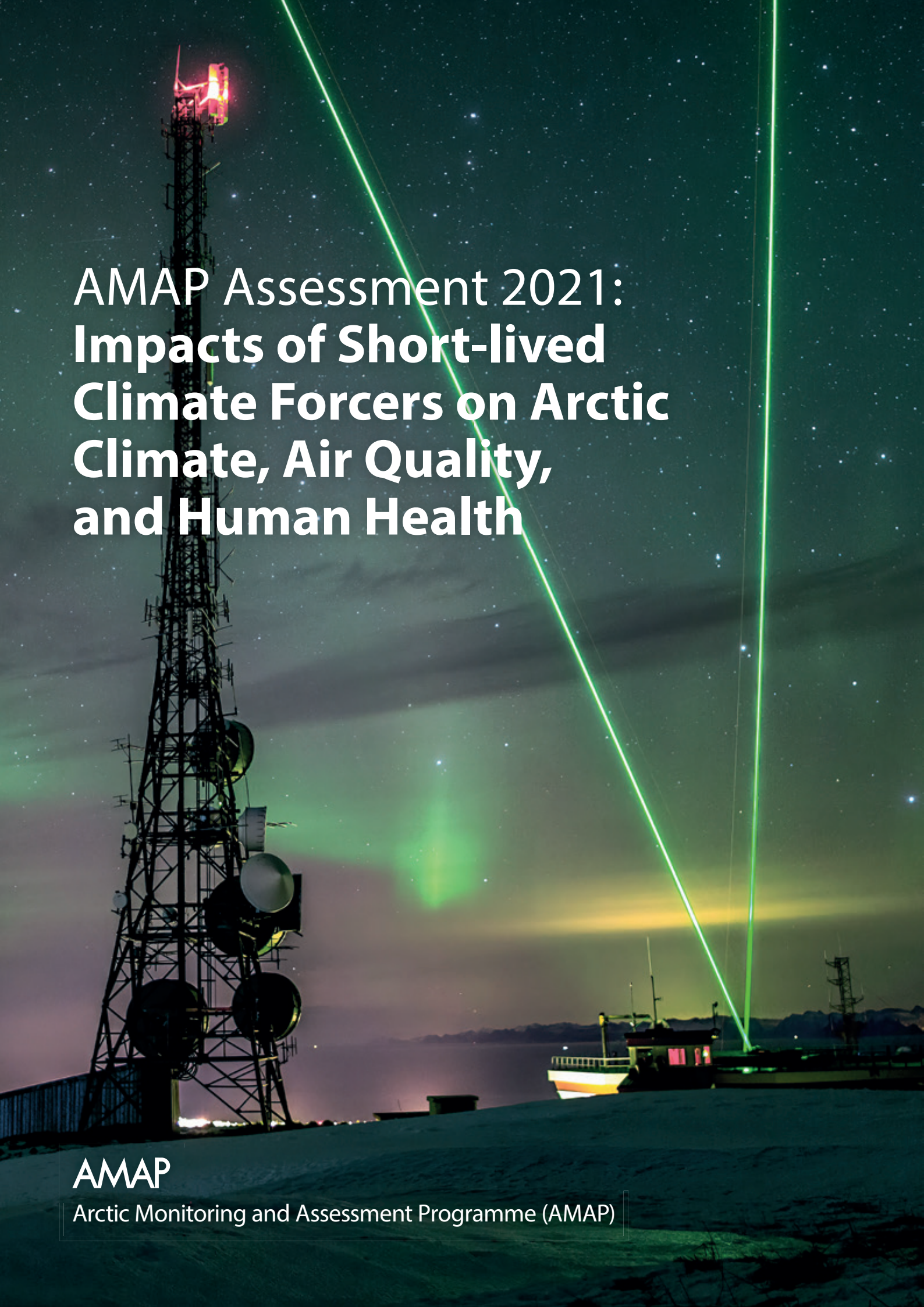

AMAP Assessment 2021: **Impacts of Short-lived Climate Forcers on Arctic Climate, Air Quality, and Human Health**

AMAP

Arctic Monitoring and Assessment Programme (AMAP)

AMAP Assessment 2021:
Impacts of Short-lived Climate Forcers on Arctic Climate, Air Quality, and Human Health

AMAP

Arctic Monitoring and Assessment Programme (AMAP)
Tromsø, 2021

AMAP Assessment 2021: Impacts of Short-lived Climate Forcers on Arctic Climate, Air Quality, and Human Health

ISBN – 978-82-7971-202-2

Citation
AMAP, 2021. AMAP Assessment 2021: Impacts of Short-lived Climate Forcers on Arctic Climate, Air Quality, and Human Health. Arctic Monitoring and Assessment Programme (AMAP), Tromsø, Norway. x + 375pp

Published by
Arctic Monitoring and Assessment Programme (AMAP), Tromsø, Norway (www.amap.no)

Ordering
This report can be ordered from the AMAP Secretariat, The Fram Centre, P.O. Box 6606 Stakkevollan, N-9296 Tromsø, Norway
This report is also published as an electronic document, available from the AMAP website at www.amap.no

Production

Production management
Simon Wilson (AMAP Secretariat)

Scientific, technical and linguistic editing
Carolyn Fry (frycaro@gmail.com), Matthew Perkins (https://matthewjperkins.com) (mattjohnperkins@gmail.com)

Layout and technical production
Burnthebook, United Kingdom (www.burnthebook.co.uk)

Design and production of computer graphics
Burnthebook, United Kingdom (www.burnthebook.co.uk)

Cover photograph
The Rayleigh/Mie/Raman lidar and the Natrium lidar on the island of Andøya in northern Norway (69.28°N, 16.01°E), which is part of the Arctic Lidar Observatory for Middle Atmosphere Research. © Leif Jonny Eilertsen/Andøya Rocket Range

Printing
Narayana Press, Gylling, DK-8300 Odder, Denmark (www.narayanapress.dk)

Acknowledgments

AMAP expresses its thanks to the following for their contributions to this assessment. Coordinating chapter leads/lead authors are indicated (**in bold**), followed by authors (*in italics*)/contributing authors/contributors listed alphabetically, by chapter. Affiliations are given at first occurence. **For details of chapter authorship see individual chapters.** We apologize for any errors or unintentional omissions.

1. Introduction
Mark Flanner (University of Michigan, USA), **Kaarle Kupiainen** (Ministry of the Environment, Finland), **Sabine Eckhardt** (Norwegian Institute for Air Research)

2. Emissions of short-lived climate forcers in an Arctic context
Kaarle Kupiainen, Zbigniew Klimont (International Institute for Applied Systems Analysis, Austria),**Ville-Veikko Paunu** (Finnish Environment Institute), *Jesper Christensen* (Aarhus University, Denmark), *Joshua Fu* (University of Tennessee, USA), *Lena Höglund-Isaksson* (International Institute for Applied Systems Analysis, Austria), *Vigdis Vestreng* (Norwegian Environment Agency)

3. Natural sources of methane within the Arctic
Frans-Jan W. Parmentier (University of Oslo, Norway/Lund University, Sweden), **Torben R. Christensen** (Aarhus University, Denmark), *Brett F. Thornton* (Stockholm University, Sweden)

4. Open biomass burning
Jessica L. McCarty (National Aeronautics and Space Administration, USA), *Juha Aalto* (Finnish Meteorological Institute/ University of Helsinki, Finland), *Sabine Eckhardt, Nikolaos Evangeliou* (Norwegian Institute for Air Research), *Justin J. Fain* (Miami University, USA), *Lin Huang* (Environment and Climate Change Canada), *Zbigniew Klimont, Kaarle Kupiainen, Ari Venäläinen* (Finnish Meteorological Institute)

5. Advances in measurement techniques and observational capacity
Stefano Decesari (National Research Council of Italy), **Kathy Law** (Sorbonne Université, UVSQ, CNRS, LATMOS, France), **Lise Lotte Sørensen** (Aarhus University, Denmark), **Abhay Devasthale** (Swedish Meteorological and Hydrological Institute), *Steve Arnold* (University of Leeds, United Kingdom), *Lori Bruhwiler* (National Oceanic and Atmospheric Administration, USA), *David Cappelletti* (University of Perugia, Italy), *Hans Christen Hansson* (Stockholm University, Sweden), *Jens Liengaard Hjorth* (Aarhus University, Denmark), *Lin Huang, Antti-Pekka Hyvärinen* (Finnish Meteorological Institute), *Makoto Koike* (University of Tokyo, Japan), *Yutaka Kondo* (National Institute of Polar Research/University of Tokyo, Japan), *Joakim Langner* (Swedish Meteorological and Hydrological Institute), *Outi Meinander* (Finnish Meteorological Institute), *Andreas Massling* (Aarhus University, Denmark), *Meri Ruppel* (University of Helsinki, Finland), *Julia Schmale* (Federal Institute of Technology, Switzerland), *Sangeeta Sharma* (Environment and Climate Change Canada), *Henrik Skov* (Aarhus University, Denmark), *Manu Anna Thomas* (Swedish Meteorological and Hydrological Institute), *Brett Thornton, Marco Zanatta* (Alfred-Wegener-Institute/ Karlsruhe Institute of Technology, Germany)

6. Observations, origins and trends of SLCFs and clouds in the Arctic
Julia Schmale, Kathy Law, Lise-Lotte Sorensen, Manu Anna Thomas, *Steve Arnold, Silvia Becagli* (University of Florence, Italy), *David Cappelletti, Stefano Decesari, Abhay Devasthale, Hans-Christen Hansson, Jens Liengaard Hjorth, Lin Huang, Antti-Pekka Hyvärinen, Makoto Koike, Yutaka Kondo, Joakim Langner, Andreas Massling, Joseph R. McConnell* (Desert Research Institute, USA), *Outi Meinander, Olga Popovicheva* (Lomonosov Moscow State University, Russia), *Meri Ruppel, Sangeeta Sharma, Henrik Skov, Rita Traversi* (University of Florence, Italy), *Peter Tunved* (Stockholm University, Sweden), *Marco Zanatta, Christian Zdanowicz* (Uppsala University, Sweden)

7. Modeling of short-lived climate forcers
Cynthia H. Whaley (Environment and Climate Change Canada), *Rashed Mahmood* (University of Montreal, Montreal, Canada), *Knut von Salzen, Sabine Eckhardt, Barbara Winter* (Environment and Climate Change Canada), *Lori Bruhwiler, Joakim Langner, Manu Anna Thomas, Abhay Devasthale,* Stephen Arnold, Stephen Beagley (Environment and Climate Change Canada), Silvia Becagli, Rong-You Chien (University of Tennessee, USA), Jesper Christensen, Sujay Manish Damani (Environment and Climate Change Canada), Xinyi Dong (University of Tennessee, USA), Nikolaos Evangeliou, Greg Faluvegi (NASA Goddard Institute for Space Studies/Columbia University, USA), Mark Flanner, Joshua Fu, Michael Gauss (Norwegian Meteorological Institute), Fabio Giardi (University of Florence, Italy), Wanmin Gong (Environment and Climate Change Canada), Jens Liengaard Hjorth, Lin Huang, Ulas Im (Aarhus University, Denmark), Yugo Kanaya (Japan Agency for Marine-Earth Science and Technology), Zbigniew Klimont, Srinath Krishnan (Centre for International Climate and Environmental Research, Norway), Thomas Kühn (Finnish Meteorological Institute), Kathy Law, Louis Marelle (Sorbonne Université, UVSQ, CNRS, LATMOS, France), Andreas Massling, Tatsuo Onishi (Sorbonne Université, UVSQ, CNRS, LATMOS, France), Naga Oshima (Japan Meteorological Agency), Yiran Peng (Tsinghua University, China), David Plummer (Environment and Climate Change Canada), Olga Popovicheva, Luca Pozzoli (European Commission Joint Research Centre, Italy), Jean-Christophe Raut (Sorbonne Université, UVSQ, CNRS, LATMOS, France), Maria Sand (Centre for International Climate and Environmental Research, Norway), Laura N. Saunders (University of

Toronto, Canada), Julia Schmale, Sangeeta Sharma, Ragnhild Skeie (Centre for International Climate and Environmental Research, Norway), Henrik Skov, Fumikazu Taketani (Japan Agency for Marine-Earth Science and Technology), Rita Traversi, Kostas Tsigaridis (NASA Goddard Institute for Space Studies/Columbia University, USA), Svetlana Tsyro (Norwegian Meteorological Institute), Steven Turnock (Met Office Hadley Centre/University of Leeds, United Kingdom), Vito Vitale (European Commission, Joint Research Centre, Italy), Kaley A. Walker (University of Toronto, Canada), Minqi Wang (Tsinghua University, China), Duncan Watson-Parris (University of Oxford, United Kingdom), Tahya Weiss-Gibbons (Environment and Climate Change Canada)

8. Simulated impacts of SLCFs on climate and air quality
Knut von Salzen (Environment and Climate Change Canada), *Stephen Arnold, Annica Ekman* (Stockholm University, Sweden), *Mark Flanner, Ulas Im, Zbigniew Klimont, Srinath Krishnan* (Centre for International Climate and Environmental Research, Norway), *Naga Oshima, Maria Sand, Steven Turnock, Cynthia Whaley,* Sabine Eckhardt, Michael Gauss, Kaarle Kupiainen, Rashed Mahmood, Dirk Olivié (Norwegian Meteorological Institute), Luca Pozzoli, Julia Schmale, Kostas Tsigaridis, Svetlana Tsyro, Rita van Dingenen (European Commission Joint Research Centre, Italy), Barbara Winter

9. Impacts of air pollution on health, ecosystems, and crops
Susan Anenberg (George Washington University, USA), **Shilpa Rao-Skirbekk** (Norwegian Institute of Public Health), *Stephen Arnold, Jørgen Brandt* (Aarhus University, Denmark), *Alfonso Diz-Lois Palomares* (Norwegian Institute of Public Health), *Joshua Fu, Camilla Geels* (Aarhus University, Denmark), *Otto Hänninen* (Finnish Institute for Health and Welfare), *Ulas Im, Joakim Langner, Kathy Law, Heli Lehtomäki* (Finnish Institute for Health and Welfare/University of Eastern Finland), *Rashed Mahmood, Maximilian Posch* (International Institute for Applied Systems Analysis, Austria), *Isabell Rumrich* (Finnish Institute for Health and Welfare/University of Eastern Finland), *Raimo O. Salonen* (Finnish Institute for Health and Welfare), *Marcus Sarofim* (Environmental Protection Agency, USA), *Julia Schmale, Svetlana Tsyro, Rita Van Dingenen, Knut von Salzen*

Contents

Preface

This assessment report presents the results of the 2021 AMAP Assessment of the Impacts of Short-lived Climate Forcers on Arctic Climate, Air Quality, and Human Health. The assessment updates information presented in earlier AMAP assessments delivered in 2015.

The Arctic Monitoring and Assessment Programme (AMAP) is a Working Group of the Arctic Council. The Arctic Council Ministers have requested AMAP to:

- produce integrated assessment reports on the status and trends of Arctic ecosystems;
- identify possible causes for the changing conditions in the Arctic;
- detect emerging problems, their possible causes, and the potential risk to Arctic ecosystems including indigenous peoples and other Arctic residents;
- recommend actions required to reduce risks to Arctic ecosystems.

This report provides the accessible scientific basis and validation for any statements and recommendations made in related derivative products, including its summary for policy-makers that was delivered to the Arctic Council Ministers at their meeting in May 2021.

The present report includes extensive background data and references to scientific literature, and details the sources for graphics reproduced in summary products. Whereas the related Summary for Policy-makers contains recommendations that focus on policy-relevant actions, the conclusions and recommendations presented in this report also cover issues of a more scientific nature, such as proposals for filling gaps in knowledge, and recommendations relevant to future monitoring and research work.

This assessment of short-lived climate forcers in the Arctic was conducted between 2017 and 2021 by an international group of experts. The expert group members and lead authors were appointed following an open nomination process coordinated by AMAP. A similar process was used to select international experts who independently reviewed this report. Information contained in this report is fully referenced and based first and foremost on the results of research and monitoring undertaken since 2015. It incorporates some new (unpublished) information from monitoring and research conducted according to well-established and documented national and international standards as well as quality assurance/ quality control protocols. Care was taken to ensure that any critical probability statements made in this assessment were based exclusively on peer-reviewed materials. Access to reliable and up-to-date information is essential for the development of science-based decision-making regarding ongoing changes in the Arctic and their global implications.

The lead authors of this assessment have confirmed that both this report and its derivative products accurately and fully reflect their scientific assessment. All AMAP assessment reports are freely available from the AMAP Secretariat and on the AMAP website (www.amap.no), and their use for educational purposes is encouraged.

AMAP would like to express its appreciation to all experts who have contributed their time, efforts and data, in particular the lead authors who coordinated the production of this report. Thanks are also due to the reviewers who contributed to the assessment peer-review process and provided valuable comments that helped to ensure the quality of the report. A list of contributors is included in the acknowledgments at the start of this report and lead authors are identified at the start of each chapter. The acknowledgments list is not comprehensive. Specifically, it does not include the many national institutes, laboratories and organizations, and their staff that have been involved in contaminants-related monitoring and research. Apologies, and no lesser thanks are given to any individuals unintentionally omitted from the list.

The support from the Arctic and non-Arctic countries implementing research and monitoring in the Arctic is vital to the success of AMAP. AMAP work is heavily based on the ongoing activities of these countries, and the countries that provide the necessary support for the experts involved in the preparation of AMAP assessments. In particular, AMAP would like to acknowledge Finland, Norway and the United States for their lead role in this assessment; AMAP would also like to thank Canada, Norway (Ministry of Foreign Affairs) and the Nordic Council of Ministers for their financial support of this assessment work.

The AMAP Working Group is pleased to present its assessment to the Arctic Council and the international science community.

Kaarle Kupiainen (Assessment co-lead, Finland)

Sabine Eckhardt (Assessment co-lead, Norway)

Mark Flanner (Assessment co-lead, USA)

Ben DeAngelo (AMAP Chair)

Rolf Rødven (AMAP Executive Secretary)

Tromsø, December 2021

1. Introduction

Authors: Mark Flanner, Kaarle Kupiainen, Sabine Eckhardt

1.1 Background

In 2015, AMAP expert groups (EGs) published comprehensive scientific reports about the impacts of black carbon and tropospheric ozone (AMAP, 2015a) and methane (AMAP, 2015b) on atmospheric chemistry and climate in the Arctic. AMAP (2015a) superseded and expanded on a prior assessment that had focused only on black carbon (AMAP, 2011). The 2015 assessments clearly acknowledged the dominant role of global anthropogenic carbon dioxide (CO_2) emissions in driving Arctic climate change, but also identified considerable potential to mitigate climate change caused by short-lived climate forcers (SLCFs). Specifically, the report estimated that a quarter of the total predicted Arctic warming of around two degrees could be avoided by 2050, if all technically feasible, global SLCF emissions-reduction measures aimed at addressing warming agents (particularly black carbon [BC] and methane [CH_4]) were implemented. Substantial uncertainties remained, however. To provide a better scientific basis for policymaking, greater effort was needed to: strengthen Earth-system monitoring; develop emissions inventories, including of present-day anthropogenic and natural emissions; and expand modeling capabilities to understand the potential Arctic impacts of adopting different mitigation options.

An additional call for robust scientific information on the impacts of climate change from SLCFs in the Arctic came from the *Arctic Council Framework for Action on Black Carbon and Methane Emissions Reductions* (Arctic Council, 2015). This called for, "continuing monitoring, research and other scientific efforts, with the inclusion of traditional and local knowledge, to improve the understanding of black carbon and methane emissions, emission inventories, Arctic climate and public health effects, and policy options". It supported, "a four-year cycle of periodic scientific reporting, including the assessment of status and trends of short-lived climate pollutants such as black carbon and methane with a focus on the impacts of anthropogenic emissions on Arctic climate and public health," and it stated that this should, "include estimates of associated costs of mitigation, as well as enhancing our state of knowledge regarding natural sources".

At the 10th Ministerial Meeting of the Arctic Council, held in Fairbanks, Alaska, in 2017, the Arctic Council agreed to: "Adopt the first Pan-Arctic report on collective progress to reduce black carbon and methane emissions by the Arctic States and numerous Observer States and its recommendations, including an aspirational collective goal, [and] acknowledge the importance of implementing those recommendations as nationally appropriate, recognizing that Arctic communities are entitled to develop in accordance with their needs and interests…". The aspirational collective goal presented in the report (EGBCM, 2017) was that: "black carbon emissions be further collectively reduced by at least 25–33 percent below 2013 levels by 2025". This goal provided impetus for further scientific analyses on emissions-reduction strategies.

In 2016, the two AMAP EGs – focusing on methane and black carbon, and tropospheric ozone – had been merged to form the new AMAP SLCF EG. The AMAP Working Group requested that the SLCF EG provide a new comprehensive assessment on the state of the science of Arctic impacts from SLCFs in advance of the 2021 Arctic Council ministerial meeting. This assessment is the response to that request.

1.2. Introduction to SLCFs

Generally, SLCFs include all agents that have the potential to directly or indirectly alter Earth's radiative energy budget, and which also have relatively short residence times in the atmosphere. Depending on how they alter the energy budget, SLCFs can either contribute to warming or cooling the planet. They encompass gaseous species – such as ozone (O_3), CH_4, and nitrogen oxides (NO_X) – and also aerosols, which can be solid or liquid and include BC, sulphate (SO_4), and mineral dust. Some SLCFs are emitted directly into the atmosphere, while others – notably O_3 and SO_4 aerosols – are formed in the atmosphere from precursor emissions. There is not a universally agreed-upon lifetime threshold for agents to be considered 'short-lived', but all agents included in the SLCF basket are shorter-lived than CO_2. CH_4, which has a lifetime of around 12 years, is only considered a SLCF by some communities. Because atmospheric CH_4 concentrations are chemically influenced by species that are clearly short-lived, however, it is reasonable to explore its impacts on climate alongside other SLCFs. Moreover, CH_4 emissions influence concentrations of O_3 and other SLCFs through chemical reactions in the atmosphere. Table 1.1 lists the SLCFs considered in this assessment, along with their key properties. A key feature that distinguishes SLCFs from long-lived substances, such as CO_2, is that atmospheric concentrations of SLCFs are governed more by their rates of emission than their cumulative emissions, so cutting emissions of SLCFs leads to rapid reductions in their atmospheric concentrations.

SLCFs influence climate through various mechanisms, as depicted in Figure 1.1. Gaseous SLCFs, such as CH_4 and O_3 amplify Earth's greenhouse effect primarily by absorbing infrared radiation emitted from Earth. Both species also absorb smaller amounts of radiation from the sun. O_3 fulfils a protective role by absorbing ultraviolet solar radiation in the stratosphere (between 10 km and 50 km from Earth's surface) and above. However, this assessment focuses primarily on O_3's warming action in the troposphere (0 km to roughly 10 km from Earth's surface). CH_4 also absorbs a small amount of solar radiation, which adds to its global warming potential (Etminan et al., 2016). In assessing the radiative and climate impacts from both of these chemical species, it is important to consider emissions of precursor species that alter the atmospheric concentrations of O_3 and CH_4. Species that can strongly affect concentrations of O_3 in the troposphere, through chemical reactions, include NO_X, carbon monoxide (CO) and volatile

Table 1.1 SLCFs considered in this assessment and their key properties

SLCF	Atmospheric lifetime	Major precursors	Spectrum of action: solar or infrared (IR)	Indirect effects	Air-quality impacts?
Gases					
Methane (CH_4)	~12 years		IR (dominant); Solar	O_3	Indirect
Tropospheric ozone (O_3)	~1 month	Nitrogen oxides (NO_x); Volatile organic compounds (VOCs); Carbon monoxide (CO)	IR (dominant); Solar	CH_4	Yes
Aerosols					
Black carbon (BC)	~1 week		Solar (dominant); IR (weak)	Snow/ice albedo; Clouds	Yes
Mineral dust	~1 week or less		Solar; IR	Snow/ice albedo; Clouds	Yes
Organic carbon (OC)	~1 week		Solar (dominant); IR (weak)	Snow/ice albedo; Clouds	Yes
Sulfate (SO_4)	~1 week	SO_2; Dimethyl sulfide (DMS)	Solar	Clouds	Yes
Volcanic ash	~1 week or less		Solar; IR	Snow/ice albedo; Clouds	Yes

organic compounds (VOCs). These species also influence CH_4, though its concentration in the atmosphere is governed more strongly by direct emissions.

Aerosols mostly affect climate by altering the amount of solar energy absorbed by Earth. BC, a product of incomplete combustion, absorbs a large fraction of interacting sunlight, thereby warming the climate system. SO_4, which is formed primarily through oxidation of sulfur dioxide (SO_2) gas, absorbs very little sunlight and cools the climate by scattering solar radiation back to space that would otherwise have been absorbed by Earth. Organic carbon (OC), which is co-emitted with BC during combustion, absorbs an intermediate proportion of sunlight and causes cooling in some environments and warming in others. Highly reflective regions, such as the Arctic, are more likely to experience warming effects from these aerosols (e.g., Myhre et al., 2013). Mineral dust and volcanic ash can also warm or cool climate depending on the content of light-absorbing minerals (especially those containing iron) in the soil or rocks from which they derive. Because some dust and volcanic ash particles are quite large, they can also absorb an appreciable amount of infrared radiation and warm Earth by enhancing its greenhouse effect (e.g., Miller and Tegen, 1998, Flanner et al., 2014). However, being larger reduces the atmospheric lifetimes of these aerosols. Typical lifetimes for SO_4, BC and OC are in the order of days to weeks, while those of larger dust and ash particles are around one to several days.

Aerosols also influence climate via indirect mechanisms. After landing on snow and ice surfaces, dark particles such as BC can hasten melting by increasing solar heating at the surface (Figure 1.1 [c]). This is a particularly important consideration when assessing the impacts of SLCFs on the Arctic climate (e.g., AMAP, 2015a). Aerosols also affect cloud properties, including their droplet size, lifetime, and vertical extent. This influences clouds' cooling and warming effects (Figure 1.1 [d], [e]). Globally, this indirect cloud forcing from aerosols is comparable to their direct forcing (Myhre et al., 2013), though the indirect effects are more uncertain and difficult to assess accurately. Moreover, impacts on climate from clouds in the Arctic are distinct from global impacts, owing to the extreme seasonality of sunlight in the Arctic, the unique characteristics of Arctic clouds (including the high frequency of mixed-phase occurrence), and rapidly evolving sea-ice distributions. In other words, complicated and unique factors govern the abundances and climate impacts of aerosols in the Arctic (e.g., Willis et al., 2018).

Moreover, it is important to consider how SLCFs originating outside of the region influence the poleward heat flux – which constitutes a substantial portion of the Arctic energy budget – and thereby the Arctic climate. AMAP (2015a), for example, found that SLCF emissions from regions such as East Asia cause perturbations to the Arctic climate primarily by altering the poleward heat flux, rather than through their direct radiative impact within the Arctic. By contrast, emissions from high-latitude regions, such as Russia and Canada, were found to primarily affect the Arctic due to their presence within (or proximity to) the region. This was because such emissions were more likely to deposit dark aerosol particles directly on to snow and ice surfaces, and to heat the lower troposphere (AMAP, 2015a; Sand et al., 2016).

Many of the SLCFs that are relevant to climate studies also adversely influence air quality and human health. These include SLCFs that constitute particulate matter (especially smaller-sized particles) and precursors of O_3. Furthermore, whereas the climate impacts of SLCFs may be positive or negative, the air-quality impacts of SLCFs are nearly universally negative. For this reason, policies to reduce emissions of SLCFs have sometimes been justified more by air-quality concerns than climate considerations.

Almost all SLCF species are emitted from both anthropogenic and natural sources, although in differing proportions. BC, for example, is emitted mostly from the anthropogenic combustion of fossil fuels and biofuels, although substantial emissions come from naturally occurring fires. Volcanic ash, on the other hand, is emitted entirely from natural processes. In cases where human activity indirectly influences emissions, it can be difficult to accurately ascribe the proportions coming from natural and anthropogenic sources. These gray areas exist for: mineral dust aerosols, which derive from both naturally occurring desert soils and those made erodible by human activity; CH_4, which

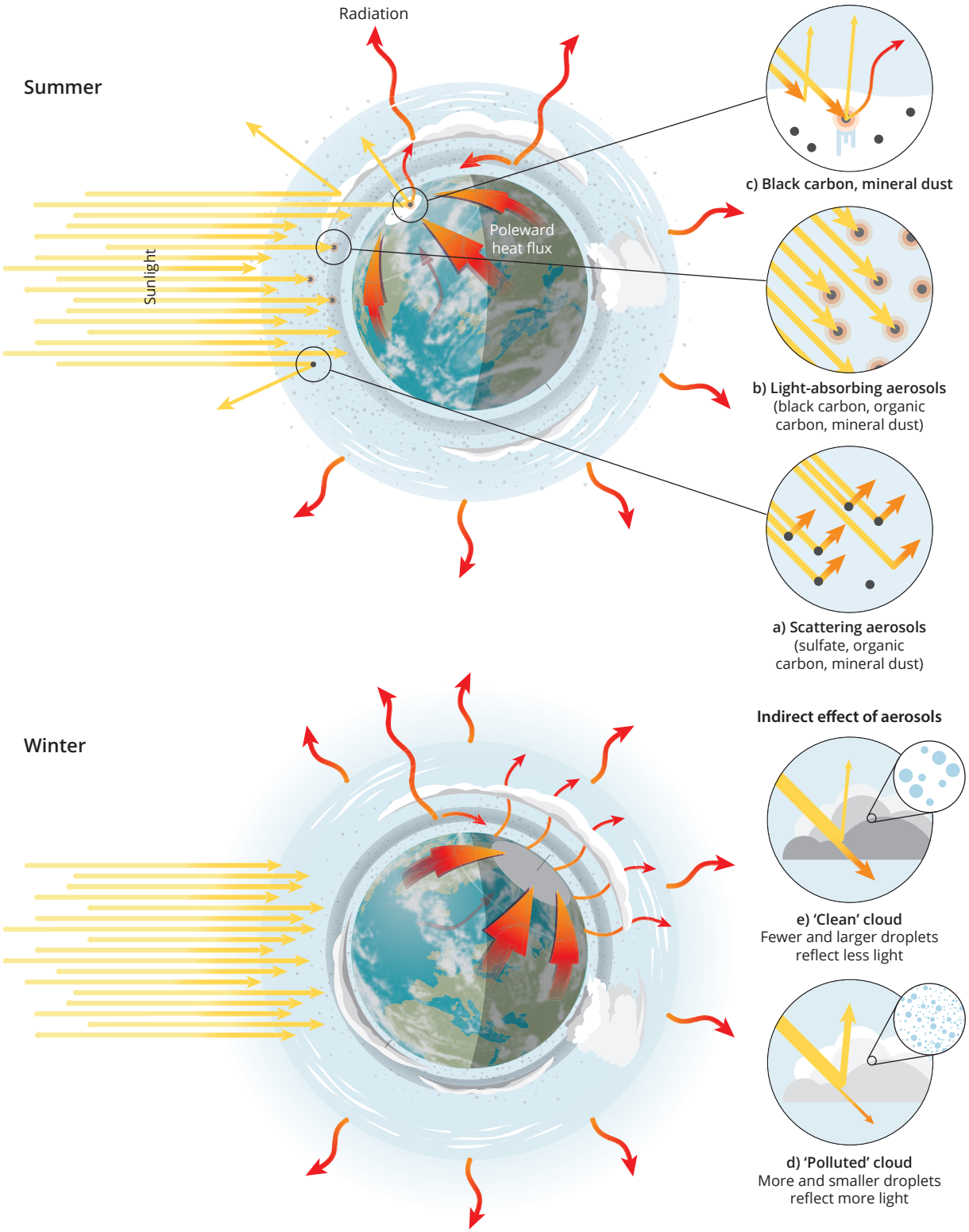

Figure 1.1 Impacts of SLCFs on the Arctic energy budget during summer (top) and winter (bottom). Greenhouse gases, and to a lesser extent aerosols, absorb infrared radiation emitted from the surface (red arrows), thereby altering the outgoing long-wave (heat) energy from Earth. Aerosols scatter (a) and absorb (b) sunlight (yellow arrows), at different layers in the atmosphere and after they are deposited on to snow and ice surfaces (c). Aerosols can also indirectly alter the way in which clouds interact with sunlight and infrared energy (d), (e). Finally, within and outside of the Arctic, SLCFs influence the poleward heat flux carried into the region by the atmosphere and oceans (thick red arrows).

is created from naturally occurring biota, but can be emitted in greater volumes where the prevalence of biota has changed due to anthropogenically induced warming or hydration of soils; and aerosol emissions from forest fires, which are increasing as fires become more intense and frequent due to human-induced climate change. How these indirect influences will change emissions in the future is even more uncertain.

Finally, the Arctic environment is changing rapidly and this also has consequences for how SLCFs affect the region. Diminishing sea ice, thawing permafrost, expanding vegetation, increasing humidity in the Arctic troposphere, and the growing prevalence of liquid clouds can affect the emissions, lifetimes and radiative forcing of SLCFs within the Arctic. The fact that these changes are occurring across the atmosphere, cryosphere and biosphere indicates the importance of adopting a multi-disciplinary, collaborative approach to studying Arctic environmental change (Thomas et al., 2019a).

1.3 Scope of this assessment

As well as considering SLCFs together, this assessment differs from AMAP (2015a; 2015b) in having a wider scope. First, the impacts of SLCFs on both climate and air quality have been included, in response to growing recognition of their importance for policymaking. The assessment also describes some impacts associated with changing SLCF emissions on ecosystems, including reduced crop productivity from surface O_3. Second, whereas AMAP (2015a) focused largely on quantifying the influence of SLCF species on absolute, equilibrium Arctic temperature, this assessment focuses more on quantifying transient Arctic climate responses due to changing emissions in the recent past and near future, as these impacts are more relevant to policymaking. The assessed impacts from each SLCF species on absolute Arctic temperature have changed between AMAP (2015a) and today due to: different baseline years being applied to emissions and assimilation of updated emissions inventories; advances in atmospheric transport models and model representations of radiative forcing components; and new regional climate sensitivity analyses. Aside from discussions of natural CH_4 and wildfire emissions, this assessment focuses more on emissions that are clearly anthropogenic, as it is within human capacity to mitigate climate change and improve air quality by changing these emissions. In assessing climate and air-quality perturbations from anthropogenic emissions, however, it is often important to know the background quantities of naturally occurring agents. To the extent possible, this assessment incorporates this knowledge, though significant gaps remain in this and other key areas.

Due to its emphasis on anthropogenic SLCFs, and the limited number of experts within the SLCF EG, the scope of this assessment is necessarily limited. As Table 1.1 outlines, the assessment includes the following SLCF species: CH_4; tropospheric O_3 and its associated precursors, including NO_X, CO and to a lesser extent VOCs; and a suite of aerosol species that includes BC, OC, SO_4 (and its precursor SO_2 emissions), and mineral dust. Volcanic ash is also discussed, though its impacts are not comprehensively assessed. Halocarbons are not treated in this assessment. Nitrate and secondary organic aerosols (SOA) are treated in some of the models applied in the assessment but impacts from these species are not rigorously explored.

The COVID-19 pandemic enormously disrupted the global economy. Reduced activity across sectors resulted in dramatically lowered emissions of many of the SLCF species studied here, with associated impacts on radiative forcing and air quality in the Arctic and elsewhere. By early 2021, emissions had rebounded substantially, following the reopening of economies. However, long-term changes in SLCF emissions will depend on the nature and degree of economic recoveries, and on any durable changes to behavior and policy that result from the pandemic. There is an enormous opportunity to learn more about atmospheric chemistry, aerosol, and transport processes from these rapid reductions in emissions, as well as the potential effectiveness of climate and air-quality mitigation strategies. But such studies take time and, as they were only at a preliminary stage when this assessment was being prepared, they are not included here.

Finally, considerable attention has been given to the possibility of exploiting the cooling effects from aerosols to geoengineer the Arctic climate via solar-radiation management (e.g., National Research Council, 2015). Although the impacts from aerosols on climate reported here can help to inform assessments of the efficacy and side effects of solar-radiation-management scenarios, this assessment does not cover geoengineering.

Beyond this chapter, the content is as follows: Chapter 2 describes historical SLCF emissions and scenarios of future anthropogenic emissions, with explanations of the key inventories applied in the modeling work conducted specifically for this assessment (Chapters 7–9). Chapters 3 and 4 review the state of understanding around natural CH_4 emissions and wildfire activity, respectively, in the context of the Arctic and drivers of temporal changes, including climate change. Chapter 5 provides an update on recent advances in measurement techniques. Chapter 6 assesses our current understanding of observations and origins of, and trends in, SLCFs in the Arctic. Chapter 7 introduces the models used in this assessment and evaluates their performance with respect to key observations. Chapter 8 describes simulated impacts of SLCFs on climate and air quality, and Chapter 9 builds on Chapter 8 to assess the impacts of changes in SLCF emissions on health and ecosystems. Finally, in planning the scope of this assessment, the AMAP SLCF EG drafted policy-relevant questions that the assessment's scientific findings could help to address. These questions were also used to communicate the scope of the assessment with stakeholders. Chapter 10 presents those questions – and answers to them – at the same time serving as a summary of the main findings and conclusions for the whole assessment. To the extent possible, the assessment focuses on new results and knowledge obtained since the AMAP 2015 assessments, and we refer readers to the reports of those earlier studies for additional background information.

2. Emissions of short-lived climate forcers in an Arctic context

Authors: Kaarle Kupiainen, Zbigniew Klimont, Ville-Veikko Paunu, Jesper Christensen, Lena Höglund-Isaksson, Joshua Fu, Vigdis Vestreng

2.1 Introduction

This chapter outlines current understanding of anthropogenic emissions of key air pollutants and short-lived climate forcers (SLCFs), within the context of the Arctic. The discussion focuses on literature and datasets that have become available since AMAP's 2015 assessment. Nonetheless, the reports published as a result of this and prior work remain important references on Arctic emission issues (AMAP, 2011 and AMAP, 2015a, 2015b).

This chapter has a distinctive regional focus, aligning it with the Arctic Council's work on mitigating black carbon (BC) and methane (CH_4) emissions. The eight Arctic Council Member states (Canada, Denmark, Finland, Iceland, Norway, Russia, Sweden, USA) and the 13 Observer countries (China, France, Germany, India, Italy, Japan, Netherlands, Poland, Singapore, South Korea, Spain, Switzerland, UK) are treated as separate groups, facilitating the evaluation of emissions in relation to the Arctic Council Member states' common vision, "… to take enhanced, ambitious, national and collective action to accelerate the decline in our overall black carbon emissions and to significantly reduce our overall methane emissions" and the aspirational collective goal that "black carbon emissions be further collectively reduced by at least 25–33 percent below 2013 levels by 2025", as set out in the *Arctic Council Framework for Action on Black Carbon and Methane Emissions Reductions* and subsequent work (Arctic Council, 2015: Arctic Council 2017). Emissions information for other regional groups and at the national level is available in Appendix 2.

A key mission of this chapter is to present emissions data used in the model evaluation (Chapter 7) and impact-modeling work (Chapters 8 and 9) undertaken for this assessment. These were produced using the Greenhouse gas–Air-pollution Interactions and Synergies (GAINS) model developed by the International Institute for Applied Systems Analysis (IIASA) (Amann et al., 2011; Klimont et al., 2017; Höglund-Isaksson et al., 2020) for the time period 1990 to 2050 (Box 2.1, overleaf). The model is hereafter referred to as IIASA-GAINS. Key background information about drivers and assumptions behind the emission scenarios used in the assessment, is presented. The IIASA-GAINS datasets developed to support this assessment provide comprehensive global emissions by country for key pollutants and relevant time periods. They include scenarios outlining possible future emissions pathways considering existing and decided policies, as well as indicating where there is scope for further emissions reductions. These emissions datasets, used further in the modeling analyses (Chapters 7, 8 and 9), include all relevant SLCF species (both warming and cooling). However, the discussion in this chapter focuses on emissions trends and mitigation opportunities for selected species, primarily BC, CH_4, and sulfur dioxide (SO_2), while Appendix 2 (Section A2.2) also provides information for other compounds. Historical emissions are examined using the most recent available datasets from scientific literature, as well as national data reported to the United Nations Economic Commission for Europe (UNECE) Convention on Long-Range Transboundary Air Pollution (CLRTAP) and the United Nations Framework Convention on Climate Change (UNFCCC), which Arctic Council Member states also report to the Expert Group on Black Carbon and Methane (EGBCM).

AMAP (2015a, 2015b) outlined the warming action of BC, ozone (O_3) and CH_4 in connection with the Arctic climate, and presented an emissions-mitigation scenario that would strongly reduce emissions of these SLCFs but which did not include dedicated control of sulfur emissions. However, air-pollution mitigation policies around the world tend to consider several objectives, and consequently focus on a larger set of pollutants – including specific policies to reduce sulfur. Sulfur emissions, which have a cooling effect on climate, have reduced significantly since the 1980s (Grennfelt et al., 2020) and policies continue to be strengthened in many countries, driven primarily by health concerns. Aligning with such approaches, this 2021 assessment analyzes emissions-mitigation scenarios that consider a broader set of air-pollution mitigation opportunities and that target a larger set of pollutants, including both climate warming and cooling species.

Section 2.2 defines the scenarios used in this assessment and outlines the key drivers behind them. Section 2.3 addresses the historical trends and expected development of emissions given current and decided air-pollution policies. Section 2.4 focuses on selected emissions sources in the Arctic, with particular attention to Arctic shipping and fossil fuel extraction. Section 2.5 discusses the mitigation scenarios, and examines potential for further emissions reductions. Comparisons with other emissions information is given in Section 2.6, and uncertainties related to emissions datasets are discussed in Section 2.7. Section 2.8 provides a summary detailing the main findings and identifying further research needs, as well as revisiting the recommendations from AMAP (2015a, 2015b). Policy Relevant Science Questions (PRSQs) related to this chapter can be found in Chapter 10.

2.2 Defining scenarios for the assessment

As with AMAP's 2015 assessment, the emissions scenarios used in this 2021 study were developed using the IIASA-GAINS model (Amann et al., 2011). They update and expand on the previously used dataset, providing historical emissions until the year 2015 and projections extending to 2050. They include all key air pollutants (SO_2, nitrous oxide [NO_X], BC, organic carbon [OC], non-methane VOCs [NMVOCs], carbon monoxide [CO], ammonia [NH_3], fine particulate matter [$PM_{2.5}$]) and greenhouse gases (carbon dioxide [CO_2], CH_4) at a global scale. An overview and a more detailed description of assumptions made and of the scenario characteristics has been published in Höglund-Isaksson et al. (2020) for CH_4.

Box 2.1 The IIASA-GAINS model

IIASA-GAINS is widely used to identify cost-effective policy interventions aimed at reducing the impacts of air pollution on health, while maximizing co-benefits with other policy priorities. In recent years, the GAINS team has strengthened links with several integrated assessment modeling (IAM) groups, and applied IIASA-GAINS to develop fine-scale global projections of air-pollutant emissions and assess the potential impacts on health arising from such emissions. The model outputs have also been used to parameterize air-pollution storylines for the Shared Socioeconomic Pathways (SSPs), used by the Intergovernmental Panel on Climate Change (IPCC) in the Sixth Assessment Report (see for example Rao et al., 2017; IPCC, 2021). The model has underpinned the development of global and regional scenarios examining the future evolution, potential for mitigation, and impacts of BC, including dedicated work for AMAP (2015a). As a scientific tool for integrated policy assessment, IIASA-GAINS describes the air-pollution pathways from atmospheric driving forces to environmental impacts. It brings together information on: economic, energy-related and agricultural developments; emissions-control measures and costs; and atmospheric dispersion and chemistry (Figure 2.1). IIASA-GAINS quantifies the emissions and impacts of nine air pollutants (SO_2, NO_X, coarse particulate matter [PM_{10}] and $PM_{2.5}$, BC, OC, CO, NH_3, volatile organic compounds [VOCs]) and six greenhouse gases (CO_2, CH_4, nitrogen dioxide [N_2O], hydrofluorocarbons [HFCs], perfluorocarbons [PFCs], sulfur hexafluoride [SF_6]) on human health, crop losses, acid deposition, and long-term radiative forcing from a multi-pollutant and multi-effect perspective. IIASA-GAINS explores the co-control of some 2000 specific measures on multiple air-pollutant and greenhouse-gas emissions, identifies trade-offs and win-win measures, and assesses their impacts on ambient air quality, population exposure, health, vegetation, and various climate metrics. IIASA-GAINS has a global coverage and is currently implemented for 180 countries/world regions. The GAINS model and databases are accessible over the Internet.

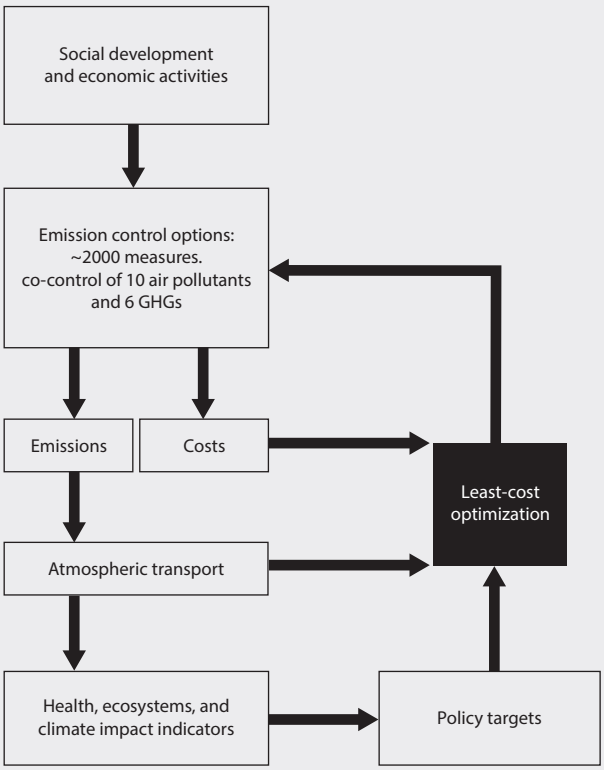

Figure 2.1 The IIASA-GAINS model explores linkages between human activities, emissions-control measures, atmospheric pollutants and impacts on health, climate and ecosystems.

Box 2.2 provides information about the key sources of activity data and projections used in the assessment, as well as on the evolution and comparison of fossil fuel CO_2 emissions to SSPs developed for the sixth cycle of the IPCC report (see, for example, IPCC, 2021; Riahi et al., 2017). The three underlying activity scenarios implemented in IIASA-GAINS for the 2021 assessment provide a wide range of possible future developments – from the case of fossil-fuel use remaining high to a scenario that assumes the rapid decarbonization necessary to constrain additional warming to below 2°C, globally, compared to the pre-industrial period.

For this assessment, the IIASA-GAINS model was updated to include statistical data for 2015; assumptions on new policies and their implementation were reviewed; spatial gridding of emissions was improved; and several new scenarios were developed.

One particular aspect worth highlighting is improvements in the spatial distribution of emissions. The spatial proxies for many sources have been revised since the 2015 assessment, including those for the residential sector, transportation, shipping, power plants, and oil and gas operations (including flaring) (Böttcher et al., 2021). In all cases, new data was used – either providing a higher resolution than previously available or a more up-to-date representation of the source location. Two elements that appear visibly different in the updated ECLIPSE v6b dataset are the distribution of residential (heating) emissions and the flaring of associated gas. Figure 2.3 shows not only higher granularity of emissions of BC in many regions but also identifies more emissions in sparsely populated areas at high latitudes, which had been identified as a challenge in the past (e.g., AMAP, 2015a; Winiger et al., 2019). The new dataset has implications for the distribution of all species, not only BC, and should facilitate improved modeling of pollutant concentrations and impacts.

The emissions scenarios developed for this assessment, combining energy and emissions-mitigation policies, can be categorized into three types: (i) baseline, (ii) mitigation, and (iii) failure. The scenario identifiers include explicit reference to the emissions policy (first three characters) and energy policy (the last three characters). This is the case except for when the New Policy Scenario (NPS) is used, which is considered the baseline energy scenario in this work; in this case only emissions policies are indicated in the identifier. A selection of the scenarios described in the following text and summarized in Table 2.1 were used in the model evaluations (presented in Chapter 7), and in the modeling (discussed in Chapters 8 and 9).

Box 2.2 Key assumptions behind the 2021 assessment's anthropogenic emissions scenarios

The energy data for the research came from International Energy Agency (IEA) statistics (Data ref. 2.1), while the projections were drawn from the 2018 World Energy Outlook (IEA, 2018) and then implemented in the IIASA-GAINS model framework. The macro-economic assumptions in IEA (2018) include a 25% growth in global population and a 90% increase in global gross domestic product (GDP) by 2050. The energy scenarios applied were as follows:

- New Policy Scenario (NPS). This scenario assumes implementation of national energy programs and revised (in 2018) commitments of the Nationally Determined Contributions (NDCs) of the Paris Climate Agreement. Its CO_2 emissions appear comparable to SSP2–4.5 evolution (Figure 2.2), and it is used in the IIASA-GAINS baseline current legislation (CLE) scenario.

- Current Policy Scenario (CPS). In this scenario, NDCs are not included, resulting in higher fossil-fuel use and a CO_2 emissions trajectory that resembles SSP4–6.0 (Figure 2.2).

- Sustainable Development Scenario (SDS). The CO_2 trajectory for this scenario is similar to the SSP1–2.6 decarbonization scenario (Figure 2.2), due to a rapid shift away from fossil fuels, greater access to clean energy for cooking, and the achievement of several other United Nations (UN) Sustainable Development Goals (SDGs).

Agricultural projections were derived from the Food and Agriculture Organization (FAO) of the UN (FAO, 2012). Figure 2.2 compares the CO_2 emission trajectories of the above scenarios (derived from the IIASA-GAINS ECLIPSE v6b dataset [Data ref. 2.2]) with the key SSP cases, and shows CO_2 emissions for the aggregate of Arctic Council Member states.

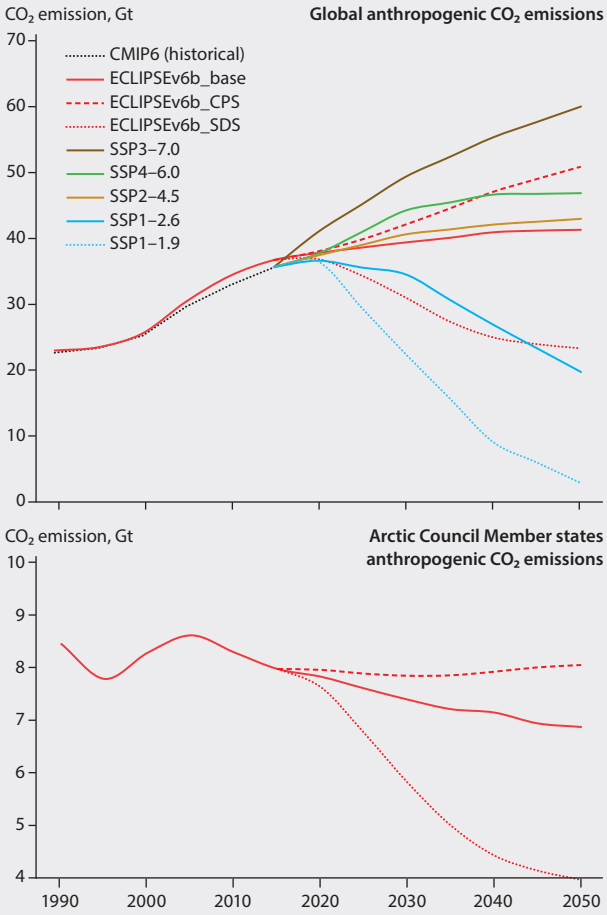

Figure 2.2 Top: How global anthropogenic CO_2 emissions under IIASA-GAINS ECLIPSE v6b scenarios compare to the SSP scenarios. Bottom: Combined CO_2 emissions for Arctic Council Member states, as depicted by IIASA-GAINS ECLIPSE v6b scenarios. Gt = gigatonnes

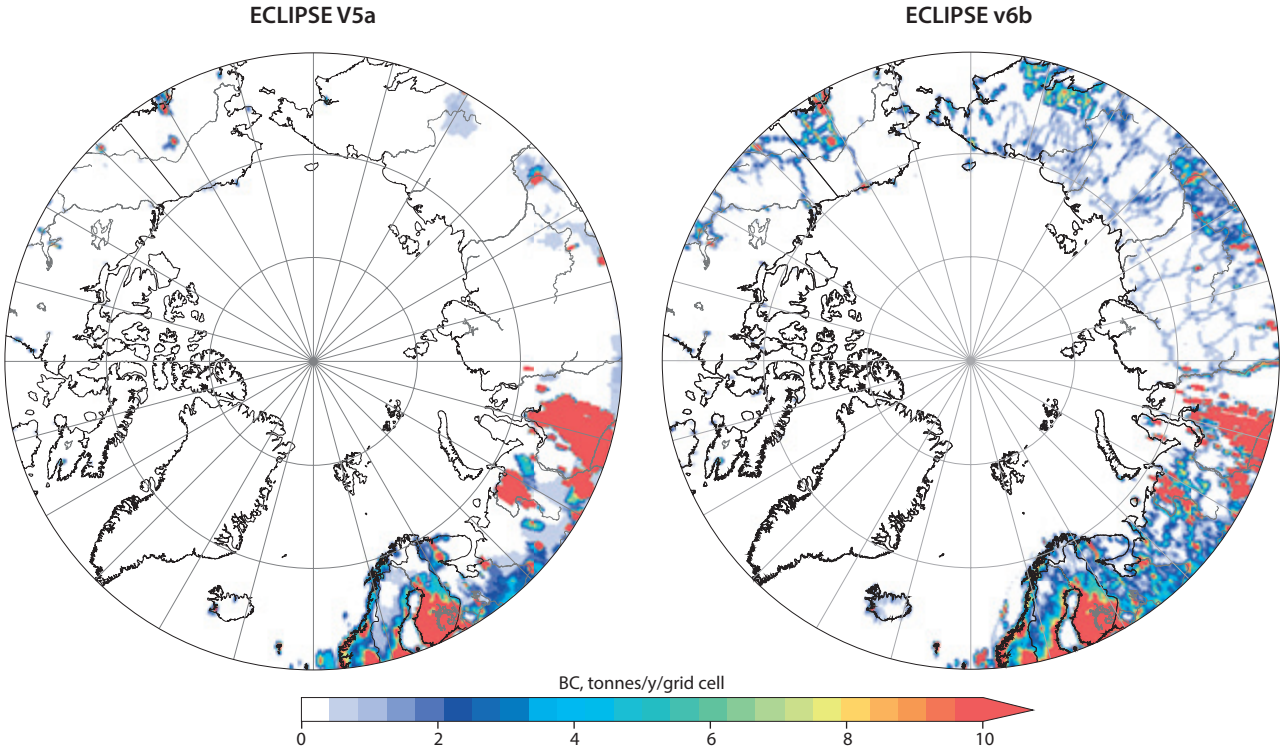

Figure 2.3 Spatial distribution of total BC emissions for 2015, north of 60°N latitude, in the ECLIPSE v5a dataset (left, [Data ref. 2.3] used in AMAP (2015a) and its successor ECLIPSE v6b (right).

Table 2.1 Studied scenarios and their identifiers. The CLE is from 1990 to 2050, with others spanning 2025 to 2050. ESM = Earth system model; CTM = chemical transport model

Scenario type	Scenario identifier	Energy scenario	Emission control policy	Model category (Chapter 8)
Baseline	CLE	NPS	CLE	ESM; CTM; Emulators
Failure scenarios	NFC	NPS	NFC	
	NFC_CPS	CPS	NFC	
Mitigation scenarios	MFR	NPS	MFR	ESM; CTM; Emulators
	CFM	NPS	Warming SLCFs	ESM; Emulators
	MFR_SDS	SDS	MFR	

- **Baseline** (CLE): Assumes NPS energy projection and efficient implementation of current air-pollution legislation (committed to before 2018).
- **Mitigation**: These scenarios focus on additional (beyond baseline) reductions in emissions. Two types of mitigation scenarios were developed:
    - Maximum technically feasible reduction (MFR) case. This is where implementation of the best available and technically feasible emissions-mitigation technologies is included for all pollutants defined in the IIASA-GAINS model and CH_4. The introduction of measures is not constrained by their costs (or current political obstacles) but there are limitations on how quickly certain measures achieve high market penetration; no premature scrapping of equipment is assumed. Under this case, two scenarios were developed: (i) MFR for baseline (NPS) activity projections (MFR); and (ii) MFR for the sustainable development case, in which the energy projections follow the SDS scenario (MFR_SDS).
    - Climate forcing mitigation (CFM) case. Here, the focus is on further reducing emissions of warming SLCFs, applying technologies that result in lower net climate forcing after abatement. Principally, this assumes MFR-type mitigation for CH_4, and ambitious reduction of BC emissions. It accounts for changes in co-emitted species, in other words, technologies that achieve strong BC reduction will also reduce cooling species (OC, SO_2, and NO_X), as well as CO and NMVOC, while NH_3 remains at the level of CLE. This type of scenario was developed to facilitate comparison with the mitigation simulations performed in the AMAP 2015 assessment, as well as to explore futures in which less-pronounced reduction of cooling species occurs while emissions of warming SLCFs are minimized. A single CFM scenario was developed using the NPS energy landscape.
- **Failure**: No further control (NFC) case. This scenario type demonstrates the importance of current policies, and assumes a failure in implementation of recent policies by freezing legislation at pre-2015 level. Two scenarios were developed under this case: (i) NFC for baseline (NPS) energy projections (NFC); and (ii) NFC for the higher fossil fuel (CPS) case outlined in Box 2.2, which assumes that national energy efficiency and structural goals resulting from the Paris Climate Agreement, as well as recent air-pollution laws, are not efficiently implemented (NFC_CPS).

The following text provides analysis of trends in emissions for Arctic Council Member states and Observer countries, as well as the potential available for mitigation.

2.3 Trends in SLCF emissions of Arctic Council Member states and Observer countries

Figure 2.4 shows global emissions of SLCFs over the period 2010 to 2050, as per the baseline scenario (CLE) of the IIASA-GAINS model. Global anthropogenic BC emissions are estimated at 66 teragrams (Tg[1]) for 2010 and 5.9 Tg for 2020. Following the CLE scenario, the emissions decline to 5.4 Tg in 2030, and further to 5.3 Tg in 2050. The most important source sectors globally throughout the period are residential combustion (contributing about half) and surface transportation (roughly a quarter).

Global SO_2 emissions are estimated to be 89 Tg in 2010 but, under the CLE scenario, decline significantly to 55 Tg by 2020 and to 48 Tg by 2030, after which they slightly increase if no further policies beyond those committed to by 2018 are introduced. The reductions are mainly due to developments in the energy and industrial sectors, and in international shipping. The former include the introduction of more stringent emissions standards, reduced coal use, and access to clean energy in the residential sector of Observer countries (particularly China and India), while the latter results from a new International Maritime Organization (IMO) rule limiting sulfur in fuel oil from 2020 onwards.

Global anthropogenic CH_4 emissions are estimated at 340 Tg in 2015 and 350 Tg in 2020. Following the baseline CLE scenario, the emissions increase to 380 Tg in 2030 and further to 440 Tg in 2050. The largest sources in 2015 are: agriculture (42% of total emissions); oil and gas, primarily through extraction and distribution (18%); waste (18%); and energy production, including coal mining (16%). These are projected to still be the most important sources in 2050. According to Höglund-Isaksson et al. (2020), the global emissions trend is primarily driven by the anticipated increase in solid waste and wastewater generation – as populations grow and countries become wealthier – as well as by greater extraction of natural gas, as gas and renewables replace coal (translating to a levelling-off of future emissions from coal mining). In addition, about a fifth of the increase in future emissions is attributed to livestock production.

[1] 1 Tg = 1000 kt

For 2015, the Arctic Council Member states are estimated to account for 8%, 13% and 20% of the global anthropogenic emissions of BC, SO_2 and CH_4, respectively (Figure 2.4). Under the baseline CLE scenario, the corresponding values for 2050 are 6%, 12% and 17%. Respective values for the Arctic Council Observer countries are much larger. These nations contribute 40%, 40%, and 30% in 2015 for BC, SO_2, and CH_4, respectively, with the corresponding baseline values for 2050 being 23%, 30%, and 29%. Jointly, Arctic Council Member states and Observer countries currently contribute about half of the global anthropogenic emissions of these pollutants. Provided the baseline development takes place until 2050, the collective share would decrease in the case of BC (to 29%) and SO_2 (43%), but would remain at around 50% for CH_4. International shipping is only a minor source of BC and CH_4 globally. For 2010, the share of SO_2 emissions from shipping is approximately 10%, but this is estimated to decline significantly by 2020 following regulation on the sulfur content of maritime fuels. Steady reductions in emissions of CO and NO_X, of around 20% and 10%, respectively, are also expected in the coming decades. These are driven by a decline in solid fuel use for cooking (important for CO, VOC) and tighter emissions standards for vehicles (CO, NO_X, VOC) and, in several countries, also for power plants (NO_X). International shipping is important with regard to NO_X, accounting for about 20% of total emissions. In spite of improving access to clean energy and lower transport emissions, anthropogenic VOC remains roughly constant under the baseline CLE scenario, as the increasing contribution of VOCs from the chemical industry and solvent use counteracts other trends.

Open biomass burning (forest fires, savannah burning) are discussed in detail in Chapter 4; Figure 2.4 illustrates the importance of this source for considered species at a global level, with about a quarter and two-thirds of total BC and OC, respectively, originating from fires.

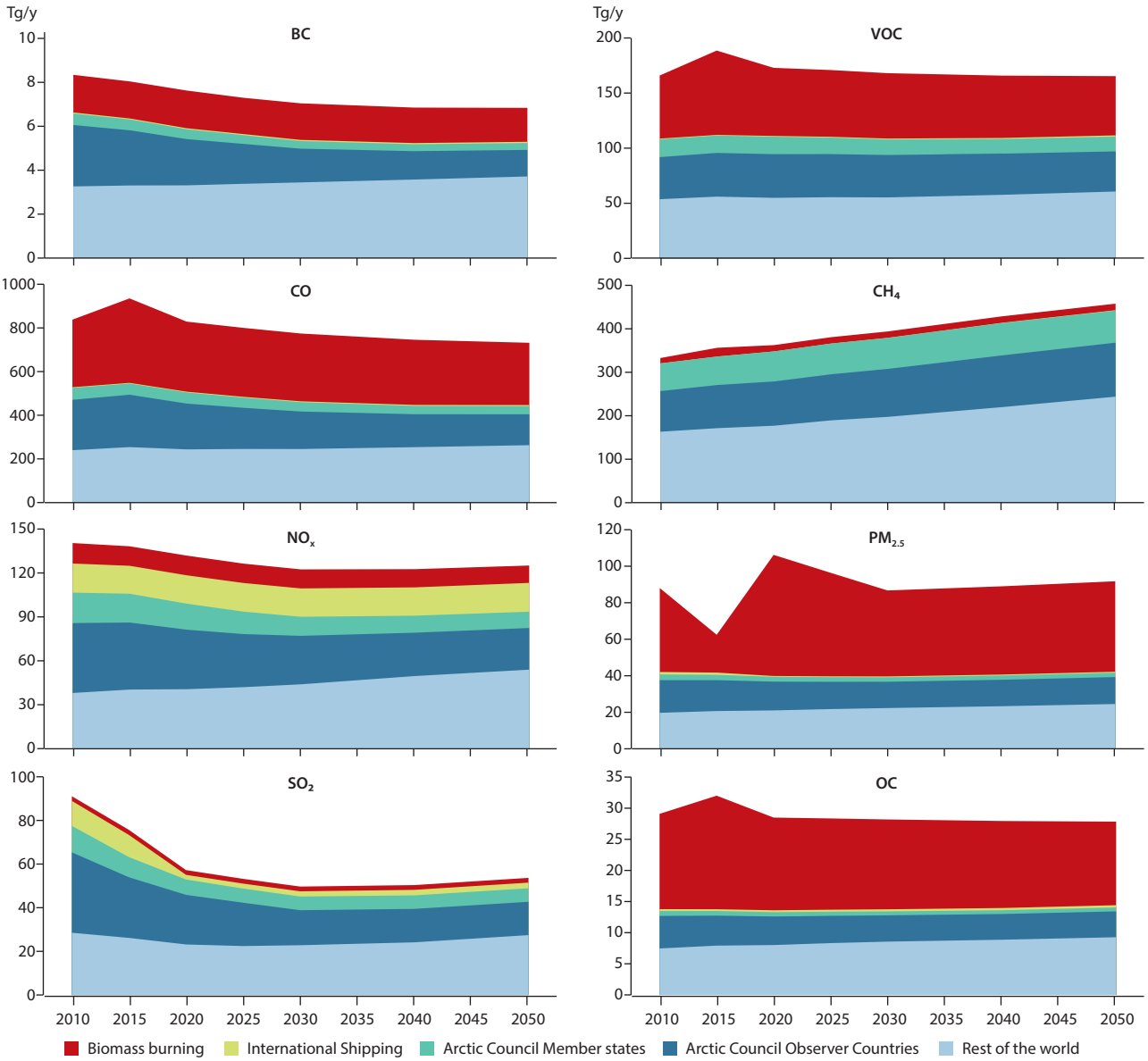

Figure 2.4 Emissions of SLCFs, other air pollutants and O_3 precursors under the baseline scenario (CLE), as estimated by the IIASA-GAINS model, and open biomass burning (including forest and savannah fires) from van Marle et al. (2017). For CH_4 and VOCs, biogenic sources are not included (natural releases of CH_4 are discussed in detail in Chapter 3). Emissions from international shipping and open biomass burning are not allocated to any country but are shown separately as global totals.

Figure 2.5 shows levels of anthropogenic BC, SO_2 and CH_4 emissions until 2050 in the Arctic Council Member states and Observer countries, as estimated under various scenarios by the IIASA-GAINS model (presented emissions do not include those from international shipping and forest fires). All analyzed emissions scenarios indicate a declining trend for BC emissions for these two groups, in contrast to the 'rest of the world' where emissions of BC are expected to increase under the baseline (CLE) scenario (Figure 2.4).

Failure to implement post-2015 legislation in the Arctic Council Member countries (NFC, NFC_CPS), would move the BC emissions trajectory further from meeting the 2025 goal, and would lead to approximately 15% and 11–19% higher emissions of BC and SO_2, respectively, towards the end of the period, compared with the baseline (CLE). CH_4 levels are relatively similar in the baseline and the failure scenarios (for both Arctic Council Member states and Observer countries), since there has been little new legislation introduced recently; most of the observed difference is for the NFC_CPS case, where it is due to the exclusion of Nationally Determined Contributions (NDCs) included in the Paris Agreement (see Section 2.2 for full scenario description). For Observer countries, the BC emissions are about 7% and 14% higher for the 2030–2050 period in the NFC scenario, respectively, and 15% and 26% higher, respectively, in the NFC_CPS scenario. The most significant difference is seen for SO_2 emissions, which are almost double the baseline values (under the NFC scenario) or more than double (in the NFC_CPS scenario) by 2030–2050, and follow an increasing trend rather than following the reducing trend of the baseline. These results highlight the importance of timely and effective enforcing of existing policies and legislation.

Figure 2.5 also includes an ECLIPSE v5a_base baseline scenario that represents the emissions trajectory driven by IEA projections from the Energy Technology Perspectives (ETP) project (IEA, 2012) and air-pollutant legislation that was current when the AMAP 2015 assessment was in progress. Comparison with the current baseline scenario (CLE), indicates the effect of subsequent legislative changes and the adoption of new policies. Emissions of BC from the Arctic Council Member states appear similar in both baseline scenarios. However, the estimates for past years are higher in the latest (CLE) estimates due mostly to an increase in emission factors for gas flaring – drawing on recent measurements (Conrad and Johnson, 2017) – resulting in higher estimates for Russia (Dong et al., 2019; Böttcher et al., 2021). For the Arctic Council Observer countries, the updated BC emissions (CLE) are lower by approximately a third compared to the AMAP 2015 baseline (V5a) but both exhibit a similar declining future trend. The major reason for

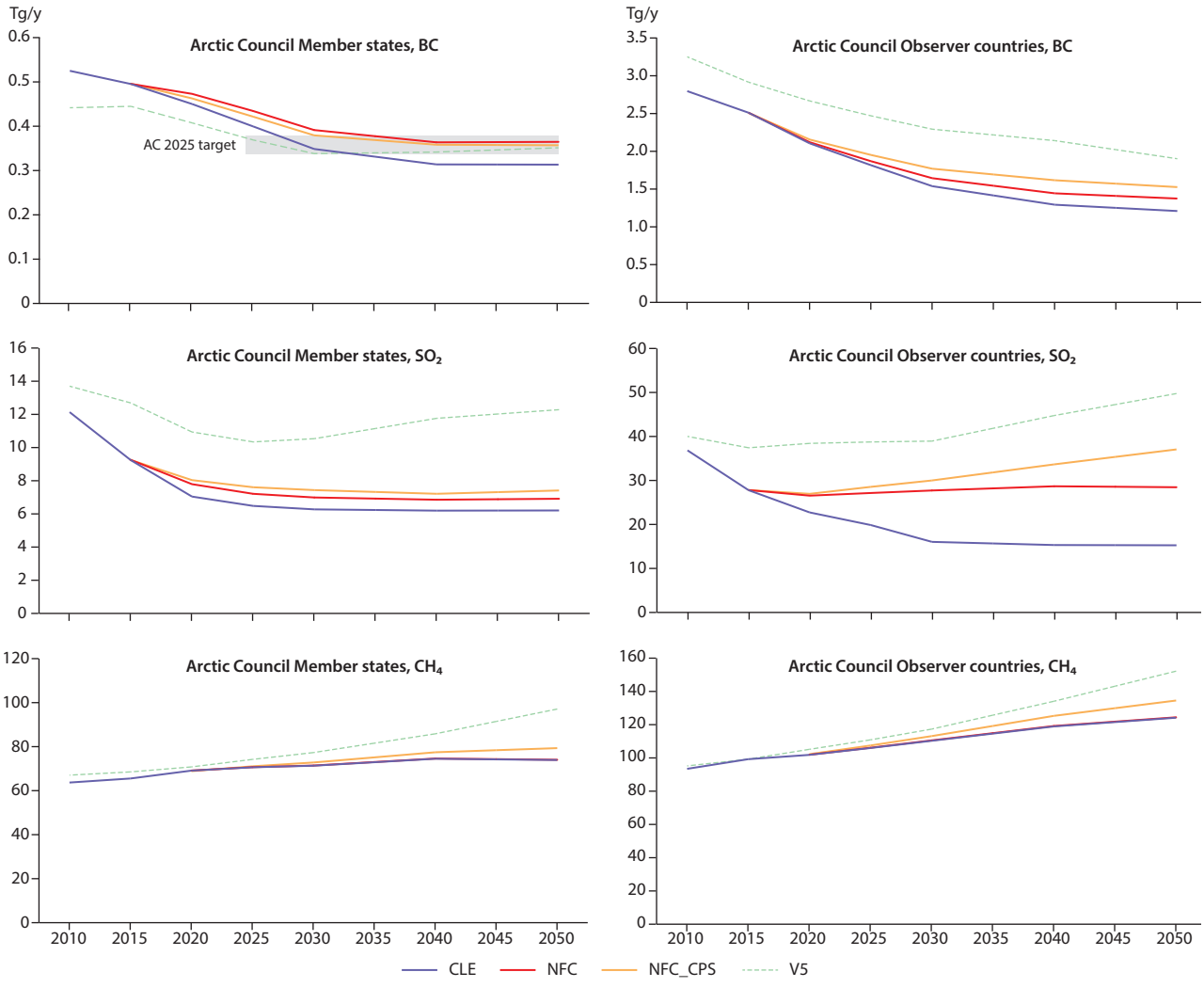

Figure 2.5 BC, SO_2 and CH_4 emissions under the baseline CLE and failure (NFC and NFC_CPS) scenarios developed for this assessment, as well as the baseline scenario (v5a) used in the AMAP 2015 assessment. A time series for these emissions dating back to 1990 is presented in Appendix 2 (Section A2.4), along with national data (Section A2.1).

the lower overall estimate is lower coal use for China (current data originates from IEA (2018) while v5a used the estimates of the Tsinghua University (Beijing) drawing on the provincial Chinese statistics). Meanwhile, the future decline is driven by a combination of more stringent vehicle standards, and policies to reduce coal and fuelwood use for heating and cooking in China and India.

The future trajectory of SO_2 emissions in the updated baseline (CLE) shows a strong decline for both Arctic Council Member states and Observer countries, unlike in the previous baseline (v5a). Determining factors for this difference include the introduction and effective enforcement of reduction measures in power plants and industry in China and the USA, and, for the coming decades, also in India. At the same time, the new data and energy projections indicate reduced coal use in the power sector (in several countries), and increased capacity for gas and renewable energy; this trend is expected to continue. CH_4 emissions increase for the 2010–2050 period in both the Arctic Council Member states and the Observer countries. However, the rise towards the end of the period is lower under the newer baseline (CLE) than with the 2015 baseline.

Figure 2.6 shows sector shares for 2015 emissions of BC, SO_2 and CH_4 in the Arctic Council Member states and the Observer countries. The 'surface transport' sector dominates BC emissions in Arctic Council Member states (47%), followed by 'residential combustion' for heating (21%), 'flaring' from 'oil and gas' extraction (14%), 'agricultural waste burning' (9%), and combustion in 'industry' (6%). In Arctic Council Observer countries, 'residential combustion' comprises 56% of BC emissions, followed by 'surface transport' (21%), combustion in 'industry' (12%) and 'agricultural waste burning', as well as household 'waste' (5% each). SO_2 emissions are dominated by combustion in 'industry' and 'energy' production, with 95% and 83% in the Arctic Council Member states and Observer countries, respectively. The remaining share originates from the 'residential combustion' sector. Key sources of CH_4 include 'agriculture', 'waste', 'coal mining (energy)', and 'oil and gas (extraction and distribution)', with a minimal contribution from energy use in 'residential' and 'industry' sectors. In Arctic Council Member states, most of the CH_4 is emitted from fossil-fuel production, storage and distribution; intended venting and unintended leakage during extraction and distribution of 'oil and gas' account for 52%, with the release of CH_4 in

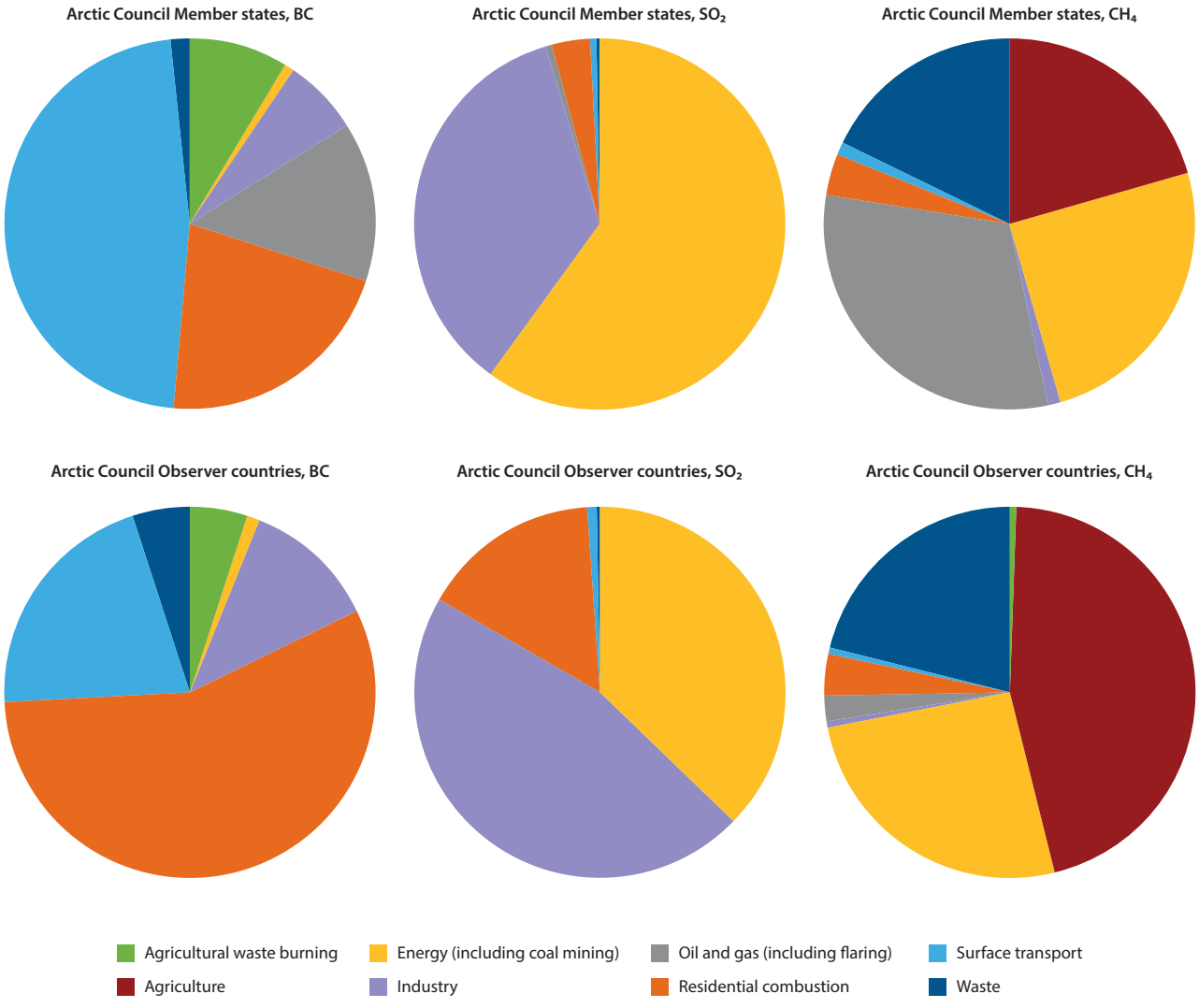

Figure 2.6 Share of BC, SO_2 and CH_4 emissions in 2015 by major sectors under the CLE scenario in the Arctic Council Member states and Observer countries.

ventilation air during 'coal mining' contributing 9%. Other significant sources of CH_4 are from biological processes, for example the anaerobic decomposition of organic materials in 'waste' and wastewater management (18%) or from livestock metabolism and manure management within 'agriculture' (20%). Incomplete combustion processes, in particular from 'agricultural waste burning' and burning of biomass in the 'residential' sector, contribute minor (1%) CH_4 emissions. In the Arctic Council Observer countries, 'agriculture' accounts for 45% of total anthropogenic emissions followed by 'coal mining' (25%), 'waste and wastewater' (21%), 'combustion' sources (4%) and the 'oil and gas' sector (5%).

Figure 2.7 presents relative emissions changes by 2030 and 2050, compared to the 2015 emissions under the CLE scenario. In the Arctic Council Member states, the surface-transport sector delivers a large share of the 30% reduction in BC emissions under the baseline scenario (CLE) between

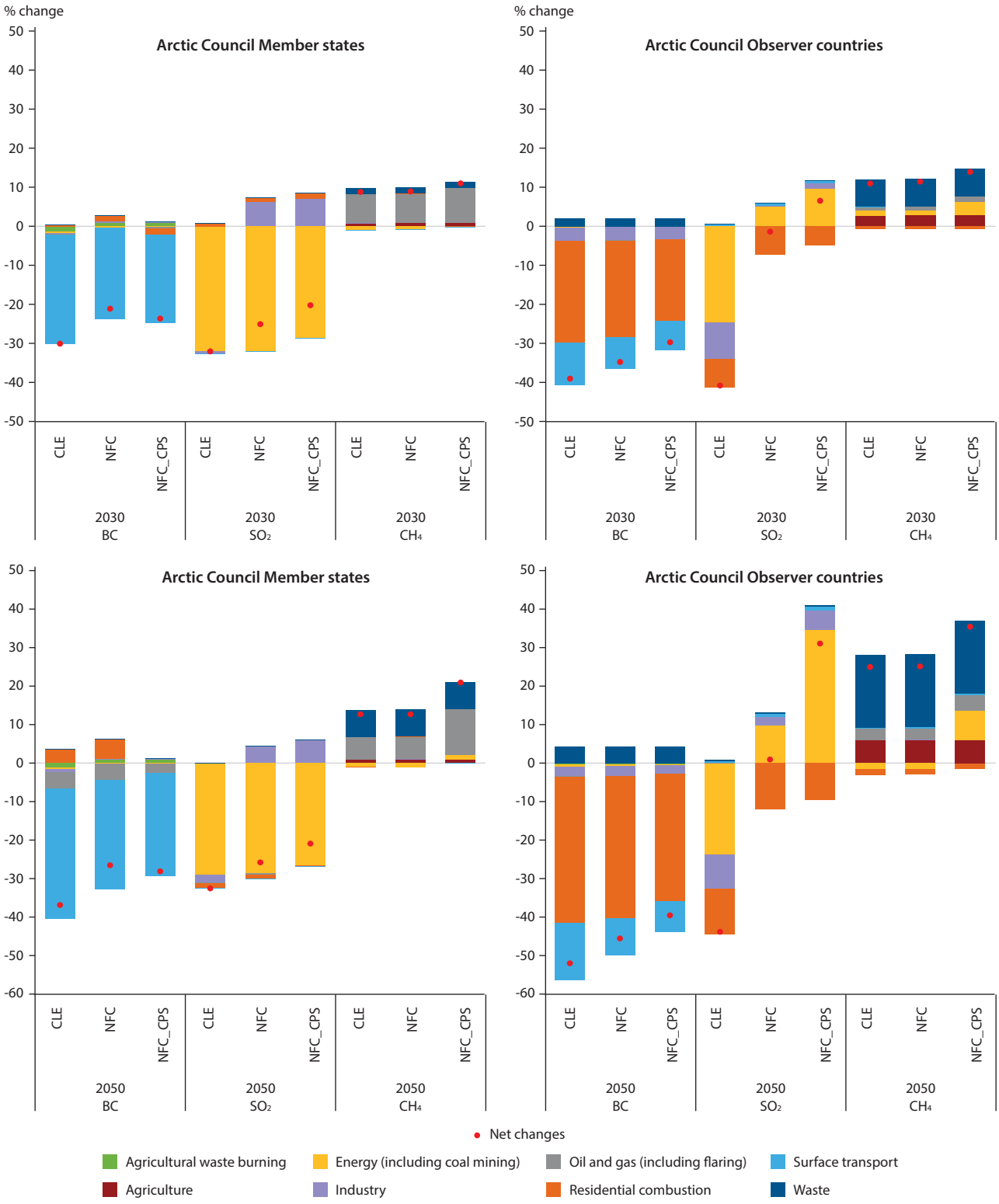

Figure 2.7 Relative change in emissions from 2015 to 2030 and 2050 under the baseline scenarios. All changes are in relation to the 2015 emissions of the CLE scenario.

2015 and 2030. Surface transport, flaring (in the oil and gas sector) and agricultural waste burning are responsible for the further reductions to BC emissions of about 10% expected between 2030 and 2050 (counteracted, however, by a few percent increase in residential combustion emissions). SO_2 emissions decline in the baseline scenario until 2030 by approximately 50% and 30%, compared with 2010 and 2015 emissions, respectively (Figures 2.4 and 2.6). This is due to reductions in the energy sector (Figure 2.7). The post-2015 policy failure scenarios (NFC and NFC_CPS) would particularly influence emissions from the industrial sector, offsetting 7%–8% or so of the reductions in the energy (power plants) sector. From 2030 to 2050, SO_2 emissions remain fairly constant – or even slightly increase – in the baseline scenario, owing to lack of further legislation. CH_4 emissions in Arctic Council Member states increase under the baseline scenario by almost 10% by 2030, and a further 5%–10% between 2030 and 2050. This rise is, however, lower than the 40% increase projected for 2015–2050 under the AMAP 2015 assessment's baseline scenario (AMAP 2015b). The oil and gas sector is responsible for the exhibited increase by 2030, supplemented by the waste sector to 2050.

BC emissions in the Arctic Council Observer countries are anticipated to decline by 39% from 2015 to 2050 in the CLE baseline developed for this report, which is greater than the 20% reduction estimated in the 2015 assessment. This is due to further clean-air policies that have been introduced for the residential and surface-transport sectors, and to some extent also in industry, since 2015. The difference between the 2015 assessment baseline, the current baseline (CLE) and the failure scenarios is very large for SO_2. This is due to a number of post-2015 mitigation policies introduced within the residential, energy and industry sectors, and to re-evaluation of the enforcement of previous policies in the energy and industry sectors, particularly in the Asian Observer countries. In total, these add up to 40% reductions in emissions by 2030 compared to 2015. Failure to implement these policies would lead to stagnation of, or even an increase in, emissions by 2030, and an even greater rise by 2050. Compared with the situation in 2015, CH_4 emissions in the Arctic Council Observer countries are anticipated to increase by 10%–15% and by 25%–35% by 2030 and 2050, respectively, mostly due to development in the agriculture and waste sectors. These are, however, lower than the increases estimated in AMAP's 2015 assessment (20% and 55% in 2030 and 2050, respectively).

2.4 Arctic emissions sources

Sources close to, or within, the Arctic have a higher relative impact on the region compared to those farther south (AMAP, 2015a). Additionally, local sources can lead to high air-pollution concentrations in remote communities and elevated exposure levels for the inhabitants (Aliabadi et al., 2015; Schmale et al., 2018a). Key reasons include: (i) energy production for electricity and heating is decentralized (diesel generator sets, old boilers) and often uses outdated and polluting equipment; and (ii) often poor waste-management practices, including open burning of waste, result in emissions of toxic air pollutants. Local air pollution in the Arctic can often be overlooked because some of the characteristics and sources may not be recognized in national-level emissions inventories, and the contributing emissions sources are not well identified and quantified in terms of locations or amounts (i.e. Aliabadi et al., 2015; Schmale et al., 2018a; see also the discussion in Section 2.7).

Industrial operations, such as fossil-fuel extraction and mining, and the traffic supplying these sites and remote communities, are additional sources of air pollution in the Arctic. The changing ice conditions in Arctic waters have led to an increase in the transit traffic of ships, as the Northern Sea Route and the Northwest Passage have become more accessible. Boreal forest fires emit significant amounts of air pollutants during summer (Schmale et al., 2018a; see also Chapter 4). The following pages provide an update of two major High-Arctic emissions sources: Arctic shipping and fossil-fuel extraction. Quantitative emissions inventories from Arctic communities are not available, so issues related to them are not discussed here. Additionally, Chapter 9 includes a section discussing how Arctic emissions sources contribute to the health impacts of air pollution.

2.4.1 Arctic shipping

The AMAP 2015 assessment included a review of emissions inventories of air pollutants from shipping (AMAP, 2015a). Since then, new work has become available that has utilized continuous data on the position and speed of ships logged on Automatic Identification Systems (AIS) and includes improved coverage of the Arctic Ocean (Johansson et al., 2017a). AIS data is retrieved from AIS satellite receivers and, in some cases, from terrestrial base stations, and can include other information about the ship's characteristics, including its type and engine operation. Combining AIS data with ship engine power functions and emission factors has allowed for more realistic estimation of emissions from individual ships, and facilitated the creation of 'bottom-up' emissions inventories. Additionally, updated emission-factor data taking into account recent regulations on ship emissions have also become available.

Regulatory changes since 2015 have taken place under the auspices of the IMO, a United Nations agency responsible for the safety and security of shipping, and for the prevention of marine and atmospheric pollution by ships. The IMO has agreed to introduce a 0.5% sulfur-content cap for marine fuels starting in 2020. The regulation will reduce total PM and SO_2 emissions from marine engines, but the impact these changes will have on BC emissions is less clear (ICCT, 2017). The IMO has provided a definition of BC for use by the community and has recommended the measurement methods to be used in connection with marine-engine emissions. Additionally, a review of available control technologies has been conducted. However, for the time being, the IMO is not regulating BC emissions from ships (ICCT, 2017). In the case of smaller marine engines, national legislation on PM exists – for example, in the European Union, the USA and Canada – which is expected to indirectly influence BC emissions (ICCT, 2017).

This section discusses those Arctic shipping emissions inventories that have become available since 2015. The IMO

regulation has decreased emissions of sulfur in comparison with the estimates given in AMAP (2015a), but BC emissions estimates remain similar. Shipping activities in the area may increase in the future due to more traffic within the Arctic, as well as from traffic being diverted from more southerly lanes. Compared with the emissions situation for 2015–2016, the SO_2 and NO_X emissions are estimated to decrease, whereas BC emissions remain unchanged. These general statements are based on an assessment of recent inventories, which are discussed in more detail below.

Johansson et al. (2017a) provided a global shipping emissions inventory based on AIS 2015 data and the Ship Traffic Emission Assessment Model (STEAM3). In 2017, the International Council of Clean Transport (ICCT) published a global emissions inventory of BC for shipping based on combined terrestrial- and satellite-based AIS and ship registry data. The inventory by DCE (2017), which uses 2012–2016 AIS data for shipping north of 60°N latitude, updates the Winther et al. (2014) work that was used in the AMAP 2015 assessment (AMAP, 2015a).

The global ECLIPSE v6b emissions dataset (Data ref. 2.2), used as input for the impact estimates in this assessment, also includes emissions from shipping based on 2015 shipping activities from Johansson et al. (2017a). The different fuel types (heavy fuel oil [HFO], light fuel oil [LFO], liquified natural gas [LNG]) have separate emission factors, and since the shares of the fuels change over time and also by region (being different across Emission Control Areas (ECAs)), the implied emission factors are also regionally specific and change over time.

In terms of current shipping activity in the Arctic sea areas, the DCE (2017) inventory indicated that north of 60°N latitude, for the time period 2012–2016, annual fuel use increased from approximately 5 megatonnes (Mt) of fuel in 2012 to 6.5 Mt in 2015, but fell back to 5.5 Mt in 2016. The Arctic Council's Protection of the Arctic Marine Environment (PAME) Working Group's Arctic Ship Traffic Data (ASTD) System provides additional insight, indicating that the sailed distance within the Polar Code Area (a subdomain of the area north of 60°N latitude) increased by 75% from 6.1 million nautical miles in 2013 to 10.7 million nautical miles in 2019 (PAME, 2020). According to PAME (2020), fishing vessels dominate, accounting for 45% of the activity. It is important to note that the trends in the DCE (2017) and PAME (2020) studies are not comparable, due to the different geographical scope; significantly more shipping activities take place outside of the Polar Code Area than within it. AMAP (2015a) reported that only 10%–15% of ship traffic north of 60°N took place inside the Polar Code Area.

Translating the ship activities into emissions, Figure 2.8 presents SO_2, NO_X and BC emissions from shipping activities north of 60°N, as estimated by the available emissions inventories. The ECLIPSE v6b inventory has the highest SO_2 emissions at 85 Mt/y, which are about 50% higher than those detailed in DCE (2017) and 85% higher than those presented by Johansson et al. (2017a). Overall, as a consequence of lower sulfur content in the fuel, the SO_2 emissions are lower than those estimated in the 2015 assessment (AMAP, 2015a). DCE (2017) uses a higher fuel-consumption estimate, which is why the NO_X emissions (360 Mt/y), are about 80%–100% higher than in ECLIPSE v6b and Johansson et al. (2017a), but relatively similar to the estimate in AMAP (2015a).

ECLIPSE v6b, DCE (2017) and ICCT (2017) estimated emissions of BC from Arctic shipping to be between 0.3 and 0.5 tonnes per year (t/y) whereas the Johansson et al. (2017a) inventory was 1.3 t/y, 2.6–4 times higher than the other three. The relatively large difference between Johansson et al. (2017a) and the rest is explained by the choice of emission factor. At 0.47 grams per kilogram (g/kg) fuel, the emission factor is relatively high in Johansson et al. (2017a), as compared with the ICCT (2017) global mean figure of 0.25 g/kg fuel; the ECLIPSE v6b figure of 0.11 g/kg fuel for shipping outside the ECAs and <0.05 g/kg fuel within the ECAs; and that in DCE (2017) of 0.10 g/kg fuel (mean). The BC emission estimates by ECLIPSE v6b (Data ref. 2.2), DCE (2017) and ICCT (2017) are also lower than the AMAP 2015 assessment (AMAP, 2015a), which assumed a constant 0.35 g/kg fuel emission factor based on work by Corbett et al. (2010).

For estimating future Arctic shipping activities and emissions, DCE (2017) used the same growth scenarios for different ship types as AMAP (2015a). In the baseline scenario, total

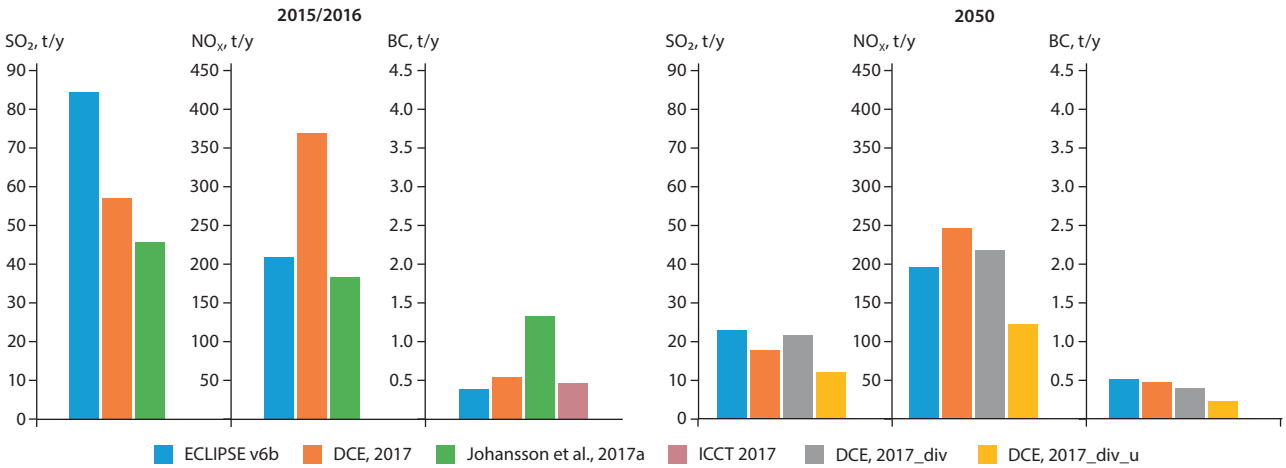

Figure 2.8 Left: emissions of SO_2, NO_X and BC in tonnes per year (t/y) from shipping north of 60°N latitude for the year 2015/2016 from the ECLIPSE v6b, DCE (2017), Johansson et al. (2017a) and ICCT (2017) emissions inventories. Right: baseline and diversion (from southerly shipping lanes) scenarios from the ECLIPSE v6b dataset and DCE (2017) for the year 2050. Please note the pollutant-specific scaling as indicated on the x-axis.

fuel use by shipping in the Arctic is estimated to increase by 14% between 2016 and 2050 (without additional fuel consumption from the diversion of ships from traditional southern routes into Arctic waters). ECLIPSE v6b, on the other hand, assumes that future shipping activities in the Arctic increase by 60% between 2015–2050, reflecting the general trend in international shipping presented in the World Energy Outlook 2018 projections (IEA, 2018). An additional aspect is that, with changing ice conditions in the future, more shipping activity and emissions may divert from the traditional southern routes into Arctic waters (see also AMAP, 2015a). DCE (2017) includes scenarios with additional shipping activities due to the diversion of ships from more southerly areas to the Arctic routes, whereas ECLIPSE v6b does not.

Figure 2.8 also presents SO_2, NO_X and BC baseline emissions scenarios for shipping North of 60°N latitude in 2050. Compared with the 2015/2016 situation, the SO_2 and NO_X emissions are estimated to decrease by 60%–75% and 10%–30%, respectively, whereas the BC emissions are estimated to remain at a similar level. In addition, the diversion of ships from more southerly sea lanes (DCE, 2017_div and DCE, 2017_div_u on the right-hand graph) could increase the emissions by up to 50%–100% depending on the pollutant and the diversion scenario (DCE, 2017).

Compared with the baseline scenario presented in AMAP (2015a), the emissions from more recent studies are approximately 80%, 50%–75% and 80%–90% lower for SO_2, NO_X and BC, respectively, due to updated emission factors taking into account the expected changes in ships and fuel sulfur content. The emissions levels estimated by ECLIPSE v6b and DCE (2017) are relatively similar for all studied pollutants.

2.4.2 Fossil fuel extraction and distribution

Extraction of crude oil and natural gas is a source of BC and CH_4. BC is emitted from the flaring of associated gas during oil extraction. CH_4 emissions originate primarily from the venting of associated gas during oil extraction, as well as due to unintended leakages along the production process chain from wellhead to upgrading and storage (Höglund-Isaksson, 2017). CH_4 can also be released during coal mining and from abandoned coal mines.

According to Stohl et al. (2013), a large share of BC in the high latitudes originates from the oil and gas sector, mostly from Russia. While the amount of flared gas has declined in recent years (WB/GGFR, 2020), the ECLIPSE V6b emissions dataset confirms that flaring remains the largest source of anthropogenic BC emissions in the high latitudes, with major sources located in Russia, the North Sea and the USA (Figure 2.9). The spatial pattern used for emissions data relies on the work of Böttcher et al. (2021); that work also shows that new fields have been developed (with associated flares) further north (Figure 2.10). Even though flaring activity has declined, and it is expected it will be reduced further, data on emissions from Conrad and Johnson (2017) indicate that actual emission factors might be higher than previously used, stressing the importance of developing policies to reduce routine flaring.

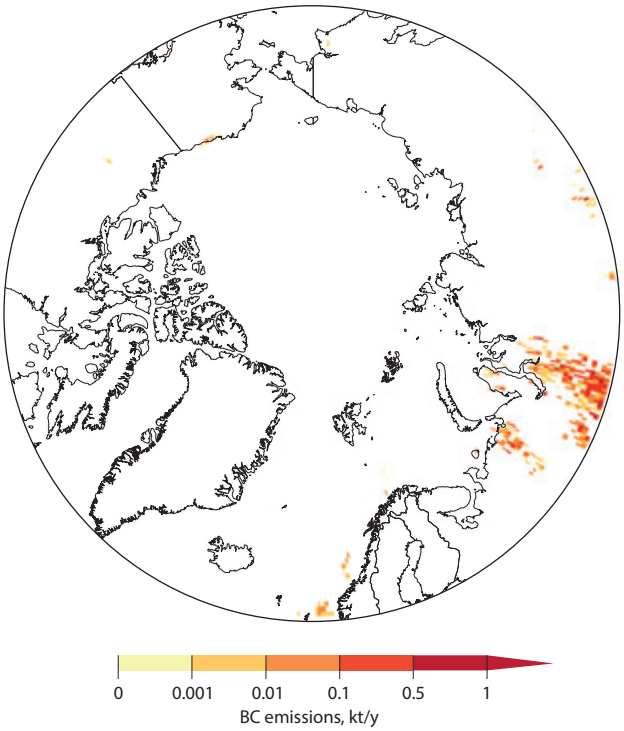

Figure 2.9 Black carbon emissions in kilotons per year (kt/y) from gas flaring in 2015, according to the ECLIPSE V6b emissions dataset.

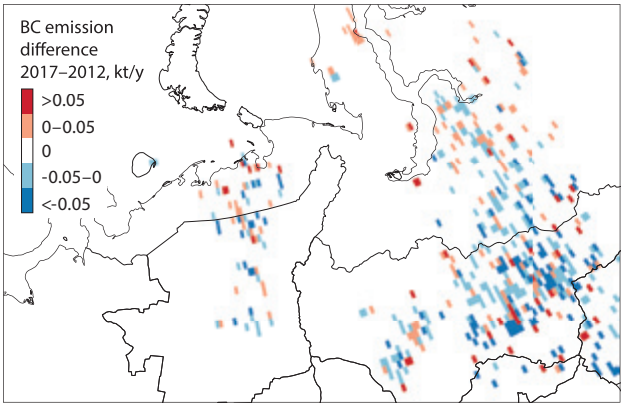

Figure 2.10 Change in black carbon emissions in kilotons per year (kt/y) from gas flaring in northern Russia between 2017 and 2012, based on Visible Infrared Imaging Radiometer Suite (VIIRS) satellite data (Böttcher et al., 2021).

2.5 Policy scenarios for further mitigation of emissions

The current legislation (CLE) scenarios presented in Section 2.2 assume no further abatement of emissions than that prescribed in already adopted legislation. The IIASA-GAINS model enables identification of a portfolio of technical measures for reducing emissions – such as improved stoves, catalysts, filters and so on – but ignores the potential for further mitigation through policies addressing energy efficiency, fuel switching, premature equipment scrapping, or even behavioral changes. The latter can be modeled, however, using externally developed scenarios where such structural changes are implemented. The mitigation scenarios discussed in this section assume maximum feasible implementation of existing best available abatement technologies, for different types of future activity

scenarios. Some of them include structural changes compared to the baseline development (e.g, the Sustainable Development Scenario [SDS] – see also Section 2.2 for a brief characterization of scenarios). However, the scenarios discussed do not consider any potential effects from future technological development (Höglund-Isaksson et al., 2020; Amann et al., 2013).

The AMAP 2015 assessment (AMAP, 2015a, 2015b) analyzed a mitigation scenario that focused primarily on the role and importance of reducing emissions of the warming SLCFs BC and CH_4 in connection with the Arctic climate. It presented an emissions-mitigation scenario that strongly reduced emissions of BC and CH_4, but did not include further dedicated control of sulfur emissions. In contrast, this 2021 assessment analyzes emissions-mitigation scenarios incorporating a broader set of air pollution-mitigation opportunities, and targeting a larger set of pollutants that include both climate warming and cooling species (Figure 2.11). This is justified by the fact that emissions-reduction policies for sulfur continue to be strengthened around the world, driven primarily by air-quality concerns.

Significant potential for further reducing BC emissions using existing technologies has been identified (MFR, CFM, MFR_SDS scenarios). In the Arctic Council Member states, adoption of best available mitigation technologies for road and non-road transport (such as the European emissions standard Euro 6/VI and enforcement of policies to remove high-emitting vehicles from the road), residential heating and cooking (advanced solid fuel boilers and stoves) and in the oil and gas sectors (reduced flaring, particularly in Russia) would approximately halve BC emissions by 2030 (Figure 2.11 and 2.12). A further 10% reduction could be achieved with measures in industry and effective enforcement of bans addressing open burning of agricultural residues. Assuming immediate implementation,

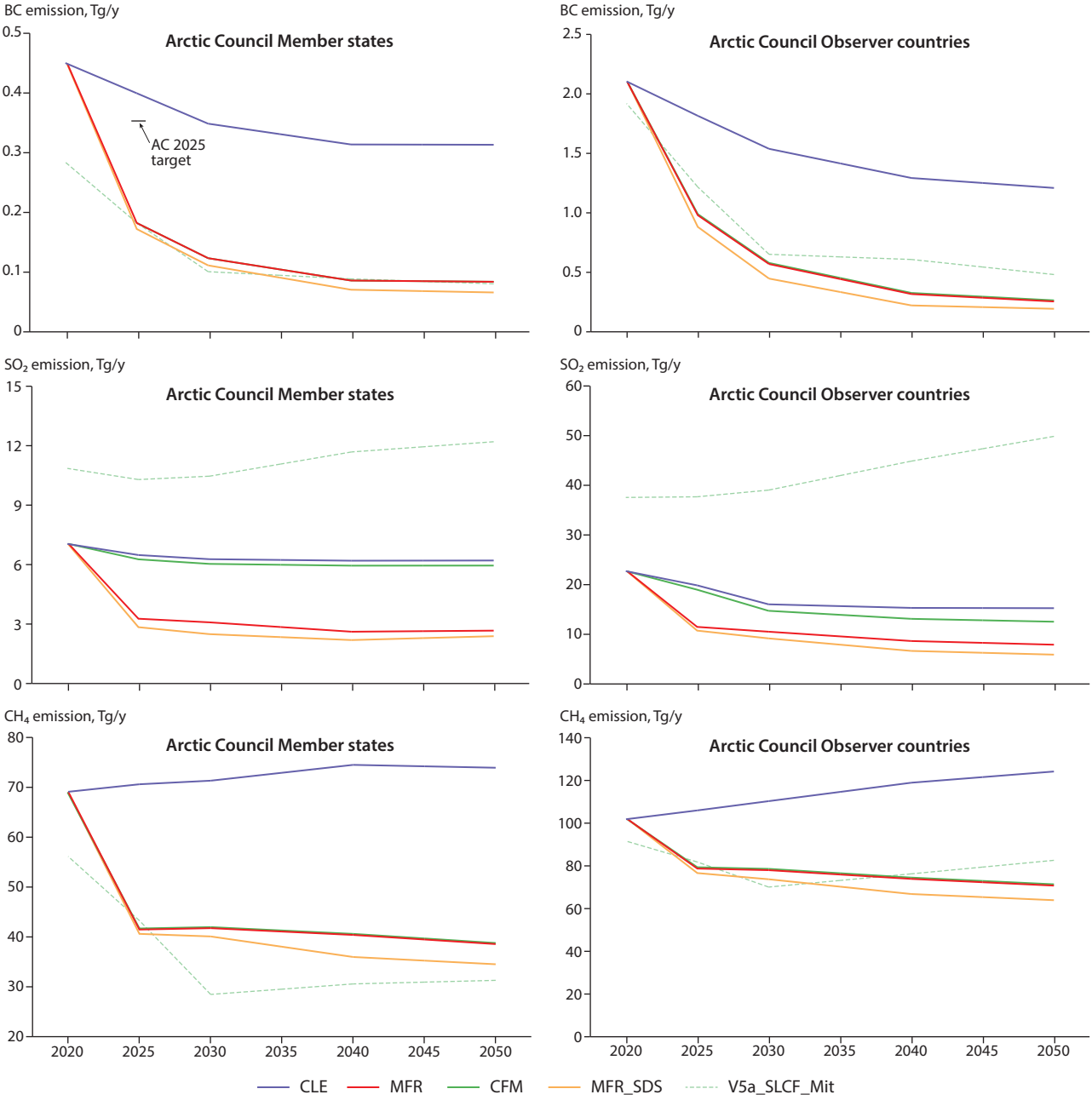

Figure 2.11 BC, SO_2 and CH_4 emissions under the current legislation baseline (CLE) scenario, mitigation scenarios (MFR, MFR_SDS, CFM), and the climate forcing scenario used in the AMAP 2015 assessment (v5a_SLCF_Mit).

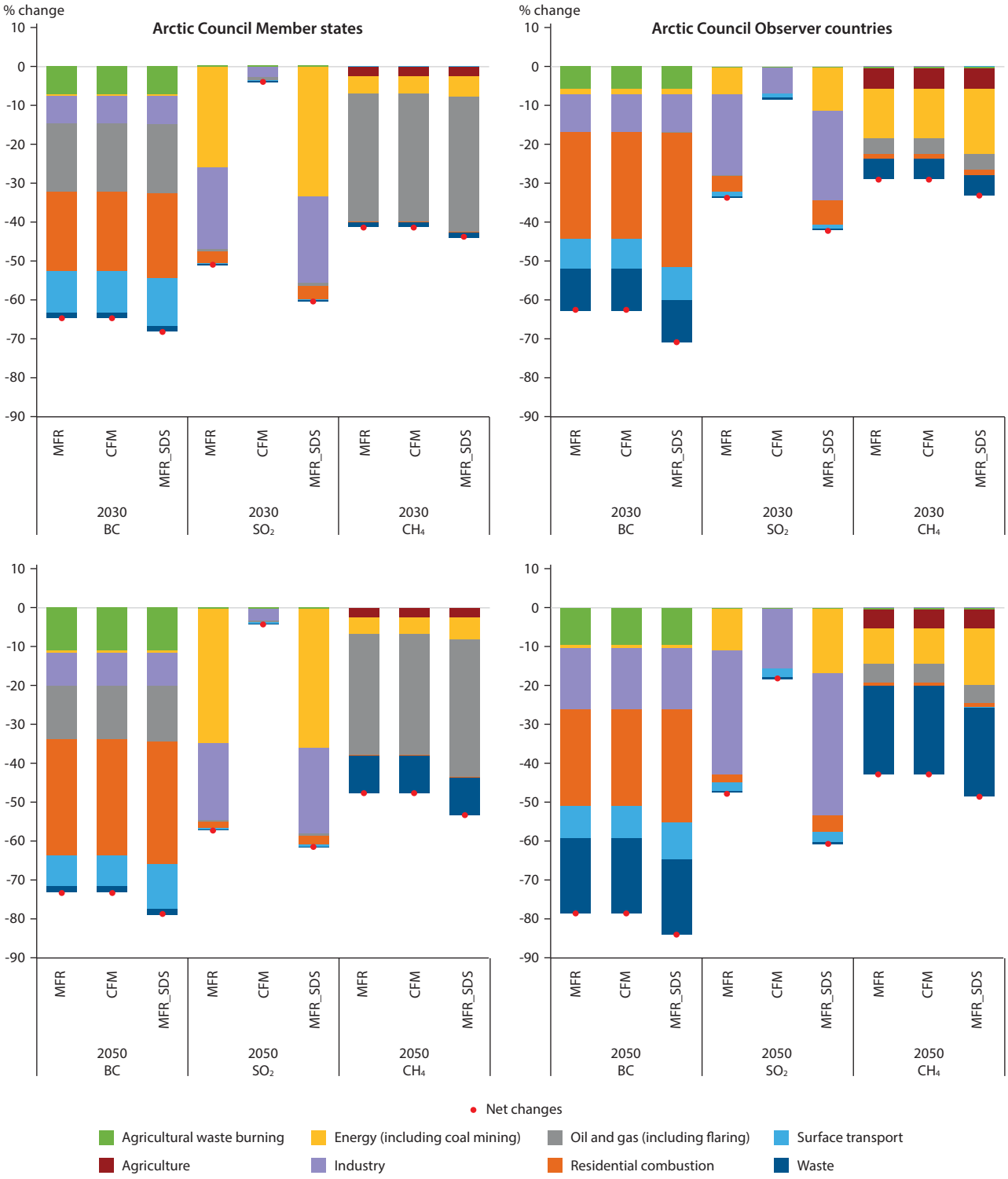

Figure 2.12 Relative changes in emissions by 2030 and 2050 under the mitigation scenarios (MFR, MFR_SDS, CFM), compared to the CLE scenario.

and strict and effective enforcement of policies, almost full potential could be achieved by 2030, and only 10% additional reduction potential would remain between 2030 and 2050. In the Arctic Council Observer countries, depending on the scenario, a reduction in BC emissions of 60%–70%, could be achieved by 2030 by implementing measures targeting practically the same sectors as in the Arctic Council member states (Figure 2.11 and 2.12). Outstanding potential to reduce emissions by a further 20% would remain for the period 2030–2050, which could be achieved by widening access to clean energy for cooking and improving municipal solid-waste management to the extent that virtually no open burning of waste remains.

The global anthropogenic CH_4 emissions in the IIASA-GAINS model are discussed in more detail by Höglund-Isaksson et al. (2020). The maximum technically feasible reduction (MFR) of global anthropogenic CH_4 in 2050 is estimated at 54% below baseline CLE emissions for that year. This corresponds to global emissions that are 30% below the 2015 level, and reflects that baseline emissions are expected to grow by 30% between 2015 and 2050 (Höglund-Isaksson et al., 2020). For the oil and gas sector, the global emissions reduction potential under the MFR scenario compared with CLE is 74%, achievable through recovery of associated petroleum gas and, in addition, leakage detection and repair (LDAR)

programs to reduce unintended leakage during extraction, transmission and distribution of natural gas (Höglund-Isaksson et al., 2020). Maximum reduction potential in solid waste management is estimated at 80%, assuming that, over 20 years, the infrastructure for source separation, recycling and energy-recovery schemes is extended globally, a ban on all landfill of organic waste is introduced and the carbon content of waste is utilized (Gómez-Sanabria et al., 2018; Höglund-Isaksson et al., 2020). In agriculture, the maximum technical reduction potential is estimated to be 21%, with about half attributed to measures related to rice cultivation and the other half to changes within the livestock sector. The latter encompass better control of emissions from enteric fermentation – achieved through changes to animal feed, as well as breeding schemes that simultaneously target genetic traits for improving productivity and enhancing animal health, longevity and fertility, – and reductions in emissions brought about by treating manure in anaerobic digesters with biogas recovery (Höglund-Isaksson et al. 2020).

For Arctic Council Member states, the technical mitigation opportunities for CH_4 are relatively extensive, potentially achieving emissions about 50% below baseline CLE in 2050 (Figure 2.11 and Figure 2.12). About 60% of this mitigation potential relates to measures that abate emissions from oil and gas extraction, storage and distribution. Meanwhile, measures to improve waste and wastewater management, for example by avoiding landfilling of organic waste through source separation and treatment, make up about fifth of the technical mitigation potential.

Further potential for reducing SO_2, beyond the CLE baseline, is assessed in the MFR scenarios. For the Arctic Council Member states and Observer countries, up to 60% and 40% reductions, respectively, could be achieved by 2030 by implementing the best available technologies. These reductions would mostly result from changes within the energy and industrial sectors and, to a smaller extent, the residential sector. The measures to reduce SO_2 emissions include after-treatment devices to remove sulfur compounds from flue gases, as well as cuts in the sulfur content of fuel. The maximum reduction potential of Arctic Council Member states could be almost entirely reached by 2030, whereas in the Observer countries, an additional 15% to 20% could be abated in the period between 2030 and 2050.

Some interconnections exist between the opportunities for mitigating BC, CH_4 and SO_2, but generally these effects are estimated to be relatively minor. Key CH_4-mitigation measures primarily affect CH_4, but have some co-benefit to air pollutants including BC. For example, proper waste management will eliminate open burning of waste; production of biogas can lead to lower use of solid fuels and reduce air-pollutant emissions; and gas recovery and reuse can also reduce flaring volumes. Measures to reduce BC, meanwhile, – such as applying diesel particulate filters that require desulfurized fuel, and reducing coal use for heating and cooking – will have a relatively small effect on total SO_2 emissions. The CFM scenario includes these associated reductions of cooling species (e.g., SO_2, NO_X, OC) while focusing on significant mitigation of BC and CH_4.

Figure 2.13 illustrates IIASA-GAINS scenarios of anthropogenic BC and CH_4 emissions in the Arctic Council Member states for the 2010–2030 period. The baseline (CLE) and failure (NFC, NFC_CPS) scenarios indicate a declining trend of BC emissions, suggesting that the voluntary Arctic Council BC goal can almost be achieved with current policies. An additional reduction of 19–60 kilotons (kt) BC appears necessary by 2025 to reach the collective BC goal. This appears feasible, since the mitigation scenarios (MFR and MFR_SDS) indicate significant further emissions-reduction potential that can be achieved primarily with technical measures (important, as the additional potential due to structural changes shown in the MFR_SDS is less than 5% in the short term).

The Arctic Council CH_4 emissions are expected to increase by 2050 and thus do not comply with the Arctic Council vision "...to significantly reduce our overall methane emissions". However, significant mitigation potential exists to reduce CH_4 emissions, as illustrated in the mitigation scenarios (MFR, MFR_SDS, CFM).

Comparing the sector-specific data on the maximum reduction potential of the best available technologies (Figure 2.12) with the recommendations for further actions outlined by the Arctic Council's EGBCM (Expert Group on Black Carbon and Methane) (Arctic Council, 2019) indicates that the Expert Group has identified and targeted key sources of BC and CH_4.

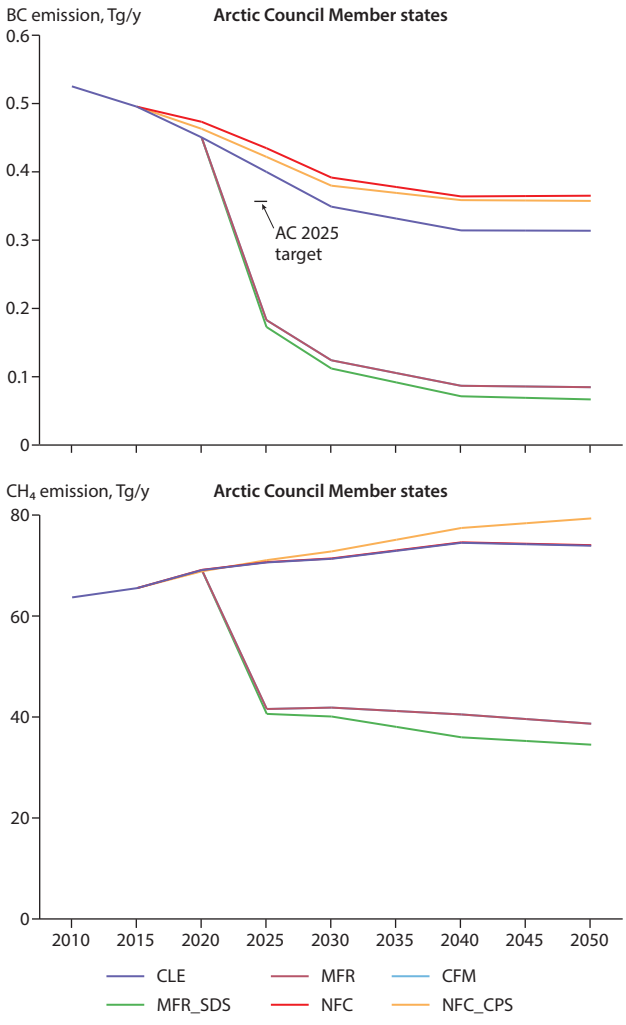

Figure 2.13 BC and CH_4 emissions in Arctic Council Member states in the baseline (CLE), mitigation and failure scenarios.

2.6 Comparing official national emissions data and research inventories

This section presents emissions reported by countries to international fora (CLRTAP, UNFCCC and the Arctic Council), the emissions data used in this assessment (IIASA-GAINS ECLIPSE v6b [Data ref. 2.2]), and other independent emissions inventories (such as the Emissions Database for Global Atmospheric Research [EDGAR v5.0 – Data ref. 2.4]). The chapter presents the data and discusses the main differences between datasets, but does not provide detailed analyses. More in-depth comparisons can be found for BC emissions in EU-funded Action on Black Carbon in the Arctic (EUA-BCA, 2019a), Hoesly et al. (2018), Huang et al. (2015), Evans et al. (2017), and Klimont et al. (2017). Further information regarding CH_4 is provided by Höglund-Isaksson et al. (2020).

2.6.1 Black carbon

Tables 2.2 and 2.3 show BC emissions for Arctic Council Member states and Observer countries from national sources, as well as from the independent ECLIPSE v6b (developed with the IIASA-GAINS model) and EDGAR v5.0 emissions inventories. The IIASA-GAINS historical estimates are discussed in Klimont et al. (2017) but were further updated with new statistical data for 2015, as well as for the European Union, during the development of the Clean Air Outlook (IIASA, 2018) where 2005 and 2010 emissions were reviewed and compared to the CLRTAP submission 2017 (Data ref. 2.5). National sources include emissions as reported to the CLRTAP in 2020 (Data ref. 2.6). For countries that do not report to the CLRTAP, the latest emissions data reported to the EGBCM was included (Arctic Council, 2019).

Table 2.2 Black carbon emissions (kilotons) from the Arctic Council Member states in 2015 from national data sources, ECLIPSE v6b and EDGAR v5.0. National data was taken from the CLRTAP 2020 submissions and, for the USA, from national reports to the EGBCM (Arctic Council, 2019).

2015	National data	ECLIPSE v6b (IIASA-GAINS)	EDGAR v5.0
Canada	37.7	46.6	32.6
Denmark	2.9	3.5	2.3
Finland	4.2	4.9	8.2
Iceland	0.2	0.1	0.1
Norway	3.3	4.3	2.7
Russia	*	171.2	34.8
Sweden	2.7	4.1	6.8
USA	260†	260.6	198.7
Total		495.3	286.1

* Russia didn't report black carbon emissions
† 2014

Table 2.3 Black carbon emissions (kilotons) from the Arctic Council Observer countries in 2015 from national sources, ECLIPSE v6b and EDGAR v5.0. National data was taken from the CLRTAP 2020 submissions, with values for Japan and the Republic of Korea coming from national reports to the EGBCM (Arctic Council, 2019).

2015	National data	ECLIPSE v6b (IIASA-GAINS)	EDGAR v5.0
China		1170.3	1313.8
France	31.3	46.2	23.0
Germany	16.1	15.8	19.5
India		1110.4	794.4
Italy	21.9	33.1	19.2
Japan	17*	14.9	38.8
Republic of Korea	13.4†	16.9	20.2
Netherlands	3.1	3.0	2.9
Poland	14.2	51.2	20.1
Singapore		1.2	3.0
Spain	37.1	27.3	17.0
Switzerland	1.5	1.8	1.9
United Kingdom	19.2	18.2	13.5
Total (excluding China, India and Singapore)	179.8	228.4	176.1
Total		2510.2	2287.3

* 2013, from national reports to the Arctic Council EGBCM (Arctic Council, 2019)
† 2014, from national reports to the Arctic Council EGBCM (Arctic Council, 2019)

The largest differences between the estimates are for Russia, for which the emissions from ECLIPSE v6b are approximately five times higher than those of the EDGAR v5.0 inventory; this is primarily due to emissions from oil and gas flaring being missing from EDGAR v5.0. This raises the question of differences in the inclusion of source sectors between the inventories.

Some non-European Arctic Council Observer countries lack official national emissions inventories with which to make comparisons with other assessments. In general, ECLIPSE v6b emissions are closer to national CLRTAP 2020 submissions than EDGAR v5.0, except for those from Poland, France, and Italy, which are estimated highest in ECLIPSE v6b. According to EU-funded Action on Black Carbon in the Arctic (EUA-BCA, 2019a), the differences for these countries between the previous version of EDGAR (v4.3.2) and the current IIASA-GAINS (ECLIPSE v6b) originate mainly from residential combustion. ECLIPSE v6b makes the highest estimates for total emissions from the Arctic Council Observer countries, while the sum from EDGAR v5.0 (excluding China, India and Singapore) is close to the total of the national inventories. For the largest Observer countries, ECLIPSE v6b estimates higher emissions for India, and EDGAR v5.0 for China. A recent study (Kanaya et al., 2020) discussed the magnitude and trends of BC emissions in China, analyzing data from measurement stations on islands east of China. This confirmed the results of the IIASA-GAINS model, and the trajectory in the ECLIPSE v6b emissions dataset.

EU-funded Action on Black Carbon in the Arctic (EUA-BCA, 2019a) compared BC emissions for 2010 from independent inventories to CLRTAP national submissions. The comparison highlighted some variation in the inclusion and handling of important emissions sectors between the inventories. Of the main source sectors, road-transport emissions showed the smallest variation between inventories. Non-road machinery showed higher variation than road transport. For residential combustion (household heating, cooking, lighting), and commercial and agricultural heating different methods were used to estimate the activity (amount of combusted fuel) and allocation between technologies, causing variations in the emissions estimated by different inventories. For most countries, emissions reported to CLRTAP for residential combustion were close to the ECLIPSE v6b numbers used in this assessment. Emissions from flaring showed the largest variation between the inventories. Overall, significant improvements were made in the reporting completeness in several countries. In recent years, Russian emissions have received considerably more attention, which has resulted in several studies involving Russian scientists. An exhaustive discussion of that process and progress is presented in Box 2.3.

2.6.2 Methane

Table 2.4 compares anthropogenic CH_4 emissions in Arctic Council Member states for the year 2015, as estimated in three different bottom-up inventories: national reporting to UNFCCC (Data ref. 2.7), IIASA-GAINS ECLIPSE v6b, and EDGAR v5.0. There are a few noteworthy differences between the estimates of the three inventories. IIASA-GAINS' estimates of emissions from the oil and gas sector are considerably higher than the others, with almost double or higher emissions for Canada, the USA and Russia. The difference can primarily be related to higher emissions from venting of associated petroleum gas (APG). In the IIASA-GAINS model, these are estimated using a consistent methodology that attributes country-specific amounts of APG generated to either recovery (for reinjection or utilization), flaring or venting (see Höglund-Isaksson, 2017). A description of IIASA-GAINS estimates for 2015 using national statistics as input data is presented in Section S6 of the Supplement to Höglund-Isaksson et al., 2020. The USA estimate for 2015 is calibrated to the average national leakage rate for the oil and gas sector as estimated by Alvarez et al. (2018) and assumes considerably higher average leakage for shale gas extraction (2.7%) than for extraction of conventional gas (1%). For Russia, the estimate for 2015 reflects assumptions about an average CH_4 content of APG of 60% (derived from Huang et al., 2015) and an average APG recovery rate increasing from 55%–68% between 2010 and 2015, as indicated by the changes in the volumes of gas flared (measured from satellite images [Elvidge et al., 2016]), and controlling for changes in production volumes.

Another notable difference between the CH_4 emissions values in the three bottom-up inventories is that EDGAR v5.0 estimates considerably higher emissions for Finland, Norway and Sweden than the other two inventories. The difference here can primarily be related to the wastewater sector and, more specifically, to assumptions about the release of CH_4 from the degradable organic content in wastewater from the pulp and paper industry. IIASA-GAINS and EDGAR v5.0 values do not contain land use, land-use change and forest (LULUCF)

Table 2.4 CH_4 emissions, in kt, from the Arctic Council Member states in 2015 from national reporting to UNFCCC, IIASA-GAINS and EDGAR v5.0.

2015	UNFCCC without LULUCF	IIASA-GAINS	EDGAR v5.0	UNFCCC with LULUCF
Canada	3822	4787	5348	3848
Denmark	288	262	356	299
Finland	194	173	913	226
Iceland	26	38	21	172
Norway	202	254	798	208
Russia	14,520	28,105	17,294	15,433
Sweden	184	171	477	202
USA	25,539	31,829	25,289	26,185
Sum	44,776	65,618	50,496	46,573

Box 2.3. Recent developments in black carbon emissions inventories for Russia

In recent years, out-of-date or missing information has affected the quality of Russian BC estimates, leading to biases in both rates and spatial distribution of emissions. This bias is a key reason why chemical transport models struggle to accurately reproduce BC levels over the Arctic. To improve the accuracy of Russian BC emissions estimates, sources including flaring, transportation, residential, energy, industry, wildfires, and agricultural burning have been much studied of late.

Flaring in the oil and gas industry

Flaring is estimated to contribute significantly to Russia's total anthropogenic BC emissions. However, there are significant uncertainties around estimating volumes of flared gas, as well as BC emission factors. Data based on satellite observations indicate that higher volumes of gas have been flared than those reported in Russian official statistics. The satellite-based data has been extensively used in peer-reviewed studies (Stohl et al., 2013; Huang et al., 2015; Evans et al., 2017; Klimont et al., 2017; Böttcher et al., 2021). Evans et al. (2017) reviewed the emission factors from available literature and established Russia-specific emission factors. The authors adopted the approach described in Huang et al. (2015), and adjusted data input to McEwen and Johnson (2012) to derive an average emission factor of 2.27 gram per cubic meter (g/m^3), with a range from 0.51 to 2.56 g/m^3, for 2010. BC emissions in 2014 were estimated to be 32.2 kt, with an uncertainty range from 10.0–54.1 kt. Reducing the uncertainty in the emissions estimates would require more site-specific information on gas composition and the corresponding heating value, as these factors can vary over time and across different production sites.

Transportation

Vehicles, vessels and machinery emit significant amounts of BC. The actual amounts emitted depend on the relative shares of diesel and gasoline vehicles, vehicle types and the respective emissions standards they comply with, and are estimated based on fuel consumption or mileage. BC emissions can be estimated directly based on BC emission factors or indirectly using $PM_{2.5}$ emission factors combined with $BC/PM_{2.5}$ ratios. Other factors that need to be accounted for include the distribution of traffic by road type, ambient temperature (for cold starts), average speed, and the presence of super-emitters (vehicles that, due to a malfunctioning or tampered-with exhaust treatment system, have very high emissions compared to regular ones). For rail and shipping, most studies use a fuel-consumption-based method to estimate BC emissions. The 2014 emissions values available from literature were 3.9–8.0 kt for Russian rail, and from 0.5–0.6 kt for shipping (Hoesly et al., 2018; Kholod et al., 2016; Evans et al., 2017). According to Evans et al. (2017), total BC emissions from the transportation sector (diesel and gasoline vehicles, locomotives and ships) ranged from 16.3–41.2 kt with a central value of 29.8 kt.

Residential combustion

Most of the households in Russia rely on district heating systems (84%) and natural gas supply (69%) for heating and cooking. About 10% of all households in rural areas rely on wood. Evans et al. (2017) collected BC emission estimates from the literature, which ranged from 13–102 kt with a central estimate 27.0 kt.

Energy and industry

In Russia, natural gas is the predominant fuel for district heating (60%), while coal and oil provide 20% and 5%, respectively. Hoesly et al. (2018) estimated emissions of BC from the heat and power sectors to be 16.4 kt, and Evans et al. (2017) estimated the uncertainty range to be from 11.9–26.7 kt. Natural gas accounts for about 80% of the energy used in industry, but the largest emissions are from diesel combustion (85%). The mining industry alone is the largest source of BC emissions (about 40% of industrial BC emissions). Hoesly et al. (2018) estimated emissions from industry to be 5.2 kt of BC, and Evans et al. (2017) estimated the uncertainty range to be 1.0–51.3 kt of BC with a central value of 5.1 kt. The uncertainty in BC emissions from industry in Russia is very large. There are no Russia-specific emission factors for BC, and emission factors from other countries may not be comparable to those in Russia.

Wildfires

BC emissions are calculated as the product of the burned area, fuel load, combustion completeness, and the emission factors for the specific plant species burned. Either satellite data or official government statistics can be used to quantify the burned area, but official statistics are several times lower than the satellite data on area burned. Because official statistics may overlook remote areas where there is no direct land-based observation, researchers often prefer using satellite data. Data on fuel load and combustion completeness are limited for Russia, and direct use of data from other countries is not always appropriate. Since information on Russia-specific emission factors is limited, Evans et al. (2017) assumed 0.93 g/kg and 1.36 g/kg, respectively, for forest and non-forest fires. This was based on a study by Hao et al. (2016), which conducted aircraft measurements in the USA and used an emission factor of 0.69 g/kg for agricultural residue from McCarty et al. (2012). Evans et al. (2017) estimated the total annual BC emissions from wildfires in forests, grasslands, and other natural areas to be 569 kt during the 14-year period from 2002 to 2015, with uncertainty ranging from 345–793 kt. They attributed most of the uncertainty to burned areas.

Emission factors contribute comparable uncertainty when the inventories are applied in atmospheric models. The most widely adopted factor, from Akagi et al. (2011), organized factors into three broad types of forests susceptible to wildfire: tropical, temperate and boreal. But in reality, one type of forest may have various types of plant species, which may have substantially different emission factors. For example, May et al. (2014) reported the factor for BC was 1.11 g/kg for black spruce (*Picea mariana*) and 2.72 g/kg for white spruce (*Picea glauca*). But the emission factor used by the Global Fire Emission Database (GFED) for burning of boreal forest is 0.56 g/kg, suggesting that emission factors at terrestrial biome scale contain large uncertainty. The high-latitude boreal forests in Siberia are important contributors of BC in the Arctic region. Thus, developing a better emission factor database for biomass burning should be an urgent priority in order to constrain the uncertainties associated with this phenomenon.

emissions. In general, emissions from LULUCF sectors are small compared to the anthropogenic sources; they represent 4% of total CH_4 emissions from the Arctic Council Member states and 2% from Observer countries.

Table 2.5 shows the corresponding comparison across the three bottom-up emissions inventories for the Arctic Council Observer countries. For China, the EDGAR v5.0 inventory estimates 16% higher CH_4 emissions in 2015 than the IIASA-GAINS or national estimate reported to UNFCCC, with the higher estimate for rice cultivation in EDGAR v5.0 being the main reason for the difference. Both IIASA-GAINS and EDGAR v5.0 estimate 32–33 Tg CH_4 emissions for India in 2015, which is considerably higher than the figure of about 20 Tg CH_4 reported by India for the year 2010. The IIASA-GAINS estimate for year 2010 is about 30 Tg CH_4, and a comparison for this year reveals that the difference to the national estimate can be related to the roughly double estimates of emissions from rice cultivation (8.4 versus 3.4 Tg CH_4), and waste and wastewater sources (5.2 versus 2.5 Tg CH_4). The higher emissions estimate for Japan in IIASA-GAINS and EDGAR v5.0 can be traced to these inventories having higher emissions estimates for livestock and for waste and wastewater management than the national reports to the UNFCCC. Finally, the double CH_4 emissions estimated for the UK in EDGAR v.5.0, compared to the other two inventories, can be related to higher emissions estimated from solid waste management.

2.7 Uncertainties within anthropogenic emissions inventories

This report discusses and, to a large extent, uses bottom-up emissions inventories to support modeling. Additionally, many international conventions, such as the CLRTAP and the UNFCCC, oblige countries to calculate national emissions data with such methodologies. Arctic Council Member states are also committed to provide that national emissions information to the Arctic Council, and Observer countries are encouraged to do so. National estimates often support the design of mitigation strategies and policies.

It is important to acknowledge that the calculated emissions are subject to uncertainties, due to missing or incomplete information or limited understanding of emissions relevant parameters. These apply to all key elements underlying the estimates, including: data on activities and their temporal distribution; aggregation of individual sources or more detailed information; emissions-relevant parameters, such as technology type, emission factors; as well as spatial distribution and vertical profiles of sources. A systematic uncertainty analysis has not been performed for this study, but a quantitative comparison (Section 2.6) and qualitative assessment have been made of the robustness of several national and international inventories.

Activities for major industrial and transport sectors are relatively well documented, regularly updated and can be accessed from national and international sources, such as the IEA (Klimont et al., 2017). Some other major source categories, for example non-commercial fuel use in heating or cooking stoves or local vehicle fleets, are not well known (Klimont et al., 2017). Moreover, there is considerable temporal variation for some activities. A good example is the heating need in northern latitudes, which has a considerable monthly – and even daily – variability between cold and warm seasons and periods. The temporal distribution can also be an important source of uncertainty related to emissions data, as generalized temporal weight factors are often used instead of real meteorological data. Considering the above, significant differences in uncertainties may exist between subsectors and fuel types (Super et al., 2020)

For SO_2, the sulfur content of the fuel is the prime determinant of the emission factor for residential combustion and transport,

Table 2.5 CH_4 emissions, in kt, from the Arctic Council Observer countries in 2015 from UNFCCC submissions, IIASA-GAINS and EDGAR v5.0.

CH_4 2015	UNFCCC without LULUCF	IIASA-GAINS	EDGAR v5.0	UNFCCC with LULUCF
China	53,570*	52,450	62,331	55,290*
France	2332	2302	2616	2380
Germany	2271	1887	3152	2305
India	19,623**	31,796	33,339	19,776**
Italy	1755	1709	1639	1766
Japan	1243	1685	2095	1246
Republic of Korea	1238	1063	1384	1252
Netherlands	728	639	854	728
Poland	1992	1628	2528	1993
Singapore	4***	29	79	4***
Spain	1568	1418	1715	1575
Switzerland	199	180	218	199
UK	2125	2076	4234	2126
Total	88,648	98,861	11,6184	90,640

*2014 **2010 ***2012

while for power plants and industrial boilers, the presence and efficiency of flue gas treatment is key. For other species, including NO_X, CO, BC and OC, the emissions depend on several factors, primarily the combustion conditions and applied exhaust treatment technology, which vary according to the source. This results in high variability in emissions estimates (Super et al., 2020; Klimont et al., 2017; Bond et al., 2013). Operating modes and user behavior can affect the combustion process or engine performance and consequently also the emissions (Bond et al., 2013) but information is too scarce to include such factors systematically into emissions inventories. In the case of BC, the lack of a consistent definition, and the use of various measurement methods for determining emission factors, makes comparing results difficult (Bond et al., 2013).

Proxies that support the spatial distribution of emissions can introduce uncertainties to the datasets used in atmospheric transport and climate models. Important sources may be wrongly placed, or emissions in a specific location may be weighted inappropriately (see also discussion in AMAP, 2015a). Additionally, the resolution of the spatial proxies may be so coarse that important local characteristics of emissions are lost.

Comparing emissions results obtained with different calculation frameworks or models can be used as an indicator of uncertainty, and it is common practice to provide such analyses when new emissions datasets are introduced. A comparison of newly available emissions inventories is presented in Section 2.6 for BC and CH_4. There are also methodologies, for example the Monte Carlo method, which quantify uncertainties around emissions by combining individual uncertainty distribution estimates of the various inventory calculation elements and provide an aggregated emissions distribution from which minimum, maximum and mean estimates can be derived (see e.g., Super et al., 2020). The uncertainties inherent in the estimates of emissions of individual pollutants vary depending on the specific characteristics of the calculation elements.

Conducting a quantitative uncertainty analysis of a global emissions database is a laborious task, but some estimates for individual pollutants exist. The previous AMAP reports (AMAP, 2011, 2015a) quoted the work by Bond et al. (2004, 2013) on BC. Bond et al. (2004) gave a 95% confidence interval of 31–10 Tg/y (-30% to +120%) for anthropogenic emissions and 16– to 9.8 Tg/y (-40% to +200%) for open biomass burning. Solazzo et al. (2021) assessed the uncertainty for greenhouse gas emissions in the EDGAR v5.0 inventory; global uncertainties for CH_4 emissions from the IPCC sectors are presented in Table 2.6. Solazzo et al. (2021) assessed uncertainties separately for industrialized and developing countries, and concluded that uncertainties for many sectors were lower for the industrialized countries.

Table 2.6 Uncertainties for global CH_4 emissions for the EDGAR v5.0 emissions inventory (Solazzo et al., 2021).

IPCC sector	Lower uncertainty (%)	Upper uncertainty (%)
1 Energy	60.4	94.2
2 Industrial	53.4	35.4
3 Agriculture	30.6	37.5
4 Waste	77.7	78.8
5 Other	117.3	117.3

The uncertainty estimate for Russian BC emissions conducted by Huang et al. (2015) gave a range of 59.1%–349.2% (95% confidence level). Karvosenoja et al. (2008), assessed $PM_{2.5}$ emissions uncertainties for 2000 in Finland, estimating emissions for traffic exhaust to be 4.2 kt/y (3.72–4.73 kt/y with 95% confidence intervals) and for residential wood combustion to be 7.58 kt/y (4.87–11.4 kt/y). According to Statistics Norway (2001), NO_X and NMVOC emissions for Norway had an uncertainty of 12% and 15%, respectively, while the uncertainty in SO_2 was estimated to be 5%. Uncertainties for emissions from wood stoves in Norway were estimated at 7% for PM, and at 45% and 27% for EC for new and old stoves, respectively (SINTEF, 2013).

This report discusses a suite of emissions estimates and presents in more detail the data calculated with the IIASA-GAINS model. At the time of writing, the ECLIPSE v6b dataset of IIASA-GAINS discussed in this report had not undergone a quantitative uncertainty estimate, but Amann et al. (2011) and Schöpp et al. (2005) described the treatment of uncertainties in the context of the IIASA-GAINS model. Since the 2015 AMAP assessment, steps have been taken to reduce the uncertainty in emissions datasets, including using: updated activity data; more data on source structure and emission factors originating from new regional studies (for example, see discussion in Box 2.3 on emissions from Russia); new emission factors for flaring, as well as venting and leakage for CH_4 (see Höglund-Isaksson et al., 2020); and updated spatial proxies.

The spatial proxies for many sources have been revised – including for the residential sector, shipping, transportation, power plants, and oil and gas operations (including flaring) (Böttcher et al., 2021). In all cases, new data was used, either providing higher resolution or a more up-to-date representation of source locations.

Amann et al. (2013) argued that, even though uncertainties can be quantified and the quantification may indicate a large uncertainty range, another element to consider besides the statistical uncertainties is the robustness of the emissions inventories. The authors define robustness to imply that emissions control needs and priorities between countries, sectors and pollutants do not significantly change due to changes in the uncertain model elements. The scenarios developed and used in this assessment are deemed to be robust from the above perspective, highlighting the importance of mitigation in particular sectors regardless of the uncertainties associated with them.

2.8 Summary and main messages

In 2015, the Arctic Council Member states accounted for 8%, 13% and 20% of the global anthropogenic emissions of BC, SO_2 and CH_4, respectively. Jointly, Arctic Council Member states and Observer countries currently account for about half of the global anthropogenic emissions of these pollutants.

- The surface transport sector dominates the BC emissions in the Arctic Council member states (47%), followed by residential combustion for heating (21%), flaring in oil and gas extraction (14%), agricultural waste burning (9%), and

industrial combustion (6%). In the Arctic Council Observer countries, residential combustion comprises 56% of BC emissions, followed by surface transport (21%), combustion in industry (12%) and burning of household and agricultural wastes (5% each).

- SO_2 emissions are dominated by combustion in industry and energy production, with 95% and 83% in the Arctic Council Member states and Observer countries, respectively.
- In the Arctic Council Member states, most of the CH_4 emitted comes from fossil fuel production, storage and distribution (intended venting and unintended leakage during extraction and transportation of oil and gas [53%], and release of CH_4 in ventilation air during coal mining [8%]). Other significant sources of CH_4 are anaerobic decomposition of organic materials in waste and wastewater management (17%), as well as livestock metabolism and manure management (19%). Incomplete combustion processes, in particular from agricultural waste burning and burning of biomass in the residential sector, contribute minor (2%) CH_4 emissions. In the Arctic Council Observer countries, agriculture accounts for 46% of total anthropogenic emissions, followed by fossil fuel production (29%), waste and wastewater (21%) and combustion sources (5%). Notably, the oil and gas sector is estimated to be responsible for only 4% of total CH_4 emissions in the Arctic Council Observer countries.

Considering the recent energy outlook, existing and decided environmental legislation (if effectively enforced) are expected to reduce BC and SO_2 emissions, but CH_4 emissions are anticipated to continue to increase.

- The baseline scenario (CLE), studying anthropogenic emissions trajectories under current legislation, indicates a declining trend for BC emissions in the Arctic Council Member states (up to 37% by 2050 compared with 2015, with reductions mainly due to the surface-transport sector) as well as the Observer countries (up to 52% by 2050 compared with 2015, with reductions due to the surface-transport and industry sectors), in contrast to the 'rest of the world' where baseline emissions are expected to increase.
- Also, under the CLE scenario, SO_2 emissions decline significantly by 2050 compared with 2015 in both regions – by up to 30% and 40%, respectively, for Arctic Council Member states and Observer countries. This is due to the further policies in the energy (Arctic Council Member states and Observer countries), industry and residential sectors (Observers).
- CH_4 emissions are projected to increase in the 2010 to 2050 period by 16% and 33% in the Arctic Council Member states and Observer countries, respectively. The oil and gas and the waste sectors account for the increase in Arctic Council Member states, whereas the waste and agriculture sectors are the key drivers in the Observer countries.

Significant opportunities exist to reduce emissions of BC, SO_2 and CH_4 in the Arctic Council Member states and Observer countries, as well as globally, as indicated by the MFR, CFM and MFR_SDS scenarios.

- There is significant outstanding potential to further reduce BC emissions, globally, using existing technologies. In the Arctic Council Member states, adopting the best available mitigation technologies for road and non-road transport, residential heating and cooking, and in the oil and gas sectors would roughly halve BC emissions by 2030 compared with the baseline. A further 10% reduction could be achieved by implementing measures within industry and by enforcing bans on the open burning of agricultural residues. In the Arctic Council Observer countries, BC emissions could be reduced by 60%–70% by 2030 by implementing measures targeting practically the same sectors as for the Arctic Council Member states. Additional reduction potential of up to 20% would remain for the 2030–2050 period, which could be achieved by widening access to clean energy for cooking, and improving municipal solid waste management to the point where virtually no open burning of waste remains. Achieving such deep cuts in BC emissions will be also associated with some reduction of SO_2, NO_X, CO, and OC, since these species are co-emitted from many sources and reduction technologies simultaneously affect several pollutants; this is reflected in the SLCF-targeted scenario (CFM).
- The maximum technically feasible reduction (MFR) of global anthropogenic CH_4 by 2050 is estimated to be 54% below the CLE baseline emissions for that year. In the Arctic Council Member states, the technical mitigation opportunities for CH_4 results in about 50% lower emissions than the baseline for 2050. A third of this can be achieved via measures to abate emissions from oil and gas extraction, storage and distribution, while changes to improve waste and wastewater management contribute around a fifth of the technical mitigation potential.
- The potential to further reduce SO_2 emissions was estimated in the MFR scenarios at up to 60% and 40% by 2030, respectively, for Arctic Council Member states and Observer countries. These cuts are feasibly mostly through implementation of further measures in the energy and industrial sectors, and, to a lesser degree, in the residential sector.

Further actions are needed to reach the Arctic Council commitments to mitigate emissions of BC and CH_4.

- According to the baseline scenario (CLE), the voluntary Arctic Council BC goal that the "black carbon emissions be further collectively reduced by at least 25–33 percent below 2013 levels by 2025" could almost be achieved with current policies. The remaining reduction gap, estimated at 19–60 kt, could be achieved by 2025 with additional, primarily technical, mitigation measures.
- The Arctic Council Member state's CH_4 emissions are expected to increase by 2050 and thus would not comply with the Arctic states' common vision "...to significantly reduce our overall methane emissions", as expressed in the *Arctic Council Framework for Action on Black Carbon and Methane Emissions Reductions* (Arctic Council, 2015). However, significant potential to reduce CH_4 emissions exists if the best available technologies are implemented.
- Failure to implement the post-2015 legislation would move the BC emissions trajectory further from meeting the 2025

goal, and would lead to approximately 15% higher emissions levels of BC and SO_2 towards the end of the period, compared with the CLE baseline. CH_4 emissions remain relatively similar in the baseline (CLE) and failure (NFC and NFC_CPS) scenarios for both Arctic Council Member states and Observer countries. These results highlight the importance of timely and effective enforcing of existing policies and legislation.

- Comparing the potential for reducing emissions using best available technologies with the recommendations for further actions by the EGBCM (Arctic Council, 2019) indicates that the Expert Group has identified and targeted key sources of BC and CH_4.

Current emissions inventories are known to be missing some important local pollution sources. Local Arctic air-pollution sources identified in the scientific literature include: boreal forest fires; outdated and polluting equipment used for energy production (diesel generators and old boilers); burning of waste; land transport and shipping; and industrial operations. These can be overlooked if they are not recognized in national-level emissions inventories (because the contributing emissions sources are not well identified and quantified in terms of locations or amount).

Comparing the emissions inventories used in this study with official national submissions and other independent datasets indicates that there is variation in the inclusion and handling of important emissions sectors, as well as in activity and emissions parameters between the inventories. The calculated emissions are subject to uncertainties, due to missing or incomplete information or limited understanding of calculation parameters. The scenarios developed and used in this AMAP assessment are robust in their approach to, and inclusion of, uncertainty; however, it remains important to mitigate emissions in particular sectors regardless of the uncertainties associated with them.

2.8.1 Remaining challenges and recommendations for further work

As identified in AMAP (2015a, 2015b), work to further develop emissions inventories for high latitudes should continue. More detailed spatial emissions inventories for Arctic communities would benefit local emissions mitigation planning. Arctic states should work to better identify and quantify local Arctic emissions sources, and to include them in national-level emissions inventories. Further effort to validate assumptions about the potential to mitigate emissions, especially the pace at which some necessary transitions could take place, is recommended.

While current work draws on a number of national assessments of local emissions sources, the future projections of activities rely entirely on international sources, such as the IEA and FAO. Explicit consideration of national visions and plans could be better integrated in analyses, and compared to the internally consistent projections used now. Such analyses could also highlight national priorities and sensitivities that could be better addressed in subsequent modeling work, to better inform policy discussions.

2.8.2 Follow-up of recommendations from the 2015 assessment

The AMAP 2015 assessment included recommendations to support and guide further development of anthropogenic emissions datasets, particularly in the Arctic area. This section provides a follow-up on these recommendations and specifically outlines how the datasets used in this assessment take these recommendations into account.

- *Recommendation 1 (AMAP, 2015a): A comparison of several global emissions inventories has shown that relative uncertainties in the total emissions per latitude band increase with latitude and are largest in the Arctic. The global inventories thus need improvement, especially at high latitudes. This could be achieved by including information from regional and Arctic Council national inventories.*

The spatial representation of emissions in the Arctic area has been improved in the anthropogenic emissions datasets used and assessed in this study. Since the AMAP 2015 assessment, a new population pattern has been introduced to significantly improve allocation of certain activities to Arctic communities. Effort has been made to enhance datasets representing Arctic shipping, including the local traffic and that on rivers. Improvements in mapping road networks, power plants, and industrial facilities (including oil and gas activities, and encompassing flares) in the Arctic have been made.

- *Recommendation 2 (AMAP, 2015a): Further analysis of observed and modeled historical trends of SLCFs should be made.*

This recommendation does not directly address anthropogenic emissions datasets. However, emissions are a key driver in explaining the trends of SLCFs in atmospheric concentrations and thus such comparisons can provide important insights into further improvements of emissions datasets. In this assessment we have continued, as in previous assessments, to analyze and compare observed and modeled historical trends of SLCFs. Chapter 6 of this assessment addresses trends in observations and Chapter 7 evaluates the performance of models used in this assessment against observations.

- *Recommendation 3 (AMAP, 2015a): Future work should develop emission scenarios that describe a strong increase in anthropogenic activities within the Arctic and quantify the projected impacts these activities would have on the Arctic climate and environment.*

An emissions scenario representing high-growth in activities in the Arctic area still remains an interesting topic for further work. However, the scenario representing slower energy transition (CPS) and failure to comply with existing air-quality legislation (NFC) addresses some potential aspects of such development.

- *Recommendation 1 (AMAP, 2015b): Undertake additional direct or on-site source measurements (at scales that support extrapolation), harmonize development and application of emission factors internationally, and improve the temporal (interannual) resolution of reported emissions in order to improve estimation of anthropogenic methane emissions.*

This recommendation points out an ongoing, overarching effort to iteratively improve our understanding of CH_4 emissions and to streamline the flow of information from source measurements

to emissions evaluations. The recommendation remains valid, and AMAP could endeavor to find ways to facilitate such efforts.

- *Recommendation 2 (AMAP, 2015b): Subsequent assessment efforts should focus on fugitive emissions from all aspects of oil and gas systems from exploration through production and distribution.*

Since AMAP (2015b) was published, extensive work has been conducted to better understand the magnitude of fugitive emissions from the upstream oil and gas sector. A wide range of methodological approaches have been applied, including ground-based monitoring, airborne-measurement campaigns, measurements of isotopic shifts in the atmospheric CH_4 concentration, atmospheric transport modeling, bottom-up inventories, inverse modeling, and the development of satellite-based monitoring technology. Without claiming to be exhaustive, a short summary of findings so far indicates that CH_4 emissions from fossil-fuel sources have likely been underestimated in past bottom-up inventories, but that the very strong increase in atmospheric CH_4 concentrations observed in the last decade can only be partly ascribed to increased emissions from fossil-fuel activities and partly is of biogenic origin (Nisbet et al., 2019; Saunois et al., 2020).

Chapter 2 Appendix

A2.1 National emissions

Table A2.1 National emissions in kilotons per year (kt/y) under the baseline scenario and failure scenarios. Baseline: CLE (CLE = current legislation; assumes recent policies implemented, including Nationally Determined Contributions [NDCs] of Paris Climate Agreement); Failure: NFC (NFC = no further control; assumes failure of recent policies); NFC_CPS (CPS = current policy scenario; with NDCs excluded).

	CLE			NFC		NFC_ CPS	
kt/y	2015	2030	2050	2030	2050	2030	2050
Arctic Council Member states							
Canada							
BC	46.6	40.4	45.0	42.5	47.6	30.4	33.2
CH_4	4793.1	5421.9	6636.0	5422.0	6636.2	5460.9	7294.7
SO_2	1073.0	1062.1	1102.1	1062.9	1102.9	1131.1	1247.5
Denmark							
BC	3.5	1.2	0.7	1.8	1.3	1.8	1.4
CH_4	253.8	214.0	210.2	216.2	219.2	215.6	216.9
SO_2	14.4	13.7	14.2	15.5	16.0	15.6	17.7
Finland							
BC	4.9	3.1	2.6	3.2	2.7	3.1	2.9
CH_4	172.4	131.6	140.2	131.7	140.8	130.9	140.0
SO_2	45.1	30.3	25.7	30.3	25.7	33.8	32.7
Iceland							
BC	0.1	0.1	0.1	0.1	0.1	0.1	0.1
CH_4	38.1	44.2	48.7	44.2	48.8	44.2	48.6
SO_2	5.9	1.9	1.9	6.8	7.3	7.5	9.9
Norway							
BC	4.3	1.5	1.2	1.8	1.7	1.9	1.8
CH_4	254.1	234.8	207.6	235.4	208.5	231.4	199.5
SO_2	50.2	41.8	47.2	67.6	75.2	71.4	88.9
Russia							
BC	171.2	154.3	128.5	157.6	133.0	158.3	144.3
CH_4	28,018.1	30,176.7	30,957.5	30,177.5	30,960.6	30,608.8	34,450.1
SO_2	3864.6	3055.0	3240.5	3710.6	3880.8	3905.9	3930.0
Sweden							
BC	4.1	1.7	1.4	2.6	2.4	2.5	2.5
CH_4	174.8	167.5	187.8	173.5	195.4	171.8	190.6
SO_2	23.5	26.3	26.2	26.4	26.2	25.6	26.4
USA							
BC	260.6	146.4	133.8	181.7	176.0	181.4	170.8
CH_4	31,819.1	34,940.4	35,536.9	35,009.7	35,623.7	35,932.5	36,789.1
SO_2	4160.8	2041.4	1748.6	2068.0	1776.8	2242.3	2057.0
Arctic Council Observer countries							
China							
BC	1170.4	696.5	466.8	735.5	534.1	843.5	647.1
CH_4	52,526.4	60,456.9	65,455.0	60,484.0	65,468.4	62,435.0	72,111.2
SO_2	16,394.2	9710.3	7738.8	11,275.5	9146.2	12,079.1	11,150.6
European Observers							
BC	197.1	85.3	60.7	121.2	96.8	120.9	100.1
CH_4	12,011.7	9412.6	9235.4	9564.6	9398.9	9580.3	9538.1
SO_2	2117.4	967.2	762.6	1199.5	998.0	1363.5	1240.9
India							
BC	1110.7	739.7	666.2	768.5	726.0	785.3	759.7
CH_4	31,930.2	37,902.2	46,662.0	37,947.0	46,723.3	38,547.5	50,025.0
SO_2	8121.2	4448.3	5958.3	13,977.7	17,128.8	15,208.2	23,208.6
Other Asian Observers							
BC	33.0	16.8	15.6	18.8	17.6	19.7	19.2
CH_4	2776.4	2534.3	2826.6	2547.6	2837.7	2550.9	2847.9
SO_2	1149.4	913.5	801.2	1264.8	1182.5	1345.7	1456.5

Table A2.2 National emissions under the mitigation scenarios: MFR (MFR = maxium feasible reduction; assumes recent policies implemented, including Nationally Determined Contributions [NDCs] of Paris Climate Agreement, and best available, technically feasible emissions-mitigation takes place); CFM (CFM = climate forcing mitigation; assumes MFR-type mitigation, with a focus on using technologies that result in lower net climate forcing); MFR_SDS (SDS = sustainable development scenario, assumes MFR technologies and rapid emissions reductions that result in achievement of several UN Sustainable Development Goals).

	MFR		CFM		MFR_SDS	
kt/y	2030	2050	2030	2050	2030	2050
Arctic Council Member states						
Canada						
BC	12.2	9.5	12.2	9.5	8.9	5.7
CH_4	3715.3	3308.7	3715.3	3308.7	3529.3	2425.0
SO_2	677.1	690.4	917.6	947.9	643.9	629.8
Denmark						
BC	0.6	0.4	0.6	0.4	0.6	0.4
CH_4	188.3	189.7	188.3	189.7	188.0	187.0
SO_2	12.0	12.2	13.7	14.3	11.0	10.2
Finland						
BC	1.4	1.0	1.4	1.0	1.4	1.0
CH_4	115.3	111.5	115.3	111.5	115.4	110.8
SO_2	25.3	19.3	30.2	25.8	22.9	16.7
Iceland						
BC	0.0	0.0	0.0	0.0	0.0	0.0
CH_4	43.1	26.0	43.1	26.0	43.0	25.7
SO_2	0.7	0.7	1.9	2.0	0.6	0.4
Norway						
BC	0.8	0.6	0.8	0.6	0.7	0.4
CH_4	211.4	179.1	211.4	179.1	194.6	141.8
SO_2	28.0	32.8	41.6	47.0	26.3	32.0
Russia						
BC	34.5	17.7	34.5	17.7	31.5	12.5
CH_4	11,448.2	7784.3	11,448.2	7784.3	10,694.7	6679.4
SO_2	980.4	878.4	2977.5	3162.2	889.0	981.4
Sweden						
BC	0.9	0.8	0.9	0.8	0.9	0.7
CH_4	151.9	164.8	151.9	164.8	151.7	162.9
SO_2	26.1	25.9	26.3	26.3	24.9	23.7
USA						
BC	72.8	53.9	72.8	53.9	67.3	45.2
CH_4	25,988.4	26907.9	25,988.4	26908.0	25,178.4	24,785.7
SO_2	1336.6	1008.1	2026.2	1725.3	871.9	692.7

	MFR		CFM		MFR_SDS	
	2030	2050	2030	2050	2030	2050
China						
BC	264.4	73.1	264.4	73.2	220.7	58.0
CH_4	38841.4	30674.4	38841.4	30674.6	35789.2	27106.9
SO_2	7225.8	4802.7	9002.3	6093.8	6326.3	3323.7
European Observers						
BC	52.4	36.2	52.4	36.2	47.9	30.9
CH_4	7822.7	6804.6	7822.7	6804.8	7768.0	6757.0
SO_2	641.7	471.3	939.6	735.5	558.2	404.9
India						
BC	248.8	143.9	248.8	143.9	170.8	99.7
CH_4	29680.2	31961.0	29686.8	31968.6	28219.7	28481.5
SO_2	2072.9	2169.7	3885.8	4913.5	1783.6	1783.2
Other Asian Observers						
BC	8.7	6.6	8.7	6.6	8.1	5.0
CH_4	1953.4	1624.9	1953.4	1625.1	1955.6	1591.1
SO_2	583.3	464.6	905.7	792.3	509.7	393.8

A2.2 Emissions as per modeling regions

Table A2.3 Baseline (CLE) emissions figures in kilotons per year (kt/y) by modeling region (see also Chapter 8, Figure 8.1).

kt/y	1990	2010	2015	2025	2030	2050
Arctic Council (East)						
BC	528	217	188	179	162	135
CH_4	61,774	30,638	28,911	31,078	30,969	31,752
CO	27,544	15,337	12,798	12,001	11,384	9744
NH_3	1846	963	990	1058	1095	1129
NO_X	10,021	5337	4772	4376	3971	3282
OC	550	268	253	243	232	224
$PM_{2.5}$	3611	1420	1316	1274	1226	1160
SO_2	11,777	4480	4005	3259	3169	3356
VOC	7895	4470	3952	3800	3690	3568
Arctic Council (West)						
BC	371	308	307	221	187	179
CH_4	25,430	33,050	36,612	39,534	40,362	42,173
CO	111,613	39,240	38,524	34,763	31,532	27,838
NH_3	3488	4527	4653	4827	4919	5195
NO_X	29,002	15,475	14,897	10,944	9051	7852
OC	614	525	497	422	404	407
$PM_{2.5}$	2352	1717	1604	1276	1215	1235
SO_2	23,729	7655	5234	3223	3104	2851
VOC	21,599	11,745	11,801	11,178	10,435	9887
Asian Observers						
BC	2378	2539	2314	1688	1453	1149
CH_4	59,215	80,297	87,233	95,986	100,893	114,944
CO	168,373	214,677	226,844	179,510	164,431	136,019
NH_3	16,540	23,064	24,276	26,907	28,326	31,308
NO_X	16,947	40,023	39,036	32,025	29,733	25,993
OC	5429	4901	4542	4177	4065	4032
$PM_{2.5}$	16,711	16,739	15,930	14,190	13,796	14,255
SO_2	21,813	33,931	25,665	18,710	15,072	14,498
VOC	24,780	33,002	35,033	35,065	34,630	32,761
European Observers						
BC	535	411	337	242	180	150
CH_4	33,122	22,971	20,605	17,845	17,169	17,257
CO	64,106	27,139	22,601	17,747	15,683	15,008
NH_3	5912	4361	4395	4406	4425	4421
NO_X	20,963	11,745	10,176	6833	5757	4739
OC	927	639	582	467	375	315
$PM_{2.5}$	4610	2316	2034	1694	1452	1318
SO_2	30,276	7036	5262	2407	2198	2125
VOC	19,249	8032	7137	6192	5776	5402

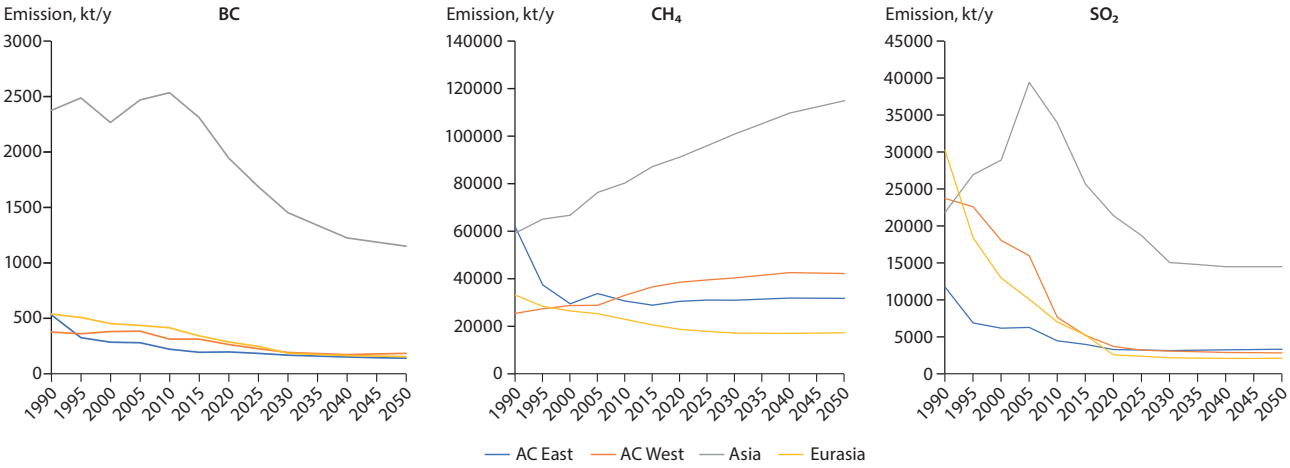

Figure A2.1 Baseline (CLE) emissions figures in kilotons per year (kt/y) 1990 – 2050 by modeling region (see also Chapter 8, Figure 8.1).

A2.3 Share of emissions from Arctic Council Member states, Observer countries and rest of the world

Table A2.4 Anthropogenic emissions of BC, SO_2 and CH_4, and the shares of the global total contributed by the Arctic Council Member states and Observer countries, and the rest of the world, for 2015, 2025 and 2050 under the baseline scenario (CLE).

	kt/y	2015	2025	2050
Arctic Council Member states	BC	495 (8%)	400 (7%)	313 (6%)
	SO_2	9239 (13%)	6482 (13%)	6207 (12%)
	CH_4	65,523 (20%)	70,612 (20%)	73,925 (17%)
Arctic Council Observer countries	BC	2511 (40%)	1816 (33%)	1209 (23%)
	SO_2	27,782 (40%)	19,859 (40%)	15,261 (30%)
	CH_4	99,245 (30%)	105,966 (30%)	124,179 (29%)
Rest of the World	BC	3205 (52%)	3313 (60%)	3680 (71%)
	SO_2	33,170 (47%)	23,446 (47%)	28,666 (57%)
	CH_4	162,865 (50%)	181,656 (51%)	236,736 (54%)

A2.4 Baseline emission scenarios from 1990–2050

Chapter 2 presents emissions from 2010 onwards. It has a distinctive regional focus to link the data with the SLCF work of the Arctic Council. However, the original emissions datasets start from 1990 onwards, and were developed and operate at the sub-national or national level. Examining the period between 1990 and 2010 indicates that, in Arctic Council Member states, BC emissions approximately halved, and SO_2 emissions reduced by about two thirds. After an initial 25% decline between 1990 and 2000, CH_4 emissions started to steadily increase, with the rise projected to continue until 2050. The trends are different in the Arctic Council Observer countries. Here, between 1990 and 2010, BC emissions were stable, while those of SO_2 and CH_4 increased by approximately 10% and 20%, respectively.

Figure A2.2 Trends in emissions of SLCFs for Arctic Council Member states (left) and Observer countries (right) between 1990 and 2050 under the scenarios: CLE (CLE = current legislation; assumes recent policies implemented, including Nationally Determined Contributions [NDCs] of Paris Climate Agreement); NFC (NFC = no further control; assumes failure of recent policies); NFC_CPS (CPS = current policy scenario; with NDCs excluded); and V5a (represents the emissions trajectory driven by International Energy Agency projections and air-pollutant legislation that was current during the AMAP 2015 assessment).

A2.5 Spatial changes in emissions

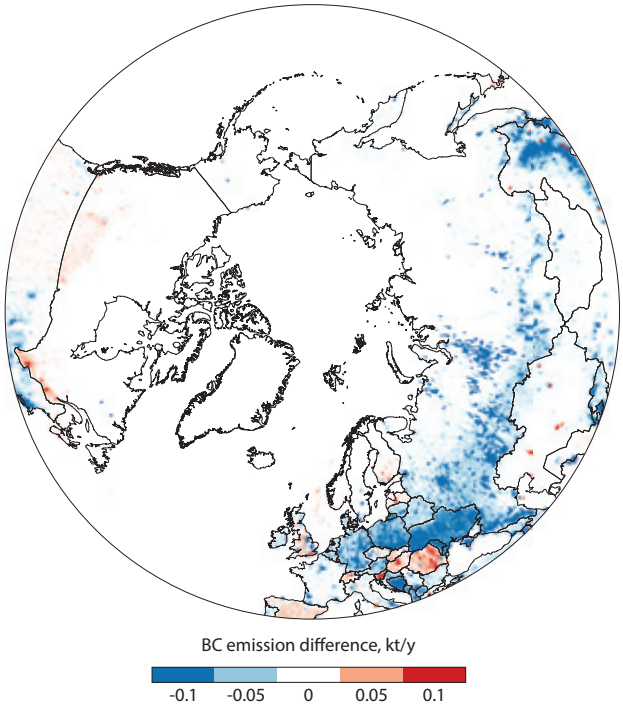

Figure A2.3 Difference in BC emissions in kilotons per year (kt/y) between 1990 and 2000

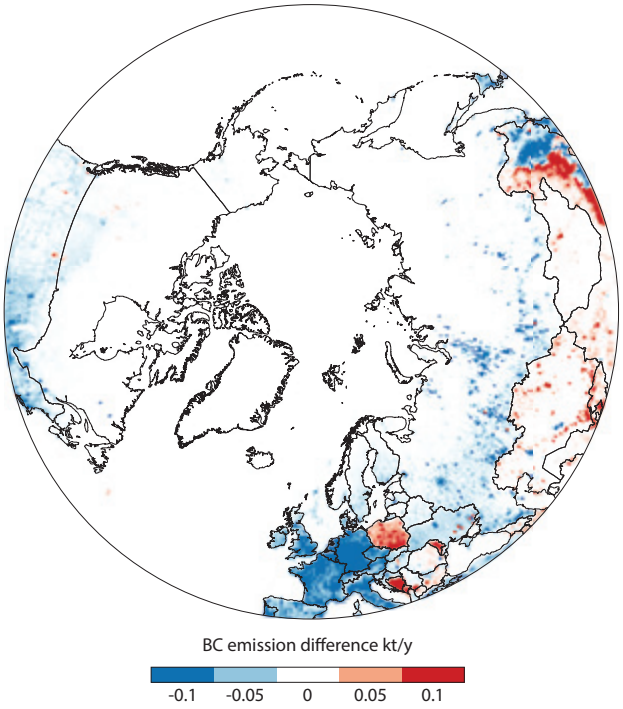

Figure A2.4 Difference in BC emissions in kilotons per year (kt/y) between 2000 and 2015

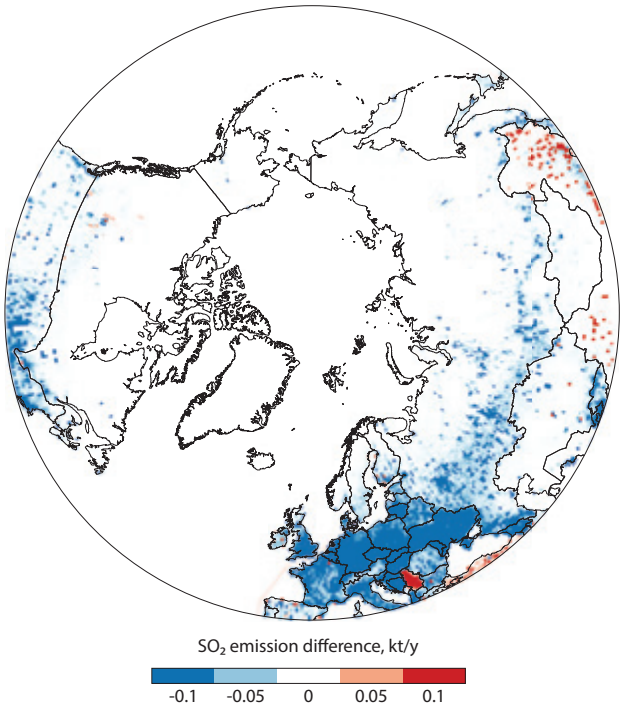

Figure A2.5 Difference in SO_2 emissions in kilotons per year (kt/y) between 1990 and 2000

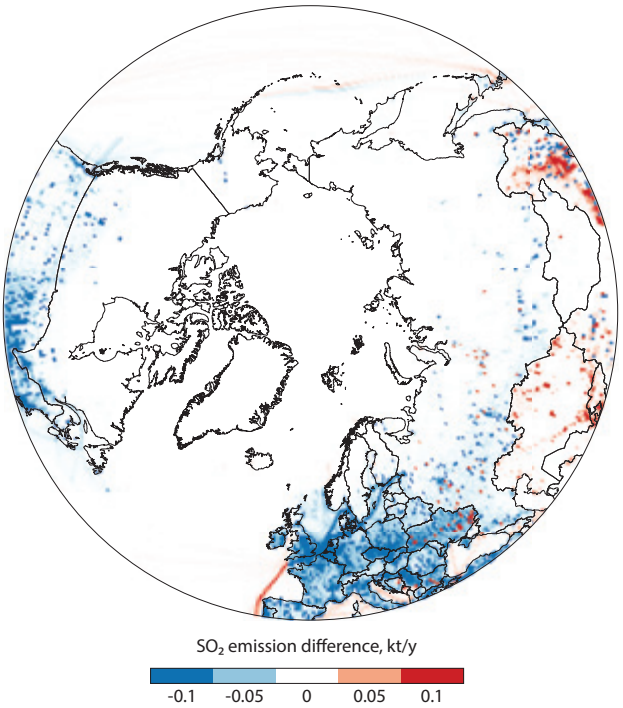

Figure A2.6 Difference in SO_2 emissions in kilotons per year (kt/y) between 2000 and 2015

3. Natural sources of methane within the Arctic

Authors: Frans-Jan W. Parmentier, Torben R. Christensen, Brett F. Thornton

3.1 Introduction

Sources of methane (CH_4) within the Arctic are predominantly natural (AMAP, 2015b). Wetlands and lakes, which cover large expanses of the region, emit CH_4 to the atmosphere, as does the Arctic Ocean. Aside from a few limited areas in which fossil-fuel extraction takes place, the region has little human activity that releases CH_4 to the atmosphere. These characteristics stand in contrast to the black carbon (BC) that affects the Arctic, sources of which are primarily anthropogenic and originate from outside the region. Acknowledging these differences, this section focuses on natural sources of CH_4 in the Arctic that originate from marine, freshwater and terrestrial environments. Anthropogenic CH_4 emissions – of Arctic and non-Arctic origin – originating from within the borders of the Arctic nations are discussed in Chapter 2.

3.1.1 Terrestrial and freshwater sources and sinks

Early studies of global atmospheric CH_4 identified wetlands as a major natural source (Ehhalt, 1974). The overall emissions values calculated by these studies, of 140–280 teragrams of CH_4 per year (Tg CH_4/y), are still within the uncertainty range for the total estimates of CH_4 in the most recent budgets (Christensen, 2014; Saunois et al., 2020). Although these global emissions are dominated by tropical wetlands, which contribute about 65% (Saunois et al., 2020), a considerable amount comes from northern wetlands, including wet tundra and surrounding environments. The overarching context for these substantial emissions is the waterlogged nature of organic soils in the Arctic, which host stable anaerobic environments with optimal conditions for methanogenic activity.

Such anaerobic conditions exist below the water table, where CH_4 is produced from soil organic matter by archaea (single-celled prokaryotic organisms that are distinct from bacteria). In places where the water table drops below the surface, CH_4 may be oxidized into CO_2 by other microorganisms when it diffuses upwards through the aerobic top layers of the soil. However, it may also bypass this zone when channelled through plant tissues or by bubbling upwards through the process of ebullition (Christensen et al., 2003; Ström et al., 2003). The microbial processes of methanogenesis (production) and methanotrophy (consumption) are both temperature dependent, with the position of the water table being dominant amongst controls on their relative importance (Olefeldt et al., 2013). The production of CH_4 in lakes and ponds follows the same pathway as in wetlands, but ebullition comprises a relatively larger fraction of the emissions to the atmosphere from lakes, since diffusive CH_4 fluxes can be oxidized more readily in lake surface waters (Walter et al., 2008a; Wik et al., 2016b). Compared to emissions

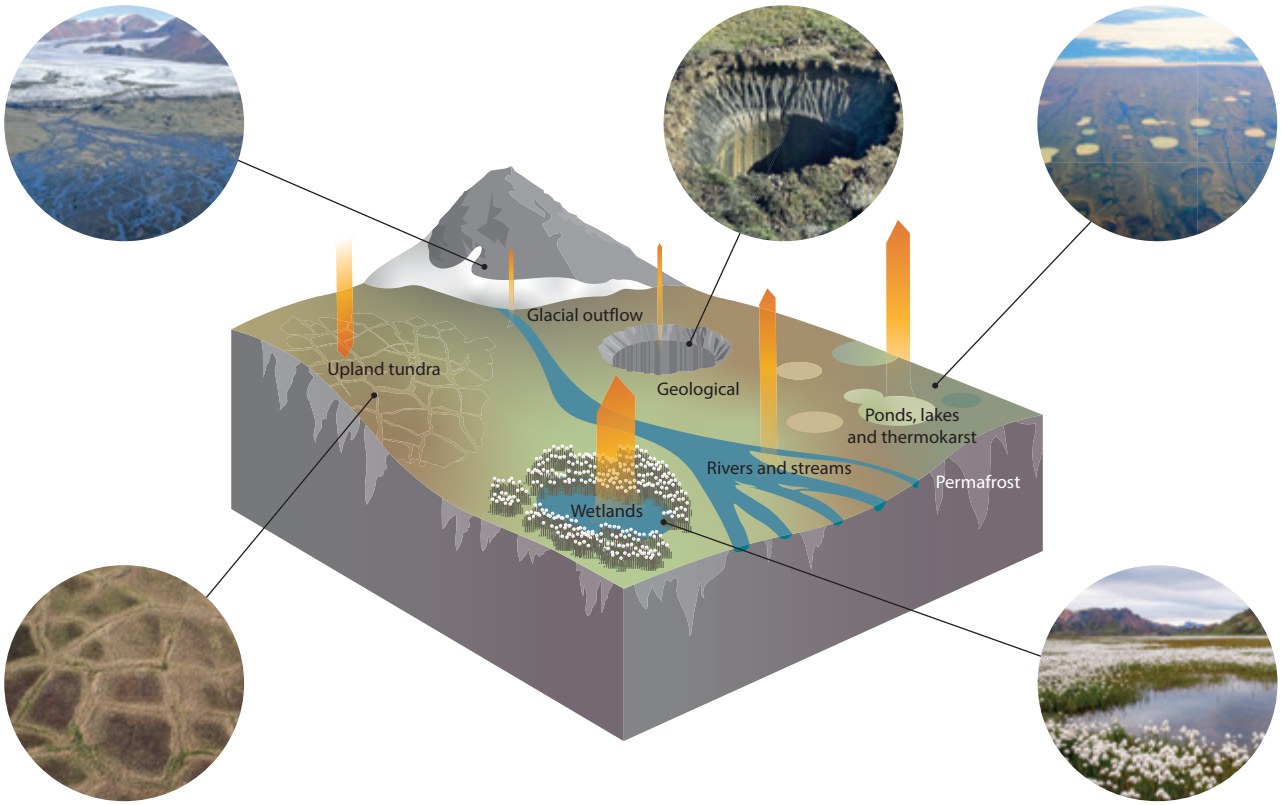

Figure 3.1 An overview of the diversity in natural sources and sinks of methane (CH_4) in the terrestrial Arctic. The widths of the arrows provide a very rough indication of the relative importance of each component, given the high uncertainties in estimates of their actual magnitude.

from tropical wetlands, which are heavily influenced by seasonal flooding, wet northern source areas tend to be more stable in their extent, with emissions subject to the balance between CH_4 production at depth and microbial oxidation in aerobic surface layers (Reay et al., 2010). Many factors – such as the available nutrients, vegetation composition, soil carbon content, topography and hydrology – modulate the size of emissions. However, a stable, non-tidal, natural wetland will under normal circumstances always be a source of atmospheric CH_4.

Within the context of the wider landscape, the constantly emitting wet-soil environments are surrounded by and intermixed with uplands, glaciers, lakes and rivers as depicted in Figure 3.1. As these all have distinct, and sometimes very different, CH_4 flux characteristics, spatial detail is needed to estimate landscape-wide emission estimates. This is particularly important in areas where small lakes and ponds abound; these water bodies are poorly constrained, which may lead to the double-counting of emissions, inflating budget estimates (Thornton et al., 2016a). Due to this high heterogeneity of CH_4 sources, large temporal and spatial uncertainties exist in estimates of overall composite landscape emissions. Therefore, new observations of unexpected fluxes remain possible.

Recently, glacial outflow of CH_4 has been identified as a hitherto unknown source of atmospheric CH_4 in the terrestrial domain (Christiansen and Jørgensen, 2018; Lamarche-Gagnon et al., 2019), although its relative contribution to the Arctic CH_4 budget appears minor since it is restricted to areas of rapid glacier or ice-sheet retreat. Another interesting new discovery is that of crater-like formations, tens of meters across and deep, in Siberian Russia – notably on the Yamal Peninsula (Bogoyavlensky et al., 2020). It has been suggested that they are the result of explosive degassing events, or cryovolcanism, although the exact mechanism for their formation remains under debate (Buldovicz et al., 2018; Bogoyavlensky et al., 2020). The dramatic and sudden appearance of these craters in the landscape, and the high CH_4 concentrations measured within them, have attracted much media attention. However, they do not seem to represent a significant new source of CH_4 to the atmosphere, given their seemingly limited extent and indications that they may revert to lakes a few years after formation (Chuvilin et al., 2020).

Most uncertainties in the Arctic CH_4 budget arise from temporal and spatial shortages in current monitoring efforts. Once CH_4 enters the atmosphere, it can be taken up again by drained upland soils and oxidized by methanotrophs, which may lower estimates when included in models (Oh et al., 2020). However, these areas are often overlooked in observational studies. The winter period is also under-sampled, even though the cold season may account for up to half of annual emissions (Treat et al., 2015). Short-lived pulses caused by freeze-thaw actions can contribute significantly to cold season emissions, but observations remain sparse (Mastepanov et al., 2013; Pirk et al., 2015; Raz-Yaseef et al., 2017). The extent to which observed CH_4 emissions are due to the release of ancient carbon from thawing permafrost soils remains uncertain, although site-level studies have shown that most CH_4 comes from modern carbon (Cooper et al., 2017). Improved mapping of Arctic landscapes and year-round monitoring are needed to provide more accurate budget estimates.

3.1.2 Marine sources and sinks

How CH_4 is produced, consumed and transported differs significantly between terrestrial and marine environments. Some similarity exists on the production side, since methanogens produce CH_4 in ocean sediments (Garcia et al., 2000), but thermogenic processes are also an important producer of CH_4 deep down in the ocean sediment (Archer, 2007). When CH_4 of biogenic or thermogenic origin migrates up towards the sea floor, it can be captured in gas hydrates (crystalline compounds that are stable under high pressure and low temperatures [Buffett, 2000]), or geological traps, and it can be anaerobically oxidized in the sulfate-methane transition zone near the ocean floor (Knittel and Boetius, 2009). In areas with high production or hydrate dissociation, this transition zone may be bypassed, with CH_4 bubbles escaping the seafloor through gas seeps and entering the water column. Whether this CH_4 reaches the atmosphere depends on the rate of dissolution of CH_4 from these bubbles into the ocean water (Rehder et al., 2009), and the amount of aerobic CH_4 oxidation in the water column (Steinle et al., 2015). The importance of these processes depends on water depth, since the probability of CH_4 dissolving into and microbially oxidizing in the ocean (Valentine et al., 2001) before reaching the atmosphere becomes greater with increasing depth. Finally, in the mixed surface layer, CH_4 can be produced aerobically (Damm et al., 2010) or, alternatively, taken up from the atmosphere in undersaturated areas. An overview of the processes that lead to the formation, oxidation and migration of CH_4 in the ocean and its sediments is depicted in Figure 3.2.

3.2 Natural methane sources: estimates from observations and process models

3.2.1 Terrestrial methane emissions

From a ground-based measurement perspective, extrapolated estimates of northern wetland emissions have, for a long time stayed between 20 and 100 Tg CH_4/y. Sebacher et al. (1986) estimated that Arctic and boreal wetlands contributed 45–106 Tg CH_4/y, while Crill et al. (1988) estimated that 72 Tg CH_4/y came from undrained peatlands north of 40°N. Whalen and Reeburgh (1992) derived an estimate of 42±26 Tg CH_4/y, from their measurements in wet-meadow and tussock-shrub tundra, and Christensen (1993) estimated 20±5 Tg CH_4/y from measurements taken in comparable habitats in the Alaska North Slope region. Reviewing the literature available at the time, Bartlett and Harriss (1993) estimated mean emissions from wetlands north of 45°N to be 38 Tg CH_4/y – a value not far from the early estimates of 42–45 Tg CH_4/y made using inverse modeling for the northern hemisphere to derive an estimate for total emissions (Chen and Prinn, 2006).

All of these early, mostly ground-based, extrapolated estimates lie at the higher end of the ranges that emerged once dynamic process models capable of simulating CH_4 emissions became available. Historically, these models focused on wetlands; not only did these ecosystems represent the largest source of CH_4 in the Arctic but they provided a longer and more extensive record of observations for testing and validating the models.

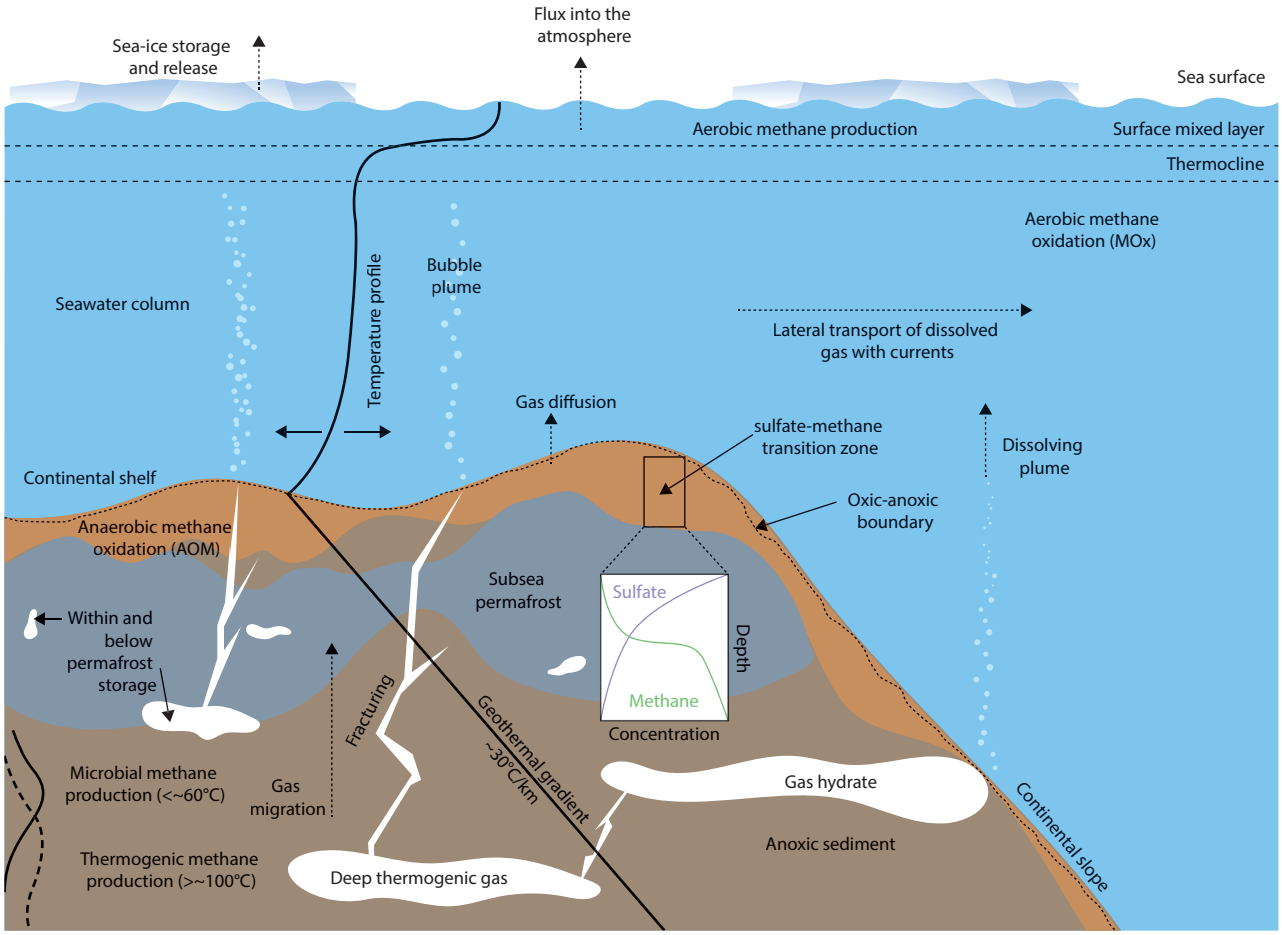

Figure 3.2 Typical areas of CH_4 production, oxidation and migration within the ocean and subsea sediments (not drawn to scale).

One of the earliest modeling attempts to establish a budget for northern wetlands modified a vegetation model by allocating a fixed fraction of heterotrophic respiration to CH_4 production (Christensen et al., 1996). This built upon the assumptions that CH_4 production generally correlates with net primary production (NPP – the amount of CO_2 taken in by vegetation through photosynthesis, minus that released by plants through respiration) and that forested and open wetlands each showed a narrow range of CH_4/CO_2 ratios. This study estimated that wetlands north of 50°N emitted 20±13 Tg CH_4/y. Surprisingly, this was comparable to the 21.3 Tg CH_4/y estimated by a more process-based study released in the same year, which modeled CH_4 production in relation to soil and vegetation carbon pools, temperature and the position of the water table (Cao et al., 1996). Nonetheless, both of these estimates were lower than the ~35 Tg CH_4/y that atmospheric inversions and extrapolations from flux measurements indicated at the time (Christensen et al., 1996).

The representation of CH_4 production and consumption in these early model runs was rudimentary. This meant they were mostly useful to estimate steady-state budgets rather than the response of wetland emissions to future change. Seeking to overcome this limitation, Walter and Heimann (2000) designed a CH_4 model that improved upon these pioneering studies, and was both process-based and climate sensitive. This made it useful for studies of global change. Production and consumption of CH_4 were modeled as temperature-sensitive processes, while diffusion, transport via plants and ebullition were explicitly represented. Most CH_4 schemes that are used in land-surface models today incorporate some or all of the concepts introduced by the studies above (see e.g. Kaiser et al., 2017; Parmentier et al., 2015; Wania et al., 2010, 2013; Zhuang et al., 2004). Moreover, new processes continue to be added, such as the inclusion of microbial mechanisms (Xu et al., 2015), sensitivity to pH (Zhuang et al., 2004) and improved oxidation of atmospheric CH_4 in upland soils (Oh et al., 2016). These continued improvements to how processes are represented has made CH_4 models capable of estimating CH_4 emissions, and their outputs compare well to field observations made at the site level (see e.g. Treat et al., 2018b).

Efforts to obtain accurate budgets for the entire terrestrial Arctic have been hampered by a lack of knowledge on the total surface area of wetlands and where they are located. It is telling that, despite valuable attempts to overcome this challenge, the global wetland map presented in the seminal paper by Matthews and Fung (1987) was still in use several decades later (see e.g. McGuire et al., 2012; Parmentier et al., 2015). This was mostly due to a lack of alternatives proven to perform substantially better in the Arctic. Depending on the prescribed wetland extent, budget estimates can easily vary by a factor of four (Petrescu et al., 2010). Still, even if static wetland maps were perfect representations of the location of current wetlands, it could not be expected that this extent would stay constant for decades – especially under a changing climate. This hampers the modeling of an accurate transient response.

In recent years, this problem has been tackled by combining the knowledge gleaned from static wetland maps with that of the dynamics of surface-inundation products derived from microwave remote sensing data (Poulter et al., 2017). In practice, this is a shift away from defining wetlands ecologically, such as by vegetation composition, to describing them in relation to a physical property, such as the water table. However, this method assumes that wetlands do not emit CH_4 in winter when soil water is frozen, even though up to half of annual emissions from permafrost wetlands may originate from deeper unfrozen layers during the winter (Mastepanov et al., 2008; Treat et al., 2018a; Zona et al., 2016). Despite these limitations, though, combining wetland maps with inundation products is a valuable advance from the perspective of modeling global emissions of CH_4.

The study by Saunois et al. (2020) is one of the most recent applications of a hybrid wetland and inundation product. The authors used the global remote-sensing-based Wetland Area Dynamics for Methane Modeling (WAD2M) dataset with 13 biogeochemical models to determine global wetland emissions. For the region north of 60°N, these models estimated that wetlands emitted 9 [2–18] Tg CH_4/y in the time period 2008–2017. This is more than three times lower than the 35 [21–47] Tg CH_4/y estimate derived using two process models for the significantly smaller area of Arctic tundra (McGuire et al., 2012). This lower estimate was likely influenced by two main factors. First, WADM2 has a lower wetland extent at high latitudes than the previously used Sustainable Wetlands Adaptation and Mitigation Program – Global Lakes and Wetlands (SWAMPS–GLWD) monthly wetland dataset (Saunois et al., 2016a). This is due to the subtraction of surface area covered by ponds and small lakes to avoid double-counting (Thornton et al., 2016a). Second, the exclusion of frozen soils also reduced the extent of CH_4-emitting wetlands in the winter, which may have led to an underestimation of fluxes. While observations of winter fluxes remain limited, a recent study estimated that, for the region north of 60°N, they may contribute as much as 1.6±0.6 Tg CH_4/y (Treat et al., 2018a). Then again, biogeochemical models may also underestimate the oxidation of atmospheric CH_4 in drained upland soils by as much as 5.5 Tg CH_4/y for the area north of 50°N (Oh et al., 2020). These errors cancel each other out to some extent, and the estimate by Saunois et al. (2020) could therefore be relatively close to the emissions from Arctic wetlands minus the uptake by drained uplands.

3.2.2 Freshwater methane emissions

Freshwater systems (lakes, ponds, rivers, streams) are abundant in the Arctic, and are subject to strong seasonal variability in their CH_4 emissions due to freeze-thaw cycles. Although formerly thought to be mostly inert during the ice-covered or winter season, it is now well known that CH_4 is actively produced and destroyed in below-ice processes, with a rapid release of stored CH_4 at spring thaw (Jammet et al., 2015). The dynamic nature of these systems, combined with the fact that current freshwater studies are taking place within a wider landscape that is already experiencing effects from climate change (Callaghan et al., 2010), complicates interpretation of observations when extrapolating to the Arctic as a whole.

3.2.2.1 Lakes and ponds

Wik et al. (2016a) elevated the relative importance of lakes and ponds as a source of CH_4 in the Arctic, when they derived a pan-Arctic estimate of emissions from these bodies of 16.5 Tg CH_4/y. Although the overlapping and conflation of small, shallow lakes and ponds with wetlands, and lake-wetland interface zones, continued to be a challenge (Thornton et al., 2016a), this estimate by Wik et al. (2016a) indicated that CH_4 emissions from Arctic lakes were of a similar magnitude to those from wetlands. Local hydrology is a key regulator of carbon cycling and CH_4 emissions in landscapes underlain by thawing permafrost. For example, terrestrially produced CH_4 can be transported from the active layer within wetlands into lakes via groundwater flow (Paytan et al., 2015).

Large numbers of Arctic lakes lie in thermokarst environments, which are characterized by the thawing of ice-rich permafrost and subsequent surface subsidence. Such lakes are often quite shallow, which makes them more vulnerable to heating and increased permafrost thaw taking place below and around them under climate warming (e.g. Arp et al., 2016). The net contribution of small lakes and thaw ponds has proven difficult to determine; such lakes are numerous and rich in dissolved organic carbon (DOC) and CH_4 (e.g. Langer et al., 2015; Wik et al., 2016a). However, one recent study of lakes in the West Siberian Lowlands (a well-known major terrestrial wetland CH_4 source) found only a minimal contribution to total CH_4 from the small thaw lakes within this landscape (Polishchuk et al., 2018).

Similar to wetlands, it has become more recognized in recent years that, during the so-called 'edge' seasons of spring and autumn, lakes can be major and variable contributors to total annual CH_4 emissions, depending on lake ice-out and freeze-up conditions. Moreover, these edge seasons are anticipated to experience the most dramatic warming changes in the future, as ice-free seasons of lakes are extended. Year-round eddy covariance observations have demonstrated that lake spring CH_4 efflux varies from year to year (Jammet et al., 2015, 2017), being lower in years with less snowmelt (Jansen et al., 2019). Spring contributions to total annual emissions vary hugely (from 4% to 74%) between years (Denfeld et al., 2018a), driven by the build-up of sub- and within-ice CH_4 over winter (e.g. Juutinen et al., 2009; Walter Anthony and Anthony, 2013; Wik et al., 2011; Langer et al., 2015; Denfeld et al., 2018b). Although the spring emission of CH_4 was once thought to be a single large burst or pulse at ice-out and lake overturn (mixing of the entire water column), recent measurements have shown more variability (Denfeld et al., 2015).

CH_4 emissions from lakes occur via various pathways (Bastviken et al., 2004). Ebullition- and turbulence-driven diffusion are generally the most important, although very shallow lakes can contribute substantial emissions via transport through vascular plants. Ebullition is historically the most difficult to quantify, due to its episodic and often stochastic nature. Approaches have included ice-bubble surveys of frozen lakes (Walter Anthony et al., 2010; Wik et al., 2011), bubble traps (e.g. Wik et al., 2013; Walter et al., 2008a), and synthetic aperture radar surveys of frozen lake surfaces (Walter et al., 2008b; Engram et al., 2020). The high temporal variability of ebullition, combined with the difficulty and expense of long-

term ebullition sampling from lakes in the Arctic, has likely led to many studies underestimating CH_4 emissions from lakes (Wik et al., 2016b).

The development of large lake-site-specific datasets (e.g. Jansen et al., 2020) has facilitated detailed analysis of how different regulators of CH_4 emissions, such as wind shear and temperature, control emissions over short and long timescales. Proposed controls for ebullition include the energy input to lakes (Wik et al., 2014), as well as temperature and lake productivity (DelSontro et al., 2016). Shallow lakes in permafrost regions appear more vulnerable to warming (Arp et al., 2016), while all lakes are experiencing increased energy input due to longer ice-free seasons (Wik et al., 2014; Thornton et al, 2015). These observations indicate that lakes will become a sustained CH_4 source under climatic warming (Wik et al., 2018), a prediction not confined to the Arctic (see e.g. Zhu et al., 2020).

3.2.2.2 Streams and rivers

A compilation of measurements from freshwater fluvial systems indicated that 7.5 Tg CH_4/y are emitted from streams and rivers alone north of 66°N (Stanley et al., 2016; Thornton et al., 2016a). This figure was 25 times higher than a similarly derived earlier estimate of 0.3 Tg CH_4/y (Bastviken et al., 2011). Both compilations were quite limited in their number of observations. However, the influence of large freshwater fluvial systems on coastal marine CH_4 cannot be understated, as large increases in dissolved CH_4 in surface waters have been frequently observed near major river outlets (Bussmann, 2013; Shakhova et al., 2010a,b; Kohnert et al., 2017; Schneider et al., 2014).

3.2.2.3 Process modeling of methane emissions from freshwater sources

While many advances have been made in simulating the biogeochemistry of wetlands and their extent, very few studies have attempted to model CH_4 emissions from lakes – and even fewer have been able to estimate a budget for lakes across the entire Arctic. One of the few studies that did attempt this estimated the pan-Arctic budget to be 11.9 [7.1–17.3] Tg CH_4/y (Tan and Zhuang, 2015). In this model, CH_4 production in lake sediment, and transport through diffusion and ebullition, were explicitly represented (Tan et al., 2015). Since there are no other comparable lake models that have been used at the pan-Arctic level, and limited validation data exists, this number is uncertain but it compares reasonably well to the above-mentioned bottom-up estimates based on extrapolations of flux measurements (Bastviken et al., 2011; Saunois et al., 2020; Wik et al., 2016a). Ongoing development, such as the integration of nutrient loading and primary production into models, (see e.g. Bayer et al., 2019), will lead to more precise simulations of the Arctic freshwater budget and its transient response to climate change.

3.2.3 Marine methane emissions

Not long ago, marine emissions of CH_4 to the atmosphere were thought to be almost negligible globally, and were not considered to have contributed to recent atmospheric CH_4 increases (Reeburgh, 2007). This point of view was reasonable, as ocean water and sulfate-rich seawater in sediments are hostile to CH_4, rapidly dissolving any of the gas contained in small bubbles and then readily oxidizing it into CO_2 once dissolved. Seafloor vents of CH_4 and its widespread production in and release from the oxic surface layer of the ocean, while scientifically interesting, were not seen as liable to change under a warming climate. In the Arctic seas, early measurements supported this view (Kvenvolden et al., 1993). However, over the past decade, this view has shifted, especially regarding emissions from shallow seas where the water-column depth is more favorable for mixing dissolved or bubbled CH_4 out of the water and into the atmosphere (McGinnis et al., 2006). It is clear that some CH_4 from seafloor gas seeps reaches the atmosphere via bubble transport (Leifer and Patro, 2002), although the total amount of CH_4 reaching the atmosphere via this pathway is controversial.

The Arctic Ocean has extensive shelf seas that are relatively shallow (Jakobsson, 2002), with known large petroleum basins (Cramer et al., 2005), and subsea permafrost that contains large amounts of frozen organic material laid down when the land was exposed to the air in previous ice ages (Romanovskii et al., 2000). Even larger stores of CH_4 exist as methane hydrates (clathrates), a solid methane-water compound that is stable at great depths (Romanovskii et al., 2005; Ruppel and Kessler, 2017). Despite these large potential sources of CH_4, loss processes in the sediment (e.g. Overduin et al., 2015; Stranne et al., 2019) limit present-day CH_4 releases to the ocean water, and ultimately the atmosphere. The past decade has seen a wide variety of estimates put forward for present-day CH_4 emissions from the Arctic Ocean – and considerable uncertainty remains – but the most recent studies have supported total emissions of less than 10 Tg CH_4/y, with most studies pointing to less than 5 Tg CH_4/y. Significant uncertainty remains about the net emissions from the surface waters from the Arctic Ocean proper, and how that may change in the future. Finally, it is worth noting that reductions in sea-ice coverage will likely affect not only marine CH_4 emissions, but also terrestrial Arctic CH_4 emissions. This is because the sea-ice albedo effect increases atmospheric warming, which ultimately extends to the land (Parmentier et al., 2013, 2015).

3.2.3.1 East Siberian Arctic Shelf and other marine regions

Interest continues to be focused on shallow shelf areas of the Arctic seas, especially the East Siberian Arctic Shelf (ESAS; consisting of the Laptev, East Siberian, and in most definitions, the Chukchi Sea), for example as in Kosmach et al. (2015). Emissions are, in some areas, enhanced by direct bubble transport from the sediment to the atmosphere, and resupply of CH_4 to surface waters by dissolving bubbles. Berchet et al. (2016) used a regional inverse model to propose that ESAS emissions had been overestimated in early studies, and suggested a range of 0–4.5 Tg CH_4/y. A global modeling study (Warwick et al., 2016) indicated that Arctic wetland emissions would have to be overestimated to accommodate the previously suggested large ESAS emissions. Thornton et al. (2016b) used surface water and atmospheric measurements in the central ESAS to suggest 2.9 Tg CH_4/y from the ESAS region, dramatically lower than earlier estimates of 17 Tg CH_4/y (Shakhova et al., 2014).

Meanwhile, an eddy covariance-based study (Thornton et al., 2020), estimated 3.02 Tg CH_4/y for the ESAS, even though emission 'hotspots' above seafloor gas seeps reached emission rates of >600 milligrams per square metre per day (mg/m^2/d) – roughly an order of magnitude higher than onshore sources. The apparent spatial rarity of these large emissions seems to limit their influence at the regional scale.

The ultimate source of emissions from marine shelf areas has been controversial. CH_4 could conceivably originate from organic material eroded from thawing permafrost onshore, thawing submerged permafrost, surface seawater CH_4 sources (see below), sub-seafloor transport of CH_4-rich terrestrial freshwater (Charkin et al., 2017), or deep thermogenic (petroleum-associated) sources. The existence of extensive petroleum sources in the ESAS is well established (Cramer and Franke, 2005). However, the presence of vast subsea petroleum reserves is not enough to imply that emissions of CH_4 are being released to the atmosphere. For example, while old thermogenic CH_4 is present at depth on the petroleum-rich Beaufort Shelf, it does not reach the surface and atmosphere in substantial quantities (Sparrow et al., 2018). Nonetheless, a study of carbon-14 (C^{14}) in CH_4 and stable methane isotopologues from water samples collected near a large gas seep in the outer Laptev Sea has also pointed to a deep thermogenic source (Steinbach et al., 2021). Measurements in other regions of the Arctic – primarily in the North American Arctic (Fenwick et al., 2017) and near Svalbard (Westbrook et al., 2009; Lund Myhre et al., 2016) – have revealed much smaller CH_4 emissions to the atmosphere than from the ESAS. In one study conducted in the waters near Svalbard, CO_2 uptake from the atmosphere above active seafloor CH_4 seeps resulted in a net negative radiative forcing, despite some CH_4 reaching the atmosphere (Pohlman et al., 2017).

3.2.3.2 Gas hydrates

For decades, the concept of large-scale releases of CH_4 from subsea hydrates to the atmosphere in rapid cataclysmic events, has been seen as a potential climate tipping point (e.g. Nisbet, 1990; Dickens, 2003; Dickens, 2011). Such methane hydrates are present beneath the Arctic continental shelves, and can be exposed on some Arctic continental slopes (e.g. Westbrook et al., 2009). However, due to the processes that destroy CH_4 in the ocean water (explained in Section 3.1.2), the scale of hydrate emissions reaching the atmosphere is thought to be relatively insignificant (James et al., 2016). Nonetheless, uncertainties remain with respect to hydrate stabilities and rapid transport through sediments under certain circumstances (Stranne et al., 2017). Over glacial-interglacial cycles, the expansion and contraction of massive ice sheets has modulated the location of the hydrate stability zone (e.g. Portnov et al., 2016). The current understanding from modeling is that CH_4 releases from hydrates under a warmer climate will most likely take place over timescales of centuries or millennia (Kretschmer et al., 2015; Archer, 2015).

3.2.3.3 Emissions from the ocean surface

In the central Arctic Ocean, where deep water prevents seafloor CH_4 sources from reaching the atmosphere, the connection between below-ice CH_4 production and the more general 'marine methane paradox' of CH_4 production in oxygenated surface waters remains somewhat unclear. However, Damm et al. (2010) proposed a model whereby phosphate-poor, Pacific-origin seawater led to more near-surface CH_4 production than phosphate-rich, Atlantic-derived seawater.

Sea ice may modulate emissions of CH_4 from the ocean surface (Damm et al., 2015), with polynya openings within ice potentially emitting CH_4, even during winter (Damm et al. 2007; Shakhova et al., 2010b). Aircraft measurements have demonstrated CH_4 emissions from ice leads (long, linear fractures) in the deep Arctic Ocean. These areas seem unlikely to be influenced by seafloor CH_4 sources (Kort et al., 2012), although the Transpolar Drift (a major current in the Arctic Ocean) seems to move some dissolved CH_4 from shallow shelf seas to the central Arctic Ocean (Damm et al., 2018). The discovery of supersaturations of CH_4 under sea ice in the ESAS (Shakhova et al., 2010a,b) and in the Canadian Arctic (Kitidis et al., 2010) support the idea of wintertime accumulation and later release of CH_4.

Recent studies show that the production of CH_4 in oxic surface waters is more prevalent than previously believed (Bižić et al., 2020; Klintzsch et al., 2020) and this provides a likely additional source of CH_4 from the marine environment in the Arctic. However, the scale of this process in the Arctic marine environment and the amount it contributes to the atmosphere remain to be quantified.

3.2.3.4 Process modeling of methane emissions from marine sources

While detailed biogeochemical models exist to estimate terrestrial sources of CH_4 to the atmosphere, the situation is quite different for the Arctic Ocean. Although the presence and evolution of gas hydrates has been modeled in great detail (Archer, 2015; Kretschmer et al., 2015), these models typically calculate the release of CH_4 into the ocean, not the atmosphere. Since the ocean is an efficient filter for CH_4 (Reeburgh, 2007), even when CH_4 is released from the seafloor as bubbles (Sparrow et al., 2018), only a small amount is expected to reach the atmosphere. At the same time, there is a paucity of reliable data and insufficient understanding of related processes to parameterize and validate models. More knowledge is needed on the depth and location of gas hydrates, the carbon content of the sediment, the extent of subsea permafrost, the thickness of the sulfate-methane transition zone, the oxygen content of the water column at different depths, and the influence of sea ice and microbial processes on CH_4 production in surface waters.

Because of these issues, there are no process models that can deliver a reliable estimate of the total release of CH_4 from the Arctic Ocean to the atmosphere, although models are useful to study the interaction of processes and their hypothetical impact on the atmospheric budget (see e.g., Wåhlström and Meier, 2014). Other approaches, such as machine learning, can provide insights in the meantime. A recent machine learning-based study (Weber et al., 2019) compiled surface seawater CH_4 concentration measurements globally from the MarinE MethanE and NiTrous Oxide data collection (MEMENTO) database (Data ref. 3.1; Kock and Bange, 2015) and suggested

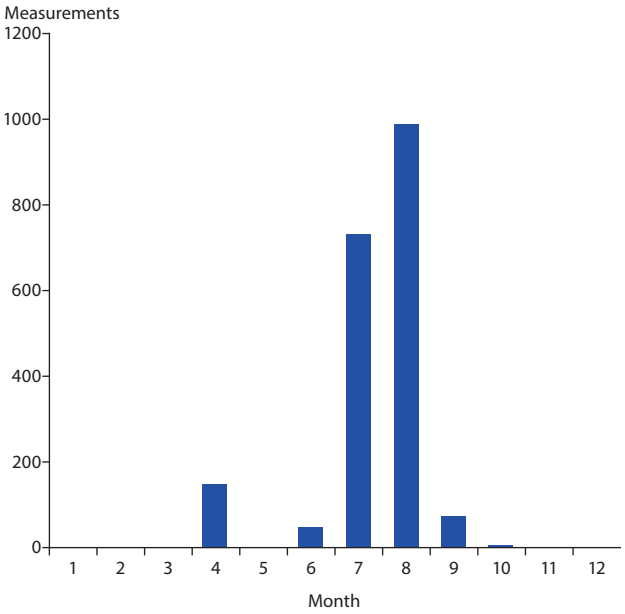

Figure 3.3 CH_4 measurements in Arctic marine surface water (<10 m depth) at >60°N as of September 2020, from the MEMENTO database of global marine methane measurements (Kock and Bange, 2015). Measurements were made almost entirely in July and August, with almost no sampling during the edge or winter seasons.

that a strong correlation existed between surface ocean CH_4 emissions and NPP. This may be a way forward for the modeling of CH_4 emissions from the Arctic Ocean, although it remains unclear how this correlation plays out in regions with seasonal sea-ice cover. The vast majority of Arctic marine CH_4 measurements have been collected during the Arctic summer season (Figure 3.3). Additionally, the Arctic marine environment is undergoing dramatic changes in seasonal ice-cover extent and thickness, which are predicted to continue (e.g. Barnhart et al., 2016). Incorporating these disparate effects into models remains an enormous challenge.

3.2.4 Total natural methane emissions

Table 3.1 shows a range of CH_4 budget estimates from terrestrial, freshwater and marine sources, most of which have been published within the last ten years. These studies reflect the wide range of estimates currently present in the literature, and include both low and high estimates of CH_4 from Arctic sources. A simple average across these northern CH_4 budgets suggests that: terrestrial sources emit 23 [0–47] Tg CH_4/y; freshwater sources 18 [7–33] Tg CH_4/y; and the Arctic Ocean, including shelf seas, 7 [2–29] Tg CH_4/y. According to these estimates, the total budget for natural sources of CH_4 with a high northern signature is 49 [9–109] Tg CH_4/y.

Table 3.1 Estimates for the CH_4 budgets of terrestrial, freshwater and marine sources in the Arctic.

Source	Method	CH_4 emissions (Tg/y)	Study
Terrestrial			
Wetlands >60°N	Process models (13)	9 (2–18)	Saunois et al. (2020)
Wetlands >50°N	Process model (1)	31±5	Bousquet et al. (2011)
Wetlands and mineral soils >60°N	Process model (1)	21	Zhuang et al. (2004)
Wetlands and mineral soils >50°N	Process model (1)	29.3±3	Oh et al. (2020)
Tundra	Process models (2)	35 (21–47)	McGuire et al. (2012)
Tundra	Upscaled flux measurements	15 (0–29)	McGuire et al. (2012)
Freshwater			
Lakes and ponds >50°N	Upscaled flux measurements	16.5±9.2	Wik et al. (2016a)
Lakes and ponds >60°N	Process model (1)	11.9 (7.1–17.3)	Tan and Zhuang (2015)
Rivers and streams >54°N	Upscaled flux measurements	7.5	Stanley et al. (2016)
Rivers and streams >54°N	Upscaled flux measurements	0.3	Bastviken et al. (2011)
Marine			
Arctic Ocean + Beaufort and Chukchi Seas (<82°N)	Upscaled airborne flux measurements	2*	Kort et al. (2012)
East Siberian Arctic Shelf (ESAS)	Upscaled diffusive fluxes and ebullition measurements	17 (12.9–26.5)	Shakhova et al. (2014)
ESAS	Upscaled diffusive fluxes	2.9	Thornton et al. (2016b)
ESAS	Upscaled eddy covariance flux measurements	3.02	Thornton et al. (2020)
ESAS	Regional atmospheric inversion	0–4.5	Berchet et al. (2016)
ESAS	Regional atmospheric inversion	0.58±0.47	Tohjima et al. (2021)
Beaufort Sea	Upscaled diffusive fluxes	0.05	Lorenson et al. (2016)
Arctic Ocean (seas >60°N, ESAS excluded)	Regional atmospheric inversion	2 (1.7–2.2)**	Tohjima et al. (2021)

*2 Tg/y is upscaled from the emission rates given in Kort et al. (2012), extended for a year and scaled to the area they surveyed.

**Tohjima et al. (2021) reported 1.8±0.1 Tg CH_4/y for a September inversion and 2.1±0.1 Tg CH_4/y for a November inversion.

This estimate is double that indicated by global atmospheric inversions for the area north of 60°N (Saunois et al. 2020), which suggests that our central estimate is at the high end. However, some of the studies listed in Table 3.1 define the area between 50°N and 60°N latitude as part of the Arctic, which explains some of this discrepancy. The varying definitions of the Arctic domain by biome, permafrost status, watershed or latitude range make it difficult to directly compare source estimates. To compensate for this, this assessment included studies with a broad definition of the Arctic (>50°N), as well as those with a narrow definition, such as the tundra biome at sea level. The latter excludes the treeless tundra of northern highlands, despite having the same vegetation types and being of similar extent (Virtanen et al., 2016). Double-counting of sources is another factor that can contribute to overestimations by bottom-up methods (Thornton et al. 2016a). It is worth noting that the bottom-up-versus-top-down discrepancy observed in this chapter was also noted by Saunois et al. (2020), and that the AMAP assessment's central estimate is close to their bottom-up estimate of 43 [26–72] Tg CH_4/y – albeit with a higher uncertainty range. Global bottom-up estimates of natural CH_4 sources suggest a total budget of 371 [245–488] Tg CH_4/y (Saunois et al. 2020), which means that the Arctic constitutes 13% [10%–20%] of all global natural CH_4 sources – about 2.5 times lower than global emissions from fossil fuels.

3.3 Conclusions and recommendations

At present, the Arctic terrestrial and marine environment is most likely a modest source of CH_4 to the atmosphere of 49 [9–109] Tg CH_4/y. According to this study's central estimates, terrestrial ecosystems are responsible for around 48% of this budget; lakes, ponds and rivers approximately 37%, and the Arctic Ocean in the region of 15%. However, the absolute and relative sizes of these estimates carry high uncertainties. Despite decades of research on the processes that govern CH_4 emissions from northern wetlands, there is only medium confidence on the size of this source. Freshwater budget estimates are even less constrained and carry medium-to-low confidence, while there is low confidence in the proposed marine contributions. The reasons for these low confidence levels are many, but include the difficulty of performing fieldwork in the harsh Arctic environment, the high spatial heterogeneity of terrestrial and freshwater systems, and the inadequate accuracy of spatial datasets used for upscaling.

Since the 2015 AMAP assessment on Arctic methane was undertaken (AMAP, 2015b), progress has been made at the site level to attain year-round monitoring of CH_4 fluxes from terrestrial ecosystems (Treat et al. 2018a). There is now also increased airborne coverage at the regional level (Miller et al. 2019). And, remote sensing instruments – airborne or from orbital platforms – are increasingly capable of mapping CH_4-emitting landforms (see e.g., Elder et al., 2020; Engram et al., 2020). However, these studies still need to be validated with reliable ground-based monitoring, which remains sparse outside of Alaska and northern Scandinavia due to logistical limitations, such as transport and the availability of a stable power supply. Increased monitoring in Siberia and the Canadian Arctic (especially in carbon-rich landforms), aided by novel techniques, such as drone surveys, are essential to quantify pan-Arctic variability in CH_4 emissions from both terrestrial and freshwater systems. Equally important are greater efforts to place existing infrastructure in a wider regional context through an enhanced focus on capturing the high heterogeneity of Arctic landscapes (Siewert et al. 2021), and scaling this information up from the site level to the regional scale and the entire Arctic. Leveraging remote sensing products to develop high-resolution maps of CH_4-emitting landforms, such as fens, bogs, marshes, lakes and ponds, is essential to achieve this.

Significant advances have also been made in the marine domain over the past six years, where shipborne observations and atmospheric monitoring have delivered budget estimates for the ESAS that were much lower than previous studies (Berchet et al., 2016, Tohjima et al., 2021, Thornton et al., 2016b; 2020). This suggests that the Arctic Ocean is a rather small component of the global CH_4 budget, contributing less than 2% of natural CH_4 sources globally. However, it remains uncertain how these emissions will develop in the future in response to bottom-water warming, sea-ice decline and the thawing of subsea permafrost. Vast knowledge gaps remain on the drivers of marine fluxes, including the extent of gas hydrate deposits, the size of the vulnerable carbon pool in subsea permafrost, emissions rates from seafloor sediments to the ocean, and the fraction of CH_4 that may pass directly through the water column and reach the atmosphere. Quantification of these processes is essential and can provide data with which to validate models for simulating responses to climate change. A recent expert assessment suggests a moderate increase of 25% [13%–55%] could be expected this century under the strong warming scenario known as the Representative Concentration Pathway (RCP) 8.5 (Sayedi et al., 2020). However, marine emissions – given the small size of this source currently – would have to show an extraordinary rise, vastly exceeding this expert estimate, to strongly affect global atmospheric concentrations (Christensen et al., 2019).

Whether the Arctic will play a larger role in the global CH_4 budget with future climate change remains uncertain. This will strongly depend on whether the region continues to harbor environments favorable to methanogenesis, such as wetlands and lakes. If the Arctic becomes wetter as a result of climate change, it is anticipated that CH_4 emissions will rise with further temperature increases (Watts et al., 2014). If the Arctic becomes drier, CH_4 emissions may not increase at the same pace, although soil carbon could be respired by microorganisms and released as CO_2 instead (Schuur et al., 2015). Abrupt thawing of permafrost could further amplify the loss of soil carbon, a process which present-day Earth system models do not account for (Turetsky et al., 2020). Wetting and drying will also affect the natural release of nitrous oxide (N_2O) from the Arctic, emissions that probably take place across a quarter of the Arctic terrain (Voigt et al., 2017). To fully understand these feedbacks, and because of the close interactions among processes, we recommend that future assessments consider the full greenhouse gas budget of the Arctic – including the long-lived greenhouse gases CO_2 and N_2O.

At the pan-Arctic level, there is significant evidence for an increased seasonal cycle of CO_2, with an enhanced uptake in summer and a stronger release in winter. However, natural CH_4

emissions may only have increased marginally (Bruhwiler et al., 2021). This could change in the future, although likely scenarios of Arctic CH_4 release – from terrestrial, freshwater and marine sources – are lower than the maximum feasible reduction in CH_4 emissions from anthropogenic sources (Christensen et al., 2019). Reducing anthropogenic emissions carries the added benefit of reducing global warming, and lowering the risk of Arctic climate feedbacks, such as an increased release of CH_4 into the atmosphere.

Acknowledgments

Frans-Jan W. Parmentier received funding from the Research Council of Norway (grant agreement 274711) and the Swedish Research Council (registration number 2017–05268). Torben R. Christensen acknowledges Danish governmental support associated with the Greenland Ecosystem Monitoring program. Brett F. Thornton acknowledges support from the Swedish Research Council (registration number 2018–04350). The MEMENTO database is administered by the Kiel Data Management Team at GEOMAR Helmholtz Centre for Ocean Research and supported by the German Federal Ministry of Education and Research project Surface Ocean Processes in the Anthropocene (SOPRAN) (Data ref. 3.1).

4. Open biomass burning

Authors: Jessica L. McCarty, Sabine Eckhardt, Juha Aalto, Nikolaos Evangeliou, Justin J. Fain, Ari Venäläinen, Lin Huang, Zbigniew Klimont, Kaarle Kupiainen

4.1 Introduction

Open biomass burning is a known disturbance in the ecosystems of the Arctic Council region. Krylov et al. (2014) found that stand-replacement wildfires, fires that kill most aboveground vegetation and trigger ecological succession, are responsible for 66% of total forest disturbance in the Russian Federation. Results from the Global Fire Emissions Database Version 4s (GFED4s [including small fires]; Data ref. 4.1) found that between 1990 and 2016, fires in boreal forests of Russia and North America, but excluding Fennoscandia, accounted for 15% of global methane emissions (van der Werf et al., 2017). In terms of burned area, 2015 was the largest fire year for the southwestern Alaskan tundra ecoregion since monitoring by satellites began in 1971 (Michaelides et al., 2019). Recent evidence suggests that northern and Arctic ecosystems will become more susceptible to fire as the climate warms (York et al., 2017).

Broadly speaking, wildfire regimes are driven by climate and weather, fuels and fuel conditions, and the presence of people as ignition sources (Silva and Harrison, 2010; de Groot et al., 2013). Human-caused fires are driven by management needs and sometimes cultural practices (Granström and Niklasson, 2008; Bowman et al., 2011). Fuels and anthropogenic ignition sources can be managed to reduce open biomass burning. Astrup et al. (2018) argued that boreal forests should be managed to increase broad-leaved stands to reduce wildfire risk and fire emissions, and increase surface albedo, since broad-leaf trees reduce surface temperatures locally (Schwaab et al., 2020). Given these complexities, management strategies are best defined by regional needs. This chapter will focus on three biophysical regions of the Arctic: North America and Greenland, Fennoscandia and European Russia, and Siberia and the Russian Far East.

Figure 4.1 depicts anticipated ecological and meteorological shifts and the potential impact of these transitions on fire risks, as reported in the scientific literature, with the locations of fire-risk indicators on the map derived from the locations of these studies. First, boreal forests experience permafrost thaw, with initially wet soils (Wrona et al., 2016; O'Neill et al., 2020) desiccating to eventually become dry ground fuels (Turetsky et al., 2015; Box et al., 2019). In response to this progression, the risk of fire rises, then falls, then rises again. Second, the predicted transition of boreal forest to deciduous stands decreases fire risk in eastern Canada and small regions of interior Alaska (Terrier et al., 2013; Foster et al., 2019; Mekonnen et al., 2019). Third, grassland ecosystems expand in northwestern Canada and Alaska (Whitman et al., 2019; Wang et al., 2020a).

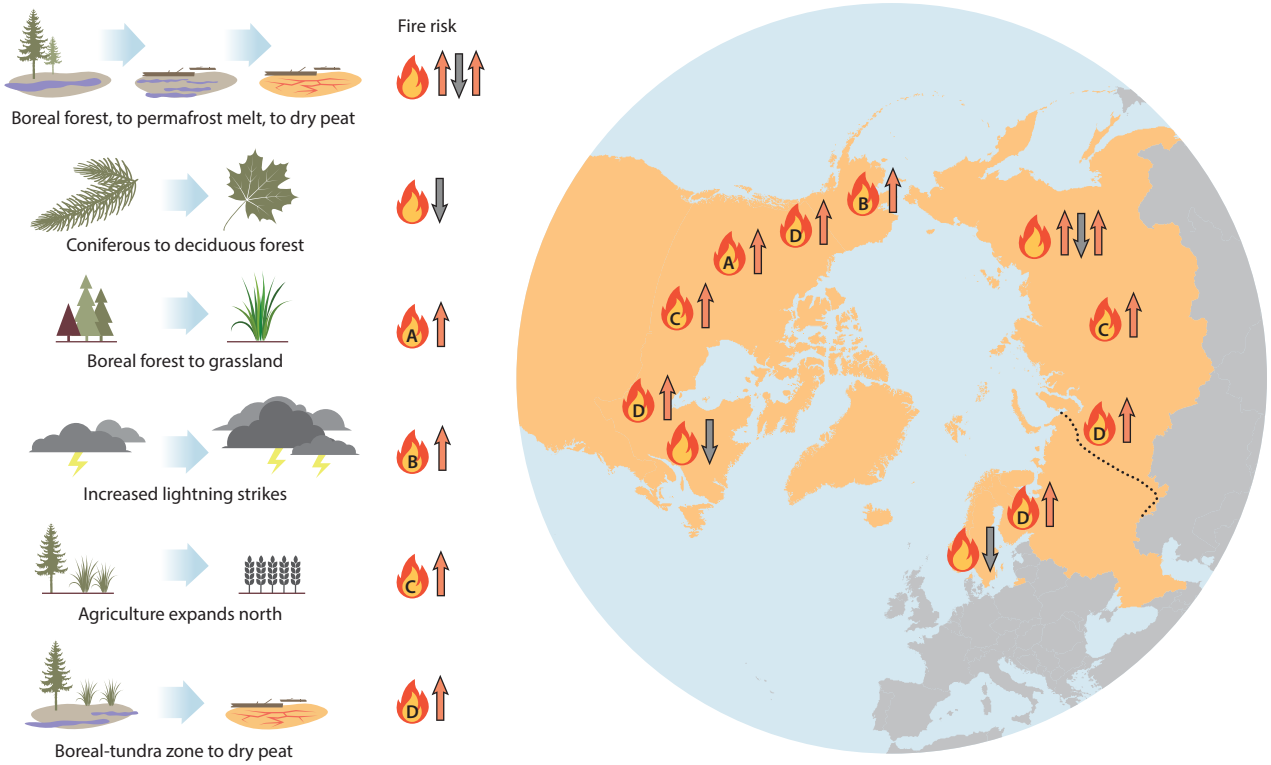

Figure 4.1 A sample of future Arctic fire-risk variables faced by Arctic Council Member states, drawn from peer-reviewed studies. The increases and decreases to fire risk relate to expected ecological and meteorological transitions forecast for the mid- to late-21st century due to climate change. Arrows indicating the anticipated changes to fire risk (up arrow, increasing risk; down arrow, decreasing risk) are placed in general locations where one or more studies predict this transition, although many of these changes could be possible across the Arctic.

Fourth, increased lightning strikes increase fire risk in Alaska (Veraverbeke et al., 2017) and also northern Europe (Púčik et al., 2017). Fifth, as wheat and maize cultivation are established in areas of West Siberia previously characterized by permafrost (Parfenova et al., 2019), and expand thereafter into the cold regions of the boreal zone (King et al., 2018) in North America, human-caused agricultural burning may increase. Finally, a threefold increase of permafrost thaw in the boreal zone by 2100 under the Representative Concentration Pathway (RCP) 4.5 will potentially increase the amount of peat (Nitzbon et al., 2020), also increasing fire risk.

Open biomass burning, as defined in this chapter, includes both wildland fires (wildfires, forest fires) and fires in human-dominated landscapes, such as agricultural and grassland areas. Throughout the chapter, open biomass burning is referred to using several terms that have specific meanings. Agricultural burning and agricultural open burning define fires used to manage croplands. Wildland fires are fires occurring in wild landscapes, whether ignited naturally or by human activity. Smouldering fires are those that take place in peat landscapes, or as surface fires in the understoreys of boreal forests. Reported statistics and geospatial methods from Earth observations were used to quantify and differentiate open biomass burning as human-caused fires (related to agricultural open burning, timber and agroforestry) and natural fires (caused by lightning strikes).

Many approaches taken to model the future risk of fires use RCPs to define the possible impacts of climate change on temperature and precipitation, as these variables influence fuel conditions and the availability of fuels for ignition and subsequent burning (Veira et al., 2016). Outlined in the AR5 report of the Intergovernmental Panel on Climate Change (IPCC) (IPCC, 2013a), the RCP scenarios outline a range of future climate-forcing conditions that can be used for considering potential impacts, and appropriate mitigation and adaptation measures (Moss et al., 2010). RCP4.5 (~650 ppm CO_2 equivalent [CO_2 eq]; low-emissions scenario) and RCP8.5 (~1370 ppm CO_2 eq; high emissions scenario) stabilize radiative forcing in the year 2100 at 4.5 watts per square meter (W/m^2) and 8.5 W/m^2 respectively. These are commonly used for sub-national, national, and regional studies (Krause et al., 2014; Sherstyukov and Sherstyukov, 2014; Girardin and Terrier, 2015; Lehtonen et al., 2016; Wotton et al., 2017), but not exclusively (Young et al., 2016). While the overall modeling work for this assessment relies on biomass burning emissions represented in the more recent Shared Socioeconomic Pathways (SSPs; O'Neill et al., 2017) – featured in IPCC AR6 – comparable assessment for the biomass burning conditions and impacts have not yet been published (Chapters 6, 7 and 8 all refer to GFED in some form as a proxy for biomass burning emissions within the SSPs). For a detailed description of the SSPs, and their relation to the RCPs, see IIASA (2019). It should be noted that the RCP2.6, RCP4.5, RCP6.0, and RCP8.5 all project temperature increases for the boreal and Arctic regions of between 1.5°C and 3.0°C by mid-century (see Figure TS15-3 of IPCC [2013]). By the end of the century, however, the RCP forecasts diverge for these regions, with anticipated temperature rises of: 2°–4°C (RCP2.6); 3°–7°C (RCP4.5); 4°–9°C (RCP6.0); and 7°–11°C (RCP8.5).

The 2015 AMAP assessment on black carbon (BC) and ozone as Arctic climate forcers (AMAP, 2015a) noted the key characteristics of open biomass burning. In this 2021 assessment, many of the open biomass burning assumptions remain the same, including human influence on both ignition and suppression, as well as on fuels management (Parisien et al., 2016), significant interannual variation in fire events and emissions, spatial and seasonal clustering of burning related to active land management, and fuel conditions. Since 2015, however, evidence for the direct influence of climate change on early season megafires has increased (Wang et al., 2017), as well as on the fuelling of extreme wildfires in more populated areas (rather than just in remote boreal forests) and in Arctic tundra (Abatzoglou and Williams, 2016; Kirchmeier-Young et al., 2019). Further, this 2021 assessment provides clarification of 'what is open biomass burning?' for the Arctic Council region and of the specific language of fire-emissions sources. Specifically, it determines landscape-scale fire types in the Arctic and boreal regions to be either wildland (boreal forest, hemi-boreal forest, taiga, tundra, grasslands and steppe, peatlands) or anthropogenic (croplands, pasture and rangeland, timber and agroforestry). Ignition sources are classified as natural or human-caused, providing needed context for policy recommendations. Finally, current uncertainties of quantifying future emissions from open biomass burning in the Arctic Council region are noted.

4.2 Understanding emissions in the Arctic

Open biomass burning is a source of many short-lived climate forcers (SLCFs), including black carbon (BC), organic carbon (OC), sulfur dioxide (SO_2), methane (CH_4), carbon monoxide (CO), nitrogen oxides (NO_X), non-methane volatile organic compounds (NMVOC), and ammonia (NH_3) (AMAP, 2015a and 2015b). Much of this chapter will focus on BC and CH_4, as mitigation of BC has been found to contribute the most of any SLCF to reducing warming in the Arctic (Sand et al., 2016) and CH_4 is a potent greenhouse gas.

4.2.1 Long-term emissions from open biomass burning

Comparison of five biomass burning emissions models including GFED (van der Werf et al., 2017), the Fire Inventory from NCAR (FINN; Wiedinmyer et al., 2011), the Global Fire Assimilation System (GFAS; Kaiser et al., 2012), the Quick Fire Emissions Dataset (QFED; Koster et al., 2015), and the Fire Energetics and Emissions Research (FEER; Ichoku and Ellison, 2014), was completed for the period 2005–2018 (Appendix 4, Figure A4.1). This built on the previous work of the 2015 AMAP assessment of BC and ozone (AMAP, 2015a), which included 2005 biomass burning emissions from GFAS, GFED, and FINN. It should be noted that GFED is used in the CMIP5 and CMIP6 inventories and analyses (van Marle et al., 2017). For each global fire emissions model, the area of interest was defined roughly as 45°–80° North (N) globally, split by latitude ranges of 45°–50°N, 50°–60°N, 60°–70°N, and 70°–80°N. Average annual emissions from open biomass burning from all sources (agriculture, boreal forest, tundra, peat, and so on) were calculated for 2005–2018 for BC, CH_4, CO, and fine particulate matter ($PM_{2.5}$). As open biomass burning emissions models are often constrained by the satellite epoch, roughly beginning in the 1980s, we have

provided a historical perspective from van Marle et al. (2017) (Figure A4.3), which shows an increase in emissions from high northern latitudes after 2000.

A custom AMAP open biomass burning emissions model was developed for this report (Figure A4.4). This model improved on the other global fire emissions models through the inclusion of higher-resolution spatial fire data (375 meters [m] compared to 1 kilometer [km] or greater) and region-specific land-use products for attributing fuel type, loadings, and emission factors. The Visible Infrared Imaging Radiometer Suite (VIIRS) active fire from day and night detections (Oliva and Schroeder, 2015) were assumed to completely burn each 375 m^2 pixel. A 'best-guess' land cover was created from three land-cover products, with a sample validation (n = 30 locations) of land-cover type performed for each country. Ultimately, the 750 m VIIRS Surface Type land-cover product (Zhang et al., 2018) was used for North America, Greenland, and the Russian Federation, augmented by the revised 1 km Circumpolar Arctic Vegetation Map (Raster CAVM; Raynolds et al., 2019) for missing values in the high northern latitudes. For Norway, Sweden, and Finland, the 10 m Land Cover Map of Europe 2017 from the Sentinel-2 Global Land Cover Project (Data ref. 4.2) was used. All land-cover maps were reclassified into the International Geosphere-Biosphere Program (IGBP) classes (Loveland et al., 1999) for ease of emissions calculations. Fuel loadings and combustion completeness were taken from van Leeuwen et al. (2014), with tundra values used for Greenland. Emission factors were taken from Akagi et al. (2011), with updates from Andreae (2019). The international scientific community's reliance on two main emission-factor sources (Akagi et al., 2011; Andreae, 2019, as an update to Andreae and Merlet, 2001) for estimates on open biomass burning makes it challenging to carry out a robust uncertainty analysis for fire emissions models (Pan et al., 2020).

First, this study reports the emissions from the most commonly cited fire emissions models: GFEDv4s, GFASv1.2, and FINNv1.5. Most of the fire activity and emissions occur between 50°N and 60°N, with very few emissions from open biomass burning found between 70°N and 80°N, and no satellite observations of fire above 80°N (Figure 4.2). The latitude band of 50°N–60°N corresponds to the southern extent of the boreal region. This area is experiencing increasing fires due to climate change (de Groot et al., 2013); in summer 2017 the most extensive wildfires in British Columbia's history occurred here, burning 1.2 million hectares (ha) (Kirchmeier-Young et al., 2019). Across these three models, 2008 and 2012 are peak years for emissions, with 2007 or 2009 having the lowest emissions. These models have high interannual variability.

The models GFEDv4s and GFASv1.2 have a relatively high level of agreement. While they do not use the same satellite-based approaches to quantify fire activity, these versions mainly rely on MODIS-based burned area (GFEDv4s) and fire radiative power (GFASv1.2) data products, and use the same land-cover maps to determine fire type (Kaiser et al., 2012). FINNv1.5 relies on MODIS active fire points only to detect fires. This makes it less capable of detecting fires than the other models – including the AMAP custom fire emissions model which relies on VIIRS. The VIIRS sensor is known to detect more fires than MODIS,

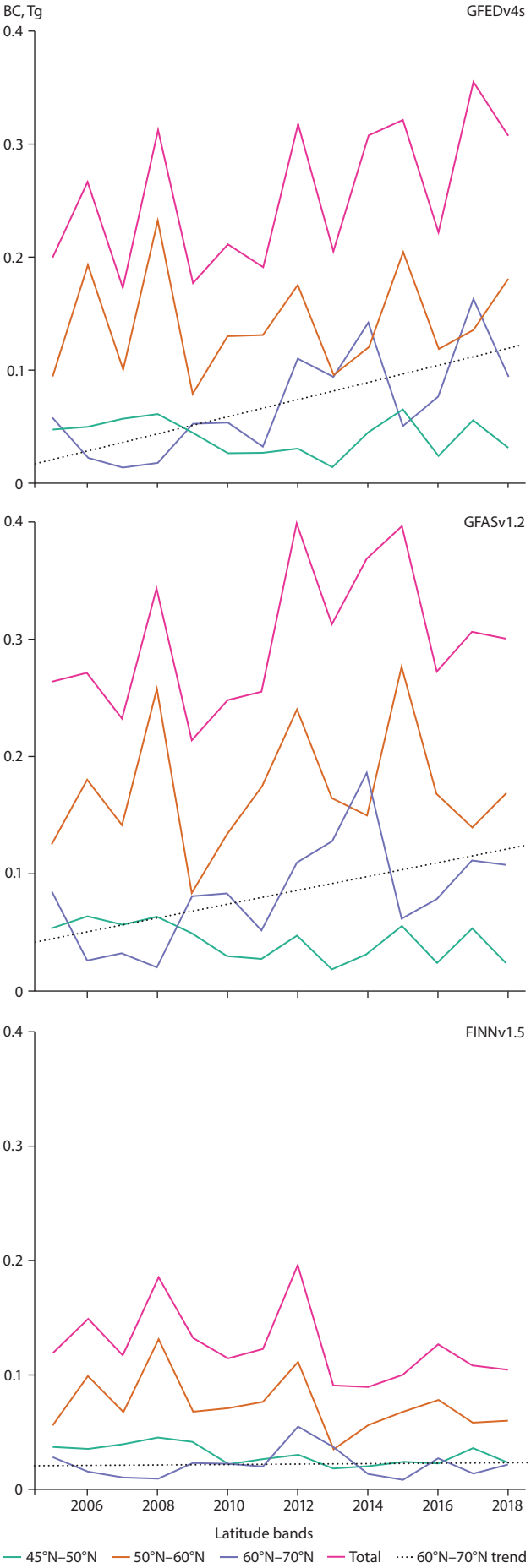

Figure 4.2 Annual black carbon (BC) emissions (1 Tg = 1 million tonnes) from three commonly used global fire emissions models, split by latitude ranges, covering the Arctic Council region for the period 2005–2018.

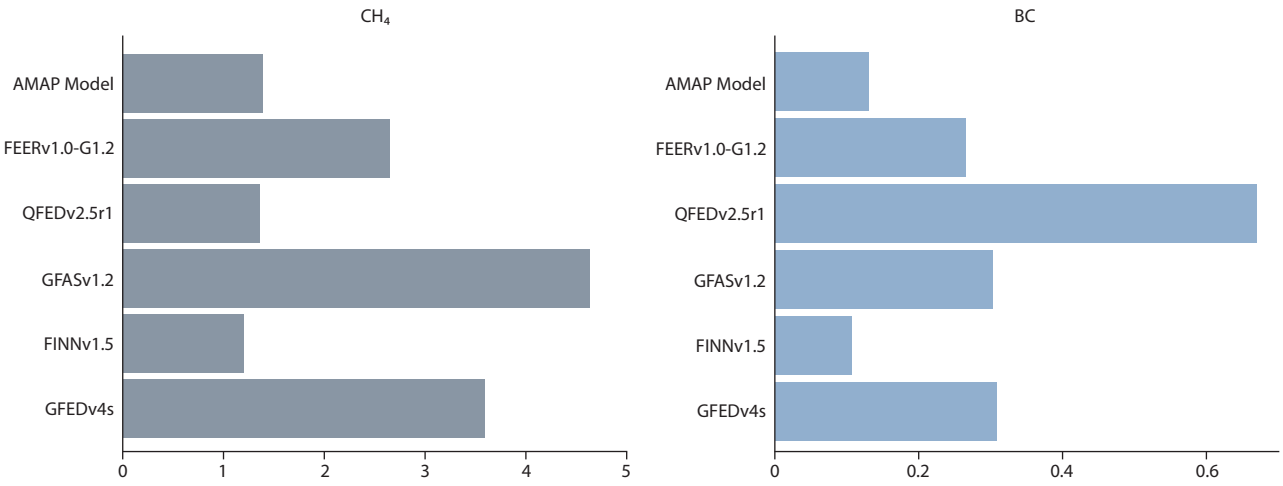

Figure 4.3 Annual 2018 BC and CH_4 emissions in Tg from five global fire emissions models and a custom-built AMAP fire emissions model for the Arctic Council region.

including smaller and cooler fires (Oliva and Schroeder, 2015), a capability that is important for high northern latitudes. By relying on MODIS active fire only, FINNv1.5 underestimates the number of fires above 60°N, as the sub-Arctic boreal ecosystem transitions to Arctic landscapes.

In the 14-year emissions estimates from GFAS, GFED, and FINN, a clear increasing trend is apparent from the mid-2000s, with there being more emissions from fire above 60°N than in the temperate zone of 45°N–50°N, where human-caused burning and wildfires are common throughout North America, Europe, and Eurasia (Figure 4.3). This trend is more pronounced in GFED and GFAS than in FINN, although all models show a positive trend (note the dotted line in Figure 4.2). Further, while there is a slight positive trend for BC emissions between 50°N–60°N for FINN and GFED, GFAS indicates a decline in emissions for this latitudinal region, which includes much of the boreal forest (Appendix Table A4.2). Both GFED and GFAS have larger, positive trends in BC emissions above 60°N and for 50°–60°N. Since it is based on 1 km MODIS active fire data, it is not surprising that FINN shows a higher positive trend for 50°N–60°N than for 60°N–70°N, as the MODIS active fire product performs less well at high northern latitudes and does not detect cool fires, such as those from burning peat.

As well as differing in their trends, these fire emissions models disagree in the absolute values for total emissions (Figure 4.2). The 2005–2018 multi-model (GFED, GFAS, FINN, FEER, QFED, and AMAP) average of annual emissions from all open biomass burning sources is 340,000 tonnes. The years with the highest multi-model average BC emissions are 2012, 2008, and 2015, being 450,000 tonnes, 440,000 tonnes, and 410,000 tonnes, respectively. The years with the lowest annual average BC emissions from across the models are 2008 and 2013, with both at approximately 270,000 tonnes. Again, across all five models, most fire emissions originate between 50°N–60°N. The AMAP custom fire emissions model, produced at a finer spatial resolution, assumes a smaller per-fire burned area than the other fire emissions models. This may be why its emissions outputs are lower than the other models, apart from FINN.

To determine specific fire activity from Arctic Council Member states, ground-based official statistics were used to report country or sub-region burned area for circa 2019 (Table 4.1). The Russian Federation had the highest burned area, with over 100,000 km^2 burned, resulting in approximately 25.6 tonnes of BC. In 2019, open biomass burning in European Russia – comprising Northwestern, Central, Southern, North Caucasian, and Volga Federal Districts – accounted for only 190 km^2 of

Table 4.1. Summary table of BC, $PM_{2.5}$, CH_4, SO_2, and CO_2 emissions from reported statistics on burned area in the Arctic Council Member states. Sources for burned area from: Alaska Division of Forestry (2020a)[a]; CIFFC (2020)[b]; Markuse (2019)[c]; DSB (2020)[d], SOU (2019 – in Swedish)[e]; Ketola (2020)[f], Data ref. 4.3[g]; and Data ref. 4.4[h]. Fuel loadings and combustion completeness came from van Leeuwen et al. (2014) for boreal forests, with tundra values used for Greenland and temperate forests for the USA/CONUS. Emission factors were taken from GFED (Data ref. 4.5).

Country/region	Year	Official burned area (km^2)	BC (tonne)	$PM_{2.5}$ (tonne)	CH_4 (tonne)	SO_2 (tonne)	CO_2 (tonne)
USA/Alaska	2019	10481[a]	2.660	81.40	31.71	5.85	8140
Canada	2019	18389[b]	4.667	142.81	55.63	10.27	14300
Denmark/ Greenland	2019	8[c]	1.27E-04	0.0288	0.0659	1.27E-03	5.04
Norway	2019	0.03[d]	7.61E-06	2.33E-04	9.08E-05	1.68E-05	0.0233
Sweden	2018	250[e]	0.063	1.94	0.76	0.14	194
Finland	2019	6[f]	0.002	0.05	0.02	0.003	4.66
Russia	2019	100785[g]	25.579	782.72	304.90	56.27	78300
USA/CONUS	2019	18876[h]	10.196	342.96	96.40	12.98	29100
Total		148795	32.97	1008.95	393.09	72.53	130000

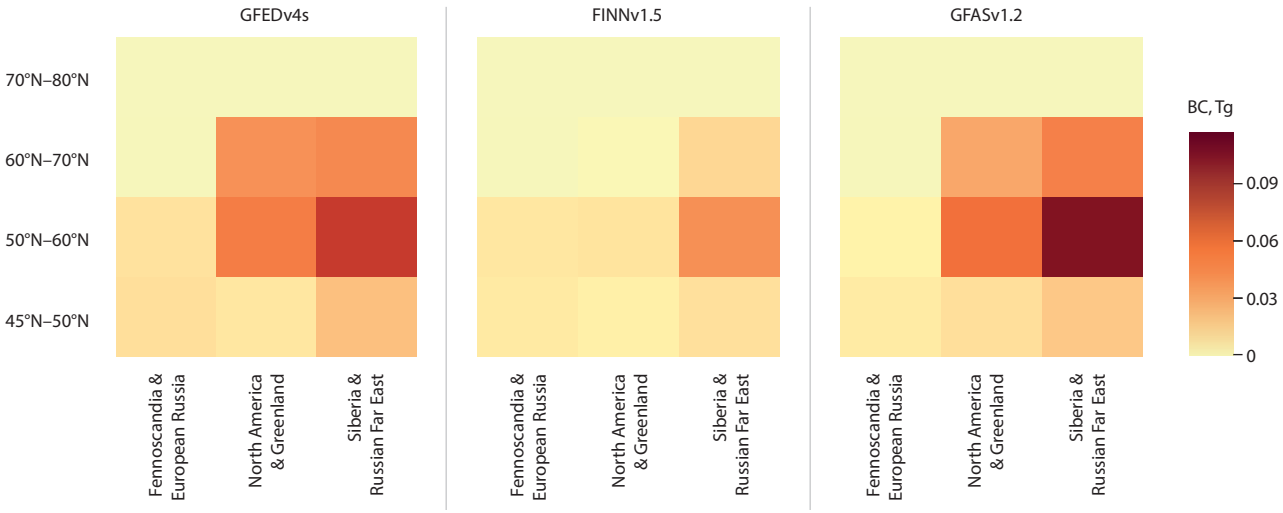

Figure 4.4 Average black carbon (BC) emissions in Tg for 2015–2018 from three global fire emission models – GFEDv4s, FINNv1.5, and GFASv12 – split by latitude ranges for the three biomass-burning regions.

burned area (Data ref. 4.3). Approximately 98.2% of burned area in Russia occurred in the Ural, Siberian, and Far Eastern Federal Districts. In general, the region encompassing Fennoscandia and European Russia had the lowest burned area and open biomass burning emissions (Figure 4.4), with all regions experiencing the most burning in the latitudinal band of 50°N–60°N, and the second-most burning in 60°N–70°N. Alaska (USA) and Canada accounted for approximately 29,000 km^2 of total pan-Arctic biomass burning and 17% of the BC emissions, with the contiguous United States (CONUS) accounting for 24% of BC emissions (Appendix Table A4.1). Note that while Canada and CONUS reported similar official statistics for burned area, fires in the temperate forests of CONUS tended to emit more emissions than boreal ecosystems. Greenland is a novel fire regime in the Arctic, with two relatively significant wildfires in 2017 and 2019 that accounted for more burned area and emissions than Norway or Finland. However, in 2019, the majority of open biomass burning and related emissions for the Arctic Council countries originated in Siberia and the Russian Far East, followed by the CONUS, Canada, and Alaska.

4.2.2 Climate change will increase natural fire emissions

In all future climate-change scenarios, the global temperature increases by 2100, but with regional variability. Here we present findings for studies focusing on the high northern latitudes. An overall increase in natural fire risk is expected in the Arctic, as well as associated emissions. Natural fires, caused by lightning rather than being ignited by human activity, are estimated to increase, as lightning strikes are predicted to increase in northern Europe and Alaska (Púčik et al., 2017; Veraverbeke et al., 2017), respectively. Lightning strikes, fire weather (dictated by temperature, precipitation, and relative humidity), and fuel conditions are the controlling processes for natural fires.

Boreal and Arctic landscapes are diverse, and thus so are natural fires – burning habitats from forests to grasslands and peatlands. Near-term warming will lead to more ignitions from lightning (Veraverbeke et al., 2017), with degraded permafrost increasing dry ground fuels, such as peat (Turetsky et al., 2015), and fire severity (Teufel and Sushama, 2019). By the end of the century, wildland fire risk is expected to increase, with the length of fire seasons – measured in the number of days of severe fire weather – predicted to increase by as many as 20 days for high northern latitudes using the IPCC A1B, A2, and B1 scenarios (Flannigan et al., 2013). Similarly, Sherstyukov and Sherstyukov (2014) predict an increase of more than 50 high fire-risk days for Russia under the RCP8.5 scenario, with potential for the area of forest fire burned to double by 2100. Using CMIP5 model intercomparisons, Lehtonen et al. (2016) found that large (≥ 10 ha) boreal forest fires in Finland may double or even triple in extent by the end of century, using RCP4.5 and RCP8.5 scenarios, but with large inter-model variability. Making robust predictions of the future burned area in wildland and human-dominated landscapes for the boreal and Arctic requires an understanding and quantitative simulation of the major drivers of fire (specifically climate, fire weather, ignition, fuels and human activity), including coupled dynamics between and among these drivers (Riley et al., 2019).

Increased fire risk will not be uniform across the Pan-Arctic (Figure 4.1). For example, thawing of the permafrost will moisten soils (Wrona et al., 2016), reducing above- and below-ground fire risk. Further, changing precipitation regimes that deliver more rainfall in the Arctic for the months of March through December by the end of the century under RCP8.5 projections (Bitanja and Andry, 2017) could, on the one hand, reduce fire risk through increased wetness but, on the other hand, increase fire risk through greater vegetation growth and/or shifting fuel regimes.

Increased convective cloud formation has been documented in the Russian Arctic (Chernokulsky and Esau, 2019) and the North American boreal forest (Veraverbeke et al., 2017), with a 5% increase in convective storms in Northern Europe (Púčik et al., 2017). Meanwhile, 5%–20% more lightning is projected to occur under RCP4.5, and 10%–40% under RCP8.5 (Rädler et al., 2019), by the end of the century. Krause et al. (2014) predict that burned area will increase by 40%–50% in the high latitudes under RCP8.5, given predicted changes in fuel loads, fuel moisture, and increased lightning frequency. And end- of-century estimates made under RCP6.0 by Young et al. (2016) for Alaska showed that summer temperature and annual moisture are the most important climatic variables

Case study: Elemental carbon concentrations in Arctic and boreal Canada

A case study of Arctic and boreal sites by Environment and Climate Change Canada (ECCC) measured long-term observed concentrations of elemental carbon (EC) at Alert (82°27'N, 62°31'W) and East Trout Lake (54°21'N, 104°59'W). Figure 4.5 shows the locations of these two sites. The observations were compared with corresponding assembled GFED/CMIP6 emissions from biomass burning for Northwest Canada over the same period of 2006–2015. Alert is mainly influenced by emissions sources from Northern Eurasia and North America, depending on the season (Hirdman et al., 2010a; Stohl et al., 2013; Xu et al., 2017). Biomass burning from North America influences Alert more during summer than winter. East Trout Lake, a boreal forest site, is largely affected in the summertime from the widespread fires across Canada, particularly in western Canada.

Comparing the time series and seasonal variation of EC from these two sites provides insight as to how biomass burning in North America affects levels of EC transported to the Canadian Arctic. Figure 4.6 shows a six-month means timeseries for EC for 2006–2015. Observations from Alert are plotted in the top panel (winter–spring: November–April; and summer–fall: May–October); those from East Trout Lake are shown in the middle panel; and the corresponding time series of assembled biomass burning from GFED emissions in CMIP6 (van Marle et al., 2017) from the upwind area of East Trout Lake are presented in the lower panel. It is obvious that the interannual variation of EC in the middle panel is well correlated with the changes of biomass burning emissions in the bottom panel (R^2 = 0.89), indicating that about 90% of the interannual changes in observed EC at the boreal East Trout Lake site can be explained by the changes in biomass burning emissions from the upwind area, i.e., Northwestern Canada. It is also noticeable that the interannual variations in

Figure 4.5 The carbonaceous aerosols sampling network for EC/OC and carbon isotope measurements used by ECCC, showing the locations of the Alert and East Trout Lake sites discussed in the text.

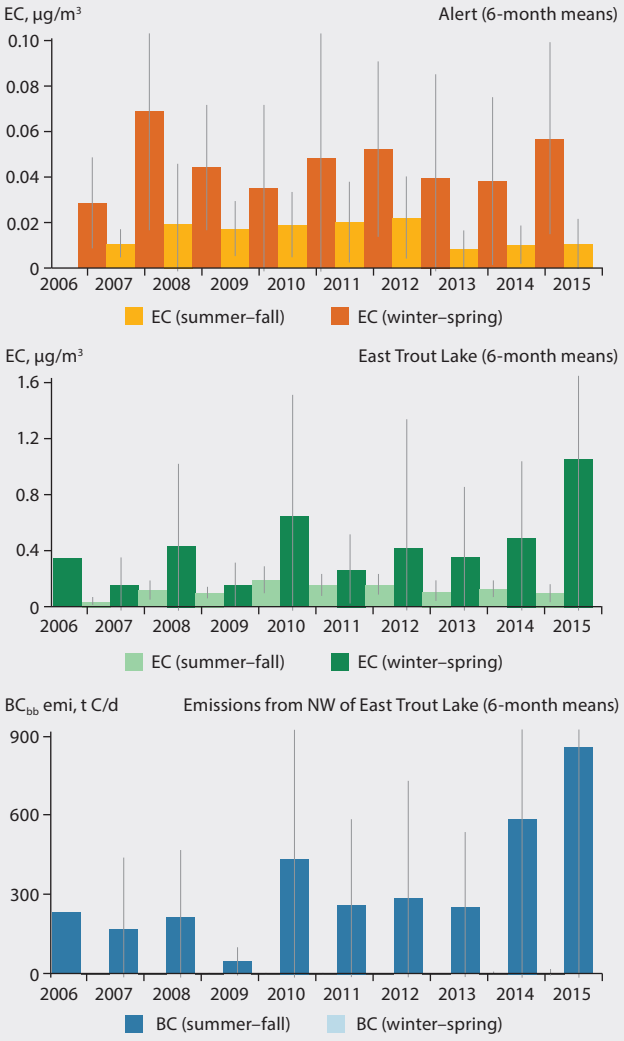

Figure 4.6 Comparison between the observed interannual seasonal trends in EC at Alert (top panel) and East Trout Lake (mid panel), with the corresponding assembled GFED/CMIP6 emissions (https://gmd.copernicus.org/articles/10/3329/2017/) from the upwind area (bottom panel) for the period 2006–2015. There is good correlation between the variables in the lower two panels: y=0.001x + 0.110 (R^2 = 0.89), where y is the EC concentration in the middle panel, and x is the BC emissions in the lower panel. Data sources: Huang, personal communication, 2020; Rodríguez et al., 2020.

EC at Alert in the top panel differ greatly from those observed at East Trout Lake in both winter–spring and summer–fall seasons. This may imply that the interannual variations of EC at Alert were not due to the impacts of biomass burning in North America.

Comparing the seasonal variability of EC monthly means from East Trout Lake with biomass burning emissions, Figure 4.7 shows that the seasonal variation of atmospheric EC at this boreal site is well correlated with the corresponding profile of GFED/CMIP6 biomass burning emissions (R^2 = 0.93). This suggests that more than 90% of the possibility of EC seasonal variability at East Trout Lake was caused by the biomass emissions from the upwind area. Seasonal variation in EC at Alert (top panel) shows an opposite pattern from that of East Trout Lake (middle panel), with the relatively higher concentrations during winter–spring months and relatively lower concentrations during summer–fall months. The seasonal variabilities are likely due to planetary boundary layer (PBL)

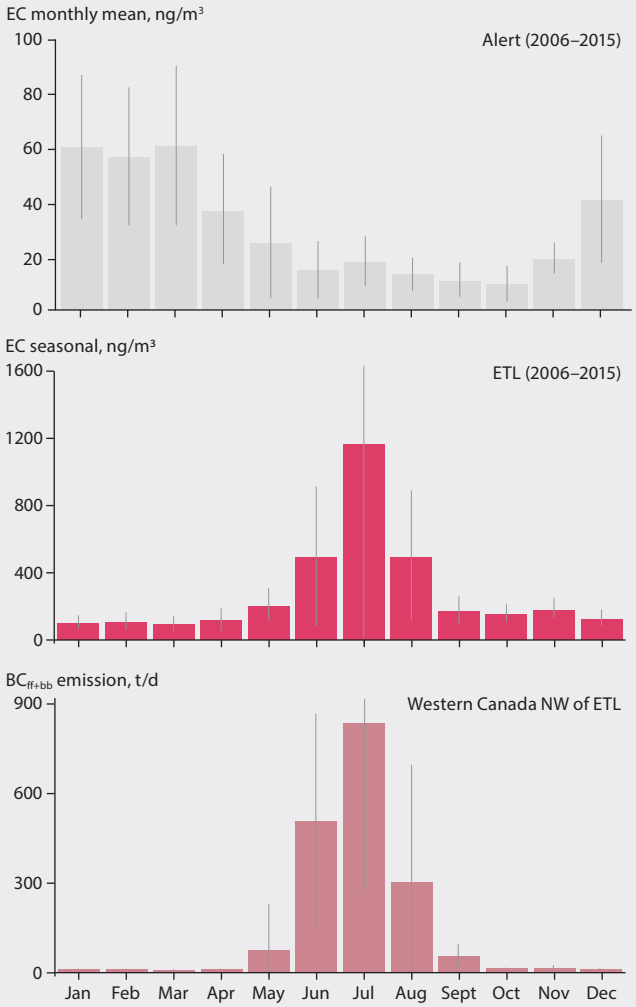

Figure 4.7 Comparison of the observed seasonal variations in EC at Alert (top panel) and East Trout Lake (ETL; middle panel), with the corresponding assembled GFED/CMIP6 emissions (https://gmd.copernicus.org/articles/10/3329/2017/) from the upwind area (bottom panel) for the period of 2006–2015. There is good correlation between the variables in the lower two panels: y=0.831x - 86.3 (R^2 = 0.94), where y is the EC concentration in the middle panel, and x is the BC emissions in the lower panel. Data sources: Huang, personal communication, 2020; Rodríguez et al., 2020.

dynamics, and a higher scavenging rate by precipitation during summer months. The small peak apparent in July implies that, while EC emitted from biomass burning in North America is not the main source of the EC concentration seen in the Arctic overall, the influence of EC emitted by biomass burning during summer seasons in North America could not be ruled out, taking account of the fact that a larger portion of EC was removed via precipitation and aerosol-cloud interactions while transported towards Alert. Using ^{14}C measurements in conjunction with the Lagrangian dispersion model provides a way to further quantify the relative fraction of pollutants from biomass burning transferred to the Arctic region.

driving the likelihood of new wildland fire regimes in tundra and the boreal forest-tundra transition zone. In general, lightning frequency is expected to increase over areas north of 50°N. The strongest relative increase is approximately 100% – across far northern Europe under the RCP8.5 scenario by the end of the century (Groenemeijer et al., 2016). Moreover, since summers are expected to become drier in the future, the relative role of lightning as an ignition source for wildfires may increase across northern Europe. These future models align with lessons learned from studies of historical drivers of natural fires in the Arctic region. Meta-analysis of palaeofires during the Holocene (4,000 BP–200 BP), for the boreal zone of North America and Fennoscandia, suggests that general trends in boreal biomass burning were primarily controlled by climatic changes – mainly mean annual precipitation in Alaska, northern Quebec, and northern Fennoscandia, and summer temperatures in central Canada and central Fennoscandia (Molinari et al., 2018). The composition of boreal needleleaf evergreen fuel at the landscape-level across Alaska, and central and southern Fennoscandia, was secondary to climatic controls.

Climate-induced vegetation shifts, which would also modify fire risk and related emissions, present a complex matrix for the Arctic Council Member states. Predictions of boreal forest transition to deciduous forest stands would decrease fire risk in eastern Canada and Interior Alaska (Terrier et al., 2013; Foster et al., 2019; Mekonnen et al., 2019). Using three decades of Landsat imagery at 30 m resolution, Wang et al. (2020a) found that these trends are already occurring in Alaska and northwestern Canada, as climate shifts drive grass and shrub expansion in the Arctic, and wildfires drive most of the evergreen forest reduction and deciduous forest expansion in the boreal sub-Arctic region. Further work in mature deciduous forests of Interior Alaska show that current canopy 'gaps' are related to ecological shifts to evergreen shrubs, lichens, and mosses. These small patches of highly flammable coniferous species within low flammability deciduous stands are increasing overall fire risk (Alexander and Mack, 2017).

Climate change may have both positive and negative impacts on boreal forests and forestry (Reyer et al., 2017). Further, changes may be positive in the near future, but become negative in the mid- and long-term. In general, climate change accelerates forest growth at high northern latitudes by lengthening the growing season. Moreover, elevated CO_2 concentration decreases transpiration and increases photosynthetic rate, also enhancing forest growth (Peltola et al., 2002; Ellsworth et al., 2012; Kellomäki et al., 2018). However, abiotic and biotic damage may have the opposite effect (Seidl et al., 2014). For example, drought increases the risk of forest fires, but also negatively affects the growth of Norway spruce (*Picea abies)* and exposes trees to biotic damage. Late winter temperature increases in southern Siberia (at 45°N–55°N) are associated with early snowmelt, early green-up and establishment of ground vegetation in larch (*Larix spp.*) forests, drier air conditions, and increased early-season fires in March and April (Kim et al., 2020). Masrur et al. (2018) found that, for circumpolar tundra landscapes, an increase in winter surface temperature increased the likelihood of wildfires occurring during the following summer, while a decrease in average winter surface precipitation and soil moisture were associated with higher-intensity wildfire events. Damage from

snow is estimated to increase in northeastern Europe but to decrease elsewhere in Europe by the end of the century under the RCP4.5 and RCP8.5 scenarios (Gronemeijer et al., 2016). Wind damage risk is expected to increase, due to the shortening of the soil frost period (Venäläinen et al., 2020).

4.2.3 Emissions from human-caused open biomass burning

Open biomass burning from anthropogenic activities, such as agriculture, forestry, and energy-related extraction and production – as well as from accidental ignition – will increase in boreal areas and the Arctic, as climate change facilitates the northward expansion of human-dominated landscapes, increasing potential ignition sources (Figure 4.1). The 2019 wildfire that occurred in Greenland was caused when a campfire ignited dry ground near a public camping site on the world-renowned Arctic Circle Trail (McGwinn, 2019). This incident indicates that tourism will need to adapt to the increased fire risk in tundra landscapes. Greenland wildfires in 2017 and 2019 occurred during warm, dry, and sunny summers. The areas that burned were east of Sisimiut, in tundra areas that had low vegetation cover and degraded permafrost but high-carbon soils (Evangeliou et al., 2019). Timber logging and site preparation currently cause large wildfires in boreal landscapes, including the 2014 Västmanland fire – the largest single wildfire event in Sweden's history (Lidskog et al., 2019). Northward agricultural expansion will likely increase human-caused agricultural burning, as wheat and maize become established in previously permafrost areas of West Siberia (Parfenova et al., 2019) and expand into the cold regions of the boreal zone (King et al., 2018). Cultivation could even potentially expand up to the Arctic Circle from Central Siberia (Tchebakova et al., 2016). Of course, this northward agricultural expansion will be controlled by local conditions, with inferior soils, existing land uses incompatible with agricultural conversion, and unsuitable topography presenting potential limitations (Ioffe and Nefedova, 2004; Dronin and Kirilenko, 2011).

4.2.4 Climate change will increase non-forest fire emissions

Under RCP8.5, Stralberg et al. (2018) estimated that by 2100, grasslands will replace much of the upland conifer, mixed forests, and deciduous forests for a large area of the boreal forest zone of northern Alberta. Shorter fire-return intervals combined with climate change-induced drought will reduce the capacity of evergreen and broadleaf species to re-seed and/or re-establish after wildfires, leading grassland ecosystems to expand in present-day northern Canadian forests (Whitman et al., 2019). The wider presence of grass-dominated landscapes would create a new fire regime of frequent but low-severity fires, with short-lived climate pollutants (SLCPs) and SLCFs likely being transported to the Arctic in the spring months of March to May (Hall and Loboda, 2018). Grassland fires produce less energy, with smoke plumes similar to crop-residue burning that are unlikely to breach the tropopause and cause consistent, year-round transport of smoke to the Arctic (Hall and Loboda, 2017), unlike the current observed deposition from boreal forest fires in the Arctic (Thomas et al., 2017). Further, Smirnov et al. (2015) found that forest fires in European Russia during 2008–2012 occurred mainly in June and August, with Siberia and the Russian Far East being the main sources of BC emissions during a time when transport to the Arctic is unfavorable. In the Sakha Republic, Kirillina et al. (2020) found that since 2011, fire seasons have, on average, been 13 days longer than previously, and that since 2009, fire seasons have started earlier in April than in previous years. Peak fire occurrence across the three-month period of May to July persists in Sakha. This indicates that BC from early-season burning in and near Arctic Siberia could be available for transport. This is also relevant because Arctic snow and sea-ice coverage are much more widespread in the early burning season than late season. Emission factors for biomass burning in grassland and steppe ecosystems are different from those of boreal forests (Akagi et al., 2011; Andreae, 2019), which

Case study: A novel Arctic fire regime in Greenland

Unusual open fires were observed by pilots in western Greenland and confirmed by satellite imagery between 31 July and 21 August 2017, after a period of warm, dry and sunny weather. The fires burned more than 2000 ha of high-carbon soils (most likely peat, due to smouldering and fire-spread behavior), which had become vulnerable due to degradation of the permafrost (Daanen et al., 2011). Evangeliou et al. (2019) estimated that the wildfire consumed around 117 kilotons (kt; 1 kiloton = 1000 tonnes) carbon (C) fuel, and emitted about 23.5 tonnes of BC and 731 tonnes of OC (including 141 tonnes of brown carbon [BrC]). Although these fires were small compared to fires burning at the same time in North America and Eurasia, a large fraction (30%) of the BC, OC and BrC emitted was deposited on the Greenland ice sheet. Measurements of aerosol optical depth (AOD) in western Greenland showed that the air was strongly affected by the Canadian forest fires. Even so, the Greenland fires had an observable impact, doubling the column concentrations of BC. The spatiotemporal evolution and, in particular, the top height of the plume was confirmed using the vertical cross-section of total attenuated backscatter (at 532 nanometers) from Cloud-Aerosol Lidar and Infrared Pathfinder Satellite Observations (CALIPSO-CALIOP) Lidar. The maximum albedo change due to BC and BrC deposition from the Greenland fires was 0.007, (albedo varies between 0 [black = absorbs all energy] and 1 [white = reflects all energy]) while the average instantaneous 'bottom of the atmosphere' (BOA) radiative forcing over Greenland at noon on 31 August 2017 (post-fire) was between 0.03 and 0.04 W/m^2, with locally occurring maxima up to 0.77 W/m^2. The summer 2017 fires in Greenland had a small impact on the Greenland ice sheet, causing almost negligible extra radiative forcing. This was due to the relatively small – in a global context – size of the fires. However, with 30% of the emissions deposited on the Greenland ice sheet, the 2017 Greenland wildfires were very efficient climate forcers on a per-unit emissions basis. Thus, while the fires in 2017 were small on a global scale, if the expected future warming of the Arctic produces more and larger fires in Greenland (Keegan et al., 2014), this may cause substantial albedo changes and, in turn, potentially contribute to accelerated melting of the Greenland ice sheet.

potentially implies different impacts on atmospheric chemistry and SLCPs. Therefore, while boreal forest fires emit more SLCPs than grasslands and cropland fires, the springtime burning of northern grasslands, peatlands, and croplands – often human-caused – means these emissions are more likely to be transported to the Arctic than summertime forest fires.

Peatland fires are more likely in dry conditions, but smouldering can persist in wet soils (Turetsky et al., 2015). Using the RCP8.5 scenario, Teufel and Sushama (2019) estimated that a 2.0°C temperature increase would be reached around 2031, causing 42% of pan-Arctic permafrost to abruptly degrade, and increasing fire severity in Russia, Canada, and Alaska (Figure 4.1). However, O'Neill et al. (2020) noted that long-term field observations in the Canadian boreal and Arctic regions did not reflect this abrupt shift to degraded and dry soils, but rather increased soil wetness. This phenomenon – which would decrease fire risk, particularly for peat – was likely missed by the model assumptions used by Teufel and Sushama (2019).

Surface fires can cause permafrost to thaw, producing thermokarst lakes (Jones et al., 2015), which previously have been considered to reduce fire risk (Sofronov et al., 2000). However, they are not perfect fire breaks, as wildfires can 'jump' over these lakes (Sofronov and Volokitina, 2010). Under RCP4.5 and RCP8.5, wildfire emissions of BC, CO, NO_X, $PM_{2.5}$, and SO_2 could exceed anthropogenic emissions in northeastern Europe by 2090, including Sweden and Finland (Knorr et al., 2016). There is a clear consensus that prolonged fire seasons will become more common, increasing in the eastern boreal forests of Canada (Boulanger et al., 2013); central and northwestern Canada (Boulanger et al., 2014); and European Russia (particularly Karelia and Leningradskaya), West Siberia, and the Far East (Sherstyukov and Sherstyukov, 2014). Wang et al. (2017) noted that a recent increase in the fire season in Canada had led to a rise in the total number of fire-spread days, resulting in large increases in total fire size and emissions for early-season fires. An example is the human-caused Fort McMurray megafire in Alberta, which burned both forests and peatlands (Hanes et al., 2019). A longer fire season, starting earlier in spring and lasting later into autumn, would bring increased potential for more and larger fire emissions throughout the season. Further, suppression of wildfires in Canadian boreal communities has increased the likelihood of flammability (Parisien et al., 2020), suggesting that other wildland-urban interfaces in the Arctic region may have similar risks due to long-term aggressive fire suppression.

4.2.5 Fire management and open biomass burning emissions in the Arctic

Current fire management is being addressed in future work planned under the Arctic Council's Working Group on Emergency Prevention, Preparedness and Response (EPPR) and work by other relevant Arctic Council groups, with leadership and contributions from the six Permanent Participants who represent Arctic Indigenous peoples. Below are some specific considerations of fire management in the context of understanding and managing emissions.

McWethy et al. (2019) argued that active "fuels management, prescribed fires and allowing wildfires to burn under moderate fire weather conditions will protect and promote ecological and cultural resources, and communities" more effectively than by managing fire risk through suppression and/or efforts to eliminate all fire from the landscape, including novel fire landscapes caused by warming in the Arctic. Privately owned grassy tussock tundra and dwarf shrub tundra vegetation types are more likely to burn than low shrub tundra in Alaska (Hu et al., 2015), showing relatively rapid vegetation re-greening within a decade after burning for grassy tussock tundra and dwarf shrub tundra (Rocha et al., 2012). Prescribed burning could therefore be effective in fuel management for tussock and dwarf shrub landscapes of the tundra. In boreal forest and forest-tundra landscapes, mulching treatments that convert canopy and surface fuels to a masticated fuel bed can limit peat burn depth in black spruce (*Picea mariana*) stands (Wilkinson et al., 2018). However, managing fuels will be more complicated in dried and degraded peatlands outside of these vegetation zones.

The effectiveness of prescribed burning for peatlands is unclear. Peat fire risk and burn depth, however, are influenced less by canopy and ground vegetation and more by soil bulk density (which affects the availability of air in soils), water-table depth, and precipitation (Kieft et al., 2016). After devastating fires in 2010 in the Moscow region, the regional government undertook an ambitious 70,000 ha peatland rewetting project to reduce fire risk (Sirin et al., 2014), a landscape-scale process that can be monitored using existing Earth observation sensors at the moderate resolution (30 m Landsat to 10 m Sentinel-2; Sirin et al., 2018). To date, the effectiveness of this campaign is unclear but, in practical terms, it should reduce fire risk. In the larger context of CH_4, Günther et al. (2020) used a radiative forcing model to determine that CH_4 emissions from rewetting peatlands were less significant in the short-term than the CO_2 emissions from degraded or drained peatlands increasing long-term warming when rewetting is postponed.

Adaptive management strategies of the timber industry in Fennoscandia could also reduce fire risk. Intensive management to maintain ditch networks and fertilize drained peatlands will increase timber values while also rewetting the peat (Ahtikoski and Hökkä, 2019). Prescribed burning for silvicultural retention, and maintaining and regenerating pure stands, can also reduce fuel loadings while increasing biodiversity (Lindberg et al., 2020).

The variable with the highest uncertainty is people – both as ignition sources and in determining how demographic, migration, and/or development patterns in these changing landscapes will affect fire activity and related emissions (Robinne et al. 2016; Reilly et al. 2019). For example, consider agricultural landscapes as one source of fire. Expanding climate-driven agricultural frontiers in the high northern latitudes under the RCP8.5 scenario for 2060–2080 could add 8.5 million km^2 of new croplands in Canada and Russia alone, expanding wheat and maize production into areas with carbon-rich or peat soils (Hannah et al., 2020). Further, Parfenova et al. (2019) found crop-growing conditions would be established in the permafrost zone of West Siberia under RCP2.6 and RCP8.5 by 2080, favorable for wheat and maize production. These crops are commonly managed via open burning practices in the USA, eastern Europe, and Russia (Kutcher and Malhi, 2010; McCarty et al., 2017; Theesfeld and Jelinek, 2017; Shiwakoti et al., 2019). While open agricultural burning in Canada is minor (ECCC,

2020 – see Annex 3, Section A3.4.7), recent research estimated that the risk of wildfires from the spread of agricultural burning peaks in Alberta in late April and early May (Thompson and Morrison, 2020). Thus, seasonality of burns and management of croplands, grasslands, and deciduous forests may occur at times when transport of emissions to the Arctic is likely, in other words in late winter and early spring for Russia (Hall and Loboda, 2018; Qi and Wang, 2020), and Canada and north central USA (Viatte et al., 2015), respectively.

4.3 Uncertainties in future open biomass burning emissions

Uncertainties in emissions from fires in the boreal and Arctic remain, due to complexities in the fire regimes. For example, peat fires can smoulder for months, years, or even decades (Hu et al., 2018), burning laterally and vertically below the surface, appearing to be extinguished, but releasing smoke at the surface in locations away from the original ignition site. In Alaska, this phenomenon is referred to as 'holdover', 'overwintered' or 'zombie' fires. Such fires are difficult to allocate to a single – albeit complex – fire event from cumulative satellite active-fire and burned-area pixels. In April 2020, the Alaska Division of Forestry was monitoring several active smoldering peat fires from the ~5 km^2 Deshka Landing Fire of August 2019 that had overwintered near Willow, Alaska, despite heavy snow melt (Alaska Division of Forestry, 2020b). Preliminary results by Scholten and Veraverbeke (2020) indicated that overwintering fires were more likely to be holdovers from high-severity fires, emerging more frequently in lowland black spruce-dominated forests. While zombie or holdover fires are an interesting phenomenon in Arctic peat systems, improving estimates of BC emissions from wildland and human-caused fires – particularly peat fires in the boreal and Arctic, – should be a priority in terms of filling data gaps.

4.3.1 Satellite-based fire emissions

Earth observations from satellite products are powerful tools for forecasting (Pickell et al., 2017), improving rapid-response post-fire modeling (Miller et al., 2017), and quantifying fire in the boreal and Arctic regions (Hislop et al., 2020). Uncertainties in satellite-based emissions estimates are driven by the availability and quality of fire-activity data from satellite- and ground-based sources, as well as imperfect knowledge of vegetation types and cover, fuel conditions and loadings, and emission factors. Current global fire emissions inventories rely on satellite-derived fire activity from detected active fires, mapping of burned areas, and calculations of fire radiative power (Liu et al., 2020). In the Arctic, as in other northern regions, satellite-based observations tend to underestimate open burning in agricultural landscapes, forest-surface fires and smouldering peat fires. For example, Zhu et al. (2017) found that current emissions inventories based on satellite-derived products of burned area, such as GFEDv4, underestimated human-caused burning in agricultural landscapes and mixed forests in Eurasia between 50°N–65°N by around 2,100 km^2 annually for 12 regions of interest. This indicates that the actual burned area from anthropogenic sources in the Eurasian boreal zone is currently underestimated by as much as 16%.

Surface fires under forest canopies dominate fire regimes in much of northern Eurasia, but are not well quantified in current satellite-based burned-area products (Duncan et al., 2020) and thus emissions inventories. Smouldering fires in carbon-rich humus and peat landscapes are difficult to detect, as smouldering combustion occurs at much lower temperatures than flaming combustion; 500°C–700°C versus 1500°C–1800°C, respectively (Rein et al., 2008). Daily, global observations of low-intensity fire from existing satellite systems are limited currently to VIIRS (Johnston et al., 2018). Smouldering fires in Arctic landscapes can be mapped via regionally-tuned algorithms that have been designed to ingest daily active-fire detections from multispectral VIIRS (Waigl et al., 2017) and hyperspectral Hyperion (Waigl et al., 2019). In general, it is difficult for satellites and drones to detect (Burke et al., 2019) smouldering peat fires because these ground fires are low temperature and can burn underground and re-emerge in new locations (Rein, 2016). The coarse resolution (>1 km) of global satellite sensors, and obstructive canopy and cloud cover add further constraints to detecting fires. (Johnston et al., 2018).

Fire emissions models are often based on satellite observations, with ground-based information, such as country-reported statistics, often needed to validate the results. There has consistently been little correlation between satellite-derived and official estimates of burned area (Fusco et al., 2019). Loepfe et al. (2012) found that multiple satellite fire products had high correlation with official reports of burned areas for Sweden, but little-to-no correlation with official statistics for Finland (see Table 4.2). And agreement between official Russian burned-area statistics from fires in Siberian forests and four satellite-based burned-area products was less than 10% (Kukavskaya et al., 2013). The Global Wildfire Information System (GWIS), a joint program between the Group on Earth Observations (GEO), the European Union's earth observation programme Copernicus, and the US National Aeronautics and Space Administration, uses the MODIS MOD64A1 Collection 6 Burned Area product (Giglio et al.,

Table 4.2 Burned area and black carbon (BC) emissions from official burned-area statistics compared to Global Wildfire Information System satellite-derived burned area (Data ref. 4.5) and calculated BC emissions. The fuel loadings, emission factor, and combustion completeness used in Table 4.1 were also used for making these emissions calculations.

Country	Year	Official burned area (km^2)	GWIS burned area (km^2)	BC (tonne) from official estimate	BC (tonne) from GWIS
Norway	2019	0.03	13	7.61E-06	3.30E-03
Sweden	2018	250	154	0.063	0.039
Finland	2019	6	28	0.002	0.007

2018) to create country-level burned-area statistics. GWIS's satellite-derived estimate for burned area overestimates open biomass burning in both Norway and Finland by 199% and 129%, respectively, when compared to official statistics. GWIS underestimates by approximately 48% the total open biomass burning in Sweden. Note, this comparison was done for one year only, and comparisons of satellite and official burned-area data should be made over a longer time period to determine if this disagreement persists.

4.3.2 Climate-driven ignitions, vegetation shifts, and fuel conditions

Ignition likelihood is often modeled by considering the moisture conditions of ground fuels (i.e., litter) and the organic layer (i.e., forest canopy), with humans the most likely source of fire on the ground, and lightning for canopy fires (Wotton et al. 2003). Veraverbeke et al. (2017) introduced a self-reinforcing feedback loop between climate, lightning, fires and northward forest expansion, in which surface energy fluxes from forests appeared to be statistically increasing the probability of lightning in Alaska. Just as warming from climate change increases lightning, it also facilitates northward expansion of the forest via the thawing of permafrost and fires that consume a layer of organic matter. This alters the soil composition to expose mineral soil, making it easier for saplings to take root. These additional trees in the north not only produce more fuel for future fires, but increase surface albedo, encouraging more melting and increasing the potential for lightning-caused fires. Predicting lightning for the Pan-Arctic will require more measurements, including region-specific assessments (Mäkelä et al., 2014), to best understand where climate change is increasing lightning (Witze, 2021).

Many forest insects responsible for killing trees will benefit from climate change due to the established linkage of increased habitat range and higher winter temperatures (Pureswaran et al., 2018). Such climate-driven 'bug kill' increases the amount of easily burnable material in forests and can influence fire risk. For example, a large-scale bark beetle invasion could increase the amount of fuels by adding to the amount of dead wood, increasing ignition and crown-fire risk, as well as increasing the need for, danger from, and cost of managing fuels and fire within forests attacked by insects. (Jenkins et al., 2014). According to Venäläinen et al. (2020), a warming climate is likely to increase the risk of bark beetle outbreaks, as well as wood decay caused by *Heterobasidion spp*. root rot in Finland's coniferous forests. Moreover, the probability of cascading and compounding forest-damaging events – such as large-scale wind damage followed by a widespread bark beetle outbreak – may increase significantly in the future for the high northern latitudes. This may all contribute to increasing fuels available for fires.

4.3.3 Constraining fire intensity and plume injection height for fire emissions

Projections of future fire emissions in the boreal zone must consider fire intensity. Wotton et al. (2017) found that, by mid- to late-century, under both RCP4.5 and RCP8.5 scenarios, a typical fire season will have approximately 24 additional days where the intensity of wildfires (i.e., crown fires) in the Canadian boreal zone will be practically unmanageable by ground crews, even if supported by aerial support, such as water bombers. Emissions from such functionally uncontrollable fires – megafires – in boreal forests are not well quantified. This is due to uncertainties in combustion-efficiency observations and estimates (Xu et al., 2020), and the lack of fine-scale burned-area products that account for small waterbodies and have the capacity to map combustion in 'wet', intermediate drainage, high-carbon soils that are often dominated by species such as black spruce (*Picea mariana*) (Walker et al., 2018). Shvetsov et al. (2019) found that the combination of high fire frequency and positive surface temperature anomalies in the Zabaikal region of southern Siberia was more likely to negatively affect post-fire reforestation than severe burns – which actually had higher rates of vegetation recovery.

Smoke injection and detrainment height are critical for estimating the transport of smoke plumes (Sokolik et al., 2019). Detrainment occurs when turbulence moves smoke particles beyond plume boundaries or when the smoke plume is weak enough to be torn apart by turbulence of the surrounding air. For accurate plume transport estimates, current satellite-based injection-height models must model smoke detrainment (Val Martin et al., 2018), with direct observations of detrainment height used to determine the transport and deposition capacity of a smoke plume (Sokolik et al., 2019). Yu et al. (2019) found that a wildfire in August 2017 in British Columbia, Canada, produced a pyrocumulonimbus event that injected smoke into the stratosphere. The initial smoke injection height of 12 km eventually rose to 23 km in the atmosphere, due to solar heating of BC over a two-month period.

Further, most research to date has focused on the transport of BC to the Arctic from open burning of agricultural fields and grasslands in eastern Europe and Russia during the late winter and early spring (Hall and Loboda, 2017; Qi and Wang, 2020). Because of this limited geographical and temporal focus, uncertainties must still exist in quantifying the impacts of human-caused burning on transport for much of northern Europe, Canada, and the USA (Viatte et al., 2015), particularly as many modeling studies have relied on broad ecoregion datasets (i.e., Olson et al., 2001) to attribute the potential biomass fuel sources of observed deposits.

4.3.4 More future fires in boreal and Arctic peatlands, but where and how much?

Peat smouldering can emit large quantities of smoke, contributing to hazardous air quality (Hu et al., 2018). However, current global fire emissions inventories underestimate peat fires, as forest fuel types currently drive fuel maps and profiles (Liu et al., 2020). Peatland fires in the boreal zone are not well quantified in terms of fuel loadings (Van Leuwen et al., 2014). High uncertainty in emission factors for boreal peat fires (Hu et al., 2018) has led to improved laboratory-derived emission factors, which were calculated using peat sampled from Russia and Alaska (Watson et al., 2019).

With a warming climate comes a risk of increasing peatland and 'legacy carbon' fires (Ingram et al., 2019) in boreal forests. This is particularly the case in stands younger than 60 years,

where drying limits the resilience of the carbon-rich soils (Walker et al., 2019), and in drying fen watersheds near large settlements. The Horse River/Fort McMurray fire that occurred in May 2016 – the costliest wildfire in Canada's history – is an example of the latter (Elmes et al., 2018). Future estimates for emissions from peat fires will need to be informed by the location and condition of these carbon-rich soils, particularly as forecast moderate-to-severe droughts in boreal peatlands in western Canada are expected to increase fire size by over 500% (Thompson et al., 2019). Presently, pan-Arctic maps of peatlands are still incomplete (Yu et al., 2010; Xu et al., 2018), but improving (Hugelius et al., 2020).

Climate adaptation and mitigation efforts, such as to restore or rewet peatlands, do not eliminate the risk of wildland fire in peat landscapes, nor rule-out the use of fire as a management tool (Davies et al., 2016). Thus, estimates of future fire emissions will need to assimilate complexities associated with peat-fuel conditions and loadings. For example, restoring peat is not a linear process, with results from Canada showing that between one and two decades are needed to restore and rewet degraded peatlands that have residual peat and vegetation in order to 'seed' the sites (Nugent et al., 2019). Until these restored peatlands have sufficient moisture and vegetation cover, they remain susceptible to fire risk (Gewin, 2020). Burn depth in peat can be limited in naturally wet and rewetted peatlands if the surface maintains a high moisture content via hydrological and vegetation processes (Granath et al., 2016). Maintaining these needed hydrological processes is difficult for degraded, unmanaged peatlands. In Alberta, wildland peat sites lacking constant sources of water and depositional inputs (such as sand, sediment and detritus that would replenish high-carbon soils) experienced severe burning on the margins (Ingram et al., 2019), while Wilkinson et al. (2019) found that forested peatland margins were extremely vulnerable to peat smouldering combustion, especially in previously burned areas without a fire for 60 or more years. Ronkainen et al. (2013) expected that a warmer climate would lower water tables via evapotranspiration in unmanaged peatlands in Finland, thus increasing wildfire risk. Further, Thompson et al. (2019) estimated that fragmented dry peatlands would act as fire corridors between more flammable upland vegetation types, creating a landscape mechanism to increase fire sizes. Producing more complete estimates of fuel loadings for peatlands across the Arctic region can follow methodologies set by Johnston et al. (2015) to augment dynamic boreal and taiga fuel loadings, such as provided by Ivanova et al. (2020).

4.3.5 Uncertainties in permafrost degradation

Permafrost areas, especially at their southern distributions, are being disturbed by wildfires (Holloway et al., 2020). In Alaska and northwestern Canada, the impacts of wildfire disturbances on permafrost have been well quantified. For example, post-fire permafrost change in Alaska showed greater surface warming in boreal sites than tundra, with surface temperatures higher for previously burned sites than unburned sites, even after vegetation recovered for one to four decades (Jiang et al., 2015). Though the vast majority of fires in the continuous and discontinuous permafrost zones occur in deciduous needleleaf forests (Loranty et al., 2016), work is needed to fill knowledge gaps on the resilience of post-fire permafrost that exist for larch-dominated forests (*Larix* spp.) in Siberia. For example, recent work in Sakha Republic found that a 36 km^2 wildfire in a landscape of open larch with shrub and moss lichen, some 25 km northwest of the Batagaika megaslump, resulted in approximately 3.5 million m^3 of permafrost thaw five years later (Yanagiya and Furuya, 2020). Likewise, uncertainties persist as to the resilience of permafrost, post-fire, in the boreal forests of eastern Canada, such as Quebec and Labrador (Holloway et al., 2020).

The IPCC Special Report on the Ocean and the Cryosphere in a Changing Climate (IPCC, 2019) concluded with very high confidence that permafrost thaw and degradation will increase throughout the 21st century. However, exact quantification is still lacking. This certainty of degradation but uncertainty in how much and where is an important consideration regarding future fire emissions in the Arctic Council region. For example, while not all permafrost is confined to peatlands, many discontinuous permafrost sites are dominated by peatlands in Canada (Estop-Aragonés et al., 2018; Gibson et al., 2018), Russia (Hugelius et al., 2014), and Sweden (Chang et al., 2019), with recent work estimating that approximately half of all northern peatland carbon is presently in soils classified as permafrost (Hugelius et al., 2020). Further, current climate models may be missing the link between melting soil ice – sometimes referred to as thermokarst processes – and potential permafrost degradation of the currently stable and carbon-rich northeast Siberian Arctic lowlands (NESAL). When thermokarst processes were combined with increased temperature projections in numerical modeling by Nitzbon et al. (2020), the results indicated that a threefold increase of permafrost thaw could be expected in the NESAL region by 2100 under RCP4.5, potentially increasing the amount of peat fuels in a region already experiencing high fire activity. Combining current peatland distribution maps with newer modeled datasets of predicted mid-century and late-century permafrost extent and geohazard indices under climate-forcing scenarios (Karjalainen et al., 2019) can reduce uncertainties to determine: 1) increased peat-fire risk and locations due to permafrost melt; and 2) decreased capability to deploy ground-level wildland firefighting, thus limiting ability to control future peat fires and fire emissions in the Pan-Arctic.

4.3.6 The role of people in future Pan-Arctic fire regimes

The impact of humans on fire risk is dependent on local- to national-scale actions that may increase fire and emissions via deforestation, transportation networks, energy extraction, and agricultural open burning, as well as decrease fire and fire emissions via active suppression. Riley et al. (2019) noted that humans on the global scale have been able to disrupt and sometimes uncouple the direct relationship between temperature and biomass burning, and asked "is there a threshold in the magnitude of climate change after which humans will no longer be able to affect this relationship?" More input from the Permanent Participants on Indigenous burning practices could clarify some of these uncertainties.

As elsewhere, while human activity in the boreal and Arctic may be a significant ignition source, human proximity tends

to reduce the area burned because of effective fire suppression; as a result, remote fires ignited by lightning lead to larger areas being burned. In Interior Alaska, where lightning-caused fires accounted for 95% of total burned area (Veraverbeke et al. 2017), 52% of total ignitions were human in origin but occurred in areas of high fire suppression; as a result that they contributed only 5% of total burned area from 1990 to 2016 (Calef et al. 2017). Archard et al. (2008) estimated that 65% of all forest fires in the Russian Federation were caused by human ignition, while a more recent study found that approximately half of all the fires in Sakha Republic were caused by anthropogenic activities (Kirillina et al., 2020). Throughout boreal Canada, anthropogenic factors increase fire probability (Parisien et al., 2016), with humans igniting most fires close to roads but lightning-caused fires responsible for the majority of burned area in remote areas (Gralewicz et al., 2012). Blouin et al. (2016) found that 45% of wildfires in Alberta were started by lightning, but were responsible for 71% of the burned area. In Finland, lightning-caused fires account for less than 15% of forest fires (Larjavaara et al., 2005). Machines used for forestry operations in stony areas of Sweden accounted for 330 to 480 annual ignitions, and 40% of total burned area (Sjöström et al., 2019). Of fires and ignition sources reported by 19 European countries to the European Forest Fire Information System (EFFIS), EC (2017) determined that only 4% were from natural sources, with half of the fire records lacking a verified cause. It should be noted that population densities vary widely across Arctic Council Member states in the boreal and Arctic regions, and therefore the influence of human activity, including Indigenous cultural burning, may be location-specific.

4.4 Summary and main messages

In 2019, the majority of open biomass burning and related emissions for the Arctic Council member countries originated in Siberia and the Russian Far East, followed by CONUS, Canada, and Alaska. The average annual BC emissions from all open biomass burning sources is 340,000 tonnes. Open biomass burning emissions have increased above 60°N, with fires above 66°N occurring earlier in the year and burning later into the growing season. Increased length in fire seasons is coupled with a prediction of increased fire severity, and potentially physically unmanageable crown fires in the boreal as soon as 2050 (Wooton et al., 2017). Future emissions from fires are difficult to predict; here more work is needed, as emissions from functionally uncontrollable fires in boreal forests are not well quantified due to uncertainties in combustion-efficiency observations and estimates (Xu et al., 2020).

Pan-Arctic fire emissions in the coming decades of the 21st century will likely be driven by climate-change impacts on fuels, including the interactions between peat and permafrost, fire weather, and ignition sources. The consensus of current literature is that climate change and human activity will increase fire risk in the Arctic, via increased lightning strikes, the thawing of permafrost, and transitions to grasslands and steppe and dry peat. In eastern Canada, northward expansion of deciduous forests will likely decrease fire risk. Human-caused fires are likely to increase, driven by the expansion of extraction processes for energy, transportation networks, and tourism.

Boreal and Arctic landscapes are complex, with high levels of localized heterogeneity, complex and endemic vegetation types, and diverse communities (Raynolds et al., 2019) and topography. Estimates of future fire emissions will need to integrate multiple datasets to accurately quantify fires in the Arctic (Masrur et al., 2018), incorporating data on climate, permafrost conditions, aboveground and peat fuels, topography, land use, Indigenous and local fire management, and ignition sources. In the short-term, better understanding of the differences between official estimates of fire activity based on ground reports (bottom-up) and Earth observation estimates of fire activity (top-down) is needed to achieve accurate assessment of emissions. Importantly, the official statistics offer a different view of fire activity and emissions. Calculating future open biomass burning emissions will need improved satellite-based fire-detection methodologies for the Arctic region, fire model intercomparisons (with a potential to learn from the ongoing international coordination and multi-scale and local-to-global evaluation efforts of the Fire Model Intercomparison Project [FireMIP]), and also shorter latency in ground reports and statistics from official agencies. An additional research priority is to identify and quantify specific drivers of fire across heterogenous boreal and Arctic landscapes, countries, and ignition sources. Further, policy-relevant research needs to quantify not only emissions but the transport of pollutants – especially BC – from fires in the Arctic (and from Arctic states) that have an impact on the Arctic, ideally accounting for errors and uncertainties. Understanding of the likelihood of Arctic and boreal fire emissions and transport in the near-term, by mid-century, and by end-of-century is also needed, building on current estimates of 12%–15% of annual BC deposition in the Arctic from forest fires in the source regions of Siberia, Alaska, and Canada when compared to global anthropogenic and biomass emissions (Ikeda et al., 2017). It should be noted that these source regions experience BC deposition due to transport from Eurasia, East Asia, and North America.

Human activity and communities in the Arctic will need to adapt to increasing fire risk. Fire management and fighting strategies in the boreal may not work or might even cause more damage in the Arctic. Climate change will also affect the effectiveness of current wildland firefighting techniques. For example, Canadian wildland firefighters operationally use several key thresholds to guide fire operations based on fire intensity. Wotton et al. (2017) reported that at 2 Megawatts per meter (MW/m) fire-line intensity, ground resources request aerial fire support to hold the fire line; at 4 MW/m, aerial fire suppression by air tankers becomes ineffective at directly controlling a fire line; at 10 MW/m, heavy air tankers cannot hold or suppress a fire line. From the policy perspective, understanding if, or how much, fire management – from reducing or eliminating ignitions, to prescribed burning for reducing fuel and resulting wildland fires – can reduce BC emissions needs to be better understood. Mitigating future emissions may require a Pan-Arctic fire management and monitoring strategy, with buy-in from the Arctic Council Member states and Arctic Indigenous communities.

Chapter 4 Appendix

A comparison of five biomass burning emission models, including the Global Fire Emissions Database (GFED; van der Werf et al., 2017); the Fire Inventory from NCAR (FINN; Wiedinmyer et al., 2011); the Global Fire Assimilation System (GFAS; Kaiser et al., 2012); the Quick Fire Emissions Dataset (QFED; Koster et al., 2015); and the Fire Energetics and Emissions Research (FEER; Ichoku and Ellison, 2014), was completed for the entire Pan-Arctic region. Figures A4.1, A4.2, A4.4, and A4.5 show details of the variation in these peer-reviewed satellite-based emissions inventories. It should be noted that GFED was used in the current CMIP runs and analyses (van Marle et al., 2017; Figure A4.3).

The fire emissions model with the consistently highest BC emissions is QFED, with an annual average of 680,000 tonnes (Figure A4.4). FEER, GFAS, and GFED exhibit greater agreement, with annual BC emissions averages of 320,000 (±70,000) tonnes, 300,000 (±71,800) tonnes, and 250,000 (± 61,000) tonnes, respectively (Figures A4.1 and A4.5). FINN had the lowest annual average BC emissions of 130,000 tonnes, with higher emissions in outlier years – 2012 (197,000 tonnes) and 2008 (186,000 tonnes). The custom AMAP model produced emissions estimates slightly higher than FINN (Figure A4.4) for 2018. The AMAP model predicted BC emissions of 129,000 tonnes and CH_4 emissions of 1,390,000 tonnes, compared to FINN's 105,000 tonnes of BC and 1,190,000 tonnes of CH_4. When compared for 2018 only, GFED showed marginally higher BC emissions than GFAS, while CH_4 emission estimates from GFAS were substantially higher than GFED.

The current satellite-based fire emissions models are not consistent in their ranking of which produces the highest overall emissions estimates, particularly when considering emissions from CH_4, CO, and $PM_{2.5}$ (Figure A4.4). Fire emissions calculations are not linear and thus these differences are expected. Consistently, FINN is the model with the lowest emissions estimates.

Table A4.1 Black carbon (BC) emissions from reported statistics on burned area in the Arctic Council Member states.

Country/Region	Year	Official burned area (km^2)	Fuel Loading (kg/km^2)	Black carbon emission factor (g/kg)	Combustion completeness (%)	Black carbon emissions (g converted to tonne)
USA/Alaska	2019	10481[a]	1080	0.5	47	2.660
Canada	2019	18389[b]	1080	0.5	47	4.667
Denmark/Greenland	2019	8[c]	1650	0.04	24	1.27E-04
Norway	2019	0.03[d]	1080	0.5	47	7.61E-06
Sweden	2018	250[e]	1080	0.5	47	0.063
Finland	2019	6[f]	1080	0.5	47	0.002
Russia	2019	100785[g]	1080	0.5	47	25.579
USA/CONUS	2019	18876[h]	1610	0.55	61	10.196

Sources for burned area from Alaska Division of Forestry (2020a)[a], CIFFC (2020)[b] , Markuse (2019)[c], DSB, personal communication, 2020[d], SOU (2019 – in Swedish)[e], Ketola, personal communication, 2020[f], and Data ref. 4.2[g]; fuel loadings and combustion completeness from van Leeuwen et al. (2014) for boreal forests, with tundra values used for Greenland and temperate forests for the contiguous United States (CONUS); emission factors for BC taken from GFEDv4s with 0.5 g/kg assigned to boreal forest ecosystems, 0.55 g/kg assigned to temperate forests, and 0.04 g/kg assigned to peat for Greenland.

Table A4.2 Slope of trends lines for GFEDv4s, GFASv1.2, and FINN1.5 for 50°N–60°N and 60°N–70°N for 2005–2018.

Fire emissions model	Slope (50°N–60° N)	Slope (60°N–70°N)
GFEDv4s	0.0014	0.0076
GFASv1.2	-0.0019	0.0058
FINNv1.5	0.0022	0.00019

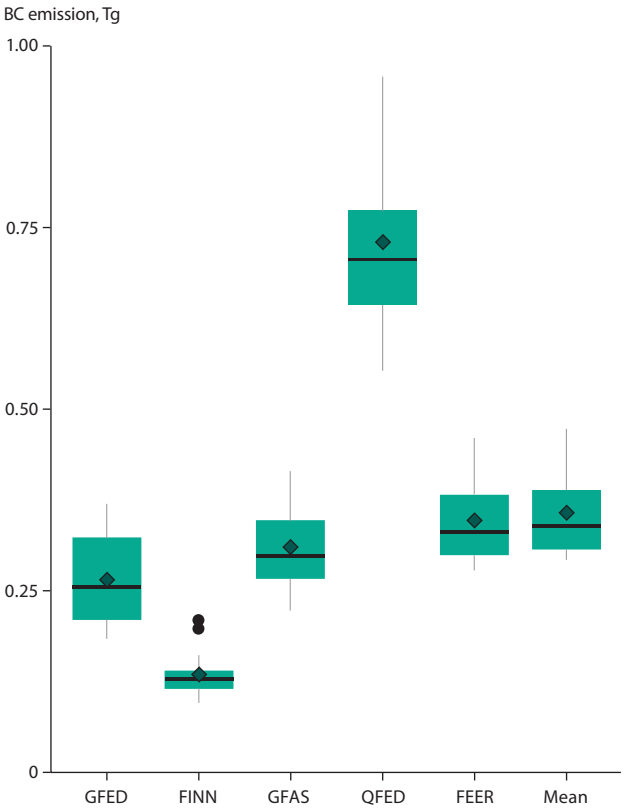

Figure A4.1 Boxplot summaries of total annual emissions of BC in Tg for 45°N–80°N from 2005–2018. Emissions from GFED, FINN, GFAS, QFED, and FEER, plus an average of the five models, are included. The horizontal bar is the median, with the mean indicated as a diamond. The box shows the 25th to the 75th percentiles, and the vertical lines show 1.5 times the interquartile range. Points outside of the interquartile range are shown as dots; the FINN outliers are for years 2008 and 2012.

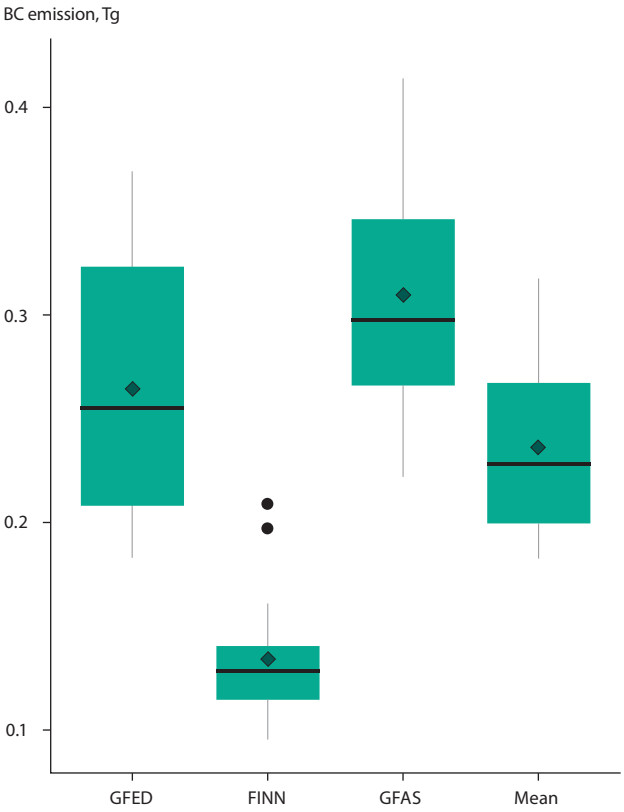

Figure A4.2 Boxplot summaries of total annual emissions of BC in Tg for 45°N–80°N from 2005–2018. Emissions from GFED, FINN, GFAS, plus an average of the three fire emission models are included. The horizontal bar is the median, with the mean indicated as a diamond. The box shows the 25th to the 75th percentiles, and the vertical lines show 1.5 times the interquartile range. Points outside of the interquartile range are shown as dots; the FINN outliers are for years 2008 and 2012.

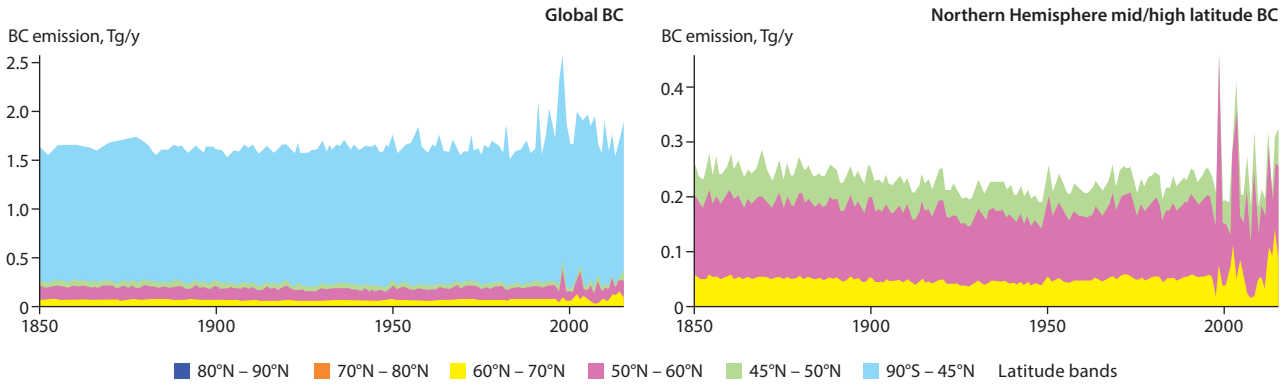

Figure A4.3 Modeled historical open biomass burning emissions from van Marle et al. (2017) for the globe (left) and the Arctic Council Member states' area of interest (right).

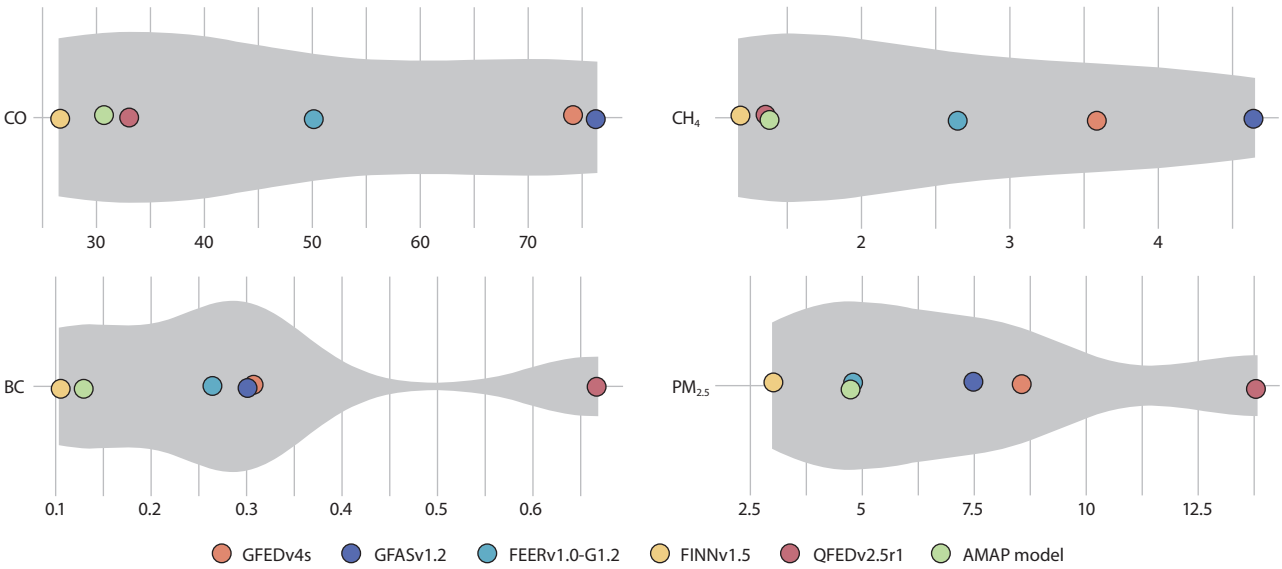

Figure A4.4 Density plot of the 2018 annual emissions (Tg) for CH_4, CO, BC, and $PM_{2.5}$ from six satellite-based global biomass-burning emissions models: GFEDv.4s, GFAS v1.2, FEER v1.0–G1.2, FINN v1.5, and the custom AMAP SLCF model produced by chapter co-authors McCarty and Fain (Data ref. 4.7) for 45°N–80°N.

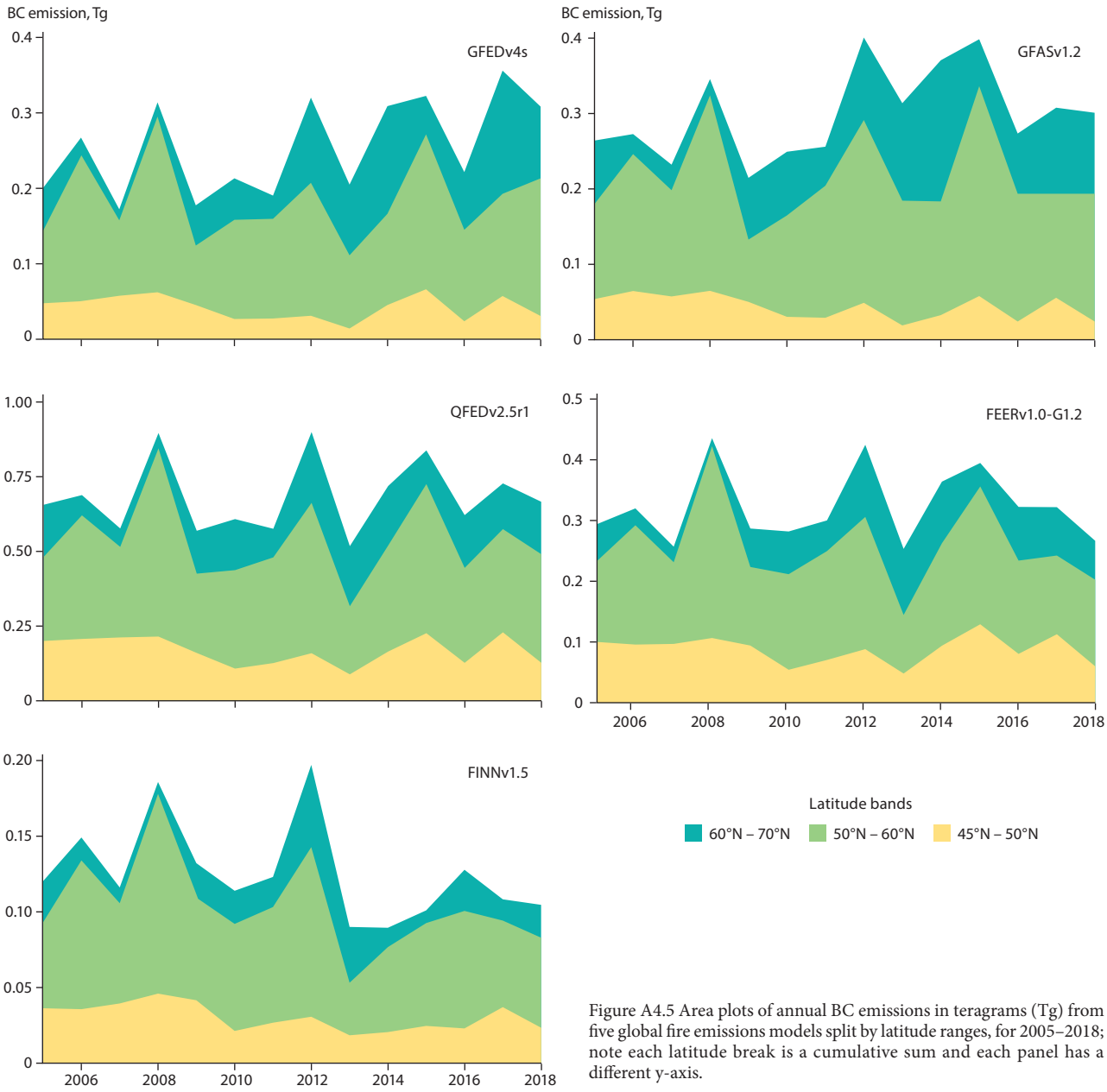

Figure A4.5 Area plots of annual BC emissions in teragrams (Tg) from five global fire emissions models split by latitude ranges, for 2005–2018; note each latitude break is a cumulative sum and each panel has a different y-axis.

5. Advances in measurement techniques and observational capacity

Authors: 5.2: Stefano Decesari, Julia Schmale, Sangeeta Sharma, Lin Huang, Hans Christen Hansson, Marco Zanatta, Andreas Massling, David Cappelletti, Outi Meinander, Antti Hyvärinen, Meri Ruppel, Makoto Koike, Yutaka Kondo

5.3: Kathy Law, Henrik Skov, Steve Arnold, Joakim Langner, Jens Liengaard Hjorth

5.4: Lise Lotte Sørensen, Lori Bruhwiler, Brett Thornton

5.5: Abhay Devasthale, Manu Anna Thomas, Joakim Langner, Makoto Koike, Yutaka Kondo

5.1 Introduction

This chapter introduces advances in techniques for measuring SLCFs, as well as discussing the current capabilities for measuring SLCF concentrations across the Arctic. The principles of established measurement methods are not presented in detail, as they can be found elsewhere (e.g., AMAP, 2015a, 2015b). Instead, the focus is on new developments and uncertainties.

5.2 Current monitoring capabilities for aerosols

Black carbon (BC) is the main aerosol component responsible for climate warming. Activities for monitoring BC have become more systematic and expanded to cover a greater number of geographical regions over time (see Appendix Figure A5.1). Other aerosol components that can contribute to warming beside BC are iron oxides in mineral dust and light-absorbing organic carbon (OC, referred to as "brown carbon"). Aerosol compounds, meanwhile, such as sulphate and nitrate salts and sea salt, contribute to light scattering, and have a cooling action on the atmosphere. Of these, sulphate and nitrate salts and sea salt have been monitored over the long-term at a few sites. However, observations of dust and organic particles appear to still be very limited. Measurements relating concentrations of aerosols to specific sources have not been regularly carried out.

Concentrations of aerosols observed at Arctic sites are modulated by atmospheric transport, with considerable interannual variability resulting from climate and seasonal weather anomalies. For this reason, assessing the effects of changes in emissions often requires multi-annual records of observations, normally spanning one or two decades. Therefore, to evaluate the effectiveness of mitigation policies over time, long-term monitoring remains essential. As climate warming is progressing at increasing rates in the Arctic, observations of its feedbacks on the production and transport of atmospheric aerosols is becoming another priority objective for monitoring in this part of the world.

5.2.1 Techniques used to monitor aerosols in the Arctic

A variety of platforms are used for measuring atmospheric aerosols. Most long-term data is recorded at surface-based observatories that measure particles either using real-time techniques or by collecting samples for subsequent analysis. Such types of observations yield detailed information on chemical and microphysical particle properties. Remote sensing, either from the ground or from space, also produces longer-term timeseries, mostly of aerosol optical properties. Intensive, but short-term, field campaigns contribute more detailed knowledge on aerosol processes, since more complex and advanced instrumentation can be operated in these circumstances. Field campaigns take place regularly at ground-based observatories, as well as on research vessels and aircraft.

Taking measurements of SLCFs in snow and ice (both in precipitation and snowpack) typically involves taking samples in the field for subsequent analysis in the laboratory. At some ground-based observatories, snow samples are collected regularly. Snowpack sampling is also carried out using transects across large areas. This approach is mostly limited to one-off efforts or a small number of repetitions. Ice-core samples are taken from specific drilling locations in the North American and European Arctic. In the Eurasian sector of the Arctic, no ice caps or glaciers exist that are suitable for ice coring. Here lake sediments can be collected instead. However, of all particulate SLCFs, only BC can be analysed from lake sediments (Ruppel et al., 2021).

5.2.1.1 Measuring atmospheric black carbon and co-emitted aerosol compounds

BC aerosols strongly absorb solar radiation, contributing to atmospheric heating and snow melt that could potentially accelerate Arctic warming (AMAP, 2015a). These particles are distinct from other forms of carbon and carbon compounds contained in atmospheric aerosol (Bond et al., 2013), having a unique combination of properties. These properties are: having strong visible light absorption with a mass absorption cross-section (MAC) of at least five square-meters per gram (m^2/g) at 550 nanometers (nm) (Petzold et al., 2013; Bond and Bergstrom, 2006); being refractory with a vaporization temperature near 4000 Kelvin (K) (Schwarz et al., 2006); having aggregate morphology (Medalia and Heckman, 1969); and being insoluble in water and common organic solvents (Fung, 1990).

BC mass concentrations (M_{BC}) are measured directly using incandescent and/or thermal techniques, or indirectly from absorption measurements using appropriate MAC values as the conversion factor (Petzold et al., 2013). Different terms are used depending on the property being measured. Refractory black carbon (rBC) refers to incandescent measurements, elemental carbon (EC) is used for thermal techniques, and equivalent black carbon (eBC) is the term for optical or photoacoustic techniques. Globally, there are various measurement networks related to air quality (Chow et al., 2004; Cavalli et al., 2010; Brown et al., 2017) and climate forcing (Collaud Coen et al., 2020) that utilize such

techniques. Several methods have been used to measure BC in the Pan-Arctic. Intercomparison of different techniques show agreement within a factor of two uncertainty at Alert in Nunavut, Canada (Sharma et al., 2006, 2017), Ny-Ålesund on Svalbard, Norway, and Utqiaġvik, in Alaska, USA (Sinha et al., 2017). It is hence possible to derive upper and lower bounds on BC measurements at these locations. Similar studies are needed at other locations in the Arctic. Below is a brief description of relevant measurement techniques that have been published elsewhere in detail (AMAP, 2015a; Petzold et al., 2013; Lack and Langridge, 2013; Sharma et al., 2017; Sinha et al., 2017; Huang et al., 2021).

The main technique to emerge in the last decade is based on single particle soot photometers (SP2). The SP2 measurement of BC involves using an online laser-induced incandescent (LII) technique to directly measure BC mass (rBC) of individual aerosols. The SP2 provides the size distribution of rBC for volume-equivalent diameters between 70 and 850 nm (Schwarz et al., 2010; Gysel et al., 2011; Moteki and Kondo, 2010; Kondo et al., 2011a), and total mass concentrations of refractory BC (M_{rBC}) can be derived directly (Moteki and Kondo, 2010) or by integrating size distributions – assuming an effective density with an analytical uncertainty of about 10% (rest of SP2 community). Considering error propagation from all factors (calibration procedures, detection efficiency, possible interference of refractory organic carbon, linearity range of instrument response and so on) an overall uncertainty for ambient BC measurements could be up to 25% (Schwarz et al., 2010; Gysel et al., 2011; Laborde et al., 2012). The SP2 can also provide information on the mixing state of BC (a ratio of BC to total particle diameters). This technique has been shown to be uninfluenced by the mixing state of BC and co-existence of non-BC particles. There is a well-established standard for calibrating the SP2 (i.e., the relationship between refractory BC mass and LII signal intensity). It involves using fullerene soot combined with an aerosol particle mass analyzer (APM) or centrifugal particle mass analyzer (CPMA) (Moteki and Kondo, 2010; Laborde et al., 2012). Ambient BC particles can also be used after removing compounds coating BC particles by heating them to 300°C–400°C, although this is more time consuming due to the lower BC concentration (Kondo et al., 2011a). Aquadag colloidal graphite can also be used, provided the difference in the sensitivity between it and fullerene soot is taken into account (Laborde et al., 2012). If a differential mobility analyzer (DMA) is used for SP2 calibration instead of APM or CPMA, accurate values for the effective densities of standard BC samples (fullerene soot or Aquadag) must be determined first (Moteki and Kondo, 2010; Gysel et al., 2011; Ohata et al., 2021.

The SP2 is considered one of the most reliable instruments with which to measure M_{BC} in various atmospheric environments, including in the well-aged airmass (Bond et al., 2013). However, SP2 underestimates when particles sizes smaller than 70 nm dominate the size distribution. In the Arctic, SP2 instruments have been used for ground-based, shipborne, and airborne measurements (Sharma et al., 2017; Zanatta et al., 2018; Schulz et al., 2019; Ohata et al., 2019). These measurements were made mainly on a campaign basis due to the challenges of maintaining such systems for long-term observations, and the amount of data they generate. That said, longer-term (>1 year) SP2 measurements have been made at Alert since 2011 and at Zeppelin since 2019. Moreover, SP2 measurements are used to validate various long-term BC measurements made in the Arctic utilizing other techniques. This involves making side-by-side measurements for comparisons over short periods of time (Ohata et al., 2019; Ohata et al., 2021).

For long-term monitoring of M_{BC} in the atmosphere, two independent techniques are currently used. Both of these have individual advantages and inherent limitations. The first are the thermal-evolution/thermal-optical methods, which directly measure EC. Using the thermal methods is one of the most accepted approaches employed by long-term monitoring networks for M_{BC} measurements around world (Chow et al., 2007; Cavalli et al., 2010; Chan et al., 2019). An advantage of the thermal methods is that they can also measure OC at the same time. Different protocols to quantify EC have been adopted by different networks. IMPROVE_A (Chow et al., 2001, 2004, 2007) is used in several North American monitoring networks; EUSAAR-2 (Cavalli et al., 2010) is the standard protocol in European networks; and EnCan-total-900 (ECT9) is the thermal method applied in the Canadian Aerosol Baseline Measurements network (Huang et al., 2006; Chan et al., 2019; Sharma et al., 2017; Huang et al., 2021). NIOSH-5040 (1999) protocols have also been used in long-term observations at Arctic sites (e.g. EUA-BCA, 2019b). The measurement principles and the details of individual protocols can be found in WMO/GAW (2016), as well as in the literature listed above. EC or OC concentrations presented in Chapters 4 and 6 were measured using either ECT9 or NIOSH-5040 protocols. EC/OC data measured using ECT9 and reported to the World Meteorological Organization World Data Center for Aerosols (WDCA) were based on the data submission guidelines (Data ref. 5.1) and associated with corresponding uncertainties (including field blank factors). The mean uncertainties (reported to WDCA) of OC and EC at Alert are 22% and ~30% (Sharma et al., 2017) on average, respectively.

Thermal methods usually include thermal-evolution and thermal-optical protocols. The main difference between the two is that the former does not monitor optical properties separating EC from OC, whereas the latter does. Total carbon mass measurements by thermal protocols are well calibrated by direct volumetric injection of sucrose solution with an uncertainty of 5%–10% (Chow et al., 1993, 2001; Cavalli et al., 2010; Huang et al., 2021). The separation of OC from EC using thermal-optical methods is not only achieved by temperature protocols but also in combination with signal changes in optical properties (either reflectance or transmittance). Consequently, no suitable EC standards are available for thermal-optical methods, resulting in protocol dependent EC/OC values. The disadvantage of the thermal-optical methods is the inherent uncertainty in the separation between EC and OC, due to charring corrections and associated assumptions (WMO/GAW 2016; Karanasiou et al., 2015; Malm et al., 2020). However, in contrast to thermal-optical protocols, the separation of EC from OC by thermal-evolution protocols only depends on refractory carbon, similar to SP2. No optical signals are used in thermal-evolution methods, and standards are used for EC and OC separation (Huang et al., 2006, 2021). Results

from replicating OC/EC ratios using different EC and OC standards for measuring are within the range of 2%–5%, and the effectiveness of separating EC from OC is well demonstrated (Huang et al., 2021).

A literature review conducted to compare various thermal and thermal-optical analysis techniques (Karanasiou et al., 2015) revealed that EC measurements differ, on average, by a factor of two or less, due to differences in protocols, instruments, and laser signals, as well as corrections of charring that depend on the chemical properties of organic matter. Recently Chan et al. (2019) showed that OC and EC measurements differed on average by 15% and 75% (and up to 83%), respectively, over a period of ten years among three North America national networks co-located at a single site. These intercomparison differences were consistent despite the use of different sampling systems, frequencies, size cut-offs, analytical protocols (IMPROVE_thermal-optical versus ECT9_thermal-evolution, for example) different instruments (such those from the Desert Research Institute [DRI] versus those from Sunset Laboratory) and different charring corrections. To identify emissions changes over time and to assess the effectiveness of mitigation policies by studying long-term trends, it is important to ensure that atmospheric measurements are consistent and traceable over long periods of time. Absolute values are also important to reveal spatial variations in M_{BC} measured by different techniques over the Arctic, because this information is used to validate numerical model calculations to evaluate the impacts of BC in the region. Maximizing the scientific value of historical data and harmonizing the EC data generated by different networks, laboratories and techniques for accurately evaluating models and constraining emissions, calls for mechanisms for assessing the comparability of EC measurements in the Arctic (as also recommended in WMO/GAW [2016]). For example, long-term intercomparison of filter samples at various co-located sites is needed, and regular reference intercomparisons should be made between networks, laboratories and techniques over decadal timescales. Given that SP2 is one of the most reliable techniques for measuring M_{BC}, regular site-specific intercomparisons of SP2 measurements with thermal-evolution/thermal-optical methods are recommended for monitoring BC in the Arctic. This is particularly important because errors resulting from the EC/OC separation by thermal-optical methods are related to the chemical properties of the samples. Different techniques can be also cross-evaluated for individual Arctic sites and protocols.

The use of filter-based optical methods is another approach taken for long-term monitoring of M_{BC} in the atmosphere, providing outputs in equivalent black carbon (eBC). Multi-decadal results discussed in the trends section of Chapter 6 (Section 6.1.4) were derived mostly from eBC measurements in the Arctic. At many locations, the particle soot absorption photometer (PSAP; Radiance Research, USA), continuous light absorption photometer (CLAP; National Oceanic and Atmospheric Administration [NOAA]/Earth System Research Laboratory [ESRL]), Aethalometer (Magee Scientific, USA) or multi-angle absorption photometer (MAAP; ESM Andersen Instruments, Germany) (Petzold and Schönlinner, 2004) have been used. However, the accuracies of the M_{BC} values derived from these measurements have not been critically evaluated in the Arctic. Possible differences in the M_{BC} arising from the various techniques would not largely affect the long-term trends in these measurements, as long as they were recorded by a single instrument type (and assuming that MAC for each individual instrument is stable – the stability of MAC needs to be confirmed accordingly, such as in work carried out by Sinha et al. [2017]). There are two major uncertainties in the filter-based absorption techniques that are caused by non-BC aerosol compounds. First, absorption coefficients b_{abs} (Mm^{-1}) must be derived from measured attenuation (absorption and scattering) of light. This is achieved by subtracting scattering of aerosol in the filter medium (largely determined by non-BC compounds) based on the empirical relationship using independent measurements of aerosol-scattering coefficients (b_{scat}), which can be derived using, for example, a nephelometer. For the MAAP, by measuring reflectance at two angles, as well as transmittance with which radiative transfer is calculated across the filter, insensitivity to the co-existing light-scattering particles (LSPs) has been evaluated (Petzold and Schönlinner, 2004). Second, M_{BC} in micrograms per cubic meter ($\mu g/m^3$) is derived as $M_{BC} = b_{abs}$ /MAC, where MAC is measured in m^2/g. The MAC value is apparently affected partly by errors in b_{abs} for given M_{BC} values and partly by coating the BC particles by LSPs, which produce a lensing effect (although the degree of the latter effect is not fully quantified for filter-based instruments). Previous studies have recommended a wide range of MAC values (10–29 m^2/g) for individual locations and seasons (Eleftheriadis et al., 2009; Hirdman et al., 2010b; Sharma et al., 2006, Zanatta et al., 2016). There has been a concerted effort to develop correction schemes to account for the above-mentioned effects in the Aethalometer absorption conversion from measured mass values (Backman et al., 2017): the suggested corrected scheme gives an approximate factor 4 reduction in absorption at all Arctic locations. The Continuous Soot Monitoring System (COSMOS) instrument was designed to overcome the difficulties of the previous filter-based optical technique (Kondo et al., 2011a). It uses a heated inlet (300°C–400°C) to evaporate major fractions of LSPs in the incoming air sample. As a result, one does not need to subtract a scattering contribution of LSPs and can use a constant MAC value of about 8.7 m^2/g, which depends only on the size distribution of bare BC particles. In fact, an agreement within 10% was found between COSMOS and SP2 measurements at Ny-Ålesund and in Asia (Ohata et al., 2019), indicating that COSMOS is comparable to the SP2. In general, M_{BC} measured by COSMOS (M_{BC} [COSMOS]) was highly correlated with b_{abs} for PSAP or CLAP (b_{abs} [PSAP] or b_{abs} [CLAP]) at Utqiaġvik, Ny-Ålesund, (Sinha et al., 2017) and Alert and b_{abs} (MAAP) at Pallas, in Finland (Ohata et al., 2021). Consequently, it is possible to construct harmonized eBC multidecadal datasets obtained by PSAP/CLAP, MAAP, and Aethalometer by scaling their values to agree with M_{BC} (COSMOS) simultaneously obtained in the Arctic. This approach is reasonable because b_{abs} values obtained by individual instruments are not fully calibrated for the PSAP, Aethalometer, and MAAP instruments (WMO/GAW, 2016), whereas M_{BC} (COSMOS) for each COSMOS is calibrated using atmospheric BC particles (Kondo et al., 2011a). As cautioned for EC measurement, it is critical to keep the consistency and traceability, as well as the absolute accuracy of the measurements. It is therefore recommended to make long-

term intercomparisons of various filter-based optical methods with COSMOS, and to perform regular intercomparisons with SP2 measurements in the Arctic. Comparisons between thermal and optical methods are also critical to establish harmonized measurement networks in the Arctic.

The methodologies discussed above for measuring different states of BC have evolved over the decades. Filter-based absorption photometers other than COSMOS — namely, PSAP, the Aethalometer, and MAAP — are still comparable to direct mass measurement techniques (SP2 and COSMOS) within a factor of about two (Sharma et al., 2017; Ohata et al., 2021); this means it is possible to refer to these measurements as upper and lower bounds in BC measurements. Limiting uncertainty in BC by using upper and lower bounds is very useful to minimize the propagating of uncertainties in model outputs.

5.2.1.1.1 **Inorganic chemical speciation**

Chemical characterization provides key information about the contributions of aerosols from different sources, and is therefore important in SLCF monitoring programs. The methodologies developed for determining the refractory components of aerosols, such as BC and dust, are complemented by a large suite of analytical techniques that provide offline filter extraction and chromatographic analysis for chemical speciation. The main targets of chromatographic methods are water-soluble ionic inorganic and organic compounds, and a range of solvent-extractable organic compounds. At Arctic locations, integrated aerosol samples are normally collected at up to weekly frequency using high-volume flow systems for offline analysis of sulfate, nitrate, MSA (methane-sulfonic acid) and other compounds. Teflon or mixed-cellulose ester filters represent the most common substrates. The details of these techniques pertinent to the measurement locations used in Chapter 6 can be found elsewhere (Sharma et al., 2012; Quinn et al., 1998; Maenhaut et al., 1997, Heidam et al., 2004; Massling et al., 2015). Several studies report filter extraction with 10 milliliters (ml) of ultrapure water and analysis with Dionex 4500i Ion Chromatography (Li and Barrie, 1993; Quinn et al., 2002; Maenhaut et al., 1994; Becagli et al., 2011; Heidam et al., 2004) and a specific chromatographic column – to meet the particular laboratory technique requirements. Very stringent standardization techniques are employed (Li and Barrie, 1993; Sharma et al., 2012; Quinn et al., 1998; Maenhaut et al., 1997, Heidam et al., 2004; Massling et al., 2015). The analytical uncertainty of inorganic ions for data used in Chapter 6 is up to +/- 20%.

Recently, online methods have been developed using mass spectrometric (MS) techniques, as described in detail in Section 5.2.2.2. These include Aerodyne C-Aerosol Mass Spectrometer (C-AMS) and Aerodyne Aerosol Chemical Speciation Monitor (ACSM) and are suitable for chemical speciation of particles of less than one micrometer (μm) size. Such methods provide higher-time-resolution chemical speciation than the off-line techniques but particle concentrations may be reduced due to oven collection and inlet transmission efficiencies less than unity (Liu et al., 2007; Matthew et al., 2008). A scaling factor needs to be applied to the Aerosol Mass Spectrometer (AMS) or ACSM measurements obtained by comparing the results to those arrived at using speciation with filter measurements (Leaitch et al., 2009, 2011). The overall uncertainty on the basis of filter comparison OM could be within +/- 25%. (Leaitch et al., 2009, 2011).

5.2.1.1.2 **Organic chemical speciation**

Compared to the inorganic ionic composition, the organic fraction of the aerosol exhibits a huge molecular complexity; as a result, a large diversity of analytical methods have been developed for speciation. Such methodologies have been applied to organic aerosol (OA) characterization mostly during intensive field campaigns or short-term observation periods. However, the development of techniques suitable for longer-term monitoring, which are currently limited to a few target species (such as MSA), is expected to expand in the future. The individual organic compounds typically represent a very small amount of total OC, and they are mainly used as tracers for specific sources (or source types). Organic tracers must exhibit good stability during transport of the aerosol in the atmosphere; the atmospheric lifetimes of the most important ones have been extensively characterized, to demonstrate, for example their reactivity with atmospheric oxidants (Hoffmann et al., 2010). The most common organic tracers include markers for biomass burning (levoglucosan and its isomers, phenolic compounds, and resin acids), anthropogenic fossil-fuel combustion (hopanes, n-alkanes and fatty acids with a low "carbon preference index") and biogenic sources (sugars, sugar-alcohols, amino acids, fatty acids with a high carbon preference index, and photo-oxidation products of volatile terpenes), as well as for natural and anthropogenic combustion polycyclic aromatic hydrocarbons (PAHs) and other industrial emissions (phthalates, persistent organic pollutants [POPs] and so on) (Fu et al., 2009, 2013, 2015, 2016; von Schneidemesser et al., 2009; Scalabrin et al., 2012; Zangrando et al., 2013; Karl et al., 2019). Among the most versatile and well-established analytical methods are techniques involving gas chromatography coupled to mass spectrometry (GC/MS) determination with chemical derivatization for the polar compounds (Fu et al., 2009, 2015). Recent developments of high performance liquid chromatography (HPLC) techniques, such as HPLC/high-resolution mass spectrometry (HRMS)-time of flight and HPLC/(−)-electrospray ionization (ESI)-MS/MS, have enabled the reduction of preanalytical steps and increased the sensitivity for low concentrations (Zangrando et al., 2013; Yttri et al., 2014). Trace-level concentrations represent a constant analytical challenge for organic speciation in remote environments. Even the most abundant components, such as levoglucosan, occur at concentrations ranging between three picograms (pg)/m^3 and 1 ng/m^3 (Fu et al., 2009; Zangrando et al., 2013). Nevertheless, by providing sufficiently long sampling times in a high-volume system, limits of detection in the range of 0.3–1 pg/m^3 can be achieved. All analytical protocols employ isotopically labelled internal standards for estimating the recovery of extraction and clean-up. There is still, however, a lack of suitable standards for emerging organic tracers, such as the photochemical products of isoprene and other biogenic terpene compounds (Fu et al., 2013). Clean-room facilities (class-1000 standard) are recommended, as well as stringent standard operation protocols covering the entire life-time of the samples. All the above methodologies rely on the in-field deployment of high-volume sampling systems, which are susceptible to failure and collection problems (for example, wind and snowpacking of sampling inlets) in harsh environmental conditions.

Mineral dust is another very important fraction of atmospheric aerosols in the Arctic. During so-called "dust events", when soil erosion by strong winds leads to the formation of thick surface aerosol layers, dust can reduce visibility to 200 m (Dagsson-Waldhauserova et al., 2013, 2014). Below is a brief summary of the vast range of physical and chemical methods used to measure dust in the background Arctic atmosphere. There is great heterogeneity in the methods, and the term "dust" is loosely defined.

Mineral dust can be measured using offline or online methods. Offline sampling includes passive and active methods. Active sampling is preferable, as it accurately determines atmospheric concentrations. The gravimetric determination of total suspended particles (TSP) and coarse particulate matter (PM_{10}) samples is used to estimate mineral dust aerosol concentrations near dust sources. In addition, Feret diameter and shape factors of mineral dust have been characterized at ground and in the free atmosphere by tethered-balloon experiments (Moroni et al., 2016). Composition measurements are helpful for identifying sources of sampled dust, as well as possible processes during transport. In background areas, offline chemical analysis is undertaken on the filters. In particular, water-soluble ions (dust is typically water-insoluble, with an exception of Ca^{2+} and Mg^{2+} [e.g. Galindo et al., 2013]) are measured with ion chromatography (IC). The elemental composition of crustal species may be measured with, for example, inductively coupled plasma mass spectrometry (ICP-MS), particle-induced x-ray emission (PIXE) or instrumental neutron activation analysis (INAA) (e.g. Calastrini et al., 2012; Fialho et al., 2014; Telloli et al., 2018). Mineralogical information can be obtained with, for example, x-ray diffraction (XRD) or SP2 methods (Yoshida et al., 2016). Electron microscopy is the best choice for detailed topographical visualization of mineral dust structures at micro and nano scales. Typical methods include secondary electron imaging, scanning electron microscopy (SEM) and transmission electron microscopy (TEM) (Kandler et al., 2007). In addition, SEM-energy dispersive spectroscopy (EDS) can be used to deduce the elemental composition of mineral dust (Moroni et al., 2018; Bachelder et al., 2020) and single aerosol particles from biomass burning (Moroni et al., 2020).

Online measurements of atmospheric dust are desirable, as they can produce accurate, high time-resolution data, available in real time. Measuring dust chemical composition online is extremely challenging. Recently, the SP2 instrument was used to detect light-absorbing dust particles, such as iron oxides, by applying the laser-induced incandescence (LII) technique (Moteki et al., 2017; Yoshida et al., 2016, 2020). Aerosol physical properties are not as specific as chemical composition in discerning mineral particles from other aerosol populations. However, coarse-skewed size distributions are often indicative of dust particles, especially when measured in elevated layers of the atmosphere. Relevant physical properties include PM concentrations measured with, for example, beta-attenuation monitors, and aerosol size-distribution measurements made utilizing scanning mobility particle sizer (SMPS), differential mobility particle sizer (DMPS) or aerodynamic particle sizer (APS) systems, or optical particle counters (OPCs). Optical parameters of the aerosol are less characteristic of dust, because of the variability in dust composition and the interference of organic light-absorbing compounds (brown carbon). Nevertheless, some approaches to discriminate dust aerosols on the basis of combinations of optical parameters (scattering and absorption coefficients) have been proposed (Cazorla et al., 2013). Aerosol scattering coefficients can be measured online with integrating or polar nephelometers. For absorption coefficients, the same instruments are typically utilized as those used to measure BC.

5.2.1.1.3 Particle physical properties – *in situ* monitoring

Optical particle counters and APS are used to measure the size distribution of atmospheric dust aerosols at micrometer scale (e.g. Denjean et al., 2016; Schladitz et al., 2009). Both types of instruments have their caveats. OPC results are affected by the refractive index and the shape (asymmetry parameter) of the measured particles. In contrast, the aerodynamic diameters determined by the APS are dependent on the density of the particles. Therefore, care has to be taken when comparing the results from these two methods. In the submicron size range, coupling electrostatic classifiers and DMAs to condensation particle counters (CPC) to form SMPS and DMPS automatic systems, is the standard method for measuring aerosol size distribution.

The most relevant aerosol optical parameters are the scattering coefficient, the absorption coefficient, the sum of these (the extinction coefficient), and Ångstrom exponent (ÅE, which relates to the wavelength dependence of the above coefficients). From these measurements, refractive indexes and asymmetry parameters can be deduced (e.g. Kandler et al., 2007). Scattering coefficients can be measured with integrating or polar nephelometers. The integrating nephelometer measures the total scattered light (ideally from 0° to 180°, but technically less) at one or several wavelengths, while the polar nephelometer determines light scattering as a function of the scattering angle. Absorption coefficients can be measured using filter-based absorption photometers, such as the PSAP and the Aethalometer. Both absorption coefficients and scattering coefficients can be measured using photoacoustic instruments, such as Droplet Measurement Technologies' Photoacoustic Extinctiometer. Determining scattering and absorption coefficients is necessary when estimating the effect of single scattering albedo (SSA) on the direct radiative effect of aerosols. Measurements are typically taken in dry conditions (<40% relative humidity [RH]); therefore calculating aerosol optical properties (especially scattering) at ambient RH levels requires information about particle hygroscopicity. It is important to know either the hygroscopic growth factor of the observed particles (measured by a hygroscopicity tandem differential mobility analyzer [HTDMA]) or the enhancement factor (measured using dry and wet nephelometers set up simultaneously). These data are needed to correct for the change in optical properties that occurs when particles take up water; however such data are very scarce in the Arctic.

5.2.1.1.4 Particle physical properties – remote sensing

The measurement methodologies listed above are suited to *in situ* observations. They represent the benchmark for monitoring surface concentrations of BC, co-emitted aerosol compounds and mineral dust at the main Arctic observatories. However,

remote sensing is another important tool used to detect atmospheric aerosol loads, and provides additional information on the three-dimensional structure of the atmosphere. Remote sensing can take place from ground-based locations, aircraft or satellite. From the ground, the standard method of observing particles is by using the sun-photometer or the radiometer. These provide the columnar aerosol optical depth (AOD) as the basic parameter (e.g. Oduber et al., 2019). The wavelength dependence of AOD (Ångström exponent) gives additional information on aerosol size, and enables spectral de-convolution algorithm (SDA) retrievals. These yield separate AOD estimates for the fine- and coarse-mode particles, at 500 nm wavelength. During the polar winter, AOD retrieval is still possible by means of lunar and star photometry (Barreto et al., 2019; Baibakov et al., 2015). While photometers provide information on the integrated atmospheric column, lidar technology can be used to ascertain the vertical distribution of aerosols. An example is the PollyXT Raman Lidar (e.g. Baars et al., 2016). The PollyXT yields vertically resolved data from 90 m to 10 km altitude, including, for example, the backscatter coefficient, extinction coefficient, lidar (extinction-to-backscatter) ratio and the ÅE. Atmospheric aerosol load may also be observed remotely from the radiometer measurements of environmental satellites, such as Terra and Aqua Moderate Resolution Imaging Spectroradiometer (MODIS), Geostationary Operational Environmental Satellite Network (GOES) -13 and -15, and Suomi National Polar-orbiting Partnership. Glantz et al. (2014) showed that AOD values retrieved between March and September over the Svalbard area using MODIS data precisely mapped the *in situ* observations made by sun photometers. Satellite retrievals can provide excellent aerial coverage for measuring atmospheric aerosols. They are also ideal for identifying long-term changes in the regional distribution of atmospheric aerosol, and can track the transport of aerosol layers from strong emission sources, such as wildfires, dust areas, and volcanoes. Estimating the integral emissions from certain territories and administrative units over time is more challenging, especially when AOD levels are small. The most common aerosol parameters detected by satellites encompass AOD, its fine- and coarse-mode fractions, the absorption optical depth, and aerosol layer thickness and height. Discerning distinct aerosol classes – such as dust, pollution aerosol, or sea salt – is possible by applying an aerosol model with class-specific phase functions. However, satellite passive sensors still have trouble distinguishing between dust and light-colored backgrounds (such as snow, ice, and clouds), and development work is needed to make the separation algorithms more accurate. Space-based active sensors, however, based on lidar technologies, can provide the vertical distributions of aerosol over the globe with little disturbance from surface effects. Cloud-Aerosol Lidar with Orthogonal Polarization (CALIOP) measures the vertical profiles of attenuated backscatter intensity at two wavelengths and polarizations, allowing the classification of clouds and aerosols (with several subtypes) between 0–40 km altitude with 30 m vertical resolution (Winker et al., 2009). Extinction and aerosol optical thickness are calculated from backscattering using the extinction-to-backscatter ratio (lidar ratio), which is function of the aerosol type (Winker et al., 2009). In the recently updated source-attribution algorithm (version 4; Kim et al., 2018), all aerosol subtypes are identified on a global scale regardless of the surface type. In the Arctic region, this facilitates identification of the following tropospheric aerosol subtypes: dust, smoke, clean continental, polluted continental, polluted dust, clean marine and dusty marine (Kim et al., 2018; Omar et al., 2018). The update also makes it possible to investigate the vertical variability and source regions of the different aerosol types during the Arctic winter (Di Biagio et al., 2018). However, the background aerosol concentration within the Arctic atmosphere is generally below the detection limit of CALIOP. As an example, 80%–95% of night-time spring observations in the Canadian and Alaskan Arctic are below the CALIOP detection limit (Di Pierro et al., 2013). There is much greater sensitivity when taking night-time measurements in the troposphere (Winker et al., 2009) because the scattering of solar radiation causes less-accurate measurements during the day-time (Di Pierro et al., 2013) This day-night sensitivity difference has the potential to introduce substantial bias in the quantification of the seasonal aerosol cycle over the Arctic (Di Pierro et al., 2013), and can lead to marked differences in estimates of seasonal aerosol cycle when compared to ground-based lidar (Shibata et al., 2018). In general, validation studies indicate that CALIOP products agree relatively well with independent Arctic measurements, such as airborne- and ground-based lidar and in-situ observations (Rogers et al., 2011; Di Pierro et al., 2013). However, for detecting high-concentration aerosol events, applying CALIOP extinction is better when compared to ground-based lidar (Shibata et al., 2018). In general, substantial differences can be observed between different seasons and altitudes (Shibata et al., 2018). Finally, CALIOP retrievals of vertical aerosol distributions are currently possible only up to 82°N of latitude (Di Pierro et al., 2013) and are therefore unsuitable for probing the atmosphere over the central Arctic ocean.

5.2.1.2 Aerosol compounds in the cryosphere – surface-snow, ice and precipitation

BC, dust and other impurities in snow can affect melting by altering the albedo, and snow and ice metamorphism. Recent literature provides important research findings about such processes, and about possible assessment methods (Meinander et al., 2014; Peltoniemi et al., 2015; Dragosics et al., 2016; Möller et al., 2016; Skiles and Painter 2016; Svensson et al., 2018; Boy et al., 2019; Manninen et al., 2021). The following section is focused on ways of determining the impurities – particularly BC – in the snowpack, because this remains the most important task for monitoring the anthropogenic impact on snow albedo in the Arctic.

5.2.1.2.1 Black carbon and dust in snow

Because BC in snowpack lowers the albedo and potentially accelerates the ice-albedo feedback, accurate measurements are crucial for understanding and evaluating the resulting impacts, and for improving transport models.

There are no analytical protocols for detecting atmospheric carbon deposited in snow, and no standardized methods for sampling and filtering it. The snowpack chemistry monitoring protocol for the Rocky Mountain Network is available in Ingersoll (2009); the protocol for BC in snow for seasonal

Svalbard snowpacks on glaciers can be found in Norwegian Polar Institute (2018); and the sampling, filtering and analysis protocols used to detect BC, OC and total carbon in seasonal surface snow in urban backgrounds and Arctic Finland are presented in Meinander et al. (2020a).

A review of the existing methodologies for determining concentration of BC in snow samples can be found in AMAP (2015a). A brief summary with references to recent studies in the Arctic area is provided below.

The size distributions of BC in snow and rainwater can be measured accurately using SP2 based on a laser-induced incandescence technique, combined with a nebulizer (Jacobi et al., 2019; Kaspari et al., 2011; Lim et al., 2014; Macdonald et al., 2017; McConnell et al., 2007; Mori et al., 2016, 2019; Sinha et al., 2018; Wendl et al., 2014). Mass concentrations of BC in snow and rain (C_{MBC}) are obtained by integrating the BC size distributions. Melted snow or rain samples are injected into a concentric pneumatic nebulizer to generate airborne BC particles, which are introduced into an SP2 for detecting the BC. The detectable mass equivalent diameter of BC is typically 70–600 nm (Lim et al., 2014). The upper limit of detectable BC size has been expanded to about 4170 nm, with the overall accuracy of the measured BC concentrations in water estimated to be about 16% (Mori et al., 2016). BC size distributions in snow samples obtained in the Arctic have been shown to be stable for 10–42 months after being melted and stored in glass bottles at about 4°C. This indicates that BC losses due to adhesion on the inner walls of the glass bottles are small. This method has been applied to measurements of BC in snowpack across the Arctic (Mori et al., 2019) and in hydrometeors (snow and rain) at Ny-Ålesund (Sinha et al., 2018) and Utqiaġvik (Mori et al., 2020), as described in Chapter 6.

C_{MBC} has also been measured by the thermal-optical transmittance (TOT) method (EC-OC technique) (Aamaas et al., 2011; Forsström et al., 2009, 2013). Lim et al. (2014) reported both overestimations and underestimations of C_{MBC} measured by the TOT method, depending on the sample origin.

C_{MBC} in snowpack in Arctic regions has also been measured by the integrating sphere/integrating sandwich spectrometer (ISSW) method (AMAP, 2015a; Doherty et al., 2010). In this method, C_{MBC} is estimated from spectrally resolved measurements of the absorption coefficient of solid particles collected on a filter, assuming a unitary absorption ÅE for BC and associating most long-wavelength (650–700 nm) absorption to BC. However, this technique has large uncertainties (up to a factor of two) attributed mainly to interference from co-existing non-BC solid particles, such as mineral dust, and filter undercatch (Doherty et al., 2010, 2016; Schwarz et al., 2012).

A systematic way to harmonize the techniques for sampling and determining BC in snow is still lacking, and efforts to remedy this are highly recommended (Svensson et al., 2019) since the variability between methods can be as high as a factor of two with the lower bound from SP2. Moreover, BC and mineral dust may mutually interfere in some measurement techniques, which poses a question on the ability to disentangle their individual effects and relative abundances. The European Cooperation in Science and Technology (COST) framework action Harmosnow makes an effort to harmonize measurement and modeling approaches.

Mineral dust in snow, on the ice surface and in cryoconite samples can be detected with various chemical and physical methods that are also used for measuring dust in atmosphere (see Section 5.2.1.1), as well as using remote-sensing techniques (e.g., Boy et al., 2019, IPCC 2019). Collected samples can be analyzed for their dust contents and particle properties, either as water samples (for example, using IC and SP2); melted and evaporated particle samples (using electron microscopy); melted and filtered samples (using gravimetry and optical methods); and as snow (via cold-room techniques).

5.2.1.2.2 **Aerosol compounds in ice cores**

Besides determining the effects of deposited anthropogenic compounds on snow albedo, the other research field of paramount importance in cryospheric sciences for assessing climate impacts is the reconstruction of past atmospheres using ice-core records. Over the years, many research groups have undertaken ice-core drilling and analysis of BC mass (rBC and EC), metals, and inorganic/organic ion species (e.g., McConnell et al., 2002, 2017; Zdanowicz et al., 2018; Ruppel et al., 2014) at the locations outlined in Chapter 6, Section 6.1.4.2, including Greenland, Devon Island and Svalbard. Typically, ice cores are processed in class-100 clean cold rooms, with the inner, uncontaminated portion of core segments melted and sampled. These samples are then analyzed using techniques, such as SP2 for rBC mass, IC for inorganic and organic ion speciation, and ICP-MS for metals and other trace elements. Several groups now use so-called continuous flow analysis (CFA) systems in which an ice-core melter is directly coupled, by meltwater flow lines, to analytical instruments such as SP2, IC or ICP-MS (e.g., McConnell et al., 2002, 2017). Appropriate calibrations are applied for each method, with internal standardization techniques used to determine losses. CFA systems offer the advantage of very high-depth (time) resolution measurements, while minimizing contamination risks, and are most suitable for polar region ice-cores. For continuous measurements of BC in ice cores, uncertainties are estimated to be +/-10% based on replicate measurements in parallel samples from the same or nearby cores (McConnell, 2010). For discrete snow- and ice-sample measurements, uncertainties may be much higher because BC measurement recoveries depend on sample handling and measurement protocols that differ between studies (Wendl et al., 2014).

The analysis of ice-core samples must be performed in laboratories well equipped with clean-room facilities. The amount of BC can be determined using TOT techniques and, more recently, using SP2 methods. Inorganic and organic tracers are analyzed in parallel with BC to detect past changes in anthropogenic emissions, biological activity and other natural events, such as volcanic eruptions. Organic markers in ice-core records are often used to reconstruct past changes in biological activity and emissions from fires. Optimal tracers must be refractory to post-depositional processes. The analysis of snow and snow-pit samples provides a way to test new proxies for their characteristics of stability (Toom-Sauntry and Barrie, 2002). For example, the analyses of snow-pit samples from Summit performed by Kehrwald et al. (2012) showed that

levoglucosan, a universal marker for biomass burning, appeared to have survived the early stages of ice metamorphism. A comprehensive review of the analytical challenges involved in determining organic tracers in ice cores is presented by Giorio et al. (2018). Drilling fluids are potentially very serious sources of contamination in the field, so great care must be taken when carving sub-samples for analyzing offline. Precautions must be followed in the laboratory, too, as traditional clean rooms designed for metal analysis contain a lot of plastics. Nevertheless, by following stringent preparation and analytical protocols, GC/MS and HPLC/ESI-MS/MS techniques enable researchers to now achieve detection limits in the range of 0.1 grams per liter (g/L) down to three nanograms per liter (ng/L) for the most common organic tracers, such as levoglucosan, phenolic compounds and fatty acids.

The depth-age scale in ice cores is typically developed using methods such as ice-flow modelling combined with analysis of time-varying isotopic or glaciochemical signals (e.g., water isotopes, major ions), often constrained by fixed-time markers such as signatures of surface nuclear explosions or past volcanic eruptions (Schwander, 2007). Optimal, annual to sub-annual resolution can only be attained in cores drilled from the dry firn zone in the interior regions of the large ice sheets or high-altitude ice caps. In smaller circumpolar ice caps (such as in the Canadian and Russian Arctic, and Svalbard, Norway) or in alpine glacier and ice caps (as in the Alps or central Asia), the time resolution is typically poorer (sub-decadal or lower) and limited by the effects of surface melt and percolation.

5.2.1.3 Black carbon in lake sediments

In addition to ice cores, lake sediments play an irreplaceable role in determining historical BC deposition trends, and are abundantly available throughout the terrestrial Arctic. However, BC constitutes a minor component and must be separated from inorganic minerals and thermally unaltered OC (such as plant or animal material, and humic substances) that comprise the bulk of the sediment (Rose and Ruppel 2015). For this, different chemical and/or thermal pre-treatments are required, and these may determine which fraction of total BC is quantified. A widely used method developed for use with sediment and atmospheric samples (e.g. Gustafsson et al., 2001, 2009) is the chemothermal oxidation method (CTO-375), which uses acid to eliminate mineral matter and heat to remove organic material before quantifying the remaining carbon as soot-BC. CTO-375 effectively quantifies the most condensed, high-refractory soot-BC that forms from the combustion of biofuels and fossil fuels at high temperatures, excluding less-condensed forms of char-BC (Elmquist et al., 2006). The soot-BC detected by CTO-375 is similar to the rBC to which SP2 measurements are most sensitive (Chellman et al., 2018). In a valuable and promising recent advance in sediment BC analyses Chellman et al. (2018) modified the SP2 instrument to detect rBC from sediment samples. When comparing BC records determined from lake sediments using different methodologies, or to ice-core or atmospheric measurements, it is critical to consider the potentially different fractions of total BC quantified. It is also important to keep in mind that, while lake sediments are invaluable for recording BC deposition trends, they are – unlike ice cores – unable to detect exact amounts of BC directly deposited from the atmosphere. This is due to potential material influx from the catchment area (Ruppel et al., 2015, 2021).

5.2.2 Advanced techniques for characterizing aerosols and source apportionment

In addition to the methodologies developed for monitoring aerosol concentrations, a vast suite of observation techniques have been developed for characterizing, in detail, the aerosol fraction, particularly for particulate matter source apportionment and identifying source areas. Many such techniques have been employed, mostly during intensive field campaigns, to study specific formation and transport processes. Some of these are candidates for becoming new advanced monitoring techniques. We discuss below two main types of analytical methods that are emerging as new tools for diagnosing and characterizing particle sources.

5.2.2.1 Isotopic measurements

The best-established techniques for attributing sources of BC involve analyzing carbon isotopes ($^{13}C/^{12}C$ and $^{14}C/^{12}C$) in EC samples; these have emerged as a new frontier of BC monitoring in the Arctic (e.g., Barrett et al., 2015; Winiger et al., 2016, 2017, 2019; Rodríguez et al., 2020). The $^{13}C/^{12}C$ isotopic fingerprint can indicate different sources of fossil-fuel combustion (gas, liquid fuels, and coal), while the $^{14}C/^{12}C$ measurements can identify the BC fraction generated by biomass burning (see Figure 5.1).

It is known that ^{14}C is constantly formed by the interaction of neutrons with nitrogen in the Earth's atmosphere. Plants and vegetation take ^{14}C from CO_2 in the air via photosynthesis. The biosphere on the Earth's surface has a relatively high and characteristic $^{14}C/^{12}C$ ratio (described as "modern" carbon). When the plants die, they stop taking ^{14}C and radioactive decay of ^{14}C ensues (with a half-life of 5700±30 years). The dead plants in ancient biospheres were subsequently buried into the deep Earth and subjected to geological processes over millions of years (thousands of the half-life of ^{14}C). They formed into fossil fuels, including natural gas, crude oil and coal, which have distinguishable $^{13}C/^{12}C$ ratios (relatively lighter isotopic ratios in the gas phase, and heavier ones in the solid phase), with almost zero ^{14}C (described as "dead" carbon). The observed $^{13}C/^{12}C$ and $^{14}C/^{12}C$ in carbonaceous aerosols result from mixing of different emission sources in the atmosphere (Figure 5.1); accurate source apportionment can be achieved by mass-balance analysis of triple isotopic measurements. Vienna Peedee belemnite (VPDB) and the hypothetical specific activity of atmospheric carbon of 1950 are the primary standards for $\delta^{13}C$ and fraction of modern ($FM^{14}C$), respectively.

The expression of $^{13}C/^{12}C$ and $^{14}C/^{12}C$ measurements are shown on Figure 5.1 as $\delta^{13}C$ and fraction of modern ($FM^{14}C$). Such measurements require the physical separation of OC and EC mass fraction. Various methods have been developed in the past 15 years for analyzing the $^{14}C/^{12}C$ isotope ratio, including CTO-375 (Zencak et al., 2007), Swiss_4S protocol (Zhang et al., 2012; Mouteva et al., 2015a), National Institute for Occupational Safety and Health (NIOSH)(Winiger et al., 2017) and hydro-pyrolysis (Zhang et al., 2019). These methods use distinct temperature protocols, gas

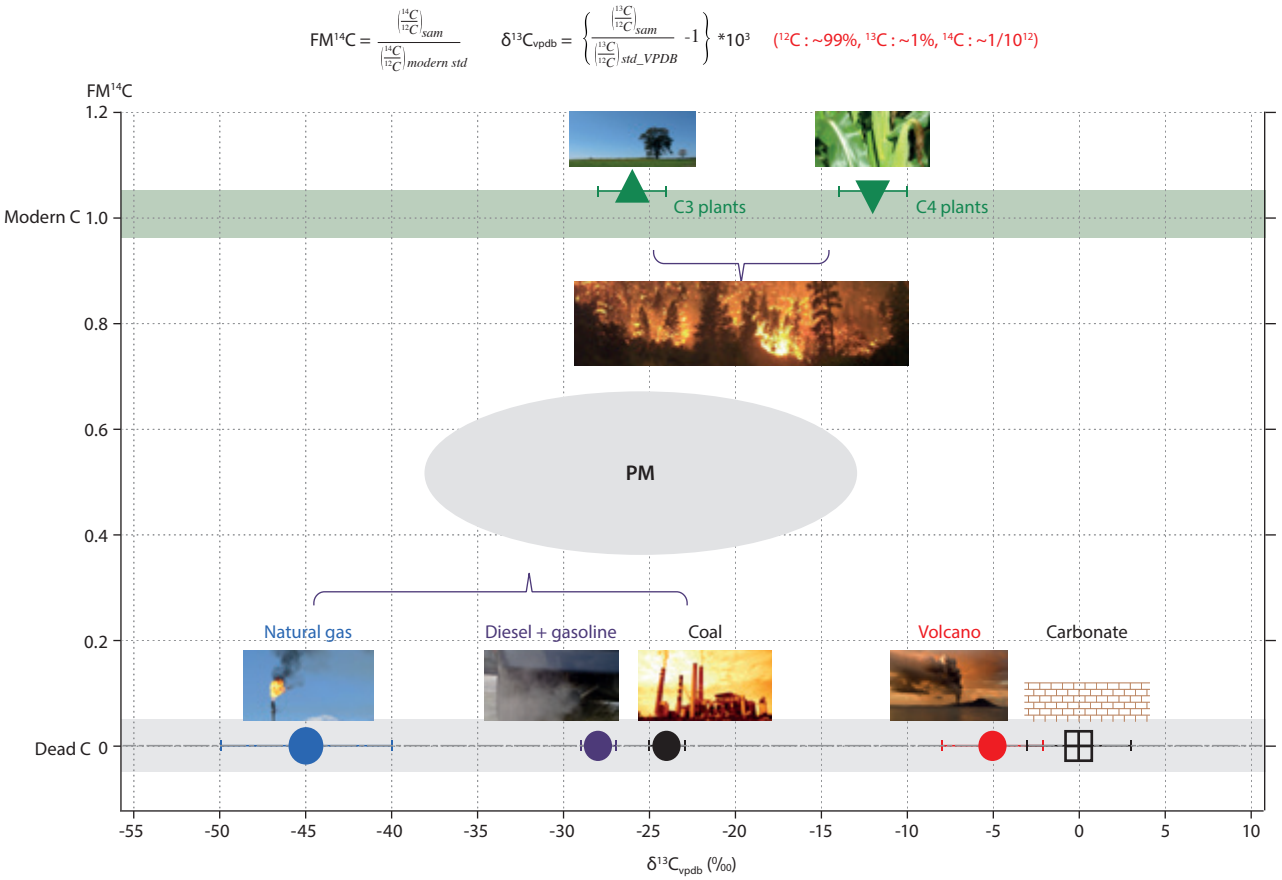

Figure 5.1 Isotopic signatures of possible sources of carbonaceous aerosols ($^{14}C/^{12}C$ and $^{13}C/^{12}C$ for attributing emissions sources in BC mass. The Y-axis stands for the fraction of modern carbon, in other words, the ratio of the sample to the hypothetical specific activity of atmospheric carbon standard of 1950 in ($^{14}C/^{12}C$). The X-axis stands for $\delta^{13}C_{VPDB}$ – the relative deviation of the sample from the VPDB standard in ($^{13}C/^{12}C$), expressed in parts per thousand (‰). On the Y-axis, the C3 and C4 plants on the Earth's surface represent "modern carbon", with the fraction of modern equal to 1, whereas all fossil fuels (natural gas, diesel and gasoline, and coal), carbon from volcanic eruptions and carbonates are "dead carbon" with fraction of modern equal to zero. On the X-axis, although both contribute "modern carbon", C3 and C4 plants (which follow different photosynthesis pathways) differ by more than 10‰ in $\delta^{13}C_{VPDB}$. Similarly, the "dead carbon" sources can be allocated to individual fossil fuel, volcanic carbon and carbonate carbon, with values from these different sources ranging from a few parts per thousand to >20‰. Atmospheric carbonaceous aerosols result from two major emissions sources – biomass burning and fossil-fuel combustion – with ambient particle matter usually comprising a mixture of the two. Thus, applying the dual carbon isotopic measurements ($\delta^{13}C$ and $FM^{14}C$) to carbonaceous aerosols (here for BC) is a direct approach to tie atmospheric concentration measurements to specific sources.

mixture and treatments prior to EC extraction (such as removing water-soluble OC or inorganic carbon) to remove or minimize OC charring and interference with EC physical separation. Usually, sample size would have the greatest bearing on analytic uncertainty. An overall uncertainty range is less than 0.5 parts per thousand (‰) and 0.05‰ for ^{13}C and $FM^{14}C$, respectively. A few of these methods derive from the thermal-optical protocols widely used for EC/OC mass measurements in monitoring networks (e.g., IMPROVE_A, EUSAAR-2), thereby limiting the relevance of the isotopic data to those corresponding mass concentrations. The EnCan-Total-900 (ECT9) method, however, was originally developed for $\delta^{13}C$ measurements in EC (Huang et al., 2006), and later applied to a long-term EC/OC mass-measurement network over Canada, including Alert site. A recent study demonstrated that the ECT9 protocol can effectively separate fossil EC from modern OC for either $\delta^{13}C$ or $FM^{14}C$ analysis. It was shown that measured OC and EC from mixed standards could reach their corresponding consensus values within an uncertainty of ~5% or less, on average, via the ECT9 protocol (Huang et al., 2021). By providing a consistent method for OC and EC concentration and isotope measurements, the ECT9 protocol is expanding the existing opportunities for characterizing and monitoring sources of carbonaceous aerosol, particularly for the Arctic.

The Alert observatory has routinely performed $\delta^{13}C$ isotopic analysis of EC since 2006 (EUA-BCA, 2019b), with $FM^{14}C$ measurements recorded since 2014 (Rodríguez et al., 2020). Multiple datasets have been acquired at Utqiaġvik, Zeppelin (in Spitsbergen, Norway) and Tiksi (in Siberia, Russia) during field campaigns (up to one-year long but with a small number of samples), and Winiger et al. (2016) have summarized results obtained at the Swedish site of Abisko. An overview of the observations made at all the above stations between 2011 and 2015, including a comparison with the source attribution from an atmospheric transport model, was presented by Winiger et al. (2019). Those results show that anthropogenic emissions are still the major sources of BC loaded over the Arctic region; this conclusion is further supported by higher-time-resolution radiocarbon measurements made at Alert (Rodríguez et al., 2020). Taking regular (preferably monthly) isotope measurements to track BC source changes over time is recommended for assessing the effectiveness of mitigation policies.

Using $\delta^{13}C/FM^{14}C$ measurements for source apportionment is attractive because it is relatively simple to do and suited to addressing policy-relevant questions about the origin of

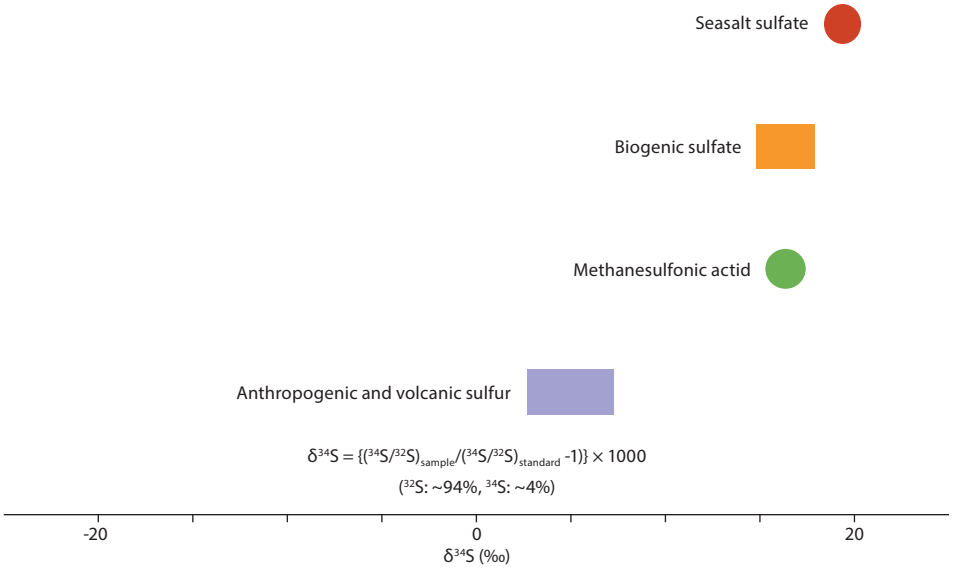

Figure 5.2 Atmospheric variations in $\delta^{34}S$ values for aerosols in Arctic airmasses represent a mixture of ^{34}S-rich seawater and biogenic S from DMS and MSA, which is in contrast to well-mixed anthropogenic and volcanic S, which typically comes from long-range transport. The data compiled from literature varies more, as the values measured at individual locations are not as exact as at the emission source due to mixing and fractionation.

BC. Although the analytical uncertainties are only 0.2‰ and 0.05‰ for $\delta^{13}C_{VPDB}$ and $FM^{14}C$, respectively, for samples of >10 micrograms (µg), the uncertainties in the end-member isotopic composition nevertheless complicate source attribution. In addition, the high analytical costs are still a major limitation for long-term measurements.

New isotopic methods have also been used for particulate sulfate source apportionment in the Arctic. Sulfates can be associated with sea salt, or originate from anthropogenic combustion or biogenic emissions (for example, Dimethyl sulfide [DMS] from microbiota). The abundance of ^{34}S in relation to the most abundant natural isotope (^{32}S) ($\delta^{34}S$, in other words, the relative deviation of samples to standard in ($^{34}S/^{32}S$) value, expressed as parts per thousand) can be particularly useful for determining the anthropogenic fraction of non-sea salt sulfate in aerosol. Details of this methodology are found elsewhere (Norman et al., 1999; Ghahremaninezhad et al., 2016). Precision for any particular measurement ranges from 0.1–0.5‰.

Different fuel types used globally contain various proportions of $\delta^{34}S$. However, measurements show that atmospheric variation in $\delta^{34}S$ values for aerosols in Arctic air masses represents a mixture of ^{34}S-rich seawater (+21‰±0.5‰) and DMS and MSA (biogenic S; +18‰±1.5‰), in contrast to well-mixed anthropogenic and volcanic sulfur (+3‰ to +7‰), typically from long-range transport (Figure 5.2). The fraction of non-sea salt-sulfate from marine biogenic sources was obtained using a two-source mixing model (Norman et al., 1999).

5.2.2.2. High-resolution chemical compositions via aerosol mass spectrometry

Taking long-term observations of aerosol chemical composition, including major ions and bulk OC in the Arctic, typically involves collecting particles on filters and subsequently analyzing them in the laboratory. The drawback of this approach is the relatively low time resolution, of several days or weeks. More recently, online mass-spectrometric methods have been developed, which enable high-time-resolution measurements (in the order of minutes) of aerosol chemical composition to be made. The Aerodyne aerosol mass spectrometer (AMS, Canagaratna et al., 2007) can measure the size-resolved, non-refractory components of particles. Typically, only aerosols up to 1 µm in diameter can be analyzed, but newer developments of the inlet lens assembly allow for sub-2.5 µm measurements. The particles are drawn through an aerodynamic lens and introduced into a vacuum chamber, in which their diameter is determined based on their time in flight. Particles are then flash-vaporized at 600°C and ionized by electron impact at 70 electronvolts (eV). The ions are extracted into a time-of-flight (ToF) mass spectrometer. Depending on the ToF, chemical information is based on unit mass resolution or can be highly resolved. Roughly, the uncertainty in quantifying the measured mass is within a factor of two. The advantage of this technique is that it provides real-time and high-resolution information on particulate sulfate, nitrate, ammonium and organics. The organic composition can be further speciated into, for example, hydrocarbon-like, highly oxygenated, marine or terrestrial biogenic, or biomass-burning compounds based on statistical methods, such as positive matrix factorization (PMF; Zhang et al., 2011; Section 5.2.2.3 of this chapter). PMF is commonly applied for source apportionment, as it can differentiate between natural and anthropogenic sources, as well as local fresh or remote aged particle sources (see section 5.2.2.3 below). AMS is, however, not capable of quantifying refractory aerosol components, such as mineral dust and BC, and is not the best option for quantifying the organic and inorganic components of sea spray. Also, particles larger than the inlet lens permits to pass are not accounted for. A further disadvantage is the high cost of the instrument, the need for highly trained personnel to continuously run it and the requirement for lengthy data analysis. However, the instrument has been deployed in numerous field campaigns in the Arctic on platforms including ground-based observatories, ships and aircraft (Nielsen et al., 2019; Schmale et al., 2011; Chang et al., 2011).

To overcome the challenges of cost and personnel, a mass spectrometer aimed specifically at continuous monitoring has been developed: the Aerosol Chemical Speciation Monitor (ACSM, Fröhlich et al., 2013). The instrument has a slightly lower time resolution (several minutes to half an hour), does

not measure particle size, and has a lower mass resolution, which puts some constraints on source apportionment. However, routine observations using the ACSM are ongoing at several sites belonging to European research-infrastructure networks, such as the Aerosol, Clouds and Trace Gases Research Infrastructure (ACTRIS). The ACSMs has also been operated at Alert (2011–2015) and Ny Ålesund. While AMS and the ACSM measure the composition of the bulk aerosol fraction, mass spectrometers also exist that measure the composition of single particles (Noble and Prather, 2000). These are based on laser ablation and can hence detect refractory particles as well. While they provide very detailed information, particularly on particle populations that are not well captured by AMS or the ACSM, single particle mass spectrometry cannot quantify mass concentrations of the aerosol compounds. Moreover, the strong molecular ion fragmentation reduces the amount of information on organic composition that can be extracted from the single particle mass spectrometry spectra. The instruments are also expensive, and call for highly trained operators and skilled data analysts. Very few deployments have been achieved so far in the Arctic (Sierau et al., 2014).

Among the newest approaches is one that combines collecting aerosols on filters and aerosol mass spectrometry to deduce detailed information on the OA. Aerosol mass is extracted from the filters into a liquid solution, which is nebulized and subsequently measured with an AMS or any other highly mass-resolving spectrometer (Daellenbach et al., 2016). This approach focuses on the water-soluble aerosol components. One of the first circum-Arctic OA composition and source apportionment studies was carried out under the Integrative and Comprehensive Understanding on Polar Environments program (iCUPE) (Petäjä et al., 2020; Moschos et al., 2022).

The above methods are all based on aerosol mass, putting an emphasis on determining the chemical composition of the larger, accumulation-mode particles (roughly >70 nm). This means that information on the Aitken mode particles (roughly 20–100 nm) is largely missing. However, some chemical ionization mass spectrometers can selectively collect Aitken-mode particles and determine their composition (Lawler et al., 2014). Such an instrument was deployed in the High Arctic on the Swedish ship-based Arctic Ocean 2018 expedition. As with other mass spectrometers, these instruments are costly, and involve intensive care and lengthy data analyses.

Understanding the composition of even smaller particles, such as those of few nanometers and in the size range of clusters (1.2–2 nm), is of high importance. New particle formation (NPF) in the Arctic is a topic that is currently being intensively studied, as NPF has implications for cloud condensation nuclei (CCN) and is a sign of climate change in the region (see Chapter 6). The atmospheric pressure interface ToF mass spectrometer (Api-Tof; Junninen et al., 2010) uses chemical ionization (CI) to determine the chemical composition of condensable vapors that can form new particles – such as sulfuric acid, iodic acid, and highly oxygenated organic molecules – and can hence reveal the detailed mechanisms of NPF and elucidate whether natural or anthropogenic factors are at play. The instrument has recently been deployed in the Arctic at Villum Research station in north Greenland (Sipilä et al., 2016), Ny Ålesund and during the Arctic Ocean 2018 and the 2019–2020 Multidisciplinary drifting Observatory for the Study of Arctic Climate (MOSAiC) ship-based field campaigns. The same drawbacks apply as for the other mass spectrometers.

In summary, a wide range of mass spectrometers have already been deployed in the Arctic, and have significantly advanced our understanding of aerosol composition, processes and sources. Due to their complexity, most versions are not feasible for long-term monitoring efforts. However, recent developments, such as the ACSM, are promising and would be very useful for Arctic stations to use in source-apportionment studies. The most viable option at present for increasing knowledge on OA and conducting source apportionment, is to combine filter collection with subsequent offline aerosol mass spectrometry in the laboratory.

5.2.2.3 Chemical mass balance (CMB) and positive matrix factorization (PMF)

Factor analysis and other receptor models are increasingly employed to derive quantitative information on source contributions of PM, based on the statistical analysis of the time series of inorganic ions, trace elements and organic tracers concentrations. Chemical mass balance (CMB) and PMF are established techniques for assessing main source contributions to variability of chemical composition at a receptor site (von Schneidemesser et al., 2009; Karl et al., 2019). The reliability and the performance of such approaches, in particular PMF, depend on the actual variability in composition and on the level of detail in chemical speciation which, in turn, is always a compromise between the costs and time dedicated to laboratory analyses. In an alternative approach, atmospheric transport models (ATMs) are employed to reconstruct source-receptor relationships, in other words, to assess source areas or "footprints" of the emissions. Examples of applications developed for datasets of organic markers for biomass burning are presented by Yttri et al. (2014), Fu et al. (2015) and Karl et al. (2019).

5.2.3 Capacity to track aerosol source regions and long-term changes in concentrations

The state of BC observations was thoroughly reviewed in a dedicated technical report of the EU Action on Black Carbon in the Arctic initiative (EUA-BCA, 2019b). The availability of year-long records of BC concentrations from observatories in both the Western and Eastern regions of the Arctic has now increased. This has enabled models to better constrain key parameters controlling aerosol transport, cloud scavenging and deposition (Eckhardt et al., 2015). Although large sectors of the Eastern Arctic remain uncovered by systematic measurements, continuous eBC measurements in Tiksi have been gathered since 2009, and periodical observations are made at Ice Base Cape Baranova station on Bolshevik Island in Russia (Popovicheva et al., 2019). In addition to the main observatories that have provided long-term BC records for the High Arctic (Utqiaġvik, Alert, Ny Ålesund and Tiksi), EUA-BCA (2019b) reported eBC measurements performed over periods of one-to-three years at nine other stations in North America and Europe. At Villum, eBC data have been

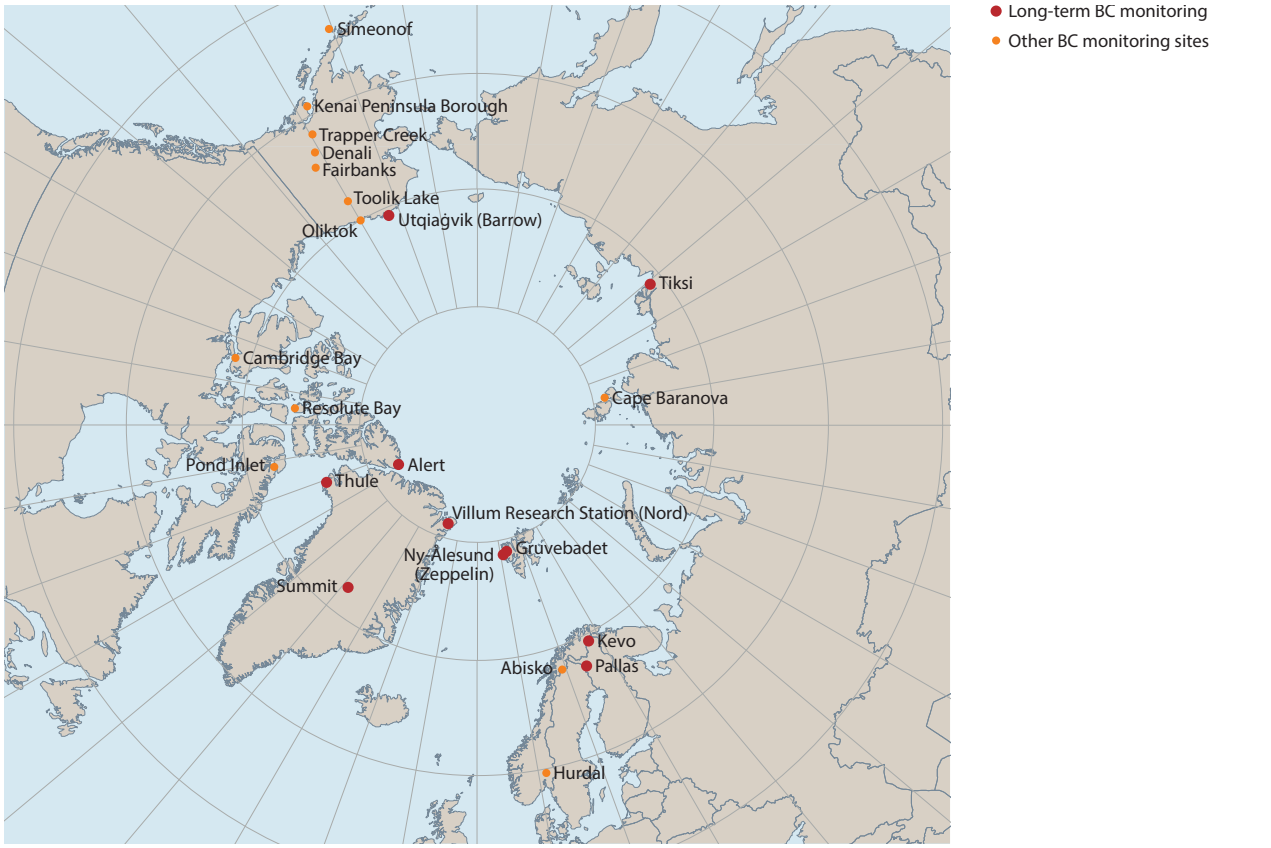

Figure 5.3 Locations of Arctic sites providing datasets of aerosol EC or eBC concentration records (adapted from EUA-BCA, 2019b).

available since 2011, and systematic measurements began in 2017. Long-term observations of elemental carbon (EC) have been undertaken at Alert, Villum, and Zeppelin in the lower Arctic, at Kevo (Finland), and at IMPROVE monitoring sites in Alaska. A comprehensive discussion on BC data coverage and accessibility is available in EUA-BCA, 2019b. Figure 5.3 presents a map showing locations of all the Arctic stations for which eBC or EC measurements have been performed.

New observations have been made and existing monitoring continued for other inorganic aerosol compounds, including anthropogenic substances co-emitted with BC. However, year-round particulate OC measurements are only available from specific sites. Currently, the only long-term record of aerosol total OC measurements in the High Arctic, dating from 2006, is that from Alert (Leaitch et al., 2018), but multi-year observations are available for Ny Ålesund (2011–2015 at Gruvebadet, and from 2017 at Mount Zeppelin) and for Villum (from 2008).

Long-term measurements of geogenic elements (such as aluminum [AI], iron [Fe] and calcium [Ca]) provide important information on concentrations and variability of atmospheric dust in the High Arctic. The corresponding datasets are at least partially available on the EBAS database of atmospheric measurements or other repositories (such as the Canadian National Atmospheric Chemistry [NAtChem] database) for the stations of Villum, Alert and Zeppelin. The increasing emissions of dust particles caused by the retreat of snow surfaces over land have become a frontier research topic. Extensive data about atmospheric dust in the Arctic are still lacking.

Aerosol physical parameters – such as particle number size distributions, scattering and absorption coefficients, and number of CCN or ice-nucleating particles (INPs) – have only partly been established in monitoring programs (Freud et al., 2017; Schmeisser et al., 2018; Jung et al., 2018, Schmale et al., 2018b). Long-term series of these parameters are key to evaluating the role of aerosols as SLCFs in the sensitive Arctic regions. Measuring of chemical components began in the Arctic in the early 1980s, with efforts to take systematic observations of physical aerosol properties beginning during the late 1990s at five sites: Ny Ålesund (Zeppelin Mountain site at Svalbard); Tiksi in the Lena river delta; Utqiaġvik on the northern coast of Alaska; Eureka and Alert on Ellesmere Island of the Canadian archipelago; and Villum Research Station at Station Nord in northernmost Greenland. However, only Ny Ålesund and Alert have continuously measured particle size distributions, from about 2000 and 2011, respectively; observations made at other locations were established later or have longer periods of interruption.

According to Tomasi et al. (2015), lidar measurements were carried out at: Utqiaġvik, Eureka (Nunavut, Canada) between 1993–1997; Alert during 1984–1986; Summit, since 2010; Andøya Rocket Range (northern Norway), since 2006; and at Ny-Ålesund and Hornsund in Spitsbergen, where several lidar systems have been deployed since the 1980s. In Ny-Ålesund, a micropulse lidar of the NASA Micro-Pulse Lidar Network (MPLNET) network has operated since 2003, while a Raman lidar (Koldewey-Aerosol-Raman-Lidar [KARL]), with aerosol channels, depolarization, and ultraviolet and visible water-vapor channels has operated since 1999. Finally, an aerosol lidar (CL51 ceilometer [Vaisala]) was installed at Villum research

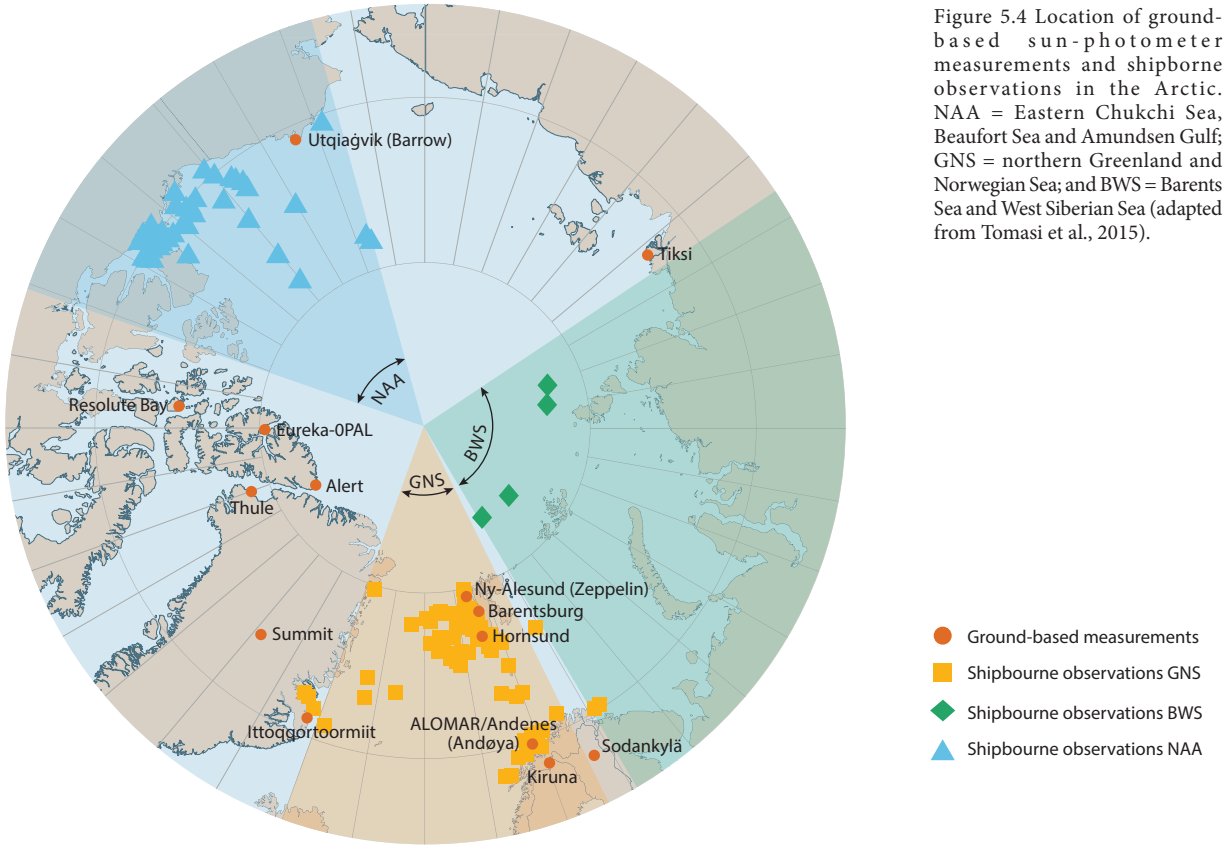

Figure 5.4 Location of ground-based sun-photometer measurements and shipborne observations in the Arctic. NAA = Eastern Chukchi Sea, Beaufort Sea and Amundsen Gulf; GNS = northern Greenland and Norwegian Sea; and BWS = Barents Sea and West Siberian Sea (adapted from Tomasi et al., 2015).

station in spring 2011. More common measurements are based on sun-photometer observations of AOD taken mostly at fixed locations but also from ships (Figure 5.4).

The sampling and analysis of snow for determining light-absorbing inclusions, primarily BC and dust, started in the early 1980s, but still only a few areas are covered by systematic observations. A compilation of data collected between 2005 and 2010 by Dou and Xiao (2016) shows that spatial coverage in the Arctic basin is largely made up of short-term field studies. Observations of BC in snow over sea ice are limited to the western sector of the Arctic Ocean (Dou et al., 2012) and the Greenland Sea (Forsström et al., 2013), as well as to the summer season.

At Villum, snow sampling began in 2016 and is carried out on a weekly basis to investigate the EC content. From 2007, the Norwegian Polar Institute and Stockholm University initiated a program of snow monitoring for EC at two locations on the outskirts of Ny Ålesund. The program was extended in 2016 to 22 sites on seven glaciers of Spitsbergen and Nordauslandet, making Svalbard one of the best characterized areas in the Arctic for BC in snow (Zdanowicz et al., 2020). The experiments in Svalbard demonstrate that, in geographical regions exhibiting a complex orography, spatial patterns of wet deposition and BC loadings in snow samples can vary at fine scales. In recent years, additional observations have been made in the Canadian Arctic, as part of the Network on Climate and Aerosols – Addressing Key Uncertainties in Remote Canadian Environments (NETCARE) project (Macdonald et al., 2017, 2018), with continuous year-round snow sampling at Alert. Another record of BC in snowpack, from samples collected between 2012–2016 each year in spring in Greenland, Finland, Alaska and Siberia, is presented by Mori et al. (2020). A similar technique was used to measure BC deposition over the Greenland ice sheet in 2014 (Thomas et al., 2017). Moreover, systematic long-term weekly OC/EC observations from the seasonal surface snow have been available from Sodankylä (Finland) since 2009 (Meinander et al., 2020b). Finally, snow sampling has been undertaken in the central Arctic Ocean during most seasons under the framework of the MOSAiC expedition. Samples are being processed at the time of preparing this report. The continuous presence of the research vessel's exhaust might pose a challenge to interpreting the results in future.

Ice cores provide a historical perspective on deposited aerosol chemical compounds. BC (dust) has been studied in ~7 ice cores across Greenland, two from Svalbard and several in Canada. Fewer ice-cores are available from sites in the Eastern Arctic, where glaciers are rarer and more remote. Instead, lake sediments have been analyzed for soot-BC, five from northern Fennoscandia (Ruppel et al., 2015) and four from northwestern Arctic Russia (Ruppel et al., 2021). To interpret the deposition flux of aerosol to glaciers, atmospheric processes such as precipitation must be known, adding an additional level of complexity when compared to present-day measurements made directly from the atmosphere. In the case of lake sediments, deposition-flux interpretations are further complicated by the potential influx of material from the catchment area (Ruppel et al., 2015, 2021). Greenland cores generally reflect pollution outflow from North America, as well as the aerosol characteristics of the free troposphere, because of the high elevation of the ice sheet. The composition of snow samples from Svalbard is aligned with European emissions, while Canadian snow composition reflects North American and Russian emissions.

In addition to the ground-based observations made at research stations, other important aerosol concentrations and composition datasets have emerged from the deployment of mobile platforms, such as tethered balloons, research aircraft and ships. More than 20 aerosol-focused airborne campaigns have been performed across the Arctic since 2007. These have been undertaken in the European Arctic, Greenland, the Canadian Arctic, Alaska, the Arctic Ocean, Iceland and Russia. The spatial coverage is not homogeneous, with most of the surveys covering the European and North American Arctic sectors only. Only two sets of airborne observations are currently available for the Russian Arctic and Subarctic. Most of the in-situ airborne campaigns are performed below 85°N. Considering that only few single flights are performed above 85°N and that the northern limit of CALIOP lidar observations is 82°N, very limited aerosol data are available for the High Arctic. Concerning the vertical extent of airborne observations, the altitude range among the different projects varies depending on the platform, with a top ceiling of 1 km in the case of tethered balloons (Ferrero et al., 2016), 4 km for non-pressurized propeller aircraft (Abbatt et al., 2019), and 14 km for pressurized jet aircraft (Schwarz et al., 2013). Overall, most of the airborne campaigns provide almost complete coverage of the boundary layer and free troposphere. The majority of airborne observations are made in April and March. Nine airborne surveys are available for May and September, while only three observation campaigns have been undertaken in the winter period.

Multiple-year projects such as the High-performance Instrumented Airborne Platform for Environmental Research Pole-to-Pole Observations (HIPPO) (Schwarz et al., 2013) and NETCARE (Abbatt et al., 2019) initiatives provide data that are useful for identifying the influence of different sources and transport patterns on Arctic pollutants. Meanwhile, multiple-year projects with extended spatial range – such as the Polar Airborne Measurements and Arctic Regional Climate Model Simulation Project (PAMARCMiP) (Herber et al., 2012) – enable examination of the source-receptor relationship across the Arctic. And single-year observations are useful for investigating specific atmospheric processes in particular locations, including combustion sources. Examples of these include the Polar Study using Aircraft, Remote Sensing, Surface Measurements and Models, of Climate, Chemistry, Aerosols, and Transport (POLARCAT), (Paris et al., 2009); the Arctic Climate Change, Economy, and Society (ACCES) program, (Schmale et al., 2011, Roiger et al., 2015), the high-latitude dust sources investigation (Dagsson-Waldhauserova et al., 2019) and the Arctic Cloud Observations Using Airborne Measurements during Polar Day (ACLOUD) study, exploring aerosol-cloud interactions (Wendisch et al., 2019).

Shipborne monitoring provides unique opportunities to assess concentrations and deposition of BC and other aerosols at the highest latitudes of the Arctic. Fluxes of SLCFs over oceanic regions in ice-free areas and over sea ice can also be explored. Finally, latitudinal transects in the lower Arctic Ocean can provide useful information about the transport patterns of pollutants from specific regions in the mid-latitudes. A typical challenge that arises when measuring aerosols from onboard a ship is the pollution produced by the ship itself. At low wind speeds, it can be difficult to avoid contamination from the ship exhaust at the sampling inlets, which biases the sampling time to clean periods only. The availability of fast and high time-resolution aerosol monitors, such as the SP2 for BC, has partly overcome this problem, because pollution periods can be removed from the time series *a posteriori*.

The MOSAiC expedition is extraordinary for its long duration (it involved a 13-month ice drift); the complexity of the instrumental set-up; and the measurement coverage it achieved in very remote areas of the Arctic Ocean – including during the winter under highly variable weather conditions. In past experiments, the North Pole was reached by icebreakers carrying aerosol instrumentation, but only for a few weeks in the summer and freeze-up seasons. This was the case for a series of Arctic Ocean Expeditions undertaken from the early 90s until 2018, with instrumental set-ups of increasing complexity. Measurements of BC or EC and other aerosol chemical and physical parameters have been performed at lower latitudes in other sectors of the Arctic basin: in the Chukchi, East Siberian and Beaufort Seas on the CAREX 2014 cruise (Wang et al., 2020b); during the ARA08C Cruises in 2017 and 2018 (Park et al., 2020); on the 2014 R/V *Mirai* cruise (Taketani et al., 2016); in Baffin Bay and around the Canadian archipelago on the 2014 and 2016 NETCARE campaigns (Collins et al., 2017; Burkart et al., 2017), in the Norway sea on the AREX 2011–2012 cruises (Ferrero et al., 2019); by the PASCAL and SiPCA campaigns in 2017 (Kecorius et al., 2019; Wendisch et al., 2019) and in the Barents and Kara Seas on the AARI marine expedition in 2015 (Popovicheva et al., 2019. In addition, Gao et al. (2019) reported measurements of atmospheric dust being taken in the central Arctic Ocean during the 2015 US GEOTRACES cruise. Finally, the Maritime Aerosol Network (MAN) of NASA's Aerosol Robotic Network (AERONET) (Smirnov et al., 2009) has provided coordination and calibration services for global shipborne measurements with sun photometers since 2004. In the past decade, MAN has contributed to about 25 cruises in the Arctic area. The list of the most relevant research cruises up to 2012 and a compilation of the sun-photometer observations organized in geographical sectors of the Arctic Ocean is presented by Tomasi et al. (2015).

Other remote sensing observations, such as satellite measurements, are not as limited *per se* in space and time as atmospheric in-situ observations or snow- and ice-core sampling programs. However, the most important satellite instrument for aerosol observations, CALIOP, only reaches up to 82°N, leaving latitudes farther north unobserved. Also, concentrations of aerosol in the Arctic are generally below the detection limit for CALIOP, which detects aerosol between 10%–15% of the time.

5.3 Ozone

5.3.1 Introduction

Very few stations provide long-term monitoring of surface ozone (O_3) and ozone vertical profiles in the Arctic. In many cases, records are not continuous and large data gaps exist,

especially in the eastern Arctic, and over the Arctic Ocean and terrestrial locations. Long-term continuous measurements of O_3 precursors (such as carbon monoxide [CO] and volatile organic compounds [VOCs]) exist at very few surface sites, and long-term records of species important for diagnosing O_3 sources (such as nitrogen oxides [NO_X], peroxyacetyl nitrate [PAN]) and sinks – notably halogens – are lacking. This data is needed to evaluate model estimates of changes in O_3 sources and sinks, as well as to understand long-term trends, and to standardize measurement techniques. Information is also required on how chemical composition in the Arctic atmosphere varies with altitude, as well as on the origins of O_3 and processes that affect it. While recent airborne missions have provided important snapshots in different seasons, there has not been an airborne campaign dedicated to process-level understanding since 2008. Satellite data provide spatial information about O_3 and certain precursors and oxidants, as well as limited vertical information, but more attention is needed to improve retrievals, and to understand biases and instrument limitations at high latitudes. Long-term monitoring of atmospheric composition at existing stations is essential to accurately determine trends. This effort needs to be continued and integrated into a Pan-Arctic observation network building on, for example, International Arctic Systems for Observing the Atmosphere (IASOA) and the World Meteorological Organization (WMO) Global Atmosphere Watch (GAW). The development of new techniques is providing additional opportunities for regular monitoring (such as from tethered balloons, unmanned aerial vehicles, and the use of platforms such as commercial aircraft and shipping).

Observations of O_3, as well as of key species that can indicate O_3 sources and sinks, are needed to understand the Arctic O_3 budget, including the contribution from anthropogenic emissions, and to quantify changes in O_3 trends. In particular, there is a need to maintain and improve long-term monitoring in regions where local emissions are increasing (both urban and rural locations) as well as in areas where natural sources and sinks are changing in response to climate change (such as along coastlines and forest-tundra boundaries). Long-term records of O_3 are needed throughout the depth of the troposphere, requiring regular airborne missions, to quantify changes to the perturbation of tropospheric O_3 by anthropogenic emissions.

This section discusses different measurements of O_3 and its precursors, in particular NO_X, CO and VOCs, including *in-situ* techniques used to make observations at the surface and to record vertical profiles from airborne platforms and ozone soundings. Remote sensing measurements by lidar and from satellite are also discussed. Methane (CH_4) is a key precursor for tropospheric O_3 , when oxidized in the presence of sufficient NO_X. Anthropogenic CH_4 emissions are estimated to be responsible for around half of the radiative forcing due to tropospheric O_3 from pre-industrial to present-day (Stevenson et al., 2013). The capacity of current observational infrastructure to provide information about the distribution of O_3 and its precursors, and trends in O_3 concentrations and budgets, is also addressed.

5.3.2 Measurement techniques

5.3.2.1 Surface data

Surface O_3 is generally measured using optical methods, where air samples are continuously drawn through an ultraviolet (UV) lamp chamber, and O_3 is measured by UV absorption at 254 nm. The stability of the instruments is ensured by adding known concentrations of O_3 from an internal O_3 generator that are traceable to a primary calibration standard. The uncertainty of the UV source is within 7% on a 95% confidence interval following EN 14625 standard (e.g. Skov et al., 2020). More recently, the absorption cross-section of O_3 has been re-evaluated and most likely will be decreased by 1.23%, leading to higher O_3 concentrations (Tarasick et al., 2019 and references therein). The UV absorption instruments are robust, and provide accurate measurements with only minor interferences from other compounds (e.g. Ollison et al., 2013).

Other types of instruments are less frequently used in the Arctic, such as chemiluminescence of O_3 with methylene, which was used more in the past, or differential optical absorption spectroscopy (DOAS). DOAS uses an open pass of, typically, a few kilometers path length with a Xenon lamp as the light source (e.g. Lorenzen-Schmidt et al., 1998).

5.3.2.1.1 Ozone precursors

In the Arctic, NO_X and VOC concentrations are generally low, posing additional difficulties when compared to measuring at more southerly latitudes, where pollution levels are higher. NO_X is most often measured with monitors using chemiluminescence. Sample air is split into two sub-streams. The first leads directly to the analytical chamber where nitrogen oxide (NO) is detected by the chemiluminescence reaction of NO with O_3. The second sub-stream passes over a catalyst (such as gold) where nitrogen dioxide (NO_2) is reduced to NO. This enables the sum of NO and NO_2 (NO_X) to be calculated. The catalysts are not specific for NO_2 but also reduce other nitrogen species such as PAN (e.g. Skov et al., 1997). Instruments are available that can measure nitrogen species, with low interference from other compounds, for example: NO_X monitors using a photolytical converter; DOAS; cavity ring-down spectroscopy; and cavity-attenuated phase shift spectroscopy (e.g. Kebabian et al., 2005). CO has been measured approximately weekly from air samples by NOAA at Alert, Utqiaġvik and Ny Ålesund from 1994 onwards, and prior to that in 1989 and 1992. Online technologies for measuring CO today are: Fourier-transform infrared spectroscopy (FTIR) using a white cell; cavity ring down techniques; or on-line gas chromatography. Gautrois et al. (2003) reported long-term VOC concentrations for Alert, where a seven-year timeseries of VOC mixing ratios was determined using off-line techniques (gas chromatography mass spectrometry; GC-MS), with a time resolution of nine days. A few campaigns have focused on taking VOC measurements with high time resolution at specific surface stations (e.g. Mungall et al., 2018a) and during ship cruises (e.g. Sjostedt et al., 2012). Oxidized and aromatic VOCs were measured with high time resolution (April 2018–October 2018) using a Proton Transfer Reaction ToF Mass Spectrometer (PTR-MS) at Villum Research Station in northern Greenland (Pernov et al., 2021).

5.3.2.2 Vertical profiles

Ozone soundings provide a long-term record of Arctic O_3 throughout the depth of the troposphere. Since 1990, regular vertical profiles for longer time periods (years) have been available from ~10 stations north of 60°N. The measurements are mainly conducted using the balloon-borne Electrochemical Concentration Cell (ECC) ozonesonde, reaching an altitude of about 30 km. Biases in tropospheric measurements are reported to be 1.0±4.4% in the lower troposphere, and 5.3±4.4% in the upper troposphere (UT) (Tarasick et al., 2019).

Tropospheric measurements of O_3 using ground-based differential absorption lidar (DIAL) are also available in the Arctic, for example at Eureka (Seabrook and Whiteway, 2016). DIAL measurements offer temporal resolution down to minutes and vertical resolution comparable to ozonesonde measurements, depending on the operational set-up. Precision and bias in tropospheric measurements are reported to be better than 10% and 1±8%, respectively (Tarasick et al., 2019). Similar techniques to those used at ground-based monitoring sites are also deployed on airborne platforms. Since AMAP (2015a) was published, additional observations from aircraft campaigns in the Arctic have become available, including EU-ACCESS (Roiger et al., 2015), PAMARCMIP 2018 (Herber et al., 2012) and NASA AToM (Brune et al., 2020) providing profile measurements of ozone and its precursors.

5.3.2.3 Satellite data

An increasing number of space-borne sensors retrieve tropospheric trace-gas distributions, offering regular, continuous coverage in poorly observed regions, such as the Arctic. Polar orbiting and sun-synchronous orbiting satellites give global coverage with regular overpass times. Many instruments have accumulated long-term, multi-annual datasets with which to assess inter-annual variability and trends in tropospheric composition. Tropospheric ozone columns and some profile information are available from sensors in the UV/visible (Global Ozone Monitoring Experiment [GOME]-1 and GOME-2, Ozone Monitoring Instrument) and infra-red (IR) (Tropospheric Emission Spectrometer [TES]) wavelength ranges. Limb sounders such as the Atmospheric Infrared Sounder (AIRS) and TES instruments, and the Microwave Limb Sounder (MLS) instrument, offer improved vertical-profile resolution at the expense of spatial coverage and horizontal resolution (Pittman et al., 2009). In addition, satellite sensors retrieve information on O_3 precursor species and oxidants, including NO_2, CO, CH_4 and bromine oxide (BrO). The recently launched TROPOspheric Monitoring Instrument (TROPOMI) is capable of broad spectral retrieval across UV, visible and IR wavelengths, facilitating measurement of a range of pollutants (NO_2, O_3, formaldehyde [HCHO], CH_4, CO) with a spatial resolution of less than 7 km. Profiles of PAN have been retrieved from the Michelson Interferometer for Passive Atmospheric Sounding (MIPAS) and TES IR instruments (Pope et al., 2016; Zhu et al., 2015), and the Atmospheric Chemistry Experiment FTIR instrument (ACE-FTIR) provides information on a wide range of species (see model evaluation in Chapter 7) in the UT region.

Despite the potential for extensive Arctic data coverage from satellite sensors, there are challenges in the reliable use of satellite observations to inform our understanding of tropospheric O_3 and precursor distributions at high latitudes. Vertical sensitivity is limited, and varies according to environmental factors, implying that fully resolving vertical profiles with layers of different composition and corresponding source influences is difficult. At Arctic latitudes, the sampled altitude range of limb instruments can often be within the lower stratosphere, limiting information available on tropospheric O_3 and precursors. Moreover, UV and visible wavelength instruments are unable to retrieve data in darkness, negating their use during polar winter. IR retrievals may also have limited reliability at high latitudes, due to problems with lower surface-atmosphere thermal contrast (Clerbaux et al., 2009), extensive Arctic cloud cover, and high surface albedo. Finally, a paucity of *in-situ* observations for evaluating satellite data may lead to poor confidence in retrieved abundances in the Arctic troposphere, and make it difficult to assess the impacts of instrument drift and inter-comparability between satellite platforms for the region (for example between different sensors).

5.4 Methane

5.4.1 Introduction

Long-term, systematic measurements of atmospheric CH_4 are essential to support the assessment of long-term trends, as well as shorter-term variability (Kulmala, 2018); however short-term process studies to understand the sources of CH_4 are also important. Research is also needed to evaluate whether current measuring techniques and monitoring infrastructure are sufficiently capable of detecting trends in atmospheric concentration and fluxes. Over the past five years, the observation capacity for CH_4 has been enhanced through new long-term, inter-calibrated tall-tower measurements, and the establishment of flux towers within the Integrated Carbon Observation System (ICOS). Furthermore, new measurement instruments and analysis methods have been developed, or become more affordable, improving the coverage and frequency of measurements.

5.4.2 Methane concentration measurement methods and networks

Observations of CH_4 in the Arctic atmosphere were described in detail in AMAP (2015); here the sites in the NOAA Global Greenhouse Gas Reference Network (GGGRN) are presented (see Figure 5.5). The measurement programs include: Measurements at four NOAA Atmospheric Baseline Observatories and multiple tall towers in the USA; air samples collected by volunteers at more than 50 sites around the world; air samples collected regularly from small aircraft, mostly in North America; and vertical profiles using balloons and the AirCore sampling system. All measurements are subject to stringent quality-control procedures, and, where possible, are directly traceable to internationally accepted calibration scales. Since the previous report, some new sites have come on-line, although data are not necessarily widely available. Surface *in situ* and baseline observatory data are submitted to the WMO/GAW World Data Centre for Greenhouse Gases.

Figure 5.5 (update of the Figure 6.1 from AMAP [2015b]). Long-term CH_4 atmospheric monitoring sites in the Arctic and sub-Arctic region. Remote background sites are shown by blue circles, with regionally influenced sites shown by red circles. The Arctic ICOS sites are marked with red triangles, and sites reported in Chapter 6 (NOAA/ESRL Global Greenhouse Gas Reference Network) are marked with green squares. CARVE Tower and Cherskii only reported between 2011–2015 and 2008–2016, respectively.

The European ICOS network provides standardized and open data from more than 130 measurement stations across 12 European countries, four of which are located in the Arctic (Station Nord and Zackenberg in Greenland; Zeppelin; and Pallas). The stations observe CH_4 concentrations in the atmosphere, as well as CH_4 fluxes between the atmosphere, the land surface and the oceans. ICOS produces standardized, high-precision and long-term observations that are used by scientists and decision-makers to predict and mitigate impacts from climate change. The ICOS atmosphere stations have recently been recognized as a contributing network to WMO/GAW for greenhouse gases.

Atmospheric CH_4 can be measured using a variety of techniques. Close to ground level, a gas analyzer can be set up to sample ambient air and determine the CH_4 concentration. Some of the NOAA sites, and all the ICOS atmospheric sites, use cavity ring-down spectroscopy (CRDS) for high-frequency and stable measurements of CH_4, but the most common measurement systems still involve collecting air samples in a flask and analyzing them in a laboratory. Ground-based networks with flask sampling and CRDS *in-situ* measurements of the CH_4 mixing ratio deliver the most reliable measurements.

Recently, ground-based remote sensing has become more common for measuring atmospheric concentrations of CH_4. Using this method, the total column of CH_4 can be retrieved by measuring the absorption of direct solar radiation at near-infrared or mid-infrared wavelengths. This method is used by the Total Carbon Column Observing Network (TCCON) and the Network for the Detection of Atmospheric Composition Change (NDACC).

Satellite observations of CH_4 offer new insights into the magnitude of regional sources and sinks, and can help to overcome large uncertainties associated with the upscaling and interpretation of surface-concentration data. The infrared radiation back-scattered by the atmosphere and the surface is used by satellite instruments, such as TROPOMI onboard Sentinel 5 Precursor satellite (S5P) and TANSO-FTS onboard GOSAT.

5.4.3 Methane flux measurement methods

This section describes methods used for measuring fluxes of CH_4 in terrestrial and marine ecosystems.

5.4.3.1 Terrestrial ecosystems

Surface flux measurements of CH_4 exchange between terrestrial ecosystems and the atmosphere rely primarily on closed chamber and eddy-covariance methods, with the latter usually deployed on ground-based flux towers. However, airborne eddy-covariance flux measurements and gradient flux estimates have been conducted and reported (Roiger et al., 2015), but for practical reasons this method is not suitable for flux-monitoring purposes.

In boreal and Arctic ecosystems, CH_4 flux measurements are still predominantly performed with chambers, which usually cover <1 m^2 (Whalen and Reeburgh, 1990; Christensen et al., 1995; Corradi et al., 2005; Mastepanov et al., 2008; Sachs et al., 2010, Pirk et al., 2016). Ecosystem-scale eddy covariance observations of integrated fluxes over larger areas (typically hectares) have become available relatively recently due to advances in IR and CRDS instruments. Class 1 ICOS-ecosystem stations have standardized eddy-covariance (Nemitz et al., 2018) and chamber (Pavelka et al., 2018) flux measurements of CH_4 and CO_2 but the stations in the Arctic are predominately Class 2, which do not measure CH_4 eddy-covariance (see Box 5.1).

Box 5.1 Methods commonly used to measure fluxes of CH_4

The closed-chamber technique

The closed-chamber technique is widely used to measure the exchange of methane (CH_4) and carbon dioxide (CO_2) from terrestrial ecosystems. The method has been extensively tested (Pavelka et al., 2018; Pirk et al., 2016; Christiansen et al., 2011; Pumpanen et al., 2004) and is generally accepted to provide good results. However, the models used for calculating the fluxes based on data from the chamber measurements are often debated. Studies suggest the exponential flux calculation model gives the most reliable flux results (Pihlatie et al., 2013; Pirk et al., 2016), however, Pavelka et al. (2018) suggest using a combination of linear and non-linear flux calculation methods. The chamber method measures the fluxes over a small area. Static chambers are based on "Ficks law of diffusion", and quantify emissions by multiplying the change in CH_4 concentration in the chamber over short monitoring periods by the ratio of volume/area in the chamber.

The eddy-covariance technique

The eddy-covariance technique has been used less frequently than the chamber technique (Rinne et al., 2007). The advantage of the eddy-covariance technique is the minimal disturbance on the measured surface, and the potential to measure long timeseries. However, only a few studies have reported using the eddy-covariance technique to make continuous measurements of annual CH_4 emissions from northern ecosystems (Rinne et al., 2007; Richardson et al., 2019). The eddy-covariance technique is the most direct way to measure vertical fluxes, and is becoming more common for studies of CH_4 fluxes over terrestrial ecosystems where an "ICOS" standard has been developed (Nemitz et al., 2018). The eddy-covariance method obtains turbulent flux data by calculating the covariance of fluctuations in the vertical wind velocity and in the physical quantity being measured. This method is also able to directly measure the carbon, water, and heat flows between plant communities and the atmosphere. The eddy-covariance technique directly and continuously determines the carbon and water vapor flows of an ecosystem, and has been confirmed to be the most efficient method for measuring the interactions between a terrestrial biosphere and the atmosphere on an ecological scale (Friend et al., 2006; Baldocchi, 2008).

5.4.3.2 Ocean

Global CH_4 emissions from the ocean are dominated by those from shallow coastal waters (Gutiérrez-Loza et al., 2019; Weber et al., 2019). The air–sea gas fluxes are commonly estimated from their ocean–atmosphere disequilibrium (denoted as Δ) using gas-transfer theory (Gålfalk et al., 2013; Platt et al., 2018). Some measurements of the distribution of CH_4 in Arctic waters exist (Lund Myhre et al., 2016; Platt et al., 2018); however only few studies to estimate and evaluate the gas transfer coefficients for air–sea exchange of CH_4 are carried out, and this AMAP assessment revealed only a single study that directly measured air–sea exchange of CH_4 in Arctic coastal waters using micrometeorological techniques (Thornton et al., 2020) (see Box 5.2).

Box 5.2 How air–sea flux is estimated

The air–sea flux of a weakly soluble gas such as CO_2 or CH_4 is water-phase controlled (Wanninkhof et al., 2009), and is commonly estimated from the difference in concentrations across the air–sea interface. The exchange is often expressed in terms of the partial pressure of the gas in air and in water by equations of the form

$$\text{Flux} = kK_0\Delta pC$$

where ΔpC is the difference in the partial pressure of CH_4 across the interface, K_0 is the aqueous-phase solubility of CH_4, and k is a gas-transfer velocity – being a function of several parameters, but usually only parameterized by the windspeed or the surface stress (Garbe et al., 2014; Wanninkhof et al., 2009). In reality, k depends on many chemical, physical, and biological processes in between the layers where the CH_4 gradient is measured. Jørgensen et al. (2020) showed how the exchange rate for CO_2 is affected by the chemical reaction rates in the carbonate buffer system. It is possible that the interaction between chemical reaction rates and turbulent exchange rate also affects the exchange rates for CH_4; however this still need to be investigated.

5.4.4 Methane isotope measurements

Because measurements cannot be made at every CH_4 source across the Arctic, atmospheric sampling is sometimes employed to determine the relative strengths and origin of

the various Arctic sources. The common tool for this "source apportionment" is isotopic analysis, generally δ^{13}C-CH_4, δD-CH_4, and Δ^{14}C-CH_4, although single studies often focus on a single isotopic system. Because of greater relative abundance of ^{13}C, it is often technically easiest to measure δ^{13}C-CH_4, and it is the most common measurement method. Ideally, each individual emitter of Arctic CH_4 would have a distinct isotopic signature. For example, thermokarst lakes are thought to be more climate-sensitive than post-glacial lakes. If the δ^{13}C-CH_4 signatures for these sources differed, that could provide a way to track increasing or decreasing emissions from certain lake types. Unfortunately, freshwater systems in the Arctic have deeply overlapping signatures, especially in δ^{13}C-CH_4 (Thornton et al., 2016a; Wik et al., 2020). However, δD-CH_4 measurements show a significant difference between thermokarst and post-glacial lakes (Wik et al., 2020: see Figure 5.6), although these measurements are currently rarer. Finding other such distinctions will depend on availability of larger and more extensive datasets of isotopic signatures of the various freshwater emission types.

Speculation has focused for some time on whether future planetary warming will release a greater proportion of old, long-stored carbon (e.g. Schuur et al., 2015), particularly as CH_4 (Dean et al., 2018). The amount of stored old carbon is immense (Hugelius et al., 2014) – nearly double the current atmospheric burden. However, understanding the stability

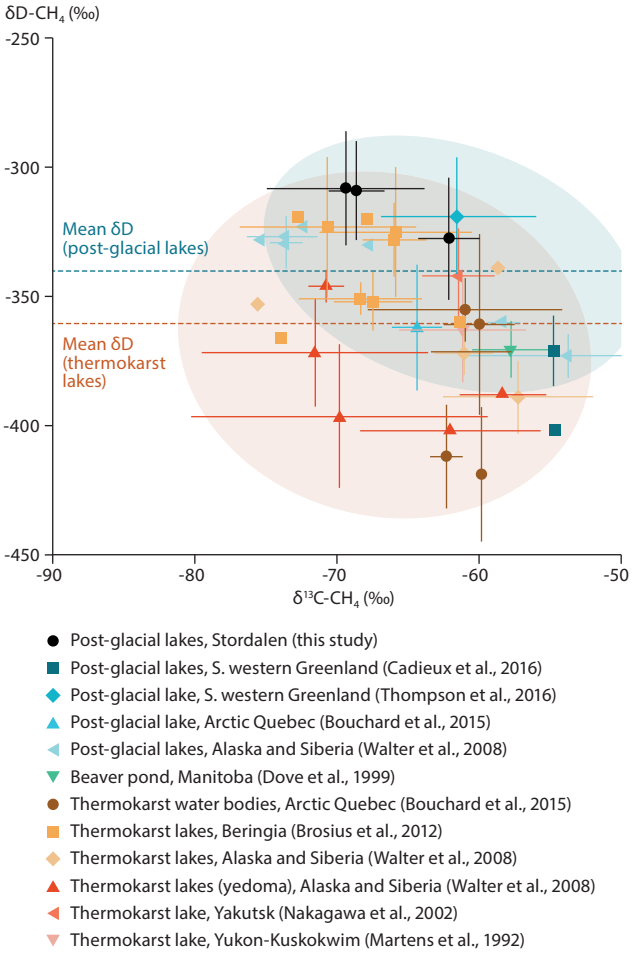

Figure 5.6 Overlap of ^{13}C and dD-CH_4 signatures for Arctic lake types. From Wik et al. (2020).

of this carbon stock against climate warming or other remobilization in the present-day is challenging. A close relationship between CH_4 emitted over decadal timescales and the amount of permafrost thawed in Arctic lakes was noted by Walter Anthony et al. (2018). Radiocarbon measurements (^{14}C-CH_4) enable a reasonably definitive determination to be made of whether any particular CH_4 emission is derived from stored old (radiocarbon-dead) or newly produced (radiocarbon-live) CH_4. Unfortunately, radiocarbon measurements are expensive and require time-consuming off-site analysis of samples, limiting the number that can be reasonably assessed (Kessler and Reeburgh, 2005). Several studies have questioned whether the CH_4 being emitted from lakes derives from new production by annual plant growth or older stored carbon being released from thawing permafrost (Bouchard et al., 2015; Elder et al., 2018). The bulk of recent studies have pointed to the majority of this carbon being relatively modern but with a quantifiable portion of ancient, radiocarbon-dead CH_4. Nonetheless, it is clear that permafrost thawing does release Pleistocene-age soil organic carbon into the modern carbon cycle, and that resulting processes such as increased erosion and runoff promote further release of old carbon (Estop-Aragonés et al., 2020).

Instead of taking samples directly from a lake or stream, another approach is to use aircraft measurements to determine the net isotopic signature from an ecosystem (France et al., 2016). Such measurements might be easier to incorporate into regional or global models, and these have been applied to locate "hotspots" of emissions within a delta landscape of varied CH_4 sources (Kohnert et al., 2017). While these studies may have some benefit, detailed underlying knowledge of the processes that control CH_4 production and loss in freshwater systems seem necessary for a true understanding of future changes.

Measuring the exotic (multiply-substituted) CH_4 isotopologues ($^{13}CH_3D$ and $^{12}CH_2D_2$) has been applied to identify the formation processes and temperatures of CH_4 in various Arctic environments (Douglas et al., 2016). These analyses currently require specialized equipment that is only available in a few laboratories worldwide.

One new focus area has been on genomic studies of the microbial species involved in CH_4 cycling in freshwater systems. A key realization from the studies of Hultman et al. (2015) and Mackelprang et al. (2016) has been that connections exist between the state of permafrost thaw and specific microbial activity, and that a variety of microbial CH_4 production pathways are active, which depend on the environmental conditions and thaw states. Combining genomic studies with isotopic analysis of CH_4 (Singleton et al., 2018) appears to be useful for determining how effective methanotrophs are at destroying CH_4 before it is released to the atmosphere.

Because there are multiple unquantified CH_4 sources in the Arctic marine environment, one necessary step is differentiating between the sources. Isotopic analysis remains the most promising, but difficult, approach to this. Isotopic studies have attempted to untangle the possible sources of CH_4 from the Arctic Ocean, but remain frustrated by overlapping isotopic signatures and variability within samples (e.g. Thornton et al., 2016b). Multi-isotope studies hold some promise. Nonetheless,

marine CH_4 isotopologue data for the Arctic remains rare, especially for atmospheric measurements (Pisso et al., 2016; Pankratova et al., 2019; Berchet et al., 2020). Sapart et al. (2016) used $\delta^{13}C\text{-}CH_4$, $\delta D\text{-}CH_4$, and $\Delta^{14}C\text{-}CH_4$ measurements in the sediment and waters in the Laptev Sea to suggest a biogenic CH_4 source, apparently forming from Pleistocene or older carbon substrate. On the Beaufort shelf north of Alaska, far lower emissions to the atmosphere were noted, with little evidence of release of CH_4 from 'old' carbon sources (Sparrow et al., 2018). In-water measurements can be challenging, requiring massive water sampling projects to obtain enough CH_4 for a single sample (Sparrow and Kessler, 2017).

Berchet et al. (2020) applied an inverse model to atmospheric shipborne measurements of $\delta^{13}C\text{-}CH_4$ in the East Siberian Arctic Shelf (ESAS), suggesting that CH_4 emissions from ESAS are dominantly thermogenic, with a smaller biogenic contribution. Thonat et al. (2017, 2019) investigated the potential to improve source apportionment of Arctic emissions of CH_4 with long-term continuous atmospheric measurements of $\delta^{13}C\text{-}CH_4$. It is hoped that such measurements will be more common in the near future. A recent study on measuring radiocarbon in CH_4 from Greenlandic ice cores and a global atmospheric inversion model suggested that global natural radiocarbon-dead, or fossil, CH_4 emissions were only ~1.6 Tg/y in pre-industrial times, with present-day rates being similar (Hmiel et al., 2020). Such a low emission rate is difficult to reconcile with what are likely multiple Arctic CH_4 sources being fed by old carbon sources – both in the marine environment and on land.

5.5 Cloud properties from satellite observations

5.5.1 Introduction

The impact of clouds on the Arctic climate is multifaceted (Kay et al., 2016). Clouds exercise radiative and dynamical control on the Arctic environment, and also interact with other components of the Arctic climate system. The importance of monitoring clouds and evaluating them in the chemistry transport and climate models in the context of AMAP can be justified due to the following reasons:

a) Cloud properties and cloud radiative effects respond to changes in aerosols and their precursor gases. Indirect effects of aerosols on clouds, and also aerosol processing by clouds in the pristine Arctic environment, are highly sensitive to changes in concentration and type of cloud condensation nuclei (CN) and ice nuclei (IN) (Garrett and Zhao, 2006; Lubin and Vogelmann, 2006; Mauritsen et al., 2011; Loewe et al., 2017; Lohmann, 2017; Zamora et al., 2017; Eirund et al., 2019). When the Arctic Ocean is locked by sea-ice during polar winters, the availability of CN is primarily driven by the transport of pollutants from more southerly latitudes; however, oceanic CN also contributes once the sea-ice melts during polar summers.

b) The net surface radiative impact of clouds in the Arctic is positive (has a warming effect) due to the dominance of longwave warming, except during a few summer months (Kay and L'Ecuyer, 2013). This implies that changes in clouds (and thus the surface longwave warming) could have an impact on seasonal sea-ice evolution in the Arctic Ocean and snow-covered land surfaces, which in turn could affect aerosol availability, optics and dynamics. This intrinsic coupling of clouds with large-scale atmospheric dynamics (the primary driver for cloud distribution), local meteorology (such as control by temperature and humidity inversions), aerosols (CCN-limited regimes), and other climate components, demands that clouds should be monitored along with other climate variables by AMAP assessments.

c) Through liquid- and ice-precipitation processes, clouds influence wet deposition of pollutants in the Arctic (Yamagata et al., 2009).

5.5.2 Available suite of satellite-based cloud climate data records

Monitoring clouds in the Arctic using the network of *in-situ* measurement stations or through dedicated monitoring campaigns is challenging because of the harsh environmental conditions and due to the central Arctic being an ocean. Space-based satellite observations offer a practical and economically viable alternative in this context. Enormous progress has been made in the last decade to improve understanding of clouds globally, including in the Arctic, using space-based observations. Polar-orbiting meteorological satellites carrying passive imaging sensors that are capable of providing cloud observations have been flying since 1978. These satellites, which are primarily operated by NOAA and European Organisation for the Exploitation of Meteorological Satellites (EUMETSAT), have flown with the Advanced Very High Resolution Radiometer (AVHRR) instrument onboard, data from which are currently available for nearly four decades. This has led to the compilation of several global cloud climate data records (CDRs).

The Arctic cloud properties from the four longest CDRs are outlined in the following paragraphs, with climatological averages calculated for the 35-year period 1982–2016. The first CDR is the most recent version from the pioneering International Satellite Cloud Climatology Project (ISCCP-HGM, Young et al., 2018a). The second is the second edition of EUMETSAT's Climate Monitoring Satellite Application Facility (CM SAF) Cloud, Albedo and surface Radiation dataset from AVHRR data (CLARA-A2, Karlsson et al., 2017). The third CDR is from the NOAA's Pathfinder Atmosphere Extended Program (PATMOS-x, Heidinger et al., 2014). And the fourth CDR is from the framework of the European Space Agency (ESA) Climate Change Initiative (CCI) program (Stengel et al., 2017). CLARA-A2, Cloud-CCI and PATMOS-x are all AVHRR-based CDRs, and employ the same AVHRR (inter)calibration. However, they differ in their approach to cloud property retrieval. The active lidar and radar sensors onboard the Cloud-Aerosol Lidar and Infrared Pathfinder Satellite Observation (CALIPSO) and CloudSat satellites, which are a part of the NASA's A-Train constellation, have been instrumental in training, evaluating and improving these CDRs in the last decade. These active sensors have revolutionized our views of clouds globally. However, the data records from the active sensors are still

not long enough to provide a climatological perspective. The strengths and limitations of the four CDRs listed above and their retrieval approaches are documented in Heidinger et al. (2014); Karlsson et al. (2017); Stengel et al. (2017); and Young et al. (2018a), respectively, and their global intercomparison is documented in Karlsson and Devasthale (2018). Note that the uncertainties in, and differences between, cloud microphysical properties such as liquid- and ice-water paths (which are based on passive sensors) are high in the central Arctic, limiting the quantitative climate-quality comparisons that can be made between retrievals from these CDRs.

5.5.2.1 Climatological overview of cloud amount and cloud-top pressure

The large-scale atmospheric circulation patterns primarily govern the spatial distribution and variability of clouds in the Arctic (Cesana et al., 2012; Kay et al., 2016; Lenaerts et al., 2017; Devasthale et al., 2020). Heat and moisture are carried to the Arctic, mainly from the Atlantic and Pacific sectors, causing shifts to the thermodynamical conditions that influence cloud processes over the ocean areas. This transport often favors high cloudiness throughout the year over the Atlantic and Pacific sectors, as visible in the climatological distribution of cloud fraction in all four CDRs (Figure 5.7). The annual average cloudiness in parts of Greenland and Norwegian Seas is about 80–90%. Such persistent cloudiness is also usually observed over the Barents and Kara Seas. The Canadian Archipelago and Beaufort Sea, on the other hand, show the lowest levels of cloudiness, which is also represented in all four CDRs. Over the Central Arctic (north of 70°N), the local thermodynamical conditions (e.g. temperature and humidity inversions) govern cloudiness. The cloudiness there is generally in the order of 60%–70%. However, the areas that have highly reflective and cold surfaces (such as permanently sea-covered parts of the Arctic Ocean, Greenland, and parts of Siberia) present a challenge for detecting clouds from the passive sensors. Thus, the CDRs have largest uncertainties and differences in cloudiness over these areas.

Temperature inversions are a dominant meteorological phenomena in the Arctic (Bradley et al., 1992; Serreze et al., 1992; Kahl et al., 1996; Devasthale et al., 2010). Inversions are persistent in all seasons, including in the summer, and exert control on the cloud-top properties (Sedlar and Tjernström, 2009; Sedlar et al., 2012; Shupe et al., 2013). The majority of clouds in the Arctic are low-level stratus and stratocumulus. They are often capped by inversions, as the boundary-layer height, cloud-top entrainment and vertical mixing are limited by these inversions. Over the ice-free parts of the oceans, all four CDRs broadly agree with one another and show cloud-top pressures larger than 700 hPa in the regions dominated by stratus and stratocumulus clouds (Figure 5.8). Over the ice-covered regions, however, the differences among the four CDRs are larger. The cloud-top heights (pressures) in PATMOS-x and ISCCP CDRs are clearly higher (lower) compared to the other two CDRs. There are many reasons for this. For example, the fraction of high clouds is higher in PATMOS-x and ISCCP, as the separability between the cold surfaces and cloud tops – as well as cloud typing in the retrieval algorithms – is different over the ice-covered regions. The handling of the cold surface temperatures, and the reliance on and usage of atmospheric temperature profiles from the reanalyses is also different among these CDRs. The evaluation of CDRs using active sensors shows that the passive retrievals, in general, overestimate cloud-top heights in the Arctic. In the lower troposphere, the presence of near isothermal vertical structures often poses a challenge for assigning accurate cloud-top heights in the retrievals.

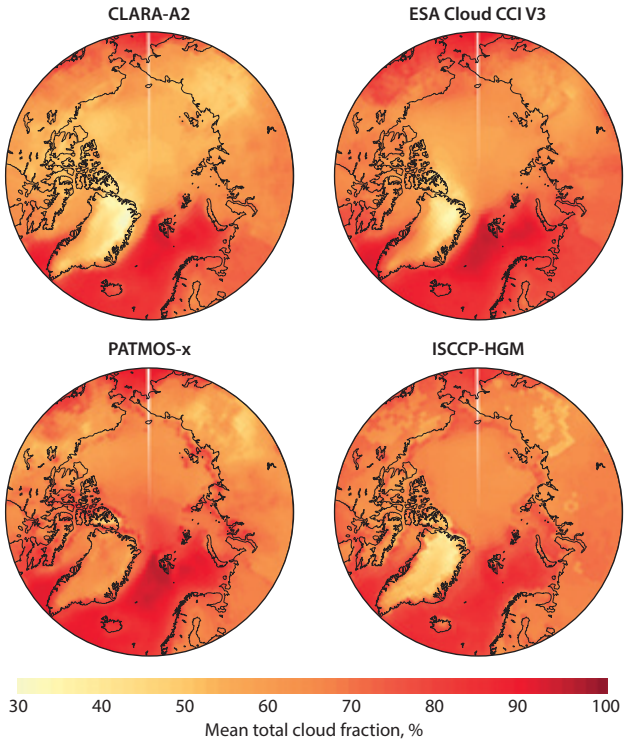

Figure 5.7 Climatological mean total cloud fraction from the four satellite-based CDRs.

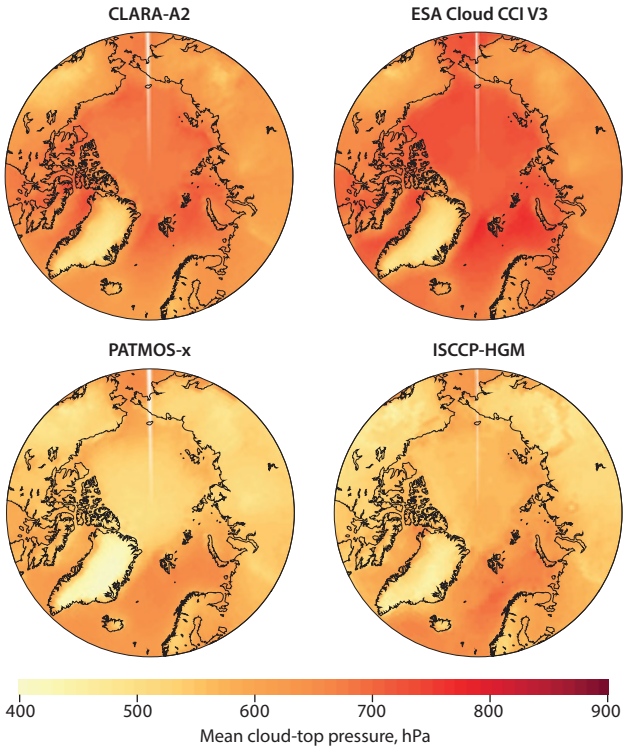

Figure 5.8 Climatological mean cloud-top pressure from the four CDRs.

5.5.2.2 Cloud radiative effects

The seasonality in incoming solar radiation primarily drives the seasonality in cloud radiative effects in the Arctic. As the optically thick low clouds are dominant over the ocean areas, their high reflection of insolation over otherwise optically black ocean areas results in a net cooling effect at the surface during the summer months, when the sea-ice is also retreating towards the seasonal minimum in September. In the absence of insolation, the longwave radiative (warming) effects dominate (Curry et al., 1996; Walsh and Chapman, 1998; Shupe and Intrieri, 2004; Wang and Key, 2005; Kay and L'Ecuyer, 2013; Kay et al., 2016; Lenaerts et al., 2017). The optically thick clouds, capped by stronger inversions, absorb and re-radiate longwave radiation to the surface, exerting positive cloud radiative effect (CRE) at the surface for most of the year (Figure 5.9).

The monthly spatial distribution of net CREs at the surface (Figure 5.10) shows that over the permanently ice-covered ocean areas and Greenland, the CREs remain positive throughout the year. Over the marginal sea-ice zones and open water northward of 60°N, net CREs at the surface follow changes in insolation through the seasons. The estimates of CREs constrained by the active CALIOP and CPR/CloudSat

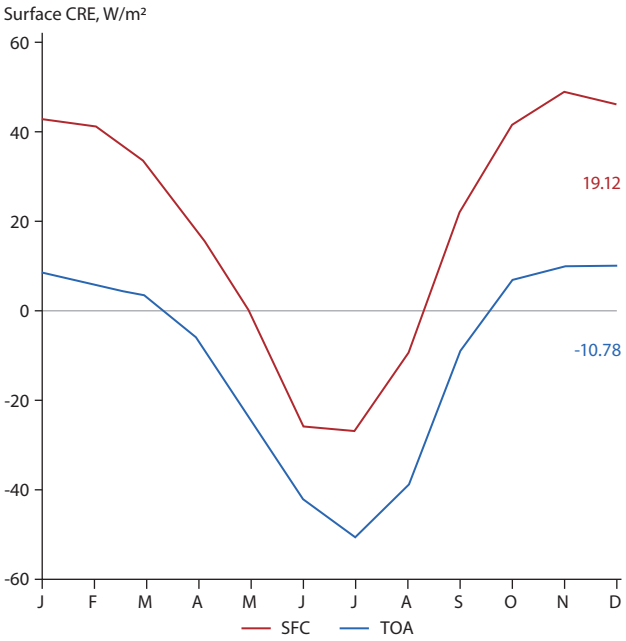

Figure 5.9 Monthly cloud radiative effects (CREs) at the surface and top of the atmosphere over the Arctic (60°N–90°N). The numbers show annual average of CRE at the top of the atmosphere (TOA) and the surface. The results are based on 15 years of data (2003–2017) from NASA's CERES instrument on board the Aqua satellite.

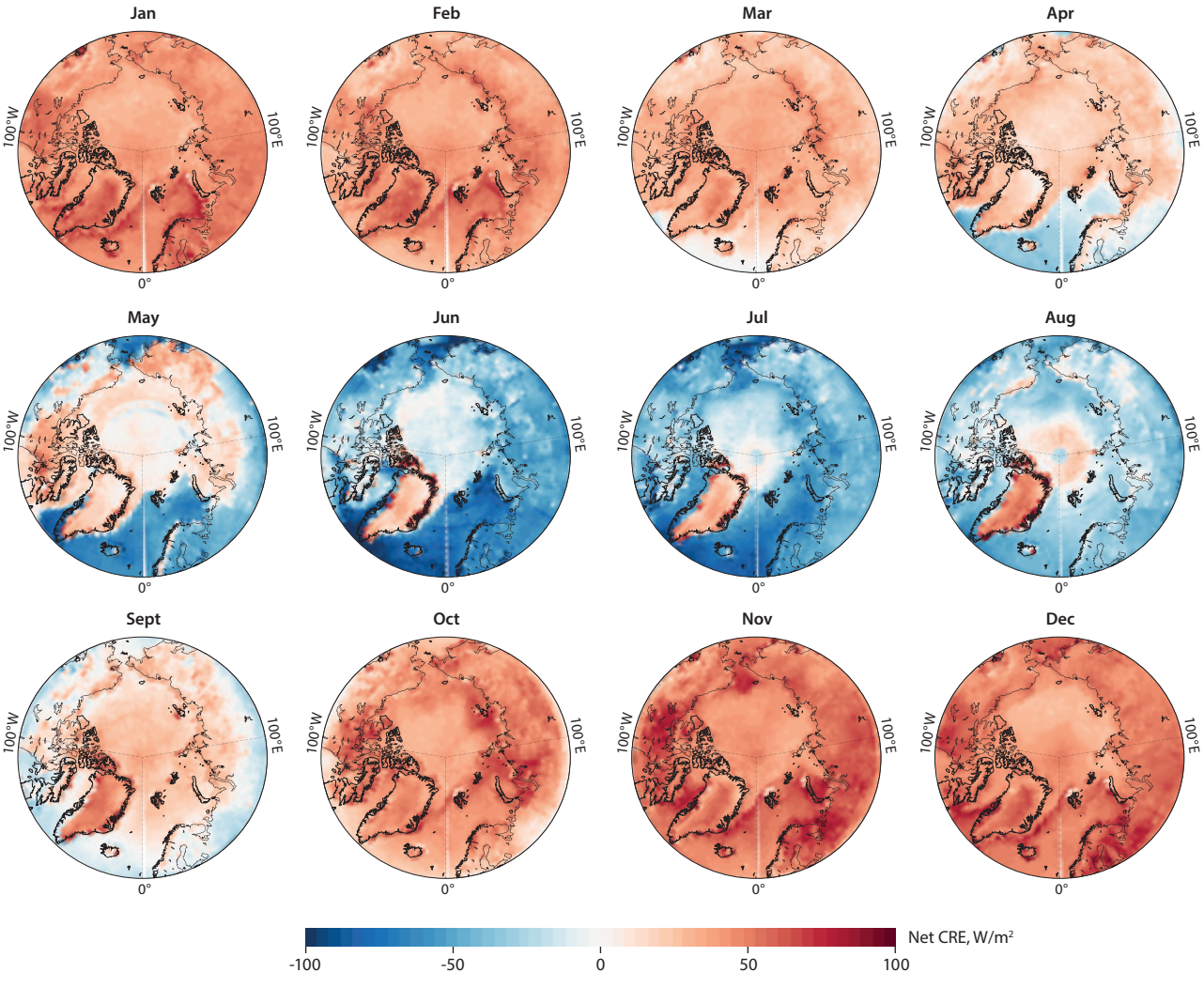

Figure 5.10 Climatological spatial distribution of CREs at the surface. The results are based on 15 years of data (2003–2017) from NASA's CERES instrument onboard the Aqua satellite.

sensors show that the clouds over the ocean areas in the Arctic warm the surface by an annual average of 10 W/m^2, and cool the top of the atmosphere (TOA) by -12 W/m^2 (Kay and L'Ecuyer, 2013).

5.5.3 *In-situ* measurements of cloud microphysical properties

Changes in anthropogenic aerosol emissions in the Arctic can affect clouds, which have a fundamental influence on the Arctic climate. Reductions in Arctic sea ice and ice cover on the land surface can increase emissions of natural aerosols, in turn affecting clouds.

In the Arctic, *in-situ* measurements of cloud microphysical properties have been made using light-scattering, imaging, and hot-wire techniques, which have also been used in other parts of the world (Baumgardner et al., 2017; McFarquhar et al., 2017). Although taking continuous *in-situ* measurements is a challenge in the Arctic, the first year-round *in-situ* measurements of cloud microphysical properties in the Arctic have now been made at a mountain site (Koike et al., 2019). More advanced cloud probes have also been developed in recent years, primarily to discriminate between liquid and ice particles, as well as to derive information about morphologies of ice particles. Some of them have been used for Arctic research. They include: probes measuring polarization in scattered light (CAS-DPOL, Baumgardner et al., 2014; Costa et al., 2017); spatial-intensity distribution of near-forward scattered light (SID-3 or PPD-HS, Vochezer et al., 2016; Mahrt et al., 2019); polar light-scattering function and stereo images (PHIPS-HALO, Abdelmonem et al., 2011; Schnaiter et al., 2018); holographic images (HOLODEC or HOLIMO II, Fugal and Shaw, 2009; Henneberger et al., 2013); and interferometric laser image (ILIDS, Porcheron et al., 2015).

In addition to the use of *in-situ* measurements, combined measurements of 94 GHz cloud radar, ceilometer, and microwave radiometer using the Cloudnet algorithm have been used to estimate vertical profiles of cloud microphysical properties (Nomokonova et al., 2019). Ground-based remote sensing is also a powerful tool for validating satellite measurements over the Arctic.

5.6 Conclusions and recommendations

5.6.1 Recommendations regarding aerosols (Section 5.2)

For continuous observations that can track long-term changes in aerosol properties across the Arctic and their sources the following actions are recommended:

- Establish a baseline proxy to standardize global BC measurements, for example by building on recent intercomparisons of SP2 and COSMOS with other methodologies, for better comparability between measurement techniques and sites.
- Add aerosol microphysical measurements, such as size distributions, at all permanent Arctic observatories to reveal aerosol processes and their relevance to climate.
- Implement a systematic snow- and precipitation-sampling program.
- Undertake systematic analyses of OC for source apportionment.
- Conduct systematic measurements of dust in the atmosphere and in snow to constrain its effects on climate.
- Establish a pan-Arctic isotopic-measurement network for better source attribution.
- Add additional measurement locations in the eastern Arctic for better geographical coverage.
- Conduct winter aircraft campaigns during the dark period in the Arctic.

5.6.2 Recommendations regarding ozone (Section 5.3)

- Maintain continuity of long-term surface O_3 measurements and vertical profiling using ozonesondes and lidars.
- Make additional measurements of O_3 precursors, especially CO, NO_X and VOCs, and important compounds such as PAN and halogens, at sites measuring surface O_3. The use of small sensors in polluted environments could be exploited.
- Expand the number of sites making surface O_3 and vertical-profile measurements, especially in the eastern Arctic and over terrestrial areas.
- Explore opportunities to make continuous measurements on new platforms, such as commercial shipping and aircraft.
- Stimulate discussions around developing new field campaigns to better understand processes governing tropospheric O_3.
- Improve understanding around O_3 and precursor satellite retrievals at high latitudes.

5.6.3 Recommendations regarding methane (Section 5.4)

- Facilitating collaborative work between monitoring stations is recommended, by standardizing instruments, and establishing automated and consistent quality checks to calibrate concentration and flux measurements.
- A homogeneous and reliable *in situ* observation network would help to support the development of remote sensing methods for CH_4 observation.
- Isotopic observations of CH_4 remain limited in the Arctic. Presently, $\delta^{13}C$-CH_4 is more common but often based on flask sampling; δD-CH_4 remains almost a curiosity in practice; and more exotic analysis of multiply-substituted isotopologues is extremely limited (Douglas et al., 2016).
- A broader set of long-term measurements of multiple CH_4 isotopologues would better constrain Arctic emissions sources; most analyses to date have relied solely on $\delta^{13}C$-CH_4.

5.6.4 Recommendations regarding clouds (Section 5.5)

Making *in-situ* measurements of clouds and aerosols in the Arctic is challenging. Satellite sensors offer a viable way forward with their continuous and homogeneous coverage, especially in the inner Arctic. However, despite significant progress made in active remote sensing in the past decade, several challenges remain in improving the retrievals from the passive satellite sensors. There are two key areas that need particular attention going forward.

1. The polar winter remains the Achilles heel for most of the data records that are based on passive sensors. Retrievals of microphysical properties depend on solar channels. Hence, they are not available in polar winters and also during the early spring and late autumn. Even cloud detection and retrievals of cloud-top properties have higher uncertainties during the polar winters.
2. Another key area is securing continued access to the vertically resolved information. This is especially true for the boundary layer clouds and aerosols, which are prevalent in the Arctic. Nearly 15 years of active space-based remote sensing has demonstrated the usefulness of having vertical information, but it has also revealed the complexities and limitations associated with observing the lowermost clouds and aerosols in the atmosphere. As a result, it is highly recommended that active space-based remote sensing and in-situ measurements continue, to ground and validate both active and passive satellite sensors.

Chapter 5 Appendix

Figure A5.1. Sites where air monitoring for SLCFs (red) or ice core BC observations (green) are conducted. Locations of sites named in Chapters 5 and 6.

6. Observations, origins and trends of SLCFs and clouds in the Arctic

Authors: Julia Schmale, Kathy Law, Lise-Lotte Sorensen, Manu Anna Thomas, Steve Arnold, Hans-Christen Hansson, Silvia Becagli, David Cappelletti, Stefano Decesari, Abhay Devasthale, Jens Liengaard Hjorth, Lin Huang, Antti-Pekka Hyvärinen, Makoto Koike, Yutaka Kondo, Joakim Langner, Andreas Massling, Joseph R. McConnell, Outi Meinander, Olga Popovicheva, Meri Ruppel, Sangeeta Sharma, Henrik Skov, Rita Traversi, Peter Tunved, Marco Zanatta, Christian Zdanowicz

6.1: Julia Schmale, Sangeeta Sharma, Stefano Decesari, Hans-Christen Hansson, Andreas Massling, Silvia Becagli, David Cappelletti, Lin Huang, Antti-Pekka Hyvärinen, Yutaka Kondo, Joseph R. McConnell, Outi Meinander, Olga Popovicheva, Meri Ruppel, Rita Traversi, Peter Tunved, Marco Zanatta, Christian Zdanowicz

6.2: Kathy Law, Henrik Skov, Steve Arnold, Joakim Langner, Jens Liengaard Hjorth

6.3: Lise Lotte Sørensen; *Contributor:* Lori Bruhwiler

6.4: Manu Anna Thomas, Abhay Devasthale

6.1 Particulate matter: black carbon, dust, and inorganic and organic aerosols

6.1.1 Introduction

Aerosols from both anthropogenic and natural sources are present in the Arctic atmosphere. During the winter season (January through April), anthropogenic particles dominate, while in the summer (June through September) natural aerosols are more influential (Schmale et al., 2022).

Anthropogenic contributions have decreased since the 1990s. In Alert, Canada (see Table 6.2 for stations referred to in this chapter), for example, anthropogenic particulate sulfate has decreased by about 50% since 1980 – especially during the haze season (January–April). Black carbon (BC) declined by 54% between 1990 and around 2010, and now remains at a steady level during the haze season. Particulate nitrate is increasing despite lower nitrous oxide (NO_X) emissions (over the period 1980–2017). This is likely due to changes to atmospheric chemistry caused by reduced emissions of sulfur dioxide (SO_2), which have led to less particulate sulfate.

The summer Arctic aerosol load is clearly dominated by emissions from natural sources, mainly sea spray and dimethyl-sulfide (DMS), which is converted to particulate sulfate or methanesulfonic acid (MSA). There are indications that the contribution of larger particles (such as sea spray) increases in summer. This has direct implications for the radiation balance through direct scattering of solar radiation and changed cloud albedo. Meanwhile, wildfires are increasingly contributing organic and black carbon aerosols to the atmosphere, which influence the absorption of solar radiation and the potential for particles to affect cloud formation. Also, mineral dust has been identified as a natural short-lived climate forcer through deposition on snow and ice, where it absorbs solar radiation (its effects on clouds have yet to be quantified). To accurately assess the role of natural sources of particles, sources both inside and outside of the Arctic need to be considered.

Current monitoring sites are much better equipped to observe tracers of anthropogenic emissions than those of natural emissions. With natural emissions – from fires, mineral dust, sea spray, and marine microbial sources – changing, new approaches in monitoring are needed to document this change. To perform source apportionment, for both natural and anthropogenic sources, more sophisticated chemical methods, such as mass spectrometry and isotopic differentiation are needed. In addition, measurements of particle size distributions can reveal changes in emissions sources and atmospheric processes but this variable is only rarely measured. With respect to locations, this report has identified knowledge gaps in the eastern Arctic and in vertical profiling.

6.1.2 Sources and distribution of aerosols in the Arctic

Various anthropogenic and natural emissions of aerosols and their precursors are responsible for climate-forcing effects, as well as for air pollution, in the Arctic. The vertical distribution of aerosols measured over the Arctic often appears layered, and particles long-range transported far from the southerly source regions of anthropogenic emissions can be confined at specific elevations, often detached from the surface (Barrie 1986; Stone et al., 2014; Sharma et al., 2013; Law and Stohl, 2007). In addition, regional and local Arctic emissions sources, such as residential heating, wildfires, shipping, and extraction activities, contribute to the aerosol burden (Schmale et al., 2018a; Mölders and Kramm, 2018). Seasonal variations, with lower aerosol concentrations during the summer (June–September), are due to a decrease in the frequency of synoptic transport from the south and more particles being removed from the atmosphere through precipitation (Arnold et al., 2016). Wintertime Arctic haze builds up between January and April. During this period, remote surface locations have a direct influence on the anthropogenic aerosol burden, with particulate matter coming from sources in Eurasia, such as Siberia, by low-level transport (Popovicheva et al., 2019). At altitudes greater than two kilometers (km), sources from Europe and North America become important, while at greater than 3 km, emissions from deserts, biomass-burning regions and Asia play a role (Koch and Hansen, 2005; Sharma et. al., 2013; Shindell et al., 2008). Local natural sources become dominant during the summer at the surface, while dust (Dagsson-Waldhauserova et al., 2014; Groot Zwaaftink et al., 2016) and aerosols from forest fires that have been transported over long distances are important aloft (Evangeliou et. al., 2016).

Below is a detailed overview of aerosols that are observed in Arctic environments and have potential for climate effects. It includes BC, dust, and aerosols of inorganic and organic composition, covering their origin and seasonal cycles, as well as historical and present-day trends. The properties of each that are responsible for current and anticipated radiative changes within the atmosphere are also described. The section is divided into observations of atmospheric near-surface and vertical

aerosol distributions, as well as particles in ice and snow. Maps indicating the locations of the observatories used to gather data are provided in Chapter 5 Appendix Figure A5.1 (see also Chapter 5 Figures 5.3 and 5.5).

6.1.3 Concentrations, seasonal cycles and origins

6.1.3.1 Surface aerosol observations

Long-term monitoring at permanent observatories in the High Arctic provides core information about aerosol concentrations and composition in the atmosphere. Monitoring coordination networks (Global Atmosphere Watch [GAW]; Aerosol, Clouds and Trace Gases Research Infrastructure [ACTRIS]; European Monitoring and Evaluation Programme [EMEP]; Interagency Monitoring of Protected Visual Environments [IMPROVE]) have greatly facilitated standardization and access to aerosol measurement data from the Arctic observatories. The stations in the western and European geographical sectors were presented in AMAP (2015a), with emerging data from the first monitoring station to operate, since 2009, in Siberia, at 71°N (Tiksi, Sakha Republic, Russia) also presented in this report. The observations gathered by this pan-Arctic network of research stations have produced a flourishing scientific literature on aerosol trends, seasonal cycles, composition and sources (Eckhardt et al., 2015; Freud et al. 2017; Popovicheva et al., 2019; Sharma et al. 2019, Schmale et al., 2022). The short review of the state of Arctic aerosol measurements presented here largely draws on this large body of information (datasets, scientific papers, technical reports), as well as on additional, selected observations carried out in the lower Arctic (e.g., Dutkiewicz et al., 2014). Short-term experimental programmes employing comprehensive aerosol measurement platforms have been conducted in recent years to target specific science questions. Among others are the Network on Climate and Aerosols (NETCARE) program (Abbatt et al., 2019) and the Multidisciplinary drifting Observatory for the Study of Arctic Climate (MOSAiC) expedition. The results available from these intensive field campaigns are only briefly treated here, as they are less relevant than long-term monitoring to the quantitative assessment of aerosol sources and trends. However, they were taken account of because of their significance in defining future directions in research and monitoring.

Figure 6.1 shows the monthly mean concentrations of equivalent black carbon (eBC) at the five observatories in the High Arctic that carry out year-round long-term monitoring. In the summer months, mean eBC levels range between 5 and 20 nanograms per cubic meter (ng/m^3) at all stations, indicating the comparable effects of large-scale transport and efficient wet scavenging in all geographical regions. Average eBC concentrations peak in late winter or early spring in correspondence with the Arctic haze advection (Eckhardt et al., 2015; Gilardoni et al., 2019) apart from at the Summit observation facility, which – due to its elevation of greater than 3000 m – is normally not affected by low-level transport. However, the highest concentrations at Summit (>95 percentiles) are also observed in winter and early spring, indicating that Arctic haze can occasionally reach the top of the Greenland plateau. The climatology of the highest 5% of eBC monthly concentrations shows a second peak in mid-summer at all observatories, which can be linked to fire activity

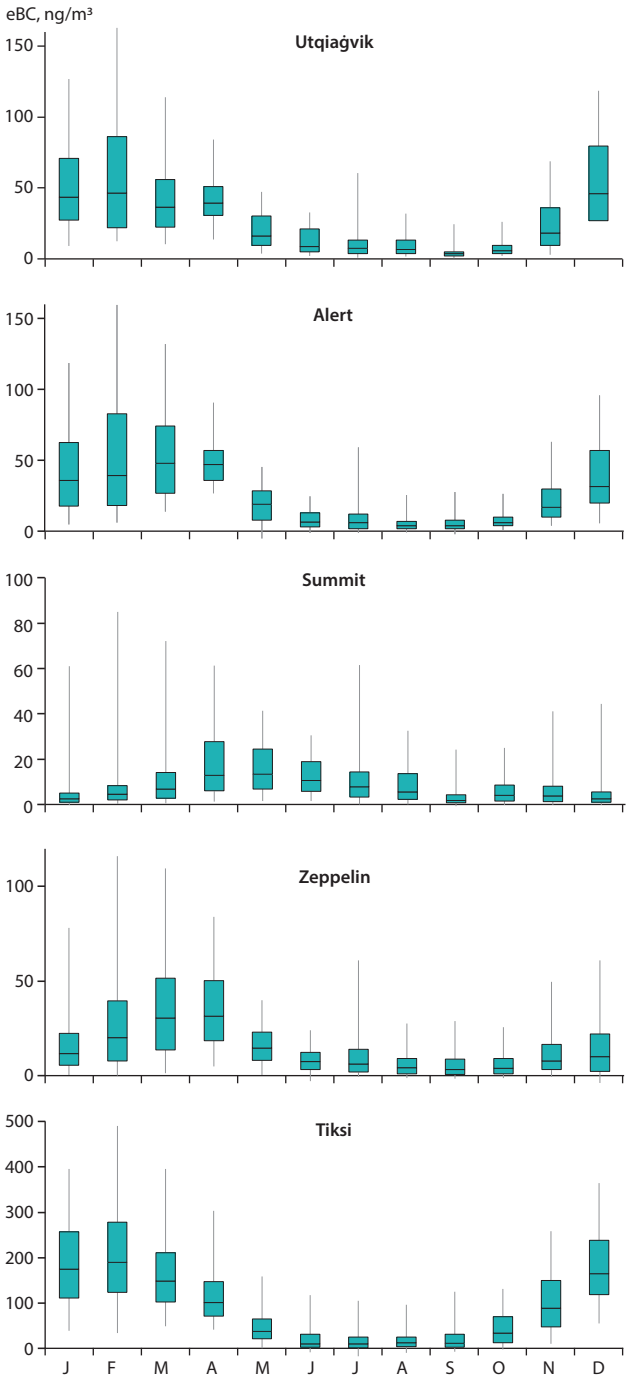

Figure 6.1. Seasonal cycles of eBC at five observatories in the High Arctic based on hourly observations during 2011–2016: Utqiaġvik (71°18'N, 3 meters above sea level (MASL); Alaska, USA); Alert (82°28'N, 30 MASL; Nunavut, Canada); Summit (72°34'N, 3216 MASL; Greenland, Denmark); Zeppelin (78°54'N, 470 MASL; Svalbard, Norway); Tiksi (71°35'N, 30 MASL; Sacha-Jacuzia, Russian Federation). Median values together with the 5%, 25%, 75% and 95% percentiles are reported. A mass absorption coefficient of 10 m^2/g was used to convert absorption coefficients into mass of BC when not internally set by the BC instruments. Data source: Data ref. 6.3 (accessed 15.01.2022).

(see Chapter 4). The other two main patterns in the yearly cycle of eBC concentrations – as summarized by Eckhardt et al. (2015) – are: (a) the more pronounced seasonality at Alert with respect to the other stations in the western Arctic; and (b) the delayed ramp-up period in late fall and winter at Zeppelin, indicating that, for most of the dark season, Svalbard experiences strong wet scavenging and might also be relatively well protected inside the polar dome from the advection of pollutants from southerly regions. The long-term observations of eBC are therefore

elucidating a consistent seasonal pattern of the transport and accumulation of eBC particles at the regional scale in the Arctic. Notice, however, that the monthly mean eBC concentrations at Tiksi (in Siberia) exceed 150 ng/m^3 in winter – more than three to four times higher than those in the western and European Arctic, where average concentrations are 20–50 ng/m^3. The higher eBC levels at Tiksi are explained by the station's proximity to strong emissions sources, and its exposure to low-level atmospheric transport from the Eurasian continent towards the Arctic Ocean during winter. The Siberian sector is still less-well covered by BC monitoring than the western Arctic. Nevertheless, the new observations performed between October 2015 and March 2016 at the Ice Base Cape Baranova station on Bolshevik Island (Russia) and reported by Manousakas et al. (2020) provide evidence for the regional-scale nature of the BC haze in the high Siberian Arctic in wintertime, where monthly means of eBC concentrations even in remote areas can reach 200 ng/m^3. Continuing to monitor BC on a long-term basis at locations such as Ice Base Cape Baranova is therefore highly recommended.

Information about the sources of BC in the Arctic can now be obtained in situ by means of carbon isotopic techniques (see Chapter 5). According to the radiocarbon data (^{14}C) discussed by Winiger et al. (2016, 2019), the biomass-burning fraction of elemental carbon (EC) in the pan-Arctic region was 39±10% in the annual mean. All sites were characterized by a pronounced seasonality, with a higher fraction from biomass burning in the summer when fire activity in the boreal forest is the highest (Mouteva et al., 2015). The stable isotopic carbon fingerprints (^{13}C) presented by Winiger et al. (2019) indicate that the combustion of liquid fuel represented the major fraction of fossil EC at all sites for the period considered (2011–2015). However, on the basis of the long-term record of δ^{13}C carried out at Alert, a significant contribution to EC from gas flaring cannot be ruled out (Stohl et al., 2013).

The recent observations of atmospheric dust (e.g., mineral particles; for a methodological definition see Chapter 5) have highlighted the importance of previously neglected sources at high latitudes. The locations of such high-latitude dust (HLD) emissions sources were identified in Bullard et al. (2016), as presented in Figure 6.2. The authors located and compared the main sources and drivers of dust emissions in the Northern hemisphere including Alaska, Canada, Greenland, and Iceland. They found an overlap between HLD areas and cold deserts, or Polar deserts, which Péwé (1974) defined as areas where

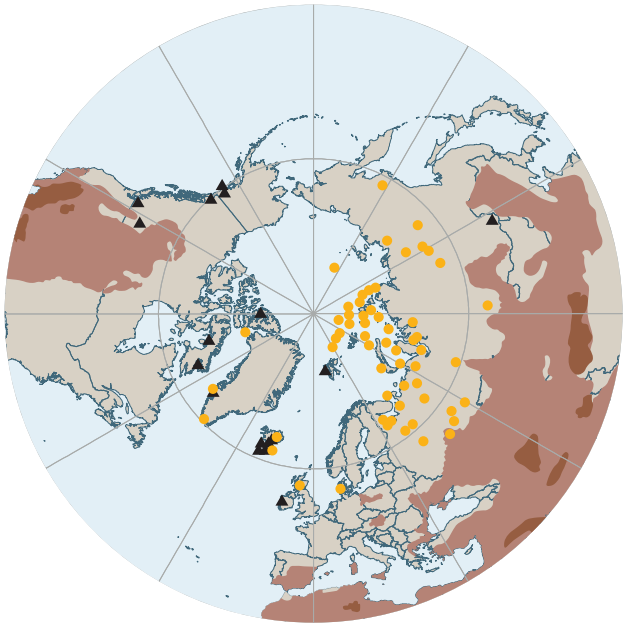

Figure 6.2. Northern hemispheric high-latitude dust sources identified on the basis of published observations (orange circles and black triangles; redrawn based on Figure 3 of Bullard et al., 2016). Orange circles indicate dust-storm frequency based on visibility data, while black triangles indicate georeferenced published observations of dust storms. For reference, light brown areas where the precipitation-to-potential-evapotranspiration ratio is <0.65 (according to the aridity index [AI] outlined in UNEP, 1997) and dark brown subtropical dust-emission zones are included.

the mean air temperature of the warmest month is <10°C and mean annual rainfall is <250 mm. Additional HLD sources have been recently identified in Meinander et al. (2019 and 2021), as presented in Figure 6.3. Meinander et al. (2021) quantify the Source Intensity (SI) values using the UNCCD Global Sand and Dust Storms Source Base Map (G-SDS-SBM), for 64 HLD sources included in their collection in the Northern (Alaska, Canada, Denmark, Greenland, Iceland, Svalbard, Sweden, and Russia) and Southern (Antarctica and Patagonia) high latitudes. Activity from most of these HLD dust sources show seasonal character. They estimate that in the Arctic HLD region, 5.5% of the land area has SI≥0.5 (1,035,059 km^2), 2.3% has SI≥0.7 (440,804 km^2), and 1.1 % has SI≥0.9 (208,701 km^2). Minimum SI values in the Arctic HLD region are about three orders of magnitude smaller, indicating that the dust sources are highly dependent on weather conditions.

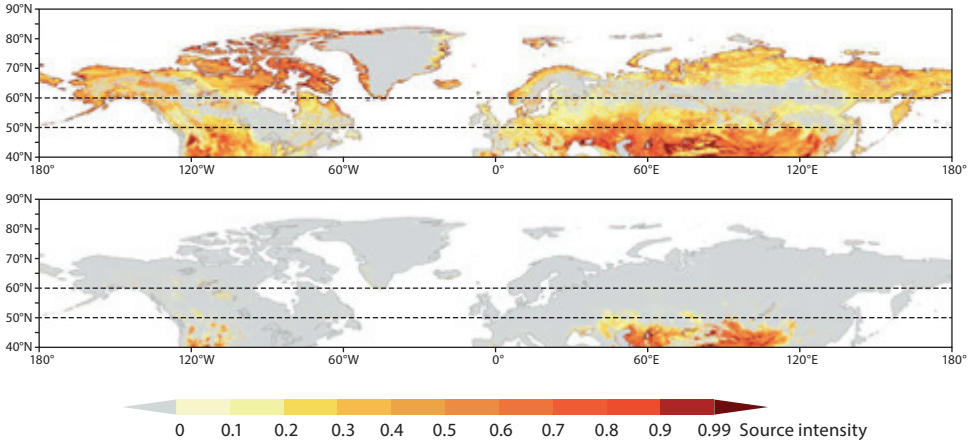

Figure 6.3. UNCCD Global Sand and Dust Storms Source Base Map (G-SDS-SBM) for annual maximum (upper panel) and minimum (lower panel) source intensity, for the northern HLD region and Arctic sub-region (north of 50°N and 60°N, respectively, marked with dashed lines); redrawn based on Figure 2 of Meinander et al. (2021).

Dust has very high temporal and spatial variability, as well as an episodic nature (Kaspari et al. 2014; Di Mauro et al., 2015), and concentrations can become very high. For example, the median annual PM_{10} dust concentration during dust events in northeast Iceland 1949–2011 was calculated as 106 µg/m³, with maxima of 122 µg/m³ in May and September (Dagsson-Waldhauserova et al., 2017). The climatology of Al concentrations compiled for Alert by Sharma et al. (2019) indicates a seasonal cycle with maxima in spring and fall, which overlaps with the months of the highest frequency of dust storms in Iceland (Dagsson-Waldhauserova et al., 2014). However, the concentrations (0.2–0.6 µg/m³ as monthly means at Alert based on weekly observations of aerosol Al between 2000 and 2006 [Fan, 2013]) appear very diluted with respect to peak levels in the source regions (e.g. Iceland). Similarly, the concentrations of geogenic elements in Ny-Ålesund peak in March and April, corresponding to the seasonality of dust in remote Arctic Canadian and Greenlandic areas.

However, as the ground is almost entirely covered by snow at this time, this dust may be transported from lower latitudes (Conca et al., 2019). Meanwhile, observations from Svalbard show that, in summertime, local sources such as dust emissions from glacial outwash plains can enhance dust concentrations (Tobo et al., 2019).

About half of annual dust events in the southern part of Iceland take place at sub-zero temperatures, when dark dust may be mixed with snow, reducing albedo (Dagsson-Waldhauserova et al., 2015). Icelandic dust contains abundant iron (Fe). Iron aerosols are emitted to the atmosphere from natural mineral-dust sources and anthropogenic processes, such as power generation. Ground-based and aircraft observations have shown that mass concentrations of anthropogenic iron oxide (FeOx) aerosols in East Asia and the Arctic were around 20%–50% of that of BC. The FeOx and BC concentrations were highly correlated, indicating that they are emitted from almost the same areas with similar emission ratios over the northern hemisphere (Yoshida et al., 2020). More research on iron oxides in atmospheric aerosols is recommended, not only because FeOx aerosols affect Earth's energy budget through their strong absorption of solar radiation, but also because they can affect global biogeochemical cycles through their role as a nutrient for oceanic phytoplankton (Matsui et al., 2018).

Aerosol sulfate and nitrate found in the Arctic environment are mainly carried from industrial and transport sources situated further south. However, sulfate in the atmosphere can also stem from natural sources as a result of volcanic emissions, the transformation of DMS gas emitted from marine microbial activity, and primary production of sulfate through sea-salt emissions. Gaseous sulfur oxides (SO_X) and NO_X oxidize in the atmosphere forming H_2SO_4 and HNO_3, respectively. These gases can readily condense onto pre-existing airborne particles or react with other compounds to form new particles. Meteorology governs the seasonality observed in the Arctic aerosol sulfate and nitrate concentrations measured at six Arctic surface stations including Alert, Utqiaġvik, Zeppelin, Gruvebadet, Thule and Villum (Figure 6.4). Similar patterns occur at all locations in the North American and European

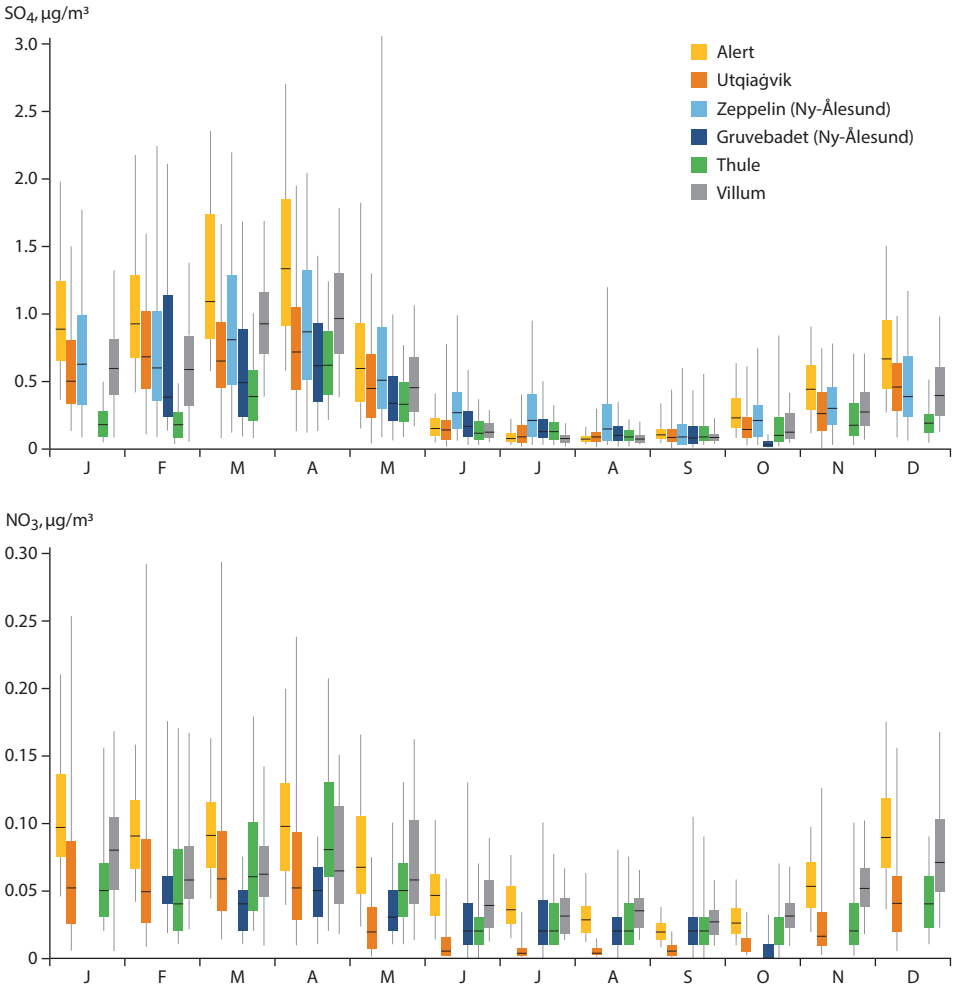

Figure 6.4. Seasonal variation in median aerosol sulfate (top) and nitrate (bottom) concentrations, over decadal or longer timescales, at: Alert (1980–2017); Utqiaġvik (1998–2012); in Ny-Ålesund at the two sites of Zeppelin (1997–2018; sulfate only) and Gruvebadet (2010–2019); Thule (2010–2018); and Villum (1991–2018) measurement stations. Sources: Data ref. 6.3; personal communication with principal investigators (PIs) of the stations.

Arctic: concentrations peak in April due to the build-up of Arctic haze, then decline and are at their minimum during the summer. The new observations emerging from the Siberian observatories also show a seasonality. Sulfate concentrations are 1–2 μg/m³ in summer, rising to 3–4 μg/m³ in winter at Tiksi (Popovicheva et al., 2019), and between 0.18±0.17 μg m^{-3} (summer) and 0.60±0.46 μg/m³ (winter) at the more remote station of Ice Base Cape Baranova (Manousakas et al., 2020). The difference in sulfate levels between the two Siberian sites points to concentration gradients in this sector of the Arctic that still need to be fully elucidated.

Aerosol nitrate median concentrations are highest at Alert and Villum followed by Thule, Gruvebadet, and Utiqiaġvik. At Utqiaġvik, concentrations of nitrate are smallest in summer, while sulfate concentrations are comparable to the other sites. Aerosol sulfate median concentrations are highest at Alert, Zeppelin and Villum, followed by Utqiaġvik and Gruvebadet, and lowest at Thule.

Few studies have estimated the contribution of different sulfate sources. At Ny-Ålesund (Zeppelin and Gruvebadet observatories), anthropogenic sources predominate during winter and spring. Crustal, sea-salt, biogenic and anthropogenic sources account for 3.3%, 12.0%, 11.5% and 74.8%, respectively (Udisti et al., 2016). In summer, the biogenic sulfate fraction extends up to 70%, becoming dominant as the anthropogenic component declines at various locations in the Arctic (Norman et al., 1999). New observations at Ice Base Cape Baranova also show that, in the Siberian Arctic, sulfate concentrations are affected by anthropogenic sources in the cold seasons and by natural sources in the warm ones (Manousakas et al., 2020). During July 2014, results from a research cruise in the Canadian Arctic Archipelago of the Arctic Ocean showed 70% of fine aerosol sulfate (<0.49 μm) and 86% of SO_2 were from biogenic sources (Ghahremaninezhad et al., 2016).

Fewer studies are published for particulate nitrate source-apportionment. While the anthropogenic sources are dominant, the source types are not explored. This is an important knowledge gap, because nitrate is one of the few aerosol components that has been clearly increasing over time in the Arctic region (see Table 6.2).

Organic aerosols (OAs) are characterized by their diverse sources, atmospheric transformation processes and composition. Such complexity means that current knowledge of the atmospheric lifecycle, sources and detailed composition of OAs in the Arctic is still very limited. Nevertheless, efforts to gather observations on the concentrations and properties of OAs have intensified significantly in recent years (Moschos, et al., 2022a; Moschos et al., 2022b). Organic compounds are thought to be important in several processes involving climate feedbacks on biogenic emissions to the atmosphere, potentially affecting the formation of new particles, cloud condensation nuclei (CCN) number and cloud formation (Abbatt et al., 2019; Boy et al., 2019; Petäjä et al., 2020; Beck et al., 2020). OAs are also associated with wildfire emissions and other anthropogenic sources, and can serve to trace BC emissions (Stohl, 2006).

The seasonal trends of organic carbon (OC) – in other words, the carbon contribution to OA – highlight the anthropogenic input during Arctic haze months (Figure 6.5). However, the summer

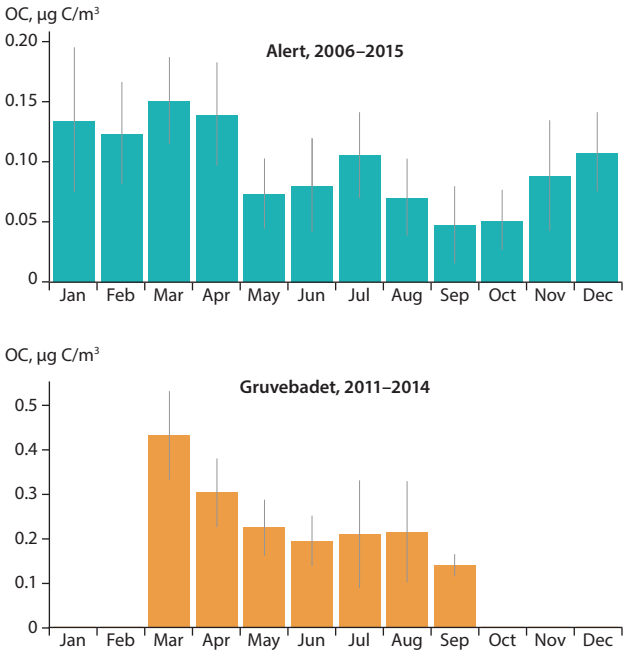

Figure 6.5. OC concentration monthly means from Alert and Gruvebadet (Ny-Ålesund). Data from Gruvebadet are not available for the dark season (Oct–Jan). Source: unpublished data from Lin Huang (Environment and Climate Change Canada) and Rita Traversi (University of Florence).

minimum is less deep than for BC (Figure 6.1). On the contrary, OC concentrations are sustained or even exhibit a second maximum in midsummer and decline to a minimum only in September (Moschos et al., 2022a). The measurements performed in the remote Siberian observatory of Ice Base Cape Baranova in 2015–2016 show a weak seasonality for OC, but generally exhibit higher concentration levels than in the western Arctic at around 800 ng/m³ throughout the year (Manousakas et al., 2020) compared to 100–400 ng/m³ at Gruvebadet and Alert (Figure 6.5). The contribution to OC provided in summertime by sources other than fossil-fuel combustion (either biomass burning or biogenic) is supported by recent studies conducted at Tiksi and Ice Base Cape Baranova on the basis of seasonal changes in the OC/EC ratios (Popovicheva et al., 2019; Manousakas et al., 2020) and, for Utqiaġvik, using OC $\Delta^{14}C$ fingerprints (Barrett and Sheesley, 2017). More stations have been investigated by Moschos et al. (2022a).

OC source-apportionment studies have highlighted the seasonal change of OA composition from the haze period – when the oxidation state of organic matter points to long-range transport, and organic markers are clearly of anthropogenic origin – to late spring and early summer season, when biogenic sources become dominant (Fu et al., 2016; Nielsen et al., 2019). The analysis of the seasonal cycles of MSA based on eight years of observations at Gruvebadet, Svalbard and Thule, Greenland (Becagli et al., 2019) suggest significant OA sources in the open ocean, as well as from the biota colonizing sea ice in the marginal ice zone (Mungall et al., 2018a; Dall'Osto et al., 2017, 2018). The source types contributing to the anthropogenic fraction of OC have been explored using isotopic and receptor modeling techniques. The application of probability source contribution functions (PSCFs), to identify pollution source areas for OAs sampled at Ice Base Cape Baranova, is an example of the latter. Results point to nearby industrial sources (including flaring)

and to forest fires and other anthropogenic emissions at the mid-latitudes in Eurasia (Manousakas et al., 2020). Further work has been undertaken using positive matrix factorization, but results were not available before publication of this report (Petäjä et al., 2020).

Further insights into the concentrations and origins of atmospheric aerosols can be gained by analyzing the physical and microphysical properties of aerosols, which have been measured in the Arctic since the late 1990s. Schmeisser et al. (2018) analyzed observations of annual mean scattering and absorption coefficients at six Arctic sites, and found a seasonality for all sites that was clearly related to variations in particle mass (the larger the particle, the greater its mass) and chemistry (see Section 5.2.1.1 for more details on optical properties).

From Zeppelin measurements (Tunved et al., 2013) noted a changing particle size distribution with seasons is clearly visible. During the Arctic haze period, relatively large submicrometer particles – 'accumulation mode', at >100 nm – dominated. However, during summer, much smaller particles– 'Aitken mode' at 20–100 nm were present in roughly equal concentration. In fall, the slow build-up of the accumulation-mode particles begins, with the concentration peaking in spring. The spring peak has long been identified as the Arctic haze period, caused by air pollution being transported over long distances, mainly from the Eurasian continent. The summer aerosol fraction has lately been hypothesized to be of natural origin, with the formation of new particles occurring at the regional scale in the atmosphere (see for example, Leaitch et al. [2018] for Alert).

For the period 2013–2015 Freud et al. (2017), Figure 6.6, found quite similar seasonality of aerosol size distribution for the other observatories around the Arctic. However, they noted some consistent differences between the sites that were beyond the year-to-year variability, caused by differences in proximity to anthropogenic source regions and the Arctic Ocean sea-ice edge. Exposure to free tropospheric air and precipitation patterns played an additional role. An important conclusion is that aerosol observations from a single Arctic site cannot fully represent the entire Arctic region.

Addressing the question of the natural Arctic aerosol sources, Dall'Osto et al. (2019) found six different types of size distributions related to natural sources and processes but only two linked

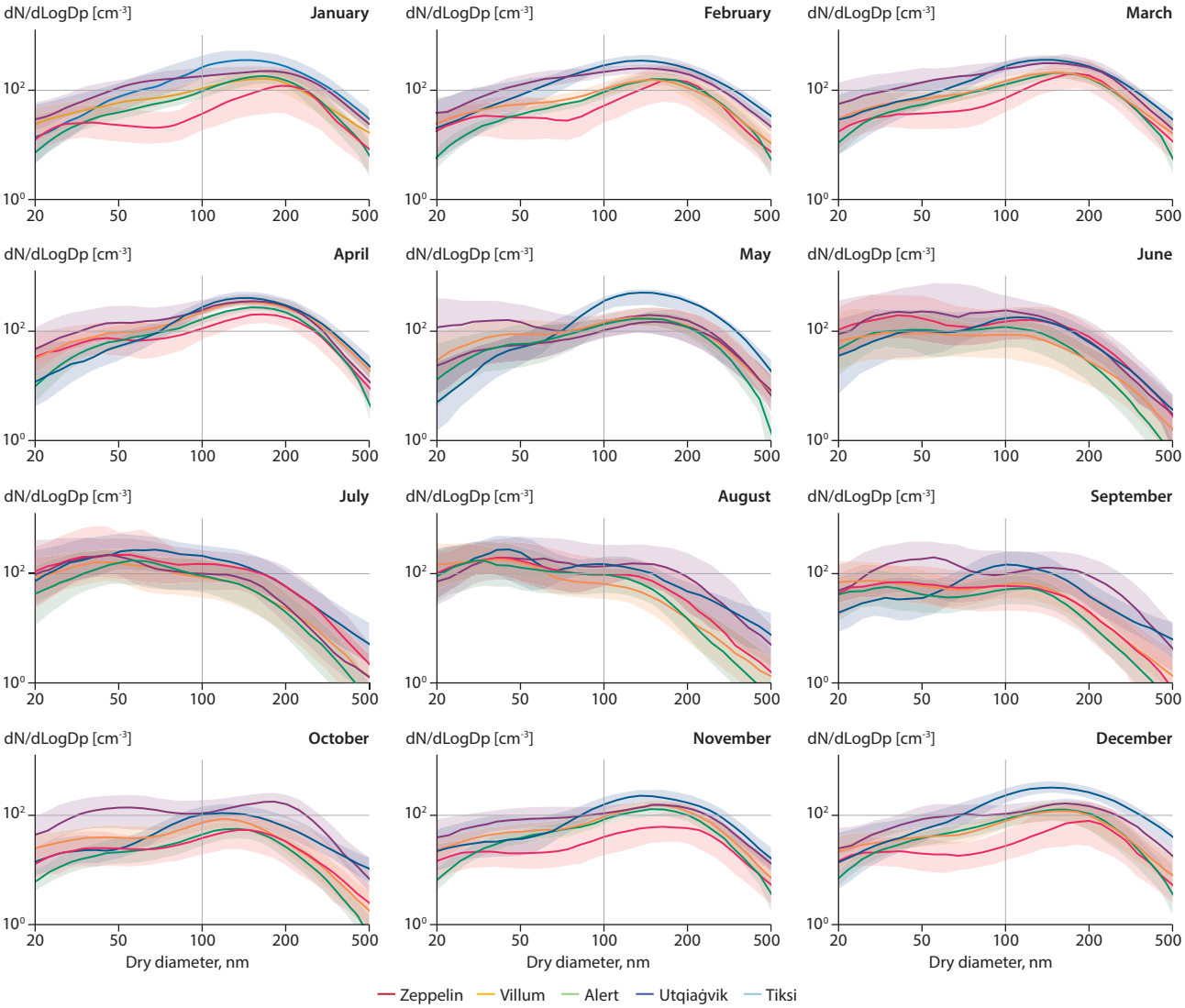

Figure 6.6. Monthly aerosol number size distributions (after Freud et al., 2017). Solid curves indicate median distributions calculated on a homogenized 29-bin size spectrum. The shaded areas denote the interquartile range. Data are from different years for each station from the period 2007–2015.

to anthropogenic sources. Natural particles dominate in the summer, with the anthropogenic contributions growing during the fall to dominate during the winter and spring.

Studying aerosol cloud interactions, Jung et al. (2018) presented five years of CCN number concentrations at different supersaturations for Zeppelin. A clear seasonal dependence was seen, which was different for low and high supersaturations (Figure 6.7). At low supersaturation, the Arctic haze period, with high concentrations of accumulation-mode, sulfate-rich particles, showed the highest number of CCN. At higher supersaturation, high summer concentrations of much smaller, mainly biogenic, particles exhibited similarly high CCN concentrations. Lange et al. (2019) concluded, from a similar study on the hygroscopic properties of aerosols, that particles from pollution transported long distances dominated the CCN in Arctic cloud formation during the winter, while natural particles dominated the CCN in summer (Figure 6.7). These studies demonstrate that it is feasible, with state-of-the-art methodologies, to apportion the sources of aerosol particles that act as CCN in the Arctic into anthropogenic and natural contributions. Extending this analysis to other geographical areas of the Arctic would greatly benefit our understanding of how human activity influences cloud-mediated aerosol impacts on climate in this part of the world.

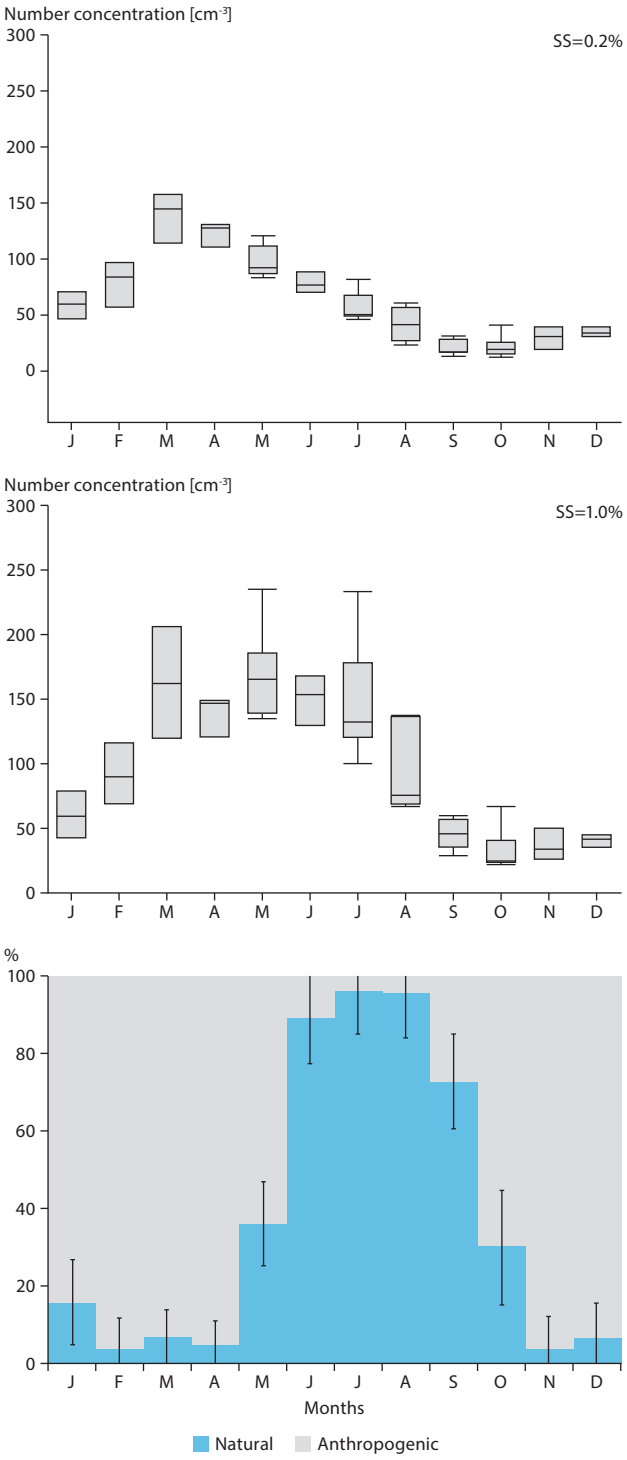

Figure 6.7. Top and middle: Box plot of monthly median CCN number concentration at 0.2% and 1.0% supersaturation (SS) for April 2007–March 2013, respectively, measured at the Zeppelin observatory in Ny-Ålesund (Jung et al., 2018). Bottom: Derived monthly contributions of natural and anthropogenic aerosol categories to total ambient CCN concentration at 0.4% supersaturation (Lange et al., 2019).

6.1.3.2 Vertical distribution

There are significantly fewer observations of the vertical profile of aerosol concentrations in the atmosphere than surface aerosol observations. The net aerosol radiative forcing strongly depends on the vertical distribution of aerosol concentrations and properties, which, in turn, is influenced by transport patterns and removal mechanisms that are also altitude dependent. The variability of aerosol vertical distribution means that this forcing differs throughout the atmospheric column (Stjern et al., 2019). As an example, the annual warming caused by BC extends from the surface (pressure above 800 hectopascals [hPa]), where it is more pronounced, up to the upper troposphere (pressure below 200 hPa), where it is less pronounced. However, the extent of the BC forcing also depends on the season, with warming along the atmospheric column dominant in summer and a combination of surface warming and upper tropospheric cooling in winter (Stjern et al., 2019). It is thus important to understand the processes controlling the distribution of aerosols in the Arctic along the atmospheric column. Also, vertical changes on decadal scales have been observed, indicating a variable influence of emerging sources and transport patterns (Stone et al., 2014).

The vertical variability of aerosols in the atmosphere between the Arctic winter and summer is due to temperature stratification in winter, with pollution being layered as a result of particles from different sources being transported at different altitudes (with, for example, aerosols from wildfires and Asian dust being transported aloft) (Di Pierro et al., 2013; Tomasi et al., 2015; Shibata et al., 2018; Thomas et al., 2019b). Remote-sensing observations, both satellite and ground-based, indicate that the highest aerosol concentration in all sectors of the High Arctic (averaged over a year) is observed in the lowest kilometer of the atmosphere, while individual biomass-burning plumes aloft can also produce a strong but temporary signal (Devasthale et al., 2011; Tomasi et al., 2015; Shibata et al., 2018).

During the Arctic haze period, BC concentrations tend to increase with altitude within the first kilometer (Ferrero et al., 2016; Markowicz et al., 2017), showing spatially well-defined pollution plumes arriving from mid latitudes (McNaughton et al., 2011; Schulz et al., 2019). These plumes, however, appear to have a significantly smaller horizontal and vertical extent than those measured during the first airborne campaigns

performed in the 1980s (Stone et al., 2014). It must be noted that improvements in BC measurements might significantly bias any comparison between recent and earlier observations. The correlation of BC with sulfate and OA strongly depends on altitude (Willis et al., 2019), and might indicate the altitudinal influence of source regions, with anthropogenic emissions being dominant below 2 km altitude and above 4 km, and episodic biomass-burning emissions at mid altitudes of 2–3 km (Marelle et al., 2015). Long-range transport from southeast Asia influences the mid and high troposphere preferentially, while transport from northern Asia (Siberia) affects lower altitudes. That from Europe and North America can influence both the lower and mid troposphere (Sharma et al., 2013; Liu et al., 2015; Xu et al., 2017). These studies report that BC was mostly emitted by anthropogenic sources in northern Asia (Siberia). Further studies indicate that open biomass burning also contributes significantly to the BC burden during spring (Stohl, A., 2006; Kondo et al., 2011b; Matsui et al., 2011), and that the injection of aerosols from biomass burning in the free troposphere can episodically lead to elevated BC concentrations at high altitudes (Roiger et al., 2015; Köllner et al., 2017; Sobhani et al., 2018). The mass concentration and particle number fraction of BC decreases abruptly within the troposphere from spring to summer (Schulz et al., 2019). This is caused by a combination of processes, including preferential wet scavenging of BC between source regions and the Arctic (Liu et al., 2015) – because BC is more hygroscopic during summer (Motos et al., 2020) – and inhibited transport from mid latitudes (Bozem et al., 2019). As a consequence, more local Arctic sources, both anthropogenic and natural, might control the summer BC population. Anthropogenic particle sources within the Arctic, such as shipping and oil-gas extraction, have been shown to enhance BC concentrations above the natural background level in the lowest layer of the atmosphere on local and regional scales (Stohl et al., 2013; Roiger et al., 2015; Ferrero et al., 2016; Law et al., 2017; Schmale et al., 2018a).

Mineral dust is a ubiquitous species of the Arctic aerosol population that is observed from the lowest to the highest layers of the troposphere. In spring, the mass concentration of mineral dust tends to increase with altitude, contributing more than 80% to the total aerosol mass concentration above 4 km altitude in the Western Arctic (McNaughton et al., 2011). A similar vertical increase is reported for the winter season in the Svalbard region (Di Biagio et al., 2018). This is mostly caused by the efficient high-altitude transport of mid-latitude desert dust suspended above Africa and Asia (Groot Zwaaftink et al., 2016). In addition to long-range transport, Arctic and sub-Arctic dust sources, such as glacial and volcanic sediments, have become more important sources of emissions in recent years (Crusius et al., 2011; Bullard et al., 2016; Groot Zwaaftink et al., 2016). Iceland represents one of the major sources of high-latitude dust, due to its geographic location and extensive desert surface (Blechschmidt et al., 2012). Icelandic dust that is injected in the free troposphere during volcanic eruptions can control the aerosol number concentration in the lowest kilometer of the atmosphere at local and regional scales (Blechschmidt et al., 2012; Groot Zwaaftink et al., 2016, 2017). Although volcanic emissions can contribute substantially to atmospheric dust loading, direct volcanic emissions are most often not included in studies of high-latitude dust, unless volcanic sediments are deposited and subsequently resuspended. Icelandic winter dust storms can lead to dust concentrations similar to Saharan conditions (Dagsson-Waldhauserova et al., 2019). However, the largest dust particles, and thus most of the mass, remain in the lowest atmospheric layer. The episodic occurrence of rain or snow can drastically change the concentration and vertical distribution of aerosols generated by dust storms (Dagsson-Waldhauserova et al., 2019). Icelandic dust can, nevertheless, be transported over long distances within the Atlantic Arctic sector (Groot Zwaaftink et al., 2017) and has been observed in the lowest kilometer of the atmosphere over Svalbard (Moroni et al., 2018). While most research has focused on Icelandic dust, it is also known that the fine-grained glacial dust in Arctic river beds can be transported through the atmosphere – for example in Alaska (Crusius et al., 2011) – but little information is available on transport pathways and climate effects.

OA shows a strong vertical variability in both summer and spring. Results obtained from airborne observations in the Canadian Arctic during the NETCARE project showed that the concentration of OA increases with altitude in spring, with the mass fraction of OA rising from approximately 20% at the surface to 40% in the high polar dome (265–280 Kelvin [K] potential temperature) (Willis et al., 2019). In that particular case, the correlation of OA with BC also increased with altitude, indicating combustion as a source of high-altitude OA in spring. Previous studies focusing on the transport of long-range pollution towards Greenland in summer highlighted the high vertical variability of OA concentrations, which was strongly driven by the emissions source type (Schmale et al., 2011). The stronger the biomass-burning influence in an air mass, the higher the fraction of OA, whereas anthropogenic sources were responsible for high-particulate sulfate fractions. Far from emissions sources, OA tends to exhibit similar characteristics, such as high oxygenation, which makes it hygroscopic and a useful CCN (Schmale et al., 2011). However, due to the high complexity, at it is not yet possible to ascribe the influence of source region, source type, chemical processing and wet removal or cloud processing during transport to vertical OA characteristics (Abbatt et al., 2019). Isolating the individual influence of such processes requires the systematic and collocated observation of trace gases, aerosol chemical and physical properties, and cloud microphysics. Although recent studies indicate that natural Arctic emissions represent an important contribution to the surface OA population in summer (Collins et al., 2017; Dall'Osto et al., 2017, 2018; Leaitch et al., 2018; Croft et al., 2019), little is known about the vertical distribution of these emissions.

Remote sensing indicates that the vertical distribution of aerosol physical properties, such as particle diameters, changes drastically throughout the seasons (Shibata et al., 2018). In spring, strong variability is observed in the lowest kilometer, as a function of atmospheric stability (Ferrero et al., 2016). Aloft, the mean diameter of both total aerosol and BC slightly decreases with altitude (Shantz et al., 2014; Schulz et al., 2019). However, the episodic influence of biomass-burning plumes leads to a shift of size distribution to larger diameters at high altitude (Brock et al., 2011; Matsui et al., 2011; Moore et al., 2011; Quennehen et al., 2012), while bimodal biomass-burning aerosol has also been observed (Schmale et al., 2011). Bimodal

distributions are also reported for anthropogenic plumes, with some having enhanced Aitken-mode particles (Quennehen et al., 2012) and others a greater fraction of coarse particles (Matsui et al., 2011). Outside of pollution plumes, nucleation and small Aitken-mode particles can dominate the number size distribution (Schmale et al., 2011). In summer, the combination of particle formation and wet removal might be responsible for the increase in, and depletion of, ultrafine- and coarse-mode particles in the boundary layer, respectively (Kupiszewski et al., 2013; Burkart et al., 2017).

Although very limited in number, studies investigating the vertical distribution of CCN generally indicate that concentration increases with altitude in spring and early summer (Hegg et al., 1995; Yum and Hudson, 2001; Moore et al., 2011). The fraction of activated aerosol increases above 1 km altitude during the occurrence of both natural and anthropogenic pollution plumes (Moore et al., 2011), and fresh biomass-burning plumes (Lathem et al., 2013). In recent surface studies (Abbatt et al., 2019), mineral dust was found to be the major source, in springtime, of ice nucleating particles (INP) at Alert from plumes transported over long distances (Si et al., 2019). The major source of INP in the summertime within the marine boundary layer of the Canadian Arctic Archipelago was found to be local mineral dust (Irish et al., 2017) and the sea-surface microlayer when mineral dust concentrations were low (Irish et al., 2017, 2019). Recent studies in Svalbard further found that INP concentrations were significantly enhanced in summertime as a result of local dust emissions (Tobo et al., 2019).

Although Arctic aerosol of marine origin has been shown to be ice-nucleation active, the studies of the vertical distribution of Arctic INP are currently limited to a few airborne observations in Alaska and the central Arctic Ocean (unpublished), and do not allow for differentiation nor quantification of the impact of anthropogenic and natural sources (Rogers et al., 2001; Prenni et al., 2009; McFarquhar et al., 2011.

6.1.3.3 Observations of aerosol components in snow

The IPCC Special Report on the Ocean and Cryosphere in a Changing Climate (IPCC, 2019) highlighted the impact that the deposition of light-absorbing particles such as BC, water-insoluble OC (WiOC) and dust has on surface snow- and ice-melt rates. Measurements of light-absorbing particles in snowpack and ice are essential, as the interaction between the cryosphere and atmosphere is important for climate forcing (Flanner et al., 2007; Boy et al., 2019; IPCC, 2019) and can only be understood when relevant data is available from both domains. Estimating climate effects, such as the reduction of albedo and increase in surface melt rates, calls for model simulations (Chapter 7 of this report, Evangeliou et al., 2018; Meinander et al., 2013; Tuccella et al., 2021). Modeling often requires assumptions to be made regarding the characteristics of snow and ice, as well as cloud coverage, and further uncertainties derive from the high spatiotemporal variability in observed concentrations of BC and dust in the Arctic cryosphere (Flanner et al., 2007; Meinander et al., 2020a; Spolaor et al., 2017).

Measurements of the BC content in snow have been carried out at numerous Arctic and sub-Arctic sites since the 1980s. However, the variety of sampling protocols and techniques used (see Chapter 5), makes it difficult to create compilations and draw comparisons from these spatial data. Data gathered from regular or repeated (weekly to monthly) multi-year monitoring using consistent protocols have so far only been reported from Finland (Sodankylä 2009–13; Meinander et al., 2020a, 2020b) and from Svalbard (Ny-Ålesund area 2007–2018; Zdanowicz et al., 2021). These and other new observations of BC in snow that have been reported since the 2015 AMAP assessment are reported below.

The first systematic measurements of BC in fresh snow from the Canadian High Arctic were obtained at Alert in the winter of 2014–15 (Macdonald et al., 2017, 2018). The median refractory black carbon (rBC) concentration was 2.3 ng/g of snow (interquartile range: 1.3–4.1 ng/g) and the estimated daily median depositional flux in snow was 0.42 millimeter per square meter per day (mm/m^2/d). For the same winter, Rodríguez et al. (2020) reported EC concentrations in fresh snow of 6.2–32.9 μg/kg. Using carbon isotope source-apportionment methods (^{13}C, ^{14}C), they inferred that elemental carbon (EC) in snow was predominantly sourced from biomass-burning emissions (53%–88%).

In Arctic Alaska, seasonal variations in rBC concentrations in snow and rain were measured between 2013 and 2017. About 50% of annual wet deposition occurred in summer, indicating the importance of wet deposition to rBC emitted from biomass burning (Mori et al., 2020). Measurements of rBC in spring and/or summer surface snow were also reported from the Juneau Icefield, southeast Alaska (Nagorski et al., 2019) and from glaciers of the Alaska Range in south-central Alaska (Konya et al., 2021). On the Juneau Icefield, median rBC concentrations in snow ranged between 0.4–3.1 ng/g, with an overall median of 0.9 ng/g. On glaciers of the Alaska Range, concentrations in snow ranged from 1.5–5.3 ng/g, with an overall mean of 2.9 ng/g. The estimated median radiative forcing caused by rBC in surface snow on the Juneau Icefield was ~3 watts per square meter (W/m^2) in May, but underwent a >10-fold increase to ~40 W/m^2 in July, as ablation caused the rBC to accumulate on the snow surface (Nagorski et al., 2019). On glaciers of the Alaska Range, the reduction in snow albedo caused by rBC and other insoluble impurities was estimated at 0.004–0.007, the largest figure (for April) being equivalent to a positive surface radiative forcing of 1.5 W/m^2 (Konya et al., 2021).

In Greenland, much research effort since 2015 has focused on quantifying the impact of BC from biomass burning, particularly forest and tundra fires, on snow and ice albedo. With this aim, Polashenski et al. (2015) measured rBC concentrations in surface snow across parts of northwest Greenland in 2013 and 2014. They found that rBC concentrations ranged between 1.1–17.4 ng/g in summer 2012, and 2.8–43 ng/g in summer 2013. They estimated that these concentrations resulted in a mean reduction in surface albedo of 0.003. As this was too small to be detected by satellites, they concluded that spring or summertime deposition of BC (and dust) could not account for the recently observed declining trend in the summer albedo of the ice sheet. These data were also used by Thomas et al. (2017) to estimate rBC deposition from Canadian forest-fire emissions

over the northwestern Greenland ice sheet in the summer of 2013. Mass deposition rates during the event were calculated at between 250–1300 mm/m^2 over roughly a one-week period.

In Svalbard, Zdanowicz et al. (2021) synthesized data obtained from snow samples collected by the Norwegian Polar Institute in the Ny-Ålesund area between 2007–18, as well as from a survey carried out on glaciers across the archipelago in the spring of 2016. Overall, the median EC concentration in surface snow varied between 1.9–6.8 ng/g at remotes sites, but was slightly higher, at 9.8 ng/g, near Ny-Ålesund. Mass loadings of EC in the late winter snowpack calculated from samples taken from Svalbard glaciers in 2016 ranged between 0.1–2.6 mg/m^2. These figures were close to, or lower than, those found by Forsström et al. (2009, 2013) at many of the same sites between 2007–2009. Mass accumulation of EC in Svalbard snow was found to increase with elevation and snow accumulation, and dry deposition is believed to play only a minor role in net accumulation. The estimated area-averaged EC load across Svalbard was 1.1 mg/m^2 for the 2015–16 winter, and the monthly mean accumulation rate was ~0.1 mg/m^2 for the winter months (September–April). The associated radiative forcing was not determined.

Further south in Sodankylä, in Arctic Finland, a five-year record of weekly sampling and analysis of EC in surface snow was presented by Meinander et al. (2020a). The overall median EC concentration in snow was 25 ng/g; with this figure more than doubling from the winter accumulation season (median 21 ng/g) to the spring season (median 57 ng/g), largely due to the surface-concentration effect during snow melt.

Concentrations of eBC were measured (using an integrating sphere) in the spring snowpack on the Arctic Ocean between 2008–2013, in the region between Greenland, Ellesmere Island, and the North Pole (82°N–89°N, 0°W–100°W) (Doherty et al., 2015). The median mixing ratio of BC across all years was 4 ng/g, with the ratio varying between around 2–7 ng/g, with no identifiable temporal trend between these years.

Large-scale geographic patterns in the BC content of Arctic snow were presented by Zdanowicz et al. (2021; Figure 6.8) using EC data compiled from 2002–18, and by Mori et al. (2019) (Figure 6.9) using rBC data from 2012–16. The lowest concentrations of EC (limited to data measured by comparable protocols) were in central Greenland and the remote mountainous parts of the western North American

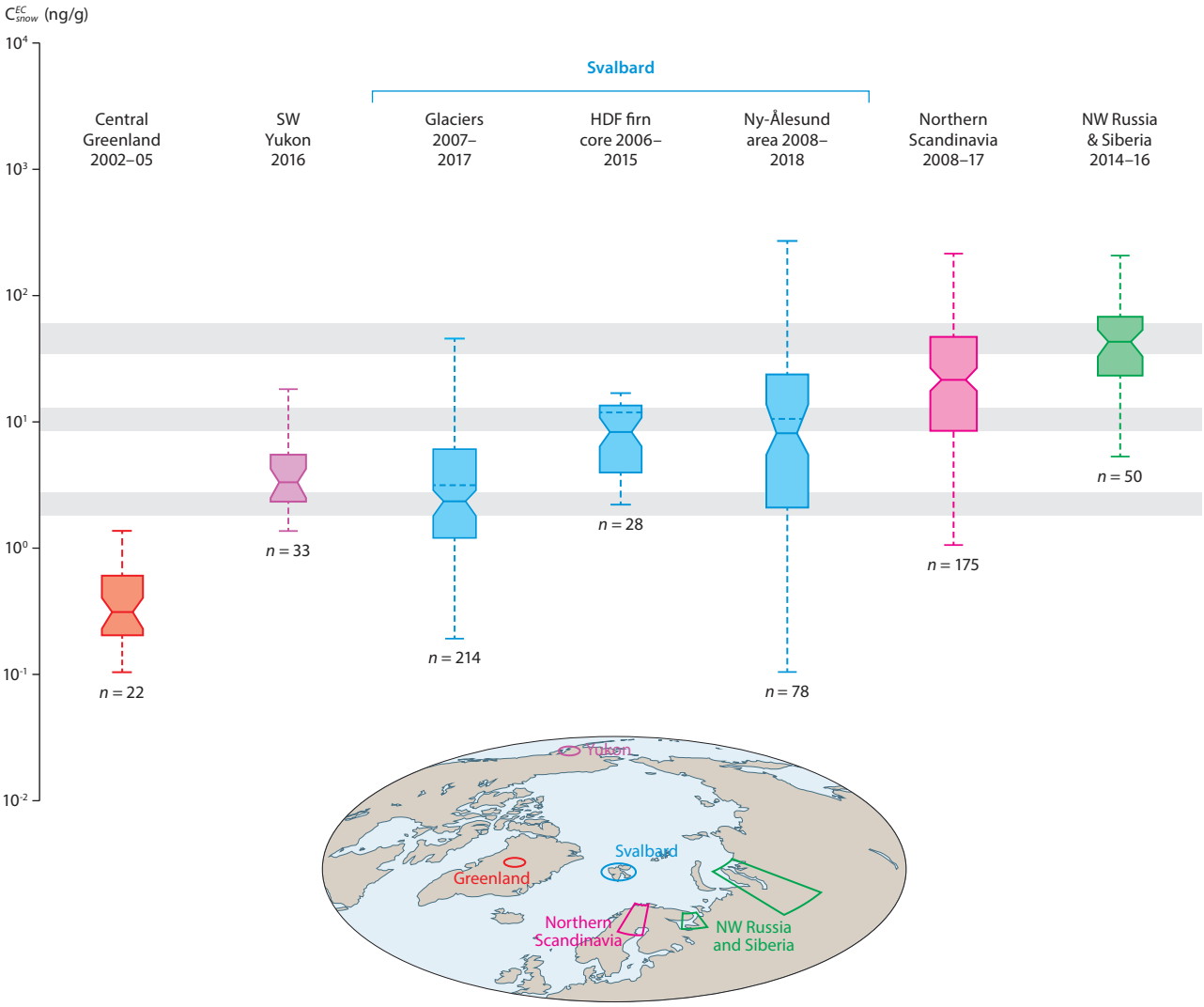

Figure 6.8. Comparison of EC concentrations in snow across different sectors of the Arctic, color-coded by region (adapted from Zdanowicz et al., 2021). Only data obtained by thermo-optical analysis using comparable protocols are included. Main data sources: Svalbard – Zdanowicz et al. (2021), Forsström et al. (2009, 2013), Ruppel et al. (2014); Greenland – Hagler et al. (2007); northern Scandinavia – Forsström et al. (2013), Meinander et al. (2013, 2020a), Svensson et al. (2013, 2018), Ingvander et al. (2013); Russia and Siberia – Evangeliou et al. (2018); and Yukon – Zdanowicz et al. (2021).

Figure 6.9. Comparison of median rBC mass concentrations in snow (C_{MBC}) across different sectors of the Arctic (from Figure 1 of Mori et al., 2019).

subarctic (Yukon). The highest concentrations were found in northern Scandinavia, western Russia and Siberia (Zdanowicz et al., 2021).

A broadly similar pattern has been observed for rBC, which Mori et al. (2019) attributed to latitudinal variations in BC source emissions fluxes, wet deposition, and the altitude of the study sites. In addition, due to the preferential wet removal of larger BC particles, the diameters of BC particles deposited in snow were found to reduce with growing distance from emissions sources. The EC and rBC concentrations in snow reported by Zdanowicz et al. (2021) and Mori et al. (2019) are within a factor of two, hence within the irreducible uncertainties arising from differences in the measurement techniques used. An earlier pan-Arctic survey of BC in snow that used yet another method (integrating-sandwich spectrophotometer) had found similar values for the North American Arctic, but higher concentrations for Svalbard and Greenland (Doherty et al., 2010, as discussed in AMAP, 2015a).

In terms of temporal variations, weekly-to-monthly sampling carried out near Ny-Ålesund by the Norwegian Polar Institute between 2011–18 showed no trends in EC concentrations in surface snow (Zdanowicz et al., 2021). Neither were any trends found in weekly measurements made between 2009–13 at Sodankylä (Meinander et al., 2020a).

Efforts to determine the concentration and radiative forcing of dust in snow, have increased in recent years (Boy et al., 2019; Dagsson-Waldhauserova and Meinander, 2019; Dagsson-Waldhauserova et al., 2015; Meinander et al., 2014; Peltoniemi et al., 2015). The components that have been measured include: optical properties of dust on snow (Peltoniemi et al., 2015; Zubko et al., 2019), chemical composition (Dordevic et al., 2019), and particle size and shape (Dragosics et al., 2016). In a modeling study, Kylling et al. (2018) estimated a surface radiative effect of 0.292 W/m^2 caused by dust deposition (largely transported from Asia) on Arctic snow. For comparison, this is approximately half of the BC central scenario estimated by Flanner et al. (2007). Influenced by temporal and spatial variability, light-absorbing dust particles can contribute to interannual fluctuations of the seasonal snow-melt rate (Painter et al., 2018); most often the particles increase melt but they can also insulate and decrease melt (Wittmann et al., 2017; Möller et al., 2016). Additionally, a reduction in the density of surface snow due to light-absorbing impurities has been documented (Meinander et al., 2014; Skiles and Painter, 2016). Understanding such reduction in snow density is important because it directly affects the amount of water the snow can hold. In addition to natural dust, dust in Arctic snow can originate from anthropogenic sources, such as from active mines (Khan et al., 2017).

The Greenland ice sheet has received special attention from researchers. According to Dumont et al. (2014), the observed decline of Greenland's albedo over the past decade has been attributed to the enhanced growth of snow grains resulting from atmospheric warming. However, Dumont et al.'s analysis of remote-sensing data indicated that the springtime darkening that has occurred since 2009 stemmed from a widespread increase in the amount of light-absorbing impurities in snow (as well as in the atmosphere). The researchers suggested that dust transported from snow-free areas of the Arctic that were experiencing earlier melt of seasonal snow as the climate warmed, may have contributed to the impurities. Newer studies from Polashenski et al. (2015) and Goelle and Boggild (2017), however, showed that long-range transport of BC or dust to the remote Greenland ice sheet is not an important factor in its melting.

Impact on snow/ice albedo and radiative forcing

Table 6.1 summarizes estimates, published since AMAP (2015a) of surface broadband albedo changes (Δα) and the associated instantaneous radiative forcing (IRF) caused by the deposition of BC or dust on snow in the Arctic or subarctic. Most studies included in this table used reported measurements of mass concentrations of BC and/or dust in snow to simulate albedo changes and estimate the IRF. An exception is the study by Kylling et al. (2018), which used modeled estimates of atmospheric dust deposition over the Arctic. Most studies used a radiative transfer model to estimate Δα caused by BC or dust (e.g., Flanner et al., 2007; Libois et al., 2013), but only a few also reported the corresponding IRF. Comparing and sythesizing results from these studies is challenging due to the lack of consistency in their methods, and in the range of parameters used in each. Where multiple results were reported, mean or median values of Δα are given for brevity.

For plausible BC concentrations, the estimated mean (or median) Δα ranges between ~16 x 10^{-4} and 87 x 10^{-4} in the central regions of the Arctic, including the Arctic Ocean (with or without snow). Such figures translate to albedo reductions that are typically less than 1% compared to clean snow or ice, and the estimated IRF, where reported, is <1 W/m^2. However, in many cases, the range of BC concentrations used to constrain such estimates was based on measurements made in late winter or early springtime snow, and may underestimate concentrations found in late spring or summer. Sectors of the circum-Arctic where larger Δα values (>100 x 10^{-4}) were estimated are presently limited to the margin of the Greenland ice sheet (during the ablation season; Goelles and Bøggild, 2017) and to subarctic mountain glaciers or icefields of Alaska (in late spring and summer; Nagorski et al., 2019). On balance, the studies compiled in Table 6.1 suggest that the radiative impact of BC deposition in snow over most of the Arctic presently remains very small, and is likely dwarfed by the IRF

Table 6.1 Estimates of albedo reduction and/or IRF due to BC and/or dust deposition on snow or ice, constrained by observations, and published since AMAP 2015. C_{BC}, C_{EC}, C_{dust} = range (median) of BC, EC or dust mass concentrations, respectively, used for albedo estimations; r_{eff} = effective optical radius of snow grains; r_{snow} = near-surface snow density; l = spectral range used in albedo estimations; Δα = albedo reduction (relative to fresh snow) caused by snow impurities; n.s. = not specified.

Region		Time period		Snow impurity content and texture			
				C_{BC} or C_{EC}	C_{dust}	r_{eff}	r_{snow}
		Year(s)	Month(s)	(ng/g)	(mg/L)	(μm)	(kg/m^3)
Arctic (undifferentiated)		2007–11	March	21–27	n.s.	100	n.s.
		2007–11	April	21–27	n.s.	1000	n.s.
		2007–11	Feb–Apr	5–137 (10)	n.s.	n.s.	n.s.
		2012	Jan–Dec	n.s.	n.s.	200	n.s.
Arctic Ocean	Sea-ice	2015	Apr–May	1.1–16.2 (5.9)	0.3–1.6 (1.6)	1000	350
	Snow on sea-ice	n.s.	spring	5–20	n.s.	55–650	250–450
	Snow on sea-ice	n.s.	n.s.	n.s.	0.1	n.s.	800
	Bare sea-ice	n.s.	n.s.	n.s.	0.1	n.s.	800
NW Greenland margin		2012–13	Apr–Aug	1.1–43	7.4–290	125	n.s.
		2009–16	n.s.	200	1	n.s.	variable
Alaska	Juneau Icefield	2016	May	0.4–3.1 (0.9)	0.2–34 (0.9)	250	300
	Juneau Icefield	2016	July	2.1–14.8 (5.1)	11–72 (25)	1250	550
	Alaska Range Glaciers	2017	April	1.5–5.3 (2.5)	0.4–1.2 (0.5)	250	360

Notes
*DISORT: Stamnes et al., (2000); TARTES: Libois et al., (2013); SNICAR: Flanner et al., (2007); G & S: Gardner and Sharp, (2010).

that arises from other factors, such as changes in snow-grain size and shape induced by temperature-induced snowpack ripening (e.g., Wang et al., 2020c).

6.1.3.4 Summary of concentrations, seasonal cycles and origin

The large body of literature that has emerged since AMAP (2015) contributes the following advances:

- Detailed intercomparisons of annual cycles between more observatories are now possible. Previously Utqiaġvik, Alert and Zeppelin mostly served this purpose; now Villum, Tiksi, Gruvebadet, Thule, Pallas, Summit and Ice Base Cape Baranova can also be included.
- Systematic annual-cycle studies for particle optical properties and size distributions across five or more observatories are now published, providing detailed information on aerosol sources and atmospheric processes. An analogue study for chemical composition has been published based on this report chapter (Schmale et al., 2022).
- With respect to the aerosol-cloud interactions, systematic measurements and analyses of CCN and INP are still missing, but first results are now available for individual stations.
- Much effort has been made to understand the concentration of light-absorbing particles, such as BC and mineral dust, deposited on snow. With regards to BC, an Arctic-wide gradient, with concentrations increasing from west to east, has become evident. It has also been demonstrated clearly that the smaller-scale spatial and seasonal variability of concentrations – and hence radiative effects – can be enormous. This highlights the need for systematic data acquisition for evaluating models and estimating climate effects. Recent data and modeling studies now also indicate mineral dust to be a natural short-lived climate forcer that should be taken into account.
- Measurements of the composition and microphysical properties of vertically distributed aerosols have increased in number but remain non-systematic, making it very difficult to extract information from the available data that is relevant beyond case studies.

6.1.4 Present-day and historical trends

6.1.4.1 Present-day trends

This assessment identified present-day trends based on measurements recorded over the past few decades at surface observatories (see also Schmale et al., 2022). Seasons were separated into the haze season from January to April, and the summer season from June to September. A seasonal trend

Albedo estimation		Albedo reduction			Inst. Radiative Forcing			Reference
Model or method*	λ	Mean or Median $\Delta\alpha$ (x 10^{-4})			Mean or Median IRF (W/m^2)			
	(μm)	BC	Dust	BC + Dust	BC	Dust	BC + Dust	
DISORT	0.20–4.00	45	n.s.	n.s.	0.06	n.s.	n.s.	Dang et al. (2017)
DISORT	0.20–4.00	87	n.s.	n.s.	0.5	n.s.	n.s.	Dang et al. (2017)
Observed	0.20–4.00	40	n.s.	n.s.	n.s.	n.s.	n.s.	Pedersen et al. (2015)
SNICAR	0.30–5.00	n.s.	n.s.	n.s.	n.s.	0.292	n.s.	Kylling et al. (2018)
SNICAR	0.38–0.78	n.s.	n.s.	26	n.s.	n.s.	n.s.	Dou et al. (2017)
TARTES	0.45–0.75	40	n.s.	n.s.	0.5	n.s.	n.s.	Donth et al. (2020)
DISORT	0.35–0.80	n.s.	7	n.s.	n.s.	n.s.	n.s.	Lamare et al. (2016)
DISORT	0.35–0.80	n.s.	18	n.s.	n.s.	n.s.	n.s.	Lamare et al. (2016)
SNICAR	0.20–5.00	16	9	31	n.s.	n.s.	n.s.	Polashenski et al. (2015)
G & S	0.20–4.00	400	190	590	n.s.	n.s.	n.s.	Goelles and Bøggild (2017)
SNICAR	0.35–2.50	30	40	50	2.83	4.05	4.47	Nagorski et al. (2019)
SNICAR	0.35–2.50	360	780	800	39.73	85.08	87.67	Nagorski et al. (2019)
SNICAR	0.20–5.00	30	n.s.	60	n.s.	n.s.	1.5	Konya et al. (2021)

line was obtained by applying a kernel-smoothing technique (Table 6.2), which involved running a median-smoothing function with a uniform weighted kernel of 1. This method is suitable for aerosol data that are log-normally distributed. The purpose of using this method was to obtain changes in the first and last five years of seasonal data timeseries for all locations, to track effects on concentrations caused by changes in emissions.

Long-term timeseries of eBC were available for the following observatories: Utqiaġvik, Alert, Kevo, Zeppelin and Gruvebadet. Data from Tiksi were also plotted, to show variability between measurements at an eastern Arctic location and western stations from 2014 onwards (Figure 6.10). The first four stations listed above exhibit a decline in eBC concentrations over the past decades, mainly due to the fall in emissions in the source regions, specifically Eurasia. The most evident changes shown in Table 6.2 were determined at Alert, with 110 ng/m^3 difference over 28 years (-52%, Sharma et al., 2019) and at Kevo, with 188 ng/m^3 difference over 47 years (-72%), both during the haze season (January–April). The eBC measurements at Kevo since 1964 are the longest measurements and generally with the highest concentrations among all locations in the western Arctic (note the different scale in the figure). The higher concentrations of eBC seen during the mid 1960s – with a median value of 300 ng/m^3 – were due to

Table 6.2. Change in all measurements between the first and last five years of running median-smoothed values. All values are significant to p<0.01 (the p-value being a statistical metric for significance) and some changes are non-significant (denoted by NS and grey shading). Coloured shading represents when the most significant decadal change occurred in each variable: green (1980–1990); red (1990–2000); light pink (2000–2010); blue (2010–2020). Single scattering albedo (SSA) is given in absolute change (relative change in %). The significance test was done by using the Student-t-test with a two-tail method with unequal variance.

Station	eBC	Sulfate	Nitrate	MSA	Absorption	Scattering	SSA
Alert	(1990–2017)	(1980–2017)	(1980–2017)	(1980–2017)	(2005–2018)	(2005–2018)	(2005–2018)
82.5°N,62.3°W, 250 MASL							
Jan–April	-54%	-50%	+26%	+3%	-27%	-15%	0.02(+2.1%)
June–Sept	-35%	-12%	+53%	-8%	-1%(NS)	+25%	0.016(+1.8%)
Utqiaġvik	(1991–2019)	(1998–2013)	(1998–2013)	(1998–2013)	(1998–2019)	(1995–2019)	(1998–2019)
71.2°N,156.8°W, 12 MASL							
Jan–April	-43%	-37%	+18%	-13%	-38%	-2.1%	0.01(+1.1%)
June–Sept	-40%	+18%	+48%	-21%	-22%	+12%	0.004(+0.5%)NS
Zeppelin	(2002–2017)	(1993–2018)		(1991–2004)	(2001–2017)	(1999–2017)	(2001–2017)
78.9°N, 11.8°E, 474 MASL							
Jan–April	-35%	-53%	-	-2%(NS)	-37%	+1%(NS)	+0.3%
June–Sept	+1%	+1%(NS)	-	-10%	-0.05 (NS)	+62%	+1.8%
Gruvebadet	(2010–2018)	(2010–2018)	(2010–2018)	(2010–2018)			
78.9°N, 11.8°E, 61 MASL							
Jan–April	-33%	-17%	-17%	+64%	-	-	-
June–Sept	-42%	+27%	+30%	+8%(NS)	-	-	-
Tiksi	(2010–2018)				(2010–2018)		
71.6°N, 156.6°W, 11 MASL							
Jan–April	+11%	-	-	-	+10%(NS)	-	-
June–Sept	-13%	-	-	-	-16%	-	-
Pallas						(2000–2018)	
67.9°N, 24.1°E, 565 MASL							
Jan–April	-	-	-	-	-	+2%	-
June–Sept	-	-	-	-	-	+14%	-
Kevo	(1965–2010)						
69.7°N, 27°E, 120 MASL							
Jan–April	-73%	-	-	-	-	-	-
June–Sept	-83%	-	-	-	-	-	-
Villum		(1990–2017)	(1990–2017)				
81.3°N, 16.4°W, 30 MASL							
Jan–April	-	-43%	+6%(NS)	-	-	-	-
June–Sept	-	-30%	+45%	-	-	-	-
Thule		(2010–2019)	(2010–2019)	(2010–2019)			
76.5°N, 68.7°W, 59 MASL							
Jan–April	-	-26%	-33%	-45%	-	-	-
June–Sept	-	+38%	-38%	-12%	-	-	-
Summit					(2012–2018)	(2012–2018)	(2012–2018)
72°N, 38°W, 3200 MASL							
Jan–April	-	-	-	-	-3%(NS)	+4.5%(NS)	-0.002(-0.2%)
June–Sept	-	-	-	-	-26%	+28%	+0.0009(+0.1%) (NS)

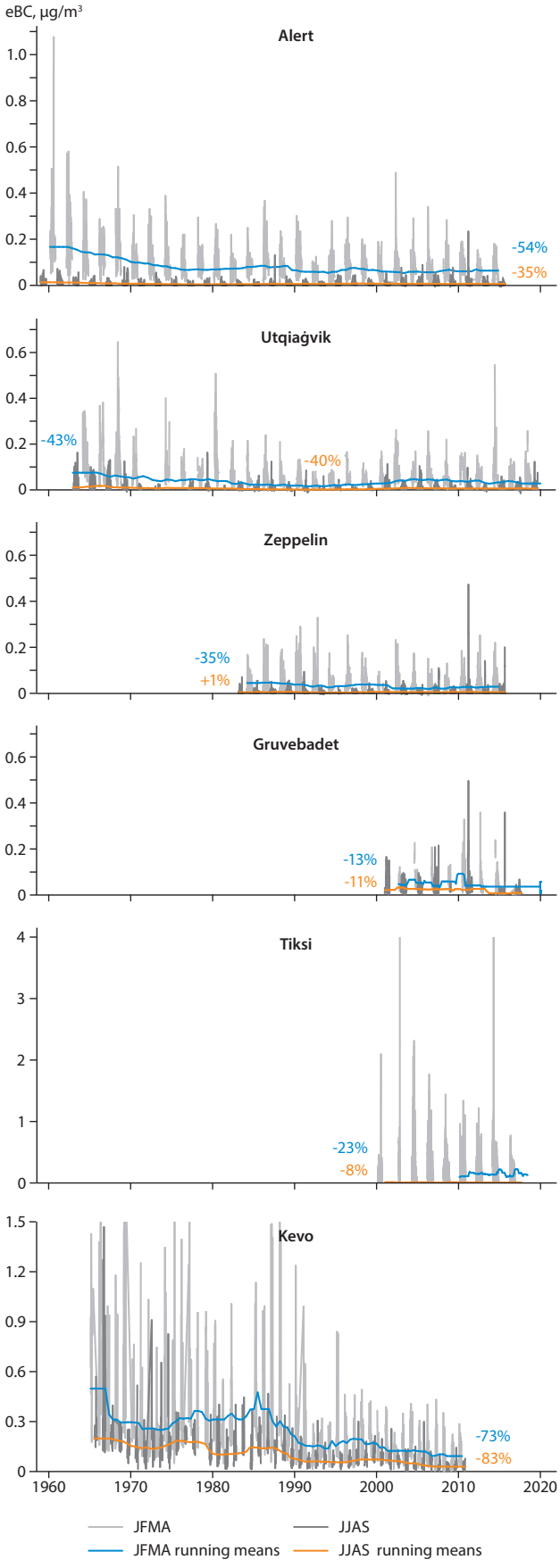

Figure 6.10. Long-term measurements of eBC at various Arctic locations. The blue (January–April) and orange (June–September) lines were obtained by taking the running median of the data, with the percentage change being the difference between first and last five years of the median values. Data sources: EBAS Kevo data – Dutkiewicz et al., 2014; Tiksi – Andrews, personal communication, 2020; Zeppelin – Eleftheriadis, personal communication, 2020.

wood burning for domestic heating. Concentrations decrease sharply from 1970–1980 due to the cessation of this practice, and thereafter a systematic decline in the BC concentrations occurs until 2010, with a median concentration of 112 ng/m^3 (Dutkiewicz et al., 2014). Kevo is closer to the source regions than Alert, and is influenced more from southern Russia and the Kola Peninsula, regions of the Former Soviet Union (FSU) and Europe (Dutkiewicz et al., 2014). At Utqiaġvik, the decrease is about 39 ng/m^3 in 28 years (43%) for the same season. It must be noted, however, that from 2008 onwards, the eBC concentrations seemed to increase again, a unique observation for Utqiaġvik. Concentration levels are still much below the ones in the 1990s, but markedly higher than during the early 2000s. These observations are in line with more vigorous emissions reductions in the FSU and Europe in the early 90s in comparison to later in the 2000s. Summer concentrations (June–September) have decreased slightly at Utqiaġvik (12 ng/m^3 in 28 years).

The increase in BC emissions in Asia until 2010, which is due to increased economic development (Hoesly et al., 2018), does not influence the eBC levels at all surface sites due to its main influence being in the upper tropospheric layers. At Alert, no significant change in eBC levels during summer was observed. At Kevo, the decline was 271 ng/m^3 in 43 years (-83%).

Observations at Zeppelin show a decline of 10 ng/m^3 over 16 years (-35%) in eBC during the haze season between 2001 and 2017. Summer values do not show a significant change. The eBC concentrations are generally lower at Zeppelin compared to Utqiaġvik, Kevo and Alert. At Gruvebadet, 400 m below Zeppelin, the timeseries of eBC are short, starting in 2010, but trends were nonetheless calculated (-33 % in winter). In winter, the eBC concentrations are around 70 ng/m^3 while summer values are around 30 ng/m^3. Concentrations at Gruvebadet are higher compared to Zeppelin, with the site potentially representing more local influence (Gilardoni et al., 2019).

Tiksi is situated in the eastern Arctic, closer to pollution sources. At times, it measured the highest episodic eBC concentrations. There were short-term increases (less than 0.1% of the data) at this location, where hourly averaged values could be as high as 4 ng/m^3. More than 80% of the data measured below 250 ng/m^3. It is noteworthy that this station exhibited generally higher concentrations of eBC (note the different scale) and more pronounced seasonal differences. Spring and summer are also influenced by episodic forest fires. The January–April median curve measures 120–180 ng m^{-3}, respectively. Summer levels are a factor of ten lower than the January–April values, and similar to the summer haze levels at the other stations.

All measurement sites have a common temporal decade between 2010–2020, over which period it can be concluded that eBC levels have stagnated in the western part of the Arctic. Kevo also exhibits a levelling off of EC concentrations since 2000. Tiksi seems to have different characteristics to the other locations. Longer-term measurements at this location will shed more light on the reasons for this.

Long-term observations of dust events in the Arctic only exist for Iceland. Iceland is one of the dustiest locations in the world, with dust emitted all year round (Dagsson-Waldhauserova et al., 2014). Counts of dust days between 1949–2011, including mineral dust and volcanic ash, indicated that there were,

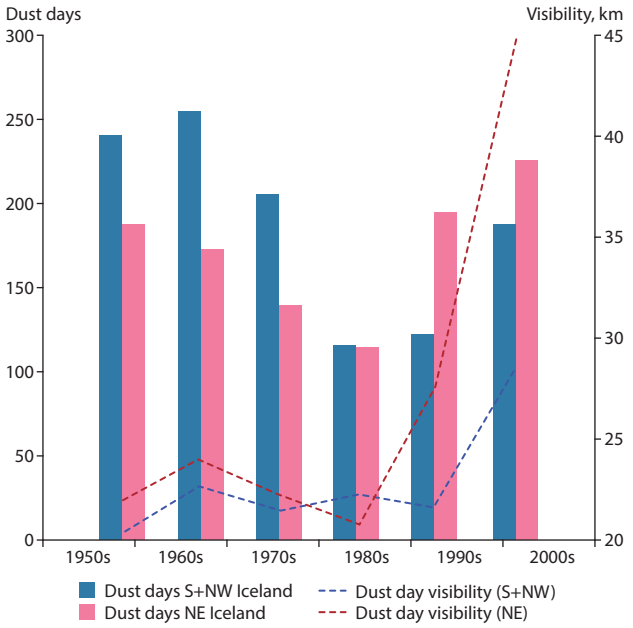

Figure 6.11. Icelandic data on dust events for 1949–2011. Total number of dust days, for all stations combined. Lines represent mean visibility at weather stations during dust events (adapted from Figure 2 of Dagsson-Waldhauserova et al., 2014).

on average, 135 dust days annually (Figure 6.11; Dagsson-Waldhauserova et al., 2014). The decades with the most frequent dust days were the 1960s for southern and northwestern Iceland, and the 2000s for northeast Iceland. A total of 32 severe dust storms (with visibility of less than 500 m) were observed over the study period, with the highest frequency of events during the 2000s in northeastern Iceland. While no decadal trend could be determined, dust events could be related to synoptic situations such as the position of the Icelandic low.

Particulate sulfate concentrations during the haze season at Alert (Figure 6.12 and Table 6.2) decreased steadily until the end of the 1990s, in line with North American and Eurasian emissions policies (Sharma et al., 2019). Since then, they have remained constant at 1.0 μg/m^3. Overall, particulate sulfate decreased by 50% between 1980–85 and 2012–2017. Other locations also show sulfate levels declining – by as much as 53% between 1993–1998 and 2008–13 at Zeppelin and by 43% between 1990–95 and 2013–2018 at Villum, with the greatest change occurring in the 2000s. A fall of 27% occurred between 1997–2002 and 2009–2014 at Utqiaġvik, and there were declines of around 18% at Gruvebadet and 26% at Thule over the shorter period between 2010–14 and 2014–2018 (both sites). The increase in sulfate in 2014 at Alert originated from a Holuhraun Fissure volcanic eruption in Iceland that started in September 2014 and lasted until May 2015. Having to assimilate the changes in chemistry at all locations over different sampling periods made it difficult to determine the spatial distribution. The only observation period that all locations have in common is 2010–2020, where spatial variability in sulfate remains constant at 0.3–1 μg/m^3.

Summertime sulfate values declined at Alert (-12%) and Villum (-30%) but increased at Utqiaġvik (+25%), Gruvebadet (+27%), Zeppelin (+1%) and Thule (+38%). Sulfate derives from natural and anthropogenic sources (see Chapter 5.2.2.1),

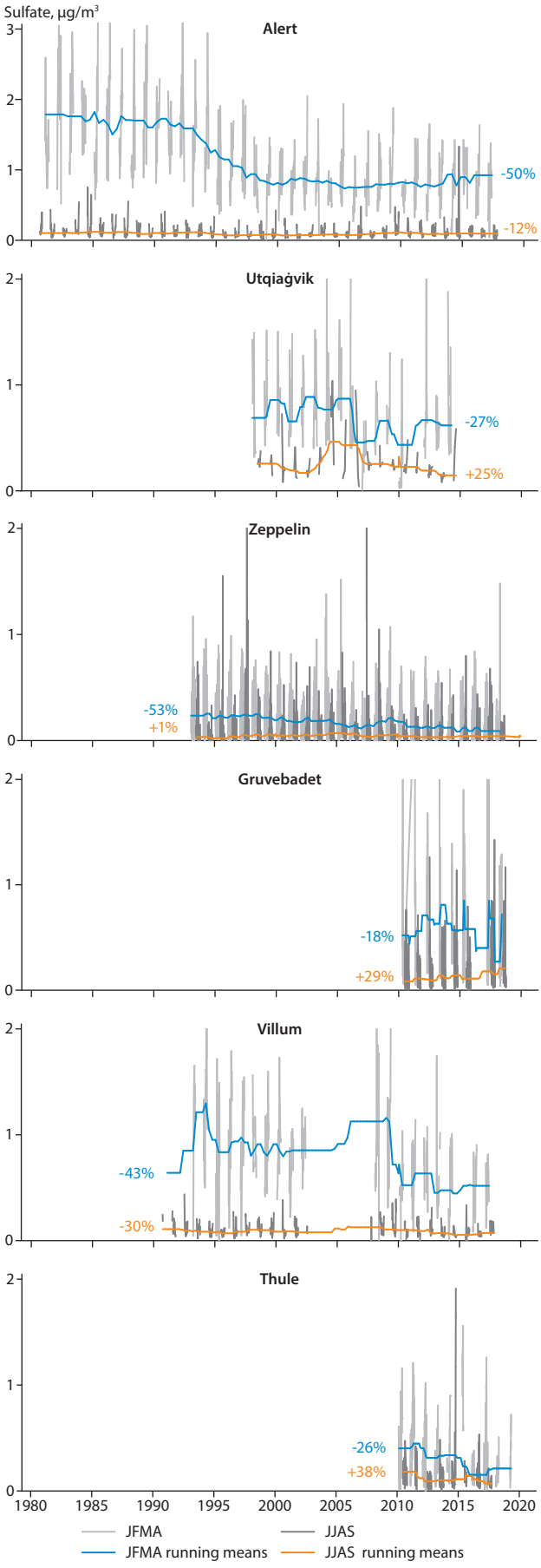

Figure 6.12. Long-term measurement of sulfate at various Arctic locations. The blue (January–April) and orange (June–September) lines were obtained by taking the running median of the data, with the percentage change being the difference between the first and last five years of the median values and statistically significant to p<0.001. Data source: Data ref. 6.3; personal communication with the PIs of the stations.

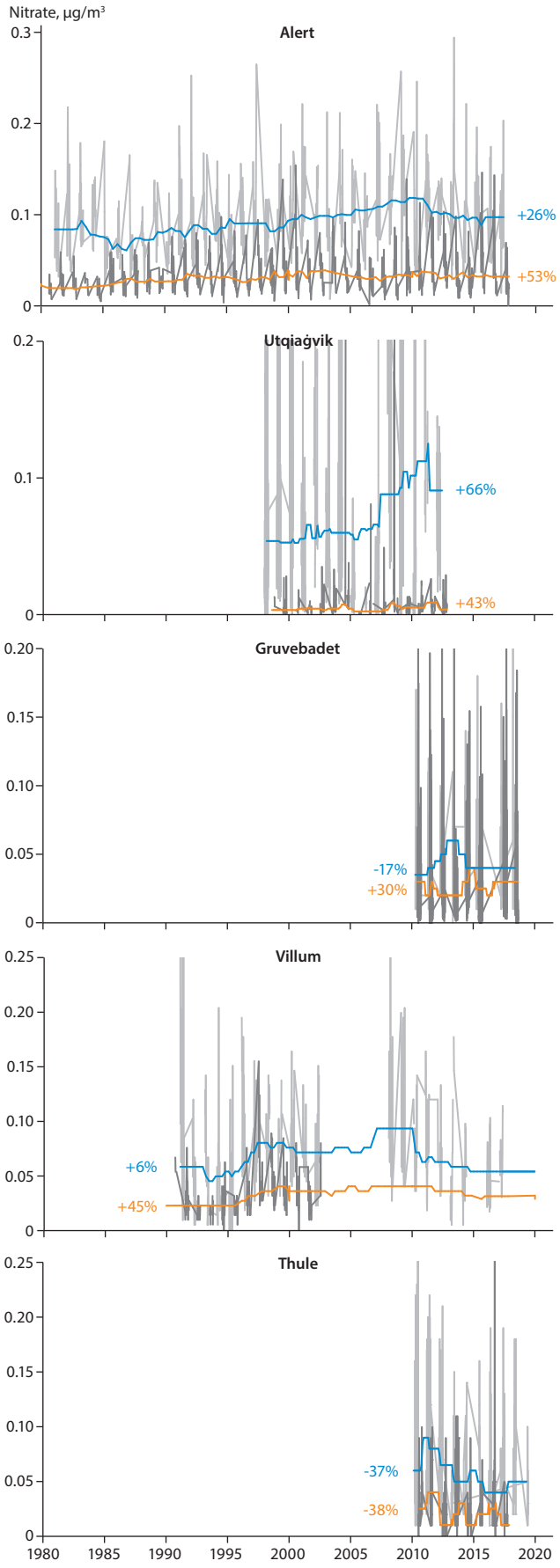

Figure 6.13. Long-term measurements of nitrate at various Arctic locations. The blue (January–April) and orange (June–September) lines were obtained by taking the running median of the data, with the percentage change being the difference between first and last five years of the median values. The difference was statistically significant to $p<0.01$. (Data sources: Data ref. 6.3; personal communication with the PIs of the stations).

and the summer increase could be due to enhanced marine emissions. Disentangling the effects of anthropogenic and natural emissions requires simultaneous measurements of specific tracer substances or isotopic analyses.

Particulate nitrate shows a positive trend, in contrast to that of sulfate and eBC at Alert, as shown in Figure 6.13. The change in the median values between the first five years and last five years are given in Table 6.2. There were changes in nitrate at Alert of +26% and Utqiaġvik of +66% during the haze season. These positive trends in nitrate were also measured during the summertime at all locations except for Thule. While emissions of nitrogen oxides have declined by 40% since the early 1980s in Eurasia, the higher particulate nitrate could be explained by decreasing aerosol acidity – with less particulate sulfate giving rise to enhanced partitioning of gaseous nitric acid into the particle phase (e.g. Sharma et al., 2019). This chemical process is widely observed over Europe and North America (e.g., Drugé et al., 2019). Also, during the cold season, nitrate partitions more readily into the particle phase than during the warmer season because of the volatility being temperature dependent. At Villum, while the overall trend since the 1990s was positive, nitrate levels began to decline slightly after 2010, from the higher early 2000s concentrations. The spatial variability of nitrate hovers around 0.05–0.1 µg/m³ during the common last decade among all sites.

The change in aerosol acidity, due to the decline in particulate sulfate concentrations, has had a significant influence on the neutralization capability of the Arctic atmosphere, potentially complicating the affects of aerosols on climate (e.g. Sharma et al., 2019). There has been a shift from sulfuric acid to the more neutral ammonium sulfate in particles, due to the decline in SO_2 emissions relative to ammonium emissions in the source regions (see Chapter 2).

The biogenic, organic aerosol MSA is an oxidation product of DMS released by the oceans during the algal growing season, usually April to August. Climatically, it is important because it changes the CCN population, which in turn can affect cloud albedo (Charlson et al., 1987). Interpreting long-term atmospheric concentrations of MSA, such as those shown in Figure 6.14, is difficult because of the complex relationships between production of the precursor gas and its emission to the atmosphere – which depend on microbial activity and ice cover (Sharma et al., 2012; Becagli et al., 2019) – and the atmospheric production of MSA and partitioning between the gas and particle phase.

The MSA data were separated into two algal blooming seasons: April–May, when MSA is is transported over longer distances to the sites due to the frozen sea surface nearby; and June–August, where local open water and closer vicinity to the marginal ice zone could be influential. Alert, Zeppelin and Utqiaġvik have longer timeseries, while Gruvebadet and Thule cover only the recent decade. Thule and Alert have a similar magnitude of MSA with median values of 0.01 µg/m³, while other locations show – at most – a median MSA concentration that is higher by a factor of five. Regarding individual sites, the trend lines for April–May at Alert and Gruvebadet are positive, with a change in the first and last five years of +3% over the 34-year timeseries and +64% ($p<0.01$) over the 10-year period. Negative

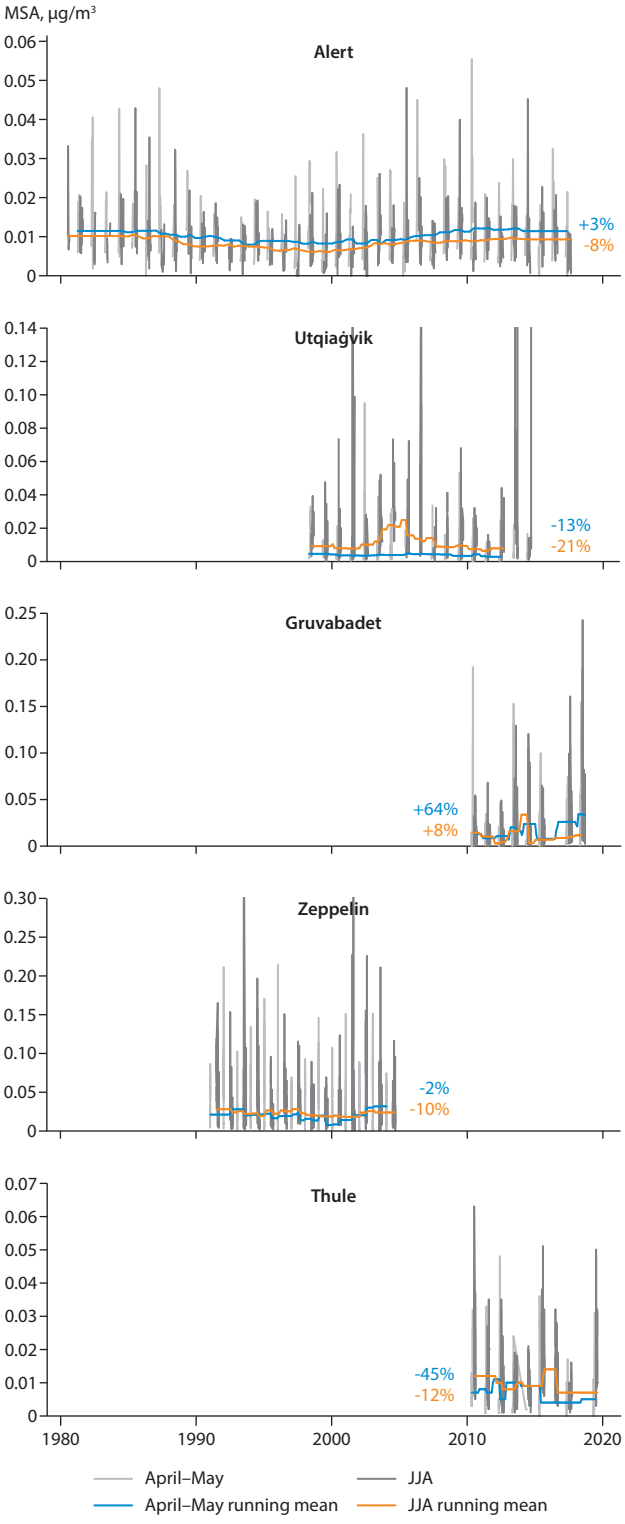

Figure 6.14. Long-term measurements of MSA at various Arctic locations. The blue (January–April) and orange (June–September) lines were obtained by taking the running median of the data, with the percentage change being the difference between the first and last five years of the median values and statistically significant to p<0.01. Data sources: Utqiaġvik – Data ref. 6.1; Zeppelin – Sharma et al., 2012; Gruvebadet and Thule – Becagli et al., 2019.

trends were observed at Utqiaġvik (-13%) and Thule (-45%), with no significant change at Zeppelin. Comparison among sites showed regional specificity of MSA measurements. The longest timeseries of MSA (1980–2017) at Alert overlaps with the 1990–2005 measurement period at Zeppelin; the change in MSA at Alert was insignificant, as was the case at Zeppelin. The common period of measurement at Alert and Utqiaġvik was 1998–2014, the change in MSA observed at Alert was +30% for this period compared to -13% for Utqiaġvik. Large spatial variability in MSA was observed for the last decade, with a change of -4% at Alert, +64% at Gruvebadet and -45% at Thule.

The summer season (June to August) showed declining trends across the various timeseries at Alert, Utqiaġvik, Thule and Zeppelin sites (-8%, -21%, -12% and -10%, respectively, with p <0.01). Sharma et al. (2012) showed that MSA values had increased at Alert, Utqiaġvik and Zeppelin stations since 2000. The periods were extended for the present analysis and the longer-term records at Alert still show higher MSA concentrations post 2000. For the available measurement time periods at Utqiaġvik and Zeppelin, an increase in MSA of 12% and 4%, respectively, were observed at Alert.The trends at Utqiaġvik and Zeppelin were difficult to assess: MSA levels at Utqiaġvik showed an initial increase but became more variable after 2004. Measurements at Zeppelin stopped in 2005 and can thus not be assessed for the more recent period. It is important to keep monitoring the trends in MSA over the coming years to identify emerging patterns and their underlying causes. The hypothesis that less ice cover allows for more microbial emissions to the atmosphere and could lead to increased aerosol MSA concentrations has already been proposed (Dall'Osto et al., 2017).

Since 2000, aerosol size-distribution measurements have been made at Zeppelin, providing a unique long-term record that can be used for trend analysis (Figure 6.15). It shows a clear decrease (-9% per year) of particles slightly larger than 100 nm (accumulation-mode), typical for an aged pollution aerosol found during the Arctic haze period. This reflects the significant decrease in sulfur emissions from Eurasian sources, and is consistent with the decrease in particulate sulfate concentrations as discussed above. A similar but smaller decrease for the same particle size is seen for the winter, also reflecting a decrease in emissions and haze burden. During the summer, an increase is observed in particles smaller than 50 nm (nucleation and Aitken-mode). This can be interpreted as an increase in new formation of natural particles, probably due to larger areas of open sea being available for the emission of precursor gases and particles (e.g., Dall'Osto et al., 2017).

Aerosol optical properties are relevant parameters that determine the radiative forcing of particulate matter. *In situ* ground-based measurements of the multidecadal timeseries of light absorption, aerosol scattering, and single scattering albedo (the ratio of light scattered to total light extinction) are presented here. The scattering values depend on the aerosol physical properties (particle size), chemical composition (sulfate, OC and others) and relative humidity, while absorption depends on the mass concentration of present absorbing components (BC, dust and other absorbing components) in the sample, as it is a filter-based measurement.

Twenty years of observations of aerosol scattering at Zeppelin and the Ångström exponent (a parameter used to provide information on aerosol size distribution) reveal an increase in scattering and a decrease in the Ångström exponent (Figure 6.16). The smaller the Ångström exponent, the more coarse particles contribute to the scattering. So, the observed trends show that more particles – particularly larger, probably

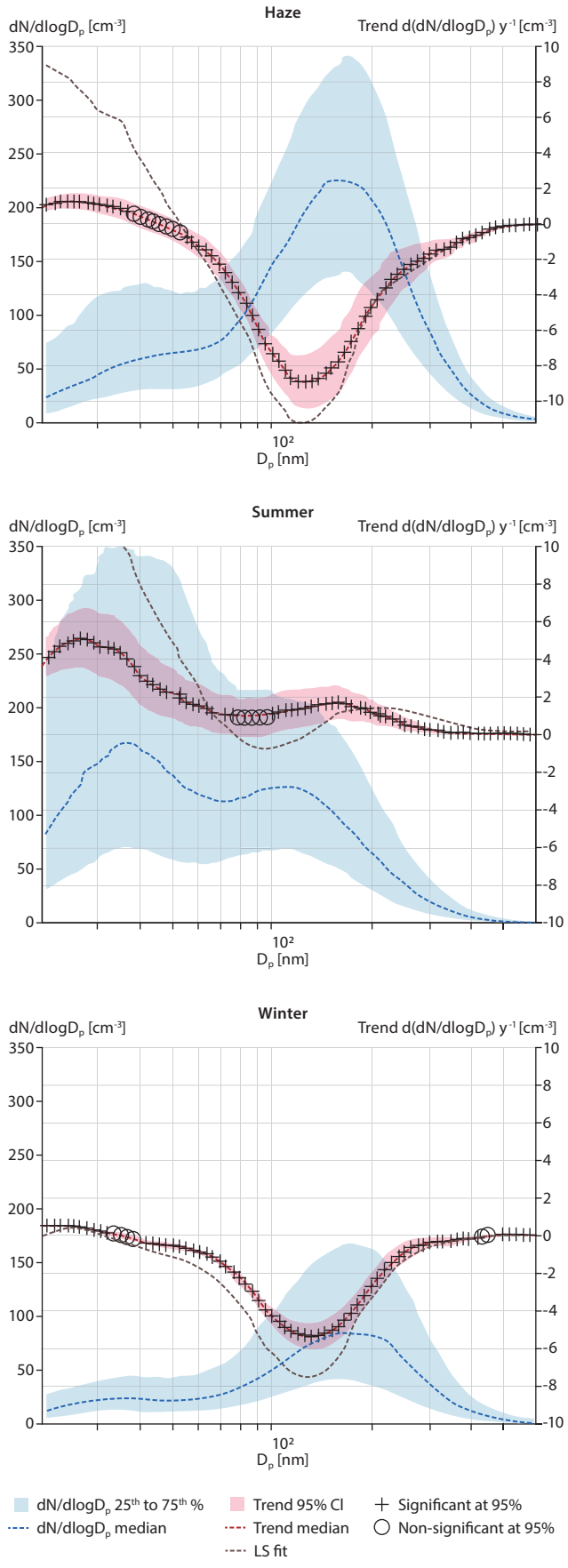

Figure 6.15. Analysis of the past 20 years of particle size-distribution data from Zeppelin (unpublished data by Peter Tunved, Stockholm University). Data were separated into the haze season, summer and winter. The blue dashed curves show the median size distribution, and the blue shaded area the interquartile range. The red dashed line indicates the median trend per size bin, and the red shaded area the trend confidence intervals at 95%. The grey dashed line is the least square fit to the trend data.

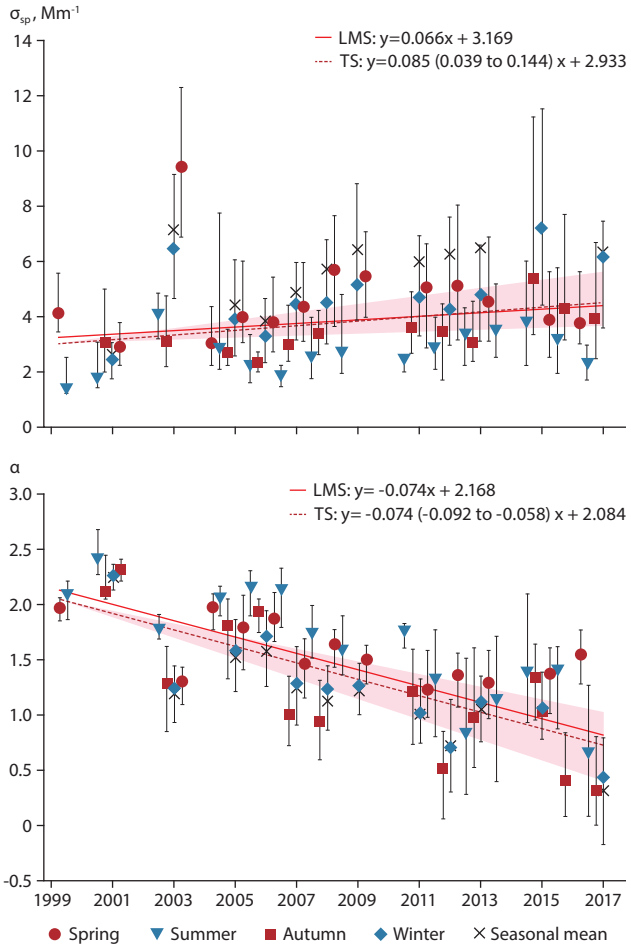

Figure 6.16 Long-term trends of the seasonal medians at Zeppelin for: (a) the particle light scattering coefficient (Mega-m^{-1}) at 550 nm; and (b) the scattering Ångström exponent (based on 450 nm and 550 nm). The seasonal medians are denoted by their respective symbols. The error bars denote the length of the 25th and 75th percentiles. The seasonal mean is marked by the crosses. The solid and dashed red lines represent the least mean square (LMS) and the Theil-Sen slope (TS) of the seasonal medians, respectively. The red shaded area denotes the associated 90% confidence interval of the TS slope. Seasons are defined as: winter = DJF, summer = JJA (Heslin-Rees et al., 2020).

super-micron ones – contribute to the scattering. Note, here results include super-micron particles but due to instrument limitation the results in Figure 6.15 only include particles up to 500 nm. Based on an air-mass trajectory analysis, Heslin-Rees et al. (2020) found a shift to higher windspeeds and more prevalent southwesterly winds. This is a possible explanation for the increase in super-micron particles, because air masses would pass over more open ocean, picking up more sea spray. The shift in air-mass trajectories is consistent with changing air-mass transport patterns into the Arctic due to climate change, as suggested by climate models (Krishnan et al., 2020).

At Utqiaġvik, Tiksi, and Alert, the scattering coefficients are higher during the Arctic haze season compared to summer, while at Pallas and Summit they are higher in summer compared to the haze period (Figure 6.17). Reasons for the increased scattering at Summit are unresolved; one hypothesis regarding Pallas is enhancement of the signal from increased secondary organic aerosol (SOA) production from the boreal forest due to warmer temperatures in recent years (Lihavainen et al., 2015).

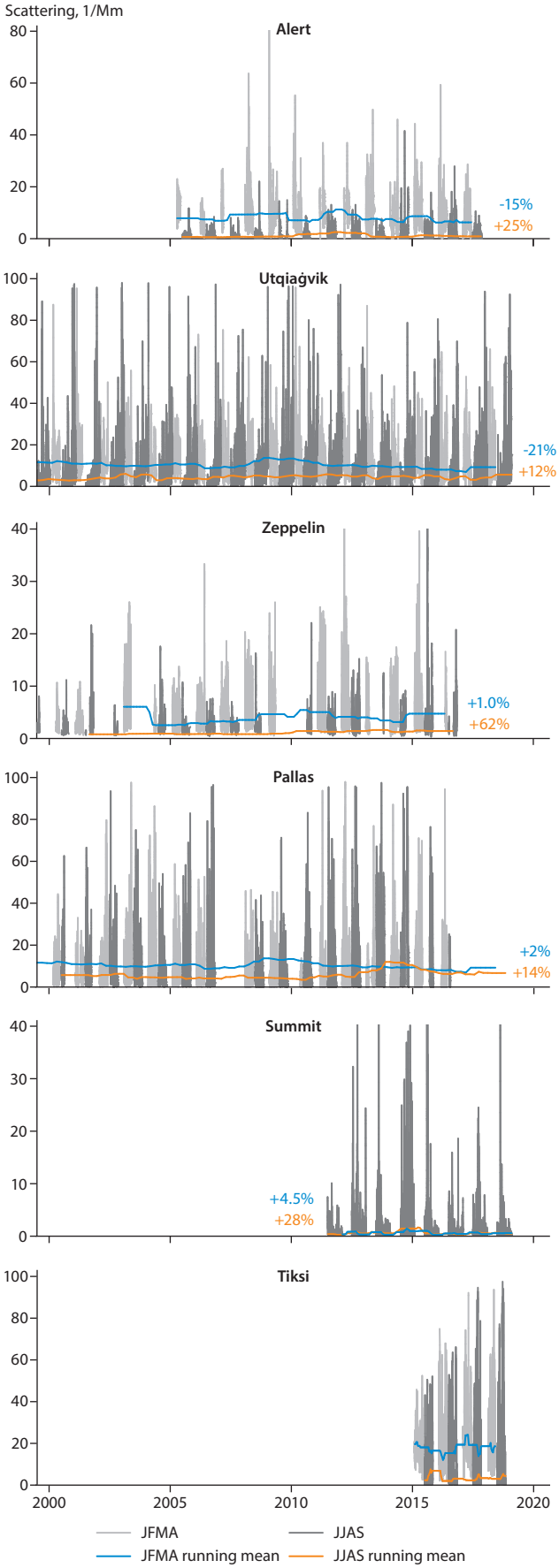

Figure 6.17. Long-term measurements of aerosol-scattering coefficients at 550 nm (measured at <50% relative humidity) at various Arctic locations. The blue (January–April) and orange (June–Sept) lines were obtained by taking the running median of the data, with the percentage change being the difference between first five and last five years of the median values, and statistically significant to p<0.01. Data sources: Data ref. 6.3; personal communication with the PIs of stations).

In the haze season, aerosol scattering shows decreasing trends at all locations except over the past decade at Pallas, where a minor +2% (p<0.01) trend is found, and Summit, where there is no significant trend (Table 6.2). Due to its high elevation (>3000 m), Summit represents the free troposphere in the cold season, which is different from all other stations. Hence different emissions sources and transport patterns likely apply there.

Positive (up to 57%) and statistically significant (p<0.01) changes are found for all the stations for summer between the first five and last five years. In relation to trends in sulfate, an aerosol-scattering component, the declining trends in scattering during the Arctic haze period may be supported more by declining trends in sulfate than in the size of the particles. Moreover, during the summer, concentrations of sulfate are an order of magnitude lower than those during the January–April period, and declining trends in sulfate do not reflect the increasing trends in scattering. An increase in particle diameters due to other natural scattering components might be influencing the size – and thus influencing the increasing trends in scattering – as speculated from results found at Zeppelin. Collaud Coen et al. (2020) analyzed trends in aerosol scattering measured across global stations, and showed that positive trends are in the minority. Hence, the positive trends observed for summer at all Arctic stations are an important exception to the global pattern. Note, although data is shown for Tiksi, trends were not calculated due to the short timeseries.

The absorption coefficients shown in Figure 6.18 reach a maximum during the haze season and a minimum in the summer at all stations except for Summit, where values are similar in both seasons. The analysis indicates that seasonal trends in absorption coefficients are decreasing, with changes between the first five and last five years negative during the haze season at all stations except for Tiksi, which shows a positive trend (+10%). During summer, absorption has decreased at all locations with the largest decline at Zeppelin station.

Using year-round data, Collaud Coen et al. (2020) showed that trends were positive for Alert between 0.002 and 0.02 Mm^{-1} per year. Globally, Alert was the only location with a statistically significant positive trend. This is somewhat contrary to the presented analysis for seasonal data, where a clear decrease of the absorption coefficient during the haze season is seen. This is in line with the emissions reductions discussed earlier. For year-round data at Tiksi, Collaud Coen et al. (2020) reported negative absorption trends of -0.08 Mm^{-1} per year, while in this AMAP analysis a positive trend for the haze period was observed.

Measurements of single scattering albedo (SSA) determine how absorbing an aerosol is with respect to its scattering components. A white aerosol has an SSA of 1, and this value decreases as the aerosol becomes darker and more absorptive. Figure 6.19 shows change in SSA between the first five years and the last five years of the timeseries, for the haze and summer periods. The aerosols are more absorptive during the Arctic haze period than in the summer at all locations. The decadal change over the haze period is positive at Utqiaġvik, Alert, and Zeppelin (0.01 [+1%], 0.02 [+2.1%], 0.025 [+3%], respectively) and only shows declining trends at Summit -0.002 (-0.2%), which is at an elevation of 3300 MASL. The decadal changes over the summer period are also increasing at all locations.

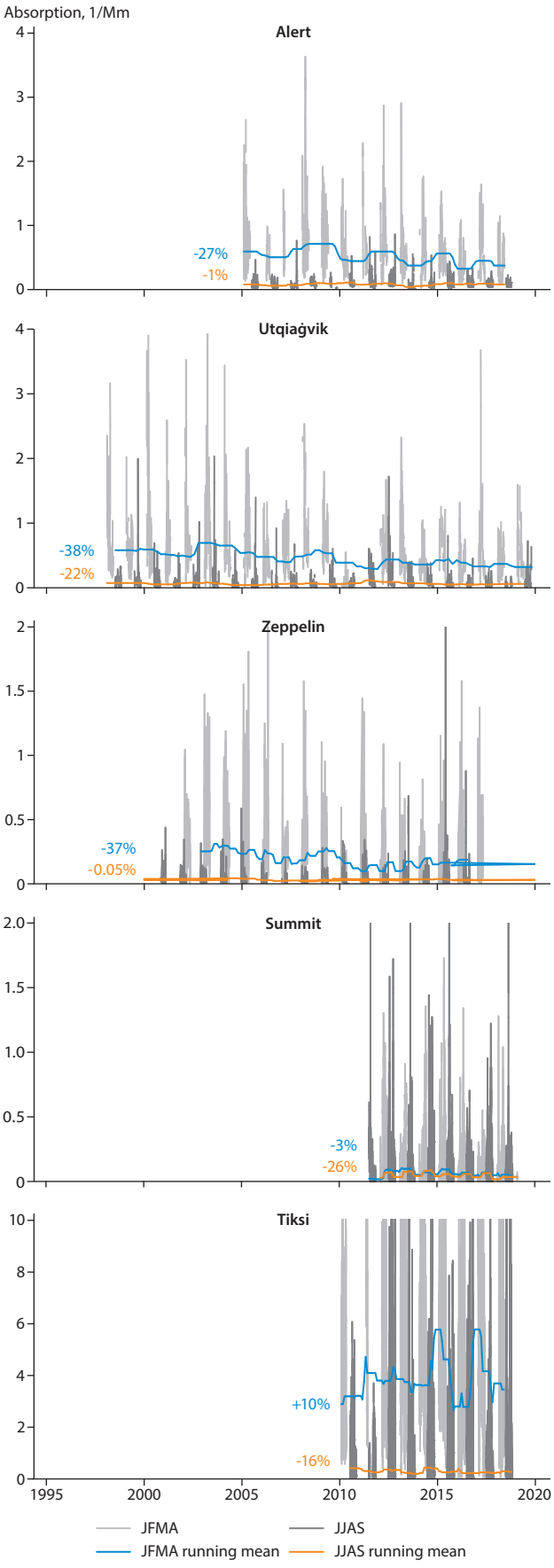

Figure 6.18. Long-term measurements of aerosol light absorption at 550 nm (measured at <50% relative humidity) at various Arctic locations. The blue (January–April) and orange (June–September) lines were obtained by taking the running median of the data, with the percentage change being the difference between first five and last five years of the median values, and statistically significant to p<0.01. All trends are significant to p<0.001. Data sources: Data ref. 6.3; personal communications with the PIs of the stations.

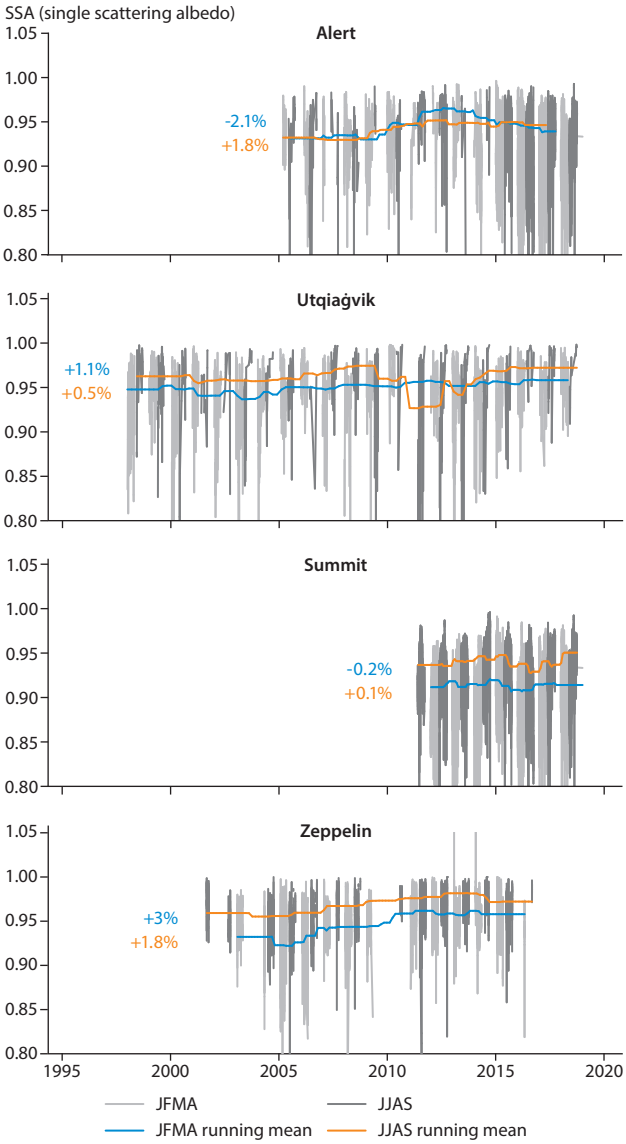

Figure 6.19. Long-term measurements of single scattering albedo at 550 nm at various Arctic locations. The blue (January–April) and red (June–September) lines were obtained by taking the running median of the data, with the percentage change being the difference between first five and last five years of the median values. All trends are found to be statistically significant to p<0.001 except for at Summit JJAS. Data sources: Data ref. 6.3; personal communications with the PIs of the stations.

This suggests that aerosols are becoming less absorptive at the four sites. In term of change in median concentrations across 34 years of aerosol chemistry (Sharma et al., 2019), all aerosol components have declined – especially eBC (absorption) and sulfate (scattering) at Alert and other locations as shown above – except for nitrate (NO_3) and seasalt (NaCl), which both exhibit increasing trends. This indicates that chemistry of Arctic aerosols might be changing with decreasing acidity and increased sea-salt concentrations (Sharma et al., 2019). This could consequently change the optical properties of the aerosol.

At Alert, the signal from the the Holuraun volcano eruption that occurred between September 2014 and May 2015 stands out. There is intra-annual variability in SSA at all locations; Zeppelin shows extremely high variability in the SSA between 2001 and 2016, with rather lower values between 2004 and 2006. Greater variability in SSA was also found during in both seasons since 2009 at Utqiaġvik, Alert and Zeppelin stations.

The discussion above focuses on surface-based trends. From measurements of vertically resolved aerosol properties, it is known that surface observations are not necessarily representative of the entire atmospheric column. Only a few studies have addressed the trends of aerosol properties integrated over the atmospheric column. Tomasi et al. (2012) and Stone et al. (2014) presented aerosol optical depth (AOD) trends over Utqiaġvik, Alert and Zeppelin between 2001 and 2012, finding that AOD increased at all locations. This is in line with the enhanced scattering found at all stations during summer and for some also during the haze season, discussed in this report.

6.1.4.2 Historical measurements from ice cores and sediments

Analysis of the concentration of aerosol chemical compounds in ice cores, as well as their deposition fluxes, provides insights into the historical evolution of the aerosol burden in the Arctic, and puts the present-day trends into a larger context. For example, detailed studies of year-by-year lead (Pb) concentrations in arrays of ice cores clearly show that mid-latitude anthropogenic emissions have contaminated large swathes of the Arctic for thousands of years, with lead pollution in Greenland and the Russian Arctic closely tracking historical events such as plagues, famines, and social unrest starting with Greek and Roman civilizations and extending to the present (McConnell et al., 2018, 2019). Arctic lead pollution increased 300-fold between the year 500 (the start of the Middle Ages) and the 1970s industrial peak. While levels have dropped by around 80% as a result of the Clean Air Act in the USA and similar legislation in other countries, Arctic lead pollution remains 60 times higher than in the year 500. Similar data from recent publications provide a regionally differentiated perspective on BC, sulfate and mineral dust deposition across the Arctic (Osmont et al., 2018; Zdanowicz et al., 2018; Ruppel et al., 2014, 2017; McConnell et al., 2007, 2019).

BC and particulate sulfate

Figure 6.20 shows reconstructed historical trends in non-sea salt sulfate (nss SO_4^{2-}) and refractory BC (rBC) concentrations in ice cores from the circum-Arctic region, developed using comparable methods. To avoid overcrowding the figures, only some of the available records from Greenland are shown. In the Atlantic sector of the Arctic, only Greenland has sufficiently high snow accumulation rates and low surface melt rates to facilitate reliable delineation of individual annual layers in ice cores, making it possible to reconstruct interannual variations of fluxes, and not just concentrations, of rBC and dust. Ice cores recovered from the smaller ice caps of the European and Canadian Arctic islands are all affected, to varying degrees, by the effects of surface melt and/or wind scouring, which makes estimates of annually-resolved fluxes obtained from these cores much less reliable, although the reconstructed interdecadal trends in both concentrations and fluxes are likely valid in most cases.

Spatial differences in the temporal patterns of BC and sulfate deposition recorded in circum-Arctic ice cores reflect different mixed contributions from emissions source regions, as well as differences in atmospheric transport pathways and scavenging patterns. For example, in winter, the high-elevation regions of central Greenland receive BC particles transported over the long range from North American sources. In contrast, ice cores from Lomonosovfonna on Spitsbergen (Svalbard) and from Akademii Nauk ice cap on Severnaya Zemlya (Russian Arctic) are likely more affected by Eurasian emissions, while Devon ice cap in the Canadian High Arctic is thought to be affected by mixed BC emissions from north-central and northwestern America, as well as from Russia and central Asia. The high-elevation icefields of the western Canadian subarctic (Eclipse, Mount Logan) are comparatively more affected by long-range transport of aerosols from eastern Asia and the North Pacific. During summer, a substantial contribution of BC deposited on Arctic and subarctic icefields also comes from biomass burning, which is partly a natural and partly an anthropogenic source (see Chapter 4 on open biomass burning).

Ice-core records from Greenland and Svalbard (Lomonosovfonna) in Norway, as well as those from Penny ice cap (southern Baffin Island) and Devon Island in the Canadian High Arctic show broadly consistent historical patterns of sulfate concentrations, with an initial rise that mostly becomes noticeable in the early 20th century, peaking around 1920. This is followed by a small decrease in the years following the Great Depression in the 1930s, and a renewed rise during the post-war economic boom of the 1950s, but peaking in different decades depending on location. In Svalbard, the peak occurs before the 1970s, in Greenland during the 1970s and in Canada in the 1980s. The 20th-century increase in sulfate concentration recorded on Devon ice cap in the Canadian High Arctic is noticeably more gradual than the trend observed in the central Greenland cores, and resembles that of the Humboldt ice core from nearby northwest Greenland. On the Prince of Wales icefield (Ellesmere Island) the 20th-century rise in sulfate is far more subdued, despite the fact that the intensity of post-depositional surface melt on this ice cap is considerably less than on Spitsbergen and Severnaya Zemlya. This may indicate a lesser influence of North American and European air pollution at this site, compared to locations farther south or in Greenland.

A general decrease in sulfate deposition is recorded from the mid-1970s or 1980s in all ice cores from the Atlantic sector of the Arctic, in agreement with trends in anthropogenic emissions from North America and western Europe/Eurasia, and reflecting the effect of air-pollution abatement measures. Sporadic peaks in sulfate deposition recorded in many Arctic ice cores are due to natural volcanic eruptions, such as the 1783 eruption of Laki volcano in Iceland and the 1815 eruption of Mount Tambora in Indonesia. While episiodic, the SO_2 emissions from these eruptions were comparable to, or much larger than, current global yearly anthropogenic SO_2 emissions.

The temporal trends in sulfate concentrations recorded in ice cores from the European Arctic islands (Spitsbergen and Severnaya Zemlya) are not as consistent as those from Greenland, possibly due to post-depositional melt effects. The late 20th-century peak sulfate concentrations in these ice cores are also in excess of 1000 ng/g (ppb) – far higher than those recorded in Greenland cores – reflecting the greater influence of polluted air masses advected from the nearby European mainland.

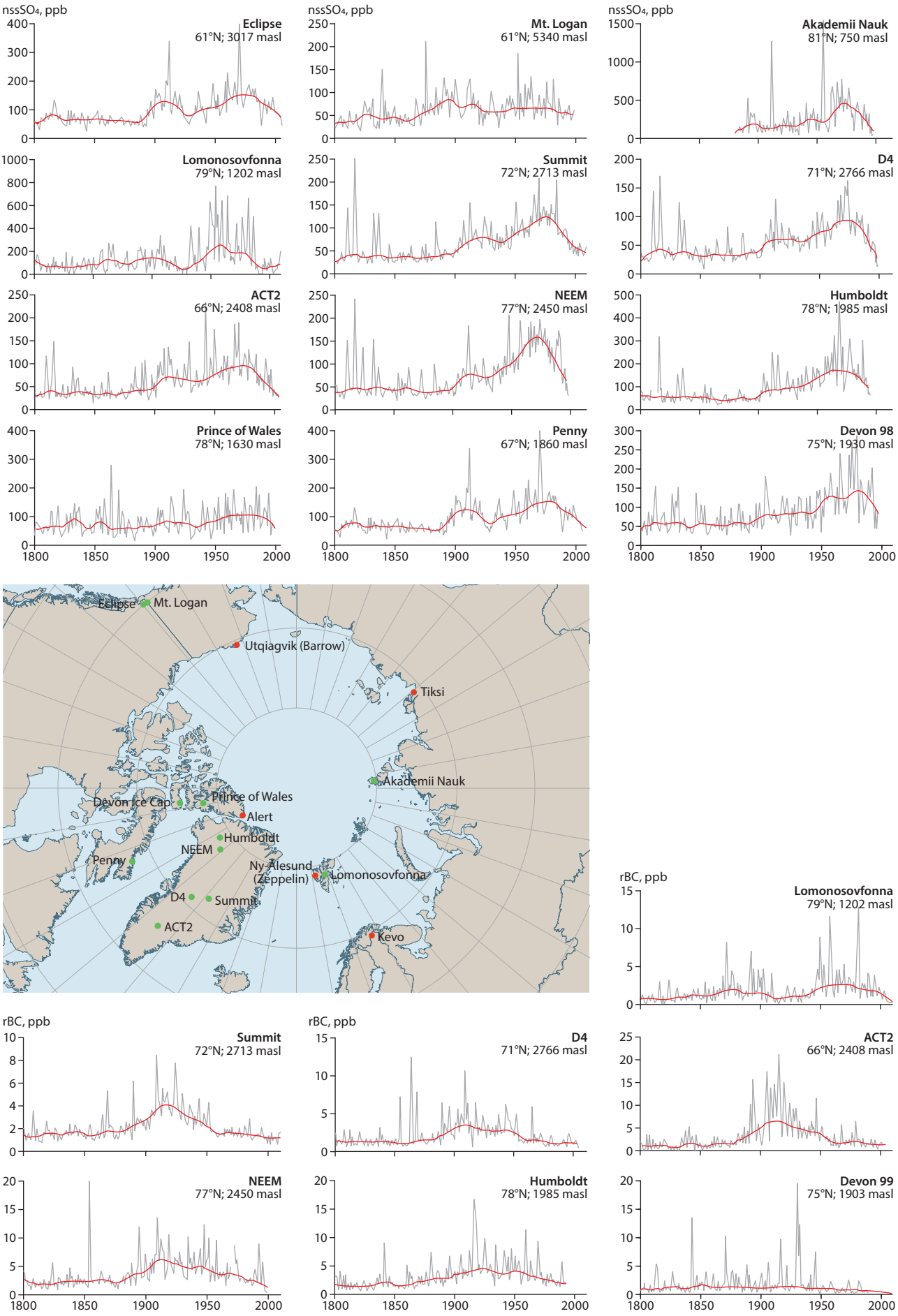

Figure 6.20. Top: Ice-core records of non-seasalt sulfate (nss SO_4) from the north circumpolar region, 1800–2010. All timeseries were resampled at approximately one-year resolution (grey lines), and a locally weighted scatter plot smoothing filter (window span = 10%) was applied to the data to emphasize the multidecadal trends (red lines). Bottom: As top but for rBC.

The two ice-core records from the western Canadian subarctic (Mount Logan, Eclipse) are from sites in close proximity, but at two different altitudes; the Mount Logan site is at 5340 MASL, while the Eclipse icefield site is at 3017 MASL. The Mount Logan core shows a modest rise in sulfate concentrations in the late 19th to early 20th century, but unlike in the Greenland or European Arctic cores, these did not peak in the late 20th century, and neither has there been a marked decline in recent decades. The difference likely reflects the unique situation of the Mount Logan ice-core site in the mid troposphere and immediately downwind of the subarctic North Pacific. Non-marine sulfate aerosols deposited in snow at this site likely primarily originate from east-Asian emissions, which steadily increased in the 20th century, but only those aerosols uplifted to, and transported at, mid-tropospheric altitudes reach the Mount Logan site. The Eclipse icefield record, for its part, shows hardly any trend in sulfate concentrations over the past two centuries. This suggests that any sulfate pollution emitted upwind in east Asia and transported across the North Pacific is largely washed out in transit before it reaches the icefield (Zdanowicz et al., 2014). A tentative inference from these two sites is that the historical ice-core records of sulfate deposition from the Atlantic sector of the Arctic (Greenland, eastern Canadian Arctic, European Arctic) are unlikely to accurately represent past trends over the more western sectors of the Arctic.

Most ice-core records of BC deposition developed from the circum-Arctic presently come from Greenland, with the exception of cores drilled on Lomonosvfonna and Holtdehalfonna on Spitsbergen (Svalbard) and one on Devon Island (Canadian High Arctic). The core from Devon ice cap comes from a site exposed to wind scouring (in other words, with low net snow accumulation) and affected by melt-freeze cycles, which might have led to an under-estimation of BC deposition and makes an overall interpretation difficult. The ensuing discussion therefore focuses on rBC deposition trends recorded in the Greenland and Svalbard cores. These are presented in Figure 6.21 as depositional fluxes (in $\mu g/m^2/y$), with corresponding trends in sulfate fluxes reconstructed from the same cores for contrast.

The deposition fluxes of rBC recorded in ice cores were more variable than those for sulfate between 1750 and 2000. Ice cores used in this analysis are located in Greenland (Humboldt, NGT_B19, D4, Summit2010, ACT2 ACT11D), and Svalbard (Lomonosovfonna icefield on central Spitsbergen; core Lomo 09_11). All ice cores from Greenland, apart from two, have similarly shaped curves between 1880 and 1950, when BC fluxes increase, followed by a sharp drop until 2000. The exceptions are: ACT11D, where the onset of higher BC fluxes was in the early 1800s, and NGT_B19, where levels remained higher until the 2000s. Apart from those two cores, the Summit 2010 and ACT2 ice cores exhibit a comparable trend. The Humboldt core also shows similar trends but with a much smaller amplitude. All cores indicate that rBC deposition fluxes close to present day have decreased to a level similar to the preindustrial time around 1800.

The Lomonosovfonna ice core in central Spitsbergen reveals a different pattern, with increased BC fluxes between 1860 and 1910, and from 1940 until the early 2000s. Osmont et al. (2018) hypothesized that the observed minimum at the beginning of the 20th century might be due to Arctic warming in the

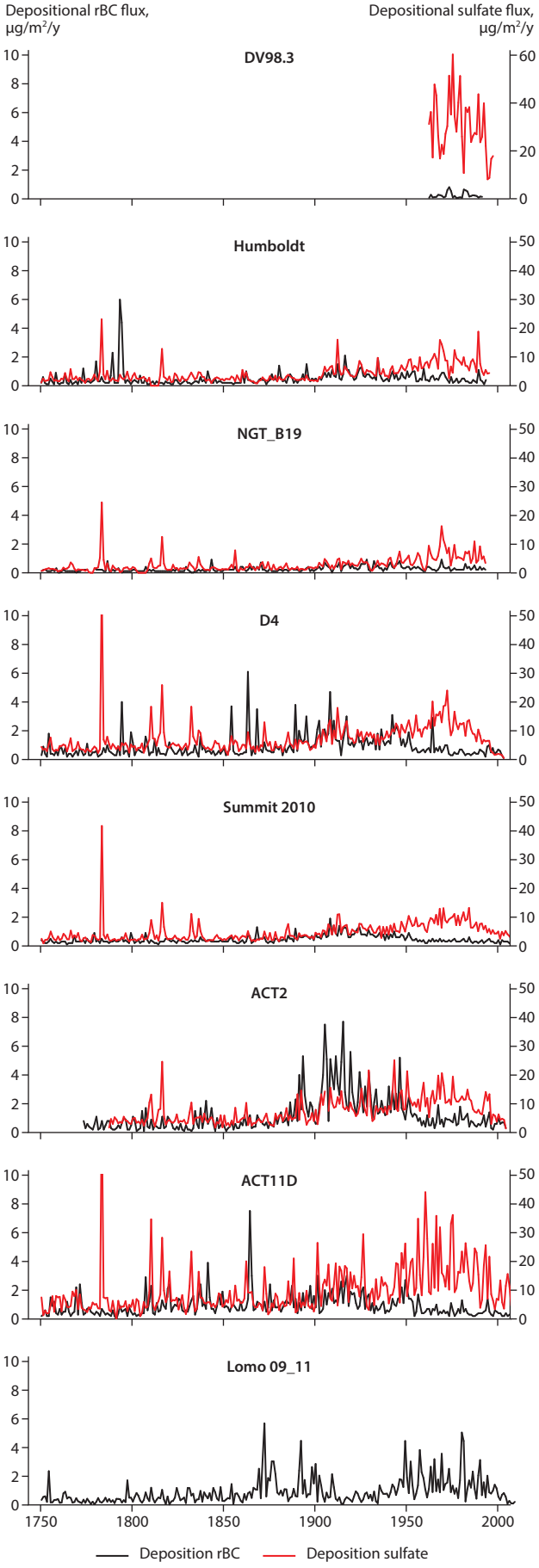

Figure 6.21. Timeseries of depositional fluxes of BC and sulfate at various Arctic locations. Data sources for Greenland cores: Humboldt, NGT-B19, D4, Summit, ACT2 and ACT11D – McConnell et al. (2007), McConnell and Edwards (2008) and McConnell, personal communication, 2020; and Lomonosovfonna, Svalbard (Lomo09_11) – Osmont et al. (2018).

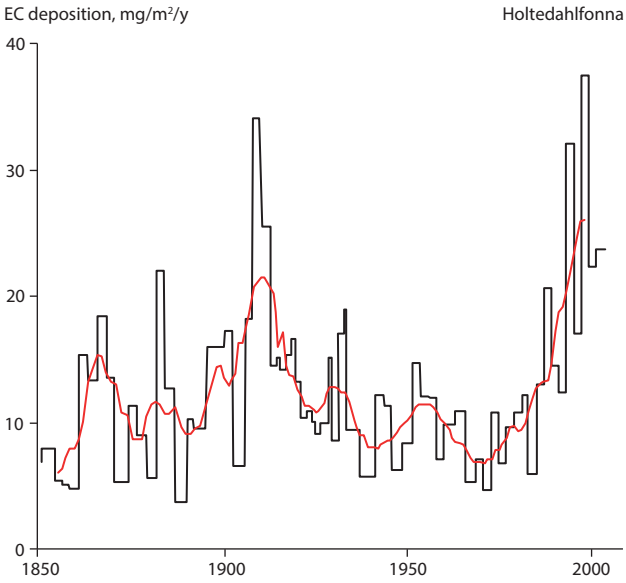

Figure 6.22. Elemental carbon (EC) deposition flux with 10-year running averages (red line) for the Holtedahlfonna (Svalbard) ice core (Ruppel et al., 2017).

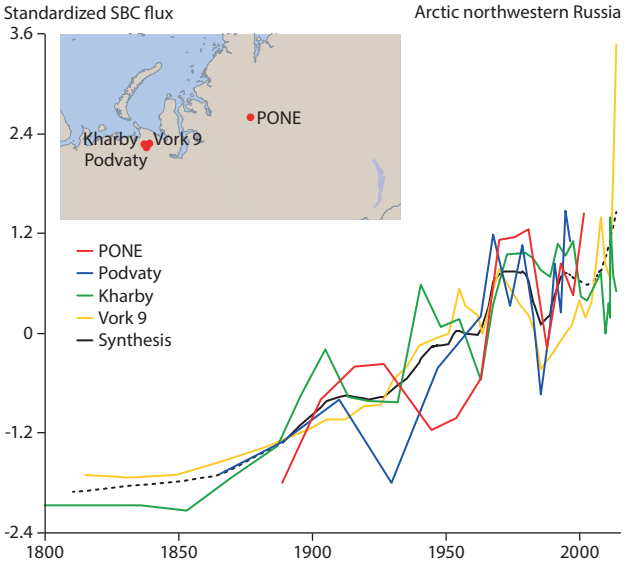

Figure 6.23. Soot-BC (SBC) fluxes for Arctic northwestern Russia. Stacked Soot-BC fluxes at northwestern Russian lakes PONE, Podvaty, Kharby and Vork 9 (data from Ruppel et al., 2021). The black curve shows a LOESS smoother (span = 0.15) of time intervals from which data is available from all lakes, and, additionally the dashed line for time intervals with data from at least two lakes. Units are standard deviations from the mean. Locations are shown on the map.

early 20th century, with artefacts from melting of the sampled ice potentially playing a role. The late timing of the recent decline in BC fluxes at the end of the 20th century marks another important difference with the Greenland records.

A separate ice-core record of EC deposition flux from Holtedahlfonna (northwestern Svalbard; Ruppel et al., 2014, 2017) shows a steady increase between 1970 and 2004, which differs markedly from the Lomonosovfonna and Greenland cores, in which the peak rBC deposition period was between 1850 and 1960 (Figure 6.22). Ruppel et al. (2014, 2017) suggest that increased gas-flaring emissions in Russia and enhanced wet scavenging of EC might explain this increase. It is noteworthy that there is a factor of 4000–5000 between the Holtedahlfonna EC deposition flux compared to the much lower rBC flux on Lomonosvfonna, even though both sites are located on Svalbard. The disagreement between these cores may reflect differences in the BC particle type quantified by each analytical method (rBC; SP2 method versus EC; thermo-optical method), and the size-dependent efficiency in the detection of particles (see Chapter 5 for a description). The rBC may not incorporate the largest (and heaviest) BC particles and EC may not include the smallest ones. This can result in different concentrations, and, if the size distribution of the particles has varied temporally, in different trends being measured from the Arctic with different methods. Importantly, Svalbard glaciers are subject to summer melt – in other words, repeated thaw-freeze cycles – which may lead to agglomeration of BC particles and a subsequent shift to larger particles in the ice (Schwarz et al., 2013). This may not be as efficiently detected with the SP2 method as with the thermo-optical method (Ruppel et al., 2014, 2017).

Soot-BC

Lake sediments give further information on the historical evolution of BC deposition in areas where ice-core records do not exist. In the Russian Arctic, records of soot-BC have been determined by a chemothermal method from lake sediments. It is not directly comparable to rBC or EC (see Chapter 5). Four lake-sediment records from an intense flaring region in Arctic northwestern Russia show a consistent increase in BC deposition from 1850 to 2014, suggesting that emissions inventories potentially underestimated and inaccurately portrayed BC emission trends for Russia, particularly after the fall of the Former Soviet Union (Ruppel et al., 2021, Figure 6.23). Furthermore, four soot-BC lake-sediment records from northern Fennoscandinavia exhibit a similar trend as the Holtedahlfonna EC record, with increasing fluxes between 1970 and 2010 (Ruppel et al., 2015).

The data presented here suggest that trends in BC deposition might be subject to greater regional variability across the Arctic than those for particulate sulfate. This is an important observation because it means that either BC emissions patterns are more variable, or atmospheric processing plays a more important role in controlling BC than sulfate deposition fluxes. Hence, comparing model performance against multiple ice-core records becomes critical. This was undertaken for this assessment and the results are presented in Chapter 7, Section 7.3.3.1. Ice-core records of BC and particulate sulfate can also be used to constrain climate models (Fyfe et al., 2013), from which radiative forcing can be calculated through direct radiation interactions of these aerosol components in the atmosphere and when deposited. Deriving information for radiative forcing from aerosol-cloud interaction is much more difficult. Here, knowing the potential CCN and INP is important to correctly simulate the cloud water phase, which is an important factor for cloud radiative properties. One study looked into the historical variability of INP in the Arctic from one ice core in Greenland and another in Svalbard (Hartmann et al., 2019). Analysis showed that no trend in INP concentrations could be observed for the time period between 1450–2000. INP are thought to be mostly made of mineral dust or biogenic material, and the emissions contributed by these natural sources could vary with a changing climate and retreating cryosphere.

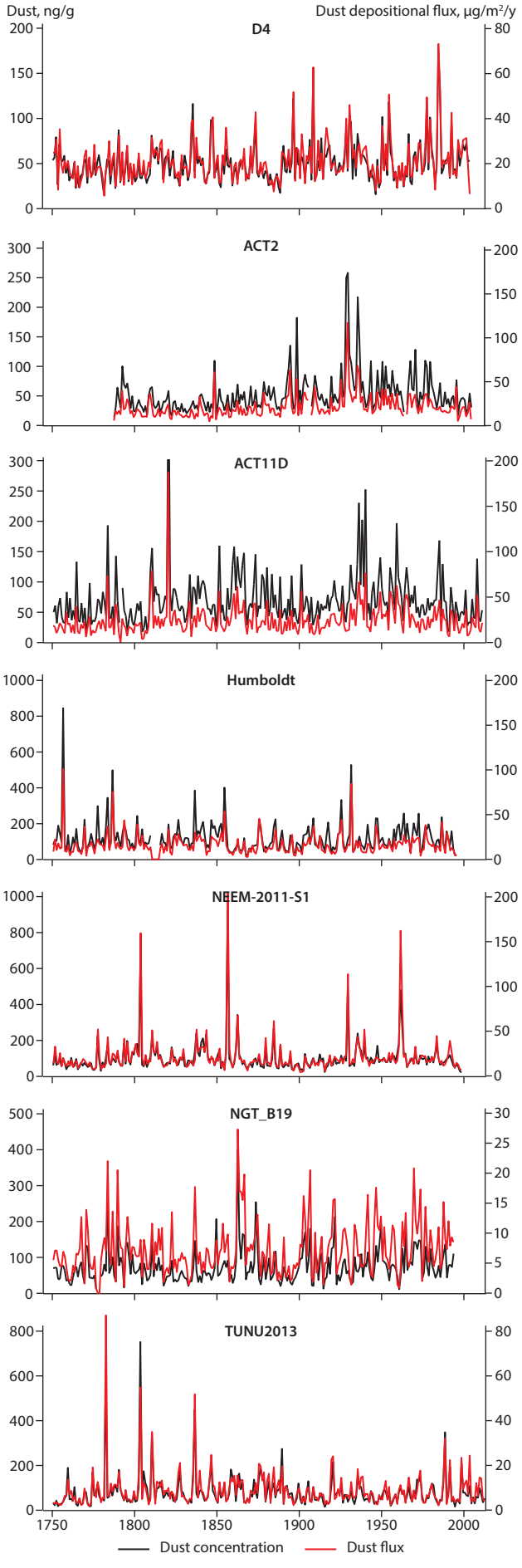

Figure 6.24. Ice-core mineral dust deposition flux data (black) and dust concentrations (red). (Data source: McConnell et al., 2019).

Mineral dust

A study by McConnell et al. (2019) investigated dust (Cerium) deposition fluxes for Greenlandic ice cores (Figure 6.24). The variability was very large, and no pattern emerged over the time period between 1750 to the present day. However, the mass deposition was between one and three orders of magnitude higher than for rBC. Mineral dust could constitute an important absorbing impurity on snow and ice in spite of having a mass absorbing efficiency that is much lower than rBC (Tuzet et al., 2019). Evaluating the relative importance of BC and mineral dust for the snow-albedo effect over time can provide insights into the contribution of natural versus anthropogenic forcing. To do so, however, more information is needed on the contribution to BC deposition from forest fires. This can be achieved by analyzing the deposition of organic tracers.

Organic tracers

The study of organic tracers in Arctic ice cores has provided detailed information on the variability of biomass burning in the boreal regions, and on its link to large-scale climate anomalies (Legrand et al., 2016; Rubino et al., 2016). Specific organic markers for biomass burning encompass levoglucosan, phenolic compounds, vanillic acid and dehydroabietic acid (Kehrwald et al., 2012; Kawamura et al., 2012; McConnell et al., 2007). The analysis of ice-core records from Svalbard (Grieman et al., 2018a), Greenland (Zennaro et al., 2014; Grieman et al., 2018b), Alaska (Pokhrel et al., 2020) and Russia (Grieman et al., 2017) suggests that fire activity in boreal regions in the last centuries was modulated by temperature and, especially, precipitation anomalies.

6.2 Ozone and precursors

6.2.1 Introduction

Tropospheric ozone (O_3) is a secondary air pollutant, which is not emitted directly but is produced photochemically in the atmosphere from precursor emissions from anthropogenic and natural sources. Analyses of Arctic surface ozone and vertical ozonesonde data have revealed small, statistically significant positive and negative trends, depending on location and the length of the observation records. Sparse precursor records in the Arctic suggest declining trends in, for example, carbon monoxide (CO), while methane (CH_4), another important ozone precursor, continues to increase globally. Seasonal cycles of O_3 vary with location in the Arctic, with episodes of very low concentrations at coastal sites in spring due to photochemistry involving halogen compounds. Possible shifts in the observed phase or amplitude of the tropospheric O_3 seasonal cycle have been reported for the first time at the surface (northern Sweden) and in the free troposphere in the Arctic. The reasons for this are not fully clarified but they may include changes in anthropogenic precursor emissions.

As well as there being significant anthropogenic sources of O_3 precursors, there are important natural sources for these species – such as boreal fires, lightning, vegetation, and transport of O_3 from the stratosphere – which show marked seasonal and inter-annual variations. Photochemistry involving halogens

and dry deposition are important O_3 sinks but remain poorly quantified. The role of natural sources in the Arctic O_3 budget relative to anthropogenic emissions is still uncertain.

Current observations are insufficient to capture anticipated changes in O_3 from anthropogenic and natural sources. Only a very limited number of stations provide long-term monitoring of ozone at the surface and O_3 vertical profiles (ozonesondes, lidar) in the Arctic. In many cases, records are not continuous. Fewer observations of species required for understanding ozone sources and sinks are collected at surface sites, and certain key measurements are lacking – particularly at terrestrial locations, which may be influenced by local anthropogenic emissions, now and in the future. Standardization of measurement techniques is required. There has been no dedicated airborne campaign to understand chemical and dynamical processes affecting tropospheric O_3 in the Arctic since International Polar Year in 2007–2008. Satellite data can provide useful spatial, and limited vertical, information about O_3 and some precursors/oxidants but retrievals have limitations that need to be improved at high latitudes.

This section reviews recent work on the origins of Arctic O_3, including natural and anthropogenic sources and sinks, and discusses observed distributions of O_3 and its precursors, and observed trends in the Arctic troposphere.

6.2.2 Ozone sources and sinks

Tropspheric O_3 is produced photochemically from anthropogenic and natural precursor emissions and transported from the stratosphere. It is destroyed by photochemistry and by dry deposition to the Earth's surface.

6.2.2.1 Ozone sources

Tropospheric O_3 is formed from the oxidation of CH_4, CO and non-methane volatile organic compounds (VOCs) (including non-methane hydrocarbons, NMHCs) in the presence of nitrogen oxides (NO_X). Fiore et al. (2008) estimated that anthropogenic CH_4 emissions contribute 15% to the annual mean total global O_3 burden (including natural and anthropogenic sources). Based on parameterized responses to O_3 precursor emission perturbations (see Chapter 8), it was found that CH_4 dominates the sensitivity of Arctic O_3 to anthropogenic emissions. CH_4 accounts for approximately 40% of the O_3 response to precursor emission perturbations. Enhancements in Arctic O_3 also result from the import of O_3 and its precursors from lower latitudes during episodes of long-range transport of pollution to the Arctic (Wespes et al., 2012; Monks et al., 2015; Ancellet et al., 2016). While very low levels of NO_X within the Arctic – away from local sources – often limit local O_3 production, O_3 can be produced from the thermal decomposition of peroxy-acetyl nitrate (PAN) transported over long distances. This can liberate NO_X in the lower troposphere during the warmer Arctic summer, leading to O_3 production (Wespes et al., 2012; Arnold et al., 2015). Recently, there has been progress in improving knowledge of local O_3 precursor sources. Surface O_3 in summer is already influenced by NO_X emissions from shipping along the northern Norwegian coast (Marelle et al., 2016, 2018) and the Northwest Passage (Aliabadi et al., 2015). Marelle et al., (2018) showed that, for a 2050 scenario in which shipping was diverted to the Arctic, shipping would become an important source of surface O_3. Tuccella et al. (2017) showed that background O_3 is influenced by emissions downwind of oil and gas extraction platforms in the southern Norwegian Sea. Investigation of long-range transport of O_3 precursors has shown efficient export of PAN (an important NO_X reservoir) from East Asia to the North Pacific, with relative contributions to long-range O_3 transport of 35% in spring and 25% in summer (Jiang et al., 2016). Ship observations over the Arctic and Bering Seas also identified long-range pollution transport events that enhanced O_3 (Kanaya et al., 2019). Natural sources of Arctic tropospheric O_3 include downward transport of O_3 from the stratosphere (Shapiro et al., 1987; Hess and Zbinden, 2013; Ancellet et al., 2016), as well as O_3 production from natural emissions of O_3 precursors. These include lightning NO_X; emissions of NO_X and reactive VOCs from the snowpack (Honrath et al., 1999; Guimbaud et al., 2002; Hornbrook et al., 2016); and natural emissions of VOCs from high-latitude vegetation (Holst et al., 2010; Ghirardo et al., 2020), and the Arctic Ocean (Mungall et al., 2017). Evidence from both observations and models shows that boreal fires are also an important source of O_3 precursors and NO_X reservoir species, like PAN, in spring and summer, with resulting impacts on Arctic O_3 (Thomas et al., 2013; Arnold et al., 2015; Viatte et al., 2015; Ancellet et al., 2016).

6.2.2.2 Ozone sinks

Photochemical loss of O_3 occurs mainly via photolysis in the presence of water vapor or through O_3 directly reacting with hydroperoxyl or hydroxyl radicals (HO_2 or OH). Photochemical destruction involving HO_2 may be particularly important in the Arctic, where water vapor abundances are low (Arnold et al., 2015), as are reactions involving halogens during the Arctic spring. The dry deposition of O_3 and precursor species to ice and ocean surfaces is slower than to vegetated terrestrial surfaces. Van Dam et al. (2016) reported O_3 dry deposition velocities that were five times higher over Arctic snow-free tundra in the summer months at Toolik Lake (northern Alaska) compared to snow-covered ground. Dry deposition, combined with possible chemical loss (such as that involving biogenic-volatile organic compounds [BVOCs]) producing lower O_3 concentrations during stable (lower light) night conditions may explain the different diurnal cycle observed at this tundra site compared to Arctic coastal locations.

During Arctic spring, photochemical cycling of halogens in so-called 'bromine-explosion' events leads to the rapid depletion of surface O_3 to low or near-zero concentrations (Barrie et al., 1988; Simpson et al., 2007). These phenomena, referred to as ozone-depletion events (ODEs), are most commonly observed at Arctic coastal locations in March–April and are attributed to bromine (halogen) sources linked to Arctic sea ice, coupled with stable surface temperature inversions (e.g. Hermann et al., 2019). Interestingly, Yang et al. (2020) were able to explain major depletion events in a model study by introducing wind-induced release of bromine from the snow pack. Figure 6.25 shows the vertical extent of low O_3 episodes observed by lidar at Eureka in northern Canada, where orographic effects were also important (Seabrook and Whiteway, 2016). Peterson et al. (2018) showed

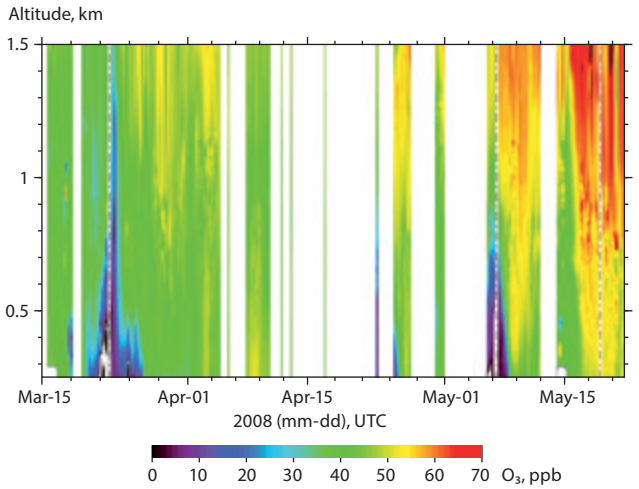

Figure 6.25. Ozone lidar measurements from Eureka in spring 2008 showing the effects of large-scale meteorology, including low O_3 in the lower troposphere, when air masses originated from the north over the Arctic Ocean, and enhanced O_3 during downward transport into the Arctic boundary layer at times when air flowed from the south over mountains. From Figure 3 in Seabrook and Whiteway (2016).

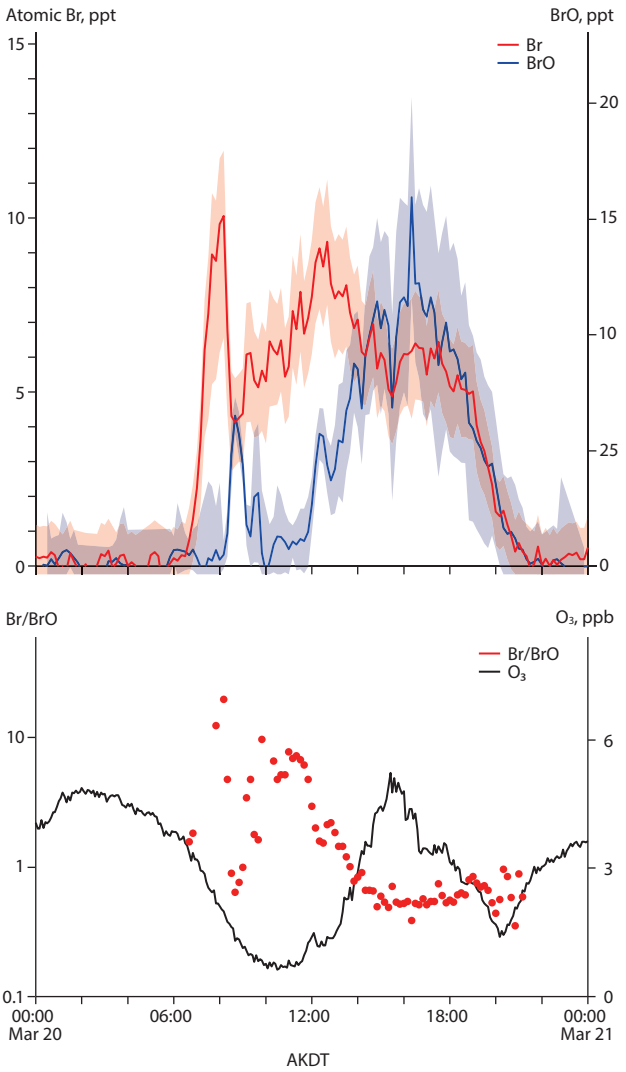

Figure 6.26. Timeseries in Alaska Daylight Time (AKDT) from 20 March 2012 of measured atomic bromine (Br) and bromine monoxide (BrO) (upper panel), and Br/BrO ratios and O_3 (lower panel). Error bars represent propagated measurement uncertainties. Data was collected during the Bromine, Ozone, and Mercury Experiment (BROMEX) conducted near Utqiaġvik (Barrow), Alaska. Based on Figure 3 in Wang et al. (2019).

that active halogen chemistry and related O_3 depletion can also occur up to 200 km inland over snow-covered tundra in Alaska. Simpson et al. (2018) reported high levels of bromine oxide (BrO) at Utqiaġvik occurring earlier in February in air masses originating from the Arctic Ocean polar night. Their findings suggest the presence of a dark wintertime source of reactive bromine that could feed halogen photochemistry at lower latitudes as the sun returns.

Earlier studies proposed indirect evidence that O_3 and mercury (Hg^0) are removed by reaction with bromine atoms (e.g. Skov et al., 2004, 2020; Dastoor et al., 2008). However, Wang et al. (2019) showed, for the first time, a direct connection between O_3 and Hg^0 with atomic bromine (Br) during O_3 and Hg^0 depletion episodes at Utqiaġvik, which lies 5 km from the northern Alaskan coast (Figure 6.26). Here, the Br/ BrO ratios are anti-correlated with O_3 concentrations, and box modeling confirmed that O_3 was removed by Br.

This result is significant since the main sources of halogens in the Arctic appear to be released from refreezing leads and from snow blowing over sea ice (e.g. Petersen et al., 2016; Yang et al., 2020). Burd et al. (2017) found a strong relationship between the end of the reactive bromine season and snowmelt timing. In the future, continued decreases in Arctic sea-ice extent or in the relative distributions of multi-year/seasonal sea-ice cover, coupled with increases in the length of the snow-free season over land, could influence the magnitude and seasonality of O_3 sinks via changes in halogen fluxes or in dry-deposition fluxes to tundra or ocean rather than snow or ice surfaces.

6.2.3 Observed concentrations

6.2.3.1 Surface site and ship *in-situ* observations

Measurements at permanent research stations in the Arctic provide long timeseries of data (typically around two decades, see Table 6.3) that allow trends to be studied, as well as the seasonality of the observations. Seasonal differences are particularly important in the Arctic because of differences in local meteorological conditions, as well as atmospheric transport, between the warm and cold seasons, and seasonal variations in O_3 sources and sinks. Figure 6.27 illustrates the range of seasonal-cycle behaviour observed in the Arctic at different measurement sites. Further analysis and comparison with the AMAP model simulations are presented in Whaley et al. (2023).

Figure 6.27 shows that the seasonality in O_3 at Villum, Utqiaġvik and Alert are similar. These stations are located at about the same latitude at High Arctic coastal sites close to sea level, with a minimum in spring due to ODEs, a slight increase in June, and a local minimum in July due to surface removal and photochemical degradation of O_3. O_3 reaches maximum during winter, when there is an absence of photochemical loss or formation of O_3. Vertical mixing is also suppressed during the polar night and the Arctic boundary layer is highly stratified, hampering removal by dry deposition (Esau and Sorokina, 2011). Zeppelin exhibits a different behaviour, with a spring maximum. This site, which is located at 450 m altitude on Svalbard, is less influenced by surface ODEs. Esrange, located in northern Sweden (67°N), also has a spring

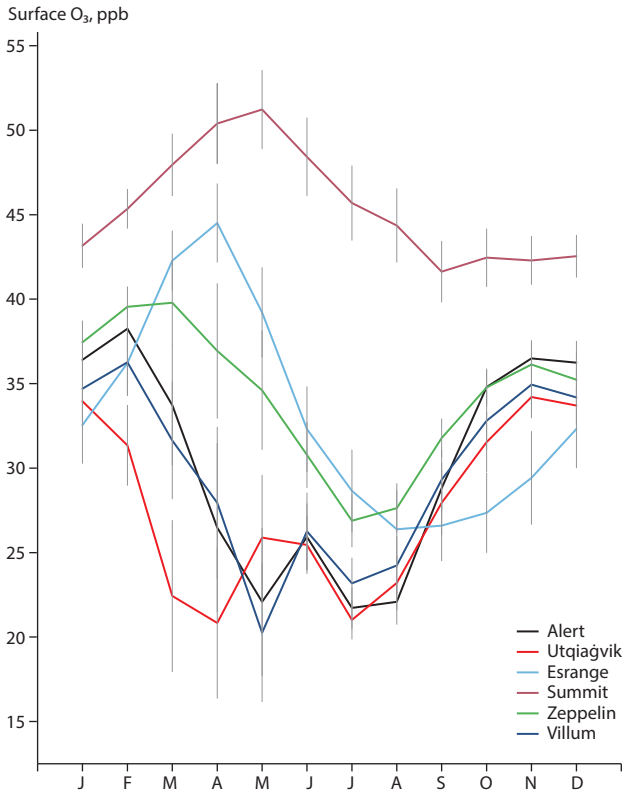

Figure 6.27. Seasonal behaviour of surface O_3 at selected Arctic stations that are representative of the coastal High Arctic (Alert, Utqiaġvik, and Villum), near the Arctic Circle, inland (Esrange), and the free troposphere (Summit). Zeppelin on Svalbard is High Arctic and close to the coast but at a higher elevation. Monthly medians are calculated for the period 2003–2018. Data were not available between 2003–2006 and for 2004 for Villum, and between 2013–2016 for Alert. The error bars show upper (75%) and lower (25%) quartiles (Data ref. 6.3).

maximum. It is far from coastal areas affected by ODEs, and its seasonal cycle is more similar to lower-latitude European stations at remote locations (see also Figure 6.30). The spring maximum is attributed to photochemical production and transport of O_3 from the stratosphere. Summit (in the free troposphere) is also unaffected by the bromine chemistry originating from sea ice or other low-altitude processes (Huang et al., 2017a). Consequently, the seasonal variation is different here, with a clear maximum in May, a minimum in September and generally higher concentrations compared to other surface stations. Short episodes of depletion have been reported (Brooks et al., 2011) but they do not appear to affect the monthly mean values (see Figure 6.27).

Note that surface O_3 can also be influenced by local anthropogenic emissions, such as those from shipping (e.g. Marelle et al., 2016, Aliabadi et al., 2015) or oil fields (McNamara et al., 2019). McNamara et al. (2019) discussed potentially important interactions between local anthropogenic O_3 emissions from the Utqiaġvik settlement or the Prudhoe Bay oil extraction facilities in northern Alaska and snowpack (chlorine) chemistry, leading to elevated concentrations of nitrogen-containing compounds with implications for Arctic tropospheric O_3. Therefore, while none of the Arctic sites currently exhibits summertime surface maxima due to photochemical production, as is often observed in polluted locations further south, this may change in the future with increasing local anthropogenic emissions (e.g. Marelle et al., 2018).

Observations of O_3 and its precursors over the oceans are important for validating models but there is a scarcity of such data from the Arctic. Two datasets from ship cruises in the Arctic have been reported: Kanaya et al. (2019) measured CO and O_3 during several ship cruises in September (2012–2017) including on legs to the Bering Sea and Arctic Ocean. Generally, it was found that halogen chemistry, stable boundary layers, and dry deposition may explain differences between measured and modeled O_3 concentrations. He et al. (2016) measured O_3 and black carbon on a ship cruise to the Arctic Ocean (31.1°N to 87.7°N and 9.3°E–90°E to 168.4°W) from June to September 2012. Comparing the observed O_3 concentrations to those measured at Utqiaġvik showed no statistically significant differences; the authors suggest that coastal stations between July and September may be representative of the entire Arctic Ocean but this hypothesis requires further investigation.

6.2.3.2 Vertical profiles

Christiansen et al. (2017) examined long-term ozonesonde records at nine Arctic stations, reporting consistent seasonal cycles as a function of altitude between sites with later maxima in the mid-troposphere, compared to the surface layers and upper troposphere.

Since AMAP (2015a), no new comprehensive aircraft campaigns have taken place with a focus on understanding processes affecting Arctic O_3 in the free troposphere. Ancellet et al. (2016) examined aircraft, lidar and ozonesonde data gathered over Canada and Greenland during the summer 2008 Polar Study using Aircraft, Remote Sensing, Surface Measurements and Models, of Climate, Chemistry, Aerosols, and Transport (POLARCAT) campaigns (described in AMAP, 2015a). This study showed clear latitudinal and longitudinal variations in the origins of sampled air masses based on back trajectories and correlations between O_3 and potential vorticity (PV). While downward transport of O_3 was important over Greenland, air masses with higher O_3 were attributed to North American boreal fires over Canada. Transport of polluted air masses from mid latitudes, for example from Asia, also contributed north of 80°N.

The airborne NASA Atmospheric Tomography (ATom) mission (Data ref. 6.2) has undertaken extensive surveying of the global troposphere (Wofsy et al., 2021). This includes repeated vertical profile measurements between 60°N and 90°N, which provide useful insights into the variation of O_3 and its precursors through the depth of the Arctic troposphere at different times of year (Figure 6.28). For example, greatly enhanced near-surface nitrogen dioxide (NO_2) during winter is associated with the relatively long lifetime of NO_2 and the accumulation of pollution in Arctic haze. Surface PAN is also enhanced in the winter and can thermally decompose in the spring and summer to release NO_X. In line with ozonesonde data and previous airborne campaigns (AMAP, 2015a), ATom profiles also demonstrate a springtime enhancement in O_3 extending throughout the troposphere, with evidence of stratospheric influence in the upper troposphere and lower O_3 in the summertime lower troposphere. Summer enhancements in O_3 precursors, such as CO and PAN in the mid-troposphere, were also observed, associated with the import of forest fire and anthropogenic emissions from lower latitudes, as also seen during POLARCAT in 2008.

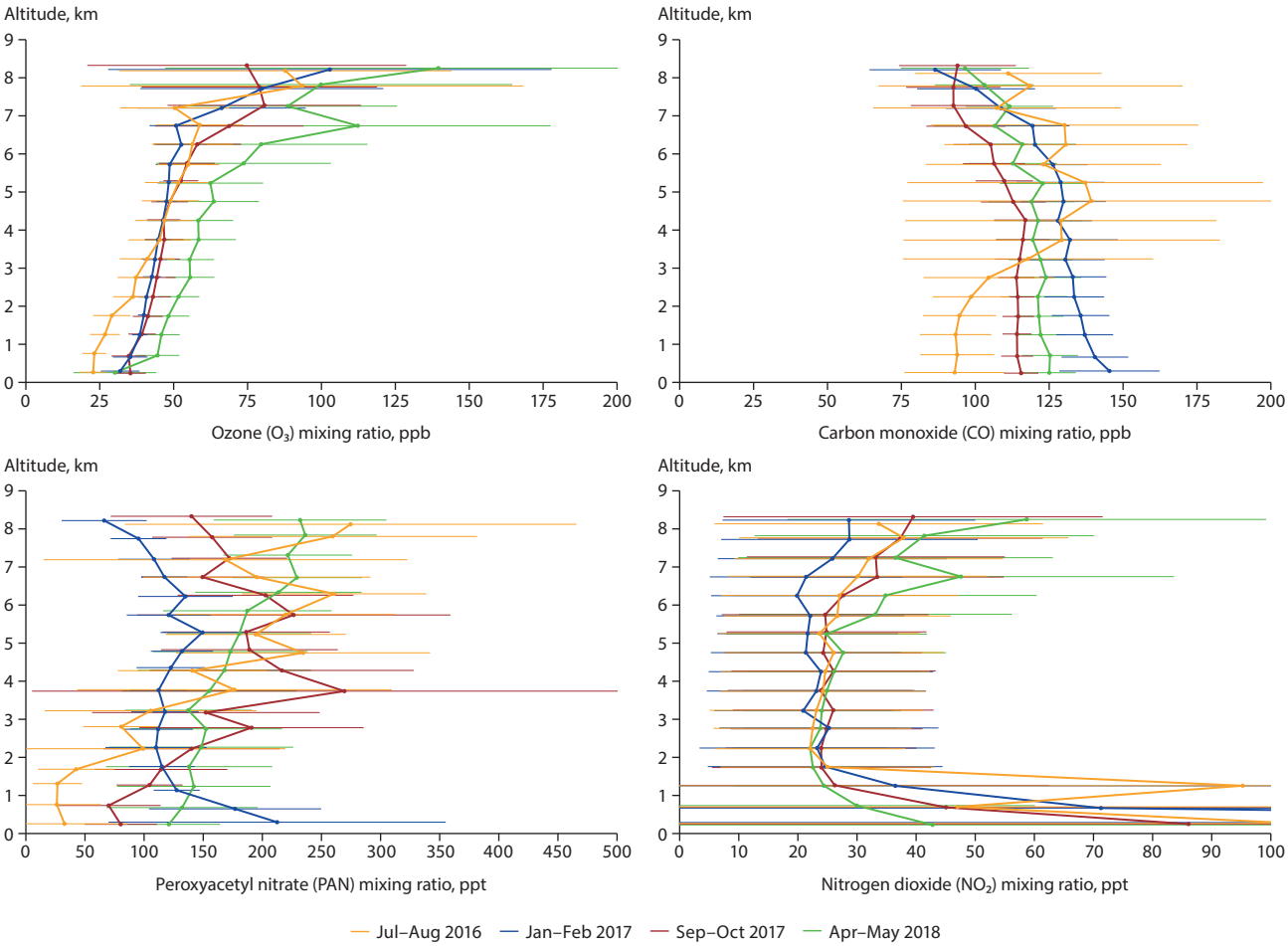

Figure 6.28. Mean vertical profiles of O_3, CO, PAN and NO_2 measured north of 60°N – from the NASA ATom missions of summer 2016, winter 2017, autumn 2017 and spring 2018. Horizontal lines indicate one standard deviation spread around mean values at each altitude (Data ref. 6.2).

6.2.3.3 Satellite data

Despite the potential limitations of some satellite data products at high latitudes (see Section 5.3, several studies have exploited satellite observations to investigate tropospheric O_3 and precursor distributions and trends relevant to the Arctic. Pommier et al. (2012) presented Infrared Atmospheric Sounding Interferometer (IASI) retrievals of 0–8 km and 0–12 km partial column O_3 for the Arctic in spring and summer 2008 (see Figure 6.29). These showed widespread enhancements in springtime (March–April) tropospheric partial column O_3 compared with during the summer (June–July), particularly over northeast Siberia, northern Canada and the Arctic Ocean. Generally good agreement with *in-situ* aircraft profiles was demonstrated, but negative IASI biases were found compared with aircraft data in the lower troposphere, due to low thermal contrast in the Arctic boundary layer. Wespes et al., (2012) showed that IASI was able to detect enhancements in mid-latitude-sourced O_3 enhancements during summer at the edge of the Arctic, but showed a lack of sensitivity over snow and ice surfaces, potentially resulting in some missed O_3 enhancements. Sodemann et al. (2011) analysed cross-polar transport of a large pollution plume originating from Asia during summer 2008 using IASI CO retrievals. IASI was able to detect features and structures of the plume consistent with in-situ aircraft data, and provided a useful comparison for evaluating transport-model simulations.

Satellite observations are also useful in evaluating the sources and export of O_3 precursors from mid-latitude regions and their subsequent transport to the Arctic. Tropospheric NO_2 columns measured from Ozone Monitoring Instrument (OMI) have been used to detect enhancements and trends in NO_X emissions due to gas flaring in high latitude (up to 67°N) areas of Russia and North America (Li et al., 2016a). Assessment of a suite of chemical transport models, using OMI tropospheric NO_2 columns for summer 2008, showed a potential overestimate in NO_2 over biomass burning regions in eastern Siberia, with lower biases over European and North American source regions, and model under-estimates over China (Emmons et al., 2015). Monks et al., (2015) exploited limited profile information from Measurement of Pollution in the Troposphere (MOPITT) CO satellite retrievals to evaluate relationships between CO seasonal cycles in the lower and upper troposphere over the Arctic and over mid-latitude source regions. Inter-annual variability in PAN, retrieved by the Tropospheric Emission Spectrometer (TES) instrument over Eastern Siberia for the month of April (2006–2010), was documented by Zhu et al., (2015); a main source of variability was boreal fire emissions at this time of year. More recently, PAN data from TES were used to help characterize Asian influence on exported PAN and downwind O_3 production (Jiang et al., 2016). A temperature-dependent high bias in TES PAN was found at cold temperatures over high latitudes. In Chapter 7, data from satellite instruments, TES and ACE-FTS are used to evaluate modeled O_3 (as well as MOPITT for CO) in the Arctic and Northern Hemisphere.

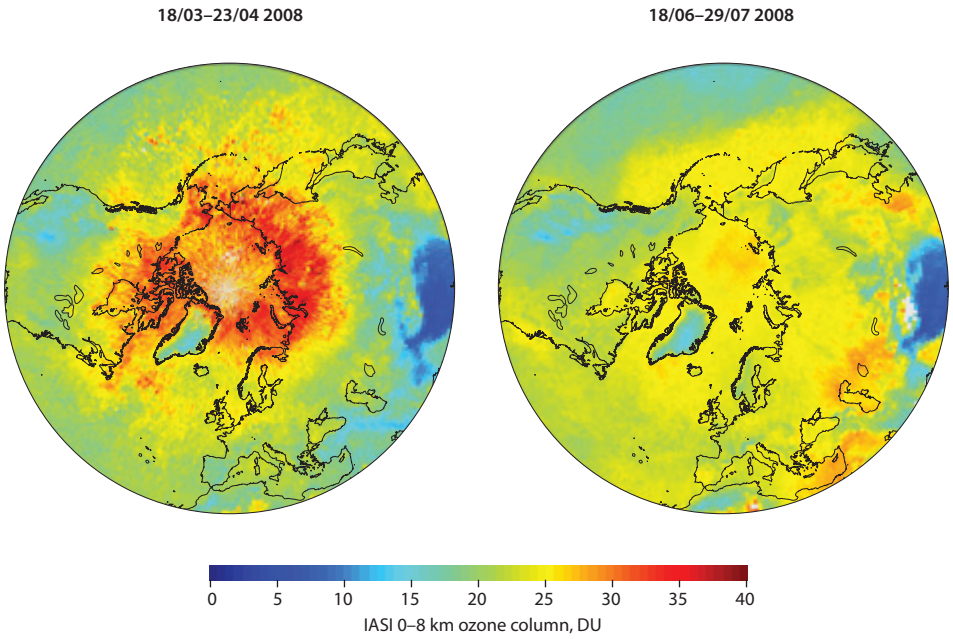

Figure 6.29. Tropospheric (0–8km) ozone partial columns in Dobson Units (DU) measured by IASI in the 2008 spring (left) and summer (right), based on an analysis presented in Pommier et al. (2012). Figure courtesy of the the IASI team at Laboratoire Atmosphères, Observations Spatiales (LATMOS), Sorbonne Université, France. It was made using IASI data retrieved with FORLI-O3 version 20151001 (Boynard et al., 2018).

6.2.4 Observed trends in ozone

Growth in anthropogenic emissions of O_3 precursors since pre-industrial times has led to an increase in tropospheric O_3 throughout the Northern Hemisphere (e.g. Tarasick et al., 2019; Young et al., 2018b). This increase in tropospheric O_3 has contributed to the observed rise in global temperature over the past century, and is likely to have made an important contribution to observed Arctic warming (Shindell, 2007; AMAP, 2015a). Since 1990, the contribution of O_3 precursor emissions has largely shifted from Europe and North America to Asia, causing a change in the global pattern of surface O_3 concentrations (Gaudel et al., 2018).

6.2.4.1 Observed trends in surface ozone and precursors

Trends in surface O_3 at several Arctic (and near Arctic) stations were determined by applying the Mann-Kendall test and Sen's slope methodology (Salmi et al., 2002) to yearly and seasonally averaged concentrations. The results are presented in Table 6.3. Trends from these stations are also used to evaluate model trends in Chapter 7 (Section 7.3.1.2). The station locations are provided in Chapter 5 Appendix Figure A5.1.

Table 6.3. Annual and seasonal trends (in %/y) in surface O_3 at Arctic and near-Arctic measuring stations (see Figure A5.1) for the range of years indicated. Sign = significance level, in other words, the probability that the data have a random distribution. With a significance level of >0.1, there is a more than 10% probability that the observed trend is just the result of random variations; therefore, these trends are considered not statistically significant and are not discussed in the text. DJF = December–February; MAM = March–May; JJA = June–August; SON = September–November. Data were obtained from EBAS (Data ref. 6.3) and, in the case of Alert, from the Canadian Air and Precipitation Monitoring Network (CAPMoN; Data ref. 6.4). A more extensive analysis of Arctic tropospheric O_3 trends is presented in Law et al. (2023).

Site	%/y	Sign.	DJF	Sign.	MAM	Sign.	JJA	Sign.	SON	Sign.	Period
Alert	0.06	>0.1	0.40	0.001	-0.04	>0.1	0.01	>0.1	0.01	>0.1	1992–2018
Denali	0.12	>0.1	0.58	0.1	-0.09	>0.1	-0.24	>0.1	0.47	>0.1	1998–2014
Esrange	0.10	>0.1	0.23	>0.1	-0.03	>0.1	-0.07	>0.1	0.10	>0.1	1996–2018
Hurdal	-0.31	>0.1	0.13	0.1	-0.35	>0.1	-0.62	>0.1	-0.21	>0.1	1997–2015
Karasjok	0.11	>0.1	0.28	>0.1	0.57	>0.1	0.01	>0.1	0.03	>0.1	1997–2009
Karvatn	-0.34	>0.1	-0.17	>0.1	-0.50	0.05	-0.33	>0.1	-0.29	>0.1	1989–2018
Pallas	-0.26	0.05	-0.29	>0.1	-0.22	>0.1	-0.40	0.01	-0.37	0.05	1995–2019
Summit	-0.40	0.05	-0.41	0.1	-1.02	0.01	0.09	>0.1	-0.34	0.05	2000–2019
Tustervatn	0.38	>0.1	0.33	0.1	0.21	>0.1	0.03	>0.1	0.23	>0.1	1992–2018
Utqiaġvik	0.21	0.05	0.31	0.001	0.35	>0.1	0.17	>0.1	0.20	0.05	1973–2018
Villum Research Station	1.62	>0.1	0.46	>0.1	0.23	>0.1	0.07	>0.1	0.20	>0.1	1996–2018
Zeppelin	0.28	0.05	0.45	0.01	0.28	>0.1	-0.27	>0.1	0.11	>0.1	1989–2018

Summit and Pallas exhibit significant negative trends of -0.40%/y and -0.26%/y, respectively. There are significant negative trends at both sites for all seasons except winter and spring for Pallas and summer for Summit. The general negative trend at Summit, a site in the free troposphere, is reported in this assessment for the first time, based on data collected from 2000–2019. Gaudel et al. (2018) examined trends from 2000–2014 only, and reported no significant trends at Summit other than a decrease in spring. Pallas is located downwind of Europe, where anthropogenic emissions have been declining.

There are significant positive trends at Utqiaġvik (Alaska) and Zeppelin (Svalbard): 0.21%/y and 0.28%/y, respectively, based on long 30–40-year data records. These positive trends appear to be mainly due to increases during winter (DJF) at Zeppelin while Utqiaġvik also has positive trends in autumn (SON). The analysis by Gaudel et al. (2018) also reported positive trends in Alaska but only in winter. The trend found in this assessment for the winter season at Alert is +0.4%/y using 1992–2018 data. Sharma et al. (2019) analysed a longer timeseries of Alert O_3 data from 1980 to 2013, and found a lower positive trend during the winter of 0.14%/y. However, since the two trends are determined by different statistical methods, they are not directly comparable. This illustrates the sensitivity of trend analysis to the chosen methodology and record length.

O_3 observations at Villum and Esrange are shown in Figure 6.30 to illustrate the different long-term seasonal behavior at these sites (see also earlier trend discussion, and seasonal cycles in Figure 6.27). Significant inter-annual variability is apparent, as well as variations in the magnitude of the seasonal cycle from year to year. Analysis of surface O_3 data in northern Sweden over the period 1990–2013, combined with modeling, suggests a shift in the O_3 seasonal cycle, with the summer O_3 maximum occurring earlier in the year (Andersson et al., 2017). Changes were attributed to rising hemispheric background concentrations, meteorological variations and European emissions reductions. These results are in line with seasonal cycle shifts first reported based on surface site data at mid-latitudes (e.g. Parrish et al., 2013).

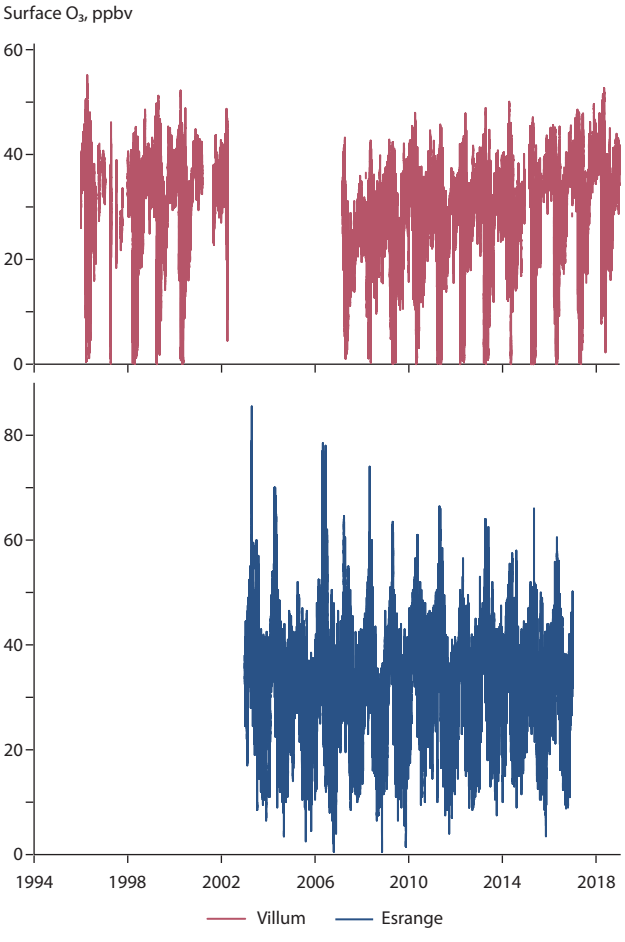

Figure 6.30. Timeseries of surface O_3 at Villum Research Station, northern Greenland (top) and Esrange, northern Sweden (bottom) (Data ref. 6.3).

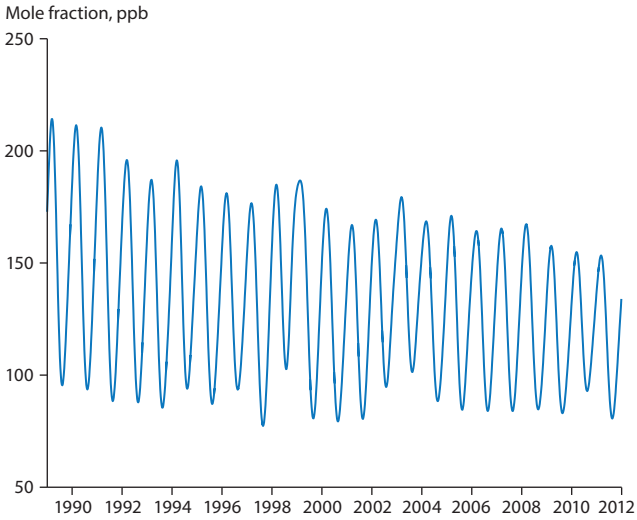

Figure 6.31. Atmospheric CO mole fraction at Utqiaġvik, Alaska, between 1989–2012. The data was smoothed using wavelet transformation, and periods with less than six months of data were removed. From Mackie et al. (2016).

Reported trends in O_3 precursors, notably CH_4, CO and VOCs, may also provide insights into factors driving trends in Arctic tropospheric O_3. Mackie et al. (2016) showed decreasing CO trends of about -1.0 ppb/y at three Arctic surface sites, covering the period 1989–2012, with the largest statistically significantly trends in winter and spring, and a reduced amplitude in the seasonal cycle at Utqiaġvik, Alaska driven by a decrease in seasonal maxima (see Figure 6.31). Associated modeling attributed observed changes to decreasing anthropogenic CO emissions in Europe and North America. NMHCs also show decreasing trends based on Greenland firn, ice-core, and Arctic surface-site data but with decreases often starting in the 1970–1980s (Helmig et al., 2014). In contrast, CH_4 increased at sites in the Arctic with changes anti-correlated with CO (Lawrence and Mao, 2019) (see also Section 6.3).

6.2.4.2 Vertical profile ozone trends

Long-term data on the vertical distribution of tropospheric O_3 in the Arctic is limited and confined to the European and North American Arctic. Ozonesondes are the only source of data that can currently be used for long-term trend analysis in the Arctic. Tarasick et al. (2019) provides a thorough review of available data and their accuracies. AMAP (2015a) reported positive trends of O_3 in the upper troposphere for the European Arctic for 1996–2010 (Hess and Zbinden, 2013) and identified positive trends at levels 500 hPa and above in ozonesonde data for Scoresbysund on the east coast of Greenland for the period

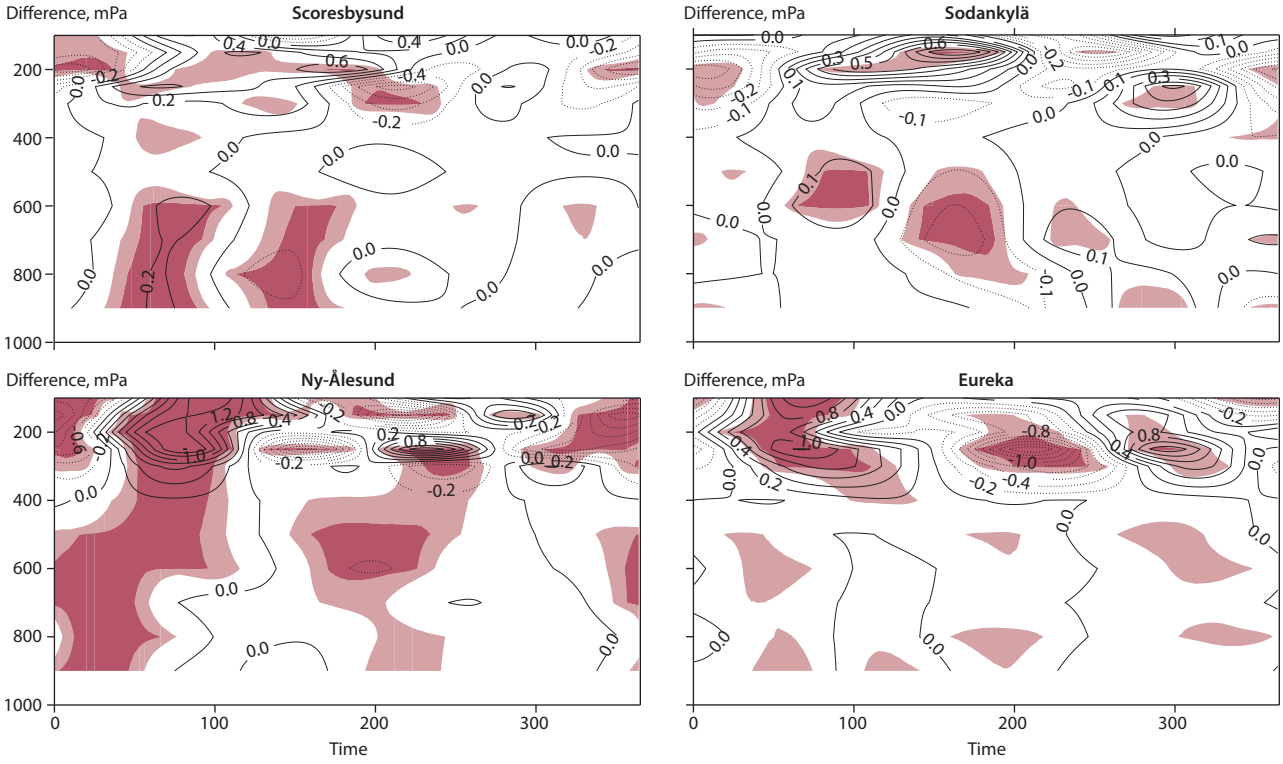

Figure 6.32. The difference between average O_3 seasonal cycles in partial pressure (millipascals, mPa) between the periods 2012–2007 and 1995–2000, as a function of pressure level and day of the year. Note that 0.1 mPa corresponds to about 2 ppbv at 500 hPa and 1 ppbv at 1000 hPa. Shaded regions are where the anomalies are statistically significant at the 99% and 95% confidence intervals. Data source: Figure 11 from Christiansen et al. (2017), which also provides details about the data analysis.

1989–2013. In an extended study, Christiansen et al. (2017) analysed trends and annual variability in ozonesonde data at nine Arctic sites (including Scoresbysund) for the period 1990–2015, with record length depending on location. Significant increases in free tropospheric O_3 were observed up to around 2005, followed by decreases at European Arctic sites. In contrast, at Eureka, in the Canadian Arctic, increases were found from 2008 onwards. Christiansen et al. (2017) also reported evidence for a possible shift in the O_3 seasonal cycle in the free troposphere, with the late May/early June summer maximum occurring earlier in the year. This is illustrated in Figure 6.32, where stations, except for Eureka, show earlier peak O_3 in the free troposphere, although the anomalies vary with altitude between stations. This is in line with the analysis of northern Scandinavian surface O_3 data (Andersson et al., 2017). Eureka, on the other hand, shows weak signals, but together with Alert and Resolute (not shown) there are indications of O_3 increasing in the summer and decreasing in the autumn. As noted by Christiansen et al. (2017) and other studies, regional differences are apparent in changes to O_3 observed in the Arctic. While further analysis is needed, increased springtime photochemical production resulting from rising Asian precursor emissions since the 2000s, and decreasing summertime photochemical production due to decreasing European and North American emissions, are likely to be playing a role. Changes in the large-scale circulation, for example, influencing the transport of O_3 from the stratosphere, may also be contributing, as well as changes in natural emissions such as those from boreal fires.

The length of available records and datasets analysed are important factors when assessing trends, and may lead to different results. In contrast to Christensen et al. (2017), who analysed longer ozonesonde records, Bahramash Shams et al. (2019) combined data from ozonesondes and the Microwave Limb Sounder (MLS) on the Aura satellite for Alert, Eureka, Summit and Ny-Ålesund for the period 2005–2017. They found significant annual mean trends in partial tropospheric O_3 columns at Ny-Ålesund, with negative trends in tropospheric O_3 in the spring and positive trends in summer. As noted above, further analysis of surface and vertical tropospheric Arctic O_3 trends, and comparison with AMAP model results, is discussed in Law et al. (2023).

6.3 Methane

6.3.1 Introduction

The growth rate of CH_4 concentration has increased since 2007, with further increases between 2015–2020. The annual amplitude is large but has decreased over the last three decades. New data from high-resolution measurements also show high variability in concentration within the same season.

Measurements of isotopic ratios suggest a change in the relative proportions of emissions from biogenic, thermogenic and pyrogenic sources of CH_4, or a decline in the atmospheric sink of methane, or both. The decreasing annual amplitude also suggests a shift in the relative proportion of the emissions, indicating an increase in biogenic emissions. Further studies involving the high-resolution measurements and back trajectory analysis are needed to confidently explain the increasing growth rate.

It is still not clear what the primary drivers of the variability are but early studies suggest natural emissions can cause

the observed late summer/early fall peaks. High-resolution atmospheric concentration measurements have become more abundant lately and the coming years of data can be used to reveal the development of the local Arctic CH_4 sources. Additional studies are needed to identify the causes of the individual peaks.

Methane is the second most important anthropogenic greenhouse gas, after carbon dioxide (CO_2), contributing to about 20% of radiative forcing from long-lived greenhouse gases. The change in methane concentration from 700 to 1877 ppb (nmol/mol) between 1850 and 2019 represents an increase of 168% since the start of industrialization. The balance of surface sources and sinks determines the global methane budget. Surface sources can be biogenic (from wetlands, lakes, agriculture, waste/landfill, permafrost); thermogenic, (from fossil fuel usage and natural seeps); pyrogenic (from burning of biomass and biofuels); or mixed (from hydrates, other geological origins). Dominant sinks include methane oxidation by the hydroxyl radical (OH) (Saunois et al., 2016b). Long-term, systematic measurements of atmospheric CH_4 from a well-calibrated network of air-sampling sites are essential to assess trends, sources and sinks of atmospheric CH_4 in the Arctic.

6.3.2 Significance of methane for the Arctic and new observations since 2015

Atmospheric CH_4 monitoring has taken place at several Arctic sites since the early 1980s using discrete flask sampling followed by gas chromatography analysis (AMAP, 2015b). Data compatibility and accuracy are ensured through participation in the World Meteorological Organization (WMO) Global Atmosphere Watch (GAW) program. However, over the past five years an increasing number of stations have initiated measurements with monitors, which can measure at hourly resolution. As described in Section 5.3, the Integrated Carbon Observation System (ICOS) network was established in 2015 and has been growing ever since, providing uniform calibrated measurements of atmospheric CH_4 concentrations and CH_4 fluxes at some Arctic sites. Recently, the ICOS atmosphere network has been recognized as a contributing network to WMO GAW for greenhouse gases. Data from the ICOS stations, and several data products, can be downloaded from the ICOS's Carbon Portal. The evolution of CH_4 concentrations in the network, including five stations above 60°N, is shown in Figure 6.33.

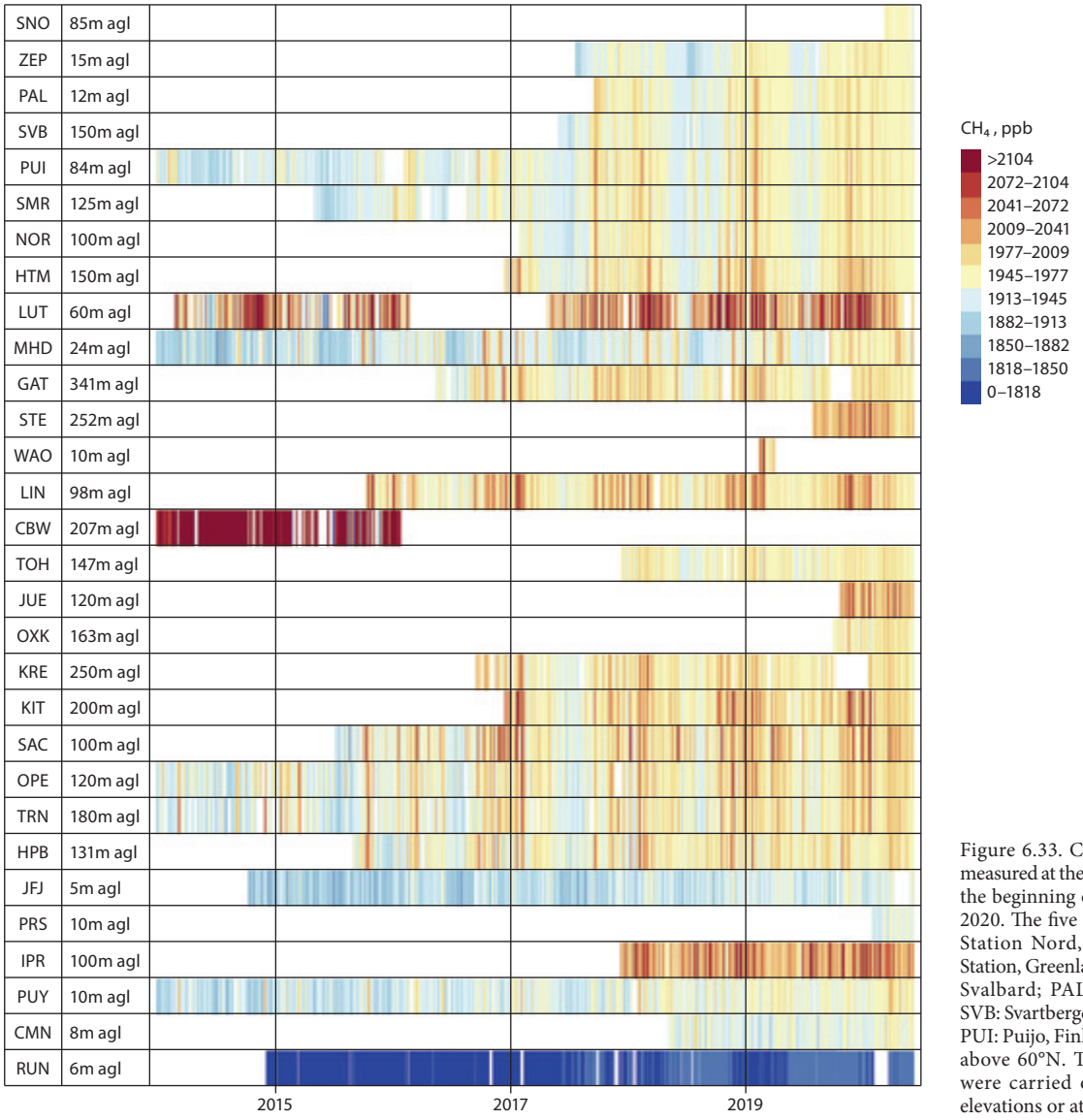

Figure 6.33. CH_4 concentrations measured at the ICOS stations from the beginning of 2014 to summer 2020. The five top stations (SNO: Station Nord, Villum Research Station, Greenland; ZEP: Zeppelin, Svalbard; PAL: Pallas, Finland; SVB: Svartbergen, Sweden and and PUI: Puijo, Finland) are all located above 60°N. The measurements were carried out either at high elevations or at coastal sites.

6.3.3 Trends in concentrations of methane in the Arctic

Methane emissions mix through the troposphere on timescales shorter than the globally averaged atmospheric lifetime (AMAP, 2015b), thus the average trend in atmospheric concentration is roughly the same everywhere on Earth. While global concentrations have increased at varying rates, the mechanisms behind these variations are still not fully understood. Between approximately 2000–2005 there was no growth in global CH_4 mixing ratios, including in the Arctic atmosphere (Figure 6.34a and Figure 6.34b) but from about 2007, the growth increased and then accelerated from 2015 (Nisbet et al., 2019) till today (See Figure 6.34b). Explanations for the stabilization and increases encompass changes in tropical wetlands, livestock, fossil fuels, biomass burning, and the methane sink. Contradictions in these hypotheses have arisen because our current observational network cannot clearly link recent methane variations to specific sources (Nisbet et al., 2019; Turner et al., 2019).

Lawrence and Mao (2019) examined long-term trends in atmospheric CH_4 mixing ratios at Summit, Alert, Utqiaġvik and Tiksi, and concluded from transect calculations and correlations between CH_4 and CO that long-range transported CH_4 contributed to the increasing trend of CH_4 in the Arctic atmosphere. This was also concluded by Platt et al. (2018); however, Platt et al., also suggest that hotspots of Arctic emissions potentially add to the growing trend. Lawrence and Mao (2019) found a decrease in the amplitude of the average seasonal variation of the CH_4 concentration, indicating an increase in local sources in the Arctic summer that contributed to a rise in the summer mean concentration.

Figure 6.34c shows a decreasing change in the amplitude of the seasonal variation from 1985–2020 at Utqiaġvik, supporting the findings of Lawrence and Mao (2019). Nisbet et al. (2019) analyzed timeseries of CH_4 mole fraction and the $^{13}C/^{12}C$ isotopic ratio from 2000 to 2017 and the analysis showed the isotopic ratio has changed, now trending negative for more than a decade. They suggested that the causes of methane's recent mole fraction increase are therefore either a change in the relative proportions (and totals) of emissions from biogenic, thermogenic and pyrogenic sources, or a decline in the atmospheric sink of methane, or both. However further studies are needed to investigate the causes of the decreasing trend.

6.3.4 Concentrations, seasonal cycles and origin

Figure 6.35 compares annual methane cycles from 2012 to 2020 at two remote Arctic sites (Summit and Zeppelin) with two regionally influenced Arctic sites (Pallas and Tiksi). The figure shows the seasonal variation in CH_4 concentration extended from the variation plotted in the assessment report from 2015 (AMAP, 2015b). The characteristics observed during the eight-year period are relatively consistent at each of the remote background sites, showing an annual CH_4 cycle with an amplitude of about 40–50 ppb from the minimum observed in July/August to the maximum observed in February, with a 'shoulder' in early November. The seasonal variation was likely caused by the transport of polluted air masses from lower latitudes during winter, and a stronger photochemical OH sink during summer, when the transport

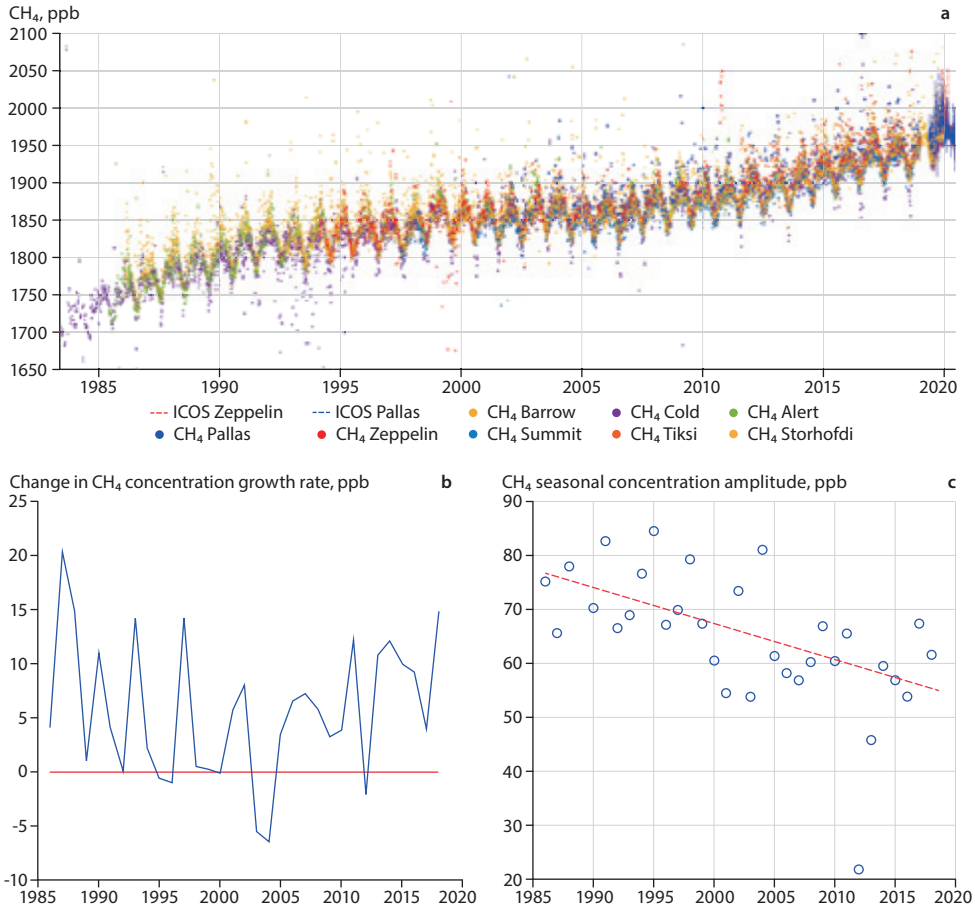

Figure 6.34. (a) CH_4 concentrations measured using flask sampling at eight Arctic sites, including two sites in the ICOS network (Pallas and Zeppelin), plus measurements made using monitors at the ICOS sites. (b) Changes in the CH_4 concentration growth rate using the data from Utqiaġvik, which has the longest CH_4 concentration timeseries of these Arctic sites. (c) The CH_4 seasonal concentration amplitude between 1985–2020, using data from Utqiaġvik. The line shows the least square fit ($R^2 = 0.28$)

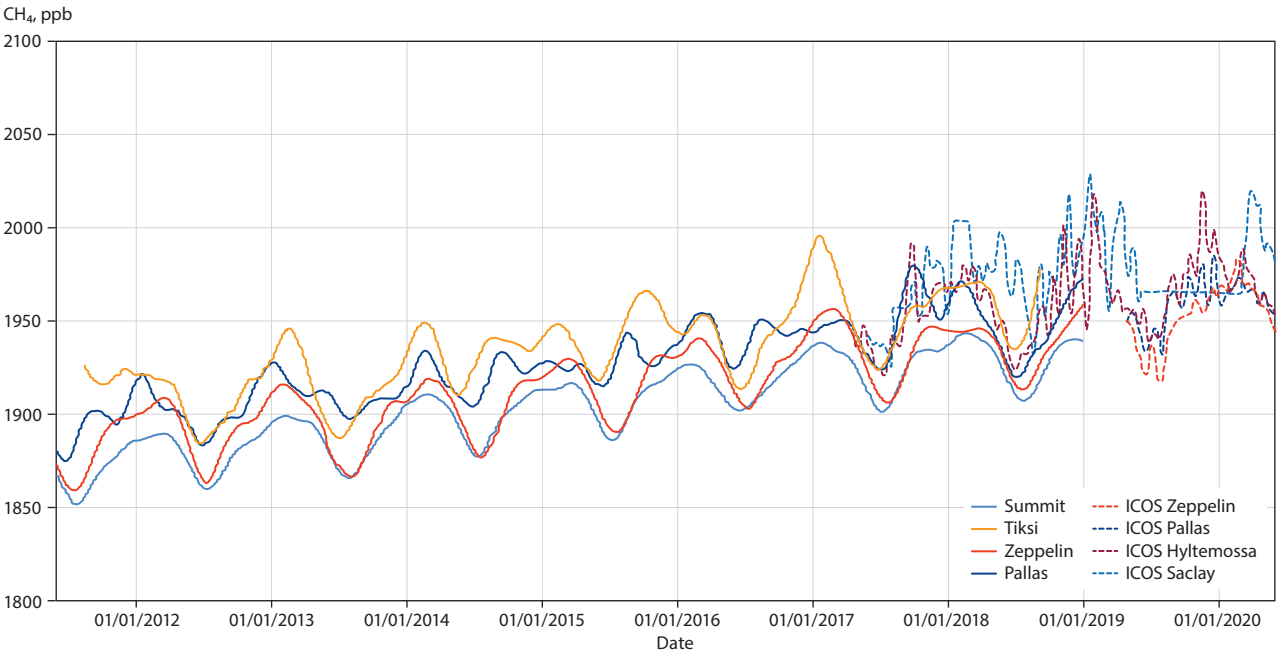

Figure 6.35. CH_4 concentrations measured between 2012–2020. The solid lines show data gathered using discrete flask sampling at two Arctic remote sites (Summit and Zeppelin) and at two regionally influenced sites (Tiksi and Pallas). The dashed lines show continuous (1-hour mean) sampling of CH_4 using online monitors between 2019–2020 at Zeppelin and Pallas, and 2017–2020 at two lower-latitude ICOS stations (Hyltemossa and Saclay).

from lower latitudes also decreases. Lower-latitude ICOS CH_4 concentration data from Hyltemossa in Sweden and Saclay in France (Figure 6.35) show, in general, higher concentrations in winter and summer but there is less difference between summer and winter for Saclay, probably due to there being less difference in photochemical removal between the summer and winter seasons.

The annual methane cycle at the two regionally influenced sites also shows a maximum during winter, but this is elevated relative to the remote sites, probably due to the latter's closer proximity to anthropogenic source regions. An additional feature in the annual methane cycle of the regionally influenced sites is the presence of a distinct secondary peak in late summer. AMAP 2015b ascribed this secondary peak to emissions from wetlands, and it is likely that this peak, as well as the shoulder occurring slightly later at the remote sites, originates from natural emissions in late summer or early autumn (Pirk et al., 2017). These seasons are referred to as edge seasons in AMAP's 2015 assessment. However, higher-resolution concentration measurements can possibly reveal more details that can be used to identify sources or sinks. Data from the last year (2020) in Figure 6.35 are taken from the ICOS portal; the data measured with an online monitor gives a better time resolution (hourly measurements) revealing several peaks during the fall at Pallas and several smaller peaks at Zeppelin. Comparing lower-latitude data to that from Pallas and Zeppelin (Figure 6.35) shows similar peaks in the fall season; however, the high-resolution data also reveal a clear peak in the summer at the Arctic sites which possibly originates from local Arctic sources. The high-resolution data from the Arctic stations only covers one season but the coming years of data will reveal how local Arctic CH_4 sources develop. Additional studies are needed to identify the causes of the peaks.

6.4 Trends in cloud properties based on satellite observations

6.4.1 Assessment of trends based on satellite-based climate data records

Changes in clouds can be considered as one of the harbingers of climate change, as clouds respond to the underlying changes in surface properties, atmospheric circulation and pollutant concentrations. Understanding the climate trends in cloud properties is therefore useful for understanding how the Arctic climate system is responding to changes in greenhouse gas emissions, including SLCFs, and the associated aerosol-cloud interactions. Figure 6.36 shows the trends in total cloud fraction, in percentages per decade, from the four satellite-based climate data records (CDRs) spanning the 35 years between 1982–2016, introduced earlier in Section 5.5.2. It is difficult to identify a pattern that holds across all CDRs, indicating the challenges that remain in cloud property retrievals from passive satellite sensors. The two regions where trends in all CDRs agree are the northeast Atlantic and the Barents/Kara sea sectors of the Arctic, albeit with different magnitudes. The total cloud fraction is decreasing over the first area, while it is increasing over the latter. However, over other regions, either the magnitude alone or both the magnitude and the sign of trends are different in the four CDRs, or the trends are not statistically significant.

An interesting feature that holds across all three AVHRR-only based CDRs (i.e. CLARA-A2, PATMOS-x and ESA Cloud CCI) is the statistically significant decreasing cloud fraction over the Fram Strait. This region is an important pathway for the export of sea-ice out of the Arctic (Min et al., 2019). Any change in cloudiness would potentially influence the rate of sea-ice export, due to change in the cloud longwave forcing at the surface, which could potentially precondition the seasonal wintertime sea-ice recovery (e.g. Letterly et al., 2016).

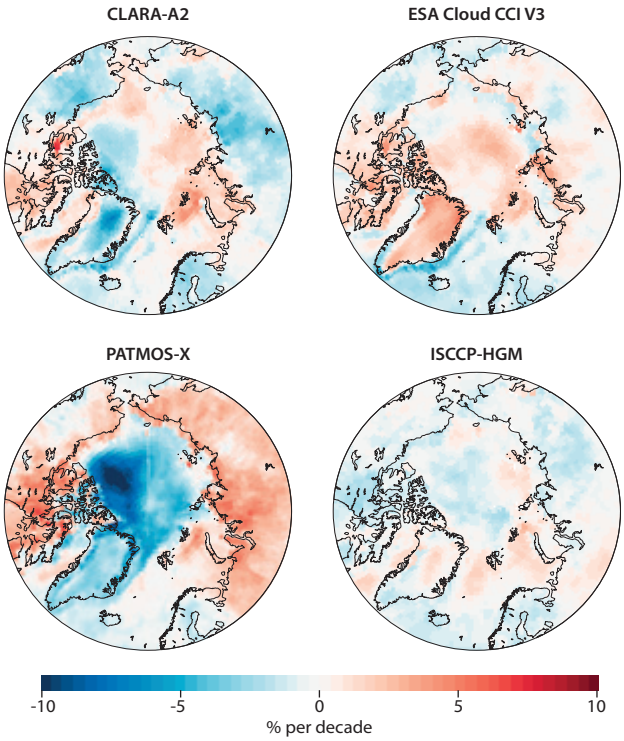

Figure 6.36. Trends in total cloud fraction (in % per decade) based on four satellite-based CDRs between 1982–2016. Only trends that are statistically significant at 90th confidence percentile are shown.

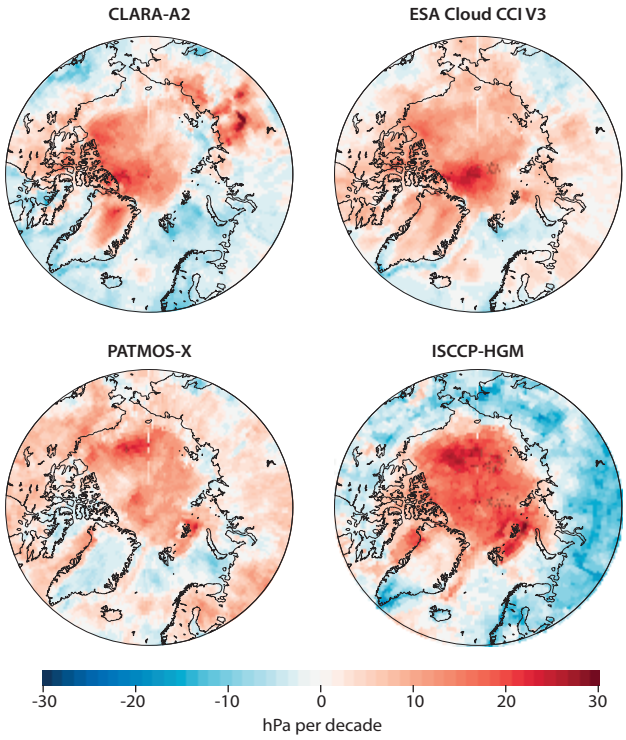

Figure 6.37. Trends in cloud-top pressures (in hPa per decade) in the four CDRs between 1982–2016.

Figure 6.37 shows the trends in cloud top pressures (CTP). In the Arctic, CTP is sensitive to the changes in boundary-layer processes, being influenced by trends in temperature inversions, surface properties and vertical mixing in the boundary layer. CTPs are also influenced by changes in atmospheric circulation, especially the transport of heat and moisture. A striking pattern that holds across all four CDRs is the increase in CTPs across the majority of the Arctic Ocean, suggesting a decrease in cloud-top altitudes. It is difficult at present to conclude if this trend is physical or a retrieval artifact. The retrievals of CTPs depend heavily on the quality of temperature profiles from the reanalyses. In general, the passive retrievals have a tendency to overestimate cloud-top altitudes. But as the quality of temperature profiles has likely improved every decade, due to the availability of more and better sensors, it is also likely that in the last 10–15 years, the assignment of cloud-top altitude has become more accurate, reducing the overestimations and thereby artificially introducing the trends seen in Figure 6.37.

6.4.2 Seasonal aspects

In the context of AMAP, investigating and monitoring seasonality in the trends of cloudiness is of scientific interest for a number of reasons. In the polar winter, when the majority of the Arctic Ocean is locked by ice, pollutant transport is the primary source of cloud nuclei. At the same time, this transport, which in turn responds to large-scale circulation patterns, is also responsible for shaping the thermodynamical conditions needed for cloud processes. In the polar summer, as the sea-ice retreats, marine biogenic and sea-salt aerosols become additional sources of cloud nuclei (Chang et al., 2011; Heintzenberg et al., 2015; Dall'Osto et al., 2017). While it is expected that the changes in large-scale circulation and sea-ice would have a first-order impact on the trends in cloudiness, aerosol-cloud interactions are also important in the Arctic, where the amount of nuclei is generally low, increasing the susceptibility of clouds to changes in pollutant concentrations.

Figure 6.38 shows the seasonal trends per decade in the total cloudiness from the CLARA-A2 CDR. The most noticeable feature is the strong increasing trend in cloudiness during boreal

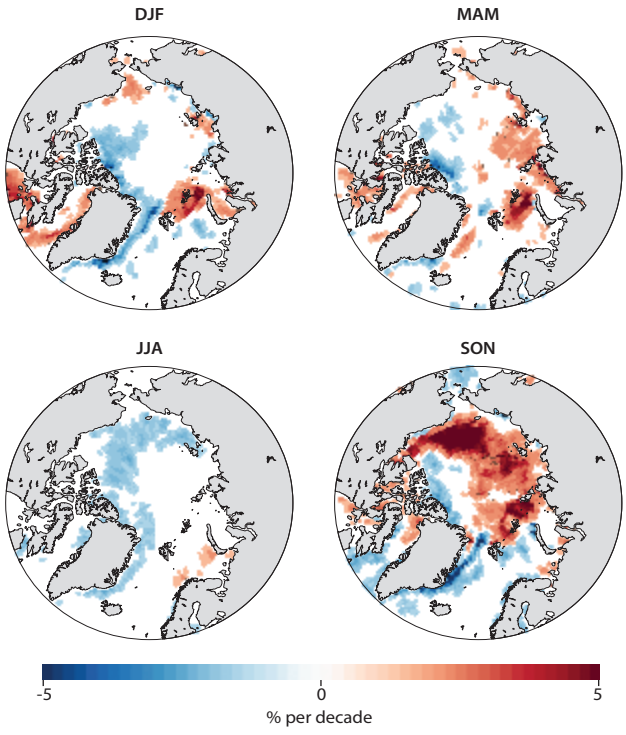

Figure 6.38. Seasonal trends in total cloud fraction (in % per decade) based on CLARA-A2 CDR data between 1982–2016.

autumn in the Laptev, East Siberian, Chukchi and Beaufort Seas. It is to be noted that the other CDRs also show similar, statistically significant trends over these regions. These are regions where the sea-ice is diminishing strongly (Devasthale et al., 2020). A number of studies have shown that the correlation between decreasing sea-ice and increasing cloudiness is strong over this region, which has been explained mainly by changes in the thermodynamical conditions as more moisture is being made available due to the loss of sea-ice (Schweiger et al., 2008; Kay and Gettelman, 2009; Eastman and Warren, 2010; Vavrus et al., 2011; Liu et al., 2012a; Wu and Lee, 2012; Devasthale et al., 2020).

In the late winter and spring, a statistically significant increase in cloudiness is also observed in the inner Arctic, in the Barents and Kara Seas. This is also the region where the winter and springtime transport of not only heat and moisture, but also of pollutants from the mid-latitudes, is commonly observed (Stohl, 2006; Brock et al., 2011; Coopman et al., 2016; Johansson et al., 2017b; Thomas et al., 2019b).

The decreasing cloudiness in the Fram Strait, mentioned earlier in Section 6.4.1, is mainly observed in the autumn and winter months. Over the same region, the sea-ice has a decreasing trend during the same months. The contradictory relationship between sea-ice and cloudiness over two regions is worth noticing. In the Pacific sector, cloudiness is increasing while the sea-ice is decreasing, and in the Fram Strait both the sea-ice and cloudiness are decreasing. In the summer months (July–August) there is a slight decreasing trend in cloudiness over the Pacific sector of the Arctic Ocean. It is to be noted that the role of pollutant aerosols (e.g. Browse et al., 2014; Wang et al., 2018), if any, in influencing the trends in cloudiness has not yet been studied sufficiently to draw robust conclusions valid for the entire Arctic Ocean.

6.5 Conclusions and recommendations

6.5.1 Particulate matter

Our understanding of the surface concentrations of aerosols in the Arctic, their seasonal variation and trends has improved considerably since the first AMAP report on BC climate effects in 2011, and can now be considered as good. Several permanent observatories measure aerosol species, including particulate sulfate and BC. Longer-term trends now clearly show that BC concentrations have stagnated in the past 10-plus years, after decreasing for decades. Aerosols have, in general, become less acidic, owing to the decrease of particulate sulfate. Ammonium is also decreasing, while nitrate increases. These changes can be due to changed emissions but can also result from changing atmospheric chemistry as the mix of chemical species changes. This concerns all constituents that are converted from gases to particulate matter (secondary aerosols). Mass concentrations of primary aerosols, such as BC and mineral dust, are not influenced by changed atmospheric chemistry.

Clear trends for the haze and summer seasons are emerging. During the haze period from fall through early spring, fewer particles in the accumulation mode (100–500 nm; typical of Arctic haze) are seen, and the overall scattering by the aerosol population decreases. Arctic aerosol in this season remains dominated by anthropogenic sources. By contrast, in summer, the numbers of accumulation- and coarse-mode particles (>1 μm) increase, which simultaneously increases the overall scattering by the aerosol population. The summer fraction of aerosols is becoming more dominated by particles from natural sources. In particular, contributions from directly emitted sea salt (>1 μm) and fires are rising. Methanesulfonic acid, which is formed from gases emitted by phytoplankton, has increased in some locations across the Arctic in spring and summer over the past ten years. This contributes to the marked increase in accumulation-mode particles at the surface. Long-term observations to determine particle-size distribution and optical properties are needed to fully understand the ongoing changes and their potential effects on climate. Greater numbers of scattering particles in summer will reflect more sunlight, while increased concentrations of particles in the size range of CCN (accumulation mode) will change cloud properties and their radiative effects.

There is presently a lack of observations for organic aerosols. However, these data are needed for apportionment of particles to natural and anthropogenic sources. It would also help to improve understanding of mineral dust, which is strongly implicated in radiative forcing; with current data it is only possible to partially quantify the importance of this effect. There is a clear need to complement ongoing surface-based observations with additional monitoring of organic and mineral dust aerosols.

Moreover, information from the atmosphere aloft, beyond the reach of surface-based observatories, is only captured sporadically in short-term and spatially limited aircraft campaigns. Systematic and vertically resolved data that clearly show the evolution of any single aerosol component in the free troposphere is not available. This is a particular constraint for quantifying the impact of biomass-burning emissions in the Arctic or transported from outside the region. The same is true for the transport of dust and volcanic ash plumes to the Arctic. The aerosol optical depth, which is retrieved from ground-based AERONET and satellite observations, represents the combined aerosol load over the full atmospheric column, and indicates that the particle load is increasing. However, the information is not detailed enough to distinguish between aerosol types and their vertical distribution. Lidar observations provide more detailed information on the vertical particle distribution, and the sizes and shapes of individual aerosols. However, there are very few lidar instruments being operated systematically in the Arctic (one example is at Ny-Ålesund's AWIPEV[1] station). Enhancing the ground-based remote-sensing network would greatly improve knowledge of vertical aerosol layers. There is a clear need to both enlarge the ground-based aerosol remote-sensing network and develop satellite-retrieval methods further because only remote sensing can deliver the continuous observations required to better quantify impacts from forest fires, mineral dust and volcanic ash.

[1] Operated by the French Polar Institute (IPEV) and its German counterpart, the Alfred Wegener Institute for Polar and Marine Research (AWI)

6.5.1.1 How natural sources contribute to aerosol emissions and concentrations

A clear pattern is emerging from currently available data of the summer aerosol fraction being dominated by particles from natural, rather than anthropogenic, sources. However, deducing trends in concentrations of natural aerosol components is currently a challenge for two main reasons: a) longer-term observations are still targeted at capturing changes in anthropogenic contributions, and b) natural emissions are changing at a magnitude that is only slightly above the natural variability. More dedicated efforts are needed to monitor natural aerosol components.

So far, longer-term observations of MSA show that concentrations are highly variable but that there is potentially an increase in particulate matter MSA due to the observed increase in marine microbial emissions. Sea salt has been found to increase, which could be due to retreating sea-ice in summer. Importantly, though, it has been found to be mainly related to changed atmospheric transport patterns with enhanced contributions from the North Atlantic towards Svalbard. Dust originating from high latitudes has recently been identified as an important contributor to radiative forcing in the Arctic, but other than ice-core and lake-sediment records, no long-term, systematically recorded atmospheric observations exist. Forest fires contribute a mixture of natural and anthropogenic emissions because they can be triggered naturally or by human activity. This assessment considers them as mainly natural. An increase in emissions has been observed, particularly in the recent past. However, the available data cannot yet answer the question of whether BC concentrations are becoming enhanced due to increased emissions from fires.

6.5.1.2 Measurement gaps exist that need to be filled

The locations of surface observatories are mostly adequate, but large measurement gaps exist in the eastern Arctic. In terms of data on chemical composition, which enables the attribution of concentrations and climate impacts to specific sources, there is a lack of observations targeted at natural aerosol components such as sea spray, MSA and mineral dust. The complex mixture of organic aerosols can reveal detailed information on local versus long-range and natural versus anthropogenic contributions but organic aerosol is not well characterized around the Arctic. Enhanced isotopic analysis of nitrogen and sulfur could put better constraints on natural versus anthropogenic sources and climate change-induced shifts.

Valuable information on sources, atmospheric processes and climate effects is also contained in data on aerosol size distributions. Only a few of the permanent observatories measure this on a continuous basis. Systematically equipping observatories to measure aerosol size distributions would therefore be beneficial. Information on the vertical distribution of aerosols remains sparse; enhancing the ground-based remote-sensing network and putting more effort into developing algorithms that can retrieve detailed aerosol information from ground-based and space-borne remote sensing could help to close this knowledge gap. In terms of analysis, very little research has been undertaken to explore the linkages between observed cloud changes and changes in the aerosol population. Clouds are a key player for the Arctic radiative balance, and models do not yet adequately represent the interaction between aerosols and clouds.

6.5.1.3 Recommendations

Natural aerosol components

- Develop the capacity for collecting observations of aerosols to enable the evaluation of changes in the occurrence of natural Arctic aerosol compounds – which might be affected by climate change throughout complex feedback mechanisms. Components of particular interest include sea spray, high-latitude dust (including old deposits of volcanic sediments that have become resuspended) and biological emissions, such as DMS and MSA.

BC

- Continue monitoring activities of BC mass concentrations at Arctic sites.
- Establish systematic monitoring of BC in snow and precipitation at more Arctic sites to better understand the influence of forest-fire emissions, and intensified shipping and industrial activities on BC. With regard to anthropogenic activities, observational sites should be established close to sites of activity.
- Harmonize measurement techniques to enhance comparability across Arctic sites.

Mineral dust

- Develop facilities to enable identification of dust sources and concentrations for all Arctic regions.
- Promote research into wet and dry particle deposition rates and amounts around the Arctic, including accumulation in snow and ice.
- Promote studies on the effects of dust to improve understanding of, for example, the influence of dust as ice nucleation particles in clouds, on snow albedo reduction, and as a nutrient to ecosystems.

Inorganic aerosol components

- Continue existing monitoring of inorganic aerosol components to understand ongoing changes, such as increasing nitrate, and potential changes in sulfate and ammonium from marine microbial emissions.

Organic aerosol components

- Establish systematic measuring, with a high-temporal resolution, of organic aerosol. Understanding the component species of organic aerosol gives essential insights into the sources – anthropogenic and natural – of Arctic aerosol and how they are shifting as the climate changes.

Aerosol microphysical properties

- Enlarge the network for measuring aerosol particle number size distribution at Arctic stations, especially in the eastern Arctic.

- Record optical properties, in combination with chemical measurements, to understand the drivers (natural and anthropogenic) of the changing atmospheric composition in the Arctic and climate effects.
- Include the monitoring of scattering and absorption at stations where this is not currently undertaken to better quantify climate effects and changes in aerosol sources.
- Increase observations and especially timeseries on CCN and INP number concentrations to enhance understanding of the roles anthropogenic and natural aerosols play in cloud and fog formation, and related climate effects.

6.5.2 Ozone

Tropospheric ozone (O_3) is a secondary air pollutant, which is not directly emitted but is produced photochemically in the atmosphere from precursor emissions produced from anthropogenic and natural sources. It can also originate from the stratosphere and is lost by surface dry deposition or photochemical reactions. Small, statistically significant trends in O_3 have been determined based on analyses of surface and vertical ozonesonde data. O_3 in the free troposphere increased up to the mid-2000s, and has since decreased at sites in the European Arctic, whereas O_3 increased since the late 2000s at Eureka in the Canadian Arctic. At the surface, certain sites, including Utqiaġvik and Zeppelin, show increasing trends over the last 30–40 years, with statistically significant trends especially in the winter (also found at Alert), whereas other sites, such as Pallas and Summit (a free tropospheric site), exhibit negative trends since the mid-1990s and early-2000s, respectively. Other sites, including Villum and Esrange, show no significant trends. Overall, reported trends vary with location and are influenced by the length of the observation records. Trends in O_3 precursors are available at only a very limited number of sites. Certain precursors show declining surface trends (CO, NMHCs) but CH_4 (an important ozone precursor) is still increasing in the Northern Hemisphere. Meanwhile, information on trends in NO_X and PAN (an important NO_X reservoir) is missing, due to a lack of routine measurements in the Arctic. The seasonal cycle of O_3 at the surface varies across the region, with coastal sites (Utqiaġvik, Villum, Alert) showing a winter or early spring maxima and very low values in the spring due to O_3 loss by halogens, so-called O_3-depletion events. Other sites, located at altitude or inland, (Zeppelin, Summit, Esrange) show maxima occurring in the spring and little or no influence from halogen-induced O_3 loss is observed.

Ozonesonde data exhibits spring maxima at most Arctic sites in the free troposphere. Possible shifts in the observed tropospheric ozone seasonal cycle are reported for the first time at the surface (northern Sweden) and in the Arctic free troposphere. A shift to an earlier summer maximum is reported in the free troposphere in the European Arctic (also seen at the surface), while there are indications of increasing summer and decreasing autumn ozone in the Canadian Arctic. Reasons for these observed trends, and possible changes to the seasonal cycle, have not yet been determined. They may be driven, in part, by declines in precursor emissions, such as NO_X, in North America and Europe, and increases in Asian emissions (at least up to the late 2000s), combined with interannual variability affecting long-range transport and the flux of O_3 from the stratosphere. Improved understanding about the causes of changes in O_3 abundances, including perturbations due to local and remote changes in anthropogenic precursor emissions, requires improved understanding about processes responsible for O_3 production and loss in the troposphere. Improved assessment of the contribution from CH_4 oxidation is also needed.

6.5.2.1 Contribution of natural sources to emissions and concentrations

Tropospheric O_3 is formed from the photo-oxidation of VOCs, CO and CH_4 in the presence of NO_X. As well as there being significant anthropogenic sources of these ozone precursors, there are also important natural sources, such as boreal fires, lightning, vegetation and transport from the stratosphere, all of which show marked seasonal and interannual variations. Photochemical reactions involving halogens and dry deposition are important O_3 sinks but remain poorly quantified in the Arctic. Uncertainties remain with regard to the contribution of anthropogenic, relative to natural, sources to the Arctic O_3 budget, including temporal and spatial variations at the surface and in the free troposphere. Understanding of how natural sources are changing in response to climate change is also highly uncertain.

6.5.2.2 Capacity for measuring ozone needs to be improved

Current observations are insufficient to capture anticipated changes in tropospheric O_3 due to changes in anthropogenic and natural sources and sinks. Tropospheric O_3 is a secondary pollutant that is influenced by a range of complex chemical and dynamical processes. Long-term monitoring of atmospheric composition at existing stations is essential for accurately determining O_3 sources and sinks, seasonal cycles and trends and needs to be continued and integrated into a Pan-Arctic observation network building on, for example, AMAP, IASOA, and WMO GAW. Standardization of measurement techniques used at existing and new sites is required. At present, only a very limited number of stations provide long-term monitoring of surface O_3 and O_3 vertical profiles (ozonesondes, lidar) in the Arctic. In many cases, records are not continuous and large data gaps exist, especially in the eastern Arctic, and over the Arctic Ocean. Measurements of O_3 and associated species are also lacking at terrestrial locations that may be influenced by local anthropogenic emissions now and in the future. Long-term continuous measurements of ozone precursors (e.g. CO, VOCs/NMHCs) exist at very few surface sites, and long-term records of species important for diagnosing O_3 sources (NO_X, PAN) and sinks, notably halogens, are lacking. Measurements of these additional compounds are needed to: understand changes in O_3 sources and sinks; evaluate model estimates of the O_3 budget; and understand processes influencing seasonal and inter-annual O_3 variability and long-term trends. Understanding clearly how sources are affecting tropospheric O_3 also requires information about vertical Arctic chemical composition, origins and processes. Vertical ozone sonde profiles are only available at a limited number of sites in the western and European

Arctic. Records are often not continuous and measurement techniques vary over time and between sites. Regular profile data are missing in the eastern Arctic. While recent airborne missions have provided important snapshots in different seasons, there has not been a dedicated airborne campaign focusing on process-level understanding since POLARCAT in 2008. Satellite data can provide useful spatial information about O_3 and certain precursors/oxidants, as well as limited vertical information, but more attention is needed to improve retrievals, and understand biases and instrument limitations at high latitudes. The development of new techniques provides opportunities for regular monitoring on new platforms, such as tethered platforms, unmanned aerial vehicles, and measurements on commercial aircraft and shipping.

6.5.2.3 Recommendations

- Initiate collection of more routine data, in addition to maintaining existing measurements for ozone, its precursors and species that are important for studying O_3 sources and sinks in urban/industrial, rural and background locations in the Arctic. This includes NO and NO_2 (not only NO_X), and NO_X reservoir species (e.g PAN, RNO_3, $HOONO_2$), VOCs and CO, as well as species important for diagnosing ozone sinks, in particular, halogens and halogen-containing organic species. Additional ozonesonde profile measurements co-located with radiosonde measurements, particularly in the eastern Arctic, together with more regular vertical profile information on source/sink species are needed.
- Implement the Findable, Accessible, Interoperable, and Reusable (FAIR) principle to measured concentrations of O_3 and its precursors, including source attribution and emission validation, particularly in the eastern Arctic, and for standardized measurement techniques.
- There is an ongoing need to improve understanding of the processes governing ozone production from anthropogenic and natural sources and ozone sinks in the Arctic troposphere, and their representation in models. In addition to routine data, this requires dedicated ground-based and airborne measurement campaigns examining processes at the surface and in the boundary layer/free troposphere across different seasons.
- Promote research to improve understanding of natural emissions and their response to global and Arctic climate warming.

6.5.3 Methane

The concentration of Arctic atmospheric methane has been recorded since the early 1980s, and an increase observed, but with zero growth from 2000 to about 2005. Since 2007, the growth rate has risen again, with an increasing rate from 2015 to 2020. Arctic CH_4 concentration measurements reveal an annual variation, with a higher concentration in late winter and a minimum in summer. The annual amplitude varied from 70–80 ppb in the 1980s but the amplitude has decreased over the last three decades and is now about 40–50 ppb. New data from high-resolution measurements show high variability in CH_4 concentration within the same season; this is especially evident in the winter season but variations over the summer also occur. The high variation during winter is likely due to varying meteorological conditions transporting polluted air from lower-latitude sources. The measurements expose a distinct peak of atmospheric CH_4 during summer at several sites, as well as a 'shoulder' occurring slightly later in early fall. The variability found in the high-resolution data is large, being about the same magnitude as the annual amplitude; however, it is not known if this variability has changed in recent years as high-resolution measurements were only initiated recently.

Anthropogenic, as well as natural, processes can drive CH_4 variability. It is still not clear what the primary drivers of the observed variability are but early studies suggest natural emissions can cause the late summer/early fall peaks. More high-resolution data and emissions studies are needed to qualify the primary drivers of such short-term variability. High-resolution atmospheric concentration measurements have become more abundant lately, but so far, the high-resolution data from the Arctic stations only covers one season. The coming years of data can be used to study the development and drivers of the local Arctic CH_4 variability.

An increasing number of measurement sites exist that can monitor the natural emissions of Arctic methane and also isotopic ratios, which can be used to categorize sources. Data on the isotopic ratios suggest a change in the relative proportions (and totals) of emissions from biogenic, thermogenic and pyrogenic sources, or a decline in the atmospheric sink of methane, or both.

The decreasing annual amplitude also points to a shift in the relative proportion of the emissions, with an increase in biogenic emissions during summer. Further studies involving the high-resolution measurements and back trajectory analysis are needed to confidently explain the increasing growth rate.

6.5.3.1 Recommendations

- Promote studies involving the high-resolution measurements and back trajectory analysis.
- Make provision for gathering more high-resolution data and undertaking emissions studies to qualify the primary drivers of short-term variability of CH_4.

6.5.4 Clouds

A statistically significant increase in cloudiness has been observed during boreal autumn in the Laptev, East Siberian, Chukchi and Beaufort Seas. This increasing trend in cloudiness is consistent and robust across all climate data records. However, large differences remain over other regions and seasons when intercomparing cloud property trends from satellite based CDRs, especially during the polar winter months.

6.5.4.1 Recommendations

Continued access to the data from active sensing instruments, such as cloud radar and lidar in space, will be crucial in future to further improve, re-train and evaluate cloud property retrieval algorithms applied to the data from historical passive sensors.

Given the complexity of the Arctic climate system, and the existing large uncertainties in both observations and models, continuous improvements and evaluations of cloud properties and trends in the Arctic are necessary.

Acknowledgment

RFBR projects #20-55-12001 is acknowledged. Olga Popovicheva's research was performed according to the Development program of the Interdisciplinary Scientific and Educational School of M V Lomonosov Moscow State University «Future Planet and Global Environmental Change».

Kathy S Law, Jean-Christophe Raut, Louis Marelle, and Tatsuo Onishi (LATMOS, France) acknowledge support from EU iCUPE (Integrating and Comprehensive Understanding on Polar Environments) project (grant agreement no. 689443) under the European Network for Observing our Changing Planet (ERA-Planet) and from access to IDRIS HPC resources (GENCI allocations A011017141 and A013017141) as well as the IPSL mesoscale computing center (CICLAD: Calcul Intensif pour le CLimat, l'Atmosphère et la Dynamique) for model simulations and analyses. Kathy S Law also acknowledges support from French Space Agency (CNES) MERLIN (contract 7752).

7. Modeling of short-lived climate forcers

Coordinating lead author: Cynthia H. Whaley

Lead Authors: Rashed Mahmood, Knut von Salzen, Sabine Eckhardt, Barbara Winter, Lori Bruhwiler, Joakim Langner, Manu Anna Thomas, Abhay Devasthale

Co-authors: Stephen Arnold, Stephen Beagley, Rong-You Chien, Jesper Christensen, Sujay Manish Damani, Xinyi Dong, Nikolaos Evangeliou, Greg Faluvegi, Mark Flanner, Joshua Fu, Michael Gauss, Wanmin Gong, Jens Liengaard Hjorth, Lin Huang, Ulas Im, Yugo Kanaya, Srinath Krishnan, Thomas Kühn, Kathy Law, Louis Marelle, Andreas Massling, Tatsuo Onishi, Naga Oshima, Yiran Peng, David Plummer, Olga Popovicheva, Luca Pozzoli, Jean-Christophe Raut, Maria Sand, Laura N. Saunders, Julia Schmale, Sangeeta Sharma, Ragnhild Skeie, Henrik Skov, Fumikazu Taketani, Kostas Tsigaridis, Svetlana Tsyro, Steven Turnock, Kaley A. Walker, Minqi Wang, Duncan Watson-Parris, and Tahya Weiss-Gibbons

Contributors: Silvia Becagli, Fabio Giardi, Zbigniew Klimont, Rita Traversi, Vito Vitale

7.1 Introduction

Observations of short-lived climate forcers (SLCFs) in the Arctic are invaluable for enhancing our understanding of how these chemicals behave in the atmosphere. However, measurements of SLCFs can be limited in space and time, and collecting such data is expensive and sometimes labor intensive. It is also difficult, from observations alone, to attribute sources and make projections for how SLCFs might behave in the future. Models, on the other hand, allow us to estimate the full three-dimensional distribution of SLCFs in the atmosphere, as well as their radiative forcing and optical properties over any given time period. Models can also be useful in helping to attribute SLCF sources, and in simulating the anticipated behavior of SLCFs and their climate and health impacts under different emissions scenarios (covered in Chapters 8 and 9, respectively). In order to have confidence in the model outputs, in this chapter, new atmospheric model simulations (which all use the same input anthropogenic emissions) are compared to observations of SLCFs. The performance of the models is evaluated and their biases quantified, to aid understanding of their characteristics.

In the previous AMAP report on black carbon (BC) and ozone (O_3) as climate forcers (AMAP, 2015a), model results were compared with observations from a handful of Arctic surface monitoring stations, aircraft campaigns, and ozonesondes. For this report, the data used in comparisons with models has been expanded to include multiple satellite retrievals, ship-based measurements and hundreds of surface observations from the Northern Hemisphere, to aid understanding of long-range transport issues from the models, and because the Arctic climate is not only influenced by greenhouse gases and SLCFs in the Arctic, but also by climate forcing from the mid-latitudes via heat and moisture transfer.

The previous AMAP report revealed that some models did not simulate the seasonal cycle of Arctic BC and sulfate (SO_4) well (AMAP, 2015a; Eckhardt et al., 2015), with many models not able to reproduce the high concentrations of the Arctic haze season (in winter and spring). With the relevant models having been subsequently updated, and the greater number of model-measurement comparisons, this chapter explores that issue again. The AMAP (2015a) report evaluated O_3 and carbon monoxide (CO) in the Arctic, finding O_3 to be overestimated by models and CO to be underestimated. The O_3 overestimation was thought to be due to O_3 descent from the stratosphere being over represented, and transport from mid-latitudes insufficiently represented for both CO and O_3 (AMAP, 2015a). In this chapter, analysis of O_3 is expanded to include new datasets and more O_3-precursor species, such as nitrogen dioxide (NO_2) and methane (CH_4), in addition to CO.

In the AMAP report on methane as a climate forcer (AMAP, 2015b), the anthropogenic CH_4 emissions needed for the climate models as input data were not available in time to carry out new simulations for the report; thus modeled CH_4 was not evaluated. In the current report, some of the participating models simulate CH_4, but not in a detailed way. Rather, they prescribe CH_4 concentrations based on simplified 'box model' results, which utilized the anthropogenic CH_4 emissions described in Chapter 2, along with assumptions for natural emissions. The models, described in Section 7.2, thus have very homogenous CH_4 fields, but are nonetheless evaluated against measurements later in this chapter (Section 7.3.2). To provide further information, however, the next subsection provides an overview from the literature of current modern CH_4 modeling (from models not employed in this report) and its challenges.

7.1.1 Modeling atmospheric methane (CH_4): the Arctic CH_4 budget

The concentration of atmospheric CH_4 in the Arctic results from a balance between that from local emissions (mainly from wetlands but with some emissions from fossil-fuel production) combined with that added by transport from lower latitudes, and that removed by chemical destruction in the atmosphere and microbes in soils. Arctic emissions are small relative to global emissions (about 4%, according to Saunois et al., 2016a; AMAP, 2015b), with the largest contribution to the atmospheric budget added through transport from the lower latitudes (e.g. Bruhwiler et al., 2021). All of the terms in the Arctic CH_4 budget are difficult to quantify. Atmospheric transport can be simulated using general circulation models or chemical transport models driven with meteorological analyses. However, the spatial distribution and temporal variability of emissions are uncertain, which results in uncertainty in the CH_4 contribution from lower latitudes. Atmospheric transport itself may also be uncertain, especially at small scales and where meteorological observations are relatively sparse, as is the situation for the Arctic (e.g. Schuh et al., 2019; Shindell et al., 2008).

Anthropogenic emissions of CH_4 fall into the broad categories of agriculture (including livestock), waste and fossil-fuel production. For all three categories, emissions occur through unintended leakage or as a by-product of microbial processes. This makes them difficult to quantify in comparison to, say, carbon dioxide (CO_2), which has emissions that directly relate to the consumption of

fossil fuels. In the Arctic, CH_4 emissions are dominated by natural sources (AMAP, 2015b), and, as discussed in Section 6.3 of this report, many site-level studies are presently being conducted to quantify natural emissions of CH_4 from wetlands, lakes and ponds. However, these are difficult to scale-up to the pan-Arctic region because of the spatial heterogeneity of ecosystems, inundation, and soil hydrology. A particular problem for quantifying the spatial distribution of emissions from wetlands and inland waters has been a lack of knowledge on where these systems are. Progress is currently being made in mapping vegetation-free surface-water bodies using remote-sensing techniques and machine-learning analysis approaches (Kyzivat et al., 2019; Cooley et al., 2019). It may therefore soon be possible to combine information gained at the site level with the satellite-based spatial data to quantify emissions and predict how they will change in the future as the Arctic climate continues to change.

The lifetime of CH_4 in the global atmosphere due to photochemical destruction is about ten years (Nicely et al., 2017). The atmospheric chemical sink of methane in the troposphere is mainly due to reaction with the hydroxyl radical (OH), initiating a reaction chain that ultimately leads to oxidation of CH_4 to CO_2. Reaction with excited-state oxygen ($O(^1D)$) and atomic chlorine (Cl) also contribute to the photochemical destruction of CH_4, but contribute less than 10% to the total chemical loss (Saunois et al., 2020). All three reactants – OH, Cl and $O(^1D)$ – are extremely short-lived in the atmosphere and are very difficult to measure. Models with detailed photochemistry also have large uncertainties in simulated OH (Nicely et al., 2016; Naik et al., 2013). Currently, the most reliable estimates of OH abundance are inferred from observations of the trace gas methyl chloride (MCL, Kirschke et al., 2013). Emissions of MCL are thought to be relatively well known, and the halocarbon's only atmospheric sink is through reaction with OH; therefore OH abundances can be deduced across large scales using global network observations of MCL and transport models. OH abundance in the atmosphere is thought to be stable, with small interannual variability (Nicely et al., 2018; Montzka et al., 2011).

OH abundances are largest in the tropics where both ultraviolet (UV) solar radiation and water vapor are highest (e.g. Naik et al., 2013), since OH is produced by dissociation of water (H_2O) by reaction with $O(^1D)$, which is produced by O_3 photolysis. In the Arctic, OH abundances are lower due to lower water vapor, more absorption of UV over long atmospheric path lengths and prolonged periods with little or no sunlight. Because of the difficulty in quantifying sources and sinks of CH_4, model simulations of CH_4 often fail to closely match observed features of the atmospheric CH_4 distribution, such as the latitudinal gradient and seasonal cycle (e.g. Saunois et al., 2020; Bruhwiler et al., 2014). Bottom-up estimates of emissions come from a wide variety of sources, such as economic inventories of fossil-fuel production, ruminant populations and age distributions, and so on. Terrestrial ecosystem process models can also be used to quantify wetland emissions and uptake in soils. Simulations using these estimates can be compared with observations to

Table 7.1 Models and their characteristics used in this study.

Model name	Model type	Horizontal grid information	Vertical grid information
CanAM5-PAM	GCM	128 × 64, Gaussian grid, T63	Hybrid/sigma, 49 levels to 1 hPa
CESM2.0	ESM	1.9° × 2.5° lat/long grid	32 levels, lid near 3 hPa
CESM2.1.1	ESM	0.9° × 1.25° lat/long grid	32 levels, lid near 3 hPa
CIESM-MAM7	GCM	0.9° × 1.25° lat/long grid	31 levels, up to ~3 hPa
CMAM	CCM	96 × 48 Gaussian grid, T47 (CanAM3.1)	Hybrid sigma-pressure, 71 levels to 0.0005 hPa
DEHM	Offline CTM, hemispheric	50km, >150 × 150 grid points, polar stereographic	Sigma up to 100 hPa, 29 levels
ECHAM6-SALSA	GCM	T63	47 levels, lid around 0.01 hPa, hybrid sigma-pressure
EMEP MSC-W	CTM	0.5° × 0.5 °regular lat/long grid	Hybrid (eta) coordinates, 20 levels from the surface up to 100 hPa
FLEXPART	Lagrangian Transport Model	Met. input data, 1° × 1° lat/long grid, global	Met. input, 137 levels, up to 100 hPa
GEM-MACH	Regional online air quality prediction model	Arctic LAM*, rotated lat/long at 0.1375° (15 km) horizontal resolution	81 hybrid levels up to 0.1 hPa
GEOS-Chem	CTM	2° × 2.5° lat/long grid	72 hybrid sigma-pressure levels up to 0.01 hPa
GISS-E2.1	ESM	2° × 2.5° lat/long grid	40 levels, up to 0.1 hPa
MATCH	Offline CTM, hemispheric	rotated lat/long, 186 × 186, 0.75° resolution	38 levels, up to ~50 hPa, hybrid
MATCH-SALSA-RCA4	Offline coupled CCM, hemispheric	rotated lat/long, 188 × 198, 0.75° resolution	40 levels, hybrid up to 20 hPa
MRI-ESM2	ESM	TL159 (AGCM), TL95 (aerosol), T42 (O_3)	80 levels up to 0.01 hPa, hybrid sigma-pressure
NorESM1-Happi	ESM and CTM	0.9° × 1.25° lat/long grid	26 levels, lid ~1 hPa, hybrid sigma-pressure
Oslo CTM3	CTM	2.25° × 2.25° lat/long	60 sigma levels, up to 0.1 hPa
UKESM1	CCM/ESM	145 × 192 (1.875° × 1.25° lat/ long grid)	85 (hybrid height terrain following grid) levels, up to ~0.001 hPa
WRF-Chem	Regional Arctic chemistry-aerosol climate model	100 km	50 levels, lid at 50 hPa

* LAM=limited area (regional) model; AGCM=atmospheric global climate model

supply information about where source/sink processes need to be adjusted for better agreement with observations. The canonical example of this type of approach applied to atmospheric CH_4 is the study of Fung et al. (1991), who comprehensively tested multiple possible CH_4 budgets that were all constrained by global mass balance, and comprised spatial distributions of emissions from anthropogenic and natural sources, as well as chemical loss and oxidation in soils. Lelieveld et al. (1998) applied a similar forward-modeling approach to study the role of CH_4 in climate forcing, and confirmed they could reproduce the global distribution of CH_4 using reasonable assumptions about emissions. Another approach is to use inverse modeling to refine bottom-up estimates of CH_4 emissions (e.g. Saunois et al., 2016a, 2020). A more detailed discussion of atmospheric inversions appears in Sections 3.2 and 5.3.

7.1.2 Chapter organization

Eighteen models provided entirely new simulations for this report. All used the same anthropogenic emissions data – described in Chapter 2 – as inputs. The models are briefly described in Section 7.2, and then comprehensively evaluated against observations in Section 7.3. The evaluation covers SLCF concentrations, aerosol optical properties, and clouds in the Arctic and Northern Hemisphere throughout the troposphere and lower stratosphere. Section 7.4 summarizes our main findings about the models' performance.

7.2 Model description

For this report, 18 atmospheric and earth system models (ESMs) ran simulations specifically aimed at assessing SLCFs and their impacts (Data ref. 7.1). The models are briefly described in this section, with further details about their processes and properties in the Appendix in Section A7.1. All models were input with the same set of anthropogenic emissions (Data ref. 7.2) but they drew on a variety of natural emissions sources and other model inputs (see Tables 7.1 and A7.2). Emissions are described in detail in Chapter 2.

Thirteen of the models used in this study are atmospheric models, simulating most atmospheric processes, including emissions, advection, convection, chemical reactions, aerosol microphysics, cloud processes, precipitation, and wet and dry deposition. Of these, eight models (DEHM, EMEP MSC-W, FLEXPART, GEM-MACH, GEOS-Chem, MATCH, Oslo CTM and WRF-Chem) have an emphasis on air quality, a relatively high horizontal resolution, and a lower atmospheric 'lid' (top modeled level). They are focused on the troposphere, with many trace gas and aerosol species, and chemical reactions. Two models (CMAM and MATCH-SALSA are chemistry climate models (CCMs), meaning they are focused on climate, with a lower horizontal resolution and higher atmospheric 'lid' (including the stratosphere). These incorporate a significant amount of atmospheric chemistry – particularly in the stratosphere. In the troposphere, CCMs have less chemistry

References	Selected SLCF and related output	Years simulated
von Salzen (2000, 2006, 2013); Ma et al. (2008); Peng et al. (2012); Mahmood et al. (2016, 2019)	BC, SO_4, OA, $PM_{2.5}$, AOD, AAOD, AE	1990–2015
Danabasoglu et al. (2020); Liu et al. (2016a)	O_3, CO, NO_2, BC, SO_4, OA, $PM_{2.5}$, AOD, AAOD, AE	2008–9, 2014–15
Danabasoglu et al. (2020); Liu et al. (2016a)	BC, SO_4, OA, $PM_{2.5}$, AOD	2015–2050
Lin et al. (2020); Liu et al. (2012b)	BC, SO_4, OA, $PM_{2.5}$, AOD, AAOD, AE	1990–2015
Jonsson et al. (2004); Scinocca et al. (2008)	O_3, CO, NO_2, CH_4	1990–2015
Christensen (1997); Brandt et al. (2012); Massling et al. (2015)	O_3, CO, NO_2, CH_4, BC, SO_4, OA, $PM_{2.5}$, AOD, AAOD, AE	1990–2015
Tegen et al. (2019); Schultz et al. (2018); Kokkola et al. (2018)	BC, SO_4, OA, $PM_{2.5}$, AOD, AAOD, AE	2008–9, 2014–15
Simpson et al. (2012); Simpson et al. (2019a)	O_3, CO, NO_2, CH_4, BC, SO_4, OA, $PM_{2.5}$, AOD	1990–2015
Pisso et al. (2019)	BC, SO_4	2014–2015
Moran et al. (2013); Makar et al. (2015a, 2016b); Gong et al. (2015)	O_3, CO, NO_2, BC, SO_4, OA, $PM_{2.5}$	2015
Bey et al. (2001)	O_3, CO, NO_2, CH_4, BC, SO_4, OA, $PM_{2.5}$, AOD, AAOD, AE	2008–9, 2014–15
Kelley et al. (2020); Miller et al. (2020); Bauer et al. (2020)	O_3, CO, NO_2, CH_4, BC, SO_4, OA, $PM_{2.5}$, AOD, AAOD, AE	1990–2015
Robertson et al. (1999)	O_3, CO, NO_2, BC, SO_4, OA, $PM_{2.5}$, AOD, AAOD, AE	2008–9, 2014–15
Robertson et al. (1999); Andersson et al. (2007); Kokkola et al. (2008)	O_3, CO, NO_2, BC, SO_4, OA, $PM_{2.5}$, AOD, AAOD, AE	2008–9, 2014–15
Yukimoto et al. (2019); Kawai et al. (2019); Oshima et al. (2020)	O_3, CO, NO_2, CH_4, BC, SO_4, OA, $PM_{2.5}$, AOD, AAOD	1990–2015
Bentsen et al. (2013); Iversen et al. (2013); Gent et al. (2011); Graff et al. (2019)	BC, SO_4, OA, AOD, AAOD, AE	2008–9, 2014–15
Søvde et al. (2012); Lund et al. (2018)	O_3, CO, NO_2, CH_4, BC, SO_4, OA, $PM_{2.5}$	2008–9, 2014–15
Sellar et al. (2019); Kuhlbrodt et al. (2018); Williams et al. (2018)	O_3, CO, NO_2, CH_4, BC, SO_4, OA, $PM_{2.5}$, AOD, AAOD, AE	1990–2015
Marelle et al. (2017); Marelle et al. (2018)	O_3, CO, NO_2, BC, SO_4, OA, $PM_{2.5}$, AOD, AAOD, AE	2014–2015

than the air-quality models. The remaining three atmospheric models (CanAM5-PAM, CIESM-MAM7, and ECHAM6-SALSA) have a tropospheric climate focus. With fewer chemical reactions, they can be run for long periods of time, and are used to simulate important atmospheric processes for climate.

Five of the models used (CESM, GISS-E2.1, MRI-ESM2, NorESM and UKESM1) are ESMs, which means that they simulate the atmosphere in a similar way to the climate models mentioned above, but also include an interactive land surface and ocean. In addition to atmospheric processes, these models can simulate changes to ocean temperatures and salinity, sea-ice thickness and extent, and land-air exchange in an interactive way, whereas these variables are prescribed in the 13 atmospheric models of the preceding paragraph.

Table 7.1 lists the individual models and their properties. Appendix Section A7.1 contains a table describing the model simulations (Table A7.1), and a table listing the emissions inputs and meteorology details (Table A7.2). Individual model descriptions are also included in Appendix A7.1. A subset of the selected models prescribe CH_4 concentrations based on box model results described in Olivié (2021) and from Meinshausen et al. (2017) for years prior to 2015. The former utilized the ECLIPSE v6b anthropogenic CH_4 emissions (Chapter 2; Data ref. 7.2), along with assumptions for the natural emissions (Chapter 2; Olivié et al., 2021; Prather et al., 2012) to provide as input to models' surface CH_4 concentrations.

7.3 Comparisons of simulated and observed short-lived climate forcers

The validation of the models, described in Section 7.2, focuses on SLCFs O_3, CH_4, BC and SO_4. Fine particulate matter ($PM_{2.5}$) validation is also included, as $PM_{2.5}$ is an SLCF due to its direct and indirect climate effects. It is composed of BC, SO_4, nitrate (NO_3), ammonium (NH_4), mineral dust (DU), sea salt (SS) and organic compounds. $PM_{2.5}$ also has important implications for health (e.g., US EPA, 2019; WHO Europe 2013a; Chapter 9 of this report). Derived measurements of aerosol optical properties are additionally utilized to evaluate models' simulations of a broader set of aerosol characteristics – including abundance and size distribution – as well as cloud properties, which have a large and highly uncertain impact on climate (Chapter 8). In the Appendix, model validation of organic aerosol (OA) and O_3-precursor species CO and NO_2 (Sections A7.6 and A7.2.3, respectively) are also presented, to help us to better understand the results. In addition to evaluating the models, the intercomparison approach used – with multiple types of measurements of the same quantity – reveals uncertainties in the measurements as well, which tend to be large for some derived quantities from satellite observations.

This section provides the results from model simulations covering four recent years: 2008–9 (which was the time period covered for model evaluation in AMAP [2015a]) and 2014–15 (a more recent time period for evaluation), as well as the period from 1990 to 2015, which is the time period for which the ECLIPSE v6b emissions (Data ref. 7.2) are available. In many cases, figures in Section 7.3 show examples for just one set of years (either the mean of 2008–9 or 2014–15) but for brevity, not both.

Details regarding some of the measurement methods and datasets are in given Chapters 5 and 6. Section 7.3 is divided by SLCF, with model performance discussed for the Arctic (considered to be >60°N for simplicity in this chapter, although this is not a standard definition) and for the Northern Hemisphere. It is important to include the latter to assess long-range transport of SLCFs to the Arctic from their largest sources and climate forcing from outside of the region. Long-term (1990–2015) trend analyses for BC, SO_4, O_3 and aerosol optical depth (AOD) are also included, as there have been significant changes to associated emissions of these SLCF species, and long-term measurements are available.

7.3.1 Ozone (O_3)

O_3 is a secondary pollutant, and its distribution is dependent on emissions of precursors, *in situ* photochemistry, and atmospheric transport (see Chapter 6 for more information). Surface *in situ* O_3 measurements are made via various types of UV absorption monitors, which have uncertainty ranges of approximately 3%, or one-to-two parts per billion by volume (ppbv) (see Chapter 5). O_3 can also be measured indirectly from remote sensors mounted on satellite instruments. We used both kinds of measurements to evaluate simulated O_3 in this section.

7.3.1.1 Arctic O_3

Mean concentrations and seasonal variability in surface air

Figure 7.1 shows volume mixing ratios (VMRs) of O_3 in surface air at 20 Arctic observation stations. Annual mean concentrations are of the order of less than 40 ppbv, with individual model biases ranging from -20% to +52% on average in the region for 2014–15. The multi-model mean in the Arctic has a bias of 11%. Nearly all models simulate too much surface O_3 in Alaska and too little in Greenland and northern Europe. These model biases are similar to those reported in AMAP (2015a).

The observed and modeled seasonal cycles of Arctic surface O_3 is shown in Figure 7.2. Whereas the observations show a maximum in the spring (consistent with those reported in Chapter 6) – due to descent of O_3 from the stratosphere and photochemical production from mid-latitude O_3 precursors – most of the models (eight of the 12) display the maximum in the summer – similar to the mid-latitude seasonal cycle (see Section 7.3.1.3) – or a late-summer secondary peak. It is possible that the models are transporting too much O_3 from mid-latitudes to the Arctic in the summer, and/or they are producing too much O_3 from summer wildfires. Conversely, models may also be underestimating O_3 sinks, such as deposition or chemical destruction, in the summer (see Chapter 6).

As with the pattern seen in the surface O_3 biases shown in Figure 7.1, there is also a western-versus-eastern pattern in the modeled seasonal cycles. The models were better able to simulate the observed spring peak at the eastern (European) Arctic locations, with the erroneous modeled summer peak only appearing for the western (North American) Arctic locations, despite both west and east observations having spring peaks in their seasonal cycles.

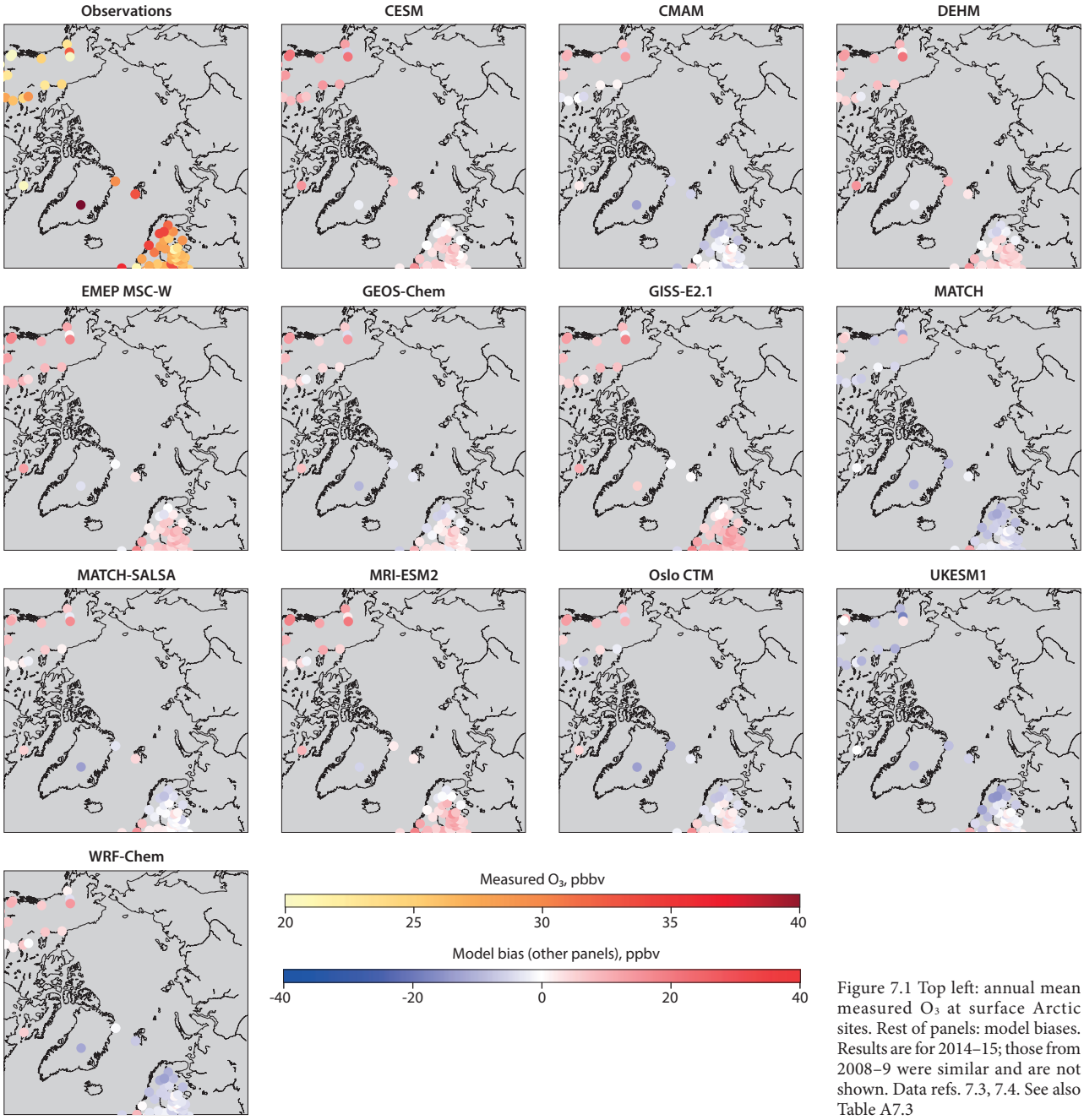

Figure 7.1 Top left: annual mean measured O_3 at surface Arctic sites. Rest of panels: model biases. Results are for 2014–15; those from 2008–9 were similar and are not shown. Data refs. 7.3, 7.4. See also Table A7.3

O_3 in the troposphere and lower stratosphere

In AMAP (2015a), ozonesondes were used in model validation to assess O_3 throughout the troposphere. In this assessment, however, satellite measurements of O_3, and O_3-precursor species, such as CH_4, CO and NO_X were used. Not only do these data provide vertical information, they have better spatial coverage than the ground sites and ozonesondes, and often have a longer time series. They also map the distribution of SLCFs in a way that better facilitates comparisons to models. Aircraft and sonde measurements have very high spatial resolution, being gathered from a very small area that is not representative of the coarse grid-cells of the models. Conversely, the satellite measurements, because of the sensors' viewing geometries, tend to have a larger spatial footprint that is more representative of model resolution. Satellites retrieve the VMRs of trace gases from the measured absorption spectra (see Chapter 5 for more detail); this method has about a 15% uncertainty on the measurements (e.g., Verstraeten et al., 2013). This study utilized data from the Atmospheric Chemistry Experiment-Fourier Transform Spectrometer (ACE-FTS) (Data ref. 7.5), the Tropospheric Emission Spectrometer (TES) (Data ref. 7.6), and Measurements Of Pollution In The Troposphere (MOPITT) satellite instruments (Data ref. 7.7), and compared those results to the modeled VMRs of O_3 in this section, CH_4 in Section 7.3.2, and CO and nitrogen oxides (NOx) in Appendix A7.2.3. Note that while TES and MOPITT spatial coverage is global, it does not extend into the High Arctic due to the viewing geometries of these instruments. Therefore, in Figures 7.3 and 7.9 the model biases are only shown where there are TES measurements. The ACE-FTS satellite has a high-inclination solar-occultation viewing geometry, which gives it more coverage at Arctic latitudes, though this limb-viewing instrument does not have a large spatial footprint, and its vertical profiles span only the upper troposphere and stratosphere, and do not extend into the lower troposphere.

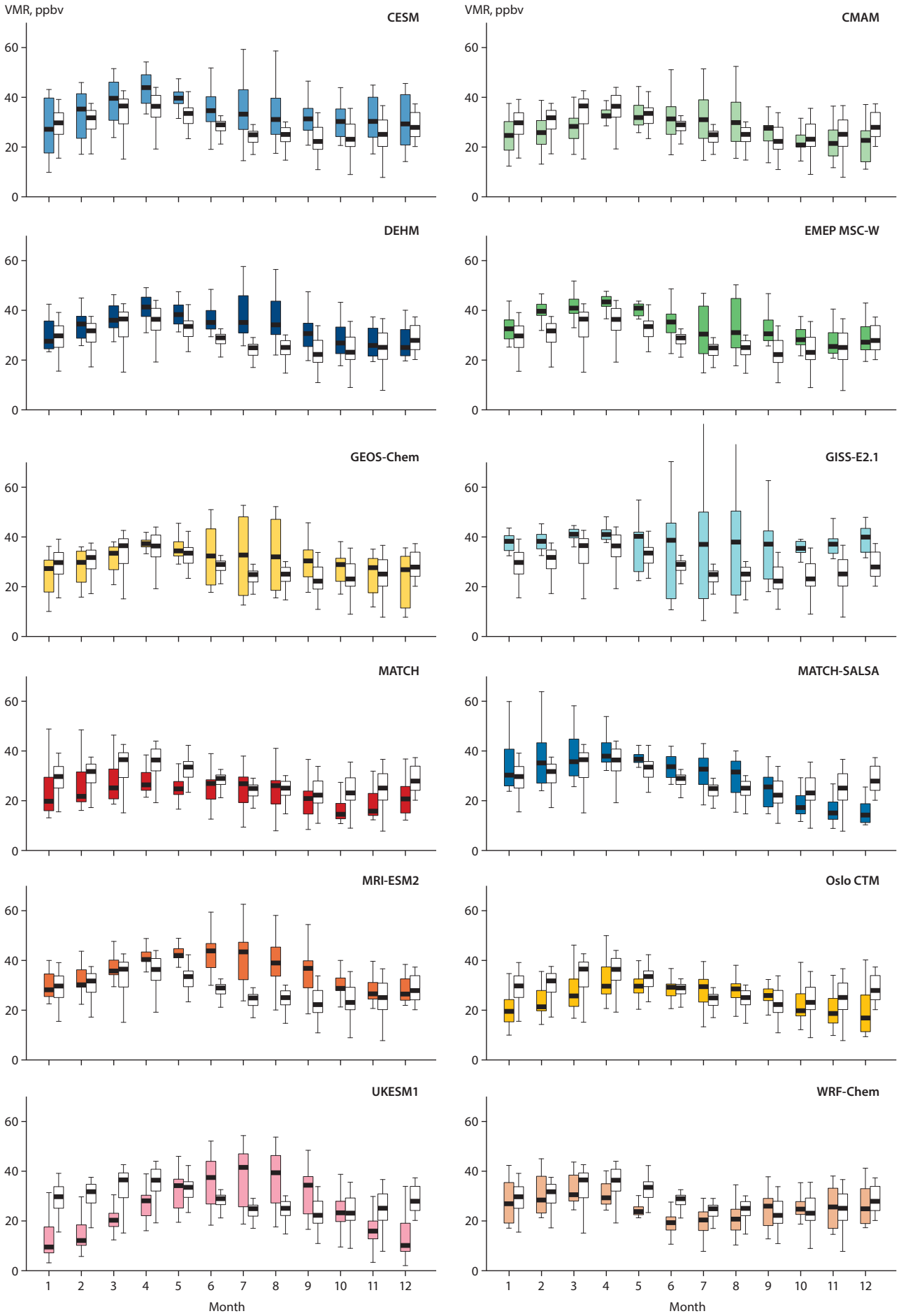

Figure 7.2 Monthly O_3 volume mixing ratios (VMRs) from all Arctic observations (black and white), and models (colors) sampled at the measurement locations for 2014–15. Horizontal lines are the median, and the boxes extend to the inter-quartile range. The vertical lines depict the maximum of the range.

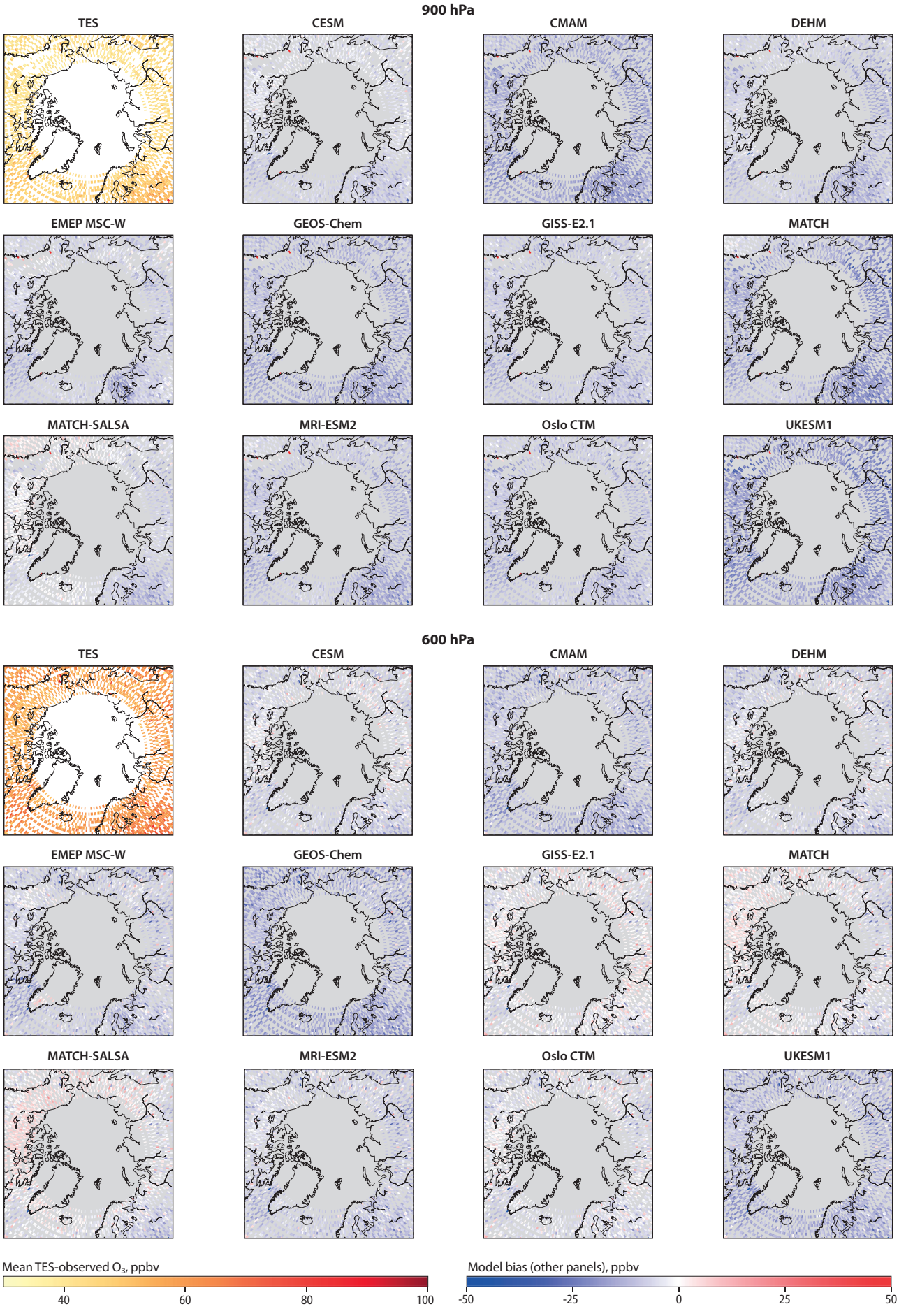

Figure 7.3 Mean TES-observed O_3 in the lower-troposphere (900 hPa) and mid-troposphere (600 hPa). Rest of panels: model biases. Results are for 2008–2009.

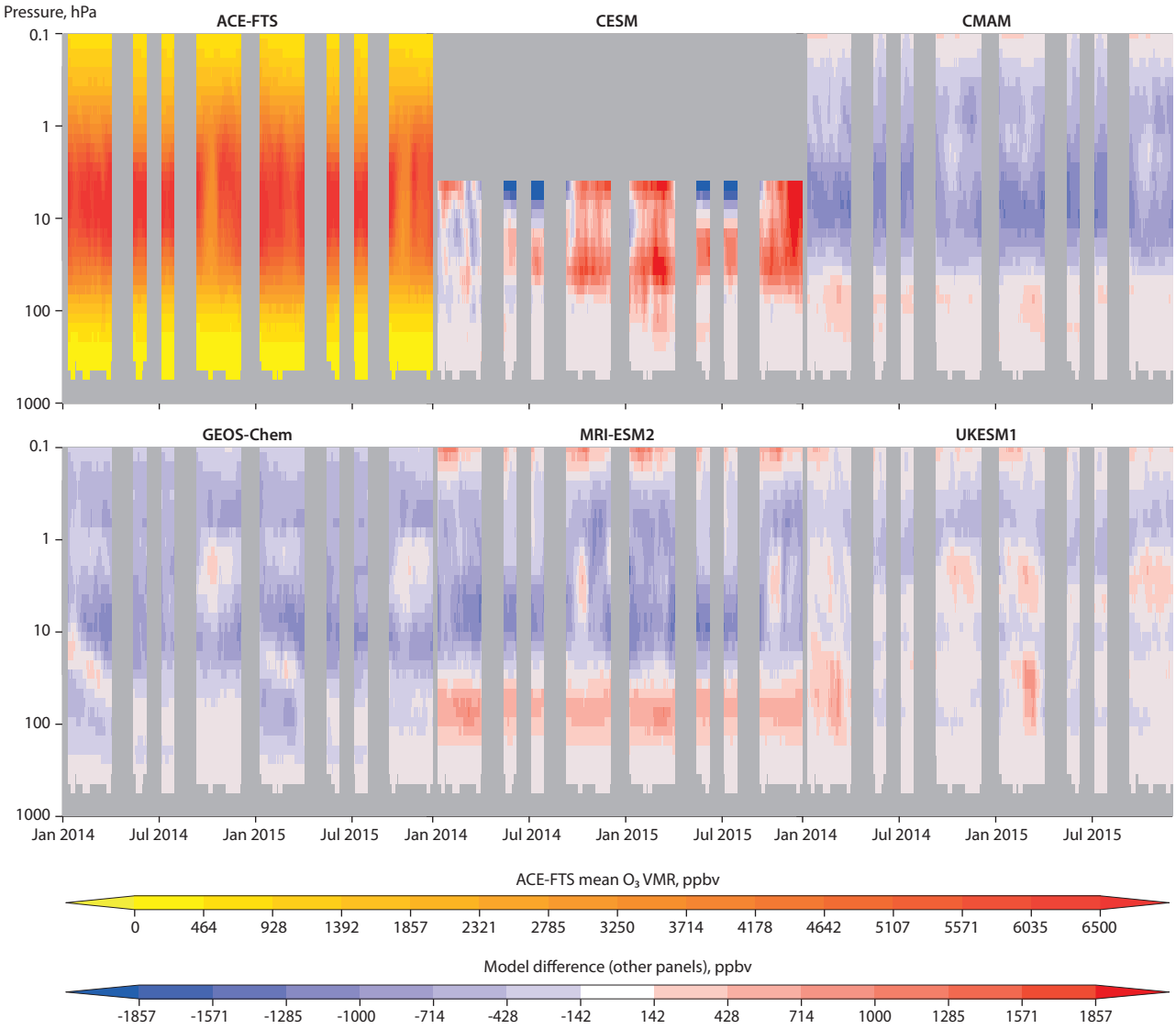

Figure 7.4 Top left: mean Arctic O_3 from ACE-FTS measurements (VMRs in ppbv, top color bar). Rest of panels: model-measurement differences (ppbv, bottom color bar). Results are for 2014–15; those for 2008–9 were very similar and are not shown.

After interpolating all model and TES results to a 1° × 1° latitude/longitude horizontal grid, the monthly mean O_3 from the TES-lite data products were matched in space and time with models. Models were smoothed with the TES mean averaging kernels and compared. The averaged differences are shown in Figure 7.3 for two different pressure levels in the lower (900 hectopascals [hPa]) and middle (600 hPa) troposphere for the 2008–2009 time period. TES measurements started in 2004 and stopped in late 2015. They had poorer coverage in the spectrometer's last few years, which is why 2014–15 results are not shown here. However, the model biases in those years were similar to what they were for 2008–9.

As seen in Figure 7.3, the distribution of O_3 in the free troposphere is more homogeneous, and all models underestimate free tropospheric Arctic O_3. This is in contrast to the results for surface O_3, which were simulated too high in Alaska, and lower in northern Europe. However, TES O_3 measurements have been shown to be biased high by +7 ppbv or +13% at northern latitudes (Verstraeten et al., 2013), and this is roughly the same amount by which the models are biased low. Therefore, the models may be simulating free tropospheric O_3 fairly accurately. The vertical distribution of the model biases is discussed further in Section 7.3.1.3.

Five models (CMAM, CESM, GEOS-Chem, MRI-ESM2, and UKESM1) have detailed stratospheric processes and provided three-hourly output of trace gases. The three-hour time frequency is required for accurate comparisons of models to ACE-FTS measurements (Kolonjari et al., 2018). O_3 results from these five models were compared to measurements from ACE-FTS in the upper troposphere, a region where O_3 is a potent greenhouse gas, and in the stratosphere, where O_3 concentrations greatly increase in the ozone layer. ACE-FTS O_3 has an uncertainty range of between 5% and 10% when compared to O_3 from other satellite limb-view observations (Sheese et al., 2017).

Figure 7.4 shows ACE-FTS O_3 measurements and model biases for the Arctic region as a time series throughout a vertical cross-section. It shows that several models underestimate the O_3 distribution in the upper stratosphere (<10 hPa) in the Arctic. This may be due to the climatological values that were used to define the upper boundary conditions in the models. In the upper troposphere-lower stratosphere (UTLS), the mean multi-

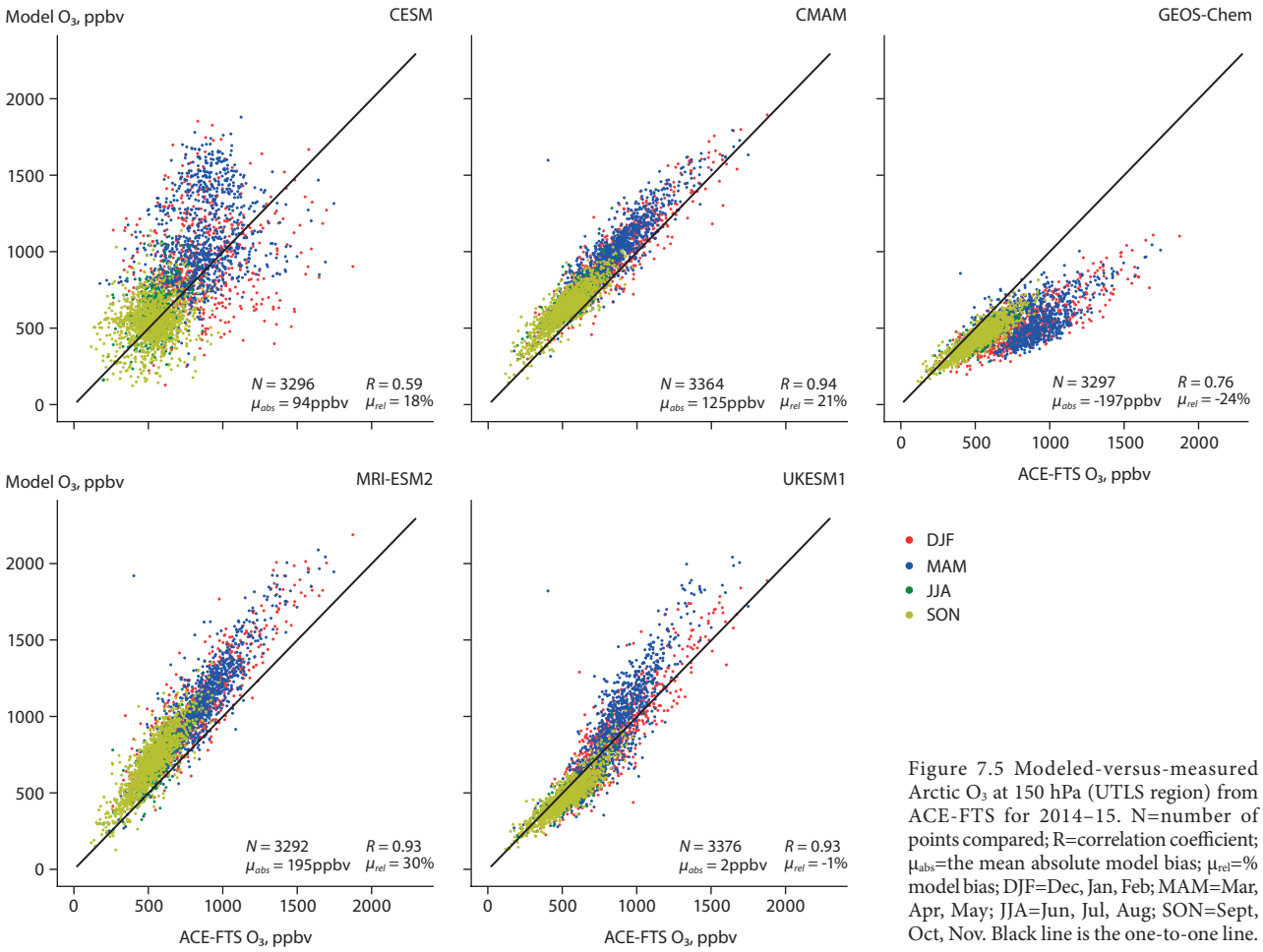

Figure 7.5 Modeled-versus-measured Arctic O_3 at 150 hPa (UTLS region) from ACE-FTS for 2014–15. N=number of points compared; R=correlation coefficient; μ_{abs}=the mean absolute model bias; μ_{rel}=% model bias; DJF=Dec, Jan, Feb; MAM=Mar, Apr, May; JJA=Jun, Jul, Aug; SON=Sept, Oct, Nov. Black line is the one-to-one line.

model biases of Arctic O_3 are smaller, at -0.9% (at 150 hPa) to -6.1% (at 100 hPa), which is within the measurement uncertainty range.

Figure 7.5 shows the model-versus-measurement scatter plot at the 150 hPa vertical level in the UTLS. Here we see the models' varied performances in capturing the spatial variability, with different seasons highlighted in different colors. This figure shows that UKESM1 has the best performance with the smallest % bias (μ_{rel}) and highest correlation coefficient (R). This is in contrast to its simulation of surface O_3, where this model had one of the largest negative biases. The Taylor diagram is a way to show multiple comparison statistics and models on the same plot. The closer the model point is to the black measurement point (located at 1 on the x-axis), the closer the model agrees with the measurements. Taylor diagrams for trace gases are shown in Figure A7.8. They show that MRI-ESM2 and UKESM1 perform the best for O_3 in the UTLS. O_3 precursors are shown in Figure A7.8 as well, and those results are discussed further at the end of Section 7.3.1.3.

7.3.1.2 O_3 trends in the Arctic, 1990–2015

Five models simulated O_3 for 1990–2015, and one for 1995–2015. The 1990–2015 time period was chosen because of the availability of emissions data for it. Over this period, emissions of O_3-precursors, such as NOx and many volatile organic compounds (VOCs), have been decreasing in North America and Europe, while increasing in Asia (Mijling et al., 2013; Miyazaki et al., 2017; Huang et al., 2017b; Kurokawa and Ohara, 2020). O_3-precursor CH_4 has been increasing globally during this time (Turner et al., 2019; NOAA GML, 2021). These complex changes in O_3-precursors have resulted in ground-level Arctic O_3 remaining steady, with little-to-no discernable trend in both the modeled and measured annual means from 1990 to 2015 (Figure 7.6).

The trends in surface O_3 at five Arctic locations (Alert, Utqiaġvik, Summit, Villum, and Zeppelin) were computed seasonally and annually in Section 6.3.3 from the measurements (using Mann-Kendall Test and Sen's slope; Gilbert, 1987). Using the same method for the same locations but a different set of years, the modeled trends (%/year) were computed for the 1990–2015 (1995–2015 for GISS-E2.1) time period (see Table A7.4 in the Appendix). Both measurements and models exhibited small (<1%/year) but significant increasing trends in the winter, and little-to-no trends for the summer. The annual trends were generally weak and often not significant, at a 0.1 level of significance. There was no consensus among the models about the trends but most of them tended to give positive trends for the winter months (December, January, February [DJF]) and negative trends in summer (June, July, August [JJA]) and autumn (September, October, November [SON]) (Table A7.4). The positive trend in DJF is consistent with the observations at Alert, Utqiaġvik and Zeppelin. This may be due to declining winter NOx emissions in Europe and North America resulting in less O_3 titration (loss). For summer and autumn, the observations did not show any clear trends. For spring (March, April, May [MAM]), neither the models nor the observations showed clear trends. Generally, the data

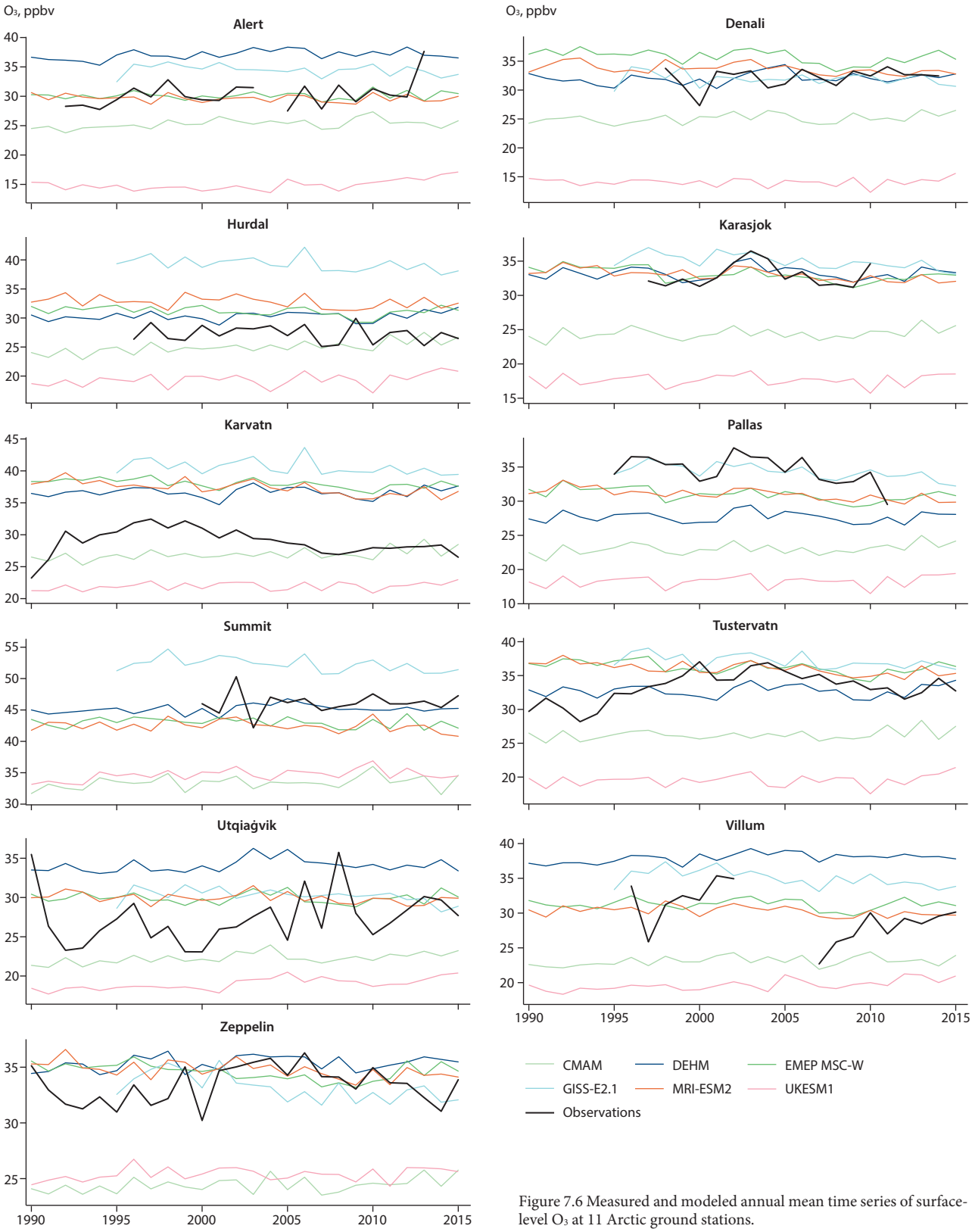

Figure 7.6 Measured and modeled annual mean time series of surface-level O_3 at 11 Arctic ground stations.

for calculating the trends in the observations covered a shorter time span than the models, and they included years after 2015.

While the models were not compared to the exact same set of years as in Section 6.3.3, there were many similarities between the model and measurement O_3 trend results (Table A7.4).

It is worth noting that UKESM1 particularly underestimates Arctic O_3 (Figure 7.6). UKESM1 is known to display too much O_3 loss over precursor-source regions, which is likely due to too much titration of O_3 via nitrogen oxide (NO) caused by insufficient boundary-layer mixing. Levels of Arctic surface O_3 are subject to heavy influence from Eurasian pollution, particularly in winter and spring when the titration reaction can be an important O_3 sink. O_3 modeled by CMAM is also particularly underestimated at Zeppelin and Summit stations, which are both located at high elevations. CMAM is missing tropospheric VOC chemistry, which might be a cause for this underestimation.

7.3.1.3 Hemispheric O_3

Since a significant fraction of Arctic pollution and climate forcing comes from long-range transport (e.g., Stohl, 2006; Wespes et al., 2012; AMAP 2015a), some of the model performance in the Arctic needs to be interpreted with additional information from larger spatial scales. In this section, model performance throughout the Northern Hemisphere is examined to help interpret the Arctic O_3 results.

Ground-level O_3

As ground-level O_3 is an important component of smog with negative impacts on health, agriculture, and ecosystems (Chapter 9), great efforts are taken to accurately simulate surface O_3 concentrations in models – particularly at mid-latitudes where agriculture and human populations are widespread. As a criteria air pollutant (pollutants for which national ambient air-quality standards are set by the United States Environmental Protection Agency), O_3 is measured widely in several countries' surface monitoring networks. Most of these measurements are archived in the Tropospheric Ozone Assessment Report (TOAR) database; Table A7.3 lists the sources of the O_3 measurements that are shown in Figure 7.7.

Figure 7.7 shows that surface O_3 is overestimated in most parts of the world, with a multi-mean model bias of +28%, and individual models ranging from -2% to +105% for the 2014–15 average. Overprediction of modeled surface O_3 is well documented (e.g., Solazzo et al., 2012; Im et al., 2015; AMAP 2015a). This may be due to a lack of forest canopy modeling (Makar et al., 2017), which reduces the amount of light to photochemically produce O_3 in surface air, or it could be due to simulated transboundary transport of O_3 (Fiore et al., 2009). MATCH and MATCH-SALSA are the only models that generally underestimate O_3, though these air-quality models have very small biases. Several models (DEHM, EMEP MSC-W, GISS-E2.1, and MRI-ESM2) overestimate O_3 in China more than other parts of the world. Since all models were run with the same anthropogenic emissions, the regional differences among the models' biases are due to differences in their chemistry schemes (such as how they treat VOCs), meteorology, spatial resolution (Table 7.1), and treatments of biogenic emissions (Table A7.2).

Figure 7.8 shows the seasonal cycle of O_3 using the global measurements, and models sampled at those measurement locations. Both measurements and models show similar seasonal cycles, with a maximum in the summer due to photochemical production peaking in polluted, mid-latitudinal areas.

Free-tropospheric O_3

Monthly mean modeled trace gases are compared to the O_3 retrieved from TES satellite measurements (Data ref. 7.6) in Figure 7.9. Note that TES measurements at high-elevation locations (such as the Himalaya) do not have reliable retrievals, thus these show up as big differences between the models and TES in the plots.

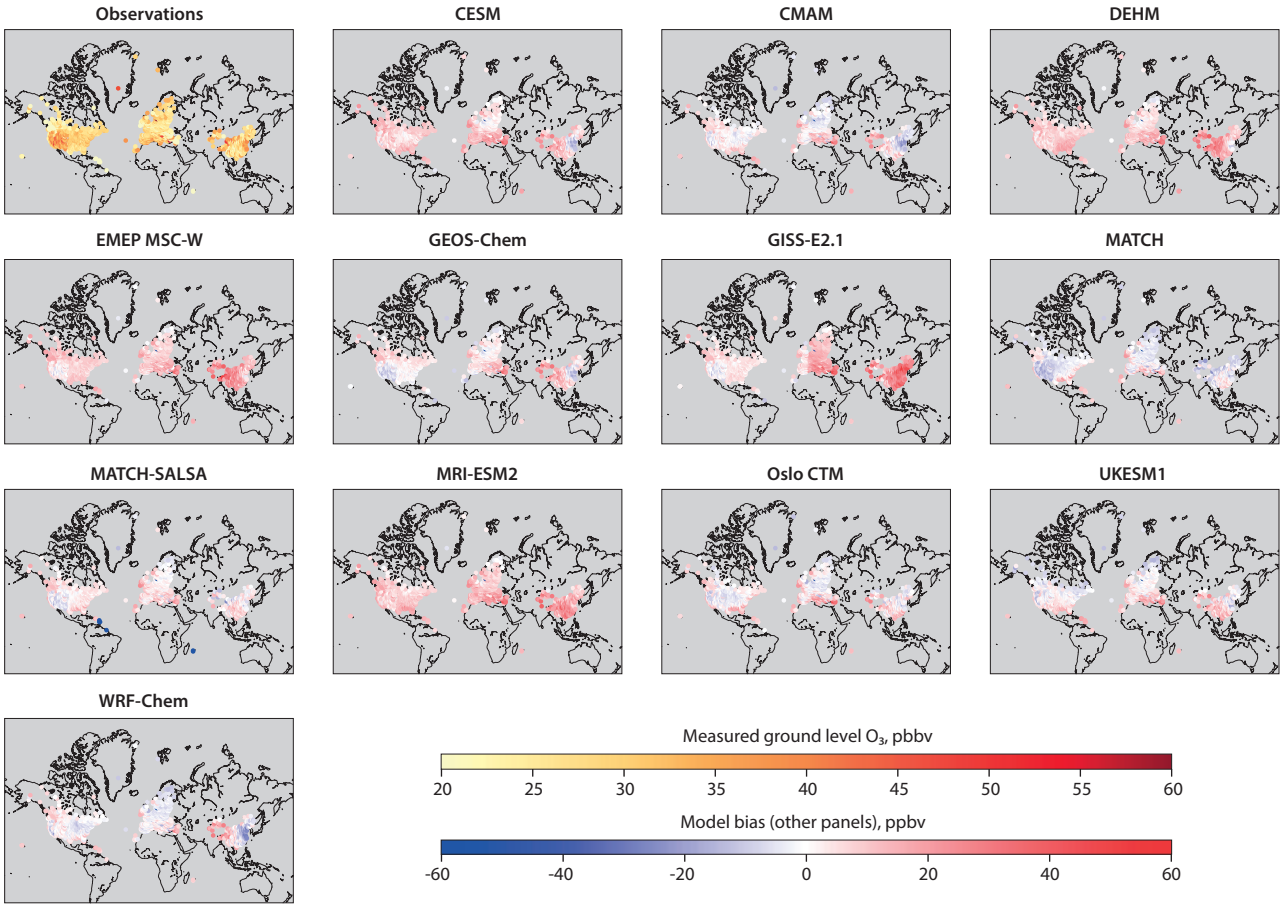

Figure 7.7 Top left: mean measured ground-level O_3. Rest of panels: model biases. Results are for 2014–15. Data refs. 7.2, 7.3. See also Table A7.3.

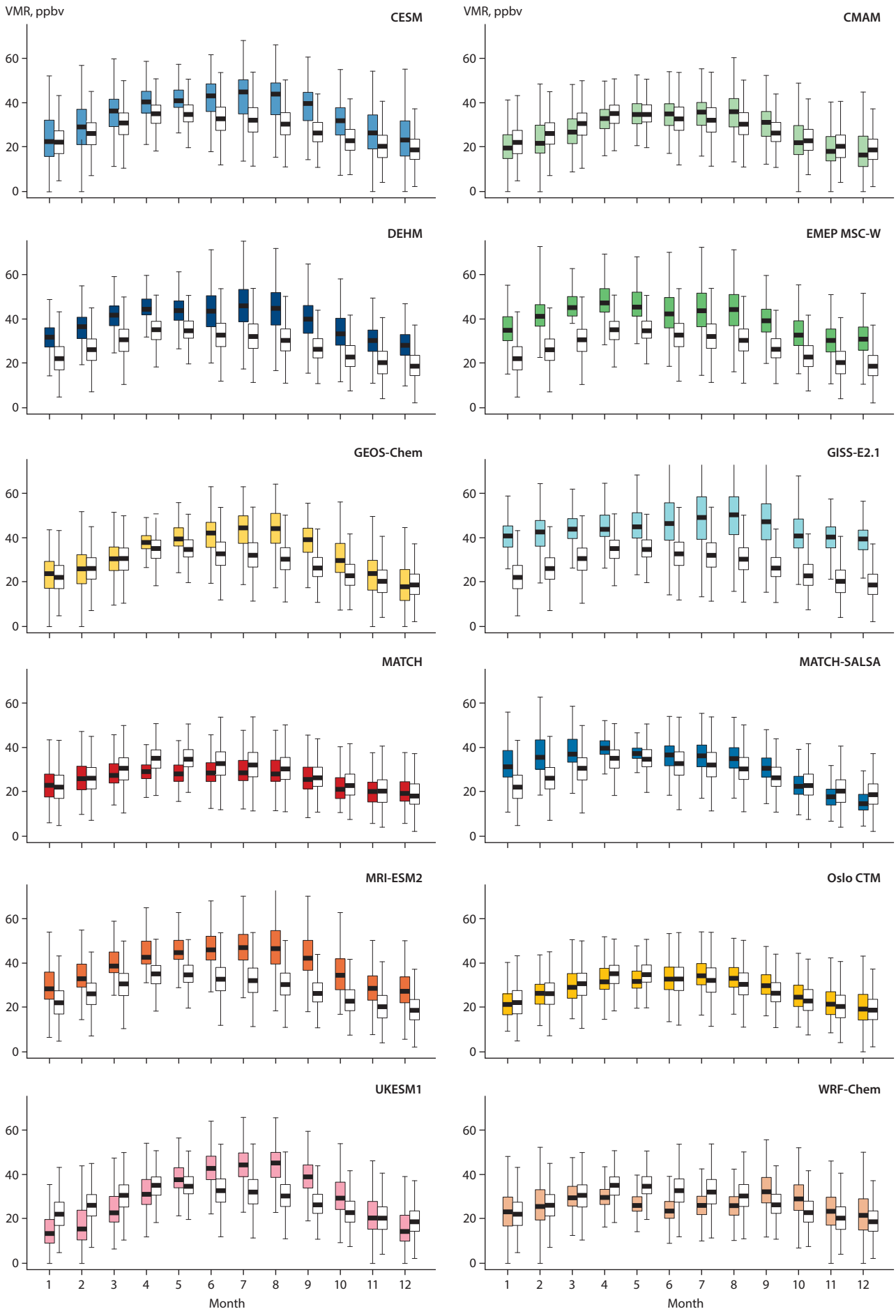

Figure 7.8 Seasonal variability of ground-level O_3 (VMRs, in ppbv) for 2014–15 from all measurement sites globally. Observations in black and white, and models in color.

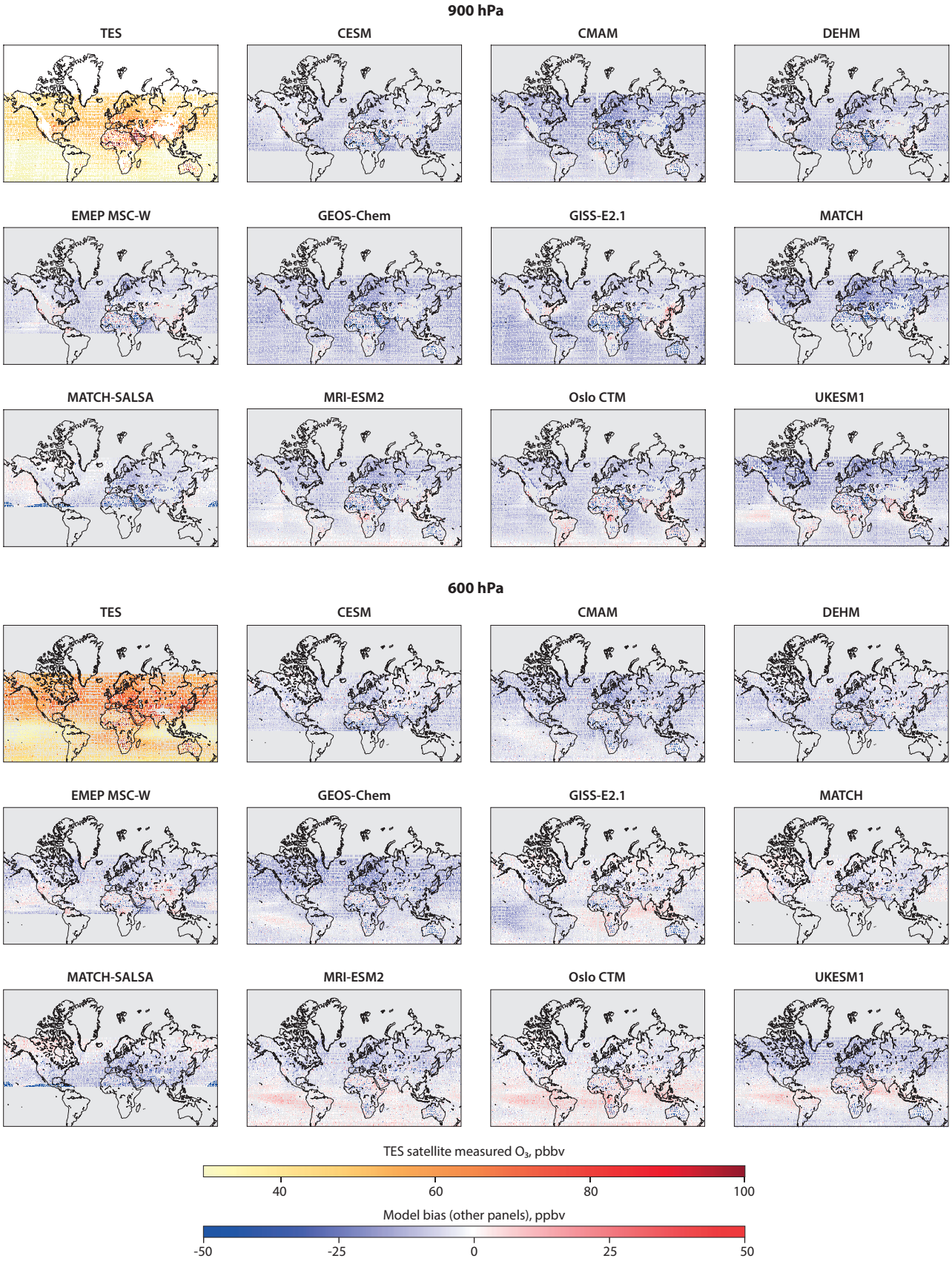

Figure 7.9 TES satellite measurements of O_3 in the lower-troposphere (900 hPa) and mid-troposphere (600 hPa) for 2008–2009. Rest of panels: model biases. Results for 2014–15 were similar and are not shown.

Figure 7.9 shows that O_3 increases from the lower- (a) to the mid-troposphere (b), and that models have relatively small biases compared to these measurements. The average model bias for individual models at the 900 hPa level is -30% to -6%, with the multi-model mean bias of -17%. At the 600 hPa level, the range is similar, at -30% to +3%, and the multi-model mean bias is -10%. As mentioned in Section 7.3.1.1, the mean biases are within the error range of the TES measurements, so the models are in quite good agreement with global free-tropospheric O_3.

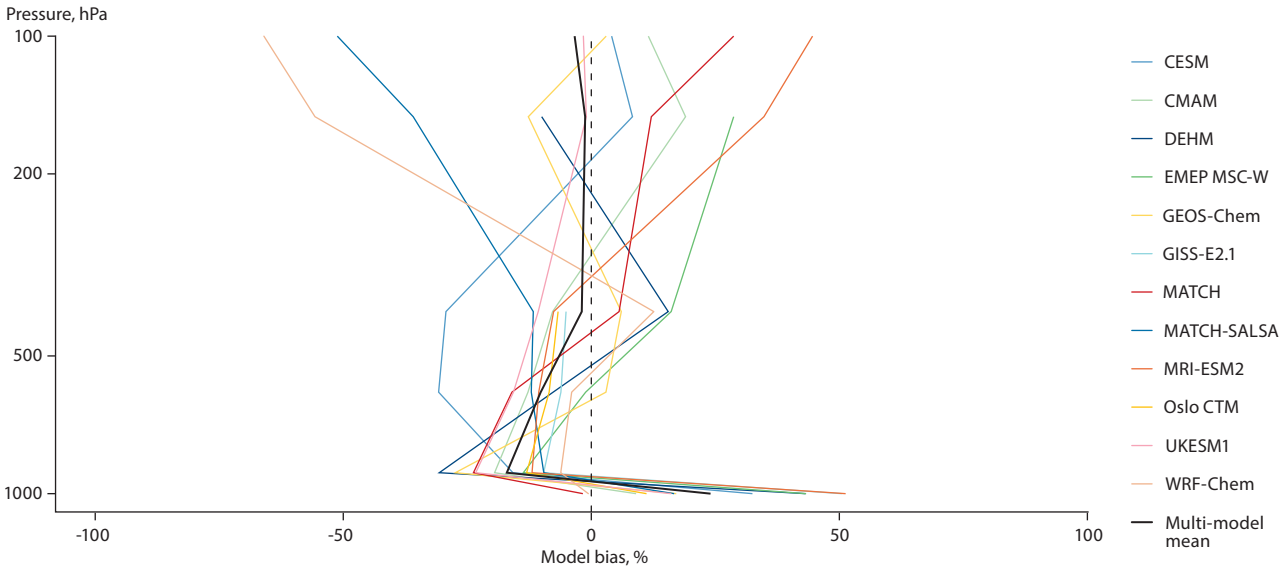

Figure 7.10 Global O_3 percent biases for all models at selected vertical levels (1000 hPa [surface], 900 hPa, 600 hPa, and 400 hPa from TES comparisons, and 150 hPa and 100 hPa from ACE-FTS comparisons) for the 2014–15 mean.

To summarize the O_3 biases across selected vertical levels, Figure 7.10 shows the global model percent biases, and the multi-model mean (thick black line) for each vertical level studied. While the mean percent bias is fairly consistent at vertical levels in the free troposphere, there is a large range in model results, particularly at the surface and in the upper troposphere. Model biases and spread may be due to deficiencies in the upper boundary O_3 climatologies that were employed, influencing UTLS O_3. They could also be due to too little modeled transport of O_3 (and its precursors) out of the boundary layer over emission source regions (Quennehen et al., 2016) or a lack of photochemical O_3 production during transport downwind from emitting regions (Arnold et al., 2015).

However, by showing positive biases in surface O_3 and generally more negative biases from 900–400 hPa, Figure 7.10 implies that there is not enough modeled vertical mixing up from the boundary layer. The lack of vertical mixing would then result in less tropospheric O_3 transport from mid-latitudes to the Arctic, and thus may be an explanation for why surface O_3 is underestimated in some regions of the Arctic.

O_3-precursors

CO and NO_x ($NO+NO_2$) are precursors to O_3 in the troposphere, and pollutants in their own right. Model outputs are compared to measurements in the troposphere for both these chemical species in Appendix A7.2.3 (Figures A7.3 to A7.8). Some of the model biases in O_3 could be due to biases in precursors such as CH_4 (Section 7.3.2) and NO_2, although in the case of CH_4, concentrations were constrained by surface data, and, as we will see in the next section, simulated CH_4 has little-to-no bias. Figures A7.3 and A7.4 show the surface CO and NO_2 measurements. These figures suggest that all models underpredict CO and NO_2 on average by -65% and -29%, respectively, except in northern Canada where modeled CO is biased high. AMAP (2015a) reported similar findings for simulated surface CO concentrations. Figure A7.5 shows CO in the free troposphere, as measured by MOPITT, at (a) 900 hPa and (b) 600 hPa vertical levels. There, modeled CO continues to be biased low throughout the northern mid-latitudes, though shows some high biases at the 900 hPa level at lower latitudes over the oceans. Figures A7.6 and A7.7 show CO and NO_X in the UTLS, as measured by ACE-FTS in the Arctic region. Figure A7.8 summarizes all of the ACE-FTS comparisons at the 150 hPa vertical level.

To summarize and conclude the O_3 model evaluation, models overestimate surface O_3, which needs to be kept in mind when considering how the modeled surface O_3 is used towards determining its health impacts (such as in Chapter 9). But in the free troposphere, where O_3 is a greenhouse gas, the model biases are within the satellite-measured error range, thus, we have higher confidence in the modeled climate impacts of O_3 (Chapter 8). Models do well at simulating the Arctic surface O_3 trends, which are very small or negligible depending on the location and season.

7.3.2 Methane (CH_4)

7.3.2.1 Arctic CH_4

Methane (CH_4) is a strong greenhouse gas, O_3-precursor, and important SLCF. Its measurements in surface-level air are shown along with model biases in the Arctic in Figure 7.11. Surface *in situ* CH_4 measurements were obtained from the World Data Centre for Greenhouse Gases. These measurements are made via gas chromatography, which has a <1% uncertainty range.

As mentioned at the end of Section 7.2, CH_4 concentrations are prescribed in the models, based on box model calculations using CH_4 emissions as input. All models use this same set of prescribed CH_4 concentrations; however, the models differ in how they distribute and advect the atmospheric CH_4 after that initialization. Some keep CH_4 concentrations prescribed as a constant distribution, while others allow CH_4 to be advected. Arctic CH_4 VMRs do not have much variability due to being distant from major sources, and CH_4 being well-mixed in the atmosphere (Figure 7.11).

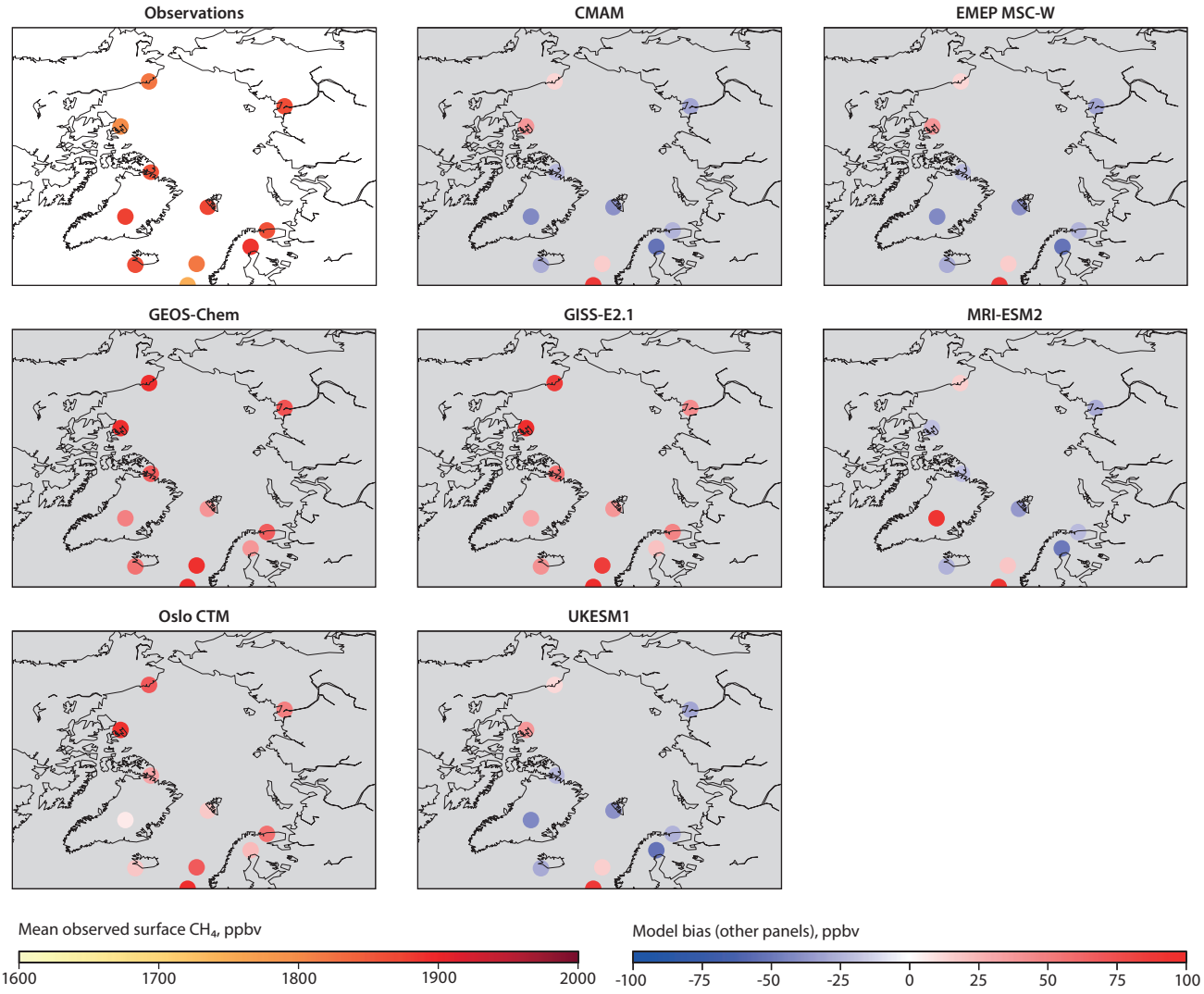

Figure 7.11 Top left panel: mean CH_4 concentrations at surface Arctic measurement sites. Rest of panels: model biases. Results are from 2014–2015; those from 2008–9 were similar and are not shown.

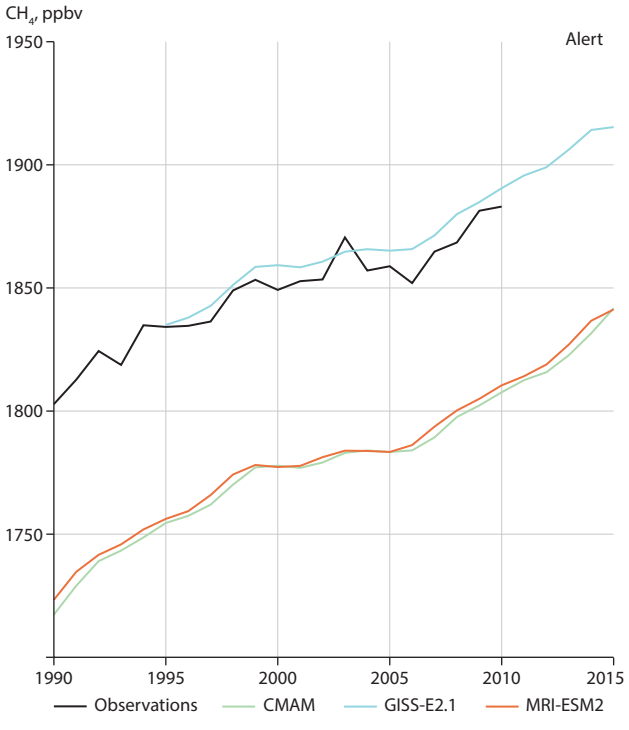

Figure 7.12 Surface CH_4 volume mixing ratios at Alert.

CMAM, MRI-ESM2 and GISS-E2.1 provided longer-term CH_4 results, which are shown in Figure 7.12 for Alert, along with observed CH_4. All three models simulate the slope of the increasing CH_4 VMRs well, however, CMAM and MRI-ESM2 are about 75 ppbv (~4%) too low. As explained in the next subsection, these two models fail to capture the north-south gradient in the global CH_4 distribution. Thus, they are biased low in the High Arctic, but biased high in the south.

Modeled CH_4 is assumed to be well mixed in the atmosphere because of its relatively long lifetime. Unlike at the surface, discussed above, in the Arctic UTLS where ACE-FTS measures, this assumption is valid, as can be seen in the relatively smooth CH_4 distribution of the top left panel of Figure 7.13, and the relatively small model biases of the order of +/-<10%. Figure 7.14 shows that the models have relatively high correlation coefficients as well. ACE-FTS has an uncertainty range of +/-10% when compared to other satellite profile measurements (Saunders, Sheese and Walker, personal communication, 2020). Thus, the modeled CH_4 agrees with these measurements within that uncertainty range.

MRI-ESM2 has the best correlation coefficient (R=0.86) of the three models that provide UTLS CH_4 VMRs (Figure 7.14), and is the best performing model in the Taylor diagram (Figure A7.7).

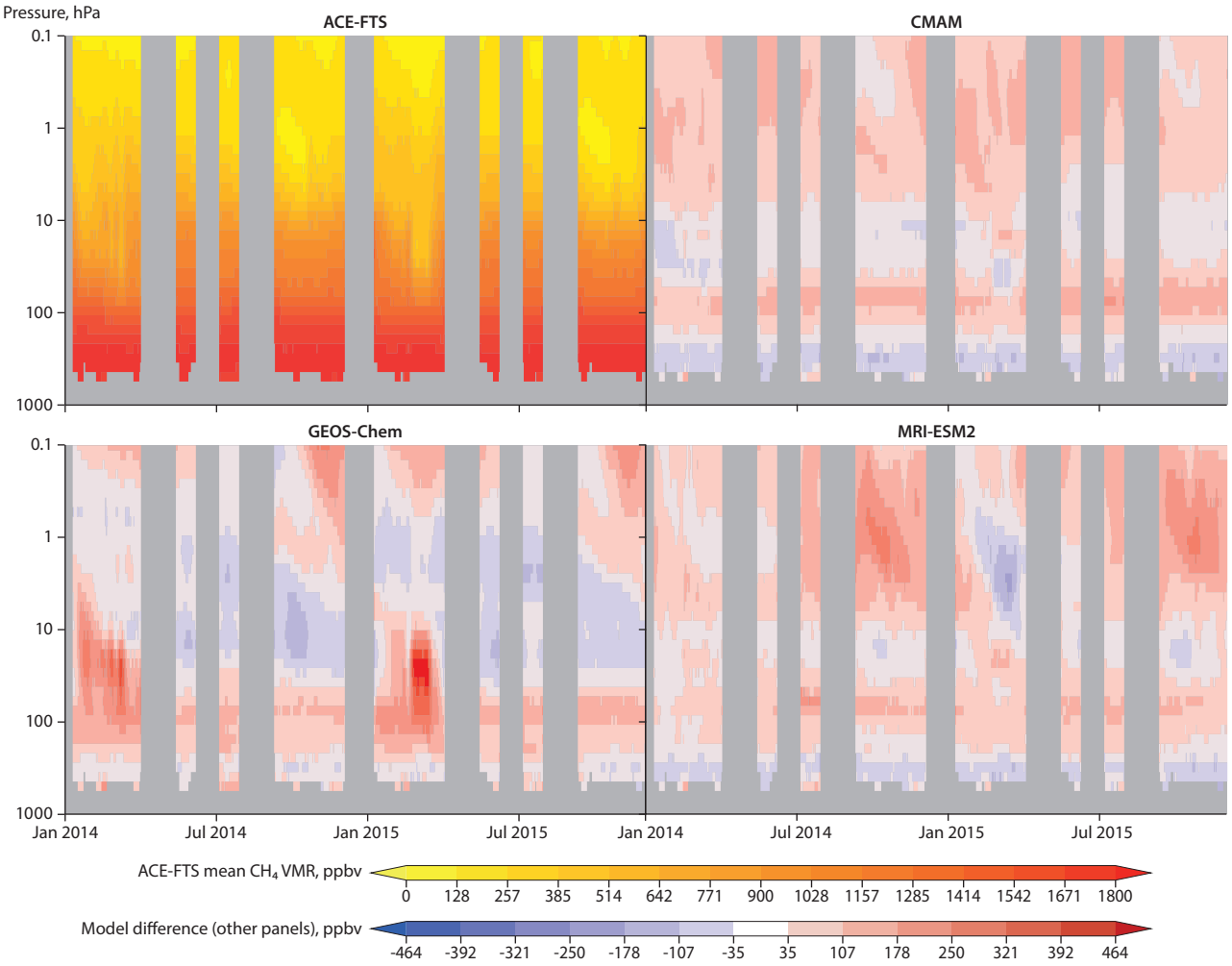

Figure 7.13 Top left: mean Arctic CH_4 from ACE-FTS measurements. Rest of panels: model-measurement differences. Results are for 2014–15; those for 2008–9 were very similar and are not shown.

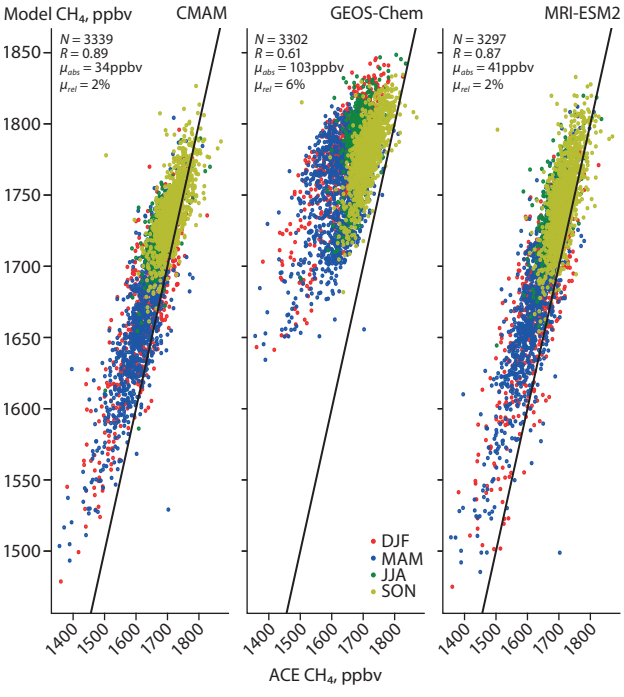

Figure 7.14 Modeled-versus-measured Arctic CH_4 at 150 hPa (UTLS region) from ACE-FTS for 2014–15. N=the number of points compared; R=correlation coefficient; μ_{abs}=the mean absolute model bias; μ_{rel}=% model bias; DJF=Dec, Jan, Feb; MAM=Mar, Apr, May; JJA=Jun, Jul, Aug; SON=Sept, Oct, Nov. Black line is the one-to-one line.

7.3.2.2 Hemispheric CH_4

Surface CH_4 on a global scale is shown in Figure 7.15 for 2014–15, along with model biases. The mean biases shown are small; the multi-model mean bias is -50 ppbv (or -3%), which means that the models simulate the magnitude of surface CH_4 well – though not within the measurement uncertainty range, which is <1%. There is a gradient in CH_4 concentrations (higher in the northern hemisphere and lower in the southern hemisphere) that is seen in the measurements (top left panel of Figure 7.15) and reported in the literature (e.g., Dlugokencky et al., 1994). As the models have more negative biases in the northern hemisphere, and more positive biases in the southern hemisphere, they do not have a strong enough latitudinal gradient in CH_4.

In Figure 7.16, we see that half of the models (CMAM, MRI-ESM2, and UKESM1) do not have nearly as large a range in CH_4 mixing ratios as the measurements do. The other models (GEOS-Chem, GISS-E2.1, and Oslo CTM) do have a similar range, with data points following the one-to-one model-versus-measurement slope more reasonably. All of these models have prescribed CH_4 concentrations, as mentioned above. It is therefore difficult to simulate realistic variability in surface-level CH_4, which varies by a few hundred ppbv according to the observations.

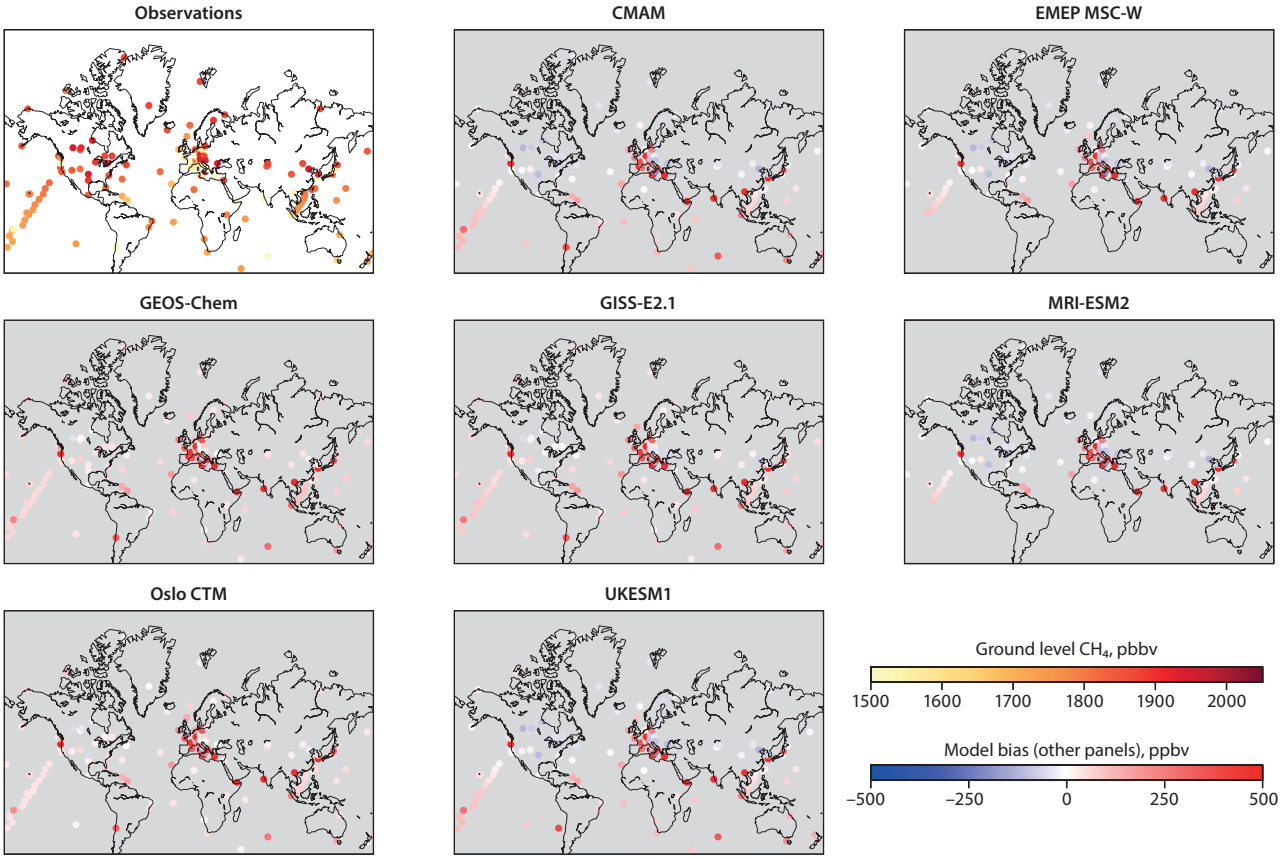

Figure 7.15 Top left panel: measured ground-level CH_4. Rest of panels: model biases. Results are for 2014–15; those from 2008–9 were similar and are not shown.

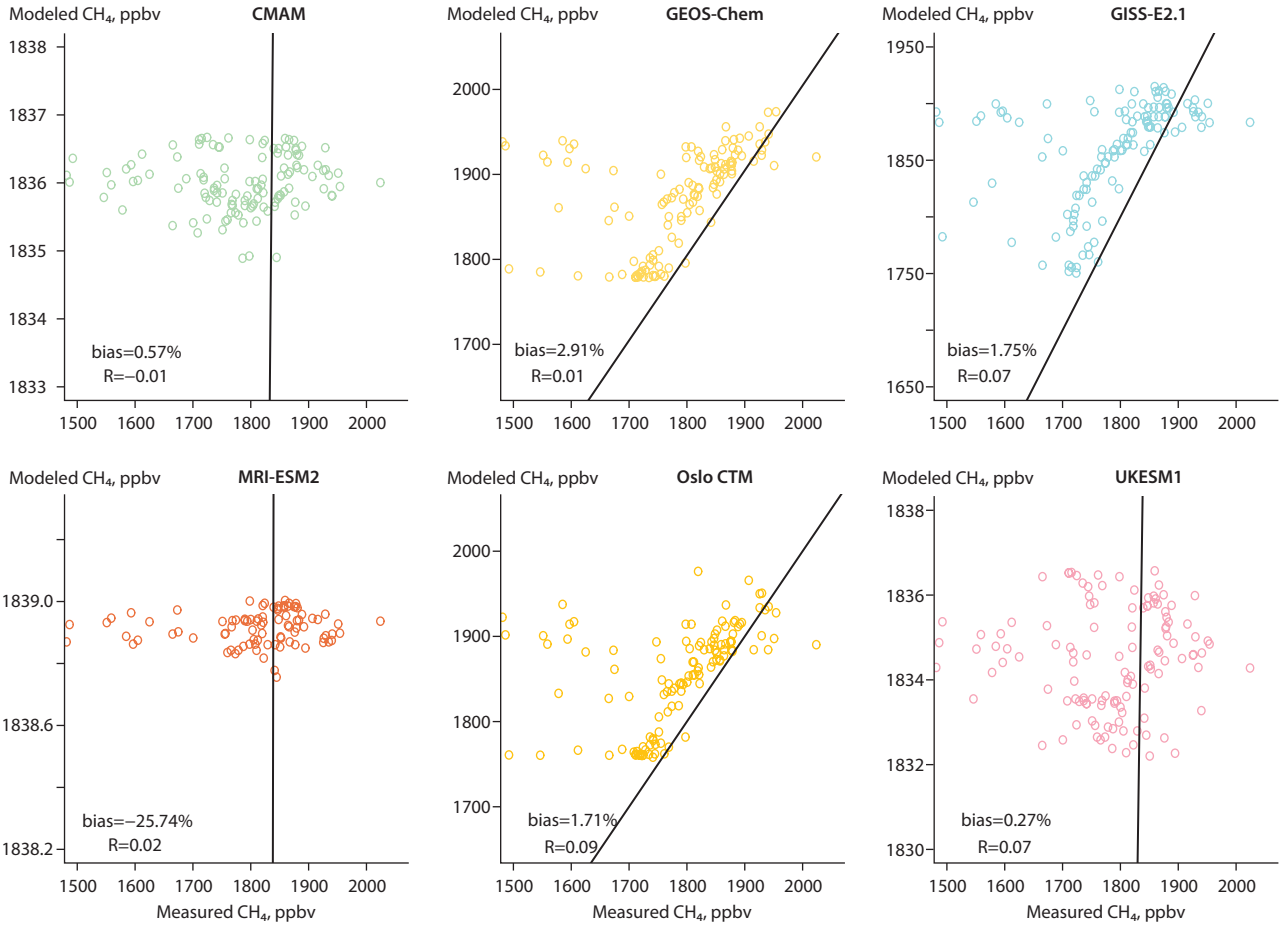

Figure 7.16 Modeled-versus-measured ground-level CH_4 (in ppbv) for 2014–2015 (annual mean). Black line is one-to-one model-versus-measurement slope. Results for 2008–9 were similar, albeit with lower VMRs, and are not shown.

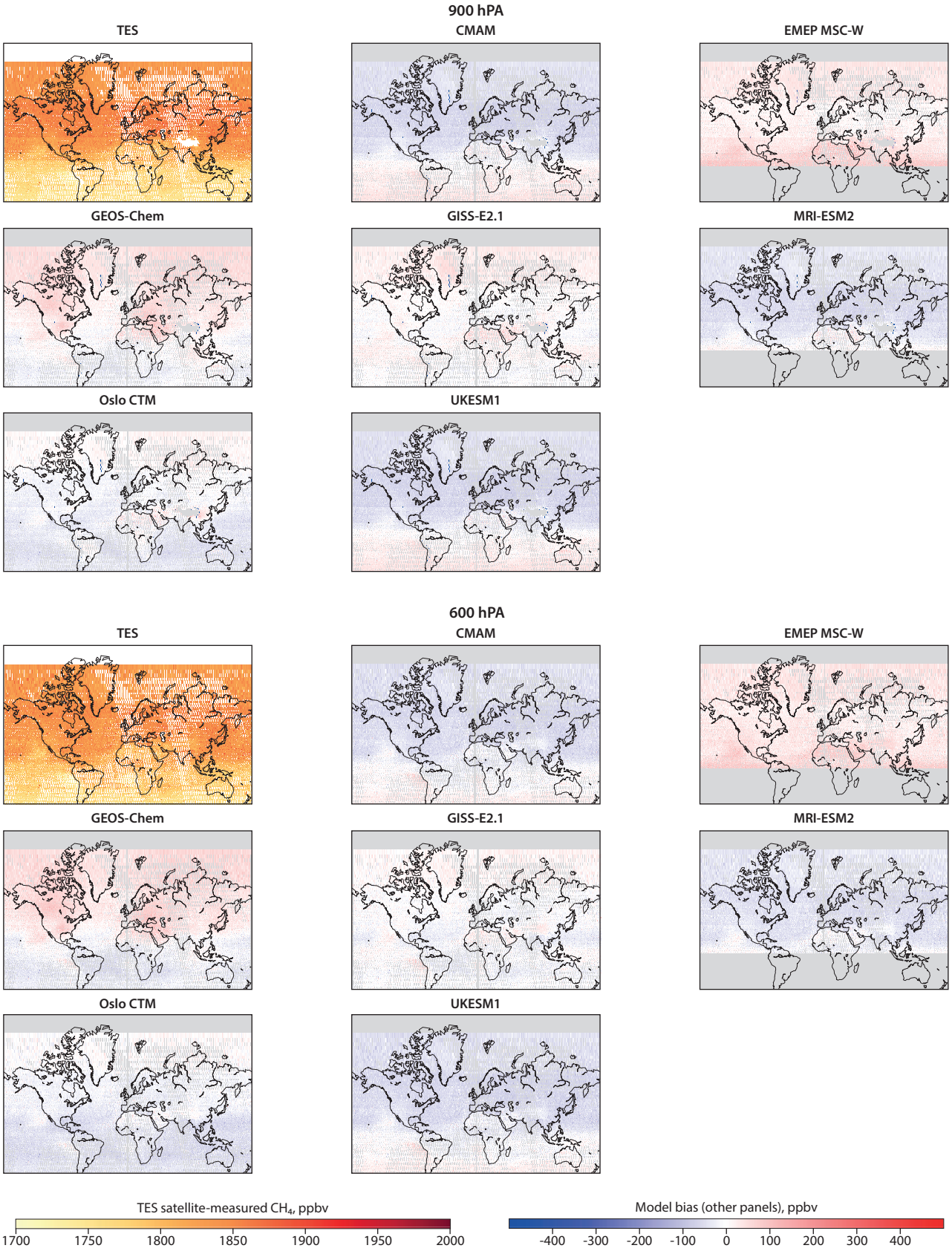

Figure 7.17 TES satellite measurements of CH_4 in the lower troposphere (900 hPa) and mid troposphere (600 hPa), and model biases for 2008–9. Results for 2014–15 (not shown) were similar but had less spatial coverage by the satellite.

Slightly higher in the troposphere, CH_4 is well mixed, as shown in the TES satellite observations in Figure 7.17 (top left), where there is a smooth distribution of CH_4. The model comparisons in Figure 7.17 and 7.13 of the previous section show that their CH_4 simplification aloft is more realistic, as their biases are distributed smoothly as well. The results for 2014–15 had less spatial coverage. The model biases are, on average, slightly negative, ranging from -13% to -4% at the 900 hPa level (lower troposphere), and -0.7% to 1.5% at the 600 hPa level (mid-troposphere) for 2014–15. The multi-model mean bias

is -7% and 0.13% for the 900 hPa and 600 hPa vertical levels, respectively, for 2014–15 (-2.5% at 900 hPa and -0.5% at 600 hPa for 2008–9). This implies that models are distributing slightly too much CH_4 near the surface and less aloft. Figure 7.17 also shows the lack of simulated northern-to-southern gradient, as CMAM, MRI-ESM2, Oslo CTM, and UKESM1 all have more negative biases towards the north, and more positive ones towards the south. Only EMEP MSC-W and GISS-E2.1 do not have that problem.

To summarize modeled CH_4 results, on average, models have higher biases at the surface and lower biases aloft, indicating insufficient vertical mixing of CH_4. Models generally do not have a strong enough north-to-south gradient in CH_4, and because they have prescribed CH_4 concentrations (instead of modeling emissions fluxes and chemistry), they do not capture the variability in CH_4 at the surface. However, the increasing Arctic trend and the magnitude of the simulated CH_4 VMRs are highly accurate. Model biases are smaller for CH_4 than any other SLCF species, as will be shown in the summary (Section 7.4).

7.3.3 Black carbon (BC)

There are various BC measurement methods, responding to different properties of BC and thus measuring different quantities (see Chapter 5 and Table A7.8). Therefore, when using BC observational data for evaluating models, it is important to know which measurement method was used. The method is typically reflected by the names of measured quantities following World Meteorological Organization Global Atmosphere Watch programme recommended terminology (Petzold et al., 2013), with elemental carbon (EC) determined by thermal-optical methods, equivalent BC (eBC) by optical absorption methods, and refractory BC (rBC) by incandescence methods (see details in Chapter 5). Correlations between methods (and measured quantities) are frequently high but relationships vary among sites, seasons and aerosol types. For example, no significant differences were found between eBC and EC for aerosols dominated by diesel traffic sources, whereas measured EC concentrations tended to be lower than eBC where a significant contribution came from biomass burning emissions from residential heating (Reisinger et al., 2008) or waste burning (Singh et al., 2014). However, the different BC measurement types usually agree within a factor of two (Chapter 5).

As BC emissions inventories, including ECLIPSE v6b (Data ref. 7.2), are mainly based on emission factors derived from thermal-optical methods, the modeled BC results are representative of EC. The major observing networks for Europe (European Monitoring and Evaluation Programme, EMEP), Canada (Canadian Aerosol Baseline Measurement, CABM), and the USA (Interagency Monitoring of Protected Visual Environments, IMPROVE) measure EC with approximately 10% uncertainty. Another complexity with model evaluation of BC is that some of the eBC measurements that models are compared to were made from collected particulate matter (PM) comprised of particles with different maximum diameters (measured in micrometers; e.g., PM_1, $PM_{2.5}$, and PM_{10}). These are included in Table A7.8 for each of the measurement locations. For the models, BC from $PM_{2.5}$ was used.

7.3.3.1 Arctic BC

Figure 7.18 shows the measurement locations of BC in the Arctic. Atmospheric concentrations in surface-level air are measured at the red locations, while BC deposition flux is measured in ice cores at the black locations. Surface-level

Figure 7.18 Locations for BC deposition (ice cores; black) and atmospheric measurements (red).

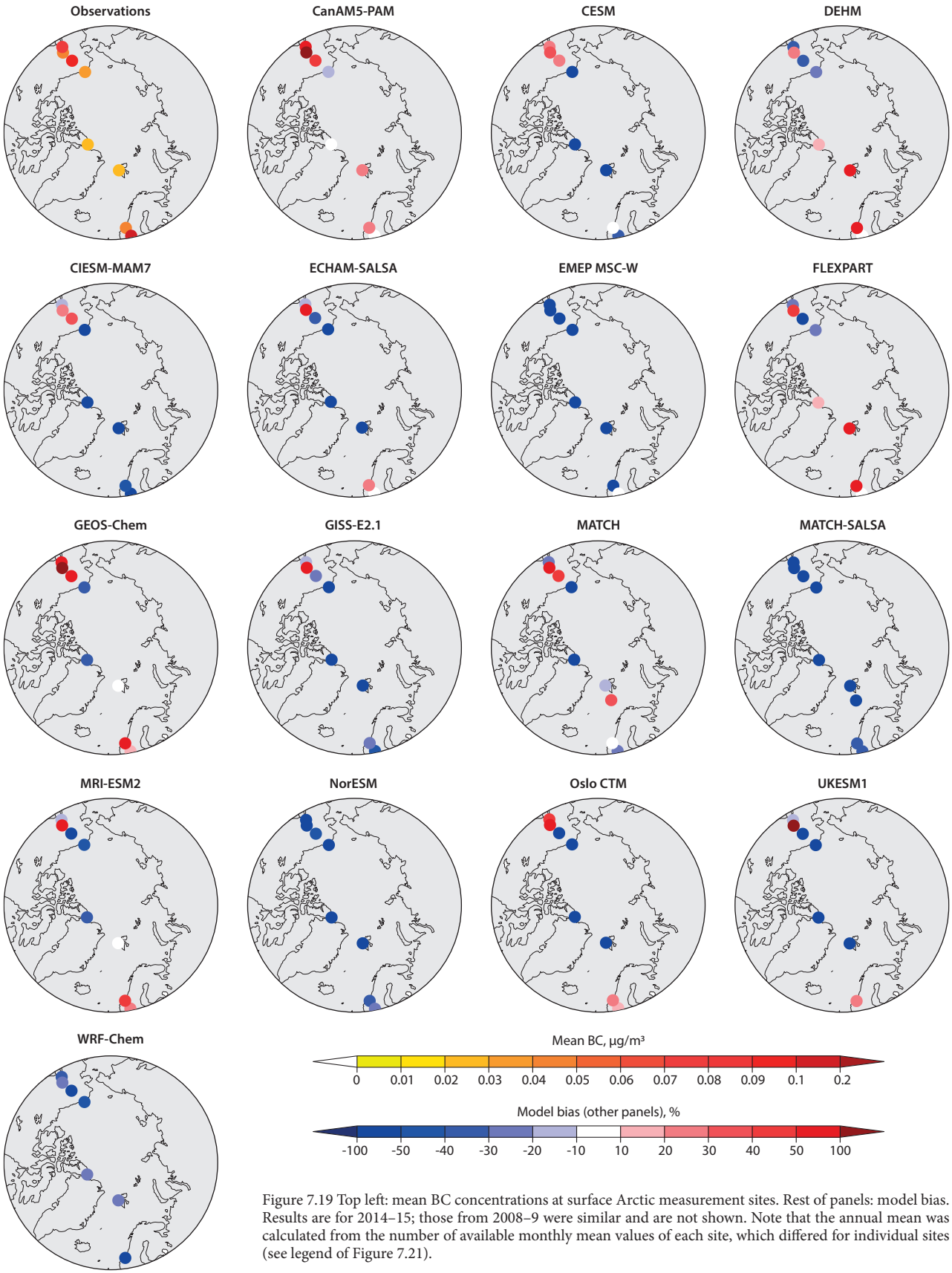

Figure 7.19 Top left: mean BC concentrations at surface Arctic measurement sites. Rest of panels: model bias. Results are for 2014–15; those from 2008–9 were similar and are not shown. Note that the annual mean was calculated from the number of available monthly mean values of each site, which differed for individual sites (see legend of Figure 7.21).

atmospheric BC over the ocean was also evaluated using two Arctic ship-based campaigns that measured BC (and other pollutants) within the 2014–2015 model validation period (see later in this section). To better evaluate models' performances in the Arctic, further measurement locations would be helpful, particularly in northern Russia, northern Canada, and in Greenland.

Figure 7.19 shows observed and modeled concentrations of BC in surface air at nine Arctic observation stations (some atmospheric locations in Figure 7.18 did not have BC data for the years of interest or were otherwise difficult to obtain). Annual mean concentrations are of the order of less than one microgram/meter^3 (µg/m^3), and most models tend to underestimate BC in the High Arctic while overestimating it

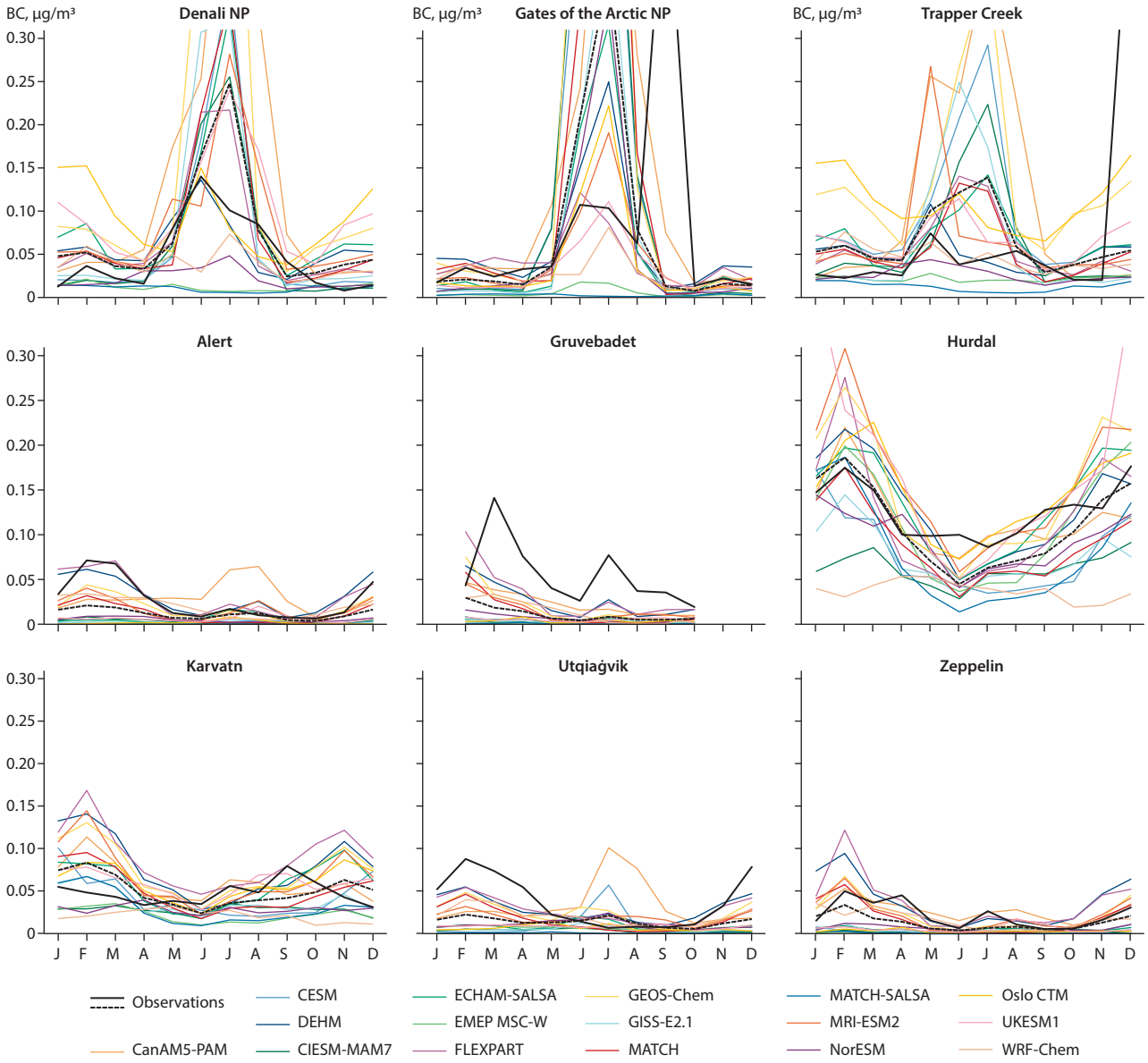

Figure 7.20 Modeled (colored lines) and measured (thick black line) monthly mean BC concentrations at surface Arctic measurement sites in 2014–15. Multi-model mean is shown by the black dashed line.

in Alaska and Scandinavia. However, a few models (CanAM5-PAM, DEHM, and FLEXPART) also overestimate BC in the High Arctic. Overall individual model biases range between +/-100% at individual sites.

It has previously been reported that most models were not able to represent the higher winter BC concentrations (AMAP 2015a; Eckhardt et al., 2015; Mahmood et al., 2016). As can be seen in Figure 7.20, some models still underestimate winter BC, but many models now have similar seasonality to the observations. The multi-model mean also captures the monthly variations well, including the summer peak at some Alaskan sites caused by fire emissions. The multi-model mean Arctic BC is underestimated in the winter (-24%), and overestimated in the summer (+32%). However, overall, this is an improvement in model performance in simulating Arctic BC since AMAP (2015a) was published – which reported a -59% winter bias and +88% summer bias for BC (AMAP, 2015a; Eckhardt et al., 2015). That said, it is difficult to make direct comparisons with the 2015 report, as those values were for a smaller set of Arctic locations, over different observation periods, and with a different set of models (although many overlap with this report). The model improvement may be due to improved data on anthropogenic emissions of BC, particularly from northern Russia, which were absent in the emissions data used for AMAP (2015a) (Chapter 2).

Most models have reasonable spatial correlation with the measurements across the Arctic, in that they correctly simulate the range of BC concentrations that appear across the Arctic (higher concentrations at Hurdal, lower concentrations at Zeppelin, and so on), as shown in Figure 7.21. However, there are still large differences and low correlation-coefficient values in the statistics shown in Figure 7.21, as is common when simulating aerosol species (e.g. Im et al., 2015).

The EMEP MSC-W model tends to underestimate BC. This is consistent with the model intercomparison presented in Gliß et al. (2021), which indicated a relatively short lifetime of BC in the EMEP MSC-W model. Also note that, differently from the other models, the FINN forest fire data (Wiedinmyer et al., 2011) was used by EMEP MSC-W in these simulations.

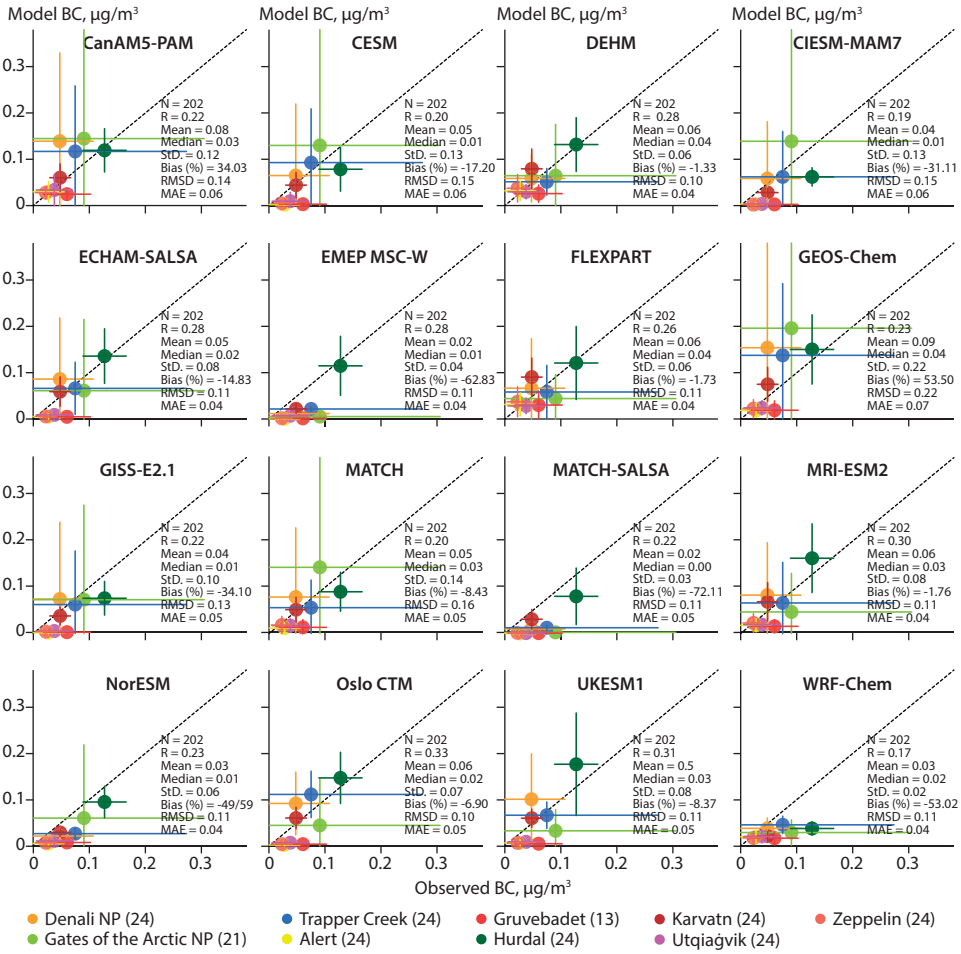

Figure 7.21 Modeled-versus-measured BC concentrations at surface Arctic measurement sites in 2014–15. Filled circles represent the mean for each location, while the lines dissecting them represent +/- one standard deviation from mean. N=number of data points, R=correlation coefficient, Mean=model mean value in mg/m³, Median=model median value in mg/m³, StD=model standard deviation, Bias (%)=percent model bias, RMSD=root mean standard error in mg/m³, MAE=mean absolute error in mg/m³. Results for 2008–9 (not shown) had lower correlation coefficients and higher biases. The number of monthly mean values available from individual sites is shown in brackets next to site names in the legend, with a max of 24 months in the two years.

BC over the Arctic Ocean

In addition to the stationary measurement locations, there were three ship-based measurement campaigns during 2014–2015. These were the Japanese campaigns in September of 2014 and 2015 (tracks from Japan to north of Alaska in Figure 7.22; Taketani et al., 2016), and the Russian campaign in October 2015 (track north of Russia in Figure 7.22; Popovicheva et al., 2017). Models that provided three-hourly BC output were compared to these observations in Figures 7.22 and 7.23. The Russian measurements are of eBC, whereas the Japanese measurements are of rBC. The two are related by a factor of 1.8 (eBC=1.8*rBC; Zanatta et al., 2018). Therefore, eBC measurements in this section were first converted before comparisons to the models were made.

There is a consistent overestimate of BC in the Pacific region, where measured concentrations are very low (Figures 7.22 and 7.23). Indeed, Taketani et al. (2016) reported that BC concentrations were in the range 0–66 µg/m³, with an overall mean value of just 1.0 +/- 1.2 µg/m³. The models, possibly due to their coarse resolutions, were not able to simulate such low background BC concentrations. However, even the model with the highest resolution (GEM-MACH at 15 km resolution) overestimated BC there – although that limited area model (LAM), in that region near the boundary, would have been heavily influenced by the assumed upwind boundary conditions. The high bias in the Pacific may be due to all models overestimating the amount of BC that gets transported off of the Asian continent.

Conversely, the model results generally agree in the Russian Arctic Ocean, though they are mostly biased slightly low. Popovicheva et al. (2017) attributed the higher BC concentrations measured near the Kara Straight (north of 70°N) to gas-flaring emissions, with mid-latitude biomass burning, transportation, and combustion (residential and commercial) being important sources near Arkhangelsk (White Sea). Since models were able to simulate this well, their improvement is likely due to improved Russian anthropogenic emissions data in ECLIPSE v6b (see Chapter 2 for more details about those emissions).

BC deposition flux compared to ice cores

Ice-core analyses give derived values of deposition during the last decades and are valuable for investigating how past concentrations have changed. As noted in Chapter 6 (Section 6.1.4.2), fluxes are not a measured value, but derived from measurements of BC concentrations in the ice and modeled assumptions about precipitation. Before the industrial period (defined as starting in 1850) the only source of BC was biomass burning. After 1850, anthropogenic emissions influenced deposition of BC in Arctic locations. Most ice cores show a peak in BC deposition flux early in the 20th century (see also Chapter 6 Section 6.1.4.2 and Figure 6.20), with a decreasing trend over the last few decades. Ice-core observations of the last two decades were used to evaluate the performance of BC (and SO_4 in Section 7.3.4.1) deposition flux in the models. Six ice cores in Greenland were analyzed, plus one in the European Arctic, in Spitsbergen (Lomonosovfonna; Figure 7.18). Ice-core data were available from 1750 until the

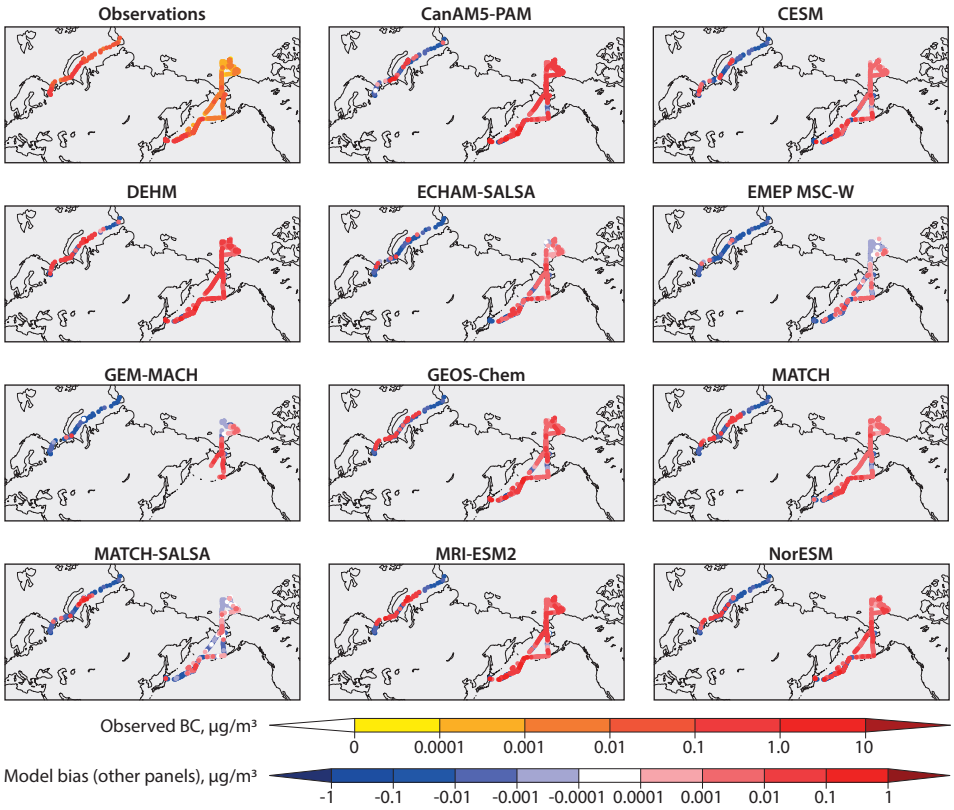

Figure 7.22 Top left: Observed BC concentrations along the Japanese and Russian ships' paths. Rest of panels: The model biases.

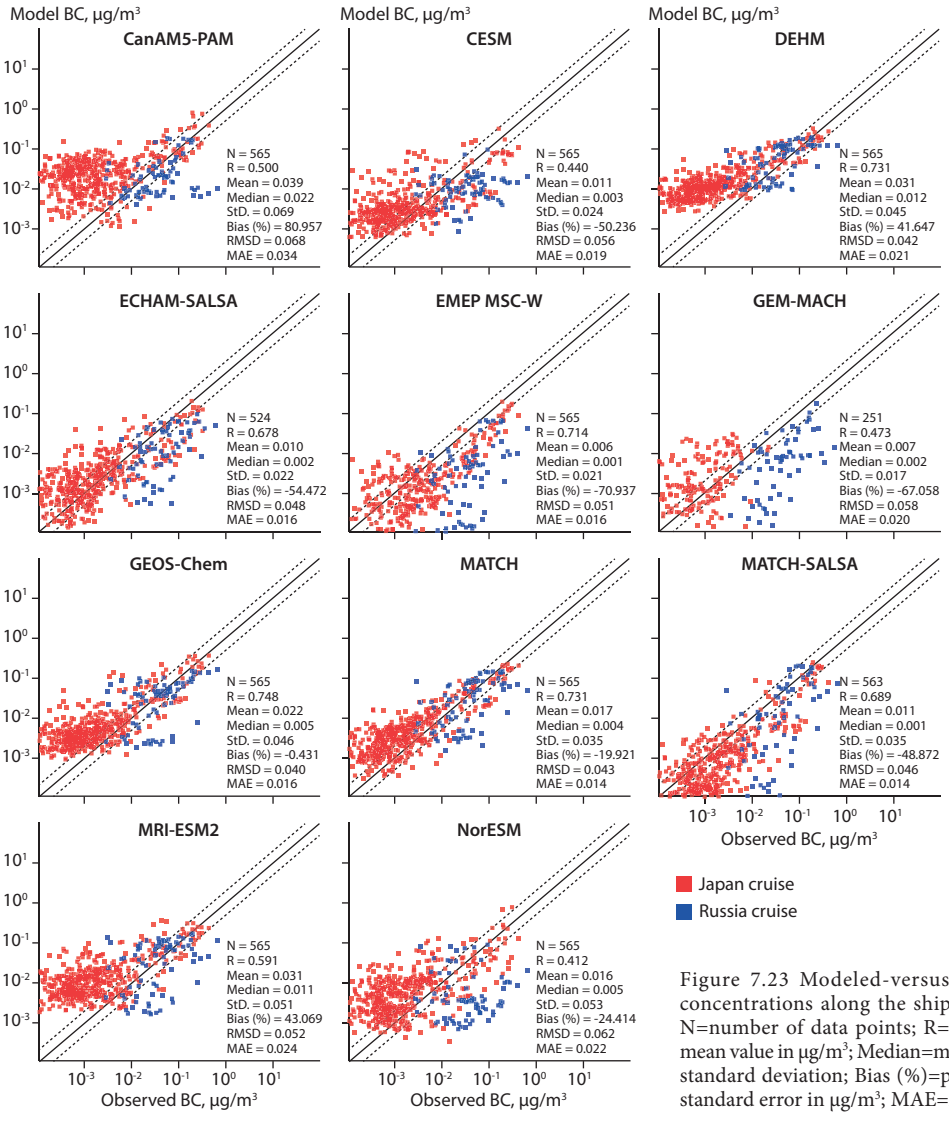

Figure 7.23 Modeled-versus-measured three-hour average BC concentrations along the ships' paths. Note the logarithmic scale. N=number of data points; R=correlation coefficient; Mean=model mean value in µg/m³; Median=model median value in µg/m³; StD=model standard deviation; Bias (%)=percent model bias; RMSD=root mean standard error in µg/m³; MAE=mean absolute error in µg/m³.

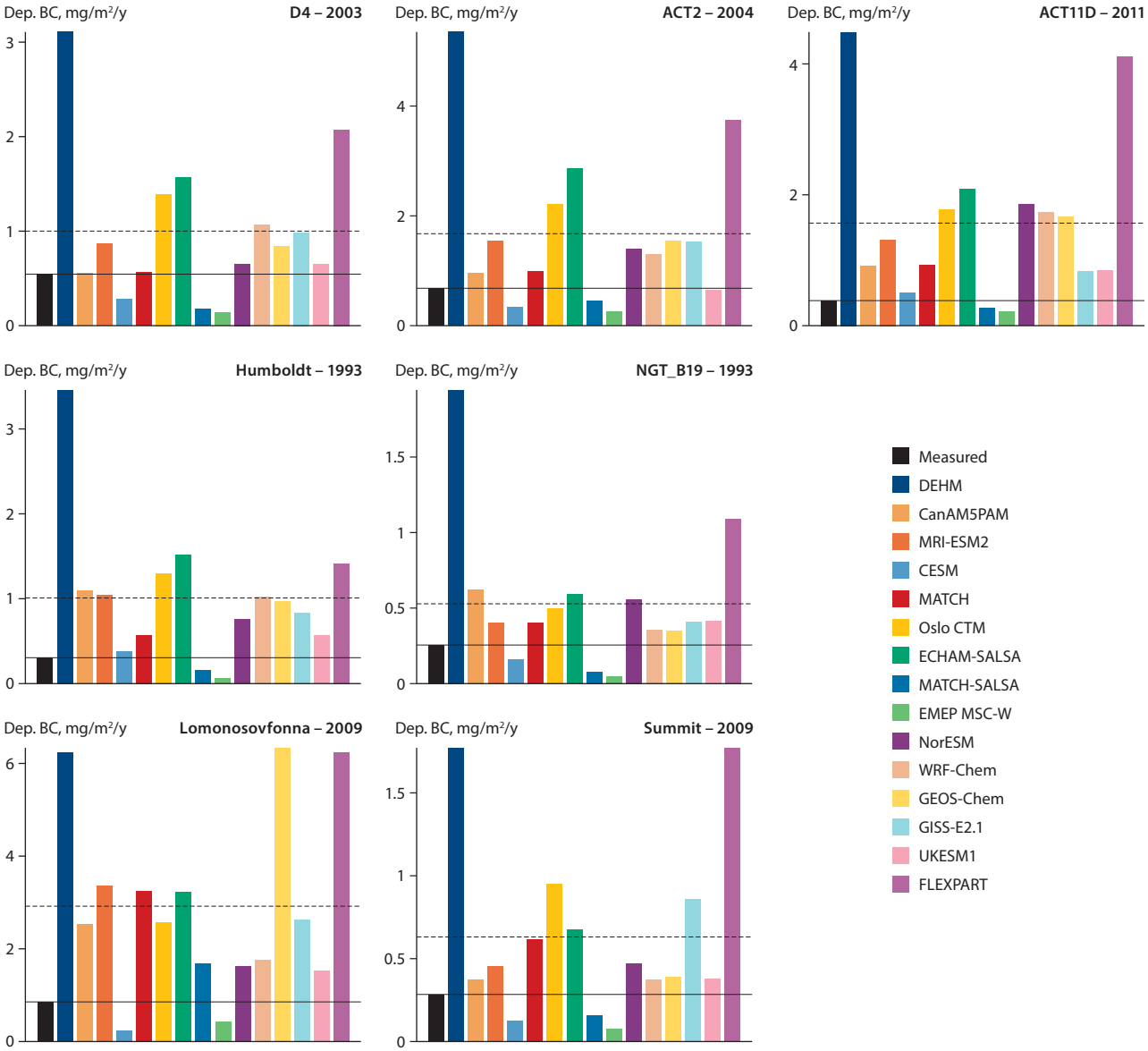

Figure 7.24 Annual average BC deposition flux values for the seven ice-core locations (Figure 7.18) for each model, based on values from 2008–2009 and 2014–2015. The observed fluxes are plotted in black, with solid black lines indicating the level of the average observed flux, and black dashed lines depicting the model mean for each location. The period used for plotting is based on all available years after 1990; the title indicates the last year available from the ice-core record.

years between 1993 and 2011 (depending on when the ice cores were drilled), as indicated in the panel titles in Figure 7.24. Only data after 1990 were used to match the modeled time periods [1990–2015, 1995–2015, 2008–9 and 2014–15, depending on the model (Table 7.1)].

The measured BC deposition flux values in Greenland vary with elevation, being lower at higher elevations. Summit (3177 meters above sea level [MASL]) had an average of 285 μg/m^2 per year (μg/m^2/y) in contrast to ACT2 (2461 MASL) with 676 μg/m^2/y. BC deposition was highest in the European Arctic at Lomonosovfonna (Spitsbergen), with 856 μg/m^2/y. For all seven ice cores used in this comparison, the averaged model mean was three times as high as the observations. At D4 (2728 MASL) the modeled mean corresponded best to the observations, with a mean bias of -83%. At ACT11 (2296 MASL) the models had four times the deposition flux compared to the measurements. Generally though, the mean was skewed higher by FLEXPART and DEHM models (Figure 7.24).

7.3.3.2 BC trends in the Arctic, 1990–2015

Some measures to reduce BC emissions have been undertaken in recent years. To assess the impacts of those emissions changes, it is important to evaluate the changes in Arctic BC concentrations. Breider et al. (2017) computed that the combined SO_4 and BC trends caused about a quarter of net warming of the Arctic surface during 1980–2010, which means the impact of BC was greater than SO_4, as SO_4 has a cooling effect. Those findings were consistent with an earlier study by Shindell and Faluvegi (2009). Six models simulated BC from 1990 to 2015, and one model from 1995 to 2015. As shown in Figure 7.25, the measurements (black line) at Alert and Utqiaġvik exhibit a decline in BC concentrations during the

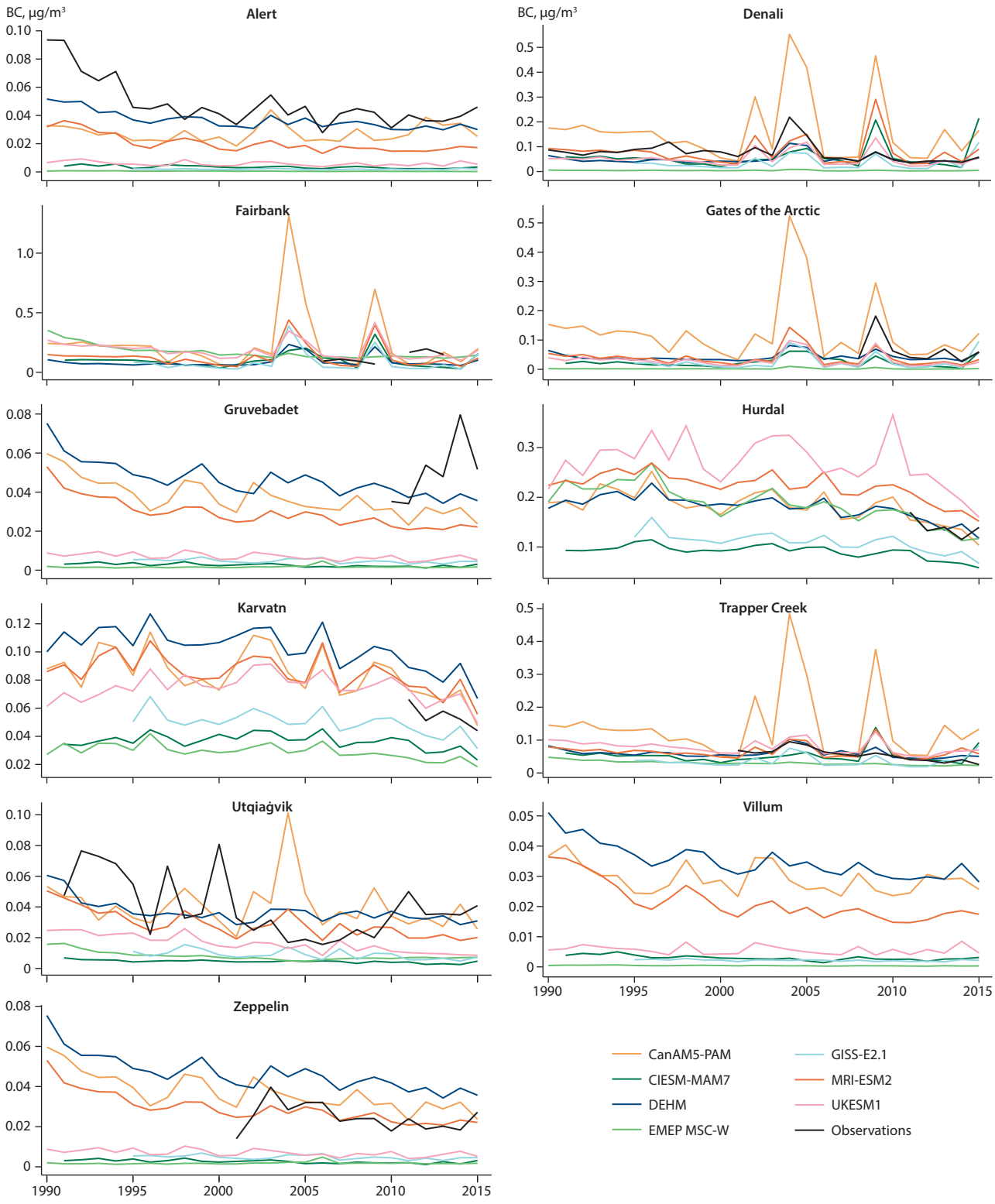

Figure 7.25 Measured (black lines) and modeled (coloured lines) annual mean time series of surface-level BC at 11 Arctic ground stations.

1990s that the models also simulate. Other stations' time series, including those of Denali and Trapper Creek, indicate that BC remained stagnant in both observations and models.

In Section 6.1.4.1, the BC and SO_4 trends were examined by comparing the last five years of the time series to the first five years of the time series after smoothing and separating out the seasons (haze season – January to April [JFMA], and summer season – June to September [JJAS]). The same calculation was made for the models' results, which are tabulated in Table 7.2.

The models generally show a large decrease in BC during the haze season at all Arctic locations, which is consistent with the measurements (Table 6.2 in Section 6.1.4.1). For the summer season, the models do not agree on whether BC is increasing or decreasing, however, the measurements show a decrease in BC at all Arctic locations, except for Zeppelin. The comparison to measurements is not perfect because the time periods are different for the models (generally 1990–2015) and measurements (usually starting later and ending in 2018). Nonetheless, the anthropogenic emissions have accurately

Table 7.2 Percent changes to modeled BC. Data for the last five years (2011–2015) were divided by those for the first five years (1990–1994 for all models except GISS-E2.1, for which 1995–1999 data were used) for winter (JFMA, top), and summer (JJAS, bottom).

	CanAM5-PAM	CIESM-MAM7	DEHM	EMEP MSC-W	GISS-E2.1	MRI-ESM2	UKESM1
Alert							
JFMA	-20%	-44%	-44%	-52%	-28%	-65%	-50%
JJAS	20%	-9.5%	16%	-25%	-18%	18%	17%
Gruvebadet							
JFMA	-49%	-56%	-37%	-16%	-45%	-48%	-43%
JJAS	1.3%	-20%	-23%	21%	-6%	-16%	-12%
Villum							
JFMA	-33%	-45%	-38%	-53%	-30%	-53%	-33%
JJAS	53%	7.2%	16%	-23%	34%	4.7%	6.1%
Utqiaġvik							
JFMA	-37%	-27%	-43%	-44%	-45%	-59%	-66%
JJAS	-9.4%	-52%	5.1%	-41%	-45%	-31%	-47%
Zeppelin							
JFMA	-47%	2.2%	-37%	-22%	-46%	-48%	-42%
JJAS	14%	-19%	-22%	28%	-5.4%	-15%	-11%

driven the modeled trends in the right direction for the winter haze season. The models are less certain for the summer, when BC concentrations are more influenced by biomass burning.

7.3.3.3 Hemispheric BC

BC is measured extensively in the USA, as well as at several locations in Canada (six sites), and Europe (~16 sites – the actual number varies from year to year). Unfortunately, the authors of this report were unable to find further global measurements of BC at the surface. And, some eastern countries did not have freely available BC measurements for the time periods required for this chapter. Figure 7.26 shows BC measurements along with the model biases. According to these comparisons, some models overestimate BC in the USA by factor of two or more, while others seem to compare well. CanAM5-PAM, Oslo CTM and WRF-Chem overestimate BC while EMEP MSC-W underestimates BC over most US sites. That BC is overestimated in the USA by many models suggests that the climate (e.g., temperature) impacts of BC may be overestimated in the models over these regions. However, because a few models also underestimate the BC concentrations, the multi-model mean results can still provide robust estimation of climatic impacts of BC. These domain-limited BC comparisons do not allow for generalizations of the results on global scales. However, Sections 7.3.5 on $PM_{2.5}$ and 7.3.6 on aerosol optical properties — although not specific only to BC — help to fill in the gaps using related variables on global scales.

Vertical profiles of BC using aircraft observations

Gridded BC outputs at three-hourly intervals were provided by 11 of the participating models. The purpose of this high-frequency modeling is to enable comparisons of model outputs to aircraft measurements – using the tracks of the aircraft in the grid space of each model. The interpolation of model output to flight-track coordinates was carried out using tools from the Community Intercomparison Suite (CIS, Watson-Parris et al., 2016), which paired the extracted model tracks with the corresponding observed values. There is naturally some coarsening of information, as the aircraft observations are of considerably higher spatial and temporal resolution than the model outputs. Nonetheless, this approach provides meaningful comparisons when flight tracks are grouped over specific areas or times.

The aircraft campaigns considered in our comparisons are shown on Figure 7.27. Note that most aircraft campaigns with BC measurements took place in the years 2008–2009, with the exception of the High-Arctic Network on Climate and Aerosols: Addressing Key Uncertainties in Remote Canadian Environments (NETCARE) campaigns, which provided observations for 2014–2015. Furthermore, most campaigns were carried out during the boreal spring and summer months (April to July), except for the High-Performance Instrumented Airborne Platform for Environmental Research (HIAPER) Pole-to-Pole Observations (HIPPO) campaign (January and November). Variability of atmospheric BC concentrations is very high on short timescales and exceeds interannual variation, therefore data from all years or campaigns were combined.

Aeroplane (map) views of observations and model biases are provided for three different height bins in Section A7.3 (Figure A7.9). The bias maps have three purposes: first, the map of the lowest heights (Figure A7.9) supports the model biases found in BC surface values in Section 7.3.3.1 and illustrated in Figure 7.19; second, all maps demonstrate the large spread among models, and within models at different heights; and third, the positive bias of all models with respect to the HIPPO campaign underscores the very low HIPPO campaign measurements. These low HIPPO measurements

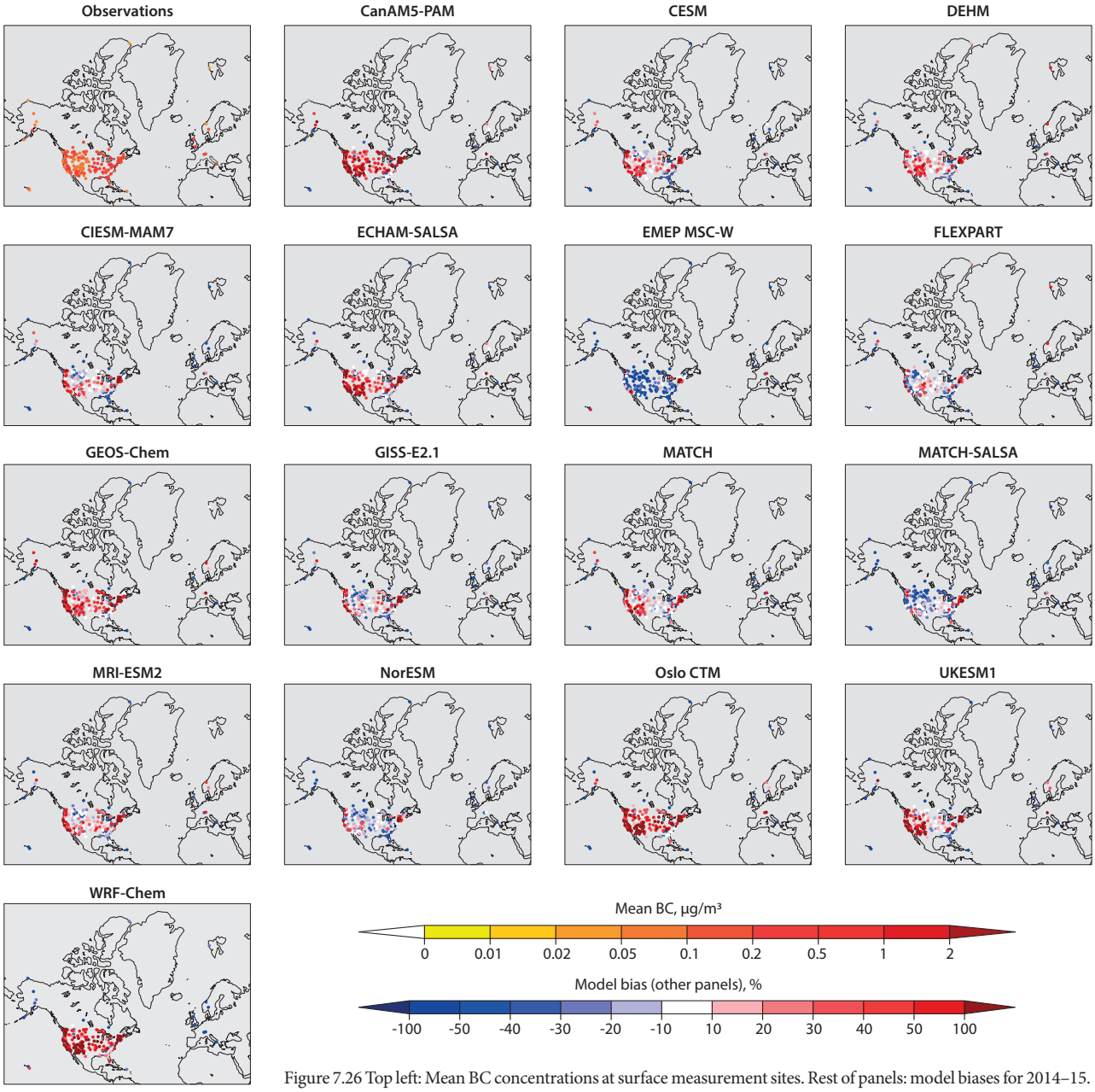

Figure 7.26 Top left: Mean BC concentrations at surface measurement sites. Rest of panels: model biases for 2014–15.

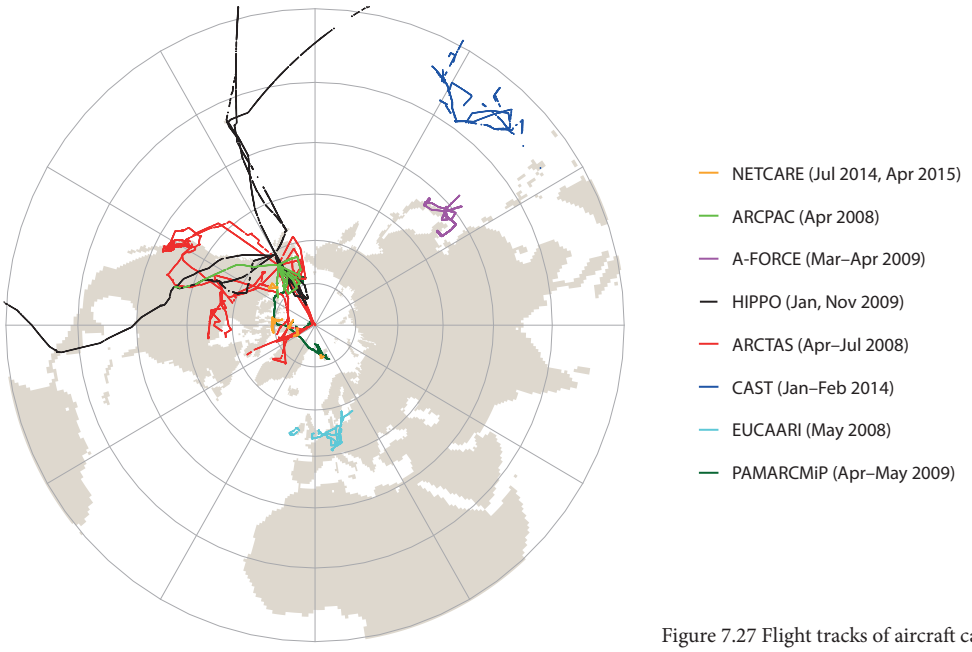

Figure 7.27 Flight tracks of aircraft campaigns used in this section.

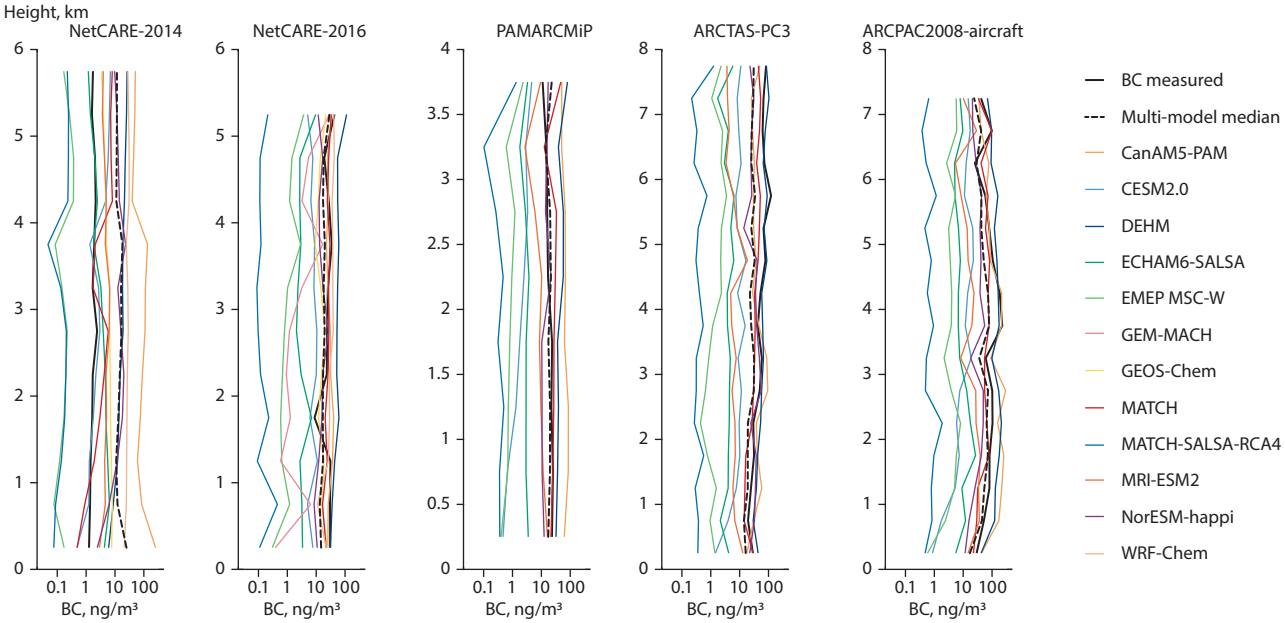

Figure 7.28 Vertical profiles of measured (solid black line) and modeled (colored lines) concentrations of BC in the High Arctic. The dashed black line is the multi-model median.

over the northwestern Pacific are consistent with particularly low BC concentrations measured from ships in the same region, as discussed in Section 7.3.3.1 and shown on Figure 7.22.

The focus of the present section is on vertical profiles of BC concentrations. Profiles of aircraft measurements made exclusively in the High Arctic (north of 70°N) are shown on Figure 7.28. For these plots, all points from a given campaign were taken together and binned by height (every 500 m); the lines of the graph show the median values for each bin. Observations are indicated by the solid black line, while the dashed black line represents the multi-model median. Because BC concentrations can span several orders of magnitude, and because of the high inter-model spread, median values are more meaningful than means, and median absolute deviations (MADs) were used to quantify spread.

A distinguishing feature of all High-Arctic profiles is the vertical homogeneity of the concentrations: lines are nearly vertical from the surface to the top of the measurements, which were at 4–7 km in altitude. Inter-model spread in the magnitude of BC is considerable, but the multi-model medians are generally very close to the observed values. The one exception is the NETCARE–2014 campaign, which covered a very small area. Most models are biased low with respect to observations recorded at these high latitudes.

In contrast, Figure 7.29 presents the profiles from flight campaigns that covered the mid-latitudes to the sub-Arctic (30–70°N). At mid-latitudes, there is considerably greater coherence among models near the surface, where concentrations are higher than in the Arctic. Model values are generally closer to observations, and all concentrations diminish with height. The greatest agreement among models and with observations is noted for the Aerosol Radiative Forcing in East Asia (A-FORCE) campaign (Oshima et al., 2012, Figure 7.29), which has near-surface BC concentrations an order of magnitude greater than all other aircraft campaigns. The HIPPO measurements, as

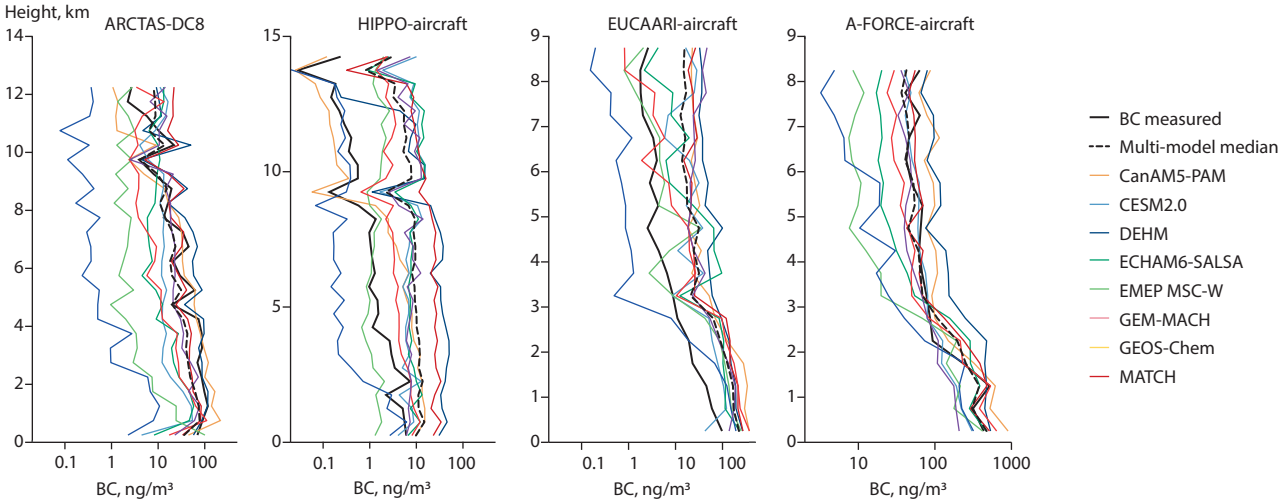

Figure 7.29 Vertical profiles of measured (solid black line) and modeled (colored lines) concentrations of BC extending from mid-latitudes into the Arctic (30–70°N). The dashed black line is the multi-model median.

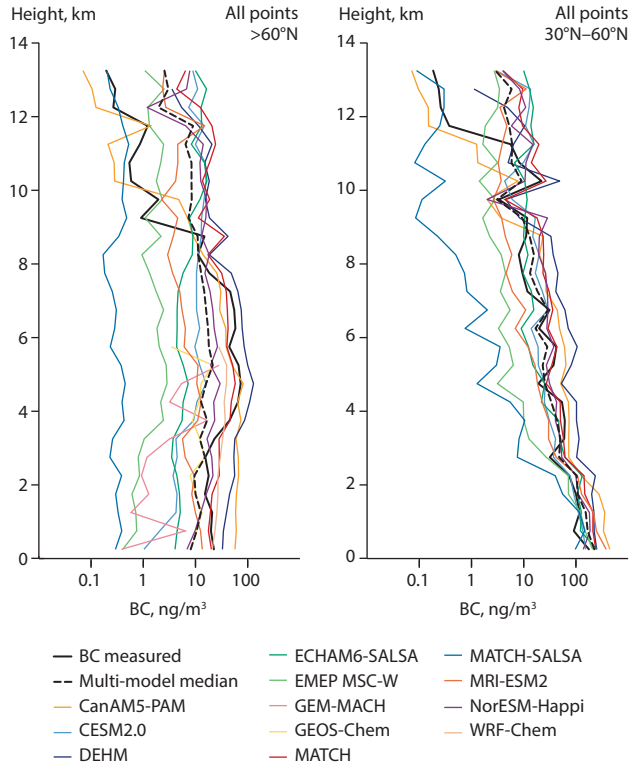

Figure 7.30 Median vertical profiles of observed (heavy black line) and modeled (colored lines) BC concentrations for all aircraft campaigns combined, separated into (left) Arctic (60°N–90°N) and (right) mid-latitude (30°N–60°N). The multi-model median is shown by the dashed black line, and the observations are the solid black line.

indicated earlier, show very low concentrations, with poorer agreement between models and with observations.

Combining the data from all campaigns, but separating points into those lying between latitudes 30°N to 60°N, and those north of 60°N, yields Figure 7.30. The general features of the previous two figures are repeated: models are in better agreement with one another and with observations in the mid-latitudes than in the Arctic, and BC profiles indicate vertically homogeneous concentrations in the Arctic, while they diminish with height in mid-latitudes.

Furthermore, at mid-latitudes, the multi-model median is in very good agreement with observations, since models are about evenly divided between low and high biases. In the latitudes north of 60°N, most models are biased low between altitudes of 2 km to 8 km, leading to a low multi-model median there. They are mostly biased high at altitudes above 8 km, with the multi-model median correspondingly much higher than observed (Figure 7.30). Note that this contrasts with the individual campaigns of the High Arctic, north of 70°N in Figure 7.28, where multi-model medians track the observations well.

The left and right panels of Figure 7.31 give an indication of model spread for the two latitude zones of Figure 7.30. Black curves and dark gray shading represent the observations, while colored curves and shading depict the model results. The GEM-MACH, GEOS-Chem and WRF-Chem models provided only one or two years, and their extracted aircraft tracks can therefore only be compared to the NETCARE campaigns of 2014–2015, hence the different observational profiles for these models. The shaded areas around the curves cover +/-1 MAD around the median value of each vertical bin. There are several hundred data points per vertical bin up to 8 km for all models, falling off to only several tens of points at higher altitudes. Tables A7.5, A7.6 and A7.7 list the bin counts, medians, and MAD for observations and for every model, in every vertical bin.

The dominant source of BC emissions in latitudes from 60°N to 70°N is boreal fires that occur yearly between April and September across a range extending from Alaska eastwards through Canada's Northwest Territories. North of 70°N, for example, in the area of the NETCARE campaigns, there are small local sources of BC emissions. Near-surface concentrations of BC in all Arctic latitudes come from local sources. However, upper tropospheric concentrations in these high latitudes primarily reflect emissions from remote industrial sources that have been transported north. The BC emissions from industrial sources in latitudes from 30°N to 60°N are an order of magnitude greater than those from boreal fire emissions. Atmospheric BC concentrations measured by aircraft in the mid-latitudes therefore reflect the high emissions from mid-latitude industrial sources.

Since all participating models used the same anthropogenic emissions dataset, it is not surprising that modeled BC concentration profiles agree best with one another and with observations in regions where surface emissions are strongest. This is most evident in the A-FORCE campaign in Figure 7.29, and is also clearly seen when mid-latitude points of all campaigns are combined, as on the right panel of Figure 7.30. The European Integrated Project on Aerosol Cloud Climate and Air Quality Interactions (EUCAARI) campaign on Figure 7.29 stands out because nearly all models agree strongly with one another from the surface up, but disagree with observations.

In Arctic latitudes, modeled BC concentrations depend on how accurately models simulate the transport north of remotely emitted BC. The term 'transport' is used here in a general sense and does not refer strictly to large-scale winds. Key factors also include deep convection processes operating at tropical latitudes, as well as isentropic transport of emissions from those latitudes, scavenging in mid-latitude convective clouds, and wet deposition rates of BC in the Arctic. The multi-model median line on the left panel of Figure 7.30 is biased high in the upper troposphere above 9 km, suggesting overly efficient long-range transport and convective processes in the models. Conversely, the low multi-model median in the lower and mid-troposphere (2 km to 8 km) in the Arctic indicates that models may have difficulty in capturing emissions from local sources, or local rates of wet deposition.

It is beyond the intent of this report to identify which process dominates the bias in each model, and the reader is referred to examinations of this question by Mahmood et al. (2016) and Kipling et al. (2016). A first-order representation of inter-model differences caused by the interplay between all processes is given in Figures A7.9 and A7.10. These show the relationship between height and zonal-mean concentration for all model grid points (not limited to the extracted aircraft tracks) in the two latitude ranges 30°N–60°N and 60°N–90°N. No comparison to observations is made; this is a model intercomparison only, intended to highlight differences. In the mid-latitudes (Figure A7.9), all models show large surface concentrations tapering off to lower values with height,

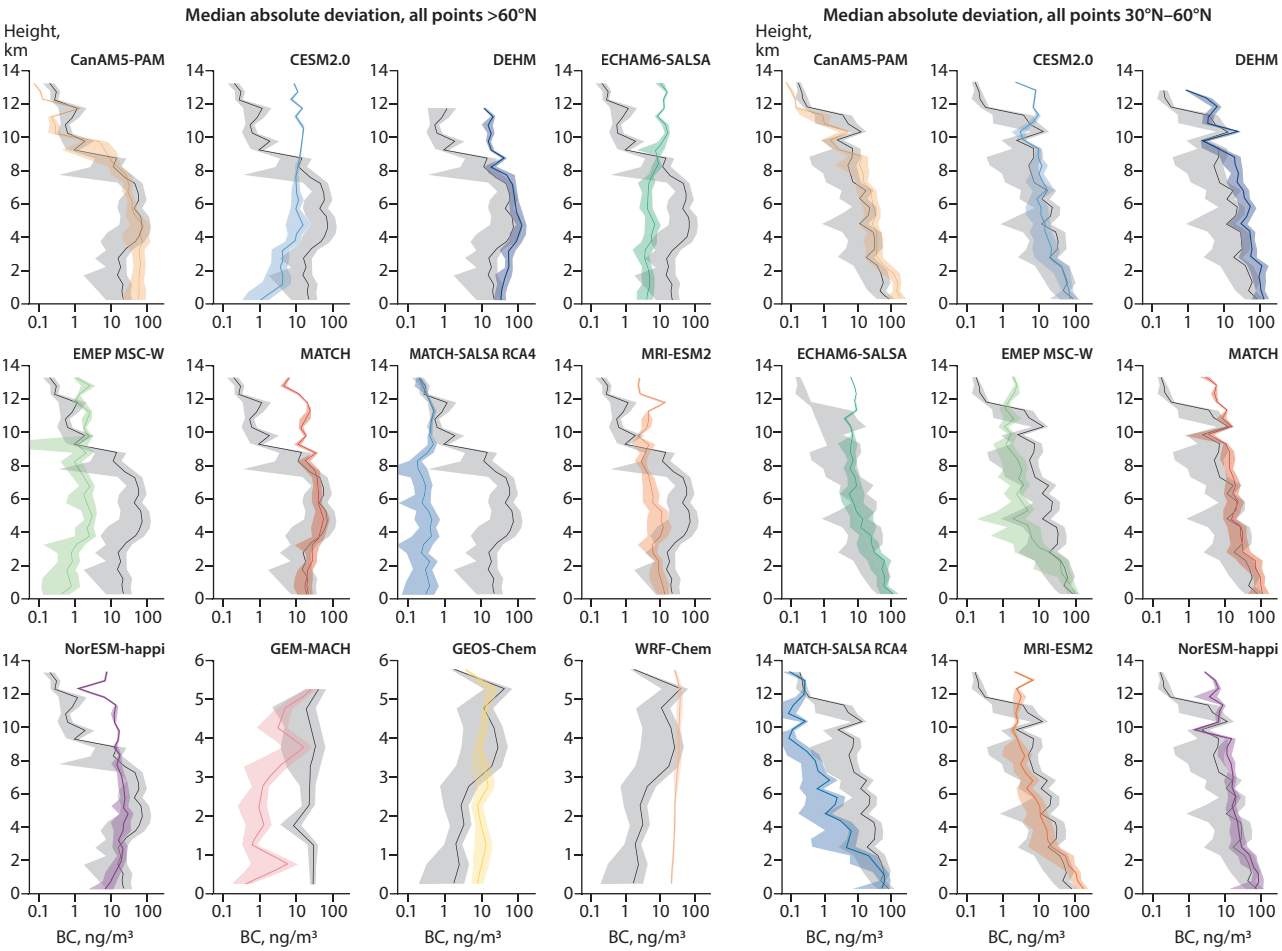

Figure 7.31 Model spread of BC concentrations given as +/-1 median absolute deviation (shading) around median (lines) for each model profile (colored), compared to observations (black line with gray shading). The left panels show all points north of 60°N and the right panels show points in the mid-latitudes (30°N–60°N). Note the different vertical and horizontal scales.

roughly following curves of the same shape: this suggests that the physical processes governing the vertical profiles are represented similarly in all models. In contrast, at Arctic latitudes (Figure A7.10), the distribution with height follows very different curves in different models, indicating that the processes dominating the vertical profiles vary from model to model.

To summarize and conclude this section, within the mid-latitudes (30°N–60°N) where the main sources of BC emissions are located, individual models represent observed concentrations reasonably well, and the multi-model median is a close fit. However, the presence of atmospheric BC in the Arctic is primarily due to long-range transport and depends on deep convective processes at low latitudes; this is especially true at the highest latitudes, where there are no significant local sources of BC emissions. Models generally underrepresent concentrations of BC in the low and mid-troposphere north of 60°N. The only model to track Arctic BC concentrations well from the lower (4 km) to the uppermost Arctic troposphere is CanAM5-PAM, although it exhibits high bias near the surface.

Although only available for limited areas and years, and made at much higher spatial and temporal resolutions than general circulation models can provide, aircraft measurements are invaluable for assessing models' ability to represent the vertical distribution of BC concentrations in the atmosphere. The profile intercomparison enabled by the CIS tools' extraction of flight tracks from model output can help to identify the source of model biases. Biases at different heights in the Arctic indicate how well a model represents both the processes that govern long-range transport into the Arctic, and those that control lower-tropospheric BC concentrations within the Arctic.

7.3.4 Sulfate (SO_4)

7.3.4.1 Arctic SO_4

Surface *in situ* sulfate (SO_4) measurements in the major observing networks typically use ion chromatography methods, which have approximately 3% uncertainty range (Solomon et al., 2014). However, SO_4 measurements have been shown to have up to 20% analytical uncertainty (Chapter 5). Monthly mean surface-level observations of SO_4 from 18 Arctic sites were used to evaluate models. Figure 7.32 shows that, as for BC, the SO_4 concentrations in the high northern Arctic are underestimated by most models. A few models overestimate SO_4 in Scandinavia and Alaska.

The models' underestimations of SO_4 could be mainly due to their higher efficiencies in removing aerosols during the long-range transport to the High Arctic. This is consistent with a previous study based on the model simulations, reported in AMAP (2015a), which found that the convective wet

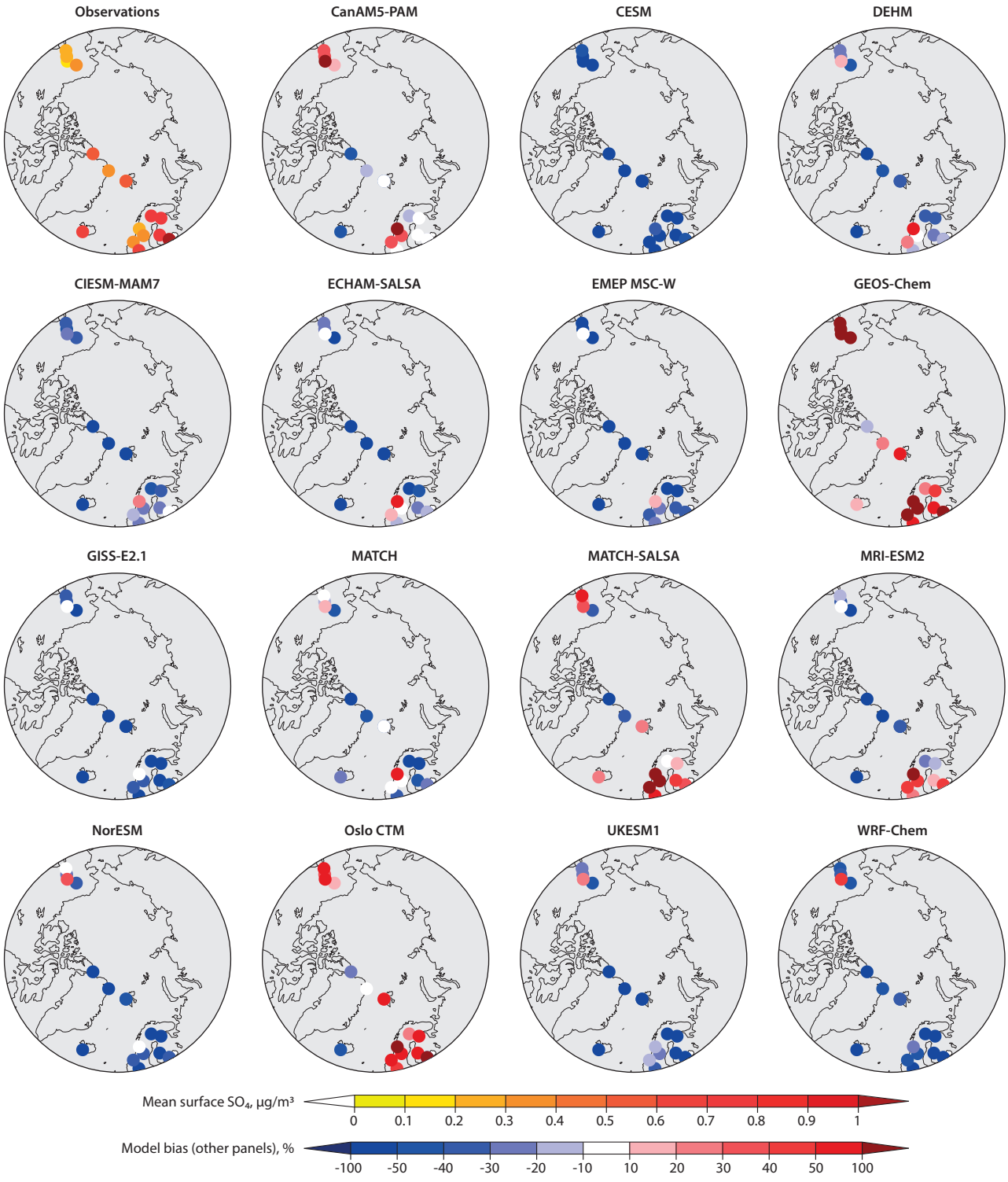

Figure 7.32 Top left: mean surface SO_4 concentrations. Rest of panels: model biases. Results are for 2014–15.

deposition outside the Arctic region may have led to different seasonal cycles of overall SO_4 concentrations in the Arctic (Mahmood et al., 2016). Dimethylsulfide (DMS), a naturally occurring source of sulfur emissions from marine algae, may also be misrepresented in models. This source would be more pronounced in the summer, when there is less sea ice in the High Arctic, but it does not appear that models underestimate DMS only in the summer (Figure 7.33). Rather, some models appear to also underestimate it in the winter and spring, pointing to a lack of transport from mid-latitudes as the cause of this inaccuracy. Despite the individual model differences in representing the seasonal cycle, the multi-model mean compares well with observations at most locations. However, the multi-model mean SO_4 is significantly underestimated at the Alert and Irafoss sites. Mean model biases for all Arctic sites range between -65% to 80% among different models, and correlation coefficients are typically around 0.5 (Figure 7.34).

The seasonal cycle for observations from all sites grouped together for 2008–9 is shown in Figure A7.12. These graphs exhibit a consistent seasonal cycle, as was the case in Figure 6.12 of Chapter 6, although that depicted observations

Figure 7.33 Modeled (colored lines) and measured (thick black line) monthly mean surface SO_4 concentrations at Arctic measurement sites for 2014–15. The multi-model mean (MMM) is shown by the thick black dashed line.

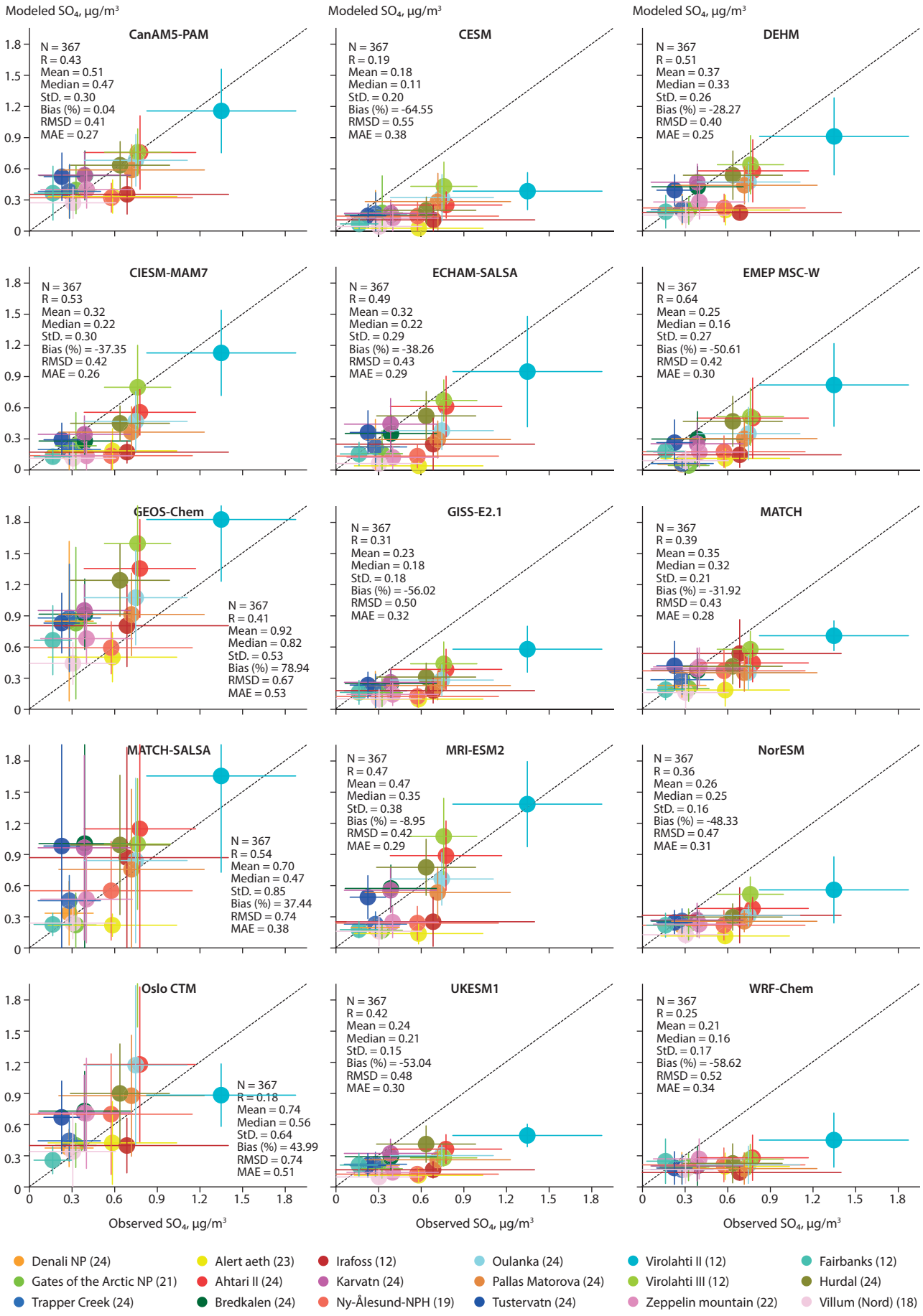

Figure 7.34 Modeled-versus-measured surface SO_4 concentrations at Arctic measurement sites for 2014–15. Filled circles represent the mean at a site and the lines represent +/- one standard deviation from mean based on available monthly mean data. N=number of data points, R=correlation coefficient, Mean=model mean value in µg/m³, Median=model median value in µg/m³, StD=model standard deviation, Bias (%)=percent model bias, RMSD=root mean standard error in µg/m³, MAE=mean absolute error in µg/m³. Numbers in brackets show the number of months used, with a maximum of 24.

from different set of Arctic sites and time period. Most models (e.g. CanAM5-PAM, DEHM, MATCH, Oslo CTM) are able to capture the seasonal cycle well. However, several models (e.g. CESM, CIESM-MAM7, ECHAM-SALSA, and EMEP MSC-W) strongly underestimate observed springtime peak values. Conversely, the modeled data and, to a lesser extent, the measurements for the 2014–15 time period exhibit little seasonal cycle, as shown in Figure A7.13. Part of the reason may be local winter pollution at some Arctic locations, such as Fairbanks, Alaska. Such highly localized pollution events, caused by local emissions becoming trapped in a stable boundary layer, occur on scales smaller than the model resolutions employed in this study can represent. As mentioned above, the uncertainty in wet deposition could also be a factor. Previous studies have shown models representing too much washout (where pollutants are removed from the atmosphere by precipitation) in winter and not enough wet deposition in summer, leading to a 'flatter' seasonal cycle than observed (e.g., Figure 7.33; Browse et al., 2012; Mahmood et al., 2016). Many models are also missing chemical formation processes for SO_4 that do not require sunlight, which may account for underestimations in winter (e.g. Moch et al., 2018; Alexander et al., 2009). Modeled SO_4 deposition is evaluated below.

SO_4 deposition compared to ice cores

As with BC (Section 7.3.3.1), the SO_4 deposition was evaluated and the average measured SO_4 deposition fluxes from ice cores for all locations (only Greenland data was available) is 18 mg/m^2/y (Figure 7.35). The lowest observed fluxes are found at D4 (12 mg/m^2/y) and highest at ACT11D (30 mg/m^2/y). The model average for all locations is overestimated by around 20%. This is similar to the surface concentrations visualized in Figure 7.33, where models capture SO_4 quite well, even though some underestimate the concentrations.

7.3.4.2 SO_4 trends in the Arctic, 1990–2015

Six models simulated sulfate for 1990–2015, and one model for 1995–2015; they are shown alongside observations at 13 Arctic locations in Figure 7.36.

The modeled and measured trend of ambient SO_4 was for a decrease from 1990 to 1995 and then stagnation until 2015 (Figure 7.36). This is consistent with publications on the topic such as that by Breider et al. (2017) and Ren et al. (2020), the latter which attributes the reduction in sulfate from the 1980s to early 1990s to reduced emissions in Europe, Russia, and local Arctic sources.

As with observed BC in Section 6.1.3.1, the SO_4 measured trends were examined by comparing the last five years with the first five years of the time series, after smoothing and separating

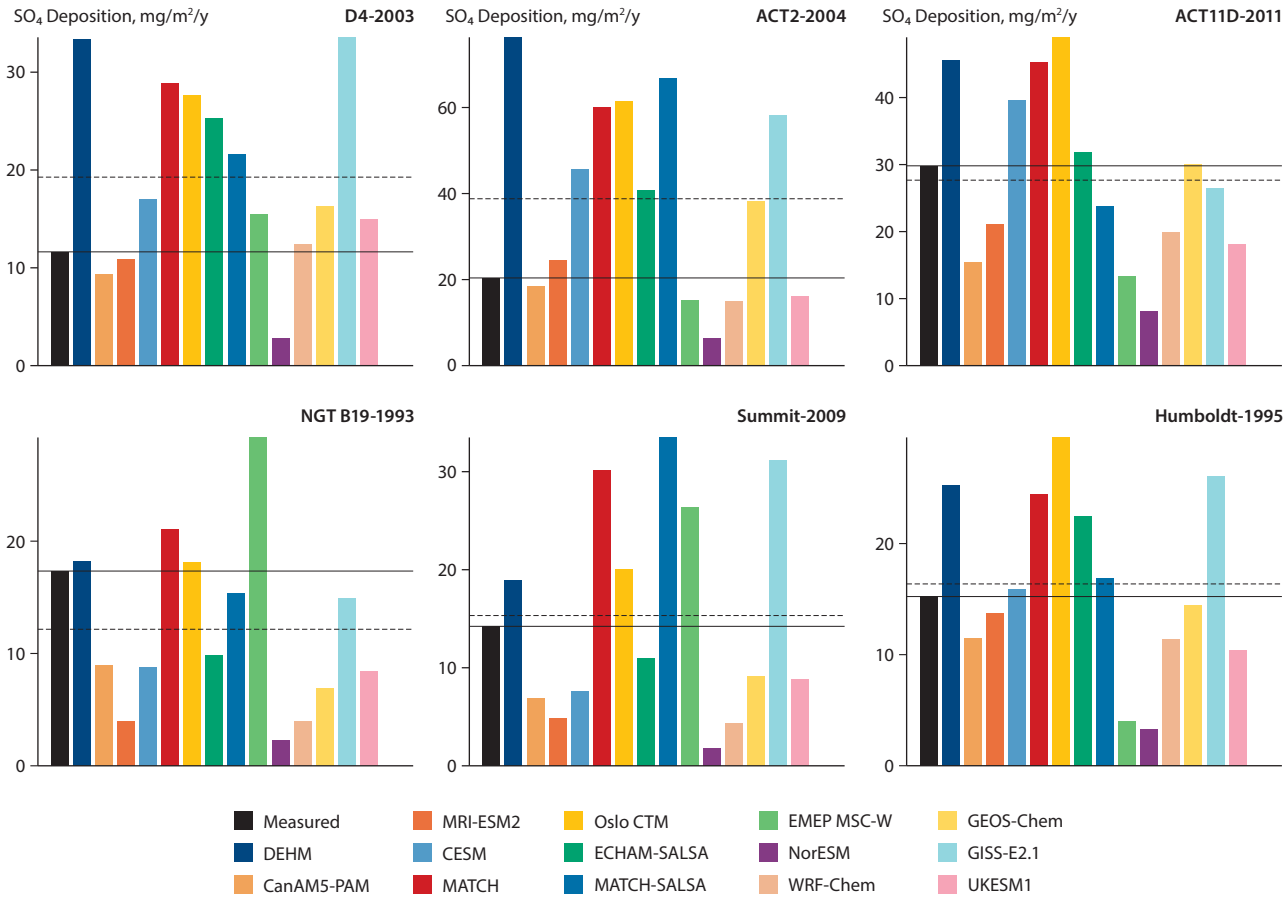

Figure 7.35 SO_4 deposition fluxes for the Greenland ice-core locations shown in Figure 7.18. The observed fluxes are plotted in black, with a black line indicating the level of the average observed flux, and a black dashed line the multi-model mean at that location. The period used for plotting is based on all available years after 1990, the title states the last available year from the ice-core record.

Figure 7.36 Measured and modeled annual mean time series of surface-level SO_4 at 13 Arctic locations.

Table 7.3 Modeled SO_4 percent change of the last five years (2011–2015) over the first five years (1990–1994 for all models except GISS-E2.1, which is for 1995–1999) for winter (JFMA, top), and summer (JJAS, bottom).

	CanAM5-PAM	CIESM-MAM7	DEHM	EMEP MSC-W	GISS-E2.1	MRI-ESM2	UKESM1
Alert							
JFMA	-47%	-53%	-43%	-49%	-23%	-58%	-39%
JJAS	-32%	-27%	-8.1%	8.1%	-22%	-18%	-19%
Gruvebadet							
JFMA	-46%	-53%	-37%	-38%	-17%	-50%	-38%
JJAS	-36%	-34%	-46%	-38%	-14%	-43%	-40%
Villum							
JFMA	-44%	-56%	-45%	-55%	-17%	-55%	-32%
JJAS	-45%	-12%	-22%	-24%	-22%	-24%	-32%
Utqiaġvik							
JFMA	-42%	-57%	-41%	-44%	-36%	-62%	-56%
JJAS	-58%	-64%	-65%	-32%	-21%	-51%	-70%
Zeppelin							
JFMA	-46%	-52%	-37%	-46%	-18%	-50%	-38%
JJAS	-36%	-34%	-46%	-37%	-14%	-44%	-39%

out the seasons (haze season, January to April [JFMA]; summer season, June to September [JJAS]). The same calculation was made for the models' results, which are tabulated in Table 7.3.

The models all generally show a large decrease in SO_4 during the haze season at all Arctic locations, which is consistent with the measurements (Table 6.2 in Section 6.1.4.1). In the summer, most models simulate a decrease in SO_4 at all locations (except for EMEP MSC-W at Alert), however, at Utqiaġvik and Gruvebadet, the observations show an increase in summertime SO_4 and a decrease at the other locations. Note that the time periods are different for the models (1990–2015) than for measurements (mostly starting in the 1990s and ending around 2018). The decrease in SO_4 is driven by the reduction in anthropogenic emissions, which is showing up accurately in the modeled winter trends. In the summer, when SO_4 concentrations are lower, the modeled trends are less accurate.

7.3.4.3 Hemispheric SO_4

SO_4 has more measurement locations than BC in Europe, but there is still limited publicly available data for SO_4 at the global scale. Figure 7.37 shows those observations, and the model biases. It is interesting to note that many models are consistent in the spatial pattern of their biases over most regions. Most models overestimate SO_4 over western USA and underestimate it over eastern USA. The reasons for this east-west model bias asymmetry in the USA is unknown. Over Europe, most models underestimate SO_4, although a few models overestimate it. At individual locations, most model biases vary between 10% to 100%, with the exception being GEOS-Chem and Oslo CTM, which overestimate SO_4 by more than 200% at many locations. The EMEP MSC-W model tends to underestimate SO_4 in Europe, consistent with Gauss et al. (2020). SO_4 aerosols in the EMEP MSC-W model have a relatively short lifetime compared to those in the Aerocom models (Gliß et al., 2021), and thus shorter transport distances from the SO_4 sources.

7.3.5 Fine particulate matter ($PM_{2.5}$)

$PM_{2.5}$ is particulate matter (PM) of less than 2.5 μm diameter. At that size, PM can be inhaled and carried deep into the lungs and possibly into the circulatory system. For that reason, $PM_{2.5}$ is a health concern (e.g., Schwartz et al., 1996; Brunekreef and Holgate, 2002; Xing et al., 2016), discussed further in Chapter 9. Atmospheric $PM_{2.5}$ is also partly connected to direct and indirect climate effects via the particles' interactions with clouds. Surface *in situ* $PM_{2.5}$ measurements are usually made via gravimetric analysis of particulate matter collected on a filter (such as a Teflon substrate), which has around 1–6% uncertainty range (Malm et al., 2011). $PM_{2.5}$ is mainly composed of BC, SO_4, OA, NO_3, and NH_4, as well as crustal material, sea salt and water. This study did not examine NO_3 or NH_4, as their radiative forcing is much smaller than that of BC and SO_4, although NO_3 is becoming more important as a PM component, as SO_4 is decreasing. However, a similar analysis to that for BC (Section 7.3.3) and SO_4 (Section 7.3.4) was undertaken for OA, which is discussed briefly below – with figures in the Appendix Section A7.6.

Organic aerosol (OA)

Not many observation stations measure this aerosol species (only six stations in the Arctic), and, importantly, only data from one remote High-Arctic station was available. All other datasets used in this study came from the sub-Arctic, in closer proximity to terrestrial emissions of biomass and biomass burning. Both observed and modeled OA tended to be highest in the summer due to the large emissions from biomass burning that occur via wildfires and due to increased biogenic secondary organic aerosols (SOAs) from biogenic VOCs. All models captured that seasonal cycle, although many of them overestimated summertime concentrations (Figure A7.15), particularly in 2008–9. There is some variability in wildfires between Arctic locations and different years. Local combustion emissions in the winter can produce large quantities of OA, as happens, for

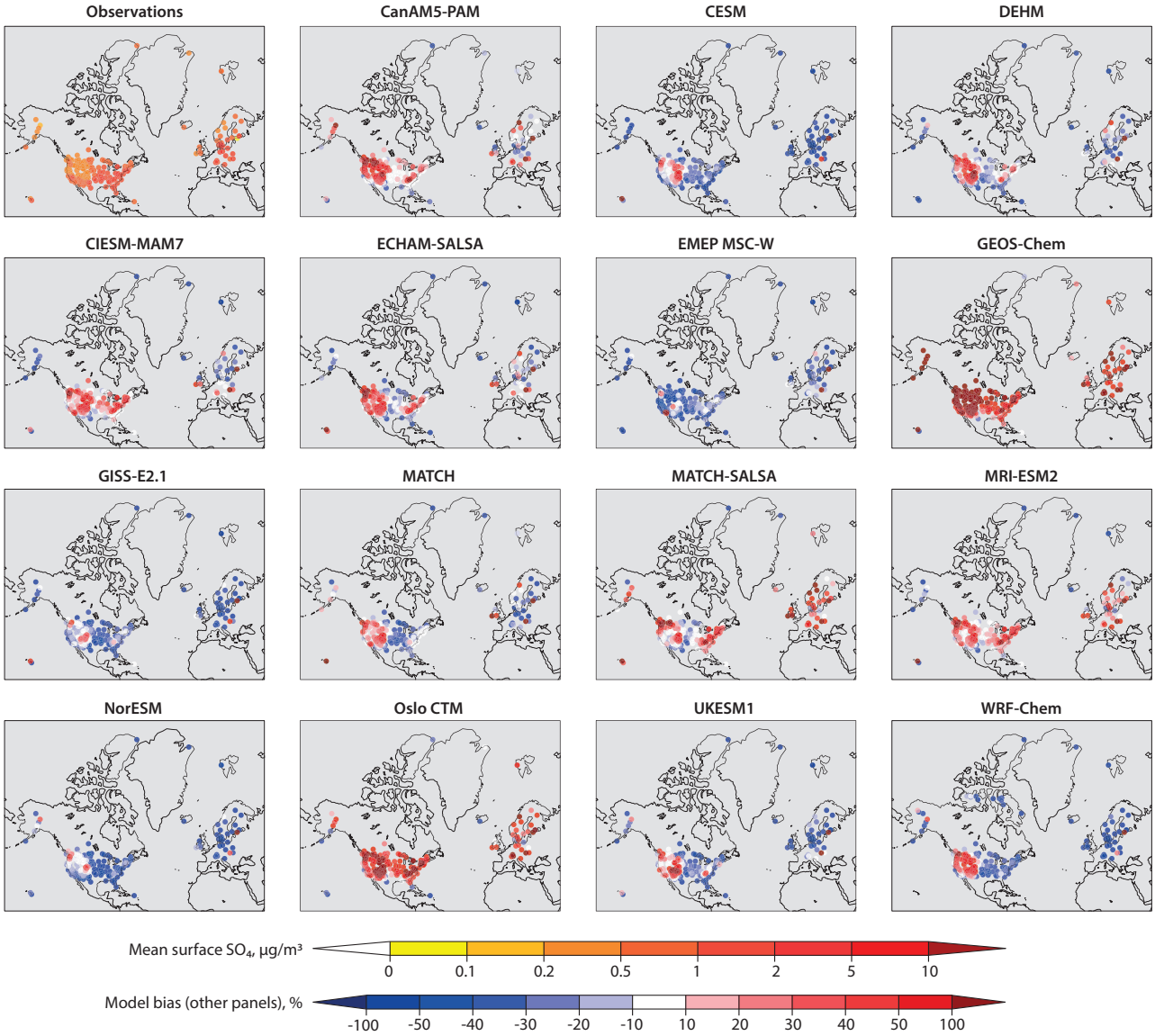

Figure 7.37 Top left: mean measured surface SO_4 concentrations. Rest of panels: model biases for 2014–15.

example, at Fairbanks, Alaska, but those emissions are poorly characterized and global models do not capture their effects.

High-Arctic seasonal cycles and spatial variability cannot be explored at present due to the lack of OA measurements there. The lack of Arctic OA measurements will become a pressing issue in the future, once VOC emissions from the ocean and natural sources increase under ice-free conditions. Furthermore, many models capture the spatial variability of OA poorly (Figure A7.15); they display concentrations that are too high at sub-Arctic latitudes, and too low in the High Arctic. This could be due to the insufficient capability of those models to simulate long-range transport, or to the absence of local sources or secondary production.

7.3.5.1 Arctic $PM_{2.5}$

Models simulate the processes and transport of many aerosol components (such as BC, SO_4, and OA discussed above) in a number of particle-size bins or following a size function, and often calculate $PM_{2.5}$ as a sum of those species in the fine particle mode. Below we evaluate models' $PM_{2.5}$ output, which is either the sum of the species in the 0–2.5 µm size bin or a pre-calculated dry $PM_{2.5}$ output. Note that this analysis focuses on sub-Arctic sites closer to human populations, rather than remote High-Arctic sites, due to the lack of available data. $PM_{2.5}$ is not a typical measurement included in the longer-term remote Arctic observations.

The spatial patterns in the model biases, such as being higher in Alaska and lower in Northern Canada, were the same for both 2008–9 (not shown) and 2014–15 (Figure 7.38), although the biases were overall skewed slightly lower for 2008–9 than they were for 2014–15. The EMEP MSC-W results are consistent with European Monitoring and Evaluation Programe (EMEP) annual evaluations for Europe – including a few Arctic sites in Norway and Finland (Gauss et al., 2020) – where the model underestimates $PM_{2.5}$ by 10–25%, and annual model evaluation reports from EMEP carried out under the Convention on Long-range Transboundary Air Pollution (CLRTAP).

Meteorological patterns were different for 2008–9 than for 2014–15 (including differences in boundary-layer stability and levels of photochemistry), which the models' surface-level SLCFs are quite sensitive to. There were also fewer wild

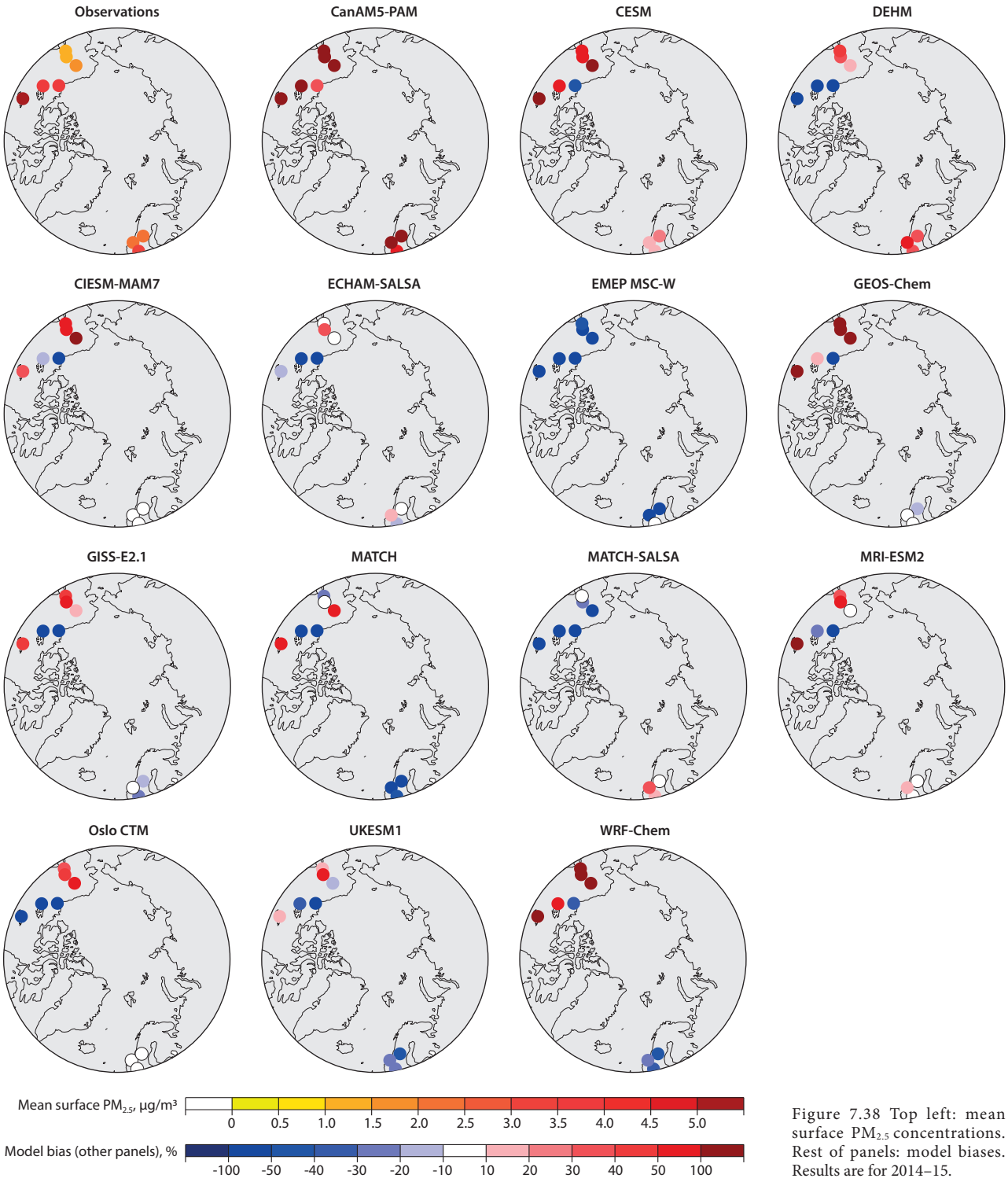

Figure 7.38 Top left: mean surface $PM_{2.5}$ concentrations. Rest of panels: model biases. Results are for 2014–15.

fires in 2008–9 than in 2014–15. According to the CMIP6 emissions data (van Marle et al., 2017) used in most of the models, emissions of BC from Canadian wildfires in 2008–9 were 340% lower than in 2014–15, whereas the emissions from the USA and Russia were similar for these periods. Given the very intense wildfire but low anthropogenic emissions in northern Canada during 2014–15, differences in simulated $PM_{2.5}$ concentrations over Canada and Alaska can be partly attributed to differences in simulations of wildfire aerosols in the models (Figure 7.38).

Some models (CanAM5-PAM, CESM, CIESM-MAM7, GEOS-Chem, and WRF-Chem) exhibit higher $PM_{2.5}$ and more variable $PM_{2.5}$ for the summer (Figure 7.39). While this is also apparent to some extent in the observations, it may be due to the way that fire and sea-salt emissions are treated in these models. Fire emissions, fire-plume injection height, and plume rise are all highly uncertain model parameters and the subject of ongoing research (e.g., Urbanski, 2014; Heilman et al., 2014; Paugam, et al., 2016). Indeed, as will be shown later (Section 7.4.1), the individual model $PM_{2.5}$ Arctic biases are more tightly clustered for 2008–9 when there were fewer fires (Figure 7.67). Mölders and Kramm (2018) showed that Arctic $PM_{2.5}$ seasonal pollution is mainly due to local air pollution in the winter and fires in the summer.

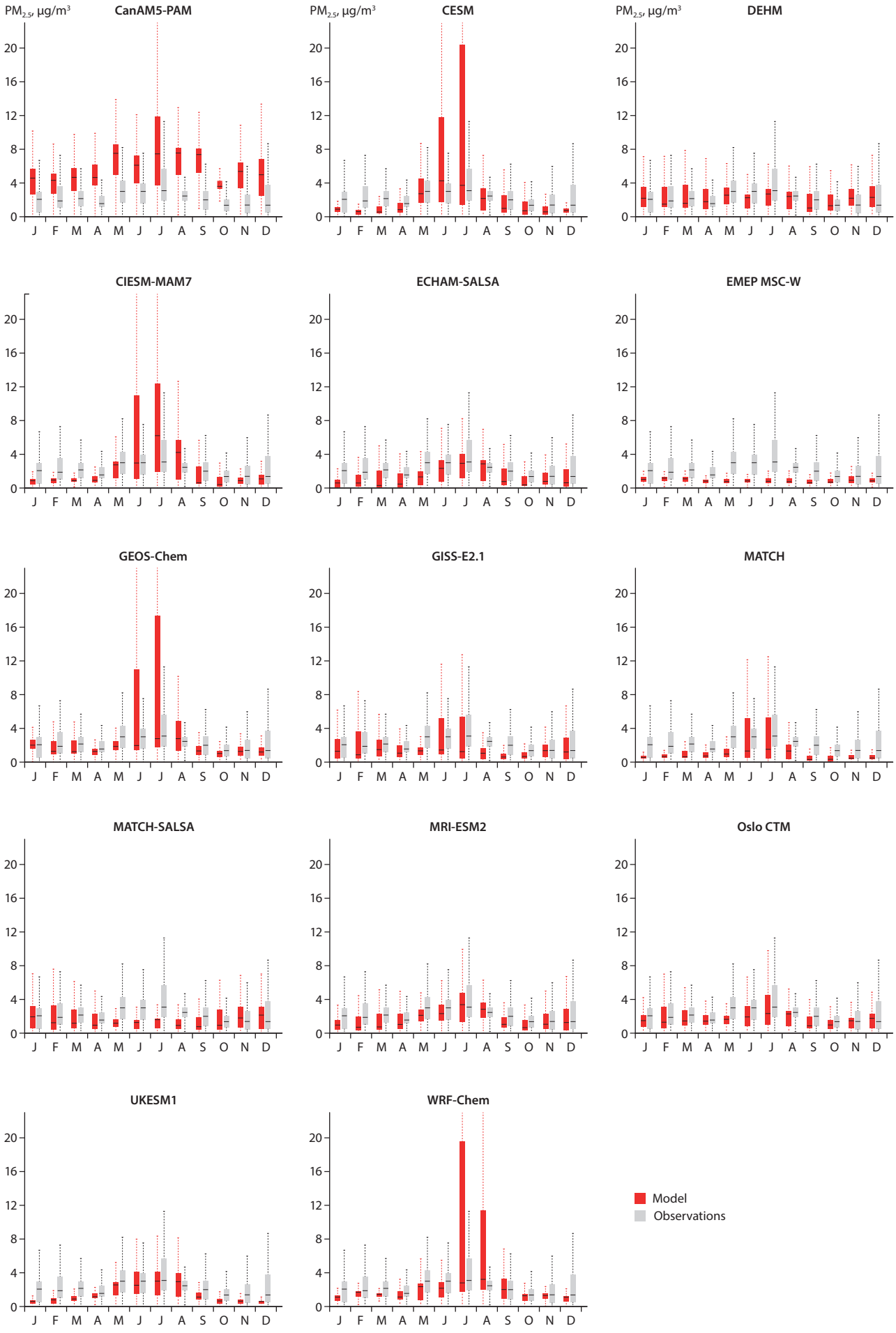

Figure 7.39 Modeled and measured monthly mean surface $PM_{2.5}$ concentrations in the Arctic for 2014–15.

7.3.5.2 High-resolution hemispheric $PM_{2.5}$

Figures 7.40 and 7.41 show the surface $PM_{2.5}$ concentrations in the Northern Hemisphere. As discussed previously, $PM_{2.5}$ has important health impacts, and thus it is well measured in populated areas via surface monitoring networks. Hemispheric concentrations of $PM_{2.5}$ were evaluated for 2014–2015 in the Appendix (Figure A7.21), and in this section for 2015 only, as these results inform Chapter 9 – where future health impacts are calculated with 2015 as the base year. First, the simulated $PM_{2.5}$ concentrations for 2015 were downscaled (the horizontal resolution of the models' results was increased) using a global, non-Arctic satellite-based dataset from Dalhousie University (Data ref. 7.8) at a resolution of 0.5°, to improve on the standard model output. This was not done for models that already had

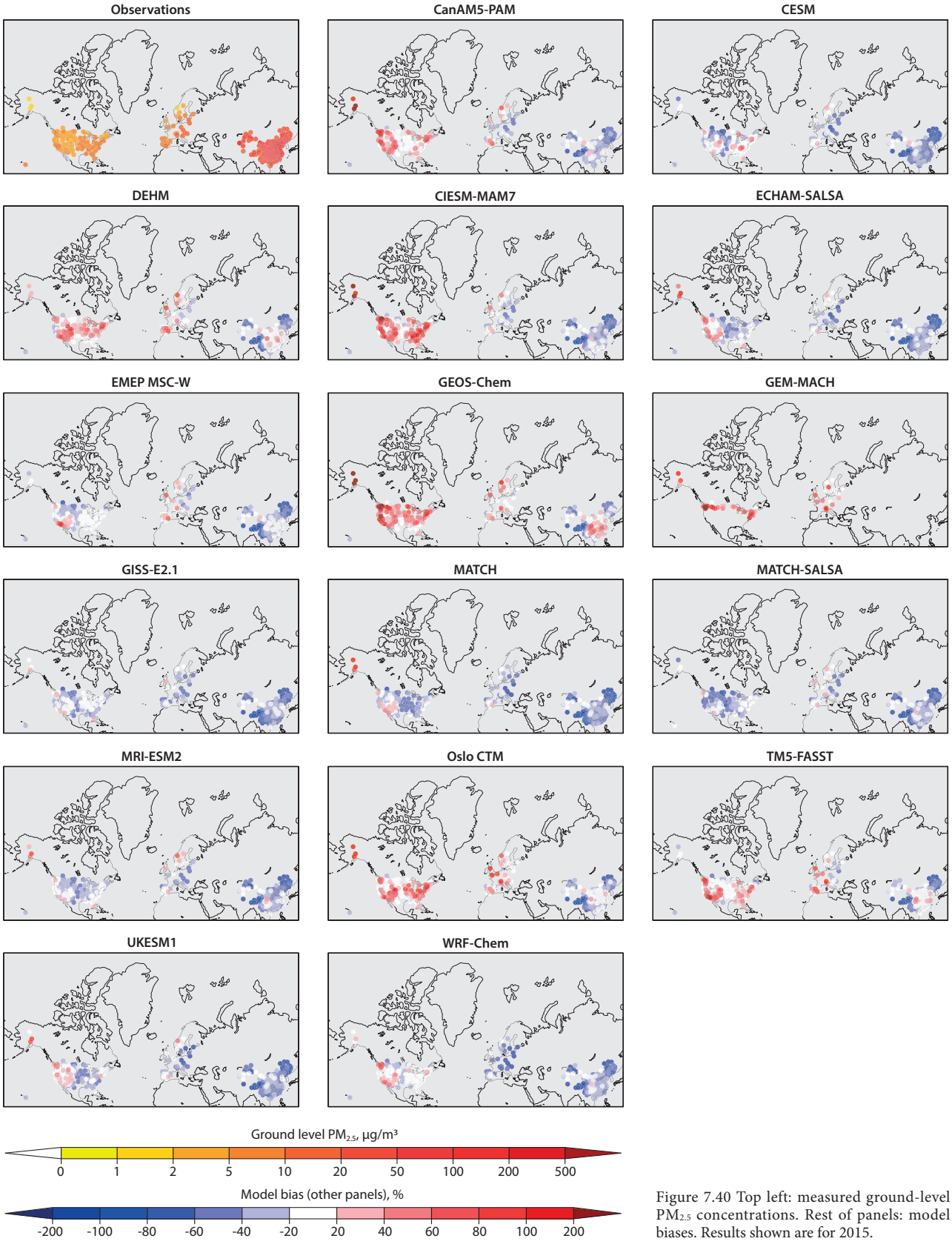

Figure 7.40 Top left: measured ground-level $PM_{2.5}$ concentrations. Rest of panels: model biases. Results shown are for 2015.

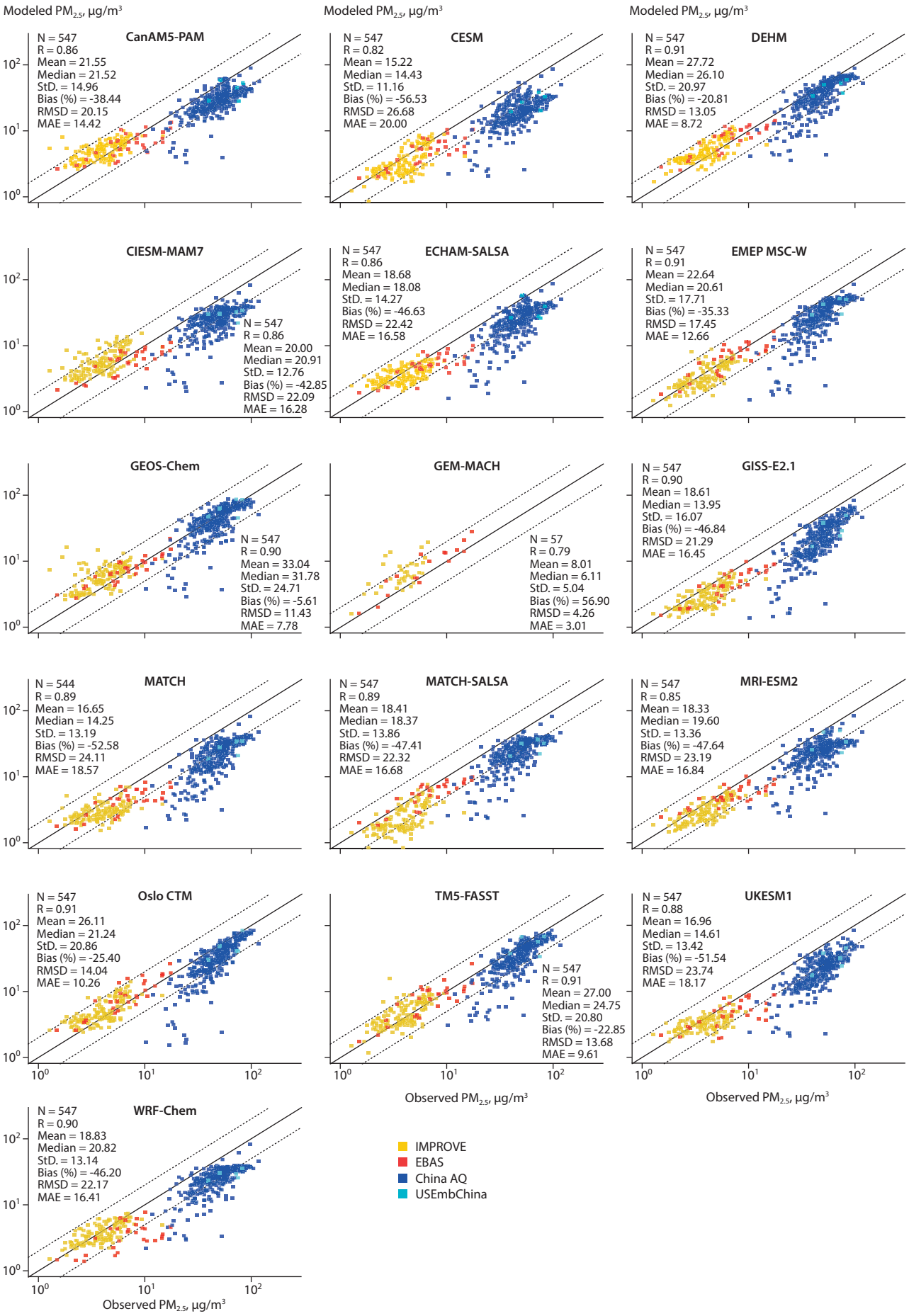

Figure 7.41 Annual mean $PM_{2.5}$ comparisons between station observations and model simulations for year 2015. N=number of data points, R=correlation coefficient, Mean=model mean value in µg/m³, Median=model median value in µg/m³, StD=model standard deviation, Bias (%)=percent model bias, RMSD=root mean standard error in µg/m³, MAE=mean absolute error in µg/m³.

a native resolution of 0.5° or greater. The downscaling method is described in Section A7.7. Downscaling is important for determining health impacts (Chapter 9), due to the fine spatial scales of population density involved in those health-impact calculations. There is no need for downscaling for other SLCF species, since the focus for those is on climate impacts, which depend on long-range transport and SLCF burdens across large regions. The post-processed $PM_{2.5}$ model results are shown as model-minus-measurement percent differences in Figure 7.40 suggesting that the model $PM_{2.5}$ biases at several locations in the USA, Europe and China are within 60%–80% range. However, some models (CanAM5-PAM, CIESM-MAM7, GEOS-Chem, GEM-MACH and Oslo CTM) show biases larger than 200%, especially in the Western USA and Alaska.

Figure 7.41 shows that the annual mean simulated $PM_{2.5}$ concentrations compare well with observations, and the correlation coefficients are relatively high (R=~0.8 or higher for all models). The high concentrations in China and low concentrations in the USA and Europe are captured by the models, providing confidence for the assessments on health impacts presented in Chapter 9.

As $PM_{2.5}$ is a pollutant with significant policy focus – for reasons discussed at the beginning of Section 7.3.5 – it is also estimated globally using data-assimilation techniques. There are three additional $PM_{2.5}$ global estimates that are based on satellite AOD measurements and models to fill in the gaps. They are: the MERRA-2 reanalysis (Gelaro et al., 2017), the Global Burden of Disease (GDB) dataset (Shaddick et al., 2018), and the University of Dalhousie $PM_{2.5}$ product (Data ref. 7.8; van Donkelaar et al., 2015a). $PM_{2.5}$ data from all measurement types are highly variable. Different measurement techniques and derivations are used; for example, estimates of $PM_{2.5}$ are made with varying levels of relative humidity, which causes large differences in the measurements and derived products. The parameters of the data assimilation and model inputs are another source of uncertainty in the derived $PM_{2.5}$ products. Figures A7.18, A7.19 and A7.20 show how the models compare to these derived $PM_{2.5}$ products. The derived $PM_{2.5}$ datasets agree well with the surface *in situ* measurements, and while the models are generally biased low, their results have similar spatial patterns when compared with the observations. Simulated $PM_{2.5}$ concentrations are also within the range of the $PM_{2.5}$ observations and the derived products. Compared to the MERRA-2 reanalysis, GBD, and Dalhousie University $PM_{2.5}$ datasets, modeled annual mean biases are within a factor of two over most locations. The model biases are consistently negative on average, but some models (CanAM5-PAM, CESM2.0, CIESM-MAM7, GEOS-Chem) overestimate $PM_{2.5}$ in some regions.

7.3.6 Aerosol optical properties

This section evaluates model simulations of aerosol optical properties, such as aerosol optical depth (AOD), which indicates how much aerosol is in the atmosphere, and the Ångström exponent (AE), which indicates the size of the aerosols. The smaller the AE, the more coarse particles are present; the larger the AE, the more fine particles are present.

7.3.6.1 Aerosol optical depth (AOD)

The primary goal of the model aerosol optical depth (AOD) evaluations is to qualitatively assess atmospheric column aerosols in the Arctic and, as discussed later in this section, in regions across the globe. Observed AOD from the AErosol RObotic NETwork (AERONET) (Holben et al., 1998; Eck et al., 1999) at 500 nanometers (nm) was interpolated to 550 nm AOD using the Ångström formula (Ångström, 1929; Wei et al., 2019) to ensure compatibility between datasets. Since satellite-based retrievals are limited in the Arctic for various reasons – including difficulties in taking measurements during the polar night, differences in viewing geometries, and reflections from bright surfaces – a satellite-based optical properties comparison is not included in this section. However, a model-based evaluation of aerosol optical properties at global scales, using both satellite-based products and AERONET observations, is included in the next section. It is important to note that the monthly aggregates of observations depend on the availability of data and are not likely to be the true aggregate of observations for a whole month. In addition, many polar-orbiting satellites take one observation per day, at the same time each day. Nevertheless, these datasets are the main observations currently available for evaluating model performance. Information about the uncertain nature of AOD observations can be found in previous studies (e.g., Wei et al., 2019; Schutgens, 2020). Schutgens et al. (2020) evaluated and intercompared 14 satellite-based AOD products against AERONET AOD and found that the regional biases among different products can reach up to +/-50%, while a typical bias can be 15–25% depending on the product. Furthermore, the models use their own software for computing AOD and other aerosol optical properties. It is unknown how much this variability is responsible for the model biases.

Arctic AOD

Figure 7.42 compares the spatial distribution of mean AOD from ground-based AERONET observations and the model biases. According to Eck et al. (1999), the uncertainty for AERONET AOD measurements is ~0.01–0.02. Note that the mean AOD at each AERONET site is based on the mean of available monthly observed values and therefore the number of values for each site is likely to be different (see Figure A7.22 for the number of months at each location). Also, AERONET observations are mostly missing during the months of December, January and February; therefore mean AODs are largely based on monthly means from March to November (depending on the availability of data at individual sites). Modeled AOD was sampled for the same months as the measurements, to provide a fair comparison. The observed mean values of AOD were lowest on the Atlantic side of the Arctic, while highest values occurred in northern Russia at Tiksi. Most models seemed capable of capturing mean AOD at many AERONET sites. CanAM5-PAM and WRF-Chem overestimated mean AOD at most locations, likely due to fire emissions in the summer, while most other models underestimated it. UKESM1 performed better compared to other models, exhibiting the smallest bias at most locations except at Tiksi and northern Canada. Overall, model biases were lower than ~50% at most locations, providing confidence in model simulations of the column-integrated aerosols burden over the Arctic region.

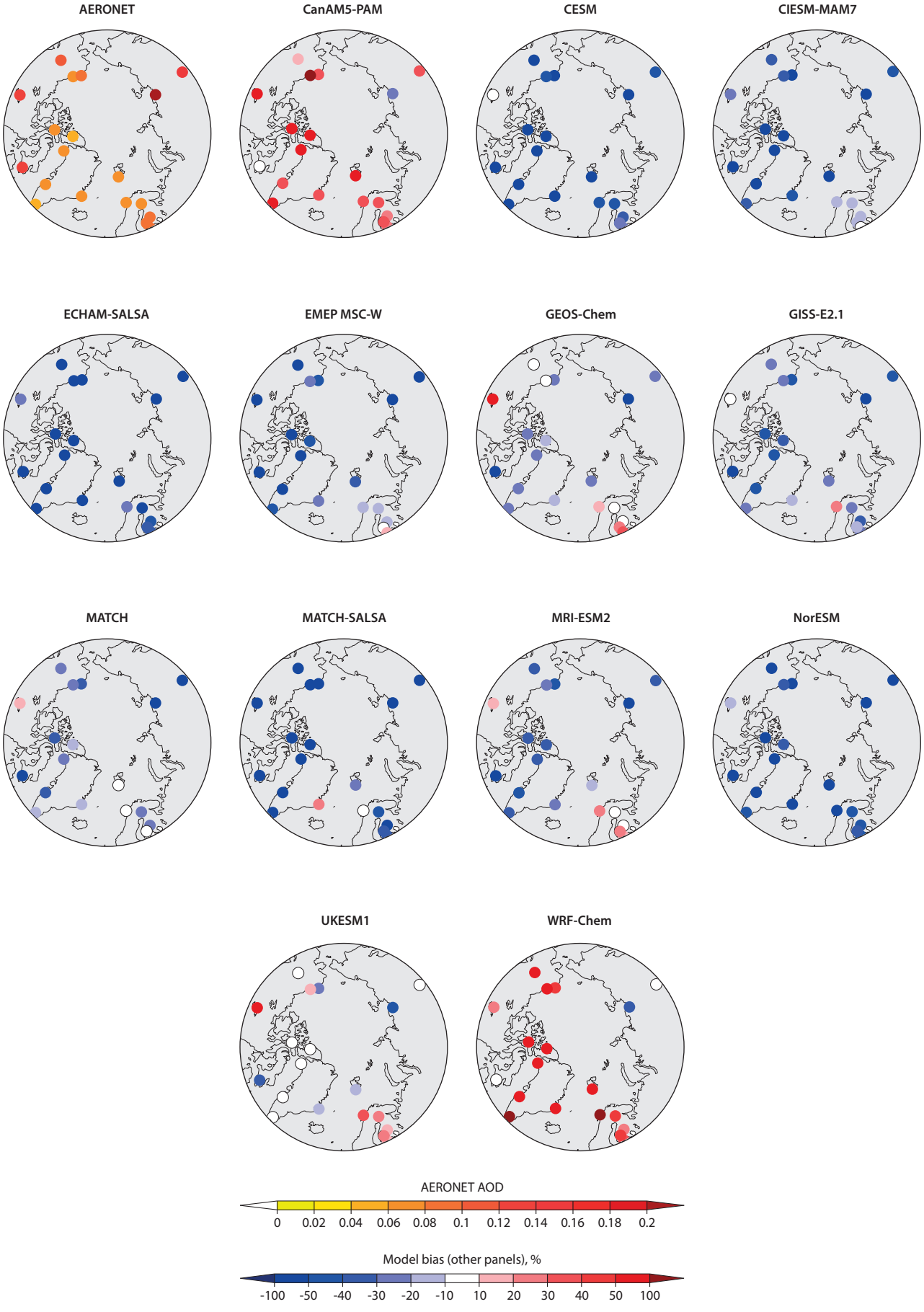

Figure 7.42 Top left: mean AOD from AERONET. Rest of panels: model mean biases, for 2014–15. Note that the annual mean is calculated from the number of available monthly values, which vary at each site (the legend of Figure 7.44 shows the number of months' data used at each site).

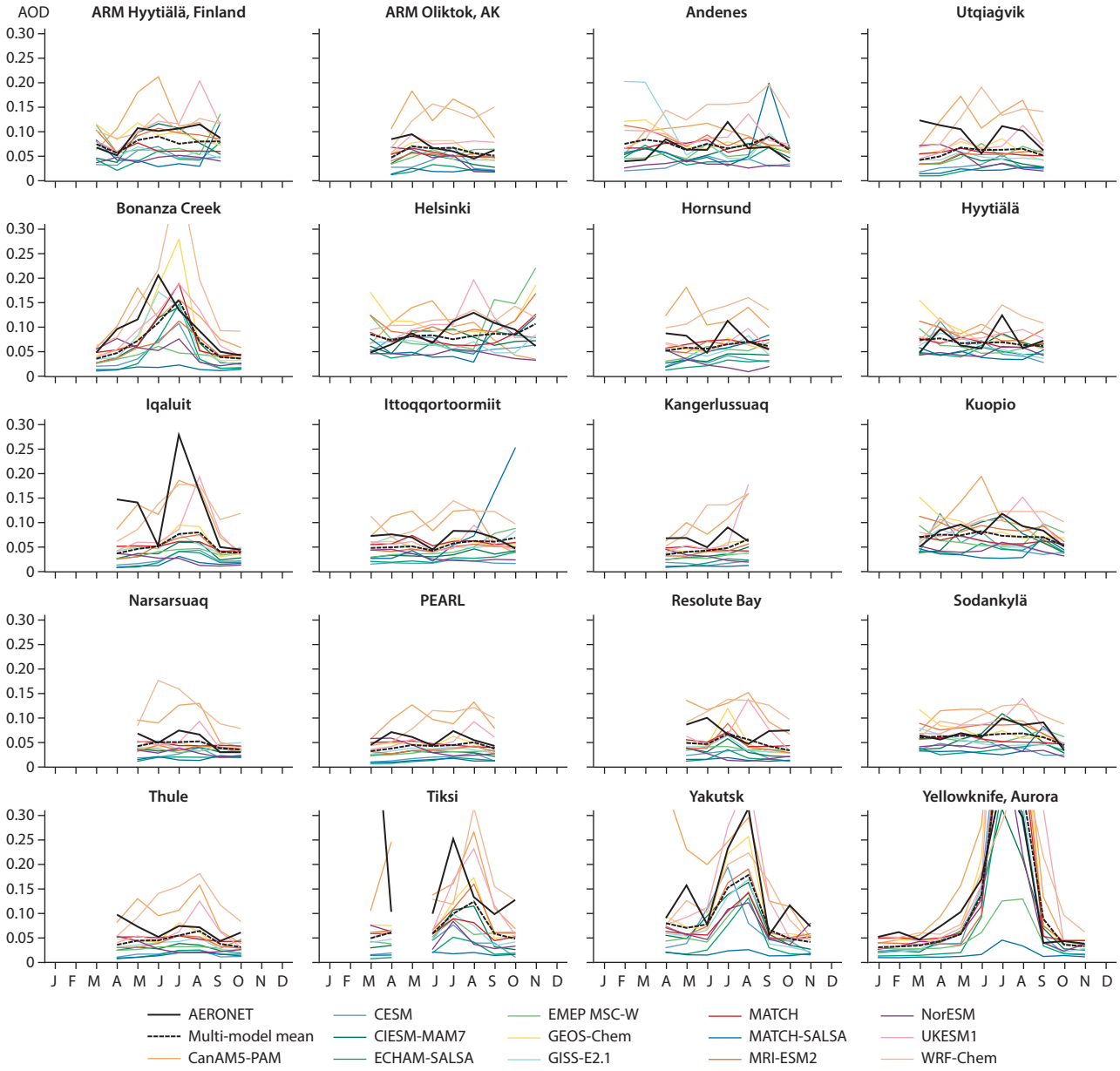

Figure 7.43 Comparison of AOD annual cycles at Arctic locations for 2014–15. The color lines depict the model results, thick black lines represent AERONET measurements, and the dashed thick black lines represent multi-model mean AOD.

Figure 7.43 compares the seasonal cycle of AOD in the Arctic at AERONET sites. At most observed sites, the AOD peaks in the summer, mainly as a result of enhanced biogenic emissions (Breider et al., 2014; Mahmood et al., 2019), SOA formation, sea salt, and increased forest fires. Most models are capable of simulating the observed seasonal cycle, although they do so with varying degrees of success. The multi-model mean AOD compares well with observed AOD at most locations, except at Iqaluit and Tiksi. Potential reasons for seasonal differences among the models could be differences in the data for biogenic and fire emissions used (Table A7.1) and differences in aerosol removal efficiencies during transport (e.g. Garrett et al., 2011; Mahmood et al., 2016).

Figure 7.44 shows the modeled-versus-measured AOD at AERONET sites, with the number of available monthly values at each location shown in brackets. Most models correlate well with AERONET AOD, with correlation coefficient values of R=0.6 or higher (except for MATCH-SALSA and WRF-Chem). Mean model biases range between -63.4% to +41%. All models underestimate AOD at Tiksi, which is known to have high levels of local pollution, making it difficult to simulate using coarse-resolution models. Mean observed AOD after accumulating monthly means from all AERONET sites is 0.09, while model mean AOD ranges between 0.03 to 0.13. This multi-model AOD range seems to be consistent with an AeroCom-based multi-model evaluation of Arctic AOD by Sand et al. (2017).

Global AOD

This sub-section evaluates modeled AOD on the global scale using observations from AERONET and numerous satellite-based monthly AOD products, including Moderate Resolution Imaging Spectroradiometer (MODIS) AOD at 550 nm (Remer et al., 2005; Hsu et al., 2013; Sayer et al., 2014), Multi-angle Imaging Spectroradiometer (MISR) AOD at 550 nm (Witek et al., 2018), Advanced Along-Track Scanning Radiometer (AATSR) AOD at 550 nm (North et al., 1999;

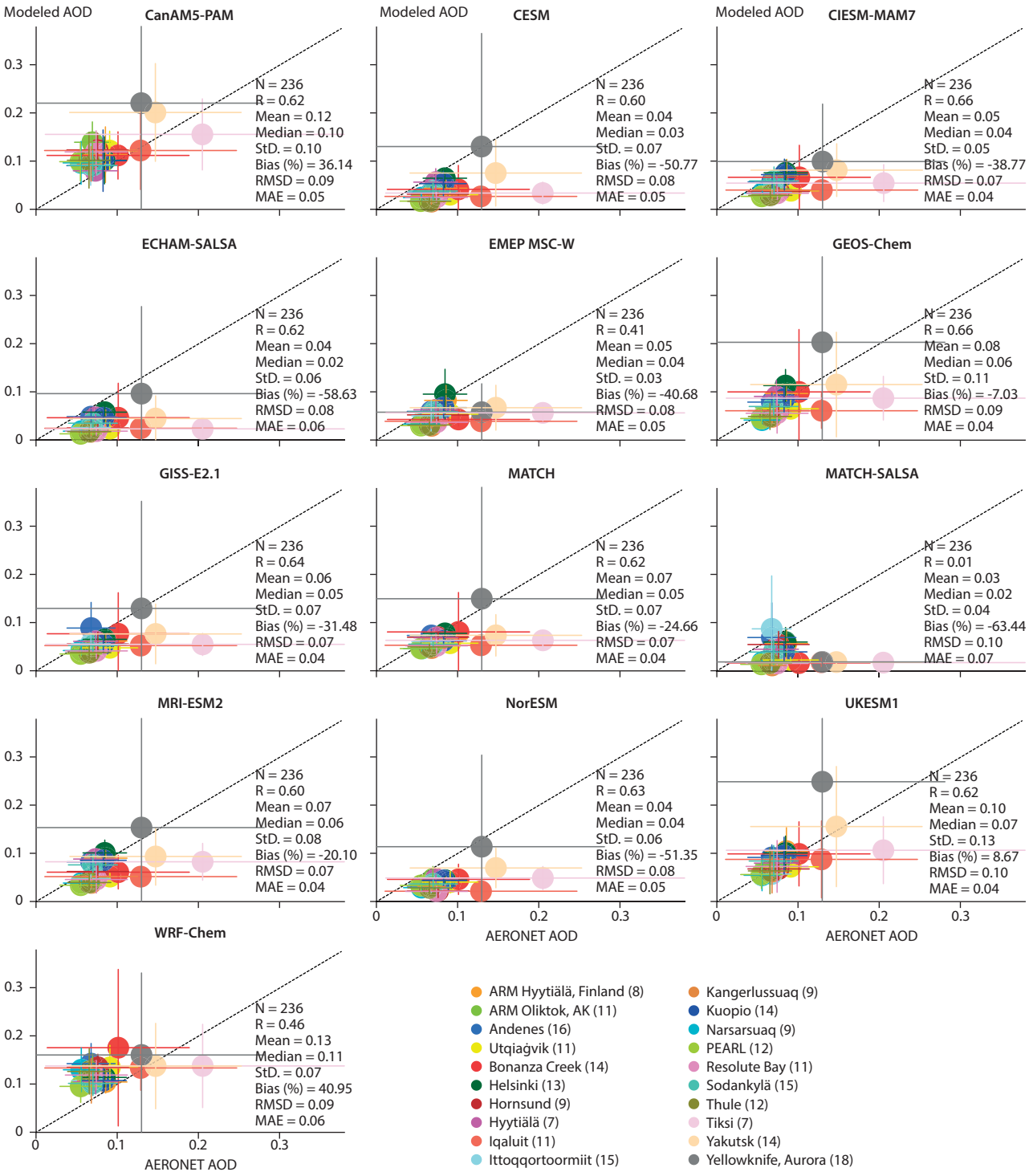

Figure 7.44 Modeled-versus-measured AOD at Arctic sites for 2014–15. Results were very similar for 2008–9, which are not shown. Filled circles represent the mean at a site and the lines represent +/- one standard deviation from the mean. The statistics insets of each plot are based on accumulated monthly mean values from all sites. N=number of data points, R=correlation coefficient, Mean=model mean value, Median=model median value, StD=model standard deviation, Bias (%)=percent model bias, RMSD=root mean standard error, MAE=mean absolute error.

Thomas et al., 2009; Veefkind and de Leeuw, 1998; Holzer-Popp et al., 2013), Sea-viewing Wide-field-of-view Sensor (SeaWiFS) AOD at 550 nm (Sayer et al., 2012), and Cloud-aerosol Lidar with Orthogonal Polarization (CALIOP-CALIPSO) AOD at 532 nm (Winker et al., 2009, 2013). The model and satellite AOD were remapped to a uniform 1° × 1° latitude/longitude grid for all satellite-based comparisons.

Figure A7.23 compares annual mean model AOD with observations from MODIS, MISR, and CALIOP-CALIPSO sensors. Most models are able to simulate the large features of AOD, including higher values in the dust source regions of Africa and Asia, and the higher concentrations of anthropogenic pollution in Asian countries. However, most models seem to underestimate AOD over parts of biomass-burning regions of Africa (for example, in Sahel and Congo forests), South Asia and China (Figure A7.24). CESM has large AOD biases attributed to its overestimating dust aerosols.

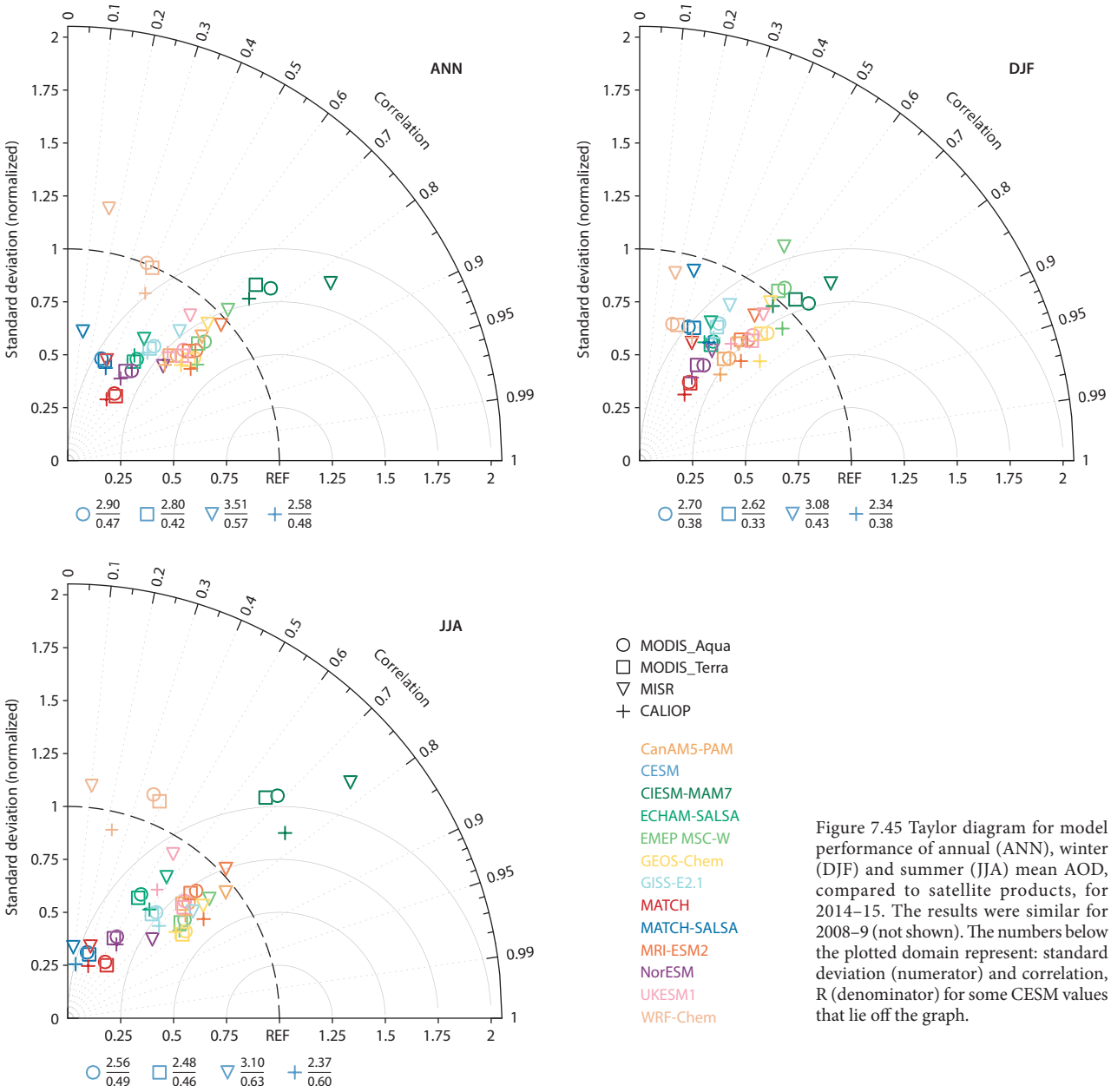

Figure 7.45 Taylor diagram for model performance of annual (ANN), winter (DJF) and summer (JJA) mean AOD, compared to satellite products, for 2014–15. The results were similar for 2008–9 (not shown). The numbers below the plotted domain represent: standard deviation (numerator) and correlation, R (denominator) for some CESM values that lie off the graph.

As mentioned above, the uncertainties among different satellite-based products could be significant, which makes comparisons with model simulations very challenging. Figure 7.45 shows a Taylor diagram for annual and seasonal mean AOD compared to four satellite-based products. Most models seem to underestimate observed AOD variance except CIESM-MAM7 and CESM2.0 (the latter being off the chart). Nevertheless, most models have high spatial pattern correlations – with R values greater than 0.5, and clustering in between values of 0.5 and 0.8. It is worth mentioning that some models provided data for a limited spatial domain (WRF-Chem, MATCH, MATCH-SALSA), which, along with missing data in satellite AOD would significantly limit these comparisons, since only a small region is left after accounting for missing values (for example Figure A7.23). In addition, it is clear from this analysis that comparison with different satellite products should be considered for a better evaluation of model simulations of AOD. This is because each satellite product differs in terms of the data values and spatial coverage it provides.

Compared to AERONET, AOD model biases are within a factor of two at most locations, including several sites where model biases are less than +/-10% (Figure 7.46). Most models seem to overestimate AOD over Europe, the Mediterranean and central USA. ECHAM-SALSA and MATCH-SALSA significantly underestimate AOD over the USA and Canada. For biomass-burning regions, such as southern Africa and East Asia, models tend to underestimate observed aerosols. However, model biases are not consistently positive or negative across all models.

Long term trends in AOD, 1995–2015

Five models provided long-term monthly mean AOD, and their trends are shown in Figure 7.47 along with satellite-measured trends from the Advanced Very-high-Resolution Radiometer (AVHRR) instrument (Data ref. 7.9). A common time period of 1995–2015 was chosen because of the availability of model simulation data from the different models. The choice of this period, although arbitrary, is useful because it does not include

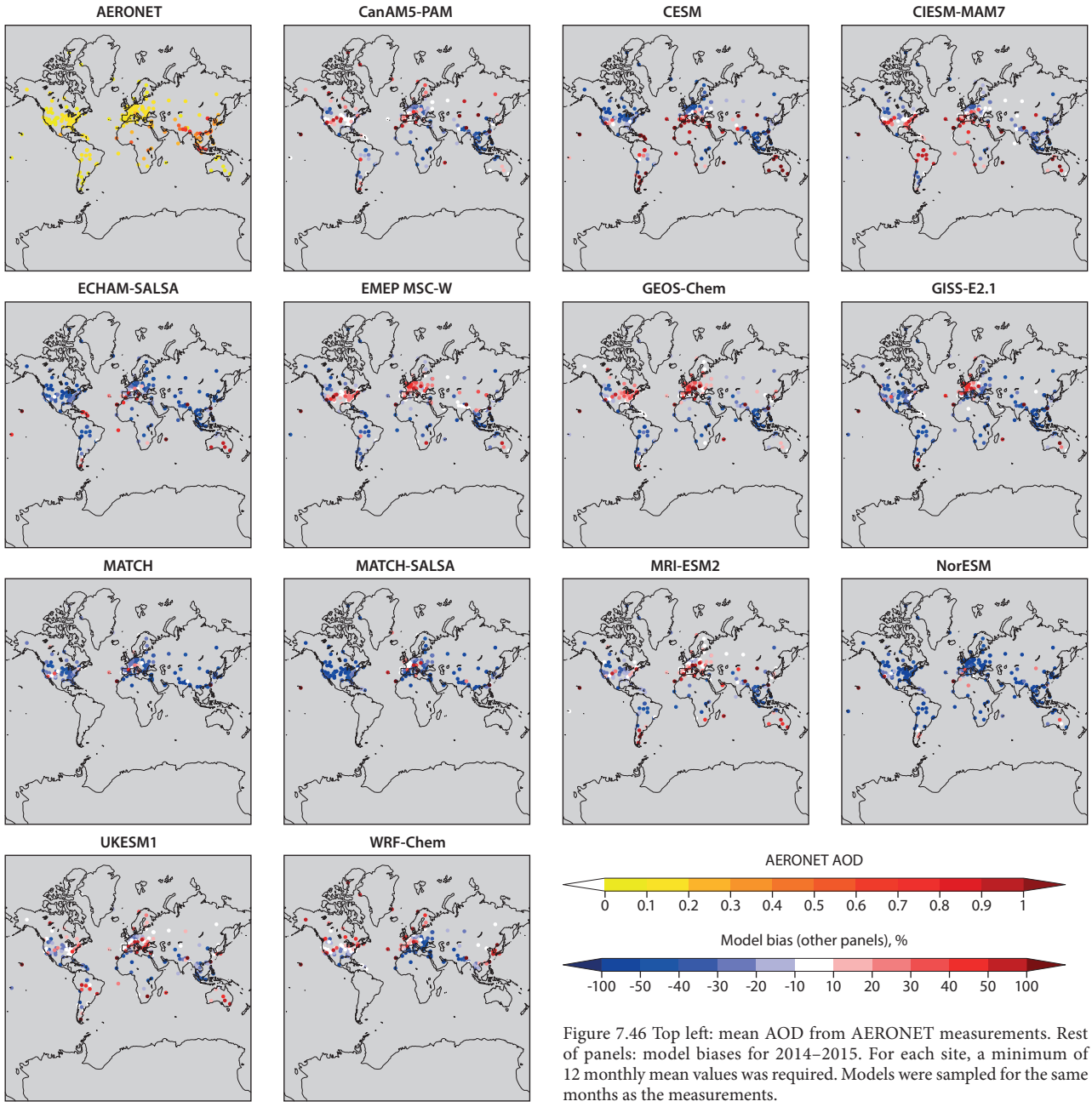

Figure 7.46 Top left: mean AOD from AERONET measurements. Rest of panels: model biases for 2014–2015. For each site, a minimum of 12 monthly mean values was required. Models were sampled for the same months as the measurements.

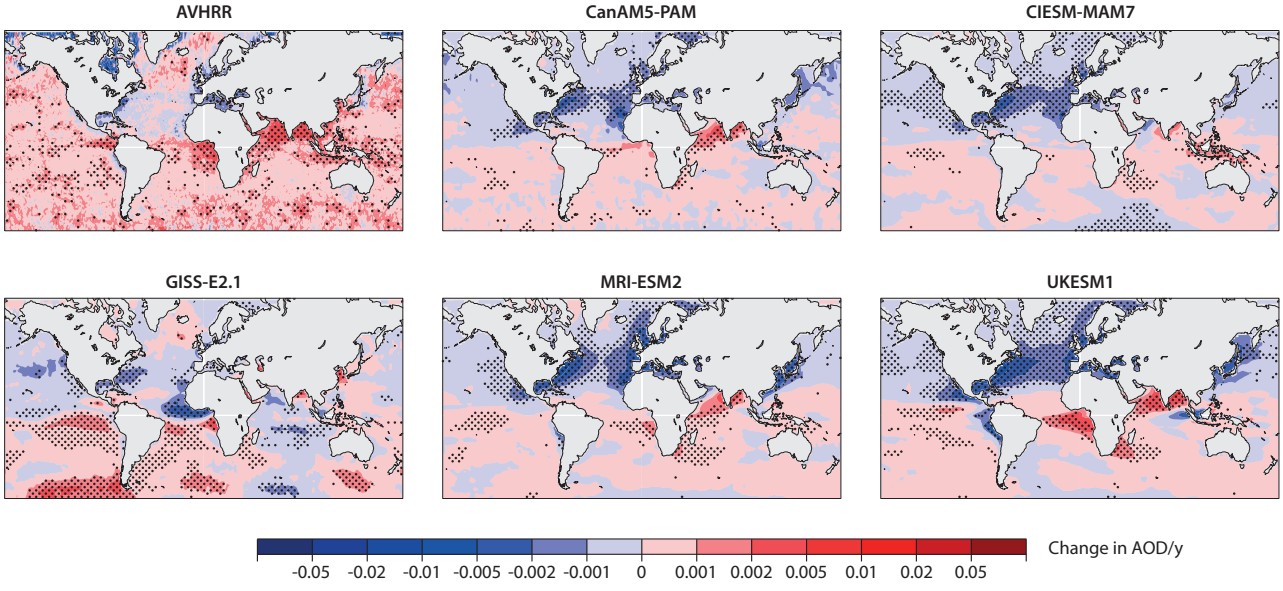

Figure 7.47 Top left: AVHRR 1995–2015 AOD trend (calculated from monthly mean AODs, multipled by ten). Rest of panels: model simulations for comparison. Stippling represents regions where trends are statistically significant for 95% confidence level based on Student's t-test (Gosset, 1908).

the large volcanic eruptions of Mount Pinatubo in 1991. The AVHRR aerosol optical thickness at 630 nm was obtained from Zhao et al. (2013) (Data ref. 7.9). All models and measurements were remapped to a uniform 1° × 1° latitude/longitude spatial grid before performing the analysis.

Figure 7.47 shows a negative AVHRR AOD trend along eastern coasts of North America, Europe and the Mediterranean, which is consistent with decreasing aerosol emissions. Over the Arabian Sea, Bay of Bengal, southwest coasts of Africa, and East Asia the aerosol AOD is increasing. All models reproduced the spatial distribution of dominant patterns of observed AOD trends to varying degrees of magnitude, depending on the particular model. All models agree in terms of the negative AOD trend over eastern North America and Europe, and positive trends in the northern Indian Ocean (except GISS-E2.1) and southeast coasts of Africa. However, most models (except GISS-E2.1) failed to reproduce the increasing observed AOD trend off the coast of northeast China. AVHRR does not have good coverage of the High Arctic, where Tomasi et al. (2012), and Stone et al. (2014) found an increasing trend in AOD over Utqiaġvik, Alert, and Zeppelin between 2001 and 2012 (see Chapter 6 for this discussion). The AVHRR trends are positive in regions around Iceland, and negative off the coast of Alaska and northeast coast of Canada – while the model simulated trends are small and not statistically significant in these regions (Figure 7.47).

7.3.6.2 Ångström Exponent (AE)

Arctic AE

Seven models simulated Ångström Exponent (AE), which give an overall indication of modeled aerosol size distribution. Particle size is important for determining the transport and fate of aerosols, their ability to absorb and scatter radiation and their contribution to cloud microphysics properties. It is worth noting that the AE-based comparisons can only provide qualitative information about aerosol sizes, since AE is obtained from AOD at two different wavelengths and is not a surrogate for aerosol-size distribution as can be obtained from direct aerosol size measurements. Figure 7.48 compares modeled AE to Arctic AERONET measurements. The uncertainty in measured AE values ranges between 0.03–0.04 (Schuster et al., 2006).

MATCH and CESM strongly underestimated observed AE, which implies that simulated particles may be too large in the Arctic region in these models. Conversely, CIESM-MAM7 and UKESM1 overestimated AE compared to observations, suggesting that their overall particle sizes were too small. ECHAM-SALSA, CanAM5-PAM and MATCH-SALSA had relatively small biases compared to Arctic AERONET observations.

All models, except MATCH, were able to reproduce some features of the seasonal cycle, shown in Figure 7.49, which peaks in late summer. This peak is likely due to the contribution of new particle formation caused by biogenic and other natural emissions (e.g. Abbatt et al., 2019; Mahmood et al., 2019). The multi-model mean annual cycle also compares well with observations, although there is a large range across the models.

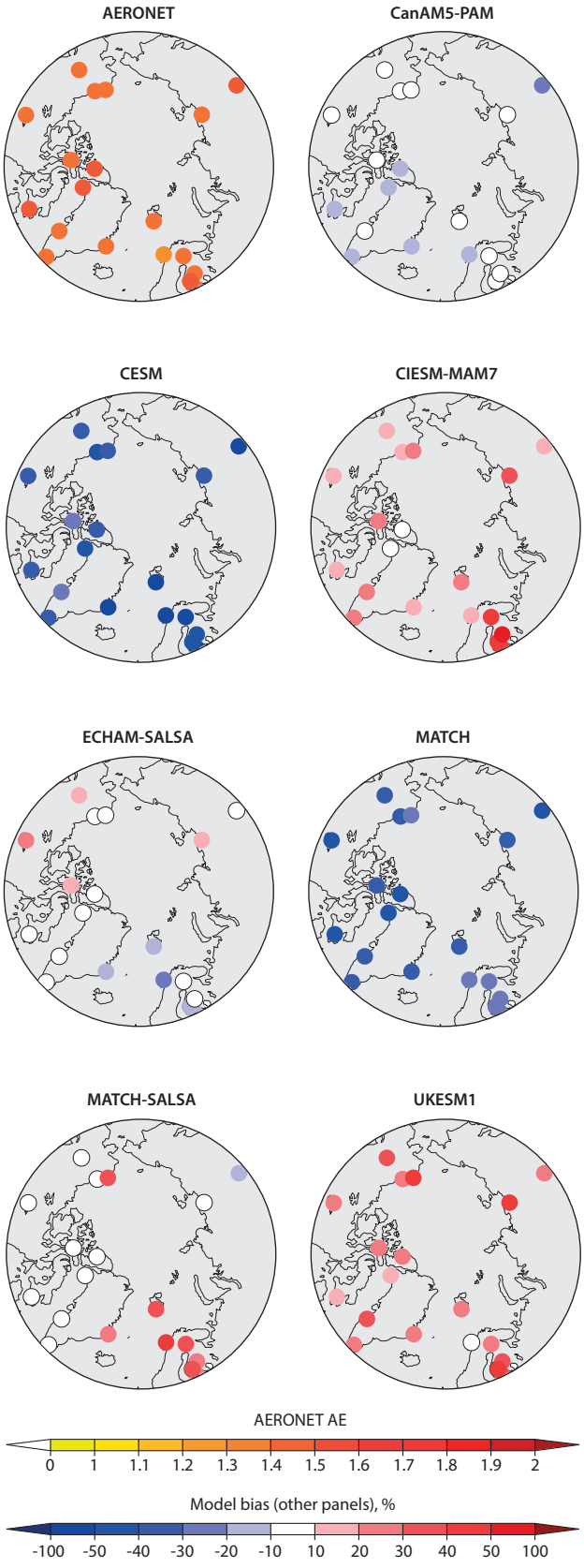

Figure 7.48 Top left: mean AE from AERONET (note the interval of 0 to 1 for the first section of the colour bar). Rest of panels: model mean biases, for 2014–15. Note that the mean is calculated from the number of monthly mean values available at each site, as shown in the legend of Figure 7.50.

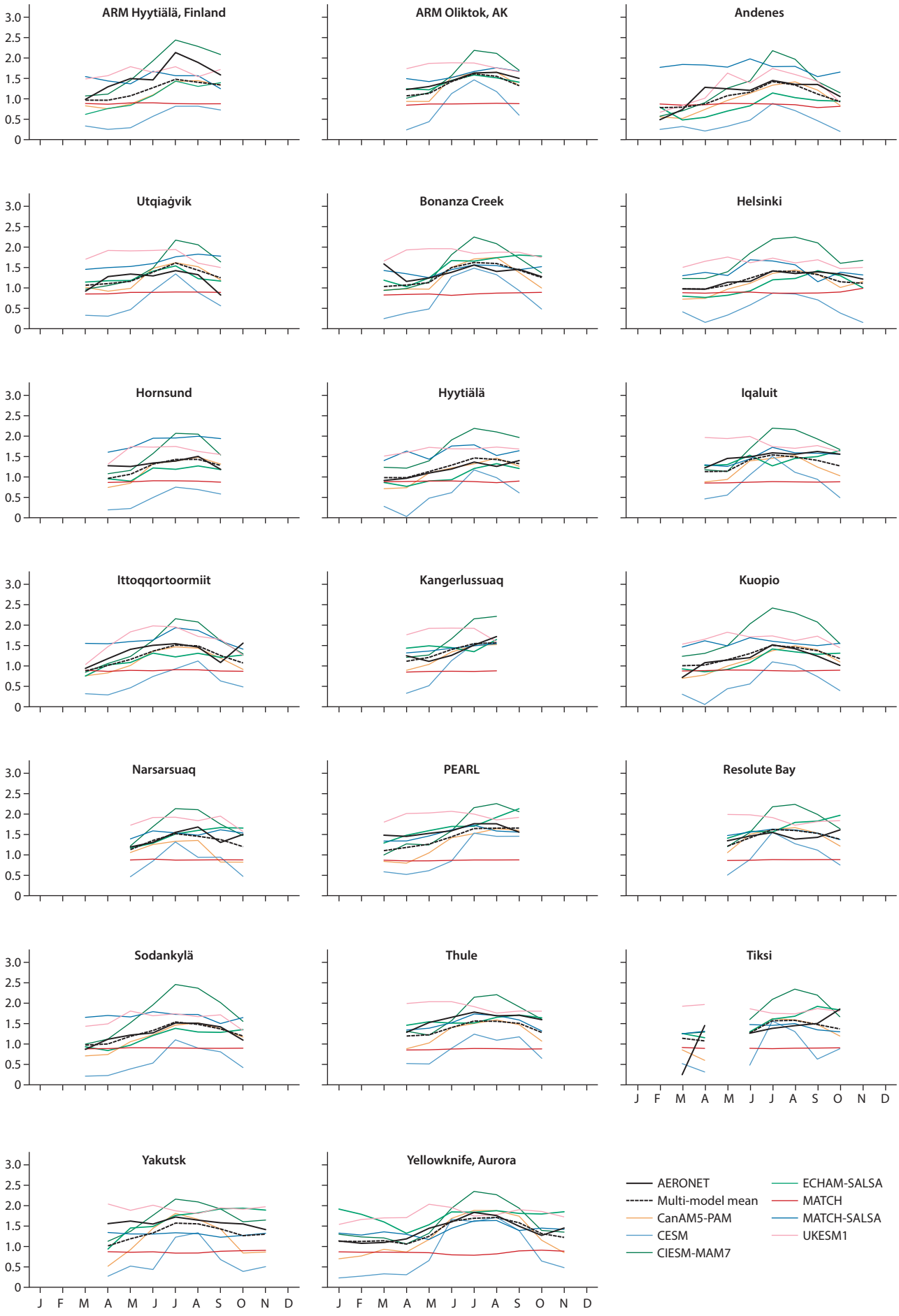

Figure 7.49 Comparison of modeled AE seasonal cycle (colored lines) at Arctic locations for periods with AERONET measurements (solid black line) available for 2014–15. The dashed black line represents the multi-model mean.

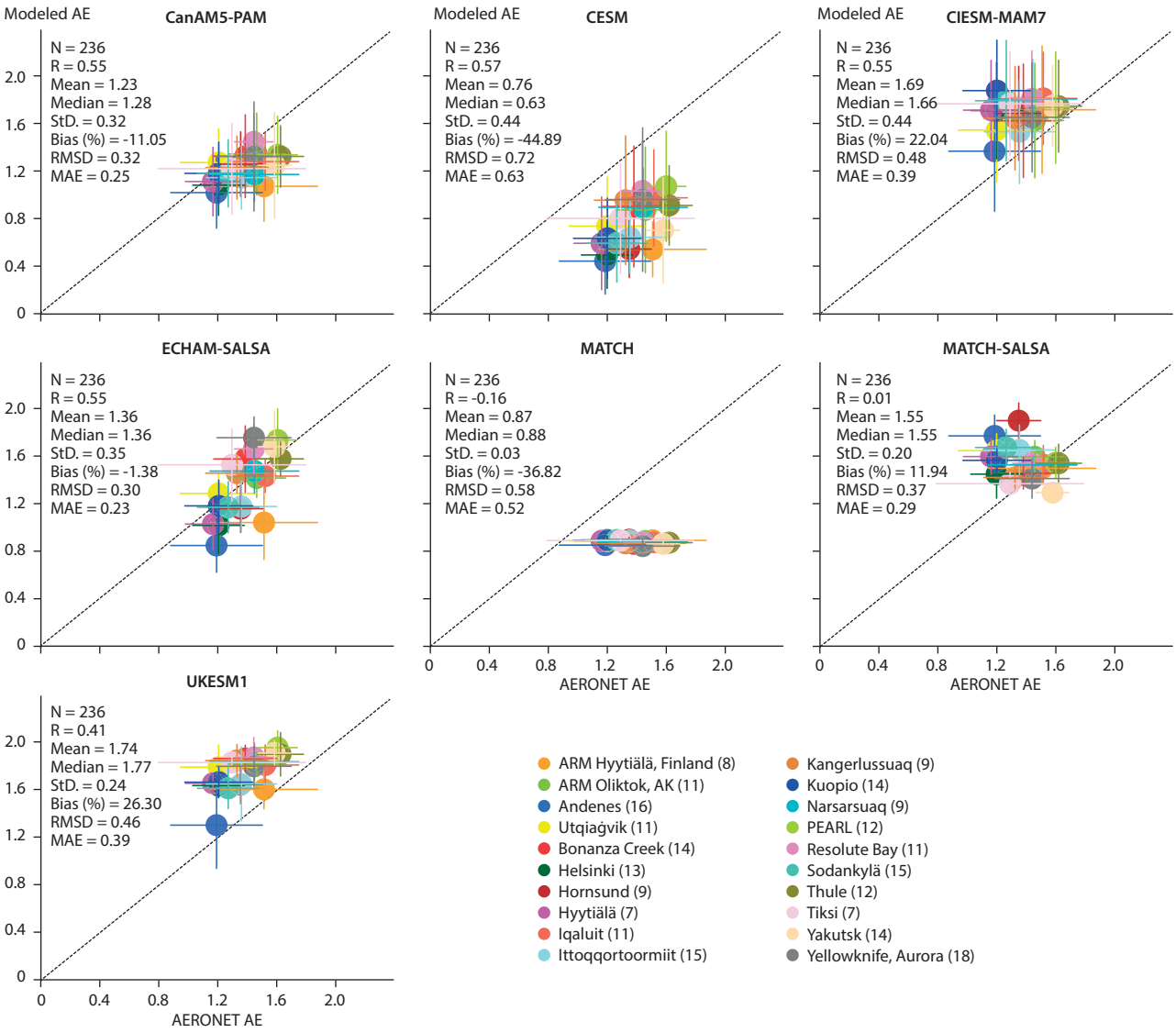

Figure 7.50 Modeled-versus-measured monthly mean AE at individual Arctic AERONET sites for 2014–15. The filled circles are the mean values at each location. The horizontal and vertical lines represent +/- one standard deviation. The statistics insets of each plot are based on accumulated monthly mean values from all sites. N=number of data points; R=correlation coefficient; Mean=model mean value; Median=model median value; StD=model standard deviation; Bias (%)=percent model bias; RMSD=root mean standard error; MAE=mean absolute error. Numbers in brackets indicate number of months for which data were available at each site.

The modeled-versus-measured AE is shown in Figure 7.50, along with the comparison statistics. The mean biases among the models range between -44.9% and +26.3%, while correlation coefficients (R) range from -0.16 (MATCH, which had a flat seasonal cycle) to 0.57 (CESM).

Global AE

The Taylor diagram in Figure 7.51 shows how models performed at simulating AE globally in comparison to three satellite AE estimations. Comparing Figure 7.51 to Figure 7.45, shows that all models are less capable of accurately simulating AE than AOD, with annual mean correlation coefficients ranging between 0.3 and 0.62 (Figure 7.51).

Figure 7.52 shows that models are able to simulate AERONET AE within a factor of two, with several locations having model biases within 10%. Thus, models simulate the overall aerosol-size distributions reasonably well. Most models (except CESM) overestimate AERONET AE over dust source regions of Africa. CESM underestimated AE over almost all sites, which could, in part, be related to its simulated dust aerosols.

7.3.6.3 Absorption aerosol optical depth (AAOD)

In addition to AOD and AE, absorption aerosol optical depth (AAOD) was evaluated. This qualitatively indicates the column aerosol loading of light-absorbing aerosols – an important parameter for radiative forcing and thus climate impacts. The satellite-based AAOD estimations from the AATSR satellite instrument provide global coverage; however, the temporal coverage stops in 2011, making comparisons for the period 2014–15 not possible. The AATSR AAOD comes from two retrieval algorithms. The first is termed AATSR_ORAC; part of Oxford Rutherford-Appleton Laboratory [RAL] Aerosol and Clouds, it uses an optimal-estimation retrieval scheme for multi-spectral images (Sayer et al., 2010). The second is called AATSR_SU (AATSR Swansea University: North et al., 1999; Beven et al., 2012). Most models have spatial-pattern correlations with satellite AAOD, with R values ranging

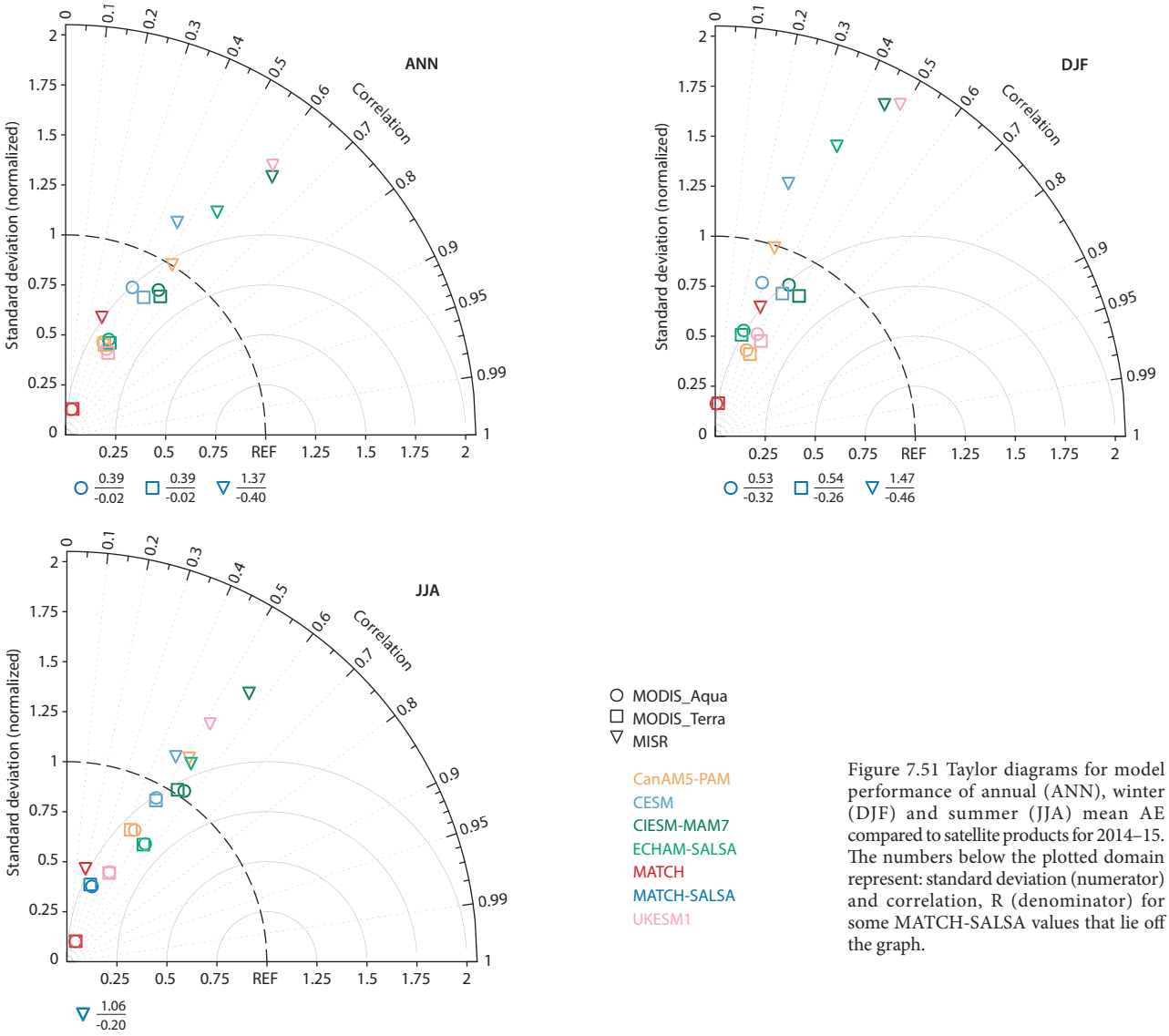

Figure 7.51 Taylor diagrams for model performance of annual (ANN), winter (DJF) and summer (JJA) mean AE compared to satellite products for 2014–15. The numbers below the plotted domain represent: standard deviation (numerator) and correlation, R (denominator) for some MATCH-SALSA values that lie off the graph.

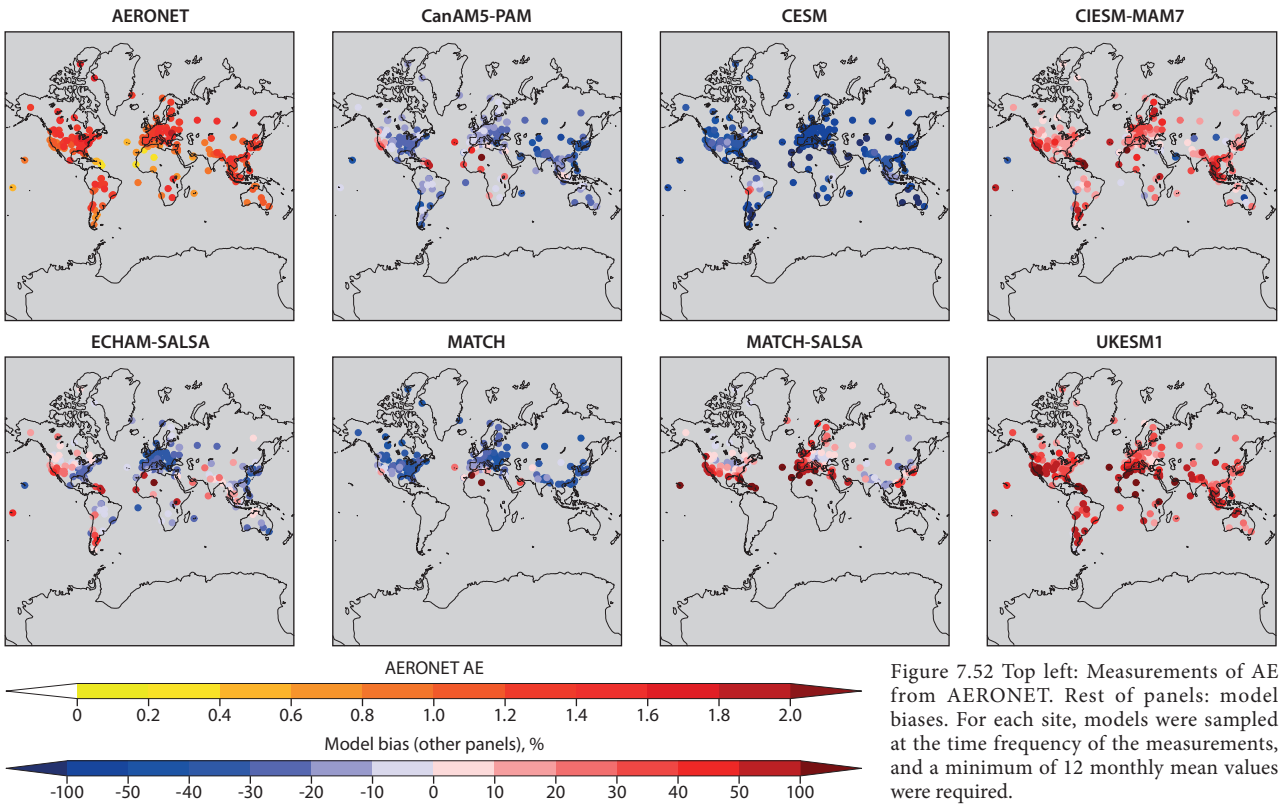

Figure 7.52 Top left: Measurements of AE from AERONET. Rest of panels: model biases. For each site, models were sampled at the time frequency of the measurements, and a minimum of 12 monthly mean values were required.

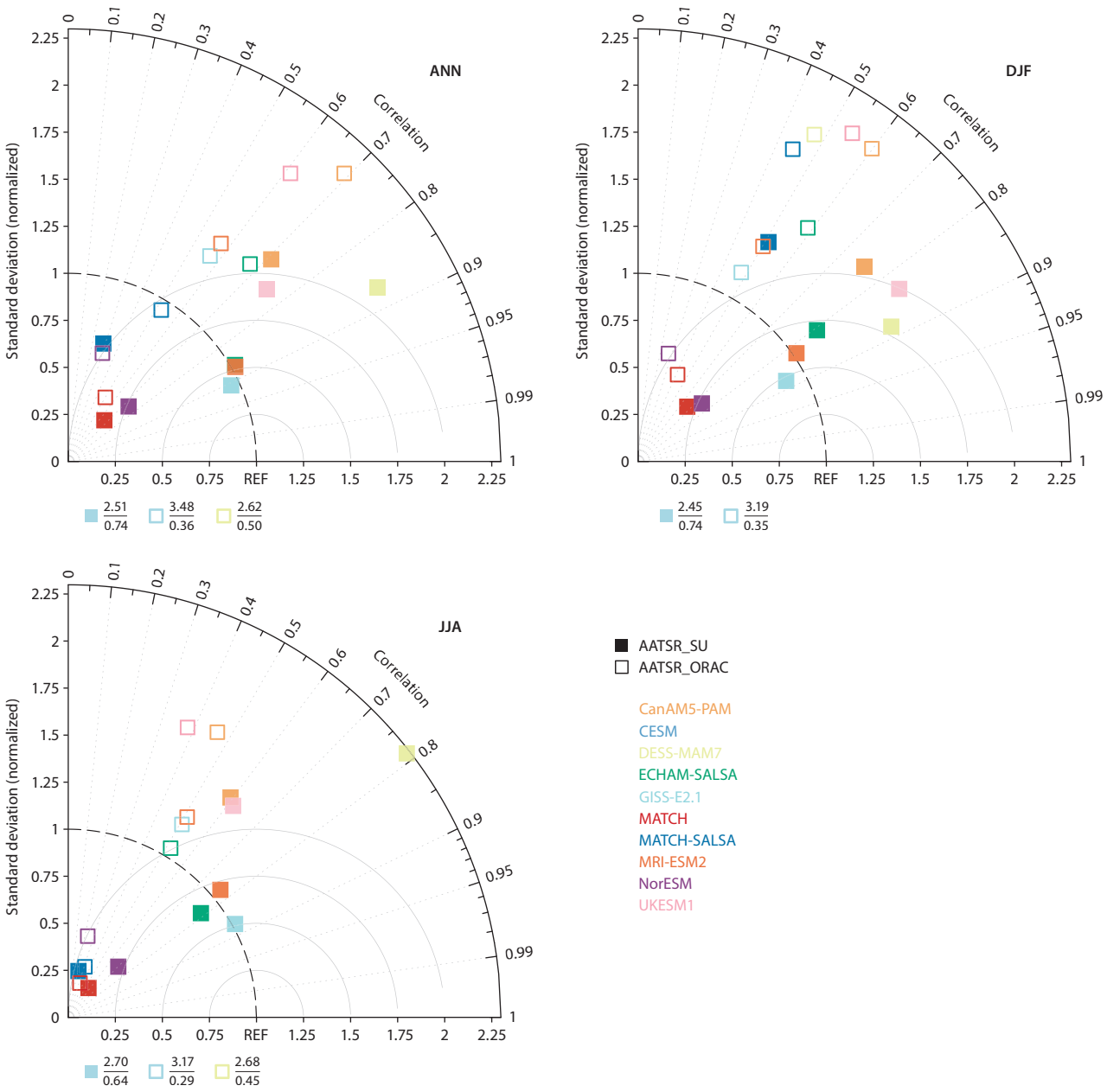

Figure 7.53 Taylor diagrams for model performance of annual (ANN), winter (DJF) and summer (JJA) mean AAOD compared to AATSR products for 2008–9. There were no AATSR data for 2014–15. The numbers below the plotted domain represent: standard deviation (numerator) and correlation, R (denominator) for some CESM, GISS-E2.1 and DESS-MAM7 values that lie off the graph.

between 0.3 and 0.9 (Figure 7.53). Models agree better with AATSR_SU retrievals than with AATSR_ORAC, which highlights the importance of taking into account uncertainties among different types of observations for the same variable.

Figure 7.54 shows model comparisons with AERONET-based AAOD for the 2014–15 period. Due to the limited number of available AAOD observations at AERONET sites, the means at each location are based on the available number of monthly mean values. This approach differs from AERONET-based AOD and AE comparisons (Sections 7.3.6.1 and 7.3.6.2, respectively), where at least 12 monthly values were required to calculate means at individual sites. Most model biases have similar spatial patterns in locations such as the USA and southern Africa, where models tend to underestimate AAOD – and northern Africa, the Mediterranean and the Middle East – where several models overestimate AAOD (Figure 7.54). Most model overestimates are for locations over dust sources, while underestimates are for areas near biomass-burning regions. However, some models, such as NorESM and MATCH, underestimate AAOD at almost all AERONET sites.

To summarize the aerosol optical properties of Section 7.3.6, model evaluations of AOD, AE and AAOD suggest that models are capable of simulating these quantities within a factor of two, although individual models differ in terms of overall biases according to location. In the Arctic, the mean model biases range between -63.4% to +41% (Figure 7.44) and have a multi-model mean AOD bias of -23.2% in the Arctic and -25% globally. AE is also simulated well by most models in the Arctic region, with mean biases among the models ranging between -44.9% and +26.3% (Figure 7.50). The AAOD observations were not available for the Arctic region; however, the global analysis shows that most models are underestimating absorbing

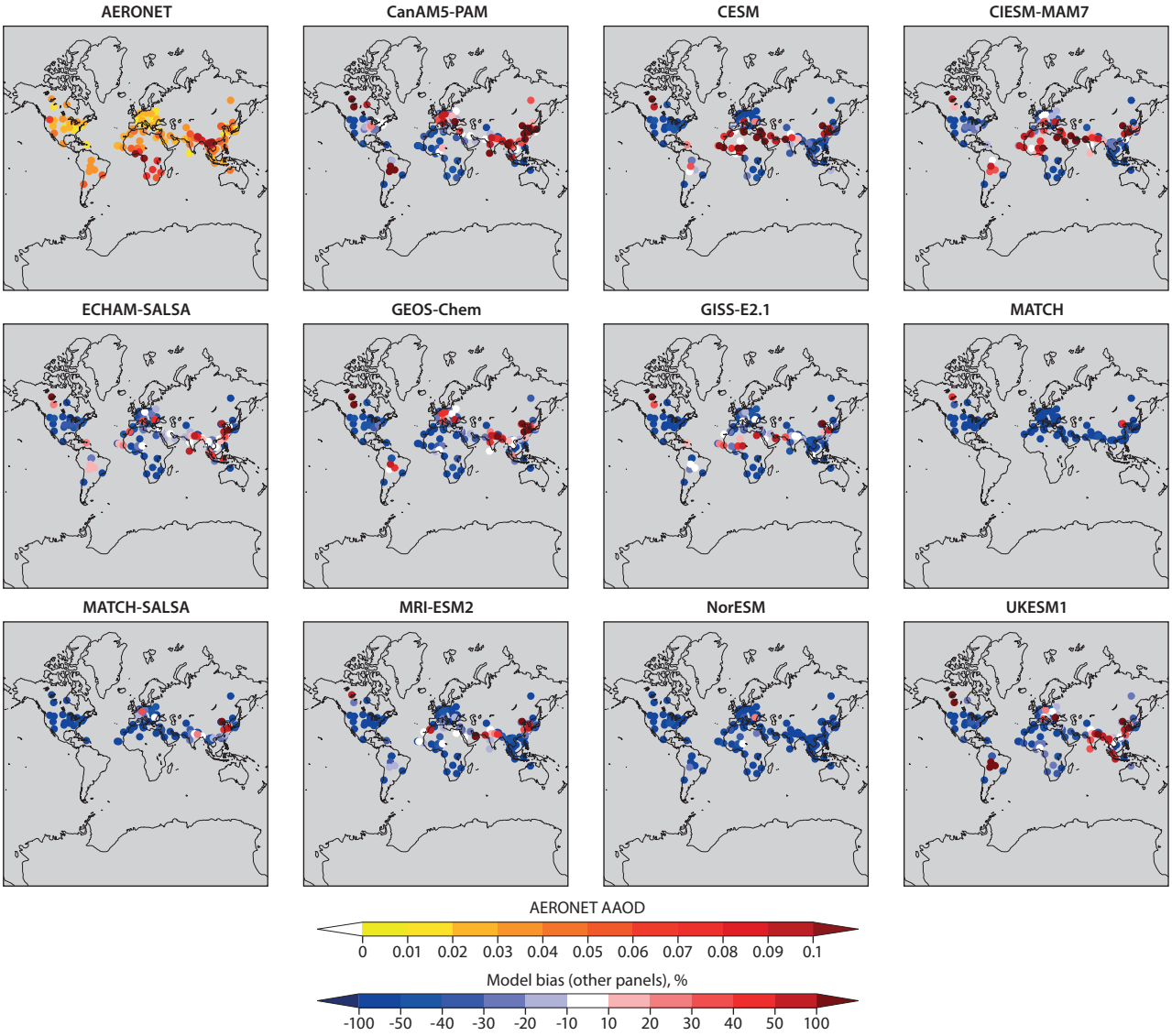

Figure 7.54 Top left: mean AAOD from AERONET. Rest of panels: model biases for 2014–15. For any given site, models were matched to the time frequency of the measurements, and the mean calculated if at least one valid month was available.

aerosols over dust sources and underestimating in biomass-burning regions. That said, some models underestimated AAOD everywhere. The evaluation of aerosol optical properties has not been carried out in previous AMAP reports; therefore these evaluations could be useful in improving models for future simulations.

7.3.7 Clouds

Clouds have some of the largest impacts on the atmosphere's radiative budget but their simulation remains very challenging. Thus, clouds present one of the largest sources of uncertainty in climate simulations. It is important to understand how well individual models simulate certain cloud characteristics that are linked to changes in cloud microphysics. In this way, we can better understand the linkages between SLCFs that influence cloud formation and properties, and the climate impacts of those clouds. Thus, in this section, simulated cloud properties are evaluated against satellite-based observations. Cloud liquid water path (CLWP), cloud ice water path (CIWP), cloud fraction, and cloud droplet number concentration (CDNC) were analysed as a mean over four simulated years: 2008, 2009, 2014 and 2015.

7.3.7.1 Cloud fraction

Evaluating the total cloud fraction provides a first-order indication of how clouds and their coupling to the large-scale thermodynamic conditions in the Arctic are simulated in the models. Cloud fraction also provides primary constraint on the cloud forcing and cloud processing of aerosols. Figures 7.55 and 7.56 show intercomparisons of total cloud fraction between the models and satellite products for the winter (DJF) and summer (JJA) months, respectively. Cloud fraction derived from three satellite sensors – two passive (Climate Monitoring-Satellite Application Facility [CM-SAF] Clouds, Albedo Radiation Data Record, AVHRR-based, Edition 2 [CLARA-A2] and MODIS) and one active (Cloud-Aerosol Lidar and Infrared Pathfinder Satellite Observation [CALIPSO]) – is shown to represent variability in the observations. The CLARA-A2 climate data record based on AVHRR sensors represents a family of heritage sensors that have been flying since 1978, while MODIS represents a more advanced, later-generation family of multi-spectral sensors. CALIPSO is used as a *de facto* standard, as it provides the most accurate description of cloudiness to date. Since these three types of sensors have different sensitivities to clouds,

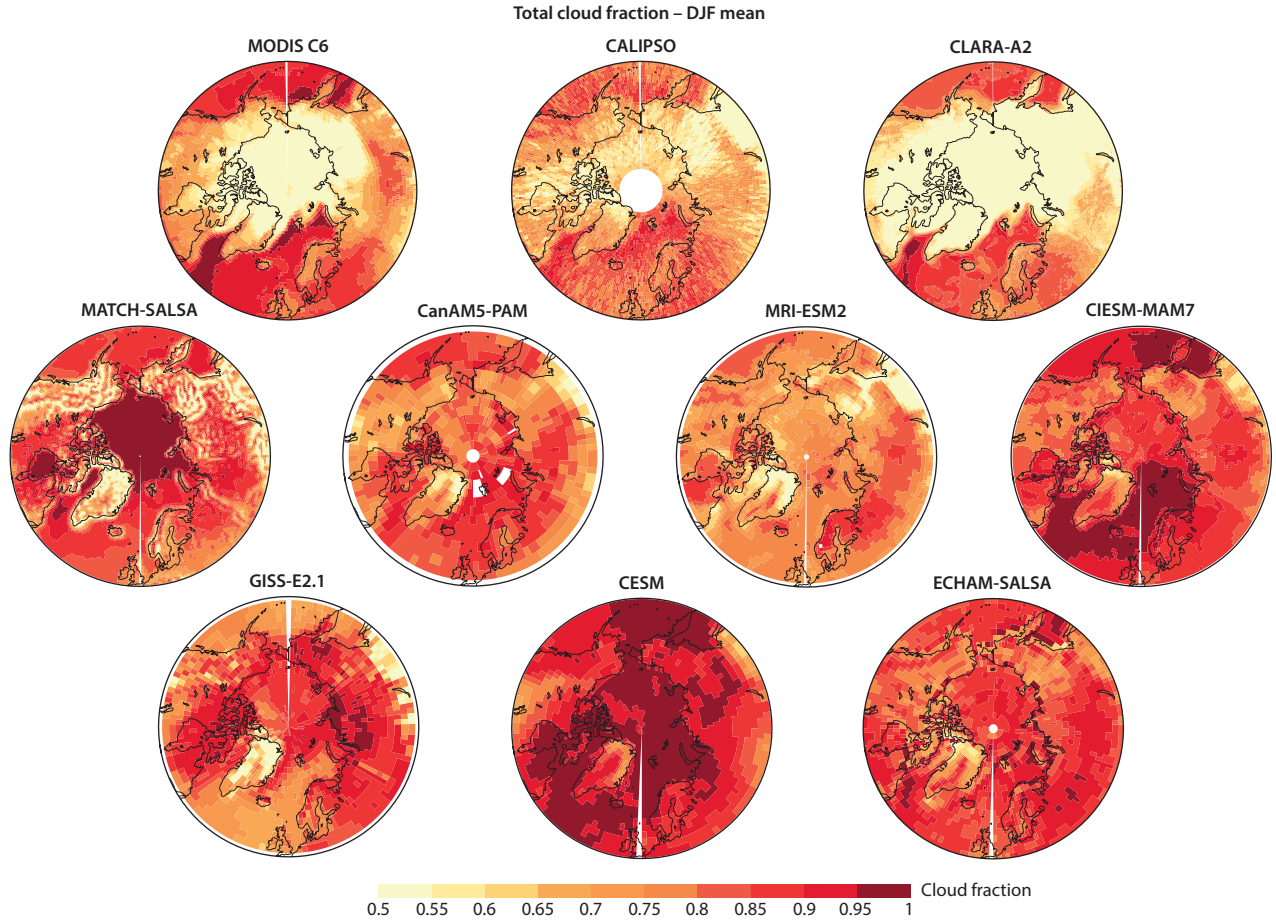

Figure 7.55 Top row: observed cloud fraction. Other rows: modeled cloud fraction. Mean for winter months (DJF) of 2008, 2009, 2014, and 2015.

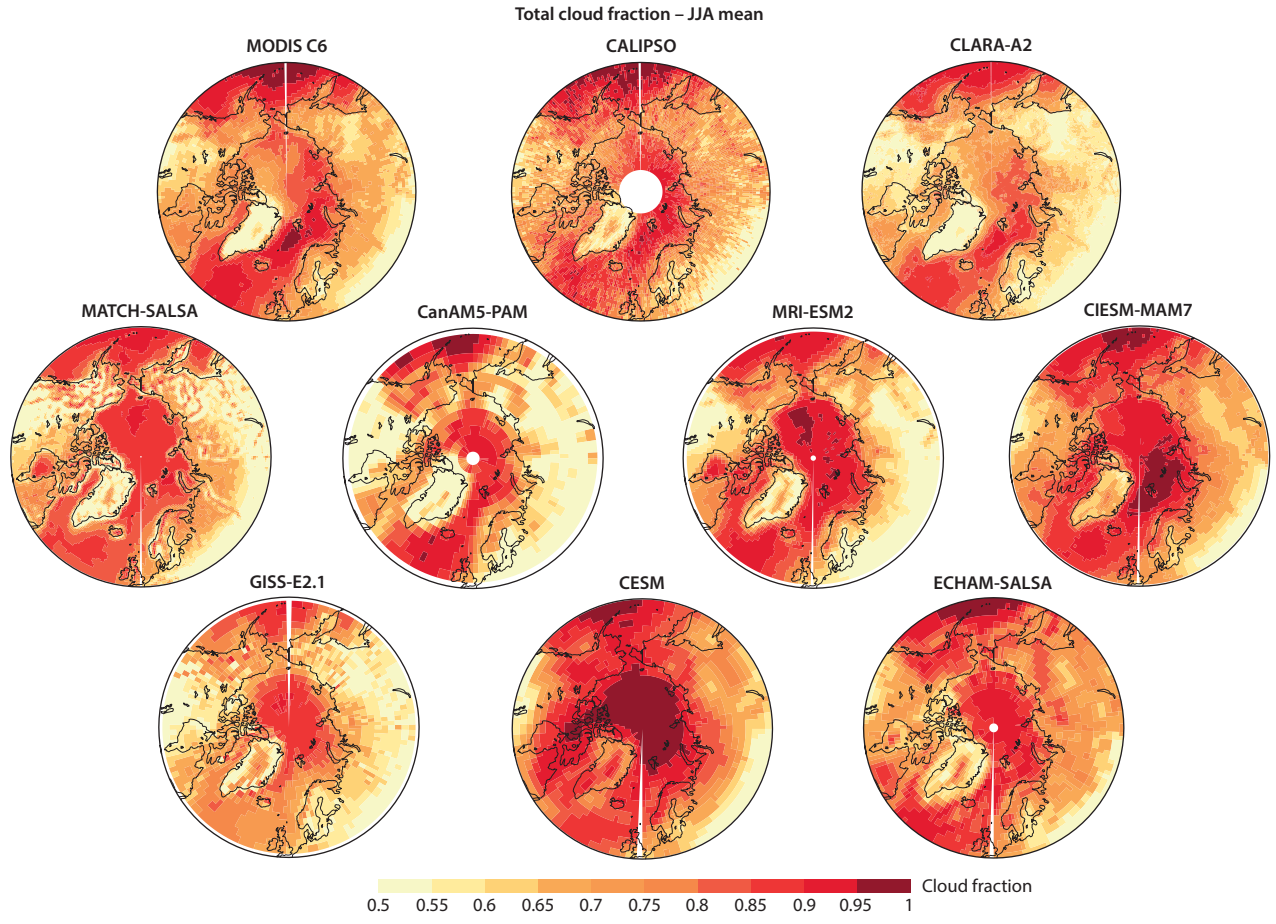

Figure 7.56 Top row: observed cloud fraction. Other rows: modeled cloud fraction. Mean for the summer months (JJA) of 2008–9 and 2014–15.

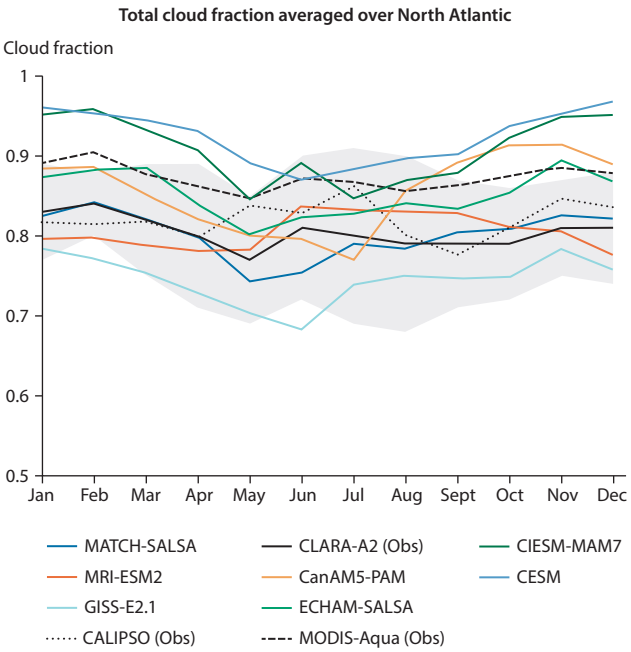

Figure 7.57 Seasonal variability of observed (black lines) and simulated (colored lines) cloud fraction over the North Atlantic (15°W–20°E, 60°N–75°N). The shaded area shows the natural variability in the CLARA-A2 observations indicated by one standard deviation in the cloud fraction.

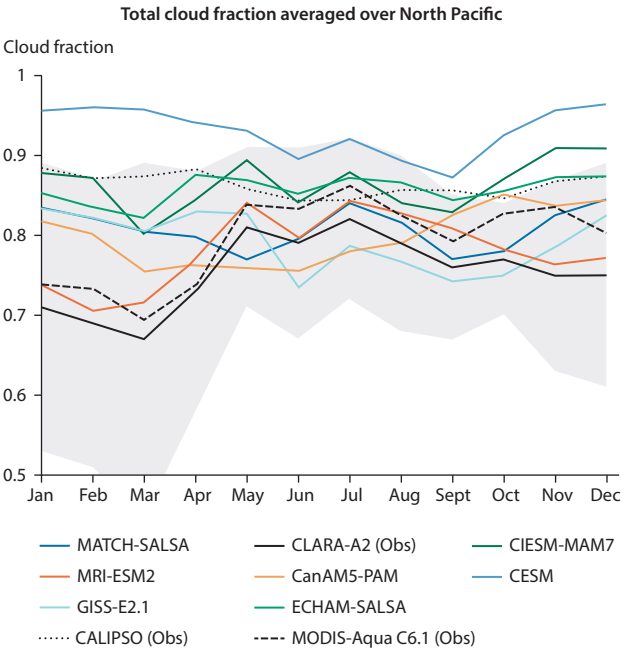

Figure 7.58 Seasonal variability of observed (black lines) and simulated (colored lines) cloud fraction averaged over the North Pacific (160°E–160°W, 50°N–70°N). The shaded area shows the natural variability in the CLARA-A2 observations indicated by one standard deviation in the cloud fraction.

they represent the typical variability to be expected in the observations, making the model evaluation more fair and meaningful.

Figure 7.55 shows fewer differences among satellite observations over ice-free waters during DJF, but greater differences over ice-covered parts of the Arctic Ocean and land areas. The differences between the models are also large during the winter months, as much as 15–20% in the central Arctic. When compared to the CALIPSO observations, the overestimations in some models reach as much as 20–25% regionally. During winter, the differences among models and the observations are also large over polluted high-latitude regions, such as in the Eurasian and East Asian sectors. However, during summer (Figure 7.56), the inter-model differences are less pronounced and also agree better with the observations. Historically, there has been better availability and quality of data from different observational systems during the polar summer, which has led to greater understanding and representation of Arctic clouds in models during the summer season. The polar winter remains a challenge in terms of both observations and models.

Figures 7.57 and 7.58 show evaluation of the annual cycle of monthly mean cloud fraction over two oceanic areas, the North Atlantic (15°W–20°E, 60°N–75°N) and North Pacific (160°E–160°W, 50°N–70°N), respectively. These areas were chosen as they are the two important pathways of long-range transport for pollutants into the Arctic. In the North Atlantic, the total cloud fraction in all three observational datasets remains high (above 80%) throughout the year, with the annual cycle being very flat. The majority of models exhibit similar features, with their cloudiness estimates within the observational variability. However, a few models (GISS-E2.1, CIESM-MAM7 and CESM) overestimate or underestimate the magnitude of cloudiness, outside the variability range during the polar winter months.

In the North Pacific, CALIPSO shows a very flat annual cycle, but the CLARA-A2 and MODIS observations differ from CALIPSO during the polar winter months. This is mainly because, while the North Atlantic remains ice-free throughout the year, parts of the North Pacific are frozen during winter months. Differentiating sea ice from low-level clouds over the frozen ocean becomes challenging for the passive sensors (MODIS and CLARA-A2), as the information from the solar channels is missing during the winter months. The cloud-masking algorithms of CLARA-A2 and MODIS have to rely solely on the information provided by the thermal channels, making it difficult to separate sea ice from low-level clouds, and thus introducing large uncertainties. Since the retrieval algorithms deem a pixel to be cloudy only under high confidence, this cloud conservative nature of the CLARA-A2 and MODIS retrieval algorithms leads to the underestimates of the cloud fraction during the winter months.

In general, the majority of the models also show flatter annual cycles in line with CALIPSO in the North Pacific. The differences among the models are largest during the winter months. Except for the CESM model, all the other models simulate the cloud fraction realistically well and are within the observational uncertainty.

Note that the different satellite sensors have varying sensitivity to clouds. To enhance the fairness of evaluations, satellite simulators are often used to harmonize these different sensitivities and to take into account the differences in the temporal samplings and retrieval philosophies between the models and satellite observations. However, unlike with global climate models, chemical transport models are not yet geared to use the cloud satellite simulators. In the absence of these simulators, current evaluations can still be justified for the several reasons. First, the diurnal cycles of cloudiness are much flatter in the Arctic than at lower latitudes. Therefore, any

variations arising from different overpass times are expected to be minimal. Second, the spatial sampling from the imager observations is far better in the Arctic. And third, CALIOP-CALIPSO, used additionally for evaluation, is able to detect even the most tenuous clouds with very low optical depths, providing a good description of variability in the observations.

7.3.7.2 Cloud liquid water path

Quantifying cloud water is important for studying the microphysical processes and indirect effects of aerosols. Cloud water is often expressed in the column-integrated quantities of CLWP and CIWP. However, retrievals of these elements from passive satellite sensors, such as MODIS, depend heavily on the quality of data from the solar channels, satellite and solar geometry, and the accuracy of cloud fraction over highly reflective surfaces in the Arctic. These retrievals are therefore restricted to only a few summer months, and the uncertainties among various satellite sensor datasets remain very high in the Central Arctic (Taylor et al., 2015). This is clear from Figure 7.59, which shows an intercomparison of CLWP from MODIS and CLARA-A2 with the models. Over the ice-free oceans, MODIS and CLARA-A2 retrievals of CLWP agree well with one another. However, over landmasses and the permanently frozen parts of the central Arctic Ocean, the differences between the two datasets are very high, reaching up to 100%. Differences among the models are large as well, and the land-sea contrast in CLWP varies from model to model. It is difficult to find a pattern that commonly holds across all the models and observations, indicating the challenges that remain in the passive observations and representation of CLWP in the Arctic. The model estimates of CLWP in the Atlantic and Pacific sectors of the Arctic Ocean are qualitatively closer to the estimates derived from the combined CloudSat and CALIOP-CALIPSO data (e.g. Lenaerts et al., 2017).

Figures 7.60 and 7.61 show the histograms of CLWP over the North Atlantic and North Pacific, respectively, during the summer months (JJF). In the North Atlantic, the shape of the distribution of CLWPs in CLARA-A2 and MODIS is similar, while the histogram of MODIS's data is shifted to higher values (by around 20 g/m^2). The distribution of CLWP in the majority of the models (DEHM, CanAM5-PAM, ECHAM-SALSA and CIESM-MAM7) broadly agrees with the CLARA-A2 observations, whereas CLWP in the other models peaks at the lower range of 60–80 g/m^2. All models except MATCH-SALSA

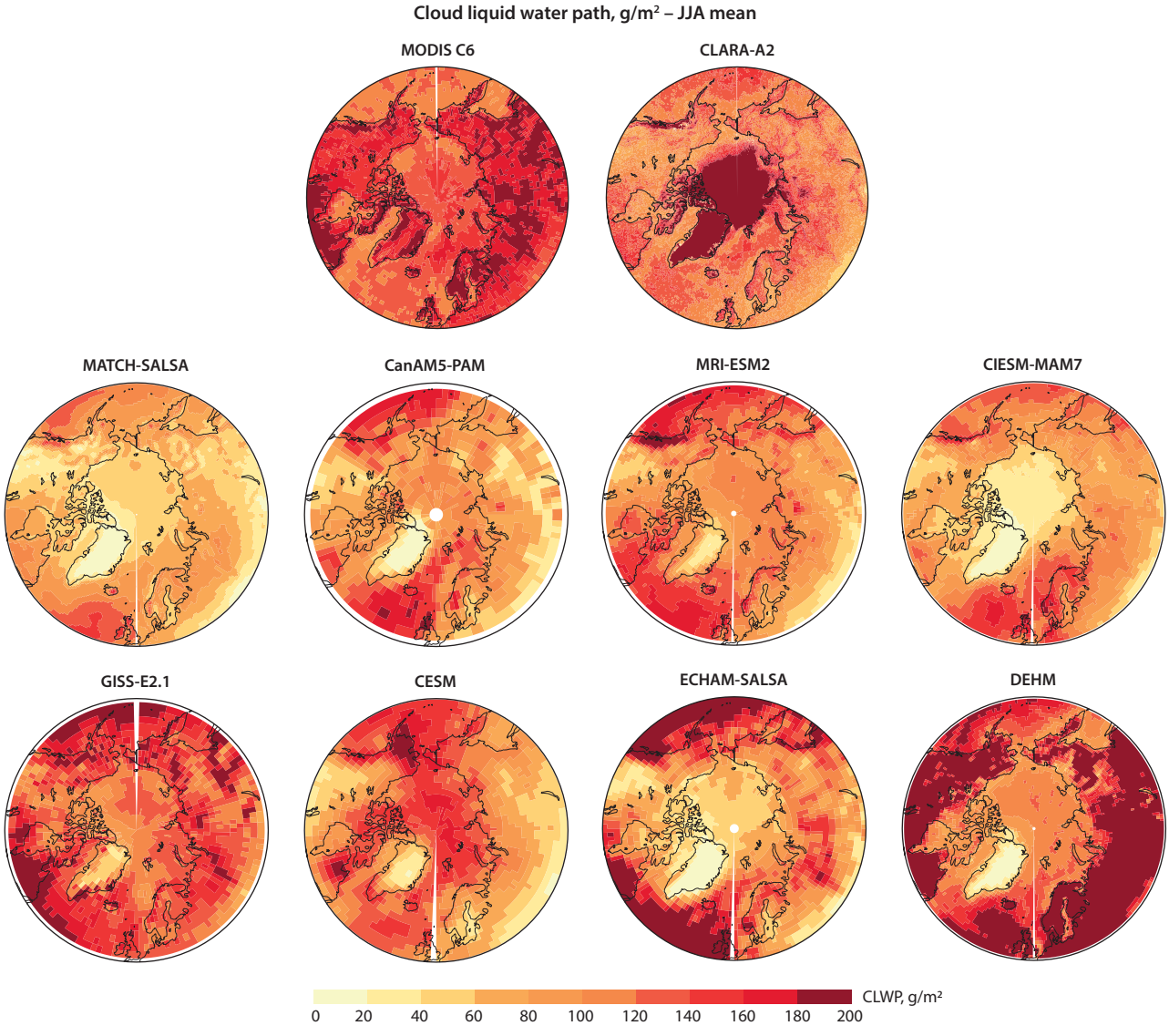

Figure 7.59 Top row: observed CLWP. Other rows: modeled CLWP. Results for the summer months (JJA).

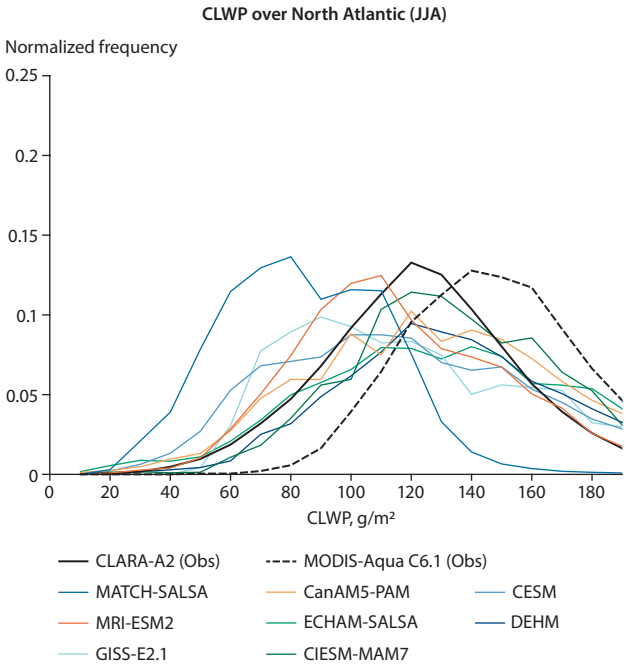

Figure 7.60 CLWP over the North Atlantic (15°W–20°E, 60°N–75°N) for the summer months (JJA), from observations (black lines) and models (colored lines).

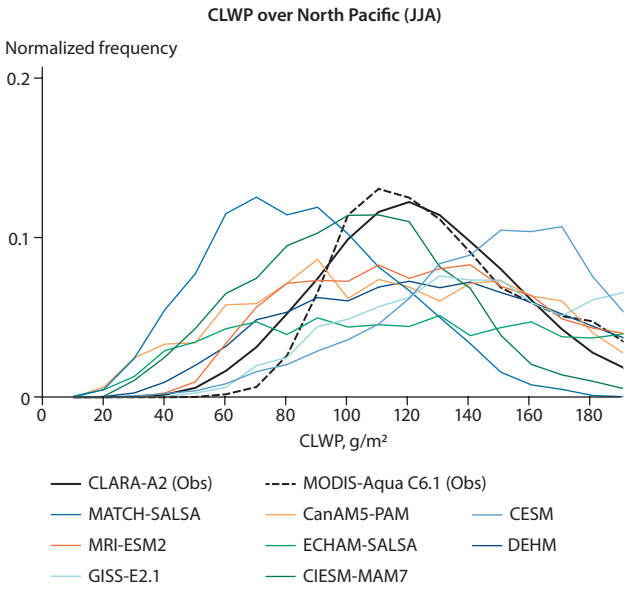

Figure 7.61 CLWP over the North Pacific (160°E–160°W, 50°N–70°N) for the summer months (JJA), from observations (black lines) and models (colored lines).

simulate CLWP realistically at the tail ends of the distribution curves. In the North Pacific, the distributions of CLWP in MODIS and CLARA-A2 agree very well with one another. Here, the modeled distributions of CLWP are flatter, and the models show distributions that are skewed both positively (MATCH-SALSA and CIESM-MAM7) and negatively (CESM and GISS-E2.1) compared to the observations.

Since the retrievals of CLWP from passive satellite sensors are available only during a few summer months, and in order to have another independent reference for the evaluation, the ground-based retrievals available from an Atmospheric Radiation Measurement (ARM) program site in Utqiaġvik,

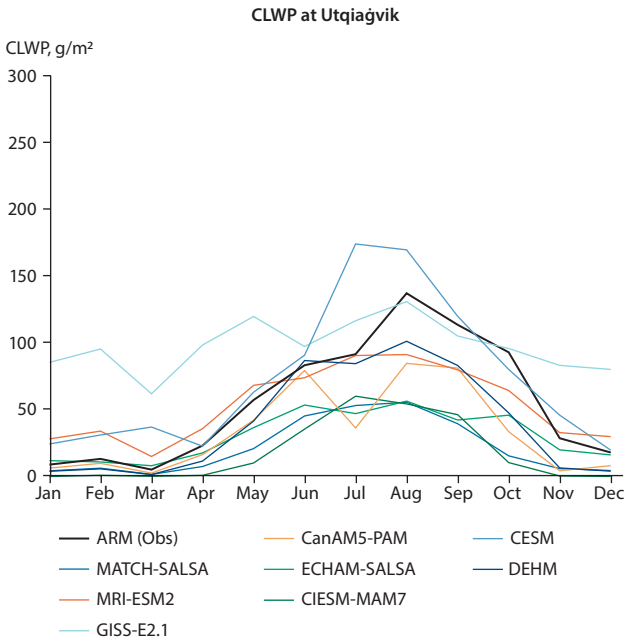

Figure 7.62 Seasonal variability of CLWP at Utqiaġvik (71.29°N, 156.78°W) from the ARM observations (black line) and models (colored lines).

Alaska, were used to evaluate the monthly mean annual cycle of CLWP in the models, as shown in Figure 7.62. Figure 7.62 shows that the annual cycle of CLWP peaks in the late summer (August) at Utqiaġvik, with the lowest values observed in the late winter and early spring months. This was expected, not only because of the prevalence of the liquid phase clouds in summer, but also due to the presence of supercooled liquid and mixed-phase clouds (Shupe, 2011). The majority of models also capture this annual cycle peaking in late summer and early autumn. The amplitude of the annual cycle is represented well in some models (DEHM, MRI-ESM2), with other models (MATCH-SALSA, ECHAM-SALSA and CIESM-MAM7) showing much flatter annual cycles.

7.3.7.3 Cloud ice water path

Figure 7.63 shows the intercomparison of cloud ice water paths (CIWPs). The CIWP estimates from earth-observing satellite CloudSat observations were used (product 2B-CWC-RVOD, R05). This dataset was chosen because it combines the strengths of CloudSat and MODIS. The cloud radar on CloudSat can penetrate the optically thick clouds, providing a realistic description of the vertical structure of ice clouds, and the visible optical depths used in the CIWP retrievals are further constrained by using MODIS retrievals, offering an advantage over other CIWP datasets. The inter-model differences are large, with most models, except CIESM-MAM7 and DEHM, underestimating the magnitude of CIWP compared to CloudSat – especially over the ice-free oceanic regions. The majority of the models have prognostic treatment of cloud ice. However, CIESM-MAM7 partitions total cloud water into liquid and ice by using the proportion of liquid and ice cloud water in large-scale clouds from the model's cloud microphysics scheme. A single ice microphysics scheme (Zhao et al., 2017; Lin et al., 2020) is used in CIESM-MAM7, where cloud ice and snow are combined into a single prognostic variable called 'total ice'. As a result, CIWP from this microphysics scheme not only

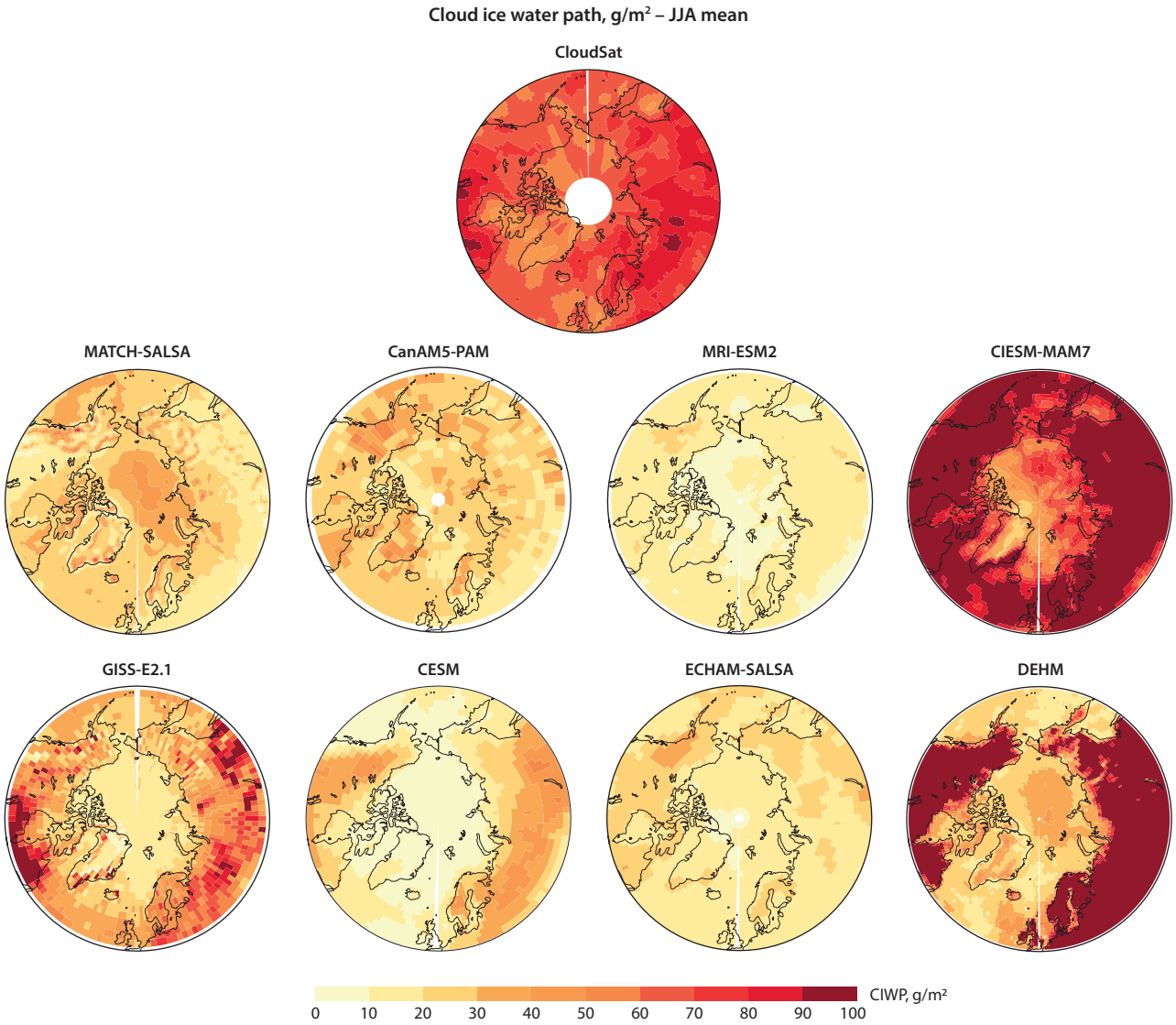

Figure 7.63 Observed CIWP (top panel) and modeled CIWP (other panels). Results are for the summer months (JJA).

includes the CIWP, but also includes the snow water path, and this may be the reason that CIESM-MAM7 overestimates CIWP everywhere. The inadequate diagnosis of CIWP is being addressed in the forthcoming version of CIESM-MAM7.

7.3.7.4 Cloud droplet number concentrations

Improved model simulations of cloud droplet number concentrations (CDNC) are important for reducing uncertainties in cloud radiative forcing. However, evaluating simulated CDNC remains challenging because of the limitations of direct observations over large domains and timescales. Bennartz and Rausch (2017) updated the CDNC climatology for liquid boundary layer clouds, first published by Bennartz (2007), using estimates from the National Aeronautics and Space Administration's Aqua MODIS. Figure 7.64 shows the observed and modeled JJA average of observed and simulated CDNC, while Figure 7.65 shows the model biases. Similar to the other cloud properties discussed above, models underestimate CDNC in most of the Arctic region, with varying regional biases.

MATCH-SALSA seems to agree better with MODIS than most other models with relatively smaller biases. MATCH-SALSA uses the Abdul-Razzak and Ghan (2002) scheme for computing CDNC, which depends on the aerosol representation, updraft velocity and the supersaturation of the air parcel. It is important to note that, although the satellite-based retrievals of cloud properties remain very important for large-scale model evaluations, these estimates can be highly uncertain, especially near the polar regions (Bennartz and Rausch., 2017).

In summary, it is challenging to draw robust conclusions from the cloud property evaluation results. While the models do, in general, simulate cloudiness reasonably during polar summers, both the inter-model differences and the uncertainties in the satellite observations are higher during the winter months. A large spread in the model estimates of CLWP and CIWP (especially over the land regions surrounding the Arctic Ocean), as well as high differences among the observations themselves, limit intercomparisons over the Arctic as a whole. However, regionally – for example over the ice-free ocean areas of the Atlantic and Pacific sectors, which are two of the main pathways of pollution transport into the Arctic – the modeled CLWP agrees better with the observations. The models tend to underestimate CIWP and CDNC over the oceanic areas.

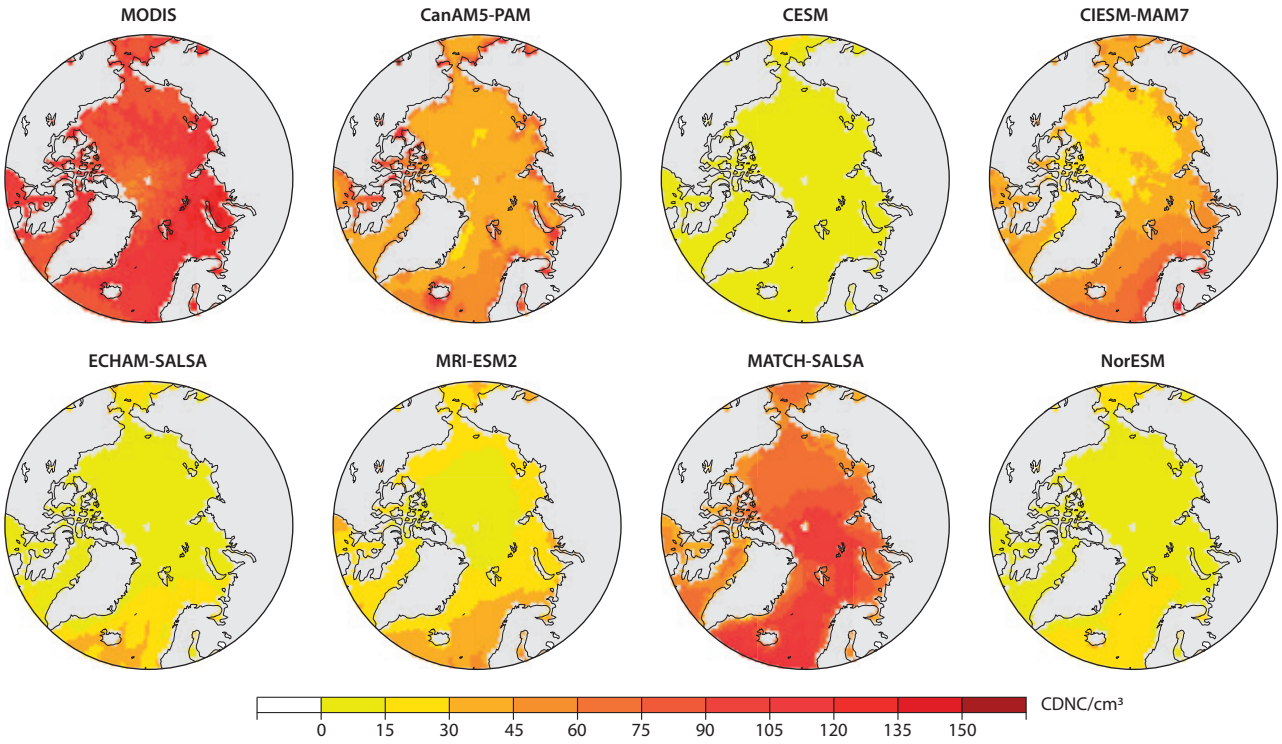

Figure 7.64 Top left: observed CDNC. Rest of panels: modeled CDNC. Results are for the summer months (JJA) of four years (2008–2009 and 2014–2015).

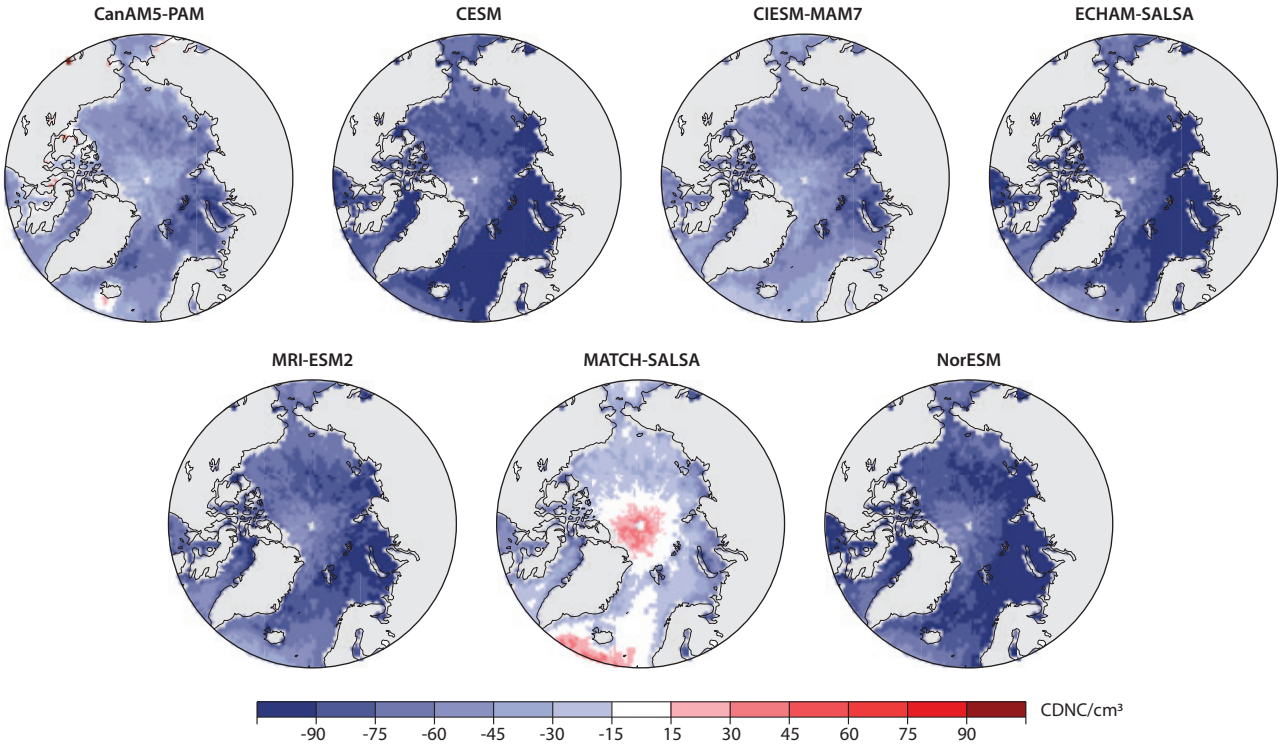

Figure 7.65 Model minus MODIS differences in cloud droplet number concentration for summer months (JJA) of four years (2008–2009 and 2014–2015).

7.4 Summary of the SLCF model evaluation

Eighteen models (eight CTMs, two CCMs, three GCMs, and five ESMs) simulated a subset of SLCFs and their properties for this report, using a common set of newly developed anthropogenic emissions (ECLIPSEv6b, Chapter 2, Data ref. 7.2). The model simulations were evaluated against numerous measurements throughout the atmosphere in the Arctic and Northern Hemisphere – more so in this report than in AMAP (2015a) and (2015b). It is with this evaluation in mind that one must interpret the model results in the next two chapters (climate impacts in Chapter 8 and health impacts in Chapter 9).

7.4.1 How well do the models perform?

Overall, the results presented in this chapter show that different models provide a range of results for different SLCF species, with some models performing better for some species and some regions than others. No one model stands out as being best for all SLCFs in all regions. However, for most SLCFs, the multi-model mean provides results that are close to the observed concentrations. For some quantities, such as Arctic surface O_3 (Figure 7.1) and global surface $PM_{2.5}$ (Figure 7.40), models share common spatial bias patterns. The representation of the seasonal cycles of aerosols in the Arctic has generally improved since the previous assessment report (Section 7.3.3.1, and Figure 7.20), and the simulated 1990–2015 trends for BC, SO_4, and O_3 are very close to the observed trends in the Arctic. In addition, simulated AOD and AAOD at high- and mid-latitudes in the participating models are generally within the range of observational uncertainty.

There are many similarities between the model performances shown here and those reported in AMAP (2015a). For example, models still overestimate surface O_3 in many regions globally (Figure 7.7), and underestimate surface CO (Figure A7.3). Models still struggle to get good results for BC in the free troposphere and in the Arctic, where there are large variations across models (e.g., Figure 7.30). The aircraft analysis of BC (Section 7.3.3.3), as well as the vertical analysis of O_3 and CH_4 based on satellite observations (Sections 7.3.1.3 and 7.3.2.2, respectively) all indicate that, on average, models lack enough vertical mixing at mid-latitudes, and that this is important for accurately simulating long-range transport to the Arctic. The BC deposition analysis (Section 7.3.3.1) shows orders of magnitude of variations among modeled depositions, which can influence each model's ability to accurately simulate Arctic concentrations of aerosol species. Among the participating

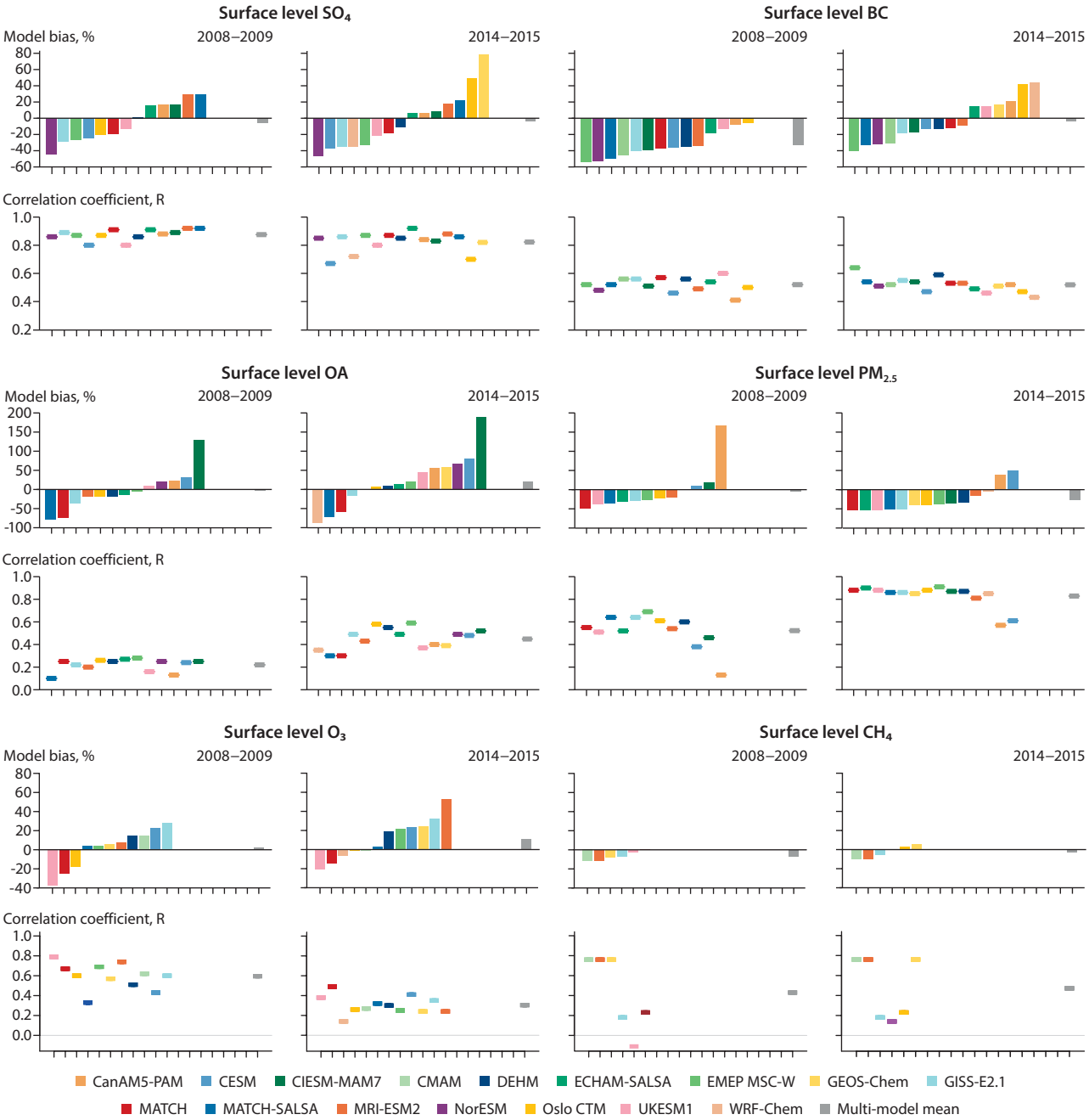

Figure 7.66 Annual model global percent biases and correlation coefficients by species and year. Note that the order of models along the x-axis changes in each panel, but the multi-model mean is always farthest right on the x-axis.

models shown in this chapter, simulated CH_4 was very close to measured CH_4 both at the surface and at higher altitudes in the Arctic. The fact that models prescribed CH_4 concentrations caused a lack of variability in the results for surface air, however.

Figure 7.66 summarizes the model biases and correlation coefficients for each SLCF measured at the surface in their global evaluation [(upper) SO_4 and BC, (middle) OA and $PM_{2.5}$, (lower) O_3 and CH_4], as well as showing the multi-model mean results (in dark gray at the right in each plot). In the case of the aerosol species (Figure 7.66 [upper] and [middle]), the multi-model mean has one of the lowest biases, and highest R values (bias and correlation coefficient of -3% and 0.8 for SO_4, and -4% and 0.5 for BC in 2014–2015, respectively, for example). This means that it is best, if possible, to use the model ensemble (multi-model mean) when computing climate and health impacts of aerosols that are based on their concentrations. The case is different for trace gases, O_3 and CH_4 (Figure 7.66 [lower]), which were consistently overestimated by all models, and thus, their multi-model mean is higher than the best-performing models (which for surface O_3 were MATCH, WRF-Chem, Oslo CTM, and CMAM, for example).

Figure 7.67 shows the results in the same way, but specifically for the Arctic region. The models perform significantly worse in the Arctic for aerosol species (Figures 7.67 [upper] and [middle]) compared to the full global results of Figure 7.66. For example, the multi-model mean bias for the Arctic is -21% and -17% for SO_4 and BC, respectively for 2014–2015, and the correlation coefficients 0.41 and 0.24, respectively. For the trace gas species, O_3 and CH_4 (Figure 7.67 [lower]), the model results are mixed – some are biased high and some low, so the corresponding multi-model mean biases are smaller for the Arctic than globally.

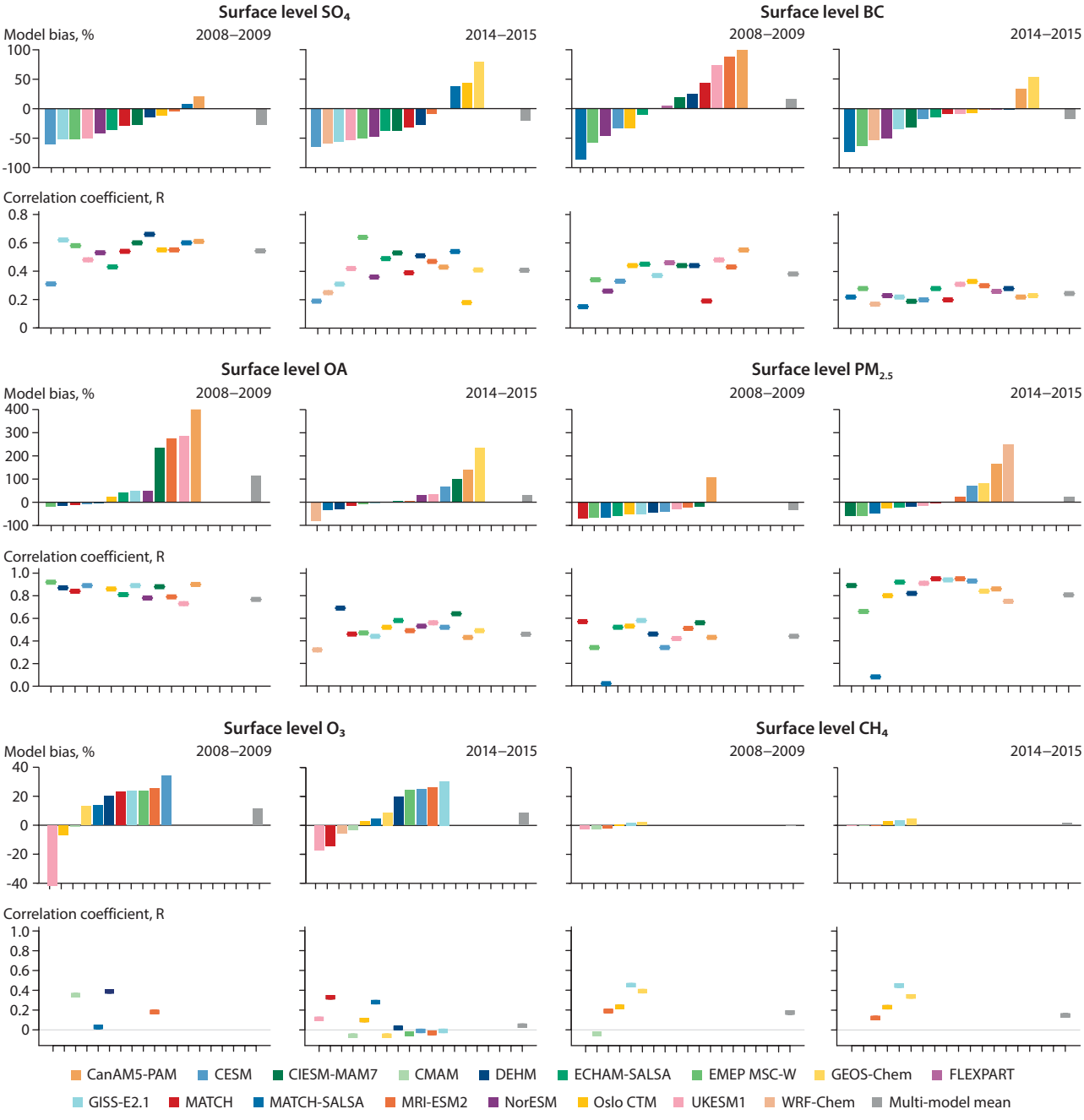

Figure 7.67 Annual model percent biases and correlation coefficients for the Arctic by species and year. Note that the order of models along the x-axis changes in each panel, but the multi-model mean is always farthest right along the x-axis.

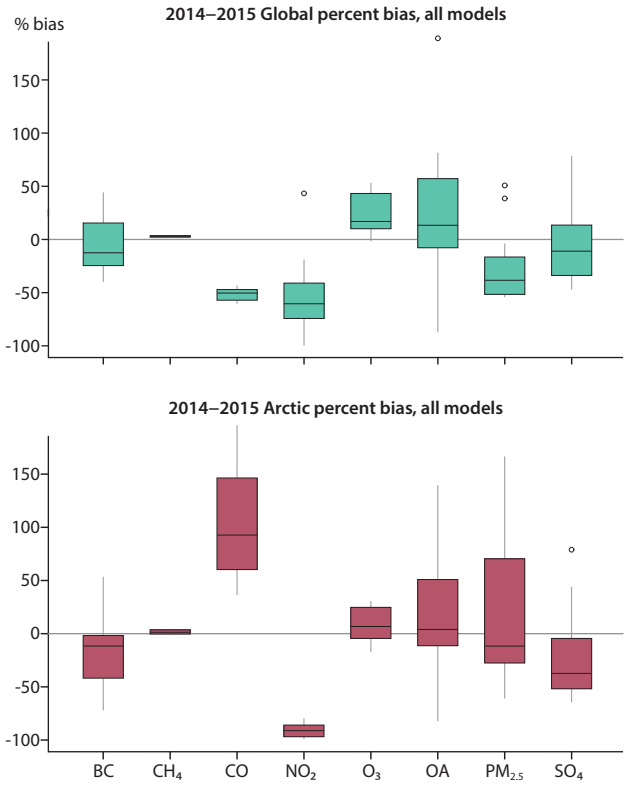

Figure 7.68 Global (upper) and Arctic (lower) % biases from all models and all species together for 2014–2015. Boxes show the median value, and extend to the 25th and 75th percentiles, and vertical lines extend to 1.5 times the interquartile range.

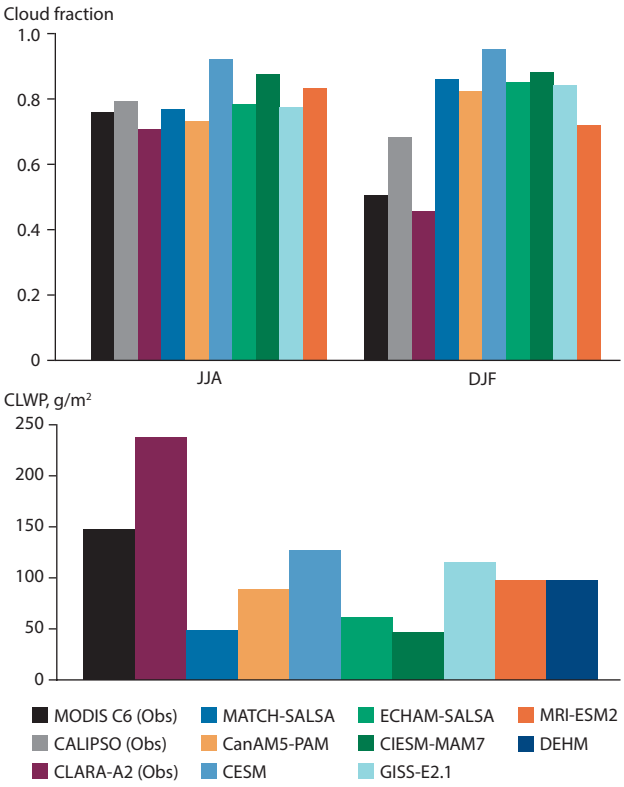

Figure 7.69 Comparison of satellite-based observations with models over the Arctic (70°N–85°N). Total cloud fraction for the JJA and DJF months (upper), and CLWP for the JJA months (lower).

Finally, Figure 7.68 summarizes the model percent biases for all SLCFs measured at the surface, both globally (upper), and in the Arctic (lower). We expect the bias of $PM_{2.5}$ to reflect the biases in its major components; BC, SO_4, and OA; however, NO_3 and NH_4 also comprise a significant portion of $PM_{2.5}$ and these were not evaluated in this report. Models are known to have particular problems with simulating NO_3 (and OA, as shown here), concentrations of which are changing in certain regions in addition to SO_4 (Chapter 6). Globally, O_3-precursors CO and NO_2 are biased low in models, yet surface O_3 is biased high. There is also a slightly smaller range in modeled O_3 in the Arctic than globally. This is likely because Arctic O_3 is close to background levels, whereas O_3 at mid-latitudes near major emissions sources exists in a more complex chemistry regime.

The model evaluations of aerosol optical properties; AOD, AE and AAOD (Section 7.3.6) suggest that the models are capable of simulating these aerosol optical properties within a factor of two, although individual models differ in terms of mean biases at different locations.

The model evaluation of cloud properties such as cloud fraction, CLWP, CIWP, and CDNC revealed large differences between satellite-based observations and models. The observations also had a large spread among themselves. This is an area where further work in both measurements, satellite-based observations and modeling will be required to narrow the range of uncertainties in cloud properties. Figure 7.69 summarizes the comparison of models with the observations for two key variables that are of primary importance for the radiation budget in the Arctic: total cloud fraction and CLWP.

7.4.2 What do model uncertainties mean for climate and health predictions?

Given that the models can never be perfect representations of atmospheric processes and SLCFs, they will not be able to simulate perfect radiative forcings (Chapter 8) and will introduce uncertainties in health analyses (Chapter 9). Thus, one must interpret the climate and health impacts outlined in the following chapters with this in mind. In those chapters, the models described and evaluated in this chapter are used to simulate two future emissions scenarios from 2015–2050: current legislation (CLE), and maximum feasible reduction (MFR) (see Chapter 2 for their descriptions). Simulated SLCF radiative forcings and their climate impacts can only be indirectly constrained by comparisons with observations as they depend on specific conditions, such as future emission changes, for which no direct observations exist. To provide indirect constraints on radiative forcings and climate impacts, the validation strategy employed in this chapter considered a broad range of observable variables linked to key climate processes, such as SLCF concentrations and their interactions with radiation and clouds. Relevant chemical, microphysical, and radiative processes were evaluated with regard to their consistency in different models and across different processes, species, regions, and years. As SLCFs often interact with radiation and clouds over deep layers of the troposphere, it is not sufficient to compare models with measurements of near-surface concentrations. Concentrations of SLCFs in the mid- and upper-troposphere tend to be much more strongly affected by long-range transport of pollutants than by emissions from sources in the underlying lower troposphere, which are more important for air quality than concentrations aloft.

Variability in meteorological conditions and emissions can be very substantial on intra- and inter-annual time scales at all levels of the atmosphere, so datasets from different seasons and years were employed in this chapter.

Overall, the findings presented here give evidence that the multi-model ensemble provides a useful basis for representing the abundance and distribution SLCFs and important climate-related processes, even though some individual model results for some observable parameters are substantially biased high or low. Below we list the annual multi-model mean biases for each SLCF species, and explain what each of those means for interpreting the climate and health impacts described in Chapters 8 and 9, respectively.

- Annual mean, simulated surface-level global and Arctic CH_4 are biased slightly low (both 3% in comparison to the measurements, which have only a 1% uncertainty). This means that confidence in the warming from CH_4 shown in Chapter 8 is high.
- Annual mean, surface-level Arctic BC is biased low compared to measurements (-17%, which is greater than the ~10% uncertainty in measured BC concentrations) in these historical simulations. However, the warming from BC is due to its concentrations throughout the atmospheric column. Underestimates in simulated concentrations at higher altitudes in the troposphere (e.g., -80% at 6km altitude for the Arctic region) generally increase with altitude and proximity to the Arctic, according to comparisons with aircraft measurements. This means that the warming due to BC shown in Chapter 8 may be underestimated.
- Annual mean Arctic SO_4 is biased low compared to measurements (-21%, well below the 3% measurement uncertainty), which means that the cooling from SO_4 in the Arctic shown in Chapter 8 may be underestimated. However, vertical profiles of SO_4 were not evaluated in the project, so their temperature impacts are highly uncertain.
- Globally, and in the Arctic, modeled surface-level O_3 is biased high (+44% global and +11% in the Arctic, with both biases greater than the 3% measurement uncertainty). This means that the detrimental health impacts of O_3 shown in Chapter 9 may be overestimated.
- Higher in the atmosphere, in the free troposphere, O_3 is an effective greenhouse gas, and at that altitude it is slightly underestimated by models (-10% to -20% compared to satellite measurements, which have ~15% uncertainty range). This means that the warming impact from O_3 shown in Chapter 8 may be slightly underestimated.
- The annual mean volumes of $PM_{2.5}$ – both globally and in the Arctic – are biased low in the historical simulations (-40% globally and -10% in the Arctic), which means that the health impacts due to $PM_{2.5}$ exposure presented in Chapter 9 may be underestimated.
- Annual mean AOD – which gives an indication of the aerosol load in the atmosphere – is biased low (-25% globally and -23.2% in Arctic) suggesting that the overall impacts of aerosols on climate and human health may be underestimated.
- The differences and uncertainties in both the satellite-based observations and model simulations of cloud properties are high over the Arctic – particularly over regions covered by multi-year sea ice, and during the polar winter months. This implies that the poor representation of the processes relevant to the interactions among aerosol-precursor gases, aerosols and clouds could be a major source of uncertainties in the climate impacts within this assessment.

There are seasonal differences in the model biases, which complicates the uncertainties associated with health and climate impacts. For example, the seasonal cycle of O_3 has health implications, since O_3 mainly exceeds health thresholds in the summer (during episodes of photochemical smog). Meanwhile, $PM_{2.5}$ exceeds health thresholds mainly in the winter (when it contributes to haze or local Arctic pollution from heating). At mid-latitudes, where human populations are much higher, the models simulate the seasonal cycles well. This means the health impacts determined in Chapter 8 for background pollution should be fairly accurate, although coarse-resolution global models are not ideal tools for simulating local pollution sources. High-resolution, regional models would be better used for that purpose. The differences in simulated seasonal cycles of O_3, BC, and SO_4 are particularly large in the Arctic. There are other regional differences in model biases as well. For example, surface-level O_3 has a much smaller positive bias in North America and Europe than in Asia, and modeled $PM_{2.5}$ is biased high in North America, but low in Asia. These, too, further complicate the interpretation of the health and climate impacts.

Given that the cloud uncertainties are so high in both observed data and the models, clouds are expected to be one of the largest sources of uncertainty when examining climate impacts. Specifically, from the AMAP perspective, it is important to note the following implications: the land regions, which are the main sources of pollutants, exhibit higher differences and uncertainties in cloud properties than the oceanic regions. This will translate into high uncertainties in the estimates of cloud forcings and feedbacks near the source regions (due, in turn, to higher uncertainties in aerosol-cloud-climate interactions). The models tend to overestimate cloudiness during polar winters, resulting in the overestimation of positive cloud radiative forcing at the surface. In summer, the models would estimate the cloud forcings and feedbacks better, as both cloudiness and CLWP are simulated relatively well. Although the CIWP is underestimated, its importance for the net surface energy budget is unclear because its vertical distribution was not evaluated. Future evaluations of cloud properties in the AMAP framework should strive to employ satellite simulators to better pinpoint the strengths and weaknesses of models and their climate implications. In addition, *in situ* measurements of cloud properties from measurement campaigns should be examined to further validate the satellite observations.

Similarities in bias patterns across different models, and the persistence of known model biases over many years of model development, emphasize the need for improvements in modellling, particularly regarding the models' tendency to underestimate SLCF concentrations in the Arctic mid-troposphere. Important seasonal biases are likely related to how wildfires and other natural sources of SLCFs are represented in the models, which limits the usefulness of

models for simulating the impacts of natural emissions on climate and air quality. Meanwhile, the coarse resolution of the models limits their capability to simulate local hotspot pollution that could be relevant for understanding air-quality and health impacts (especially if the local sources are missing in emissions inventories). However, although there is still room for improvement in the models' Arctic simulations, they nonetheless provide a more complete picture of the state of SLCFs in the atmosphere than measurements alone. The models thus remain useful tools for examining the effects of different emissions scenarios, as is carried out in the following two chapters.

Acknowledgments

The authors would like to thank all operators and technicians at the Arctic stations for the collection of observational data. Thanks are also due to the following people for providing us with data: Mauro Mazzola, Stefania Gilardoni, and Angelo Lupi from the Institute of Polar Sciences for eBC measurements at Gruvebadet lab; and Mirko Severi from University of Florence for SO_4 measurements at Gruvabadet. Zeppelin Station datasets were from Angelo Lupi. Fairbanks aerosol measurements came from William Simpson. For Villum data (Data ref. 7.4), we acknowledge the Aarhus University, Department of Environmental Science (ENVS). NOAA/ESRL/GMD, EMEP (http://ebas.nilu.no) and WMO GAW network are acknowledged for Utqiaġvik (Barrow) and Zeppelin observational datasets. Contributions by SMHI were funded by the Swedish Environmental Protection Agency under contract NV-03174-20 and Swedish Climate and Clean Air Research program (SCAC) and partly by Swedish National Space Board (NORD-SLCP, Grant agreement ID: 94/16) and EU Horizon 2020 project Integrated Arctic Observing System (INTAROS, Grant agreement ID: 727890. LATMOS acknowledges support from the EU iCUPE (Integrating and Comprehensive Understanding on Polar Environments) project (grant agreement n°689443), under the European Network for Observing our Changing Planet (ERA-Planet), and from access to IDRIS HPC resources (GENCI allocation A009017141) and the IPSL mesoscale computing centre (CICLAD: Calcul Intensif pour le CLimat, l'Atmosphère et la Dynamique) for model simulations. The Aerosol Optical Thickness CDR used in this study was acquired from NOAA's National Climatic Data Center (Data ref. 7.9). This CDR was originally developed by Xuepeng Zhao and colleagues for NOAA's CDR Program. Funding for ACE is provided by the Canadian Space Agency (CSA) and the Natural Sciences Research Council of Canada (NSERC). The ACE-FTS work was supported by NSERC. The ECHAM-HAMMOZ model is developed by a consortium composed of ETH Zurich, Max Planck Institute für Meteorologie, Forschungszentrum Jülich, University of Oxford, the Finnish Meteorological Institute and the Leibniz Institute for tropospheric research, and managed by the Center for Climate Systems Modeling (C2SM) at ETH Zurich.

Chapter 7 Appendix

A7.1 Detailed model description

A7.1.1 CanAM5-PAM

The Canadian Atmospheric Model version 5 (CanAM5), with Piecewise lognormal approximation Aerosol Model (PAM) was used. CanAM5-PAM is an improved version of CanAM4 (von Salzen et al., 2013). The improvements include a higher vertical resolution, improved parameterizations for land-surface and snow processes, DMS emissions, and clear-sky radiative transfer. CanAM5-PAM has 49 vertical levels extending up to 1 hPa with a resolution of approximately 100 m near the surface. Model simulations are performed using a spectral resolution of T63, which is equivalent to the horizontal resolution of approximately 2.8° × 2.8° latitude/longitude. The model uses separate parameterizations for layer and convective clouds. Aerosol microphysical processes are based on the piecewise lognormal approximation (von Salzen, 2006; Ma et al., 2008; Peng et al., 2012; Mahmood et al., 2016, 2019; AMAP, 2015a). The model simulates binary homogeneous nucleation of sulfuric acid and water vapor. Newly formed particles grow by condensation and coagulation.

A detailed description of parameterizations of ocean DMS flux to atmosphere, oxidation, and removal processes is provided in Tesdal et al. (2016). In-cloud production of sulfate requires O_3 and hydrogen peroxide (H_2O_2) as oxidants (von Salzen et al., 2000), with oxidant (OH, NO_3, H_2O_2, O_3) concentrations specified as climatological results from CMAM. Dry deposition of aerosol depends on concentrations of aerosols in the near-surface model layer (Zhang et al., 2001). Wet deposition includes in-cloud scavenging in both convective clouds and layer clouds, as well as below-cloud scavenging.

CDNC are calculated based on the assumption of a parcel of air that ascends from the subcloud layer into the cloud layer with a characteristic vertical velocity (Peng et al., 2005), where the standard deviation of the subgrid-scale cloud vertical velocity probability distribution is parameterized using the approach by Ghan et al. (1997). Aerosol particles that are suspended in the parcel of air may activate and grow into cloud droplets by the process of condensation of water vapor. A numerically efficient solution of the condensational droplet growth equation (e.g., Seinfeld and Pandis, 2006) is employed for this purpose. In grid cells that are affected by clouds, CanAM5-PAM accounts for cloud albedo and lifetime effects (first and second aerosol indirect effects) as well as semi-direct effects.

A7.1.2 CESM

The Community Earth System Model version 2 (CESM2.0) (Danabasoglu et al., 2020) is an ESM that can be configured in many different ways. The configuration applied for this assessment utilized the Community Atmosphere Model (CAM) version 6 and Modal Aerosol Model (MAM4) with four mixed-species aerosol modes (Liu et al., 2016a). CAM6 employs a spectral element dynamical core (Lauritzen et al., 2018). Type 0 and Type 1 CESM2.0 runs were conducted at 1.9° × 2.5° latitude/longitude horizontal resolution, while Type 3 runs at 0.9° × 1.25° latitude/longitude, all with 32 vertical layers. For Type 0 and Type 1 simulations, CESM2.0 was used with CAM6-chem representations of chemical reactions (Emmons et al., 2020), enabling prognostic simulation of tropospheric O_3 concentrations, along with a volatility basis set (VBS) parameterization for the formation of SOAs (Tilmes et al., 2019) and stratospheric chemistry. CAM6-chem is coupled to the interactive Community Land Model Version 5 (CLM5), which provides biogenic emissions, calculated online using the MEGANv2.1 algorithm (Guenther et al., 2012), and handles dry deposition. Tracked aerosol species simulated by MAM4 include sulfate, primary and aged BC and OM, dust (DU), sea salt (SS) and SOAs. Both SS and DU emissions are calculated online and are highly sensitive to the surface wind speed (Mahowald et al., 2006a, 2006b) These runs were also forced with prescribed sea surface temperatures (SSTs) and sea-ice concentrations (SIC), created from merged Reynolds/HADISST products as in Hurrell et al. (2008). Type 3 transient runs utilized CESM version 2.1.1 without atmospheric chemistry and with fully-coupled atmosphere, ocean, land, and sea-ice components (component set 'BSSP245cmip6'), as applied to simulate future scenarios for CMIP6. All CESM runs specified global-mean mixing ratios of CH_4 and CO_2.

A7.1.3 CIESM-MAM7

CIESM-MAM7 is the Community Integrated Earth System Model (CIESM) (Lin et al., 2020) using the Modal Aerosol Model (MAM7) with seven mixed-species aerosol modes (Liu et al., 2012b). Current CIESM version 1.1 (see Table 1 of Lin et al., 2020) is based on the Community Earth System Model (CESM version 1.2.1) with several novel developments and modifications aiming to overcome some persistent systematic biases, such as the double Intertropical Convergence Zone problem and underestimated marine boundary-layer clouds. CIESM-MAM7 employs a finite volume dynamical core with 0.9° × 1.25° for horizontal resolution and 31 layers for vertical resolution. The large-scale meteorology (horizontal wind field) is nudged towards reanalysis data from the ERA-Interim made by the European Centre for Medium-Range Weather Forecasts (ECMWF), and the relaxation time set to six hours.

In CIESM-MAM7, the primary emission of BC, OC, NH_3, VOCs, sulfur dioxide (SO_2) and oxidizing gases (H_2O_2, O_3 and OH) are prescribed by the input data uniformly provided by AMAP-SLCF group. The emission amounts of DU and SS are calculated online. Aerosol size distributions in CIESM-MAM7 are described by the seven overlapping log-normal distributions, including Aitken, accumulation, primary carbon, fine dust, fine sea salt, coarse dust, and coarse sea-salt modes. The geometric standard deviation of each mode is prescribed (see Table 1 of Liu et al., 2012b). A simplified gas- and liquid-phase chemistry is included in CIESM-MAM7. SO_2 and DMS can be oxidized to sulfuric acid gas (H_2SO_4), which then condenses to form the sulfate aerosols, with the evolution of oxidizing gases not

Table A7.1 Types of simulation conducted in support of the AMAP SLCF assessment and summary of features.

Name	Objective	Model set-up
Type 0	Atmospheric model intercomparison and validation	Key simulation time periods: 2008–2009 and 2014–2015, with additional simulations for 1990–2015, 2030, and 2050. Anthropogenic emissions were specified according to the IIASA GAINS ECLIPSE V6b dataset (Data ref 7.2) – future years: CLE and MFR scenarios). Natural emissions were provided by the modeling groups, with recommendation to use the Coupled Model Intercomparison Project Phase 6 (CMIP6) wildfire emission datasets, if possible. Sea surface temperatures (SSTs), sea ice and meteorological conditions were specified using reanalysis data.
Type 1	SLCF concentrations and direct radiative forcings from source-receptor modelling	Control simulations and set of atmospheric model simulations with emissions perturbations for different chemical species, emissions regions and sectors. Emissions and meteorological conditions were for 2015, with repeated annual cycles over the course of the multi-year-long simulations. Simulated source-receptor relationships for aerosols were used to subsequently assess the air-quality trends associated with different regional SLCF sources.
Type 2	Effective radiative forcings from source-receptor modeling	Control simulation and set of atmospheric model simulations with emission perturbations for different chemical species, emissions regions and sectors. Interactions of SLCFs with radiation and meteorology were included in the simulations. Emissions, SSTs, and sea ice were for 2015, with repeated annual cycles over the course of the multi-year-long simulations. Simulated source-receptor relationships for effective radiative forcings were used to subsequently assess the temperature impacts associated with different regional SLCF sources.
Type 3	Earth System Model projections for future climate and air quality	Fully coupled transient simulations with interactive ocean and sea-ice model components for 2015–2050, initialized from historical simulations, following the modeling protocol of the CMIP6. Anthropogenic emissions were specified according to the IIASA GAINS ECLIPSE V6b dataset (Data ref 7.2) – CLE and MFR scenarios)

Table A7.2 Emissions and meteorology details for the models

Model name	Biogenic emissions	Volcanic emissions
CanAM5-PAM	None	Specified climatological emissions and CMIP6 stratospheric aerosol
CESM2.0 (Type 0 and Type 1 runs)	Model of Emissions of Gases and Aerosols from Nature (MEGAN)v2.1	CMIP6
CESM2.1.1 (Type 3 runs)	CMIP6 (but only affecting SOA, not O_3)	CMIP6
CIESM-MAM7	None	CMIP6
CMAM	None	None
DEHM	MEGANv2	None
ECHAM-SALSA	Based on the Global Emissions Inventory Activity (GEIA) inventory (as particulate matter only)	3D emission fields based on AeroCom III (https://wiki.met.no/aerocom/phase3-experiments); includes emissions for Holuhraun
EMEP MSC-W	EMEP scheme (Simpson et al., 2012)	Degassing from Etna, Stromboli (as reported to EMEP), Eyjafjallajökull (2010) Grimsvotn (2011), Holuhraun (2014, 2015) For future years: 2010
FLEXPART	None	None
GEOS-Chem	MEGANv2.1 with update from Guenther et al. (2012)	NASA/GMAO
GEM-MACH	Biogenic Emission Inventory System (BEIS) v3.09	None
GISS-E2.1	Isoprene: Guenther et al. (2012); Terpenes: Organizing Carbon and Hydrology in Dynamic EcosystEm (ORCHIDEE); Online DMS, Sea-salt and dust	AeroCom
MATCH	MEGANv2	Climatological, plus separate runs with and without Holuhraun eruption
MATCH-SALSA	MEGANv2	Specified 2014–15 including Holuhraun eruption, plus climatological
MRI-ESM2	Biogenic VOCs emissions taken from Horowitz et al. (2003)	CMIP6 stratospheric aerosol dataset or specified 2014–2015 SO_2 emission with Holuhraun eruption
NorESM1-Happi	CMIP6	CMIP6
Oslo CTM	MEGAN – Monitoring Atmospheric Composition and Climate (MACC) constant at 2010 level	Emissions for continually degassing volcanoes from AeroCom (Dentener et al., 2006). Based on: Andres and Kasgnoc (1998). Volcano height based on publication of Halmer et al. (2002).
UKESM1	Isoprene and monoterpenes interactive with land surface vegetation scheme	Climatology of emissions for continually degassing volcanoes. For explosive volcanoes a zonal mean climatology of stratospheric aerosol optical properties over historical period was used from CMIP6 dataset.
WRF-Chem	MEGAN2.1	No

considered. Primary organic matter (POM) and BC are emitted to the primary carbon mode, then are aged and transferred to the accumulation mode by condensation of H_2SO_4, NH_3, and semi-volatile organics, and by coagulation with Aitken and accumulation modes. The effect of stratospheric sulfate aerosol from volcanic emissions on radiative forcing is considered by following the CMIP6 procedure (Thomason, 2012). No specific stratospheric chemistry is included in CIESM-MAM7.

A7.1.4 CMAM

The Canadian Middle Atmosphere Model (CMAM) is based on the third generation CanAM model, with the model lid raised to approximately 95 km and the necessary radiative processes for the mesosphere included (Scinocca et al., 2008). A representation of gas-phase chemistry has also been included that contains a relatively complete description of the hydrogen oxide radicals, (HO_X), nitrogen oxides (NO_X), chlorine (Cl_X) and bromine (Br_X) that control stratospheric O_3, along with the longer-lived source gases such as CH_4, nitrous oxide (N_2O) and chlorofluorocarbons (Jonsson et al., 2004). For the troposphere, the chemical mechanism can be considered as CH_4-NO_X chemistry as it does not include the chemistry of larger VOCs. The model does, however, include a description of associated tropospheric chemical processes such as wet and dry deposition, interactive NO_X emissions from lightning, corrections of clear-sky photolysis rates for clouds and dinitrogen pentoxide (N_2O_5) hydrolysis on prescribed sulfate aerosol distribution using the reaction probabilities of Davis et al. (2008).

The simulation analyzed here used a 'specified dynamics' set-up. This is where the model horizontal winds and temperature are nudged towards a meteorological reanalysis dataset representing the observed historical evolution of the atmosphere. This aligns the day-to-day variability of the model meteorology more closely with the historical evolution of the atmosphere than would be possible in a free-running model. For this study, the CMAM model was nudged to six-hourly fields from the ECMWF ERA-Interim reanalysis (Dee et al., 2011) on all model levels below 1 hPa and with a relaxation time constant of 24 hours.

Forest fire emissions	Agricultural waste burning	Meteorology
CMIP6	ECLIPSE V6b	Nudged to ERA-Interim reanalysis
CMIP6	ECLIPSE V6b	Fully interactive with prescribed sea surface temperature and sea ice concentration
CMIP6	ECLIPSE V6b	Fully interactive atmosphere, ocean, and sea ice
CMIP6	ECLIPSE V6b	Nudged to ERA-Interim reanalysis
CMIP6	ECLIPSE V6b	Nudged to ERA-Interim reanalysis
Global Fire Assimilation System (GFAS)	ECLIPSE V6b	Nudged to ERA-Interim reanalysis
CMIP6	ECLIPSE V6b	Nudged to ERA-Interim reanalysis
Fire INventory from NCAR (FINN) (based on Wiedinmyer et al., 2011)	ECLIPSE V6b	Driven by three-hourly data from the Integrated Forecast System (IFS) at ECMWF
CMIP6	ECLIPSE V6b	Driven by the three-hourly ECMWF meteorology
GFEDv4.1	ECLIPSE V6b	Driven by the GEOS meteorology from the NASA data assimilation office
CFFEPS (North America only)	ECLIPSE V6b outside North America, 2016 US National Emission Inventories for the USA, and 2015 Canadian national Air Pollution Emission Inventories for Canada	Driven by the Global Environmental Multiscale (GEM) Model numerical forecast, initialized every 24 hours using the Canadian Meteorological Centre's global objective analysis
CMIP6	ECLIPSE V6b	Nudged to National Center for Environmental Prediction (NCEP) reanalysis
CMIP6	ECLIPSE V6b	ERA-Interim reanalysis six-hourly
CMIP6	ECLIPSE V6b	Rossby Center Regional Climate model (RCA4)
CMIP6	ECLIPSE V6b	Nudged to the Japanese 55-year Reanalysis (JRA55)
CMIP6	ECLIPSE V6b	Fully interactive with prescribed SST and SIC
Global Fire Emissions Database (GFED)v4	ECLIPSE V6b	Driven by three-hourly data from the Integrated Forecast System (IFS) at ECMWF
Prescribed from CMIP6 dataset	CMIP6 emissions for Type 0 but ECLIPSE V6b for all other simulations	Nudged to ERA-Interim reanalysis
GFED	ECLIPSE v6b	Nudged to NCEP Final Analysis (FNL)

A7.1.5 DEHM

The Danish Eulerian Hemispheric Model (DEHM) (Christensen, 1997; Brandt et al., 2012; Massling et al., 2015) is a 3D Eulerian atmospheric chemistry-transport model developed at the Department of Environmental Science at Aarhus University in Denmark. The model domain covers the Northern Hemisphere using a polar stereographic projection with a grid resolution of 150 km × 150 km. It includes nesting capabilities to make simulations with a higher grid resolution in a limited area of the domain; in this work an Arctic sub-domain with 50 km × 50 km resolution has been applied covering the Arctic area down to about 40°N–54°N. The model has 29 vertical levels in sigma coordinates, where the lowest 15 levels are within 2000 m of the surface. The lowest model levels are 22 m thick, with the top of the model domain at 100 hPa (spanning the whole troposphere and the very lowest part of the stratosphere). DEHM includes a chemistry comprising sulfur oxides (SO_X), NO_X, VOC and O_3, with 71 components – including SOA calculated using VBS mechanisms, and nine particulates including hydrophobic and hydroscopic BC, primary organic aerosols (POA), primary anthropogenic dust, fine ($PM_{2.5}$) and coarse (PM_{10}) fraction of sea salt and lead (Pb). CH_4 is a prognostic species, on which the boundary conditions have a large influence. The model is driven by meteorological data from a numerical weather prediction model from the Weather Research and Forecasting model (NCAR, 2008), version 3.9, with one-hour resolution. The WRF model system is driven by reanalysis data from the ECMWF ERA-Interim by nudging.

A7.1.6 ECHAM-SALSA

ECHAM-SALSA is the general aerosol-climate model ECHAM-HAMMOZ (ECHAM6.3-HAM2.3-MOZ1.0) (Tegen et al., 2019; Schultz et al., 2018) using the Sectional Aerosol module for Large Scale Applications (SALSA) (Kokkola et al., 2018) to solve the aerosol microphysics. ECHAM6 (Stevens et al., 2013) computes the atmospheric circulation and fluxes using a semi-Lagrangian transport scheme. In the set-up used here, the large-scale meteorology (vorticity, divergence, and surface pressure, with 24-, six-, and 48-hour relaxation times, respectively) was nudged towards ECMWF ERA-Interim reanalysis data (Berrisford et al., 2011). In SALSA, the aerosol size distribution is modeled using ten size sections (or bins), which span particle sizes between 3 nm and 10 μm. The size distribution is further divided into a soluble and an insoluble sub-population, which are treated as externally mixed. Within one size bin of one sub-population, all aerosol particles are considered internally mixed. In its standard set-up, SALSA describes the aerosol compounds, BC, organic carbon (OC), SO_4, SS, and DU. In the model, BC, OC, SS, and DU are emitted as primary particles, while sulfate is emitted as either SO_2 or DMS, which are oxidized using a simplified chemistry (Stier et al., 2005) to form sulfuric acid (H_2SO_4), which then either nucleates or condenses onto existing particles. BC, OC, and SO_2 emissions are prescribed using input files, while SS and DU emissions are computed online. All greenhouse gas concentrations are fixed to pre-defined concentrations. The model resolution for the simulations performed here was T63, further using 47 hybrid sigma-pressure levels.

A7.1.7 EMEP MSC-W

The EMEP MSC-W model is a three-dimensional Eulerian chemistry transport model developed at the Norwegian Meteorological Institute within the Framework of the UN Convention on Long-range Transboundary Air Pollution. It is described in detail in Simpson et al. (2012). Although originally aimed at simulations of acidification, eutrophication and air quality over Europe, global modeling has been performed and evaluated against observations for many years (Jonson et al., 2010; Wild et al., 2012). The model uses 20 vertical levels defined as eta-hybrid coordinates. The ten lowest levels are within the planetary boundary layer (with the bottom layer being 92 m thick), and the top of the model domain is at 100 hPa. Model updates since Simpson et al. (2012), resulting in EMEP model version rv4.33 (as used here), have been described in Simpson et al. (2019) and references cited therein. The main revisions were made to the parameterizations of coarse nitrate (NO_3) formation SS and DU aerosols, N_2O_5 hydrolysis on aerosols, and additional gas-aerosol loss processes for O_3, nitric acid (HNO_3) and hydroperoxy radical (HO_2). The EMEP model, including a user guide, is publicly available as open-source code at https://github.com/metno/emep-ctm.

EMEP-modeled $PM_{2.5}$ and PM_{10} include primary and secondary aerosols, both anthropogenic and natural. Secondary aerosol consists of inorganic sulfate, nitrate and ammonium, and SOA; the latter is formed from both anthropogenic and biogenic emissions using the VBS scheme detailed in Bergström et al. (2012) and Simpson et al. (2012). The model also calculates sea-salt aerosols and windblown dust particles from soil erosion. AOD is calculated based on the mass concentrations of individual aerosols multiplied by corresponding mass extinction coefficients.

In these simulations, we did not use the BC and OC emissions from ECLIPSEV6b (Data ref. 7.2) directly, but applied ECLIPSEV6b $PM_{2.5}$ and coarse PM emissions instead, which were split into elementary carbon (EC), OM (here assumed inert) and the remaining DU. The EC and OM emissions in the fine and coarse fractions were further divided into fossil fuel and wood-burning compounds for each country and source sector. The split applied to the PM emissions is the same as used in EMEP operational runs (Klimont, personal communication, 2020). Eighty per cent of emitted EC is assumed to be hydrophobic, ageing to become hydrophilic within one to one-and-a-half days. As in Bergström et al. (2012), the OM/OC ratio of emissions by mass is assumed to be 1.3 for fossil-fuel sources and 1.7 for wood-burning sources. Note that different wildfire emissions were used here – from FINN (the Fire INventory from NCAR, version 15). The EMEP model runs were driven by three-hourly meteorological data from the ECMWF Integrated Forecast System (IFS) model at 0.5° × 0.5° latitude/longitude resolution.

A7.1.8 FLEXPART

The Lagrangian particle dispersion model FLEXPART version 10.4 (Pisso et al., 2019) releases computational particles that are simulated forward in time following three-hourly ECMWF meteorological fields with 137 vertical layers and a spatial resolution of 1° × 1° latitude/longitude. For each year,

around 330 million particles were released to calculate turbulent diffusion (Cassiani et al., 2014), unresolved mesoscale motions (Stohl et al., 2005) and convection (Forster et al., 2007). A recently updated wet-deposition scheme taking into account in-cloud and below-cloud removal was used (Grythe et al., 2017). Gravitational settling for spherical BC particles with an aerosol mean diameter of 0.25 μm, a normalized standard deviation of 3.3, and a particle density of 1500 kg/m^3 (Long et al., 2013) were used in the calculation of dry deposition. The surface concentration and deposition fields were retrieved on a monthly basis on a resolution of 0.5° × 0.5° latitude/longitude.

A7.1.9 GEM-MACH

GEM-MACH (Global Environmental Multiscale model-Modelling Air quality and CHemistry) is the air-quality prediction model of Environment and Climate Change Canada (ECCC). It consists of an online tropospheric chemistry module embedded within ECCC's GEM numerical weather forecast model (Côté et al., 1998a, 1998b; Charron et al., 2012). The chemistry module includes a comprehensive representation of air-quality processes, such as gas-phase, aqueous-phase, and heterogeneous chemistry and aerosol processes (e.g. Environment Canada, 2013; Makar et al., 2015a, 2015b; Gong et al., 2015). Specifically, gas-phase chemistry is represented by a modified Acid Deposition and Oxidant Model (ADOM)-II mechanism with 47 species and 114 reactions (Lurmann et al., 1986; EPRI, 1989); inorganic heterogeneous chemistry is parameterized by a modified version of the ISORROPIA algorithm of Nenes et al. (1999), as described in detail in Makar et al. (2003); SOA formation is parameterized using a two-product, overall or instantaneous aerosol yield formation (Odum et al., 1996; Jiang, 2003; Stroud et al., 2018); aerosol microphysical processes, including nucleation and condensation (sulfate and SOA), hygroscopic growth, coagulation and dry deposition/sedimentation are parameterized as in Gong et al. (2003); and the representation of cloud processing of gases and aerosols includes uptake and activation, aqueous phase chemistry, and wet removal, as outlined in Gong et al. (2006, 2015).

Aerosol chemical composition is represented by eight components: SO_4, NO_3, NH_4, EC, POA, SOA, crustal material (CM) and SS; aerosol particles are assumed to be internally mixed. A sectional approach was used for representing aerosol size distribution. For the 2015 Arctic simulation, a 12-bin configuration was used (between 0.01 and 40.96 μm in diameter, logarithmically spaced: 0.01–0.02, 0.02–0.04, 0.04–0.08, 0.08–0.16, 0.16–0.32, 0.32–0.64, 0.64–1.28, 1.28–2.56, 2.56–5.12, 5.12–10.24, 10.24–20.48 and 20.48–40.96 μm).

Type 0 simulation was conducted for the year of 2015 over a limited-area model (LAM) domain on a rotated latitude/longitude grid at 0.1375° × 0.1375° (or ~15 km) resolution covering the Arctic and extending to the southern USA–Canada border. Some of the model upgrades for the Arctic simulation are described in Gong et al. (2018). Anthropogenic emissions used are based on a combination of North American emission inventories (specifically, the 2016 US National Emission Inventories and 2015 Canadian national Air Pollution Emission Inventories) and global ECLIPSE v6b 2015 baseline emissions (Data ref. 7.2). North American wildfire emissions were processed using the Canadian Forest Fire Emission Prediction System (CFFEPS) from satellite-detected fire hotspot data (MODIS, AVHRR, and VIIRS). CFFEPS consists of a fire growth model, a fire emissions model, and a thermodynamic-based model to predict the vertical penetration height of a smoke plume from fire energy (see Chen et al., 2019 for details). Biogenic emissions were calculated online in GEM-MACH based on the algorithm from Biogenic Emission Inventory System (BEIS) version 3.09 with BELD3-format vegetation land cover. SS emissions were computed based on Gong et al. (2003). The chemical lateral boundary conditions were from MOZART-4/GEOS-5 (Emmons et al., 2010). The meteorology was initialized daily (at 00:00 UTC) using the Canadian Meteorological Centre's global objective analyses.

A7.1.10 GEOS-Chem

GEOS-Chem is a global 3D chemical transport model driven by assimilated meteorological observations from the Goddard Earth Observing System (GEOS) of the NASA Data Assimilation Office (DAO), which was first introduced in 2001 (Bey et al., 2001). GEOS-Chem is a grid-independent model which operates on a one-dimensional column with default or user-specified horizontal grid points, vertical grid points, and time-step. GEOS-Chem Classic can use archived GEOS meteorological data on a rectilinear latitude/longitude grid to compute horizontal and vertical transport and uses Open-Multi-Processing (MP) in parallelization. Two of the assimilated meteorological data from the NASA Global Modeling and Assimilation Office (GMAO) can be used to drive the off-line mode of GEOS-Chem. The first one is the operational data starting from 2012, the GEOS Forward Processing (GEOS-FP – NASA, 2013) for which the native resolution was 0.25° × 0.3125° latitude/longitude. The second one is the consistent MERRA-2 (Randles et al., 2017) starting from 1979–present, with the native resolution 0.5° × 0.625° latitude/longitude. Both meteorological datasets have 72 hybrid sigma-pressure levels with the top at 0.01 hPa and three-hourly temporal resolution for three-dimensional fields and one-hour resolution for two-dimensional fields. The advection scheme of GEOS-Chem uses the TPCORE advection scheme (Lin and Rood, 1996) on the latitude/longitude grid, while the convective transport scheme uses the convective mass flux described by Wu et al. (2007). The wet deposition scheme in GEOS-Chem is based on Liu et al. (2001) for water-soluble aerosols and Amos et al. (2012) for gases. The dry deposition is based on the resistance-in-series scheme of Wesely (1989). Aerosol deposition is from Zhang et al. (2001). Emission of dust aerosol, lightning NO_X, biogenic VOCs, soil NO_X, and SS aerosol are dependent on the local meteorological conditions. The Community Emissions Data System (CEDS) global inventory is the default input for anthropogenic emissions, while EDGAR v4.3.2 (Crippa et al., 2018) is also available as an alternate option to CEDS. Future anthropogenic emissions following the Representative Concentration Pathway (RCP) scenarios (Holmes et al., 2013), aircraft emissions (Stettler et al., 2011), ship emissions (from CEDS), and lighting NO_X emissions (Murray et al., 2012) are also included and configured at run-time using the Harvard–NASA Emission Component (HEMCO) module (Keller et al.,

2014). Biogenic VOC emissions in GEOS-Chem are from the MEGAN v2.1 inventory (Guenther et al., 2012). Chemical solver in the standard GEOS-Chem simulation uses KPP (Damian et al., 2002) as implemented in GEOS-Chem. The gas phase in the troposphere in GEOS-Chem included the detailed HO_X-NO_X-VOC-ozone-halogen-aerosol tropospheric chemistry mechanism, which generally follows JPL/IUPAC recommendations including the peroxyacyl nitrates (PAN) (Fischer et al., 2014), isoprene (Travis et al., 2016; Fisher et al., 2016), Halogens (Sherwen et al., 2016; Chen et al., 2017), and Criegees (Millet et al., 2015). A linearized stratospheric chemistry scheme has been implemented since GEOS-Chem v9.0. The model reads from an archived three-dimensional monthly mean production rates and losing frequency for each species at the beginning of each month. The Linoz stratospheric ozone chemistry package (McLinden et al., 2000) is also applied; it is a recommended option for the stratospheric ozone layer. The original sulfate-nitrate-ammonium aerosol simulation in GEOS-Chem coupled to gas-phase chemistry (Park et al., 2004). The BC simulation (Wang et al., 2014), OA (Pai et al., 2020), complex SOA (Pye et al., 2010), aqueous-phase isoprene SOA scheme (Marais et al., 2016) and the DU simulation (Fairlie et al., 2007) are also implemented in GEOS-Chem. The DU size distributions are from Zhang et al., 2013. GEOS-Chem v12.3.2, with uniform 2° × 2.5° latitude/longitude GEOS-Forward Processing (FP) meteorological data and Eclipse V6b emissions, was used in this study.

A7.1.11 GISS-E2.1

NASA Goddard Institute of Space Studies (GISS) Earth system model (ESM), GISS-E2.1, is a fully-coupled ESM. A full description of GISS-E2.1 and evaluation of its coupled climatology during the satellite era (1979–2014) and the historical ensemble simulation of the atmosphere and ocean component models (1850–2014) are described in Kelley et al. (2020). GISS-E2.1 has a horizontal resolution of 2° × 2.5° latitude/longitude, and 40 vertical layers extending from the surface to 0.1 hPa in the lower mesosphere. The tropospheric chemistry scheme used in GISS-E2.1 (Shindell et al., 2001, 2003) includes inorganic chemistry of odd-oxygen (O_X), NO_X, HO_X, CO, and organic chemistry of CH_4 and higher hydrocarbons using the carbon-bond mechanism CBM4 scheme (Gery et al., 1989), and the stratospheric chemistry scheme (Shindell et al., 2006), which includes chlorine and bromine chemistry, together with polar stratospheric clouds. The meteorology was nudged to the National Center for Environmental Prediction (NCEP) reanalysis.

In this study, we used the one-moment aerosol (OMA) scheme (Bauer et al., 2007a; Bauer et al., 2007b; Bauer and Koch, 2005; Koch et al., 2006; Miller et al., 2006; Tsigaridis et al., 2013; Bauer et al., 2020). OMA is a mass-based scheme in which aerosols are assumed to remain externally mixed and have a prescribed and constant size distribution. Exceptions are sea salt, which has two distinct size classes, and DU, which is described by a sectional model with the option for four-to-six bins. The OMA scheme treats sulfate, nitrate, ammonium, carbonaceous aerosols (BC and OC, including the NO_X-dependent formation of SOA and methanesulfonic acid formation), DU and SS. The model includes SOA production, as described by Tsigaridis and Kanakidou (2007). The default DU configuration used in this work includes five bins – one clay and four silt – from submicrometer to 16 μm in size. The first three dust-size bins can be coated by sulfate and nitrate aerosols (Bauer and Koch, 2005). OMA only includes the first aerosol indirect effect. The aerosol number concentration that impacts clouds is obtained from the aerosol mass as described in Menon and Rotstayn (2006).

The natural emissions of SS, DMS, isoprene and DU are calculated interactively. Anthropogenic dust sources are not represented in GISS-E2.1. DU emissions vary spatially and temporally only with the evolution of climate variables, such as wind speed and soil moisture (Miller et al., 2006). The version of the model employed in this work uses prescribed sea-surface temperature (SST) and sea-ice thickness and extent during the historical period (Rayner et al., 2003).

A7.1.12 MATCH

Multiscale Atmospheric Transport and Chemistry (MATCH) (Robertson et al., 1999) is an offline, Eulerian, three-dimensional chemistry transport model developed at the Swedish Meteorological and Hydrological Institute. MATCH can be run on global to urban domains to study a range of atmospheric chemistry/air quality problems; for this study, model runs were performed for the ~20°N–90°N region – focusing on long-range transport to the Arctic.

ECMWF ERA-Interim reanalysis data were used as the meteorological input to the model. Six-hourly data (three-hourly for precipitation) were extracted from the ECMWF archives on a 0.75° × 0.75° rotated latitude-longitude grid. The original data had 60 levels, but the 38 lowest levels – reaching about 16 km in the Arctic – were used in the model.

The scheme for gas-phase tropospheric chemistry and bulk aerosols as described in Andersson et al. (2007) was used. CH_4 concentrations were prescribed. Boundary conditions at the top of the model and at the lateral boundaries for a range of species including O_3 were based on monthly mean values from the Copernicus Atmospheric Monitoring Service. The aerosol scheme was extended with BC and OC simulated as two fractions: fresh, hydrophobic and aged, and hydrophilic. Eighty percent of anthropogenic emissions from all sectors were emitted into the hydrophobic and 20% into the hydrophilic fraction except for fire/biomass combustion, where 100% was emitted into the hydrophilic component following Genberg et al. (2013). Scavenging and aging were parameterized following Liu et al. (2011), – with aging proportional to OH and scavenging in mixed-phase clouds reduced. The hydrophobic fraction was assumed to be 5% activated in the scavenging scheme, while the hydrophilic fraction was 100% activated. If the clouds were mixed phase, then the scavenging efficiency was scaled by the ratio of cloud ice water content to total cloud water content, assuming zero scavenging for 100% ice clouds.

A7.1.13 MATCH-SALSA

The chemistry transport model, MATCH (Robertson et al., 1999; Andersson et al., 2007) described above is online coupled to the aerosol dynamics model, SALSA (Kokkola et al., 2008). SALSA describes the whole chain from nucleation to growth and deposition of particles, and computes the size distribution,

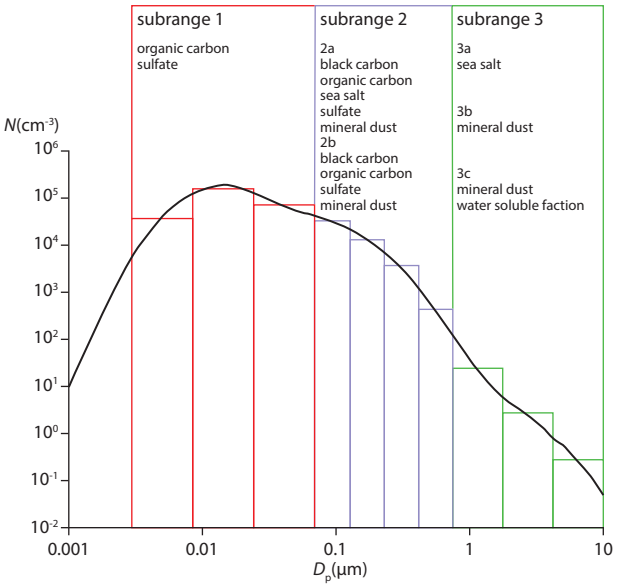

Figure A7.1 Schematic of sectional distribution of aerosol

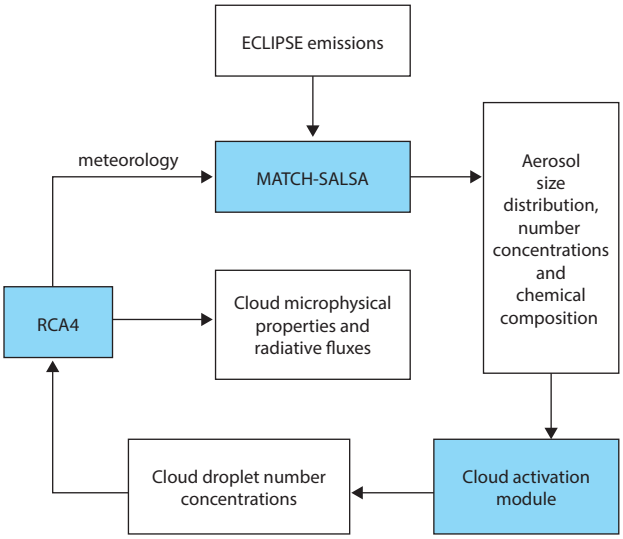

Figure A7.2 Schematic representation of the different components of the model (shown in blue) and the process links between them, as laid out in the flow chart (adapted from Kokkola et al., 2008).

number concentration and chemical composition of the aerosol species. A sectional representation of the aerosol size distribution is considered, with three main size ranges (a: 3–50 nm; b: 50–700 nm; c: >700 nm). Each range is again subdivided into smaller bins, and into soluble and insoluble bins, adding up to a total of 20 bins. A schematic of the sectional size distribution and the aerosol species considered in each bin is shown in Figure A7.1. The seasonally varying emissions are based on the sector-wise ECLIPSE inventory. Isoprene emissions are modeled online depending on the meteorology based on the methodology by Simpson et al. (1995). The terpene emissions (α-pinene) are taken from the modeled fields by the EMEP model. SS is parameterized following the scheme of Foltescu et al. (2005) but modified for varying particle sizes; the Mårtensson et al. (2003) scheme is used if the particle diameter is ≤1 μm, with the Monahan et al. (1986) scheme used otherwise. The coupling of MATCH with SALSA and the evaluation of this model set-up is described in detail in Andersson et al. (2015). A cloud activation model that computes three-dimensional CDNC based on the prognostic parameterization scheme of Abdul-Razzak and Ghan (2002) – specifically designed for aerosol representation with sectional bins – is embedded in the MATCH–SALSA model. This scheme simulates the efficiency of aerosol particles being converted to cloud droplets based on the number, concentration and chemical composition of the particles given the updraft velocity and supersaturation of the air parcel. The updraft velocity is computed as the sum of the grid mean vertical velocity and turbulent kinetic energy for stratiform clouds (Lohmann et al., 1999). These CDNCs are then offline coupled to a regional climate model, RCA4 (Samuelsson et al., 2011), which provides information on cloud properties such as cloud cover, cloud droplet radii and CLWP, as well as radiative fluxes. A schematic of the model coupling is shown in Figure A7.2. RCA4 is run with six-hourly ECMWF ERA-Interim meteorology and the three-hourly RCA4 meteorological fields, while fields needed to calculate updraft velocity are used to drive the MATCH-SALSA cloud activation model. The CDNCs are then used to re-run the RCA4 model to obtain the cloud properties and radiative effects. Additional details of the model set-up and validation are described in Thomas et al. (2015).

A7.1.14 MRI-ESM2

The Meteorological Research Institute (MRI) Earth System Model version 2.0 (MRI-ESM2), developed by the MRI of the Japan Meteorological Agency comprises four major component models; an atmospheric general circulation model (MRI-AGCM3.5) with land processes, an ocean-sea-ice general circulation model (OGCM; MRI.COMv4), and aerosol and atmospheric chemistry models (Yukimoto et al., 2019; Kawai et al., 2019; Oshima et al., 2020). However, in this study, land and OGCM were not coupled in the Type 0, Type 1, and Type 2 simulations. MRI-ESM2 uses different horizontal resolutions but employs the same vertical resolution in each atmospheric component model as follows: TL159 (approximately 120 km), TL95 (approximately 180 km), and T42 (approximately 280 km) in the MRI-AGCM3.5, the aerosol model, and the atmospheric chemistry model, respectively, all with 80 vertical layers (from the surface to a model top of 0.01 hPa) in a hybrid sigma-pressure coordinate system. Each component model is interactively coupled by a coupler, which enables an explicit representation of the effects of gases and aerosols on the climate system.

The atmospheric chemistry component model in MRI-ESM2 is the MRI Chemistry Climate Model version 2.1 (MRI-CCM2.1), which calculates the evolution and distribution of O_3 and other trace gases in the troposphere and in the middle atmosphere. The model calculates a total of 90 gas-phase chemical species and 259 chemical reactions in the atmosphere. The aerosol component model in MRI-ESM2 is the Model of Aerosol Species in the Global Atmosphere mark-2 revision 4-climate (MASINGAR mk-2r4c), which calculates atmospheric aerosol physical and chemical processes for the following species; non-sea-salt sulfate, BC, OC, SS, DU and aerosol precursor gases (SO_2 and DMS). The size distributions of SS and DU are divided into ten discrete bins, with the sizes of the other aerosols represented by lognormal size distributions.

The model assumes external mixing for all aerosol species. However, in the radiation process in MRI-AGCM3.5, hydrophilic BC is assumed to be internally mixed with sulfate

with a shell-to-core volume ratio of two (the optical properties of hydrophilic BC are calculated based on Mie theory with a core-shell aerosol treatment, in which a concentric BC core is surrounded by a uniform coating shell composed of other aerosol compounds [Oshima et al. 2009a; 2009b]). MRI-ESM2 employs BC-aging parameterization (Oshima and Koike, 2013) that calculates the variable conversion rate of BC from hydrophobic BC to hydrophilic BC (generally, this depends on the production rate of condensable materials, such as sulfate). In the radiation and cloud processes in MRI-ESM2, sulfate is assumed to be ammonium sulfate $(NH_4)_2SO_4$ and OC is assumed to be OM by lumping OC species using an OM-to-OC factor of 1.4. MRI-ESM2 represents the activation of aerosols into cloud droplets based on the parameterizations; detailed descriptions and evaluations of the cloud processes and cloud representations in MRI-ESM2 are given by Kawai et al. (2019). Evaluations of MRI-ESM2's effective radiative forcing (ERF) of anthropogenic gases and aerosols in present-day conditions relative to preindustrial conditions, both globally and in the Arctic, are given by Oshima et al. (2020).

The Type 0 simulations were performed from January 2008 (or January 1990) to December 2015 after a one-year spin-up run using the prescribed SST and sea-ice data (provided by the Atmospheric Model Intercomparison Project (AMIP) experiment in CMIP6. The horizontal wind fields were nudged toward the six-hourly Japanese 55-year Reanalysis (JRA-55 project) data (Kobayashi et al., 2015) in the simulation. Monthly anthropogenic emissions from the ECLIPSE v6b emissions dataset (Data ref. 7.2) and monthly biomass burning emissions from CMIP6 were used in the simulations. Major volcanic aerosols were provided by the stratospheric aerosol dataset used in the CMIP6 experiments (Thomason et al., 2018). Another Type 0 simulation with volcanic SO_2 emissions, including the volcanic eruption of Iceland's Holuhraun lava field, was also performed for 2014–2015.

The Type 1 simulations (see Table A7.1) were performed for four years after a one-year spin-up run using the prescribed SST and sea-ice data provided by AMIP. The horizontal wind fields were nudged toward the six-hourly JRA55 reanalysis in the simulations. The annually-repeating 2015 emissions with individually 100% perturbed (complete removal) emissions of BC and SO_2 were used for individual region and sector combinations.

The Type 2 simulations (see Table A7.1) were performed for 50 or 60 years after a one-year spin-up run using the prescribed SST and sea-ice data provided by AMIP. The annually-repeating 2015 conditions with individually 100% perturbed (complete removal) emissions of BC and SO_2 were used for individual region and sector combinations.

The Type 3 simulations (see Table A7.1) by the fully coupled ESM were performed in 2015–2050 using three time-evolving emissions (CLE, MFR, and SLCF scenarios). Five ensemble simulations were performed for each emissions scenario. These simulations branched off from the end of the CMIP6 historical simulations (1850–2014) by MRI-ESM2.

A7.1.15 NorESM1

NorESM1 (Bentsen et al., 2013; Iversen et al., 2013) is based on the fourth version of the Community Climate System Model (CCSM4) (Gent et al., 2011), with coupled models for the atmosphere, ocean, land and sea ice. In this study, a 1° horizontal resolution in the atmosphere was used (0.95° × 1.25° latitude/longitude, version 'NorESM1-Happi'). The model has 26 vertical levels on a hybrid sigma-pressure coordinate up to the model top at 2.194 hPa. The model calculates the lifecycles of a range of natural and anthropogenic aerosol components from emissions and physico-chemical processing in air and cloud droplets. The only prescribed aerosol concentrations are stratospheric sulfate from explosive volcanoes. The direct and indirect aerosol effects on climate are calculated by parameterization of aerosol interactions with schemes for radiation and warm cloud microphysics (Kirkevåg et al., 2013). The model uses a prognostic calculation of cloud droplet numbers, allowing for competition effects between aerosols with different hygroscopic properties and sizes.

A7.1.16 Oslo CTM

The Oslo CTM3 is an offline global 3D chemistry transport model driven by three-hourly meteorological forecast data from the IFS model at ECMWF. The Oslo CTM3 consists of a tropospheric and stratospheric chemistry scheme (Søvde et al., 2012), as well as aerosol modules for sulfate, nitrate, BC, primary OC, SOA, DU and SS (Lund et al. 2018).

A7.1.17 UKESM1

The United Kingdom Earth System Model (UKESM1) is a fully-coupled earth system model (Sellar et al., 2019) with the coupled atmosphere-ocean physical climate model HadGEM3-GC3.1 at its core (Kuhlbrodt et al., 2018; Williams et al., 2018). Various Earth system components are incorporated in UKESM1, with the physical climate model including ocean biogeochemistry, an interactive stratosphere-troposphere chemistry and aerosol scheme, and terrestrial carbon and nitrogen cycles coupled to interactive vegetation. The model has a horizontal resolution of ~135 km at the mid-latitudes (1.875° × 1.25° latitude/longitude), with 85 levels on a terrain-following hybrid height coordinate system, extending from the surface to the model top of 85 km. The combined stratosphere-troposphere United Kingdom Chemistry and Aerosol (UKCA) scheme is used within UKESM1, being fully described and evaluated in Archibald et al. (2020) and Mulcahy et al. (2020).

The chemical scheme in UKCA is built upon that described for the stratosphere in Morgenstern et al. (2009) and another for the troposphere outlined in O'Connor et al. (2014). Chemical reactions are included within UKCA for odd-oxygen ($O_X = O+O_3$), nitrogen (NOy=total nitrogen [NH_X + the sum of all oxidized nitrogen species, except N_2O]), hydrogen (HO_X=OH + HO_2), CO, CH_4 and short-chain non-methane volatile organic compounds (NMVOCs), including isoprene. Reactions involving NMVOCs are simulated as discrete species. UKCA includes an interactive photolysis scheme, as well as representations of both wet and dry deposition for gas and

aerosol species. Additional chemical reactions for DMS, SO_2 and monoterpenes ($C_{10}H_{16}$) are included to enable coupling to the aerosol scheme within UKCA. A two-moment aerosol microphysical scheme, GLOMAP (Global Model of Aerosol Processes; Mann et al., 2010, 2012), is used to simulate four aerosol components (sulfate, BC, OM, and SS) across five log-normal modes, ranging from submicrometer to supermicrometer sizes. DD is simulated separately using a six-bin mass-only scheme, ranging from 0.6 to 60 micrometers in diameter (Woodward, 2001). Ammonium nitrate is not currently included within the UKCA aerosol scheme. The formation of SOA is included based on a fixed yield rate of 26% from the products of monoterpene oxidation. The higher fixed yield value accounts for the underlying uncertainty in SOA formation and the absence of anthropogenic, marine and isoprene sources.

Precursor emissions fluxes are either prescribed using specified input files or calculated interactively using online meteorological variables within UKESM1. CH_4 is represented by using prescribed global concentrations. Interactive emissions fluxes are calculated online for SS, DMS, DU, lightning NO_X and biogenic volatile organic compounds (BVOCs). Emissions of isoprene and monoterpenes from the natural environment are calculated online by coupling to the land-surface scheme within UKESM1.

Simulations provided by UKESM1 were undertaken for this study using different configurations. For Type 0 and Type 1 experiments, UKESM1 was set up using an atmosphere-only configuration nudged to ECMWF ERA-Interim reanalysis data of temperature and wind fields above the boundary layer. Prescribed values of SSTs and sea ice were used for each year of simulation based on historical simulations conducted as part of CMIP6 using the fully coupled atmosphere-ocean configuration of UKESM1. For other ancillary inputs, a multi-year climatology was used (equivalent to an AMIP-type simulation). Transient emissions were used as the input for Type 0 experiments, while annually repeating 2015 emissions were used for four different years in Type 1 experiments to account for the influence of meteorological variability. The fully coupled ESM configuration of UKESM1 was used for Type 3 experiments, with free-running meteorology, enabling feedbacks of changes in SLCFs on the climate system.

A7.1.18 WRF-Chem

The Weather Research and Forecasting model with online coupled chemistry (WRF-Chem) is used to simulate the transport and chemical transformation of trace gases and aerosols simultaneously with the meteorology. The model dynamics (WRF) are non-hydrostatic. The model version used in this study was WRF-Chem version 3.8.1, including updates reported in Marelle et al. (2017) and Marelle et al. (2018). The simulation was performed on a polar stereographic projection with a horizontal resolution of 100 km, and 50 vertical hybrid terrain-following levels based on hydrostatic pressure. The center of the domain was placed at the North Pole, with the latitude of the domain's outside boundary varying from 7°S–7°N. Pressure at the model top was set to 50 hPa with stratospheric concentrations (e.g. O_3) taken from climatologies. The model was run with Morrison double-moment scheme microphysics, with long- and short-wave radiative effects treated by the Rapid Radiative Transfer Model for General Circulation Models, and the Kain-Fritsch-Cumulus Potential (KF-CuP) parameterization scheme. The SAPRC-99 chemical scheme provided gas-phase tropospheric reactions including VOCs and NO_X, while the MOSAIC eight-bin sectional scheme included VBS treatments for SOA. CH_4 concentrations were prescribed. Stratospheric and tropospheric halogen chemistries were not included. Anthropogenic emissions were from ECLIPSE v6b (Data ref. 7.2) and the GFED fire emissions. Boundary and initial meteorological conditions were given by the global NCEP Final Analysis (FNL), and used to nudge the temperature, relative humidity, and winds at every dynamical time-step above the planetary boundary layer.

A7.2 Model validation of O_3 and O_3-precursors

A7.2.1 Data sources for surface O_3 plots

Table A7.3 Data sources for surface O_3 plots (Figures 7.1 and 7.7)

Measurement Network	Region
Chemical Speciation Network – https://airquality.ucdavis.edu/csn#:~:text=CSN%20(Chemical%20Speciation%20Network)%20is,implementation%20of%20the%201997%20PM2.	USA
National Air Pollution Surveillance Network + Speciation network – https://open.canada.ca/data/en/dataset/1b36a356-defd-4813-acea-47bc3abd859b	Canada
Earth System Research Laboratory (formerly the Climate Monitoring and Diagnostics Laboratory (surface observations) of NOAA) – https://www.esrl.noaa.gov/	Global
European data from EBAS – https://ebas.nilu.no/	Europe
China air quality from Beijing Air – https://beijingair.sinaapp.com/	China
Hong Kong Environmental Protection Department (EPD) – https://www.epd.gov.hk/epd/english/top.html	Hong Kong
World Data Centre for Greenhouse Gases (WDCGG) – https://gaw.kishou.go.jp/	Global

A7.2.2 O_3 trends from models

Table A7.4a Increase in O_3 (%/y) for 1990–2015 for CMAM. NS=not significant (level of significance > 0.1). Trends are calculated as the yearly or seasonal changes compared to the average of the yearly or seasonal concentrations over all of the years.

Site	Annual	Level of significance	DJF	Level of significance	MAM	Level of significance	JJA	Level of significance	SON	Level of significance
Alert	0.17	0.05	0.59	0.001	0.40	0.05	NS		NS	
Utqiaġvik	0.22	0.01	0.63	0.001	0.24	0.10	-0.43	0.001	0.25	0.05
Summit	0.15	0.10	0.52	0.01	NS		NS		NS	
Villum	0.13	0.05	0.78	0.001	0.24	0.10	-0.57	0.010	NS	
Zeppelin	0.13	0.10	0.97	0.001	0.27	0.10	-0.83	0.001	NS	

DJF=December, January, February; MAM=March, April, May; JJA=June, July, August; SON=September, October, November

Table A7.4b Increase in O_3 (%/y) for 1990–2015 for DEHM. NS=not significant (level of significance > 0.1). Trends are calculated as the yearly or seasonal changes compared to the average of the yearly or seasonal concentrations over all of the years.

Site	Annual	Level of significance	DJF	Level of significance	MAM	Level of significance	JJA	Level of significance	SON	Level of significance
Alert	0.10	0.10	0.54	0.001	NS		NS		NS	
Utqiaġvik	NS		0.48	0.001	NS		-0.26	0.050	NS	
Summit	NS		NS		NS		NS		NS	
Villum	0.11	0.050	0.56	0.001	0.14	0.05	NS		NS	
Zeppelin	NS		0.54	0.001	NS		-0.31	0.01	NS	

DJF=December, January, February; MAM=March, April, May; JJA=June, July, August; SON=September, October, November

Table A7.4c Increase in O_3 (%/y) for 1990–2015 for EMEP MSC-W. NS=not significant (level of significance > 0.1). Trends are calculated as the yearly or seasonal changes compared to the average of the yearly or seasonal concentrations over all of the years.

Site	Annual	Level of significance	DJF	Level of significance	MAM	Level of significance	JJA	Level of significance	SON	Level of significance
Alert	NS		0.62	0.001	NS		-0.42	0.001	NS	
Utqiaġvik	NS		0.32	0.050	NS		-0.36	0.001	NS	
Summit	NS		NS		NS		NS		-0.31	0.01
Villum	NS		0.52	0.010	NS		-0.48	0.001	-0.27	0.05
Zeppelin	-0.18	0.010	0.24	0.050	NS		-0.51	0.001	-0.24	0.01

DJF=December, January, February; MAM=March, April, May; JJA=June, July, August; SON=September, October, November

Table A7.4d Increase in O_3 (%/y) for 1990–2015 for GISS-E2.1. NS=not significant (level of significance > 0.1). Trends are calculated as the yearly or seasonal changes compared to the average of the yearly or seasonal concentrations over all of the years.

Site	Annual	Level of significance	DJF	Level of significance	MAM	Level of significance	JJA	Level of significance	SON	Level of significance
Alert	-0.19	0.100	NS		NS		-0.41	0.050	-0.63	0.05
Utqiaġvik	-0.23	0.050	NS		NS		-0.91	0.001	-0.62	0.01
Summit	-0.16	0.100	NS		NS		NS		-0.63	0.01
Villum	-0.34	0.010	NS		NS		-0.98	0.050	-0.69	0.01
Zeppelin	-0.34	0.001	-0.41	0.050	NS		-0.70	0.050	-0.46	0.01

DJF=December, January, February; MAM=March, April, May; JJA=June, July, August; SON=September, October, November

Table A7.4e Increase in O_3 (%/y) for 1990–2015 for MRI-ESM2. NS=not significant (level of significance > 0.1). Trends are calculated as the yearly or seasonal changes compared to the average of the yearly or seasonal concentrations over all of the years.

Site	Annual	Level of significance	DJF	Level of significance	MAM	Level of significance	JJA	Level of significance	SON	Level of significance
Alert	NS		NS		NS		-0.25	0.010	NS	
Utqiaġvik	-0.11	0.05	NS		-0.15	0.05	-0.42	0.010	NS	
Summit	NS		NS		NS		NS		-0.24	0.05
Villum	-0.14	0.05	NS		NS		-0.18	0.050	-0.22	0.01
Zeppelin	-0.16	0.01	NS		-0.19	0.05	-0.34	0.010	-0.20	0.05

DJF=December, January, February; MAM=March, April, May; JJA=June, July, August; SON=September, October, November

Table A7.4f Increase in O_3 (%/y) for 1990–2015 for UKESM1. NS=not significant (level of significance > 0.1). Trends are calculated as the yearly or seasonal changes compared to the average of the yearly or seasonal concentrations over all of the years.

Site	Annual	Level of significance	DJF	Level of significance	MAM	Level of significance	JJA	Level of significance	SON	Level of significance
Alert	0.45	0.05	1.30	0.00	NS		NS		0.69	0.010
Utqiaġvik	0.35	0.00	1.23	0.00	NS		NS		0.49	0.050
Summit	0.14	0.10	0.46	0.05	NS		NS			
Villum	0.32	0.01	1.03	0.00	0.51	0.05	-0.27	0.100		
Zeppelin	NS		0.71	0.01	NS		-0.27	0.050		

DJF=December, January, February; MAM=March, April, May; JJA=June, July, August; SON=September, October, November

A7.2.3 Evaluation of O_3-precursors: CO and NO_x

Surface CO and NO_2 in North America, Europe, and China are shown in Figures A7.3 and A7.4, respectively, along with the model biases (model minus measurement in ppbv).

Figure A7.5 shows the MOPITT-measured CO at two different altitudes: (a) 900 hPa for lower-troposphere; and (b) 600 hPa for mid-troposphere.

Figures A7.6 and A7.7 show the CO and NO_X (= NO + NO_2), respectively, in the Arctic UTLS region from ACE-FTS and the

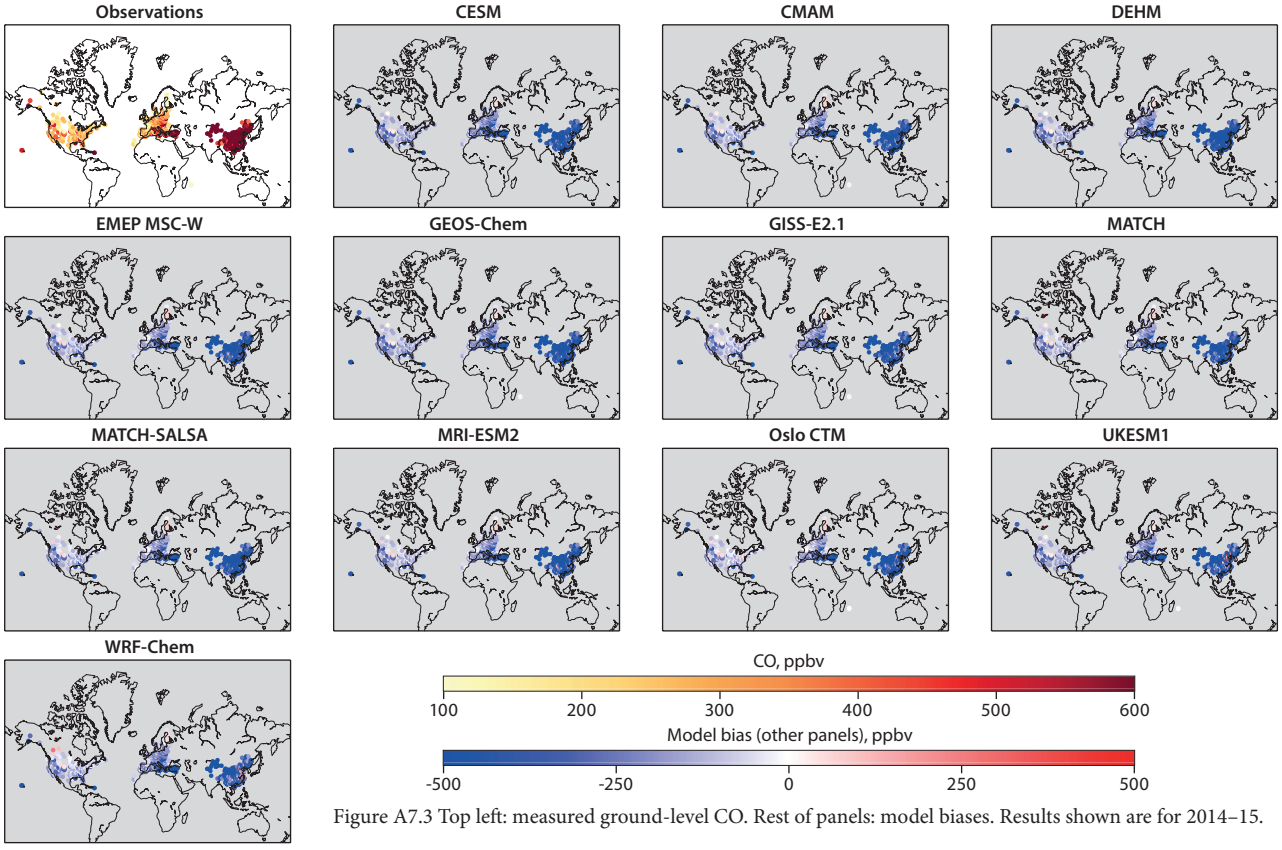

Figure A7.3 Top left: measured ground-level CO. Rest of panels: model biases. Results shown are for 2014–15.

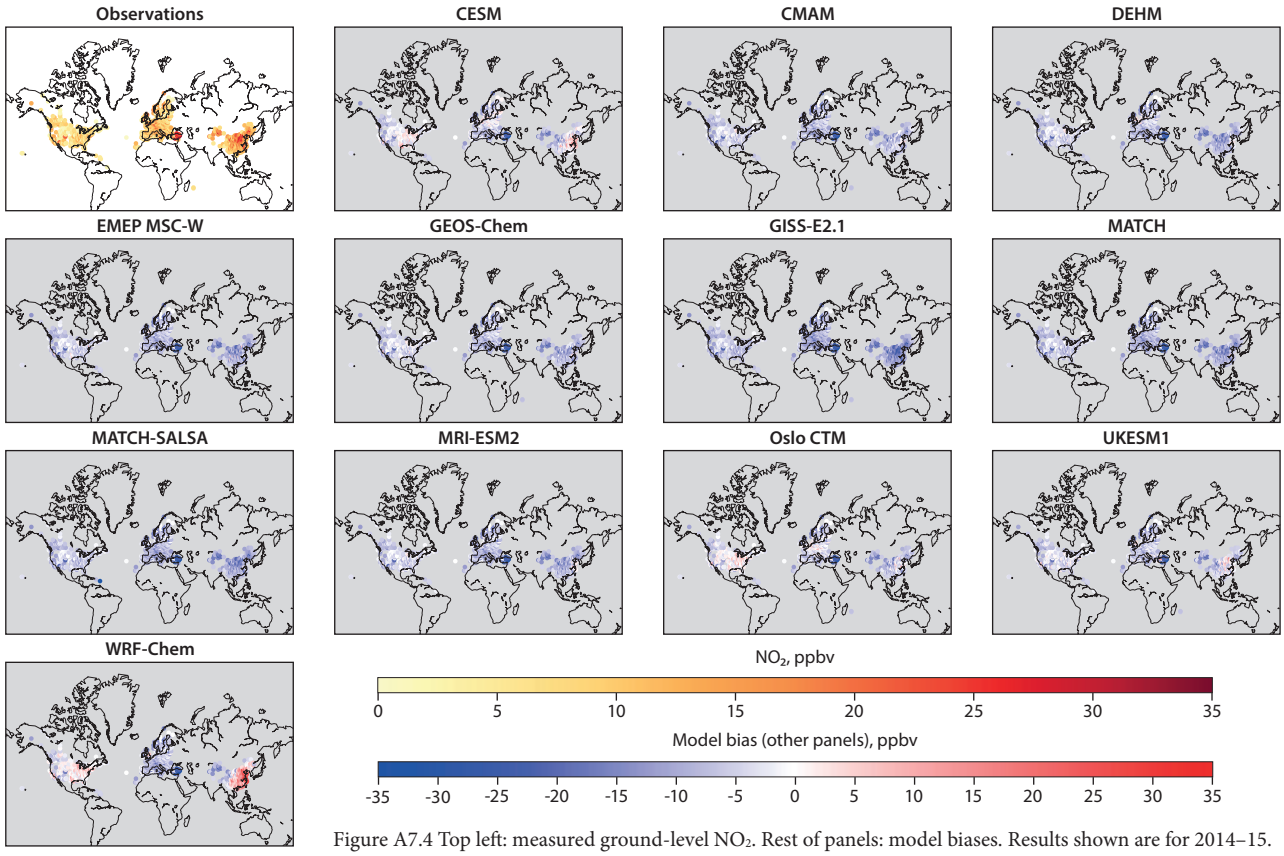

Figure A7.4 Top left: measured ground-level NO_2. Rest of panels: model biases. Results shown are for 2014–15.

model biases. CO from ACE-FTS has been shown to vary up to -35% when compared to CO from other satellite measurements. The multi-model mean bias is up to ~+/-50% in that region. NO and NO_2 from ACE-FTS vary by about 25% compared to other satellite measurements, but these comparisons did not account for diurnal variation. The multi-mean bias for NO_X is up to ~-50% during the summer in the UTLS but exceeds 200% during the winter.

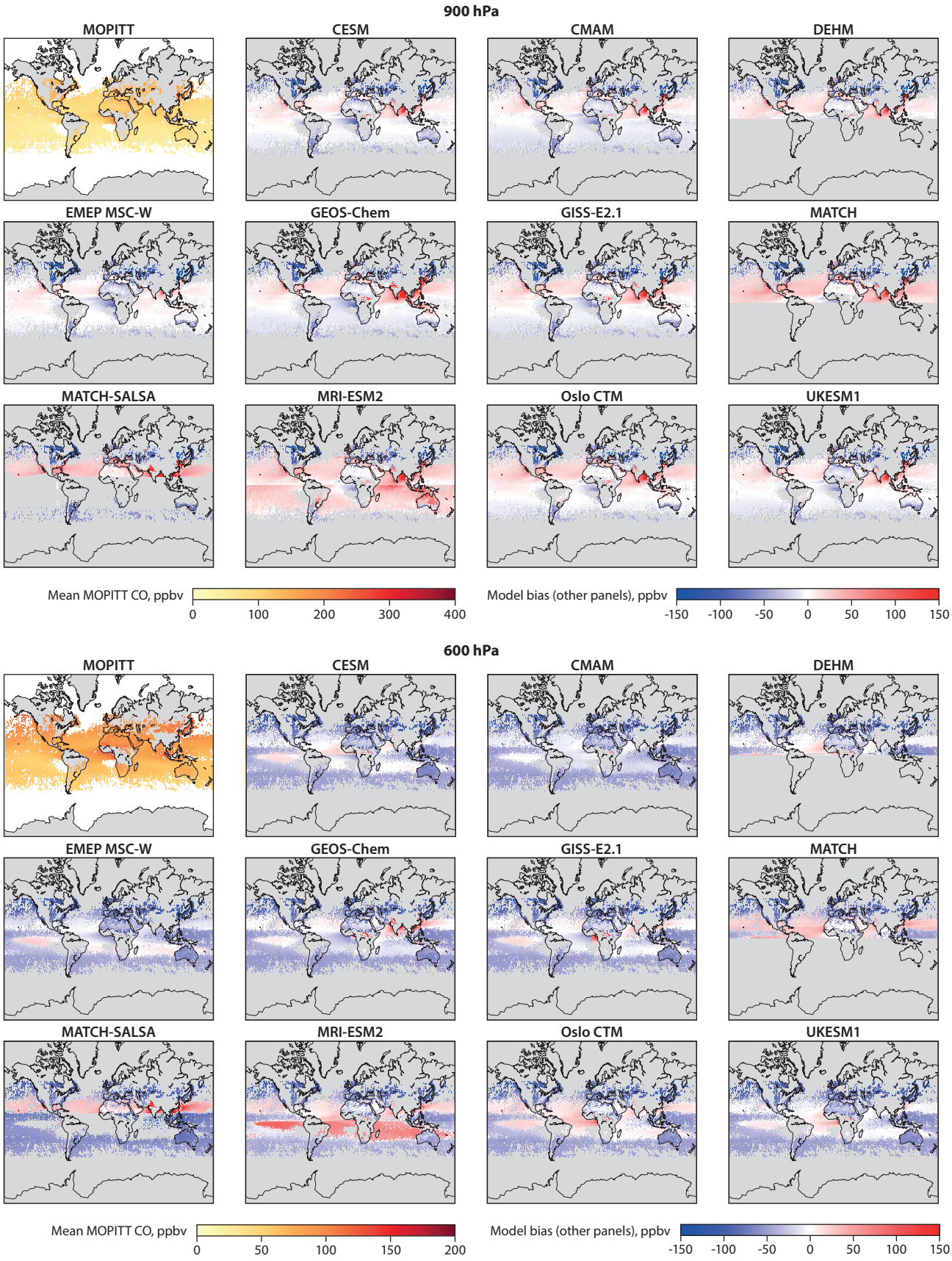

Figure A7.5 Top left: Mean MOPITT CO in the lower-troposphere (900 hPa) and mid-troposphere (600 hPa). Rest of panels: model biases. Results are for 2014–15.

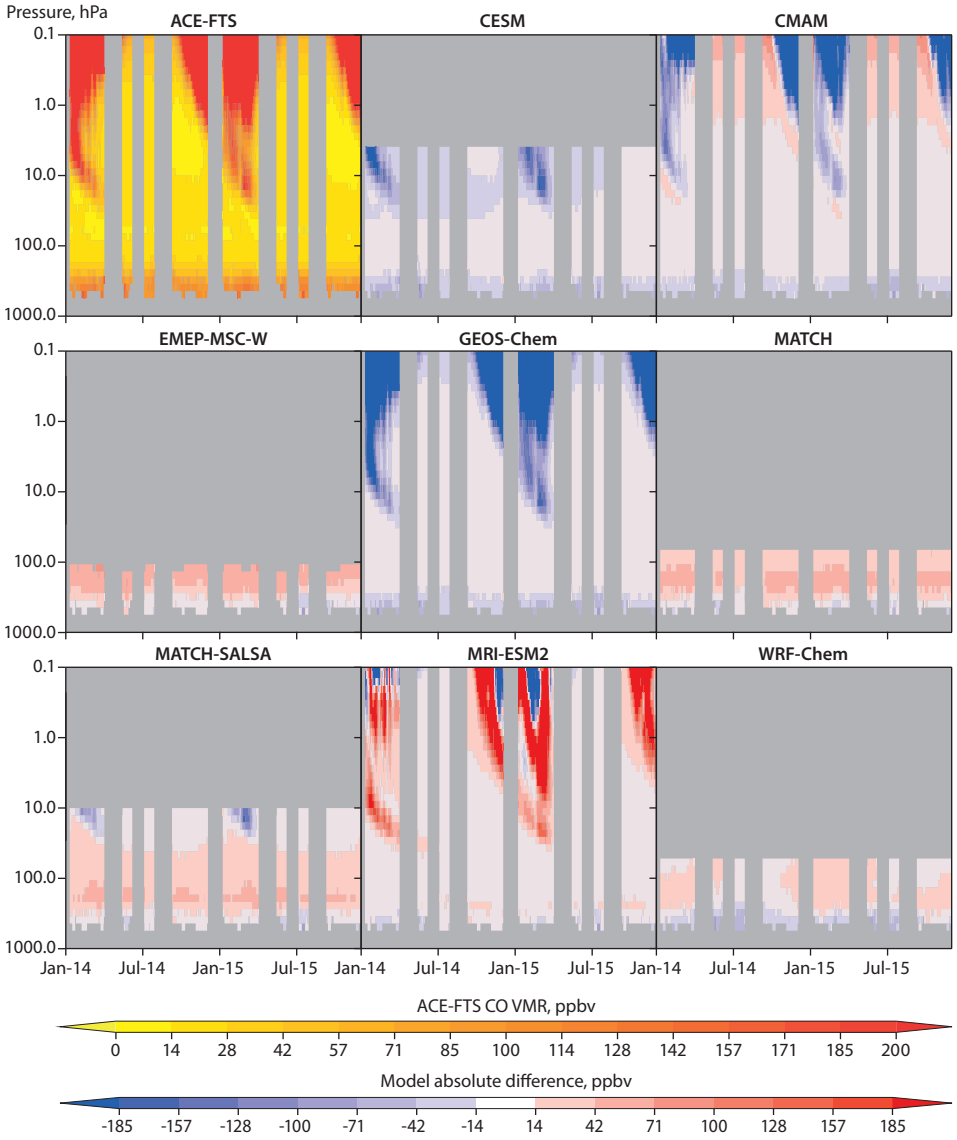

Figure A7.6 Top left: Mean Arctic CO from ACE-FTS. Rest of panels: model-measurement differences. Results shown are for 2014–15.

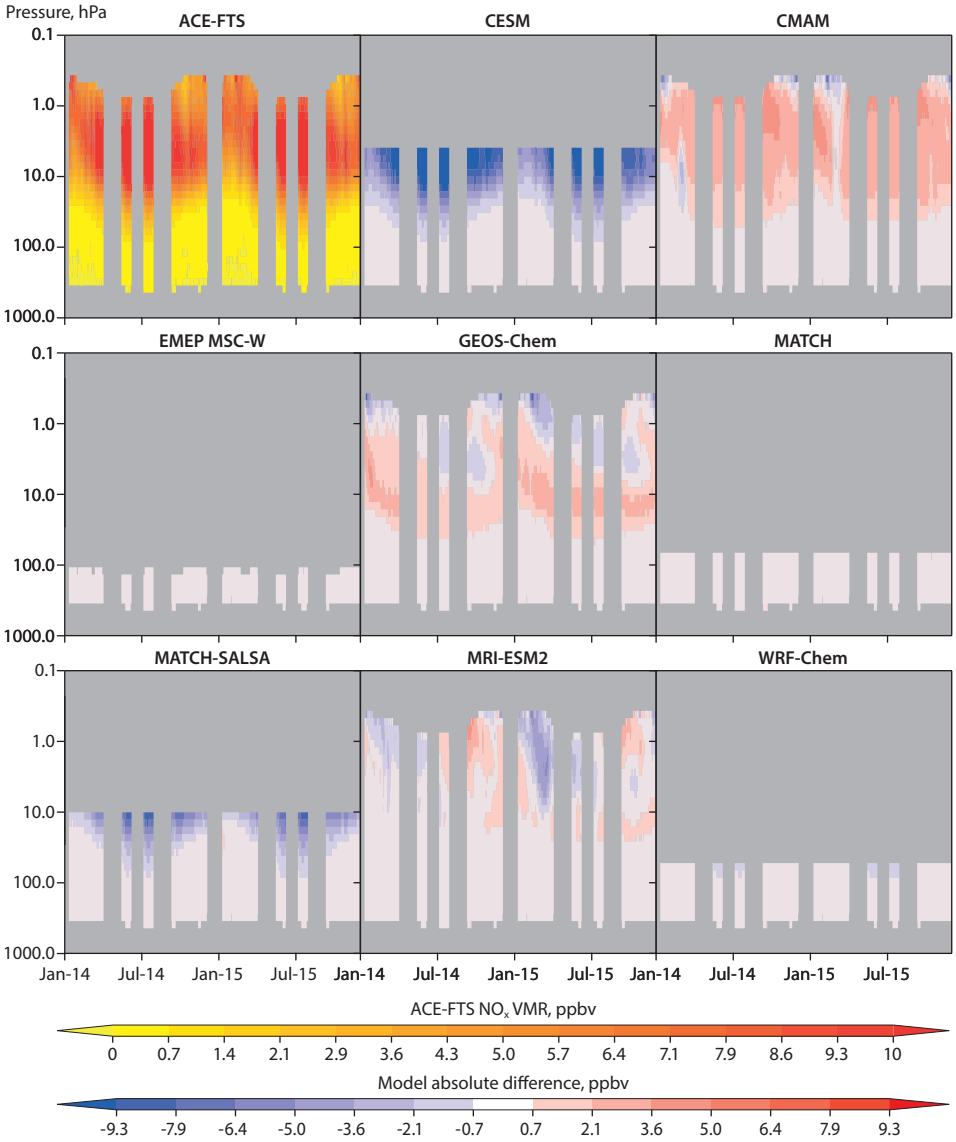

Figure A7.7 Top left: mean Arctic NO_X from ACE-FTS. Rest of panels: the model-measurement differences. Results shown are for 2014–15.

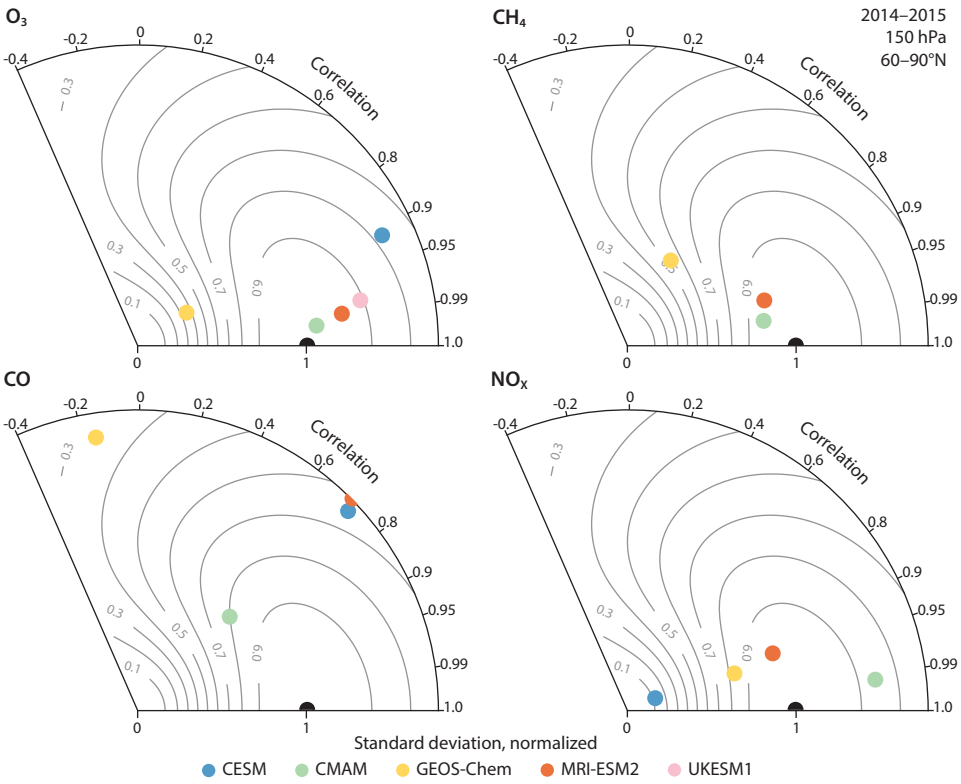

Figure A7.8 Taylor diagrams showing model performance for 2014–15 trace gases in the Arctic UTLS region at 150 hPa, as evaluated against ACE-FTS satellite measurements.

A7.3 Vertical profiles of black carbon using aircraft observations

Here, additional figures and data tables for Section 7.3.3.3 of the main text are presented.

For a more comprehensive look at model behavior, Figures A7.10 and A7.11 use all model grid points to show the relationship between zonal-mean concentrations of BC and height (using pressure as the vertical coordinate). Zonal-mean concentrations are used to reduce the otherwise intractable number of points being scattered onto the plots. Although the main emissions source regions are very localized longitudinally, transport by zonal winds and the presence of numerous smaller source regions in the mid-latitudes justifies using a zonal mean.

In the mid-latitudes, all models exhibit their highest overall concentrations in winter (DJF) below 800 m, but the highest concentrations in the mid-troposphere occur in spring (MAM). In all seasons, concentrations fall off monotonically with height, and latitudinal ranges (defined as the largest and smallest values of each model at each pressure level) shrink to a single value only above jet stream heights of about 200–300 hPa.

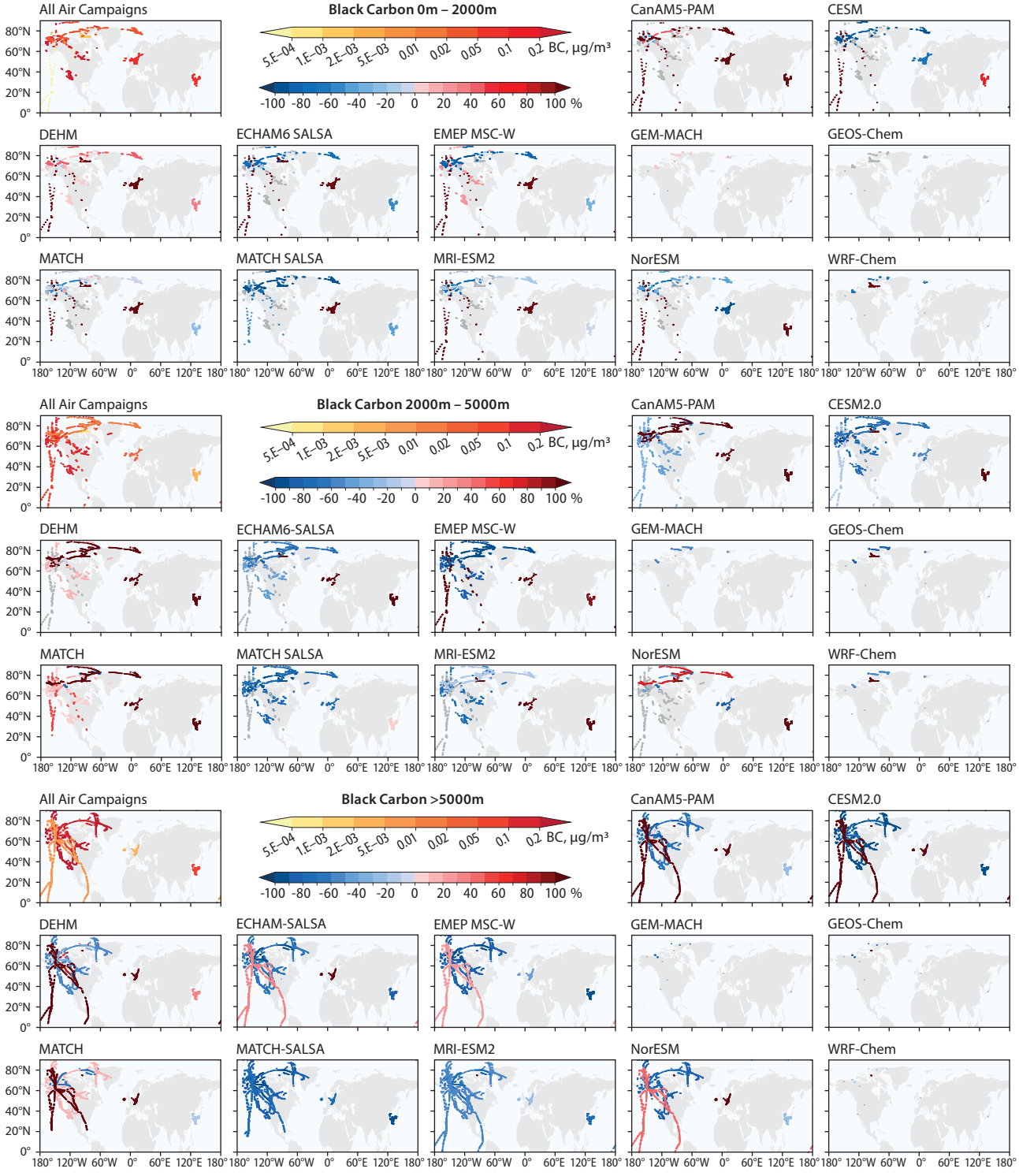

Figure A7.9 Top left: measured BC concentration (in µg/m^3, top scale bar). Rest of panels: model biases (in %, bottom scale bar). Results are for all aircraft campaigns: for measurements made between the surface and 2 km; for measurements made between 2 km and 5 km; and for measurements made above 5 km.

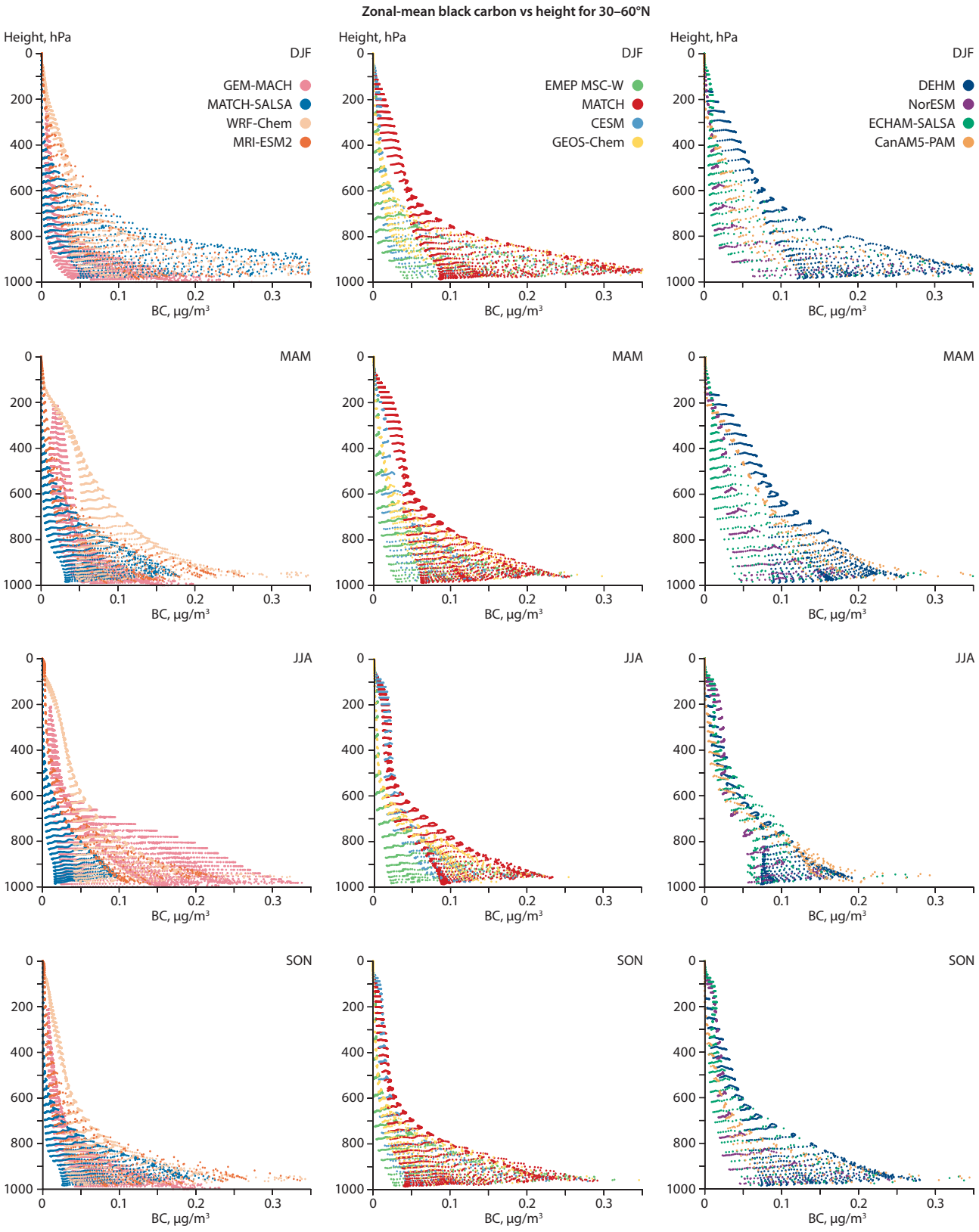

Figure A7.10 Scatter plots of zonal-mean BC concentrations against air pressure for all latitude points in the range 30°N–60°N. DJF=December, January, February; MAM=March, April, May; JJA=June, July, August; SON=September, October, November.

In the Arctic, the highest overall concentrations are found closest to the surface in summer (JJA), deriving mainly from local sources, such as high-latitude forest fires. The highest emissions extending to the mid-troposphere occur in spring (MAM). The shapes of the scattered points are very different from those in the mid-latitudes. The large variety of shapes indicates that different processes dominate the distribution of BC concentrations in the Arctic in different models.

The following tables (Tables A7.5 to A7.7) provide numerical information to accompany Figure 7.28 of the main text. For every 500 m height bin of every profile, the number of points per bin, the median BC concentration, and the MAD are tabulated.

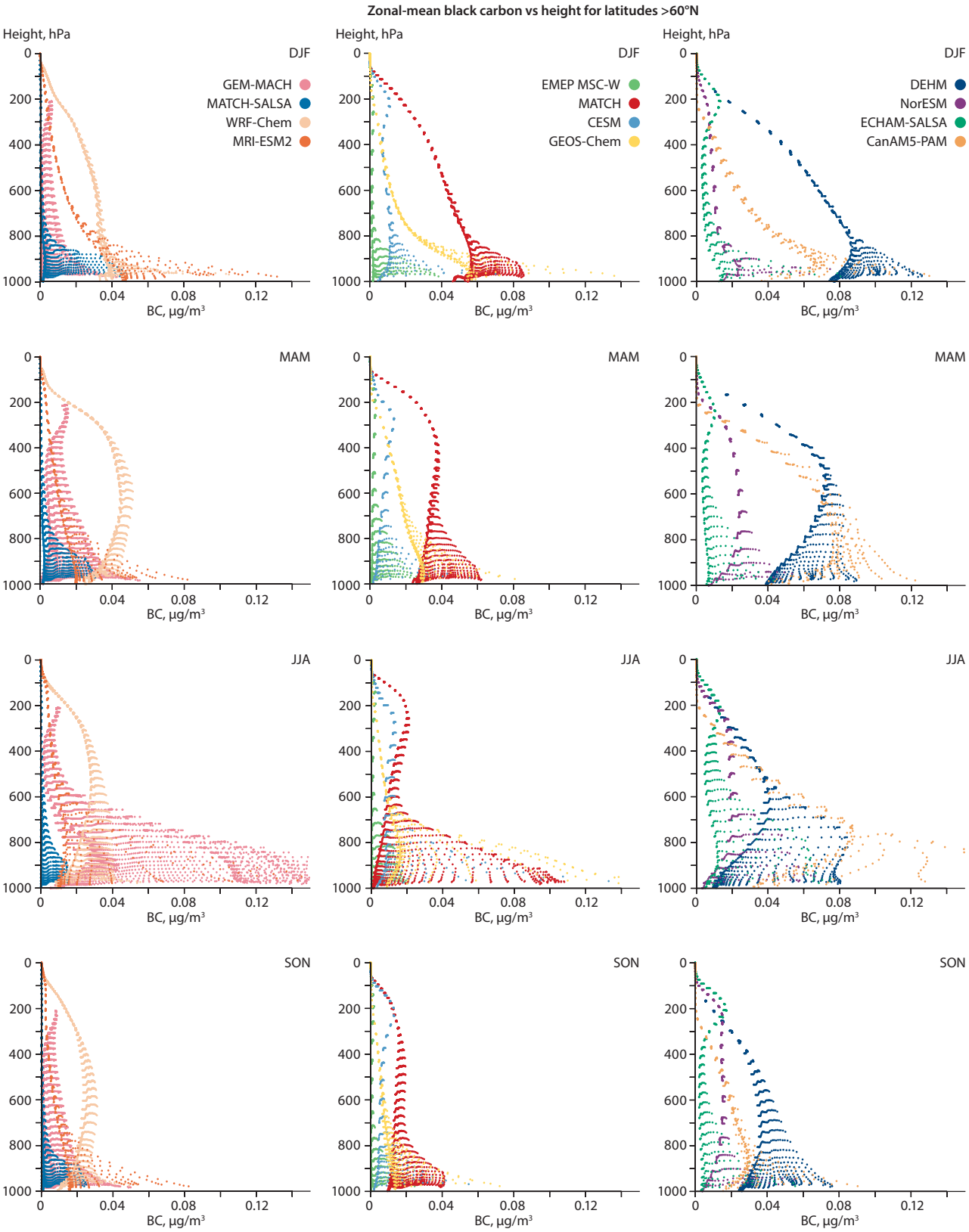

Figure A7.11 Scatter plots of zonal-mean BC concentrations against air pressure for all latitude points north of 60°N. DJF=December, January, February; MAM=March, April, May; JJA=June, July, August; SON=September, October, November. Note that the scale of the horizontal axis is smaller than on Figure A7.9

Table A7.5 Number of points (N), median BC concentration and median absolute deviation (MAD) for each height bin, for all data north of 60°N.

Height (m)	Stats (μg/m³)	Obs	CanAM5-PAM	CESM2.0	DEHM	ECHAM6-SALSA	EMEP MSC-W	MATCH	MATCH-SALSA	MRI-ESM2	NorESM-happi
0–500	N	1591	1009	642	990	1139	1441	1312	1203	1198	571
	median	0.022	0.057	0.001	0.033	0.004	4.00E-04	0.02	2.90E-04	0.014	0.007
	MAD	0.015	0.036	6.90E-04	0.012	0.002	2.80E-04	0.009	2.30E-04	0.005	0.005
500–1000	N	470	442	454	469	464	470	469	469	393	420
	median	0.02	0.06	0.002	0.034	0.004	7.50E-04	0.018	3.90E-04	0.012	0.01
	MAD	0.016	0.038	0.002	0.012	0.002	6.40E-04	0.009	3.10E-04	0.007	0.004
1000–1500	N	402	396	400	402	397	402	402	402	349	347
	median	0.021	0.059	0.004	0.039	0.005	7.20E-04	0.019	3.30E-04	0.01	0.013
	MAD	0.018	0.025	0.003	0.014	0.002	6.00E-04	0.01	2.30E-04	0.005	0.006
1500–2000	N	378	375	378	378	376	378	378	378	299	340
	median	0.015	0.061	0.004	0.045	0.005	6.00E-04	0.021	3.00E-04	0.009	0.016
	MAD	0.013	0.024	0.003	0.022	0.002	4.30E-04	0.01	1.60E-04	0.004	0.006
2000–2500	N	602	587	602	602	599	602	602	602	555	572
	median	0.018	0.067	0.004	0.056	0.004	8.50E-04	0.028	3.80E-04	0.01	0.022
	MAD	0.011	0.025	0.002	0.014	0.002	5.30E-04	0.01	2.70E-04	0.003	0.007
2500–3000	N	721	716	721	721	720	721	721	721	596	674
	median	0.015	0.066	0.004	0.054	0.003	8.00E-04	0.029	2.30E-04	0.006	0.021
	MAD	0.012	0.025	0.002	0.013	0.001	4.70E-04	0.01	1.40E-04	0.002	0.01
3000–3500	N	453	453	453	453	453	453	453	453	425	420
	median	0.023	0.056	0.004	0.057	0.004	0.001	0.028	2.60E-04	0.006	0.017
	MAD	0.016	0.025	0.002	0.025	0.002	9.20E-04	0.019	2.10E-04	0.003	0.005
3500–4000	N	282	281	282	282	281	282	282	282	240	227
	median	0.045	0.074	0.009	0.087	0.006	0.002	0.046	4.30E-04	0.011	0.023
	MAD	0.04	0.052	0.004	0.036	0.003	0.001	0.018	3.10E-04	0.007	0.012
4000–4500	N	296	290	296	296	294	296	296	296	251	202
	median	0.065	0.064	0.011	0.109	0.006	0.002	0.048	3.90E-04	0.013	0.022
	MAD	0.058	0.043	0.005	0.052	0.002	0.001	0.023	1.90E-04	0.009	0.013
4500–5000	N	332	332	332	332	332	332	332	332	312	217
	median	0.073	0.082	0.016	0.129	0.007	0.003	0.058	4.50E-04	0.011	0.03
	MAD	0.057	0.046	0.011	0.041	0.004	0.001	0.029	3.00E-04	0.006	0.013
5000–5500	N	288	287	288	288	288	288	288	288	265	235
	median	0.067	0.05	0.012	0.1	0.006	0.003	0.052	3.70E-04	0.011	0.019
	MAD	0.049	0.024	0.006	0.04	0.002	0.001	0.019	2.10E-04	0.006	0.01
5500–6000	N	254	243	254	249	245	251	251	251	245	223
	median	0.044	0.039	0.01	0.086	0.004	0.002	0.04	2.30E-04	0.006	0.026
	MAD	0.029	0.012	0.003	0.031	0.002	0.001	0.012	1.80E-04	0.003	0.008
6000–6500	N	175	175	175	175	175	175	175	175	175	138
	median	0.058	0.038	0.012	0.078	0.004	0.002	0.042	2.80E-04	0.006	0.023
	MAD	0.042	0.009	0.005	0.021	0.002	0.001	0.015	1.30E-04	0.003	0.007
6500–7000	N	187	178	187	185	181	187	187	187	181	159
	median	0.055	0.029	0.01	0.075	0.004	0.002	0.041	3.00E-04	0.006	0.021
	MAD	0.028	0.009	0.003	0.019	0.002	0.001	0.011	1.60E-04	0.002	0.007
7000–7500	N	201	201	201	201	201	201	201	201	201	147
	median	0.046	0.031	0.01	0.065	0.005	0.002	0.039	2.50E-04	0.005	0.019
	MAD	0.031	0.008	0.003	0.022	0.002	0.001	0.011	1.40E-04	0.002	0.004
7500–8000	N	134	134	134	134	134	134	134	134	134	118
	median	0.018	0.026	0.01	0.048	0.006	0.001	0.032	1.80E-04	0.004	0.015
	MAD	0.018	0.015	0.001	0.032	0.001	8.60E-04	0.013	1.70E-04	8.50E-04	0.006
8000–8500	N	139	139	139	139	139	139	139	139	139	139
	median	0.011	0.014	0.011	0.018	0.009	9.40E-04	0.017	1.70E-04	0.003	0.018
	MAD	0.009	0.006	0.002	0.006	0.003	5.70E-04	0.007	6.50E-05	0.001	0.002
8500–9000	N	170	170	170	170	170	170	170	170	170	163
	median	0.015	0.009	0.013	0.042	0.009	0.002	0.036	3.40E-04	0.004	0.013
	MAD	0.011	0.007	0.001	0.009	7.90E-04	0.001	0.006	1.70E-04	0.001	0.002
9000–9500	N	51	51	51	51	51	51	51	51	51	50
	median	9.00E-04	0.007	0.013	0.019	0.008	0.001	0.011	4.80E-04	0.005	0.016
	MAD	3.40E-04	0.007	5.30E-04	0.003	0.005	0.001	0.003	1.40E-04	0.003	7.00E-04
9500–10000	N	29	29	29	29	29	29	29	29	29	29
	median	0.002	0.005	0.015	0.015	0.012	0.002	0.019	3.90E-04	0.002	0.016
	MAD	0.002	0.003	0.002	0.003	0.003	6.50E-04	0.002	5.14E-05	1.50E-04	0.002
10000–10500	N	18	18	18	18	18	18	18	18	18	17
	median	5.90E-04	2.80E-04	0.016	0.018	0.017	0.002	0.014	4.20E-04	0.004	0.013
	MAD	2.80E-04	1.10E-04	6.90E-04	0.004	0.003	1.50E-04	0.002	2.80E-05	0.001	8.20E-04
10500–11000	N	10	10	10	10	10	10	10	10	10	7
	median	5.40E-04	2.80E-04	0.015	0.015	0.015	0.002	0.019	4.30E-04	0.005	0.012
	MAD	1.60E-04	9.00E-05	0.002	0.005	0.004	6.90E-04	0.006	4.90E-05	0.002	0.003
11000–11500	N	18	18	18	18	18	18	18	18	18	15
	median	8.60E-04	2.10E-04	0.001	0.021	0.008	0.002	0.024	5.20E-04	0.005	0.014
	MAD	5.00E-04	3.80E-05	0.001	0.003	0.001	4.10E-04	0.005	5.30E-05	1.60E-04	0.002
11500–12000	N	15	15	15	15	15	15	15	15	15	15
	median	0.001	0.001	0.015	0.011	0.013	0.001	0.021	4.10E-04	0.015	0.007
	MAD	8.80E-04	1.80E-04	0.001	4.50E-04	0.001	5.70E-04	6.40E-04	1.30E-05	7.20E-04	2.70E-04
12000–12500	N	27	27	27	4	27	27	27	27	27	27
	median	2.70E-04	1.20E-04	0.007	0.005	0.013	0.001	0.012	3.30E-04	0.003	0.001
	MAD	5.90E-05	4.90E-07	2.80E-04	---	6.40E-05	3.60E-05	9.10E-04	3.90E-05	2.60E-04	1.10E-05
12500–13000	N	21	21	21	14	21	21	21	21	21	21
	median	2.90E-04	1.00E-04	0.011	0.004	0.016	0.002	0.004	2.30E-04	0.002	0.007
	MAD	9.10E-05	1.30E-06	7.60E-05	4.50E-04	4.70E-05	0.001	9.10E-04	8.50E-05	4.90E-05	2.10E-04
13000–13500	N	85	85	85	0	85	85	85	85	85	85
	median	1.90E-04	7.00E-05	0.009	—	0.01	0.001	0.006	2.00E-04	0.003	0.008
	MAD	7.20E-05	9.10E-06	3.20E-04	—	0.004	2.30E-04	7.80E-04	3.10E-05	1.70E-04	1.10E-04

Table A7.6 Number of points (N), median BC concentration and median absolute deviation (MAD) for each height bin, for locations north of 60°N with output from 2014–2015 only.

Height (m)	Stats (μg/m³)	2014-2015			2015 only	
		Obs	GEOS-Chem	WRF-Chem	Obs	GEM-MACH
0–500	N	520	272	292	91	62
	median	0.002	0.008	0.021	0.03	3.80E-04
	MAD	0.002	0.003	0.002	0.004	2.10E-04
500–1000	N	177	177	174	72	63
	median	0.02	0.011	0.024	0.03	0.006
	MAD	0.002	0.005	0.003	0.005	0.006
1000–1500	N	138	138	138	49	40
	median	0.002	0.013	0.026	0.031	5.80E-04
	MAD	0.001	0.007	0.002	0.011	2.60E-04
1500–2000	N	151	151	151	77	72
	median	0.003	0.01	0.027	0.009	0.001
	MAD	0.002	0.003	0.002	0.005	8.60E-04
2000–2500	N	117	117	117	44	41
	median	0.003	0.008	0.027	0.023	9.20E-04
	MAD	0.002	0.003	0.002	0.009	6.80E-04
2500–3000	N	262	262	262	124	124
	median	0.004	0.015	0.03	0.024	0.001
	MAD	0.004	0.008	0.006	0.011	6.10E-04
3000–3500	N	38	38	38	28	28
	median	0.018	0.012	0.033	0.025	0.003
	MAD	0.016	0.007	0.008	0.02	0.003
3500–4000	N	48	48	48	41	41
	median	0.028	0.009	0.037	0.035	0.017
	MAD	0.025	0.003	0.011	0.031	0.012
4000–4500	N	46	46	46	43	43
	median	0.021	0.012	0.036	0.027	0.003
	MAD	0.018	0.003	0.007	0.023	0.002
4500–5000	N	26	26	26	20	20
	median	0.011	0.013	0.039	0.019	0.005
	MAD	0.009	0.003	0.008	0.017	0.003
5000–5500	N	26	26	26	23	23
	median	0.041	0.021	0.04	0.043	0.028
	MAD	0.03	0.01	0.008	0.025	0.01
5500–6000	N	5	5	5		
	median	0.002	0.003	0.028		
	MAD	3.10E-04	5.70E-05	0.008		

Table A7.7 Number of points (N), median BC concentration and median absolute deviation (MAD) for each height bin, for all data between 30°N and 60°N.

Height (m)	Stats (μg/m³)	Obs	CanAM5-PAM	CESM2.0	DEHM	ECHAM6-SALSA	EMEP MSC-W	MATCH	MATCH-SALSA	MRI-ESM2	NorESM-happi
0–500	N	443	218	174	252	230	407	304	307	263	163
	median	0.172	0.435	0.149	0.243	0.247	0.203	0.235	0.094	0.37	0.135
	MAD	0.102	0.314	0.115	0.137	0.153	0.078	0.152	0.084	0.152	0.113
500–1000	N	482	450	454	459	453	474	451	459	453	432
	median	0.089	0.328	0.133	0.218	0.119	0.145	0.206	0.144	0.24	0.182
	MAD	0.053	0.095	0.056	0.068	0.051	0.061	0.073	0.059	0.092	0.071
1000–1500	N	464	463	462	463	463	464	453	464	460	413
	median	0.115	0.347	0.109	0.216	0.124	0.12	0.207	0.114	0.213	0.176
	MAD	0.09	0.116	0.046	0.09	0.056	0.058	0.079	0.063	0.093	0.049
1500–2000	N	355	350	350	350	350	355	352	355	351	304
	median	0.097	0.269	0.089	0.195	0.104	0.07	0.144	0.054	0.125	0.107
	MAD	0.081	0.161	0.042	0.104	0.06	0.059	0.082	0.045	0.082	0.056
2000–2500	N	323	321	321	317	316	323	323	321	320	293
	median	0.072	0.123	0.075	0.229	0.129	0.07	0.139	0.039	0.104	0.097
	MAD	0.06	0.076	0.053	0.145	0.093	0.057	0.098	0.03	0.083	0.055
2500–3000	N	178	178	178	178	178	178	178	178	178	169
	median	0.031	0.071	0.036	0.1	0.059	0.026	0.06	0.007	0.041	0.052
	MAD	0.027	0.043	0.024	0.056	0.041	0.023	0.043	0.007	0.033	0.031
3000–3500	N	229	229	229	229	229	229	229	229	229	212
	median	0.058	0.071	0.04	0.112	0.047	0.012	0.056	0.008	0.029	0.05
	MAD	0.052	0.039	0.03	0.059	0.033	0.01	0.031	0.007	0.02	0.024
3500–4000	N	248	248	248	248	248	248	248	248	248	213
	median	0.06	0.072	0.03	0.1	0.045	0.01	0.049	0.01	0.029	0.039
	MAD	0.052	0.047	0.019	0.044	0.026	0.009	0.027	0.009	0.018	0.017
4000–4500	N	163	163	163	163	163	163	163	163	163	138
	median	0.053	0.07	0.024	0.1	0.021	0.01	0.049	0.005	0.022	0.042
	MAD	0.048	0.035	0.016	0.05	0.012	0.008	0.029	0.005	0.017	0.016
4500–5000	N	230	230	230	230	230	230	230	230	230	219
	median	0.019	0.05	0.025	0.051	0.024	0.003	0.026	0.001	0.018	0.03
	MAD	0.018	0.028	0.014	0.031	0.015	0.003	0.012	0.001	0.011	0.013
5000–5500	N	182	182	182	182	182	182	182	182	182	157
	median	0.036	0.063	0.019	0.079	0.015	0.006	0.034	0.003	0.016	0.026
	MAD	0.032	0.036	0.012	0.043	0.007	0.005	0.019	0.003	0.011	0.009
5500–6000	N	239	239	239	239	239	239	239	239	239	208
	median	0.041	0.059	0.018	0.103	0.012	0.005	0.042	0.003	0.012	0.037
	MAD	0.03	0.033	0.012	0.057	0.007	0.003	0.023	0.003	0.008	0.016
6000–6500	N	292	292	292	292	292	292	292	292	292	205
	median	0.019	0.047	0.014	0.069	0.009	0.003	0.028	7.30E-04	0.007	0.027
	MAD	0.015	0.026	0.006	0.031	0.004	0.002	0.013	5.40E-04	0.003	0.008
6500–7000	N	188	188	188	188	188	188	188	188	188	169
	median	0.03	0.043	0.028	0.06	0.015	0.005	0.035	0.002	0.011	0.028
	MAD	0.026	0.028	0.018	0.034	0.007	0.003	0.018	0.002	0.006	0.013
7000–7500	N	258	258	258	258	258	258	258	258	258	245
	median	0.011	0.026	0.022	0.04	0.014	0.003	0.03	8.00E-04	0.006	0.028
	MAD	0.01	0.011	0.016	0.022	0.006	0.003	0.011	5.60E-04	0.003	0.007
7500–8000	N	199	199	199	199	199	199	199	199	199	156
	median	0.009	0.026	0.016	0.044	0.009	0.004	0.023	7.10E-04	0.004	0.025
	MAD	0.008	0.016	0.008	0.018	0.004	0.003	0.006	5.00E-04	0.002	0.01
8000–8500	N	226	226	226	226	226	226	226	226	226	196
	median	0.008	0.02	0.019	0.036	0.012	0.004	0.023	4.90E-04	0.006	0.019
	MAD	0.007	0.017	0.011	0.02	0.004	0.002	0.018	4.10E-04	0.005	0.009
8500–9000	N	169	169	169	169	169	169	169	169	169	115
	median	0.011	0.023	0.015	0.032	0.01	0.002	0.023	2.20E-04	0.004	0.019
	MAD	0.01	0.015	0.003	0.02	0.004	0.001	0.01	1.60E-04	0.003	0.01
9000–9500	N	89	89	89	89	89	89	89	89	89	79
	median	0.011	0.004	0.016	0.008	0.01	0.002	0.018	8.30E-05	0.004	0.028
	MAD	0.009	9.10E-04	0.003	0.005	0.007	9.90E-04	0.003	7.80E-05	5.10E-04	0.008
9500–10000	N	89	89	89	89	89	89	89	89	89	65
	median	0.003	0.002	0.006	0.004	0.011	0.003	0.004	1.10E-04	0.003	0.002
	MAD	0.002	9.30E-04	8.30E-04	0.001	0.002	6.60E-04	0.003	2.30E-05	5.60E-04	4.40E-04
10000–10500	N	34	34	34	34	34	34	34	34	34	31
	median	0.021	0.008	0.004	0.048	0.01	0.001	0.026	3.10E-04	0.004	0.01
	MAD	0.012	0.004	0.002	0.009	9.20E-04	4.80E-04	0.007	1.00E-04	6.50E-04	0.001
10500–11000	N	50	50	50	50	50	50	50	50	50	50
	median	0.008	0.001	0.01	0.005	0.007	0.003	0.014	8.00E-05	0.003	0.011
	MAD	0.007	5.30E-04	0.003	0.002	0.001	0.002	0.005	7.10E-05	4.80E-04	0.003
11000–11500	N	21	21	21	21	21	21	21	21	21	20
	median	0.005	0.001	0.015	0.006	0.015	0.002	0.019	1.20E-04	0.004	0.014
	MAD	0.005	0.001	0.003	0.003	0.002	6.50E-04	0.001	9.80E-05	0.001	0.003
11500–12000	N	52	52	52	52	52	52	52	52	52	52
	median	3.60E-04	1.50E-04	0.011	0.01	0.013	0.002	0.009	2.40E-04	0.005	0.006
	MAD	1.20E-04	8.80E-06	7.90E-04	0.003	9.10E-04	3.30E-04	0.001	9.50E-05	0.002	0.004
12000–12500	N	156	156	156	156	156	156	156	156	156	156
	median	2.50E-04	1.40E-04	0.012	0.005	0.015	0.003	0.008	2.90E-04	0.003	0.011
	MAD	1.10E-04	2.30E-05	0.001	0.002	3.00E-04	0.001	0.002	3.00E-05	4.00E-04	0.002
12500–13000	N	48	48	48	8	48	48	48	48	48	48
	median	2.30E-04	9.40E-05	0.013	0.001	0.013	0.003	0.009	2.90E-04	0.011	0.008
	MAD	6.30E-05	2.50E-06	9.30E-04	4.70E-05	2.10E-04	4.10E-04	4.00E-04	3.70E-05	0.003	0.001
13000–13500	N	22	22	22	0	22	22	22	22	22	22
	median	1.80E-04	7.00E-05	0.003	—	0.01	0.003	0.004	8.60E-05	0.003	0.004
	MAD	3.50E-05	8.10E-06	8.90E-05	—	5.40E-04	4.00E-04	0.001	5.80E-05	4.60E-04	3.60E-05

A7.4 Arctic black carbon (BC)

Table A7.8 Information about global BC measurements used for model evaluation in Section 7.3.3.

Measurement location or network	BC measurement method	Comments/references
IMPROVE (including Fairbanks)	Elemental carbon via thermo-optical method	Malm et al. (1994)
EMEP	Elemental carbon via thermo-optical method from $PM_{2.5}$ and PM_{10}	Tørseth et al. (2012); EMEP manual, 2014
CABM (including Alert)	Elemental carbon via thermo-optical method from total suspended particle (2005–2011) and PM_1 (2011 to present) At Alert, also equivalent BC via aethalometer for PM_1	Sharma et al. (2014)
Gruvebadet Lab	Equivalent BC via particle soot absorption photometer (PSAP) from PM_1	Gogoi et al. (2016)
Zeppelin Mountain	Equivalent BC via aethalometer	Eleftheriadis et al. (2009); Eleftheriadis, personal communication, 2020.
Villum Research Station	Multi-angle absorption photometer (MAAP, 24-hour) and aethalometer (weekly)	MAAP data not used in model validation in this chapter as not for the relevant years of study. Aethalometer data also not used as not available in time.
Utqiaġvik (Barrow)	Equivalent BC via aethalometer and via PSAP from PM_1	Delene and Ogren (2002); Andrews, personal communication, 2020.
Japanese Arctic cruise	Refractory BC via single particle soot photometer (SP2) from PM_{10}	Taketani et al. (2016)
Russian Arctic cruise	Equivalent BC via aethalometer	Popovicheva et al. (2017)
Aircraft campaigns	Refractory black carbon (rBC) from SP2	Moteki and Kondo (2010); Schwarz et al. (2006); Stephens et al. (2003)

The 2014–2015 monthly modeled and measured BC appears in Figure A7.12 for all Arctic locations shown in Figure 7.19

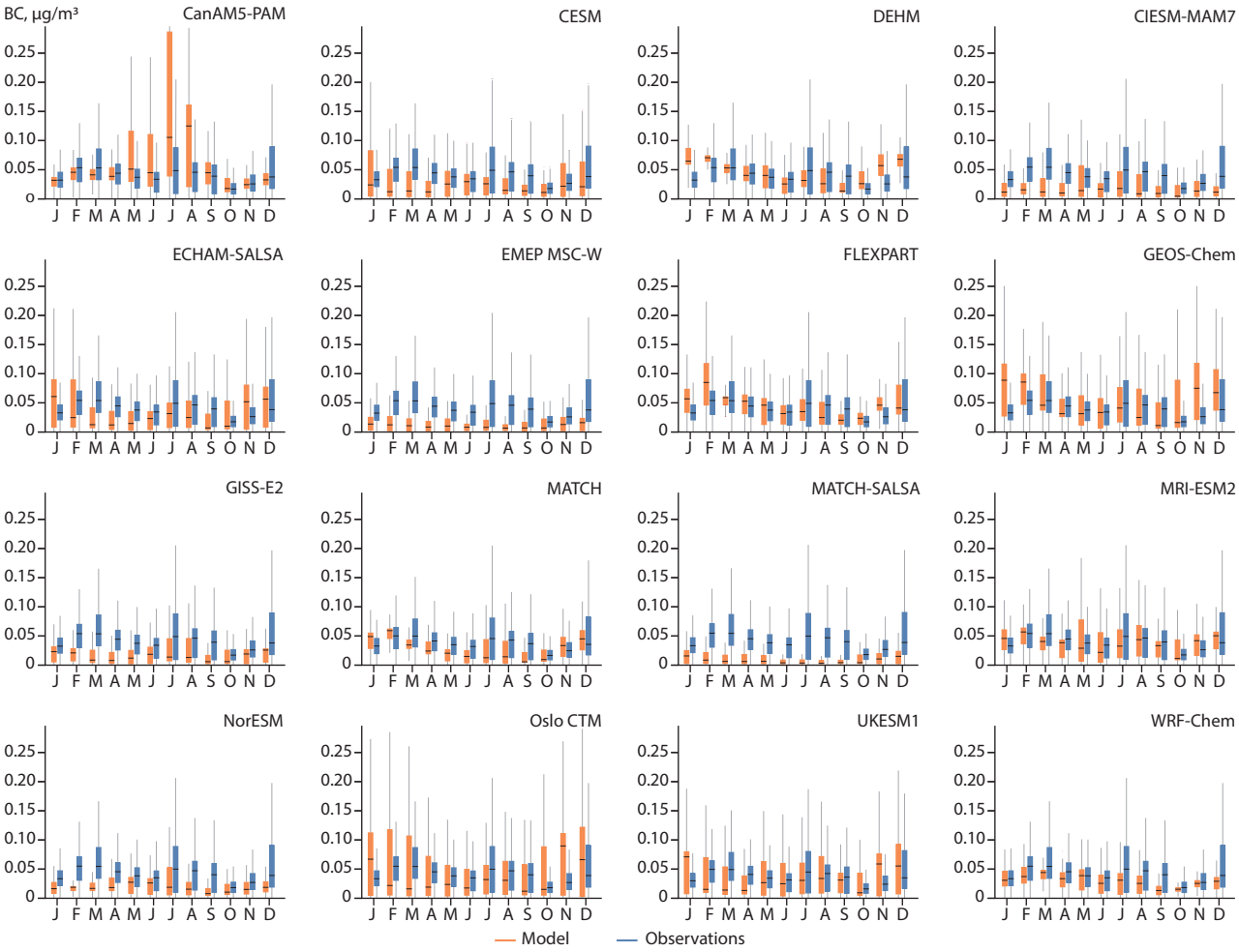

Figure A7.12 Modeled and measured monthly mean BC concentrations at surface Arctic measurement sites in 2014–2015.

A7.5 Arctic sulfate for 2014–15

Figures A7.13 and A7.14 show the monthly modeled and measured SO_4 in the Arctic for years 2008–9 and 2014–15, respectively. The Arctic locations are shown in Figure 7.33. Note that 2008–9 has a more consistent seasonal cycle than 2014–15.

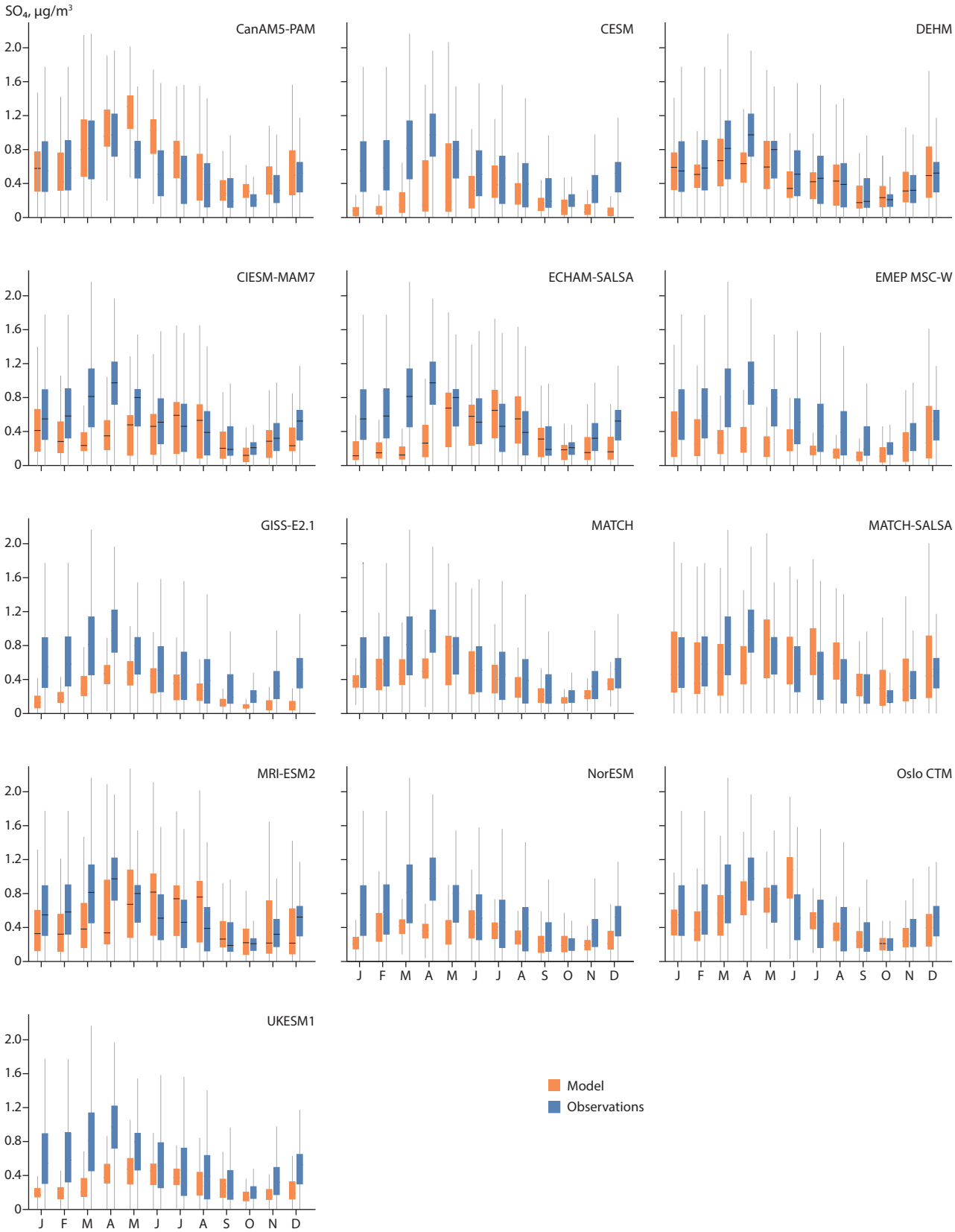

Figure A7.13 Modeled and measured monthly SO_4 concentrations at surface Arctic measurement sites in 2008–2009.

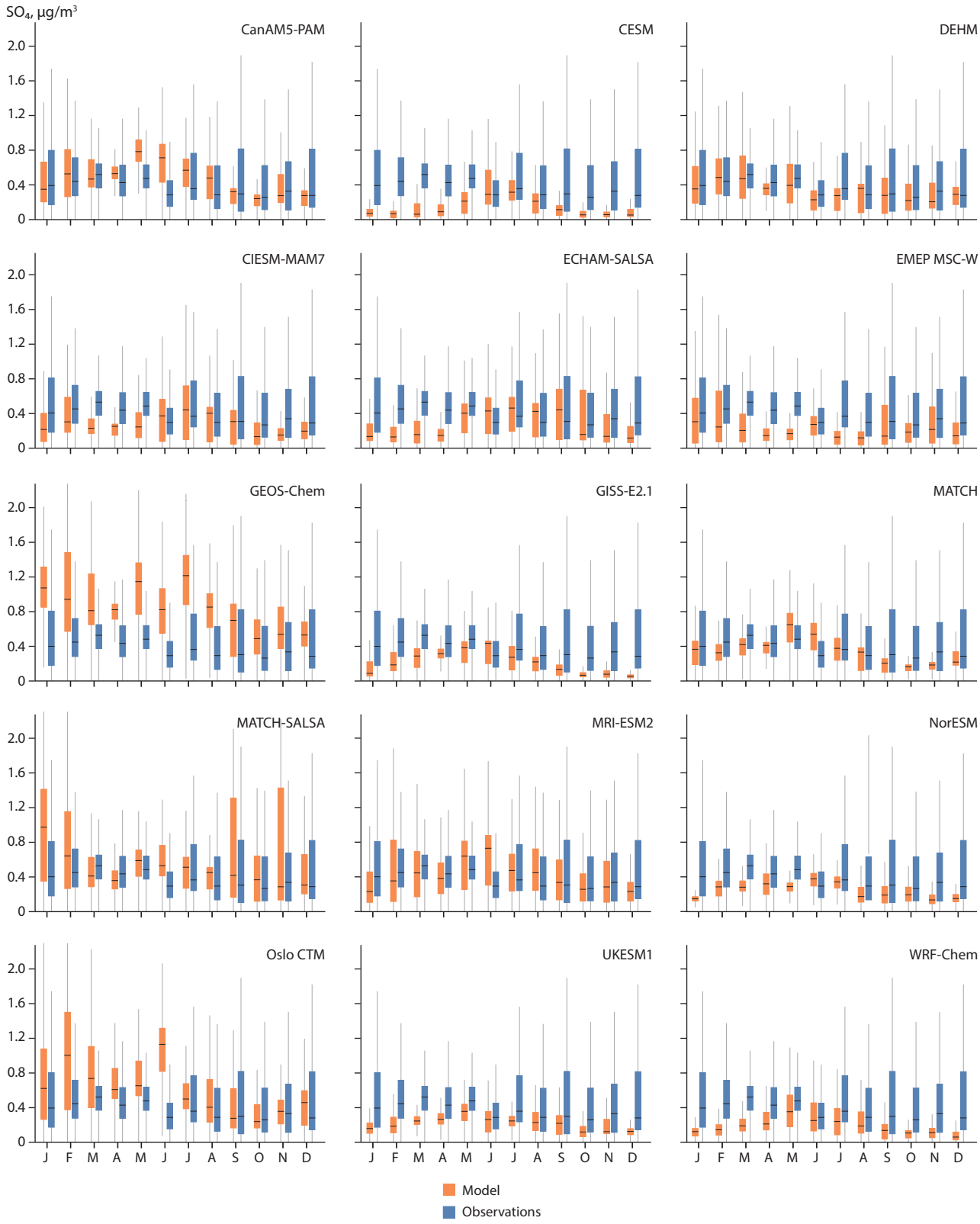

Figure A7.14 Modeled and measured monthly SO_4 concentrations at surface Arctic measurement sites in 2014–15.

A7.6 Organic aerosol

Most OA is measured by thermal optical method (as are EC and OC), with approximately 20% uncertainty (e.g., Sharma et al., 2017). To compare these data to models, we applied a conversion factor of 1.4 to report it as OA. Figures A7.15 to A7.17 are discussed in the main text in Section 7.3.5.

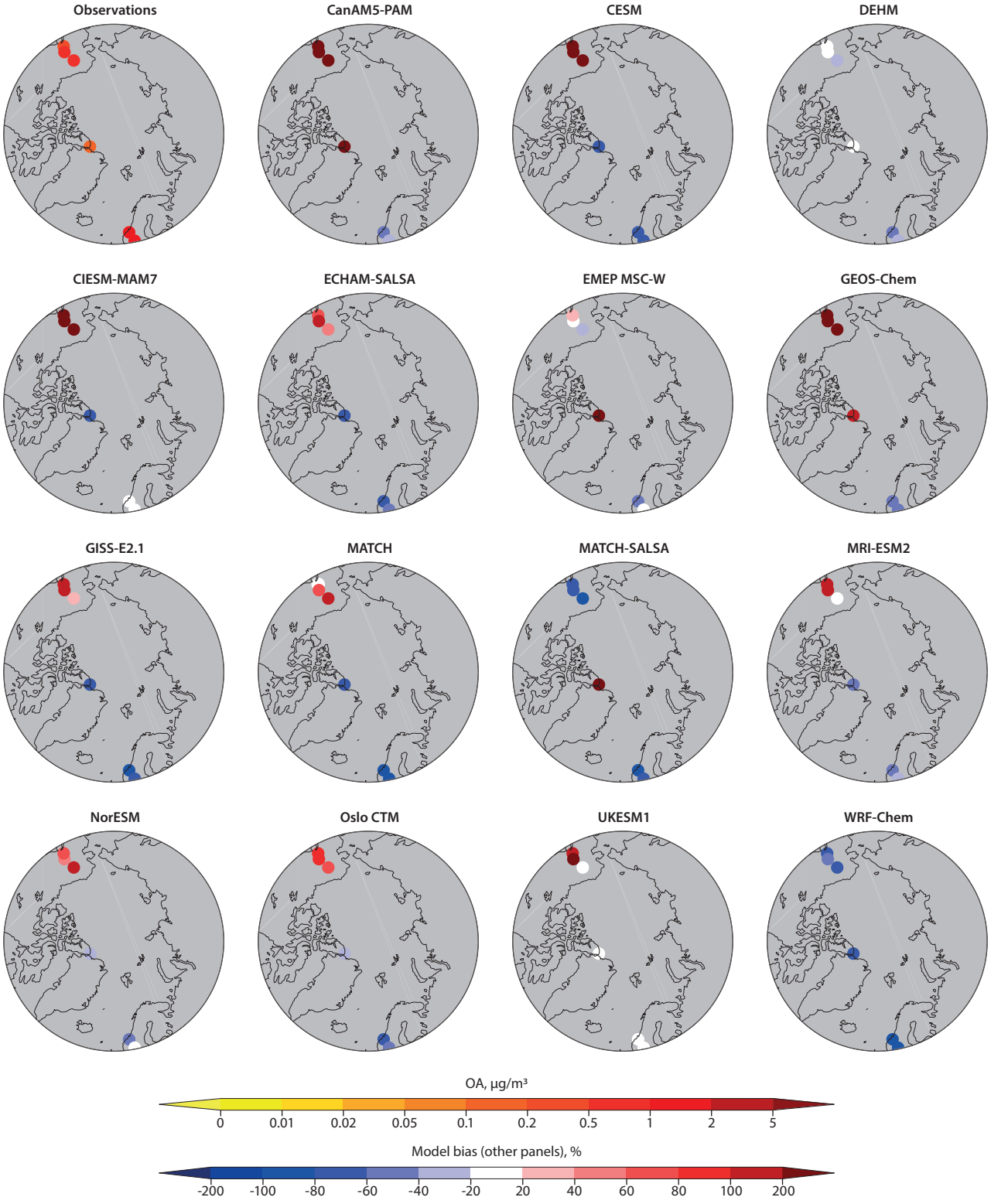

Figure A7.15 Top left: mean Arctic OA at observing sites. Rest of panels: the model mean biases for 2014–2015.

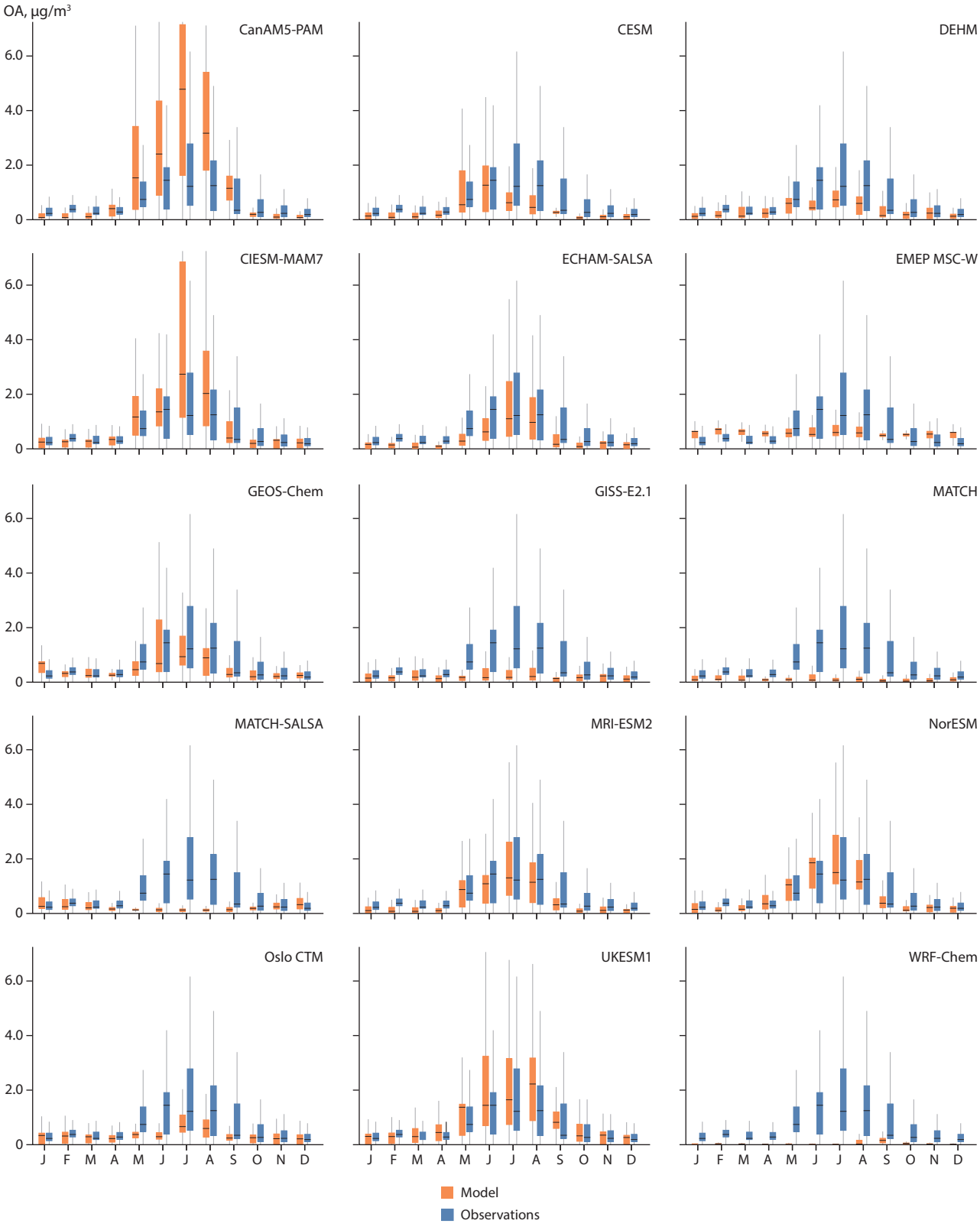

Figure A7.16 Monthly Arctic OA from models and measurements for 2014–2015.

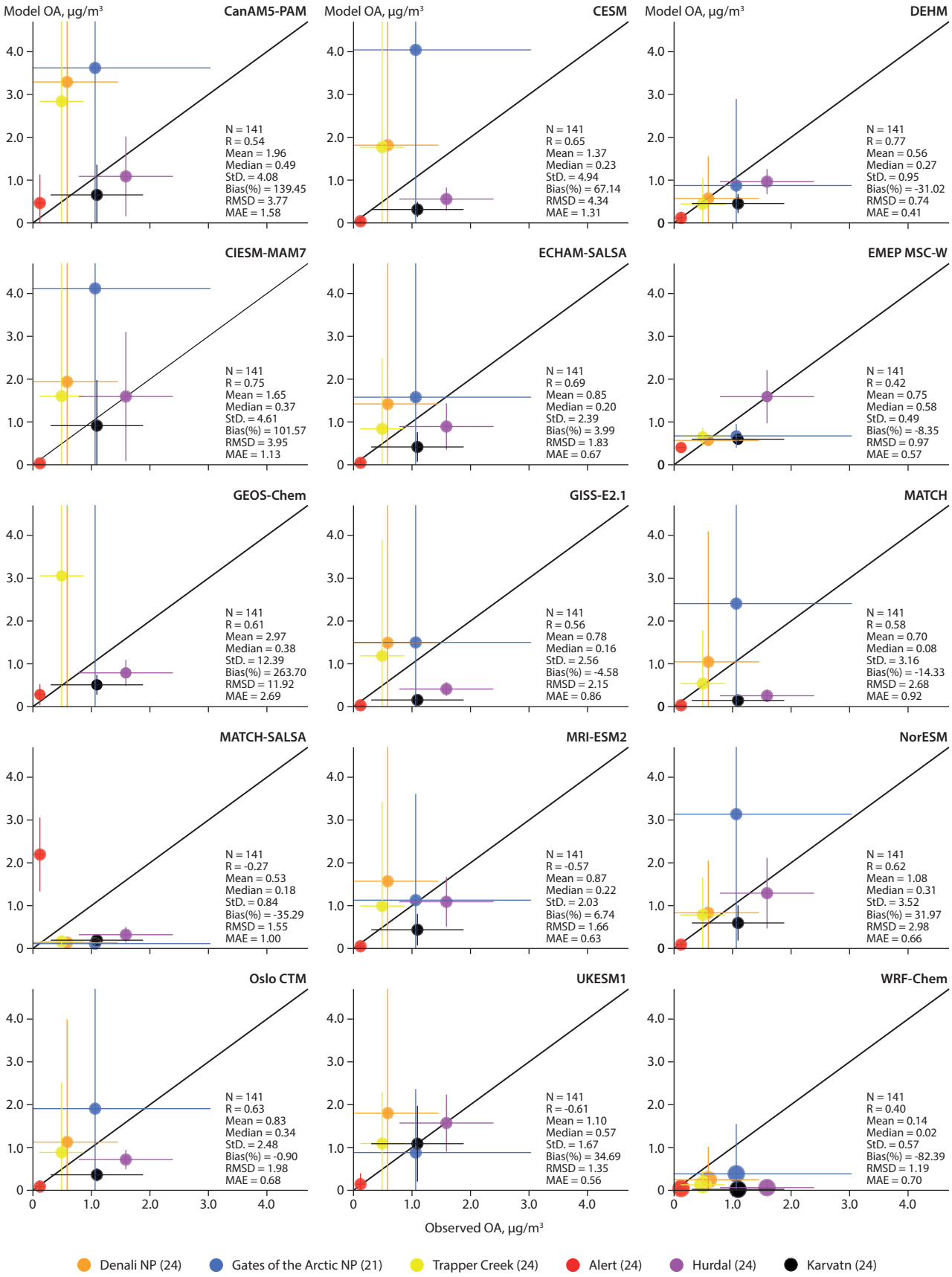

Figure A7.17 Modeled-versus-measured Arctic OA for 2014–2015. Circles show the means, and horizontal/vertical lines represent standard deviation from the mean. N=number of data points; R=correlation coefficient; Mean=model mean value; Median=model median value; StD=model standard deviation; Bias (%)=percent model bias; RMSD=root mean standard error; MAE=mean absolute error. Numbers in brackets indicate number of months for which data were available at each site.

A7.7 Global $PM_{2.5}$ evaluation

A wide range of horizontal resolutions are employed in the models, ranging from approximately 0.14° (GEM-MACH) to 2.8° (CanAM5-PAM) longitude. Observations provide clear evidence for steep gradients in annual mean $PM_{2.5}$ concentrations between urban and rural regions that cannot be well resolved by most of the available models. To better reproduce concentration gradients – with the hope of enhancing health-impact analyses – and to more directly compare model results obtained at different resolutions, the simulated $PM_{2.5}$ concentrations for 2015 were first downscaled. This involved increasing the horizontal resolution of the models' results using a global, non-Arctic satellite-based dataset from Dalhousie University (Data ref. 7.8) at a resolution of 0.5° for that year.

The overall goal was to enhance regional $PM_{2.5}$ concentration patterns by introducing spatial $PM_{2.5}$ variability at scales unresolved by the model. An important requirement was that the approach needed to preserve the large-scale features resolved by the model, so that the enhancement of spatial patterns should not affect mean model results.

For each individual model with a nominal resolution coarser than 0.5°, the downscaling approach involved the following steps for merging the model-simulated $PM_{2.5}$[1] results and externally specified high-resolution $PM_{2.5}$ dataset:

[1] This method was applied to models' $PM_{2.5a}$ (SO_4 + BC + OA + NO_3 + NH4). A common dataset of $PM_{2.5b}$ (DU + SS) was added to each models' $PM_{2.5a}$ in order to estimate total $PM_{2.5}$ for each model.

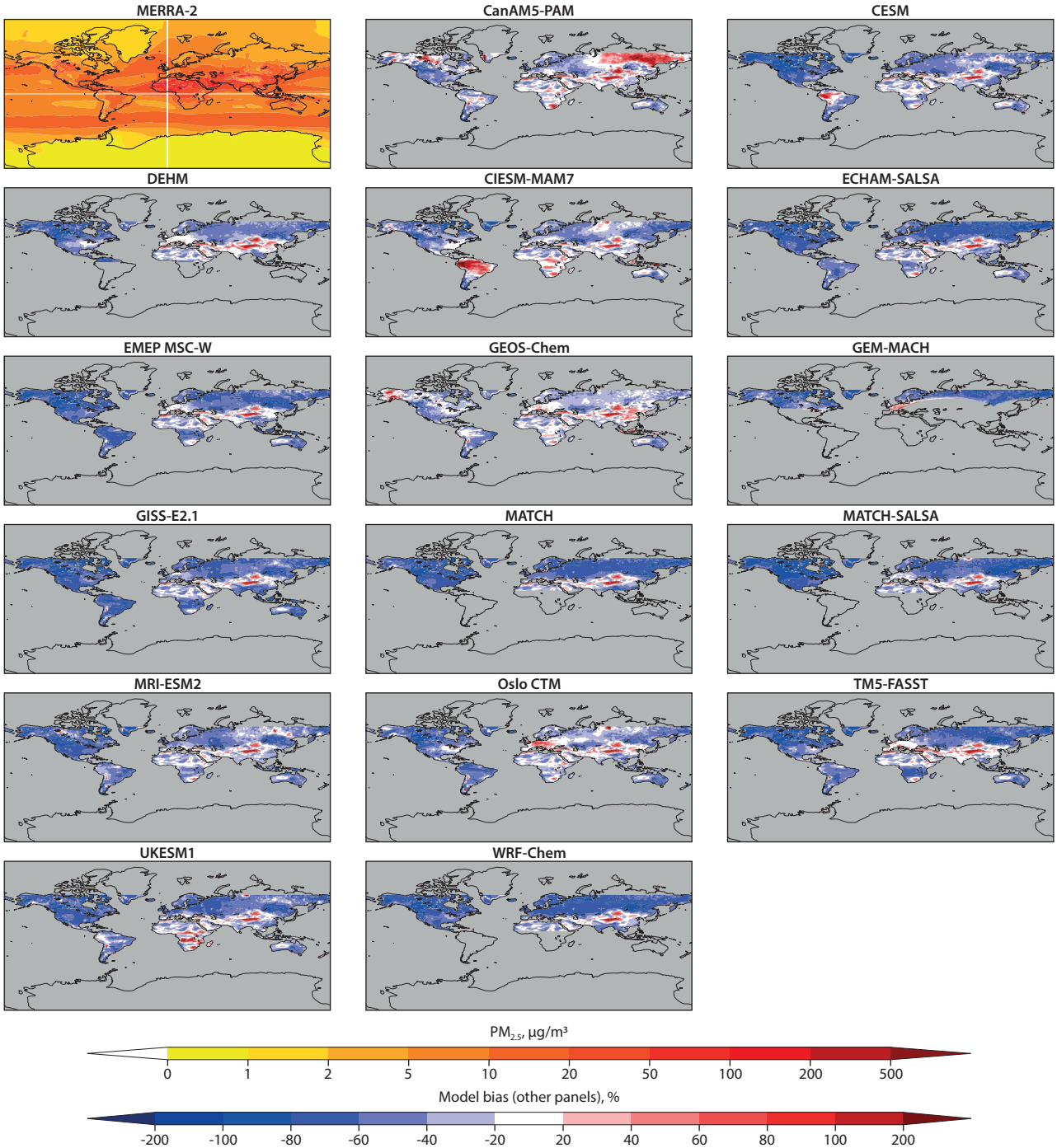

Figure A7.18 Top left: $PM_{2.5}$ from MERRA-2 reanalysis. Rest of panels: model biases. Results shown are for 2015.

1. Remapping the external high-resolution $PM_{2.5}$ dataset onto the model grid.
2. Calculating the ratio of externally specified $PM_{2.5}$ concentrations obtained in Step 1 over the simulated mean $PM_{2.5}$ concentrations.
3. Remapping the ratio from Step 2 onto a grid with a resolution of 0.5°.
4. Remapping the model results onto a grid with a resolution of 0.5°.
5. Multiplying the ratio from Step 3 by the external high-resolution $PM_{2.5}$ concentrations (a bi-linear remapping method was used for this).

Undertaking the outlined calculations produced downscaled model results at a resolution of 0.5°, which were compared with observations and used to analyze health impacts. Comparisons with observed $PM_{2.5}$ concentrations from measurement networks showed that this approach systematically improved the agreement of simulated results with observations in 2015, compared to the datasets at the native resolution of the models.

Figures A7.18, A7.19 and A7.20 show $PM_{2.5}$ produced from different data assimilation systems, and the downscaled-model differences for 2015.

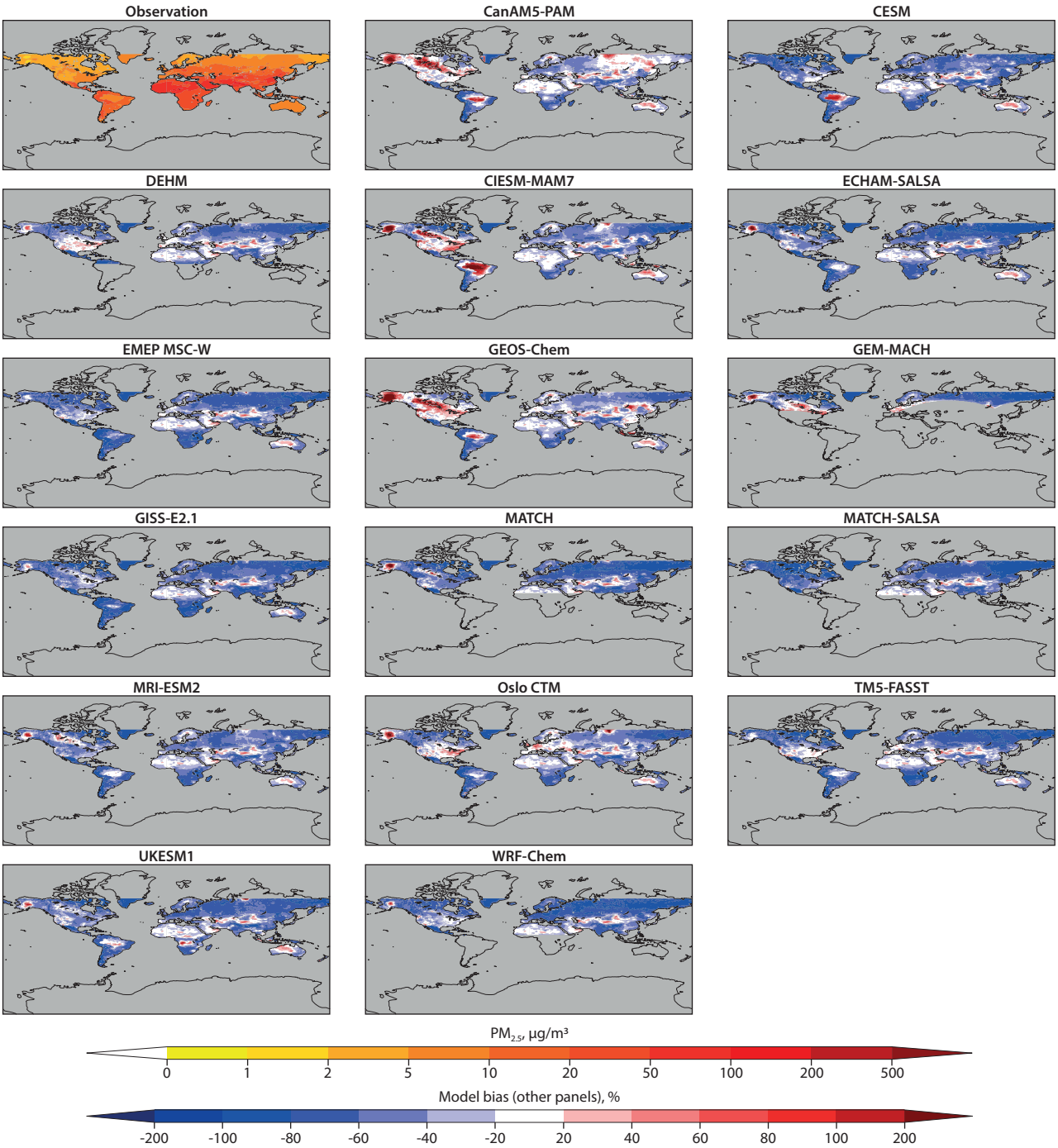

Figure A7.19 Top left: annual mean $PM_{2.5}$ from GBD. Rest of panels: model biases. Results shown are for 2015.

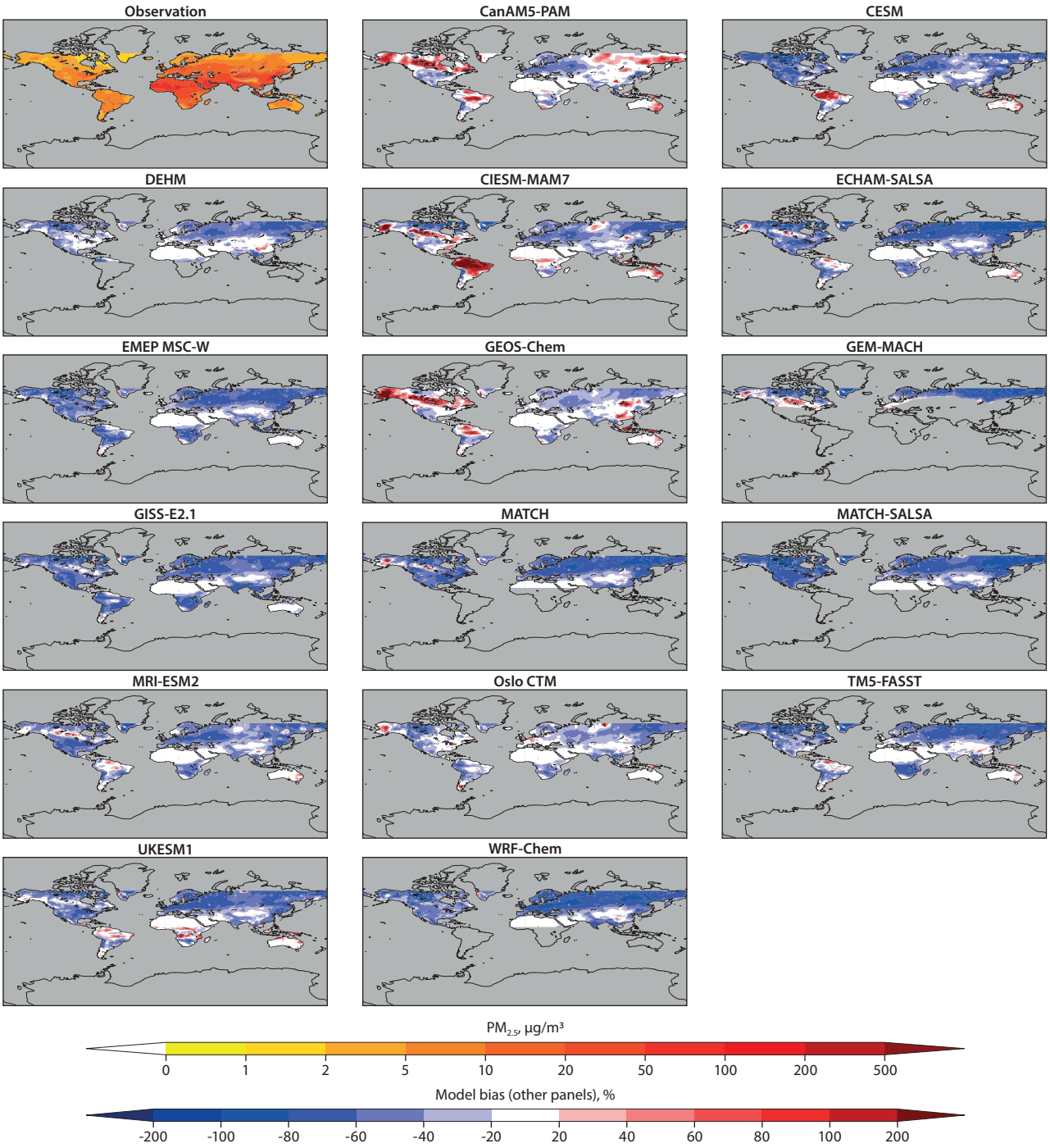

Figure A7.20 Top left: annual mean $PM_{2.5}$ from University of Dalhousie (Data ref. 7.8). Rest of panels: model biases. Results shown are for 2015.

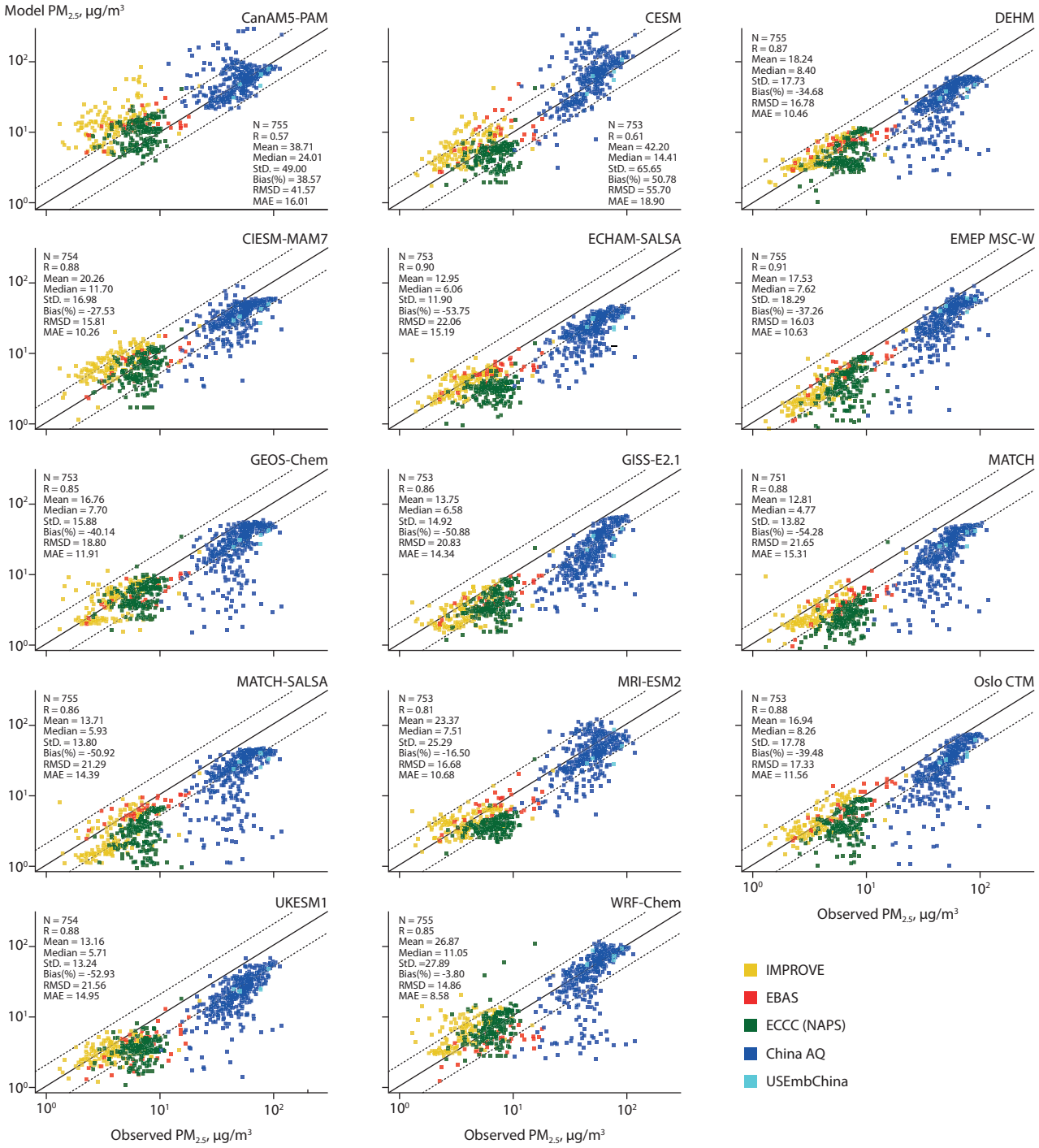

Figure A7.21 Annual mean modeled-versus-measured $PM_{2.5}$ for 2014–2015. Note this is for original model output (not downscaled). N=number of data points; R=correlation coefficient; Mean=model mean value; Median=model median value; StD=model standard deviation; Bias (%)=percent model bias; RMSD=root mean standard error; MAE=mean absolute error.

A7.8 Global aerosol optical properties

This section contains additional information about the AOD comparisons from Section 7.3.6. Figure A7.22 shows the number of months that AERONET AOD data was available, globally. Figures A7.23 shows the annual mean AOD from four different satellite products, as well as the models. We see a range of AOD from the measurements that is similar to the range in the different models. Finally, Figure A7.24 shows the absolute differences of the modeled AOD to just one of the satellite instruments, CALIOP-CALIPSO.

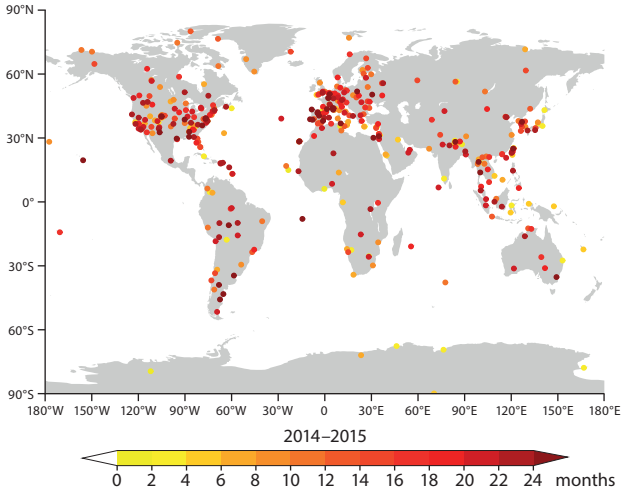

Figure A7.22 Number of months for which AERONET AOD data was available.

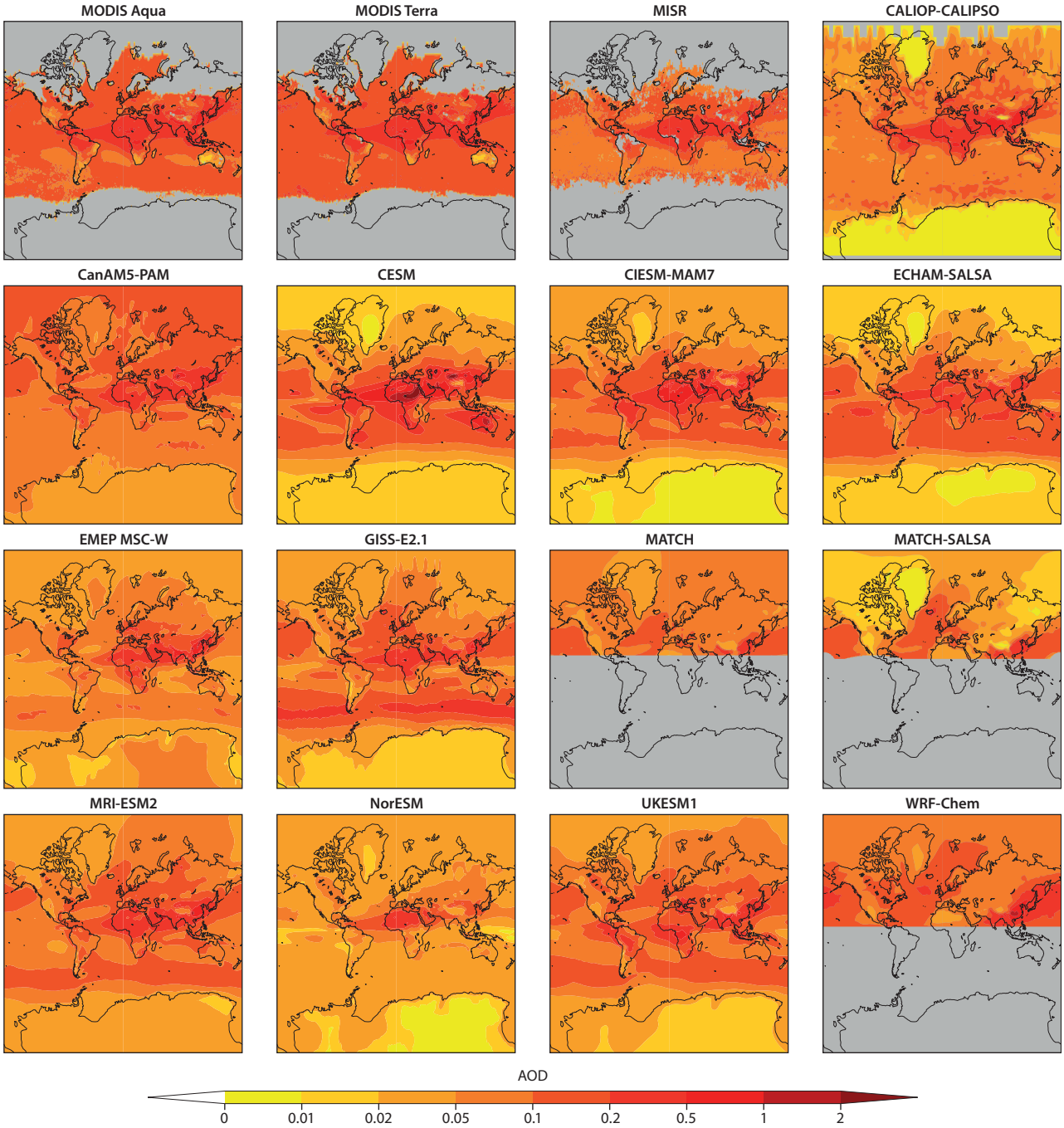

Figure A7.23 Top row: annual mean AOD from four satellite-based retreivals. Rest of panels: modeled AOD.

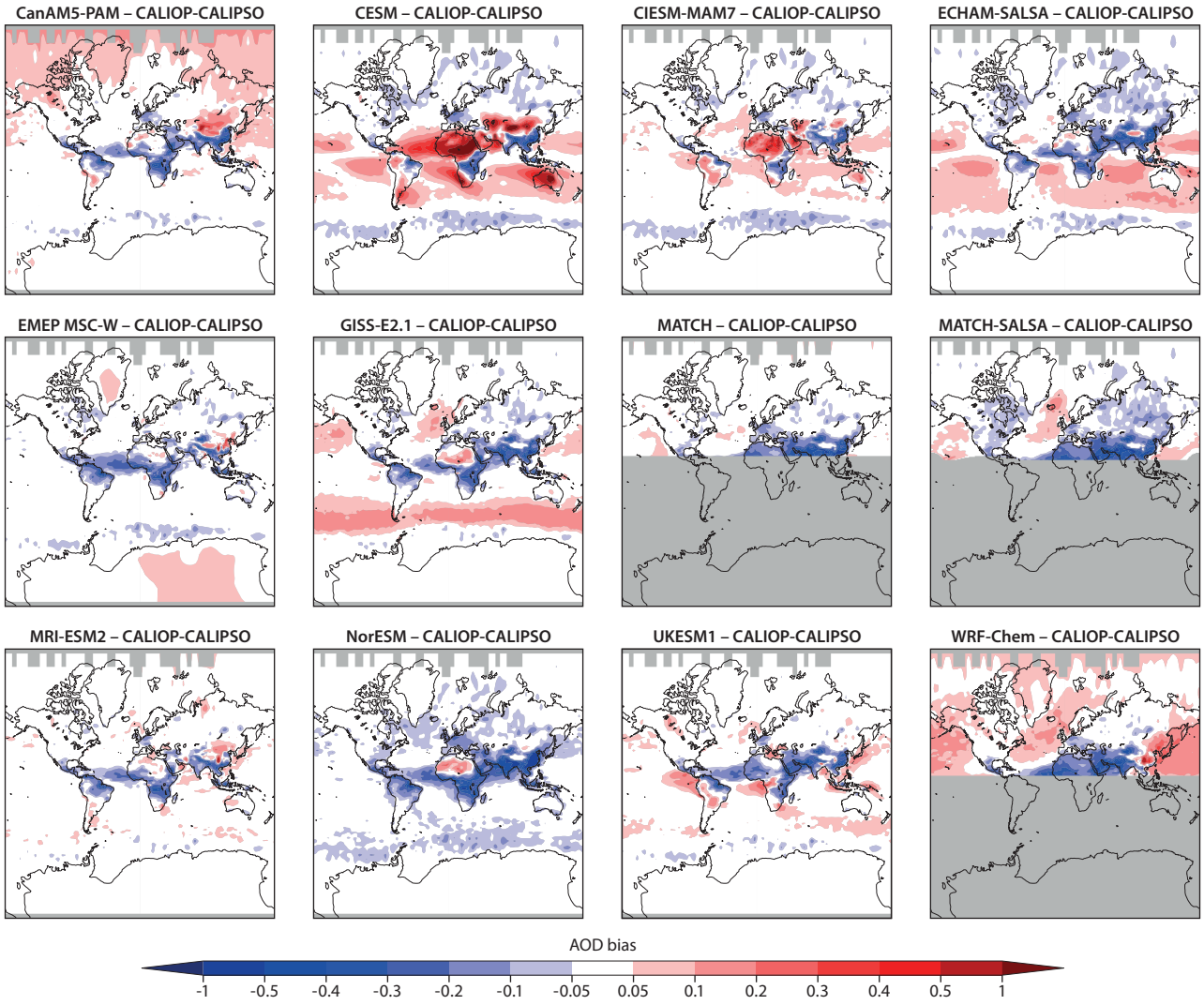

Figure A7.24 Model AOD biases compared to CALIOP-CALIPSO.

8. Simulated impacts of SLCFs on climate and air quality

Lead authors: Knut von Salzen, Stephen Arnold, Annica Ekman, Mark Flanner, Ulas Im, Zbigniew Klimont, Srinath Krishnan, Naga Oshima, Maria Sand, Steven Turnock, Cynthia Whaley

Contributing Authors: Sabine Eckhardt, Michael Gauss, Kaarle Kupiainen, Rashed Mahmood, Dirk Olivié, Luca Pozzoli, Julia Schmale, Michael Sigmond, Kostas Tsigaridis, Svetlana Tsyro, Rita van Dingenen, Barbara Winter

8.1 Introduction

Arctic warming is a manifestation of global warming, with the main driver being carbon dioxide (CO_2) radiative forcing (IPCC 2013b). Arctic warming is amplified by feedbacks from sea-ice and snow, and affected by local radiative forcings in the Arctic, including those caused by the actions of SLCFs.

The relatively short residence time of SLCFs in the atmosphere means that the resulting impacts on the global and regional climate vary greatly, both temporally and spatially (Wilcox et al., 2013; Marvel et al., 2019). In this report, methane (CH_4) is defined as a SLCF even though it has a lifetime of about ten years and is sometimes included under the category of 'well-mixed greenhouse gases'. CH_4 does not exhibit the same temporal and spatial variability as the other SLCFs with shorter lifetimes. While CO_2 and CH_4 concentrations have increased more or less steadily during the 20th and 21st centuries, the emissions of different chemical components of anthropogenic aerosol particles as well as ozone (O_3) precursors (nitrogen oxides [NO_X]; carbon monoxide, [CO]; and non-methane volatile organic compounds [NMVOCs]) first increased over Europe and North America when industrialization began but then generally decreased after the 1980s (Lamarque et al., 2010, also Chapter 2, Section 2.3; Chapter 6, Section 6.1.4 and Chapter 7, Section A7.2.2). The decrease in these air pollutants has been primarily in response to the introduction of air-pollutant control measures in these regions. Conversely, anthropogenic emissions of O_3 precursors and aerosols over South and East Asia increased between the 1950s and early 21st century. In general, there has been a shift from the largest emissions sources being in North America and Europe to being in Asia since the 1990s (Granier et al., 2011). Since 2010, efforts to mitigate poor air quality prompted by concerns for public health have led to a rapid reduction in sulfur (S) emissions in China, while India is on an opposite trajectory, its sulfur emissions having more than doubled during the same time period (Li et al., 2017).

The impacts on the Arctic climate of SLCFs with lifetimes of weeks to months often depend on where the pollution is emitted. The climate can change due to local emissions of SLCFs, transport of SLCFs into the region, and remote influences (occurring outside of the Arctic region) prompting changes to SLCFs and subsequent perturbations, for example, in the transport of heat (Krishnan et al., 2020; Acosta-Navarro, 2016; Sand et al., 2016; Yang et al., 2014; Ren et al., 2020).

In general, changes in emissions and concentrations of SLCFs are largest outside of the Arctic region, meaning that Arctic climate change through SLCFs is mainly driven by a response to remote forcings (Gagné et al., 2015; Westervelt et al., 2015). The Arctic surface temperature response to black carbon (BC) emissions in Europe and North America, for example, has been estimated to be 0.06–0.1 degrees centigrade (°C) per teragram (Tg) per year (y) (Sand et al., 2020). For Asian emissions, the Arctic response was slightly lower (0.05–0.08°C/Tg/y). The Arctic temperature change per unit of S emission was estimated to be -0.020 to -0.025°C per Tg/y in a companion paper by Lewinschal et al. (2019), perturbing sulfur dioxide (SO_2) emissions in the same regions. In general, considerable uncertainties exist with regard to the magnitude of the impact of sulfur emissions on the production of sulfate aerosols (SO_4) and their impacts on climate.

Nevertheless, local Arctic SLCF emissions and forcing changes may have a disproportionately large impact on Arctic surface temperatures per unit of emissions compared to remote emissions changes (Shindell and Faluvegi, 2009; Sand et al., 2016; Sand et al., 2013; Flanner, 2013). This means that, from a climate perspective it is still important to characterize local emissions sources and SLCF concentrations (Cho et al., 2019). For example, Kühn et al. (2020) found that BC mitigation in the Arctic Council Member states alone could reduce BC deposition in the Arctic by about 30%.

Emissions of non-CH_4 O_3 precursors contribute to both warming and cooling, in the Arctic and globally. Model simulations suggest that tropospheric O_3 has increased from pre-industrial times (1850) to the present day, although there are limited observations to validate the projected change. Output from models that contributed to the Coupled Model Intercomparison Project Phase 5 (CMIP5) indicate that the change in O_3 precursor emissions has resulted in around a 30% increase in the global tropospheric burden since 1850, which has resulted in an O_3 radiative forcing of 0.4 Watts per square meter (W/m^2) (Stevenson et al., 2013; Young et al., 2013). Previous model studies have estimated the Arctic surface temperature response over the historic period since 1890 to be between +0.2°C and +0.4°C, caused by changes in tropospheric O_3 that were mostly due to remote O_3 forcing at lower latitudes (Shindell and Favulvegi, 2009). Tropospheric O_3 produced from NO_X, VOCs and CO emissions was estimated to produce an equilibrium temperature response of 0.05°C in the Arctic, while the response estimated for O_3 produced from CH_4 oxidation was estimated to be 0.07°C (AMAP, 2015a).

Due to uncertainties in emissions, transport, residence time, mixing, chemical and physical processing, and the interactions of SLCFs with clouds, it is challenging to quantify the impact of SLCFs on Arctic climate. The internal climate variability in the Arctic is also particularly large, with strong seasonal contrasts and year-to-year fluctuations. To our knowledge, a careful evaluation of the impacts on climate of different SLCFs due to recent past and future trends in SLCF emissions has not yet been undertaken using a multi-model framework. However, the overall impact from aerosols on global and Arctic climate is likely to have been a continuous cooling until about 1980 (Fyfe et al., 2013; Wilcox et al., 2013; Najafi et al., 2015; Marvel et al., 2019). The strong reductions in North American

and European SO_2 emissions after the 1980s may have resulted in an enhanced global and Arctic warming (Yang et al., 2014; Acosta-Navarro et al., 2016). Regardless of these reductions, the increase in aerosol emissions over Asia during the same period may have masked some of the greenhouse warming (Zhao et al., 2019). Reducing all anthropogenic SO_2 emissions would likely lead to a global mean warming (0.7°C, range 0.4°C–0.8°C), while reducing all anthropogenic BC emissions would likely lead to cooling (-0.05°C, range -0.15°C–0.08°C), with amplified signals in the Arctic (Gillett and von Salzen, 2013; Stohl et al., 2015; Baker et al., 2015). Studies have reported a relatively small global temperature response to reductions in BC emissions, because of indirect and semi-direct effects partly offsetting the direct aerosol radiative effect (Baker et al., 2015; Stjern et al., 2017). However, considerable uncertainties exist for simulations of these effects in models.

In AMAP, 2015a, a multi-model ensemble was used to estimate the contributions of present-day emissions from different geographical regions and source sectors on concentrations of BC, organic carbon (OC), sulfate, and O_3. The source sectors were: domestic; energy and industry; transport; agricultural fires; grass and forest fires (natural and anthropogenic); and flaring. The models calculated the top-of-atmosphere (TOA) direct and snow/ice radiative forcing for all sectors, compounds and regions individually. The equilibrium Arctic surface temperature response to the emissions perturbations was estimated using a modified version of the regional temperature potential (RTP) concept of Shindell and Faluvegi (2009). The largest contributions to warming in the Arctic were found to come from domestic emissions originating in East and South Asia, and those from Russian grass and forest fires, and flaring. Regarding the emissions from East and South Asia, the greatest contribution to Arctic warming came from BC outside of the Arctic, while for Russia a greater proportion of the warming came from BC within the Arctic. The net Arctic surface temperature response due to the direct effect of the total emissions was estimated to be 0.35°C (0.40°C from atmospheric BC; 0.22°C from BC in snow; -0.04°C from OC; and -0.23°C from SO_4). Note that these were equilibrium responses to total emissions, and represent an upper limit of possible future temperature changes. Due to high computing costs, only one climate model was used for transient fully coupled simulations. The model ran an aggressive mitigation scenario that was designed to achieve large reductions in temperature response in the short term at the global scale for SLCFs. The reduced Arctic warming from this scenario was estimated to be 0.3°C by 2050 (compared to 2015).

While AMAP (2015a) assessed the impacts BC and O_3 on Arctic climate, AMAP (2015b) showed that strong future reductions in global emissions of CH_4 could potentially reduce Arctic surface air temperature by between 0.26°C±0.26°C and 0.40°C±0.14°C for the time period 2036–2050, relative to currently legislated methane emissions. This finding was based on simulations with three global climate models (CanESM2, CESM1, and NorESM; Christensen et al., 2019). Differences and uncertainties in these estimates have been attributed to the simulation of atmospheric chemical processes, feedbacks of natural emissions and sinks, and climate variability in the models.

For this assessment, we expanded on the work conducted for the two previous reports by 1) investigating the climate and air-quality impacts of SLCF emissions, including aerosol and O_3 precursors, and CH_4, and 2) using transient simulations with five fully coupled ocean-atmosphere general circulation models or Earth system models (hereafter referred to as ESMs). To investigate impacts of future concentrations of CH_4, BC and co-emitted species on the Arctic climate, newly developed scenarios for future SLCFs emissions were used, which are discussed in Section 8.2. The SLCF changes forecast in the ESM simulations are given in Section 8.3.2, and the climate response to these changes is given in Section 8.3.3. The modeling simulates all climate effects in detail, including aerosol-cloud interactions and ocean/sea-ice feedbacks. Furthermore, all five ESMs also incorporate feedbacks from changes in the burden of dust and sea salt, and most of them consider feedbacks from changes in dimethyl sulfide (DMS) and secondary organic aerosols (SOAs). As global emissions of anthropogenic aerosols are expected to decrease in the future, these often poorly quantified natural aerosol feedbacks may become increasingly important for the Arctic climate (Mahmood et al., 2019; Boy et al., 2019, Willis et al., 2018; Browse et al., 2014; Struthers et al., 2011). Feedbacks from fires on aerosol emissions are, however, not explicitly simulated by the models but are prescribed. Furthermore, the models do not include any natural feedbacks on CH_4 emissions.

A summary and overview of ESM results is given in Section 8.3, with the climate penalties and benefits associated with the various cooling and warming SLCF species discussed in detail in Sections 8.4 and 8.5. The air-quality impacts are also assessed. The analysis in these sections is focused on how key emitted chemical species from the Arctic Council Member states and Observer countries contribute to the net Arctic warming rate, based on results from simulations with the global ESMs, Chemistry Transport Models (CTMs), and simplified models. Finally, the impacts of changing natural SLCF emissions are discussed in Section 8.6, with conclusions drawn in Section 8.7 and recommendations made in Section 8.8.

8.2 Emissions scenarios

8.2.1 Introduction

Several of the future anthropogenic emissions scenarios from IIASA-GAINS ECLIPSE v6b (Chapter 2) were made available for the simulations of future climate and air quality summarized in this assessment. In the following sections, emissions of SLCFs, SLCF precursors, and CO_2 are analyzed to determine the impacts of anthropogenic emissions sources within large geographic regions on the Arctic climate and regional air quality.

A distinction is made between emissions from upstream oil and gas production sources (oil and gas flaring) and combined fossil-fuel and biofuel sources related to energy consumption (fossil fuel and biofuel). The former includes storage and distribution (encompassing intended venting and unintended leakage occurring during the extraction and transportation of oil and gas), the release of ventilation-air CH_4 during coal mining, and the flaring of excess gases and liquids. The latter includes: land-based emissions from residential and

commercial sources; agriculture and waste burning on fields; power plants, energy conversion and extraction; industrial combustion and processing; surface transportation; and waste processing. In addition to these upstream and downstream sources, emissions from international shipping sources (shipping) are also considered.

In the models, emissions from aviation, vegetation fires, and other natural sources – which are not part of the IIASA-GAINS ECLIPSE v6b emissions scenarios – are based on emissions specified according to the Shared Socioeconomic Pathway (SSP) 2–4.5 scenario (van Marle et al., 2017). Exceptions exist for some of the models (see the Appendix of Chapter 7 for details).

The global baseline scenario used here assumes that current legislation (CLE) to mitigate future air pollution emissions is implemented. In addition, a mitigation scenario based on the application of best available technologies to reduce future air-pollutant emissions (the maximum feasible reductions [MFR] scenario) is used. In the MFR scenario, which is for baseline activity data, the introduction of measures is not constrained by their costs but there are limitations on how quickly certain measures achieve high market penetration (Chapter 2). The CLE and MFR scenarios employ 2015 as the base year for the future projections, with identical emissions for that year.

Neither the CLE or the MFR scenario considers mitigation measures that are specifically aimed at improving the Arctic climate. Therefore, an additional scenario is also examined in Section 8.5 – aimed at mitigating SLCFs – which produces a lower net climate forcing than the MFR scenario. This so-called CFM scenario is achieved by focusing on mitigating emissions of warming SLCFs. Specifically, strong mitigation measures are assumed for CH_4 and BC that are similar to the MFR scenario. Only minor additional reductions of cooling species (OC, SO_2, and NO_X) occur, relative to the CLE scenario, which are necessary to achieve full BC mitigation. CO and VOCs are reduced strongly, while ammonia (NH_3) remains at the level of CLE measures. A brief summary of scenarios is provided in Table 8.1, for reference.

Given large-scale variations in atmospheric processes and the long-range atmospheric transport patterns of SLCFs, it is useful to broadly distinguish between emissions from western and eastern Arctic Council Member states, Arctic Council Observer countries, and other nations (Figure 8.1). Although this choice is somewhat arbitrary, it helps to facilitate the analysis of climatic changes in the Arctic (defined here as the region north of 60°N) and air quality at regional scales in Section 8.4. The consequences of changes in emissions from individual countries are beyond the scope of current modeling and analysis capabilities.

Table 8.1 Anthropogenic emissions scenarios in climate and air-quality simulations. Details are provided in Chapter 2.

Scenario	Key assumptions
CLE	Current emission-control legislation
MFR	Best available technologies to reduce future air-pollutant emissions
CFM	Best available technologies to reduce future air-pollutant emissions focusing on mitigating emissions of warming SLCFs

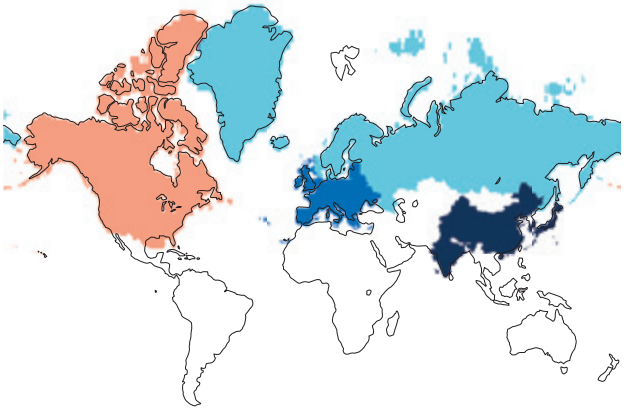

Figure 8.1 Regions selected for the analysis of impacts on climate and air quality of anthropogenic emissions from land-based sources, including oil- and gas-flaring sources. Arctic Council Member states include Canada and the USA (western Arctic Council; orange), and the Kingdom of Denmark, Finland, Iceland, Norway, the Russian Federation, and Sweden (eastern Arctic Council; light blue). European Arctic Council Observer countries and western Eurasian states are represented by a single region (rest of Europe; mid-blue). Arctic Council Observer countries in southern and eastern Asia are also represented by a single region (Asian Observers; dark blue). Impacts from international marine transport by sea and other waterways are analyzed separately for Arctic (latitudes >60°N) and non-Arctic (latitudes <60°N) regions. Note that emissions from Svalbard are omitted.

8.2.2 Historic and future changes in emissions fluxes

For 2015, 26% of global anthropogenic CH_4 emissions under the CLE and MFR emissions scenarios originated from Asian Observers. Arctic Council Member states contributed 11% (west) and 8.6% (east) to global anthropogenic CH_4 emissions, respectively. The Rest of Europe contributed 6.1%. Almost half (48%) of the emissions were generated by the Rest of the World. Most of the emissions were produced by the fossil-fuel and biofuel sector (82%). The oil-and-gas sector produced 18%. Contributions from shipping amounted to less than 0.001% (Figure 8.2, Table A8.1).

Relatively small net changes in global CH_4 emissions between 1990 and 2015 are attributable to reductions in oil-and-gas-sector emissions from eastern Arctic Council Member states, which partly compensates for increases in fossil-fuel- and biofuel-burning emissions from Asian Observer countries and the Rest of the World (Figure 8.2, Table A8.2).

Under the CLE scenario, global emissions of CH_4 are projected to increase steadily by 32% from 2015 to 2050, mainly due to a ramping up of fossil-fuel and biofuel emissions from Asian Observer countries and the Rest of the World (Table A8.3). Alternatively, with maximum feasible reductions in emissions across a broad range of regions and sectors (MFR scenario), global emissions of CH_4 are projected to decrease by 30% from 2015 to 2050, after an initial increase in emissions (Table A8.4).

The lifetime of CH_4 in the atmosphere is influenced by chemical reactions, which involve reactive gases that control tropospheric hydroxyl radical concentrations, including CO, VOCs, and NO_X (Prather et al., 2012; Naik et al., 2013). All regions considered here contributed to increases in global NO_X emissions over the 20th century, corresponding to a steady increase in fossil-fuel and biofuel combustion. However,

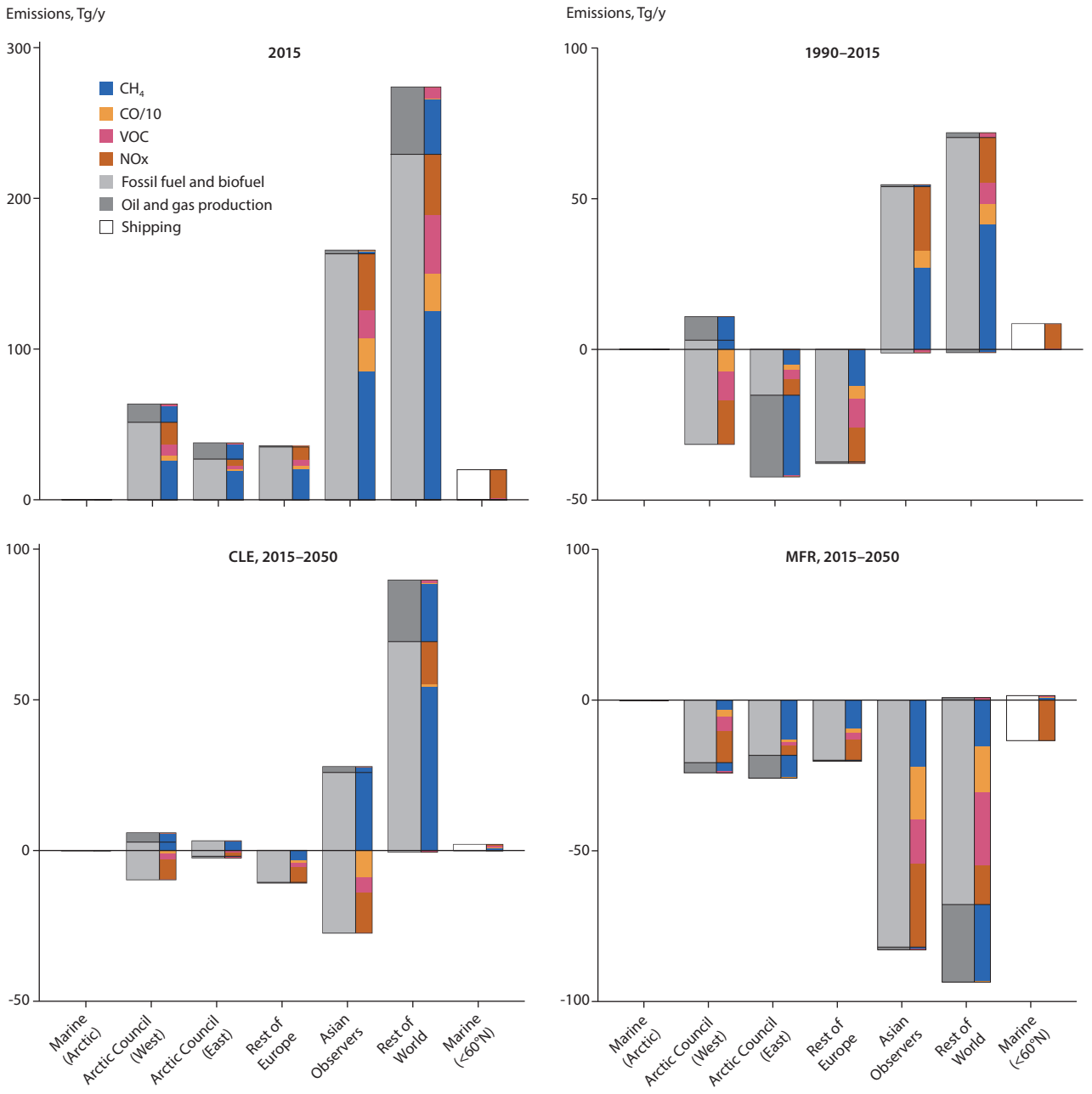

Figure 8.2 Summary of regional emissions in Tg/y of CH_4, CO, VOCs, and NO_X in 2015 (top left), changes in emissions between 1990–2015 (top right), and during 2015–2050 under the CLE (bottom left) and MFR (bottom right) scenarios. CO is scaled by a factor of 0.1 for clarity. Grey shades are used to distinguish contributions from different sectors. See Chapter 2 for definition of the sectors.

NO_X emissions from western Arctic Member states and the Rest of Europe declined between 1990–2015 (Table A8.2). Emissions of CO and VOCs followed similar trends as NO_X emissions, reflecting policy actions targeting air pollutants in Europe and North America. Under the MFR scenario, substantial reductions in emissions of NO_X, CO, and VOCs are projected to occur between 2015–2050 (by -60%, -68%, and 57%, respectively; Table A8.4).

In 2015, about 8% of the global BC emissions under the CLE and MFR scenarios originates from Arctic Council Member states (3% from eastern and 4.8% from western Arctic Council Member states, Figure 8.3, Table A8.5) – figures that exclude emissions sources that are predominantly caused by natural processes. In comparison, Asian Observer countries and the Rest of the World generated 36% and 50% of the global anthropogenic BC emissions, respectively. Non-Arctic and Arctic shipping contributed 0.7% and 0.007% to the global BC emissions, respectively. The fossil-fuel and biofuel sectors account for almost all of the emissions (97%). However, large regional differences exist. The oil-and-gas sector accounts for 35% of total BC emissions from eastern Arctic Council Member states for 2015, for example.

Total emissions of BC changed little between 1990–2015 (-0.4%), with steady increases in emissions from the Rest of the World but reductions in all other regions during this time period (Figure 8.3, Table A8.6). In the future, global BC emissions are projected to decrease by between 17% (CLE) and 77% (MFR), largely due to reductions in fossil-fuel and biofuel combustion (Tables A8.7 and A8.8), mainly in Asian Observer countries (-51% [CLE] to -90% [MFR]) and the Rest of the World (+14% [CLE] to -66% [MFR]). Oil and gas sector emissions from eastern Arctic Council

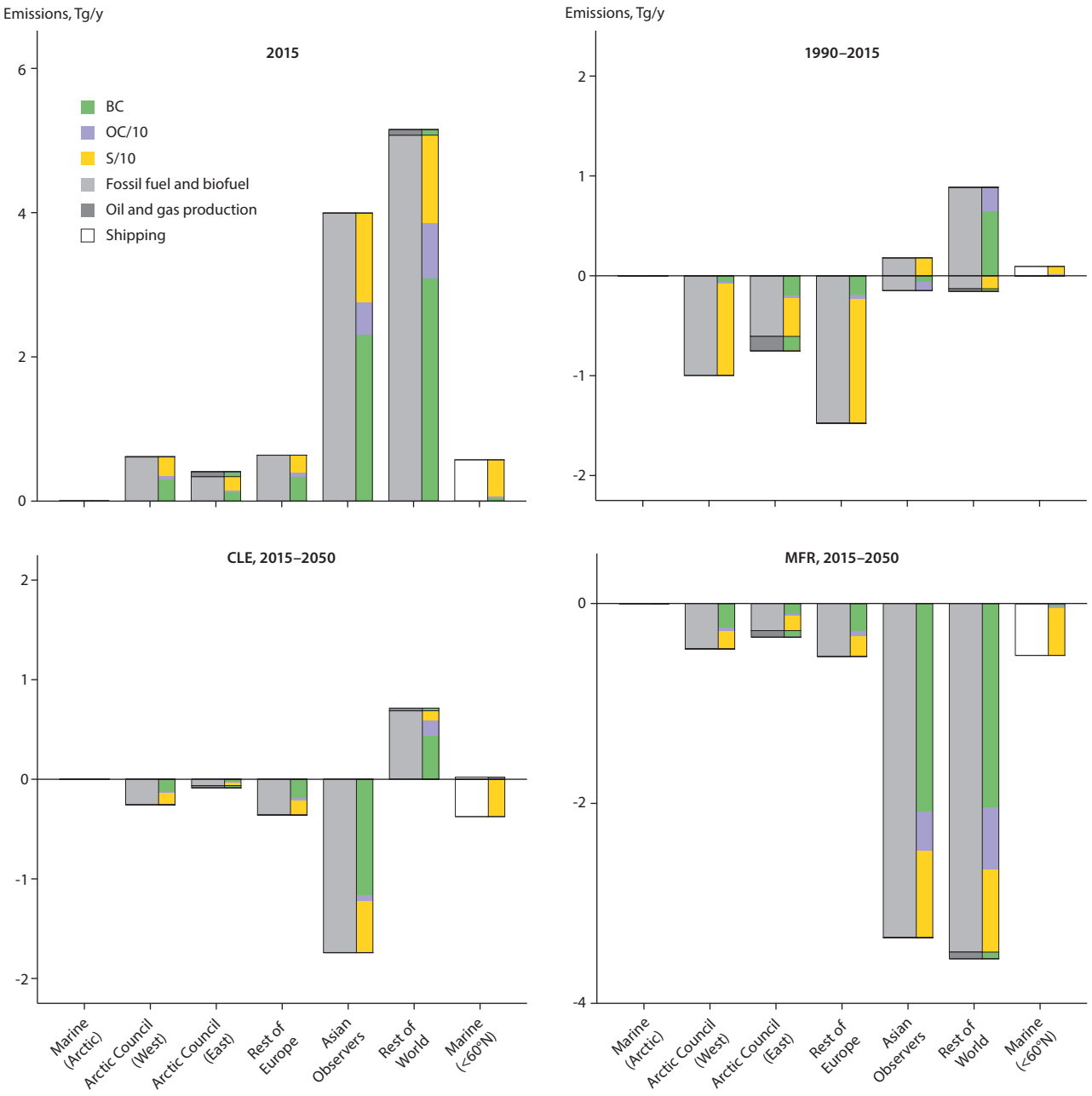

Figure 8.3 Regional emissions in Tg/y of sulfur (S), organic carbon (OC) and black carbon (BC) in 2015 (top left), changes in emissions between 1990–2015 (top right), and during 2015–2050 according to the CLE (bottom left) and MFR (bottom right) scenarios. Emissions of OC and S are scaled by a factor 0.1 for clarity. Grey shades are used to distinguish contributions from different sectors.

Member states are projected to decrease by between 33% (CLE) and 96% (MFR).

Sulfate aerosols are produced from oxidized sulfur compounds during the combustion of fossil fuels and biofuels, and subsequent chemical reactions in the clear atmosphere and in clouds. Most of the sulfur is emitted into the atmosphere in the form of SO_2. About 12% of global sulfur emissions in 2015 originated from Arctic Council Member states (7.1% from eastern and 5.4% from western Arctic Council Member states, Figure 8.3, Table A8.5). Asian Observer countries and the Rest of the World generated 34% and 33% of global sulfur emissions, respectively. The fossil-fuel and biofuel sector, and shipping, account for nearly all the emissions (86% and 14%, respectively).

Sulfur emissions were substantially higher in 1990 than in 2015 in the Arctic Council Member states and the Rest of Europe (by 354% for western Arctic Council Member states; 196% for eastern Arctic Council Member states; 508% for the Rest of Europe), consistent with efficient policy actions targeting air pollutants and acid deposition.

In the future, sulfur emissions are projected to decline steadily for nearly all regions and sectors, including emissions from global shipping (Figure 8.3). Emissions reductions in Asian Observer countries are particularly large, especially under the MFR scenario, where projected emissions decline by 74% (global mean) and 70% (Asian Observers) between 2015–2050 (Table A8.8).

8.2.3 Changes in the abundance of CO_2 and CH_4

The abundance of global mean CO_2 is projected to steadily increase from 2015 to at least 2050 under the SSP2–4.5 scenario, used here for non-SLCF species (Figure 8.4), based on simulations with a climate and air-quality emulator (Box 8.1). The projected increase is largely driven by increasing emissions from Asian Observers and the Rest of the World, although there are considerable contributions from emissions sources in western Arctic Council Member states and the Rest of Europe, too. In the emulator, lifetimes of CO_2 are specified for different carbon sink processes in order to empirically account for the combined effects of these processes on global mean CO_2 mass budgets.

While the results from exploratory simulations of the CH_4 lifecycle in ESMs are encouraging, CH_4 abundances are commonly simulated using reduced-complexity models, including emulators (Chapter 7.1.1). For this assessment, the emulator (Olivié et al., 2021) was also used to simulate changes in global mean CH_4 tropospheric abundance based on specified anthropogenic emissions of CH_4, NO_X, CO, and VOCs. The emulator accounts for changes in the lifetime of CH_4 in the atmosphere, which result from changes in emissions of NO_X, CO, and VOCs. However, the simulated CH_4 lifetime does not respond to changes in the rate of CH_4 loss in the stratosphere, CH_4 uptake by soils, reactions with tropospheric chlorine, atmospheric temperature, or feedbacks in natural sources and sinks of CH_4. Global mean natural emissions of CH_4 are specified as 202 Tg/y (Prather et al., 2012).

The global mean observed abundance of CH_4 rose slowly between 1990–2015 (Figure 8.5), which is consistent with relatively small changes in anthropogenic CH_4 emissions over this period. Simulated results are largely consistent with the observed changes. In particular, the time period spanning 1999–2007 represents an unusual hiatus in the increase in abundance of CH_4, which has been previously linked to emissions reductions due to the break-up of the Soviet Union in 1991.

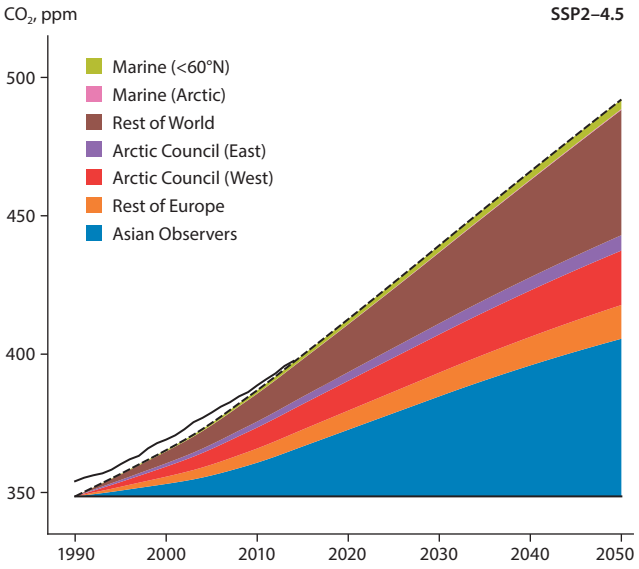

Figure 8.4 Changes in simulated volume mixing ratios of CO_2 under the SSP2–4.5 scenario (dashed black line). Observed mixing ratios (Meinshausen et al., 2017) are shown for comparison (solid black line). Contributions of emissions from different regions to simulated mixing ratios are indicated by the colored shading. The simulated values match the observed ones in 2014 by construction of the emulator. Note that due to the relatively small magnitude of the emissions from Arctic marine shipping, these contributions may not be discernible in the graph.

Rising CH_4 emissions from Asian Observer countries and the Rest of the World were largely responsible for a slowly increasing abundance of CH_4 between 1990–2015, with additional contributions from western Arctic Council Member states (Section 8.2.2). Increases in emissions from these regions were partly compensated for by declining emissions from eastern Arctic Council Member states and the Rest of Europe, which considerably slowed the net CH_4 growth rate over this period.

Box 8.1: Climate and air-quality emulator

Assessing the impacts of emissions controls on air-pollutant concentrations and climate in this report included using results from simulations undertaken with a climate and air-quality emulator, alongside results from 3D climate and air-quality grid-point models. The emulator is based on specified relationships between concentrations and radiative forcing responses to emissions changes, which are derived from simulations with the comprehensive 3D climate and air-quality grid-point models. The emulator consists of model components for climate and air quality (Olivié et al., 2021).

The climate emulator component is based on linearized and highly approximated mass and energy balances of the climate system. It simulates the forced response in regional mean surface air temperature to a series of instantaneous pulse emissions of different chemical species, which affect the energy balance of the climate system by changing radiative forcings of greenhouse gases and SLCFs in the atmosphere. The temporal evolution of the regional mean temperature in response to the pulse emission is approximated using a specified climate sensitivity, time scales of heat dissipation, and other parameters derived from simulations with more comprehensive models, in addition to regional temperature potentials (RTPs) which were previously used for AMAP (2015b). Furthermore, radiative forcings of CO_2 and CH_4 are simulated, based on global atmospheric mass budgets that account for key physical- and chemical-loss processes. Given the simplicity of the calculations, the emulator cannot be used to simulate changes in sea ice, precipitation, or other important climate variables. Further, natural climate variability on inter-annual to multi-decadal scales is not simulated; instead, results from simulations with the 3D climate models are used for that purpose.

The air-quality emulator component is based on pre-calculated relationships between emissions and concentration responses from more comprehensive 3D grid-point models. Source-receptor relationships are used to simulate impacts of emissions on annual mean air-pollutant concentrations. As with the climate emulator component, efficiency of calculations is achieved by applying rigorous approximations of complex physical and chemical atmospheric processes.

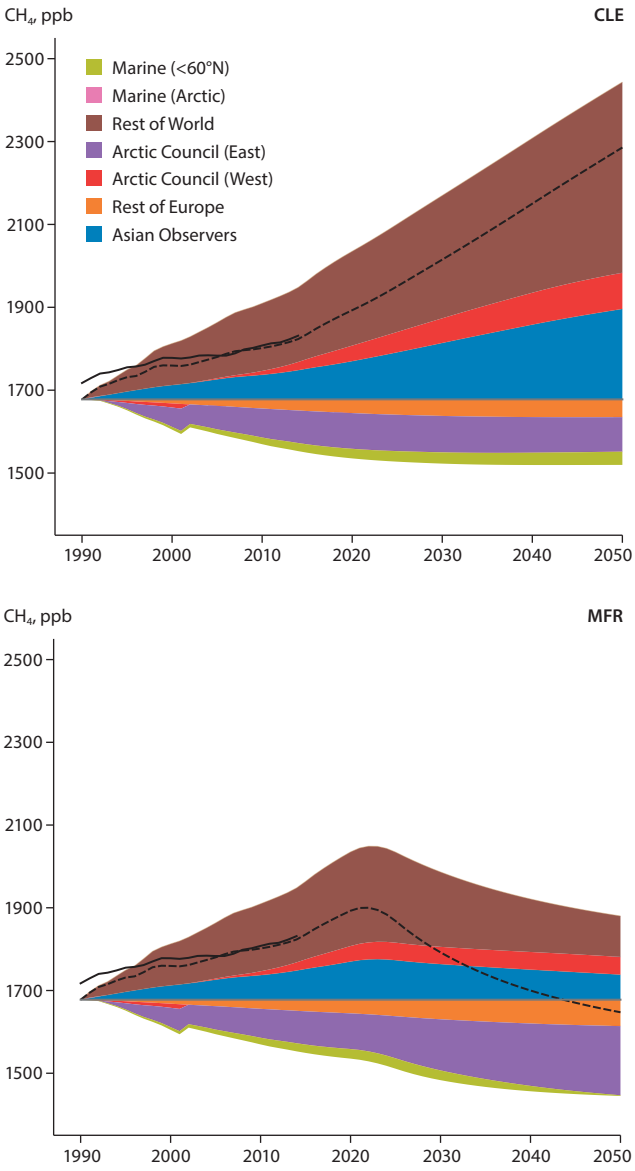

Figure 8.5 Changes in simulated global and annual mean volume mixing ratios of CH_4 according to the CLE (upper) and MFR (lower) scenarios (dashed black lines). Observed mixing ratios (Meinshausen et al., 2017) are shown for comparison (full black lines). Note that, due to the relatively small magnitude of the emissions from Arctic marine shipping, these contributions may not be discernible in the graph.

Increasing NO_X emissions from marine transport caused small reductions in the lifetime of CH_4 between 1990–2015. This also helped to slow the net CH_4 growth rate, despite increasing CH_4 emissions from marine transport sources.

The simulated increase in CH_4 abundance during 2015–2020, according to both scenarios, is largely consistent with recent observations of a more rapidly increasing trend in 2019 (Data ref. 8.1). With current legislation (under the CLE scenario), the CH_4 abundance is projected to steadily increase beyond 2020 at least until until 2050. The change is largely attributable to increases in CH_4 emissions from Asian Observers and the Rest of the World, although emissions from western Arctic Council Member states also contribute to the increase. With maximum feasible reductions in SLCF emissions (under the MFR scenario), the abundance of CH_4 is projected to decline from the 2020s until at least 2050, eventually reaching levels last observed in the 1990s. CH_4 emissions and abundance from sources in Asian Observer states and the Rest of the World are projected to decrease from 2015 to 2050. The reductions in global mean CH_4 abundance are largely due to decreases in emissions from Asian Observers and the Rest of the World, combined with continued reductions in emissions from eastern Arctic Council Member states over this period. Despite emissions reductions from Asian Observers and the Rest of the World under the MFR scenario, CH_4 abundance from sources in Asian Observer states and the Rest of the World is still projected to be higher in 2050 than in 1990. This is due to the delay in emission changes being reflected in the abundance, as a consequence of the roughly nine-year atmospheric half-life of CH_4.

ESM simulations in the following sections employ specified global and annual mean CH_4 and CO_2 abundances that were generated using a method similar to the emulator used in this and subsequent chapters (Olivié et al., 2021). However, a linear increase in global mean temperature of 0.2°C per decade from 2019 to 2050 was assumed for the calculation of specified CH_4 abundances in the ESMs, which approximately matches simulated warming rates for the SSP2–4.5 scenario (Section 8.3.3). This leads to a lower projected increase in the specified CH_4 abundances between 2015–2050 (356 ppb versus 417 ppb, for the CLE scenario), compared to the emulator results that are discussed in this chapter. In the ESMs, the specified CH_4 abundance in 2050 differs by 625 ppb between the CLE and MFR scenarios, compared to a difference of 614 ppb in the emulator simulations.

The specified annual and global mean abundance of CO_2 in the ESMs increases from 399.9 ppm from 2015 to 507 ppm in 2050, according to the SSP2–4.5 scenario (Meinshausen et al., 2020), whereas the emulator simulates an increase to 493 ppm in 2050 for the same emissions. These differences are caused by differences in parameterizations of CO_2-related processes in the reduced-complexity models.

The analysis above does not account for future changes in natural emissions that are associated with climate change. According to AMAP (2015b) natural emissions changes in an 'extreme' case would lead to a 357 ppb increase in global mean CH_4 abundance by 2050. This corresponds to about 60% of the 614-ppb difference between the CLE and MFR scenarios. Consequently, any additional warming from natural CH_4 emission feedbacks would likely be smaller than temperature changes associated with differences in anthropogenic emissions between these scenarios. However, substantial uncertainties in natural emissions exist (Section 8.6).

8.3 Future changes in global and Arctic climate systems

8.3.1 Introduction

Five fully-coupled ESMs with interactive ocean and sea-ice components were used to determine the full climate impacts of SLCF emissions scenarios, including on temperature, precipitation, and sea ice. These are: NorESM (three ensemble members), CESM2 (four ensemble members), MRI-ESM2 (five

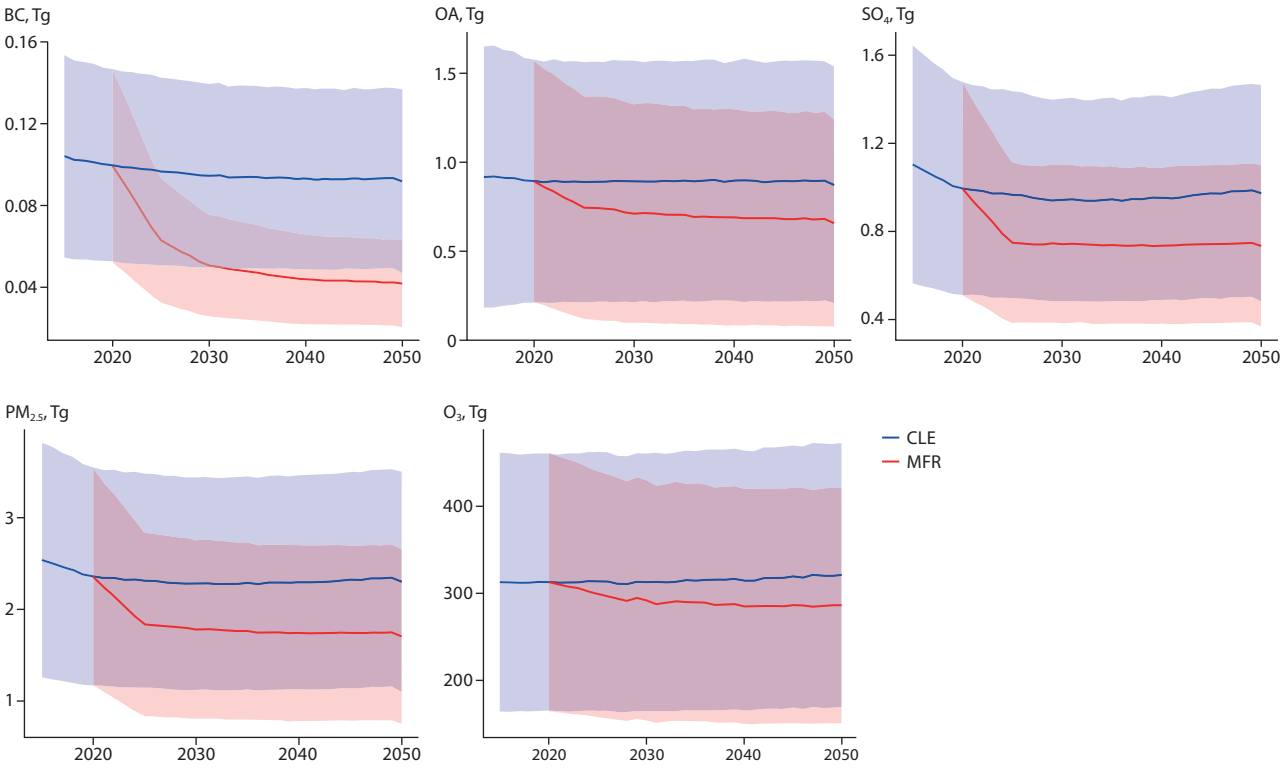

Figure 8.6 Multi-model means (MMMs) and spread of global BC, organic aerosol (OA), sulfate (SO_4), anthropogenic $PM_{2.5}$ and O_3 burdens under the CLE and MFR scenarios. The figure shows MMMs over the number of ensembles from all ESMs, along with the standard deviation.

ensemble members), GISS-E2.1 (three ensemble members), and UKESM1 (three ensemble members). The models were initialized from the Coupled Model Intercomparison Project Phase 6 (CMIP6) historical simulations. The simulations for four models (CESM2, MRI-ESM2, GISS-E2.1, and UKESM1) were branched off from the year 2000 and NorESM was branched off from 2011. Between the branch-off time and 2020, all simulations follow the IIASA-GAINS ECLIPSE V6b emissions scenarios CLE, while after 2020 the CLE and MFR runs follow their respective, diverging emissions pathways. Results are shown for 2015–2050.

8.3.2. Multi-model mean SLCF burden, air quality, and top-of-atmosphere radiative forcing changes

8.3.2.1 Burdens

The multi-model mean (MMM) global and Arctic burdens of BC, OA, SO_4, anthropogenic fine particulate matter ($PM_{2.5}$), and O_3 are presented in Figures 8.6 and 8.7, respectively. All individual aerosol species and $PM_{2.5}$ decrease under both the CLE and MFR scenarios, with MFR leading to greater reductions. The figures also show the large variability between the ESMs. The CLE scenario reduces the global [Arctic] aerosol burdens by 5–12% [17–22%] by 2050 compared to 2015, while the MFR scenario leads to reductions of 10–48% [8–44%] by 2050, with the largest relative changes simulated for the BC burdens. In contrast, under CLE, the tropospheric O_3 burden is projected to rise again after 2030, leading to a slight increase of 2.5% [0.5%] compared to 2015, while MFR leads to an initial sharp reduction of 7% [9%] in 2030 followed by a slight increase – giving an overall reduction of 9% [10%] in 2050 compared to 2015. The burdens simulated by the ESMs for each component are shown in Figures A8.1, A8.2, A8.3, A8.4, and A8.5 in the Appendix.

8.3.2.2 Projected future radiative forcings of individual aerosol components

Among the five ESMs, GISS-E2.1 was the only model to perform the simulations with a double call to the radiation code, facilitating attribution of the total direct aerosol radiative forcing to individual components (BC, OC, SO_4, and nitrate [NO_3]). Figures 8.8 and 8.9 show the TOA longwave and shortwave direct radiative forcings, and contributions of the individual aerosol species (BC, OC, SO_4, NO_3, and total, respectively) for the CLE scenario, as well as the difference between the MFR and CLE scenarios, calculated by GISS-E2.1.

Globally, the TOA longwave radiative forcing due to aerosols stayed at around 0.060±0.003 W/m^2 between 2015 and 2050 in the CLE scenario (Figure 8.8), mainly due to an increase in nitrate aerosol (NO_3) forcing and a decrease in SO_4 forcing, with BC and OC forcings remaining constant. Over the Arctic, the total aerosol forcing in the CLE scenario increased slightly from 0.042±0.003 W/m^2 in 2015 to 0.043±0.003 W/m^2 in 2050. In the MFR scenario, the model projects a rapid decrease in both the global and Arctic TOA longwave forcing from all aerosol species between 2020–2025, leading to a further decrease of the total aerosol forcing by 0.010 W/m^2, which remains at that level until 2050, with some year-to-year variability.

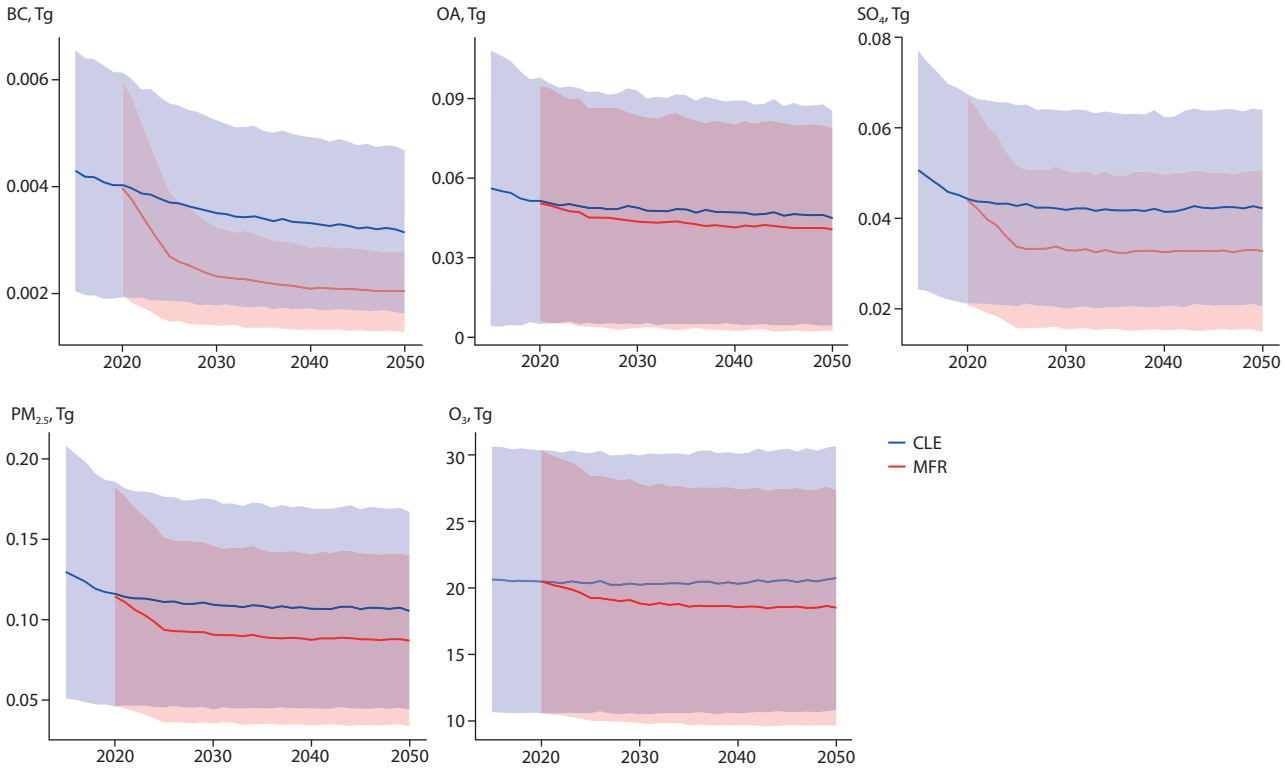

Figure 8.7 Multi-model means and spread of global BC, organic aerosol (OA), sulfate (SO_4), anthropogenic $PM_{2.5}$ and O_3 burdens over the Arctic in CLE and MFR scenarios. The figure shows multi-model means (MMMs) over the number of ensembles from all ESMs, along with the standard deviation.

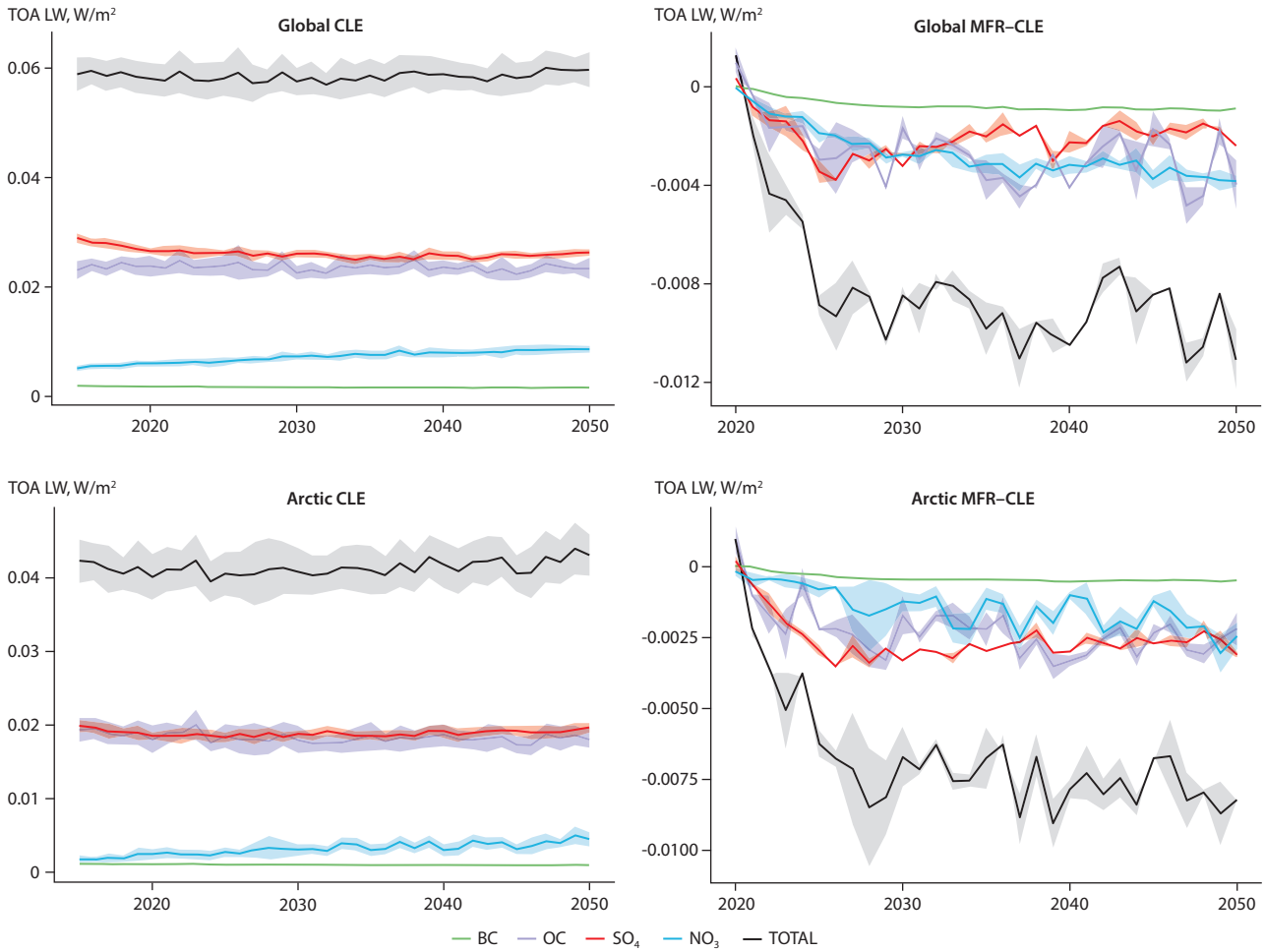

Figure 8.8 Global (upper panel) and Arctic (lower panel) TOA longwave (LW) direct radiative forcing for the different aerosol species (in W/m²), as simulated by the GISS-E2.1 model. The mean over three ensembles is shown, along with the standard deviation. The left panel shows CLE for 2015–2050, while the right panel shows the difference between MFR and CLE scenarios (MFR–CLE) for 2020–2050.

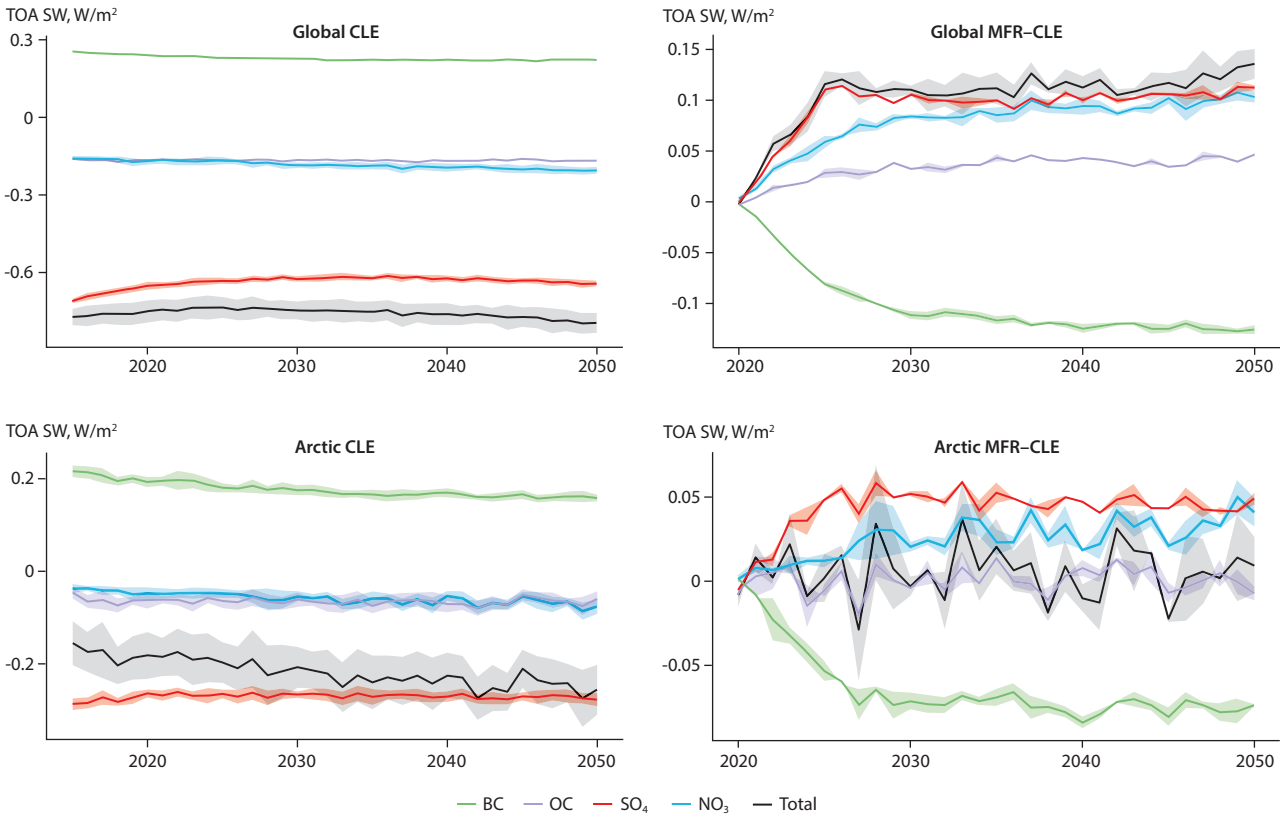

Figure 8.9 Global (upper panel) and Arctic (lower panel) TOA shortwave (SW) radiative forcing for the different aerosol species (in W/m²) as simulated by the GISS-E2.1 model. The mean over three ensembles is shown, along with the standard deviation. The left panel shows CLE for 2015–2050, while the right panel shows the difference between MFR and CLE scenarios (MFR–CLE) for 2020–2050.

Regarding the TOA shortwave radiative forcing (Figure 8.9), the CLE scenario produces a slight increase in global total aerosol forcing in 2050 (-0.794±0.038 W/m²) compared to the 2015 forcing (-0.772±0.032 W/m²), which is mainly driven by the increase in the negative NO_3 forcing, with the decreases in the negative SO_4 and the positive BC forcing counterbalancing each other. Over the Arctic, the total aerosol forcing decreases throughout the simulation period, driven mainly by the decrease in BC forcing, while forcings due to other aerosol types remain constant. The MFR scenario leads to a net increase of TOA shortwave aerosol forcing, in particular during 2020–2025, of 0.012 W/m². This is driven by the larger decrease in SO_4 forcing, together with OC and NO_3 forcings, while the decrease in BC forcing is smaller than the change in shortwave forcing from other species. Over the Arctic, the BC and SO_4 forcings compete, with the decrease of the positive BC shortwave forcing outweighing the decrease in the negative shortwave SO_4 forcing. This leads to the net aerosol forcing being around the same level projected under the CLE scenario.

8.3.3 Climate response to future scenarios

In this section, trends are presented for the temperature at the lowest atmospheric level (here referred to as the near-surface air temperature [NSAT]), precipitation, and sea-ice changes for all ESMs.

Figure 8.10 shows the global mean and Arctic mean NSAT anomalies relative to the 2015–2025 mean for the CLE and MFR emissions scenarios, with SSP2–4.5 scenario for non-SLCF emissions, as detailed in Section 8.2. Over the 2010–2050 period, global mean temperatures are projected to increase by about 1.0°C, while Arctic temperatures are projected to increase by more than twice the global mean. The UKESM1 model projects greater warming than the other four models, which can be explained by its high-equilibrium climate sensitivity (Zelinka et al., 2020).

To put these changes in the context of other ESMs, Figure 8.11 shows the changes in Surface Air Temperature (SAT; 2-m air temperature) for the 34 CMIP6 models that were available as of March 2020. Comparison with Figure 8.10 shows that, while CMIP6 models employ different scenarios for SLCFs (Chapter 2), the mean of the MFR and CLE simulations project warming at a very similar rate to the mean of the 34 CMIP6 models. The UKESM1 MFR and CLE simulations project warming at a similar, or slightly faster, rate than the fastest warming projected by the CMIP6 models.

With regards to quantifying the impacts of the CLE and MFR emissions scenarios on warming rates, comparison of the dashed (MFR) and solid (CLE) lines in Figure 8.10 shows this impact to be small. Figure 8.12 (a) shows that by 2045–2050, the ensemble median global NSAT difference is close to zero, while, averaged over the Arctic, four of the five models are slightly warmer under the MFR scenario than the CLE one, although this warming is not statistically significant for any of the models. Figure 8.12 (b) shows NSAT long-term linear trends (2015–2050). For both the global and Arctic means, there are no statistically significant different trends between the MFR and CLE scenarios. Furthermore, spatial evaluation of the trends shows that, while northern

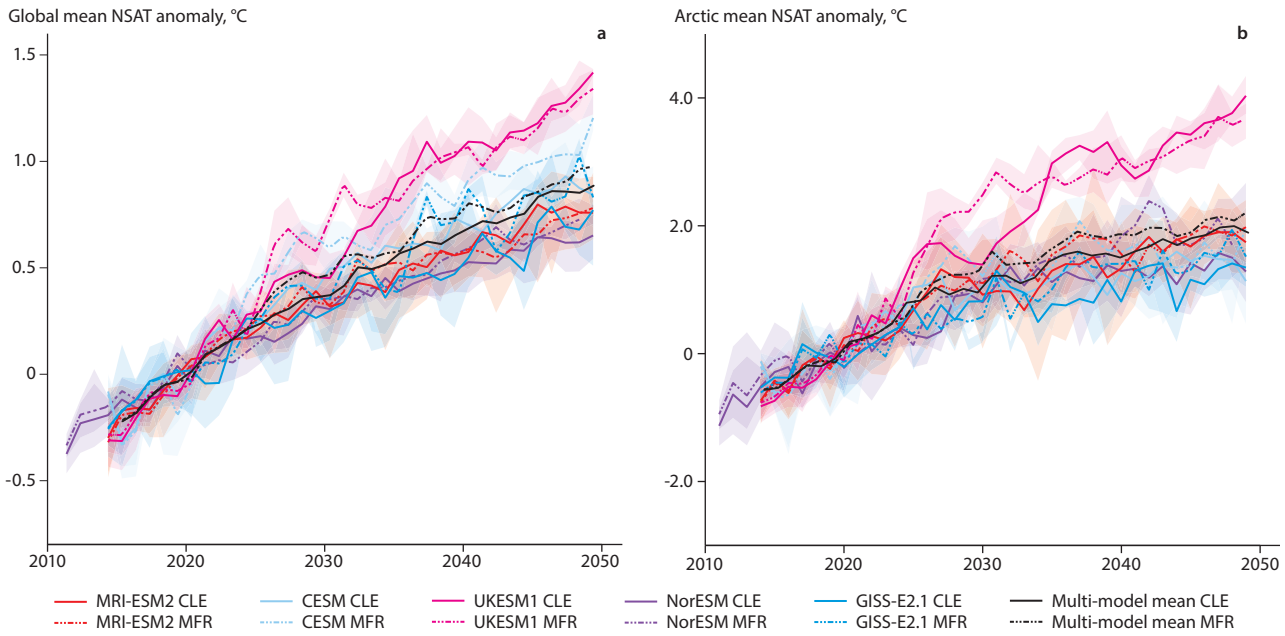

Figure 8.10 (a) Global mean and (b) Arctic mean near surface air temperature (NSAT) anomaly compared to the 2015–2025 mean in CLE (solid) and MFR (dashed) simulations. Note the different scales in temperature anomalies between (a) and (b). Lines represent means from single model ensembles, with shading depicting the ranges.

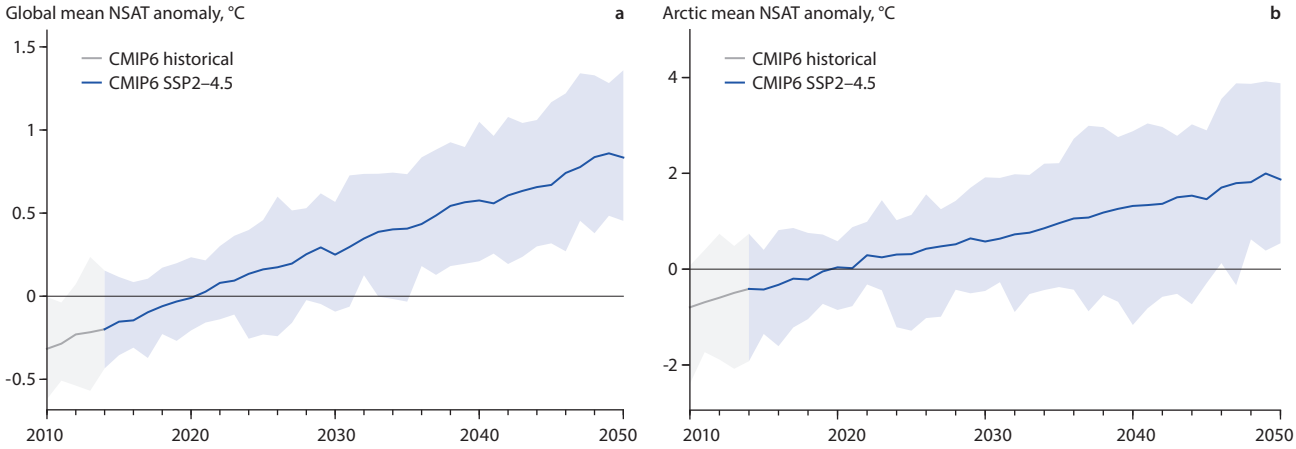

Figure 8.11 (a) Global mean and (b) Arctic mean near surface air temperature (NSAT) anomaly compared to the 2015–2025 mean in CMIP6 simulations. Note the different scales in temperature anomalies between (a) and (b). The lines represent the mean of 34 CMIP6 models and shading depicts the multi-model range.

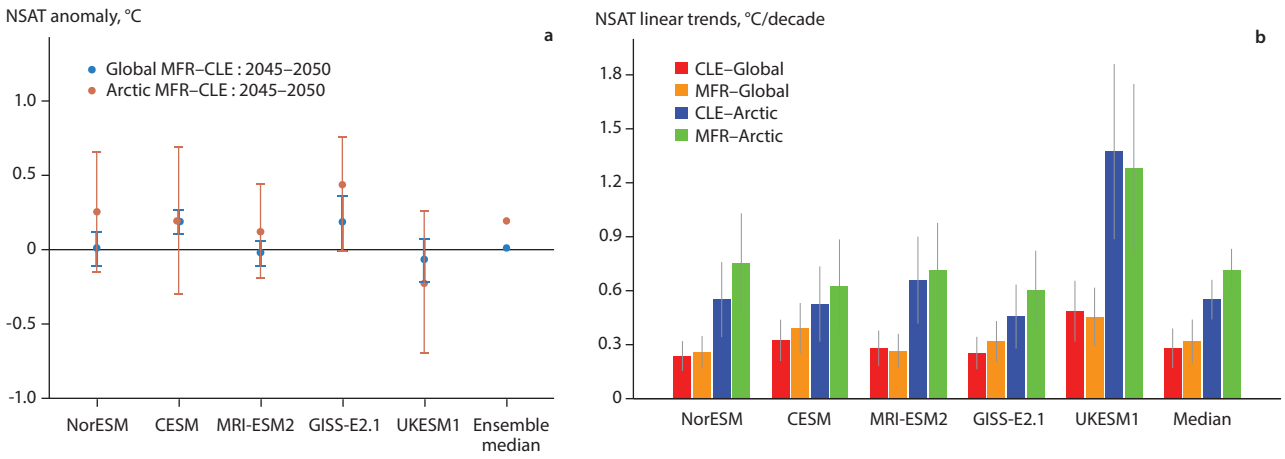

Figure 8.12 (a) Arctic and global mean NSAT change for the MFR scenario compared to CLE, with positive values indicating where the MFR scenario is warmer than the CLE scenario. Vertical bars represent the 95% confidence interval of the differences. The confidence intervals for all models cross the zero line, indicating that the differences are not statistically significant. (b) Linear trends for Arctic and global mean NSAT change from 2015–2050 for CLE and MFR for the different models. Vertical lines represent the 95% confidence interval of the trends. The overlap between the confidence intervals for the two scenarios for all models indicates that the trends are statistically indistinguishable.

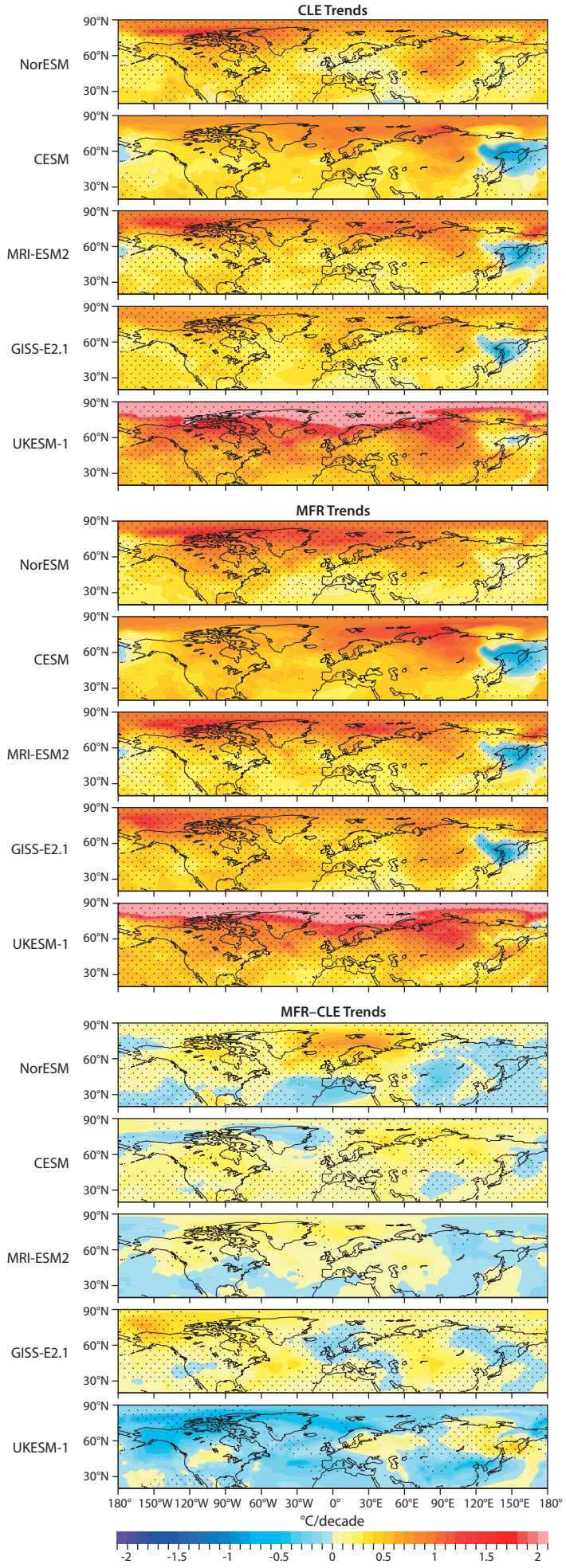

Figure 8.13 Spatial patterns for linear trends for NSAT change from 2015–2050 for the CLE and MFR scenarios, and the difference between them. Stippling indicates significance, as calculated using the Mann-Kendall trend test.

Europe is projected to a warm slightly across the different models under the MFR scenario, there are no regions that have a consistent and significant pattern of temperature change across all models (Figure 8.13).

A reduction in Arctic sea-ice extent of ~1–3 x 10^{12} m^2 is observed across most models (Figure 8.14) but the change projected by UKESM1 is the largest, at ~5 x 10^{12} m^2. The responses for the CLE and MFR scenarios are similar to each other, and the differences between the two scenarios are not statistically significant.

Global mean precipitation (Figure 8.15) increases towards 2050 following the trend of warmer surface temperatures (Figure 8.10), as has been predicted for warmer climates (Trenberth, 1998). The difference between the two scenarios is small, but there is a slightly larger increase in precipitation under the MFR scenario than the CLE scenario (Figure 8.16). This matches the temperature difference between the two scenarios, where the MFR scenario is slightly warmer than the CLE scenario. The small increase in precipitation under the MFR scenario is also observed in the difference in precipitation climatology across most months in the Arctic for 2045–2050 (Figure 8.17), although most of these changes are not significant. No significant changes to cloud cover were found.

To summarize the above findings, all ESMs project warming during 2020–2050, similar to the CMIP6 ESMs. The multi-model NSAT responses for the MFR and CLE emissions scenarios are similar, with a small (non-statistically-significant) warming under the MFR scenario compared to CLE. The precipitation response follows a similar pattern to temperature, with a small (non-statistically-distinguishable) increase under the MFR scenario, compared to CLE. There does not seem to be any difference in the Arctic sea-ice extent for the two scenarios. Thus, from an ESM perspective, the difference between the two SLCF emissions strategies on global and Arctic climate variables are small. This is further evaluated using the emulator approach in Section 8.4.5.

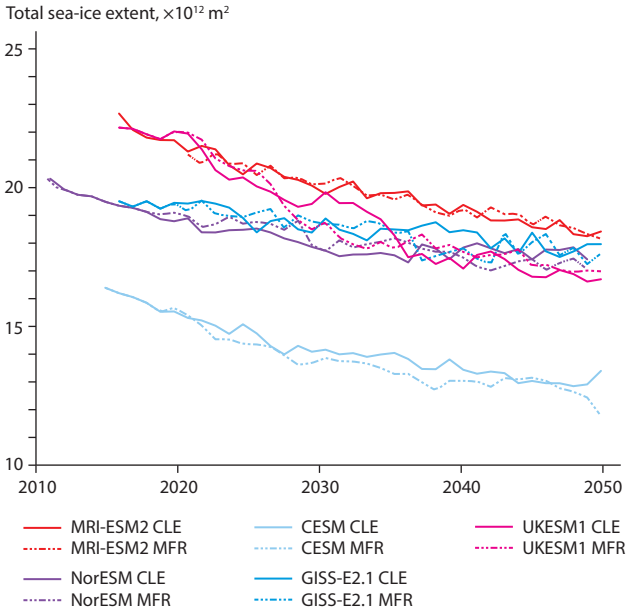

Figure 8.14 Changes in the total Arctic sea-ice extent for the ESMs for CLE (solid) and MFR (dashed) scenarios.

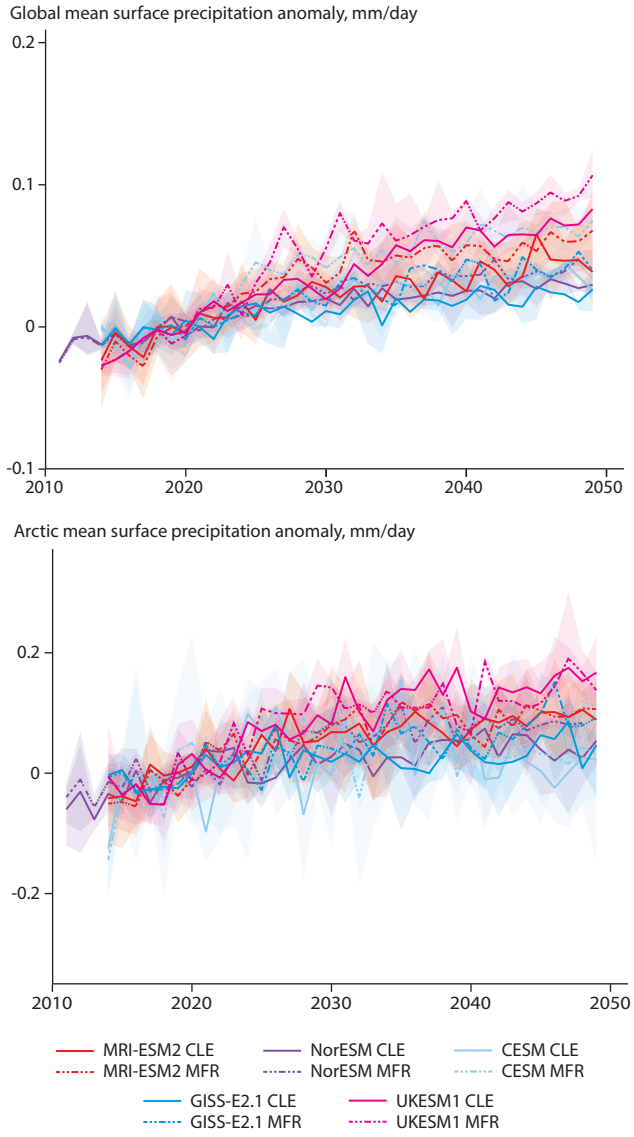

Figure 8.15 Global and Arctic mean total surface precipitation anomalies (2015–2025) for all models for the CLE (solid) and MFR (dashed) scenarios. Shading indicates the range for the individual ensemble members.

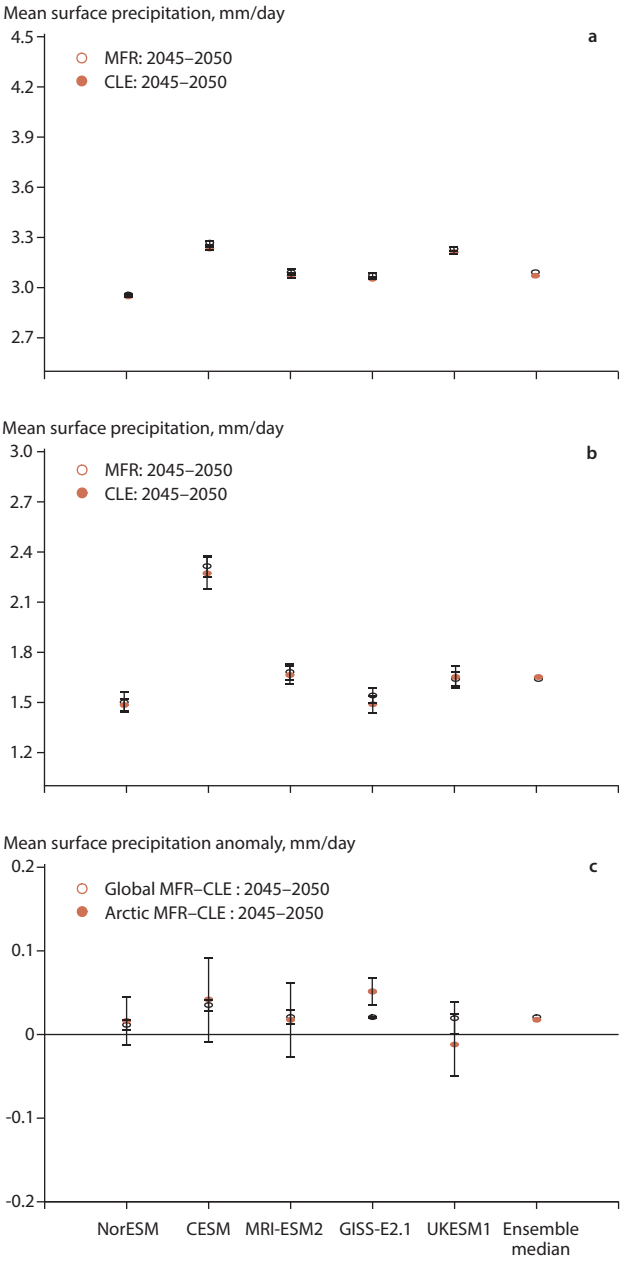

Figure 8.16 Global mean (a) and Arctic mean (b) precipitation (averaged over 2045–2050) for the MFR and CLE scenarios, and the difference between the global mean and Arctic mean precipitation (c) (averaged over 2045–2050) between the MFR and CLE scenarios.

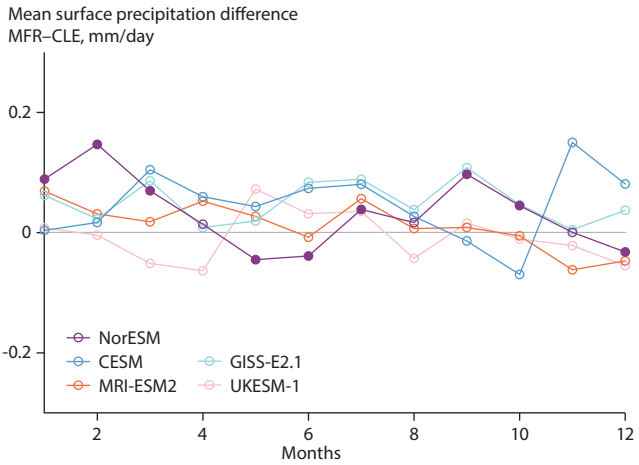

Figure 8.17 Differences in the seasonal Arctic mean surface precipitation change (2045–2050) under the MFR scenario compared to CLE. Filled circles represent significant changes.

8.4 Linking sources of air pollution in Arctic Council Member countries and Observer states to Arctic climate

8.4.1 Introduction

The global CLE and MFR emission scenarios produced considerable differences in SLCF concentrations and radiative forcings, yet differences in simulated Arctic warming rates are indiscernible, according to the analysis of global ESM results in Section 8.3.3. The cause of the simulated Arctic temperature differences are analyzed in the following text, with a focus on how the key chemical species emitted from Arctic Council Member states and Observer countries contribute to the projected Arctic warming rate and air-quality trends. In particular, air pollutants are considered historically to have had significant warming (CH_4, BC, and O_3) and cooling (sulfur) influences on global climate.

The analysis builds on the available results from the coupled ESMs for 2015–2050, in addition to further results from tropospheric Chemistry Climate Models (CCMs), atmospheric climate models, CTMs, and the emulator (Section 8.2.3). Three emission scenarios are considered: CLE, MFR, and CFM. Analysis of changes in the regional emissions of the different chemical species is presented in Section 8.2. Changes in emissions between 1990 and 2015 are also considered, to give a historical context. Throughout the whole chapter, changes caused by emissions of different SLCF chemical species are compared with impacts of CO_2 emission changes.

To show the sensitivity of O_3 (surface concentrations and radiative forcing) to changes in precursor emissions, additional idealized experiments were conducted (Section 8.4.2). In these, 20% reductions were made for regional anthropogenic emissions from different source regions and sectors, in a similar way to those used to calculate direct aerosol radiative forcings. The projected influences of regional emissions on concentrations of aerosols and particulate matter are discussed in Section 8.4.3, with the potential impacts of these concentration changes on health discussed in Chapter 9. The impacts of regional emissions on radiative forcings are summarized in Chapter 8.4.4, followed by an analysis of the impacts on Arctic temperature.

8.4.2 Response of O_3 to regional changes in precursor emissions

Tropospheric O_3 is a secondary pollutant, formed photochemically in the atmosphere from emissions of NO_X and VOC precursors. It is a greenhouse gas, and a harmful pollutant in the surface atmosphere. Details of the formation of tropospheric ozone and its sources are given in Chapter 6, Section 6.2. For this assessment, a simple parameterized model was used to assess the impacts of reductions in regional SLCF emissions on surface O_3 – from the perspectives of air-quality and climate (via O_3 radiative effects). The O_3 parameterization uses source-receptor relationships derived from atmospheric chemistry models that participated in emissions perturbation experiments conducted as part of the Hemispheric Transport of Air Pollutants (HTAP) project, and introduces a level of uncertainty based on the diversity of input models (Turnock et al., 2018; 2019). The parameterization uses changes in regional precursor emissions (NO_X, CO and NMVOCs), as well as changes in global CH_4 abundances, to scale the source-receptor relationships of the tropospheric O_3 response from the individual models used to construct the parameterization. A linear scaling factor is used to calculate the O_3 response from changes in CO and NMVOCs emissions, with a quadratic scaling factor used to account for the non-linear responses from changes in NO_X emissions and CH_4 abundances. The parameterization has a baseline year of 2010 and is therefore not able to account for impacts on O_3 from changes in climate, chemical environment (O_3 production or loss) and the long-term feedback of emission changes on oxidants and CH_4 lifetime.

The change in global and regional O_3 concentrations is calculated based on the response to the emissions perturbation scenarios. The calculated changes in tropospheric O_3 are combined with the O_3 radiative kernel of Rap et al. (2015) to estimate the instantaneous O_3 radiative effect and direct O_3 radiative forcings from regional emissions perturbations analogous to those in Section 8.3.2. For further details on the development and previous uses of the parameterization see Wild et al. (2012) and Turnock et al. (2018, 2019).

The response of surface O_3 and direct O_3 radiative forcing to idealized 20% reductions in regional anthropogenic emissions from different source regions and sectors was estimated in order to show the sensitivity of O_3 to changes in precursor emissions and to compare the direct aerosol radiative forcings in section 8.4.4. The tropospheric O_3 response to regional changes in anthropogenic O_3 precursor emissions over the historical period (1990–2015) and for the CLE and MFR future scenarios (2015–2050) was also calculated from the parameterization for comparison to that from aerosols in section 8.4.3 and 8.4.5. It is important to note that the calculated surface and tropospheric O_3 changes account only for the direct response of O_3 to changes in precursor emissions and global CH_4 abundance. They do not include the longer-term impacts of changes in these emissions on the tropospheric hydroxyl radical (OH) distribution and CH_4 lifetime (e.g. the atmospheric chemical methane feedback; Holmes, 2018), and the subsequent response of the tropospheric O_3 distribution. They also do not include the effects of climate change over these periods.

8.4.2.1 Surface O_3 response to regional emissions perturbations

In response to an idealized 20% reduction in all O_3 precursor emissions (NO_X, CO, NMVOCs and CH_4), surface O_3 was reduced by 1.5 ppb (~5%) over the Arctic and Rest of the World and by more than 3 ppb (~7%) across the Asian Observers. The largest reductions in surface O_3, of 1.5 ppb, are due to reductions in CH_4 emissions, particularly from fossil-fuel emission sources (Figure 8.18). The Asian Observers represent the only region where the combined 20% emissions reductions from local fossil-fuel sources of NO_X, CO and NMVOCs were able to reduce surface O_3 concentrations by a similar amount to that from CH_4. The reduction in emissions from Asian Observers also showed a relatively large impact on surface O_3 changes in the Arctic. This indicates that long-range transport

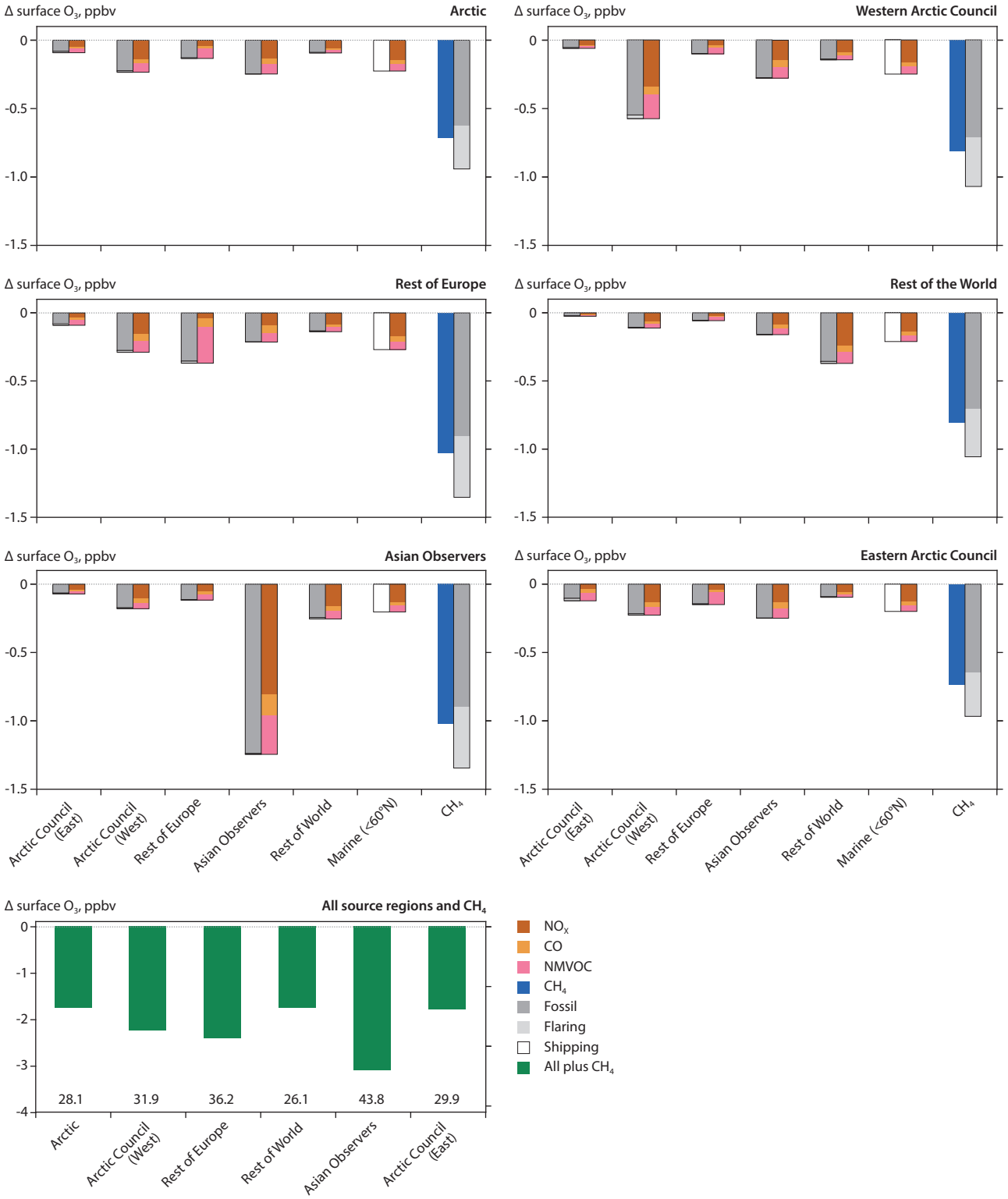

Figure 8.18 How 20% emission reductions in NO_X, CO, NMVOCs and CH_4 from different source regions and sectors contribute to the change in surface O_3 in six receptor regions (individual panels). For CH_4, a 20% reduction in global emissions was used. The total response in each receptor region to the combined 20% emissions reductions for NO_X, CO, NMVOCs and CH_4 is shown in the last panel, with baseline surface O_3 values for each region shown below the bars.

from the Asian Observers has an important influence in the Arctic and is comparable to more local emission changes from the eastern and western Arctic Council Member states. Apart from changes in global CH_4, reductions in local emission sources induced larger regional reductions in surface O_3 than those from remote regions. These changes were dominated by the response to NO_X emissions from fossil-fuel sources. Across all regions, flaring emissions made a small contribution to the change in surface O_3, with shipping emissions an important contribution from the marine source region.

Regional changes to emissions of O_3 precursors (Chapter 2 and Section 8.2.2) from the different source regions over the historical period of 1990–2015 and for the future MFR and CLE scenarios (2015–2050), were applied in the parameterization. The resulting timeseries of surface O_3 responses from the

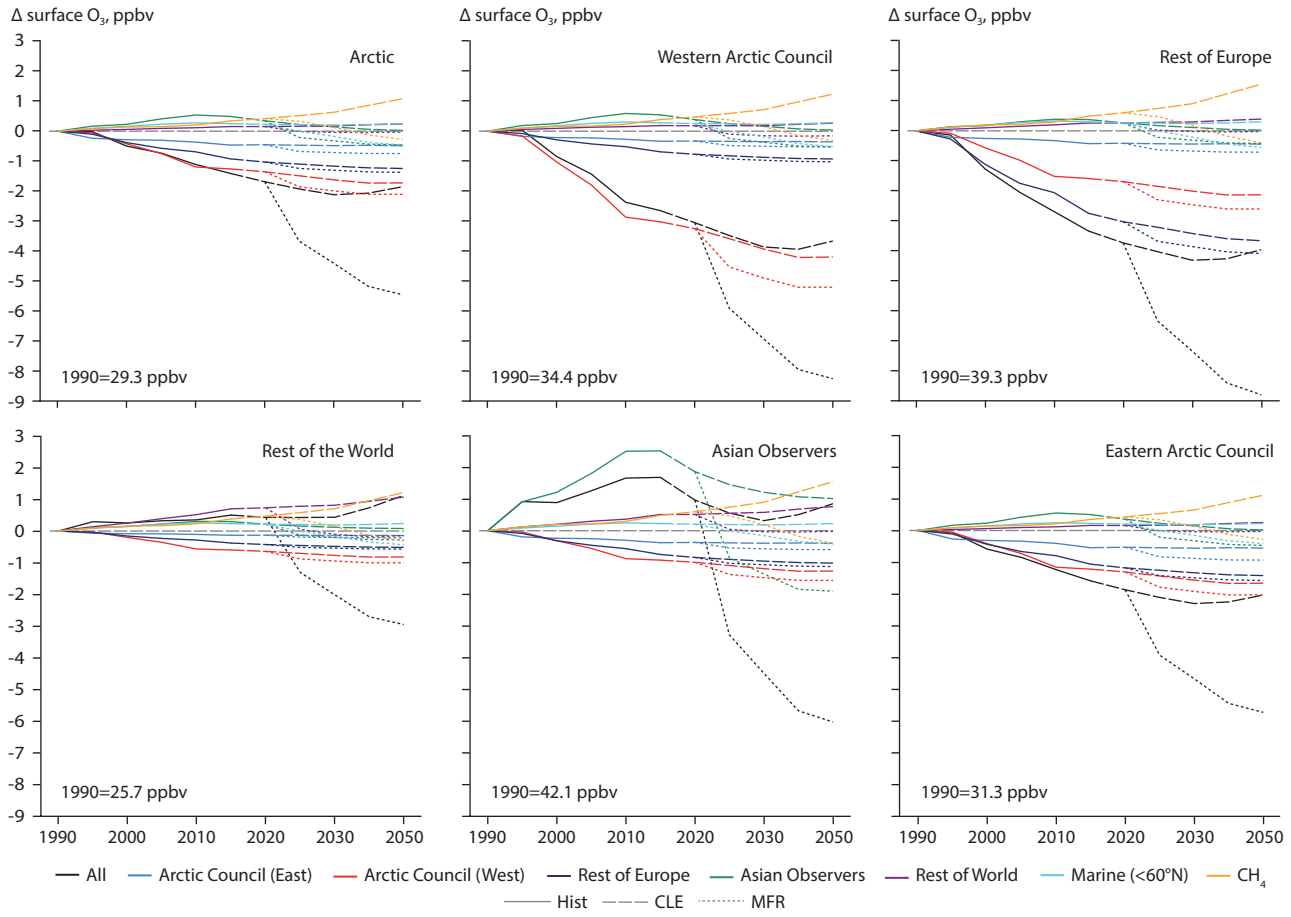

Figure 8.19 Contributions from reductions in regional precursor emissions and changes in global CH_4 abundance (yellow line) to the response in surface O_3 concentrations, across six receptor regions in the historical time period 1990–2015 (solid line), under CLE during 2015–2050 (dashed line) and in the MFR scenario 2020–2050 (dotted line). Values for 1990 are given at the bottom left-hand side of each plot.

parameterization (Figure 8.19) indicates that surface O_3 across the Arctic would be lower by a maximum of 2±0.2 ppb (~7%) in 2050, relative to 1990 values, driven mainly by reductions of O_3 precursor emissions from the western Arctic Council Member states and the Rest of Europe, with smaller contributions from the eastern Arctic Council Member states. Overall, surface O_3 concentrations across the Arctic decreased by approximately 1±0.3 ppb over the period 1990–2015. Small increases in surface O_3 evident across the Arctic during this period, were driven by emissions from Asian Observer source regions and also from changes in global CH_4.

The parameterization predicts reductions in Arctic surface O_3 for the historical period, in contrast to the small increase in annual mean surface O_3 observed at individual Arctic monitoring locations (Chapter 6, Section 6.2) and also simulated by composition models at these locations (Chapter 7, Section 7.3.1.2). The parameterization is a simple statistical model used to represent the regional average response of tropospheric O_3 to regional perturbations in precursor emissions, and neglects the effects of climate change and meteorological variability. Therefore, it is not anticipated to be able to reproduce observed regional trends in surface O_3 at point locations, but can be used to represent the impact solely from continental-scale emissions mitigation measures.

Post-2015 reductions in Arctic surface O_3 concentrations of up to 2±0.2 ppb occur by 2050 (relative to 1990) under the CLE scenario, due to reductions in emissions from all source regions. The only exception to this is the increase in surface O_3 concentrations of 1±0.1 ppb that occurs from changes in global CH_4 concentrations under CLE. The large regional emissions reductions that occur in the MFR scenario reduce Arctic surface O_3 concentrations by more than 5±0.3 ppb by 2050 (relative to 1990) due to the combined impact of changes in all emissions source regions.

Similar temporal changes in surface O_3 are shown for other receptor regions, driven by changes in local emissions sources and global CH_4. Over the western Arctic Council Member states and the Rest of Europe, surface O_3 concentrations are reduced by 4±0.4 ppb (~10%) by 2050, relative to 1990, in the CLE scenario, and by approximately 8±0.5 ppb (~20%) in the MFR scenario. Smaller reductions in surface O_3 are predicted for the eastern Arctic Council Member states and the Rest of the World of up to 2±0.2 ppb (~7%) by 2050 in CLE, and up to 6 (~20%) ±0.3 ppb in MFR.

Changes in surface O_3 across the Asian Observers are notably different, with increases of 2.5±0.4 ppb (~6%) in 2015, relative to 1990, driven by increases in local O_3 precursor emissions within this region. In the CLE scenario, surface O_3 changes in the Asian Observers decline after 2015, to a 1±0.3 ppb (~2%) increase in 2050, relative to 1990, as the contribution of O_3 from local sources declines. Decreases in emissions in all the Arctic Council Member states as well as the Rest of Europe source regions contribute to reducing surface O_3 across the Asian Observer countries, in both the historical and future projection periods.

8.4.3 Response of $PM_{2.5}$ to regional emissions changes

Reductions in emissions of SLCFs and SLCF precursors from sources in Arctic Council Member states and the Rest of Europe during 1990–2015 (Chapter 2 and Section 8.2.2) have produced notable reductions in concentrations of local and Arctic aerosols over this time period (Chapters 6 and 7).

In 2015, SLCF emissions from Asian Observer countries exceeded the combined total emissions from the Arctic Council Member states and the Rest of Europe (Figure 8.3). According to projections under the MFR scenario, applying emissions-reduction strategies (Chapter 2) would avoid most of the emissions from Asian Observer states and the Rest of the World anticipated by 2050 under CLE. Doing so would likely produce substantial improvements in local air quality and long-range transport of $PM_{2.5}$ to the Arctic.

Responses in regional concentrations of near-surface $PM_{2.5}$ to changes in regional emissions of sulfur, BC, and OC during 2015–2050 were simulated by four ESMs (CESM, GISS-E2.1, MRI-ESM2, and UKESM1), one CTM (EMEP MSC-W), and one atmospheric global climate model (CanAM5-PAM). In addition, results for total $PM_{2.5}$ from a source-receptor model (TM5-FASST) are available (see Chapter 7 Appendix for model details). The following analysis only considers the contributions to $PM_{2.5}$ of BC, OC, and SO_4; aerosol chemical species that are strongly affected by anthropogenic sources and simulated in all models. Although ammonium and nitrate concentrations are predicted by some of the models (Chapters 7 and Section 8.3.2), these aerosol species are not explicitly included in the analysis of $PM_{2.5}$ concentrations, due to the limited amount of available data (from the multi-model ensemble and observations) for model comparisons. Instead, it is assumed that sulfate is fully neutralized by ammonium. As shown in Chapter 6, Arctic aerosols have become less acidic with time and this assumption should be sufficient for analyzing $PM_{2.5}$ concentrations.

The available models simulate the long-range transport of pollutants and average pollutant concentrations for model grid cells that are considerably larger than the footprints of local Arctic communities and cities. This situation arises due to the high computational demands of the models, the relatively low spatial resolution of the emissions datasets (Chapter 2), and constraints imposed by the parameterizations of physical and chemical processes in the models. Results from the models were post-processed – 'downscaled' – to enhance the spatial resolution of the model datasets and to allow analysis at a resolution of 0.5° latitude × 0.5° longitude, corresponding to the resolution of the emissions datasets. The post-processed model datasets cannot be used to assess the local variability at scales smaller than this, where long-range advection of air pollutants is less efficient at changing local $PM_{2.5}$ concentrations than the emissions from local sources. See Chapter 7 for details.

Contributions of natural emissions to future changes in $PM_{2.5}$ concentrations are discussed in Section 8.6. Possible changes in the simulated concentrations of DMS in the ocean and emissions of SOA precursors are not explicitly accounted for in the following analysis. Although impacts of changes in wildfire emissions are implicitly included in ESM and CCM model results (Chapter 7), their climate impacts have not been assessed.

Despite considerable differences in model complexity and how they treat natural emissions sources, all the models simulate reductions in $PM_{2.5}$ concentrations in China, Europe, and North America during 2015–2050, according to the CLE scenario (Figure 8.20). This consistency indicates that simulated changes

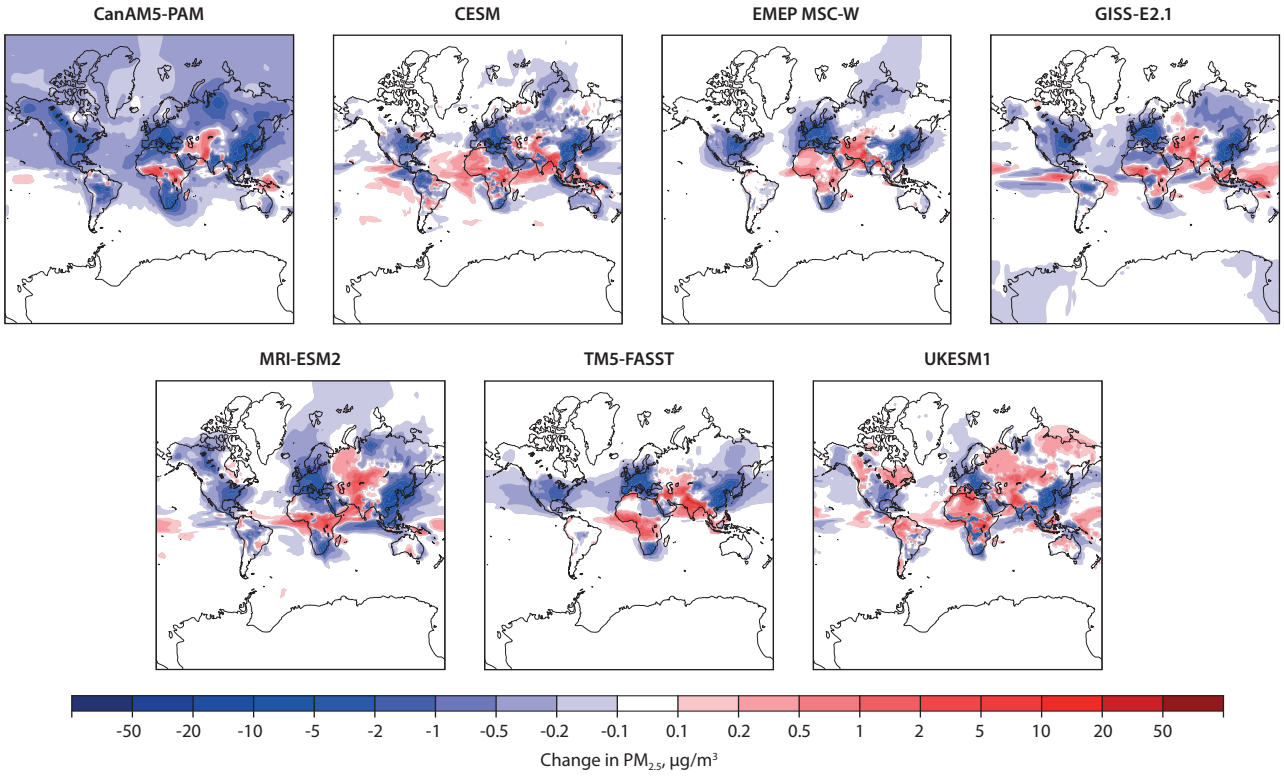

Figure 8.20 Projected change in annual mean near-surface $PM_{2.5}$ concentration under the CLE scenario between 2015–2050. Only contributions of sulfate, ammonium, BC, and OC to $PM_{2.5}$ are included.

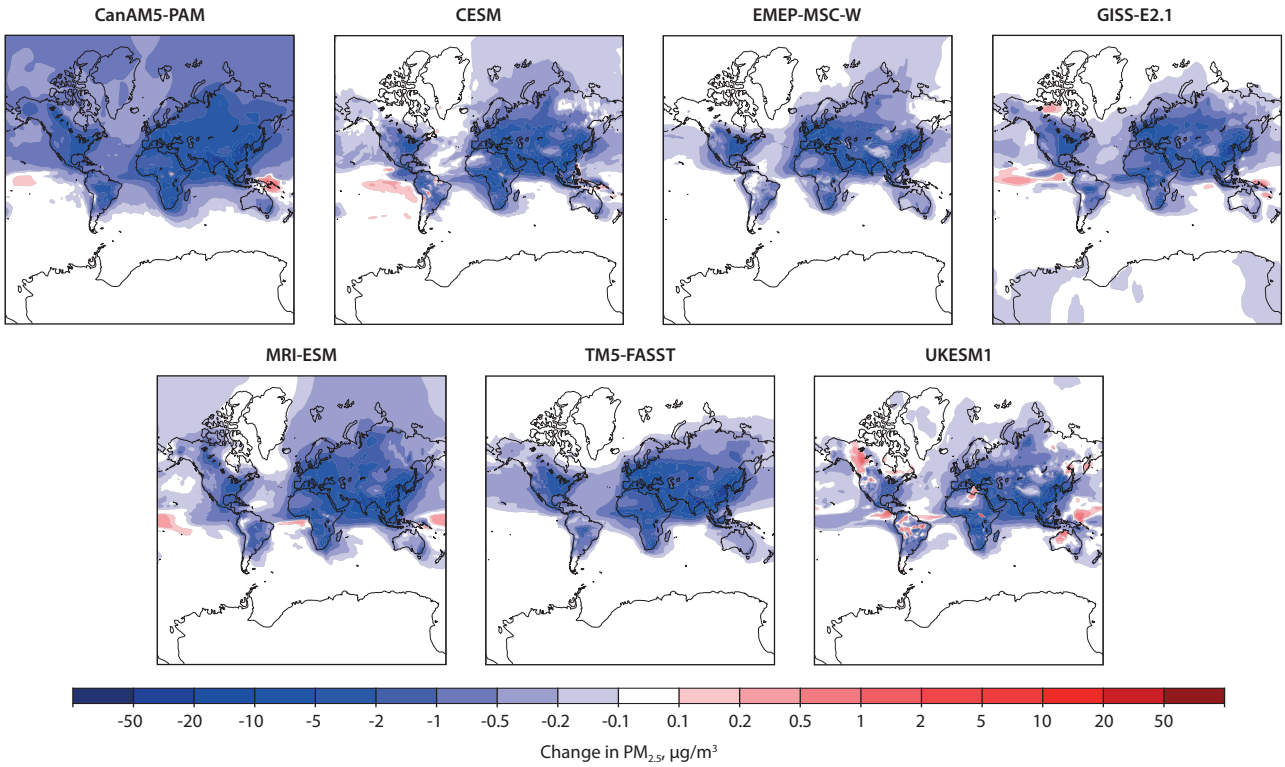

Figure 8.21 Projected change in annual mean near-surface $PM_{2.5}$ concentration under the MFR scenario between 2015–2050. Only contributions of sulfate, ammonium, BC, and OC to $PM_{2.5}$ are included.

are likely robust, given the available emissions scenarios. The simulated changes in near-surface concentrations are of the order of 10–20 µg/m³ for China and generally less than 10 µg/m³ for all other regions.

Under the MFR scenario, future $PM_{2.5}$ concentrations are reduced much more strongly, especially in Asian Observer states and the Rest of the World, where reductions locally exceed 50 µg/m³ (Figure 8.21).

Although the models are consistent in projecting regional changes that are associated with large reductions in local emissions, differences exist for regions that are located downstream of large source regions and strongly affected by the long-range transport of pollutants. This particularly includes concentrations over Siberia and other regions at high latitudes. The differences can be partly attributed to model uncertainties in aerosol transport and efficiencies of physical and chemical processes (Chapter 7). However, given the relatively small size of the multi-model ensemble and limited amount of available data, it is not possible to attribute differences to any particular group of models or processes.

Adopting the policy context of the MFR scenario would lead to systematic future reductions in annual mean $PM_{2.5}$ concentrations in the Arctic, Arctic Council Member states, and Asian Observer countries, relative to the CLE scenario (Figure 8.22). The modeling indicates most of these reductions would occur during 2020–2025, corresponding to rapid changes in emissions in the MFR scenario over this period. The reductions are projected to be particularly large for Asian Observers.

The models agree well in their simulations of concentration reductions, especially in regions with large reductions in emissions. For example, for Asian Observer countries, the difference in mean $PM_{2.5}$ concentration in 2050 between the MFR and CLE scenarios amounts to about 45% of the anthropogenic $PM_{2.5}$ concentrations in 2015 in this region (or about 6 µg/m³), with a model range from -53.4% to -43.4%. The impacts of simulated natural emissions on these results are likely to be small compared to uncertainties related to the simulated transport and atmospheric transformations of aerosols in the models. For example, CanAM5-PAM and GISS-E2.1 use identical datasets for natural emissions, yet large differences in simulated air pollutant concentrations exist.

Additional results are available for an analysis of how emissions of BC, OC, and S contribute to $PM_{2.5}$ concentrations. These are based on additional simulations with four CCMs and climate models (CanAM5-PAM, CESM, MRI-ESM2, UKESM1) with perturbed emissions in 2015. In detail, concentration responses to changes in emissions of the various species from different regions and sectors were simulated in the CCMs and climate models using specified meteorological conditions, which do not respond to changes in emissions. Subsequently, the concentration responses were determined by comparing the perturbed to original (unperturbed) concentrations. Finally, the diagnosed concentration responses were used – under the assumption of a linear response – to determine concentrations for different years.

The approach described above is conceptually equivalent to the calculations of effective radiative forcings and climate, which also employ emission perturbations and linearized source-receptor relationships (Section 8.4.4). These approaches were combined to develop the emulator for air quality and climate (Section 8.2.3 and Olivié et al., 2021). Although assuming that aerosol concentrations and radiative forcings respond in a linear way may lead to substantial biases under certain conditions, it considerably simplified and harmonized analysis of the impacts of emissions on air quality and climate presented in this chapter.

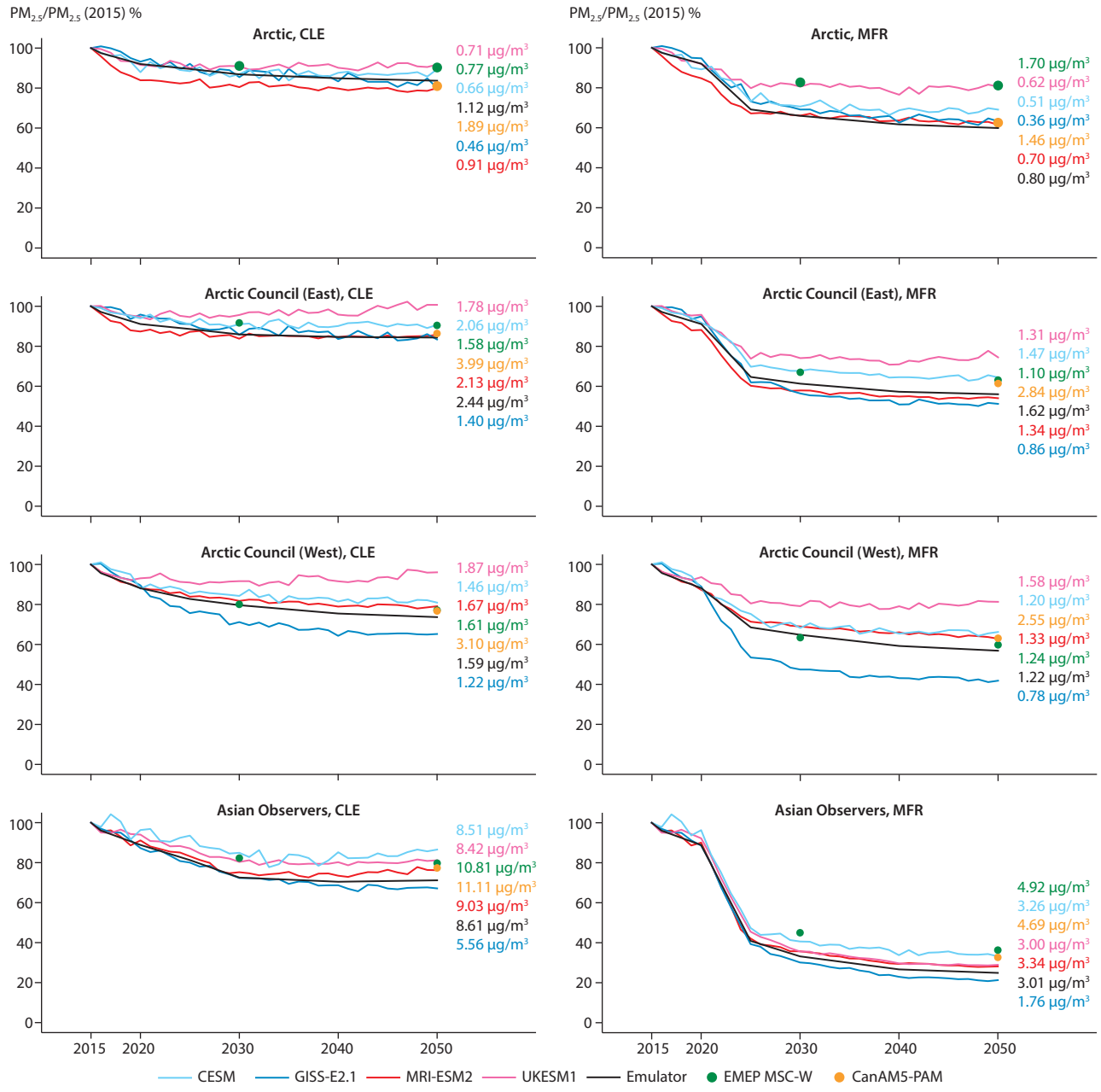

Figure 8.22 Future annual and regional mean anthropogenic near-surface $PM_{2.5}$ concentrations under the CLE (left) and MFR (right) scenarios in four receptor regions (one region indicated in each panel). Future concentrations are normalized by the concentration in 2015 to facilitate the comparison of trends across regions. Ensemble mean results for ESMs (CESM, GISS-E2.1, MRI-ESM2, UKESM1), the atmospheric climate model CanAM5-PAM (orange bullet), and the CTM EMEP MSC-W (green bullet) are shown. The black line refers to the emulator results. Corresponding changes in absolute concentrations during 2015–2050 are also included for each model (to right of graphs).

Future changes in BC concentrations within $PM_{2.5}$ ($BC_{2.5}$) simulated in the emulator agree well with mean diagnosed concentrations from the ESM and CTM simulations in Asian Observer countries. However, they tend to be smaller for other regions (Figure 8.23). By 2050, reductions in $BC_{2.5}$ concentrations are even greater than the reductions in $PM_{2.5}$ concentrations, relative to the concentrations in 2015. Similar results for emissions of sulfur and OC are provided in the Appendix (Figures A8.6 and A8.7).

The emulator simulation results indicate that reductions in emissions of sulfur are more important than those of OC and BC for reducing total anthropogenic $PM_{2.5}$ concentrations in the MFR scenario, exemplifying the importance of mitigating sulfur emissions for enhanced future air quality. This is generally true for all regions but is particularly important for the Arctic and eastern Arctic Council Member states (Table 8.2). However, reduced emissions of OC also contribute considerably to reducing $PM_{2.5}$ concentrations in the MFR scenario, especially in Asian Observer countries and the Rest of the World. For these regions, reductions of sulfur and OC emissions contribute almost equally to the projected reduced total $PM_{2.5}$ concentrations.

Emissions of different aerosol species are often coupled due to shared emissions sources and processes, which is particularly the case for contributions of BC and OC to total $PM_{2.5}$. Although the analysis presented here assesses the $PM_{2.5}$ components in the CLE and MFR scenarios, it may also be useful for developing emissions scenarios that focus on mitigation options for

Table 8.2 Difference in annual and regional mean anthropogenic near-surface $PM_{2.5}$ concentrations by 2050 between the MFR and CLE scenarios, relative to concentrations in 2015. The first number in each cell in the table refers to results from the emulator for emissions of BC, OC, and S under the MFR and CLE scenarios. Numbers in brackets indicate the range of speciated $PM_{2.5}$ concentrations of BC, OA, and sulfate in simulations of anthropogenic $PM_{2.5}$ with the ESMs, atmospheric climate model, and CTM.

	Difference in $PM_{2.5}$, between MFR and CLE scenarios (%)			
	BC	OC	S	Total
Arctic	-1.0 (-1.6, -0.3)	-4.4 (-5.5, -0.8)	-16.9 (-13.9, -8.2)	-22.2 (-20.4, -9.2)
Eastern Arctic Council	-1.5 (-2.6, -1.3)	-6.0 (-9.3, -3.2)	-19.7 (-24.7, -14.6)	-27.3 (-32.2, -25.0)
Western Arctic Council	-1.2 (-1.8, -1.1)	-5.6 (-9.2, -5.1)	-6.6 (-9.0, -4.8)	-13.4 (-23.4, -13.4)
Rest of Europe	-2.1 (-3.4, -1.0)	-7.6 (-14.3, -3.7)	-13.5 (-15.9, -7.7)	-23.2 (-27.6, -21.8)
Asian Observers	-4.8 (-6.3, -3.6)	-21.9 (-32.7, -8.3)	-18.7 (-24.4, -10.6)	-45.4 (-53.4, -43.4)
Rest of the World	-2.3 (-3.4, -2.3)	-11.5 (-14.4, -6.0)	-13.4 (-17.6, -9.3)	-27.2 (-31.9, -25.8)

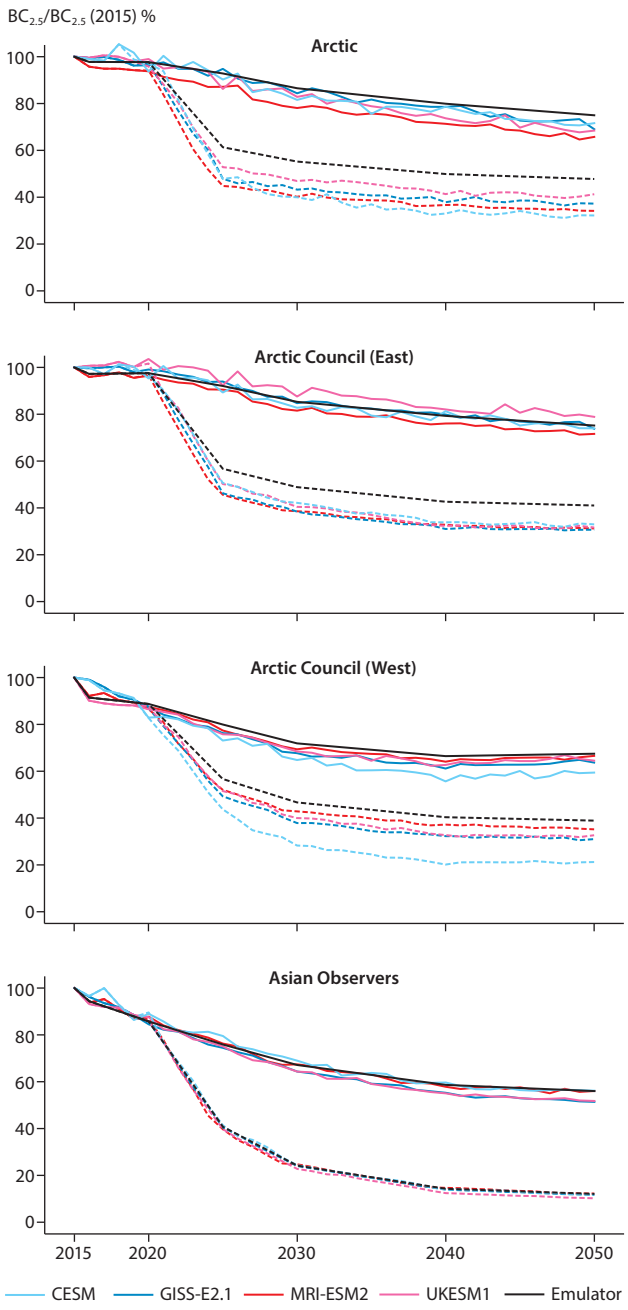

Figure 8.23 Impacts of the CLE (solid lines) and MFR (dashed lines) emissions scenarios on the future mean atmospheric near-surface concentration of BC particulate matter ($BC_{2.5}$) in different regions, normalized by the concentration in 2015. Colored lines refer to ESMs and black lines to the emulator (see Figure 8.22).

individual species. Note that the coupling of emissions through shared sources is not considered here.

Projected reductions of BC emissions by 2050 under the MFR scenario (relative to the CLE scenario) result in reduction of anthropogenic $PM_{2.5}$ concentrations ranging from -4.8% to -1.0% of the total anthropogenic $PM_{2.5}$ concentrations in 2015. (Table 8.2). The benefits from lower BC emissions are particularly high for Asian Observers, where reductions in BC account for 10.6% of the total reductions for all species. Benefits are also considerable for western Arctic Council Member states and the Rest of Europe, where reductions in BC account for 9.2% and 9.1% of the total reductions, respectively.

Asian Observer countries and the Rest of the World are responsible for a major part of global emissions, and the potential for reducing emissions is projected to be significant in these regions under both the MFR and CLE scenarios. As a consequence, particularly large reductions in emissions of SLCFs are projected to occur in Asian Observer countries and the Rest of the World (Chapter 2, Section 8.2.2). The net long-range transport of aerosols from these regions to the Arctic is projected to decrease during 2015–2050 under the CLE and MFR scenarios, with resultant reductions in $PM_{2.5}$ concentrations in the mid and upper Arctic troposphere – as is also indicated from large changes in aerosol radiative forcings (Section 8.4.4).

Although the long-range transport of pollutants from sources in Asian Observer countries and the Rest of the World is important for total tropospheric aerosol and $PM_{2.5}$ burdens in the Arctic, mean near-surface concentrations of $PM_{2.5}$ in the Arctic are mostly sensitive to changes in emissions from sources in eastern Arctic Council Member states, which generate most of the emissions produced by sources near and above 60°N (Chapter 2). Therefore, projected future reductions in concentrations are very similar in the Arctic and eastern Arctic Council Member states, relative to 2015 (Figure 8.24).

For Arctic Council Member states, the Rest of Europe, and Asian Observers, diminishing emissions from local sources of aerosols within state or country boundaries are considerably more important for reducing net regional mean $PM_{2.5}$ concentrations than diminishing long-range transport of aerosols that arrive from other regions (Figure 8.24). The long-range transport of aerosols from sources in the Rest of the World is important for $PM_{2.5}$ concentrations in all regions (Figure 8.24). Given that reductions in SLCF emissions from

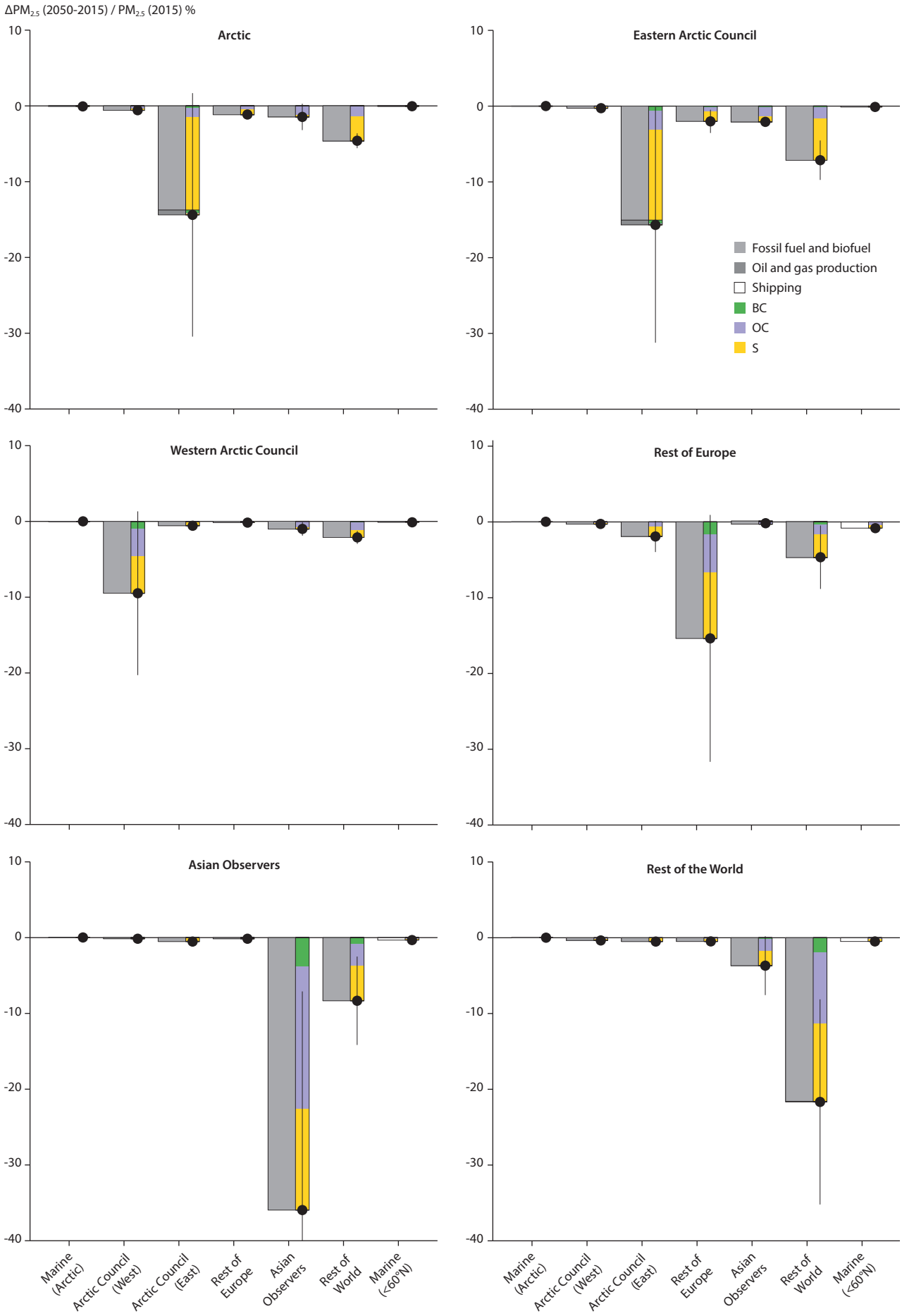

Figure 8.24 How BC, OC and S from different regions and sectors contribute to the difference in near-surface $PM_{2.5}$ concentrations between MFR and CLE scenarios in six receptor regions; values are normalized by concentrations in 2015. The vertical lines indicate the standard deviation of the multi-model mean total $PM_{2.5}$, based on emulated results from simulations with perturbed emissions in CanAM5-PAM, UKESM1, and MRI-ESM2.

sources in the Rest of the World and Asian Observer countries are very similar (Section 8.2.2), long-range transport from the former is more likely than that from the latter to influence near-surface concentration trends elsewhere. Although this evidence strengthens the case for taking mitigation action in the Rest of the World, a more detailed analysis of the long-range transport of aerosols from the Rest of the World is beyond the scope of this assessment.

8.4.4 Radiative forcings of CO_2 and SLCFs

SLCFs modify the flux of radiant energy through the atmosphere, affecting its energy budget. Radiative forcings provide a convenient measure of the impacts of SLCF concentrations on radiation and climate. As with other climate assessments, radiative forcings are used here to analyze the impacts of historic and future projected changes to SLCFs and greenhouse gases on temperatures. Commonly available methods for global forcings were applied to SLCFs from different emission regions and sectors to support an analysis of the impacts of regional emissions on radiative forcings and climate.

CH_4, O_3, and aerosols share common atmospheric chemical processes, with emissions of one pollutant potentially affecting radiative forcings of several SLCFs. The analysis presented here accounts for the impacts of NO_X, VOCs, and CO on CH_4 radiative forcings, but not on aerosol radiative forcings. The impacts of O_3-precursor emissions on total aerosol radiative forcings are relatively small (Shindell et al., 2009). Therefore, changes in O_3 concentrations (Section 8.4.2) and O_3 radiative forcings (Section 8.4.4.3) are analyzed separately from changes in aerosol concentrations (Section 8.4.3) and radiative forcings.

Two methods for determining radiative forcings of SLCFs are used in the following, based on radiative transfer calculations in the models. Previously, in AMAP (2015a), radiative forcings of BC and O_3 were determined by comparing net radiative fluxes at the TOA through multiple calls of the radiative transfer schemes in the models. For each radiation calculation, a single SLCF was removed from the atmosphere in order to determine an instantaneously perturbed radiative flux, without the contributions of scattering and absorption of radiation by the SLCF to the radiative fluxes. Comparing the perturbed flux with the original (unperturbed) flux then yielded the net radiative forcing of the SLCF. Removing the SLCFs did not change the temperature, humidity, and clouds in the simulations. The resulting radiative forcing is referred to as a direct radiative forcing (or instantaneous radiative forcing). Direct radiative forcing contributions of SLCF emissions from specific source regions and sectors were determined, either by employing source-tagged SLCF tracers or by conducting full climate model simulations with perturbed emissions.

Calculations of direct radiative forcings are numerically efficient and can be performed in CTMs, which otherwise cannot be used to simulate responses of temperatures to changes in SLCF concentrations. In addition, the climate research community has recently embraced the use of effective radiative forcings. These are extensively used in the following text to analyze aerosol climate impacts. Similar to the approaches used by Ghan (2013) and the IPCC (2013a), the diagnosed effective radiative forcings account for the radiative impacts of different emitted SLCFs or their precursors. In contrast to direct radiative forcings, they additionally account for impacts from rapid physical feedbacks on radiative transfer, which are semi-directly or indirectly associated with changes in SLCF concentrations. For example, this includes responses in amounts and optical properties of clouds and snow, which can have substantial impacts on atmospheric radiative fluxes and climate.

All calculations of emissions source- and sector-specific effective radiative forcings were conducted using CCMs with specified Sea Surface Temperatures (SSTs) and sea ice. Perturbed radiative fluxes were calculated by simulating the climate model responses (in radiative and other physical processes in the atmosphere, and on land surfaces, and snow) to a perturbative removal of the emissions of individual SLCFs from different regional sources. Subsequently, the radiative forcings were determined by comparing the perturbed with the original (unperturbed) simulated radiative fluxes.

Different components of the net effective radiative forcings were diagnosed, associated with interactions between the SLCFs and radiation, clouds, and surface albedo (Ghan, 2013). The effective radiative forcing from interactions of SLCFs with radiation is closely related to direct radiative effects of SLCFs in the atmosphere which, for example, may result from the scattering or absorption of solar radiation by aerosols. The effective radiative forcing from SLCFs interacting with clouds includes instantaneous changes in cloud albedo, and changes to cloud amounts, lifetimes, and microphysical processes, in response to SLCF concentration changes, which are primarily related to aerosol indirect and semi-direct effects. The effective radiative forcings from SLCFs interacting with surface albedo particularly accounts for the dynamic responses of snow radiative properties, and amounts to the darkening of snow from BC snow impurities.

Simulating effective SLCF radiative forcings generally requires substantial computing resources because of the influence of natural atmospheric variability on simulated radiative fluxes in climate models. This places considerable limits on the use of this method in assessing the impacts on SLCFs on climate.

Finally, the effective radiative forcing of CO_2 implicitly accounts for adjustments in stratospheric temperature. This has a substantial impact on changes in radiative fluxes that result from changes in CO_2 abundance.

8.4.4.1 CO_2

The annual and global mean CO_2 abundance of 399.9 ppm in 2015 (Section 8.2.3) yields a global mean effective radiative forcing of 1.83 W/m^2, relative to a pre-industrial abundance of 284.3 ppm in 1850, based on the emulator employed here (Olivié et al., 2021). By comparison, Etminan et al. (2016) determined an effective radiative forcing of 1.95 W/m^2 in 2015, which accounted for impacts of changes in nitrous oxide (N_2O) on the CO_2 radiative forcing and was relative to an abundance of 278 ppm in 1750. IPCC (2013a), meanwhile, determined a radiative forcing of 1.82 (1.63–2.01) W/m^2 for the period 1750–2011, for an abundance of 390.5 ppm in 2011. Most recently, Smith et al. (2020) analyzed results from the CMIP6 multi-model ensemble (Pincus et al., 2016) and determined an

effective radiative forcing of 1.81±0.09 W/m² for 1850–2014. Overall, different estimates of historic forcings of CO_2 are largely consistent with each other.

For 1990–2015, the effective forcing simulated by the emulator is 0.74 W/m². For 2030, differences in CO_2 abundances in the available SSP scenarios (Riahi et al., 2017) range from 434.32 ppm under the SSP1–1.9 scenario to 452.13 ppm in the SSP5–3.4 overshoot scenario (where emissions follow the SSP5–8.5 pathway until 2040 before declining). Therefore, the SSP2–4.5 scenario used here can be considered a 'middle-of-the-road' scenario, with a CO_2 abundance of 444.14 ppm in 2030 (Meinshausen et al., 2020). The projected CO_2 forcing according to the SSP2–4.5 scenario for 2015–2030 is 0.61 W/m². The abundance differences between the SSP1–1.9 and the SSP5–3.4 overshoot scenarios implies a range in the radiative forcing from -24% to +19%. The projected forcing for 2015–2050 is 1.15 W/m², with an SSP scenario range from -71% to +52%.

8.4.4.2 CH_4

The annual and global mean CH_4 abundance of 1834.2 ppb in 2015 (Section 8.2.3) yields a global mean effective radiative forcing of 0.55 W/m², relative to a preindustrial abundance of 808.3 ppb in 1850. By comparison, Etminan et al. (2016) determined an effective radiative forcing of 0.62 W/m² in 2015, relative to an abundance of 722 ppb in 1750. Meanwhile, IPCC (2013a) determined a radiative forcing of 0.48±0.05 W/m² for 1750–2011, for an abundance of 1803 ppb in 2011. Thornhill et al. (2021) determined an effective radiative forcing for CH_4 of 0.67±0.17 W/m² between 1850–2014, based on simulations with eight ESMs from CMIP6 (including results from simulations with interactive chemistry). In the latter estimate, O_3 and sulfate concentrations responded to changes in CH_4 emissions in some of the models, which may account for the relatively large forcing compared to the other estimates (Shindell et al., 2009; O'Connor et al., 2021). Oshima et al. (2020) estimated the global and Arctic mean effective radiative forcings of CH_4 to be 0.71 W/m² and 0.35 W/m², respectively, for 1850–2014 using one of the CMIP6 models, MRI-ESM2.

The net CH_4 effective radiative forcing between 1990–2015 is 0.044 W/m², which is much smaller than the change during 1850–2015, corresponding to a relatively weak increase in the abundance of CH_4 over this period (Section 8.2.3). As with the shift in CH_4 abundance, increasing emissions from Asian Observer countries and the Rest of the World acted to increase the radiative forcing, whereas reductions in emissions from eastern Arctic Council Member states acted to reduce the radiative forcing (Figure 8.25). Further reductions in radiative

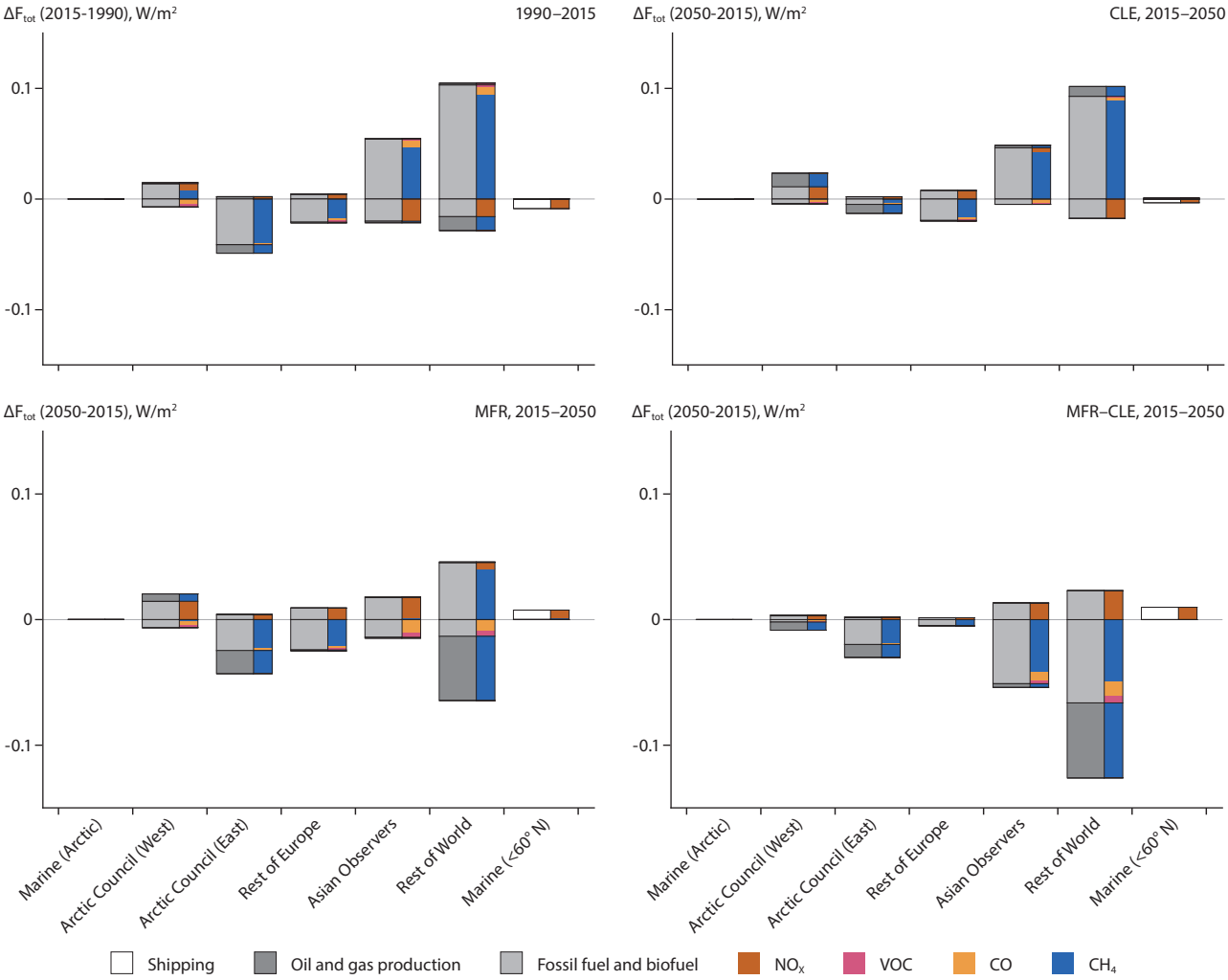

Figure 8.25 The impact of emissions of CH_4, CO, VOCs, and NO_X from different regions and sectors to the total effective radiative forcing from interactions of CH_4 with radiation and other physical climate processes between 1990–2015 (top left) and 2015–2050 (other panels). Projected changes according to the CLE and MFR scenarios are shown in the top right and bottom left panels, respectively, with the difference between them presented bottom right.

forcing resulted from increasing NO_X emissions from Asian Observers and the Rest of the World.

Between 2015–2050, the radiative forcing is 0.122 W/m², under the CLE emissions scenario. Increases in forcing over this period are mainly associated with emissions from fossil-fuel and biofuel combustion sources in Asian Observer countries and the Rest of the World.

Under the MFR scenario, the radiative forcing is reduced to -0.048 W/m², largely owing to reduced emissions from Asian Observers and the Rest of the World. A considerable fraction of the reduction is associated with reduced emissions from sources within the oil and gas sector in eastern Arctic Council Member states and the Rest of the World.

8.4.4.3 O_3

The tropospheric O_3 changes predicted by the parameterization (Section 8.4.2) in response to the 20% regional and sectoral emission perturbations were applied with an O_3 radiative kernel to calculate the resulting O_3 direct radiative forcings (Figure 8.26). Direct O_3 radiative forcings were also calculated over the historical and future time periods using the simulated changes in tropospheric O_3 over these periods (Figure 8.27).

A direct radiative forcing of up to -80 milliwatts (mW)/m² was calculated over Asian Observer countries for a 20% reduction in all O_3-precursor emissions across all source regions and globally for CH_4. Across the Arctic a smaller direct radiative forcing of -36 mW/m² resulted from the 20% change in emissions.

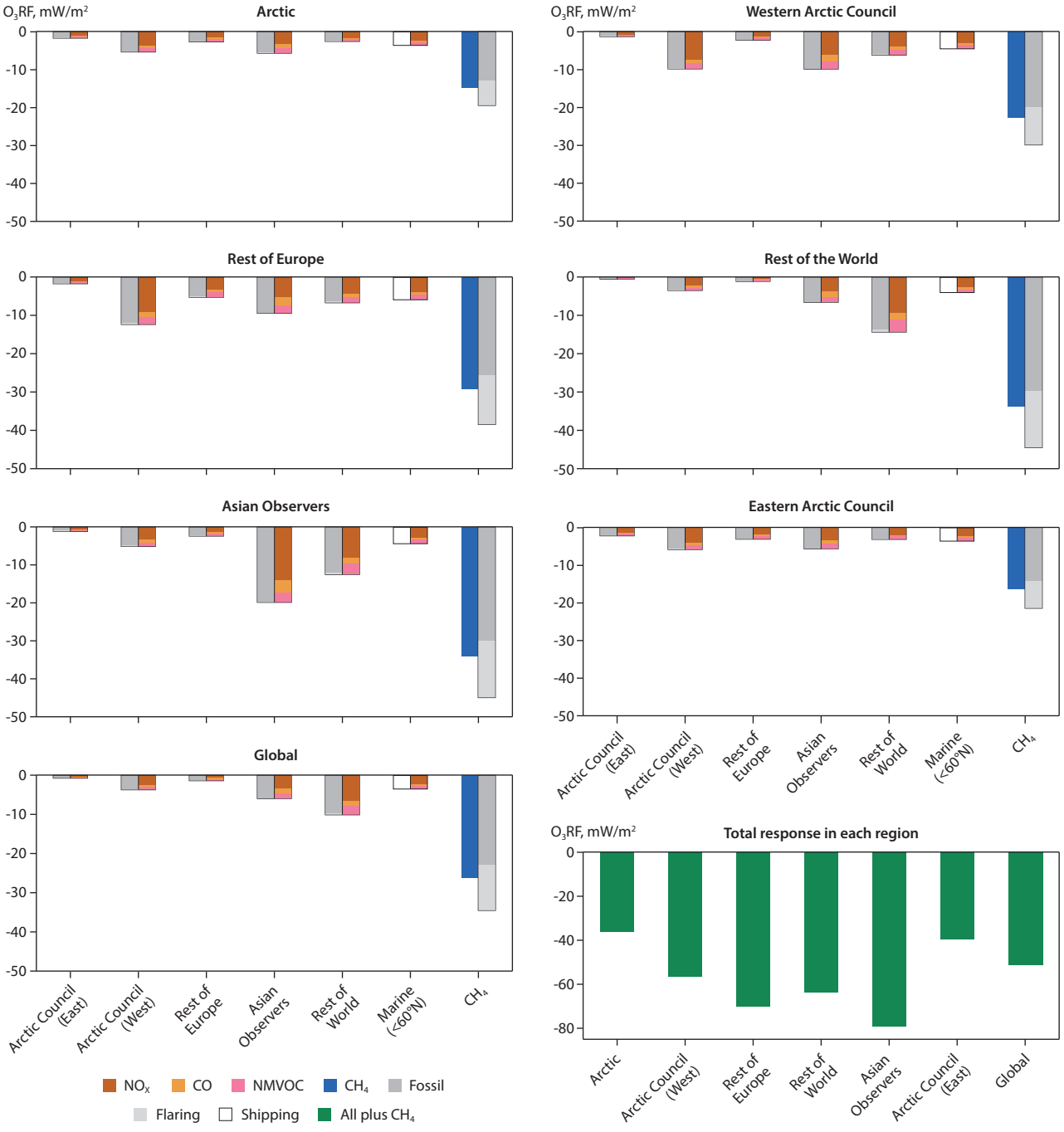

Figure 8.26 How a 20% reduction in emissions of NO_X, CO, NMVOCs and CH_4 from different regions and sectors contributes to the O_3 direct radiative forcing (RF) in six receptor regions. For CH_4, a 20% reduction in total global emissions was used. The total response in each receptor region to the combined 20% emission reductions for NO_X, CO, NMVOCs and CH_4 is shown in the bottom right panel.

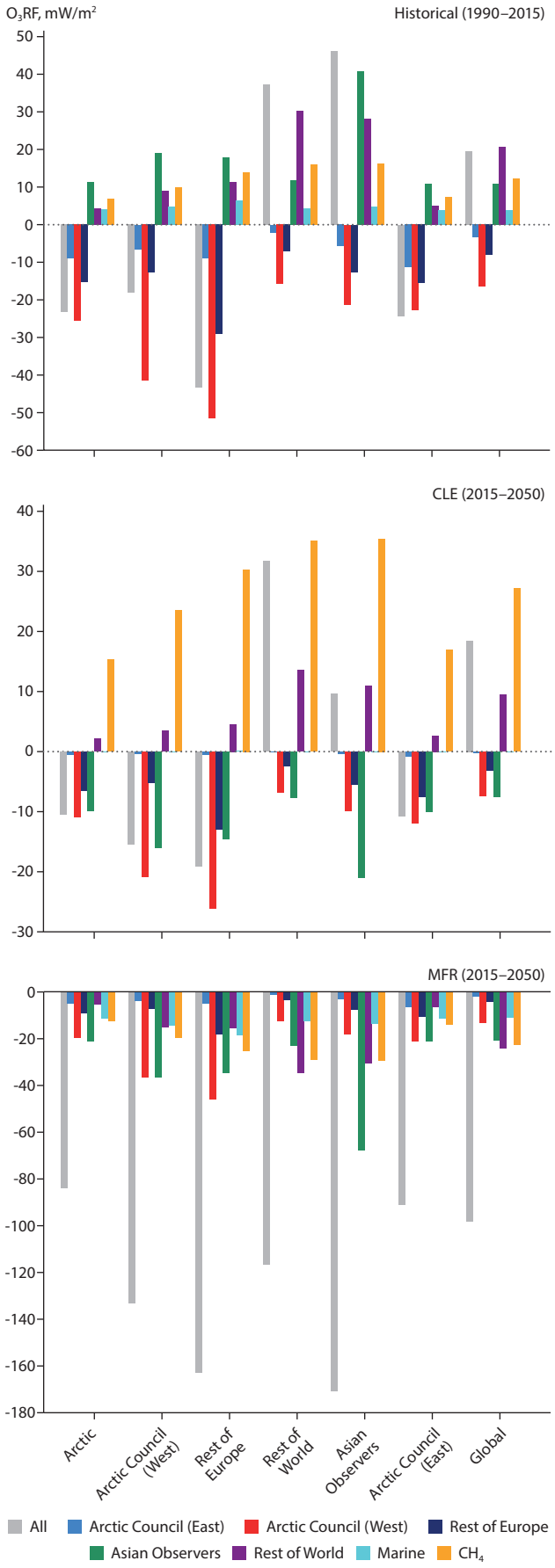

Figure 8.27 How changes in emissions of NO_X, CO and NMVOCs from different source regions and from changes in global CH_4 abundances contribute to the O_3 direct radiative forcing (RF) in six receptor regions and globally. The O_3 direct radiative forcing was calculated as the difference between O_3 radiative effects between 1990–2015 for the historical period and between 2015–2050 for the two future scenarios (CLE and MFR).

A 20% change in global CH_4 emissions, mainly from fossil-fuel sources, produced the largest O_3 direct radiative forcing across all receptor regions, with a -35 mW/m² contribution over Asian Observers and the Rest of the World. Over the Arctic region, the largest contributions to the O_3 direct radiative forcing came from reduced fossil-fuel NO_X emissions over the Asian Observers and the western Arctic Council states. Over other receptor regions, changes in local NO_X emissions from fossil-fuel sources dominated the O_3 direct radiative forcing from sources other than CH_4.

The O_3 direct radiative forcing across the Arctic between 1990–2015 from all emissions source regions was approximately -23 mW/m² (Figure 8.27), with negative contributions to this forcing arising from emissions reductions over both the eastern and western Arctic Council states and the Rest of Europe. Changes in O_3-precursors in the same source regions resulted in negative O_3 direct radiative forcings in all the other receptor regions, with the largest overall O_3 direct radiative forcing of more than -43 mW/m² occurring over the Rest of Europe. Small positive O_3 direct radiative forcings in the Arctic region occurred from emissions changes in the marine, Asian Observers and the Rest of the World source regions, as well as from global CH_4 changes. The positive direct radiative forcings from these source regions resulted in an overall positive O_3 direct radiative forcing across the Asian Observers and Rest of the World regions, with a 46 mW/m² direct radiative forcing over the period 1990–2015 across the Asian Observers.

Future changes in emissions of NO_X, NMVOCs and CO from most source regions under the CLE scenario tended to result in a negative O_3 direct radiative forcing between 2015–2050 across the majority of receptor regions, including a -10 mW/m² direct radiative forcing over the Arctic (and all Arctic Council Member states) and -19 mW/m² over the Rest of Europe. However, global CH_4 concentrations increased for the period 2015–2050 under the CLE scenario, resulting in a positive O_3 direct radiative forcing from changes in CH_4 across all receptor regions, with the largest being 35 mW/m² over Asian Observers and the Rest of the World. Coupled with increases in O_3-precursor emissions across the Rest of the World under the CLE scenario between 2015–2050, an overall positive O_3 direct radiative forcing of 32 mW/m² was calculated for the Rest of the World, and a slightly lower result of 10 mW/m² over the Asian Observer countries.

The large reductions in O_3 precursor emissions under the MFR scenario across all source regions and globally for CH_4 induced a corresponding negative O_3 direct radiative forcing between 2015–2050 across all receptor regions and of -98 mW/m² globally. An O_3 direct radiative forcing of -84 mW/m² occurred between 2015–2050 under the MFR scenario across the Arctic region, with the largest contributing source region being the western Arctic Council Member states and the Asian Observer countries. The largest overall O_3 radiative forcing of -171 mW/m² was calculated over the Asian Observers, with a strong contribution from changes in local emissions sources.

8.4.4.4 Aerosols

Simulated aerosol direct radiative forcings are available for 2015, relative to an approximated pre-industrial atmosphere

Table 8.3 Arctic and global MMM direct radiative forcing and standard deviation in 2015, for emissions from all anthropogenic sources of BC, OC, and S.

	Direct radiative forcing, F_{dir} (W/m^2)			
	BC	OC	S	Total
Arctic	0.31±0.17	0.03±0.03	-0.15±0.02	0.19±0.17
Global	0.40±0.13	0.01±0.03	-0.22±0.12	0.18±0.18

with negligible anthropogenic emissions and the same natural emissions as in 2015 (Table 8.3). The preindustrial reference year for the purpose of diagnosing direct radiative forcings is 1850, although it should be noted that pre-industrial concentrations of SLCFs and radiative forcings are subject to large uncertainties (Carslaw et al., 2013). Possible forcing biases that may result from assuming a steady natural background, are probably small, compared to these forcing uncertainties. Two of the models (CESM and CanAM5-PAM) provided separate direct radiative forcings for global emissions of BC, OC, and sulfur, based on the IIASA-GAINS ECLIPSE V6b anthropogenic emissions in 2015 (Chapter 2). In addition, one ESM provided separate direct radiative forcings for BC and sulfur emissions (MRI-ESM2) and another (UKESM1) for BC emissions only. Contributions of longwave radiative fluxes to the direct radiative forcing are omitted in the following analysis. Simulated longwave radiative flux contributions to aerosol radiative forcings are small in simulations with GISS-E2.1 (Section 8.3.2.2).

In contrast to the other models, the simulation with GISS-E2.1 involved feedbacks between aerosols and climate, which can cause differences in diagnosed direct radiative forcings. Therefore, MMM forcing estimates provided in the following analysis do not include results from GISS-E2.1.

Global MMM direct radiative forcings from emissions of BC in 2015 (Table 8.3) are within the range of uncertainty of radiative forcings from interactions with radiation for 1750 to 2005, according to CMIP5 simulations (0.40 W/m^2, range from +0.05 to +0.80 W/m^2) for BC from fossil fuel and biofuel (IPCC, 2013c).

The forcing from emissions of OC is slightly larger than the CMIP5 forcing for primary OC from fossil-fuel and biofuel sources for 1750–2005 (–0.09 W/m^2, range –0.16 to –0.03 W/m^2) (IPCC, 2013c). All the available OC global forcing estimates are close to nil, even considering uncertainties in the forcing. On a regional scale, OC forcings can be positive or negative, depending on the importance of absorption versus scattering of solar radiation by the aerosol and the surface albedo.

The forcing from emissions of sulfur (Table 8.3) is also within the previously reported range but the mean forcing is weaker for the current study (-0.40 W/m^2, range -0.60 to -0.20 W/m^2; IPCC, 2013c). It is also weaker than the MMM direct radiative effect from sulfate of -0.34 W/m^2, according to simulations for 1750–2010 from the Aerosol Comparisons between Observations and Models (AeroCom) initiative (Myhre et. al., 2013). These differences may be partly related to reductions in global sulfur emissions after 2005 and 2010, respectively. In addition, reductions in sulfur emissions from China are considerably larger in the AMAP emissions data set than simulated in CMIP5 (Chapter 2), which likely explains part of the differences.

Direct radiative forcings are similar to estimates for 2010 from AMAP (2015a) in Figure 8.28. In particular, the global mean direct BC radiative forcing of 0.38 W/m^2 in 2010 agrees very well with the forcing in 2015, for similar global mean BC emissions in 2010 and 2015 (5.92 Tg/y in 2010 and 6.35 Tg/y in 2015). The Arctic direct radiative forcing associated with anthropogenic BC emissions in 2010 is 0.40 W/m^2, which is higher than the forcing in 2015.

The contributions of BC emissions from Arctic Council Member states to the Arctic forcing were 0.067 W/m^2 (2010) and 0.050 W/m^2 (2015), respectively, much weaker than contributions of other regions of the world to the total Arctic forcing. In comparison, anthropogenic sources of BC in Arctic Observer countries contributed 0.16 W/m^2 to the total Arctic forcing in 2015. Although sources in Arctic Observer countries produced 36% of the total emissions of anthropogenic BC, these emissions contributed 50% of the Arctic and 35% of the global mean BC anthropogenic direct radiative forcings in 2015. In turn, the Arctic Council Member states produced 8% of the total anthropogenic BC emissions, which caused 16% of the Arctic and 6% of the global mean BC anthropogenic direct radiative forcings.

The diagnosed direct Arctic BC radiative forcing emissions from oil-and-gas-sector sources in eastern Arctic Council Member states in 2015 was weaker than the corresponding value for emissions in 2010 from AMAP (2015a) (0.017 W/m^2 and 0.008 W/m^2, in 2010 and 2015, respectively), although both estimates were based on very similar emissions (about 0.066 Tg/y). Consequently, reduced radiative forcings in 2015 were likely caused by differences in the models. In general, uncertainties in aerosol concentrations and optical properties in the Arctic tend to be large compared to global mean results, owing to uncertainties associated with the long-range transport of pollutants to the Arctic and their deposition thereafter (Chapters 6 and 7).

Direct radiative forcings from emissions of sulfur were also similar in 2010 and 2015. In comparison to Table 8.3, the total Arctic and global mean direct radiative forcings in 2010 were -0.16 W/m^2 and -0.20 W/m^2, respectively. As was the case with BC emissions, Arctic forcings associated with emissions of sulfur from Arctic Council Member states were relatively weak, compared to other regions (-0.056 W/m^2 in 2010 and -0.037 W/m^2 in 2015).

In addition to direct radiative forcings, effective radiative forcings were available for emissions of BC, OC, and sulfur from simulations with CanAM5-PAM for all regions and sectors for 2015, based on IIASA-GAINS ECLIPSE V6b emissions data (Section 8.2.2). Additionally, effective radiative forcings were available from simulations with MRI-ESM2 for emissions of BC and sulfur from fossil-fuel and biofuel sources, and emissions

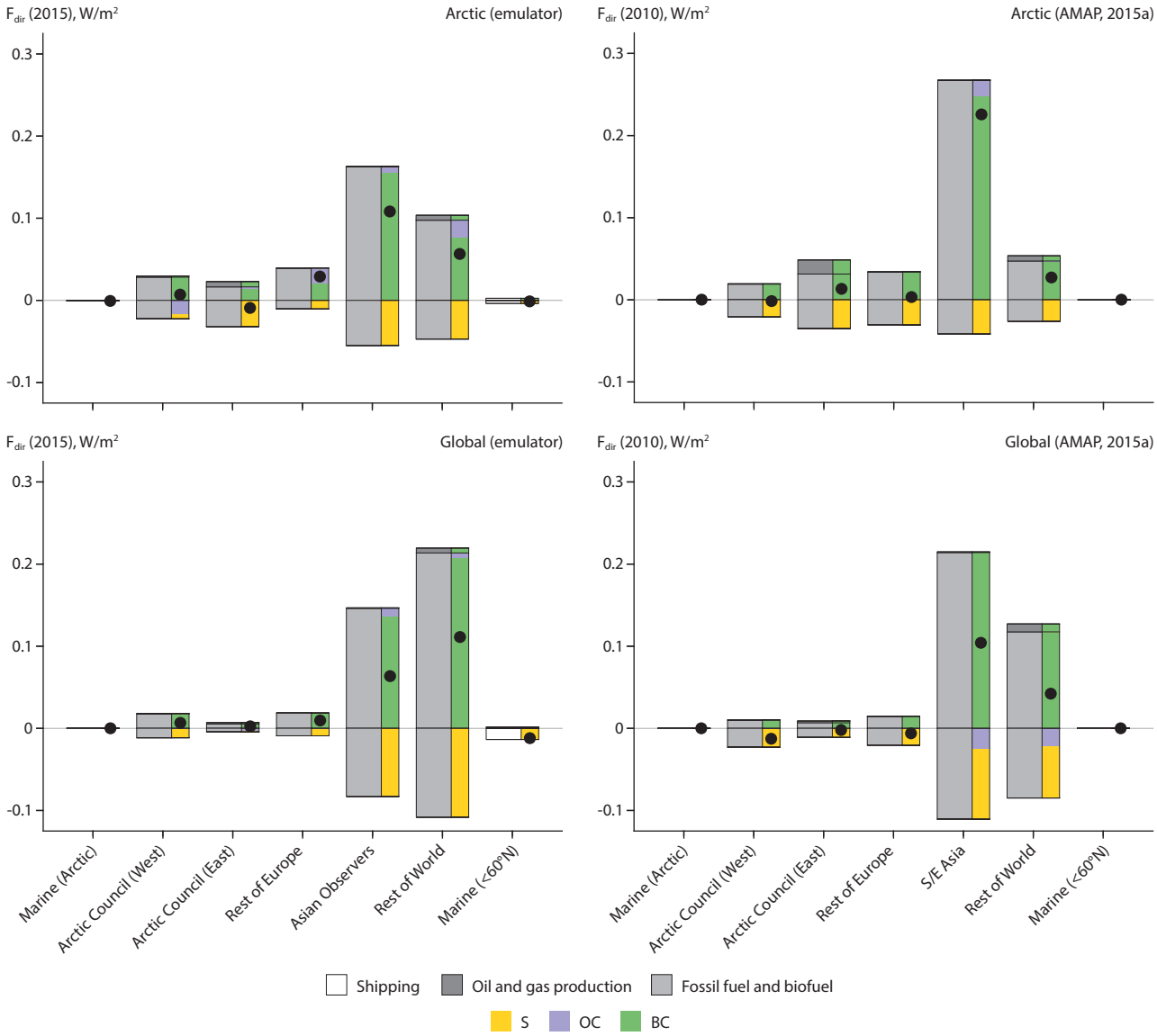

Figure 8.28 Contributions of OC, S, and BC emissions in 2015 (left) and 2010 (right), from different regions and sectors, to the total anthropogenic aerosol direct radiative forcing in the Arctic (top) and global mean (bottom). Bullets indicate net forcings. Multi-model results for emissions in 2010 (right) are taken from AMAP (2015a) and are based on different models and emissions, to those used for 2015 (left). In addition, different region boundaries were used for emissions from Asia and the Rest of the World in AMAP (2015a), which limits comparisons of results for these two regions in the graphs. Furthermore, direct radiative forcings for shipping sources were not included for results for AMAP (2015a).

of BC from oil-and-gas-sector sources, in east Arctic Council Member states, based on the same emissions data. According to the available results from CanAM5-PAM, emissions from the regions and sectors simulated in MRI-ESM2 could be expected to account for nearly all of the net global mean effective radiative forcing from interactions with radiation due to emissions of BC (>97%) and S (>94%).

Although for each emissions perturbation the models were integrated over 100 years (CanAM5-PAM) and 50 years (MRI-ESM2), respectively, the temporal variability in simulated effective radiative forcings is considerable and causes notable uncertainties in mean results. For the following analysis, uncertainties in simulated radiation forcings were determined based on 10–90 percentile ranges of simulated annual mean radiative forcings using perturbed emissions for different combinations of aerosol species, regions, and sectors. Uncertainties in the combined total aerosol radiative forcing were calculated under the assumption that emissions perturbations generate radiative forcings that can be combined linearly and are statistically independent of each other. Considering that aerosol radiative forcings can be strongly coupled through atmospheric physical and chemical feedback processes, this should be regarded as a conservative approach that overestimates statistical uncertainties in total radiative forcings. The absolute statistical uncertainty in total effective radiative forcings is lower than the estimated statistical uncertainty. However, it is useful to consider the relative magnitudes of the estimated statistical uncertainties as a measure of the robustness of the impacts on temperature of the various forcing mechanisms and emitted species. Beyond the statistical uncertainties, the analysis from the emulator simulations of radiative forcings and Arctic temperatures in the assessment did not account for any other sources of uncertainty. Given that results from only two models were available, systematic uncertainties in radiative forcings could not be evaluated.

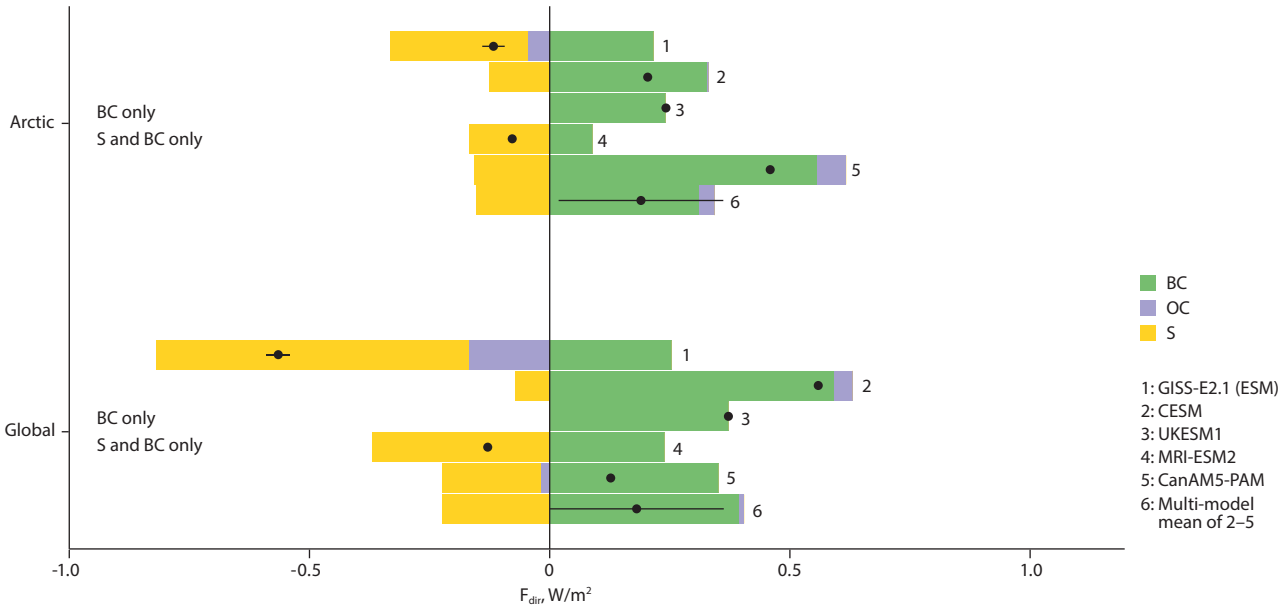

Figure 8.29 Arctic global annual mean anthropogenic aerosol direct radiative forcings in simulations with CCMs, climate models, and one ESM (GISS-E2.1) for 2015, relative to 1850. The bottom bar refers to multi-model mean (MMM) results for CESM, UKESM1, MRI-ESM2, and CanAM5-PAM. Bullets indicate net combined direct radiative forcings resulting from emissions of S, OC, and BC. The horizontal black lines (top and bottom bars) depict standard deviations of the ensemble-mean net radiative forcing for GISS-E2.1 (Section 8.3.2.2) and the MMM-weighted CCM and climate model radiative forcings, respectively. Only direct radiative forcings from emissions of BC are available for UKESM1 ('BC only') and from emissions of BC and S for MRI-ESM2 ('S and BC only'). Direct radiative forcings for CanAM5-PAM and GISS-E2.1 include emissions from all fossil-fuel and biofuel sources, shipping, and the oil and gas sector. Results from CESM and MRI-ESM2 include fossil-fuel and biofuel sources, and oil-and-gas sector BC emissions from eastern Arctic Council Member states (which are the dominant contributions to the BC direct radiative forcing according to results from the other models).

Unless stated otherwise, the mean results from simulations of effective radiative forcings undertaken with CanAM5-PAM and MRI-ESM2 are assessed here (where they were available in both models for the same species, sectors, and regions). Results from CanAM5-PAM were used where corresponding results were not available from MRI-ESM2. Subsequently, these forcings are also used in the emulator simulations (Olivié et al., 2021) of temperature changes in following chapters.

For emissions of BC, the global and annual mean effective aerosol radiative forcing from interactions with radiation is systematically weaker than the corresponding direct radiative forcing in the same models in 2015 (Tables 8.3 and 8.4, and Figure 8.29), which largely reflects the impact of rapid physical feedbacks on effective radiative forcings, as described at the beginning of this section (Section 8.4.4). Consequently, net mean aerosol effective radiative forcings from interactions of all aerosol species with radiation are lower than the net mean direct radiative forcings. However, uncertainties are substantial for mean effective radiative forcings in the Arctic.

Considerable statistical uncertainties exist for effective radiative forcings from interactions of SLCFs with clouds and surface albedo (Olivié et al., 2021). The calculations of these forcings are more sensitive to the variability in cloud albedo in the model simulations than forcings from interactions with radiation, which mostly explains the large uncertainties.

Net global mean effective radiative forcings from interactions of anthropogenic aerosols with radiation in the two models and the emulator agree with the results from simulations with four ESMs for CMIP6, including MRI-ESM2, for 1850–2014 (Thornhill et al., 2021). Similarly, net mean effective radiative forcings from interactions with surface albedo and clouds in the emulator are also within the range of uncertainty of the CMIP6-based results for emissions of BC, OC, and S (Figure 8.30 and Table A8.9 in the Appendix).

The estimated statistical uncertainties in the total forcings are very substantial, for the reasons outlined above (Figure 8.30). Uncertainties in forcings from interactions of aerosols with radiation are lower than those from surface albedo and cloud interactions, which provides a high degree of confidence in the statistical robustness of the former.

Global effective radiative forcings from interactions of BC with surface albedo may also be compared to global snow albedo direct radiative forcings associated with deposition of BC on snow and ice from CMIP5 (0.04 W/m^2, with a range of 0.02 W/m^2–0.09 W/m^2) and from Lee et al. (2013) for 1850–2000 (with a range of 0.014 W/m^2–0.019 W/m^2). These are less than the effective radiative forcing from interactions of BC with surface albedo in the current assessment (0.09±0.41 W/m^2). This is partly due to the effective forcing accounting for amplifying feedbacks of snow radiative properties. It amounts to the instantaneously increased absorption of solar radiation by BC impurities in snow, which are not included in snow albedo direct radiative forcings.

The net global mean effective radiative forcing from all species and forcing mechanisms in the emulator is within the range of uncertainty of the CMIP6 models according to Thornhill et al. (2021) and Smith et al. (2020). The latter study is based on simulations with an ensemble of 17 ESMs, and employs the same emissions that were used by Thornhill et al. (2021). Both

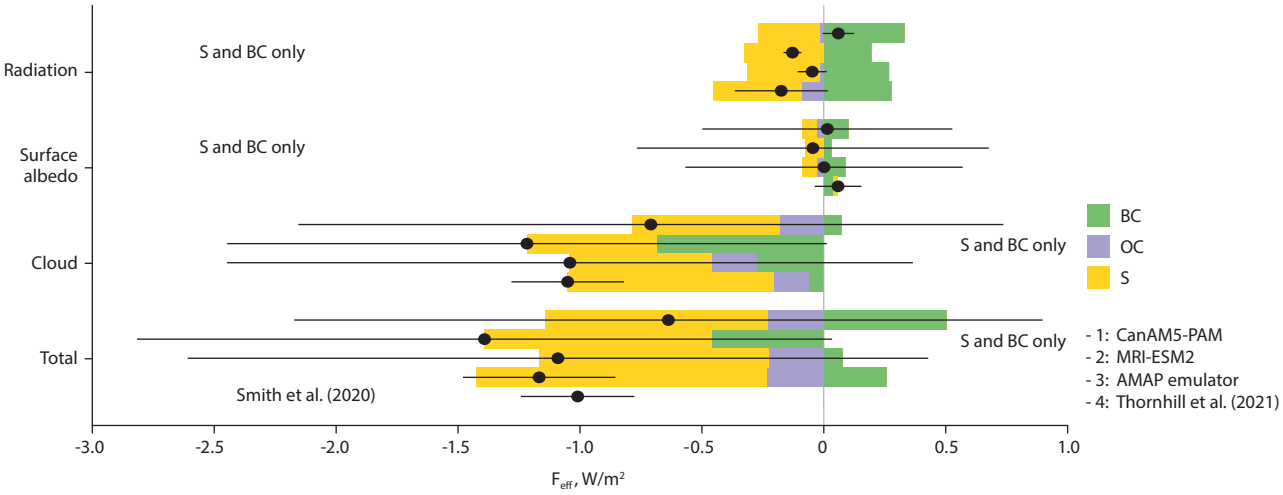

Figure 8.30 Global mean effective radiative forcings from aerosols in the AMAP emulator and CMIP6 models, as indicated on the right. Forcings are for 2015 (AMAP) and 2014 (CMIP6), relative to 1850. Bullets refer to net direct radiative forcings. Black horizontal lines represent statistical uncertainty ranges for CanAM5-PAM, MRI-ESM2, and the emulator; and standard deviations across multi-model estimates for results from Thornhill et al. (2021) and Smith et al. (2020).

studies include contributions of longwave and shortwave fluxes to diagnosed effective radiative forcings.

According to Smith et al. (2020), the MMM effective radiative forcing from interactions with both radiation and clouds (-1.04±0.20 W/m²) is comprised of a shortwave contribution of -1.26±0.46 W/m² offset by a longwave contribution of 0.23±0.36 W/m². The approximate partial radiative perturbation (APRP) method (Taylor et al., 2007) was used to deconstruct the shortwave effective radiative forcing into interactions of aerosol with radiation and clouds in Smith et al. (2020). The large inter-model spread in both the shortwave and longwave forcings is driven by the models that include aerosol interactions on ice clouds, which show the strong negative shortwave and positive longwave forcings (Smith et al., 2020; Oshima et al., 2020). Contributions of longwave fluxes tend to be small in most models that exclude ice-cloud interactions, and are subject to considerable uncertainties related to diagnostic calculations and interactions of aerosols with ice clouds (Smith et al., 2020).

The earlier assessments of global net effective radiative forcings from CMIP5 for 1750–2011 (IPCC, 2013c) for interactions of aerosol with radiation (-0.45 W/m² [-0.96 W/m²–to 0.05 W/m²]) and clouds (-0.45 W/m² [-1.2 W/m²–0.0 W/m²]) differ from the corresponding results from CMIP6 (Thornhill et al., 2021) and from results in Table 8.4. This reflects improvements in models and observational constraints (McCoy et al., 2020; Bellouin et al., 2020).

Although there is relatively good agreement in net cloud forcings between the emulator and results from Thornhill et al. (2021), the relative contributions from the various aerosol types to the net forcing differ greatly between

Table 8.4 Mean Arctic and global effective radiative forcings and uncertainty in 2015, for interactions of anthropogenic aerosols with radiation, surface albedo, and clouds.

	Effective radiative forcing from interactions with radiation, F_{rad} (W/m²)			
	BC	OC	S	Total
Arctic	0.21±0.19	0.02±0.03	-0.30±0.09	-0.07±0.22
Global	0.27±0.04	-0.02±0.03	-0.30±0.03	-0.05±0.06
	Effective radiative forcing from interactions with surface albedo, F_{alb} (W/m²)			
	BC	OC	S	Total
Arctic	0.85±0.54	0.10±0.21	0.06±0.42	1.01±0.71
Global	0.09±0.41	-0.03±0.21	-0.06±0.32	0.00±0.57
	Effective radiative forcing from interactions with clouds, F_{cld} (W/m²)			
	BC	OC	S	Total
Arctic	-0.10±1.06	0.20±0.60	-0.16±0.80	-0.06±1.46
Global	-0.28±1.00	-0.18±0.60	-0.58±0.78	-1.04±1.40
	Total effective radiative forcing, F_{tot} (W/m²)			
	BC	OC	S	Total
Arctic	0.96±1.21	0.31±0.64	-0.39±0.91	0.88±1.64
Global	0.08±1.08	-0.23±0.64	-0.94±0.85	-1.09±1.52

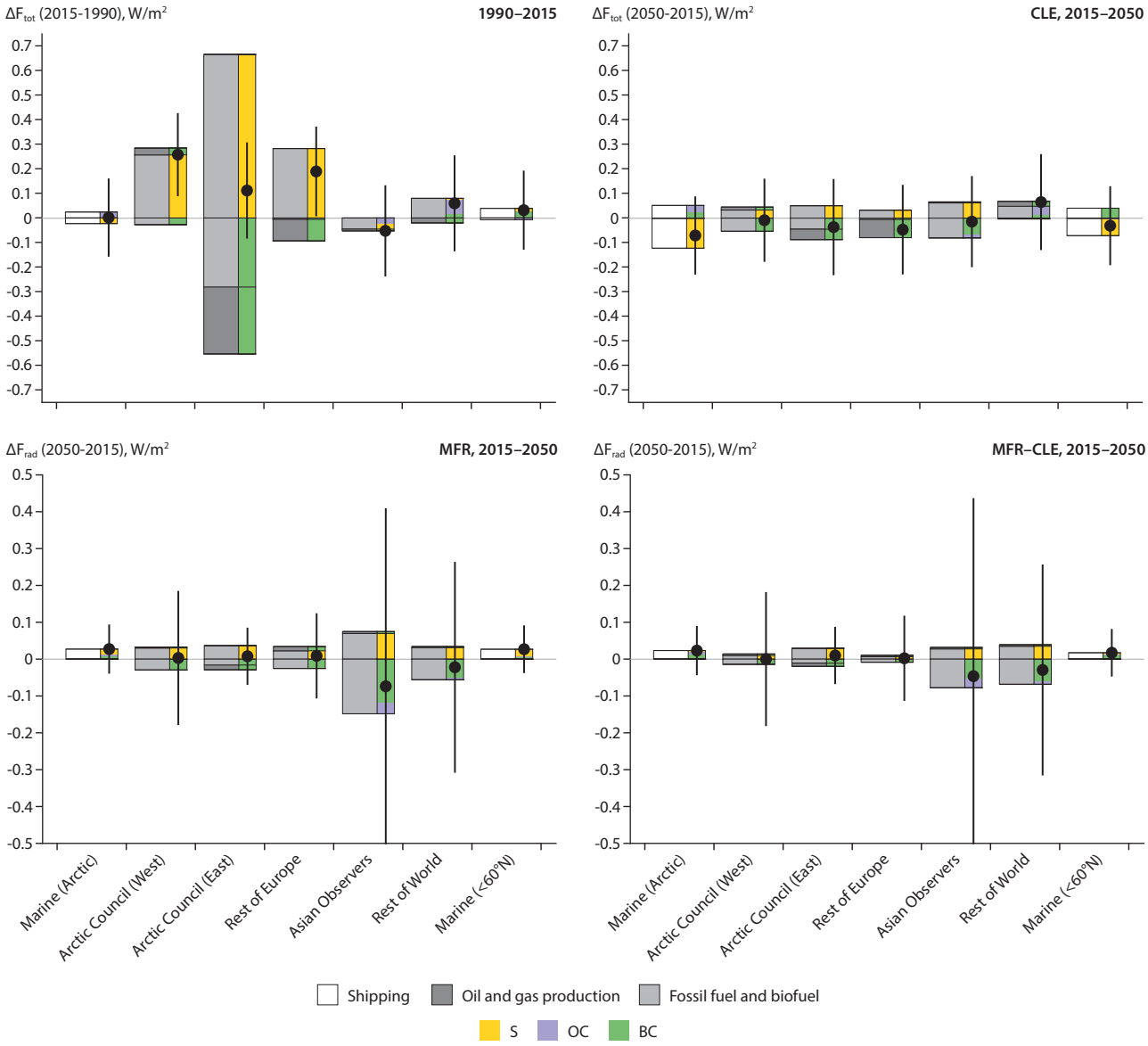

Figure 8.31 Contributions of S, OC, and BC emissions to the Arctic effective radiative forcing from interactions of aerosols with radiation for 1990–2015 (top left) and 2015–2050 (other panels). Projected changes according to the CLE and MFR scenarios are shown in the top right and bottom left panels, respectively, with the differences between them depicted in the bottom right panel. Bullets indicate net mean forcings, and vertical black lines refer to their uncertainties.

the models. In particular, interactions of BC aerosols with clouds produce negative forcings in MRI-ESM2 but weak positive forcings in CanAM5-PAM. These differences are plausible, given large uncertainties in simulated cloud microphysical properties and impacts of aerosols on cloud albedo (Chapter 7, Stjern et al., 2017).

Simulated effective radiative forcings in 2015 were used to determine radiative forcings for different time periods between 1990–2050, under the assumption that forcings respond linearly to changes in emissions. In particular, forcings for individual regions, sectors, and species were scaled by emissions according to the CLE and MFR scenarios.

During 1990–2015, considerable reductions in emissions of sulfur from fossil-fuel and biofuel sources in Arctic Council Member states and the Rest of Europe (Section 8.2.2) caused positive effective radiative forcings in the Arctic, due to the diminishing interactions of aerosols with radiation over this time period (Figure 8.31). This largely caused a net Arctic effective radiative forcing of 0.30±0.22 W/m^2 and global mean forcing of 0.17±0.06 W/m^2 for this period.

For 2015–2050, net effective radiative forcings from interactions with radiation are relatively weak under the CLE scenario, which reflects relatively small trends in projected sulfur emissions. Considerable projected reductions in emissions of BC from sources in Asian Observer countries lead to a net negative forcing over this period, which is partly compensated by the positive radiative forcing arising from diminishing interactions of aerosols with radiation from reduced emissions of sulfur.

Applying best available technologies to reduce emissions of air pollutants globally (MFR scenario) would lead to even greater reductions in emissions of BC from fossil-fuel and biofuel

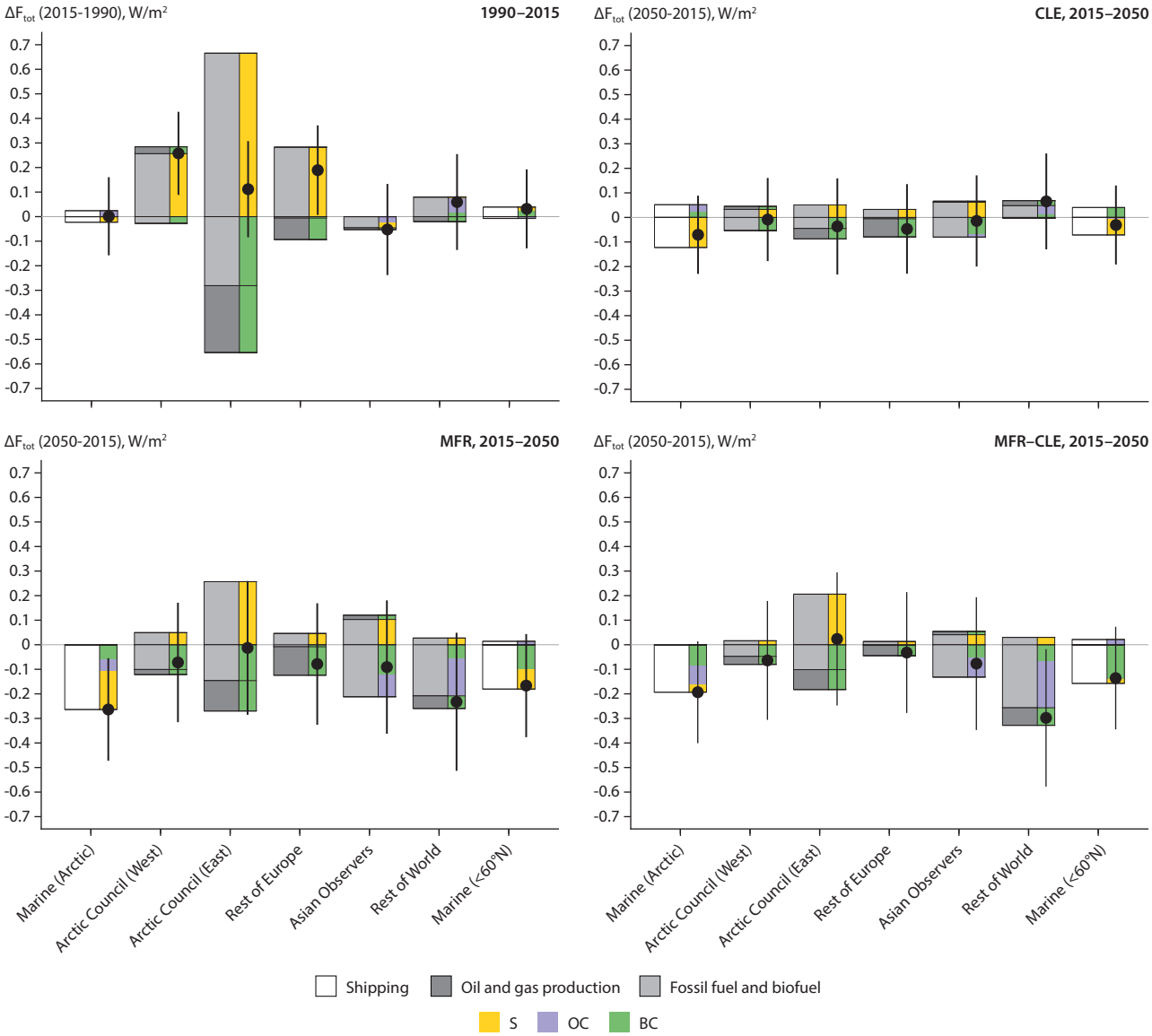

Figure 8.32 Contributions of S, OC, and BC emissions to the effective radiative forcing in the Arctic from interactions of aerosols with radiation, surface albedo, and clouds – for 1990–2015 (top left) and 2015–2050 (other panels). Projected changes according to the CLE and MFR scenarios are shown in the top right and bottom left panels, respectively, with the differences between them depicted in the bottom right panel. Bullets indicate net mean forcings, and vertical black lines refer to their uncertainties. Note that uncertainty ranges are scaled by a factor of 0.1 for clarity (they are larger than shown).

sources in Arctic Observer countries, leading to more negative net forcings by 2050 in comparison to the CLE scenario.

The differences in the net Arctic and global mean forcings between the MFR and CLE scenarios by 2050, from all emissions changes, are -0.02±0.22 W/m^2 and -0.02±0.06 W/m^2, respectively, which is small when compared to radiative forcings for 1990–2015. The weak forcings agree well with net mean effective radiative forcings in the ESM simulation with GISS-E2.1 of -0.03±0.03 W/m^2 (Arctic) and 0.03±0.02 W/m^2 (global), for the same aerosol components but with additional changes in SSTs and sea ice.

Total effective radiative forcings tend to be much greater than those from interactions with radiation alone (Figure 8.32). In general, forcing magnitudes are substantially enhanced by interactions of BC with surface albedo, and interactions of sulfate containing aerosols with clouds.

For 1990–2015, the total Arctic and global mean effective radiative forcings are 0.60±1.64 W/m^2 and 0.79±1.52 W/m^2, respectively. Diminishing aerosol interactions with clouds are largely responsible for positive forcings over these time periods. However, considerably larger forcings would have occurred without reductions of emissions of BC from eastern Arctic Council Member states over this time period.

From 2015–2050, maximum feasible reductions in emissions are projected to reduce the total mean effective radiative forcings by 0.78±1.64 W/m^2 (Arctic), relative to the CLE scenario. However, the corresponding global mean forcing is projected to increase by 0.68±1.52 W/m^2 at the same time. This rise is largely caused by diminishing interactions of aerosols with clouds from reduced emissions of sulfur, OC and BC from sources in the Rest of the World and Asian Observer countries.

8.4.5 Historical and projected Arctic temperature changes

8.4.5.1 Arctic temperature changes in ESM and emulator simulations

ESMs provide evidence for significant future increases in projected Arctic and global mean temperatures between 2015–2050, with a high level of confidence (Section 8.3). MMM simulated rates of Arctic warming differ slightly between the CLE and MFR scenarios in the ESMs (Table 8.5 and Figures 8.10 and 8.33). The warming is consistent with increasing concentrations of CO_2 and greenhouse gas radiative forcings over this period. However, although significant differences exist in simulated concentrations of CH_4, O_3, and aerosol species between these scenarios (Section 8.3.2.1), the net impact of these differences on simulated warming rates are small and uncertain.

The emulator (Olivié et al., 2021) provides contributions of emissions of CH_4, NO_X, CO, VOCs, S, BC, and OC from different source regions and sectors (Section 8.2.1) to net warming rates between 1990–2050. Note that the impacts of changes in O_3 abundances on radiative forcings and temperature are analyzed separately (Section 8.4.5.3).

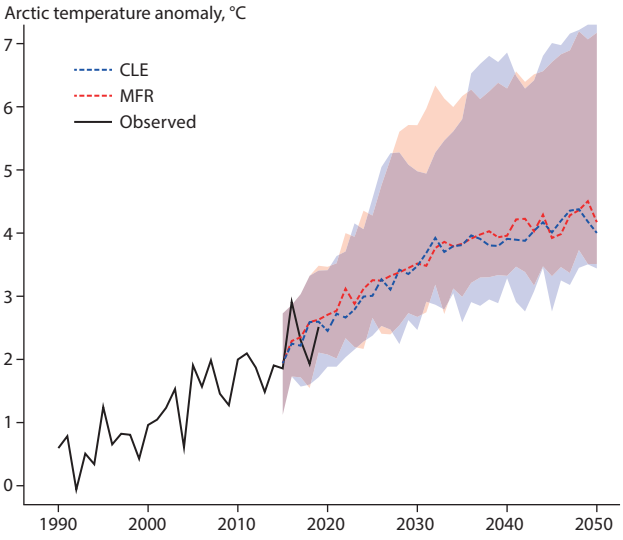

Figure 8.33 ESM Multi-model ensemble median simulated annual NSAT anomaly in the Arctic under CLE (blue dashed lines) and MFR (red dashed lines) scenarios between 2015–2050, relative to the mean observed temperature during 1951–1980. The black line shows observed annual mean temperature anomalies during 1990–2019, according to GISS Surface Temperature Analysis, GISTEMP v4 (Lenssen et al., 2019; Data ref. 8.2). Confidence intervals (shading) reflect the combined uncertainty arising from the multi-model ensemble spread and temperature variability in each individual model ensemble. Constant temperature offsets were added to the model results to match mean simulated and observed temperatures in 2015 to facilitate visualizing the simulated temperature trends.

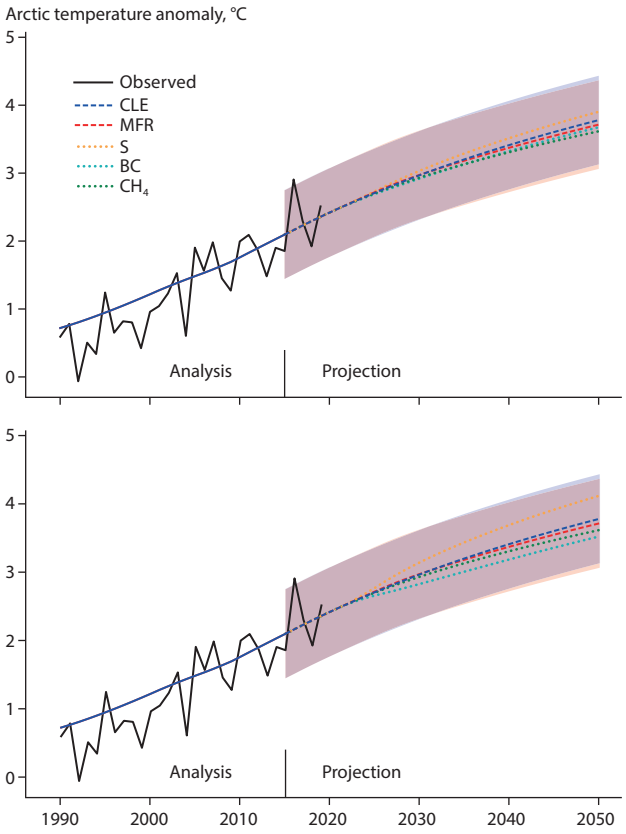

Figure 8.34 Arctic NSAT anomaly, simulated by the emulator. The CLE scenario (blue line) produces steadily increasing temperatures between 2015–2050. The MFR scenario (red line) produces slightly reduced warming trends relative to the CLE scenario during 2015–2050. Black dashed lines show how individual SLCFs contribute to net warming trends in the CLE scenario, either through interactions with radiation (top panel) or all interactions (including with clouds and surface radiation; bottom panel). In the top panel, maximum feasible reductions in emissions of BC or CH_4 produce reductions in warming trends through reduced interactions of BC and CH_4 with radiation (lower black dashed lines), relative to the CLE scenario. In contrast, maximum feasible reductions in S lead to increased warming trends through reduced interactions of sulfate with radiation (upper black dashed line). The shading delineates the statistical uncertainties for the CLE and MFR scenario simulations.

The primary purpose of undertaking the emulator simulations was to understand better how CH_4, aerosols and CO_2 contribute to net simulated changes in temperatures in ESMs. Given the simplicity of the emulator, the approach is suitable for approximating contributions of individual SLCFs to temperature changes on time scales of several decades, averaged over large geographic regions. The emulator does not simulate changes in any other climate variables, such as precipitation or sea ice. Further, it does not account for important contributions to temperature variability. For example, it does not account for inter-annual to multi-decadal natural climate variability, or for radiative forcings associated with volcanic eruptions, vegetation fires, and land-use changes.

Table 8.5 Arctic warming rate and temperature anomaly according to ESM simulations (multi-model ensemble medians).

	Arctic warming rate (°C/decade)		Arctic temperature anomaly (°C)		
Scenario	2015–2030	2015–2050	2015	2030	2050
CLE	1.03±0.99	0.59±0.63	1.94±0.80	3.48±1.26	4.00±2.07
MFR	1.05±1.15	0.64±0.57	1.94± 0.80	3.52±1.52	4.17±1.83

Table 8.6 Arctic warming rates and temperature anomalies according to emulator simulations

	Arctic warming rate (°C/decade)			Arctic temperature anomaly (°C)			
Scenario	1990–2015	2015–2030	2015–2050	1990	2015	2030	2050
CLE	0.55±0.37	0.58±0.62	0.48±0.26	0.72±0.65	2.10±0.65	2.97±0.65	3.79±0.65
MFR	0.55±0.37	0.59±0.62	0.46±0.26	0.72±0.65	2.10±0.65	2.98±0.65	3.72±0.65

Despite the emulator's simplicity, the Arctic warming rate according to the GISTEMP analysis (0.71±0.22°C/decade) is within the statistical uncertainty range of the forced warming rate in the emulator (0.55±0.37°C/decade) from 1990–2015 (Figure 8.34 and Table 8.6). Radiative forcings of CO_2 and CH_4 have increased over this time period, contributing to the simulated and observed warming trends over this period.

The forced warming trend simulated by the emulator continues steadily from the historic time period to the near-term future. Projected near-term warming rates from 2015 to 2030 are within the range of the analyzed historic warming rate from 1990 to 2015. The simulated warming rates decline steadily during 2015–2050. Differences between mean temperatures simulated under the CLE and MFR scenarios are small and well within estimated uncertainty ranges (Table 8.6). In particular, the simulated temperature in 2015 under the MFR scenario differs from the simulated temperature for the CLE scenario by -0.07±0.92°C.

Overall, these results are consistent with results from the ESMs, although rates of warming are systematically higher in the ESMs, especially during the time period 2015–2030 (Table 8.5). This may be related to the ESM simulations being initialized from ESM-simulated conditions in 2015; differences in simulated radiative forcings and CO_2 abundance; natural emissions; or variations in transient climate sensitivity between the models. An analysis of these differences is beyond the scope of this report.

8.4.5.2 How emissions of aerosol chemical species and CH_4 contribute to net Arctic temperature changes

Reduced emissions of CH_4 and BC under the MFR scenario lead to lower Arctic warming rates than those projected for the CLE scenario. Consequently, Arctic mean temperatures in 2050 are reduced by 0.164°C (CH_4) and 0.105°C (BC) from temperatures in 2015. This is because these SLCFs interact less with radiation in the MFR scenario than in the CLE scenario (Table 8.7), given the lower SLCF concentrations. If additional, but uncertain, interactions of BC with clouds and surface albedo are also considered, the decrease in Arctic mean temperature from lower BC emissions is enhanced (0.258°C in 2050, Table 8.8). The relatively small differences in net warming rates between

Table 8.7 Contribution of SLCF species to the net Arctic warming rate and temperature change under the MFR scenario relative to the CLE one, for interactions of the SLCFs with radiation only. Results for each species in the table represent the cooling (negative) or warming (positive) that would be achieved if emissions followed the MFR, rather than the CLE, scenario. Note that temperature responses to emissions of CO, NO_X, and VOCs are due to the impacts of these species on the CH_4 radiative forcing. Further, statistical uncertainties in CH_4 radiative forcing and associated temperature trends are not available and could not be assessed.

Emitted SLCF species	Arctic warming rate (°C/decade)		Arctic temperature change (°C)	
	2015–2030	2015–2050	2030	2050
CH_4	-0.023	-0.047	-0.035	-0.164
BC	-0.033±0.084	-0.030±0.036	-0.049±0.089	-0.105±0.089
S	0.043±0.024	0.035±0.010	0.065±0.025	0.123±0.025
OC	0.000±0.008	0.000±0.003	-0.001±0.008	-0.001±0.008
CO + NO_X + VOCs	0.001	0.004	0.001	0.014
Total	-0.013±0.088	-0.038±0.038	-0.019±0.093	-0.134±0.093

Table 8.8 Contribution of SLCF species to the net Arctic warming rate and temperature change under the MFR scenario relative to the CLE scenario, for interactions of the SLCFs including interactions of BC with radiation, clouds and surface albedo.

Emitted SLCF species	Arctic warming rate (°C/decade)		Arctic temperature change (°C)	
	2015–2030	2015–2050	2030	2050
CH_4	-0.023	-0.047	-0.035	-0.164
BC	-0.094±0.574	-0.074±0.246	-0.141±0.609	-0.258±0.609
S	0.118±0.614	0.097±0.263	0.177±0.651	0.339±0.651
OC	0.003±0.226	0.001±0.097	0.004±0.240	0.004±0.240
CO + NO_X + VOCs	0.001	0.004	0.001	0.014
Total	0.005±0.870	-0.019±0.373	0.006±0.923	-0.065± 0.923

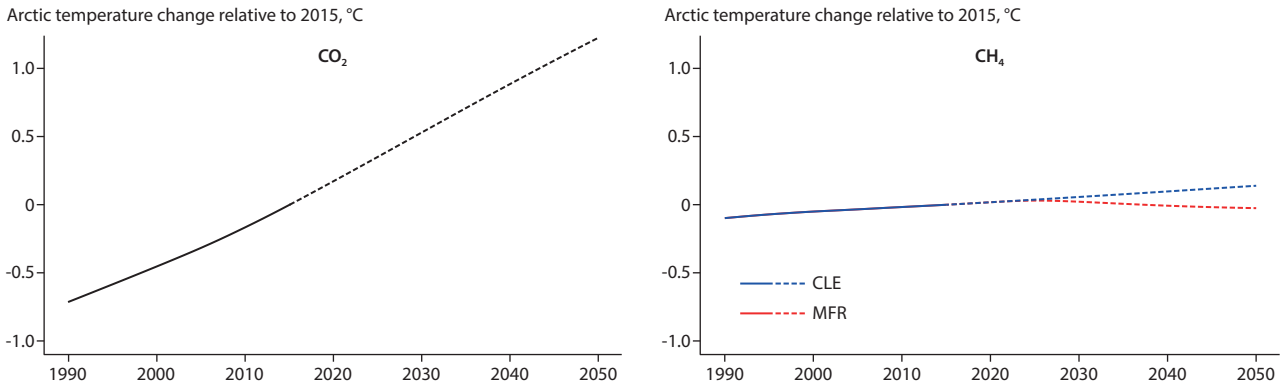

Figure 8.35 Arctic temperature changes associated with a change in mixing ratios of CO_2 (left) according to the SSP2–4.5 scenario and of CH_4 (right) according to CLE and MFR scenarios, both relative to 2015. Full and dashed lines indicate results before and after 2015, respectively.

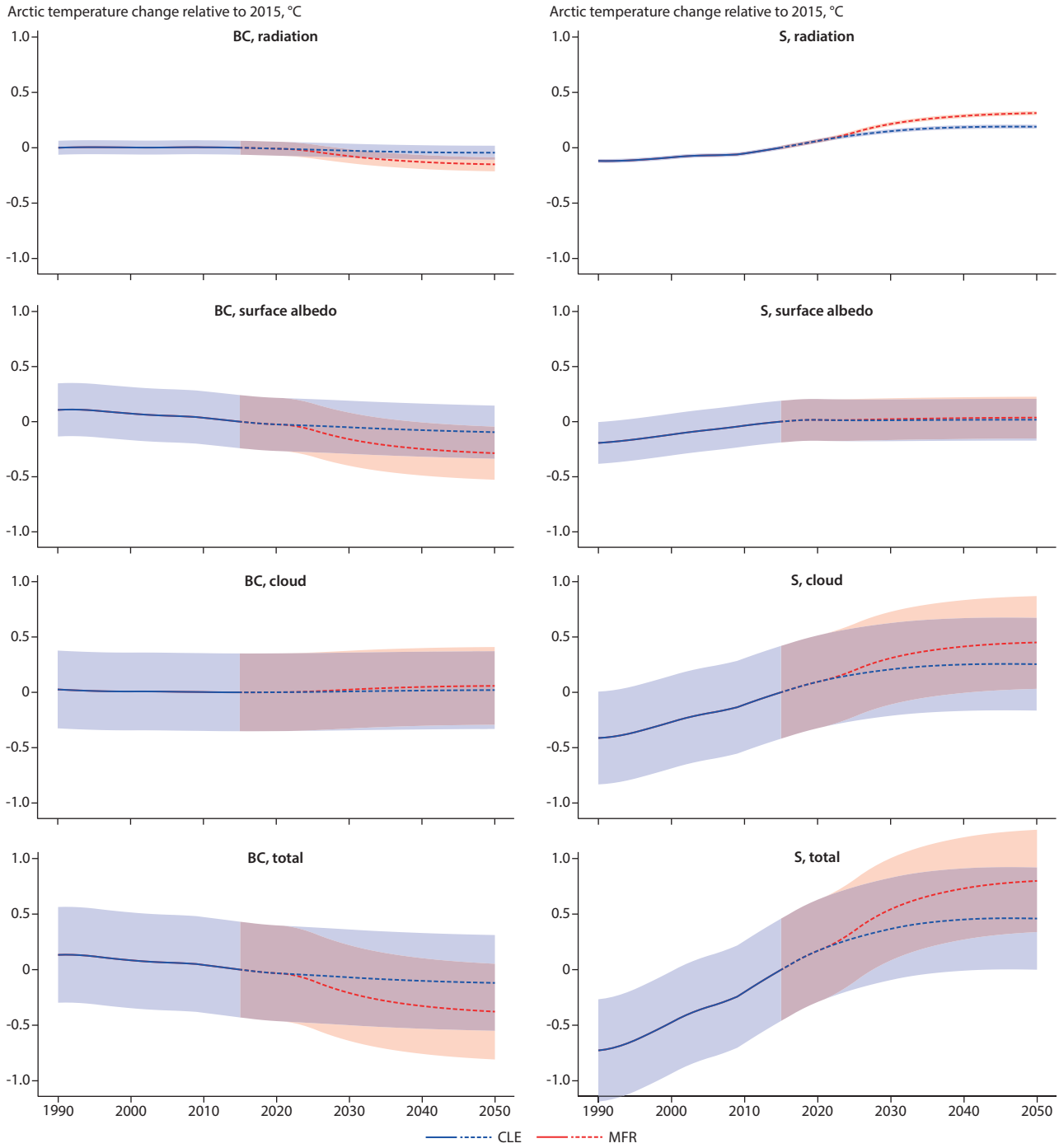

Figure 8.36 Arctic temperature changes in response to changes in emissions of BC (left) and S (right) under the CLE and MFR scenarios, relative to 2015. Rows refer to different aerosol/climate process interactions.

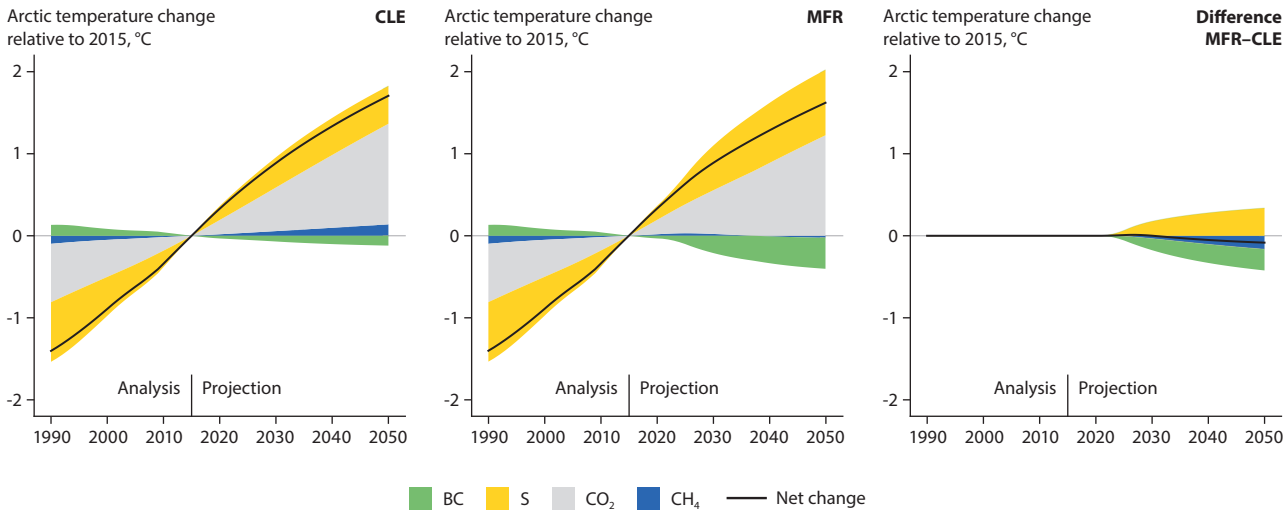

Figure 8.37 Mean Arctic temperature changes in the MFR and CLE scenarios. The shaded areas indicate the contributions of emitted pollutants to the net changes (black lines).

the two scenarios are attributable to reduced S emissions; this causes warming in the MFR scenario relative to the CLE scenario because it results in lower concentrations of sulfate aerosol, which leads to weaker interactions with radiation in the MFR scenario. The net temperature difference between MFR and CLE scenarios from changes in emissions of all SLCF species in 2050 ranges from -0.134°C (for interactions with radiation only) to -0.066°C (for interactions with radiation, clouds, and surface albedo).

Between 1990–2015, interactions of CO_2 with radiation are associated with an Arctic warming rate of 0.285°C/decade. They contributed much more strongly to Arctic warming than interactions of CH_4 or BC with radiation (with warming rates of 0.039°C/decade and 0±0.036°C/decade, respectively [Tables A8.10 and A8.11, and Figures 8.35 and 8.36]). Furthermore, reductions in interactions of sulfate aerosols with radiation also produced relatively small contributions to Arctic warming rates over this time period, with a warming rate of 0.048±0.010°C/decade.

If (more uncertain) interactions of BC and sulfate aerosols with surface albedo and clouds are considered, on top of interaction with radiation, the warming rate contributions are -0.053±0.244°C/decade (BC) and 0.290±0.260°C/decade (S). This indicates that anthropogenic emissions of CO_2 and sulfur contributed nearly equally to net Arctic warming during this time period. However, considerable statistical uncertainties exist, as explained above and analyzed in the following pages. Furthermore, the general scientific understanding of how aerosols and clouds interact is very limited, compared to other relevant forcing processes, which further adds to overall uncertainties around climate. Although it cannot be ruled out that the impacts of reduced sulfur emissions on warming rates are substantially less than estimated here, the consistency of radiative forcings and impacts on temperature seen across the different model simulations and scenarios supports the results (also see Sections 8.4.4.4 and 8.5).

Projected future changes in emissions of CH_4 and BC under the MFR scenario lead to reduced Arctic warming rates in the short and longer term through interactions of these SLCFs with radiation, relative to the CLE scenario (Table 8.7). For 2015–2050, contributions to the warming rate from interactions of CH_4 with radiation range from 0.040°C/decade (CLE) to -0.007°C/decade (MFR). Meanwhile, contributions to the warming rate from interactions of BC with radiation range from -0.013±0.026°C/decade (CLE) to -0.043±0.026°C/decade (MFR). If (more uncertain) interactions with clouds and surface albedo are also considered, contributions to the warming rate associated with BC emissions range from -0.034±0.174°C/decade (CLE) to -0.108±0.174°C/decade (MFR) (Tables A8.10, A8.11, A8.13, and A8.14).

Projected reductions in emissions of sulfur significantly contribute to future Arctic warming rates in both scenarios (Tables 8.7 and 8.8). For 2015–2050, contributions to the warming rate from interactions of sulfate aerosols with radiation range from 0.054±0.007°C/decade (CLE) to 0.089±0.007°C/decade (MFR). If (more uncertain) interactions with clouds and surface albedo are also considered, contributions to the warming rate from S emissions range from 0.132±0.186°C/decade (CLE) to 0.228±0.186°C/decade (MFR) (Tables A8.12 and A8.15).

By comparison, simulated warming rates associated with CO_2 are 0.354°C/decade during 2015–2030 and 0.350°C/decade between 2015–2050.

In the short term, between 2015–2030, the warming rate associated with sulfur reductions under the MFR scenario (0.363±0.434°C/decade) exceeds the warming rate associated with CO_2 (0.354°C/decade). With S emissions following the CLE scenario, the associated warming rate is reduced to 0.245±0.434°C/decade, which is still large compared to the warming that is associated with CO_2 (Figure 8.37).

8.4.5.3 Impacts of tropospheric O_3 changes on net Arctic temperature changes

For 1990 to 2015, changes in emissions of NO_X, CO, VOCs, and CH_4 produce an increase in O_3 globally and a decrease in Arctic mean direct radiative forcings (Section 8.4.4.3). The O_3 forcing changes result in a net Arctic warming impact of 0.0013°C/decade over this time period (Figure 8.38), based on a parameterization of Arctic temperature changes (Olivié et al., 2021).

Between 2015–2050, the global mean O_3 forcing is projected to increase according to the CLE scenario and to decrease under the MFR one. The projected forcings imply an increase in Arctic temperature under the CLE scenario of 0.0012°C/decade, and a decrease of 0.0056°C/decade for the MFR scenario.

The temperature difference between the MFR and CLE scenarios in 2050 is projected to be -0.024°C, with changes in emissions of non-CH_4 precursors (NO_X, VOCs, and CO) contributing -0.014°C and changes in emissions of CH_4 contributing -0.009°C. However, these temperatures are based on tropospheric O_3 changes calculated from a simple parameterization, which does not account for the atmospheric chemical CH_4 feedback or the impacts of climate change (Section 8.4.2).

8.4.5.4 Impacts of regional aerosol and CH_4 emissions sectors

The previous sections provide evidence for the considerable warming and cooling impacts of different SLCFs on Arctic temperature. The magnitudes of these impacts differ between the CLE and MFR scenarios, and depend on which chemical species are emitted. The following analysis shows how emissions from different sources contribute to the net Arctic temperature changes. The analysis distinguishes between different emission regions and sectors (Section 8.2.1). As the previous section showed, O_3 forcing-induced temperature changes are considerably smaller than the impacts of changes in radiative forcings of CH_4 and aerosols on Arctic temperatures (Sections 8.4.5.2 and 8.4.5.3). Consequently, the following analysis only addresses the impacts of CH_4 and aerosol emissions on Arctic climate.

Between 1990–2015, increases in temperature caused by interactions of CH_4 with radiation can be largely attributed to Asian Observer and Rest of the World emissions sources (Figure 8.39, Table A8.16). Even though emissions of NO_X from eastern and western Arctic Council Member states and the Rest of Europe declined over this time period, reduced CH_4 lifetimes from increases in NO_X emissions before 1990 result in a cooling impact on Arctic temperature that still persisted between 1990–2015.

Considerable net Arctic warming from aerosols that occurred during 1990–2015 mainly resulted from reduced sulfur emissions from fossil-fuel and biofuel sources in western Arctic Council Member states (0.325±0.210°C) and the Rest of Europe (0.376±0.257°C) (Figures 8.40 and 8.41, Tables A8.19 and A8.22). The warming was partly compensated for by reductions in BC emissions from eastern Arctic Council Member states (-0.122±0.257°C), which led to reduced interactions with surface albedo during this time. Although similar reductions in

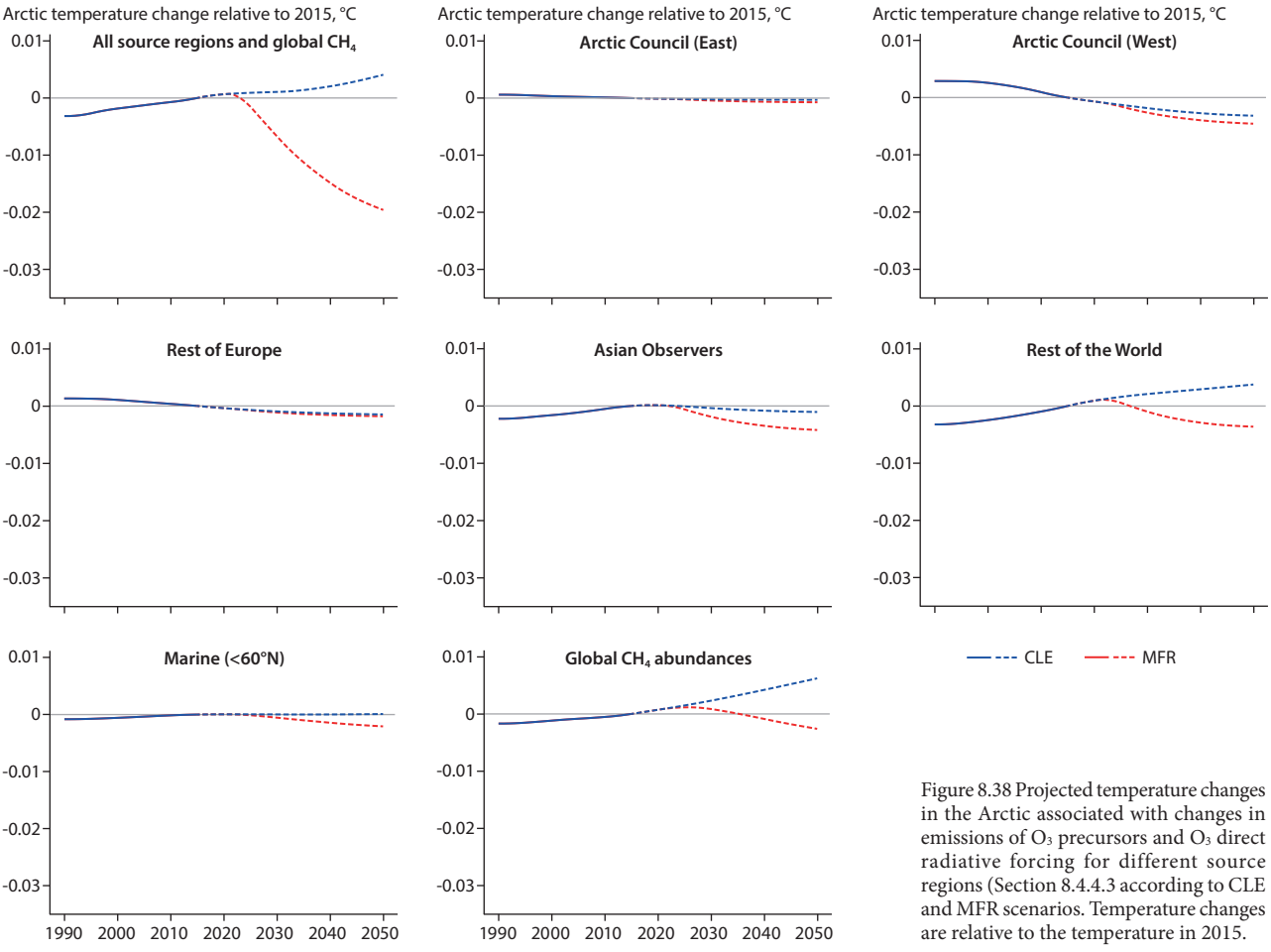

Figure 8.38 Projected temperature changes in the Arctic associated with changes in emissions of O_3 precursors and O_3 direct radiative forcing for different source regions (Section 8.4.4.3 according to CLE and MFR scenarios. Temperature changes are relative to the temperature in 2015.

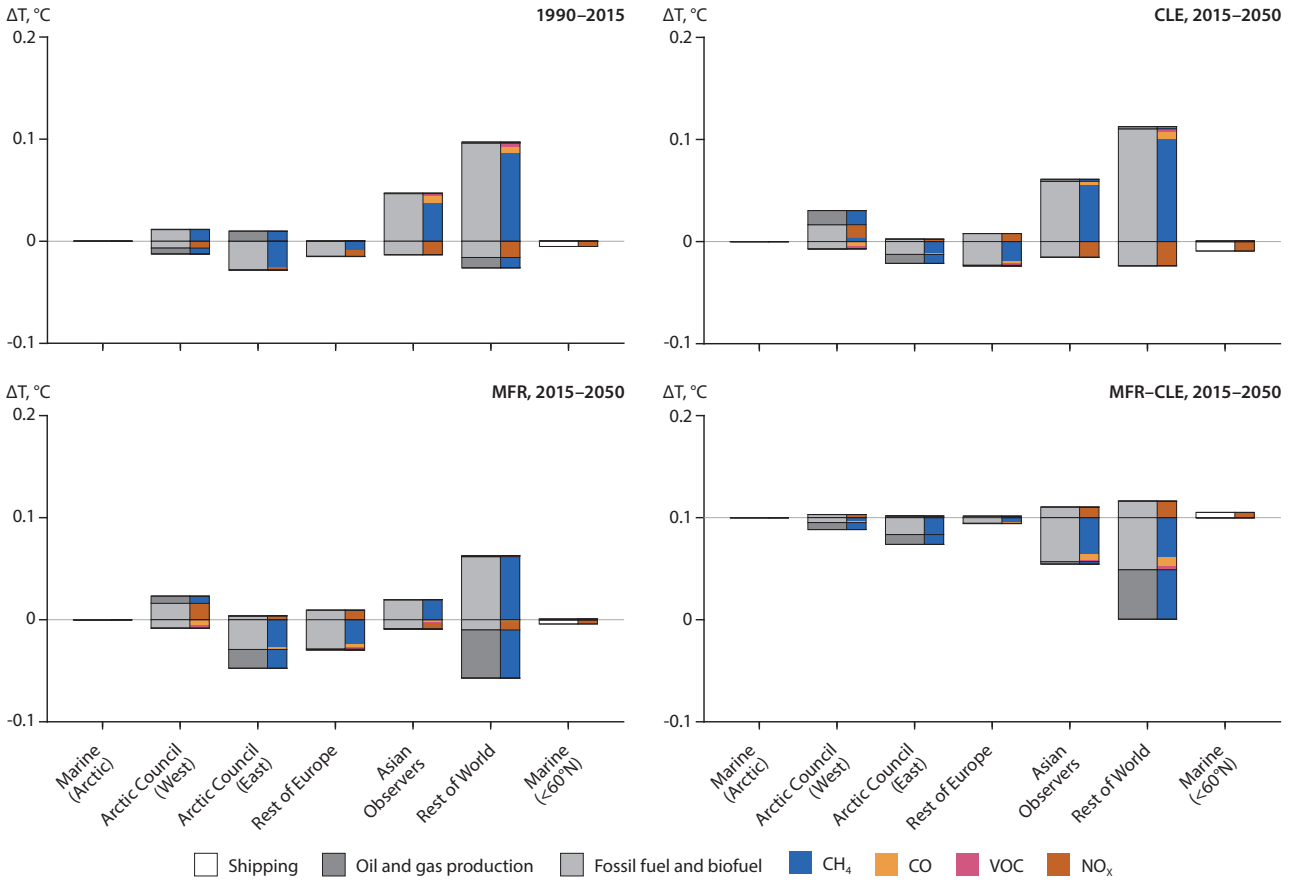

Figure 8.39 Contributions of CH_4, CO, VOCs, and NO_X from different regions and sectors to the Arctic temperature change during 1990–2015 (top left) and 2015–2050. Projected changes under CLE and MFR scenarios are shown in the top right and bottom left panels, respectively, with the difference between them presented in the bottom right panel.

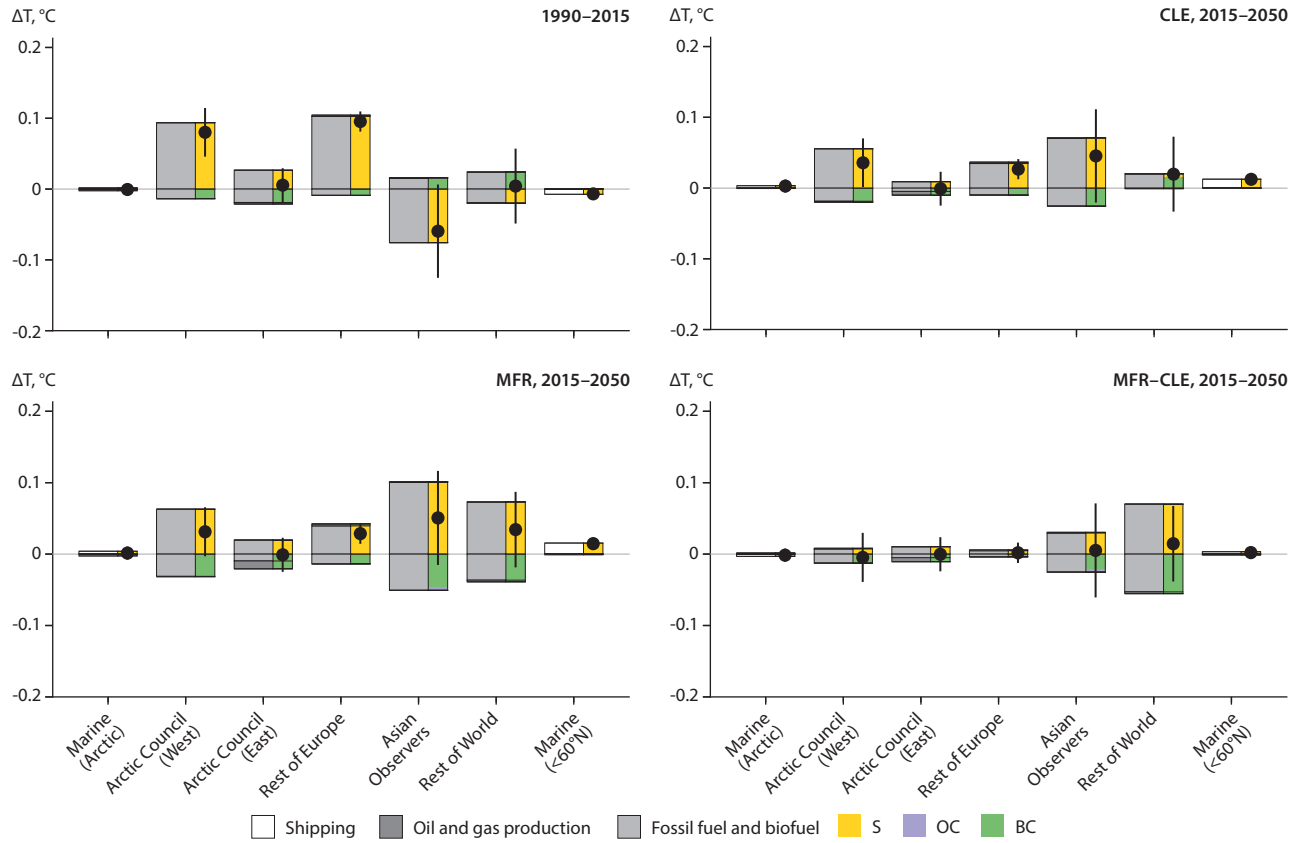

Figure 8.40 Contributions of S, OC, and BC emissions from different regions and sectors to the Arctic temperature change during 1990–2015 (top left) and 2015 to 2050, for interactions of aerosols with radiation only. Projected changes under CLE and MFR scenarios are shown in the top right and bottom left panels, respectively, with the difference between them presented in the bottom right panel. For each emission region, the bullets refer to net temperature changes from all sectors and species. Statistical uncertainties are indicated by the vertical lines.

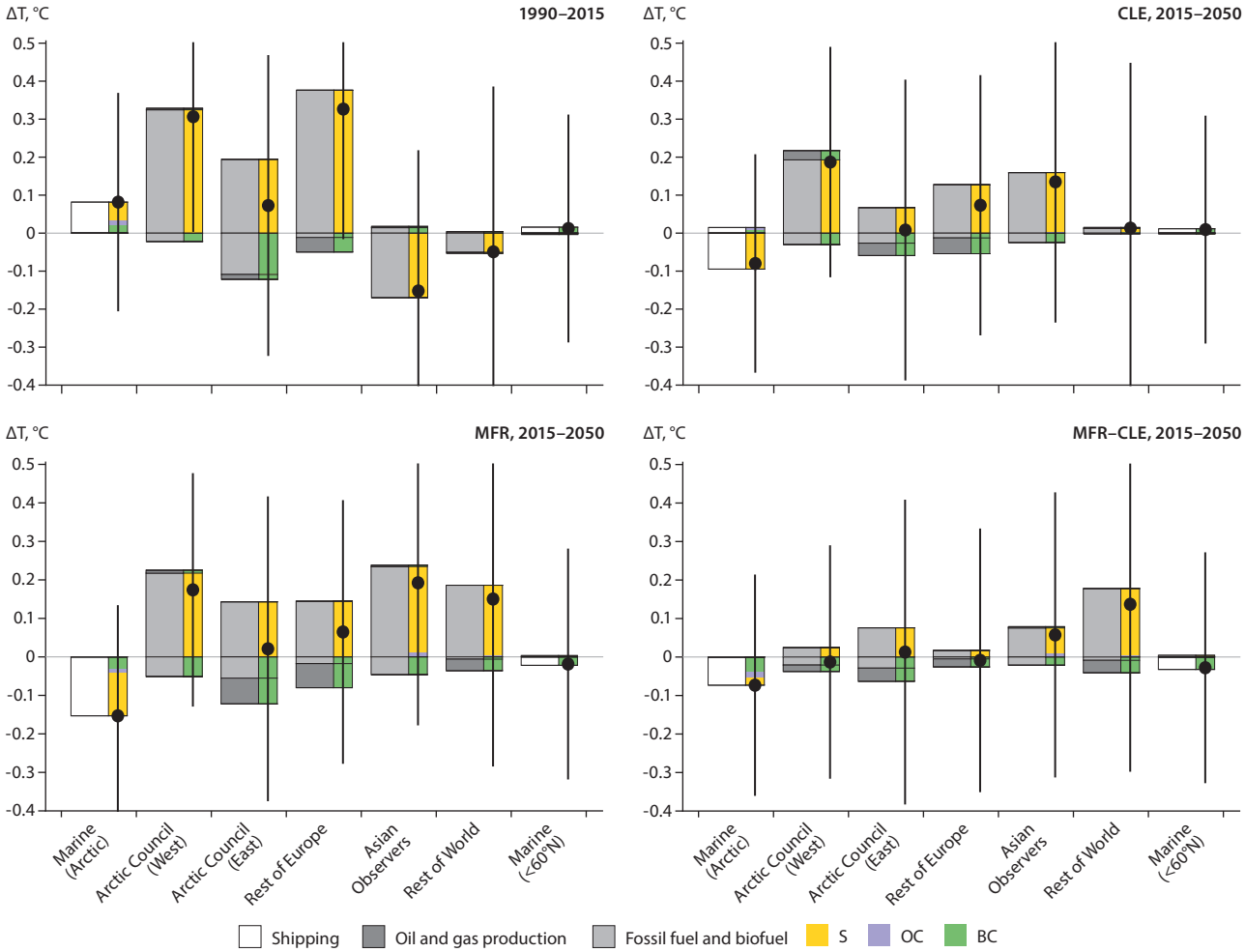

Figure 8.41 Contributions of S, OC, and BC emissions from different regions and sectors to the Arctic temperature change during 1990–2015 (top left) and 2015–2050, for interactions of aerosols with radiation, surface albedo, and clouds. Projected changes under CLE and MFR scenarios are shown in the top right and bottom left panels, respectively, with the difference between them presented in the bottom right panel. For each emission region, the bullets refer to net temperature changes from all sectors and species. Statistical uncertainties are indicated by the vertical lines.

BC emissions also occurred in the Rest of Europe, the impacts on the warming trend were weaker due to the lower sensitivity of Arctic surface albedo and temperatures to sources outside the Arctic (Olivié et al., 2021).

Emissions of CH_4 from fossil-fuel and biofuel sources in Arctic Observer countries under the CLE and MFR scenarios, (causing 0.055°C and 0.020°C of warming, respectively) and the Rest of the World (causing 0.101°C and 0.062°C of warming, respectively) continue to be the dominant source of CH_4-induced Arctic warming for 2015–2050 (Tables A8.17 and A8.18). However, CH_4 emissions are substantially lower under the MFR than the CLE scenario, which causes the considerably reduced CH_4-induced Arctic warming rate under the MFR scenario.

Projected warming during 2015–2050 is considerably enhanced by declining sulfur emissions from fossil-fuel and biofuel sources in eastern and western Arctic Council Member states, the Rest of Europe, and Asian Observers (Figures 8.40 and 8.41). The warming contributions are particularly large under the MFR scenario. Reductions in BC emissions from eastern Arctic Council Member states have a notable cooling influence, especially if interactions of BC with surface albedo are considered (-0.059±0.257°C change for CLE and -0.122±0.257°C change for MFR; Tables A8.20, A8.21, A8.23, A8.24). Under the MFR scenario, reduced BC emissions from oil-and-gas-sector sources from eastern Arctic Council Member states (-0.067±0.208°C change relative to 2015) and the Rest of Europe (-0.063±0.119°C change relative to 2015) are particularly efficient at counteracting the overall temperature increase.

8.5 The impacts of mitigating warming SLCFs on Arctic temperature

As shown in the previous sections, reduced SLCF concentrations under the MFR scenario lead to weak net responses in Arctic temperature, as a result of the diminishing impacts of both cooling and warming SLCFs, in particular BC and sulfur. An additional scenario is available where the focus is on mitigating the impacts of SLCFs using technologies that result in lower climate forcing of net emissions after abatement. Under this CFM scenario (Chapter 2), emissions of BC and CH_4 are very similar to those of the MFR scenario. Emissions of sulfur under the CFM scenario roughly equate to those in the CLE scenario but they are higher than those projected by the MFR scenario. Consequently, the CFM scenario can be analyzed to isolate the effects of reducing warming versus cooling SLCFs in the other scenarios.

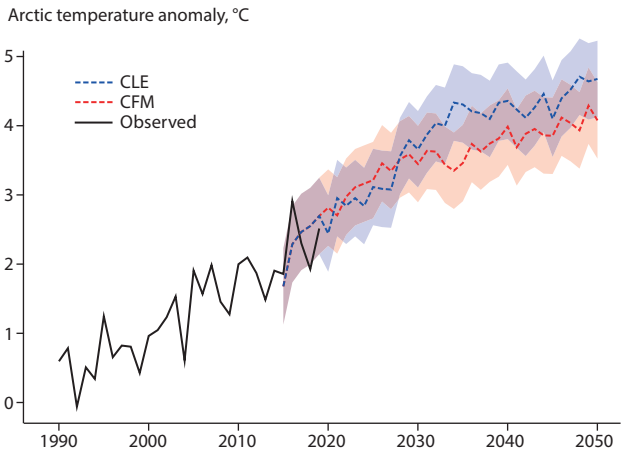

Figure 8.42 Arctic NSAT anomaly, for the CLE (blue) and CFM (red) scenarios for 2015–2050, relative to 1951–1980 mean observed temperature, based on simulations with MRI-ESM2. The black line shows observed annual mean temperature anomalies during 1990–2019, according to GISS Surface Temperature Analysis, GISTEMP v4 (Lenssen et al., 2019; Data ref. 8.2). Confidence intervals (shading) reflect the combined uncertainty arising from the multi-model ensemble spread and temperature variability in each individual model ensemble. Constant temperature offsets were added to the model results to match mean simulated and observed temperatures in 2015 to facilitate visualizing the simulated temperature trends.

Projected Arctic temperatures under the CFM scenario are systematically reduced relative to the CLE scenario, according to simulations undertaken with MRI-ESM2 (Figure 8.42). In 2050, the ensemble mean temperature is projected to be lower by 0.60±0.78°C, corresponding to a reduction in the Arctic warming trend by 0.171±0.316°C/decade from 2015–2050.

Arctic temperatures simulated in the emulator largely agree with those projected by the MRI-ESM2 (Figure 8.43). In 2050, the ensemble mean temperature is projected to be 0.36±0.92°C lower, corresponding to a decline in the Arctic warming trend by 0.103±0.373°C/decade between 2015–2050.

The results confirm that mitigation measures for BC and CH_4 proposed in the CFM and MFR scenarios effectively reduce the projected future Arctic warming trend (Figure 8.44).

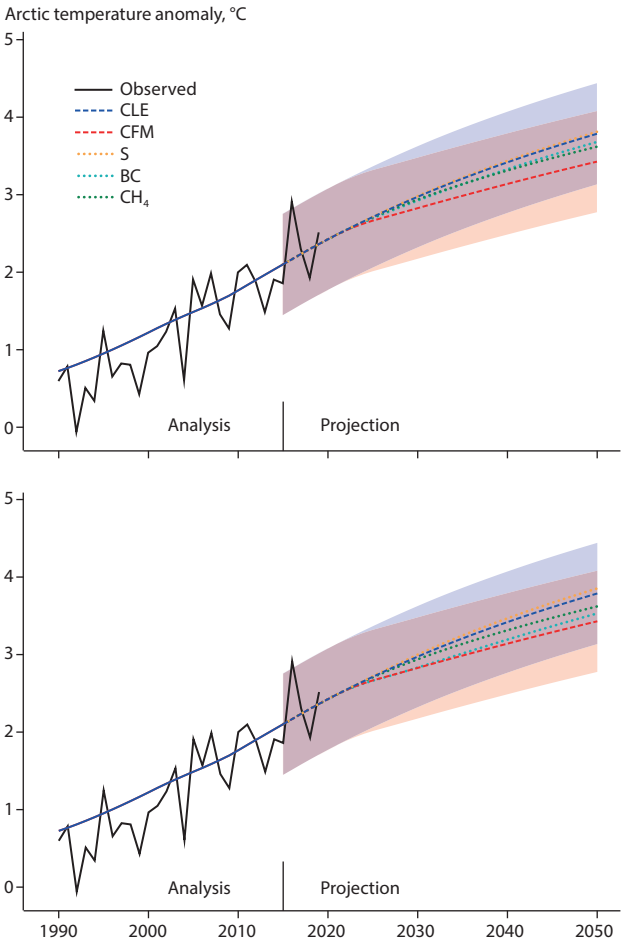

Figure 8.43 Emulator-simulated Arctic NSAT anomaly for the CLE (blue dashed lines) and CFM scenarios (red dashed lines). Contributions of individual SLCFs to net warming trends are shown (black dashed lines), either through interactions with radiation (top panel) or all interactions (including interactions with clouds and surface radiation; bottom panel). Reductions in emissions of BC or CH_4 according to the CFM scenario produce reductions in warming trends in both panels, relative to the CLE scenario. Small differences in emissions of S between the CFM and CLE scenarios lead to small impacts on temperature trends in both panels.

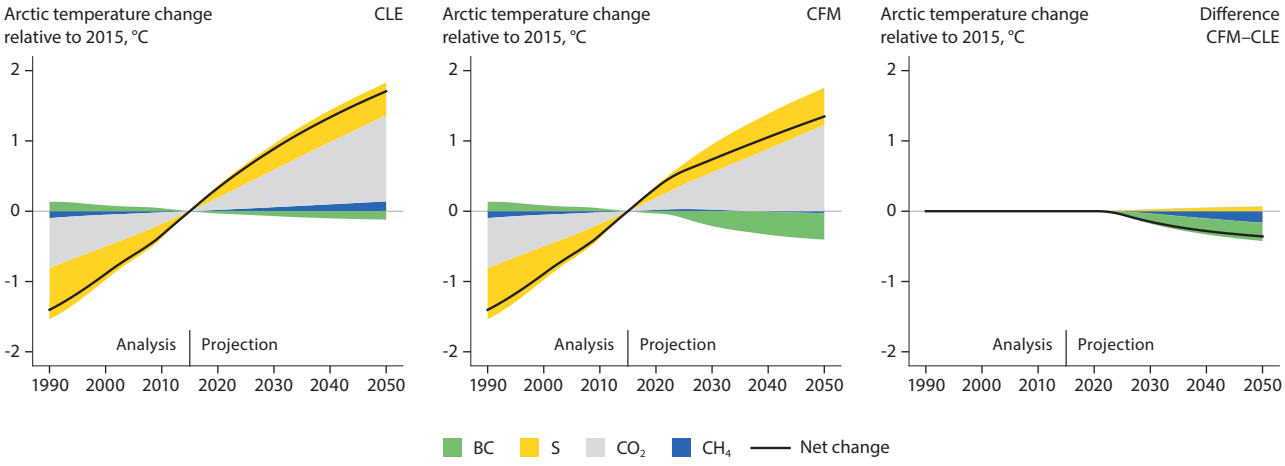

Figure 8.44 Mean Arctic temperature changes, relative to 2015, under the CFM and CLE scenarios. The shaded areas indicate the contributions of emitted pollutants to the net changes (black lines).

8.6 The potential role of natural SLCF emissions

To assess the relative importance of anthropogenic emissions and their impacts – both today and in the future – it is necessary to differentiate them from the effects caused by natural emissions. Here, the term natural emissions refers primarily to: CH_4 from terrestrial, freshwater and marine sources; emissions from natural fires; mineral and soil dust; sea spray and secondary aerosol formed from marine precursor emissions (DMS, from phytoplankton); and terrestrial trace gases (such as biogenic volatile organic compounds [BVOCs] from vegetated areas).

Both anthropogenic and natural emissions change over time. While anthropogenic emissions are changed through policy action, such as that simulated by the ESMs for the CLE and MFR emissions scenarios, natural emissions change as a consequence of climate and environmental shifts. For example, natural emissions of CH_4 from wetlands, lakes and oceans are projected to increase in the Arctic, but the absolute magnitude of these is uncertain (Chapter 3; Tan and Zhuang, 2015; James et al., 2016; Dean et al., 2018; Koffi et al., 2020; Zhang et al., 2017; Shindell et al., 2013; Sultan et al., 2020). This natural increase could potentially be mitigated by a strong reduction in anthropogenic CH_4 emissions (Christensen et al., 2019).

Forest fires are expected to become more frequent and severe in the future due to rising temperatures, lower relative humidity and more frequent lightning strikes – potentially leading to increased emissions if not carefully managed (Chapter 4). The increased release of surface dust in the future is conceivable, as ground snow cover becomes sparser and remains for shorter periods (Bormann et al., 2018; Allchin and Déry, 2020). Land ice, such as glaciers and the Greenland ice sheet, are retreating rapidly, exposing areas covered by fine sediments. Glacial dust is already the dominant factor in reducing snow and ice albedo on Greenland (Goelles and Boggild, 2017), and the effect could become more severe in the future. In addition, areas razed by forest fires become another source of ash and soil dust. This material could be transported to snow- and ice-covered regions of the Arctic, where it might reduce the surface albedo by darkening the snow or act as a nutrient for algae (Cook et al., 2020), accelerating melt processes.

With sea ice retreating, sea-spray formation on the open ocean is set to increase (Struthers et al., 2011; Zábori et al., 2012; Browse et al., 2014). Such change can already be observed, as discussed in Chapter 6, where measurements of aerosol optical properties indicate an increase of coarse-mode particles, particularly in the area around Svalbard (Heslin-Rees et al., 2020). Sea-spray aerosols are also lofted from sea ice by blowing snow, and can function as cloud condensation nuclei (CCN), potentially enhancing the albedo of clouds. With less sea ice cover, and with rain increasing at the expense of snow fall in the future (Bintanja and Andry, 2017) this source of CCN might diminish. In spring and summer, retreating sea ice makes more microbial activity possible, leading to enhanced emissions of DMS and other trace gases (Søreide et al., 2010; Ardyna et al., 2014). Not only are more, smaller particles formed (new particle formation), but existing particles can also grow larger. BVOCs, which are increasingly emitted from thawing permafrost (Kramshøj et al., 2016) and also from the surface ocean (Abbatt et al., 2019), can function over land analogously to DMS at sea, contributing more and larger particles. The overall effect is to alter the Arctic CCN population in terms of number, size and composition, changing the radiative properties of clouds and influencing the Arctic rate of warming positively and potentially negatively, too. Moreover, these shifts are linked to a chain of complex environmental processes that are themselves subject to climate change, and hence have uncertain effects. As a result, the overall net effect of changing natural emissions on Arctic climate is still unknown.

It is difficult to represent all these complex chemical and physical processes in climate models with sufficient detail; there is currently no single model set up for the task. However, several modeling studies have investigated individual processes. For example, (Browse et al., 2014) identified small effects after studying the aerosol climate effects due to diminishing sea ice. Other studies (Struthers et al., 2011; Gilgen et al., 2018; Mahmood et al., 2019) concluded that the aerosols would lead to enhanced cloud albedo, prompting cooling over the open ocean. The fate of enhanced emissions of DMS was studied by Mahmood et al. (2019). They found that with sea-ice retreat, wet deposition efficiently scavenges newly formed sulfate aerosols from DMS emissions but that the remaining sulfate aerosols are more efficient at nucleating new cloud droplets and enhancing the cloud radiative forcing. More effort dedicated to measuring and modeling is needed to constrain these uncertainties.

For the MFR and CLE simulations performed for this report, all five ESMs consider climate feedbacks from changes in the burden of dust, sea salt and fires – although the latter is prescribed and not explicitly represented in each model. Most of the models also consider feedbacks from changes in DMS and SOA. No explicit feedback on natural CH_4 emissions is included in the ESM simulations, however. In other words, the climate response simulated by the ESMs for the MFR and CLE scenarios includes a partial climate response from changes in natural aerosol emissions only. Even though the models include these feedbacks, they do not all provide the necessary outputs to fully explore the magnitude of the different natural feedback mechanisms of each model. Furthermore, the models describe the underlying feedback processes in a rudimentary – and sometimes substantially different – manner. This simplification is partly due to computational limitations; it is simply not possible to include all the details of all chemical and physical processes in an ESM. There is also a lack of suitable model parameterizations, to a large extent caused by insufficient understanding of the natural processes. For fire emissions, the models use the same future emissions scenario of OC and BC from CMIP6 (see Feng et al., 2020); in other words, the fires and the fire emissions do not respond to the simulated climate change in each model. Sea salt emissions are dependent on changes in sea ice and wind in all models but the descriptions are different and not all models consider the effects of changes in ocean temperature. Emissions of organic matter from the ocean also differ between the models. The description of dust emissions is substantially different between the models and is not dependent on any change in, for example, glacier extent as the models do not include dynamic land-ice models. Nevertheless, the simulated changes in dust and sea-salt

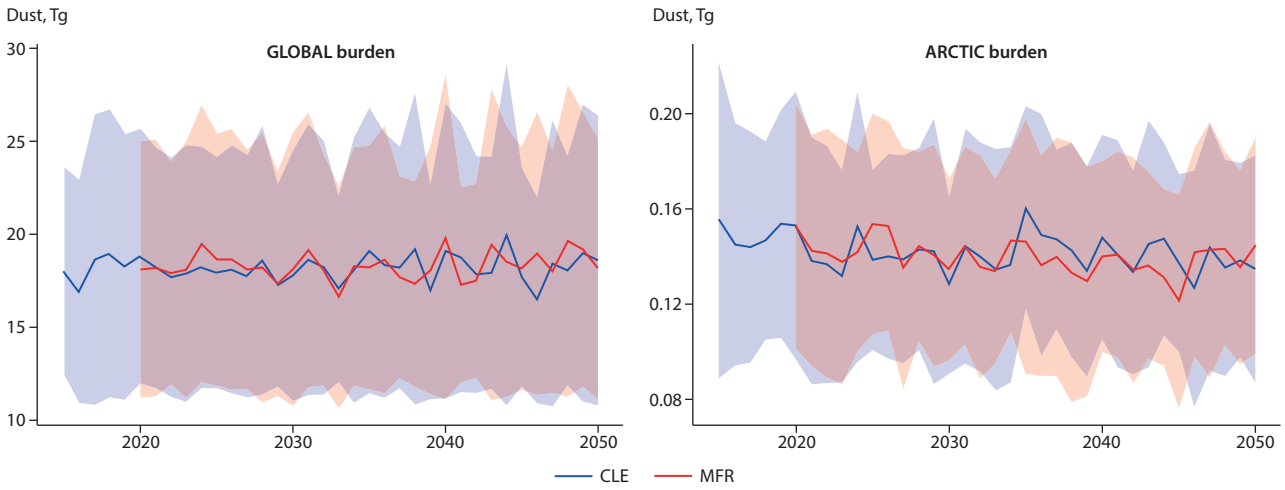

Figure 8.45 MMM Global and Arctic fine-fraction dust burdens. The figure shows MMMs over the number of ensembles from all ESMs along with the standard deviation

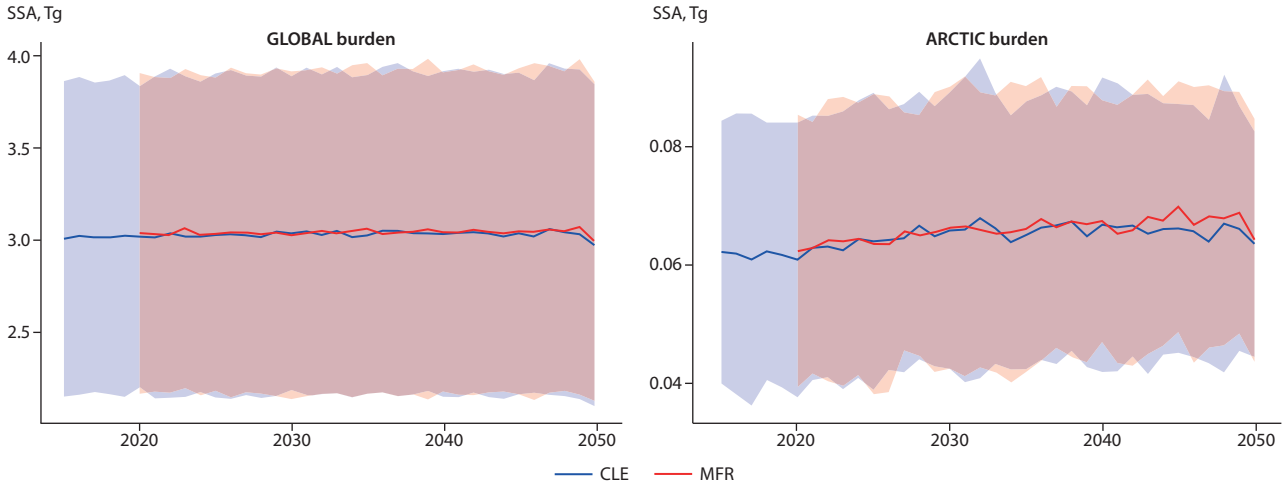

Figure 8.46 MMM global and Arctic fine fraction sea-salt burdens. The figure shows MMMs over the number of ensembles from all ESMs, along with the standard deviation.

burdens under the CLE and MFR scenarios are discussed below for all models, as a rough indication of possible future trends. A task for the future is to better constrain natural aerosol and gas emissions changes, alongside any anthropogenic effects, to improve our overall understanding of the Arctic climate system.

Based on the mean of all five ESMs, the burden of fine-fraction dust in 2015 is calculated to be 20 Tg and 0.15 Tg globally and over the Arctic, respectively. As seen in Figure 8.45, the models produce large differences in simulated dust concentrations, up to a factor of three, both globally and over the Arctic. The simulated global MMM dust burdens increase slightly in the future in both scenarios. The trend is statistically significant in the MFR scenario (at a 95% confidence level according to a Mann-Kendall test) but is not significant in the CLE scenario. In the CLE scenario, the global mean dust burden decreases slightly by 1.4% in 2030 compared to 2015 levels, but then increases by 4.9% in 2050 compared to 2030. In the MFR scenario, the global 2030 burden is 4% lower than the 2015 burden, while the 2050 burden is 2.3% higher than the 2015 burden. The changes over the Arctic are larger (Figure 8.45); under the CLE scenario, the models estimate an 18% and 13% decrease of the Arctic dust burden in 2030 and 2050, respectively, compared to 2015 levels, and a 13% and 7% decrease, respectively under the MFR scenario. The decreasing trend in the CLE scenario is not statistically significant, while the trend in the MFR scenario is statistically significant. The results suggest that the global dust burden increases while the anthropogenic aerosol burden decreases, meaning that mineral dust aerosols will become more important in the future.

Regarding fine sea-salt aerosols, as with dust, there are large differences between the models in terms of the simulated global and Arctic burdens (Figure 8.46). Trend analyses based on the MMM show a small but statistically significant increase in the global sea-salt concentrations under both CLE and MFR scenarios. The global MMM sea-salt burden increases slightly by up to 1% in 2030 compared to 2015 in both scenarios, while the 2050 levels are 1–1.5% lower than the 2015 levels. The changes over the Arctic are larger; the 2030 burden is 6–7% higher than the 2015 levels, while the 2050 levels are 2–3% higher than in 2015. This can be attributed to decreased sea ice over the Arctic (Section 8.3.3), leading to an expanded open sea-surface and increasing sea-spray fluxes. The increasing trend over the Arctic in the CLE scenario is statistically significant, while in the MFR scenario the increase is not statistically significant.

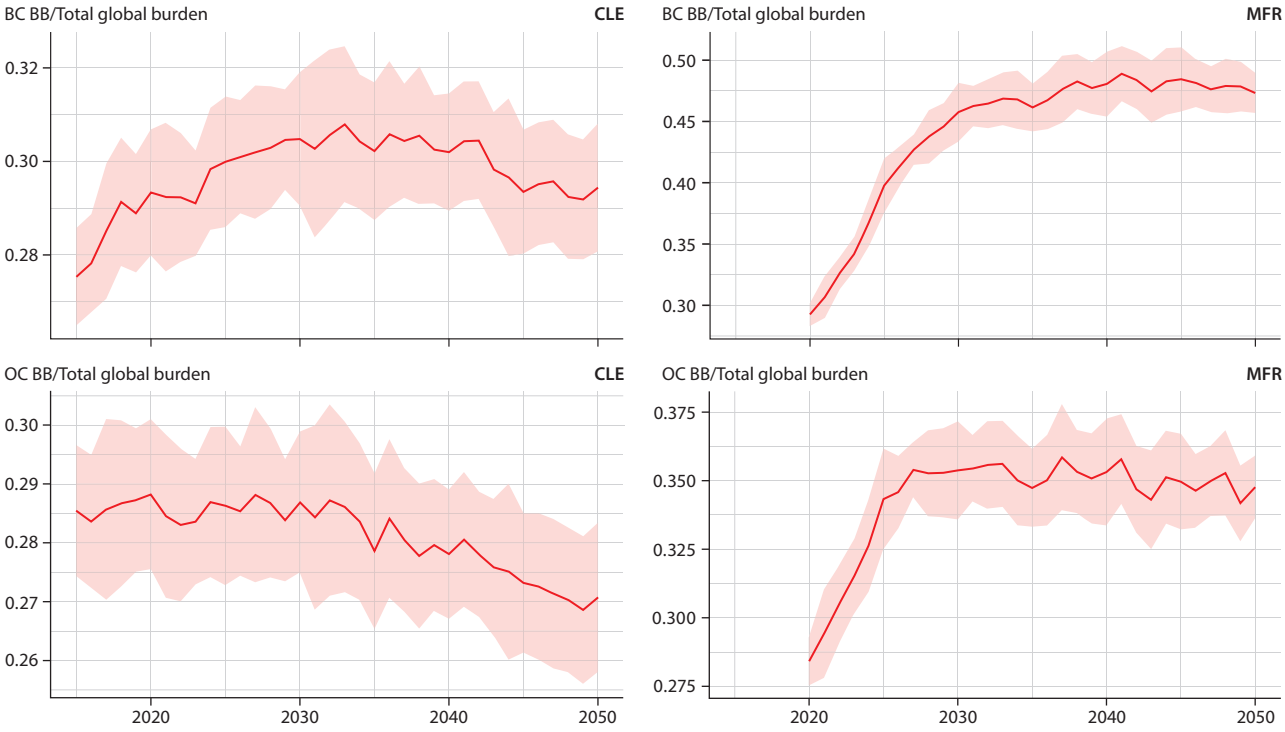

Figure 8.47. Evolution of the biomass-burning fraction of BC and OC versus the total global burden, under the CLE and MFR scenarios. The figure shows MMMs over three ensembles of the GISS-E2.1 model, along with the standard deviation.

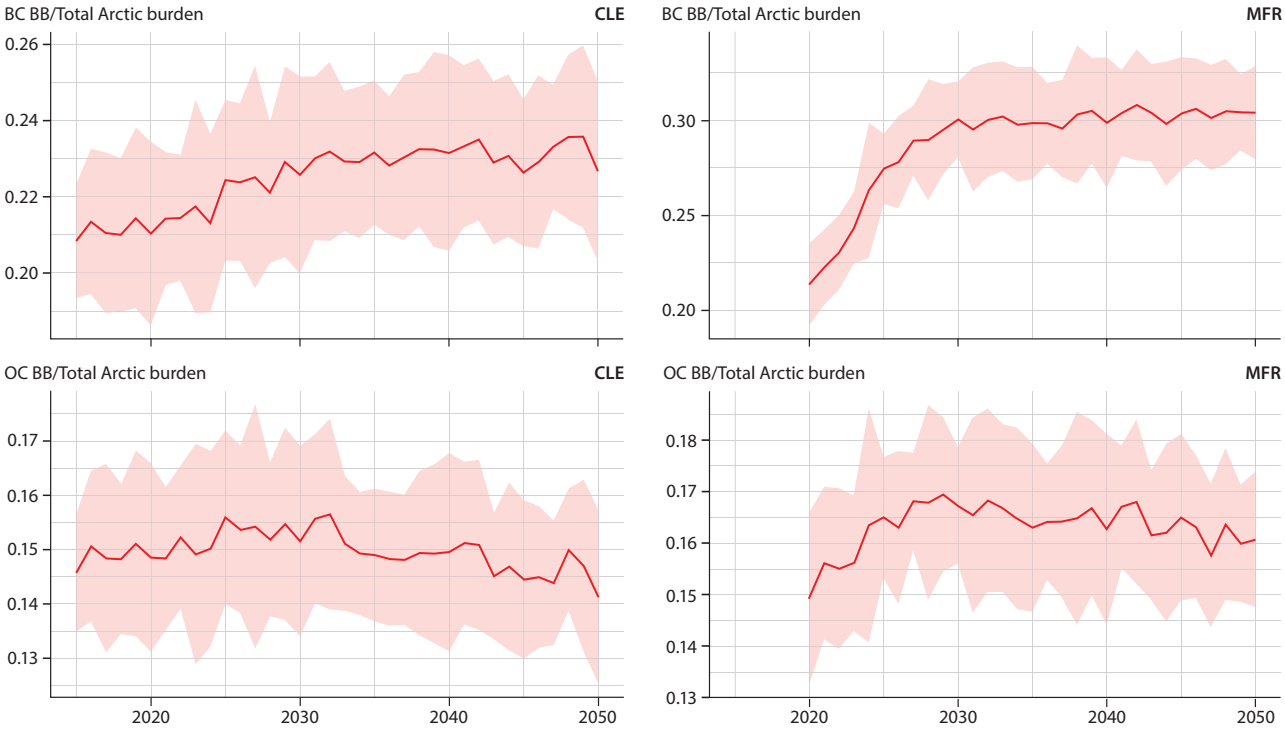

Figure 8.48. Evolution of the biomass-burning fraction of BC and OC versus the total Arctic burden, under the CLE and MFR scenarios. The figure shows multi-model means over three ensembles of the GISS-E2.1 model, along with the standard deviation.

The GISS-E2.1 model was further used to estimate the change of biomass-burning fraction of BC and OC in comparison to the total global (Figure 8.47) and Arctic (Figure 8.48) burdens, and changes to this ratio over time due to the anthropogenic emissions reductions applied in the model. It should be noted that the biomass burning includes both natural and anthropogenic fires. The GISS-E2.1 model tracks the anthropogenic and biomass burning BC and OC separately, and therefore can distinguish and calculate the anthropogenic and biomass burning fractions of BC and OC concentrations, implying that, depending on the reductions in anthropogenic emissions, the ratio between the biomass burning and total BC and OC concentrations can

change over time. The model calculated that in 2015, 27%–29% of the global OC mass was due to biomass burning. Under the CLE scenario, this ratio slightly increases to 31%–32%, while in the MFR scenario, the ratio increases by up to 52%. This suggests that, due to the decrease of anthropogenic emissions, the biomass burning fraction of BC will become dominant. Regarding global OC, the model simulated a slight decrease in the biomass-burning fraction under the CLE scenario, while in the MFR scenario, the global biomass burning ratio increased from 30% in 2015 to almost 40% in 2030 and 2050. Over the Arctic, the biomass-burning fraction of BC increased from around 20% in 2015 to 24% in 2050 under the CLE scenario, with the ratio increasing to more than 30% under the MFR scenario. Arctic OC does not change much by 2050 in the CLE scenario, and increases only slightly in the MFR scenario.

8.7 Conclusions

- Model simulations for the period 1990–2015 provide evidence that the slightly declining global anthropogenic BC emissions during this time period had a relatively small cooling impact on recent Arctic warming (-0.053°C/decade), compared to the simulated net Arctic warming from global emissions of CO_2 and other SLCFs during this time (0.55 °C/decade). At the same time, the slight increase in global anthropogenic CH_4 emissions produced a relatively small warming impact (0.039°C/decade).
- Global anthropogenic emissions of CO_2 and reductions in global sulfur emissions contributed strongly and equally to Arctic warming between 1990–2015, highlighting the importance of declining global sulfur emissions and reduced interactions of sulfate aerosols with clouds, following the steady increase in global emissions of sulfur and aerosol/cloud radiative forcings during the 20th century. The magnitude of the warming from declining sulfur emissions is large but very uncertain, mainly due to uncertainties in aerosol/cloud radiative forcings.
- With the available emissions scenarios, the Arctic is projected to continue to warm until 2050, at least. Simulations with the ESMs and the emulator consistently show that the forced warming rates are stronger in the near-term (2015–2030) than in the mid-term (2015–2050), and that the warming is mainly due to a combination of strong warming impacts of CO_2 and diminishing global sulfur emissions (of similar magnitude).
- From 2015–2030, with maximum feasible reductions in global emissions of CH_4 and BC, the net rate of Arctic warming could be reduced by 20%, relative to emissions changes from current legislation. If maximum feasible emission reductions are sustained until 2050, the net Arctic warming rate over this time period could be reduced by 25% (10% from CH_4 and 15% from BC emissions reductions).
- Reductions in global sulfur emissions will reduce the cooling impact of global CH_4 and BC emission-mitigation measures on Arctic warming. Combined maximum feasible SLCF emissions reductions are unlikely to produce a notable net change in Arctic temperature between 2015–2050. The weak response in Arctic temperature to global SLCF emissions mitigation is consistent in all the models.
- Projected future changes in O_3 abundance imply a relatively small change in Arctic warming of less than 0.006°C/decade between 2015–2050, consistent with simulated changes in concentrations and radiative forcings.
- There is strong evidence that maximum feasible reductions in SLCF emissions would produce measurable improvements in air quality in all Arctic Council Member states and Asian Observer countries, compared to current legislation in the near- and mid-term. For Asian Observers, maximum feasible reductions in local emissions could lead to particularly large reductions in projected annual mean anthropogenic PM concentrations of up to about 60% by 2030, relative to 2015. These reductions are robustly simulated in the different models. However, simulated changes in absolute concentrations are more uncertain. Additionally, maximum feasible reductions in O_3 precursor emissions (mainly from fossil-fuel and biofuel sources) also yield large decreases in surface O_3 concentrations by 2050 across all regions.
- Future global mean precipitation rates display a small and non-significant increase with maximum feasible reductions in SLCF emissions compared to the CLE scenario (0.7% difference in 2050), which is caused by changes in surface energy budgets from reductions in concentrations of CH_4, sulfate, BC and OC. In the Arctic, the mean precipitation increase is 1.4% (non-significant).
- The introduction of further air-pollution mitigation options reduces the emissions of sulfur and other precursors of particulate matter in the scenarios considered here. This will likely lead to significant health benefits in large regions of the World. Regardless of far-reaching air quality improvements, the overall impact of declining global sulfur emissions is to unmask the greenhouse gas warming impact on Arctic temperature, which could be considerable. This emphasizes the need to reduce global emissions of CO_2, CH_4, and BC in order to slow the rate of Arctic warming. Furthermore, air-quality benefits could be enhanced by targeting emissions of OC, without detrimental impacts on Arctic climate.
- Maximum feasible reductions in fossil-fuel and biofuel emissions of CH_4 from Asian Observer countries and the Rest of the World are projected to reduce the Arctic warming rate each by about 2%, relative to current legislation and from 2015–2050. This is a substantial portion of the Arctic cooling impact from reductions in global emissions from all anthropogenic CH_4 sources (10% reduction in warming rate).
- Maximum feasible reductions in SLCF emissions from the oil-and-gas sector are beneficial for the Arctic climate from 2015–2050. In particular, BC emissions reductions from gas flaring in eastern Arctic Council Member states are particularly beneficial (2% reduction in Arctic warming rate, relative to current legislation). Furthermore, global CH_4 emissions from the oil-and-gas sector account for 40% of the projected cooling impact of the maximum feasible reductions in global CH_4 emissions from all anthropogenic sources.

- In a warming Arctic, emissions of natural aerosols and their precursors will change. All ESMs consider climate feedbacks on dust and sea-spray emissions. The simulations indicate that the Arctic dust burden will decrease while the sea-salt burden will increase in the future. However, these changes are associated with large uncertainties and need better quantification. Only a subset of the models include climate feedbacks on DMS concentrations in the ocean and emissions of SOA precursors, and these models do not provide the necessary output to quantify the feedbacks. Emissions from wildfires follow prescribed future scenarios and are not explicitly calculated by the models.
- Due to the chemical complexity, future changes in CH_4 are currently considered in a simplistic way in the ESM projections (Chapter 7). Furthermore, there is no feedback from the modeled climate change on natural CH_4 emissions.
- The development of an integrated modeling capacity for climate and air quality is essential for understanding the inherent trade-offs and synergies in policy and regulations. Substantial uncertainties still exist with regard to the magnitude of future simulated warming and regional SLCF concentrations. Future development of ESMs needs to support the creation of emissions mitigation pathways and adaptation priorities that respond to diverse societal, cultural, health, economic, and environmental priorities and values.
- Rapid-assessment tools such as emulators provide additional options for making an integrated assessment of emissions mitigation strategies for climate and air quality. They are fundamentally based on results from more complex models. Emulator projections are highly idealized and are limited to changes of a small number of variables over multi-year-long time scales. The limited availability of long integrations with complex models poses substantial challenges for assessing the impacts of SLCFs on climate and air quality. In contrast to these models, emulators can be easily adapted in response to an improved scientific understanding of the impacts of emissions on SLCF concentrations, radiative forcings, and climate sensitivity.

8.8 Recommendations

- Promote studies aimed at expanding knowledge of natural aerosols. Future reductions of global anthropogenic aerosol and aerosol precursor emissions imply that changes in natural aerosol emissions (fires, sea spray, DMS, organic vapors) will become increasingly important. These emissions are closely connected to changes in different climate variables and need to be better understood, represented, and evaluated in models.
- Develop better observational datasets and models to address current uncertainties in aerosol indirect effects and cloud adjustments (including long-wave feedbacks) – which are substantial.
- Initiate studies to better constrain the Arctic warming effect from reduced anthropogenic sulfur emissions, in particular for the historical time period.
- Undertake longer and more computationally expensive simulations with Earth system and atmospheric global climate models to reduce statistical uncertainties in radiative forcings and climate caused by natural variability in clouds and surface albedo. The current lack of studies limits the scientific understanding of SLCF and cloud processes, and also affects the assessment of the impacts of SLCF emissions on climate.
- Support efforts to integrate models for climate and air quality to facilitate the evaluation of co-benefits of emissions reductions for climate and health. In particular, the spatial resolution and time periods of global model datasets need to be increased for robust assessments of changes in local air quality and regional climate over multiple decades.

Appendix 8

A8.1 Regional SLCF emissions

Table A8.1 Emissions of CH_4-chemistry-related chemical species (in Tg/y) for different regions and sectors in 2015.

Species	Sector	Asian Observers	Rest of Europe	Arctic Council (West)	Arctic Council (East)	Rest of World	Marine (Arctic)	Marine (<60°N)	Sector total
CH_4	Fossil fuel and biofuel	85.04	20.13	25.80	19.34	125.49			275.79
	Oil and gas flaring	1.96	0.45	10.68	9.64	36.91			59.64
	Shipping						0.00	0.03	0.03
	Region total	87.00	20.58	36.48	28.98	162.40	0.00	0.03	335.46
CO	Fossil fuel and biofuel	225.25	22.48	38.04	12.64	244.36			542.77
	Oil and gas flaring	0.01	0.00	0.03	0.17	0.48			0.70
	Shipping						0.03	3.02	3.05
	Region total	225.27	22.48	38.07	12.81	244.84	0.03	3.02	546.52
VOC	Fossil fuel and biofuel	18.27	3.71	7.42	2.02	38.80			70.22
	Oil and gas flaring	0.37	0.22	1.34	0.92	7.53			10.37
	Shipping						0.01	0.60	0.61
	Region total	18.64	3.93	8.76	2.94	46.33	0.01	0.60	81.20
NO_X	Fossil fuel and biofuel	37.34	8.94	14.34	4.35	40.46			105.43
	Oil and gas flaring	0.00	0.00	0.01	0.03	0.10			0.14
	Shipping						0.21	19.00	19.21
	Region total	37.34	8.94	14.35	4.38	40.56	0.21	19.00	124.77

Table A8.2 Change in emissions of CH_4-chemistry-related chemical species (in Tg/y) from 1990 to 2015.

Species	Sector	Asian Observers	Rest of Europe	Arctic Council (West)	Arctic Council (East)	Rest of World	Marine (Arctic)	Marine (<60°N)	Sector total
CH_4	Fossil fuel and biofuel	27.05	-12.23	3.05	-5.25	41.54			54.16
	Oil and gas flaring	0.49	-0.24	7.76	-26.66	-0.97			-19.62
	Shipping						0.00	0.01	0.01
	Region total	27.53	-12.47	10.81	-31.90	40.57	0.00	0.01	34.55
CO	Fossil fuel and biofuel	57.36	-41.74	-75.70	-14.48	66.86			-7.70
	Oil and gas flaring	0.01	0.00	0.01	-0.28	-0.09			-0.35
	Shipping						0.01	1.33	1.34
	Region total	57.36	-41.74	-75.68	-14.76	66.77	0.01	1.33	-6.71
VOC	Fossil fuel and biofuel	-1.09	-9.49	-9.32	-3.24	7.09			-16.05
	Oil and gas flaring	0.09	-0.21	-0.04	-0.30	1.52			1.07
	Shipping						0.00	0.26	0.26
	Region total	-1.00	-9.70	-9.35	-3.54	8.61	0.00	0.26	-14.71
NO_X	Fossil fuel and biofuel	21.22	-11.42	-14.53	-5.26	14.98			4.99
	Oil and gas flaring	0.00	0.00	0.00	-0.06	-0.02			-0.07
	Shipping						0.09	8.04	8.13
	Region total	21.22	-11.42	-14.53	-5.31	14.96	0.09	8.04	13.05

Table A8.3 Change in emissions of CH_4-chemistry-related chemical species (in Tg/y) from 2015 to 2050, according to the CLE scenario.

Species	Sector	Asian Observers	Rest of Europe	Arctic Council (West)	Arctic Council (East)	Rest of World	Marine (Arctic)	Marine (<60°N)	Sector total
CH_4	Fossil fuel and biofuel	25.89	-3.23	2.78	3.16	54.27			82.88
	Oil and gas flaring	1.89	-0.13	2.84	-0.39	19.31			23.51
	Shipping						0.01	0.84	0.84
	Region total	27.78	-3.36	5.62	2.77	73.58	0.01	0.84	107.23
CO	Fossil fuel and biofuel	-89.16	-7.77	-10.34	-3.10	9.52			-100.85
	Oil and gas flaring	0.00	0.00	0.01	-0.06	0.14			0.08
	Shipping						0.02	1.72	1.74
	Region total	-89.16	-7.78	-10.33	-3.16	9.66	0.02	1.72	-99.03
VOC	Fossil fuel and biofuel	-5.07	-1.55	-1.97	-0.31	-0.51			-9.41
	Oil and gas flaring	-0.14	-0.05	0.18	-0.08	1.03			0.94
	Shipping						0.01	0.47	0.47
	Region total	-5.21	-1.59	-1.79	-0.40	0.52	0.01	0.47	-7.99
NO_X	Fossil fuel and biofuel	-13.23	-5.01	-6.65	-1.29	14.08			-12.10
	Oil and gas flaring	0.00	0.00	0.00	-0.01	0.03			0.02
	Shipping						-0.03	0.50	0.46
	Region total	-13.23	-5.02	-6.65	-1.30	14.11	-0.03	0.50	-11.62

Table A8.4 Change in emissions of CH_4-chemistry-related chemical species (in Tg/y) from 2015 to 2050, according to the MFR scenario.

Species	Sector	Asian Observers	Rest of Europe	Arctic Council (West)	Arctic Council (East)	Rest of World	Marine (Arctic)	Marine (<60°N)	Sector total
CH_4	Fossil fuel and biofuel	-22.10	-9.52	-3.31	-13.11	-15.48			-63.52
	Oil and gas flaring	-0.71	-0.31	-2.95	-7.42	-25.63			-37.02
	Shipping						0.01	0.84	0.84
	Region total	-22.81	-9.83	-6.26	-20.53	-41.11	0.01	0.84	-99.69
CO	Fossil fuel and biofuel	-177.01	-13.85	-23.24	-8.07	-151.40			-373.58
	Oil and gas flaring	-0.01	0.00	-0.01	-0.16	-0.42			-0.61
	Shipping						0.02	1.72	1.74
	Region total	-177.02	-13.86	-23.25	-8.24	-151.83	0.02	1.72	-372.44
VOC	Fossil fuel and biofuel	-14.53	-2.31	-4.66	-1.24	-24.30			-47.04
	Oil and gas flaring	-0.14	-0.06	-0.43	-0.09	0.82			0.09
	Shipping						0.01	0.47	0.47
	Region total	-14.67	-2.37	-5.09	-1.33	-23.48	0.01	0.47	-46.47
NO_X	Fossil fuel and biofuel	-27.63	-6.72	-10.46	-3.18	-12.89			-60.87
	Oil and gas flaring	0.00	0.00	0.00	-0.03	-0.08			-0.12
	Shipping						-0.15	-13.45	-13.60
	Region total	-27.63	-6.72	-10.46	-3.21	-12.97	-0.15	-13.45	-74.59

Table A8.5 Emissions of aerosol-related chemical species (in Tg/y) in 2015.

Species	Sector	Asian Observers	Rest of Europe	Arctic Council (West)	Arctic Council (East)	Rest of World	Marine (Arctic)	Marine (<60°N)	Sector total
BC	Fossil fuel and biofuel	2.31	0.34	0.30	0.12	3.09			6.16
	Oil and gas flaring	0.00	0.00	0.00	0.07	0.08			0.15
	Shipping						0.00	0.04	0.04
	Region total	2.31	0.34	0.31	0.19	3.17	0.00	0.04	6.35
OC	Fossil fuel and biofuel	4.52	0.57	0.49	0.24	7.64			13.45
	Oil and gas flaring	0.00	0.00	0.00	0.01	0.02			0.03
	Shipping						0.00	0.28	0.28
	Region total	4.52	0.57	0.49	0.25	7.66	0.00	0.28	13.76
S	Fossil fuel and biofuel	12.30	2.45	2.60	1.94	12.20			31.49
	Oil and gas flaring	0.00	0.00	0.00	0.02	0.00			0.03
	Shipping						0.04	5.03	5.07
	Region total	12.30	2.45	2.60	1.96	12.20	0.04	5.03	36.59

Table A8.6 Change in emissions of aerosol-related chemical species (in Tg/y) from 1990 to 2015.

Species	Sector	Asian Observers	Rest of Europe	Arctic Council (West)	Arctic Council (East)	Rest of World	Marine (Arctic)	Marine (<60°N)	Sector total
BC	Fossil fuel and biofuel	-0.06	-0.20	-0.07	-0.20	0.65			0.13
	Oil and gas flaring	0.00	0.00	0.00	-0.14	-0.03			-0.16
	Shipping						0.00	0.01	0.01
	Region total	-0.06	-0.20	-0.06	-0.34	0.62	0.00	0.01	-0.03
OC	Fossil fuel and biofuel	-0.89	-0.35	-0.12	-0.27	2.36			0.73
	Oil and gas flaring	0.00	0.00	0.00	-0.03	-0.01			-0.03
	Shipping						0.00	0.08	0.08
	Region total	-0.89	-0.35	-0.12	-0.30	2.35	0.00	0.08	0.78
S	Fossil fuel and biofuel	1.80	-12.45	-9.20	-3.79	-1.30			-24.94
	Oil and gas flaring	0.00	0.00	0.00	-0.05	0.00			-0.05
	Shipping						-0.01	0.77	0.76
	Region total	1.80	-12.45	-9.20	-3.84	-1.30	-0.01	0.77	-24.22

Table A8.7 Change in emissions of aerosol-related chemical species (in Tg/y) from 2015 to 2050, according to the CLE scenario.

Species	Sector	Asian Observers	Rest of Europe	Arctic Council (West)	Arctic Council (East)	Rest of World	Marine (Arctic)	Marine (<60°N)	Sector total
BC	Fossil fuel and biofuel	-1.17	-0.19	-0.13	-0.03	0.44			-1.08
	Oil and gas flaring	0.00	0.00	0.00	-0.02	0.03			0.00
	Shipping						0.00	0.01	0.01
	Region total	-1.17	-0.19	-0.13	-0.05	0.47	0.00	0.01	-1.06
OC	Fossil fuel and biofuel	-0.52	-0.27	-0.09	-0.03	1.48			0.57
	Oil and gas flaring	0.00	0.00	0.00	0.00	0.01			0.00
	Shipping						0.00	0.08	0.08
	Region total	-0.52	-0.27	-0.09	-0.03	1.49	0.00	0.08	0.66
S	Fossil fuel and biofuel	-5.18	-1.44	-1.18	-0.29	1.00			-7.09
	Oil and gas flaring	0.00	0.00	0.00	-0.01	0.00			-0.01
	Shipping						-0.03	-3.75	-3.78
	Region total	-5.18	-1.44	-1.18	-0.30	1.00	-0.03	-3.75	-10.88

Table A8.8 Change in emissions of aerosol-related chemical species (in Tg/y) from 2015 to 2050, according to the MFR scenario.

Species	Sector	Asian Observers	Rest of Europe	Arctic Council (West)	Arctic Council (East)	Rest of World	Marine (Arctic)	Marine (<60°N)	Sector total
BC	Fossil fuel and biofuel	-2.09	-0.28	-0.24	-0.10	-2.04			-4.76
	Oil and gas flaring	0.00	0.00	0.00	-0.06	-0.07			-0.13
	Shipping						0.00	-0.03	-0.03
	Region total	-2.09	-0.28	-0.24	-0.17	-2.11	0.00	-0.03	-4.92
OC	Fossil fuel and biofuel	-3.93	-0.47	-0.36	-0.21	-6.21			-11.18
	Oil and gas flaring	0.00	0.00	0.00	-0.01	-0.01			-0.03
	Shipping						0.00	-0.16	-0.16
	Region total	-3.93	-0.47	-0.36	-0.22	-6.22	0.00	-0.16	-11.37
S	Fossil fuel and biofuel	-8.61	-2.01	-1.76	-1.46	-8.26			-22.10
	Oil and gas flaring	0.00	0.00	0.00	-0.02	0.00			-0.02
	Shipping						-0.04	-4.70	-4.74
	Region total	-8.61	-2.01	-1.76	-1.48	-8.26	-0.04	-4.70	-26.87

A8.2 Burden changes in individual ESMs

A8.2.1 BC

All ESMs simulated a continuous decrease of BC burden over the Arctic (Figure 8.7). The ensemble-mean simulated BC burden of 5.1±1.9 kilotons (kt; 1 kiloton = 1000 tonnes) over the Arctic in 2015 decreased to 4.7±1.9 kt (7%) in 2020, 4.0±1.4 kt (21%) in 2030 and 3.4±1.3 kt (32%) in 2050, under the CLE scenario. The MFR scenario reduced an additional 1.8±1.1 kt (32%) in 2030 and 1.7±1.1 kt (32%) in 2050. The largest absolute reductions under the CLE scenario were simulated by the CESM2 and NorESM models, which also simulated the largest additional reductions under the MFR scenario (Figure A8.1). The annual mean BC surface concentrations were also projected to decrease over the Arctic, with MRI-ESM2 simulating the highest surface concentrations under the CLE scenario and therefore the largest additional decrease under the MFR scenario. However, this additional decrease was projected to get smaller from 2025 onwards (Figure 8.7).

A8.2.2 Ozone

Only GISS-E2.1, MRI-ESM2 and UKESM1 models simulated O_3, while CESM2 and NorESM used prescribed O_3 concentrations. All available ESMs simulated a continuous increase of O_3 burden over the Arctic (Figure 8.7). The models did not agree on the change in the surface O_3 mixing ratios over the Arctic (Figure A8.2). The GISS-E2.1 projected a decrease until 2030,

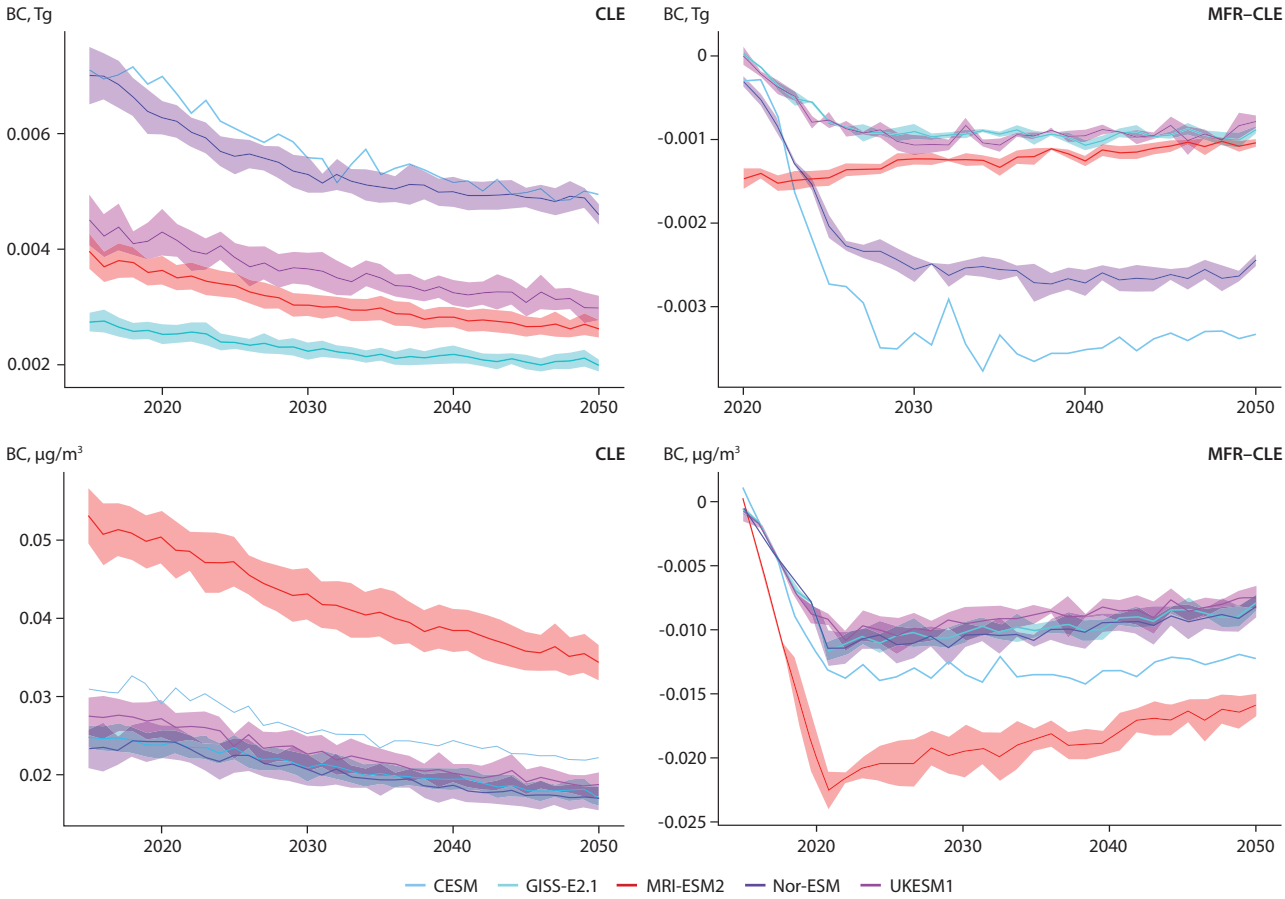

Figure A8.1 BC burden in teragrams [Tg] (upper panel) and surface concentration in µg/m³ (lower panel) over the Arctic for the five ESMs, for the CLE scenario and the difference between the MFR and CLE scenarios (MFR–CLE), along with spread for each model.

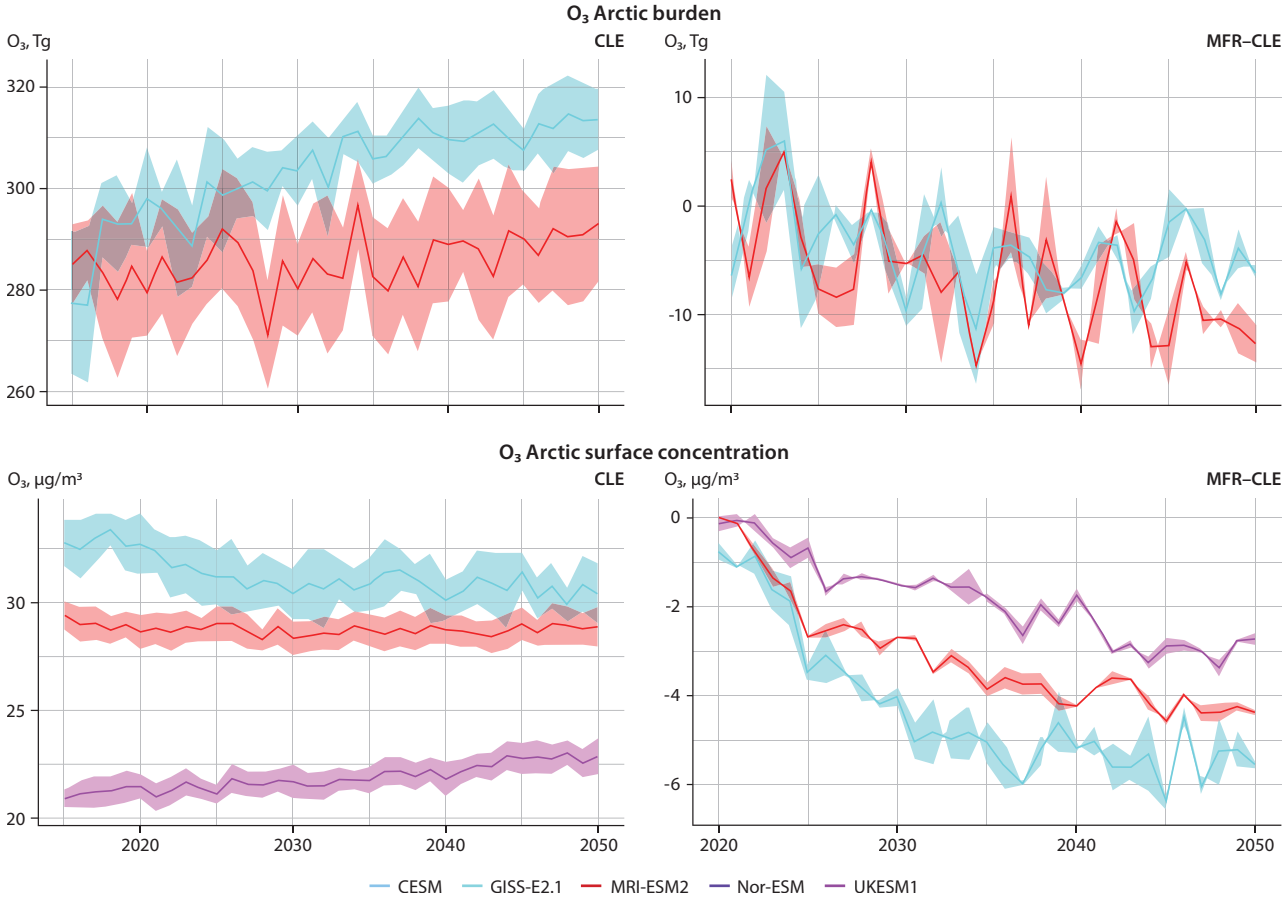

Figure A8.2 O_3 burden in teragrams [Tg] (upper panel) and surface concentration in µg/m³ (lower panel) over the Arctic for the five ESMs, for the CLE scenario and the difference between MFR and CLE scenarios (MFR–CLE), along with spread for each model.

then relatively stable onwards, while MRI-ESM2 projected O_3 levels to remain stable throughout the simulation period, and UKESM1 projected a continuous increase in surface O_3 levels. All models agreed that following the MFR scenario would further decrease the surface O_3 mixing ratios over the Arctic.

A8.2.3 Sulfate and OC

All ESMs simulated a significant decrease of sulfate (SO_4) burden over the Arctic until around 2030 (Figure A8.3). After 2030, burdens remain almost constant until 2050, with the exception of the CESM2 model, which simulated a slight increase of burdens after around 2040. The ensemble-mean simulated sulphate burden of 58.8±17.7 kt over the Arctic in 2015 decreased to 50.8±16.3 kt (14%) in 2020, 48.04.0±15.4 kt (19%) in 2030 and 48.5±13.3 kt (17%) in 2050 under the CLE scenario (Figure 8.7). The MFR scenario produced an additional reduction of 10.9±4.1 kt (19%) in 2030 and 12.1±3.4 kt (12%) in 2050. The largest reductions in the CLE scenario were simulated by the UKESM1 model, which also simulated the largest additional reductions in the MFR scenario. Regarding the surface SO_4 levels, all models agreed on a decrease until 2020 in the CLE scenario, with concentrations remaining relatively stable thereafter. As with BC, MRI-ESM2 projected the larger surface SO_4 levels, and the largest additional decrease under the MFR scenario.

All models simulated a slight decrease in the organic aerosol (OA) burden over the Arctic, except NorESM, which projected a large decrease until 2020 (Figure A8.4). The ensemble-mean simulated organic aerosol burden of 68.2±51.0 kt over the Arctic in 2015 decreased to 63.4±53.6 kt (5%) in 2020, 60.0±42.2 kt (10%) in 2030 and 55.5±37.9 kt (17%) in 2050 under the CLE scenario. The MFR scenario produced an additional reduction of 7.1±6.1 kt (12%) in 2030 and 6.5±6.3 kt (13%) in 2050. The NorESM model simulated the largest reductions under the CLE scenario, with the largest additional reductions under the MFR scenario projected by the NorESM and CESM2 models. Surface OA levels were projected to remain constant (MRI-ESM2 and UKESM1) or slightly decrease (CESM2, NorESM and GISS-E2.1). The MFR scenario led to additional decreases until 2035 and little change thereafter.

A8.2.4 $PM_{2.5}$

The anthropogenic $PM_{2.5}$ burden, calculated as the sum of BC, OA and SO_4 (assumed to be fully neutralized), was simulated to decrease until 2020, then continue to slightly decrease (Figure A8.5). The ensemble-mean simulated anthropogenic $PM_{2.5}$ burden of 154.2±62.5 kt over the Arctic in 2015 decreased to 138.1±54.6 kt (10%) in 2020, 130.0±51.2 kt (16%) in 2030 and 125.5±43.4 kt (17%) in 2050 under the CLE scenario. The MFR scenario produced an additional reduction of 23.9±9.5 kt

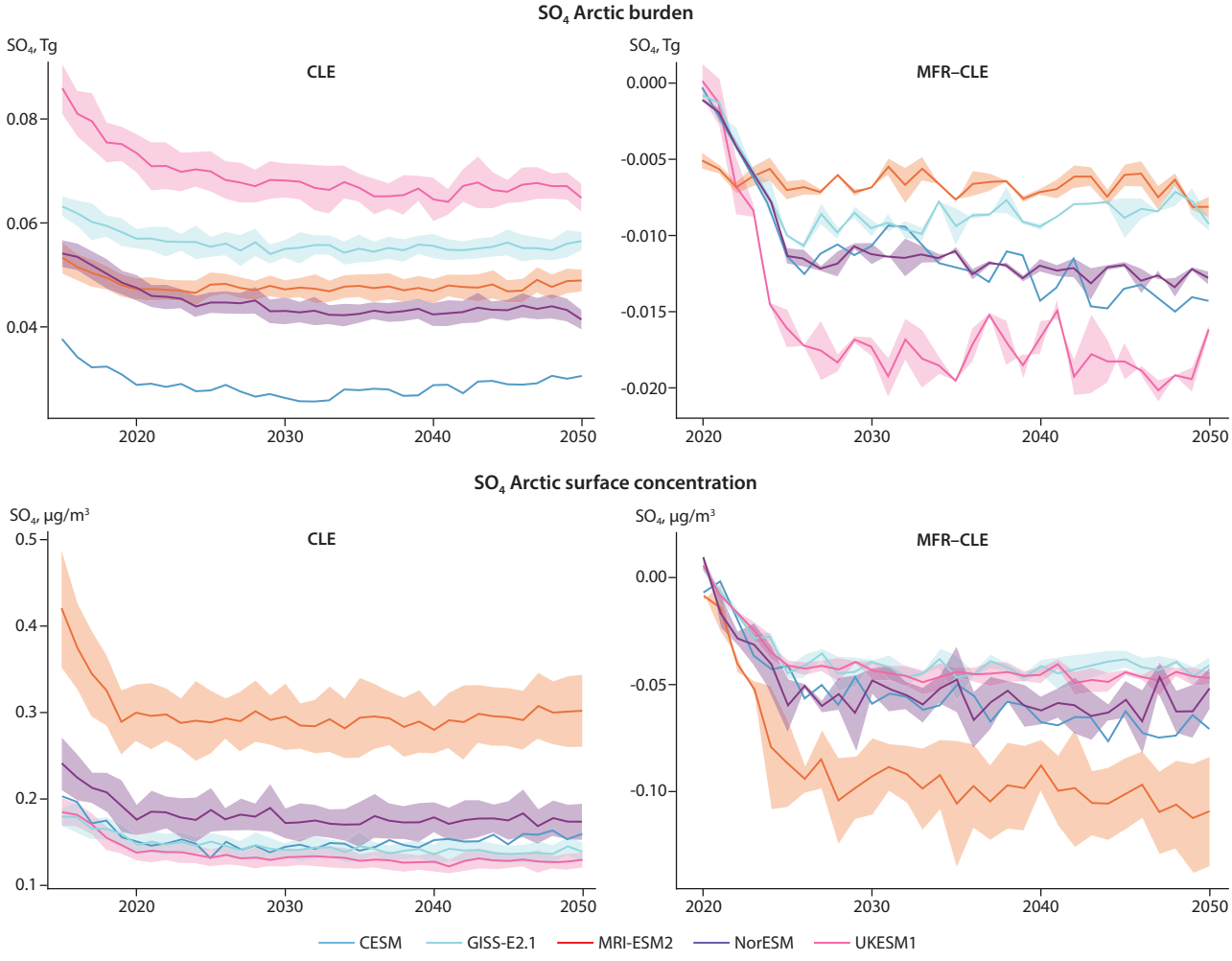

Figure A8.3. SO_4 burden in teragrams [Tg] (upper panel) and surface concentration in µg/m³ (lower panel) over the Arctic for the five ESMs, for the CLE scenario and the difference between the MFR and CLE scenarios (MFR–CLE), along with the spread for each model.

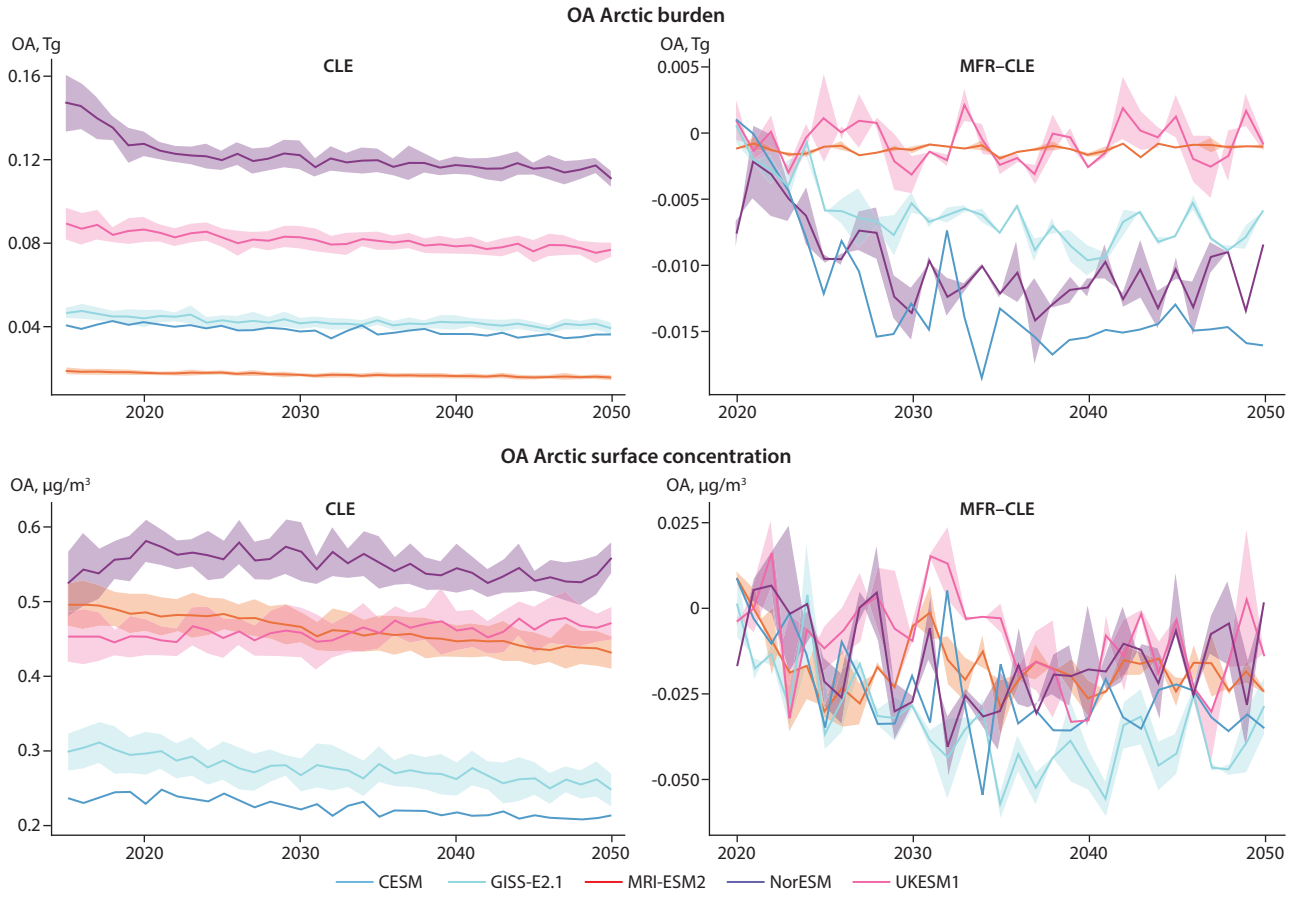

Figure A8.4. OA burden in teragrams [Tg] (upper panel) and surface concentration in µg/m³ (lower panel) over the Arctic for the five ESMs, for the CLE scenario and the difference between the MFR and CLE scenarios (MFR–CLE), along with the spread for each model.

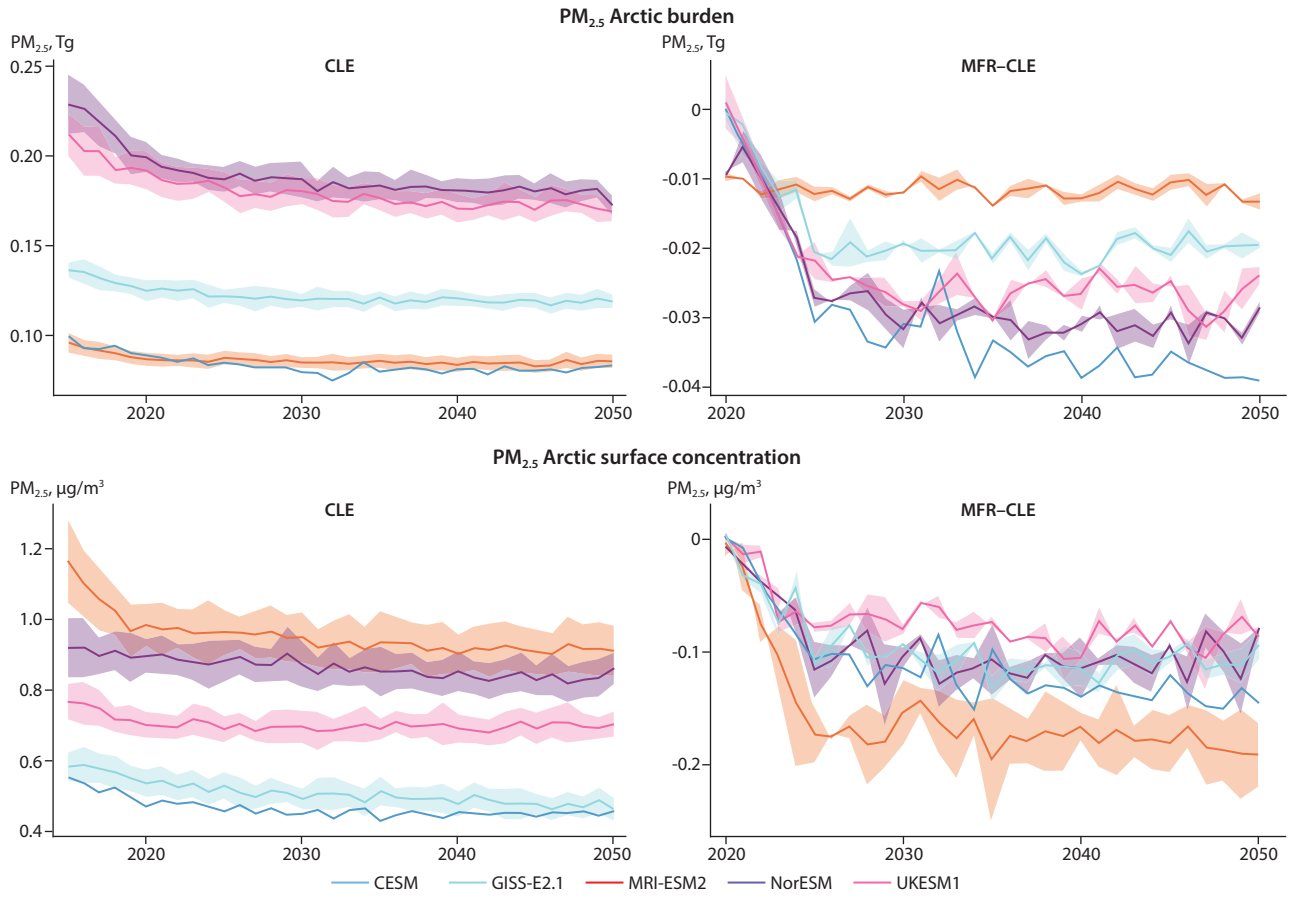

Figure A8.5. Anthropogenic $PM_{2.5}$ (BC+OA+SO_4) burden in teragram [Tg] (upper panel) and surface concentration µg/m³ (lower panel) over the Arctic for the five ESMs, for the CLE scenario and the difference between MFR and CLE scenarios (MFR–CLE), along with the spread for each model.

(16%) in 2030 and 24.9±9.7 kt (18%) in 2050. The largest reductions in the CLE scenario were simulated by the NorESM and UKESM1 models, which, in addition to the CESM2 model, also simulated the largest additional reductions in the MFR scenario. All models projected a decrease in the surface $PM_{2.5}$ levels, in particular until 2020, and nearly steady concentrations after that. The MFR scenario led to a further decrease of surface $PM_{2.5}$ levels, in particular until 2030.

A8.3 Impacts of SLCF emissions on regional aerosol concentrations

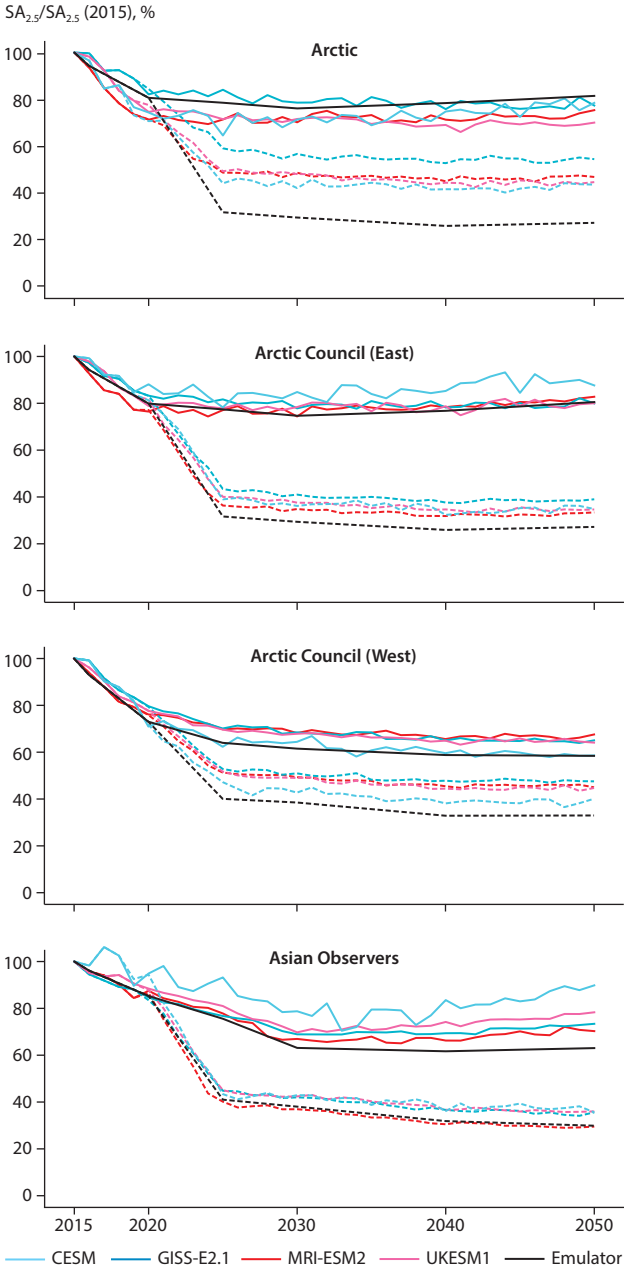

Figure A8.6 Impacts of the CLE and MFR emissions scenarios, represented by solid and dashed lines, respectively, on the future mean atmospheric near-surface concentration of sulfate aerosol in $PM_{2.5}$ ($SA_{2.5}$) in different regions, normalized by the concentration in 2015. Colored lines refer to ESMs and black lines to the emulator (Figure 8.22).

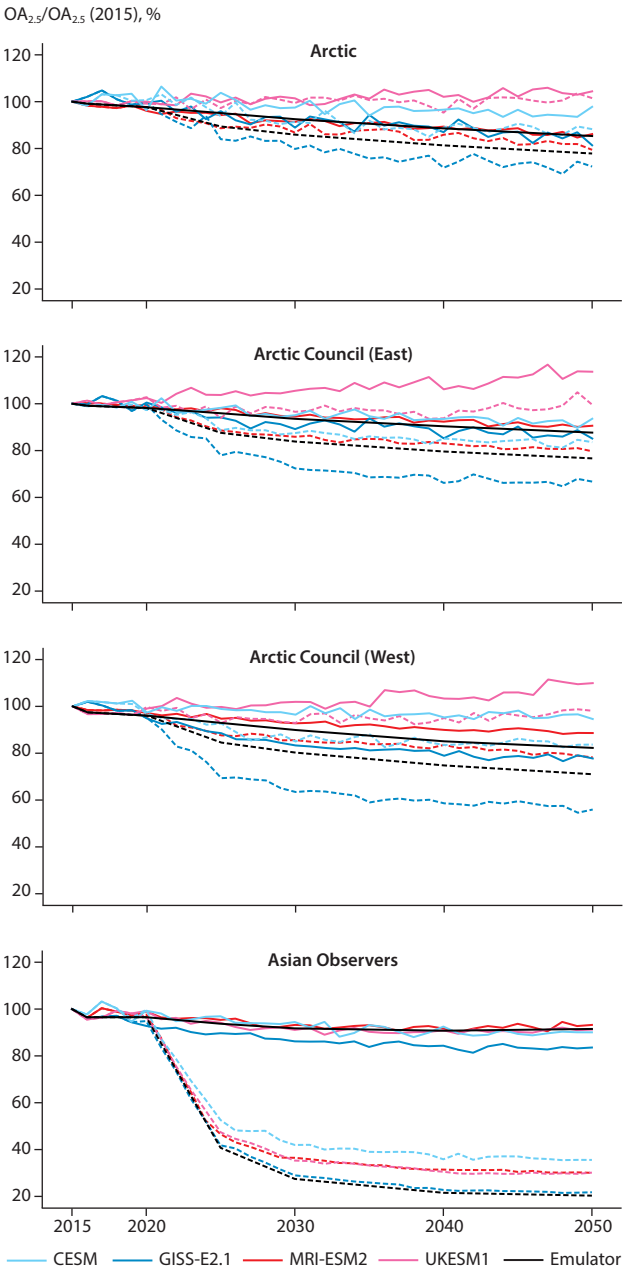

Figure A8.7 Impacts of the CLE and MFR emissions scenarios, represented by solid and dashed lines, respectively, on the future mean atmospheric near-surface concentration of organic aerosol in $PM_{2.5}$ ($OA_{2.5}$) in different regions, normalized by the concentration in 2015. Colored lines refer to ESMs and black lines to the emulator (Figure 8.22).

A8.4 Effective radiative forcings

Table A8.9 MMM of global effective radiative forcings and standard deviation in 2014, for interactions of anthropogenic aerosols with radiation, surface albedo, and clouds from CMIP6 models (Thornhill et al., 2021). The method of Ghan (2013) was used to decompose the effective radiative forcings into interactions with radiation, clouds, and surface albedo. Note that the sum of the individual forcings (total, BC+OC+S) is not the same as the total aerosol forcings (Aer), because of the nonlinearities in the aerosol and cloud process, which indicates uncertainties in the emulator calculations (which assume a linear response of the forcings to emission changes).

	Aer	BC	OC	S	Total
Effective radiative forcing from interactions with radiation, F_{rad} (W/m^2)					
Global	-0.16±0.15	0.28±0.11	-0.09±0.04	-0.36±0.15	-0.18±0.19
Effective radiative forcing from interactions with surface albedo, F_{alb} (W/m^2)					
Global	0.05±0.05	0.04±0.04	0.00±0.04	0.02±0.07	0.06±0.09
Effective radiative forcing from interactions with clouds, F_{cld} (W/m^2)					
Global	-0.95±0.25	-0.06±0.05	-0.15±0.06	-0.85±0.21	-1.05±0.23
Total effective radiative forcing, F_{tot} (W/m^2)					
Global	-1.07±0.29	0.26±0.13	-0.24±0.08	-1.19±0.27	-1.17±0.31

A8.5 Impacts of SLCF emissions on Arctic climate

Table A8.10 Arctic warming rate and temperature anomaly associated with CH_4-related SLCF species emissions according to the CLE scenario.

Emitted SLCF species	Arctic warming rate (°C/decade)			Arctic temperature anomaly (°C)		
	1990–2015	2015–2030	2015–2050	1990	2030	2050
CH_4	0.039	0.038	0.040	-0.098	0.057	0.139
CO + NO_X + VOCs	-0.009	-0.008	-0.006	0.023	-0.012	-0.019

Table A8.11 Arctic warming rate and temperature anomaly associated with BC emissions according to the CLE scenario.

Radiative forcing process	Arctic warming rate (°C/decade)			Arctic temperature anomaly °C)		
	1990–2015	2015–2030	2015–2050	1990	2030	2050
Radiation	0.000±0.036	-0.018±0.060	-0.013±0.026	0.000±0.063	-0.027±0.063	-0.045±0.063
Surface albedo	-0.043±0.136	-0.034±0.227	-0.027±0.097	0.107±0.241	-0.051±0.241	-0.096±0.241
Cloud	-0.010±0.199	0.005±0.331	0.006±0.142	0.026±0.351	0.008±0.351	0.020±0.351
Total	-0.053±0.244	-0.046±0.406	-0.034±0.174	0.133±0.431	-0.070±0.431	-0.120±0.431

Table A8.12 Arctic warming rate and temperature anomaly associated with S emissions according to the CLE scenario.

Radiative forcing process	Arctic warming rate (°C/decade)			Arctic temperature anomaly °C)		
	1990–2015	2015–2030	2015–2050	1990	2030	2050
Radiation	0.048±0.010	0.099±0.017	0.054±0.007	-0.120±0.018	0.149±0.018	0.189±0.018
Surface albedo	0.078±0.107	0.008±0.179	0.005±0.077	-0.194±0.190	0.012±0.190	0.017±0.190
Cloud	0.165±0.237	0.138±0.395	0.073±0.169	-0.413±0.419	0.207±0.419	0.254±0.419
Total	0.290±0.260	0.245±0.434	0.132±0.186	-0.726±0.460	0.368±0.460	0.460±0.460

Table A8.13 Arctic warming rate and temperature anomaly associated with CH_4-related SLCF species emissions according to the MFR scenario.

Emitted SLCF species	Arctic warming rate (°C/decade)		Arctic temperature anomaly (°C)	
	2015–2030	2015–2050	2030	2050
CH_4	0.015	-0.007	0.022	-0.025
CO + NO_X + VOCs	-0.008	-0.002	-0.011	-0.006

Table A8.14 Arctic warming rate and temperature anomaly associated with BC emissions according to the MFR scenario.

Radiative forcing process	Arctic warming rate (°C/decade)		Arctic temperature anomaly (°C)	
	2015–2030	2015–2050	2030	2050
Radiation	-0.050±0.060	-0.043±0.026	-0.076±0.063	-0.150±0.063
Surface albedo	-0.106±0.227	-0.082±0.097	-0.159±0.241	-0.286±0.241
Cloud	0.016±0.331	0.017±0.142	0.024±0.351	0.058±0.351
Total	-0.140±0.406	-0.108±0.174	-0.210±0.431	-0.378±0.431

Table A8.15 Arctic warming rate and temperature anomaly associated with S emissions according to the MFR scenario.

Radiative forcing process	Arctic warming rate (°C/decade)		Arctic temperature anomaly (°C)	
	2015–2030	2015–2050	2030	2050
Radiation	0.142±0.017	0.089±0.007	0.214±0.018	0.313±0.018
Surface albedo	0.015±0.179	0.010±0.077	0.022±0.190	0.036±0.190
Cloud	0.206±0.395	0.129±0.169	0.308±0.419	0.450±0.419
Total	0.363±0.434	0.228±0.186	0.544±0.460	0.799±0.460

Table A8.16 Arctic temperature change (in °C) for emissions of CH_4-chemistry-related species from different regions and sectors for 1990–2015.

Species	Sector	Asian Observers	Rest of Europe	Arctic Council (West)	Arctic Council (East)	Rest of World	Marine (Arctic)	Marine (<60°N)	Sector total
CH_4	Fossil fuel and biofuel	0.03752	-0.00901	0.01141	-0.02565	0.08628			0.10055
	Oil and gas flaring	0.00037	-0.00024	-0.00579	0.00954	-0.01006			-0.00618
	Shipping						0.00000	0.00002	0.00002
	Region total	0.03789	-0.00924	0.00562	-0.01611	0.07623	0.00000	0.00002	0.09439
CO	Fossil fuel and biofuel	0.00694	-0.00022	-0.00045	0.00011	0.00668			0.01306
	Oil and gas flaring	0.00000	0.00000	0.00000	0.00002	0.00003			0.00005
	Shipping						0.00000	0.00006	0.00006
	Region total	0.00694	-0.00022	-0.00045	0.00012	0.00671	0.00000	0.00006	0.01317
VOC	Fossil fuel and biofuel	0.00218	0.00034	-0.00064	0.00005	0.00305			0.00498
	Oil and gas flaring	0.00004	0.00005	0.00019	0.00014	0.00100			0.00142
	Shipping						0.00000	0.00004	0.00004
	Region total	0.00222	0.00039	-0.00045	0.00019	0.00406	0.00000	0.00004	0.00644
NO_X	Fossil fuel and biofuel	-0.01317	-0.00551	-0.00561	-0.00263	-0.01590			-0.04282
	Oil and gas flaring	-0.00000	-0.00000	-0.00000	-0.00004	-0.00007			-0.00011
	Shipping						-0.00006	-0.00513	-0.00519
	Region total	-0.01317	-0.00552	-0.00561	-0.00267	-0.01598	-0.00006	-0.00513	-0.04812
All	**Region total**	0.03388	-0.01459	-0.00089	-0.01847	0.07102	-0.00006	-0.00501	0.06588

Table A8.17 Arctic temperature change (in °C) for emissions of CH_4-chemistry-related species from different regions and sectors for 2015–2050, under the CLE scenario.

Species	Sector	Asian Observers	Rest of Europe	Arctic Council (West)	Arctic Council (East)	Rest of World	Marine (Arctic)	Marine (<60°N)	Sector total
CH_4	Fossil fuel and biofuel	0.05545	-0.01905	0.00436	-0.01137	0.10083			0.13022
	Oil and gas flaring	0.00191	-0.00072	0.01367	-0.00880	0.00105			0.00711
	Shipping						0.00001	0.00052	0.00053
	Region total	0.05736	-0.01977	0.01803	-0.02017	0.10188	0.00001	0.00052	0.13786
CO	Fossil fuel and biofuel	0.00330	-0.00256	-0.00496	-0.00070	0.00718			0.00226
	Oil and gas flaring	0.00000	0.00000	0.00000	0.00000	0.00002			0.00002
	Shipping						0.00000	0.00017	0.00017
	Region total	0.00330	-0.00256	-0.00496	-0.00070	0.00720	0.00000	0.00017	0.00245
VOC	Fossil fuel and biofuel	0.00027	-0.00160	-0.00215	-0.00052	0.00237			-0.00163
	Oil and gas flaring	0.00004	0.00001	0.00020	0.00010	0.00119			0.00154
	Shipping						0.00000	0.00011	0.00011
	Region total	0.00031	-0.00159	-0.00195	-0.00042	0.00356	0.00000	0.00011	0.00002
NO_X	Fossil fuel and biofuel	-0.01544	0.00788	0.01215	0.00224	-0.02362			-0.01679
	Oil and gas flaring	0.00000	0.00000	-0.00001	-0.00001	-0.00005			-0.00007
	Shipping						-0.00009	-0.00926	-0.00935
	Region total	-0.01544	0.00788	0.01214	0.00223	-0.02367	-0.00009	-0.00926	-0.02621
All	**Regional total**	0.04553	-0.01604	0.02326	-0.01906	0.08897	-0.00008	-0.00846	0.11412

Table A8.18 Arctic temperature change (in °C) for emissions of CH_4-chemistry-related species from different regions and sectors for 2015–2050, under the MFR scenario.

Species	Sector	Asian Observers	Rest of Europe	Arctic Council (West)	Arctic Council (East)	Rest of World	Marine (Arctic)	Marine (<60°N)	Sector total
CH_4	Fossil fuel and biofuel	0.01963	-0.02401	0.00082	-0.02748	0.06179			0.03075
	Oil and gas flaring	-0.00054	-0.00094	0.00694	-0.01844	-0.04719			-0.06017
	Shipping						0.00001	0.00061	0.00062
	Region total	0.01909	-0.02495	0.00776	-0.04592	0.01460	0.00001	0.00061	-0.02880
CO	Fossil fuel and biofuel	-0.00239	-0.00295	-0.00572	-0.00099	-0.00106			-0.01311
	Oil and gas flaring	0.00000	0.00000	0.00000	-0.00001	-0.00001			-0.00002
	Shipping						0.00000	0.00014	0.00014
	Region total	-0.00239	-0.00295	-0.00572	-0.00100	-0.00107	0.00000	0.00014	-0.01299
VOC	Fossil fuel and biofuel	-0.00133	-0.00179	-0.00266	-0.00068	-0.00143			-0.00789
	Oil and gas flaring	0.00003	0.00000	0.00011	0.00008	0.00099			0.00121
	Shipping						0.00000	0.00009	0.00009
	Region total	-0.00130	-0.00179	-0.00255	-0.00060	-0.00044	0.00000	0.00009	-0.00659
NO_X	Fossil fuel and biofuel	-0.00512	0.00931	0.01524	0.00378	-0.00753			0.01568
	Oil and gas flaring	0.00000	0.00000	0.00000	0.00001	0.00002			0.00003
	Shipping						-0.00004	-0.00417	-0.00421
	Region total	-0.00512	0.00931	0.01524	0.00379	-0.00751	-0.00004	-0.00417	0.01150
All	**Region total**	0.01028	-0.02038	0.01473	-0.04373	0.00558	-0.00003	-0.00333	-0.03688

Table A8.19 Arctic temperature change (in °C) for emissions of aerosol-related species from different regions and sectors during 1990–2015, for interactions with radiation only.

Species	Sector	Asian Observers	Rest of Europe	Arctic Council (West)
BC	Fossil fuel and biofuel	0.01434±0.06159	-0.00891±0.01158	-0.01339±0.02995
	Oil and gas flaring	0.00098±0.00505	0.00172±0.00430	-0.00022±0.00476
	Shipping			
	Region total	0.01532±0.06180	-0.00718±0.01235	-0.01362±0.03032
OC	Fossil fuel and biofuel	0.00089±0.00416	0.00000±0.00000	0.00000±0.00000
	Oil and gas flaring	0.00000±0.00000	0.00000±0.00000	0.00000±0.00000
	Shipping			
	Region total	0.00089±0.00416	0.00000±0.00000	0.00000±0.00000
S	Fossil fuel and biofuel	-0.07566±0.01785	0.10258±0.00346	0.09377±0.01292
	Oil and gas flaring	0.00000±0.00000	0.00000±0.00000	0.00000±0.00000
	Shipping			
	Region total	-0.07566±0.01785	0.10258±0.00346	0.09377±0.01292
All	**Region total**	-0.05945±0.06446	0.09539±0.01283	0.08015±0.03296

Table A8.20 Arctic temperature change (in °C) for emissions of aerosol-related species from different regions and sectors for 2015–2050, according to the CLE scenario and for interactions with radiation only.

Species	Sector	Asian Observers	Rest of Europe	Arctic Council (West)
BC	Fossil fuel and biofuel	-0.02456±0.06159	-0.00984±0.01158	-0.01845±0.02995
	Oil and gas flaring	0.00011±0.00505	0.00187±0.00430	-0.00141±0.00476
	Shipping			
	Region total	-0.02444±0.06180	-0.00797±0.01235	-0.01986±0.03032
OC	Fossil fuel and biofuel	-0.00091±0.00416	0.00000±0.00000	0.00000±0.00000
	Oil and gas flaring	0.00000±0.00000	0.00000±0.00000	0.00000±0.00000
	Shipping			
	Region total	-0.00091±0.00416	0.00000±0.00000	0.00000±0.00000
S	Fossil fuel and biofuel	0.07087±0.01785	0.03477±0.00346	0.05572±0.01292
	Oil and gas flaring	0.00000±0.00000	0.00000±0.00000	0.00000±0.00000
	Shipping			
	Region total	0.07087±0.01785	0.03477±0.00346	0.05572±0.01292
All	**Region total**	0.04551±0.06446	0.02681±0.01283	0.03586±0.03296

Table A8.21 Arctic temperature change (in °C) for emissions of aerosol-related species from different regions and sectors for 2015–2050 according to the MFR scenario, for interactions with radiation only.

Species	Sector	Asian Observers	Rest of Europe	Arctic Council (West)
BC	Fossil fuel and biofuel	-0.04587±0.06159	-0.01367±0.01158	-0.03116±0.02995
	Oil and gas flaring	0.00113±0.00505	0.00282±0.00430	-0.00044±0.00476
	Shipping			
	Region total	-0.04474±0.06180	-0.01085±0.01235	-0.03160±0.03032
OC	Fossil fuel and biofuel	-0.00488±0.00416	0.00000±0.00000	0.00000±0.00000
	Oil and gas flaring	0.00000±0.00000	0.00000±0.00000	0.00000±0.00000
	Shipping			
	Region total	-0.00488±0.00416	0.00000±0.00000	0.00000±0.00000
S	Fossil fuel and biofuel	0.10028±0.01785	0.03949±0.00346	0.06284±0.01292
	Oil and gas flaring	0.00000±0.00000	0.00000±0.00000	0.00000±0.00000
	Shipping			
	Region total	0.10028±0.01785	0.03949±0.00346	0.06284±0.01292
All	**Region total**	0.05066±0.06446	0.02864±0.01283	0.03124±0.03296

Arctic Council (East)	Rest of World	Marine (Arctic)	Marine (<60°N)	Sector total
-0.01893±0.01326	0.02416±0.05069			-0.00273±0.08700
-0.00211±0.01674	-0.00021±0.00393			0.00017±0.01903
		0.00174±0.00506	0.00062±0.00344	0.00235±0.00612
-0.02104±0.02136	0.02395±0.05084	0.00174±0.00506	0.00062±0.00344	-0.00021±0.08927
0.00000±0.00000	-0.00070±0.00411			0.00019±0.00585
0.00000±0.00000	0.00000±0.00000			0.00000±0.00000
		-0.00090±0.00415	-0.00021±0.00395	-0.00112±0.00573
0.00000±0.00000	-0.00070±0.00411	-0.00090±0.00415	-0.00021±0.00395	-0.00092±0.00819
0.02657±0.00707	-0.01904±0.00713			0.12822±0.02446
0.00000±0.00000	0.00000±0.00000			0.00000±0.00000
		-0.00143±0.00417	-0.00718±0.00412	-0.00862±0.00586
0.02657±0.00707	-0.01904±0.00713	-0.00143±0.00417	-0.00718±0.00412	0.11961±0.02515
0.00554±0.02250	0.00421±0.05150	-0.00060±0.00776	-0.00678±0.00666	0.11847±0.09311

Arctic Council (East)	Rest of World	Marine (Arctic)	Marine (<60°N)	Sector total
-0.00460±0.01326	0.01640±0.05069			-0.04105±0.08700
-0.00535±0.01674	0.00020±0.00393			-0.00458±0.01903
		0.00063±0.00506	0.00040±0.00344	0.00103±0.00612
-0.00995±0.02136	0.01660±0.05084	0.00063±0.00506	0.00040±0.00344	-0.04459±0.08927
0.00000±0.00000	-0.00063±0.00411			-0.00154±0.00585
0.00000±0.00000	0.00000±0.00000			0.00000±0.00000
		-0.00052±0.00415	-0.00017±0.00395	-0.00069±0.00573
0.00000±0.00000	-0.00063±0.00411	-0.00052±0.00415	-0.00017±0.00395	-0.00223±0.00819
0.00919±0.00707	0.00378±0.00713			0.17432±0.02446
0.00000±0.00000	0.00000±0.00000			0.00000±0.00000
		0.00284±0.00417	0.01226±0.00412	0.01511±0.00586
0.00919±0.00707	0.00378±0.00713	0.00284±0.00417	0.01226±0.00412	0.18943±0.02515
-0.00076±0.02250	0.01974±0.05150	0.00295±0.00776	0.01250±0.00666	0.14261±0.09311

Arctic Council (East)	Rest of World	Marine (Arctic)	Marine (<60°N)	Sector total
-0.00961±0.01326	-0.03648±0.05069			-0.13678±0.08700
-0.01096±0.01674	-0.00230±0.00393			-0.00975±0.01903
		-0.00257±0.00506	-0.00086±0.00344	-0.00343±0.00612
-0.02057±0.02136	-0.03878±0.05084	-0.00257±0.00506	-0.00086±0.00344	-0.14996±0.08927
0.00000±0.00000	0.00128±0.00411			-0.00360±0.00585
0.00000±0.00000	0.00000±0.00000			0.00000±0.00000
		0.00062±0.00415	0.00014±0.00395	0.00076±0.00573
0.00000±0.00000	0.00128±0.00411	0.00062±0.00415	0.00014±0.00395	-0.00284±0.00819
0.01957±0.00707	0.07180±0.00713			0.29397±0.02446
0.00000±0.00000	0.00000±0.00000			0.00000±0.00000
		0.00337±0.00417	0.01532±0.00412	0.01869±0.00586
0.01957±0.00707	0.07180±0.00713	0.00337±0.00417	0.01532±0.00412	0.31267±0.02515
-0.00100±0.02250	0.03430±0.05150	0.00142±0.00776	0.01461±0.00666	0.15987±0.09311

Table A8.22 Arctic temperature change (in °C) for emissions of aerosol-related species from different regions and sectors for 1990–2015, for interactions with radiation, surface albedo, and clouds.

Species	Sector	Asian Observers	Rest of Europe	Arctic Council (West)
BC	Fossil fuel and biofuel	0.01436±0.20965	-0.01139±0.18793	-0.02197±0.17924
	Oil and gas flaring	0.00325±0.11756	-0.03824±0.11914	0.00388±0.11900
	Shipping			
	Region total	0.01761±0.24036	-0.04963±0.22252	-0.01809±0.21515
OC	Fossil fuel and biofuel	-0.00232±0.12186	0.00000±0.00000	0.00000±0.00000
	Oil and gas flaring	0.00000±0.00000	0.00000±0.00000	0.00000±0.00000
	Shipping			
	Region total	-0.00232±0.12186	0.00000±0.00000	0.00000±0.00000
S	Fossil fuel and biofuel	-0.16736±0.25025	0.37614±0.25692	0.32456±0.21000
	Oil and gas flaring	0.00000±0.00000	0.00000±0.00000	0.00000±0.00000
	Shipping			
	Region total	-0.16736±0.25025	0.37614±0.25692	0.32456±0.21000
All	**Region total**	-0.15207±0.36776	0.32651±0.33989	0.30647±0.30065

Table A8.23 Arctic temperature change (in °C) for emissions of aerosol-related species from different regions and sectors for 2015–2050, under the CLE scenario and for interactions with radiation, surface albedo, and clouds.

Species	Sector	Asian Observers	Rest of Europe	Arctic Council (West)
BC	Fossil fuel and biofuel	-0.02459±0.20965	-0.01259±0.18793	-0.03026±0.17924
	Oil and gas flaring	0.00038±0.11756	-0.04157±0.11914	0.02444±0.11900
	Shipping			
	Region total	-0.02421±0.24036	-0.05415±0.22252	-0.00582±0.21515
OC	Fossil fuel and biofuel	0.00236±0.12186	0.00000±0.00000	0.00000±0.00000
	Oil and gas flaring	0.00000±0.00000	0.00000±0.00000	0.00000±0.00000
	Shipping			
	Region total	0.00236±0.12186	0.00000±0.00000	0.00000±0.00000
S	Fossil fuel and biofuel	0.15676±0.25025	0.12751±0.25692	0.19285±0.21000
	Oil and gas flaring	0.00000±0.00000	0.00000±0.00000	0.00000±0.00000
	Shipping			
	Region total	0.15676±0.25025	0.12751±0.25692	0.19285±0.21000
All	**Region total**	0.13491±0.36776	0.07336±0.33989	0.18703±0.30065

Arctic Council (East)	Rest of World	Marine (Arctic)	Marine (<60°N)	Sector total
-0.10876±0.15163	0.00389±0.32630			-0.12387±0.49077
-0.01288±0.20761	-0.00268±0.12249			-0.04667±0.31667
		0.02198±0.12204	0.01576±0.12247	0.03774±0.17289
-0.12164±0.25709	0.00121±0.34853	0.02198±0.12204	0.01576±0.12247	-0.13280±0.60912
0.00000±0.00000	-0.00175±0.11994			-0.00406±0.17099
0.00000±0.00000	0.00000±0.00000			0.00000±0.00000
		0.01199±0.11716	-0.00284±0.12118	0.00915±0.16856
0.00000±0.00000	-0.00175±0.11994	0.01199±0.11716	-0.00284±0.12118	0.00508±0.24010
0.19438±0.29768	-0.04851±0.22616			0.67920±0.55902
0.00000±0.00000	0.00000±0.00000			0.00000±0.00000
		0.04774±0.22923	-0.00070±0.24232	0.04704±0.33356
0.19438±0.29768	-0.04851±0.22616	0.04774±0.22923	-0.00070±0.24232	0.72625±0.65097
0.07273±0.39333	-0.04905±0.43245	0.08170±0.28490	0.01223±0.29732	0.59853±0.92328

Arctic Council (East)	Rest of World	Marine (Arctic)	Marine (<60°N)	Sector total
-0.02641±0.15163	0.00264±0.32630			-0.09121±0.49077
-0.03267±0.20761	0.00258±0.12249			-0.04685±0.31667
		0.00792±0.12204	0.01036±0.12247	0.01828±0.17289
-0.05908±0.25709	0.00522±0.34853	0.00792±0.12204	0.01036±0.12247	-0.11978±0.60912
0.00000±0.00000	-0.00158±0.11994			0.00077±0.17099
0.00000±0.00000	0.00000±0.00000			0.00000±0.00000
		0.00690±0.11716	-0.00224±0.12118	0.00466±0.16856
0.00000±0.00000	-0.00158±0.11994	0.00690±0.11716	-0.00224±0.12118	0.00543±0.24010
0.06721±0.29768	0.00962±0.22616			0.55396±0.55902
0.00000±0.00000	0.00000±0.00000			0.00000±0.00000
		-0.09470±0.22923	0.00119±0.24232	-0.09351±0.33356
0.06721±0.29768	0.00962±0.22616	-0.09470±0.22923	0.00119±0.24232	0.46045±0.65097
0.00813±0.39333	0.01326±0.43245	-0.07989±0.28490	0.00931±0.29732	0.34610±0.92328

Table A8.24 Arctic temperature change (in °C) for emissions of aerosol-related species from different regions and sectors for 2015–2050, under the MFR scenario and for interactions with radiation, surface albedo, and clouds.

Species	Sector	Asian Observers	Rest of Europe	Arctic Council (West)
BC	Fossil fuel and biofuel	-0.04593±0.20965	-0.01749±0.18793	-0.05110±0.17924
	Oil and gas flaring	0.00376±0.11756	-0.06258±0.11914	0.00770±0.11900
	Shipping			
	Region total	-0.04217±0.24036	-0.08006±0.22252	-0.04340±0.21515
OC	Fossil fuel and biofuel	0.01271±0.12186	0.00000±0.00000	0.00000±0.00000
	Oil and gas flaring	0.00000±0.00000	0.00000±0.00000	0.00000±0.00000
	Shipping			
	Region total	0.01271±0.12186	0.00000±0.00000	0.00000±0.00000
S	Fossil fuel and biofuel	0.22183±0.25025	0.14480±0.25692	0.21750±0.21000
	Oil and gas flaring	0.00000±0.00000	0.00000±0.00000	0.00000±0.00000
	Shipping			
	Region total	0.22183±0.25025	0.14480±0.25692	0.21750±0.21000
All	**Region total**	0.19237±0.36776	0.06474±0.33989	0.17409±0.30065

Arctic Council (East)	Rest of World	Marine (Arctic)	Marine (<60°N)	Sector total
-0.05520±0.15163	-0.00588±0.32630			-0.17559±0.49077
-0.06694±0.20761	-0.02998±0.12249			-0.14804±0.31667
		-0.03251±0.12204	-0.02193±0.12247	-0.05444±0.17289
-0.12214±0.25709	-0.03585±0.34853	-0.03251±0.12204	-0.02193±0.12247	-0.37808±0.60912
0.00000±0.00000	0.00321±0.11994			0.01592±0.17099
0.00000±0.00000	0.00000±0.00000			0.00000±0.00000
		-0.00826±0.11716	0.00190±0.12118	-0.00636±0.16856
0.00000±0.00000	0.00321±0.11994	-0.00826±0.11716	0.00190±0.12118	0.00956±0.24010
0.14312±0.29768	0.18292±0.22616			0.91017±0.55902
0.00000±0.00000	0.00000±0.00000			0.00000±0.00000
		-0.11230±0.22923	0.00148±0.24232	-0.11082±0.33356
0.14312±0.29768	0.18292±0.22616	-0.11230±0.22923	0.00148±0.24232	0.79935±0.65097
0.02098±0.39333	0.15028±0.43245	-0.15307±0.28490	-0.01855±0.29732	0.43084±0.92328

9. Impacts of air pollution on health, ecosystems, and crops

Authors: Susan Anenberg, Shilpa Rao-Skirbekk, Stephen Arnold, Jørgen Brandt, Alfonso Diz-Lois Palomares, Joshua Fu, Camilla Geels, Otto Hänninen, Ulas Im, Joakim Langner, Kathy Law, Heli Lehtomäki, Rashed Mahmood, Maximilian Posch, Isabell Rumrich, Raimo O. Salonen, Marcus Sarofim, Julia Schmale, Svetlana Tsyro, Rita Van Dingenen, Knut von Salzen

9.1 Introduction

This chapter presents the results of the authors' efforts to quantify the impacts of present-day pollutant emissions on human health, ecosystems, and crop yields and to understand the benefits that can be gained by reducing emissions in the future. Black carbon (BC) and methane (CH_4) influence public health and ecosystems globally, and in the Arctic specifically. These short-lived climate forcers (SLCFs) negatively affect public health by contributing to air pollution and climate change. Air pollution also affects ecosystems through the acidification and eutrophication of water bodies, by damaging trees and soil, and by harming biodiversity and aquatic life. Tropospheric ozone, meanwhile, can reduce crop yields by damaging leaves, potentially affecting food security and nutrition.

SLCFs affect health within Arctic communities through two pathways. First, BC, as a component of fine particulate matter ($PM_{2.5}$), and CH_4, through its role as a precursor to tropospheric ozone (O_3), contribute to air pollution-related health effects. $PM_{2.5}$ and O_3 are health-damaging air pollutants, associated with a range of negative outcomes that include respiratory and cardiovascular diseases. Air pollution is considered the fifth leading global health risk factor, and the leading environmental and occupational health risk factor, ranking among the top global health risk factors in all Arctic Council Member states and Observer countries. Over the past decades, many nations around the world have established health-based regulations to limit $PM_{2.5}$ and O_3 exposure. Mitigation measures that reduce BC and CH_4 emissions often also reduce other co-emitted pollutants – such as organic carbon (OC) and nitrogen oxides (NO_X) – leading to large air-quality and health benefits from their combined impact on $PM_{2.5}$ and O_3 concentrations, as is shown in this chapter.

Second, BC and CH_4 also influence public health in the Arctic through their impacts on climate change, which may have a variety of negative consequences for public health across cities and communities in the Arctic. For example, climate change can affect natural ecosystems that sustain fish, forests, and wildlife, potentially leading to dietary risks. Climate change can also increase air pollution from wildfires, contribute to the spread of vector-borne diseases, and heighten the risk of heat stress and associated mortality. Reducing BC and CH_4 can thus help to minimize negative consequences for public health in Arctic communities, as well as throughout the world, by reducing the effects of both climate change and exposure to air pollution.

This chapter presents an assessment of the health and environmental impacts of the emissions scenarios described in Chapter 2. Understanding the benefits to both health and ecosystems under different contexts can help to inform the design and implementation of emissions-reducing policies. Health and environmental impact assessments are often used in decision-making analyses, such as those used to explore cost-benefit trade-offs or the cost-effectiveness of particular actions. However, quantitatively estimating the public health and environmental benefits of reduced climate change in the Arctic is challenging due to limited data and modeling. Estimating health impacts from changes in air quality is currently easier. Averting air quality-related health impacts would lead to immediate reductions in premature death and disease, with societal benefits accruing each year; meanwhile, climate benefits may be realized in the longer-term. Methods also exist for estimating pollution deposition, which can reduce crop yields and damage ecosystems through acidification and eutrophication. This chapter therefore focuses on how changes to $PM_{2.5}$ and O_3 resulting from current legislation (CLE) and maximum feasible reduction (MFR) scenarios could affect public health, ecosystems, and crop yields in Arctic Council Member states and Observer countries. The additional health and environmental benefits from reduced climate change are also important, but are not quantified here.

Section 9.2 reviews the evidence for health impacts related to air quality, including what is known from the body of scientific literature that has accrued over decades on epidemiological, toxicological, environmental and other research studies globally. Section 9.3 reviews the evidence for air pollution's effects on ecosystems and crop yields. Section 9.4 presents new quantitative analyses of the impacts of air pollution on health, ecosystems, and crop yields in the Arctic, as well as of the degree to which these impacts could be avoided by policies that reduce BC, CH_4, and other emissions. Finally, Section 9.5 synthesizes the existing body of literature with the new quantitative analyses to outline the present-day impacts of pollutant emissions on human health, ecosystems, and crop yields – and the potential benefits that can be achieved by mitigating emissions in the future.

9.2 Review of evidence of how air quality affects health

9.2.1 Epidemiological evidence

9.2.1.1 Systematic reviews of the effects of $PM_{2.5}$ and O_3 on health

$PM_{2.5}$ and O_3 are associated with a range of deleterious health outcomes, including premature mortality. However, assessing people's exposure to air pollution in the Arctic region is challenging due to: ground monitors being historically sited away from settlements in order to measure background air quality; the incomplete coverage of satellite observations over snow- and ice-covered regions; and limited high-resolution modeling of air quality. For these reasons and others, empirical research on the

health effects from air pollution on Arctic communities is limited. However, the health effects of being exposed to air pollution have been extensively studied since the early 20th century, mostly in the USA and Europe, and more recently in Asia. Based on this large body of literature, the World Health Organization (WHO), United States Environmental Protection Agency (US EPA), and Institute for Health Metrics and Evaluation (IHME), among others, periodically conduct comprehensive, systematic literature reviews to determine whether the evidence supports a causal association between different pollutants and health outcomes (WHO Europe, 2013a; US EPA, 2019; GBD 2019 Risk Factor Collaborators, 2020). For example, the latest Integrated Science Assessments conducted by the US EPA concluded that long-term exposure to $PM_{2.5}$ is causally associated with mortality and cardiovascular effects specifically, and likely to be causally associated with respiratory effects (US EPA, 2019). The US EPA also concluded that short-term exposure to O_3 is causally associated with respiratory effects and likely to be causally associated with metabolic effects, and that long-term exposure to O_3 is also likely to be causally associated with respiratory effects (US EPA, 2020). Growing evidence also supports associations between exposure to $PM_{2.5}$ and diabetes, negative birth outcomes – including short gestational age and low birth weight – and neurological effects in children and adults (GBD 2019 Risk Factor Collaborators, 2020; Perera et al., 2019; Power et al., 2016).

Some epidemiological, toxicological, and human studies have explored potential differences in the health effects of individual components of $PM_{2.5}$ or of different component mixtures. Evidence from these studies is mixed, with some assessments, including by WHO, finding that traffic-related air pollution, such as BC and other pollutants from vehicle tailpipe emissions, leads to elevated risk (WHO, 2012; WHO Europe, 2013a). Despite some support for differential effects of $PM_{2.5}$ components in the scientific literature, the US EPA and WHO have concluded that there is insufficient evidence to support the setting of guidelines or standards for individual $PM_{2.5}$ components, such as BC (US EPA, 2012; WHO Europe, 2013a). A more recent literature review by US EPA is consistent with this conclusion (Luben et al., 2017). Future research may disentangle the roles of air-pollution mixtures, particle components, and sources in characterizing air pollution risks to human health.

9.2.1.2 Arctic- and Nordic-specific epidemiological studies

Most air-pollution epidemiology studies that have been carried out in the Arctic region are from the Nordic countries (Denmark, Finland, Iceland, Norway and Sweden). Although epidemiological studies in Alaska are more limited in number, the findings are broadly consistent with studies from the contiguous USA. For example, Kossover (2010) found significant associations between short-term exposure to $PM_{2.5}$ and hospital admissions in Fairbanks, Alaska. Residential heating, in particular wood burning, is a major source of wintertime $PM_{2.5}$ in the Fairbanks area (e.g. Ward et al., 2012). Studies focusing on the replacement of wood stoves with cleaner alternatives in rural communities found that reduced $PM_{2.5}$ concentrations resulting from stove changeouts led to a decrease in community-level respiratory problems (Noonan et al., 2012), although changeouts were less effective than installing air-filtration systems for individual homes (Ward et al., 2017). Improving understanding of the health effects of indoor and outdoor winter pollution is now the subject of a major international study – the Alaskan Layered Pollution And Chemical Analysis (ALPACA). The ALPACA White Paper provides an extensive review of the sources and processes affecting $PM_{2.5}$ in Fairbanks (Simpson et al., 2019b). In summer, smoke from local forest fires also contributes to enhanced $PM_{2.5}$ levels over Alaska (Schmale et al., 2018a).

Among the Nordic countries, overall concentrations of air pollution decrease northwards, resulting in generally low levels of pollution in Finland and Iceland, although associations with health outcomes have been reported even at these low levels. Thus, the Nordic region warrants attention in epidemiological studies, including exploration of potential thresholds for health effects reported in studies from other regions. The NordicWelfAir project is examining air-pollution levels, chemical composition, and related health and welfare impacts in the five Nordic countries. By the end of 2020, the project had contributed to 27 epidemiological studies estimating the health effects of short- and long-term exposure to $PM_{2.5}$ and coarse particulate matter (PM_{10}) and their components (NO_X, ammonia, O_3, hydrogen sulfide [H_2S], and ambient benzene). These studies explored the increased risk for mortality, cancer, asthma, hospital admissions, psychological and cognitive disorders, and preterm birth (Table 9.1).

In the Nordic and wider Arctic regions, air pollution has been shown to have statistically significant associations with a wide range of health outcomes. Here, we report some of the findings in those regions, relating air-pollution exposure to mortality, mental and behavioral disorders, cardiovascular and respiratory disease, cancer, and prenatal impacts.

Exposure to air pollution has, for example, been associated with premature mortality. Specifically, statistically significant associations have been reported between long-term exposure (mean durations of 9–18 years) to $PM_{2.5}$, PM_{10}, nitrogen dioxide (NO_2), NO_X, BC and OC, and secondary inorganic aerosols (SIA) and all-cause, cardiovascular, and respiratory mortality (e.g. Christidis et al., 2019; Crouse et al., 2015; Hvidtfeldt et al., 2019a, 2019b; Nafstad et al., 2003, 2004; Raaschou-Nielsen et al., 2020). In addition, short-term peak exposure to $PM_{2.5}$ has been associated with all-cause, circulatory and respiratory mortality (Kollanus et al., 2016; Madsen et al., 2012; Olstrup et al., 2019).

Exposure to air pollution has also been linked with increased risk for some outcomes related to mental and behavioral disorders. Long-term exposure to $PM_{2.5}$, PM_{10}, NO_X, and NO_2 have been associated with an increased risk for attention deficit hyperactivity disorder (ADHD) and schizophrenia (Antonsen et al., 2020; Horsdal et al., 2019; Thygesen et al., 2020). Exposure to $PM_{2.5}$ and NO_2 has been associated with dementia in Canada (Smargiassi et al., 2020). And short-term exposure to PM_{10} has been associated with increases in psychiatric emergency visits (Oudin et al., 2018), with a similar association observed in children and young adults for $PM_{2.5}$ and NO_2 (Szyszkowicz et al., 2020). A study including two independent, very large datasets from the USA and Denmark, showed that air pollution is significantly associated with an increased risk of bipolar disorder, depression and other psychiatric disorders (Khan et al., 2019).

Table 9.1. Statistically significant exposure-response associations found in studies published under the NordicWelfAir project up to the end of 2020.

Pollutant	Exposure type	Outcome	Concentration (μg/m³)	Type	Risk metric[1]	Risk estimate (95% confidence interval)	Reference
$PM_{2.5}$	Long-term	Malignant non-glioma brain tumors	5.39 (contr.); 5.31 (cases)	IQR	OR	1.267 (1.053–1.524)	Poulsen et al., 2020a
	Long-term	Childhood non-Hodgkins lymphoma (NHL)	5	μg/m³ increment	OR	2.11 (1.10–4.01)	Hvidtfeldt et al., 2020a
	Long-term	Adult leukemia	5.6	IQR	OR	1.09 (1.02–1.17)	Taj et al., 2020b
	Long-term	Adult acute myeloid leukemia	5.6	IQR	OR	1.14 (1.00–1.29)	Taj et al., 2020b
	Long-term	Childhood NHL	4.83	IQR	OR	2.05 (1.10, 3.83)	Hvidtfeldt et al., 2020b
	Long-term	Adult leukemia	10	μg/m³ increment	OR	1.19 (1.05–1.35)	Puett et al., 2020
	Long-term	Stroke	3.9	IQR	OR	1.13 (1.01–1.25)	Amini et al., 2020
	Long-term	Ischemic stroke	3.9	IQR	OR	1.14 (1.01–1.27)	Amini et al., 2020
	Long-term	All-cause mortality	10	μg/m³ increment	HR	1.28 (1.1–1.46)*	Hvidtfeldt et al., 2019b
	Long-term	Cardiovascular disease (CVD) mortality	10	μg/m³ increment	HR	1.66 (1.28–2.16)*	Hvidtfeldt et al., 2019b
	Long-term	Natural cause mortality	10	μg/m³ increment	MRR	1.08 (1.04–1.13)	Raaschou-Nielsen et al., 2020
	Long-term	Attention deficit hyperactivity disorder	5	increment	IRR	1.51 (1.41–1.62)	Thygesen et al., 2020
	Long-term	Asthma	5	μg/m³ increment	HR	1.05 (1.03–1.07)	Holst et al., 2020
PM_{10}	Long-term	All-cause mortality	10	μg/m³ increment	HR	1.12 (1.03–1.22)	Hvidtfeldt et al., 2019b
	Long-term	CVD mortality	10	μg/m³ increment	HR	1.3 (1.11–1.53)	Hvidtfeldt et al., 2019b
	Long-term	Schizophrenia	10	μg/m³ increment	IRR	1.04 (1–1.08)	Antonsen et al., 2020
	Long-term	Asthma	5	μg/m³ increment	HR	1.04 (1.02–1.06)	Holst et al., 2020
	Short-term	Psychiatric emergency visits	10	μg/m³ increment	% change	2.3 (0.3–4.3)	Oudin et al., 2018
O_3	Long-term	CVD mortality	10	μg/m³ increment	MRR	1.02 (1.01–1.04)	Raaschou-Nielsen et al., 2020
NO_2	Long-term	All-cause mortality	10	μg/m³ increment	HR	1.07 (1.04–1.1)	Hvidtfeldt et al., 2019b
	Long-term	CVD mortality	10	μg/m³ increment	HR	1.11 (1.04–1.17)	Hvidtfeldt et al., 2019b
	Long-term	Natural cause mortality	10	μg/m³ increment	MRR	1.05 (1.04–1.06)	Raaschou-Nielsen et al., 2020
	Long-term	Respiratory mortality	10	μg/m³ increment	MRR	1.08 (1.05–1.11)	Raaschou-Nielsen et al., 2020
	Long-term	Lung cancer mortality	10	μg/m³ increment	MRR	1.07 (1.04–1.09)	Raaschou-Nielsen et al., 2020
	Long-term	Meningioma	10.78 (contr.); 10.81 (cases)	IQR	OR	1.083 (1.016–1.154)	Poulsen et al., 2020a
	Long-term	Schizophrenia	10	μg/m³ increment	IRR	1.2 (1.09–1.33)	Antonsen et al., 2020
	Long-term	Schizophrenia	10	μg/m³ increment	HR	1.23 (1.15–1.32)	Horsdal et al., 2019
	Long-term	Attention deficit hyperactivity disorder	10	increment	IRR	1.38 (1.35–1.42)	Thygesen et al., 2020
	Long-term	Asthma	10	μg/m³ increment	HR	1.04 (1.03–1.04)	Holst et al., 2020
NO_3	Long-term	Adult leukemia	1	IQR	OR	1.08 (1.02–1.14)	Taj et al., 2020b
	Long-term	Adult acute myeloid leukemia	1	IQR	OR	1.12 (1.01–1.24)	Taj et al., 2020b
	Long-term	Asthma	5	μg/m³ increment	HR	1.03 (1.02–1.05)	Holst et al., 2020
NO_X	Long-term	Schizophrenia	10	μg/m³ increment	IRR	1.06 (1.02–1.1)	Antonsen et al., 2020
	Long-term	Asthma	10	μg/m³ increment	HR	1.04 (1.03–1.04)	Holst et al., 2020
NH_4	Long-term	Adult leukemia	0.8	IQR	OR	1.08 (1.00–1.17)	Taj et al. 2020b
	Long-term	Adult acute myeloid leukemia	0.8	IQR	OR	1.16 (1.01–1.34)	Taj et al., 2020b
SO_2	Long-term	All other NHL types	10	μg/m³ increment	OR	1.07 (1.00–1.15)	Taj et al., 2020a
	Long-term	Asthma	5	μg/m³ increment	HR	1.02 (1.01–1.04)	Holst et al., 2020
H_2S	Daily 24-hour	Emergency hospital visits	over 7	μg/m³	RR	1.07 (1.02–1.11)	Finnbjornsdottir et al., 2016

Table 9.1 continued

Pollutant	Exposure type	Outcome	Concentration (μg/m³)	Type	Risk metric[1]	Risk estimate (95% confidence interval)	Reference
BC	Long-term	Malignant intracranial CNS tumors	0.39 (contr.); 0.38 (cases)	IQR	OR	1.034 (1.005–1.065)	Poulsen et al., 2020a
	Long-term	Total brain tumor	0.39	IQR	OR	1.026 (1.001–1.052)	Poulsen et al., 2020b
	Long-term	Malignant brain tumor	0.39	IQR	OR	1.036 (1.006–1.067)	Poulsen et al., 2020b
	Long-term	Childhood NHL	1	μg/m³ increment	OR	1.68 (1.06–2.66)	Hvidtfeldt et al., 2020a
	Long-term	Adult leukemia	0.4	IQR	OR	1.02 (1.00–1.03)	Taj et al., 2020b
	Long-term	Adult acute myeloid leukemia	0.4	IQR	OR	1.03 (1.00–1.07)	Taj et al., 2020b
	Long-term	Childhood NHL	0.39	IQR	OR	1.22 (1.02, 1.46)	Hvidtfeldt et al., 2020b
	Long-term	Adult leukemia	1	μg/m³ increment	OR	1.05 (1.01–1.10)	Puett et al., 2020
	Long-term	Natural cause mortality	1	μg/m³ increment	MRR	1.05 (1.02–1.08)	Raaschou-Nielsen et al., 2020
	Long-term	Respiratory mortality	1	μg/m³ increment	MRR	1.07 (1.01–1.13)	Raaschou-Nielsen et al., 2020
	Long-term	Lung cancer mortality	1	μg/m³ increment	MRR	1.07 (1.03–1.11)	Raaschou-Nielsen et al., 2020
BC + OC	Long-term	NHL	1.15	IQR	OR	1.03 (1.00–1.07)	Taj et al., 2020b
	Long-term	Total brain tumor	1.16	IQR	OR	1.053 (1.005–1.103)	Poulsen et al., 2020b
	Long-term	Malignant brain tumor	1.16	IQR	OR	1.063 (1.007–1.123)	Poulsen et al., 2020b
	Long-term	Glioma	1.16	IQR	OR	1.067 (1.001–1.137)	Poulsen et al., 2020b
	Long-term	All-cause mortality	0.83	IQR	HR	1.06 (1.03–1.09)	Hvidtfeldt et al., 2019a
	Long-term	CVD mortality	0.83	IQR	HR	1.1 (1.04–1.16)	Hvidtfeldt et al., 2019a
	Long-term	All-cause mortality	1	μg/m³ increment	HR	1.09 (1.04–1.15)	Hvidtfeldt et al., 2019b
	Long-term	CVD mortality	1	μg/m³ increment	HR	1.16 (1.05–1.27)	Hvidtfeldt et al., 2019b
SIA	Long-term	Non-glioma	3.95	IQR	OR	1.663 (1.216–2.274)	Poulsen et al., 2020b
	Long-term	Adult leukemia	4.2	IQR	OR	1.15 (1.03–1.29)	Taj et al., 2020b
	Long-term	Adult acute myeloid leukemia	4.2	IQR	OR	1.23 (1.01–1.51)	Taj et al., 2020b
	Long-term	CVD mortality	0.26	IQR (in μg/m³)	HR	1.05 (1.02–1.08)	Hvidtfeldt et al., 2019a
SOA	Long-term	NHL	0.05	IQR	OR	1.54 (1.13–2.09)	Taj et al., 2020b
Benzene	Pregnancy	Medulloblastoma	Doubling	ppb	RR	1.3 (1.0–1.9)	Raaschou-Nielsen et al., 2017
Exhaust particles	2nd trimester of pregnancy	Small for gestational age	0.201–0.332 v. ≤ 0.061	4th v. 1st quintile	PRR	1.09 (1.01–1.17)	Olsson et al., 2020
Air-quality index	Long-term	Schizophrenia	3	Septiles (1 as ref.)	HR	1.34 (1.19–1.52)	Khan et al., 2019
	Long-term	Personality disorder	2	Septiles (1 as ref.)	HR	1.5 (1.38–1.62)	Khan et al., 2019
	Long-term	Major depression	2	Septiles (1 as ref.)	HR	1.21 (1.15–1.28)	Khan et al. 2019
	Long-term	Bipolar disorder	2	Septiles (1 as ref.)	Rate change	1.07 (1.01–1.15)	Khan et al. 2019

[1]HR: hazard ratio, IRR: incidence rate ratio, MRR: mortality rate ratio, OR: odds ratio, PRR: prevalence rate ratio, RR: relative risk; IQR = interquartile range

Exposure to air pollution is also linked with cardiovascular and respiratory diseases, and related hospital admissions. Amini et al. (2020) reported an association between long-term exposure to $PM_{2.5}$ and increased risk for stroke, while Holst et al. (2020) noted an association of exposure to air pollution (NO_2, NO_X, sulfur dioxide [SO_2], $PM_{2.5}$, PM_{10}, nitrate [NO_3], O_3) and asthma. Anderson et al. (2007) reported increased risks for hospital admissions related to cardiovascular and respiratory disease in the elderly for short-term exposures to PM_{10} and NO_2. Similar associations have been reported for O_3 and $PM_{2.5}$ in Canada (Szyszkowicz et al., 2018). In children and adolescents, short-term exposure to PM_{10}, carbon monoxide (CO) and NO_2 were associated with increased risks for asthma-related hospital admissions (Anderson et al., 2007). In Iceland, short-term exposure to H_2S has been shown to increase emergency-room visits (Finnbjornsdottir et al., 2016) and has been weakly associated with an increase in dispensing of drugs for chronic obstructive pulmonary disease (COPD) (Carlsen et al., 2012). Additionally, O_3 was associated with an increase in cardiopulmonary- and stroke-related hospital admissions in Iceland (Carlsen et al., 2013). And in a literature review by Rodriguez-Villamizar et al. (2015), exposure to outdoor air pollution was associated with respiratory emergency-room visits and hospital admissions, as well as with asthma and decreased lung function in Canadian children.

There is evidence linking air pollution with an increased risk for cancer. In Denmark, long-term exposure to air pollution components (benzene, BC and OC, ammonium, NO_2, NO_3, NO_X, O_3, $PM_{2.5}$, SIA, SO_2, secondary organic aerosol [SOA]) has been associated with increased risk for cancer (central nervous system cancer, leukemia, non-Hodgkins lymphoma) in adults and children (e.g. Hvidtfeldt et al., 2020a, 2020b; Nafstad et al., 2003; Poulsen et al., 2020a, 2020b; Puett et al., 2020; Raaschou-Nielsen et al., 2017; Taj et al., 2020a, 2020b). However, some studies have had contradicting results (e.g.

Jørgensen et al., 2016), and no association between $PM_{2.5}$ and breast cancer was observed by Andersen et al. (2017). In Canada, no clear association was found between NO_2 or $PM_{2.5}$ and adult leukemia (Winters et al., 2015).

Prenatal exposure to air pollution has been linked with adverse health effects. Prenatal exposure to NO_X was associated with type 1 diabetes (Malmqvist et al., 2015); NO_2 with pre-eclampsia and gestational diabetes mellitus (Pedersen et al., 2017a, 2017b); and exhaust particles with the risk of being born with a low birth weight (Olsson et al., 2020). No clear association between air pollution and preterm birth has been reported (Siddika et al., 2019, 2020).

It is notable that disease-register data and modeled air-pollution concentrations are used routinely in Nordic epidemiological studies. However, study designs often differ in terms of the units of exposure used or definitions of reference groups, making direct comparisons of the magnitude of effects difficult. Another challenge is that levels of several air pollutants are strongly correlated, and the single-pollutant models used by most of these epidemiological studies do not allow for considering the effects of simultaneous exposure to multiple pollutants. Despite these challenges, findings from Nordic studies are broadly consistent with the evidence from other parts of the world, as described in Section 9.2.1.1.

The availability of long-term, detailed register and national-cohort data in, for example, Canada (Crouse et al., 2015) and Denmark (e.g. Raaschou-Nielsen et al., 2020), makes it possible to study diverse health impacts over many years, and to add to general understanding of the risks associated with exposure to air pollution. However, epidemiological studies focusing on communities at elevated Arctic altitudes are presently lacking. Available studies in the northern latitudes do not report results stratified by altitude. The relatively low population and limited availability of air-quality data for the High Arctic regions contribute to the dearth of epidemiological studies.

9.2.2 Estimates of air-pollution disease burdens in Arctic Council Member states and Observer countries

9.2.2.1 Estimates from the Global Burden of Disease study

Using relationships between $PM_{2.5}$ and O_3, and health outcomes from studies conducted around the world, the IHME Global Burden of Disease (GBD) 2017 study estimated that 4.9 million premature deaths worldwide could be attributed to air pollution in 2017, including 2.9 million from ambient $PM_{2.5}$, 470,000 from ambient O_3, and 1.6 million from household air pollution from solid-fuel combustion for household energy use (GBD 2017 Risk Factor Collaborators, 2018). Air pollution is considered the fifth leading global health risk factor, and the leading environmental and occupational health risk factor. In all Arctic Council Member states and Observer countries, air pollution ranks among the top global health risk factors (Table 9.2). Regarding Member states, the percentage of all deaths attributable to air pollution ranges from 2.1% in Finland to 5.4% in Russia; for Observer countries it extends

Table 9.2. Deaths, disability-adjusted life years (DALYs), and percentage of all deaths that were attributable to the combination of ambient $PM_{2.5}$, O_3, and household air pollution in 2017, according to GBD 2017 Risk Factor Collaborators (2018). Rank indicates the position of air pollution among all health risk factors in terms of magnitude of mortality impacts. Values in parentheses indicate 95% confidence intervals reported by the GBD 2017 study.

Country/region	Deaths	DALYs	% of all deaths	Rank
Global	4,895,476 (4,415,829–5,390,166)	147,418,000 (132,345,551–161,667,283)	8.8 (7.9–9.6)	5
Arctic Council Member states				
Canada	7835 (2735–11,502)	158,122 (42,350–244,199)	2.8 (1.0–4.1)	9
Denmark	2366 (1745–3013)	48,500 (34,000–62,294)	4.4 (3.2–5.5)	8
Finland	1127 (361–1654)	23,764 (6383–38,103)	2.1 (0.7–3.0)	10
Iceland	59 (26–105)	1224 (403–2344)	2.7 (1.1–4.7)	9
Norway	1153 (829–1473)	22,610 (14,936–30,322)	2.8 (2.0–3.6)	9
Russia	99,392 (82,011–116,820)	2,316,484 (1,920,892–2,726,159)	5.4 (4.5–6.3)	9
Sweden	2257 (967–3458)	42,645 (14,736–68,588)	2.5 (1.0–3.8)	10
USA	107,507 (80,542–134,664)	2,478,386 (1,734,276–3,179,612)	3.8 (2.8–4.7)	8
Arctic Council Observer countries				
China	1,242,987 (1,081,828–1,395,446)	27,934,105 (24,391,019–31,198,105)	12 (10–13)	4
France	18,992 (14,108–24,027)	349,044 (245,213–445,560)	3.3 (2.4–4.1)	9
Germany	41,839 (32,386–52,475)	791,874 (599,537–989,048)	4.4 (3.4–5.4)	9
India	1,240,529 (1,086,201–1,385,928)	38,684,028 (34,547,725–42,409,874)	13 (11–14)	8
Italy	29,368 (20,700–38,023)	527,238 (360,332–682,441)	4.7 (3.4–6.1)	7
Japan	49,554 (40,065–60,455)	851,539 (690,685–1,023,004)	3.6 (2.9–4.4)	8
Netherlands	6714 (5330–8357)	139,067 (107,537–173,164)	4.4 (3.5–5.4)	7
Poland	24,629 (18,797–30,293)	561,000 (429,721–695,299)	6.2 (4.8–7.7)	8
Singapore	1318 (965–1640)	32,245 (24,304–39,466)	6.6 (4.9–8.3)	7
South Korea	17,343 (14,266–20,432)	432,010 (346,273–516,283)	5.8 (4.8–6.8)	5
Spain	17,133 (11,126–22,715)	295,076 (184,858–393,989)	4.1 (2.7–5.5)	9
Switzerland	2313 (1725–2915)	47,465 (33,032–61,831)	3.6 (2.7–4.5)	8
UK	24,794 (20,066–30,074)	485,471 (382,773–587,044	4.1 (3.3–4.9)	7

from 3.3% in France to 13% in India. However, the health burden from air pollution is likely to be higher than that estimated by the GBD 2017 Risk Factor Collaborators (2018) study because additional pollutants and health outcomes that scientific evidence indicates could be causally associated have not yet been included – such as NO_2 air pollution and pediatric asthma incidence (Achakulwisut et al., 2019). The GBD 2017 Risk Factor Collaborators' (2018) study included stroke, ischemic heart disease (IHD), COPD, lung cancer (LC), type 2 diabetes mellitus, and lower respiratory infection (LRI) for ambient $PM_{2.5}$ and household air pollution, and COPD for O_3.

Air pollution burden-of-disease calculations are influenced by estimates of air-pollution concentrations, as well as population size, and vulnerability due to age and baseline disease rates, among other factors. As IHME GBD studies use globally consistent methods to estimate pollution levels and population characteristics, they may lack specificity for small areas, including cities and smaller communities. For example, Health Canada estimates the burden of ambient air pollution to be 14,600 premature deaths per year (Health Canada 2019), a factor of almost two higher than the GBD estimate presented in Table 9.2 for Canada. The difference is driven by different data inputs and methods, including the choice of low-concentration cut-off; that is, the concentration below which health impacts are not calculated. That the GBD estimates lack specificity for small areas is particularly true for High-Arctic communities, where pollution levels are not well understood due to the lack of ground monitors and challenges associated with observing pollution columns from satellites over highly reflective surfaces, such as snow and ice. In addition, the health status of High-Arctic communities may differ from national averages. Therefore, the GBD estimates in Table 9.2 are provided for national-level information, but may not fully reflect the unique circumstances of individual cities and communities within these countries.

As part of NordicWelfAir, the health burdens of air pollution in the five Nordic countries were quantified and compared using three different health risk assessment tools (Lehtomäki et al., 2020). In terms of deaths attributable to ambient air pollution in 2015, estimates by the three tools ranged from 8500 to 11,400 for $PM_{2.5}$-related deaths, and from 230 to 260 deaths for O_3. A sensitivity analysis of the impacts of the spatial resolution of the exposure data underlined the importance of using high spatial resolution to avoid underestimating exposure and related health impacts.

9.2.2.2 How different emissions sources contribute to $PM_{2.5}$ disease burdens in Arctic Council Member states and Observer countries

Arctic air pollution comes from local sources within the Arctic, as well as distant sources located at lower latitudes, from where pollution gets transported through the atmosphere to the Arctic region (Mahmood et al., 2016; Monks et al., 2015; Schmale et al., 2018a; Stohl, 2006). Remote anthropogenic sources of near-surface air pollution in the Arctic are dominated by transport of emissions from northern Eurasia in winter and spring, including from the metallurgical industry, flaring to burn off gases in industrial plants, residential and traffic sources, and agricultural fires (Bourgeois and Bey, 2011; Law et al., 2014; Monks et al., 2015). Sources of $PM_{2.5}$ and its precursors that are local to the Arctic Council Member states include vehicle tailpipe emissions; residential combustion of wood, oil, coal, or natural gas; power generation from diesel, coal, or natural gas; industrial activities including oil and gas extraction, metal smelting, and mineral extraction; shipping; waste burning; and wildfires (Schmale et al., 2018a). Some sources, including vehicle tailpipe emissions, are common all over the world, while others, such as residential wood combustion (RWC), are more prevalent in Arctic communities and less extensive (although still present) at mid-latitudes. These sources have been discussed in detail in Chapter 2. Here, we briefly summarize several particularly relevant studies that have estimated the contribution of different local emissions sources to $PM_{2.5}$ in cities and countries within the Arctic Council Member states.

RWC is an important local contributor to $PM_{2.5}$ levels in many regions of the world, including the Arctic. A recent study that evaluated the contribution from RWC to urban air pollution across Denmark, Finland, Norway and Sweden found it accounted for up to 15–22% of the annual $PM_{2.5}$ level in Helsinki, Copenhagen and Umeå (Kukkonen et al., 2020). In central Oslo, the contributions from RWC exceeded 40%, due to wood stoves being used for heating in some larger apartment blocks. By contrast, in Helsinki and Copenhagen, the RWC fraction was highest in suburban areas on the outskirts of main city centers.

Shipping is another important source of air pollution in the Arctic, currently and also potentially in the future (Winther et al., 2014). Another Nordic study developed future scenarios for shipping emissions, and simulated the contribution from shipping to $PM_{2.5}$ concentrations and related health impacts across the Nordic region (Geels et al., 2021). Simulations with two chemical-transport models (DEHM and MATCH), showed that for current-day emissions (2015), up to 10–15% of the annual average $PM_{2.5}$ concentration in the Nordic area was attributable to shipping emissions, with some differences between the two models. Air pollution from shipping was estimated to have been associated with approximately 850 premature deaths (as a mean over the two models) in the Nordic region under the current-day conditions. The findings indicated that mortality would decrease to just under 600 cases in a 'business as usual' shipping scenario for 2050. Elevated O_3 pollution in marine areas around Norway has been shown to have contributions from local shipping (Marelle et al., 2016), and oil and gas extraction activities (Tuccella et al., 2017).

In addition to local emissions sources, pollutants outside of the Arctic region can have considerable impacts on Arctic air quality and health. For example, one modeling study found that 80% of the overall $PM_{2.5}$ concentration in Denmark, Finland, Norway and Sweden was linked to emissions sources outside the Nordic area in 2015 (Im et al., 2019). In Denmark, Finland and Norway, non-industrial combustion (including RWC) was the main sector contributing to the $PM_{2.5}$ levels. In Sweden, a similar share was linked to emissions from industry. Overall, OC was the main $PM_{2.5}$ component originating in-country. The same study estimated that approximately 11,000 premature

deaths per year could be linked to short-term exposure to O_3 and long-term exposure to $PM_{2.5}$ in the four Nordic countries and the Arctic. This estimate is roughly in agreement with GBD 2017 Risk Factor Collaborators (2018), as can be seen in Table 9.2.

9.2.2.3 The health benefits to Arctic communities of emissions reductions

Complementing work investigating disease burdens of air pollution, other studies have estimated the health benefits of emissions reductions – that is, the number of avoided cases of mortality and disease associated with lower air-pollution levels. In 2013, the joint report of the World Bank and International Cryosphere Climate Initiative, *On Thin Ice* estimated that approximately 47,800 air pollution-related premature deaths in the Arctic region could be avoided annually if mitigation measures were taken to reduce emissions of SLCFs (World Bank, 2013). The greatest anticipated health benefits among the Arctic population came from mitigation measures imposed on local sources, including biomass heating stoves and diesel transport. However, additional health benefits were also calculated for mitigation measures imposed on distant emissions sources due to reduced transport of pollution to the Arctic region.

9.3 Review of evidence of the impacts of air pollution on ecosystems and crops

As well as having negative consequences for public health, air pollution can damage ecosystems and reduce crop yields, potentially leading to dietary risks and impacts on livelihoods. This section reviews the current state of knowledge about air pollution's effects on ecosystems through eutrophication and acidification, as well as the effects of O_3 exposure on crop production. It is important to note that installing technologies aimed at controlling particular emissions can sometimes have unintended negative impacts on ecosystems. For example, open-loop scrubbers used to reduce sulfur oxide emissions from ships into the air can discharge zinc and copper to surface water (Turner et al., 2017). These effects have not been explored here, but should be considered when evaluating specific mitigation approaches.

9.3.1 Effects on ecosystems: deposition and critical loads

Problems associated with emissions of sulfur, NO_X and ammonia are related to eutrophication and acidification. Impacts of eutrophication in terrestrial ecosystems are associated with excess nitrogen leaching, and resulting changes to floristic composition and ecosystem function and stability. A critical load (CL) is defined as 'a quantitative estimate of an exposure to one or more pollutants below which significant harmful effects on specified sensitive elements of the environment do not occur according to present knowledge' (Nilsson and Grennfelt, 1988). CLs are deposition thresholds and are calculated for different receptors, such as a terrestrial or an aquatic ecosystem, with 'sensitive elements' referring to particular parts of the ecosystem; fine roots in forest soils or fish in a lake, for example. CLs were originally derived in the context of acidification, and provided limits for sulfur (S) and nitrogen (N) deposition – called CLs of acidity (CLaci). Limits for the eutrophying effect of N deposition were derived later – termed CLs for eutrophication (CLeutN or CL of nutrient N). Note that a CL depends on an ecosystem's properties, the local climate, and so on, and can thus take 'any' value. Accordingly, CLs are also influenced by climate change. In general, climate warming leads to a small increase in CL, except in mountainous and arid regions; for details see Posch (2002).

CLs for the acidifying and eutrophying effects of sulfur and nitrogen deposition that individual countries have determined have been collected under the Convention on Long-range Transboundary Air Pollution (LRTAP), hosted by the United Nations Economic Commission for Europe, and used to support European assessments and negotiations on emissions reductions (De Vries et al., 2015; EEA, 2014; Maas and Grennfelt, 2016; Reis et al., 2012). CL assessments were included in earlier AMAP reports, first appearing in Chapter 9 of AMAP (1998), in which terrestrial CLs of acidity for the Eurasian part of the (sub-)Arctic zone, and CLs for surface waters for the European section of the zone, as well as their exceedances, were computed and mapped (Kämäri and Joki-Heiskala, 1998). In Chapter 5 of AMAP (2006) – on terrestrial ecosystems – Derome et al. (2006) reported CLs and exceedances for northern Europe and Canada. Meanwhile, in Chapter 6 – on freshwater ecosystems – Skjelkvåle et al. (2006) reported CLs and their exceedances for surface waters in northern Fennoscandia. The first comprehensive study on CLs of acidity and their exceedances for the whole (sub-)Arctic region was carried out by Forsius et al. (2010). More recently, CLs for acidity and eutrophication and their exceedances for terrestrial ecosystems in the Northern Hemisphere (>30°N) were presented by Reinds et al. (2015). And, CLs of acidity and their exceedances for more than 1100 lakes and ponds in the Canadian Arctic were recently computed by Liang and Aherne (2019). Overall, exceedances of CLs occur mostly in Fennoscandia and some hotspots in Russia, and they have gone down in most places in recent decades.

The amount of S and N deposited in the Arctic is small compared to polluted regions, based on both observational data (AMAP, 2006; Hole et al., 2009; Vet et al., 2014) and model simulations (Tan et al., 2018; Vet et al., 2014). Deposition is largely caused by long-range transport, but is also due to anthropogenic emissions within the Arctic region. Notably, the contribution of international shipping has been increasing as melting sea ice has opened the Arctic up to navigation. According to an article in *National Geographic* magazine (Champine et al., 2019), in 2018, the number of vessels crossing waters governed by the International Polar Code – a set of strict safety and environmental rules – was nearly 60% higher than in 2012. All in all, the Arctic region is characterized by relatively large deposition-to-emission ratios for both S and N, making it a net receiver of acidifying and eutrophying pollution.

Despite the relatively dry Arctic climate, most of the total deposition of S and N in the Arctic region is due to wet deposition – by rain, snow, sleet or fog – (Tan et al., 2018; Vet et al., 2014). This is because a large portion of gaseous pollutant species

is efficiently dry-deposited much closer to the source areas, while sulfate, nitrate and ammonium aerosols are deposited more slowly and can be transported over longer distances. The exception could be areas close to international shipping lines and local land-based emissions sources. This is consistent with earlier findings (AMAP, 2006) indicating that, although air pollution in the Arctic is generally higher in winter, deposition may be highly episodic. For example, a study by Kühnel et al. (2011) based on 20-year measurements from Ny-Ålesund, Svalbard, Norway, revealed that a few precipitation events strongly influence the annual load of NO_3 and ammonium ions (NH_4). A future increase in precipitation due to climate change (Bintanja et al., 2020) would result in increasing wet deposition in the Arctic in both summer and winter.

Meanwhile, Björkman et al. (2013) found that, for the winter season (September 2009 to May 2010) in Ny-Ålesund, nitrate dry deposition accounted for, on average, 14% of the total oxidized nitrate deposition, with a range of 2–44%. Dry deposition events were associated with elevated atmospheric concentrations, corroborating previous studies that identified episodes of rapid pollution transport to and deposition in the Arctic.

The share of nitrogen that is reduced (NH_X = ammonia [NH_3] + ammonium [NH_4]) is growing in many regions of the world (Kurzyca and Frankowski, 2017). This is as a consequence of larger reductions in NO_X emissions compared to NH_3 emissions. However, deposition in the Arctic of total nitrogen – in other words, the sum of reduced [NH_X] nitrogen and oxidized [NO_y] nitrogen (excluding N_2O) – is dominated by oxidized nitrogen. A multi-model global study by Tan et al. (2018) showed moderate contributions of reduced nitrogen to total nitrogen deposition in most of the Arctic region in 2010. However, the study showed that the fraction of NH_X deposition increased from 30–40% to 50% in Alaska and by 5% in Northern Europe from 2000 to 2010. According to EMEP MSC-W model simulations for this report, the fraction of NH_X within total nitrogen deposition varies between 25–40% across the Arctic region, reaching 50–55% in small regions of Alaska, northern Canada and northeastern Russia. Biodiversity loss linked to rising nitrogen deposition has been broadly discussed in the literature, with reduced nitrogen inputs appearing more likely to decrease biodiversity than oxidized nitrogen deposition (Erisman et al., 2007 and references therein). And, van den Berg et al. (2008) pointed out that elevated NH_4/NO_3 ratios might be a strong determining factor in vegetation composition.

Dry deposition uptake of surface-level O_3 by vegetation has been shown to be an important O_3 sink over Siberia, with suppressed O_3 concentrations observed in Arctic air masses that have undergone transport across areas of extensive vegetation (Engvall Stjernberg et al., 2012; Hirdman et al., 2010). Recent results from regional model simulations over Western Siberia suggest that forest and tundra vegetation represent approximately equal surface O_3 sinks north of 60°N in spring and summer, and dominate the O_3 dry-deposition loss (Thorp et al., 2021).

9.3.2 Impacts on crops

There is evidence of widespread adverse effects of ground-level O_3 on crops and (semi-)natural vegetation (Hayes et al., 2007; Mills et al., 2011). Experimental exposure studies have shown that crops and (semi-)natural vegetation could be damaged by: reduced growth and seed production (e.g. Booker et al., 2009; Hayes et al., 2007; Mills et al., 2007); premature senescence (e.g. Tonneijck et al., 2004); and reduced ability to over-winter (e.g. Hayes et al., 2006) and withstand stresses, such as drought (e.g. Wilkinson and Davies, 2009). In many cases, an increased protein concentration was observed, while protein yield was reduced (Feng et al., 2008; Feng and Kobayashi, 2009; Grünhage et al., 2012).

Ozone is deposited from the atmosphere onto plant canopies by diffusion, and enters leaves through their stomata. Environmental, biological, and agricultural (e.g., irrigation) factors that promote stomatal opening increase the risk of injury to plants from O_3. State-of-the-art modeling of ozone damage to vegetation is moving towards a flux-based approach that can take into account environmental factors on stomatal uptake of O_3 (Emberson et al., 2018). However, because of the complexity of this approach, most risk assessments of ozone damage use methods that combine modeled O_3 concentration (rather than stomatal flux) with crop distribution and production data, using empirically derived statistical relationships between crop yield and O_3 concentration or exposure. Ozone exposure is often estimated using 'accumulated ozone exposure over a threshold of 40 ppb' (AOT40) or the seasonal mean daytime ozone concentration (M7 or M12, for a 7-hour or 12-hour daytime period, respectively).

Global yield losses due to present-day O_3 are estimated at 2%–16% for wheat, rice, maize and soybean (Avnery et al., 2011; Van Dingenen et al., 2009). These yield losses lead to global economic damages in the order of USD10–40 billion per year (Avnery et al., 2011; Sampedro et al., 2020).

As with O_3, $PM_{2.5}$ could have direct and indirect effects on crop growth; however the effects of particulate matter on crops are more uncertain than for ozone. The direct effect of $PM_{2.5}$ is to impede respiration and affect leaf temperature, as the particulate matter accumulates on the leaf surface (Hirano et al., 1995). This influences crop yields. Indirectly, $PM_{2.5}$ can affect the natural climatic conditions around crops, for example by absorbing and scattering solar radiation. In this way, $PM_{2.5}$ may reduce the solar radiation available to plants (Liu et al., 2016b), thereby reducing photosynthesis and limiting plant growth (Chameides et al., 1999).

BC aerosols can also reduce agricultural productivity through their impacts on temperature and precipitation (Burney and Ramanathan, 2014). Shindell (2016) modeled the impact on crops of temperature changes due to various pollutants, and found that at the global level, while BC caused substantial damage, this was largely offset by cooling from co-emitted OC. Schiferl and Heald (2018) examined the positive effects on agricultural yield of increased diffusion of light due to particulate matter. They found that these effects offset the negative impact of reduced direct light caused by the particles, and that – under some assumptions and in some regions – these positive influences also offset much of the damage from O_3.

The staple crops considered here are not of major importance to overall agricultural production in the Arctic. However, there may be specific Arctic conditions – for example, permanent

daylight, intrusion of stratospheric O_3 into the troposphere, long-range transport of pollutants from Asia, and off-shore oil production – that could cause O_3-related damage to ecosystems such as boreal forest and grasslands, as well as Arctic agro-crops and fuel woods. These types of impacts are not considered in the present study and, to our best knowledge, no or limited research has been undertaken on these issues. In future, rapid climate change in the Arctic region is likely to push the thermal boundaries that currently limit crop production to higher latitudes, opening up the Arctic region for new agricultural practices. This possible shift in crop production areas in future scenarios is not included in this assessment.

9.4 Modeled impacts of SLCF emissions changes on health, ecosystems and crops in Arctic Council Member states and Observer countries

This section describes new quantitative analysis of the impacts on health, ecosystems, and agriculture of air-pollution changes from modeled SLCF emissions scenarios. Air-pollution impacts were estimated by combining $PM_{2.5}$ and O_3 concentration changes simulated from the multiple chemical transport and general circulation models described in earlier chapters, with concentration-response functions for health and ecosystems, as well as agricultural outcomes, from the peer-reviewed literature. For consistency, impacts were only assessed for the emissions scenarios that were simulated by the largest ensemble of models – the Current Legislation (CLE) and the Maximum Feasible Reduction (MFR) scenarios.

9.4.1 Impacts on health

This section describes premature mortality attributable to $PM_{2.5}$ and O_3 from current exposure levels, and reductions that may be achieved through the CLE and MFR emissions scenarios. $PM_{2.5}$ and O_3 concentrations were derived from the suite of models described in Chapters 7 and 8. The spatial resolution of these models ranges from about 0.14°(GEM-MACH) to about 2.8° (CanAM5-PAM). For $PM_{2.5}$, annual averages were used to estimate health impacts. For ozone, the 'sum of ozone means over 35 ppb' (SOMO35) was used, which is a measure of accumulated annual O_3 concentrations used as an indicator of health hazards (e.g. WHO, 2008). For each day, the maximum of the running eight-hours average for O_3 was selected and the values >35ppb summed over the whole year. While these models capture to a large extent the overall exposures in Arctic Council Member states and Observer countries, the relatively coarse resolution does not allow for local-level estimations of impacts.

As the spatial resolution of the models differed, we re-gridded the model outputs to a common grid at 0.5° x 0.5° (latitude/longitude) resolution (approximately 50 km x 50 km at the equator and 25 km x 50 km at 60° north). This resolution is not sufficient to fully resolve high concentrations in urban regions, likely leading to underestimates of mortality attributable to $PM_{2.5}$. The underestimation is likely attenuated for air pollution-related health impacts in the Arctic from emissions released in other parts of the world, as long-range transported pollution is more spatially homogeneous. For $PM_{2.5}$, modeled concentrations were spatially reallocated to a grid with a 0.5° x 0.5° (latitude/longitude) resolution, using a satellite-derived $PM_{2.5}$ concentration dataset (van Donkelaar et al., 2015a, 2015b), as described and evaluated in Chapter 7.3.5.2. For O_3, modeled concentrations were bilinearly remapped to 0.5° x 0.5° (latitude/longitude) resolution to provide model data on a uniform grid; however such remapping does not provide information in addition to that obtained from the original source grid. Urban centers have been shown to have lower O_3 concentrations than coarse-resolution models can capture. Combined with the surface O_3 overestimate shown in Chapter 7.3.1, it is possible that O_3-attributable deaths based on modeled SOMO35 could be overestimated. However, this potential overestimation is likely counterbalanced by potential underestimation introduced by only including COPD mortality, and excluding other health outcomes associated with O_3 exposure.

To estimate long-term $PM_{2.5}$ and O_3-attributable health impacts, we used a set of existing health impact assessment tools that have been previously applied in multiple contexts:

- *The Economic Valuation of Air Pollution (EVA) system* (Brandt et al., 2013a, 2013b; Geels et al., 2015; Im et al., 2018, 2019) is based on the impact-pathway chain method (Friedrich and Bickel, 2001). With recent developments, EVAv6 can calculate all-cause acute and chronic mortality and morbidity based on linear risk ratios, along with cause-specific mortality based on non-linear functions following Burnett et al. (2018).
- *The ISTE tool* (Lehtomäki et al. 2018, 2020), developed at the Finnish Institute for Health and Welfare (THL), has an extensive collection of available concentration-response functions and is linked to baseline burden-of-disease data from WHO. The tool allows for probabilistic modeling of exposure variability, and calculates uncertainties using the 95% confidence interval (CI) for concentration-response functions and standard error for exposure when these are available.
- *The TM5-Fast Scenario Screening Tool (TM5-FASST)* (Van Dingenen et al., 2018) is a global reduced-form air quality source-receptor model that has been designed to compute: ambient pollutant concentrations; a broad range of pollutant-related impacts on human health and agricultural crop production; and short-lived pollutant climate metrics – based on input annual pollutant emissions data aggregated at the national or regional level.

A range of concentration-response functions are used across the different health impact assessment models to calculate mortality and morbidity end-points. For mortality, non-linear concentration-mortality relationships – based on many epidemiology studies from countries around the world – are used to estimate cause-specific mortality due to O_3 and $PM_{2.5}$. These include functions derived from the Integrated Exposure Response (IER) model (Burnett et al., 2014), which integrates studies globally for a wide range of exposures that include household air pollution and smoking, and more recent updates from the Global Exposure Mortality Model (GEMM) (Burnett et al., 2018). These functions consider cause-specific mortality due to exposure to ambient $PM_{2.5}$ for

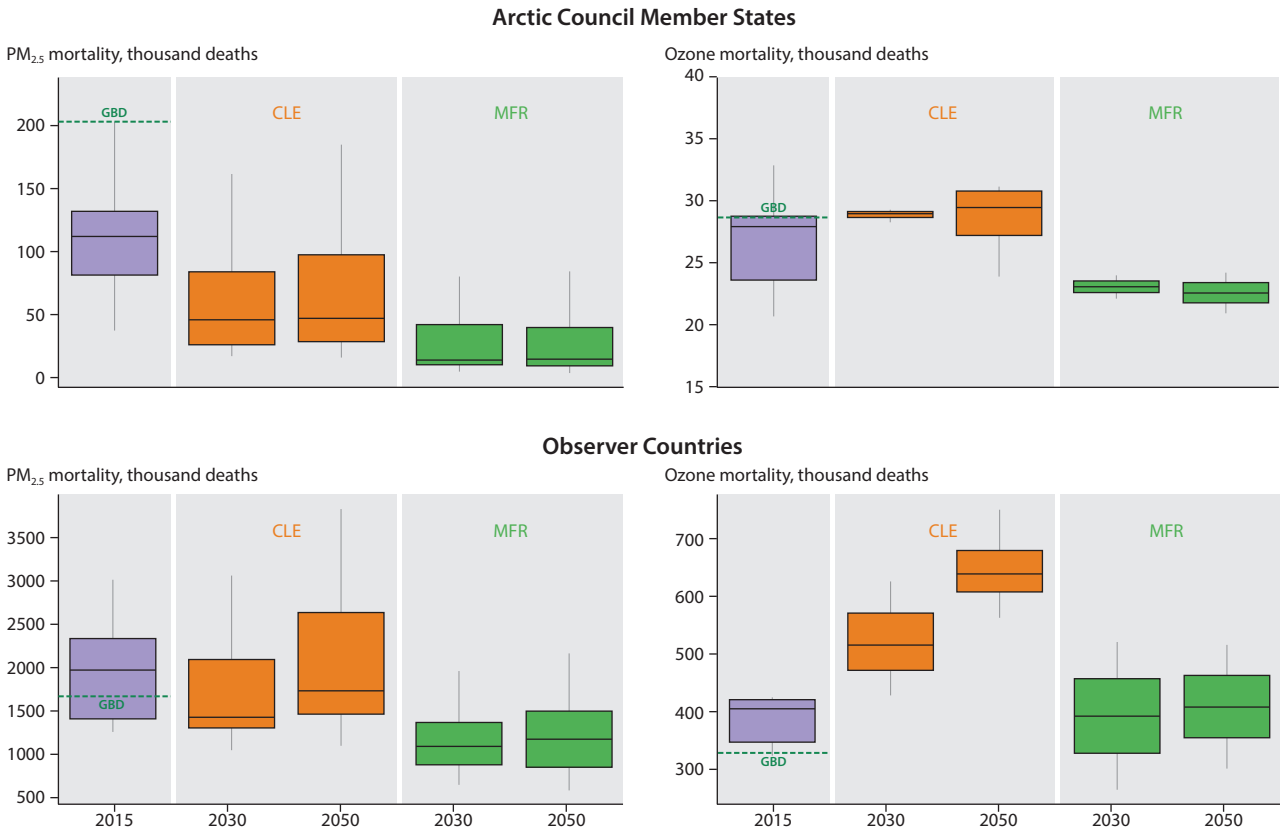

Figure 9.1. Mortality from EVA, ISTE and TM5-FASST models due to $PM_{2.5}$ (left) and O_3 (right) in Arctic Council Member states and Observer countries in 2015, and in 2030 and 2050 under the CLE and MFR scenarios, respectively. Confidence intervals account for variability across modeled concentrations and health impact assessment methods. Intervals depicted by gray horizonal lines represent the interquartile range (IQR), while the gray vertical lines represent the maximum range up to ±1.5 IQR. The green dotted lines display mortality estimates from GBD 2017 Risk factor Collaborators (2018), for comparison.

LC, COPD, cerebrovascular disease (CEV), IHD and LRI. The functions have further been sampled in Lelieveld et al. (2019) for European cohorts, and these updated versions are used in the EVA model. The EVA model also calculates different morbidity end-points (bronchitis, asthmatic children and LC) using linear concentration-response relationships derived from Héroux et al. (2015) and WHO (2013a). We used these functions in all countries in our analysis to be globally consistent and because they incorporate studies from all Arctic Council countries where available. Further information on the health-impact models and input data are provided in Appendix 9.

When considering future scenarios, population growth, ageing, and mortality rates contribute to the overall change in attributable mortality, in addition to pollutant concentration changes. Baseline mortality and morbidity data across the models were drawn from a number of sources including WHO (Data ref. 9.1), with projections of future mortality rates from the IHME Forecasting Model (Foreman et al., 2018). Population projections were derived using Shared Socioeconomic Pathways (SSPs) (Samir and Lutz, 2017); specifically the SSP2 scenario denoting a 'middle of the road' pathway in which social, economic and technological trends do not shift markedly from historical patterns. The EVA modeling further used global population density data, at a 2.5-minute spatial resolution (about 4.5 km at the equator), from the Socioeconomic Data and Applications Center (SEDAC) (Data ref. 9.2).

For 2015, the modeling results indicate that there were around 2.5 million–3.8 million deaths globally due to exposure to $PM_{2.5}$ and 425,000–530,000 due to exposure to O_3 (the range reflects different model estimates of concentrations and differences in health-impact modeling methods). These estimates correspond well to a central GBD estimate of 2.9 million $PM_{2.5}$ deaths for the same year and 472,000 O_3 deaths. More than 75% of these deaths are estimated to have occurred in Arctic Council Observer countries. Note, the regional definitions for Arctic Council Member states and Observer countries used here are the same as in Chapter 2, and we do not assume any changes in these categorizations over time.

The simulated $PM_{2.5}$ and O_3 concentration ranges across the air-quality models are an important factor in explaining the large range in the mortality estimates (see Chapter 7 for inter-model comparisons of concentrations). The concentration-response functions also contribute significantly. For example, the attributable number of deaths due to $PM_{2.5}$ exposure using the GEMM functions was about twice that predicted by the IER. This is in part because the GEMM model is based on all natural-cause mortality, while the IER approach is limited to six causes of death, and in part because the IER incorporates additional types of exposure, such as active smoking, that have lower relative risks per unit $PM_{2.5}$ than ambient air pollution (more details on different concentration-response functions are given in Appendix 9). As discussed earlier, the spatial resolution of models is also an important factor when estimating population exposures and impacts, particularly for $PM_{2.5}$. Although some of the models used to provide concentration estimates employ grids with spatial resolutions that are coarser than the areas of smaller

Nordic countries, the downscaling method described in Chapter 7 provided additional spatial detail that could not be resolved by the models directly.

The results of the scenario modeling show CLE leading to 24% fewer $PM_{2.5}$ deaths globally in 2030 and 4.5% fewer in 2050 compared with 2015. CLE also leads to substantial declines in $PM_{2.5}$-attributable mortality in Arctic Council Member states in 2030 (-59%; 66,000 fewer deaths) and 2050 (-57%; 64,000 fewer deaths) compared to 2015 (Figure 9.1). The MFR scenario results in a greater decline in $PM_{2.5}$ mortality in comparison to the CLE one (approximately -87% or 97,000 fewer deaths in 2030 and 2050).

For Arctic Council Observer countries, while declines in $PM_{2.5}$ mortality occur in 2030 compared to 2015, for both policy scenarios, $PM_{2.5}$ mortality increases in 2050 compared to 2030 (from -28% or 540,000 fewer deaths in 2030 to -12% or 235,000 fewer deaths in 2050 for the CLE scenario, and from -45% or 880,000 fewer deaths to -40% or 790,000 fewer deaths for MFR, compared to 2015 estimates). While emissions and exposures continue to decline in 2050 under these scenarios, the increases in $PM_{2.5}$ mortality can be attributed to large increases in populations at risk. For example, the population over 70 years of age increases by 140% in Arctic Council Member countries and by more than 260% in Observer countries, compared to 2010 (Data ref. 9.3). $PM_{2.5}$ mortality changes under CLE and MFR differ between Arctic Council Member states and Observer countries (Figure 9.2).

In terms of impacts on O_3 mortality, the modeling scenarios indicate that global O_3 mortality could increase by 17% in 2030 and by almost 60% in 2050 compared with 2015, due to steady O_3 concentrations but growing exposed populations. In the CLE scenario, O_3-related mortality increases slightly compared to 2015 in the Arctic Council Member states in both 2030 and 2050 (16% increment; around 4,000 more deaths), as shown in Figure 9.1. In Observer countries, there is a sustained increase in O_3-based mortality between 2015 and 2030 (23%; 95,000 more deaths) and also from 2030 to 2050 compared to 2015 (54%; 220,000 more deaths), according to the CLE scenario. In addition to the above-mentioned increases in populations at risk, these results can be explained by a rise in exposure, as exemplified by population-weighted O_3 concentrations in the 2030–2050 period. This is consistent with the estimated increase in population-weighted SOMO35 concentrations within Asian Observer countries under the CLE scenario (Chapter 8). The large population in Asia, combined with the projected O_3 increase there, could outweigh the health benefits gained from reductions in O_3 everywhere else. Similarly, under the MFR scenario, a small decrease in O_3 mortality is predicted for the Observer countries (-10%; 40,000 fewer deaths) in 2030 but this is totally outweighed by the subsequent rise from 2030 to 2050. In the Arctic Council Member states, mortality from O_3 decreases in both 2030 and 2050 under the MFR scenario, with a larger drop during the first period (-20% or 5700 fewer deaths in 2030 and -24% or 6900 fewer deaths in 2050 compared to 2015). The increase observed in O_3-attributable mortality under CLE for 2030 is not seen for $PM_{2.5}$-attributable mortality, because the large reductions in $PM_{2.5}$ concentrations counteract the rise in the population at risk.

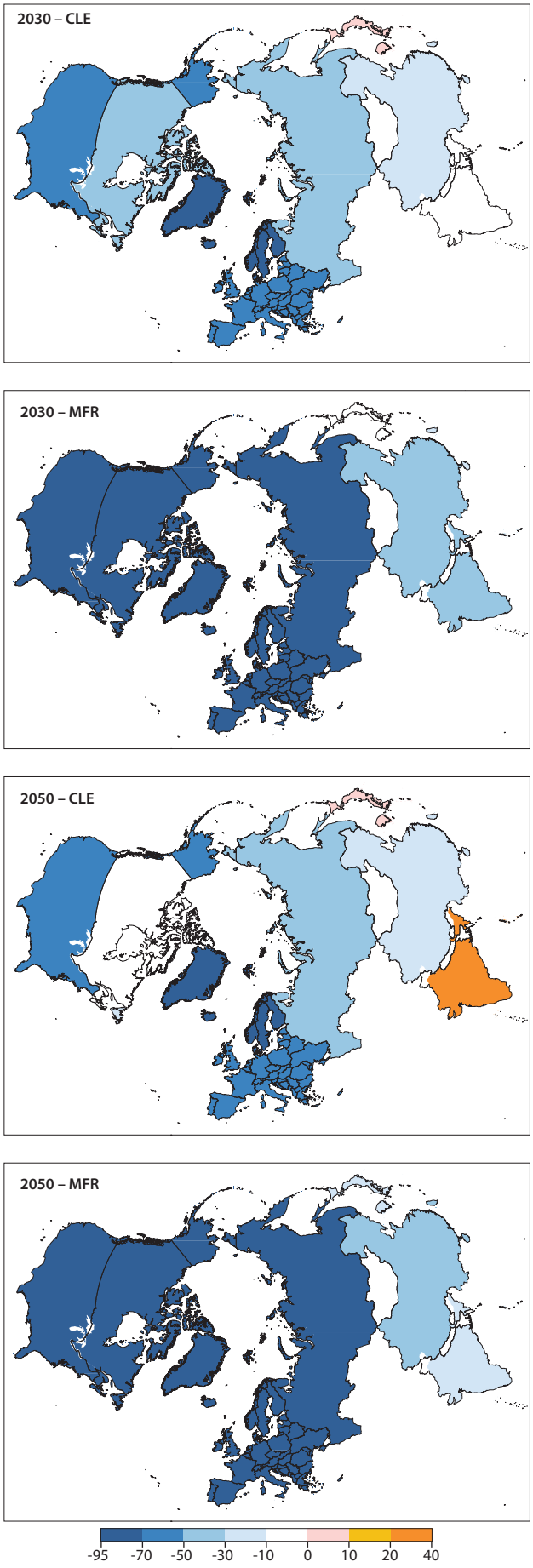

Figure 9.2. Changes in $PM_{2.5}$ mortality (average across chemical transport and health impact assessment models) in Arctic Council Member states and Observer countries by 2030 and 2050, under the CLE and MFR scenarios, compared to 2015.

As previously stated, some studies have indicated that traffic-related air pollution, such as BC and other pollutants from vehicle tailpipe emissions, leads to elevated risk beyond that associated with total $PM_{2.5}$ mass. For example, a recent meta-analysis found that the pooled estimates of relative risk (RR) per 1 μg/m^3 for all-cause mortality related to long-term exposure to $PM_{2.5}$ and BC are 1.007 and 1.06, respectively, suggesting that the concentration-response coefficient for BC could be up to 10 times larger than that for $PM_{2.5}$ (Janssen et al., 2011). However, comparing health impacts associated with BC to those associated with $PM_{2.5}$ mass requires careful consideration of the type of source (most notably, traffic versus other sources of fuel combustion). A more recent review of the epidemiological literature found that BC is consistently associated with cardiovascular morbidity and mortality, but that the current literature is not sufficient to conclude that BC is independently associated with these effects rather than being just an indicator for PM mass (Luben et al., 2017). Therefore, current evidence does not indicate that BC is a better predictor of mortality than $PM_{2.5}$ mass. The results presented above are of estimated $PM_{2.5}$-attributable mortality, driven by the emissions changes in BC and other co-emitted primary $PM_{2.5}$ and precursors to secondary aerosols. For this reason, the contribution of BC to the health impacts reported above should be considered as a subset of, rather than additional to, the estimated $PM_{2.5}$-attributable deaths.

If BC is more harmful to human health in comparison to other $PM_{2.5}$ components, as some studies have shown (e.g. Janssen et al., 2011; WHO, 2012), applying concentration-response functions that represent risk from exposure to the general $PM_{2.5}$ mixture may underestimate the health benefits of reducing SLCF emissions. We therefore conducted a sensitivity analysis to estimate impacts of the changes in concentrations of BC from the emissions scenarios on premature mortality (Figure 9.3) using $PM_{2.5}$- and BC-specific concentration-response functions, and simulated BC concentrations under the emissions scenarios. BC concentrations are from the emulator simulations with regionally perturbed emissions for 2015 in climate chemistry models (CCMs, described in Chapter 8). The simulated concentration response to emissions perturbations is scaled linearly by time-evolving emissions to estimate concentrations for future years. The emulator is based on results from three CCMs (CanAM5-PAM, UKESM1, and MRI-ESM2). To ascertain the influence of the choice in concentration-response factor on estimated BC-attributable mortality, we compared the mortality estimates calculated based on different RR functions. These approaches provide bounds for our understanding of the impacts on mortality of changes in BC concentrations, with the $PM_{2.5}$ RR estimates from the GBD 2017 Risk Factor Collaborators (2018) study as a lower estimate and the BC-specific RR estimate from Janssen et al. (2011) as an upper estimate. The results showed a different pattern to that of Figure 9.1 because of the variation in assumed health outcomes and mortality rates (only selected causes of mortality in Figure 9.1 and all-cause mortality in Figure 9.3, for example). Therefore, these results should only be used to compare the application of different RR estimates within Figure 9.3.

We see that despite stringent air-pollution control policies under the MFR scenario, the BC fraction remains significant. The high share of BC combined with high RRs and increasing population could imply there would be continued health impacts related to exposure to SLCFs, and air pollution more broadly, in both Arctic Council Member states and Observer countries. This indicates that there is a need to evaluate current policies on air pollution in these regions, and to include more targeted interventions to reduce the burden of disease associated with BC emissions.

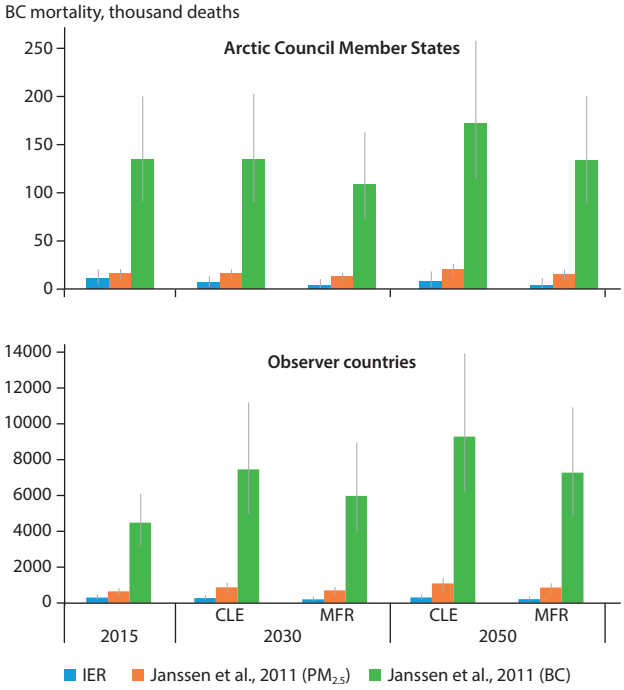

Figure 9.3. Estimated BC-related mortality for 2015, 2030 and 2050 (based on BC concentrations from the emulator simulations of three models). The blue bar (Integrated Exposure Response, IER) applies the share of BC in $PM_{2.5}$ concentrations to the mortality estimates shown in Figure 9.1. The orange and green bars indicate mortality estimated using the BC concentrations from the emulator, all-cause mortality rates from WHO (Data ref. 9.4), and linear relative risk (RR) functions for $PM_{2.5}$ and BC from Janssen et al. (2011). The confidence intervals (95% – represented by the gray vertical lines) account for the range in the parameters of the RRs. Note that different RRs, health outcomes and disease rates are used compared to those yielding the results shown in Figure 9.1, precluding comparisons to be made between the two figures.

9.4.2 Sulfur and nitrogen deposition and critical loads

This section describes how S and N deposition, critical-load exceedances, and crop yields vary for the years 2015, 2030 and 2050 under the SLCF emissions scenarios.

We used the results from the EMEP MSC-W model simulations (Section 7.2) to assess past trends in, and future scenarios of, ecosystem damage by acidifying and eutrophying depositions on terrestrial ecosystems. The CL for a site (either for acidification [CLaci] or eutrophication [CLeutN]) is derived from (simple) steady-state charge and mass balance equations, linking the chosen chemical criterion – such as an acceptable pH or N concentration in soil solution that should not be exceeded – with the corresponding deposition value(s). The chemical criterion, in turn, is linked (by observations and experiments) to the 'harmful effect' to be avoided. The CLaci for a site is not unique, since different combinations of N and S depositions (N_{dep} and S_{dep}) can lead to the same soil chemical values (e.g. pH). Thus, CLs of acidity are characterized by a so-called critical load function (CLF), which consists of all pairs of N_{dep} and S_{dep} that fulfil the chemical criterion, and which, in general, has a trapezoidal shape

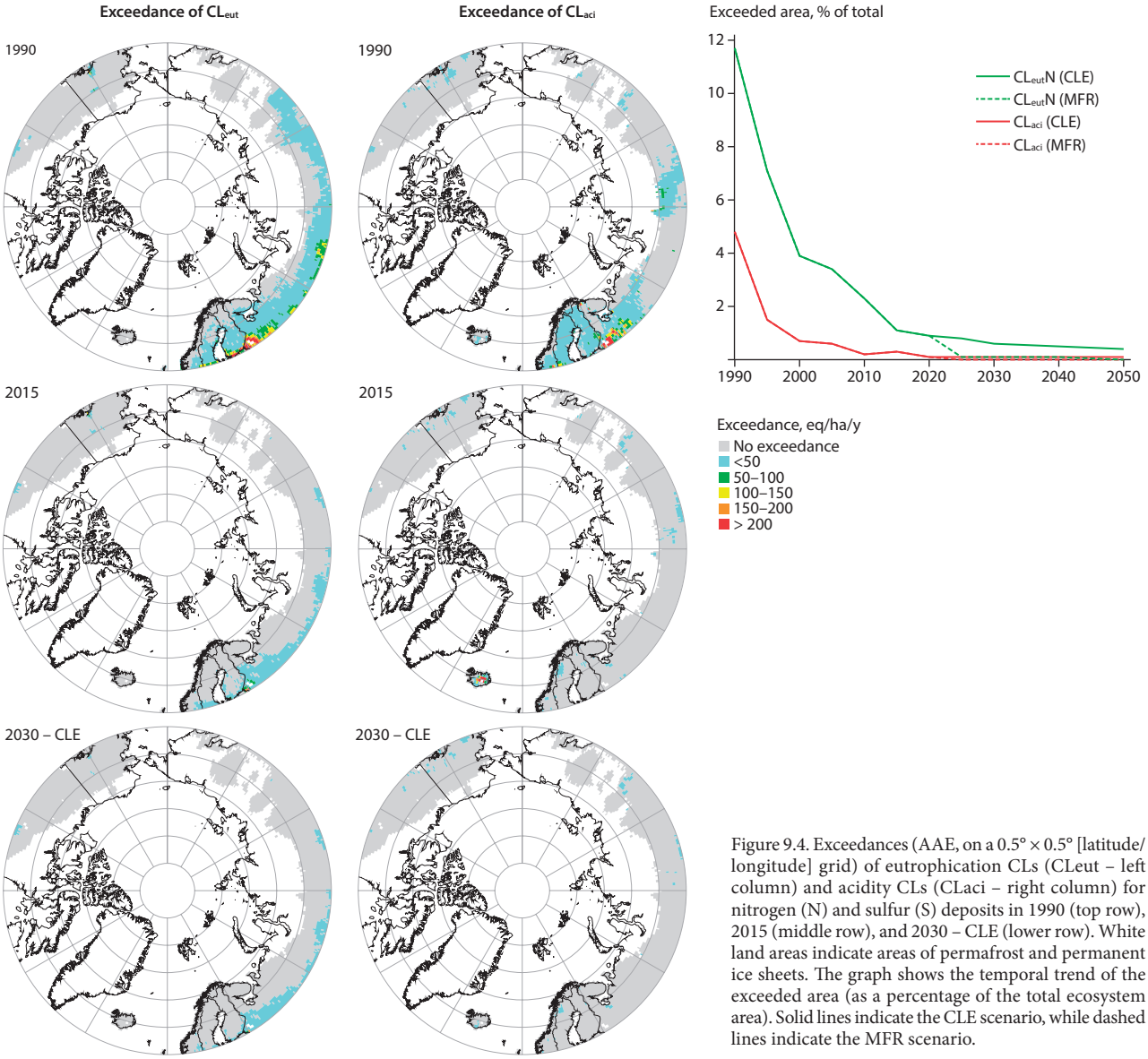

Figure 9.4. Exceedances (AAE, on a 0.5° × 0.5° [latitude/longitude] grid) of eutrophication CLs (CLeut – left column) and acidity CLs (CLaci – right column) for nitrogen (N) and sulfur (S) deposits in 1990 (top row), 2015 (middle row), and 2030 – CLE (lower row). White land areas indicate areas of permafrost and permanent ice sheets. The graph shows the temporal trend of the exceeded area (as a percentage of the total ecosystem area). Solid lines indicate the CLE scenario, while dashed lines indicate the MFR scenario.

in the (N_{dep}, S_{dep})-plane. In contrast, the CLeutN for a site is a single number. Methods to compute CLs are summarized in Posch et al. (2015). In contrast to depositions, a CL for a site is an ecosystem property and is treated as constant over time.

If the figure for deposition at a site is higher than for the CL, the CL is said to be exceeded. For acidity, the exceedance is a well-defined distance measure from the CLF. For CLeutN, the exceedance is defined as the difference between N_{dep} and CLeutN (set to zero if negative). To obtain a single exceedance number for a grid cell (or any other region) the so-called average accumulated exceedance (AAE) is used, defined as the weighted mean of the exceedances of all ecosystems within the grid cell, with the weights being the respective ecosystem areas (Posch et al., 2015).

Critical loads for acidity and eutrophication and their exceedances for terrestrial ecosystems in the Northern Hemisphere (>30°N) have been presented in Reinds et al. (2015); the CL database derived there was also used in this study. In both Reinds et al. (2015) and our assessment, global databases on soils, land cover and forest growth were overlain, with the intersection of those yielding about 1.43 million unique forest and (semi-)natural ecosystem sites, covering about 5.6 million km^2 in the (sub-)Arctic area, here defined as all land areas north of 60°N. Areas of shallow permafrost, defined as areas in which the mean monthly temperature is below zero for eight or more months, were excluded. Further databases on base cation deposition and climatic characteristics (temperature, precipitation and sunshine) were used to obtain the variables – such as soil-water percolation, via a simple hydrological model – needed to compute the CLs for all the sites. The CLs were generated using the simple mass balance (SMB) model, linking the chemical criterion to N and S depositions. For eutrophication CLs, ecosystem-dependent critical limits of N concentrations in the soil solution were used, whereas for acidity CLs, the widely used molar-aluminium-to-base-cation ratio (Al/Bc ratio) in the soil solution was applied. All the databases and methods used in this study are documented in Reinds et al. (2015) and the literature cited therein, and are presented there with maps showing the obtained CLs.

Figure 9.4 illustrates the development, over time, of the CL-exceeded area in the Arctic region. Acidity CLs were exceeded in 4.8% of the area in 1990, 0.7% in 2000 and 0.1% in 2020. In 1990,

CLeutN was exceeded in 11.7% of the area; this dropped quickly to 3.9% in 2000, and finally dropped below 1% after 2020. The exceeded area under the MFR scenario is close to zero in all cases.

The results indicate that CLs for the American Arctic were hardly exceeded, even in 1990, whereas those for the Eurasian part were exceeded, with maxima in Fennoscandia and westernmost Russia. By 2010, most of the exceedances had disappeared and the magnitude (the AAE) had fallen below 50 equivalents per hectare per year (eq/ha/y). It can be concluded that the area in which acidity and eutrophication CLs are exceeded will drop below 1% in the (sub-)Arctic region, and the remaining exceedance amounts within the region will drop to quite low values. Emissions-reduction policies of the last three decades are likely to have contributed to this trend.

9.4.3 Crop losses

Crop exposure and impacts were evaluated using the TM5-FASST tool, employing the methodology described in detail by Van Dingenen et al. (2009, 2018). This analysis focused on the key global staple crops of rice, maize, wheat and soybean. While other types of vegetation – including berries, lichens, fungi and fuelwood – are often consumed or used by people in the Arctic, these have not been included in the quantitative analysis due to lack of available exposure-response relationships.

Briefly, crop-production losses (CPL) were calculated using the equation:

$$CPL = RYL/(1- RYL) * CP$$

where CP is the 'actual' crop production and the relative yield losses (RYL) are calculated from exposure-response functions provided in the literature, as a function of the crop exposure metric. Of the four crops considered, soybean has the highest sensitivity to damage from O_3.

Available crop-O_3 exposure metrics, for which exposure-response functions were available from the literature (Mills et al., 2007; Wang and Mauzerall, 2004), were three-monthly AOT40 and seasonal mean daytime O_3 concentration (Mi – with M7 representing the 7-hour [09:00–15:59 LT] mean and M12 the 12-hour [08:00–19:59 LT] mean). AOT40 and Mi were evaluated over the three months, centred on the midpoint of the location-dependent crop growing season provided by the Global Agro-Ecological Zones (GAEZ) 2012 dataset (Data ref. 9.5). Note that in the GAEZ methodology, the theoretical growing season is determined based on prevailing temperatures and water-balance calculations for a reference crop, and can range between 0 and 365 days; however, for this analysis, three months was adopted as the standard metric accumulation or averaging period. The use of a standard three-month growing season may overestimate the exposure time of crops in high-latitude regions where the growing season is shorter but concurring low O_3 concentrations outside of the growing season mean this is not expected to overestimate the crops' exposure to O_3.

Crop distributions for evaluating the O_3 exposure (Figure 9.5) were taken from the GAEZ year 2000 dataset (Data ref. 9.6). Actual crop production losses for 2015, 2030 and 2050 were adjusted from the Food and Agriculture Organization (FAO) of the United Nations' FAOSTAT dataset of countries' crop production for the year 2000 (Data ref. 9.7)

For 2015, estimated relative yield losses are highest in Canada (14%), India (14%), Europe (13%), and the USA (12%). In terms

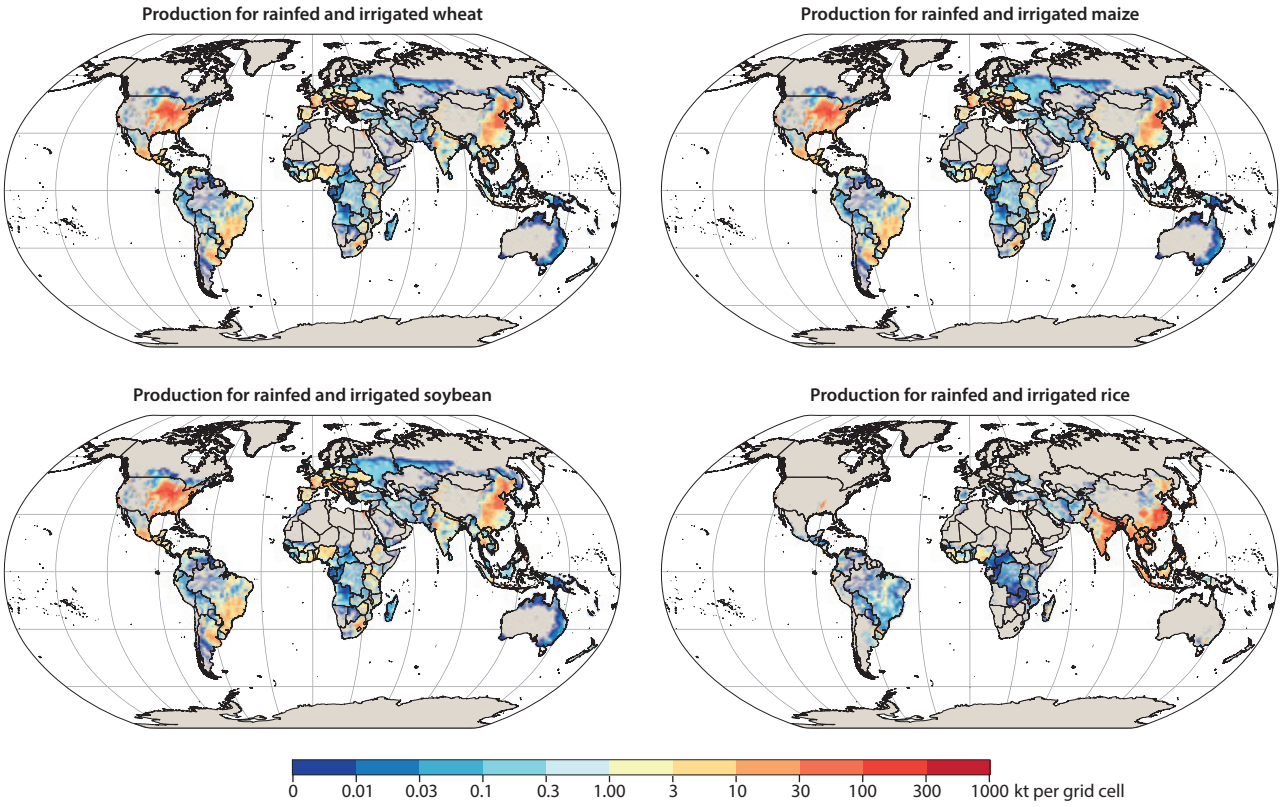

Figure 9.5. Global distribution of crop production (kt) per grid cell for the year 2000. Source: Data ref. 9.6.

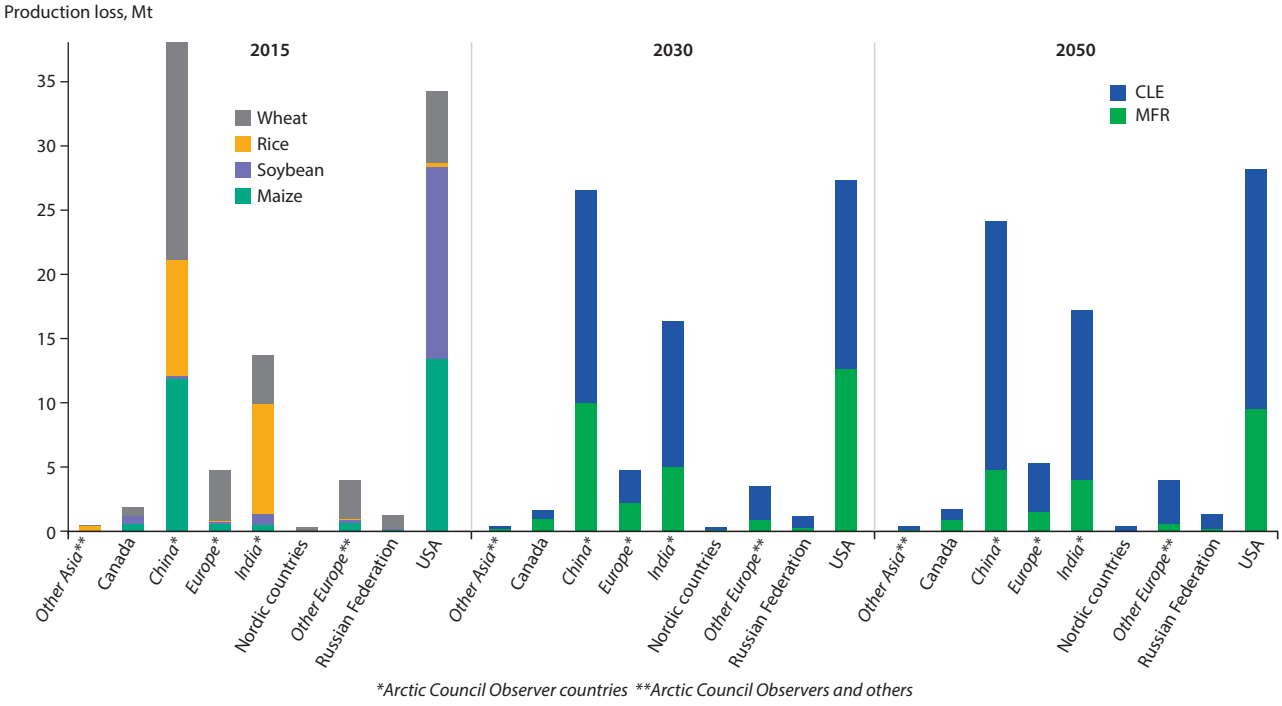

Figure 9.6. Crop losses in 2015 and estimated for 2030 and 2050 under CLE and MFR scenarios. For 2030 and 2050, production losses are summed across the four crops to show total losses under each scenario. MFR estimates are shown superimposed over CLE. Arctic Council Members are Nordic countries, Canada, Russian Federation and USA; Observers are: European observers, China and India; and also included are Other Asian Observer countries and Other European countries (non-member and non-observer).

of metric tonnes per year, the highest losses worldwide in 2015 are observed for wheat, at 39 mega tonnes (Mt), followed by rice (20 Mt), maize (18 Mt) and soybean (14 Mt). The regions experiencing the highest aggregated losses from all four crops are the USA (27 Mt) and China (26 Mt), as shown in Figure 9.6.

Crop losses are forecast to decline under CLE in China and the USA, to increase in India, and to remain stable in other regions through 2030 and 2050. Under the MFR scenario, significant reductions in crop losses are expected over all regions. While globally aggregated losses are estimated at around 84 Mt under CLE in 2050, applying MFR could reduce the crop losses by 74% to 22 Mt.

9.5 Conclusions

9.5.1 Key findings

Air pollution is a leading global health risk factor in all countries within the Arctic region and globally. A large body of evidence from epidemiology, toxicology, human and other studies indicates that air pollution is associated with premature mortality, cardiovascular and respiratory disease, lung cancer, diabetes, adverse birth outcomes, and neurological effects. Air pollution also contributes to ecosystem damage through acidification and eutrophication, and can harm crops, resulting in reduced yields.

A new quantitative analysis of the emissions scenarios presented in Chapter 2 indicates that current air-pollution levels are associated with a large number of air pollution-related deaths and morbidity cases, as well as damage to ecosystems and crops.

The emissions cuts under CLE will lead to reductions in Arctic Council Member states in future years in: $PM_{2.5}$ mortality; O_3-related crop-yield losses; and exceedances of eutrophication and acidity critical loads . The findings indicate that O_3-related mortality will have increased by 2030 and 2050 under current legislation, particularly in Arctic Council Observer countries. This trend is driven mainly by population growth and changes in disease rates. Under the MFR scenario, mortality related to $PM_{2.5}$ and O_3 are anticipated to decline dramatically, with additional reductions in critical load exceedances and crop yield losses.

In terms of quantifying the present-day impacts of pollutant emissions on human health, ecosystems, and crop yields, and identifying benefits that can be achieved by reducing emissions in the future, it is possible to draw several conclusions.

BC affects health as a component of $PM_{2.5}$, while CH_4 affects health by contributing to concentrations of O_3 in the troposphere. Together, $PM_{2.5}$ and O_3 are among the leading risk factors for all Arctic Council Member states and Observer nations, according to GBD 2017 Risk Factor Collaborators (2018). The contribution of ambient air pollution to premature mortality ranges from 2%–3% in Nordic countries, to 13% in India. While climate change is expected to result in negative consequences for human health, it has not yet been included in the prominent IHME GBD study or other global comparative disease-burden assessments. Therefore, little information is currently available about the burden of disease from climate change, either globally, in individual countries, or in the Arctic specifically.

Policies and control measures that reduce SLCFs would also reduce other co-emitted air pollutants, affecting overall $PM_{2.5}$ and O_3 levels. The health impacts from future emissions changes

under business-as-usual or policy scenarios therefore extend beyond just the health benefits from reduced SLCFs. New modeling undertaken for this integrated assessment indicates that $PM_{2.5}$ mortality globally could drop by 24% in 2030 and 4.5% in 2050 compared with 2015 levels, under current legislation. This is due mainly to declining $PM_{2.5}$ concentrations from policies that reduce SO_2 emissions. For the Arctic Council Member states in particular, our findings indicate that current air-pollution legislation could lead to even more substantial declines in annual $PM_{2.5}$-attributable mortality by 2030 (-59%; 66,000 fewer deaths) and 2050 (-57%; 64,000 fewer deaths) compared to 2015. Contrastingly, global O_3 mortality could increase by 17% in 2030 and by almost 60% in 2050 compared with 2015, due to steady O_3 concentrations but growing exposed populations. The influence of population changes is especially important in Arctic Council Observer countries, particularly in Asia, where significant population growth is expected in the future. O_3-related mortality is anticipated to have increased slightly compared to 2015 in Arctic Council Member states by both 2030 and 2050 under current legislation (16% increment; approximately 4,000 more deaths annually).

Our study indicates that if MFR approaches were implemented, global $PM_{2.5}$ mortality could be 22% lower in 2030 and 26% lower in 2050 compared with the CLE scenario. For Arctic Council Member states in particular, maximum feasible reductions would result in a greater decline in $PM_{2.5}$-related mortality than that delivered by current legislation (approximately -87% or 97,000 fewer deaths in 2030 and 2050). However, for Observer countries, while declines in $PM_{2.5}$-related mortality are indicated for 2030 compared to 2015, $PM_{2.5}$ mortality is forecast to rise by 2050 compared to 2030, due to increases in populations at risk (from -28% or 540,000 fewer deaths in 2030 to -12% or 235,000 fewer deaths in 2050 under CLE, and from -45% or 880,000 fewer deaths to -40% or 790,000 fewer deaths under the MFR scenario, compared to 2015 estimates). In addition, global O_3-related mortality would change from a future increase under the CLE scenario to a future decrease under the MFR scenario, compared with 2015. Maximum feasible control technologies are forecast to reduce global O_3 mortality by 42% by 2030 and 53% by 2050 compared with current legislation. In the Arctic Council Member states, mortality due to O_3 decreases for both 2030 and 2050 under the MFR scenario, with a larger drop in the first period (-20% or 5,700 fewer deaths in 2030 and -24% or 6,900 fewer deaths in 2050 compared to 2015).

We also estimate that past policies and current legislation will result in the area in which terrestrial acidity and eutrophication critical loads are exceeded to drop below 1% in the (sub-)Arctic region, and the remaining exceedance amounts to drop to quite low values. O_3-related damage to maize, soybean, wetland rice, and wheat is also anticipated to decline under current legislation – and far more so under the MFR scenario – through 2030 and 2050.

Human health and crop yields are affected by air pollution, climate, and socio-economic factors simultaneously. While the air-quality improvements simulated under the future emissions scenarios could potentially be very beneficial for health, they would occur simultaneously with changes in other risk factors that also affect population health, including climate change and other non-environmental influences. In addition to actions that protect environmental quality, actions that improve overall public health would result in healthier and more resilient populations, who may be better prepared to overcome the negative consequences of anthropogenic climate change and other environmental risk factors.

9.5.2 Uncertainties and limitations

Health impact assessments are subject to uncertainty in each of the parameters used as inputs to the health-impact function, including pollutant concentrations, disease rates and concentration-response relationships. The simulated $PM_{2.5}$ and O_3 concentrations from the chemical transport and Earth system models described in earlier chapters have spatial resolutions that are too coarse to capture co-location of pollution levels and populations at smaller spatial scales (see Chapter 7 for model evaluations). In addition, the emissions inputs to those models themselves are coarsely resolved, at around 50 km grid resolution. While the modeled concentration outputs were re-gridded to a finer resolution using the spatial structure from a satellite-derived $PM_{2.5}$ concentration dataset (van Donkelaar et al., 2015a, 2015b), studies indicate that coarse-resolution health impact assessments may underestimate $PM_{2.5}$-related mortality (e.g. Li et al., 2016b; Punger and West, 2013). This effect of model spatial resolution on $PM_{2.5}$ health impact analysis is likely amplified for spatially heterogeneous pollution levels from local emissions sources, and may not be as important for more spatially homogeneous pollution levels from long-distance atmospheric transport. Baseline disease rates from the IHME GBD study are also subject to uncertainty due to lack of available administrative health data from each country, and smaller-scale regions, cities, and communities (GBD 2017 Risk Factor Collaborators, 2018).

Health-impact functions are highly uncertain. $PM_{2.5}$-related mortality was calculated using different concentration-response relationships from meta-analyses of epidemiological studies conducted around the world. These concentration-response relationships lead to very large differences in estimated $PM_{2.5}$-related mortality, due to assumptions about non-linearity. Recent evidence suggests that $PM_{2.5}$ concentration-response relationships may be very steep at low concentrations (Vohra et al., 2021), which would lead to larger estimated $PM_{2.5}$-attributable disease burdens in both Arctic Council Member states and Observer countries, and elsewhere around the world. In addition, concentration-response relationships were based on total $PM_{2.5}$ mass, as opposed to relationships specific to individual $PM_{2.5}$ components, such as BC. As previously discussed, the evidence for differential effects of $PM_{2.5}$ components is mixed, with some studies showing that BC may be more strongly associated with deleterious health effects than total $PM_{2.5}$ mass. If BC is more harmful to human health compared with other $PM_{2.5}$ components, the estimated health benefits from reductions in BC emissions achieved by the mitigation measures explored in this chapter may be underestimated. In addition, concentration-response relationships used in this analysis are from meta-analyses of epidemiological studies largely conducted outside of the Arctic region. They may not necessarily apply to Arctic communities, which may have differing health statuses, access to healthcare, lifestyles, and sources of emissions. Further, evidence suggests that air pollution and heat may act synergistically on health

systems. Therefore, populations that are simultaneously exposed to warmer temperatures due to climate change and continued air pollution may be at higher risk of deleterious health outcomes. Finally, health effects from exposure to indoor air pollution were excluded here but are important in Arctic communities, particularly where residential solid fuel combustion is used for home heating and other purposes.

Estimates of crop losses are subject to uncertainties resulting from the modeled ozone exposure metric, as well as from the exposure-response functions, and uncertainties in crop spatial distribution and growing seasons. The TM5-FASST linearized reduced-form model with native 1° x 1° (latitude/longitude) resolution, as used for this assessment, tends to overestimate the crop exposure metrics compared to the full-process TM5 (Van Dingenen et al., 2018). On the other hand, the full TM5 model tends to underestimate measured springtime monthly AOT40 values, while summertime values are variable for different world regions (Van Dingenen et al., 2009). Further, the possible presence of a vertical gradient near the surface that is not resolved within the model's bottom layer may lead to overestimated O_3 exposure at crop canopy height, in locations and at times of day when vertical mixing in the boundary layer is weak. And, the applied exposure-response functions have to be considered as a highly simplified representation of real-world processes, where meteorological variables and variability in O_3 sensitivity play an important role in the actual uptake of O_3 via plant stomata. Particularly important climatic parameters include soil moisture and leaf-to-air vapor pressure deficits that moderate the flux of O_3 into the leaf stomata. Where crops are grown in arid climates without irrigation, yield losses may be lower than predicted here, due to water stress resulting in stomata closing, thereby reducing the plant's exposure to O_3 (Emberson et al., 2000).

Future reports may include impacts of air pollution on freshwater and freshwater ecosystems, given that fish populations are an important food source for Arctic communities, and that both nutrition and drinking-water quality are important for human health.

9.5.3 Recommendations

Several actions are recommended for improving the knowledge and information available on the impacts of air pollution on health, ecosystems, and crops among Arctic Council Member states and Observer countries. As the scientific evidence advances, future AMAP assessments can improve upon the estimates in this chapter of exposure to air pollution, associated damages to public health and vegetation, and outcomes of emissions mitigation scenarios. Our recommendations are:

1. *Expand observations of current air-pollution levels and their impacts on human health and vegetation in the Arctic.* Large-scale efforts to estimate levels of exposure to $PM_{2.5}$, O_3, and other air pollutants focus more on highly populated areas, particularly at the mid-latitudes, and where there are more ground monitors. While some ground monitors exist in the Arctic region, most are located in remote areas to measure background air pollution. Satellite remote sensing has been extremely valuable in providing estimates of $PM_{2.5}$ levels in places where there are no ground monitors, but such space-based monitoring is not possible over highly reflective surfaces, such as snow- and ice-covered terrain. Global chemical transport and climate models are typically limited in spatial resolution, and need to be developed with finer spatial resolutions to more adequately simulate exposure in cities and towns that have sharp spatial gradients. With limited ground monitors and satellite remote-sensing retrievals, populated areas of the Arctic are lacking estimates of current air-pollution levels that can be used for environmental and public health surveillance, for input into epidemiological studies, and as a baseline for making comparisons with simulations of concentrations and impacts on public health and vegetation under different emissions-reduction scenarios. Arctic-specific epidemiological studies can also shed light on whether the available health response functions are appropriate for these communities.
2. *Increase case studies for locally specific emissions inventories and emissions-reduction scenarios.* Most of the information currently available about the impacts of air pollution on human health and vegetation is from outside the Arctic region. Given the unique circumstances of Arctic communities and the differences in local emissions sources that affect them, studying the consequences of current emissions and more locally specific emissions-reduction scenarios can provide more relevant information — on which decisions for shaping emissions policy among Arctic nations can be based. For example, investigations into the feasibility and benefits of instigating emissions-reduction measures for wood combustion in homes, oil and gas development, shipping, and other emissions sources local to the Arctic region are needed.
3. *Conduct more research into the health and environmental benefits of limiting climate change.* Approaches for estimating the public health consequences of climate change, and the benefits that could occur under various policy scenarios, are limited. This assessment has focused only on the impacts on health, ecosystems, and crop yields occurring from exposure to $PM_{2.5}$ and O_3 air pollution, and has excluded the potential effects on health and vegetation of changes in exposure to heat, extreme weather, and other shifts that could occur as anthropogenic climate change continues. Understanding a wider range of climate-driven harms could provide a more accurate estimate of the societal impacts of climate change, and the effects that could occur under different emissions-reduction scenarios. This would provide more policy-relevant information to decision-makers. Future assessments should seek to include these effects as the scientific evidence and methodologies advance.

Chapter 9 Appendix

A9.1. Economic Valuation of Air Pollution Model

The Economic Valuation of Air Pollution (EVA) system (Brandt et al., 2013a, 2013b; Geels et al., 2015; Im et al., 2018, 2019) is based on the impact-pathway chain method (Friedrich and Bickel, 2001). The latest version, EVAv6, can calculate all-cause acute and chronic mortality and morbidity based on linear exposure-response functions, along with cause-specific mortality based on non-linear functions following Lelieveld et al. (2019).

A9.1.1. Linear approach

The EVA system estimates premature mortality, related to acute exposure to O_3, $PM_{2.5}$, SO_2 and NO_2, and chronic exposure to $PM_{2.5}$ and NO_2. EVA requires gridded surface concentrations of the above pollutants, along with gridded population density data over fixed age intervals, corresponding to babies (under one year), children (under 16), adults (above 16 and above 30), and elderly people (above 65). The linear concentration-response functions used in EVA are those recommended by the World Health Organization (WHO) (Héroux et al., 2015; WHO, 2013b). Adjustments are included that help to minimize the risk of double counting premature deaths due to short-term and long-term exposures.

The health impacts are calculated using a concentration-response function of the following form:

$$R = \alpha \times \delta c \times P$$

where R is the response of the mortality rate or the years of life lost (in cases or days), δc denotes the pollutant concentration, P denotes the affected share of the population, and α is an empirically determined constant for the particular health outcome.

The applied concentration-response functions recommended by WHO in, for example, Héroux et al. (2015), are based on a comprehensive review, and only pollutant/health outcome pairs supported by sufficient evidence for a causal association are included in the recommendations. The underlying research derives from larger meta-studies, such as Hoek et al. (2013), and includes analyses from Europe, USA and Asia, where data are most extensive and up-to-date. Some studies to develop region-specific concentration-response functions are ongoing – in Europe, and in particular in the Nordic region (the NordicWelfAir project, for example). The EVA model system was compared to other similar systems in Anenberg et al. (2016).

EVA calculates the number of lost life years for a Danish population cohort with normal age distribution, applying the RR as follows: RR=1.062 (1.040–1.083) for all-cause chronic mortality due to $PM_{2.5}$. The latency period sums to 1138 years of life lost (YOLL) per 100,000 individuals for an annual $PM_{2.5}$ increase of 10 μg/m³ following Andersen et al. (2008). The YOLL is then converted to number of cases by dividing by 10.6 following EC (2005). The counterfactual $PM_{2.5}$ concentration is assumed to be 0 μg/m³ following the European Environment Agency (EEA) methodology, meaning that the impacts have been estimated for the simulated total (anthropogenic and natural) $PM_{2.5}$ mass (EEA, 2017). Chronic mortality is also included for NO_2, but only for annual averaged levels above 20 μg/m³ and with RR of 1.0550 per 10 μg/m³ (Table A9.1).

Table A9.1. The health endpoints and RRs used in EVA – based on WHO recommendations. COPD = chronic obstructive pulmonary disease; RAD = restricted activity days; WLD = work loss days; MRAD = minor restricted activity days.

Health endpoint	Pollutant	Range	Ages	RR per 10 μg/m³
Acute mortality	O_3	>35 ppb	All	1.0029
	NO_2 (daily max)	No threshold	All	1.0027
	$PM_{2.5}$	No threshold	All	1.0123
	SO_2	No threshold	All	0.072%
Acute mortality infants	$PM_{2.5}$ (from PM_{10})	No threshold	Infants	1.0400
Chronic mortality	$PM_{2.5}$	No threshold	>30	1.062
	NO_2	>20 μg/m³	>30	1.0550
Hospital admissions (HA):				
Cardiovascular HA (including stroke)	$PM_{2.5}$	No threshold	All	1.0091
Cardiovascular HA (excluding stroke)	O_3	>35 ppb	>65	1.0089
Respiratory HA	$PM_{2.5}$	No threshold	All	1.0190
Respiratory HA	O_3	>35 ppb	>65	1.0044
Respiratory HA	NO_2	No threshold	All	1.0180
Bronchitis (COPD) in children	$PM_{2.5}$ from PM_{10}	No threshold	6–18	1.0480
Bronchitis (COPD) in adults	$PM_{2.5}$ from PM_{10}	No threshold	>18	1.1170
Asthma symptoms in children	$PM_{2.5}$ from PM_{10}	No threshold	5–19	1.0280
RAD	$PM_{2.5}$	No threshold	All	1.0470
WLD	$PM_{2.5}$	No threshold	20–65	1.0460
MRAD	O_3	>35 ppb	all	1.0154
Lung cancer morbidity	$PM_{2.5}$	No threshold	Above 30	1.14

Regarding short-term exposure and acute mortality, the number of cases related to exposure to O_3, NO_2, $PM_{2.5}$ and SO_2 are estimated in the EVA system using RR ranging from 1.0027 to 1.0123 per 10 μg/m³. For O_3, SOMO35 is applied, based on the daily maximum of 8-hour mean O_3 concentrations. The effect related to NO_2 is included as an annual mean of the daily maximum NO_2 concentration, while annual mean concentrations are used for $PM_{2.5}$ and SO_2.

The morbidity outcomes include bronchitis, asthmatic children and LC. As a main application of the EVA system is the assessment of costs, the system also includes concentration-response functions related to hospital admissions (cardiovascular and respiratory) as well as restricted-activity and lost work days. This facilitates differentiation between costs associated with days of reduced well-being and actual sick days, useful for accounting purposes. Details on the concentration-response functions for the different morbidity and mortality outcomes are presented in Table A9.1.

A9.1.2. Non-linear approach

EVA uses concentration-response functions that are modeled as a linear function, which is a reasonable approximation for the region of interest in the present study, as showed in several studies (e.g. EC, 2005; Pope III et al., 2002; UN and WHO, 2003). However, some studies showed non-linear relationships, being steeper at lower than at higher concentrations (e.g. Samoli et al., 2005). Therefore, linear relationships may lead to overestimated health impacts across highly polluted areas and underestimation of health impacts within relatively unpolluted areas.

EVA has been recently further developed to include non-linear functions, in order to estimate cause-specific mortality due to O_3 and $PM_{2.5}$, following Lelieveld et al. (2019). This method uses the GEMM model (Burnett et al., 2018), where RR is calculated through hazard ratio functions. These functions are based on 41 cohort studies from 16 countries, and model the association between $PM_{2.5}$ and non-accidental mortality. Hence, the methodology of Burnett et al. (2018) as implemented in Lelieveld et al. (2019) was followed for estimating RR as:

$$RR = \exp\{\theta \log[(z/\alpha)+1]/(1+\exp\{-(z-\mu)/\nu\})\}$$

where z = max (0, 2.4 μg/m³ $PM_{2.5}$ concentration); and θ, α, μ and ν are variables obtained from Burnett et al. (2018). Log is the natural logarithmic function. Due to the lack of long-term knowledge about the shape of the concentration-mortality association below 2.4 μg/m³, concentrations below this threshold value were taken from cohort studies where subjects were exposed to relatively low concentrations.

This method can calculate cause-specific mortality due to exposure to ambient $PM_{2.5}$, including LC, COPD, CEV, IHD and LRI. The category of non-accidental diseases, which was defined as 'non-communicable disease (NCD) + LRI'; and the so-called 'other NCD', defined as the subtraction of the above categories to NCD+LRI, were added when using GEMM. RR, and hence premature mortality has been estimated for each pathology and different ages: 25–29, 30–34, 35–39, 40–44, 45–49, 50–54, 55–59, 60–64, 65–69, 70–74, 75–79, 80+ and all ages.

For this AMAP assessment, global population density data at 2.5-minute spatial resolution from SEDAC (Data ref. 9.2) were input to EVAv6. In these data, the age breakdown is available for the year 2010. Therefore, the age distribution of other years in the assessment were scaled by a dataset of country-specific age distributions for the years 1950–2020, originally given in five-year intervals Data ref. 9.11), and subsequently interpolated to the actual year in EVAv6. By way of example, based on these data, the world population was 7.34 billion people in the year 2015 and 7.79 billion people in 2020.

The main text of this chapter included results for $PM_{2.5}$ and O_3-related mortality. Results for morbidity outcomes from changes to $PM_{2.5}$ and O_3 in each year and for each emissions scenario are shown in Table A9.2.

A9.2 TM5-FASST tool

TM5-FASST health and crop impacts were evaluated as described in Van Dingenen et al. (2018) but using updated values for RR for both $PM_{2.5}$ and O_3, and adding type 2 diabetes mellitus as an additional cause of death for $PM_{2.5}$, following GBD 2017 Risk Factor Collaborators (2018).

Base mortality rates at country level for each cause of death were downloaded from the GBD 2017 results tool (Data ref. 9.8) for model years until 2015 and applied to each grid cell belonging to a country. Projected base mortality rates were downloaded from the GBD 2016 foresight visualization tool (Data ref. 9.9). To avoid discontinuities between GBD2016 foresight and GBD 2017 data after 2015, the foresight mortality rates were scaled with their respective GBD 2017 value in 2015 and this correction factor was applied on all years beyond 2015 from GBD 2016 foresight, to smoothly transition to the foresight data until 2040. Therefore, the final foresight data in the current set differ slightly from the GBD 2016 foresight data because they were tuned to match 2015 from GBD 2017. We assume year 2050 base mortality rates to be equal to the 2040 values, the last available year in the GBD 2016 foresight set.

For IHD and stroke, age class-specific RRs and mortality rates were used, following GBD 2017 Risk Factor Collaborators (2018). While still based on SSP2 gridded total population, the age class population fractions were computed from UN World Population Prospects 2017 (Data ref. 9.10).

O_3 mortalities were computed following GBD 2017 Risk Factor Collaborators (2018), using as exposure metric the maximal 6-month daily maximal 8-hourly O_3 mean (SDMa8); O_3 mortalities were associated to COPD with RR = 1.06 (1.02, 1.10) per 10 ppb. We applied a lower threshold of 29.1 ppb (while GBD 2017 applied a uniformly distributed value between 29.1 and 35.7 ppb). All models, except TM5-FASST, provided only SOMO35 as O_3 exposure metric. As TM5-FASST provides both SOMO35 and SDMa8, we converted SOMO35 to SDMa8 using a conversion factor SDMa8/(SOMO35 + 35) computed with TM5-FASST at grid cell level.

Crop exposure and impacts were evaluated using the methodology as described in detail by Van Dingenen et al. (2009, 2018). Available crop O_3 exposure metrics for which exposure-response functions were available from the literature (Mills et al., 2007; Wang and Mauzerall, 2004) were AOT40, plus M7, M12. Mi were calculated as the three-monthly mean daytime O_3 concentration. AOT40 and Mi were evaluated

Table A9.2. Morbidity results from the EVA model. RHA = respiratory hospital admissions; CHA = cardiovascular hospital admissions; COU_C = Asthma symptoms/cough; CB = chronic bronchitis; CB_C = chronic bronchitis in children; WLD = work loss days; RAD = restricted activity days; MRAD = minor restricted activity days; LC = lung cancer; IM = infant mortality. Scenarios: CLE = current legislation; MFR = maximum feasible reduction. Region: OBS = Arctic Council Observer countries; AC = Arctic Council Member states.

Region	Outcome	Year	Scenario	Mean	Lower confidence interval	Upper confidence interval
Global	RHA	2015		4,436,336	1,653,092	5,644,235
Global	CHA	2015		3,119,165	1,160,153	3,961,334
Global	COU_C	2015		1,840,224	789,525	2,291,735
Global	CB	2015		7,659,961	2,663,876	9,826,609
Global	CB_C	2015		57,349,130	24,567,582	71,311,896
Global	WLD	2015		2,706,661	902,447	3,488,107
Global	RAD	2015		11,159,170,080	4,147,796,480	14,162,068,480
Global	LC	2015		120,719	40,053	154,812
Global	IM	2015		20,101	9033	24,631
Global	RHA	2030	CLE	3,293,671	2,770,074	3,724,458
Global	CHA	2030	CLE	2,312,077	1,944,110	2,613,867
Global	COU_C	2030	CLE	1,399,214	1,174,575	1,605,540
Global	CB	2030	CLE	5,632,349	4,732,587	6,315,468
Global	CB_C	2030	CLE	43,495,383	36,549,392	49,959,576
Global	WLD	2030	CLE	1,982,694	1,676,390	2,207,484
Global	RAD	2030	CLE	8,270,092,177	6,950,429,184	9,344,876,544
Global	LC	2030	CLE	88,122	74,404	97,977
Global	IM	2030	CLE	15,275	12,936	17,579
Global	RHA	2030	MFR	2,442,644	2,128,986	2,627,159
Global	CHA	2030	MFR	1,714,337	1,494,172	1,843,800
Global	COU_C	2030	MFR	1,068,598	944,845	1,164,949
Global	CB	2030	MFR	4,113,227	3,561,141	4,398,312
Global	CB_C	2030	MFR	33,285,326	29,400,790	36,249,832
Global	WLD	2030	MFR	1,441,539	1,244,021	1,533,698
Global	RAD	2030	MFR	6,132,433,543	5,341,854,720	6,591,784,960
Global	LC	2030	MFR	63,962	55,215	68,071
Global	IM	2030	MFR	11,841	10,505	12,900
Global	RHA	2050	CLE	4,058,851	3,342,418	4,607,694
Global	CHA	2050	CLE	2,846,782	2,345,748	3,233,796
Global	COU_C	2050	CLE	1,800,079	1,493,409	2,060,711
Global	CB	2050	CLE	6,789,623	5,572,421	7,682,275
Global	CB_C	2050	CLE	56,017,240	46,470,224	64,122,868
Global	WLD	2050	CLE	2,337,502	1,922,372	2,629,811
Global	RAD	2050	CLE	10,191,994,619	8,386,418,688	11,561,263,104
Global	LC	2050	CLE	103,790	85,321	116,721
Global	IM	2050	CLE	19,756	16,525	22,627
Global	RHA	2050	MFR	2,807,823	2,460,638	3,005,681
Global	CHA	2050	MFR	1,972,272	1,726,944	2,109,432
Global	COU_C	2050	MFR	1,298,334	1,158,131	1,400,633
Global	CB	2050	MFR	4,603,611	3,995,911	4,906,555
Global	CB_C	2050	MFR	40,371,030	36,037,348	43,583,432
Global	WLD	2050	MFR	1,572,203	1,354,839	1,668,547
Global	RAD	2050	MFR	7,041,467,057	6,174,006,272	7,541,590,528
Global	LC	2050	MFR	69,684	60,134	74,056
Global	IM	2050	MFR	14,466	12,961	15,618
OBS	RHA	2015		2,424,151	527,658	3,358,393
OBS	CHA	2015		1,710,500	370,321	2,356,984
OBS	COU_C	2015		823,357	180,429	1,162,954
OBS	CB	2015		4,538,955	979,887	6,210,291

Region	Outcome	Year	Scenario	Mean	Lower confidence interval	Upper confidence interval
OBS	CB_C	2015		25,560,038	5,614,402	36,187,678
OBS	WLD	2015		1,697,109	367,276	2,302,924
OBS	RAD	2015		6,100,828,819	1,323,943,056	8,426,516,792
OBS	LC	2015		75,115	16,301	102,212
OBS	IM	2015		8368	1814	11,737
OBS	RHA	2030	CLE	1,355,239	1,119,799	1,463,854
OBS	CHA	2030	CLE	948,909	785,894	1,027,360
OBS	COU_C	2030	CLE	408,232	325,760	448,456
OBS	CB	2030	CLE	2,615,942	2,183,020	2,812,808
OBS	CB_C	2030	CLE	12,711,662	10,136,680	13,954,600
OBS	WLD	2030	CLE	998,953	844,545	1,070,150
OBS	RAD	2030	CLE	3,396,964,482	2,809,676,296	3,672,945,080
OBS	LC	2030	CLE	44,320	37,484	47,497
OBS	IM	2030	CLE	4121	3310	4507
OBS	RHA	2030	MFR	876,719	732,384	963,558
OBS	CHA	2030	MFR	615,050	514,000	676,243
OBS	COU_C	2030	MFR	257,092	213,694	280,037
OBS	CB	2030	MFR	1,705,367	1,426,154	1,878,929
OBS	CB_C	2030	MFR	7,986,152	6,649,520	8,713,909
OBS	WLD	2030	MFR	657,659	552,108	726,194
OBS	RAD	2030	MFR	2,201,290,185	1,837,616,556	2,417,657,752
OBS	LC	2030	MFR	29,200	24,505	32,231
OBS	IM	2030	MFR	2598	2172	2834
OBS	RHA	2050	CLE	1,502,841	1,166,977	1,640,061
OBS	CHA	2050	CLE	1,053,700	819,006	1,151,024
OBS	COU_C	2050	CLE	476,765	354,877	523,708
OBS	CB	2050	CLE	2,858,236	2,241,568	3,114,704
OBS	CB_C	2050	CLE	14,831,805	11,042,707	16,296,243
OBS	WLD	2050	CLE	1,074,568	850,962	1,165,466
OBS	RAD	2050	CLE	3,775,640,040	2,928,052,900	4,115,062,296
OBS	LC	2050	CLE	47,637	37,769	51,728
OBS	IM	2050	CLE	4788	3589	5255
OBS	RHA	2050	MFR	842,995	683,989	929,037
OBS	CHA	2050	MFR	592,099	480,036	652,016
OBS	COU_C	2050	MFR	257,878	211,225	281,490
OBS	CB	2050	MFR	1,621,739	1,311,240	1,791,295
OBS	CB_C	2050	MFR	8,021,502	6,572,703	8,759,116
OBS	WLD	2050	MFR	616,216	498,290	682,615
OBS	RAD	2050	MFR	2,116,636,807	1,716,189,252	2,331,037,532
OBS	LC	2050	MFR	27,384	22,116	30,297
OBS	IM	2050	MFR	2602	2136	2838
AC	RHA	2015		88,454	48,317	115,717
AC	CHA	2015		62,157	33,910	81,213
AC	COU_C	2015		23,722	12,639	30,703
AC	CB	2015		176,179	96,759	230,948
AC	CB_C	2015		737,860	393,288	955,403
AC	WLD	2015		72,099	39,573	94,499
AC	RAD	2015		221,497,106	121,231,651	290,345,428
AC	LC	2015		3203	1756	4194
AC	IM	2015		247	129	321
AC	RHA	2030	CLE	51,407	47,052	56,138
AC	CHA	2030	CLE	36,103	33,022	39,399

Region	Outcome	Year	Scenario	Mean	Lower confidence interval	Upper confidence interval
AC	COU_C	2030	CLE	13,555	12,438	14,867
AC	CB	2030	CLE	102,898	93,992	112,092
AC	CB_C	2030	CLE	421,744	387,019	462,609
AC	WLD	2030	CLE	43,433	39,621	47,207
AC	RAD	2030	CLE	129,033,632	118,058,365	140,855,116
AC	LC	2030	CLE	1928	1759	2095
AC	IM	2030	CLE	139	127	152
AC	RHA	2030	MFR	39,562	32,029	44,917
AC	CHA	2030	MFR	27,782	22,479	31,524
AC	COU_C	2030	MFR	10,468	8,539	11,918
AC	CB	2030	MFR	78,979	63,850	89,646
AC	CB_C	2030	MFR	325,850	265,715	370,845
AC	WLD	2030	MFR	33,408	26,923	37,692
AC	RAD	2030	MFR	99,319,770	80,363,739	112,700,977
AC	LC	2030	MFR	1482	1195	1673
AC	IM	2030	MFR	107	88	122
AC	RHA	2050	CLE	55,034	47,975	59,802
AC	CHA	2050	CLE	38,626	33,669	41,970
AC	COU_C	2050	CLE	14,482	12,667	15,787
AC	CB	2050	CLE	110,029	95,861	119,499
AC	CB_C	2050	CLE	450,716	394,162	491,230
AC	WLD	2050	CLE	46,366	40,344	50,266
AC	RAD	2050	CLE	138,124,999	120,372,865	150,048,858
AC	LC	2050	CLE	2059	1791	2231
AC	IM	2050	CLE	148	129	161
AC	RHA	2050	MFR	40,838	31,510	46,863
AC	CHA	2050	MFR	28,677	22,114	32,889
AC	COU_C	2050	MFR	10,816	8,424	12,337
AC	CB	2050	MFR	81,688	62,771	93,725
AC	CB_C	2050	MFR	336,123	262,143	383,889
AC	WLD	2050	MFR	34,400	26,387	39,451
AC	RAD	2050	MFR	102,549,311	79,060,544	117,582,825
AC	LC	2050	MFR	1524	1171	1751
AC	IM	2050	MFR	110	86	126

over three months, centred on the midpoint of the location-dependent crop growing season provided by the Global Agro-Ecological Zones (GAEZ) 2012 dataset (Data ref. 9.5). Note that in the GAEZ methodology, the theoretical growing season is determined based on prevailing temperatures and water-balance calculations for a reference crop, and can range between 0 and 365 days; however, this study always took three months as the standard metric accumulation or averaging period.

A9.3. Health impacts of air pollution (ISTE) tool

For this report, the ISTE tool was used to estimate deaths attributable to $PM_{2.5}$ exposure in Nordic countries in 2015. The attributable deaths were estimated at country level. Two alternative concentration-response functions were applied: log-linear function for all-cause natural mortality, and GEMM for non-communicable and lower respiratory infections (Table A9.3). The deaths were estimated using probabilistic exposure distributions taking into account the population-weighted concentrations and standard deviations for $PM_{2.5}$ for 2015. Baseline mortality data for each Nordic country were obtained from WHO Global Health Estimates data for 2015 (Data ref. 9.1).

Table A9.3. Mortality-related assumptions in ISTE

Pollutant	Health endpoint	Threshold	Ages	Relative risk	Reference
$PM_{2.5}$	All-cause (natural) mortality	No threshold	>30	1.062 per 10 μg/m^3	Hoek et al., 2013
$PM_{2.5}$	NCD+LRI	2.4 μg/m^3	>25	GEMM	Burnett et al., 2018

(NCD + LRI = non-communicable diseases + lower respiratory infections).

10. Conclusions and recommendations

In planning the scope of this assessment, the AMAP SLCF Expert Group drafted relevant policy questions that the findings of the study could potentially help to answer. Those questions were also used to communicate the scope of the assessment with stakeholders. This chapter presents the questions – and answers to them – at the same time serving as a summary of the main findings and conclusions drawn from the whole assessment.

The results related to anthropogenic and natural emissions sources are discussed first, then observations and trends in atmospheric constituents present in the Arctic are considered, and the modelling capabilities examined. Finally, the chapter presents the assessment's conclusions relating to potential impacts of SLCFs on the climate, health and ecosystems.

10.1 Anthropogenic emissions of short-lived climate forcers in an Arctic context (Chapter 2)

10.1.1 What are the current global emissions of anthropogenic black carbon and methane (the key warming SLCFs) and how might they change in future under current legislation?[1] What are the major sectors contributing emissions globally?

Global emissions of black carbon (BC) from anthropogenic sources were estimated with the IIASA-GAINS model to be 6.6 Teragrams per year (Tg/y) in 2010 and 5.9 Tg/y in 2020. Assuming effective enforcement of current legislation and policies (the CLE scenario, as described in Chapter 2, Section 2.2), the emissions are projected to decline to 5.4 Tg/y by 2030, and further to 5.3 Tg/y by 2050. Globally, the most important source sectors (throughout the whole period) are residential combustion, constituting about half of the total, and land-based transportation, responsible for a quarter.

Global emissions of methane (CH_4) from anthropogenic sources were estimated to be 340 Tg/y in 2015 and 350 Tg/y in 2020. Under the CLE scenario, the CH_4 emissions are projected to increase to 380 Tg/y in 2030 and further to 440 Tg/y in 2050. The largest anthropogenic CH_4 sources in 2015 were agriculture (42% of total emissions), oil and gas (18%), waste (18%) and energy production and industry (16%). These sources are anticipated to remain key in 2050. The rising global trend is primarily driven by increasing solid waste generation, as populations grow and countries become wealthier, and by greater extraction of unconventional natural gas (such as shale gas through fracking) to substitute coal use in energy production.

According to the model estimates, enforcing current legislation will lead to declines in emissions of sulfur dioxide (SO_2), carbon monoxide (CO) and nitrogen oxides (NO_X) in the future, while those of fine particulate matter ($PM_{2.5}$) and volatile organic compounds (VOCs) stay close to their 2015 levels. SO_2 reductions, in particular, occur before 2030. Organic carbon (OC) and ammonia (NH_3) emissions, meanwhile, are projected to increase during the study period.

10.1.2 What are the current anthropogenic black carbon and methane emissions of Arctic Council Member states and Observer countries, and how might they change in future under current legislation?

10.1.2.1 Arctic Council Member states

Based on the IIASA-GAINS model, emissions of BC from anthropogenic sources in the eight Arctic Council Member states were estimated to be 507 Gigagrams[2] (Gg/y) in 2013 and 450 Gg/y in 2020, representing about 8% of the global total. Under the CLE scenario, when compared with 2013 and 2020 figures, the emissions are projected to decline by 21% and 11%, respectively, by 2025. Emissions continue to decline to 313 Gg/y by 2050.

The USA, Russia, Canada and the Nordic countries accounted for 51%, 36%, 10% and 4%, respectively, of the Arctic Council Member state emissions in 2013. By 2050, the corresponding shares are projected to be 43%, 41%, 14% and 2%, reflecting the different national emissions trends arising under current air-pollution legislation.

The main anthropogenic sources of BC emissions in Arctic Council Member states are land-based transportation, accounting for 46% in 2013 and 34% in 2025, followed by residential combustion with 22% and 26% percent shares, respectively. The transport sector contributes most (93%) to the projected emissions reduction of 107 Tg anticipated between 2013 and 2025 under the CLE scenario.

The Arctic Council has a collective voluntary goal to reduce emissions of BC by at least 25%–33% below 2013 levels by 2025. Analysis of the estimated emissions development, under the CLE scenario, indicates that a reduction of between 19 Gg and 60 Gg (4%–12%) must be achieved by 2025 to reach that goal.

Anthropogenic CH_4 emissions in the eight Arctic Council member states in 2020 were estimated to be 69 Tg/y, representing approximately 20% of the global total. Under the CLE scenario, emissions are projected to increase to 71 Tg/y by 2030, and to reach 74 Tg/y by 2050. This estimated trend does not comply with the Arctic Council vision "...to significantly reduce our overall methane emissions".

[1] Note: These do not include the anticipated impacts of the COVID-19 pandemic on emissions

[2] Note: 1 Gigagram = 0.001 Teragrams; 1 Megagram = 0.001 Gigagrams

10.1.2.2 Arctic Council Observer countries

According to estimates from the IIASA-GAINS model, emissions of BC from anthropogenic sources in the 13 Arctic Council Observer countries were 2625 Gg/y in 2013 and 2105 Gg/y in 2020, representing about 42% and 37% of the global total, respectively. With existing legislation, a continuous decline in emissions is anticipated, to 1816 Gg/y in 2025 and 1209 Gg/y in 2050 – less than half of the 2013 levels. Main emissions sources include residential combustion (1477 Gg/y and 950 Gg/y for 2013 and 2025, respectively) and land-based transportation (527 Gg/y, 303 Gg/y). The majority of the reductions are expected to be made within the residential combustion, transport, and industry sectors, with reductions of 527 Gg/y, 224 Gg/y and 93 Gg/y, respectively, from 2013 to 2025. Between 2025–2050 the emissions are projected to decrease further by 490 Gg/y, 156 Gg/y and 25 Gg/y, respectively. However, assuming no change in waste-management practices, emissions from the waste sector are projected to increase by 41 Gg/y between 2013 and 2025, and by a further 77 Gg/y during 2025–2050. Most of the emissions in the Arctic Council Observer countries originate from China and India; as a consequence, changes in these countries have the largest impact on emissions trajectories. Over 90% of the total decrease of BC emissions is due to policies in these countries, primarily addressing emissions from coal and fuelwood use for cooking and heating, and diesel vehicles.

CH_4 emissions from anthropogenic sources in the Arctic Council Observer countries for 2020 are estimated at 102 Tg/y, representing about 30% of global emissions. By 2025, under the CLE scenario, the emissions are projected to increase by 5% compared to 2020, reaching 106 Tg/y. The emissions are projected to increase further to 124 Tg/y by 2050.

10.1.3 How will the magnitude of black carbon, methane and sulfur dioxide emissions change in the future, and what options are there for additional emissions reduction measures beyond current legislation?

The CLE scenario for anthropogenic emissions assumes that current air-pollution legislation is effectively implemented, as are climate commitments set out in Nationally Determined Contributions towards the Paris Agreement. The Maximum Feasible Reduction (MFR) scenario considers further emissions reductions that could be achieved by adopting existing best available mitigation technologies for all air pollutants.

Compared to 2015, emissions of BC are projected to decline by nearly 40% by 2050 in the Arctic Council Member states, and by 60% in the Observer countries. In contrast, BC emissions for the Rest of the world (total of all remaining countries) are estimated to increase. However, there is significant potential to further reduce BC emissions with existing technologies. In the Arctic Council Member states, an ambitious strategy of adopting best available mitigation technologies for road and non-road transport, residential heating, and in the oil-and-gas sectors, could approximately halve BC emissions by 2030, compared with the CLE baseline. A further 10% reduction could be achieved through measures implemented in industry and the effective enforcement of existing bans on open burning of agricultural residues. In the Arctic Council Observer countries, reductions in BC emissions of 60%–70% could be achieved by 2030 by implementing measures targeting practically the same sectors as in the Arctic Council Member states. Additional reductions of up to 20% could be achieved between 2030–2050 by further improving access to clean energy for cooking and by improving municipal solid waste management to the point where virtually no open burning of waste remains.

CH_4 emissions are expected to grow by 10% and 30% by 2050 in the Arctic Council Member states and the Observer countries, respectively, relative to 2015. The maximum feasible reduction of global anthropogenic CH_4 in 2050 is estimated to be 54% below the emissions under the CLE scenario for that year. The mitigation potential in the Arctic Council Member states is somewhat higher, at 65% below that anticipated under the CLE scenario for 2050; this could be achieved by introducing measures to reduce emissions from oil- and-gas production, storage and distribution, as well as from improved municipal and industrial solid waste and wastewater management.

The CLE scenario for SO_2 emissions projects a strong decline of about 30% and 40%, respectively, for Arctic Council Member states and Observer countries. Potential exists for further declines, typically through scenarios aimed at improving air quality. The maximum mitigation potential by 2030 is estimated to be 60% for Arctic Council Member states and 40% for Observer countries. SO_2 emissions would also fall further under strategies focusing on BC mitigation, since some options (such as introducing diesel particle filters or reducing coal use) would necessitate or result in its removal. However, such additional reductions are small in comparison to those resulting from targeted SO_2 mitigation.

10.1.4 What percentage of global anthropogenic methane, black carbon and sulfur dioxide emissions are controlled by Arctic Council Member states and Observer countries?

In 2015, the Arctic Council Member states accounted for 8%, 13% and 20% of the global anthropogenic emissions of BC, SO_2 and CH_4, respectively. The corresponding values projected for 2050 are 6%, 12%, and 17%. The global shares of emissions originating from the Arctic Council Observer countries in 2015 were 40%, 40%, and 30%, respectively, for BC, SO_2, and CH_4, with figures of 23%, 30% and 29% projected for 2050.

Together, Arctic Council Member states and Observer countries contributed about half of global emissions of these pollutants in 2015. Under the CLE scenario, by 2050 the collective share decreases by 29% for BC, and 42% for SO_2. It is projected to remain at around 50% for CH_4.

10.1.5 What are the current and potential future emissions from Arctic shipping?

Although Arctic shipping is currently a relatively minor source of BC, these emissions occur close to and within the

Arctic, thus posing a higher relative risk to Arctic climate and local communities compared with sources located farther south. Regulatory changes affecting emissions from shipping have recently come into effect. The International Maritime Organization (IMO) introduced a 0.5% cap on sulfur (S) content for marine fuels from 2020. The IMO also has established a process for discussing BC emissions, but no regulation is currently in place.

Estimates of BC emissions for shipping above 60°N latitude in 2015 range between 0.3–1.5 Mg/y, while SO_2 emission estimates range between 40–80 Mg/y. These represent less than 1% of global emissions from international shipping. Future emissions will be influenced by changes in shipping activities in the Arctic area, as well as by the application of emissions regulations and consequent mitigation. Comparing the projected situation in 2050 with that of 2015, SO_2 emissions are estimated to decrease by 60%–75% under the CLE scenario, whereas BC emissions are projected to remain on a similar level, despite projected increases in Arctic shipping activities.

10.1.6 How do national emissions inventories relate to other available emissions datasets?

Comparing emissions inventories included in this study with official national submissions and other independent inventories highlights variation in the inclusion and handling of data from important emission sectors, as well as in activity and emissions parameters between the inventories.

10.1.7 What are the uncertainties in estimates of current and future anthropogenic emissions?

The calculated emissions within inventories are subject to uncertainties due to missing or incomplete information and to limitations in understanding calculation parameters.

The uncertainties apply to all key elements underlying the estimates: activity data and the temporal distribution of activities; the aggregation of individual sources or more detailed information; emissions calculation parameters, such as emission factors, as well as locations of sources in both vertical and horizontal domains. The emissions datasets used for estimating impacts in this assessment have not undergone a quantitative statistical uncertainty analysis. A comparison with emissions data estimates from other sources indicates that there is variation that depends on the pollutant, sector and region.

10.1.8 How well do we understand where emissions occur, especially in the Arctic area?

This issue was addressed in AMAP's 2015 assessment, which highlighted that "more attention is also needed on identifying the location of high-latitude sources and on improving the accuracy of the spatial distribution of emissions in the vicinity of and within the Arctic". Since that assessment, more attention has been paid to this issue, with further improvements made to the spatial dimension of emission sources.

The datasets used in this study have more detailed coverage of: the distribution of Arctic populations; shipping lanes and ship movements; road networks; and industrial and energy installations, including oil-and-gas-exploration sites. Understanding of the locations of emissions has similarly improved since previous assessments, but work in this area should continue with the aim of further characterizing resulting impacts. Local information from Arctic communities on energy, waste handling and transportation sectors is welcome.

10.2 Open biomass burning (Chapter 4)

10.2.1 What are the impacts of climate change on fire risk and fire emissions?

Near-term warming will result in more ignitions from lightning, with degraded permafrost increasing dry-ground fuels, as well as fire severity and duration in the boreal forest and Arctic tundra ecosystems. By the end of the century (using the 'business-as-usual' high emissions Representative Concentration Pathway [RCP] 8.5), wildland fire risk is expected to increase, with the length of fire seasons – measured in terms of daily severe fire weather occurrence – predicted to expand by many as 20 days globally and by greater than 50 days for Russia, with the potential for annual forest fire burned area to double. Further, under both RCP 8.5 and RCP 4.5 (stabilizing emissions), natural wildfire emissions of BC, $PM_{2.5}$ and SO_2 could exceed anthropogenic emissions in northeastern Europe, including Sweden and Finland, by 2090. Robust predictions of future burned area in wildland and human-dominated landscapes for the Arctic require an understanding and quantitative simulation of the major drivers of fire – specifically climate and fire weather, fuels, and lightning- and human-caused ignitions.

Climate-induced vegetation shifts present a complex fire risk matrix for the Arctic Council Member states. The predicted transition of boreal forest to deciduous forest stands would decrease fire risk in eastern Canada and interior Alaska. However, grass and shrub expansion in the Arctic tundra, as well as in the transition zone between boreal forest and the tundra, would increase fire risk. And in boreal Alaska and northwestern Canada, increased wildfires would reduce current evergreen forests and expand deciduous forests. Mature deciduous forests in interior Alaska show that current canopy gaps are related to ecological shifts to evergreen shrubs, lichens, and mosses. The trend is increasing fire risk as gaps within low flammability deciduous stands transition from high flammability coniferous species. Further, grasslands are predicted to replace much of the upland conifer, mixed, and deciduous forests for a large area of the boreal forest zone of northern Alberta, Canada, by 2100. Shorter fire-return intervals combined with climate change-induced drought will reduce the resiliency of evergreen and broadleaf species to reseed and reestablish after wildfires, leading to an expansion of grassland ecosystems in what are currently Northern Canadian forests. The expansion of grass-dominated landscapes would create a new fire regime of frequent but low-severity fires, with short-lived climate

pollutants (SLCPs) and SLCFs likely being transported to the Arctic in the spring months as a result.

In general, lightning frequency is expected to increase over areas north of 50°N. Increased convective cloud formation has been documented in the Russian Arctic and the North American boreal forest, with a 5% projected increase in convective storms in Northern Europe by the end of the century. Moreover, since summers are expected to become drier in the future, the role of lightning as an ignition source for wildfires may increase for Northern Europe.

10.2.2 What are current and potential future fire-management strategies in the Arctic?

Active fire management via prescribed burning, cultural fires by Indigenous peoples, fuels management, ignitions reduction, and even allowing moderate- to low-intensity wildland fires are current strategies in Arctic Council Member states. Grassy tussock tundra and dwarf shrub tundra vegetation types (often grown on private land) are more likely to burn than low shrub tundra in Alaska, with rapid vegetation regreening occurring within a decade of burning. Prescribed burning could therefore be effective for fuel management in tussock and dwarf shrub landscapes of the tundra. However, in the Zabaikal region of southern Siberia, Russia, high fire frequency combined with positive surface temperature anomalies was found to be more likely to negatively impact the post-fire reforestation process than severe burns, the latter having higher vegetation recovery rates.

The effectiveness of prescribed burning for peatlands is less clear. The risk of peat fires happening and their potential burn depth are influenced less by canopy and ground vegetation and more by soil bulk density (which affects air availability in soils), water-table depth, and precipitation. After fires in 2010 that devastated the Moscow region of Russia, the regional government undertook an ambitious 70,000-hectare (ha) peatland rewetting project to reduce fire risk. To date, the effectiveness of this campaign is unclear – given the long timescales required for peat restoration – but in practical terms it should reduce fire risk. Emissions of CH_4 from peatland rewetting are less significant in the short-term than emissions of CO_2 from degraded or drained peatlands increasing long-term warming when rewetting is postponed. In dried and degraded peatlands of the Arctic region, fuels management will be more complicated outside of the boreal forest and forest-tundra gradient, where mulching treatments that convert canopy and surface fuels to a masticated fuel bed have been found to limit peat burn depth in Black Spruce (*Picea mariana*) stands.

Adaptive management strategies enacted by the timber industry in Fennoscandia could also reduce fire risk. Intensive management involving the maintenance of ditch networks and fertilization of drained peatlands will increase timber values while also rewetting the peat. Prescribed burning for silvicultural retention, and maintaining and regenerating stands, can also reduce fuel loadings while increasing biodiversity.

Current wildland firefighting strategies may not be suitable for future 'typical' fire seasons in the boreal forest. This is because approximately 24 more days are anticipated where the intensity of wildfires (crown fires) in the Canadian boreal zone will be practically unmanageable by ground crews, even if supported by aerial support such as water bombers. Canadian wildland firefighters operationally use several key thresholds based on fire intensity to guide fire operations: at 2 Megawatts per meter (MW/m) fire-line intensity, ground resources request aerial fire support to hold the fire line; at 4 MW/m, aerial fire suppression by air tankers becomes ineffective at directly controlling a fire line; and at 10 MW/m, heavy air tankers cannot hold or suppress a fire line. Current wildland firefighting techniques in the boreal forest will not be appropriate for the more fragile permafrost- and peat-dominated Arctic tundra. Collaboration, cooperation, and innovation are needed for effective future firefighting in Arctic wildlands.

People can be considered the variable with the highest uncertainty – both as ignition sources and when seeking to determine how demographic shifts, migration, and changes to traditional uses of land and development patterns within these evolving landscapes will affect fire activity and related emissions. Expanding climate-driven agricultural frontiers in the high northern latitudes could add 8.5 million km^2 of new croplands in Canada and Russia alone, expanding wheat and maize production into areas with carbon-rich or peat soils. Crop-growing conditions favorable for wheat and maize production could be established in the permafrost zone of Siberia by 2080. These crops are commonly managed via open burning practices in Canada, the USA, eastern Europe, and Russia. Burns and management of croplands, grasslands, and deciduous forests may occur in these locations at times when the transport of emissions to the Arctic is likely, such as late winter or early spring. Understanding, managing, and preventing human-caused ignitions in the Arctic Council Member states and Observer countries will be beneficial for mitigating future fire risk.

10.2.3 What are the long-term emissions from open biomass burning?

Comparison of five satellite-based biomass-burning model runs, conducted for 2005–2018, found that most fire activity and emissions take place between 50°N–60°N, with very few emissions from open biomass burning occurring between 70°N–80°N, and no satellite observations of fire above 80°N. The latitude band 50°N–60°N corresponds with the southern boundary of the boreal region. This area is experiencing increasing fires due to climate change, and has been the site of some of the largest wildfires in Canada's history. A clear shift has occurred since the mid-2000s, with more fires occurring above 60°N than in the temperate zone of 45°N–50°N – where traditionally human-caused burning and wildfires have occurred extensively throughout North America, Europe, and Eurasia. This trend is more pronounced in the outputs from fire models such as the Global Fire Emissions Database (GFED) and the Global Fire Assimilation System (GFAS) than in the Fire Inventory from NCAR (FINN), though all models show a positive trend. The 2005–2018 multi-model annual average BC emissions from all open biomass burning sources in the Arctic (60°N–80°N) and adjacent regions known to impact smoke transport into the Arctic (between 45°N–60°N)

is 340 Gg. The years with the highest multi-model average are 2012, 2008, and 2015, with BC emissions of 450 Gg, 440 Gg, and 410 Gg, respectively. The years having the lowest annual average BC emissions according to the models are 2008 and 2013, both with 270 Gg.

Ground-based official statistics vary greatly and can be classified by both country and sub-region (for example, Greenland; Alaska). With regards to specific fire activity within Arctic Council Member states, the Russian Federation has the highest annual burned area, with over 100,000 km^2 burned (circa 2019 figures), resulting in approximately 0.025 Gg of BC and 0.305 Gg of CH_4. In 2019, approximately 98% of burned area in Russia occurred in the Urals, Siberia, and Far East Federal Districts. In general, Fennoscandia and European Russia had the lowest burned area and open biomass-burning emissions, with all Arctic Council Member states experiencing the most burning between 50°N–60°N, followed by 60°N–70°N. Alaska and Canada accounted for approximately 29,000 km^2 of total pan-Arctic biomass burning and 22% of the BC emissions. Greenland is a novel fire regime in the Arctic, with two relatively significant wildfires in 2017 and 2019; in 2019, it accounted for more burned area and emissions than Norway or Finland.

10.2.4 What are the emissions from 'natural' fires?

For this assessment, only fires started by lightning were considered to be 'natural' fires. Lightning strikes, fire weather, and fuels conditions are the controlling processes for 'natural' fires. Current satellite inventories do not distinguish between natural fires and human-caused ignitions, only differentiating land use and fuel type, and thus no emissions estimates for natural fires could be presented. Ground-based statistics from Arctic Council Member states break down emissions from known lightning sources and human-caused fires, with human-caused fires accounting for most fire activity but with lightning being the source of the largest fires in terms of burned area and therefore emissions releases. However, natural fires are not necessarily always the source of the largest total annual fire emissions.

10.2.5 What are the emissions from human-caused open biomass burning?

Open biomass burning from anthropogenic activities, including timber, agriculture, and energy extraction, will increase in the Arctic as climate change expands human-dominated landscapes northward, increasing potential ignition sources. Timber extraction and site preparation currently cause large wildfires in the Arctic Council region, with the 2014 Västmanland fire (the largest single wildfire event in Sweden's history) being an example. Northward agricultural expansion will likely increase human-caused open burning, as wheat and maize become established in areas of Siberia that are currently permafrost. The major wildfire in Greenland in 2019 was caused when an outdoor campfire ignited dry ground fuels at a public camping site on the world-renowned Arctic Circle Trail. This indicates that tourism will also need to adapt to increased fire risk in Arctic landscapes.

10.2.6 What are the uncertainties around future natural and human-caused open biomass-burning emissions?

Little is documented in the scientific literature or official statistics on Indigenous cultural burning across the pan-Arctic. This has resulted in a gap in this assessment but it presents an opportunity for future fire monitoring and management. Further uncertainties in understanding of future natural and human-caused open biomass-burning emissions include:

1. Satellite-based observations of fire in the Arctic and boreal zones underestimate open burning in agricultural landscapes, surface fires in boreal forests, and smouldering peat fires, plus they need to be improved or augmented to distinguish between natural and human-caused ignitions.
2. There is a lack of agreement between satellite-derived and official estimates of burned area.
3. Ignitions of natural fires in future will be influenced by vegetation shifts, increased lightning and extreme weather events, and fuel conditions (including increased bug kills from climate change-induced pest outbreaks).
4. More frequent fires are anticipated in Arctic and boreal peatlands – but substantial uncertainties remain around locations, intensity, duration, ignition types, and fire return intervals.
5. Better understanding is needed on permafrost thermal state, dynamics and distribution, as well as post-fire resiliency.
6. Human influence on fire risk is dependent on local- to national-scale actions that may increase fire and emissions via deforestation, transportation networks, energy extraction, tourism, cultural burning, and agricultural open burning, but may also decrease fire risk and fire emissions via active fuel management and suppression.

10.3 Natural sources of methane within the Arctic (Chapter 3)

10.3.1 What are the current emissions of methane from terrestrial, freshwater and marine sources?

Averages of the various natural CH_4 sources within the Arctic, based on scientific literature published within the past ten years, indicate that terrestrial sources emit 23 [0–47] Tg/y, freshwater sources emit 18 [7–33] Tg/y and the Arctic Ocean, including shelf seas, emits 7 [2–29] Tg/y. The total budget for natural CH_4 sources with a high northern signature according to these estimates is 49 [9–109] Tg/y. This estimate is double the amount that global atmospheric inversions indicate is being emitted from the area north of 60°N.

Global bottom-up estimates of natural CH_4 sources suggest a total budget of 371 [245–488] Tg/y (Saunois et al., 2020), which means that the Arctic constitutes 13% [10%–20%] of all global

natural sources – about 2.5 times lower than global emissions of CH_4 from fossil fuels. The Arctic is most likely a modest source of CH_4 at present, but budget estimates carry a high uncertainty. Whether the Arctic will play a larger role in the global CH_4 budget with future climate change remains uncertain; this will strongly depend on whether the region continues to harbor environments that are favorable to methanogenesis, such as wetlands and lakes. If the Arctic becomes wetter as a result of climate change, CH_4 emissions are anticipated to rise with further temperature increases (Watts et al., 2014). If the Arctic becomes drier, CH_4 emissions may not increase at the same pace, although soil carbon may be respired and released as CO_2 instead (Schuur et al., 2015).

10.3.2 To what extent might potential increases in natural emissions of methane offset mitigation of anthropogenic emissions? (Chapter 3, Chapter 2)

This question was addressed in AMAP's 2015 assessment (AMAP 2015b), which stated that until 2050, the MFR emissions reduction scenario for the eight Arctic Council Member states would be comparable to the magnitude of the potential increase in natural emissions under the 'high' scenario due to climate warming, while the achievements of other natural emissions scenarios were lower in magnitude. A reanalysis of the 2015 results by Christensen et al. (2019) shows that none of the naturally induced increases in Arctic CH_4 sources are as large in magnitude as the reduction in global anthropogenic emissions, represented by the difference between emissions according to the MFR and CLE scenarios.

10.3.3 Does the location of methane emissions matter for the Arctic climate impacts?

The 2015 assessment (AMAP 2015b), concluded that the spatial distribution of CH_4 emissions would not significantly affect the global mean concentration of CH_4 – due to the atmospheric lifetime of CH_4 exceeding a decade – and that, as a result, it need not be a major consideration in mitigation strategies. Although this has not been analysed in the 2021 assessment, this conclusion remains still valid.

10.4 Observations, origins and trends of SLCFs and clouds in the Arctic (Chapter 6)

10.4.1 What are the current abundances of SLCFs in the Arctic atmosphere? What is our current understanding of the abundance of these components?

Our understanding of the surface concentrations of aerosols in the Arctic, their seasonal variation and trends has improved considerably, and can now be considered as good. Permanent observatories measure concentrations of aerosol species, including particulate sulfate (SO_4) and BC. Longer-term trends now clearly show that BC concentrations have stagnated during the past decade or so, after decreasing between the 1990s and 2010. The aerosol component in the atmosphere has also become less acidic, owing to the decrease of particulate SO_4. Ammonium is also decreasing, while levels of nitrate are rising. These trends can be due to changes in emissions but they may also arise from changing atmospheric chemistry causing variations in the mix of chemical species.

Clear trends for the haze and summer seasons are emerging. Between fall and early spring, (the haze period), fewer particles in the accumulation mode (100–500 nanometers [nm]; typical of Arctic haze) are seen, and the overall scattering of the aerosol population decreases. Arctic aerosol in this season remains dominated by anthropogenic sources. In summer, according to data from Zeppelin station, at Ny-Ålesund on Svalbard, Norway, the number of accumulation- and coarse-mode particles (>1 micrometer [μm]) rises, simultaneously increasing the overall scattering by the aerosol population. The summer is becoming dominated by natural aerosol sources. Methane sulfonic acid (MSA), which is formed from gases emitted by phytoplankton, seemed to have increased in summer during 2000–2010 at some stations. However, these trends did not persist through the following decade. Nonetheless, this effect could help to explain the marked increase in fine-nm (MSA) and accumulation-mode particles at the surface. Long-term observations of particle-size distributions and optical properties are needed to fully understand the ongoing changes and their implications for climate change. A greater number of scattering, as opposed to absorbing, particles in summer would reflect more sunlight, and the presence of more particles in the size range of cloud condensation nuclei (accumulation mode) has the potential to change cloud properties and their radiative effects.

There is a lack of observations of organic aerosols (OA); (needed for apportionment of particles to natural and anthropogenic sources) and for mineral dust (which is strongly implicated in radiative forcing). This means that quantifying particles in the atmosphere is only partially possible. There is a clear need to complement ongoing surface-based observations.

In addition, information from the atmosphere aloft, meaning at all altitudes above the surface, is only captured sporadically in short-term and spatially limited aircraft campaigns. Systematic and vertically resolved understanding of the evolution of any aerosol component in the free troposphere is not available. This is a particular constraint for quantifying the impact of biomass-burning emissions in, or transported into, the Arctic. The same is true for dust transport to the Arctic and ash from volcanic plumes. Measurements of aerosol optical depth (AOD), which are retrieved from satellite observations and represent the integrated aerosol load throughout the atmospheric column, indicate that the particle load is increasing. However, the information is not detailed enough to distinguish between aerosol types and their vertical distribution. There is a clear need to develop satellite-retrieval methods further, as well as to enlarge the ground-based aerosol remote-sensing network to better quantify impacts from forest fires, mineral dust and volcanic ash.

Tropospheric ozone (O_3) is a secondary air pollutant, which is not directly emitted but is produced photochemically in the atmosphere from precursor emissions produced from anthropogenic and natural sources. Small, statistically significant trends in O_3 have been determined based on analyses of surface and vertical ozonesonde data. Regional differences in ozone trends are evident based on analysis of data from different sites, and of different record lengths, in the free troposphere and at the surface. Ozone in the free troposphere has decreased since the mid-2000s at sites in the European Arctic (also at Summit, central Greenland) and increased since the late 2000s at Eureka in the Canadian Arctic. At the surface, certain sites, including Utqiaġvik, Alert, and Zeppelin, show increasing trends over the last 30–40 years, especially in the winter, and some sites, such as Pallas and Summit, exhibit negative trends since the mid-1990s. Other sites, including Villum and Esrange, show no significant trends (over the periods of reported ozone concentrations). The seasonal cycle of ozone at the surface varies across the region, with coastal sites (Utqiaġvik, Villum, Alert) showing a winter or early spring maxima and very low values later in the spring. Other sites, located at altitude or inland, show maxima occurring later in the spring (Zeppelin, Esrange) or early summer (Summit).

Long-term monitoring of atmospheric composition at existing stations is essential to accurately determine trends, with a need to continue and expand current efforts to build an integrated Pan-Arctic observation network. New techniques, approaches and opportunities for monitoring exist that could be applied more widely.

The concentration of Arctic atmospheric methane (CH_4) has been observed since the early 1980s and an increase recorded but with zero growth from 2000 to about 2005. Since 2007, the growth rate has risen again, with an increasing rate from 2015 to 2020. Arctic CH_4 concentration measurements reveal an annual variation, with a higher concentration in late winter and a minimum in summer. The annual amplitude varied from 70–80 ppb in the 1980s but the amplitude has decreased over the last three decades and is now about 40–50 ppb. New data from high-resolution measurements show high variability in CH_4 concentration within the same season; this is especially evident in the winter season but variations over the summer also occur. The high variation during winter is likely due to varying meteorological conditions transporting polluted air from lower-latitude sources. The measurements expose a distinct peak of atmospheric CH_4 during summer at several sites, as well as a 'shoulder' occurring slightly later in early fall. The variability found in the high-resolution data is large, being about the same magnitude as the annual amplitude. Anthropogenic as well as natural processes can drive CH_4 variability. It is still not clear what the primary drivers of the observed variability are but recent studies (Pirk et al., 2017; Ishizawa et al., 2019) suggest natural emissions can cause the late summer/early fall peaks.

10.4.2 In what ways do natural sources contribute to emissions and atmospheric concentrations?

Deducing trends in natural aerosol components is currently a challenge for two main reasons: a) the longer-term observations have been targeted at capturing changes in anthropogenic contributions, and b) natural emissions are changing at a magnitude that is comparable to natural variability. More dedicated efforts are needed to monitor natural aerosol components.

So far, longer-term observations of MSA show that concentrations are highly variable, and trends could only be found at specific stations in particular decades. However, a general increase in concentration is arising from the greater contribution of MSA to the ultra-fine particle population. Sea-salt aerosol has been found to be increasing around Svalbard, which could be due to retreating sea ice in summer. Dust has recently been identified as an important contributor to radiative forcing in the Arctic, but no long-term and systematic observations exist yet. Forest fires release a mixture of natural and anthropogenic emissions because they can be triggered naturally or by human activity. Fire emissions within the Arctic have strongly increased in very recent years (see Chapter 4).

Observations of O_3 and key species that can indicate O_3 sources and sinks are needed to understand the Arctic O_3 budget and changes in O_3 trends. This includes a need to maintain and improve long-term monitoring in regions where local emissions are increasing and where natural sources and sinks are changing in response to climate change, as well as airborne missions to quantify changes (including perturbations due to changing anthropogenic emissions) throughout the depth of the troposphere.

10.4.3 Are the current monitoring and analysis of atmospheric aerosol concentrations sufficient to capture anticipated source changes?

Regarding aerosol properties, the locations of surface observatories are mostly adequate but large measurement gaps exist in the Eastern Arctic. In terms of chemical composition, which enables the attribution of concentrations and climate impacts to specific sources, there is a lack of data-collection stations targeted at measuring natural aerosol components, such as sea spray, MSA and mineral dust. Also, OA is not well characterized around the Arctic, yet the complex mix of organics present can reveal detailed information on local-versus-long-range and natural-versus-anthropogenic contributions. Enhanced isotopic analysis of nitrogen (N) and sulfur (S) could better constrain natural-versus-anthropogenic sources as well as climate-change-induced changes.

Valuable information on sources, atmospheric processes and climate effects is also contained in data on aerosol size distributions. Only a few of the current permanent observatories take continuous measurements of aerosol size distribution. Systematically equipping observatories to gather this data is recommended.

Vertical information remains sparse, and enhancing the ground-based remote-sensing network is also recommended, as is putting more effort into developing algorithms capable of retrieving detailed aerosol information from ground-based and space-borne remote sensing.

In terms of analysis work, very little has been done to explore whether observed cloud changes cause changes to the aerosol

population. Clouds are a key player for the Arctic radiative balance but as yet models do not represent the interaction between aerosols and clouds very well.

Current O_3 observations are insufficient to capture anticipated changes in O_3 from anthropogenic and natural sources and only a very limited number of Arctic stations provide long-term monitoring of ozone at the surface as well as vertical profiles. Standardization of measurement techniques is also required. Satellite data can provide useful spatial, and limited vertical, information about O_3 and some precursors/oxidants but retrievals have limitations that need to be improved at high latitudes.

10.5 Model description and evaluation (Chapter 7)

10.5.1 How well do models capture the current abundance and distribution of SLCFs in the Arctic atmosphere?

Model simulations of the atmosphere output global or regional three-dimensional distributions of SLCFs. While individual models vary in how well they represent SLCFs compared to measured concentrations, the multi-model average provides results that are close to, or within the uncertainty range, of the observed BC, O_3, and CH_4 at sites representative of the background atmosphere. This conclusion is based on a comprehensive evaluation of 18 models (including global climate models and chemistry transport models) in simulating global and Arctic concentrations of SLCFs for years 2008–2009 and 2014–2015, and for some, 1990–2015. Model performance for SO_4, aerosol optical properties, cloud properties, and O_3-precursors was also evaluated using a multitude of global and Arctic observations.

Generally, individual models simulate a range of SLCF concentrations, but the multi-model mean captures the abundance and distribution of SLCFs in Arctic surface ambient air, with multi-model mean biases of -17%, -21%, 10%, and 1.7% for BC, SO_4, O_3, and CH_4, respectively. For free-tropospheric O_3 and surface-level CH_4, these results are very close to the measurement uncertainty range. For aerosol species, model biases are 4–7 times greater in the Arctic than they are globally, as they have historically been tuned to the multitude of observations at mid-latitudes. Models have similar spatial patterns in their biases. However, most models show improvements in simulating seasonal cycles of aerosols in the Arctic, compared to model performance in the 2015 AMAP assessment (AMAP, 2015a).

10.5.2 What are the trends and interannual variability in simulated Arctic SLCF concentrations in the atmosphere, and what are the primary drivers of this variability?

Due to limitations in the availability of emissions datasets, the longest time period simulated by some models in this study was 1990–2015. Unfortunately, this means that post-2015 actions taken to reduce BC emissions following the task force's recommendations to the Arctic Council cannot be verified in the models.

CH_4 mixing ratios were prescribed in all of the models based on box model results, by inputting CH_4 emissions derived from IIASA-GAINS ECLIPSE v6b scenarios. Thus, the simulated CH_4 is much simpler and not as variable as observations made at the surface. However, the modeled CH_4 higher up in the troposphere agrees well with the long-lived and well-mixed observed CH_4. Two models simulated CH_4 during 1990–2015, and these show a steadily increasing trend that is consistent with measurements and expected, given increasing anthropogenic CH_4 emissions.

Seven models simulated BC and SO_4 during 1990–2015 using prescribed historical emissions. Those models captured the current abundance, including seasonal cycle, and trends in SO_4 and BC in the Arctic atmosphere, as compared to 18 Arctic measurement locations. Both models and observations suggest a decreasing SO_4 trend in the early 1990s and relatively little change during the 2000s. Wintertime (January–April) Arctic SO_4 shows a decrease of 17%–57% (depending on location) when comparing the 2011–2015 average to the 1990–1994 average. The summertime (May–August) change in Arctic SO_4 is much smaller. BC also appears to decrease for the 1990–2015 time period, particularly in the winter Arctic haze season, where models estimate a 22%–53% decrease, depending on the location. These trends are as expected, given the reductions in SO_4 and BC emissions, and the remoteness of the Arctic from source regions. SO_4 and BC show a decrease in North America and Europe for 1990–2015, with an increase in Asia. However, in the last ten years, both have started decreasing in parts of Asia as well.

Six models simulated O_3 from 1990–2015 using prescribed historical emissions. Surface O_3 has a small (<0.45%/year) increasing annual trend at some Arctic locations, dominated by the wintertime rise of ~1%/year. The other seasons show no trend, a pattern that is consistent between models and measurements. Emissions of O_3-precursors NO_X and VOCs vary regionally, decreasing in North America and Europe, but increasing in Asia. Meanwhile, CH_4 has been increasing globally. Thus, the lack of O_3 trend is expected, given these compensating changes in precursors. Models do not quite capture the seasonal cycle of surface O_3 in the Arctic; the observations have a springtime peak, while the models either have a summertime peak, or a secondary peak in late summer.

There is interannual variability in the modeled and measured SLCFs, with the primary drivers of this being the differences in meteorology (and thus transport patterns), and wildfires from year to year.

10.5.3 How useful is satellite data for validating model simulations of Arctic concentrations of SLCFs? What are the limitations?

Satellite data are very useful for monitoring Arctic concentrations of CH_4, O_3, and other gaseous SLCFs. These data provide better spatial coverage than the ground sites, and often

have a longer timeseries. They also provide information on the vertical distribution of SLCFs – often in a way that facilitates comparison with models better than very-high spatial-resolution measurements made using aircraft or sondes. Data from ACE-FTS, TES, and MOPITT are utilized in Chapter 5 (with Infrared Atmospheric Sounding Interferometer [IASI] data also used) in comparisons with the modeled mixing ratios of O_3, CO, and CH_4.

While satellite sensors cannot measure individual aerosol species, their data are very useful for estimating the optical properties of aerosols such as AOD, aerosol absorption optical depth (AAOD), and Ångström exponent (ÅE). Again, these measurements provide a wide spatial coverage compared to ground-based observations, though they can be limited in the High Arctic. Data from the Moderate Resolution Imaging Spectroradiometer (MODIS; MODIS/Aqua and MODIS/Terra), Multi-angle Imaging Spectroradiometer (MISR), Advanced Along-Track Scanning Radiometer (AATSR,) Sea-viewing Wide-field-of-view Sensor (SeaWIFS), Cloud-aerosol Lidar with Orthogonal Polarization (CALIOP) and Advanced Very-high-Resolution Radiometer (AVHRR) sensors were used in Chapter 7 for model evaluations. The aerosol optical properties measured by satellite can also be integrated or assimilated into derived $PM_{2.5}$ data products (such as the Modern-Era Retrospective analysis for Research and Applications [MERRA]; Dalhousie University; and Global Burden of Disease [GBD] datasets), which were also used in Chapter 7 chapter to validate modeled $PM_{2.5}$ concentrations.

Satellite-based data products are limited in the Arctic region for various reasons that include difficulties in taking measurements during polar nights, assumptions in the retrieval algorithms, viewing geometries, cloud contamination, and reflections from bright snow- and ice-covered surfaces (see Chapter 7, Section 7.3.6 for further discussion on this). Thus, satellite-based data products are no substitution for ground-based and aircraft measurements, but provide important complementary data.

10.5.4 How do modeled concentrations of SLCFs in snow and ice relate to observations?

Modeled deposition fluxes of BC and SO_4 in the Arctic were evaluated against ice-core data in this assessment. Ice-core data were available from 1750 until the years between 1993–2011, whereas atmospheric concentrations are continuously being measured. Sharma et al. (2019) showed decreasing trends of atmospheric BC and SO_4 in the Canadian Arctic in recent decades. Chapter 6 also reports similar decreasing trends of atmospheric concentrations in all circum-Arctic stations after 1990. Therefore, it is assumed that the deposited concentrations of the two SLCFs in the ice cores follow atmospheric concentration trends, indicating that current levels would be more or less stable compared to the 1990s. To maximize the period available for comparing modeled deposition against observations, we selected all ice-core measurements after 1990 (4–21 samples per ice core). Most models over-predicted deposition of both SLCFs. The uncertainty of measured BC in snow is comparable to that of BC concentrations in the air – around a factor of two (Lim et al., 2014; Sharma et al., 2017).

10.5.6 To what extent do models agree with the satellite-based cloud climate data records?

Four state-of-the-art satellite-based cloud climate data records (CDRs), spanning more than 30 years, were inter-compared and used to evaluate the cloud properties output by the models. All four CDRs showed similar large-scale variability in cloudiness and cloud-top properties. The agreements among CDRs were better over the ice-free ocean compared to the multi-year ice covered parts of the Central Arctic for all cloud properties. Disagreements among them were largest for the polar winter months, due to the lack of sufficient information available from passive satellite sensors. The CDRs also disagreed to a large extent in the retrievals of cloud microphysical properties.

The models simulated the large-scale climatological features in cloud fraction and cloud liquid water (CLW) well when compared to the four CDRs during polar summers. However, the differences were larger for the polar winter months when uncertainties in the CDRs were also higher. In general, the models agreed with the observations better over the ice-free ocean areas. The annual cycles of cloud properties were also simulated well by the majority of the models. The differences among the models in simulating cloud ice water (CIW) were high.

Model simulations of cloud droplet number concentrations (CDNC) in the Arctic were evaluated against satellite-based estimations for the summer season. Most models underestimated CDNC in the Arctic region compared to MODIS-based estimations. However, the satellite-based observations of CDNC were also uncertain, especially in the Arctic region where bright reflecting surfaces add noise to estimations of cloud properties. Improved observations of CDNC (including vertical profiles) are needed to better constrain model simulations of CDNC.

In general, more and better observations are needed during the polar winter months to reduce the uncertainties in both the CDRs and the models.

10.5.7 What do the model uncertainties mean for this assessment's predictions of the impacts of SLCFs on near-term climate and health?

In Chapter 7, model simulations of SLCFs (CH_4, O_3 and ozone precursors, BC, SO_4, OA, and $PM_{2.5}$), aerosol optical properties, and cloud properties were thoroughly evaluated against measurements for the years 2008–2009 and 2014–2015, in addition to some historical simulations covering 1990–2015. The spatial distribution in model biases was examined, as well as seasonal cycle, trends, and interannual variability. Generally, the multi-model mean provided the best results compared to any one particular model for most of the SLCF species. Therefore, the results in Chapter 8 (climate impacts) and Chapter 9 (health impacts) are based on the multi-model mean – representing the optimal use of these model datasets.

Below are listed the annual mean, multi-model-mean biases for each SLCF species included in the historical model simulations of Chapter 8, along with explanations of what each means for

interpreting the impacts on climate and health described in Chapters 8 and 9, respectively.

- Annual mean, simulated surface-level Arctic and global CH_4 was biased slightly high (+1.7% in the Arctic, and +2.1% globally) compared to measurements, which have only a 1% uncertainty), and biased slightly low in the free troposphere (e.g., -0.7% at 600 hectopascals [hPa]), which means that confidence in the warming from CH_4 shown in Chapter 8 is high.
- Annual mean, surface-level Arctic (>60°N) BC was biased low compared to measurements (-17%, which is greater than the ~10% uncertainty in measured BC concentrations) in the historical simulations. However, the warming from BC is due to its concentrations not just at the surface but throughout the atmospheric column. Underestimates in simulated concentrations at higher altitudes in the troposphere (e.g., -80% at z = 6 km in altitude for the Arctic region) generally increase with altitude and proximity to the Arctic, according to comparisons with aircraft measurements. This means that the warming due to BC shown in Chapter 8 may be underestimated.
- Annual mean Arctic SO_4 was biased low in the historical simulations compared to measurements (-21%, well below the 3% measured uncertainty), which means that cooling from SO_4 in the Arctic (shown in Chapter 8) may be underestimated. However, vertical profiles of SO_4 and radiative forcings were not evaluated, so temperature impacts are uncertain.
- Globally, and in the Arctic, modeled surface-level O_3 was biased high (10% in the Arctic, which is greater than the 3% measurement uncertainty). This means that the detrimental health impacts of O_3 shown in Chapter 9 may be overestimated.
- Higher in the atmosphere (in the free troposphere) O_3 is an effective greenhouse gas, and at this level it was slightly underestimated by models (-10% to -20% compared to satellite measurements, which have ~15% uncertainty range). This means that the warming impact from O_3 shown in Chapter 8 may be slightly underestimated.
- Annual mean $PM_{2.5}$ – both globally and in the Arctic – was biased low in the historical simulations (-40% globally; -10% in the Arctic), which means that the health impacts due to $PM_{2.5}$ exposure (presented in Chapter 9) may be underestimated.
- Annual mean AOD – giving an indication of the aerosol load in the atmosphere – was biased low (-25% globally; -23.2% in the Arctic) suggesting that the overall impacts of aerosols on climate and human health may be underestimated.
- The differences and uncertainties in both the satellite-based observations and model simulations of cloud properties were high over the Arctic, especially over regions covered by multi-year sea ice and during the polar winter months. This implies that the poor representation of the processes relevant to the interactions among aerosol-precursor gases, aerosols and clouds could be a major source of uncertainties in the climate impacts in this assessment.

There were seasonal differences in the model biases, which complicates the uncertainties around the potential impacts on climate and health. For example, the seasonal cycle of O_3 has health implications, since O_3 mainly exceeds health thresholds in the summertime (photochemical smog), while $PM_{2.5}$ mainly exceeds health thresholds in the wintertime (haze or local Arctic pollution). At mid-latitudes, where human populations are much higher, the models simulated the seasonal cycles well – thus the health impacts determined in Chapter 9 for background pollution should be fairly accurate. That said, coarse-resolution global models are not ideal tools for simulating local pollution sources; high-resolution regional models would be better used for that purpose. The differences in simulated seasonal cycles of O_3, BC, and SO_4 were particularly large in the Arctic. There were other regional differences in model biases as well. For example, surface-level O_3 had a much smaller positive bias in North America and Europe than in Asia, and modeled $PM_{2.5}$ was biased high in North America, but low in Asia. These, too, further complicate the interpretation of the climate and health impacts.

10.6 Modeling of climate and air quality (Chapter 8)

10.6.1 How have changes in global atmospheric concentrations of SLCFs between 1990–2015 contributed to Arctic climate warming?

In response to changing global anthropogenic emissions, SLCFs contribute to both warming and cooling of the Arctic, through changing interactions with radiation, clouds, and surface albedo. The simulated net Arctic warming during 1990–2015 – from changing interactions of warming and cooling SLCFs from global anthropogenic sources with radiation – is 0.077°C/decade. In detail, CH_4 contributed 0.039°C/decade while the contribution of BC was less than 0.001°C/decade. Global anthropogenic sulfur emissions and SO_4 aerosol concentrations declined during 1990–2015, thereby contributing 0.048°C/decade to net Arctic warming due to diminishing interactions of SO_4 aerosols with radiation. The changes in tropospheric O_3 precursors between 1990–2015 resulted in a small net Arctic warming of 0.0013°C/decade. For comparison, interactions of CO_2 with radiation during this time are associated with an Arctic warming rate of 0.285°C/decade.

In addition to the interactions with radiation, interactions of SO_4 with clouds likely had a net warming impact on the Arctic over this period. The simulated magnitude of this warming is large but very uncertain. Reductions in global sulfur emissions produced an Arctic warming impact of 0.290°C/decade from diminishing interactions of SO_4 aerosols with radiation, clouds, and surface albedo.

The net impact on Arctic warming of changing global emissions of all SLCFs from interactions with radiation, clouds, and surface albedo is 0.269°C/decade, for 1990–2015. Therefore, changes in sulfur emissions dominated the impact of all SLCFs on Arctic climate during this time period.

10.6.2 What impact will future atmospheric emissions of SLCFs have on the Arctic climate?

Regardless of the emissions scenario, model simulations indicate that the Arctic will continue to warm at a rapid rate, as interactions of both long-lived and short-lived climate forcers with radiation, clouds, and surface albedo will continue to cause global mean temperature to increase, with an amplified response in the Arctic. Most of this response is caused by changes to emissions outside the Arctic, which affects heat transport into the Arctic and subsequent climate feedbacks within the region. Under the CLE scenario, the net rate of Arctic warming between 2015–2050 caused by warming and cooling climate forcers could be as high as 0.59°C/decade, based on Earth System Model (ESM) projections.

Health concerns motivate policy actions to reduce concentrations of SLCF air pollutants, including sulfur. Under the CLE scenario, continuing reductions in anthropogenic emissions of sulfur globally would lead to diminishing interactions of SO_4 aerosols with radiation, clouds, and surface albedo – producing an impact on Arctic warming of 0.132°C/decade between 2015–2050 (the contribution of interactions with radiation only is 0.054°C/decade). With maximum feasible reductions in sulfur emissions (MFR scenario), the simulated impact on Arctic warming is considerably higher (0.228°C/decade). Furthermore, the rate of impact on Arctic warming depends on the time period, with greater impacts projected for 2015–2030 than for 2015–2050. This indicates that reductions in sulfur emissions alone, could substantially accelerate the rate of Arctic warming in the near term, with particularly large impacts if air pollutant concentrations are rapidly reduced, as simulated under the MFR scenario.

The model results also show that making the maximum feasible reductions in emissions of BC and CH_4 can nearly offset the impact of the reduced sulfur emissions on the Arctic warming rate, compared to the CLE scenario. Facilitating such reductions in CH_4 emissions from the oil-and-gas sector in Arctic Council Member states would be particularly efficient at reducing the projected warming. Maximum feasible reductions in global emissions of CH_4 from all anthropogenic combustion sources would cause cooling in the Arctic through reduced interactions of CH_4 with radiation; this could lead to a reduction in the Arctic warming rate of 0.047°C/decade during 2015–2050, relative to the CLE scenario.

To counteract accelerated warming from diminishing sulfur emissions, it will be particularly important to achieve maximum feasible reductions of global BC from gas flaring, transport, and residential combustion. Reduced deposition of BC on snow would increase the reflectivity of the snow, thereby cooling the Arctic, this is especially the case for BC emissions from Arctic Council Member states. Maximum feasible reductions in global emissions of BC from all anthropogenic sources and diminishing interactions of BC with radiation would produce a cooling impact on Arctic temperature that could reduce the rate of Arctic warming by 0.074°C/decade (the contribution of interactions with radiation only is 0.030°C/decade) from 2015–2050, relative to the CLE scenario.

Maximum feasible reductions in tropospheric O_3 precursors (mainly from fossil-fuel sources) would have a small impact on the rate of Arctic warming over the period 2015–2050, reducing it from a small increasing rate of 0.0012°C/decade under the CLE scenario to a decreasing rate of 0.0056°C/decade under the MFR one.

In summary, the simulated impacts of making maximum feasible reductions to combined global CH_4 and BC emissions (-0.121°C/decade) and sulfur emissions (+0.097°C/decade) on the net rate of Arctic warming between 2015–2050 are approximately in balance, relative to the CLE scenario. Consequently, the difference between the Arctic warming rates for the CLE scenario and the more ambitious MFR scenario is small, and within the uncertainty of the model projections. This indicates that it would be feasible to counteract near-term impacts on Arctic warming from decreasing sulfur emissions by reducing emissions of CH_4 and BC, at least until 2050.

Future simulated global and Arctic mean precipitation rates are slightly higher under the MFR than the CLE scenario (differences are less than 0.1 mm/day), due to changes in surface energy budgets from reduced concentrations of SO_4, BC and OC with maximum feasible emission reductions.

The confidence in the simulated climate impacts for 2015–2050 is high regarding the direction of change, and medium regarding the magnitude of change. The future emissions trajectory is a major source of uncertainty. Another important source of uncertainty are climate feedbacks on natural aerosol, aerosol-precursor and CH_4 emissions, such as from wildfires, oceans, wetlands, forests and deserts. These feedbacks are currently either represented in a relatively rudimentary manner in ESMs or are not included at all. To reduce the considerable uncertainties in impacts of SLCFs on climate that are related to clouds and surface albedo, further improvements in observations and models are needed. In addition, uncertainties also result from natural variability in radiative forcings and climate on annual to multi-decadal time scales, and in the initial conditions employed in models.

10.6.3 What are the climate penalties of reduced emissions of cooling species (sulfur, NO_x) versus the benefits of lower emissions of warming species (black carbon, and methane)?

The net maximum feasible reductions to anthropogenic emissions of both warming and cooling SLCFs is not likely to produce a notable impact on the Arctic climate between 2015–2050, relative to the net warming rate of 0.59°C/decade from all SLCFs and greenhouse gases simulated under the CLE scenario. This lack of notable net Arctic climate benefits can be explained by the near cancellation of cooling and warming impacts, resulting from concurrent reductions in emissions of warming and cooling SLCFs (mainly CH_4, BC, and SO_4). In particular, projected future reductions in sulfur emissions lead to reduced interactions of SO_4 with radiation and clouds in the MFR scenario relative to the CLE one, causing the rate of Arctic warming to increase. The sulfur-induced Arctic warming is greater in magnitude than the cooling from concurrent reductions in interactions of

BC with radiation and surface albedo. Given that global sulfur emissions are highly likely to continue to decline in the near term, it would be efficient to also reduce global SLCF emissions that lead to warming (CH_4 and BC) to reduce the rate of Arctic warming between 2015–2050, which could achieve particularly large climate benefits during the time period from 2015–2030.

Reductions of global S and BC emissions are necessary to mitigate future health hazards due to poor air quality. Given the near-cancellation of the climate impacts of different SLCFs, it would be possible to further improve air quality with only minor impacts on Arctic warming.

In summary, projected future reductions in global sulfur emissions emphasize the need to reduce global emissions of CO, CH_4, and BC in order to slow the rate of Arctic warming.

These conclusions are based on the analysis of the available emissions scenarios and are therefore specific to the assumptions described in Chapter 2. Different mitigation actions could lead to a different balance between temperature changes and SLCF emissions than simulated here, which points to the need to also assess the additional IIASA-GAINS model emissions scenarios (Chapter 2) in future studies.

10.6.4 How large are the climate responses to SLCFs in the context of climate changes from carbon dioxide and other greenhouse gas emissions?

The model simulations conducted for this report provide evidence that rising global anthropogenic emissions of CO_2 and diminishing global anthropogenic emissions of sulfur contributed strongly and equally to the rate of Arctic warming during 1990–2015. However, considerable uncertainties exist in the magnitude of the warming attributable to sulfur emission changes, largely owing to uncertainty in how sulfate aerosols interact with clouds and surface albedo. By comparison, the simulated changes that anthropogenic emissions of BC and CH_4 contributed to net Arctic warming were much smaller over this time period (-10% and 7%, respectively).

The Arctic warming rate associated with CO_2 emissions is projected to accelerate from 0.285 °C/decade during 1990–2015 to 0.354°C/decade for 2015–2030 according to the shared socioeconomic pathway (SSP) 2–4.5 scenario. Based on the assumption that the world follows a path in which social, economic, and technological trends that affect CO_2 emissions do not shift markedly from historical patterns, this scenario is compatible with the assumptions that were used for emissions scenarios for sulfur and other SLCFs from the IIASA-GAINS model (Chapter 2). Over the same time periods outlined above, the projected Arctic warming attributable to reductions in global sulfur emissions increases from 0.290°C/decade to 0.363°C/decade under the MFR scenario. Between 2015–2030, continuing reductions in global anthropogenic sulfur emissions will produce a mean warming impact on Arctic temperature that could lie between 69% (CLE scenario) and 103% (MFR scenario) of the warming impact of CO_2 (SSP 2–4.5 scenario). Therefore, global emissions reductions of sulfur could increasingly contribute to Arctic warming in the near term, adding to the accelerating warming impacts of CO_2. This emphasizes the need to address the impacts of near-term sulfur emissions reductions on Arctic climate.

In turn, the cooling impacts of making maximum feasible reductions in global anthropogenic emissions of BC and CH_4 could act to reduce the Arctic warming rate by up to 0.140°C/decade and 0.015°C/decade between 2015–2030. With maximum feasible reductions in global anthropogenic emissions of CH_4 and BC, the key warming SLCFs, the net rate of Arctic warming due to CO_2 and SLCF emissions during 2015–2030 could be reduced by 20%, relative to emissions changes resulting from current legislation. If the maximum feasible emissions reductions are further sustained until 2050, the net Arctic warming due to CO_2 and SLCF emissions between 2015–2050 could be reduced by 25%. However, concurrent maximum feasible reductions of global sulfur emissions could cause the net rate of Arctic warming to increase by 20% (for 2015–2030 and 2015–2050), which would largely offset the cooling impact of reduced global BC and CH_4 emissions.

In summary, based on available scenarios and model simulations, the Arctic will very likely continue to warm rapidly during 2015–2030, mainly due to a combination of strong warming impacts of CO_2 and declining global sulfur emissions on Arctic climate. The confidence in the simulated 1990–2030 impacts on temperature of emissions of CO_2, S, BC, and CH_4 is high regarding the direction of change but medium for the magnitude of change.

Additional emissions scenarios need to be considered to determine the impacts of different future social, economic, and technological trends on CO_2 emissions and Arctic temperature changes after 2030, outside of the SSP 2–4.5 scenario that was used for this assessment.

10.6.5 What is the Arctic climate response to SLCF emissions and emissions reductions, from Arctic Council states, Arctic Observers, and the Rest of the World? What sources and sectors should be prioritized to maximize the climate benefits?

The capacity of SLCF emissions to affect Arctic warming strongly depends on the type of emissions source and where located. Therefore, the response of Arctic warming rates to emissions mitigation actions should be evaluated by considering the different chemical species, the regions in which they are emitted, and the sectors targeted by the mitigation actions.

Under the MFR scenario, emissions of CH_4, BC, OC, CO, NO_X, and VOCs are projected to decline strongly in many regions of the world, including eastern and western Arctic Council Member states, the Rest of Europe, and Asian Observer countries (Japan, People's Republic of China, Republic of India, Republic of Korea, Republic of Singapore). The largest reductions in anthropogenic SLCF emissions are associated with fossil-fuel and biofuel combustion sources in the Asian Observer states and the Rest of the World. Although these emissions produce considerable impacts on Arctic temperatures, emissions from Arctic Council Member states generally affect Arctic

temperatures more (relative to their magnitude). This is because emissions sources located in the Arctic, or are close to the Arctic, affect temperatures locally through SLCFs interacting with radiation, clouds, and surface (snow and ice) albedo.

To slow Arctic warming, it would be efficient to achieve maximum feasible reductions in global BC emissions from fossil-fuel and biofuel sources (land-based emissions from residential and commercial sources; agriculture and waste burning on fields; power plants, energy conversion and extraction; industrial combustion and processing; surface transportation; and waste processing) and from flaring and venting during oil and gas production. The reduction in global anthropogenic emissions of BC (including shipping emissions) under the MFR scenario could slow the rate of Arctic warming between 2015–2050 by 0.074°C/decade more than changes achieved under the CLE scenario. Reducing emissions from oil and gas production in Arctic Council Member states, which is included in the global estimate, would be a particularly efficient way to slow the rate of Arctic warming in comparison to other SLCF emissions sources. Specifically, reducing emissions of BC from oil and gas production is projected to slow Arctic warming by 0.010°C/decade (eastern Arctic Council Member states) and 0.005°C/decade (western Arctic Council Member states), largely due to changes in surface albedo from the deposition of BC on snow. By comparison, reducing emissions of BC from fossil-fuel and biofuel sources is projected to slow Arctic warming by 0.008°C/decade (eastern Arctic Council Member states) and 0.006°C/decade (western Arctic Council Member states).

Reducing global anthropogenic emissions of CH_4 emissions by implementing maximum feasible emissions reduction technologies could slow the rate of Arctic warming during 2015–2050 by 0.048°C/decade, relative to changes under current legislation. This incorporates a contribution of 0.003°C/decade (eastern Arctic Council Member states) and 0.002°C/decade (western Arctic Council Member states) from making maximum feasible reductions to CH_4 emissions from venting during oil and gas production. By comparison, reducing emissions of CH_4 from fossil-fuel and biofuel sources is projected to slow Arctic warming by 0.005°C/decade (eastern Arctic Council Member states) and 0.001°C/decade (western Arctic Council Member states). Overall, making maximum feasible reductions in CH_4 emissions from Arctic Council Member states would yield only moderate benefits for the Arctic climate, compared to CH_4 emission cuts in the Rest of the World.

Depending on the specific emissions source and mitigation strategy, the introduction of best available technologies for tackling air pollutants can, but will not necessarily, lead to equivalent reductions in emissions of sulfur, in addition to the reducing BC emissions. Projected Arctic warming between 2015–2050 is considerably enhanced by declining sulfur emissions from fossil-fuel and biofuel sources in eastern and western Arctic Council Member states, the Rest of Europe, and Asian Observers under the MFR scenario. Contributions of sulfur emissions from oil and gas production to total anthropogenic sulfur emissions are relatively minor, and are not expected to produce any notable impacts on the Arctic climate. Their impacts have not been assessed for this report.

10.6.6 Will Arctic nations have the ability to influence climate and air-quality impacts by mitigating anthropogenic emissions?

With current legislation, the projected total contribution of anthropogenic SLCF emissions from eastern and western Arctic Council Member states to Arctic warming between 2015–2050 is 0.057°C/decade, based on interactions of CH_4 and aerosols (SO_4, BC, OC) with radiation, clouds, and surface albedo. By comparison, the projected total contribution of global anthropogenic SLCF emissions to Arctic warming is 0.131°C/decade. Therefore, 44% of the net warming contribution of global anthropogenic SLCF emissions could be associated with emissions from Arctic Council Member states, which corresponds to 12% of the projected net warming impact of combined global SLCF and CO_2 emissions.

Future BC reductions in Arctic Council states would be particularly beneficial for the Arctic climate, compared to cuts made in other countries. Following the MFR scenario, the reduction in anthropogenic BC emissions from Arctic Council states would contribute approximately 6% of the global BC emissions reduction, relative to the CLE scenario. This would cause 39% of the Arctic cooling impact from declining global BC emissions, relative to the current legislation – considerably more than the change in corresponding BC emissions. With regard to the role of different emissions sectors, reducing BC emissions from gas flaring in Arctic Council countries would account for approximately 1% of the global BC emissions reduction, yet this would cause 20% of the Arctic cooling impact from declining global BC emissions, relative to current legislation.

Regardless of the high efficacy of reductions in BC emissions from Arctic Council Member states, the net impact of making maximum feasible reductions in SLCF emissions from Arctic Council Member states on future Arctic warming could be small, due to near compensation of cooling impacts from reduced BC and CH_4 emissions (0.029°C/decade and 0.010°C/decade, respectively) and warming impacts from reduced sulfur emissions (0.029°C/decade) between 2015–2050, relative to currently legislated emissions reductions.

10.7 Impacts of air pollution on health, ecosystems, and crops (Chapter 9)

10.7.1 What are the potential present-day impacts of pollutant emissions on human health, ecosystems and crop yields, and what benefits can be achieved in the future by mitigating emissions?

BC affects health as a component of $PM_{2.5}$, and CH_4 affects health by contributing to tropospheric O_3 concentrations. Together, $PM_{2.5}$ and O_3 are among the ten leading health-risk factors in all Arctic Council Member states and Observer countries, according to the Institute for Health Metrics and Evaluation (IHME) Global Burden of Disease (GBD) 2017 Study. The

contribution of ambient air pollution to premature mortality ranges from 2%–3% in Nordic countries to 13% in India. While climate change is expected to result in negative consequences for human health, it has not yet been included in the prominent GBD study. Therefore, little information is currently available about the burden of disease from climate change, either globally, in individual countries, or in the Arctic specifically.

Maximum feasible reductions in global SLCF emissions could produce large improvements in air quality in all Arctic Council Member states and Asian Observer countries, relative to current legislation. For Asian Observer countries, maximum feasible reductions in emissions could lead to particularly large reductions in annual mean anthropogenic $PM_{2.5}$ concentrations (up to 60% by 2030, relative to 2015). In addition, large reductions in annual mean surface O_3 concentrations (up to 20%) for Arctic Council Member states and Asian Observers are also achieved by making maximum feasible reductions in all O_3-precursor emissions (mainly from fossil-fuel and biofuel sources), both local to the Arctic and remote.

Policies and control measures that reduce SLCFs would also reduce other co-emitted air pollutants, influencing overall $PM_{2.5}$ and O_3 levels. The health impacts from future emissions changes under business-as-usual or other policy scenarios therefore extend beyond the health benefits achieved from reduced SLCFs. New modeling undertaken for this assessment indicates that mortality associated with $PM_{2.5}$ globally could be 24% lower by 2030 and 4.5% lower by 2050 compared with 2015 under current legislation, due mainly to declining $PM_{2.5}$ concentrations from policies that reduce SO_2 emissions. For the Arctic Council Member states in particular, current air-pollution legislation leads to even more substantial declines in annual mortality attributed to $PM_{2.5}$ by 2030 (-59%; -66,000 deaths) and 2050 (-57%; -64,000 deaths) compared to 2015. In contrast, global O_3 mortality could increase by 17% in 2030 and by almost 60% in 2050, compared with 2015, due to steady O_3 concentrations but growing exposed populations. The influence of population changes is particularly important in Arctic Council Observer countries – especially in Asia – where significant population growth is anticipated in the future. O_3 mortality increases slightly compared to 2015 in the Arctic Council Member states in both 2030 and 2050 under current legislation (16% increment; ~4,000 deaths annually).

Given the use of maximum feasible technologies, global $PM_{2.5}$ mortality is estimated to drop by 22% and 26% in 2030 and 2050, respectively, compared with the current legislation scenario. For Arctic Council Member states in particular, such reductions result in a further decline in $PM_{2.5}$ mortality compared to current legislation (approximately -87% or -97,000 deaths in 2030 and 2050, respectively). For Observer countries, while declines in $PM_{2.5}$ mortality occur in 2030 compared to 2015, $PM_{2.5}$ mortality increases in 2050 compared to 2030 (from -28% or 540,000 fewer deaths in 2030 to -12% or 235,000 fewer deaths in 2050 under current legislation, and from -45% or 880,000 fewer deaths in 2030 to -40% or 790,000 fewer deaths in 2050 given maximum feasible emissions reductions, compared to 2015 estimates). In addition, global mortality from O_3 changes from a future increase under the CLE scenario to a future decrease under the MFR scenario, compared with the present day. Maximum feasible control technologies are projected to reduce global O_3 mortality by 42% in 2030 and 53% in 2050 compared with current legislation. In the Arctic Council Member states, O_3 mortality decreases in both 2030 and 2050 under maximum feasible controls, with a larger drop during the first period (-20% or 5,700 fewer deaths by 2030 and -24% or 6,900 fewer deaths by 2050 compared to 2015).

The findings also indicate that past policies and current legislation will result in the area in which critical loads for acidity and eutrophication are exceeded shrinking to below 1% in the (sub-) Arctic region, with the remaining exceedance areas dropping to quite low values. O_3-related damage to maize, soybean, wetland rice, and wheat is also estimated to decline through current legislation, and to fall further under maximum feasible emissions reductions, towards 2030 and 2050.

Health and crop yields are affected by air pollution, climate, and socio-economic factors simultaneously. While the air-quality improvements simulated under the future emissions scenarios appear very beneficial for health, they would occur simultaneously with changes in other risk factors that also affect population health, including climate change and other non-environmental risk factors. Actions that improve public health overall would result in healthier and more resilient populations who may be better prepared to overcome the negative consequences of anthropogenic climate change and other environmental risk factors.

References

Personal Communications

Andrews, E., 2020. NOAA/ESRL. Tiksi data. Personal communication.

DSB, 2020. Direktoratet for samfunnssikkerhet og beredskap (DSB). Personal communication.

Eleftheriadis, K., 2020. NCSR "Demokritos". Zeppelin data. Personal communication.

Huang, L., 2020. Environment and Climate Change, Canada. Personal communication.

Ketola, J., 2020. Forest fire activity and burned area for Finland, Emergency Services Academy. Personal communication to H. Lindberg, based on rescue service database PRONTO. Available at: https://prontonet.fi/Pronto3/online3/OnlineTilastot.htm (last accessed 13 September 2021).

Klimont, Z., 2020. International Institiute for Applied Systems Analysis (IIASA). Personal communication.

McConnell, J., 2020. DRI. Personal communication.

Saunders, L., 2020. University of Toronto. Personal communication.

Sheese, P., 2020. University of Toronto. Personal communication.

Walker, K., 2020. University of Toronto. Personal communication.

References

Aamaas, B., C.E. Bøggild, F. Stordal, T. Berntsen, K. Holmèn and J. Ström, 2011. Elemental carbon deposition to Svalbard snow from Norwegian settlements and long-range transport. Tellus B: Chemical and Physical Meteorology, 63(3):340–351.

Abatzoglou, J.T. and A.P. Williams, 2016. Impact of anthropogenic climate change on wildfire across western US forests. PNAS, 113(42):11770–11775.

Abbatt, J.P.D., W.R. Leaitch, A.A. Aliabadi, A.K. Bertram, J.-P. Blanchet, A. Boivin-Rioux, H. Bozem, J. Burkart, R.Y.W Chang, J. Charette, J.P. Chaubey, R.J. Christensen, A. Cirisan, D.B. Collins, B. Croft, J. Dionne, G.J. Evans, C.G. Fletcher, M. Galí, R. Ghahremaninezhad, E. Girard, W. Gong, M. Gosselin, M. Gourdal, S.J. Hanna, H. Hayashida, A.B. Herber, S. Hesaraki, P. Hoor, L. Huang, R. Hussherr, V.E. Irish, S.A. Keita, J.K. Kodros, F. Köllner, F. Kolonjari, D. Kunkel, L.A. Ladino, K. Law, M. Levasseur, Q. Libois, J. Liggio, M. Lizotte, K.M. Macdonald, R. Mahmood, R.V. Martin, R.H. Mason, L.A. Miller, A. Moravek, E. Mortenson, E.L Mungall, J.G. Murphy, M. Namazi, A.-L. Norman, N.T. O'Neill, J.R. Pierce, L.M. Russell, J. Schneider, H. Schulz, S. Sharma, M. Si, R.M. Staebler, N.S. Steiner, J.L. Thomas, K. von Salzen, J.J.B. Wentzell, M.D. Willis, G.R. Wentworth, J.-W. Xu and J.D. Yakobi-Hancock, 2019. Overview paper: New insights into aerosol and climate in the Arctic. Atmospheric Chemistry and Physics, 19: 2527–2560.

Abdelmonem, A., M. Schnaiter, P. Amsler, E. Hesse, J. Meyer and T. Leisner, 2011. First correlated measurements of the shape and light scattering properties of cloud particles using the novel Particle Habit Imaging and Polar Scattering (PHIPS) probe. Atmospheric Measurement Techniques, 4(10):2125–2142.

Abdul-Razzak, H. and S.J. Ghan, 2002. A parameterization of aerosol activation 3. Sectional representation. Journal of Geophysical Research: Atmospheres, 107(D3):AAC1.1–AAC1.6.

Achakulwisut, P., M. Brauer, P. Hystad and S.C. Anenberg, 2019. Global, national, and urban burdens of paediatric asthma incidence attributable to ambient NO_2 pollution: estimates from global datasets. The Lancet Planetary Health, 3(4):e166–e178.

Achard, F., H.D. Eva, D. Mollicone and R. Beuchle, 2008. The effect of climate anomalies and human ignition factor on wildfires in Russian boreal forests. Philosophical Transactions of the Royal Society B: Biological Sciences, 363(1501):2329–2337.

Acosta Navarro, J.C., V. Varma, I. Riipinen, Ø. Seland, A. Kirkevåg, H. Struthers, T. Iversen, H.-C. Hansson and A.M.L. Ekman, 2016. Amplification of Arctic warming by past air pollution reductions in Europe. Nature Geoscience, 9:277–281.

Ahtikoski, A. and H. Hökkä, 2019. Intensive forest management — does it pay off financially on drained peatlands? Canadian Journal of Forest Research, 49(9):1101–1113.

Akagi, S.K., R.J. Yokelson, C. Wiedinmyer, M.J. Alvarado, J.S. Reid, T. Karl, J.D. Crounse and P.O Wennberg, 2011. Emission factors for open and domestic biomass burning for use in atmospheric models. Atmospheric Chemistry and Physics, 11(9):4039–4072.

Alaska Division of Forestry, 2020a. Alaska 2019 Fire Numbers. Available at: http://forestry.alaska.gov/Assets/pdfs/firestats/2019%20Alaska%20Fire%20Statistics.pdf

Alaska Division of Forestry, 2020b. Despite heavy snow melt, Deshka Landing hot spots still smoldering. Available at: https://akfireinfo.com/2020/04/24/despite-heavy-snow-melt-deshka-landing-hot-spots-still-smoldering/

Alexander, H.D. and M.C. Mack, 2017. Gap regeneration within mature deciduous forests of Interior Alaska: implications for future forest change. Forest Ecology and Management, 396:35–43.

Alexander, B., R.J. Park, D.J. Jacob and S. Gong, 2009. Transition metal-catalyzed oxidation of atmospheric sulfur: Global implications for the sulfur budget. Journal of Geophysical Research: Atmospheres, 114(D2).

Aliabadi, A.A., R.M. Staebler and S. Sharma, 2015. Air quality monitoring in communities of the Canadian Arctic during the high shipping season with a focus on local and marine pollution. Atmospheric Chemistry and Physics, 15(5):2651–2673.

Aliabadi, A.A., J.L. Thomas, A.B. Herber, R.M. Staebler, W.R. Leaitch, H. Schulz, K.S. Law, L. Marelle, J. Burkart, M.D. Willis, H. Bozem, P.M. Hoor, F. Köllner, J. Schneider, M. Levasseur and J.P.D. Abbatt, 2016. Ship emissions measurement in the Arctic by plume intercepts of the Canadian Coast Guard icebreaker *Amundsen* from the *Polar 6* aircraft platform. Atmospheric Chemistry and Physics, 16(12):7899–7916.

Allchin, M.I. and S.J. Déry, 2020. The Climatological context of trends in the onset of Northern Hemisphere seasonal snow cover 1972–2017. Journal of Geophysical Research: Atmospheres, 125(17):e2019JD032367.

Alvarez, R.A., D. Zavala-Araiza, D.R. Lyon, D.T. Allen, Z.R. Barkley, A.R. Brandt, K.J. Davis, S.C. Herndon, D.J. Jacob, A. Karion, E.A. Kort, B.K. Lamb, T. Lauvaux, J.D. Maasakkers, A.J. Marchese, M. Omara, S.W. Pacala, J. Peischl, A.L. Robinson, P.B. Shepson, C. Sweeney, A. Townsend-Small, S.C. Wofsy and S.P. Hamburg, 2018. Assessment of methane emissions from the U.S. oil and gas supply chain. Science, 361(6398):186–188.

Amann, M., I. Bertok, J. Borken-Kleefled, J. Cofala, C. Heyes, L. Höglund-Isaksson, Z. Klimont, B. Nguyen, M. Posch, P. Rafaj, R. Sandler, W. Schöpp, F. Wagner and W. Winiwarter, 2011. Cost-effective control of air quality and greenhouse gases in Europe: modeling and policy applications. Environmental Modelling & Software, 26(12):1489–1501.

Amann, M., Z. Klimont and F. Wagner, 2013. Regional and global emissions of air pollutants: recent trends and future scenarios. Annual Review of Environment and Resources, 38:31–55.

AMAP, 1998. AMAP Assessment Report: Arctic Pollution Issues. Arctic Monitoring and Assessment Programme (AMAP), Oslo, Norway. xii + 859pp.

AMAP, 2006. AMAP Assessment 2006: Acidifying Pollutants, Arctic Haze, and Acidification in the Arctic. Arctic Monitoring and Assessment Programme (AMAP), Oslo, Norway. xii + 112pp.

AMAP, 2011. The impact of black carbon on Arctic climate. Arctic Monitoring and Assessment Programme (AMAP), Oslo, Norway. ii + 72pp.

AMAP, 2015a. AMAP Assessment 2015: Black carbon and ozone as Arctic climate forcers. Arctic Monitoring and Assessment Programme (AMAP), Oslo, Norway. vii + 116pp.

AMAP, 2015b. AMAP Assessment 2015: Methane as an Arctic climate forcer. Arctic Monitoring and Assessment Programme (AMAP), Oslo, Norway. vii + 139pp.

Amini, H., C. Dehlendorff, Y-H. Lim, A. Mehta, J.T. Jørgensen, L.H. Mortensen, R. Westendorp, B. Hoffmann, S. Loft, T. Cole-Hunter, E.V. Bräuner, M. Ketzel, O. Hertel, J. Brandt, S. Solvang Jensen, J.H. Christensen, C. Geels, L.M. Frohn, C. Backalarz, M.K. Simonsen and Z.J. Andersen, 2020. Long-term exposure to air pollution and stroke incidence: a Danish Nurse cohort study. Environment International, 142:105891.

Amos, H.M., D.J. Jacob, C.D. Holmes, J.A. Fisher, Q. Wang, R.M. Yantosca, E.S. Corbitt, E. Galarneau, A.P. Rutter, M.S. Gustin, A. Steffen, J.J.

Schauer, J.A. Graydon, V.L. St. Louis, R.W. Talbot, E.S. Edgerton, Y. Zhang and E.M. Sunderland, 2012. Gas-particle partitioning of atmospheric Hg(II) and its effect on global mercury deposition. Atmospheric Chemistry and Physics, 12:591–603.

Ancellet, G., N. Daskalakis, J.C. Raut, D. Tarasick, J. Hair, B. Quennehen, F. Ravetta, H. Schlager, A.J. Weinheimer, A.M. Thompson, B. Johnson, J.L. Thomas and K.S. Law, 2016. Analysis of the latitudinal variability of tropospheric ozone in the Arctic using the large number of aircraft and ozonesonde observations in early summer 2008. Atmospheric Chemistry and Physics, 16(20):13341–13358.

Andersen, M.S., L.M. Frohn, J.S. Nielsen, M. Nielsen, J.B. Jensen, S.S. Jensen, J.H. Christensen and J. Brandt, 2008. A non-linear Eulerian approach for assessment of health-cost externalities of air pollution. European Association of Environmental and Resource Economists 16th Annual Conference. 25–28 June 2008, Gothenburg, Sweden. pp. 1–23.

Andersen, Z.J., L. Ravnskjær, K.K. Andersen, S. Loft, J. Brandt, T. Becker, M. Ketzel, O. Hertel, E. Lynge and E.V. Bräuner, 2017. Long-term exposure to fine particulate matter and breast cancer incidence in the Danish Nurse Cohort Study. Cancer Epidemiology, Biomarkers & Prevention, 26(3):428–430.

Anderson, Z.J., P. Wahlin, O. Raaschou-Nielsen, T. Scheike and S. Loft, 2007. Ambient particle source apportionment and daily hospital admissions among children and elderly in Copenhagen. Journal of Exposure Science & Environmental Epidemiology, 17:625–636.

Andersson, C., J. Langner and R. Bergström, 2007. Interannual variation and trends in air pollution over Europe due to climate variability during 1958–2001 simulated with a regional CTM coupled to the ERA-40 reanalysis. Tellus B: Chemical and Physical Meteorology, 59(1):77–98.

Andersson, C., R. Bergström, C. Bennet, L. Robertson, M. Thomas, H. Korhonen, K.E.J Lehtinen and H. Kokkola, 2015. MATCH-SALSA – Multi-scale Atmospheric Transport and CHemistry model coupled to the SALSA aerosol microphysics model – Part 1: Model description and evaluation. Geoscientific Model Development, 8(2):171–189.

Andersson, C., H. Alpfjord, L. Robertson, P.E. Karlsson and M. Engardt, 2017. Reanalysis of and attribution to near-surface ozone concentrations in Sweden during 1990–2013. Atmospheric Chemistry and Physics, 17(22):13869–13890.

Andreae, M.O., 2019. Emission of trace gases and aerosols from biomass burning – an updated assessment. Atmospheric Chemistry and Physics, 13(19):8523–8546.

Andreae, M.O. and P. Merlet, 2001. Emission of trace gases and aerosols from biomass burning. Global biogeochemical cycles, 15(4):955–966.

Andres, R.J. and A.D. Kasgnoc, 1998. A time-averaged inventory of subaerial volcanic sulfur emissions. Journal of Geophysical Research: Atmospheres, 103(D19):25251–25261.

Anenberg, S.C., A. Belova, J. Brandt, N. Fann, S. Greco, S. Guttikunda, M.-E. Heroux, F. Hurley, M. Krzyzanowski, S. Medina, B. Miller, K. Pandey, J. Roos and R. Van Dingenen, 2016. Survey of ambient air pollution health risk assessment tools. Risk Analysis, 36(9): 1718–1736.

Ångström, A., 1929. On the atmospheric transmission of sun radiation and on dust in the air. Geografiska Annaler, 11:156–166.

Antonsen, S., P.L.H. Mok, R.T. Webb, P.B. Mortensen, J.J. McGarth, E. Agerbro, J. Brandt, C. Geels, J.H. Christensen and C.B. Pedersen, 2020. Exposure to air pollution during childhood and risk of developing schizophrenia: a national cohort study. The Lancet Planetary Health, 4(2):e64–e73.

Archer, D., 2007. Methane hydrate stability and anthropogenic climate change. Biogeosciences, 4(4):521–544.

Archer, D., 2015. A model of the methane cycle, permafrost, and hydrology of the Siberian continental margin. Biogeosciences, 12(10):2953–2974.

Archibald, A.T., F.M. O'Connor, N.L. Abraham, S. Archer-Nicholls, M.P. Chipperfield, M. Dalvi, G.A. Folberth, F. Dennison, S.S. Dhomse, P.T. Griffiths, C. Hardacre, A.J. Hewitt, R.S. Hill, C.E. Johnson, J. Keeble, M.O. Köhler, O. Morgenstern, J.P. Mulchay, C. Ordóñez, R.J. Pope, S.T. Rumbold, M.R. Russo, N.H. Savage, A. Sellar, M. Stringer, S.T. Turnock, O. Wild and G. Zeng, 2020. Description and evaluation of the UKCA stratosphere-troposphere chemistry scheme (StratTrop vn 1.0) implemented in UKESM1. Geoscientific Model Development, 13:1223–1266.

Arctic Council, 2015. Enhanced Black Carbon and Methane Emissions Reductions: an Arctic Council Framework for Action (Annex 4. Iqaluit 2015 Senior Arctic Officials report to Ministers). Arctic Council Secretariat, Tromsø, Norway. 12pp.

Arctic Council, 2017. Expert Group on Black Carbon and Methane; Summary of Progress and Recommendations. Arctic Council Secretariat, Tromsø, Norway. 49pp.

Arctic Council, 2019. Expert Group on Black Carbon and Methane; Summary of Progress and Recommendations 2019. Arctic Council Secretariat, Tromsø, Norway. 88pp.

Ardyna, M., M. Babin, M. Gosselin, E. Devred, L. Rainville and J.-É. Tremblay, 2014. Recent Arctic Ocean sea ice loss triggers novel fall phytoplankton blooms. Geophysical Research Letters, 41(17):6207–6212.

Arnold, S.R., L.K. Emmons, S.A. Monks, K.S. Law, D.A. Ridley, S. Turquety, S. Tilmes, J.L. Thomas, I. Bouarar, J. Flemming, V. Huijnen, J. Mao, B.N. Duncan, S. Steenrod, Y. Yoshida, J. Langner and Y. Long, 2015. Biomass burning influence on high-latitude tropospheric ozone and reactive nitrogen in summer 2008: a multi-model analysis based on POLMIP simulations. Atmospheric Chemistry and Physics, 15(11):6047–6068.

Arnold, S.R., K.S. Law, C.A. Brock, J.L. Thomas, S.M. Starkweather, K. von Salzen, A. Stohl, S. Sharma, M.T. Lund, M.G. Flanner, T. Petäjä, H. Tanimoto, J. Gamble, J.E. Dibb, M. Melamed, N. Johnson, M. Fidel, V.-P. Tynkkynen, A. Baklanov, S. Eckhardt, S.A. Monks, J. Browse and H. Bozem, 2016. Arctic air pollution: challenges and opportunities for the next decade. Elementa: Science of the Anthropocene, 4:000104.

Arp, C.D., B.M. Jones, G. Grosse, A.C. Bondurant, V.E. Romanovsky, K.M. Hinkel and A.D. Parsekian, 2016. Threshold sensitivity of shallow Arctic lakes and sublake permafrost to changing winter climate. Geophysical Research Letters, 43(12):6358–6365.

Astrup, R., P.Y. Bernier, H. Genet, D.A. Lutz and R.M. Bright, 2018. A sensible climate solution for the boreal forest. Nature Climate Change, 8(1):11–12.

Avnery, S., D.L. Mauzerall, J. Liu and L.W. Horowitz, 2011. Global crop yield reductions due to surface ozone exposure: 1. Year 2000 crop production losses and economic damage. Atmospheric Environment, 45(13):2284–2296.

Baars, H., T. Kanitz, R. Engelmann, D. Althausen, B. Heese, M. Komppula, J. Preißler, M. Tesche, A. Ansmann, U. Wandinger, J.-H. Lim, J.Y. Ahn, I.S. Stachlewska, V. Amiridis, E. Marinou, P. Seifert, J. Hofer, A. Skupin, F. Schneider, S. Bohlmann, A. Foth, S. Bley, A. Pfüller, E. Giannakaki, H. Lihavainen, Y. Viisanen, R.K. Hooda, S.N. Pereira, D. Bortoli, F. Wagner, I. Mattis, L. Janicka, K.M. Markowicz, P. Achtert, P. Artaxo, T. Pauliquevis, R.A.F. Souza, V.P. Sharma, P.G. van Zyl, J.P. Beukes, J. Sun, E.G. Rohwer, R. Deng, R.-E. Mamouri and F. Zamorano, 2016. An overview of the first decade of Polly^{NET}: an emerging network of automated Raman-polarization lidars for continuous aerosol profiling. Atmospheric Chemistry and Physics 16(8):5111–5137.

Bachelder, J., M. Cadieux, C. Liu-Kang, P. Lambert, A. Filoche, J.A. Galhardi, M. Hadioui, A. Chaput, M.-P. Bastien-Thibault, K.J. Wilkinson, J. King and P.L. Hayes, 2020. Chemical and microphysical properties of wind-blown dust near an actively retreating glacier in Yukon, Canada. Aerosol Science and Technology, 54(1):2–20.

Backman, J., L. Schmeisser, A. Virkkula, J.A. Ogren, E. Asmi, S. Starkweather, S. Sharma, K. Eleftheriadis, T. Uttal, A. Jefferson, M. Bergin, A. Makshtas, P. Tunved and M. Fiebig, 2017. On Aethalometer measurement uncertainties and an instrument correction factor for the Arctic. Atmospheric Measurement Techniques, 10:5039–5062.

Bahramvash Shams, S., V.P. Walden, I. Petropavlovskikh, D. Tarasick, R. Kivi, S. Oltmans, B. Johnson, P. Cullis, C.W. Sterling, L. Thölix and Q. Errera, 2019. Variations in the vertical profile of ozone at four high-latitude Arctic sites from 2005 to 2017. Atmospheric Chemistry and Physics, 19(15):9733–9751.

Baibakov, K., N.T. O'Neill, L. Ivanescu, T.J. Duck, C. Perro, A. Herber, K.-H. Schulz and O. Schrems, 2015. Synchronous polar winter starphotometry and lidar measurements at a High Arctic station. Atmospheric Measurement Techniques, 8(9):3789–3809.

Baker, L.H., W.J. Collins, D.J.L., Olivié, R. Cherian, Ø. Hodnebrog, G. Myhre and J. Quaas, 2015. Climate responses to anthropogenic emissions of short-lived climate pollutants. Atmospheric Chemistry and Physics, 15(14),:8201–8216.

Baldocchi, D., 2008. 'Breathing' of the terrestrial biosphere: lessons learned from a global network of carbon dioxide flux measurement systems. Australian Journal of Botany, 56(1):1–26.

Barnhart, K.R., C.R. Miller, I. Overeem and J.E. Kay, 2016. Mapping the future expansion of Arctic open water. Nature Climate Change, 6:280–285.

Barreto, A., R. Román, E. Cuevas, D. Pérez-Ramírez, A.J. Berjón, N. Kouremeti, S. Kazadzis, J. Gröbner, M. Mazzola, C. Toledano, J.A. Benavent-Oltra, L. Doppler, J. Juryšek, A.F. Almansa, S. Victori, F.

Maupin, C. Guirado-Fuentes, R. González, V. Vitale, P. Goloub, L. Blarel, L. Alados-Arboledas, E. Woolliams, S. Taylor, J.C. Antuña and M. Yela, 2019. Evaluation of night-time aerosols measurements and lunar irradiance models in the frame of the first multi-instrument nocturnal intercomparison campaign. Atmospheric Environment, 202:190–211.

Bartlett, K.B. and R.C Harriss, 1993. Review and assessment of methane emissions from wetlands. Chemosphere, 26(1–4):261–320.

Barrett, T.E., E.M. Robinson, S. Usenko, and R.J. Sheesley, 2015. Source contributions to wintertime elemental and organic carbon in the Western Arctic based on radiocarbon and tracer apportionment. Environmental Science & Technology, 49(19):11631–11639.

Barrie, L.A, 1986. Arctic air-pollution: An overview of current knowledge. Atmospheric Environment, 20(4):643–663.

Barrie, L.A, J.W. Bottenheim, R.C. Schnell, P.J. Crutzen and R.A. Rasmussen, 1988. Ozone destruction and photochemical reactions at polar sunrise in the lower Arctic atmosphere. Nature, 334:138–141.

Bastviken, D., J. Cole, M. Pace and L. Tranvik, L, 2004. Methane emissions from lakes: Dependence of lake characteristics, two regional assessments, and a global estimate. Global Biogeochemical Cycles, 18(4):GB4009.

Bastviken, D., L.J. Tranvik, J.A. Downing, P.M. Crill and A. Enrich-Prast, 2011. Freshwater methane emissions offset the continental carbon sink. Science, 331(6013):50.

Bauer, S.E. and D. Koch, 2005. Impact of heterogeneous sulfate formation at mineral dust surfaces on aerosol loads and radiative forcing in the Goddard Institute for Space Studies general circulation model. Journal of Geophysical Research: Atmospheres, 110(D17).

Bauer, S.E., D. Koch, N. Unger, S.M. Metzger, D.T. Shindell and D.G. Streets, 2007a. Nitrate aerosols today and in 2030: a global simulation including aerosols and tropospheric ozone. Atmospheric Chemistry and Physics, 7(19):5043–5059.

Bauer, S.E., M.I. Mishchenko, A.A. Lacis, S. Zhang, J Perlwitz and S.M. Metzger, 2007b. Do sulfate and nitrate coatings on mineral dust have important effects on radiative properties and climate modeling? Journal of Geophysical Research: Atmospheres, 112(D6).

Bauer, S.E., K. Tsigaridis, G. Faluvegi, M. Kelley, K.K. Lo, R.L. Miller, L. Nazarenko, G.A. Schmidt and J. Wu, 2020. Historical (1850–2014) aerosol evolution and role on climate forcing using the GISS ModelE2.1 contribution to CMIP6. Journal of Advances in Modeling Earth Systems, 12(8) e2019MS001978.

Baumgardner, D., R. Newton, M. Krämer, J. Meyer, A. Beyer, M. Wendisch and P. Vochezer, 2014. The Cloud Particle Spectrometer with Polarization Detection (CPSPD): A next generation open-path cloud probe for distinguishing liquid cloud droplets from ice crystals. Atmospheric Research, 142:2–14.

Baumgardner, D., S.J. Abel, D. Axisa, R. Cotton, J. Crosier, P. Field, C. Gurganus, A. Heymsfield, A. Korolev, M. Krämer, P. Lawson, G. McFarquhar, Z. Ulanowski and J. Um, 2017. Cloud ice properties: in situ measurement challenges. Meteorological Monographs, 58(1): 9.1–9.23.

Bayer, T.K., E. Gustafsson, M. Brakebusch and C. Beer, 2019. Future carbon emission from boreal and permafrost lakes are sensitive to catchment organic carbon loads. Journal of Geophysical Research: Biogeosciences, 124(7):1827–1848.

Becagli, S., C. Ghedini, S. Peeters, A. Rottiers, R. Traversi, R. Udisti, M. Chiari, A. Jalba, S. Despiau, U. Dayan and A. Temara, 2011. MBAS (methylene blue active substances) and LAS (linear alkylbenzene sulphonates) in Mediterranean coastal aerosols: sources and transport processes. Atmospheric Environment, 45(37):6788–6801.

Becagli S., A. Amore, L. Caiazzo, T. Di Iorio, A. di Sarra, L. Lazzara, C. Marchese, D. Meloni, G. Mori, G. Muscari, C. Nuccio, G. Pace, M. Severi and R. Traversi, 2019. Biogenic aerosol in the Arctic from eight years of MSA data from Ny Ålesund (Svalbard Islands) and Thule (Greenland). Atmosphere, 10(7):349.

Bellouin, N., J. Quaas, E. Gryspeerdt, S. Kinne, P. Stier, D. Watson-Parris, O. Boucher, K.S. Carslaw, M. Christensen, A.-L. Daniau, J.-L. Dufresne, G. Feingold, S. Fiedler, P. Forster, A. Gettelman, J.M. Haywood, U. Lohmann, F. Malavelle, T. Mauritsen, D.T. McCoy, G. Myhre, J. Mülmenstädt, D. Neubauer, A. Possner, M. Rugenstein, Y. Sato, M. Schulz, S.E. Schwartz, O. Sourdeval, T. Storelvmo, V. Toll, D. Winker and B. Stevens, 2020. Bounding global aerosol radiative forcing of climate change. Reviews of Geophysics, 58(1):e2019RG000660.

Bennartz, R., 2007. Global assessment of marine boundary layer cloud droplet number concentration from satellite. Journal of Geophysical Research: Atmospheres, 112(D2).

Bennartz, R. and J. Rausch, 2017. Global and regional estimates of warm cloud droplet number concentration based on 13 years of AQUA-MODIS observations. Atmospheric Chemistry and Physics, 17(16):9815–9836.

Bentsen, M., I. Bethke, J.B. Debernard, T. Iversen, A. Kirkevåg, Ø. Seland, H. Drange, C. Roelandt, I.A. Seierstad, C. Hoose and J.E. Kristjánsson, 2013. The Norwegian Earth System Model, NorESM1-M – Part 1: Description and basic evaluation of the physical climate. Geoscientific Model Development, 6:687–720.

Berchet, A., I. Pison, P.M. Crill, B. Thornton, P. Bousquet, T. Thonat, T. Hocking, J. Thanwerdas, J.-D. Paris and M. Saunois, 2020. Using ship-borne observations of methane isotopic ratio in the Arctic Ocean to understand methane sources in the Arctic. Atmospheric Chemistry and Physics, 20(6):3987–3998.

Berchet, A., P. Bousquet, I. Pison, R. Locatelli, F. Chevallier, J.-D.Paris, E.J. Dlugokencky, T. Laurila, J. Hatakka, Y. Viisanen, D.E.J. Worthy, E. Nisbet, R. Fisher, J. France, D. Lowry, V. Ivakhov and O. Hermansen, 2016. Atmospheric constraints on the methane emissions from the East Siberian Shelf. Atmospheric Chemistry and Physics, 16(6):4147–4157.

Bergström, R., H.A.C. Denier van der Gon, A.S.H. Prévôt, K.E. Yttri and D. Simpson, 2012. Modelling of organic aerosols over Europe (2002–2007) using a volatility basis set (VBS) framework: application of different assumptions regarding the formation of secondary organic aerosol. Atmospheric Chemistry and Physics, 12(18):8499–8527.

Bernath, P.F., C.T. McElroy, M.C. Abrams, C.D. Boone, M. Butler, C. Camy-Peyret, M. Carleer, C. Clerbaux, P.-F. Coheur, R. Colin, P. DeCola, M. DeMazière, J.R. Drummond, D. Dufour, W.F.J. Evans, H. Fast, D. Fussen, K. Gilbert, D.E. Jennings, E.J. Llewellyn, R.P. Lowe, E. Mahieu, J.C. McConnell, M. McHugh, S.D. McLeod, R. Michaud, C. Midwinter, R. Nassar, F. Nichitiu, C. Nowlan, C.P. Rinsland, Y.J. Rochon, N. Rowlands, K. Semeniuk, P. Simon, R. Skelton, J.J. Sloan, M.-A. Soucy, K. Strong, P. Tremblay, D. Turnbull, K.A. Walker, L. Walkty, D.A. Wardle, V. Wehrle, R. Zander and J. Zou, 2005. Atmospheric Chemistry Experiment (ACE): mission overview. Geophysical Research Letters 32(15):L15S01.

Berrisford, P., D.P. Dee, P. Poli, R. Brugge, M. Fielding, M. Fuentes, P.W. Kållberg, S. Kobayashi, S. Uppala and A. Simmons, 2011. The ERA-Interim archive Version 2.0, ERA Report Series. 23pp.

Bevan, S.L., P.R.J. North, S.O. Los and W.M.F. Grey, 2012. A global dataset of atmospheric aerosol optical depth and surface reflectance from AATSR. Remote Sensing of Environment, 116:199–210.

Bey, I., D.J. Jacob, R.M. Yantosca, J.A. Logan, B.D. Field, A.M. Fiore, Q. Li, H.Y. Liu, L.J. Mickley and M.G. Schultz, 2001. Global modeling of tropospheric chemistry with assimilated meteorology: model description and evaluation. Journal of Geophysical Research: Atmospheres, 106(D19):23073–23095.

Bintanja, R. and O. Andry, 2017. Towards a rain-dominated Arctic. Nature Climate Change, *7*(4):263–267.

Bintanja, R., K. van der Wiel, E.C. van der Linden, J. Reusen, L. Bogerd, F. Krikken and F.M. Selten, 2020. Strong future increases in Arctic precipitation variability linked to poleward moisture transport. Science Advances, 6(7):eaax6869.

Bižić, M., T. Klintzsch, D. Ionescu, M.Y. Hindiyeh, M. Günthel, A.M. Muro-Pastor, W. Eckert, T. Urich, F. Keppler and H.P. Grossart, 2020. Aquatic and terrestrial cyanobacteria produce methane. Science Advances, 6(3):eaax5343.

Björkman, M.P., R. Kühnel, D.G. Partridge, T.J. Roberts, W. Aas, M. Mazzola, A. Viola, A. Hodson, J. Ström and E. Isaksson, 2013. Nitrate dry deposition in Svalbard. Tellus B: Chemical and Physical Meteorology, 65(1):19071.

Blechschmidt, A.-M., J.E. Kristjánsson, H. Ólafsson, J.F. Burkhart, Ø. Hodnebrog and P.D. Rosenberg, 2012. Aircraft-based observations and high-resolution simulations of an Icelandic dust storm. Atmospheric Chemistry and Physics, 12(22):10649–10666.

Blouin, K.D., M.D. Flannigan, X. Wang and B. Kochtubajda, 2016. Ensemble lightning prediction models for the province of Alberta, Canada. International Journal of Wildland Fire, 25(4):421–432.

Boeke, R.C. and P.C. Taylor, 2016. Evaluation of the Arctic surface radiation budget in CMIP5 models. Journal of Geophysical Research: Atmospheres, 121(14):8525–8548.

Bogoyavlensky, V., I. Bogoyavlensky, R. Nikonov and A. Kishankov, 2020. Complex of geophysical studies of the Seyakha catastrophic gas blowout crater on the Yamal Peninsula, Russian Arctic. Geosciences, 10(6):215.

Bond, T.C. and R.W. Bergstrom, 2006. Light absorption by carbonaceous particles: an investigative review. Aerosol Science and Technology, 40(1):27–67.

Bond, T.C., D.G. Streets, K.F. Yarber, S.M. Nelson, J.-H. Woo and Z. Klimont, 2004. A technology-based global inventory of black and organic carbon emissions from combustion. Journal of Geophysical Research: Atmospheres, 109(D14).

Bond, T.C., S.J. Doherty, D.W. Fahey, P.M. Forster, T. Berntsen, B.J. DeAngelo, M.G. Flanner, S. Ghan, B. Kärcher, D. Koch, S. Kinne, Y. Kondo, P.K. Quinn, M.C. Sarofim, M.G. Schultz, M. Schulz, C. Venkataraman, H. Zhang, S. Zhang, N. Bellouin, S.K. Guttikunda, P.K. Hopke, M.Z. Jacobson, J.W. Kaiser, Z. Klimont U. Lohmann, J.P. Schwarz, D. Shindell, T. Storelvmo, S.G. Warren and C.S. Zender, 2013. Bounding the role of black carbon in the climate system: a scientific assessment. Journal of Geophysical Research: Atmospheres, 118(11):5380–5552.

Booker, F., R. Muntifering, M. McGrath, K. Burkey, D. Decoteau, E. Fiscus, W. Manning, S. Krupa, A. Chappelka and D. Grantz, 2009. The ozone component of global change: potential effects on agricultural and horticultural plant yield, product quality and interactions with invasive species. Journal of Integrative Plant Biology, 51(4):337–351.

Bormann, K.J., R.D. Brown, C. Derksen and T.H. Painter, 2018. Estimating snow-cover trends from space. Nature Climate Change, 8:924–928.

Böttcher, K., V.-V. Paunu, K. Kupiainen, M. Zhizhin, A. Matveev, M. Savolahti, Z. Klimont, S. Väätäinen, H. Lamberg and N. Karvosenoja, 2021. Black carbon emissions from flaring in Russia in the period 2012–2017. Atmospheric Environment, 254:118390.

Bouchard, F., I. Laurion, V. Prėskienis, D. Fortier, X. Xu and M. J. Whiticar, 2015. Modern to millennium-old greenhouse gases emitted from ponds and lakes of the Eastern Canadian Arctic (Bylot Island, Nunavut). Biogeosciences, 12:7279–7298.

Boulanger, Y., S. Gauthier, D.R. Gray, H. Le Goff, P. Lefort and J. Morissette, 2013. Fire regime zonation under current and future climate over eastern Canada. Ecological Applications, 23(4):904–923.

Boulanger, Y., S. Gauthier and P.J. Burton, 2014. A refinement of models projecting future Canadian fire regimes using homogeneous fire regime zones. Canadian Journal of Forest Research, 44(4):365–376.

Bourgeois, Q. and I. Bey, 2011. Pollution transport efficiency toward the Arctic: sensitivity to aerosol scavenging and source regions. Journal of Geophysical Research: Atmospheres, 116(D8).

Bousquet, P., B. Ringeval, I. Pison, E.J. Dlugokencky, E.-G. Brunke, C. Carouge, F. Chevallier, A. Fortems-Cheiney, C. Frankenberg, D.A. Hauglustaine, P.B. Krummel, R.L. Langenfelds, M. Ramonet, M. Schmidt, L.P. Steele, S. Szopa, C. Yver, N. Viovy and P. Ciais, 2011. Source attribution of the changes in atmospheric methane for 2006–2008. Atmospheric Chemistry and Physics, 11(8):3689–3700.

Bowman, D.M.J.S., J. Balch, P. Artaxo, W.J. Bond, M.A. Cochrane, C.M. D'Antonio, R. DeFries, F.H. Johnston, J.E. Keeley, M.A. Krawchuk, C.A. Kull, M. Mack, M.A. Moritz, S. Pyne, C.I. Roos, A.C. Scott, N.S. Sodhi and T.W. Swetnam, 2011. The human dimension of fire regimes on Earth. Journal of Biogeography, 38(12):2223–2236.

Box, J.E., W.T. Colgan, T.R. Christensen, N.M. Schmidt, M. Lund, F.-J.W. Parmentier, R. Brown, U.S. Bhatt, E.S. Euskirchen, V.E. Romanovsky, J.E. Walsh, J.E. Overland, M. Wang, R.W. Corell, W.N. Meier, B. Wouters, S. Mernild, J. Mård, J. Pawlak and M. Skovgård Olsen, 2019. Key indicators of Arctic climate change: 1971–2017. Environmental Research Letters, 14(4):045010.

Boy, M., E.S. Thomson, J.-C. Acosta Navarro, O. Arnalds, E. Batchvarova, J. Bäck, F. Berninger, M. Bilde, Z. Brasseur, P. Dagsson-Waldhauserova, D. Castarède, M. Dalirian, G. de Leeuw, M. Dragosics, E.-M. Duplissy, J. Duplissy, A.M.L. Ekman, K. Fang, J.-C. Gallet, M. Glasius, S.-E. Gryning, H. Grythe, H.-C. Hansson, M. Hansson, E. Isaksson, T. Iversen, I. Jonsdottir, V. Kasurinen, A. Kirkevåg, A. Korhola, R. Krejci, J.E. Kristjansson, H.K. Lappalainen, A. Lauri, M. Leppäranta, H. Lihavainen, R. Makkonen, A. Massling, O. Meinander, E.D. Nilsson, H. Olafsson, J.B.C. Pettersson, N.L. Prisle, I. Riipinen, P. Roldin, M. Ruppel, M. Salter, M. Sand, Ø. Seland, H. Seppä, H. Skov, J. Soares, A. Stohl, J. Ström, J. Svensson, E. Swietlicki, K. Tabakova, T. Thorsteinsson, A. Virkkula, G.A. Weyhenmeyer, Y. Wu, P. Zieger and M. Kulmala, 2019. Interactions between the atmosphere, cryosphere and ecosystems at northern high latitudes. Atmospheric Chemistry and Physics, 19(3):2015–2061.

Boynard, A., D. Hurtmans, K. Garane, F. Goutail, J. Hadji-Lazaro, M.E. Koukouli,C. Wespes, C. Vigouroux, A. Keppens, J.-P. Pommereau, A. Pazmino, D. Balis, D. Loyola, P. Valks, R. Sussmann, D. Smale, P.-F. Coheur and C. Clerbaux, 2018. Validation of the IASI FORLI/EUMETSAT ozone products using satellite (GOME-2), ground-based (Brewer–Dobson, SAOZ, FTIR) and ozonesonde measurements. Atmospheric Measurement Techniques, 11(9):5125–5152.

Bozem, H., P. Hoor, D. Kunkel, F. Köllner, J. Schneider, A. Herber, H. Schulz, W.R. Leaitch, A.A. Aliabadi, M.D. Willis, J. Burkart and J.P.D. Abbatt, 2019. Characterization of transport regimes and the polar dome during Arctic spring and summer using in situ aircraft measurements. Atmospheric Chemistry and Physics, 19(23):15049–15071.

Bradley, R.S., F.T. Keimig and H.F. Diaz, 1992. Climatology of surface-based inversions in the North American Arctic. Journal of Geophysical Research: Atmospheres, 97(D14):15699–15712.

Brandt, J., J.D. Silver, L.M. Frohn, C. Geels, A. Gross, A.B. Hansen, K.M. Hansen, G.B. Hedegaard, C.A. Skjøth, H. Villadsen, A. Zare and J.H. Christensen, 2012. An integrated model study for Europe and North America using the Danish Eulerian Hemispheric Model with focus on intercontinental transport of air pollution. Atmospheric Environment. 53:156–176.

Brandt, J., J.D. Silver, J.H. Christensen, M.S. Andersen, J.H. Bønløkke, T. Sigsgaard, C. Geels, A. Gross, A.B. Hansen, K.M. Hansen, G.B. Hedegaard, E. Kaas and L.M. Frohn, 2013a. Assessment of past, present and future health-cost externalities of air pollution in Europe and the contribution from international ship traffic using the EVA model system. Atmospheric Chemistry and Physics, 13:7747–7764.

Brandt, J., J.D. Silver, J.H. Christensen, M.S. Andersen, J.H. Bønløkke, T. Sigsgaard , C. Geels, A. Gross, A.B. Hansen, K.M. Hansen, G.B. Hedegaard, E. Kaas and L.M. Frohn, 2013b. Contribution from the ten major emission sectors in Europe and Denmark to the health-cost externalities of air pollution using the EVA model system – an integrated modelling approach. Atmospheric Chemistry and Physics, 13:7725–7746.

Breider, T.J., L.J. Mickley, D.J. Jacob, Q. Wang, J.A. Fisher, R.Y.-W. Chang and B. Alexander, 2014. Annual distributions and sources of Arctic aerosol components, aerosol optical depth, and aerosol absorption. Journal of Geophysical Research: Atmospheres, 119(7):4107–4124.

Breider, T.J., L.J. Mickley, D.J. Jacob, C. Ge, J. Wang, M.P. Sulprizio, B. Croft, D.A. Ridley, J.R. McConnell, S. Sharma, L. Husain, V.A. Dutkiewicz, K. Eleftheriadis, H. Skov and P.K. Hopke, 2017. Multidecadal trends in aerosol radiative forcing over the Arctic: contribution of changes in anthropogenic aerosol to Arctic warming since 1980. Journal of Geophysical Research: Atmospheres, 122(6):3573–3594.

Brock, C.A., J. Cozic, R. Bahreini, K.D. Froyd, A.M. Middlebrook, A. McComiskey, J. Brioude, O.R. Cooper, A. Stohl, K.C. Aikin, J.A. de Gouw, D.W. Fahey, R.A. Ferrare, R.-S. Gao, W. Gore, J.S. Holloway, G. Hübler, A. Jefferson, D.A. Lack, S. Lance, R.H. Moore, D.M. Murphy, A. Nenes, P.C. Novelli, J.B. Nowak, J.A. Ogren, J. Peischl, R.B. Pierce, P. Pilewskie, P.K. Quinn, T.B. Ryerson, K.S. Schmidt, J.P. Schwarz, H. Sodemann, J.R. Spackman, H. Stark, D.S. Thomson, T. Thornberry, P. Veres, L.A. Watts, C. Warneke and A.G. Wollny, 2011. Characteristics, sources, and transport of aerosols measured in spring 2008 during the Aerosol, Radiation, and Cloud Processes Affecting Arctic Climate (ARCPAC) Project. Atmospheric Chemistry and Physics, 11(6):2423–2453.

Brooks, S., C. Moore, D. Lew, B. Lefer, G. Huey and D. Tanner, 2011. Temperature and sunlight controls of mercury oxidation and deposition atop the Greenland ice sheet. Atmospheric Chemistry and Physics, 11(16):8295–8306.

Brown, R.J.C., S. Beccaceci, D.M. Butterfield, P.G. Quincey, P.M. Harris, T. Maggos, P. Panteliadis, A. John, A. Jedynska, T.A.J. Kuhlbusch, J.-P. Putaud and A. Karanasiou, 2017. Standardisation of a European measurement method for organic carbon and elemental carbon in ambient air: results of the field trial campaign and the determination of a measurement uncertainty and working range. Environmental Science: Processes & Impacts, 10:1249–1259.

Browse, J., K.S. Carslaw, S.R. Arnold, K. Pringle and O. Boucher, 2012. The scavenging processes controlling the seasonal cycle in Arctic sulfate and black carbon aerosol. Atmospheric Chemistry and Physics, 12:6775–6798.

Browse, J., K.S. Carslaw, G.W. Mann, C.E. Birch, S.R. Arnold and C. Leck, 2014. The complex response of Arctic aerosol to sea-ice retreat. Atmospheric Chemistry and Physics, 14:7543–7557.

Bruhwiler, L., E. Dlugokencky, K. Masarie, M. Ishizawa, A. Andrews, J. Miller, C. Sweeney, P. Tans and D. Worthy, 2014. CarbonTracker-CH_4: an assimilation system for estimating emissions of atmospheric methane. Atmospheric Chemistry and Physics, 14(16): 8269–8293.

Bruhwiler, L., F.-J.W. Parmentier, P. Crill, M. Leonard and P.I. Palmer, 2021. The Arctic carbon cycle and its response to changing climate. Current Climate Change Reports, 7:14–34.

Brune, W.H., D.O. Miller, A.B. Thames, H.M. Allen, E.C. Apel, D.R. Blake, T.P. Bui, R. Commane, J.D. Crounse, B.C. Daube, G.S. Diskin, J.P. DiGangi, J.W. Elkins, S.R. Hall, T.F. Hanisco, R.A. Hannun, E.J. Hintsa,

R.S. Hornbrook, M.J. Kim, K. McKain, F.L. Moore, J.A. Neuman, J.M. Nicely, J. Peischl, T.B. Ryerson, J.M. St Clair, C. Sweeny, A.P. Teng, C. Thompson, K. Ullmann, P.R. Veres, P.O. Wennberg and G.M. Wolfe, 2020. Exploring oxidation in the remote free troposphere: insights from Atmospheric Tomography (ATom). Journal of Geophysical Research: Atmospheres, 125(1):e2019JD031685.

Brunekreef, B. and S.T. Holgate, 2002. Air pollution and health. The Lancet, 360(9341):1233–1242.

Buffett, B.A., 2000. Clathrate hydrates. Annual Review of Earth and Planetary Science, 28(1):477–507.

Buldovicz, S.N., V.Z. Khilimonyuk, A.Y. Bychkov, E.N. Ospennikov, S.A. Vorobyev, A.Y. Gunar, E.I. Gorshkov, E.M. Chuvilin, M.Y. Cherbunina, P.I. Kotov, N.V. Lubnina, R.G. Motenko and R.M. Amanzhurov, 2018. Cryovolcanism on the Earth: origin of a spectacular crater in the Yamal Peninsula (Russia). Scientific Reports, 8:13534.

Bullard, J.E., M. Baddock, T. Bradwell, J. Crusius, E. Darlington, D. Gaiero, S. Gassó, G. Gisladottir, R. Hodgkins, R. McCulloch, C. McKenna-Neuman, T. Mockford, H. Stewart and T. Thorsteinsson, 2016. High-latitude dust in the Earth system. Reviews of Geophysics, 54(2):447–485.

Burd, J.A., P.K. Peterson, S.V. Nghiem, D.K. Perovich and W.R. Simpson, 2017. Snowmelt onset hinders bromine monoxide heterogeneous recycling in the Arctic. Journal of Geophysical Research: Atmospheres, 122(15):8297–8309.

Burkart, J., A.L. Hodshire, E.L. Mungall, J.R. Pierce, D.B. Collins, L.A. Ladino, A.K.Y. Lee, V. Irish, J.J.B. Wentzell, J. Liggio, T. Papakyriakou, J. Murphy and J. Abbatt, 2017. Organic condensation and particle growth to CCN sizes in the summertime marine Arctic is driven by materials more semivolatile than at continental sites. Geophysical Research Letters, 44(20):10,725–10,734.

Burke, C., S. Wich, K. Kusin, O. McAree, M.E. Harrison, B. Ripoll, Y. Ermiasi, M. Mulero-Pázmány and S. Longmore, 2019. Thermal-Drones as a safe and reliable method for detecting subterranean peat fires. Drones, 3(1):23.

Burnett, R.T., C.A. Pope, III, M. Ezzati, C. Olives, S.S. Lim, S. Mehta, H.H. Shin, G. Singh, B. Hubbell, M. Brauer, H.R. Anderson, K.R. Smith, J.R. Balmes, N.G. Bruce, H. Kan, F. Laden, A. Prüss-Ustün, M.C. Turner, S.M. Gapstur, W.R. Diver and A. Cohen, 2014. An integrated risk function for estimating the global burden of disease attributable to ambient fine particulate matter exposure. Environmental Health Perspectives, 122(4):397–403.

Burnett, R., H. Chen, M. Szyszkowicz, N. Fann, B. Hubbell, C.A. Pope, III, J.S. Apte, M. Brauer, A. Cohen, S. Weichenthal, J. Coggins, Q. Di, B. Brunekreef, J. Frostad, S.S. Lim, H. Kan, K.D. Walker, G.D. Thurston, R.B. Hayes, C.C. Lim, M.C. Turner, M. Jerrett, D. Krewski, S.M. Gapstur, W.R. Diver, B. Ostro, D. Goldberg, D.L. Crouse, R.V. Martin, P. Peters, L. Pinault, M. Tjepkema, A. van Donkelaar, P.J. Villeneuve, A.B. Miller, P. Yin, M. Zhou, L. Wang, N.A.H. Janssen, M. Marra, R.W. Atkinson, H. Tsang, T.Q. Thach, J.B. Cannon, R.T. Allen, J.E. Hart, F. Laden, G. Cesaroni, F. Forastiere, G. Weinmayr, A. Jaensch, G. Nagel, H. Concin and J.V. Spadaro, 2018. Global estimates of mortality associated with long-term exposure to outdoor fine particulate matter. Proceedings of the National Academy of Sciences, 115(38):9592–9597.

Burney, J. and V. Ramanathan, 2014. Recent climate and air pollution impacts on Indian agriculture. Proceedings of the National Academy of Sciences, 111(46):16319–16324.

Bussmann, I., 2013. Distribution of methane in the Lena Delta and Buor-Khaya Bay, Russia. Biogeosciences, 10(7):4641–4652.

Calastrini, F., F. Guarnieri, S. Becagli, C. Busillo, M. Chiari, U. Dayan, F. Lucarelli, S. Nava, M. Pasqui, R. Traversi, R. Udisti and G. Zipoli, 2012. Desert dust outbreaks over Mediterranean Basin: a modeling, observational, and synoptic analysis approach. Advances in Meteorology (2012): 246874.

Calef, M.P., A. Varvak and A.D. McGuire, 2017. Differences in human versus lightning fires between urban and rural areas of the boreal forest in interior Alaska. Forests, 8(11):422.

Callaghan, T.V., F. Bergholm, T.R. Christensen, C. Jonasson, U. Kokfelt and M. Johansson, 2010. A new climate era in the sub-Arctic: Accelerating climate changes and multiple impacts. Geophysical Research Letters, 37(14).

Canagaratna, M.R., J.T. Jayne, J.L. Jimenez, J.D. Allan, M.R. Alfarra, Q. Zhang, T.B. Onasch, F. Drewnick, H. Coe, A. Middlebrook, A. Delia, L.R. Williams, A.M. Trimborn, M.J. Northway, P.F. DeCarlo, C.E. Kolb, P. Davidovits and D.R. Worsnop, 2007. Chemical and microphysical characterization of ambient aerosols with the aerodyne aerosol mass spectrometer. Mass Spectrometry Reviews, 26(2):185–222.

Cao, M., S. Marshall and K. Gregson, 1996. Global carbon exchange and methane emissions from natural wetlands: Application of a process-based model. Journal of Geophysical Research: Atmospheres, 101(D9):14399–14414.

Carlsen, H.K., H. Zoëga, U. Valdimarsdóttir, T. Gíslason and B. Hrafnkelsson, 2012. Hydrogen sulfide and particle matter levels associated with increased dispensing of anti-asthma drugs in Iceland's capital. Environmental Research, 113:33–39.

Carlsen, H.K., B. Forsberg, K. Meister, T. Gíslason and A. Oudin, 2013. Ozone is associated with cardiopulmonary and stroke emergency hospital visits in Reykjavík, Iceland 2003–2009. Environmental Health, 12(28).

Carslaw, K.S., L.A. Lee, C.L. Reddington, K.J. Pringle, A. Rap, P.M. Forster, G.W. Mann, D.V. Spracklen, M.T. Woodhouse, L.A. Regayre and J.R. Pierce, 2013. Large contribution of natural aerosols to uncertainty in indirect forcing. Nature, 503:67–71.

Cassiani, M., A. Stohl and J. Brioude, 2014. Lagrangian stochastic modelling of dispersion in the convective boundary layer with skewed turbulence conditions and a vertical density gradient: formulation and implementation in the FLEXPART model. Boundary-Layer Meteorology, 154:367–390.

Cavalli, F., M. Viana, K.E. Yttri, J. Genberg and J.-P. Putaud, 2010. Toward a standardised thermal-optical protocol for measuring atmospheric organic and elemental carbon: the EUSAAR protocol. Atmospheric Measurement Techniques, 3(1):79–89.

Cazorla, A., R. Bahadur, K.J. Suski, J.F. Cahill, D. Chand, B. Schmid, V. Ramanathan and K.A. Prather, 2013. Relating aerosol absorption due to soot, organic carbon, and dust to emission sources determined from in-situ chemical measurements. Atmospheric Chemistry and Physics, 13(18):9337–9350.

Cesana, G., J.E. Kay, H. Chepfer, J.M. English and G. de Boer, 2012. Ubiquitous low-level liquid-containing Arctic clouds: New observations and climate model constraints from CALIPSO-GOCCP. Geophysical Research Letters, 39(20):L20804.

CEN, 2017. EN 16909: 2017, Ambient Air – Measurement of Elemental Carbon (EC) and Organic Carbon (OC) Collected on Filters. European Committee for Standardisation (CEN), Brussels.

Chameides, W.L., H. Yu, S.C. Liu, M. Bergin, X. Zhou, L. Mearns, G. Wang, C.S. Kiang, R.D. Saylor, C. Luo, Y. Huang, A. Steiner and F. Giorgi, 1999. Case study of the effects of atmospheric aerosols and regional haze on agriculture: an opportunity to enhance crop yields in China through emission controls? Proceedings of the National Academy of Sciences, 96(24):13626–13633.

Champine, R.D., R. Morris and S. Elder, 2019. National Geographic. Available at: https://www.nationalgeographic.com/environment/graphics/map-shows-how-ships-navigate-melting-arctic-feature (Accessed 19 January 2023).

Chan, T.W., L. Huang, K. Banwait, W. Zhang, D. Ernst, X. Wang, J.G. Watson, J.C. Chow, M. Green, C.I. Czimczik, G.M. Santos, S. Sharma and K. Jones, 2019. Inter-comparison of elemental and organic carbon mass measurements from three North American national long-term monitoring networks at a co-located site. Atmospheric Measurement Techniques, 12(8):4543–4560.

Chang, R.Y.-W., C. Leck, M. Graus, M. Müller, J. Paatero, J.F. Burkhart, A. Stohl, L.H. Orr, K. Hayden, S.-M. Li, A. Hansel, M. Tjernström, W.R. Leaitch and J.P.D. Abbatt, 2011. Aerosol composition and sources in the central Arctic Ocean during ASCOS. Atmospheric Chemistry and Physics, 11(20):10619–10636.

Chang, K.-Y., W.J. Riley, P.M. Crill, R.F. Grant, V.I. Rich and S.R. Saleska, 2019. Large carbon cycle sensitivities to climate across a permafrost thaw gradient in subarctic Sweden. The Cryosphere, 13(2):647–663.

Charkin, A.N., M.R. van der Loeff, N.E. Shakhova, Ö. Gustafsson, O.V. Dudarev, M.S. Cherepnev, A.N. Salyuk, A.V. Koshurnikov, E.A. Spivak, A.Y. Gunar, A.S. Ruban and I.P. Semiletov, 2017. Discovery and characterization of submarine groundwater discharge in the Siberian Arctic seas: a case study in the Buor-Khaya Gulf, Laptev Sea. The Cryosphere, 11(5):2305–2327.

Charlson, R.J., J.E. Lovelock, M.O. Andreae and S.G. Warren, 1987. Oceanic phytoplankton, atmospheric sulphur, cloud albedo and climate. Nature, 326:655–661.

Charron, M., S. Polavarapu, M. Buehner, P.A. Vaillancourt, C. Charette, M. Roch, J. Morneau, L. Garand, J.M. Aparicio, S. MacPherson, S. Pellerin, J. St-James and S. Heilliette, 2012. The stratospheric extension of the Canadian global deterministic medium-range weather forecasting system and its impact on tropospheric forecasts. Monthly Weather Review, 140(6):1924–1944.

Chellman, N.J., J.R. McConnell, A. Heyvaert, B.Vannière, M.M. Arienzo and V. Wennrich, 2018. Incandescence-based single-particle method for black carbon quantification in lake sediment cores. Limnology and Oceanography Methods, 16(11):711–721.

Chen, Y.-H. and R.G. Prinn, 2006. Estimation of atmospheric methane emissions between 1996 and 2001 using a three-dimensional global chemical transport model. Journal of Geophysical Research: Atmospheres, 111(D10).

Chen, Q., J.A. Schmidt, V. Shah, L. Jaeglé, T. Sherwen and B. Alexander, 2017. Sulfate production by reactive bromine: implications for the global sulfur and reactive bromine budgets. Geophysical Research Letters, 44(13):7069–7078.

Chen, J., K. Anderson, R. Pavlovic, M.D. Moran, P. Englefield, D.K. Thompson, R. Munoz-Alpizar and H. Landry, 2019. The FireWork v2.0 air quality forecast system with biomass burning emissions from the Canadian Forest Fire Emissions Prediction System v2.03, Geoscientific Model Development, 12: 3283–3310.

Chernokulsky, A. and I. Esau, 2019. Cloud cover and cloud types in the Eurasian Arctic in 1936–2012. International Journal of Climatology, 39(15):5771–5790.

Cho, M.-H., R.J. Park, J. Yoon, Y. Choi, J.I. Jeong, L. Labzovskii, J.S. Fu, K. Huang, S.-J. Jeong and B.-M. Kim, 2019. A missing component of Arctic warming: black carbon from gas flaring. Environmental Research Letters, 14(9):094011.

Chow, J.C., J.G. Watson, D. Crow, D.H. Lowenthal and T.M. Merrifield, 2001. Comparison of IMPROVE and NIOSH carbon measurements. Aerosol Science and Technology, 34(1):23–34.

Chow, J.C., J.G. Watson, L.-W.A. Chen, M.C.O. Chang, N.F. Robinson, D. Trimble and S. Kohl, 2007. The IMPROVE_A temperature protocol for thermal/optical carbon analysis: maintaining consistency with a long-term database. Journal of the Air & Waste Management Association, 57(9):1014–1023.

Chow, J.C., J.G. Watson, L.-W.A. Watson, W.P. Arnott, H. Moosmüller and K. Fung, 2004. Equivalence of elemental carbon by thermal/optical reflectance and transmittance with different temperature protocols. Environmental Science & Technology, 38(16):4414–4422.

Chow, J.C., J.G. Watson, L.C. Pritchett, W.R. Pierson, C.A. Frazier and R.G. Purcell, 1993. The dri thermal/optical reflectance carbon analysis system: description, evaluation and applications in U.S. air quality studies. Atmospheric Environment. Part A. General Topics, 27(8):1185–1201.

Christensen, T.R., 1993. Methane emission from Arctic tundra. Biogeochemistry, 21:117–139.

Christensen, J.H., 1997. The Danish eulerian hemispheric model – A three-dimensional air pollution model used for the Arctic. Atmospheric Environment, 31(24):4169–4191.

Christensen, T.R., 2014. Climate science: understand Arctic methane variability. Nature, 509:279–281.

Christiansen, B., N. Jepsen, R. Kivi, G. Hansen, N. Larsen and U.S. Korsholm, 2017. Trends and annual cycles in soundings of Arctic tropospheric ozone. Atmospheric Chemistry and Physics, 17(15)9347–9364.

Christiansen, J.R. and C.J. Jørgensen, 2018. First observation of direct methane emission to the atmosphere from the subglacial domain of the Greenland Ice Sheet. Scientific Reports, 8:16623.

Christensen, T.R., S. Jonasson, T.V. Callaghan and M. Havström, 1995. Spatial variation in high latitude methane flux along a transect across Siberian and Eurasian tundra environments. Journal of Geophysical Research: Atmospheres, 100(D10):21035–21045.

Christensen, T.R., I.C. Prentice, J. Kaplan, A. Haxeltine and S. Sitch, 1996. Methane flux from northern wetlands and tundra – an ecosystem source modelling approach. Tellus B: Chemical and Physical Meteorology, 48(5):652–661.

Christensen, T.R., N. Panikov, M. Mastepanov, A. Joabsson, A. Stewart, M. Öquist, M. Sommerkorn, S. Reynaud and B. Svensson, 2003. Biotic controls on CO_2 and CH_4 exchange in wetlands – a closed environment study. Biogeochemistry, 64:337–354.

Christensen, T.R., V.K. Arora, M. Gauss, L. Höglund-Isaksson and F.-J.W. Parmentier, 2019. Tracing the climate signal: mitigation of anthropogenic methane emissions can outweigh a large Arctic natural emission increase. Scientific Reports, 9:1146.

Christidis, T., A.C. Erickson, A.J. Pappin, D.L. Crouse, L.L. Pinault, S.A. Weichenthal, J.R. Brook, A. van Donkelaar, P. Hystad, R.V. Martin, M. Tjepkema, R.T. Burnett and M. Brauer, 2019. Low concentrations of fine particle air pollution and mortality in the Canadian Community Health Survey cohort. BMJ Environmental Health, 18(84).

Chuvilin, E., J. Stanilovskaya, A. Titovsky, A. Sinitsky, N. Sokolova, B. Bukhanov, M. Spasennykh, A. Cheremisin, S. Grebenkin, D. Davletshina and C. Badetz, 2020. A gas-emission crater in the Erkuta river valley, Yamal Peninsula: characteristics and potential formation model. Geosciences, 10(5):170.

CIFFC, 2020. National Fires: hectares by year. Canadian Interagency Forest Fire Centre (CIFFC). Available at: https://ciffc.net/en/hectares-by-year

Clerbaux, C., A. Boynard, L. Clarisse, M. George, J. Hadji-Lazaro, H. Herbin, D. Hurtmans, M. Pommier, A. Razavi, S. Turquety, C. Wespes and P.-F. Coheur, 2009. Monitoring of atmospheric composition using the thermal infrared IASI/MetOp sounder. Atmospheric Chemistry and Physics, 9(16):6041–6054.

Collaud Coen, M., E. Andrews, A. Alastuey, T.P. Arsov, J. Backman, B.T. Brem, N. Bukowiecki, C. Couret, K. Eleftheriadis, H. Flentje, M. Fiebig, M. Gysel-Beer, J.L. Hand, A. Hoffer, R. Hooda, C. Hueglin, W. Joubert, M. Keywood, J.E. Kim, S.-W. Kim, C. Labuschagne, N.-H. Lin, Y. Lin, C. Lund Myhre, K. Luoma, H. Lyamani, A. Marinoni, O.L. Mayol-Bracero, N. Mihalopoulos, M. Pandolfi, N. Prats, A.J. Prenni, J.-P. Putaud, L. Ries, F. Reisen, K. Sellegri, S. Sharma, P. Sheridan, J.P. Sherman, J. Sun, G. Titos, E. Torres, T. Tuch, R. Weller, A. Wiedensohler, P. Zieger and P. Laj, 2020. Multidecadal trend analysis of in situ aerosol radiative properties around the world. Atmospheric Chemistry and Physics, 20(14):8867–8908.

Collins, D.B., J. Burkart, R.Y.-W. Chang, M. Lizotte, A. Boivin-Rioux, M. Blais, E.L. Mungall, M. Boyer, V.E. Irish, G. Massé, D. Kunkel, J.-E. Tremblay, T. Papakyriakou, A.K. Bertram, H. Bozem, M. Gosselin, M. Levasseur, and J.P.D. Abbatt, 2017. Frequent ultrafine particle formation and growth in Canadian Arctic marine and coastal environments. Atmospheric Chemistry and Physics 17(21):13119–13138.

Conca, E., O. Abollino, A. Giacomini, S. Buoso, R. Traversi, S. Becagli, M. Grotti and M. Malandrino, 2019. Source identification and temporal evolution of trace elements in PM_{10} collected near to Ny-Ålesund (Norwegian Arctic). Atmospheric Environment, 203:153–165.

Conrad, B.M. and M.R. Johnson, 2017. Field measurements of black carbon yields from gas flaring. Environmental Science & Technology, 51(3):1893–1900.

Cook, J.M., A.J. Tedstone, C. Williamson, J. McCutcheon, A.J. Hodson, A. Dayal, M. Skiles, S. Hofer, R. Bryant, O. McAree, A. McGonigle, J. Ryan, A.M. Anesio, T.D.L. Irvine-Fynn, A. Hubbard, E. Hanna, M. Flanner, S. Mayanna, L.G. Benning, D. van As, M. Yallop, J.B. McQuaid, T. Gribbin and M. Tranter, 2020. Glacier algae accelerate melt rates on the south-western Greenland Ice Sheet. The Cryosphere, 14:309–330.

Cooley, S.W., L.C. Smith, J.C. Ryan, L.H. Pitcher and T.M Pavelsky, 2019. Arctic-boreal lake dynamics revealed using CubeSat imagery. Geophysical Research Letters, 46(4):2111–2120.

Cooper, M.D.A., C. Estop-Aragonés, J.P. Fisher, A. Thierry, M.H. Garnett, D.J. Charman, J.B. Murton, G.K. Phoenix, R. Treharne, S.V. Kokelj, S.A. Wolfe, A.G. Lewkowicz, M. Williams and I.P. Hartley, 2017. Limited contribution of permafrost carbon to methane release from thawing peatlands. Nature Climate Change, 7:507–511.

Coopman, Q., T.J. Garrett, J. Riedi, S. Eckhardt and A. Stohl, 2016. Effects of long-range aerosol transport on the microphysical properties of low-level liquid clouds in the Arctic. Atmospheric Chemistry and Physics, 16(7):4661–4674.

Corbett, J.J., D.A. Lack, J.J Winebrake, S. Harder, J.A. Silberman and M. Gold, 2010. Arctic shipping emissions inventories and future scenarios. Atmospheric Chemistry and Physics, 10(19):9689–9704.

Corradi, C., O. Kolle, K. Walter, S.A. Zimov and E.D. Schulze, 2005. Carbon dioxide and methane exchange of a north-east Siberian tussock tundra. Global Change Biology, 11(11):1910–1925.

Costa, A., J. Meyer, A. Afchine, A. Luebke, G. Günther, J.R. Dorsey, M.W. Gallagher, A. Ehrlich, M. Wendisch, D. Baumgardner, H. Wex and M. Krämer, 2017. Classification of Arctic, midlatitude and tropical clouds in the mixed-phase temperature regime. Atmospheric Chemistry and Physics, 17(19):12219–12238.

Côté, J., S. Gravel, A. Méthot, A. Patoine, M. Roch and A. Staniforth, 1998a. The operational CMC–MRB Global Environmental Multiscale (GEM) model. Part I: Design considerations and formulation. Monthly Weather Review, 126(6):1373–1395.

Côté, J., J.-G. Desmarais, S. Gravel, A. Méthot, A. Patoine, M. Roch and A. Staniforth, 1998b. The operational CMC–MRB Global Environmental Multiscale (GEM) model, Part II: Results. Monthly Weather Review, 126(6):1397–1418.

Cramer, B. and D. Franke, 2005. Indications for an active petroleum system in the Laptev Sea, NE Siberia. Journal of Petroleum Geology, 28(4):369–384.

Crill, P.M., K.B. Bartlett, R.C. Harriss, E. Gorham, E.S. Verry, D.I. Sebacher, L. Madzar and W. Sanner, 1988. Methane flux from Minnesota Peatlands. Global Biogeochemical Cycles, 2(4):371–384.

Crippa M., D. Guizzardi, M. Muntean, E. Schaaf, F. Dentener, J.A. van Aardenne, S. Monni, U. Doering, J.G.J. Olivier, V. Pagliari and G. Janssens-Maenhout, 2018. Gridded emissions of air pollutants for the period 1970–2012 within EDGAR v4.3.2. Earth System Science Data, 10(4):1987–2013.

Croft, B., R.V. Martin, W.R. Leaitch, J. Burkart, R.Y.-W. Chang, D.B. Collins, P.L. Hayes, A.L. Hodshire, L. Huang, J.K. Kodros, A. Moravek, E.L. Mungall, J.G. Murphy, S. Sharma, S. Tremblay, G.R. Wentworth, M.D. Willis, J.P.D. Abbatt and J.R. Pierce, 2019. Arctic marine secondary organic aerosol contributes significantly to summertime particle size distributions in the Canadian Arctic Archipelago. Atmospheric Chemistry and Physics, 19(5):2787–2812.

Crouse, D. L., P.A. Peters, P. Hystad, J.R. Brook, A. van Donkelaar, R.V. Martin, P.J. Villeneuve, M. Jerrett, M.S. Goldberg, C.A. Pope, III, M. Brauer, R.D. Brook, A. Robichaud, R. Menard and R.T. Burnett, 2015. Ambient $PM_{2.5}$, O_3, and NO_2 exposures and associations with mortality over 16 years of follow-up in the Canadian Census Health and Environment Cohort (CanCHEC). Environmental Health Perspectives, 123(11):1180–1186.

Crusius, J., A.W. Schroth, S. Gassó, C.M. Moy, R.C. Levy and M. Gatica, 2011. Glacial flour dust storms in the Gulf of Alaska: hydrologic and meteorological controls and their importance as a source of bioavailable iron. Geophysical Research Letters, 38(6): L06602

Curry, J.A., J.L. Schramm, W.B. Rossow and D. Randall, 1996. Overview of Arctic cloud and radiation characteristics. Journal of Climate, 9(8):1731–1764.

Daanen, R.P., T. Ingeman-Nielsen, S.S. Marchenko, V.E. Romanovsky, N. Foged, M. Stendel, J.H. Christensen and K. Hornbech Svendsen, 2011. Permafrost degradation risk zone assessment using simulation models. The Cryosphere, 5(4):1043–1056.

Dabek-Zlotorzynska, E., T.F. Dann, P.K. Martinelango, V. Celo, J.R. Brook, D. Mathieu, L. Ding and C.C. Austin, 2011. Canadian National Air Pollution Surveillance (NAPS) $PM_{2.5}$ speciation program: methodology and $PM_{2.5}$ chemical composition for the years 2003–2008. Atmospheric Environment, 45(3):673–686.

Daellenbach, K.R., C. Bozzetti, A. Křepelová, F. Canonaco, R. Wolf, P. Zotter, P. Fermo, M. Crippa, J.G. Slowik, Y. Sosedova, Y. Zhang, R.-J. Huang, L. Poulain, S. Szidat, U. Baltensperger, I. El Haddad and A.S.H. Prévôt, 2016. Characterization and source apportionment of organic aerosol using offline aerosol mass spectrometry. Atmospheric Measurement Techniques, 9(1):23–39.

Dagsson-Waldhauserova, P. and O. Meinander, 2019. Editorial: Atmosphere–cryosphere interaction in the Arctic, at high latitudes and mountains with focus on transport, deposition and effects of dust, black carbon, and other aerosols. Frontiers in Earth Science, 7:337.

Dagsson-Waldhauserova, P., O. Arnalds and H. Olafsson, 2013. Long-term frequency and characteristics of dust storm events in Northeast Iceland (1949–2011). Atmospheric Environment, 77:117–127.

Dagsson-Waldhauserova, P., O. Arnalds and H. Olafsson, 2014. Long-term variability of dust events in Iceland (1949–2011). Atmospheric Chemistry and Physics, 14(24):13411–13422.

Dagsson-Waldhauserova, P., O. Arnalds, H. Olafsson, J. Hladil, R. Skala, T. Navratil, L. Chadimova and O. Meinander, 2015. Snow–Dust Storm: unique case study from Iceland, March 6–7, 2013. Aeolian Research, 16:69–74.

Dagsson-Waldhauserova, P., O. Arnalds and H. Olafsson, 2017. Long-term dust aerosol production from natural sources in Iceland. Journal of the Air & Waste Management Association, 67(2):173–181.

Dagsson-Waldhauserova, P., J.-B. Renard, H. Olafsson, D. Vignelles, G. Berthet, N. Verdier and V. Duverger, 2019. Vertical distribution of aerosols in dust storms during the Arctic winter. Scientific Reports 9:16122.

Dall'Osto, M., D.C.S. Beddows, P. Tunved, R. Krejci, J. Ström, H.-C. Hansson, Y.J. Yoon, K.-T. Park, S. Becagli, R. Udisti, T. Onasch, C.D. O´Dowd, R. Simó and R.M. Harrison, 2017. Arctic sea ice melt leads to atmospheric new particle formation. Scientific Reports, 7:3318.

Dall'Osto, M., C. Geels, D.C.S. Beddows, D. Boertmann, R. Lange, J.K. Nøjgaard, R.M. Harrison, R. Simo, H. Skov and A. Massling, 2018. Regions of open water and melting sea ice drive new particle formation in North East Greenland. Scientific Reports, 8:6109.

Dall'Osto, M., D.C.S. Beddows, P. Tunved, R.M. Harrison, A. Lupi, V. Vitale, S. Becagli, R. Traversi, K.-T. Park, Y.J. Yoon, A. Massling, H. Skov, R. Lange, J. Strom and R. Krejci, 2019. Simultaneous measurements of aerosol size distributions at three sites in the European high Arctic. Atmospheric Chemistry and Physics, 19(11):7377–7395.

Damian, V., A. Sandu, M. Damian, F. Potra and G.R. Carmichael, 2002: The kinetic preprocessor KPP – a software environment for solving chemical kinetics, Computers & Chemical Engineering, 26(11):1567–1579.

Damm, E., U. Schauer, B. Rudels and C. Haas, 2007. Excess of bottom-released methane in an Arctic shelf sea polynya in winter. Continental Shelf Research, 27(12):1692–1701.

Damm, E., E. Helmke, S. Thoms, U. Schauer, E. Nöthig, K. Bakker and R.P Kiene, 2010. Methane production in aerobic oligotrophic surface water in the central Arctic Ocean. Biogeosciences, 7(3):1099–1108.

Damm, E., B. Rudels, U. Schauer, S. Mau and G. Dieckmann, 2015. Methane excess in Arctic surface water – triggered by sea ice formation and melting. Scientific Reports, 5:16179.

Damm, E., D. Bauch, T. Krumpen, B. Rabe, M. Korhonen, E. Vinogradova and C. Uhlig, 2018. The Transpolar Drift conveys methane from the Siberian Shelf to the central Arctic Ocean. Scientific Reports, 8:4515.

Danabasoglu, G., J.-F. Lamarque, J. Bacmeister, D.A. Bailey, A.K. DuVivier, J. Edwards, L.K. Emmons, J. Fasullo, R. Garcia, A Gettelman, C. Hannay, M.M. Holland, W.G Large, P.H. Lauritzen, D.M. Lawrence, J.T.M Lenaerts, K. Lindsay, W.H. Lipscomb, M.J. Mills, R. Neale, K.W. Oleson, B. Otto-Bliesner, A.S. Phillips, W. Sacks, S. Tilmes, L. van Kampenhout, M. Vertenstein, A. Bertini, J. Dennis, C. Deser, C. Fischer, B. Fox-Kemper, J.E. Kay, D. Kinnison, P.J. Kushner, V.E. Larson, M.C. Long, S. Mickelson, J.K. Moore, E. Nienhouse, L. Polvani, P.J. Rasch and W.G. Strand, 2020. The Community Earth System Model version 2 (CESM2). Journal of Advances in Modeling Earth Systems 12(2):e2019MS001916.

Dang, C., S.G. Warren, Q. Fu, S.J. Doherty, M. Sturm and J. Su, 2017. Measurements of light-absorbing particles in snow across the Arctic, North America, and China: Effects on surface albedo. Journal of Geophysical Research: Atmospheres, 122(19):10,149–10,168.

Dastoor, A.P., D. Davignon, N. Theys, M. Van Roozendael, A. Steffen and P.A. Ariya, 2008. Modeling dynamic exchange of gaseous elemental mercury at polar sunrise. Environmental Science & Technology, 42(14):5183–5188.

Davies, G.M., N. Kettridge, C.R. Stoof, A. Gray, D. Ascoli, P.M. Fernandes, R. Marrs, K.A. Allen, S.H. Doerr, G.D. Clay, J. McMorrow and V. Vandvik, 2016. The role of fire in UK peatland and moorland management: the need for informed, unbiased debate. Philosophical Transactions of the Royal Society B: Biological Sciences, 371(1696):20150342.

Davis, J.M., P.V. Bhave and K.M. Foley, 2008. Parameterization of N_2O_5 reaction probabilities on the surface of particles containing ammonium, sulfate, and nitrate. Atmospheric Chemistry and Physics, 8(17):5295–5311.

DCE, 2017. Emissions from shipping in the Arctic from 2012–2016 and emission projections for 2020, 2030 and 2050. Scientific Report from DCE No. 252. Danish Centre for Environment and Energy (DCE), Aarhus University. 124pp.

Dean, J.F., J.J. Middelburg, T. Röckmann, R. Aerts, L.G. Blauw, M. Egger, M.S.M. Jetten, A.E.E. de Jong, O.H. Meisel, O. Rasigraf, C.P. Slomp, M.H. in 't Zandt and A.J. Dolman, 2018. Methane feedbacks to the global climate system in a warmer world. Reviews of Geophysics, 56(1):207–250.

de Groot, W.J., M.D. Flannigan and B.J. Stocks, 2013. Climate change and wildfires. In: González-Cabán, A. (Tech. coord.). Proceedings of the Fourth International Symposium on Fire Economics, Planning, and Policy: Climate Change and Wildfires. General Technical Report PSW-GTR-245. pp. 1–10, US Department of Agriculture, Forest Service.

De Vries, W., J.-P. Hettelingh and M. Posch (Eds), 2015. Critical Loads and Dynamic Risk Assessments: Nitrogen, Acidity and Metals in Terrestrial and Aquatic Ecosystems. Environmental Pollution, 25. Springer, Dordrecht, Netherlands. xxvii + 662pp.

Dee, D.P., S.M. Uppala, A.J. Simmons, P. Berrisford, P. Poli, S. Kobayashi, U. Andrae, M.A. Balmaseda, G. Balsamo, P. Bauer, P. Bechtold, A.C.M. Beljaars, L. van de Berg, J. Bidlot, N. Bormann, C. Delsol, R. Dragani, M. Fuentes, A.J. Geer, L. Haimberger, S.B. Healy, H. Hersbach, E.V. Hólm, L. Isaksen, P. Kållberg, M. Köhler, M. Matricardi, A.P. McNally, B.M. Monge-Sanz, J.-J. Morcrette, B.-K. Park, C. Peubey, P. de Rosnay, C. Tavolato, J.-N. Thépaut and F. Vitart, 2011. The ERA-Interim reanalysis: configuration and performance of the data assimilation system. Quarterly Journal of the Royal Meteorological Society 137(656):553–597.

Delene, D.J. and J.A. Ogren, 2002. Variability of aerosol optical properties at four North American surface monitoring sites. Journal of the Atmospheric Sciences, 59(6):1135–1150.

DelSontro, T., L. Boutet, A. St-Pierre, P.A. del Giorgio and Y.T. Prairie, 2016. Methane ebullition and diffusion from northern ponds and lakes regulated by the interaction between temperature and system productivity. Limnology and Oceanography, 61(S1):S62–S77.

Denfeld, B.A., M.B. Wallin, E. Sahlée, S. Sobek, J. Kokic, H.E. Chmiel and G.A. Weyhenmeyer, 2015. Temporal and spatial carbon dioxide concentration patterns in a small boreal lake in relation to ice cover dynamics. Boreal Environment Research, 20:679–692.

Denfeld, B.A., H.M. Baulch, P.A. del Giorgio, S.E. Hampton and J. Karlsson, 2018a. A synthesis of carbon dioxide and methane dynamics during the ice-covered period of northern lakes. Limnology and Oceanography Letters, 3(3):117–131.

Denfeld, B.A., M. Klaus, H. Laudon, R.A. Sponseller and J. Karlsson, 2018b. Carbon dioxide and methane dynamics in a small boreal lake during winter and spring melt events. Journal of Geophysical Research: Biogeosciences, 123(8):2527–2540.

Denjean, C., P. Formenti, K. Desboeufs, S. Chevaillier, S. Triquet, M. Maillé, M. Cazaunau, B. Laurent, O.L. Mayol-Bracero, P. Vallejo, M. Quiñones, I.E. Gutierrez-Molina, F. Cassola, P. Prati, E. Andrews and J. Ogren, 2016. Size distribution and optical properties of African mineral dust after intercontinental transport. Journal of Geophysical Research: Atmospheres, 121(12):7117–7138.

Dentener, F., S. Kinne, T. Bond, O. Boucher, J. Cofala, S. Generoso, P. Ginoux, S. Gong, J.J. Hoelzemann, A. Ito, L. Marelli, J.E. Penner, J.P. Putaud, C. Textor, M. Schulz, G.R. van der Werf and J. Wilson, 2006. Emissions of primary aerosol and precursor gases in the years 2000 and 1750 prescribed data-sets for AeroCom. Atmospheric Chemistry and Physics, 6:4321–4344.

Derome, J., S. Manninen, J. Aherne, P. J. Hellstedt, J.-P. Hettelingh, K. Hicks, S. Huttunen, J. Kämäri, G. Kashulina, M. Kozlov, A. Markkola, M. Posch, A. L. Ruotsalainen, R. Salminen and E. Zvereva, 2006. Chapter 5: Effects on terrestrial ecosystems. In: AMAP Assessment 2006: Acidifying Pollutants, Arctic Haze, and Acidification in the Arctic, pp. 41–63. Arctic Monitoring and Assessment Programme (AMAP), Oslo, Norway.

Devasthale, A. and M.A. Thomas, 2011. A global survey of aerosol-liquid water cloud overlap based on four years of CALIPSO-CALIOP data. Atmospheric Chemistry and Physics, 11(3):1143–1154.

Devasthale, A., U. Willén, K.-G. Karlsson and C.G. Jones, 2010. Quantifying the clear-sky temperature inversion frequency and strength over the Arctic Ocean during summer and winter seasons from AIRS profiles. Atmospheric Chemistry and Physics, 10(12):5565–5572.

Devasthale, A., J. Sedlar, M. Tjernström and A. Kokhanovsky, 2020. A Climatological Overview of Arctic Clouds. In: Kokhanovsky, A. and C. Tomasi (Eds). Physics and Chemistry of the Arctic Atmosphere, pp. 331–360, Springer.

Di Biagio, C., J. Pelon, G. Ancellet, A. Bazureau and V. Mariage, 2018. Sources, load, vertical distribution, and fate of wintertime aerosols north of Svalbard from combined V4 CALIOP data, ground-based IAOOS lidar observations and trajectory analysis. Journal of Geophysical Research: Atmospheres, 123(2):1363–1383.

Di Mauro, B., F. Fava, L. Ferrero, R. Garzonio, G. Baccolo, B. Delmonte and R. Colombo, 2015. Mineral dust impact on snow radiative properties in the European Alps combining ground, UAV, and satellite observations. Journal of Geophysical Research: Atmospheres, 120(12):6080–6097.

Di Pierro, M., L. Jaeglé, E.W. Eloranta and S. Sharma, 2013. Spatial and seasonal distribution of Arctic aerosols observed by the CALIOP satellite instrument (2006–2012). Atmospheric Chemistry and Physics, 13(14):7075–7095.

Dickens, G.R., 2003. A methane trigger for rapid warming? Science, 299(5609):1017.

Dickens, G.R., 2011. Down the rabbit hole: toward appropriate discussion of methane release from gas hydrate systems during the Paleocene-Eocene thermal maximum and other past hyperthermal events. Climate of the Past, 7(3):831–846.

Dlugokencky, E.J., L.P. Steele, P.M. Lang, K.A. Masarie, 1994. The growth rate and distribution of atmospheric methane. Journal of Geophysical Research: Atmospheres, 99(D8):17021–17043.

Doherty, S.J., S.G. Warren, T.C. Grenfell, A.D. Clarke and R.E. Brandt, 2010. Light-absorbing impurities in Arctic snow. Atmospheric Chemistry and Physics, 10(23):11647–11680.

Doherty, S.J., M. Steele, I. Rigor, and S.G. Warren, 2015. Interannual variations of light-absorbing particles in snow on Arctic sea ice. Journal of Geophysical Research: Atmospheres, 120(21):11,391–11,400.

Doherty, S.J., D.A. Hegg, J.E. Johnson, P.K. Quinn, J.P. Schwarz, C. Dang and S.G. Warren, 2016. Causes of variability in light absorption by particles in snow at sites in Idaho and Utah. Journal of Geophysical Research: Atmospheres, 121(9):4751–4768.

Dong, X., Q. Zhu, J.S. Fu, K. Huang, J. Tan and M. Tipton, 2019. Evaluating recent updated black carbon emissions and revisiting the direct radiative forcing in Arctic. Geophysical Research Letters, 46(6):3560–3570.

Donth, T., E Jäkel, A. Ehrlich, B. Heinold, J. Schacht, A. Herber, M. Zanatta and M. Wendisch, 2020. Combining atmospheric and snow radiative transfer models to assess the solar radiative effects of black carbon in the Arctic. Atmospheric Chemistry and Physics, 20(13):8139–8156.

Dordević, D., I. Tošic, S. Sakan, S. Petrović, J. Duričic-Milanković, D.C. Finger and P. Dagsson-Waldhauserova, 2019. Can volcanic dust suspended From surface soil and deserts of Iceland be transferred to Central Balkan similarly to African dust (Sahara)?. Frontiers in Earth Science, 7:142.

Dou, T., C. Xiao, D.T. Shindell, J. Liu, K. Eleftheriadis, J. Ming and D. Qin, 2012. The distribution of snow black carbon observed in the Arctic and compared to the GISS-PUCCINI model. Atmospheric Chemistry and Physics, 12(17):7995–8007.

Dou, T.-F. and C.-D. Xiao, 2016. An overview of black carbon deposition and its radiative forcing over the Arctic. Advances in Climate Change Research, 7(3):115–122.

Dou, T., C. Xiao, Z. Du, J.J. Schauer, H. Ren, B. Ge, A. Xie, J. Tan, P. Fu and Y. Zhang, 2017. Sources, evolution and impacts of EC and OC in snow on sea ice: a measurement study in Barrow, Alaska. Science Bulletin, 62(22):1547–1554.

Douglas, P.M.J., D.A. Stolper, D.A. Smith, K.M. Walter Anthony, C.K. Paull, S. Dallimore, M. Wik, P.M. Crill, M. Winterdahl, J.M. Eiler and A.L. Sessions, 2016. Diverse origins of Arctic and Subarctic methane point source emissions identified with multiply-substituted isotopologues. Geochimica et Cosmochimica Acta, 188:163–188.

Dragosics, M., O. Meinander, T. Jónsdóttír, T. Dürig, G. De Leeuw, F. Pálsson, P. Dagsson-Waldhauserova and T. Thorsteinsson, 2016. Insulation effects of Icelandic dust and volcanic ash on snow and ice. Arabian Journal of Geosciences, 9:126.

Dronin, N. and A. Kirilenko, 2011. Climate change, food stress, and security in Russia. Regional Environmental Change, 11:167–178.

Drugé, T., P. Nabat, M. Mallet and S. Somot, 2019. Model simulation of ammonium and nitrate aerosols distribution in the Euro-Mediterranean region and their radiative and climatic effects over 1979–2016. Atmospheric Chemistry and Physics, 19(6):3707–3731.

Dumont, M., E. Brun, G. Picard, M. Michou, Q. Libois, J.-R. Petit, M. Geyer, S. Morin and B. Josse, 2014. Contribution of light-absorbing impurities in snow to Greenland's darkening since 2009. Nature Geoscience, 7:509–512.

Duncan, B.N., L.E. Ott, J.B. Abshire, L. Brucker, M.L. Carroll, J. Carton, J.C. Comiso, E.P. Dinnat, B.C. Forbes, A. Gonsamo, W.W. Gregg, D.K. Hall, I. Ialongo, R. Jandt, R.A. Kahn, A. Karpechko, S.R. Kawa, S. Kato, T Kumpula, E. Kyrölä, T.V. Loboda, K.C. McDonald, P.M. Montesano, R. Nassar, C.S.R. Neigh, C.L. Parkinson, B. Poulter, J. Pulliainen, K. Rautiainen, B.M. Rogers, C.S. Rousseaux, A.J. Soja, N. Steiner, J. Tamminen, P.C. Taylor, M.A. Tzortziou, H. Virta, J.S. Wang, J.D. Watts, D.M. Winker and D.L. Wu, 2020. Space-based observations for understanding changes in the Arctic-boreal zone. Reviews of Geophysics, 58(1):e2019RG000652.

Dutkiewicz, V.A., A.M. DeJulio, T. Ahmed, J. Laing, P.K. Hopke, R.B. Skeie, Y. Viisanen, J. Paatero and L. Husain, 2014. Forty-seven years of weekly atmospheric black carbon measurements in the Finnish Arctic: decrease in black carbon with declining emissions. Journal of Geophysical Research: Atmospheres, 119(12):7667–7683.

Eastman, R. and S.G. Warren, 2010. Interannual variations of Arctic cloud types in relation to sea ice. Journal of Climate, 23(15):4216–4232.

EC, 2005. CAFE CBA: Baseline Analysis 2000 to 2020. Service Contract for Carrying out Cost-Benefit Analysis of Air Quality Related Issues, in Particular in the Clean Air for Europe (CAFE) Programme. Available at: https://ec.europa.eu/environment/archives/cafe/activities/pdf/cba_baseline_results2000_2020.pdf

EC, 2017. Forest fire danger extremes in Europe under climate change: variability and uncertainty. JRC Technical Reports. European Commission (EC), Luxembourg. 71pp.

ECCC, 2020. National Inventory Report 1990–2018: Greenhouse Gas Sources and Sinks in Canada, Part 2. Environment and Climate Change Canada (ECCC), Gatineau, Quebec, Canada. xi + 259pp.

Eck, T.F., B.N. Holben, J.S. Reid, O. Dubovik, A. Smirnov, N.T. O'Neill, I. Slutsker and S. Kinne, 1999. Wavelength dependence of the optical depth of biomass burning, urban and desert dust aerosols. Journal of Geophysical Research: Atmospheres, 104(D24):31333–31349.

Eckhardt, S., B. Quennehen, D.J.L. Olivié, T.K. Berntsen, R. Cherian, J.H. Christensen, W. Collins, S. Crepinsek, N. Daskalakis, M. Flanner, A. Herber, C. Heyes, Ø. Hodnebrog, L. Huang, M. Kanakidou, Z. Klimont, J. Langner, K.S. Law, M.T. Lund, R. Mahmood, A. Massling, S. Myriokefalitakis, I.E. Nielsen, J.K. Nøjgaard, J. Quaas, P.K. Quinn, J.-C. Raut, S.T. Rumbold, M. Schulz, S. Sharma, R.B. Skeie, H. Skov, T. Uttal, K. von Salzen and A. Stohl, 2015. Current model capabilities for simulating black carbon and sulfate concentrations in the Arctic atmosphere: a multi-model evaluation using a comprehensive measurement dataset. Atmospheric Chemistry and Physics, 15(16):9413–9433.

EEA, 2014. Effects of air pollution on European ecosystems. Technical Report EEA 11/2014, European Environment Agency (EEA), Copenhagen, Denmark. 38pp.

EEA, 2017. Air quality in Europe, Technical report 13/2017. European Environment Agency (EEA), Copenhagen, Denmark. 74pp.

EGBCM, 2017. Expert Group on Black Carbon and Methane: Summary of Progress and Recommendations 2017. Expert Group on Black Carbon and Methane (EGBCM). Arctic Council Secretariat, Tromsø, Norway. iv + 46pp.

Ehhalt, D.H, 1974. The Atmospheric Cycle of Methane. Tellus, 26(1–2):58–70.

Eirund, G.K., A. Possner and U. Lohmann, 2019. Response of Arctic mixed-phase clouds to aerosol perturbations under different surface forcings. Atmospheric Chemistry and Physics, 19(15):9847–9864.

Elder, C.D., X. Xu, J. Walker, J.L. Schnell, K.M. Hinkel, A. Townsend-Small, C.D. Arp, J.W. Pohlman, B.V. Gaglioti and C.I. Czimczik, 2018. Greenhouse gas emissions from diverse Arctic Alaskan lakes are dominated by young carbon. Nature Climate Change, 8:166–171.

Elder, C.D., D.R. Thompson, A.K. Thorpe, P. Hanke, K.M. Walter Anthony and C.E. Miller, 2020. Airborne mapping reveals emergent power law of Arctic methane emissions. Geophysical Research Letters, 47(3):e2019GL085707.

Eleftheriadis, K., S. Vratolis and S. Nyeki, 2009. Aerosol black carbon in the European Arctic: Measurements at Zeppelin station, Ny-Ålesund, Svalbard from 1998–2007. Geophysical Research Letters, 36(2):L02809.

Ellsworth, D.S., R. Thomas, K.Y. Crous, S. Palmroth, E. Ward, C. Maier, E. DeLucia and R. Oren, 2012. Elevated CO_2 affects photosynthetic responses in canopy pine and subcanopy deciduous trees over 10 years: a synthesis from Duke FACE. Global Change Biology, 18(1):223–242.

Elmes, M.C., D.K. Thompson, J.H. Sherwood and J.S. Price, 2018. Hydrometeorological conditions preceding wildfire, and the subsequent burning of a fen watershed in Fort McMurray, Alberta, Canada. Natural Hazards and Earth System Sciences, 18(1):157–170.

Elmquist, M., G. Cornelissen, Z. Kukulska and Ö. Gustafsson, 2006. Distinct oxidative stabilities of char versus soot black carbon: implications for quantification and environmental recalcitrance. Global Biogeochemical Cycles, 20(2):GB2009.

Elvidge, C.D., M. Zhizhin, K. Baugh, F.-C. Hsu and T. Ghosh, 2016. Methods for Global Survey of Natural Gas Flaring from Visible Infrared Imaging Radiometer Suite Data. Energies 9(1):14.

Emberson, L.D., M.R. Ashmore, H.M. Cambridge, D. Simpson and J.-P. Tuovinen, 2000. Modelling stomatal ozone flux across Europe. Environmental Pollution, 109(3):403–413.

Emberson, L.D., H. Pleijel, E.A. Ainsworth, M. van den Berg, W. Ren, S. Osborne, G. Mills, D. Pandey, F. Dentener, P. Büker, F. Ewert, R. Koeble and R. Van Dingenen, 2018. Ozone effects on crops and consideration in crop models. European Journal of Agronomy, 100:19–34.

Emmons, L.K., S.R. Arnold, S.A. Monks, V. Huijnen, S. Tilmes, K.S. Law, J.L. Thomas, J.-C. Raut, I. Bouarar, S. Turquety, Y. Long, B. Duncan, S. Steenrod, S. Strode, J. Flemming, J. Mao, J. Langner, A.M. Thompson, D. Tarasick, E.C. Apel, D.R. Blake, R.C. Cohen, J. Dibb, G.S. Diskin, A. Fried, S.R. Hall, L.G. Huey, A.J. Weinheimer, A. Wisthaler, T. Mikoviny, J. Nowak, J. Peischl, J.M. Roberts, T. Ryerson, C. Warneke and D. Helmig, 2015. The POLARCAT Model Intercomparison Project (POLMIP): overview and evaluation with observations. Atmospheric Chemistry and Physics, 15(12):6721–6744.

Emmons, L.K., R.H. Schwantes, J.J. Orlando, G. Tyndall, D. Kinnison, J.-F. Lamarque, D. Marsh, M.J. Mills, S. Tilmes, C. Bardeen, R.R. Buchholz, A. Conley, A. Gettelmann, R. Garcia, I. Simpson, D.R Blake, S. Meinardi and G. Pétron, 2020. The chemistry mechanism in the Community Earth System Model version 2 (CESM2). Journal of Advances in Modeling Earth Systems, 12(4):e2019MS001882.

Engram, M., K.M. Walter Anthony, T. Sachs, K. Kohnert, A. Serafimovich, G. Grosse and F.J. Meyer, 2020. Remote sensing northern lake methane ebullition. Nature Climate Change, 10:511–517.

Engvall Stjernberg, A.-C., A. Skorokhod, J.D. Paris, N. Elansky, P. Nédélec and A. Stohl, 2012. Low concentrations of near-surface ozone in Siberia. Tellus B: Chemical and Physical Meteorology, 64(1):11607.

Environment Canada, 2013. RAQDPS Versions 1.5.0 and 1.5.1: Upgrades to the CMC Operational Regional Air Quality Deterministic Prediction System Released in October 2012 and February 2013. Environment Canada, Dorval, Quebec. 29pp. Available at: https://collaboration.cmc.ec.gc.ca/cmc/CMOI/product_guide/docs/lib/op_systems/doc_opchanges/technote_raqdps_20130226_e.pdf

EPRI, 1989. Intercomparison of the ADOM and RADM gas-phase chemical mechanisms. Electrical Power Research Institute (EPRI), Paolo Alto, California, USA, 254pp.

Erisman, J.W., A. Bleeker, J. Galloway and M.S. Sutton, 2007. Reduced nitrogen in ecology and the environment. Environmental Pollution, 150(1):140–149.

Esau, I. and S. Sorokina, 2011. Climatology of the arctic planetary boundary layer. In: Lang, P.R. and F.S. Lombargo (Eds.). Atmospheric Turbulence, Meteorological Modeling and Aerodynamics, pp. 3–58. Nova Science Publishers.

Estop-Aragonés, C., C.I. Czimczik, L. Heffernan, C. Gibson, J.C. Walker, X. Xu and D. Olefeldt, 2018. Respiration of aged soil carbon during fall in permafrost peatlands enhanced by active layer deepening following wildfire but limited following thermokarst. Environmental Research Letters, 13(8):085002.

Estop-Aragonés, C., D. Olefeldt, B.W. Abbott, J.P. Chanton, C.I. Czimczik, J.F. Dean, J.E. Egan, L. Gandois, M.H. Garnett, I.P. Hartley, A. Hoyt, M. Lupascu, S.M. Natali, J.A. O'Donnell, P.A. Raymond, A.J. Tanentzap, S.E. Tank, E.A.G. Schuur, M. Turetsky, K. Walter Anthony, 2020. Assessing the potential for mobilization of old soil carbon after permafrost thaw: A synthesis of ^{14}C measurements from the northern permafrost region. Global Biogeochemical Cycles, 34, e2020GB006672.

Etminan, M., G. Myhre, E.J. Highwood and K.P. Shine, 2016. Radiative forcing of carbon dioxide, methane, and nitrous oxide: a significant revision of the methane radiative forcing. Geophysical Research Letters, 43(24): 12,614–12,623.

EUA-BCA, 2019a. Review of Reporting Systems for National Black Carbon Emissions Inventories: EU Action on Black Carbon in the Arctic - Technical Report 2. April 2019. iv + 72pp.

EUA-BCA, 2019b. Review of observation capacities and data availability for Black Carbon in the Arctic region: EU Action on Black Carbon in the Arctic - Technical Report 1. December 2019. iv + 35pp.

Evangeliou, N., Y. Balkanski, W.M. Hao, A. Petkov, R.P. Silverstein, R. Corley, B.L. Nordgren, S.P. Urbanski, S. Eckhardt, A. Stohl, P. Tunved, S. Crepinsek, A. Jefferson, S. Sharma, J.K. Nøjgaard and H. Skov, 2016. Wildfires in northern Eurasia affect the budget of black carbon in the Arctic – a 12-year retrospective synopsis (2002–2013). Atmospheric Chemistry and Physics, 16(12):7587–7604.

Evangeliou, N., A. Kylling, S. Eckhardt, V. Myroniuk, K. Stebel, R. Paugam, S. Zibtsev and A. Stohl, 2019. Open fires in Greenland in summer 2017: transport, deposition and radiative effects of BC, OC and BrC emissions. Atmospheric Chemistry Physics, 19(2):1393–1411.

Evangeliou, N., V.P. Shevchenko, K.E. Yttri, S. Eckhardt, E. Sollum, O.S. Pokrovsky, V.O. Kobelev, V.B. Korobov, A.A. Lobanov, D.P. Starodymova, S.N. Vorobiev, R.L. Thompson and A. Stohl, 2018. Origin of elemental carbon in snow from western Siberia and northwestern European Russia during winter–spring 2014, 2015 and 2016. Atmospheric Chemistry and Physics, 18(2):963–977.

Evans, M., N. Kholod, T. Kuklinski, A. Denysenko, S.J. Smith, A. Staniszewski, W.M. Hao, L. Liu and T.C. Bond, 2017. Black carbon emissions in Russia: A critical review. Atmospheric Environment, 163:9–21.

Fairlie, T.D., D.J. Jacob and R.J. Park, 2007. The impact of transpacific transport of mineral dust in the United States. Atmospheric Environment, 41(6):1251–1266.

Fan, S-M., 2013. Modeling of observed mineral dust aerosols in the Arctic and the impact on winter season low-level clouds. Journal of Geophysical Research: Atmospheres, 118(19):11161–11174.

FAO, 2012. World agriculture towards 2030/2050: the 2012 revision. ESA Working paper No. 12–03. Alexandratos, N. and J. Bruinsma, Food and Agriculture Organization of the United Nations (FAO). Rome, Italy. vi + 147pp.

Feng, Z. and K. Kobayashi, 2009. Assessing the impacts of current and future concentrations of surface ozone on crop yield with meta-analysis. Atmospheric Environment, 43(8):1510–1519.

Feng, Z., K. Kobayashi and E.A. Ainsworth, 2008. Impact of elevated ozone concentration on growth, physiology, and yield of wheat (Triticum aestivum L.): a meta-analysis. Global Change Biology, 14(11):2696–2708.

Feng, L., S.J. Smith, C. Braun, M. Crippa, M.J. Gidden, R. Hoesly, Z. Klimont, M. van Marle, M. van den Berg and G.R. van der Werf, 2020. The generation of gridded emissions data for CMIP6. Geoscientific Model Development, 13(2):461–482.

Fenwick, L., D. Capelle, E. Damm, S. Zimmermann, W.J. Williams, S. Vagle and P.D. Tortell, 2017. Methane and nitrous oxide distributions across the North American Arctic Ocean during summer, 2015. Journal of Geophysical Research: Oceans, 122(1):390–412.

Ferrero, L., D. Cappelletti, M. Busetto, M. Mazzola, A. Lupi, C. Lanconelli, S. Becagli, R. Traversi, L. Caiazzo, F. Giardi, B. Moroni, S. Crocchianti, M. Fierz, G. Močnik, G. Sangiorgi, M.G. Perrone, M. Maturilli, V. Vitale, R. Udisti and E. Bolzacchini, 2016. Vertical profiles of aerosol and black carbon in the Arctic: a seasonal phenomenology along 2 years (2011–2012) of field campaigns. Atmospheric Chemistry and Physics, 16(19):12601–12629.

Ferrero, L., G. Sangiorgi, M.G. Perrone, C. Rizzi, M. Cataldi, P. Markuszewski, P. Pakszys, P. Makuch, T. Petelski, S. Becagli, R. Traversi, E. Bolzacchini and T. Zielinski, 2019. Chemical composition of aerosol over the Arctic Ocean from summer ARctic EXpedition (AREX) 2011–2012 cruises: ions, amines, elemental carbon, organic matter, polycyclic aromatic hydrocarbons, n-alkanes, metals, and rare earth elements. Atmosphere, 10(2):54.

Fialho, P., M. Cerqueira, C. Pio, J. Cardoso, T. Nunes, D. Custódio, C. Alves, S.M. Almeida, M. Almeida-Silva, M. Reis and F. Rocha, 2014. The application of a multi-wavelength Aethalometer to estimate iron dust and black carbon concentrations in the marine boundary layer of Cape Verde. Atmospheric Environment 97:136–143.

Finnbjornsdottir, R.G., H.K. Carlsen, T. Thorsteinsson, A. Oudin, S.H. Lund, T. Gislason and V. Rafnsson, 2016. Association between daily hydrogen sulfide exposure and incidence of emergency hospital visits: a population-based study. PLOS ONE, 11(5):e0154946.

Fiore, A.M., J.J. West, L.W. Horowitz, V. Naik and M.D. Schwarzkopf, 2008. Characterizing the tropospheric ozone response to methane emission controls and the benefits to climate and air quality. Journal of Geophysical Research: Atmospheres, 113(D8):D08307.

Fiore, A.M., F.J. Dentener, O.Wild, C. Cuvelier, M.G. Schultz, P. Hess, C. Textor, M. Schulz, R.M. Doherty, L.W. Horowitz, I.A. MacKenzie, M.G. Sanderson, D.T. Shindell, D.S. Stevenson, S. Szopa, R. Van Dingenen, G. Zeng, C. Atherton, D. Bergmann, I. Bey, G. Carmichael, W.J. Collins, B.N. Duncan, G. Faluvegi, G. Folberth, M. Gauss, S. Gong, D. Hauglustaine, T. Holloway, I.S.A. Isaksen, D.J. Jacob, J.E. Jonson, J.W.Kaminski, T.J.Keating, A. Lupu, E. Marmer, V. Montanaro, R.J. Park, G. Pitari, K.J. Pringle, J.A. Pyle, S. Schroeder, M.G. Vivanco, P.Wind, G.Wojcik, S. Wu and A. Zuber, 2009. Multimodel estimates of intercontinental source-receptor relationships for ozone pollution. Journal of Geophysical Research: Atmospheres, 114(D4).

Fischer, E.V., D.J. Jacob, R.M. Yantosca, M.P. Sulprizio, D.B. Millet, J. Mao, F. Paulot, H.B. Singh, A.-E. Roiger, L. Ries, R.W. Talbot, K. Dzepina and S. Pandey Deolal, 2014. Atmospheric peroxyacetyl nitrate (PAN): a global budget and source attribution, Atmospheric Chemistry and Physics, 14(5):2679–2698.

Fisher, J.A., D.J. Jacob, K.R. Travis, P.S. Kim, E.A. Marais, C. Chan Miller, K. Yu, L. Zhu, R.M. Yantosca, M.P. Sulprizio, J. Mao, P.O. Wennberg, J.D. Crounse, A.P. Teng, T.B. Nguyen, J.M. St. Clair, R.C. Cohen, P. Romer, B.A. Nault, P.J. Wooldridge, J.L. Jimenez, P. Campuzano-Jost, D.A. Day, P.B. Shepson, F. Xiong, D.R. Blake, A.H. Goldstein, P.K. Misztal, T.F. Hanisco, G.M. Wolfe, T.B. Ryerson, A. Wisthaler and T. Mikoviny, 2016. Organic nitrate chemistry and its implications for nitrogen budgets in an isoprene- and monoterpene-rich atmosphere: constraints from aircraft (SEAC^{4}RS) and ground-based (SOAS) observations in the Southeast US. Atmospheric Chemistry and Physics, 16(9):5969–5991.

Flanner, M.G., 2013. Arctic climate sensitivity to local black carbon. Journal of Geophysical Research: Atmospheres, 118: 1840–1851.

Flanner, M.G., C.S. Zender, J.T. Randerson and P.J. Rasch, 2007. Present-day climate forcing and response from black carbon in snow. Journal of Geophysical Research: Atmospheres, 112(D11).

Flanner, M.G., A.S. Gardner, S. Eckhardt, A. Stohl and J. Perket, 2014. Aerosol radiative forcing from the 2010 Eyjafjallajökull volcanic eruptions. Journal of Geophysical Research: Atmospheres, 119(15):9481–9491.

Flannigan, M., A.S. Cantin, W.J. de Groot, M. Wotton, A. Newbery and L.M. Gowman, 2013. Global wildland fire season severity in the 21st century. Forest Ecology and Management, 294:54–61.

Foltescu, V., S. Pryor and C. Bennet, 2005. Sea salt generation, dispersion and removal on the regional scale. Atmospheric Environment, 39(11):2123–2133.

Foreman, K.J., N. Marquez, A. Dolgert, K. Fukutaki, N. Fullman, M. McGaughey, M.A. Pletcher, A.E. Smith, K. Tang, C.-W. Yuan, J.C. Brown, J. Friedman, J. He, K.R. Heuton, M. Holmberg, D.J. Patel, P. Reidy, A. Carter, K. Cercy, A. Chapin, D. Douwes-Schultz, T. Frank, F. Goettsch, P.Y. Liu, V. Nandakumar, M.B. Reitsma, V. Reuter, N. Sadat, R.J.D. Sorensen, V. Srinivasan, R.L. Updike, H. York, A.D. Lopez, R. Lozano, S.S. Lim, A.H. Mokdad, S.E. Vollset and C.J.L. Murray, 2018. Forecasting life expectancy, years of life lost, and all-cause and cause-specific mortality for 250 causes of death: reference and alternative scenarios for 2016–40 for 195 countries and territories. The Lancet, 392(10159):2052–2090.

Forsius, M., M. Posch, J. Aherne, G.J. Reinds, J. Christensen and L. Hole, 2010. Assessing the impacts of long-range sulfur and nitrogen deposition on Arctic and sub-Arctic ecosystems. Ambio, 39(2):136–147.

Forsström, S., J. Ström, C.A. Pedersen, E. Isaksson and S. Gerland, 2009. Elemental carbon distribution in Svalbard snow. Journal of Geophysical Research: Atmospheres, 114(D19):D19112.

Forsström, S., E. Isaksson, R.B. Skeie, J. Ström, C.A. Pedersen, S.R. Hudson, T.K. Berntsen, H. Lihavainen, F. Godtliebsen and S. Gerland, 2013. Elemental carbon measurements in European Arctic snow packs. Journal of Geophysical Research: Atmospheres, 118(24):13614–13627.

Forster, C., A. Stohl and P. Seibert, 2007. Parameterization of convective transport in a Lagrangian particle dispersion model and its evaluation. Journal of Applied Meteorology and Climatology, 46(4):403–422.

Foster, A.C., A.H. Armstrong, J.K. Shuman, H.H. Shugart, B.M. Rogers, M.C. Mack, S.J. Goetz and K.J. Ranson, 2019. Importance of tree-and species-level interactions with wildfire, climate, and soils in interior Alaska: Implications for forest change under a warming climate. Ecological Modelling, 409:108765.

France, J.L., M. Cain, R.E. Fisher, D. Lowry, G. Allen, S.J. O'Shea, S. Illingworth, J. Pyle, N. Warwick, B.T. Jones, M.W. Gallagher, K. Bower, M. Le Breton, C. Percival, J. Muller, A. Welpott, S. Bauguitte, C. George, G.D. Hayman, A.J. Manning, C. Lund Myhre, M. Lanoisellé and E.G. Nisbet, 2016. Measurements of $\delta^{13}C$ in CH_4 and using particle dispersion modeling to characterize sources of Arctic methane within an air mass. Journal of Geophysical Research: Atmospheres, 121(23):14257–14270.

Freud, E., R. Krejci, P. Tunved, R. Leaitch, Q.T. Nguyen, A. Massling, H. Skov and L. Barrie, 2017. Pan-Arctic aerosol number size distributions: seasonality and transport patterns. Atmospheric Chemistry and Physics, 17(13):8101–8128.

Fröhlich, R., M.J. Cubison, J.G. Slowik, N. Bukowiecki, A.S.H. Prévôt, U. Baltensperger, J. Schneider, J.R. Kimmel, M. Gonin, U. Rohner, D.R. Worsnop and J.T. Jayne, 2013. The ToF-ACSM: a portable aerosol chemical speciation monitor with TOFMS detection. Atmospheric Measurement Techniques, 6(11):3225–3241.

Fu, P., K. Kawamura and L.A. Barrie, 2009. Photochemical and other sources of organic compounds in the Canadian High Arctic aerosol pollution during winter–spring. Environmental Science & Technology, 43(2):286–292.

Fu, P.Q., K. Kawamura, J. Chen, B. Charrière, and R. Sempéré, 2013. Organic molecular composition of marine aerosols over the Arctic Ocean in summer: contributions of primary emission and secondary aerosol formation. Biogeosciences, 10(2):653–667.

Fu, P., K. Kawamura, J. Chen, M. Qin, L. Ren, Y. Sun, Z. Wang, L.A. Barrie, E. Tachibana, A. Ding and Y. Yamashita, 2015. Fluorescent water-soluble organic aerosols in the High Arctic atmosphere. Scientific Reports, 5:9845.

Fu, P., G. Zhuang, Y. Sun, Q. Wang, J. Chen, L. Ren, F. Yang, Z. Wang, X. Pan, X. Li and K. Kawamura, 2016. Molecular markers of biomass burning, fungal spores and biogenic SOA in the Taklimakan desert aerosols. Atmospheric Environment, 130:64–73.

Fugal, J.P. and R.A. Shaw, 2009. Cloud particle size distributions measured with an airborne digital in-line holographic instrument. Atmospheric Measurement Techniques, 2(1):259–271.

Friedrich, R. and P. Bickel (Eds.), 2001. Environmental External Costs of Transport. Springer, Munich, Germany. 326pp.

Friend, A.D., A. Arneth, N.Y. Kiang, M. Lomas, J. Ogée, C. Rödenbeck, S.W. Running, J.-D. Santaren, S. Sitch, N. Viovy, F.I. Woodward and S. Zaehle, 2006. FLUXNET and modelling the global carbon cycle. Global Change Biology, 13(3):610–633.

Fung, K, 1990. Particulate carbon speciation by MnO_2 oxidation. Aerosol Science and Technology, 12(1):122–127.

Fung, I., J. John, J. Lerner, E. Matthews, M. Prather, L.P. Steele and P.J. Fraser, 1991. Three-dimensional model synthesis of the global methane cycle. Journal of Geophysical Research: Atmospheres, 96(D7):13033–13065.

Fusco, E.J., J.T. Finn, J.T. Abatzoglou, J.K. Balch, S. Dadashi and B.A. Bradley, 2019. Detection rates and biases of fire observations from MODIS and agency reports in the conterminous United States. Remote Sensing of Environment, 220:30–40.

Fyfe, J.C., K. von Salzen, N.P. Gillett, V.K. Arora, G.M. Flato and J. R. McConnell, 2013. One hundred years of Arctic surface temperature variation due to anthropogenic influence. Scientific Reports, 3:2645.

Gagné, M.-È., N.P. Gillett, and J.C. Fyfe, 2015. Observed and simulated changes in Antarctic sea ice extent over the past 50 years. Geophysical Research Letters, 42(1):90–95.

Gålfalk, M., D. Bastviken, S. Fredriksson and L. Arneborg, 2013. Determination of the piston velocity for water-air interfaces using flux chambers, acoustic Doppler velocimetry, and IR imaging of the water surface. Journal of Geophysical Research: Biogeosciences, 118(2):770–782.

Galindo, N., J. Gil-Moltó, M. Varea, C. Chofre and E. Yubero, 2013. Seasonal and interannual trends in PM levels and associated inorganic ions in southeastern Spain. Microchemical Journal 110:81–88.

Gao, Y., C.M. Marsay, S. Yu, S. Fan, P. Mukherjee, C.S. Buck and W.M. Landing, 2019. Particle-size variability of aerosol iron and impact on iron solubility and dry deposition fluxes to the Arctic Ocean. Scientific Reports, 9:16653.

Garbe, C.S, A. Rutgersson, J. Boutin, G. de Leeuw, B. Delille, C.W. Fairall, N. Gruber, J. Hare, D.T. Ho, M.T. Johnson, P.D. Nightingale, H. Pettersson, J. Piskozub, E. Sahlée, W.-t. Tsai, B. Ward, D.K. Woolf, C.J. Zappa, 2014. Transfer across the air-sea interface. In: Liss, P.S. and M.T. Johnson (Eds). Ocean-Atmosphere Interactions of Gases and Particles, pp. 55–112. Springer.

Garcia, J.-L., B.K.C. Patel and B. Ollivier, 2000. Taxonomic, phylogenetic, and ecological diversity of methanogenic *Archaea*. Anaerobe, 6(4):205–226.

Gardner, A.S. and M.J. Sharp, 2010. A review of snow and ice albedo and the development of a new physically based broadband albedo parameterization. Journal of Geophysical Research, 115(F1), F01009.

Garrett, T.J., and C. Zhao, 2006. Increased Arctic cloud longwave emissivity associated with pollution from mid-latitudes. Nature, 440:787–789.

Garrett, T.J., S. Brattström, S. Sharma, D.E.J. Worthy and P. Novelli, 2011. The role of scavenging in the seasonal transport of black carbon and sulfate to the Arctic. Geophysical Research Letters, 38(16):L1685.

Gaudel, A., O.R. Cooper, G. Ancellet, B. Barret, A. Boynard, J.P. Burrows, C. Clerbaux, P.-F. Coheur, J. Cuesta, E. Cuevas, S. Doniki, G. Dufour, F. Ebojie, G. Foret, O. Garcia, M.J. Granados-Muñoz, J.W. Hannigan, F. Hase, B. Hassler, G. Huang, D. Hurtmans, D. Jaffe, N. Jones, P. Kalabokas, B. Kerridge, S. Kulawik, B. Latter, T. Leblanc, E. Le Flochmoën, W. Lin, J. Liu, X. Liu, E. Mahieu, A. McClure-Begley, J.L. Neu, M. Osman, M. Palm, H. Petetin, I. Petropavlovskikh, R. Querel, N. Rahpoe, A. Rozanov, M.G. Schultz, J. Schwab, R. Siddans, D. Smale, M. Steinbacher, H. Tanimoto, D.W. Tarasick, V. Thouret, A.M. Thompson, T. Trickl, E. Weatherhead, C. Wespes, H.M. Worden, C. Vigouroux, X. Xu, G. Zeng and J. Ziemke, 2018. Tropospheric Ozone Assessment Report: Present-day distribution and trends of tropospheric ozone relevant to climate and global atmospheric chemistry model evaluation. Elementa: Science of the Anthropocene, 6:39.

Gauss, M., S. Tsyro. A. Benedictow, A.-G. Hjellbrekke, W. Aas and S. Solberg, 2020. EMEP MSC-W model performance for acidifying and eutrophying components, photo-oxidants and particulate matter in 2018. Supplementary material to EMEP Status Report 1/2020. Norwegian Meteorological Institute, Oslo, Norway. iv + 130pp.

Gautrois, M., T. Brauers, R. Koppmann, F. Rohrer, O. Stein and J. Rudolph, 2003. Seasonal variability and trends of volatile organic compounds in the lower polar troposphere. Journal of Geophysical Research: Atmospheres, 108(D13).

GBD 2017 Risk Factor Collaborators, 2018. Global, regional, and national comparative risk assessment of 84 behavioural, environmental and occupational, and metabolic risks or clusters of risks for 195 countries and territories, 1990–2017: a systematic analysis for the Global Burden of Disease Study 2017. The Lancet, 392(10159):1923–1994.

GBD 2019 Risk Factor Collaborators, 2020. Global burden of 87 risk factors in 204 countries and territories, 1990–2019: a systematic analysis for the Global Burden of Disease Study 2019. The Lancet, 396 (10258):1223–1249.

Geels, C., C. Andersson, O. Hänninen, A.S. Lansø, P.E. Schwarze, C.A. Skjøth and J. Brandt, 2015. Future premature mortality due to O_3, secondary inorganic aerosols and primary PM in Europe – sensitivity to changes in climate, anthropogenic emissions, population and building stock. International Journal of Environmental Research and Public Health, 12(3):2837–2869.

Geels, C., M. Winther, C. Andersson, J.-P. Jalkanen, J. Brandt, L.M. Frohn, U. Im, W. Leung and J.H. Christensen, 2021. Projections of shipping emissions and the related impact on air pollution and human health in the Nordic region. Atmospheric Chemistry and Physics, 21(16):12495–12519.

Gelaro, R., W. McCarty, M.J. Suárez, R. Todling, A. Molod, L. Takacs, C.A. Randles, A. Darmenov, M.G. Bosilovich, R. Reichle, K. Wargan, L. Coy, R. Cullather, C. Draper, S. Akella, V. Buchard, A. Conaty, A.M. da Silva, W. Gu, G.-K. Kim, R. Koster, R. Lucchesi, D. Merkova, J.E. Nielsen, G. Partyka, S. Pawson, W. Putman, M. Rienecker, S.D. Schubert, M. Sienkiewicz and B. Zhao, 2017. The Modern-Era Retrospective Analysis for Research and Applications, version 2 (MERRA-2). Journal of Climate, 30(14):5419–5454.

Genberg, J., H.A.C. Denier van der Gon, D. Simpson, E. Swietlicki, H. Areskoug, D. Beddows, D. Ceburnis, M. Fiebig, H.C. Hansson, R.M. Harrison, S.G. Jennings, S. Saarikoski, G. Spindler, A.J.H. Visschedijk, A. Wiedensohler, K.E. Yttri and R. Bergström, 2013. Light-absorbing carbon in Europe – measurement and modelling, with a focus on residential wood combustion emissions. Atmospheric Chemistry and Physics, 13:8719–8738.

Gent, P.R., G. Danabasoglu, L.J. Donner, M.M. Holland, E.C. Hunke, S.R. Jayne, D.M. Lawrence, R.B. Neale, P.J. Rasch, M. Vertenstein, P.H. Worley, Z.-L. Yang and M. Zhang, 2011. The Community Climate System Model Version 4. Journal of Climate, 24(19):4973–4991.

Gery, M.W., G.Z. Whitten, J.P. Killus and M.C. Dodge, 1989. A photochemical kinetics mechanism for urban and regional scale computer modelling. Journal of Geophysical Research: Atmospheres, 94(D10):12925–12956.

Gewin, V., 2020. How peat could protect the planet. Nature, 578:204–208.

Ghahremaninezhad, R., A.-L. Norman, J.P.D. Abbatt, M. Levasseur and J.L. Thomas, 2016. Biogenic, anthropogenic and sea salt sulfate size-segregated aerosols in the Arctic summer. Atmospheric Chemistry and Physics, 16(8):5191–5202.

Ghan, S.J., 2013. Technical note: Estimating aerosol effects on cloud radiative forcing, Atmospheric Chemistry and Physics, 13(19):9971–9974.

Ghan, S.J., L.R. Leung, R.C. Easter and H. Abdul-Razzak, 1997. Prediction of cloud droplet number in a general circulation model. Journal of Geophysical Research: Atmospheres, 102(D18):21777– 21794.

Ghirardo A, F. Lindstein, K. Koch, F. Buegger, M. Schloter, A. Albert, A. Michelsen, J. B. Winkler, J.-P. Schnitzler and R. Rinnan, 2020. Origin of volatile organic compound emissions from subarctic tundra under global warming. Global Change Biology, 26(3):1908–1925.

Gibson, C.M., L.E. Chasmer, D.K. Thompson, W.L. Quinton, M.D. Flannigan and D. Olefeldt, 2018. Wildfire as a major driver of recent permafrost thaw in boreal peatlands. Nature communications, 9:3041.

Giesemann, A., H.-J. Jaeger, A.L. Norman, H.P. Krouse and W.A. Brand, 1994. Online sulfur-isotope determination using an elemental analyzer coupled to a mass-spectrometer. Analytical Chemistry, 66(18):2816–2819.

Giglio, L., L. Boschetti, D.P. Roy, M.L. Humber and C.O. Justice, 2018. The Collection 6 MODIS burned area mapping algorithm and product. Remote Sensing of Environment, 217:72–85.

Gilardoni, S., A. Lupi, M. Mazzola, D.M Cappelletti, B. Moroni, P. Markuszewski, A. Rozwadowska, R. Krejci, P. Zieger, P. Tunved, S. Vratolis, K. Eleftheriadis and A.P. Viola, 2019. Atmospheric black carbon in Svalbard (ABC Svalbard). The State of Environmental Science In Svalbard 2019 Report. 8:196–211.

Gilbert, R.O., 1987. Statistical methods for environmental pollution monitoring. Van Nostrand Reinhold Company.

Gilgen, A., W.T.K. Huang, L. Ickes, D. Neubauer and U. Lohmann, 2018. How important are future marine and shipping aerosol emissions in a warming Arctic summer and autumn? Atmopheric Chemistry and Physics, 18(14):10521–10555.

Gillett, N.P. and K. von Salzen, 2013. The role of reduced aerosol precursor emissions in driving near-term warming. Environmental Research Letters, 8:034008.

Giorio, C., N. Kehrwald, C. Barbante, M. Kalberer, A.C.F. King, E.R. Thomas, E.W. Wolff and P. Zennaro, 2018. Prospects for reconstructing paleoenvironmental conditions from organic compounds in polar snow and ice. Quaternary Science Reviews, 183:1–22.

Girardin, M.P. and A. Terrier, 2015. Mitigating risks of future wildfires by management of the forest composition: an analysis of the offsetting potential through boreal Canada. Climatic Change, 130:587–601.

Glantz, P., A. Bourassa, A. Herber, T. Iversen, J. Karlsson, A. Kirkevåg, M. Maturilli, Ø. Seland, K. Stebel, H. Struthers, M. Tesche and L. Thomason, 2014. Remote sensing of aerosols in the Arctic for an evaluation of global climate model simulations. Journal of Geophysical Research: Atmospheres, 119(13):8169–8188.

Gliß, J., A. Mortier, M. Schulz, E. Andrews, Y. Balkanski, S.E. Bauer, A.M.K Benedictow, H. Bian, R. Checa-Garcia, M. Chin, P. Ginoux, J.J. Griesfeller, A. Heckel, Z. Kipling, A. Kirkevåg, H. Kokkola, P. Laj, P. Le Sager, M.T. Lund, C. Lund Myhre, H. Matsui, G. Myhre, D. Neubauer, T. van Noije, P. North, D.J.L. Olivié, S. Rémy, L. Sogacheva, T. Takemura, K. Tsigaridis and S.G. Tsyro, 2021. AeroCom phase III multi-model evaluation of the aerosol life cycle and optical properties using ground- and space-based remote sensing as well as surface in situ observations. Atmospheric Chemistry and Physics, 21:87–128.

Goelles, T. and C.E. Bøggild, 2017. Albedo reduction of ice caused by dust and black carbon accumulation: a model applied to the K-transect, West Greenland. Journal of Glaciology, 63(242):1063–1076.

Gogoi, M.M., S.S. Babu, K.K. Moorthy, R.C. Thakur, J.P. Chaubey and V.S. Nair, 2016. Aerosol black carbon over Svalbard regions of Arctic. Polar Science, 10:60–70.

Gómez-Sanabria, A., L. Höglund-Isaksson, P. Rafaj and W. Schöpp, 2018. Carbon in global waste and wastewater flows – its potential as energy source under alternative future waste management regimes. Advances in Geosciences, 45:105–113.

Gong, S.L., L.A. Barrie, J.-P. Blanchet, K. von Salzen, U. Lohmann, G. Lesins, L. Spacek, L.M. Zhang, E. Girard, H. Lin, R. Leaitch, H. Leighton, P. Chylek and P. Huang, 2003. Canadian Aerosol Module: a size-segregated simulation of atmospheric aerosol processes for climate and air quality models 1. Module development. Journal of Geophysical Research: Atmospheres, 108(D1):AAC3-1–AAC3-16.

Gong, W., A.P. Dastoor, V.S. Bouchet, S. Gong, P.A. Makar, M.D. Moran, B. Pabla, S. Ménard, L.-P. Crevier, S. Cousineau and S. Venkatesh, 2006. Cloud processing of gases and aerosols in a regional air quality model (AURAMS). Atmospheric Research, 82(1):248–275.

Gong, W., P.A. Makar, J. Zhang, J. Milbrandt, S. Gravel, K.L. Hayden, A.M. Macdonald and W.R. Leaitch, 2015. Modelling aerosol–cloud–meteorology interaction: A case study with a fully coupled air quality model (GEM-MACH). Atmospheric Environment, 115:695–715.

Gong, W., S.R. Beagley, S. Cousineau, M. Sassi, R. Munoz-Alpizar, S. Ménard, J. Racine, J. Zhang, J. Chen, H. Morrison, S. Sharma, L. Huang, P. Bellavance, J. Ly, P. Izdebski, L. Lyons and R. Holt, 2018. Assessing the impact of shipping emissions on air pollution in the Canadian Arctic and northern regions: current and future modelled scenarios. Atmospheric Chemistry and Physics, 18:16653–16687.

Gosset, W. S., 1908. The probable error of a mean. Biometrika, 6(1):1–25.

Graff, L.S., T. Iversen, I. Bethke, J.B. Debernard, Ø. Seland, M. Bentsen, A. Kirkevåg, C. Li and D.J.L. Olivié, 2019. Arctic amplification under global warming of 1.5 and 2°C in NorESM1-Happi. Earth System Dynamics, 10(3):569–598.

Gralewicz, N.J., T.A. Nelson and M.A. Wulder, 2012. Factors influencing national scale wildfire susceptibility in Canada. Forest Ecology and Management, 265:20–29.

Granath, G., P.A. Moore, M.C. Lukenbach and J.M. Waddington, 2016. Mitigating wildfire carbon loss in managed northern peatlands through restoration. Scientific Reports, 6:28498.

Granier, C., B. Bessagnet, T. Bond, A. D'Angiola, H. Denier van der Gon, G.J. Frost, A. Heil, J.W. Kaiser, S. Kinne, Z. Klimont, S. Kloster, J.-F. Lamarque, C. Liousse, T. Masui, F. Meleux, A. Mieville, T. Ohara, J.-C. Raut, K. Riahi, M.G. Schultz, S.J. Smith, A. Thompson, J. van Aardenne, G.R. van der Werf and D.P. van Vuuren, 2011. Evolution of anthropogenic and biomass burning emissions of air pollutants at global and regional scales during the 1980–2010 period. Climatic Change 109:163.

Granström, A. and M. Niklasson, 2008. Potentials and limitations for human control over historic fire regimes in the boreal forest. Philosophical Transactions of the Royal Society B: Biological Sciences, 363(1501):2351–2356.

Grennfelt, P., A. Engleryd, M. Forsius, Ø. Hov, H. Rodhe and E. Cowling, 2020. Acid rain and air pollution: 50 years of progress in environmental science and policy. Ambio, 49:849–864.

Grieman, M.M., M. Aydin, D. Fritzsche, J.R. McConnell, T. Opel, M. Sigl and E.S. Saltzman, 2017. Aromatic acids in a Eurasian Arctic ice core: A 2600-year proxy record of biomass burning. Climate of the Past, 13(4):395–410.

Grieman, M.M., M. Aydin, E. Isaksson, M. Schwikowski and E.S. Saltzman, 2018a. Aromatic acids in an Arctic ice core from Svalbard: A proxy record of biomass burning. Climate of the Past, 14(5):637–651.

Grieman, M.M., M. Aydin, J.R. McConnell and E.S. Saltzman, 2018b. Burning-derived vanillic acid in an Arctic ice core from Tunu, northeastern Greenland. Climate of the Past, 14(11):1625–1637.

Groenemeijer, P., A. Vajda, I. Lehtonen, M. Kämäräinen, A. Venäläinen, H. Gregow, N. Becker, K. Nissen, U. Ulbrich, D. Paprotny, O. Morales Napoles and T. Púčik, 2016. Present and future probability of meteorological and hydrological hazards in Europe. Final report of Deliverable 2.5 for the Risk Analysis of Infrastructure Networks in response to extreme weather (RAIN) project. Available at: http://rain-project.eu/wp-content/uploads/2016/09/D2.5_REPORT_final.pdf (accessed: 14 December 2021).

Groot Zwaaftink, C.D., H. Grythe, H. Skov and A. Stohl, 2016. Substantial contribution of northern high-latitude sources to mineral dust in the Arctic. Journal of Geophysical Research: Atmospheres, 121(22):13,678–13,697.

Groot Zwaaftink, C.D., Ó. Arnalds, P. Dagsson-Waldhauserova, S. Eckhardt, J.M. Prospero and A. Stohl, 2017. Temporal and spatial variability of Icelandic dust emissions and atmospheric transport. Atmospheric Chemistry and Physics, 17(17):10,865–10,878.

Grünhage, L., H. Pleijel, G. Mills, J. Bender, H. Danielsson, Y. Lehmann, J.-F. Castell and O. Bethenod, 2012. Updated stomatal flux and flux-effect models for wheat for quantifying effects of ozone on grain yield, grain mass and protein yield. Environmental Pollution, 165:147–157.

Grythe, H., N.I. Kristiansen, C.D. Groot Zwaaftink, S. Eckhardt, J. Ström, P. Tunved, R. Krejci and A. Stohl, 2017. A new aerosol wet removal scheme for the Lagrangian particle model FLEXPARTv10. Geoscientific Model Development, 10(4):1447–1466.

Guenther, A.B., X. Jiang, C.L Heald, T. Sakulyanontvittaya, T. Duhl, L.K. Emmons and X. Wang, 2012. The Model of Emissions of Gases and Aerosols from Nature version 2.1 (MEGAN2.1): an extended and updated framework for modeling biogenic emissions. Geoscientific Model Development, 5(6):1471–1492.

Guimbaud, C., A.M. Grannas, P.B. Shepson, J.D. Fuentes, H. Boudries, J.W. Bottenheim, F. Dominé, S. Houdier, S. Perrier, T.B. Biesenthal and B.G. Splawn, 2002. Snowpack processing of acetaldehyde and acetone in the Arctic atmospheric boundary layer. Atmospheric Environment, 36(15–16):2743–2752.

Günther, A., A. Barthelmes, V. Huth, H. Joosten, G. Jurasinski, F. Koebsch and J. Couwenberg, 2020. Prompt rewetting of drained peatlands reduces climate warming despite methane emissions. Nature Communications, 11:1644.

Gustafsson, Ö., T.D. Bucheli, Z. Kukulska, M. Andersson, C. Largeau, J.-N. Rounzaud, C.M. Reddy and T.I. Eglinton, 2001. Evaluation of a protocol for the quantification of black carbon in sediments. Global Biogeochemical Cycles, 15(4):881–890.

Gustafsson, Ö., M. Kruså, Z. Zencak, R.J. Sheesley, L. Granat, E. Engström, P.S. Praveen, P.S.P. Rao, C. Leck and H. Rodhe, 2009. Brown clouds over South Asia: biomass or fossil fuel combustion? Science, 323(5913):495–498.

Gutiérrez-Loza, L., M.B. Wallin, E. Sahlée, E. Nilsson, H.W. Bange, A. Kock and A. Rutgersson, 2019. Measurement of air-sea methane fluxes in the Baltic Sea using the eddy covariance method. Frontiers in Earth Science, 7:93.

Gysel, M., M. Laborde, J.S. Olfert, R. Subramanian and A.J. Gröhn, 2011. Effective density of Aquadag and fullerene soot black carbon reference materials used for SP2 calibration. Atmospheric Measurement Techniques, 4(12):2581–2858.

Hagler, G.S.W., M.H. Bergin, E.A. Smith, J.E. Dibb, C. Anderson and E.J. Steig, 2007. Particulate and water-soluble carbon measured in recent snow at Summit, Greenland. Geophysical Research Letters, 34(16):L16505.

Hall, J.V. and T.V. Loboda, 2017. Quantifying the potential for low-level transport of black carbon emissions from cropland burning in Russia to the snow-covered Arctic. Frontiers in Earth Science, 5:109.

Hall, J. and T. Loboda, 2018. Quantifying the variability of potential black carbon transport from cropland burning in Russia driven by atmospheric blocking events. Environmental Research Letters, 13(5):055010.

Halmer, M.M., H.-U. Schmincke and H.-F. Graf, 2002. The annual volcanic gas input into the atmosphere, in particular into the stratosphere: a global data set for the past 100 years. Journal of Volcanology and Geothermal Research, 115(3–4):511–528.

Hamburger, T., G. McMeeking, A. Minikin, W. Birmili, M. Dall'Osto, C. O'Dowd, H. Flentje, B. Henzing, H. Junninen, A. Kristensson, G. de Leeuw, A. Stohl, J.F. Burkhart, H. Coe, R. Krejci and A. Petzold, 2011. Overview of the synoptic and pollution situation over Europe during the EUCAARI-LONGREX field campaign. Atmospheric Chemistry and Physics, 11(3):1065–1082.

Han, Y.M., C. Wei, B.A.M. Bandowe, W. Wilcke, J.J. Cao, B.Q. Xu, S.P. Gao, X.X. Tie, G.H. Li, Z.D. Jin and Z.S. An, 2015. Elemental carbon and polycyclic aromatic compounds in a 150-year sediment core from Lake Qinghai, Tibetan Plateau, China: influence of regional and local sources and transport pathways. Environmental Science & Technology, 49(7):4176–4183.

Hanes, C.C., X. Wang, P. Jain, M.-A. Parisien, J.M. Little and M.D. Flannigan, 2019. Fire-regime changes in Canada over the last half century. Canadian Journal of Forest Research 49(3):256–269.

Hannah, L., P.R. Roehrdanz, K.B. KC., E.D.G. Fraser, C.I. Donatti, L. Saenz, T.M. Wright, R.J. Hijmans, M. Mulligan, A. Berg and A. van Soesbergen, 2020. The environmental consequences of climate-driven agricultural frontiers. PLoS One, 15(2):e0228305.

Hao, W.M., A. Petkov, B.L. Nordgren, R.E. Corley, R.P. Silverstein, S.P. Urbanski, N. Evangeliou, Y. Balkanski and B.L Kinder, 2016. Daily black carbon emissions from fires in Northern Eurasia for 2002–2015. Geoscientific Model Development, 9(12):4461–4474.

Hartmann, M., T. Blunier, S.O. Brügger, J. Schmale, M. Schwikowski, A. Vogel, H. Wex and F. Stratmann, 2019. Variation of ice nucleating particles in the European Arctic over the last centuries. Geophysical Research Letters, 46(7):4007–4016.

Hayes, F., G. Mills, P. Williams, H. Harmens and P. Büker, 2006. Impacts of summer ozone exposure on the growth and overwintering of UK upland vegetation. Atmospheric Environment, 40(22):4088–4097.

Hayes, F., M.L.M. Jones, G. Mills and M. Ashmore, 2007. Meta-analysis of the relative sensitivity of semi-natural vegetation species to ozone. Environmental Pollution, 146(3):754–762.

He, P., L. Bian, X. Zheng, J. Yu, C. Sun, P. Ye and Z. Xie, 2016. Observation of surface ozone in the marine boundary layer along a cruise through the Arctic Ocean: from offshore to remote. Atmospheric Research, 169(Part A):191–198.

Health Canada, 2019. Health Impacts of Air Pollution in Canada: Estimates of Morbidity and Premature Mortality Outcomes, 2019 Report. Health Canada, Ottawa, Canada. 24 + xiiipp.

Heede, R., 2014. Tracing anthropogenic carbon dioxide and methane emissions to fossil fuel and cement producers, 1854–2010. Climatic Change, 122:229–241.

Hegg, D.A., R.J. Ferek and P.V. Hobbs, 1995. Cloud condensation nuclei over the Arctic Ocean in early spring. Journal of Applied Meteorology and Climatology, 34(9):2076–2082.

Heidam, N.Z., J. Christensen, P. Wåhlin and H. Skov, 2004. Arctic atmospheric contaminants in NE Greenland: levels, variations, origins, transport, transformations and trends 1990–2001. Science of The Total Environment, 331(1–3):5–28.

Heidinger, A.K., M.J. Foster, A. Walther and X. Zhao, 2014. The Pathfinder Atmospheres – extended AVHRR climate dataset. Bulletin of the American Meteorological Society, 95(6):909–922.

Heilman, W.E., Y. Liu, S. Urbanski, V. Kovalev and R. Mickler, 2014. Wildland fire emissions, carbon, and climate: plume rise, atmospheric transport, and chemistry processes. Forest Ecology and Management, 317:70–79.

Heintzenberg, J., C. Leck and P. Tunved, 2015. Potential source regions and processes of aerosol in the summer Arctic. Atmospheric Chemistry and Physics, 15(11):6487–6502.

Hemig, D., V. Petrenko, P. Martinerie, E. Witrant, T. Röckmann, A. Zuiderweg, R. Holzinger, J. Hueber, C. Thompson, J.W.C. White, W. Sturges, A. Baker, T. Blunier, D. Etheridge, M. Rubino and P. Tans, 2014. Reconstruction of Northern Hemisphere 1950–2010 atmospheric non-methane hydrocarbons. Atmospheric Chemistry and Physics, 14(3):1463–1483.

Henneberger, J., J.P. Fugal, O. Stetzer and U. Lohmann, 2013. HOLIMO II: a digital holographic instrument for ground-based in situ observations of microphysical properties of mixed-phase clouds. Atmospheric Measurement Techniques, 6(11):2975–2987.

Herber, A.B., C. Haas, R.S. Stone, J.W. Bottenheim, P. Liu, S.-M. Li, R.M. Staebler, J.W. Strapp and K. Dethloff, 2012. Regular airborne surveys of Arctic sea ice and atmosphere. EOS, 93(4):41–42.

Héroux, M.-E., H.R. Anderson, R. Atkinson, B. Brunekreef, A. Cohen, F. Forastiere, F. Hurley, K. Katsouyanni, D. Krewski, M. Krzyzanowski, N. Künzli, I. Mills, X. Querol, B. Ostro and H. Walton, 2015. Quantifying the health impacts of ambient air pollutants: recommendations of a WHO/Europe project. International Journal of Public Health, 60(5):619–627.

Herrmann, M., L. Cao, H. Sihler, U. Platt and E. Gutheil, 2019. On the contribution of chemical oscillations to ozone depletion events in the polar spring. Atmospheric Chemistry and Physics, 19(15):10161–10190.

Heslin-Rees, D., M. Burgos, H.-C. Hansson, R. Krejci, J. Ström, P. Tunved and P. Zieger, 2020. From a polar to a marine environment: has the changing Arctic led to a shift in aerosol light scattering properties? Atmospheric Chemistry and Physics, 20(21):13,671–13,686.

Hess, P.G. and R. Zbinden, 2013. Stratospheric impact on tropospheric ozone variability and trends: 1990–2009. Atmospheric Chemistry and Physics, 13(2):649–674.

Hirano, T., M. Kiyota and I. Aiga, 1995. Physical effects of dust on leaf physiology of cucumber and kidney bean plants. Environmental Pollution, 89(3):255–261.

Hirdman, D., J.F. Burkhart, H. Sodemann, S. Eckhardt, A. Jefferson, P.K. Quinn, S. Sharma, J. Ström and A. Stohl, 2010a. Long-term trends of black carbon and sulphate aerosol in the Arctic: changes in atmospheric transport and source region emissions. Atmospheric Chemistry and Physics, 10(19):9351–9368.

Hirdman, D., H. Sodemann, S. Eckhardt, J.F. Burkhart, A. Jefferson, T. Mefford, P.K. Quinn, S. Sharma, J. Ström and A. Stohl, 2010b. Source identification of short-lived air pollutants in the Arctic using statistical analysis of measurement data and particle dispersion model output. Atmospheric Chemistry and Physics, 10 (2):669–693.

Hislop, S., A. Haywood, S. Jones, M. Soto-Berelov, A. Skidmore and T.H. Nguyen, 2020. A satellite data driven approach to monitoring and reporting fire disturbance and recovery across boreal and temperate forests. International Journal of Applied Earth Observation and Geoinformation, 87:102034.

Hmiel, B., V.V. Petrenko, M.N. Dyonisius, C. Buizert, A.M. Smith, P.F. Place, C. Harth, R. Beaudette, Q. Hua, B. Yang, I. Vimont, S.E. Michel, J.P. Severinghaus, D. Etheridge, T. Bromley, J. Schmitt, X. Faïn, R.F. Weiss and E. Dlugokencky, 2020. Preindustrial $^{14}CH_4$ indicates greater anthropogenic fossil CH_4 emissions, Nature, 578:409–412.

Hoek, G., R.M. Krishnan, R. Beelen, A. Peters, B. Ostro, B. Brunekreef and J.D. Kaufman, 2013. Long-term air pollution exposure and cardio-respiratory mortality: a review. Environmental Health, 12(43).

Hoesly, R.M., S.J. Smith, L. Feng, Z. Klimont, G. Janssens-Maenhout, T. Pitkanen, J.J. Seibert, L. Vu, R.J. Andres, R.M. Bolt, T.C. Bond, L. Dawidowski, N. Kholod, J.-i. Kurokawa, M. Li, L. Liu, Z. Lu, M.C.P. Moura, P.R O'Rourke and Q. Zhang, 2018. Historical (1750–2014) anthropogenic emissions of reactive gases and aerosols from the Community Emissions Data System (CEDS). Geoscientific Model Development, 11(1):369–408.

Hoffmann, D., A. Tilgner, Y. Iinuma and H. Herrmann, 2010. Atmospheric Stability of Levoglucosan: A Detailed Laboratory and Modeling Study. Environmental Science & Technology, 44(2):694–699.

Höglund-Isaksson, L., 2017. Bottom-up simulations of methane and ethane emissions from global oil and gas systems 1980 to 2012. Environmental Research Letters, 12:024007.

Höglund-Isaksson, L., A. Gómez-Sanabria, Z. Klimont, P. Rafaj and W. Schöpp, 2020. Technical potentials and costs for reducing global anthropogenic methane emissions in the 2050 timeframe – results from the GAINS model. Environmental Research Communications, 2:025004.

Holben B.N., T.F. Eck, I. Slutsker, D. Tanré, J.P. Buis, A. Setzer, E. Vermote, J.A. Reagan, Y.J. Kaufman, T. Nakajima, F. Lavenu, I. Jankowiak and A. Smirnov, 1998. AERONET – A federated instrument network and data archive for aerosol characterization. Remote Sensing of Environment, 66(1):1–16.

Hole, L.R., J.H. Christensen, T. Ruoho-Airola, K. Tørseth, V. Ginzburg and P. Glowacki, 2009. Past and future trends in concentrations of sulphur and nitrogen compounds in the Arctic. Atmospheric Environment, 43(4):928–939.

Holloway, J.E., A.G. Lewkowicz, T.A. Douglas, X. Li, M.R. Turetsky, J.L. Baltzer and H. Jin, 2020. Impact of wildfire on permafrost landscapes: a review of recent advances and future prospects. Permafrost and Periglacial Processes, 31(3):371–382.

Holmes, C.D., M.J. Prather, O.A. Søvde and G. Myhre, 2013: Future methane, hydroxyl, and their uncertainties: key climate and emission parameters for future predictions. Atmospheric Chemistry and Physics, 13(1):285–302.

Holmes, C.D., 2018. Methane feedback on atmospheric chemistry: methods, models, and mechanisms. Journal of Advances in Modeling Earth Systems, 10(4):1087–1099.

Holst, T., A. Arneth, S. Hayward, A. Ekberg, M. Mastepanov, M. Jackowicz-Korczynski, T. Friborg, P.M. Crill and K. Bäckstrand, 2010. BVOC ecosystem flux measurements at a high latitude wetland site. Atmospheric Chemistry and Physics, 10(4):1617–1634.

Holst, G.J., C.B. Pedersen, M. Thygesen, J. Brandt, C. Geels, J.H. Bønløkke and T. Sigsgaard, 2020. Air pollution and family related determinants of asthma onset and persistent wheezing in children: nationwide case-control study. BMJ, 370(8257):m2791.

Holzer-Popp, T., G. de Leeuw, J. Griesfeller, D. Martynenk, L. Klüser, S. Bevan, W. Davies, F. Ducos, J.L. Deuzé, R.G. Graigner, A. Heckel, W. von Hoyningen-Hüne, P. Kolmonen, P. Litvinov, P. North, C.A. Poulsen, D. Ramon, R. Siddans, L. Sogacheva, D. Tanre, G.E. Thomas, M. Vountas, J. Descloitres, J. Griesfeller, S. Kinne, M. Schulz and S. Pinnock, 2013. Aerosol retrieval experiments in the ESA Aerosol_cci project. Atmospheric Measurement Techniques, 6(8):1919–1957.

Honrath, R.E., M.C. Peterson, S. Guo, J.E. Dibb, P.B. Shepson and B. Campbell, 1999. Evidence of NOx production within or upon ice particles in the Greenland snowpack. Geophysical Research Letters, 26(6):695–698.

Hornbrook, R.S., A.J. Hills, D.D. Riemer, A. Abdelhamid, F.M. Flocke, S.R. Hall, L.G. Huey, D.J. Knapp, J. Liao, R.L. Mauldin lll, D.D. Montzka, J.J. Orlando, P.B. Shepson, B. Sive, R.M. Staebler, D.J. Tanner, C.R. Thompson, A. Turnipseed, K. Ullmann, A.J. Weinheimer and E.C. Apel, 2016. Arctic springtime observations of volatile organic compounds during the OASIS-2009 campaign. Journal of Geophysical Research: Atmospheres, 121(16):9789– 9813.

Horowitz, L.W., S. Walters, D.L. Mauzerall, L.K. Emmons, P.J. Rasch, C. Granier, X. Tie, J.-F. Lamarque, M.G. Schultz, G.S. Tyndall, J.J. Orlando and G.P. Brasseur, 2003. A global simulation of tropospheric ozone and related tracers: description and evaluation of MOZART, version 2. Journal of Geophysical Research: Atmospheres, 108(D24).

Horsdal, H.T., E. Agerbo, J.J. McGrath, B.J. Vilhjálmsson, S. Antonsen, A.M. Closter, A. Timmermann, J. Grove, P.L.H. Mok, R.T. Webb, C.E. Sabel, O. Hertel, T. Sigsgaard, C. Erikstrup, D.M. Hougaard, T. Werge, M. Nordentoft, A.D. Børglum, O. Mors, P.B. Mortensen, J. Brandt, C. Geels and C.B. Pedersen, 2019. Association of childhood exposure to nitrogen dioxide and polygenic risk score for schizophrenia with the risk of developing schizophrenia. JAMA Network Open, 2(11):e1914401.

Hsu, N.C., M.-J. Jeong, C. Bettenhausen, A.M. Sayer, R. Hansell, C.S. Seftor, J. Huang and S.-C. Tsay, 2013. Enhanced Deep Blue aerosol retrieval algorithm: the second generation. Journal of Geophysical Research: Atmospheres, 118(16):9296–9315.

Hsu, N.C., J. Lee, A.M. Sayer, W. Kim, C. Bettenhausen and S.-C. Tsay, 2019. VIIRS Deep Blue aerosol products over land: extending the EOS long-term aerosol data records, Journal of Geophysical Research: Atmospheres, 124(7):4026–4053.

Hu, F.S., P.E. Higuera, P. Duffy, M.L. Chipman, A.V. Rocha, A.M. Young, R. Kelly and M.C. Dietze, 2015. Arctic tundra fires: natural variability and responses to climate change. Frontiers in Ecology and the Environment, 7(13):369–377.

Hu, Y., N. Fernandez-Anez, T.E.L. Smith and G. Rein, 2018. Review of emissions from smouldering peat fires and their contribution to regional haze episodes. International Journal of Wildland Fire, 27(5):293–312.

Huang, L., J.R. Brook, W. Zhang, S.M. Li, L. Graham, D. Ernst, A. Chivulescu and G. Lu, 2006. Stable isotope measurements of carbon fractions (OC/EC) in airborne particulate: a new dimension for source characterization and apportionment. Atmospheric Environment, 40(15):2690–2705.

Huang, K., J.S. Fu, V.Y. Prikhodko, J.M. Storey, A. Romanov, E.L. Hodson, J. Cresko, I. Morozova, Y. Ignatieva and J. Cabaniss, 2015. Russian anthropogenic black carbon: Emission reconstruction and Arctic black carbon simulation. Journal of Geophysical Research: Atmospheres, 120(21):11306–11333.

Huang, Y., S. Wu, L.J. Kramer, D. Helmig and R.E. Honrath, 2017a. Surface ozone and its precursors at Summit, Greenland: comparison between observations and model simulations. Atmospheric Chemistry and Physics, 17(23):14661–14674.

Huang T, X. Zhu, Q. Zhong, X. Yun, W. Meng, B. Li, J. Ma, E.Y. Zeng and S. Tao, 2017b. Spatial and temporal trends in global emissions of nitrogen oxides from 1960 to 2014. Environmental Science & Technology. J51(14):7992–8000.

Huang L., W. Zhang, G.M. Santos, B.T. Rodríguez, S.R. Holden, V. Vetro and C.I. Czimczik, 2021. Application of the ECT9 protocol for radiocarbon-based source apportionment of carbonaceous aerosols. Atmospheric Measurement Techniques, 14:3481–3500.

Hugelius, G., J. Strauss, S. Zubrzycki, J.W. Harden, E.A.G. Schuur, C.-L. Ping, L. Schirrmeister, G. Grosse, G.J. Michaelson, C.D. Koven, J.A. O'Donnell, B. Elberling, U. Mishra, P. Camill, Z. Yu, J. Palmtag and P. Kuhry, 2014. Estimated stocks of circumpolar permafrost carbon with quantified uncertainty ranges and identified data gaps. Biogeosciences, 11(23):6573–6593.

Hugelius, G., J. Loisel, S. Chadburn, R.B. Jackson, M. Jones, G. MacDonald, M. Marushchak, D. Olefeldt, M. Packalen, M.B. Siewert, C. Treat, M. Turetsky, C. Voigt and Z. Yu, 2020. Large stocks of peatland carbon and nitrogen are vulnerable to permafrost thaw. PNAS, 117(34):20438–20446.

Hultman, J., M.P. Waldrop, R. Mackelprang, M.M. David, J. McFarland, S.J. Blazewicz, J. Harden, M.R. Turetsky, A.D. McGuire, M.B. Shah, N.C. VerBerkmoes, L.H. Lee, K. Mavrommatis and J.K. Jansson, 2015. Multi-omics of permafrost, active layer and thermokarst bog soil microbiomes. Nature, 521:208–212.

Hurrell, J.W., J.J. Hack, D. Shea, J.M. Caron and J. Rosinski, 2008. A new sea surface temperature and sea ice boundary dataset for the community atmospheric model. Journal of Climate, 21(19):5145–5153.

Hvidtfeldt, U.A., C. Geels, M. Sørensen, M. Ketzel, J. Khan, A. Tjønneland, J.H. Christensen, J. Brandt and O. Raaschou-Nielsen, 2019a. Long-term residential exposure to $PM_{2.5}$ constituents and mortality in a Danish cohort. Environment International, 133(B):105268.

Hvidtfeldt, U.A., M. Sørensen, C. Geels, M. Ketzel, J. Khan, A. Tjønneland, K. Overvad, J. Brandt and O. Raaschou-Nielsen, 2019b. Long-term residential exposure to $PM_{2.5}$, PM_{10}, black carbon, NO_2, and ozone and mortality in a Danish cohort. Environment International, 123:265–272.

Hvidtfeldt, U.A., F. Erdmann, S.K. Urhøj, J. Brandt, C. Geels, M. Ketzel, L.M. Frohn, J.H. Christensen, M. Sørensen and O. Raaschou-Nielsen, 2020a. Air pollution exposure at the residence and risk of childhood cancers in Denmark: a nationwide register-based case-control study. EClinicalMedicine, 28:100569.

Hvidtfeldt, U.A., F. Erdmann, S.K. Urhøj, J. Brandt, C. Geels, M. Ketzel, L.M. Frohn, J.H. Christensen, M. Sørensen and O. Raaschou-Nielsen, 2020b. Residential exposure to $PM_{2.5}$ components and risk of childhood non-Hodgkin lymphoma in Denmark: a nationwide register-based case-control study. International Journal of Environmental Research and Public Health, 17(23):8949.

ICCT, 2017. Greenhouse gas emissions from global shipping, 2013–2015. The International Council on Clean Transportation (ICCT), Washington DC, USA. viii + 27pp.

Ichoku, C. and L. Ellison, 2014. Global top-down smoke-aerosol emissions estimation using satellite fire radiative power measurements. Atmospheric Chemistry and Physics, 14(13):6643–6667.

IEA, 2012. Pathways to a Clean Energy System. International Energy Agency (IEA)/OECD Publishing, Paris, France. Available at: https://www.oecd-ilibrary.org/energy/energy-technology-perspectives-2012_energy_tech-2012-en

IEA, 2016. World Energy Outlook 2016. International Energy Agency (IEA), Paris, France. 684pp.

IEA, 2018. World Energy Outlook 2018. International Energy Agency (IEA), Paris, France. 661pp.

IIASA, 2018. Progress towards the achievement of the EU's air quality and emissions objectives. Amann, M. (Ed). International Institute for Applied Systems Analysis, Laxenburg, Austria. vii + 58pp.

IIASA, 2019. Linking climate and sustainable development: policy insights from national and global pathways. International Institute for Applied Systems Analysis (IIASA), Laxenburg, Austria.

Ikeda, K., H. Tanimoto, T. Sugita, H. Akiyoshi, Y. Kanaya, C. Zhu and F. Taketani, 2017. Tagged tracer simulations of black carbon in the Arctic: transport, source contributions, and budget. Atmospheric Chemistry and Physics, 17(17):10515–10533.

Im, U., R. Bianconi, E. Solazzo, I, Kioutsioukis, A. Badia, A. Balzarini, R. Baró, R. Bellasio, D. Brunner, C. Chemel, G. Curci, H.D. van der Gon, J. Flemming, R. Forkel, L. Giordano, P. Jiménez-Guerrero, M. Hirtl, A. Hodzic and S. Galmarini, 2015. Evaluation of operational online-coupled regional air quality models over Europe and North America in the context of AQMEII phase 2. Part II: particulate matter. Atmospheric Environment, 115:421–411.

Im, U., J. Brandt, C. Geels, K.M. Hansen, J.H. Christensen, M.S. Andersen, E. Solazzo, I. Kioutsioukis, U. Alyuz, A. Balzarini, R. Baro, R. Bellasio,

R. Bianconi, J. Bieser, A. Colette, G. Curci, A. Farrow, J. Flemming, A. Fraser, P. Jimenez-Guerrero, N. Kitwiroon, C.-K. Liang, U. Nopmongcol, G. Pirovano, L. Pozzoli, M. Prank, R. Rose, R. Sokhi, P. Tuccella, A. Unal, M.G. Vivanco, J. West, G. Yarwood, C. Hogrefe and S. Galmarini, 2018. Assessment and economic valuation of air pollution impacts on human health over Europe and the United States as calculated by a multi-model ensemble in the framework of AQMEII3. Atmospheric Chemistry and Physics, 18(8):5967–5989.

Im, U., J.H. Christensen, O.-K. Nielsen, M. Sand, R. Makkonen, C. Geels, C. Anderson, J. Kukkonen, S. Lopez-Aparicio and J. Brandt, 2019. Contributions of Nordic anthropogenic emissions on air pollution and premature mortality over the Nordic region and the Arctic. Atmospheric Chemistry and Physics, 19(20):12975–12992.

Ingersoll, G.P., M.A. Mast, J.M. Swank and C.D. Campbell, 2010. Rocky Mountain snowpack physical and chemical data for selected sites, 2009: U.S. Geological Survey Data Series 498. 9pp.

Ingram, R.C., P.A. Moore, S. Wilkinson, R.M. Petrone and J.M. Waddington, 2019. Postfire soil carbon accumulation does not recover boreal peatland combustion loss in some hydrogeological settings. Journal of Geophysical Research: Biogeosciences, 124(4):775–788.

Ingvander, S., G. Rosqvist, J. Svensson and H.E. Dahlke, 2013. Seasonal and interannual variability of elemental carbon in the snowpack of Storglaciären, northern Sweden. Annals of Glaciology, 54(62):50–58.

Ioffe, G. and T. Nefedova, 2004. Marginal farmland in European Russia. Eurasian Geography and Economics, 45(1):45–59.

IPCC, 2013a. Technical Summary. In: Stocker, T.F., D. Qin, G.-K. Plattner, M. Tignor, S.K. Allen, J. Boschung, A. Nauels, Y. Xia, V. Bex and P.M. Midgley (Eds.). Climate Change 2013: The Physical Science Basis. Contribution of Working Group I to the Fifth Assessment Report of the Intergovernmental Panel on Climate Change. Cambridge University Press.

IPCC, 2013b. Clouds and Aerosols. In: Stocker, T.F., D. Qin, G.-K. Plattner, M. Tignor, S.K. Allen, J. Boschung, A. Nauels, Y. Xia, V. Bex and P.M. Midgley (Eds.). Climate Change 2013: The Physical Science Basis. Contribution of Working Group I to the Fifth Assessment Report of the Intergovernmental Panel on Climate Change. Cambridge University Press.

IPCC, 2013c. Anthropogenic and Natural Radiative Forcing. In: Stocker, T.F., D. Qin, G.-K. Plattner, M. Tignor, S.K. Allen, J. Boschung, A. Nauels, Y. Xia, V. Bex and P.M. Midgley (Eds.). Climate Change 2013: The Physical Science Basis. Contribution of Working Group I to the Fifth Assessment Report of the Intergovernmental Panel on Climate Change. Cambridge University Press.

IPCC, 2019. Technical Summary. In: Pörtner, H.- O., D.C. Roberts, V. Masson-Delmotte, P. Zhai, M. Tignor, E. Poloczanska, K. Mintenbeck, A. Alegría, M. Nicolai, A. Okem, J. Petzold, B. Rama and N.M. Weyer (Eds.). IPCC Special Report on the Ocean and Cryosphere in a Changing Climate [In press].

IPCC, 2021. Climate Change 2021: The Physical Science Basis. Contribution of Working Group I to the Sixth Assessment Report of the Intergovernmental Panel on Climate Change [Masson-Delmotte, V., P. Zhai, A. Pirani, S.L. Connors, C. Péan, S. Berger, N. Caud, Y. Chen, L. Goldfarb, M.I. Gomis, M. Huang, K. Leitzell, E. Lonnoy, J.B.R. Matthews, T.K. Maycock, T. Waterfield, O. Yelekçi, R. Yu, and B. Zhou (eds.)]. Cambridge University Press, Cambridge, United Kingdom and New York, NY, USA, 2391 pp. doi:10.1017/9781009157896.

Irish, V.E., P. Elizondo, J. Chen, C. Chou, J. Charette, M. Lizotte, L.A. Ladino, T.W. Wilson, M. Gosselin, B.J. Murray, E. Polishchuk, J.P.D. Abbatt, L.A. Miller and A.K. Bertram, 2017. Ice-nucleating particles in Canadian Arctic sea-surface microlayer and bulk seawater. Atmospheric Chemistry and Physics, 17(17):10,583–10,595.

Irish, V.E., S.J. Hanna, Y. Xi, M. Boyer, E. Polishchuk, M. Ahmed, J. Chen, J.P.D. Abbatt, M. Gosselin, R. Chang, L.A. Miller and A.K. Bertram, 2019. Revisiting properties and concentrations of ice-nucleating particles in the sea surface microlayer and bulk seawater in the Canadian Arctic during summer. Atmospheric Chemistry and Physics, 19(11):7775–7787.

Irwin, M., Y. Kondo, N. Moteki, and T. Miyakawa, 2013. Evaluation of a heated-inlet for calibration of the SP2. Aerosol Science and Technology, 47(8):895–905.

Ishizawa, M., D. Chan, D. Worthy, E. Chan, F. Vogel, and S. Maksyutov. 2019. Analysis of Atmospheric CH4 in Canadian Arctic and Estimation of the Regional CH4 Fluxes. Atmospheric Chemistry and Physics, 19 (7):4637–58.

Ivanova, G.A., E.A., Kukavskaya, V.A. Ivanov, S.G. Conard and D.J. McRae, 2020. Fuel characteristics, loads and consumption in Scots pine forests of central Siberia. *Journal of Forestry Research*, 31:2507–2524.

Iversen, T., M. Bentsen, I. Bethke, J.B. Debernard, A. Kirkevåg, Ø. Seland, H. Drange, J.E. Kristjansson, I. Medhaug, M. Sand and I.A. Seierstad, 2013.The Norwegian Earth System Model, NorESM1-M – Part 2: Climate response and scenario projections. Geoscientific Model Development, 6(2):389–415.

Jacob, D.J., J.H. Crawford, H. Maring, A.D. Clarke, J.E. Dibb, L.K. Emmons, R.A. Ferrare, C.A. Hostetler, P.B. Russell, H.B. Singh, A.M. Thompson, G.E. Shaw, E. McCauley, J.R. Pederson and J.A. Fisher, 2010. The Arctic Research of the Composition of the Troposphere from Aircraft and Satellites (ARCTAS) mission: design, execution, and first results, Atmospheric Chemistry and Physics, 10(11):5191–5212.

Jacobi, H.-W., F. Obleitner, S. Da Costa, P. Ginot, K. Eleftheriadis, W. Aas and M. Zanatta, 2019. Deposition of ionic species and black carbon to the Arctic snowpack: combining snow pit observations with modeling. Atmospheric Chemistry and Physics, 19(15):10,361–10,377.

Jakobsson, M., 2002. Hypsometry and volume of the Arctic Ocean and its constituent seas. Geochemistry, Geophysics, Geosystems, 3(5):1–18.

James, R.H., P. Bousquet, I. Bussmann, M. Haeckel, R. Kipfer, I. Leifer, H. Niemann, I. Ostrovsky, J. Piskozub, G. Rehder, T. Treude, L. Vielstädte and J. Greinert, 2016. Effects of climate change on methane emissions from seafloor sediments in the Arctic Ocean: a review. Limnology and Oceanography, 61(S1):S283–S299.

Jammet, M., P. Crill, S. Dengel and T. Friborg, 2015. Large methane emissions from a subarctic lake during spring thaw: mechanisms and landscape significance. Journal of Geophysical Research: Biogeosciences, 120(11):2289–2305.

Jammet, M., S. Dengel, E. Kettner, F.-J.W. Parmentier, M. Wik, P. Crill and T. Friborg, 2017. Year-round CH_4 and CO_2 flux dynamics in two contrasting freshwater ecosystems of the subarctic. Biogeosciences, 14(22):5189–5216.

Jansen, J., B.F. Thornton, M.M. Jammet, M. Wik, A. Cortés, T. Friborg, S. MacIntyre and P.M. Crill, 2019. Climate-sensitive controls on large spring emissions of CH_4 and CO_2 from northern lakes. Journal of Geophysical Research: Biogeosciences, 124(7):2379–2399.

Jansen, J., B.F. Thornton, A. Cortés, J. Snöälv, M. Wik, S. MacIntyre and P.M. Crill, 2020. Drivers of diffusive CH_4 emissions from shallow subarctic lakes on daily to multi-year timescales. Biogeosciences, 17(7):1911–1932.

Janssen, N.A.H., G. Hoek, M. Simic-Lawson, P. Fischer, L. van Bree, H. ten Brink, M. Keuken, R. W. Atkinson, H.R. Anderson, B. Brunekreef and F.R. Cassee, 2011. Black Carbon as an additional indicator of the adverse health effects of airborne particles compared with PM_{10} and $PM_{2.5}$. Environmental Health Perspectives, 119(12):1691–1699.

Jenkins, M.J., J.B. Runyon, C.J. Fettig, W.G. Page and B.J. Bentz, 2014. Interactions among the mountain pine beetle, fires, and fuels. Forest Science, 60(3):489–501.

Jiang, W., 2003. Instantaneous secondary organic aerosol yields and their comparison with overall aerosol yields for aromatic and biogenic hydrocarbons. Atmospheric Environment, 37(38):5439–5444.

Jiang, Y., A.V. Rocha, J.A. O'Donnell, J.A. Drysdale, E.B. Rastetter, G.R. Shaver and Q. Zhuang, 2015. Contrasting soil thermal responses to fire in Alaskan tundra and boreal forest. Journal of Geophysical Research: Earth Surface, 120(2):363–378.

Jiang, Z., J.R. Worden, V.H. Payne, L. Zhu, E. Fischer, T. Walker and D.B.A. Jones, 2016. Ozone export from East Asia: The role of PAN. Journal of Geophysical Research: Atmospheres, 121(11):6555–6563.

Johansson, L., J.P. Jalkanen and J. Kukkonen, 2017a. Global assessment of shipping emissions in 2015 on a high spatial and temporal resolution. Atmospheric Environment, 167:403–415.

Johansson, E., A. Devasthale, M. Tjernström, A.M.L. Ekman and T. L'Ecuyer, 2017b. Response of the lower troposphere to moisture intrusions into the Arctic. Geophysical Research Letters, 44(5):2527–2536.

Johnston, D.C., M.R. Turetsky, B.W. Benscoter and B.M. Wotton, 2015. Fuel load, structure, and potential fire behaviour in black spruce bogs. Canadian Journal of Forest Research, 45(7):888–899.

Johnston, J.M., L.M. Johnston, M.J. Wooster, A. Brookes, C. McFayden and A.S. Cantin, 2018. Satellite detection limitations of sub-canopy smouldering wildfires in the North American Boreal Forest. Fire, 1(2):28.

Jones, B.M., G. Grosse, C.D. Arp, E. Miller, L. Liu, D.J. Hayes and C.F. Larsen, 2015. Recent Arctic tundra fire initiates widespread thermokarst development. Scientific Reports, 5:15865.

Jonson, J.E., A. Stohl, A.M. Fiore, P. Hess, S. Szopa, O. Wild, G. Zeng, F.J. Dentener, A. Lupu, M.G. Schultz, B.N. Duncan, K. Sudo, P. Wind, M. Schulz, E. Marmer, C. Cuvelier, T. Keating, A. Zuber, A. Valdebenito, V. Dorokhov, H. De Backer, J. Davies, G.H. Chen, B. Johnson, D.W.

Tarasick, R. Stübi, M.J. Newchurch, P. von der Gathen, W. Steinbrecht and H. Claude, 2010. A multi-model analysis of vertical ozone profiles. Atmospheric Chemistry and Physics, 10(12):5759–5783.

Jonsson, A.I., J. de Grandpré, V.I. Fomichev, J.C. McConnell and S.R. Beagley, 2004. Doubled CO_2-induced cooling in the middle atmosphere: photochemical analysis of the ozone radiative feedback. Journal of Geophysical Research: Atmospheres, 109(D24).

Jørgensen, J.T., M.S. Johansen, L. Ravnskjær, K.K. Andersen, E.V. Bräuner, S. Loft, M. Ketzel, T. Becker, J. Brandt, O. Hertel and Z.J. Andersen, 2016. Long-term exposure to ambient air pollution and incidence of brain tumours: The Danish Nurse Cohort. NeuroToxicology, 55:122–130.

Jørgensen, H.E., L.L. Sørensen and S.E. Larsen, 2020. A simple model of chemistry effects on the air-sea CO_2 exchange coefficient. Journal of Geophysical Research: Oceans, 125(6):e2018JC014808.

Jung, C.H., Y.J. Yoon, H.J. Kang, Y. Gim, B.Y. Lee, J. Ström, R. Krejci and P. Tunved, 2018. The seasonal characteristics of cloud condensation nuclei (CCN) in the arctic lower troposphere. Tellus B: Chemical and Physical Meteorology, 70(1):1–13.

Juutinen, S., M. Rantakari, P. Kortelainen, J.T. Huttunen, T. Larmola, J. Alm, J. Silvola and P.J. Martikainen, 2009. Methane dynamics in different boreal lake types. Biogeosciences, 6(2):209–223.

Junninen, H., M. Ehn, T. Petäjä, L. Luosujärvi, T. Kotiaho, R. Kostiainen, U. Rohner, M. Gonin, K. Fuhrer, M. Kulmala and D.R. Worsnop, 2010. A high-resolution mass spectrometer to measure atmospheric ion composition. Atmospheric Measurement Techniques, 3(4):1039–1053.

Kahl, J.D.W., D.A. Martinez and N.A. Zaitseva, 1996. Long-term variability in the low-level inversion layer over the Arctic Ocean. International Journal of Climatology. 16(11):1297–1313.

Kaiser, J.W., A. Heil, M.O. Andreae, A. Benedetti, N. Chubarova, L. Jones, J.-J. Morcrette, M. Razinger, M.G. Schultz, M. Suttie and G.R. van der Werf, 2012. Biomass burning emissions estimated with a global fire assimilation system based on observed fire radiative power. Biogeosciences, 9(1):527–554.

Kaiser, S., M. Göckede, K. Castro-Morales, C. Knoblauch, A. Ekici, T. Kleinen, S. Zubrzycki, T. Sachs, C. Wille and C. Beer, 2017. Process-based modelling of the methane balance in periglacial landscapes (JSBACH-methane). Geoscientific Model Development, 10(1):333–358.

Kämäri, J. and P. Joki-Heiskala (Eds), 1998. Chapter 9: Acidifying pollutants, Arctic haze, and acidification in the Arctic. In: AMAP Assessment Report: Arctic Pollution Issues. Arctic Monitoring and Assessment Programme (AMAP), Oslo, Norway, pp. 621–659.

Kanaya, Y., K. Miyazaki, F. Taketani, T. Miyakawa, H. Takashima, Y. Komazaki, X. Pan, S. Kato, K. Sudo, T. Sekiya, J. Inoue, K. Sato and K. Oshima, 2019. Ozone and carbon monoxide observations over open oceans on R/V *Mirai* from 67°S to 75°N during 2012 to 2017: testing global chemical reanalysis in terms of Arctic processes, low ozone levels at low latitudes, and pollution transport. Atmospheric Chemistry and Physics, 19(11):7233–7254.

Kanaya, Y., K. Yamaji, T. Miyakawa, F. Taketani, C. Zhu, Y. Choi, Y. Komazaki, K. Ikeda, Y. Kondo and Z. Klimont, 2020. Rapid reduction in black carbon emissions from China: evidence from 2009–2019 observations on Fukue Island, Japan. Atmospheric Chemistry and Physics, 20(11):6339–6356.

Kandler, K., N. Benker, U. Bundke, E. Cuevas, M. Ebert, P. Knippertz, S. Rodríguez, L. Schütz and S. Weinbruch, 2007. Chemical composition and complex refractive index of Saharan Mineral Dust at Izaña, Tenerife (Spain) derived by electron microscopy. Atmospheric Environment, 41(37):8058–8074.

Karanasiou, A., M.C. Mingguillón, M. Viana, A. Alastuey, J.-P. Putaud, W. Maenhaut, P. Panteliadis, G. Močnik, O. Favez and T.A.J. Kuhlbusch, 2015. Thermal-optical analysis for the measurement of elemental carbon (EC) and organic carbon (OC) in ambient air: a literature review. Atmospheric Measurement Techniques Discussions, 8:9649–9712.

Karjalainen, O., J. Aalto, M. Luoto, S. Westermann, V.E. Romanovsky, F.E. Nelson, B. Etzelmüller and J. Hjort, 2019. Circumpolar permafrost maps and geohazard indices for near-future infrastructure risk assessments. Scientific Data, 6:190037.

Karl, M., C. Leck, F.M. Rad, A. Bäcklund, S. Lopez-Aparicio and J. Heintzenberg, 2019. New insights in sources of the sub-micrometre aerosol at Mt. Zeppelin observatory (Spitsbergen) in the year 2015. Tellus B: Chemical and Physical Meteorology, 71(1):1613143.

Karlsson, K-G. and A. Devasthale, 2018. Inter-Comparison and evaluation of the four longest Sstellite-derived cloud Ccimate data records: CLARA-A2, ESA Cloud CCI V3, ISCCP-HGM, and PATMOS-x. Remote Sensing, 10(10):1567.

Karlsson, K.-G., K. Anttila, J. Trentmann, M. Stengel, J. Fokke Meirink, A. Devasthale, T. Hanschmann, S. Kothe, E. Jääskeläinen, J. Sedlar, N. Benas, G.-J. van Zadelhoff, C. Schlundt, D. Stein, S. Finkensieper, N. Håkansson and R. Hollmann, 2017. CLARA-A2: the second edition of the CM SAF cloud and radiation data record from 34 years of global AVHRR data. Atmospheric Chemistry and Physics, 17(9):5809–5828.

Karvosenoja N., M. Tainio, K. Kupiainen, J. Tuomisto, J. Kukkonen and M. Johansson, 2008. Evaluation of the emissions and uncertainties of $PM_{2.5}$ originated from vehicular traffic and domestic wood combustion in Finland. Boreal Environmental Research, 13(5):465–474.

Kaspari, S.D., M. Schwikowski, M. Gysel, M.G. Flanner, S. Kang, S. Hou and P.A. Mayewski, 2011. Recent increase in black carbon concentrations from a Mt. Everest ice core spanning 1860–2000 AD. Geophysical Research Letters, 38(4):L04703.

Kaspari, S., T.H. Painter, M. Gysel, S.M. Skiles and M. Schwikowski, 2014. Seasonal and elevational variations of black carbon and dust in snow and ice in the Solu-Khumbu, Nepal and estimated radiative forcings. Atmospheric Chemistry and Physics, 14(15):8089–8103.

Kawai, H., S. Yukimoto, T. Koshiro, N. Oshima, T. Tanaka, H. Yoshimura and R. Nagasawa, 2019. Significant improvement of cloud representation in the global climate model MRI-ESM2. Geoscientific Model Development, 12(7):2875–2897.

Kawamura, K., Y. Izawa, M. Mochida and T. Shiraiwa, 2012. Ice core records of biomass burning tracers (levoglucosan and dehydroabietic, vanillic and *p*-hydroxybenzoic acids) and total organic carbon for past 300 years in the Kamchatka Peninsula, Northeast Asia. Geochimica et Cosmochimica Acta, 99:317–329.

Kay, J.E. and A. Gettelman, 2009. Cloud influence on and response to seasonal Arctic Sea ice loss. Journal of Geophysical Research: Atmospheres, 114:D18204.

Kay, J.E. and T. L'Ecuyer, 2013. Observational constraints on Arctic Ocean clouds and radiative fluxes during the early 21st century. Journal of Geophysical Research: Atmospheres, 118(13):7219–7236.

Kay, J.E., T. L'Ecuyer, H. Chepfer, N. Loeb, A. Morrison and G. Cesana, 2016. Recent advances in Arctic cloud and climate research. Current Climate Change Reports, 2:159–169.

Samir, K.C. and W. Lutz, 2017. The human core of the shared socioeconomic pathways: population scenarios by age, sex and level of education for all countries to 2100. Global Environmental Change, 42:181–192.

Kebabian, P.L., S.C. Herndon and A. Freedman, 2005. Detection of nitrogen dioxide by cavity attenuated phase shift spectroscopy. Analytical Chemistry 77(2):724–728.

Kecorius, S., T. Vogl, P. Paasonen, J. Lampilahti, D. Rothenberg, H. Wex, S. Zeppenfeld, M. van Pinxteren, M. Hartmann, S. Henning, X. Gong, A. Welti, M. Kulmala, F. Stratmann, H. Herrmann and A. Wiedensohler, 2019. New particle formation and its effect on cloud condensation nuclei abundance in the summer Arctic: a case study in the Fram Strait and Barents Sea. Atmospheric Chemistry and Physics, 19(22):14339–14364.

Keegan, K.M., M.R. Albert, J.R. McConnell and I. Baker, 2014. Climate change and forest fires synergistically drive widespread melt events of the Greenland Ice Sheet. PNAS, 111(22):7964–7967.

Kehrwald, N., R. Zangrando, P. Gabrielli, J.-L. Jaffrezo, C. Boutron, C. Barbante and A. Gambaro, 2012. Levoglucosan as a specific marker of fire events in Greenland snow. Tellus B: Chemical and Physical Meteorology, 64(1):18196.

Keller, C.A., M.S. Long, R.M. Yantosca, A.M. Da Silva, S. Pawson and D.J. Jacob, 2014. HEMCO v1.0: a versatile, ESMF-compliant component for calculating emissions in atmospheric models. Geoscientific Model Development, 7:1409–1417.

Kelley, M., Schmidt, G.A., L.S. Nazarenko, S.E. Bauer, R. Ruedy, G.L. Russell, A.S. Ackerman, I. Aleinov, M. Bauer, R. Bleck, V. Canuto, G. Cesana, Y. Cheng, T.L. Clune, B.I. Cook, C.A. Cruz, A.D. Del Genio, G.S. Elsaesser, G. Faluvegi, N.Y. Kiang, D. Kim, A.A. Lacis, A. Leboissetier, A.N. LeGrande, K.K. Lo, J. Marshall, E.E. Matthews, S. McDermid, K. Mezuman, R.L. Miller, L.T. Murray, V. Oinas, C. Orbe, C.P. García-Pando, J.P. Perlwitz, M.J. Puma, D. Rind, A. Romanou, D.T. Shindell, S. Sun, N. Tausnev, K. Tsigaridis, G. Tselioudis, E. Weng, J. Wu and M.-S. Yao, 2020. GISS-E2.1: configurations and climatology. Journal of Advances in Modeling Earth Systems, 12(8): e2019MS002025.

Kellomäki, S., H. Strandman, T. Heinonen, A. Asikainen, A. Venäläinen and H. Peltola, 2018. Temporal and spatial change in diameter growth of boreal Scots pine, Norway spruce, and birch under recent-generation (CMIP5) global climate model projections for the 21st century. Forests, 9(3):118.

Kessler, J.D. and W.S. Reeburgh, 2005. Preparation of natural methane samples for stable isotope and radiocarbon analysis, Limnology and Oceanography Methods, 3:408-418.

Khan, A.L., H. Dierssen, J.P. Schwarz, C. Schmitt, A. Chlus, M. Hermanson, T.H. Painter and D.M. McKnight, 2017. Impacts of coal dust from an active mine on the spectral reflectance of Arctic surface snow in Svalbard, Norway. Journal of Geophysical Research: Atmospheres, 122(3):1767–1778.

Khan, A., O. Plana-Ripoll, S. Antonsen, J. Brandt, C. Geels, H. Landecker, P.F. Sullivan, C.B. Pedersen and A. Rzhetsky, 2019. Environmental pollution is associated with increased risk of psychiatric disorders in the US and Denmark. PLOS Biology, 17(10):e3000353.

Kholod, N., M. Evans and T. Kuklinski, 2016. Russia's black carbon emissions: focus on diesel sources. Atmospheric Chemistry and Physics, 16(17):11267–11281.

Kieft, J., T. Smith, S. Someshwar and R. Boer, 2016. Towards anticipatory management of peat fires to enhance local resilience and reduce natural capital depletion. In: Renaud, F., K. Sudmeier-Rieux, M. Estrella and U. Nehren (Eds.) Ecosystem-Based Disaster Risk Reduction and Adaptation in Practice. Advances in Natural and Technological Hazards Research, Vol 42, pp. 361–377. Springer.

Kim, M.-H., A.H. Omar, J.L. Tackett, M.A. Vaughan, D.M. Winker, C.R. Trepte, Y. Hu, Z. Liu, L.R. Poole, M.C. Pitts, J. Kar, and B.E. Magill, 2018. The CALIPSO version 4 automated aerosol classification and lidar ratio selection algorithm. Atmospheric Measurement Techniques, 11(11):6107–6135.

Kim, J.-S., J.-S. Kug, S.-J. Jeong, H. Park and G. Schaepman-Strub, 2020. Extensive fires in southeastern Siberian permafrost linked to preceding Arctic Oscillation. Science Advances, 6(2):eaax3308.

King, M., D. Altdorff, P. Li, L. Galagedara, J. Holden and A. Unc, 2018. Northward shift of the agricultural climate zone under 21st-century global climate change. Scientific Reports, 8:7904.

Kipling, Z., P. Stier, C.E. Johnson, G.W. Mann, N. Bellouin, S.E. Bauer, T. Bergman, M. Chin, T. Diehl, S.J. Ghan, T. Iversen, A. Kirkevåg, H. Kokkola, X. Liu, G. Luo, G. Myhre, T. van Noije, K.J. Pringle, K. von Salzen, M. Schulz, Ø. Seland, R.B. Skeie, T. Takemura, K. Tsigaridis and K. Zhang, 2016. What controls the vertical distribution of aerosol? Relationships between process sensitivity in HadGEM3–UKCA and inter-model variation from AeroCom Phase II. Atmospheric Chemistry and Physics, 16(4): 2221–2241.

Kirchmeier-Young, M.C., N.P. Gillett, F.W. Zwiers, A.J. Cannon and F.S. Anslow, 2019. Attribution of the influence of human-induced climate change on an extreme fire season. Earth's Future, *7*(1):2–10.

Kirillina, K., E.G. Shvetsov, V.V. Protopopova, L. Thiesmeyer and W. Yan, 2020. Consideration of anthropogenic factors in boreal forest fire regime changes during rapid socio-economic development: case study of forestry districts with increasing burnt area in the Sakha Republic, Russia. Environmental Research Letters, 15(3):035009.

Kirkevåg, A., T. Iversen, Ø. Seland, C. Hoose, J.E. Kristjánsson, H. Struthers, A.M.L Ekman, S. Ghan, J. Griesfeller, E.D. Nilsson and M. Schulz, 2013. Aerosol–climate interactions in the Norwegian Earth System Model – NorESM1-M. Geoscientific Model Development, 6(1):207–244.

Kirschke, S., P. Bousquet, P. Ciais, M. Saunois, J.G. Canadell, E.J. Dlugokencky, P. Bergamaschi, D. Bergmann, D.R. Blake, L. Bruhwiler, P. Cameron-Smith, S. Castaldi, F. Chevallier, L. Feng, A. Fraser, M. Heimann, E.L. Hodson, S. Houweling, B. Josse, P.J. Fraser, P.B. Krummel, J.-F.

Kitidis, V., R.C. Upstill-Goddard and L.G. Anderson, 2010. Methane and nitrous oxide in surface water along the North-West Passage, Arctic Ocean. Marine Chemistry, 121(1–4):80–86.

Klimont, Z., K. Kupiainen, C. Heyes, P. Purohit, J. Cofala, P. Rafaj, J. Borken-Kleefeld and W. Schöpp, 2017. Global anthropogenic emissions of particulate matter including black carbon. Atmospheric Chemistry and Physics, 17(14):8681–8723.

Klintzsch, T., G. Langer, A. Wieland, H. Geisinger, K. Lenhart, G. Nehrke and F. Keppler, 2020. Effects of temperature and light on methane production of widespread marine phytoplankton. Journal of Geophysical Research: Biogeosciences, 125(9):e2020JG005793.

Knittel, K. and A. Boetius, 2009. Anaerobic oxidation of methane: progress with an unknown process. Annual Review of Microbiology, 63:311–334.

Knorr, W., F. Dentener, S. Hantson, L. Jiang, Z. Klimont and A. Arneth, 2016. Air quality impacts of European wildfire emissions in a changing climate. Atmospheric Chemistry and Physics, 16(9):5685–5703.

Kobayashi, S., Y. Ota, Y. Harada, A. Ebita, M. Moriya, H. Onoda, K. Onogi, H. Kamahori, C. Kobayashi, H. Endo, K. Miyaoka and K. Takahashi, 2015. The JRA-55 reanalysis: general specifications and basic characteristics. Journal of the Meteorological Society of Japan. Ser. II. 93(1):5–48.

Koch, D. and J. Hansen, 2005. Distant origins of Arctic black carbon: a Goddard Institute for Space Studies ModelE experiment. Journal of Geophysical Research: Atmospheres, 110:D04204.

Kock, A. and H.W. Bange, 2015. Counting the ocean's greenhouse gas emissions. Eos, 96.

Koch, D., G.A. Schmidt and C.V. Field, 2006. Sulfur, sea salt, and radionuclide aerosols in GISS ModelE. Journal of Geophysical Research: Atmospheres, 111(D6).

Koffi, E.N., P. Bergamaschi, R. Alkama and A. Cescatti, 2020. An observation-constrained assessment of the climate sensitivity and future trajectories of wetland methane emissions. Science Advances, 6(15):eaay4444.

Kohnert, K., A. Serafimovich, S. Metzger, J. Hartmann and T. Sachs, 2017. Strong geologic methane emissions from discontinuous terrestrial permafrost in the Mackenzie Delta, Canada. Scientific Reports, 7:5828.

Koike, M., J. Ukita, J. Ström, P. Tunved, M. Shiobara, V. Vitale, A. Lupi, D. Baumgardner, C. Ritter, O. Hermansen, K. Yamada and C.A. Pedersen, 2019. Year-round in situ measurements of Arctic low-level clouds: microphysical properties and their relationships with aerosols. Journal of Geophysical Research: Atmospheres, 124(3):1798–1822.

Kokkola, H., H. Korhonen, K.E.J. Lehtinen, R. Makkonen, A. Asmi, S. Järvenoja, T. Anttila, A.-I. Partanen, M. Kulmala, H. Järvinen, A. Laaksonen and V.-M. Kerminen, 2008. SALSA – a Sectional Aerosol module for Large Scale Applications. Atmospheric Chemistry and Physics, 8:2469–2483.

Kokkola, H., T. Kühn, A. Laakso, T. Bergman, K.E.J. Lehtinen, T. Mielonen, A. Arola, S. Stadtler, H. Korhonen, S. Ferrachat, U. Lohmann, D. Neubauer, I. Tegen, C. Siegenthaler-Le Drian, M.G. Schultz, I. Bey, P. Stier, N. Daskalakis, C.L. Heald and S. Romakkaniemi, 2018. SALSA2.0: the sectional aerosol module of the aerosol–chemistry–climate model ECHAM6.3.0-HAM2.3-MOZ1.0. Geoscientific Model Development, 11:3833–3863.

Kollanus, V., P. Tiittanen, J.V. Niemi and T. Lanki, 2016. Effects of long-range transported air pollution from vegetation fires on daily mortality and hospital admissions in the Helsinki metropolitan area, Finland. Environmental Research, 151:351–358.

Köllner, F., J. Schneider, M.D. Willis, T. Klimach, F. Helleis, H. Bozem, D. Kunkel, P. Hoor, J. Burkart, W.R. Leaitch, A.A. Aliabadi, J.P.D. Abbatt, A.B. Herber and S. Borrmann, 2017. Particulate trimethylamine in the summertime Canadian high Arctic lower troposphere. Atmospheric Chemistry and Physics, 17(22):13747–13766.

Kolonjari, F., D.A. Plummer, K.A. Walker, C.D. Boone, J.W. Elkins, M.I. Hegglin, G.L. Manney, F.L. Moore, D. Pendlebury, E.A. Ray, K.H. Rosenlof and G.P. Stiller, 2018. Assessing stratospheric transport in the CMAM30 simulations using ACE-FTS measurements. Atmospheric Chemistry and Physics, 18(9):6801–6828.

Kondo, Y., L. Sahu, N. Moteki, F. Khan, N. Takegawa, X. Liu, M. Koike and T. Miyakawa, 2011a. Consistency and traceability of black carbon measurements made by laser-induced incandescence, thermal-optical transmittance, and filter-based photo-absorption techniques. Aerosol Science and Technology, 45(2):295–312.

Kondo, Y., H. Matsui, N. Moteki, L. Sahu, N. Takegawa, M. Kajino, Y. Zhao, M.J. Cubison, J.L. Jimenez, S. Vay, G.S. Diskin, B. Anderson, A. Wisthaler, T. Mikoviny, H.E. Fuelberg, D.R. Blake, G. Huey, A.J. Weinheimer, D.J. Knapp and W.H. Brune, 2011b. Emissions of black carbon, organic, and inorganic aerosols from biomass burning in North America and Asia in 2008. Journal of Geophysical Research: Atmospheres, 116(D8):D08204.

Konya, K., M. Yamaguchi, M. Takigawa, T. Miyakawa and S. O'Neel, 2021. Mass concentration and origin of black carbon in spring snow on glaciers in the Alaska Range. Polar Science, 27:100572.

Kort, E.A., S.C. Wofsy, B.C. Daube, M. Diao, J.W. Elkins, R.S. Gao, E.J. Hintsa, D.F. Hurst, R. Jimenez, F.L. Moore, J.R. Spackman and M.A. Zondlo, 2012. Atmospheric observations of Arctic Ocean methane emissions up to 82° north. Nature Geoscience, 5:318–321.

Kosmach, D.A., V.I. Sergienko, O.V. Dudarev, A.V. Kurilenko, O. Gustafsson, I.P. Semiletov and N.E. Shakhova, 2015. Methane in the surface waters of Northern Eurasian marginal seas. Doklady Chemistry, 465:281–285.

Kossover, R., 2010. Association between Air Quality and Hospital Visits – Fairbanks, 2003–2008. State of Alaska Epidemiology Bulletin, 26.

Koster, R.D., A.S. Darmenov and A.M da Silva, 2015. The Quick Fire Emissions Dataset (QFED): Documentation of Versions 2.1, 2.2 and 2.4. Volume 38; Technical Report Series on Global Modeling and Data Assimilation. Available at: https://ntrs.nasa.gov/search.jsp?R=20180005253

Krause, A., S. Kloster, S. Wilkenskjeld and H. Paeth, 2014. The sensitivity of global wildfires to simulated past, present, and future lightning frequency. Journal of Geophysical Research: Biogeosciences, 119(3):312–322.

Kramshøj, M., I. Vedel-Petersen, M. Schollert, Å. Rinnan, J. Nymand, H. Ro-Poulsen, and R. Rinnan, 2016. Large increases in Arctic biogenic volatile emissions are a direct effect of warming. Nature Geoscience, 9 (5):349–352.

Kretschmer, K., A. Biastoch, L. Rüpke and E. Burwicz, 2015. Modeling the fate of methane hydrates under global warming. Global Biogeochemical Cycles, 29(5):610–625.

Krishnan, S., A.M.L. Ekman, H.-C. Hansson, I. Riipinen, A. Lewinschal, L.J. Wilcox and T. Dallafior, 2020. The roles of the atmosphere and ocean in driving Arctic warming due to European aerosol reductions. Geophysical Research Letters, 47(7):e2019GL086681.

Krylov, A., J.L. McCarty, P. Potapov, T. Loboda, A. Tyukavina, S. Turubanova and M.C. Hansen, 2014. Remote sensing estimates of stand-replacement fires in Russia, 2002–2011. Environmental Research Letters, 9(10):105007.

Kuhlbrodt, T., C.G. Jones, A. Sellar, D. Storkey, E. Blockley, M. Stringer, R. Hill, T. Graham, J. Ridley, A. Blaker, D. Calvert, D. Copsey, R. Ellis, H. Hewitt, P. Hyder, S. Ineson, J. Mulcahy, A. Siahaan and J. Walton, 2018. The low-resolution version of HadGEM3 GC3.1: development and evaluation for global climate. Journal of Advances in Modeling Earth Systems, 10(11):2865–2888.

Kühn, T., K. Kupiainen, T. Miinalainen, H. Kokkola, V.-V. Paunu, A. Laakso, J. Tonttila, R. Van Dingenen, K. Kulovesi, N. Karvosenoja and K.E.J. Lehtinen, 2020. Effects of black carbon mitigation on Arctic climate. Atmospheric Chemistry and Physics, 20(9):5527–5546.

Kühnel, R., T.J. Roberts, M.P. Björkman, E. Isaksson, W. Aas, K. Holmén and J. Ström, 2011. 20-year climatology of NO_3^- and NH_4^+ wet deposition at Ny-Ålesund, Svalbard. Advances in Meteorology, e406508.

Kukavskaya, E.A., A.J. Soja, A.P. Petkov, E.I. Ponomarev, G.A. Ivanova and S.G. Conard, 2013. Fire emissions estimates in Siberia: evaluation of uncertainties in area burned, land cover, and fuel consumption. Canadian Journal of Forest Research, 43(5):493–506.

Kukkonen, J., M. Savolahti, Y. Palamarchuk, T. Lanki, V. Nurmi, V.-V. Paunu, L. Kangas, M. Sofiev, A. Karppinen, A. Maragkidou, P. Tiittanen and N. Karvosenoja, 2020. Modelling of the public health costs of fine particulate matter and results for Finland in 2015. Atmospheric Chemistry and Physics, 20:9371–9391.

Kulmala M., 2018. Build a global Earth observatory. Nature, 553:21–23.

Kupiszewski, P., C. Leck, M. Tjernström, S. Sjogren, J. Sedlar, M. Graus, M. Müller, B. Brooks, E. Swietlicki, S. Norris and A. Hansel, 2013. Vertical profiling of aerosol particles and trace gases over the central Arctic Ocean during summer. Atmospheric Chemistry and Physics, 13(24):12,405–12,431.

Kurokawa, J. and T. Ohara, 2020. Long-term historical trends in air pollutant emissions in Asia: Regional Emission inventory in ASia (REAS) version 3. Atmospheric Chemistry and Physics, 20(21):12761–12793.

Kurzyca, I. and M. Frankowski, 2017. Recent changes in the oxidized to reduced nitrogen ratio in atmospheric precipitation. Atmospheric Environment, 167:642–655.

Kutcher, H.R. and S.S. Malhi, 2010. Residue burning and tillage effects on diseases and yield of barley (*Hordeum vulgare*) and canola (*Brassica napus*). Soil and Tillage Research, 109(2):153–160.

Kvenvolden, K.A., M.D. Lilley, T.D. Lorenson, P.W. Barnes and E. McLaughlin, 1993. The Beaufort Sea continental shelf as a seasonal source of atmospheric methane. Geophysical Research Letters, 20(22):2459–2462.

Kylling, A., C.D. Groot Zwaaftink and A. Stohl, 2018. Mineral dust instantaneous radiative forcing in the Arctic. Geophysical Research Letters, 45(9):4290–4298.

Kyzivat, E.D., L.C. Smith, L.H. Pitcher, J.V. Fayne, S.W. Cooley, M.G. Cooper, S.N. Topp, T. Langhorst, M.E. Harlan, C. Horvat, C.J. Gleason and T.M. Pavelsky, 2019. A high-resolution airborne color-infrared camera water mask for the NASA ABoVE Campaign. Remote Sensing, 11(18):2163.

Laborde, M., P. Mertes, P. Zieger, J. Dommen, U. Baltensperger and M. Gysel, 2012. Sensitivity of the Single Particle Soot Photometer to different black carbon types. Atmospheric Measurement Techniques, 5(5):1031–1043.

Lack, D.A. and J.M. Langridge, 2013. On the attribution of black and brown carbon light absorption using the Ångström exponent. Atmospheric Chemistry and Physics, 13(20): 10535–10543.

Lamarche-Gagnon, G., J.L. Wadham, B. Sherwood Lollar, S. Arndt, P. Fietzek, A.D. Beaton, A.J. Tedstone, J. Telling, E.A. Bagshaw, J.R. Hawkings, T.J. Kohler, J.D. Zarsky, M.C. Mowlem, A.M. Anesio and M. Stibal, 2019. Greenland melt drives continuous export of methane from the ice-sheet bed. Nature, 565:73–77.

Lamare, M.L., J. Lee-Taylor and M.D. King, 2016. The impact of atmospheric mineral aerosol deposition on the albedo of snow & sea ice: are snow and sea ice optical properties more important than mineral aerosol optical properties? Atmospheric Chemistry and Physics, 16(2):843–860.

Lamarque, J.-F., T.C. Bond, V. Eyring, C. Granier, A. Heil, Z. Klimont, D. Lee, C. Liousse, A. Mieville, B. Owen, M.G. Schultz, D. Shindell, S.J. Smith, E. Stehfest, J. Van Aardenne, O.R. Cooper, M. Kainuma, N. Mahowald, J.R. McConnell, V. Naik, K. Riahi and D.P. van Vuuren, 2010. Historical (1850–2000) gridded anthropogenic and biomass burning emissions of reactive gases and aerosols: methodology and application. Atmospheric Chemistry and Physics, 10(15):7017–7039.

Lamarque, R.L. Langenfelds, C. Le Quéré, V. Naik, S. O'Doherty, P.I. Palmer, I. Pison, D. Plummer, B. Poulter, R.G. Prinn, M. Rigby, B. Ringeval, M. Santini, M. Schmidt, D.T. Shindell, I.J. Simpson, R. Spahni, L.P. Steele, S.A. Strode, K. Sudo, S. Szopa, G.R. van der Werf, A. Voulgarakis, M. van Weele, R.F. Weiss, J.E. Williams and G. Zeng, 2013. Three decades of global methane sources and sinks. Nature Geoscience, 6:813–823.

Lange, R., M. Dall'Osto, H. Wex, H. Skov and A. Massling, 2019. Large summer contribution of organic biogenic aerosols to Arctic cloud condensation nuclei. Geophysical Research Letters, 46(20):11500–11509.

Langer, M., S. Westermann, K. Walter Anthony, K. Wischnewski and J. Boike, 2015. Frozen ponds: production and storage of methane during the Arctic winter in a lowland tundra landscape in northern Siberia, Lena River delta. Biogeosciences, 12:977–990.

Larjavaara, M., T. Kuuluvainen and H. Rita, 2005. Spatial distribution of lightning-ignited forest fires in Finland. Forest Ecology and Management, 208(1–3):177–188.

Lathem, T.L., A.J. Beyersdorf, K.L. Thornhill, E.L. Winstead, M.J. Cubison, A. Hecobian, J.L. Jimenez, R.J. Weber, B.E. Anderson and A. Nenes, 2013. Analysis of CCN activity of Arctic aerosol and Canadian biomass burning during summer 2008. Atmospheric Chemistry and Physics, 13(5):2735–2756.

Lauritzen, P.H., R.D. Nair, A.R. Herrington, P. Callaghan, S. Goldhaber, J.M. Dennis, J.T. Bacmeister, B.E. Eaton, C.M. Zarzycki, M.A. Taylor, P.A. Ullrich, T. Dubos, A. Gettelman, R.B. Neale, B. Dobbins, K.A. Reed, C. Hannay, B. Medeiros, J.J. Benedict and J.J. Tribbia, 2018. NCAR release of CAM-SE in CESM2.0: a reformulation of the spectral element dynamical core in dry-mass vertical coordinates with comprehensive treatment of condensates and energy. Journal of Advances in Modeling Earth Systems, 10(7):1537–1570.

Law, K.S. and A. Stohl, 2007. Arctic air pollution: origins and impacts. Science, 315(5818):1537–1540.

Law, K.S., A. Stohl, P.K. Quinn, C.A. Brock, J.F. Burkhart, J.-D.Paris, G. Ancellet, H.B. Singh, A. Roiger, H. Schlager, J. Dibb, D.J. Jacob, S.R. Arnold, J. Pelon and J.L. Thomas, 2014. Arctic air pollution: new insights from POLARCAT-IPY. Bulletin of the American Meteorological Society, 95(12):1873–1895.

Law, K.S., A. Roiger, J.L. Thomas, L. Marelle, J.-C. Raut, S. Dalsøren, J. Fuglestvedt, P. Tuccella, B. Weinzierl and H. Schlager, 2017. Local Arctic air pollution: sources and impacts. Ambio, 46:453–463.

Law, K.S., J. Liengaard Hjorth, J.B. Pernov, C.H. Whaley, H. Skov, M. Collaud Coen, J. Langner, S.R. Arnold, D. Tarasick, J. Christensen, M. Deushi, P. Effertz, G. Faluvegi, M. Gauss, U. Im, N. Oshima, I. Petropavlovskikh, D. Plummer, K. Tsigaridis, S. Tsyro, S. Solberg and S.T. Turnock, 2023. Arctic Tropospheric Ozone Trends. Geophysical Research Letters (under revision), available ESS Open Archive. February 20, 2023, doi: 10.22541/essoar.167690073.34678721/v1

Lawler, M.J., J. Whitehead, C. O'Dowd, C. Monahan, G. McFiggans and J.N. Smith, 2014. Composition of 15–85 nm particles in marine air. Atmospheric Chemistry and Physics, 14(21):11557–11569.

Lawrence, C. and H. Mao, 2019. Anthropogenic and natural factors affecting trends in atmospheric methane in Barrow, Alaska. Atmosphere, 10(4):187.

Leaitch, W.R., A.M. Macdonald, K.G. Anlauf, P.S.K. Liu, D. Toom-Sauntry, S.-M. Li, J. Liggio, K. Hayden, M.A. Wasey, L.M. Russell, S. Takahama, S. Liu, A. van Donkelaar, T. Duck, R.V. Martin, Q. Zhang, Y. Sun, I. McKendry, N.C. Shantz and M. Cubison, 2009. Evidence for Asian dust effects from aerosol plume measurements during INTEX-B 2006 near Whistler, BC. Atmospheric Chemistry and Physics, 9(11):3523–3546.

Leaitch, W.R., A.M. Macdonald, P.C. Brickell, J. Liggio, S.J. Sjostedt, A. Vlasenko, J.W. Bottenheim, L. Huang, S.-M. Li, P.S.K. Liu, D. Toom-Sauntry, K.A. Hayden, S. Sharma, N.C. Shantz, H.A. Wiebe, W. Zhang, J.P.D. Abbatt, J.G. Slowik, R.Y.-W. Chang, L.M. Russell, R.E. Schwartz, S. Takahama, J.T. Jayne and N.L. Ng, 2011. Temperature response of the submicron organic aerosol from temperate forests. Atmospheric Environment, 45(37):6696–6704.

Leaitch, W.R., L.M. Russell, J. Liu, F. Kolonjari, D. Toom, L. Huang, S. Sharma, A. Chivulescu, D. Veber and W. Zhang, 2018. Organic functional groups in the submicron aerosol at 82.5°N, 62.5°W from 2012 to 2014. Atmospheric Chemistry and Physics, 18(5):3269–3287.

Lee, Y.H., J.-F Lamarque, M.G. Flanner, C. Jiao, D.T. Shindell, T. Berntsen, M.M. Bisiaux, J. Cao, W.J. Collins, M. Curran, R. Edwards, G. Faluvegi, S. Ghan, L.W. Horowitz, J.R. McConnell, J. Ming, G. Myhre, T. Nagashima, V. Naik, S.T. Rumbold, R.B. Skeie, K. Sudo, T. Takemura, F. Thevenon, B. Xu, and J.-H. Yoon, 2013. Evaluation of preindustrial to present-day black carbon and its albedo forcing from Atmospheric Chemistry and Climate Model Intercomparison Project (ACCMIP). Atmospheric Chemistry and Physics, 1395):2607–2634.

Legrand, M., J. McConnell, H. Fischer, E.W. Wolff, S. Preunkert, M. Arienzo, N. Chellman, D. Leuenberger, O. Maselli, P. Place, M. Sigl, S. Schüpbach and M. Flannigan, 2016. Boreal fire records in Northern Hemisphere ice cores: a review. Climate of the Past, 12(10):2033–2059.

Lehtomäki, H., A. Korhonen, A. Asikainen, N. Karvosenoja, K. Kupiainen, V.-V. Paunu, M. Savolahti, M. Sofiev, Y. Palamarchuk, A. Karppinen, J. Kukkonen and O. Hänninen, 2018. Health impacts of ambient air pollution in Finland. International Journal of Environmental Research and Public Health, 15(4):736.

Lehtomäki, H., C. Geels, J. Brandt, S. Rao, K. Yaramenka, S. Åström, M.S. Anderson, L.M. Frohn, U. Im and O. Hänninen, 2020. Deaths attributable to air pollution in Nordic countries: disparities in the estimates. Atmosphere, 11(5):467.

Lehtonen, I., A. Venäläinen, M. Kämäräinen, H. Peltola and H. Gregow, 2016. Risk of large-scale fires in boreal forests of Finland under changing climate. Natural Hazards and Earth System Sciences, 16:239–253.

Leifer, I. and R.K. Patro, 2002. The bubble mechanism for methane transport from the shallow sea bed to the surface: a review and sensitivity study. Continental Shelf Research, 22(16):2409–2428.

Lelieveld, J., P.J. Crutzen and F.J. Dentener, 1998. Changing concentration, lifetime and climate forcing of atmospheric methane. Tellus B: Chemical and Physical Meteorology, 50:128–150.

Lelieveld, J., K. Klingmüller, A. Pozzer, U. Pöschl, M. Fnais, A. Daiber and T. Münzel, 2019. Cardiovascular disease burden from ambient air pollution in Europe reassessed using novel hazard ratio functions. European Heart Journal, 40(20):1590–1596.

Lenaerts, J.T.M., K. Van Tricht, S. Lhermitte and T.S. L'Ecuyer, 2017. Polar clouds and radiation in satellite observations, reanalyses, and climate models. Geophysical Research Letters, 44(7):3355–3364.

Lenssen, N.J.L., G.A. Schmidt, J.E. Hansen, M.J. Menne, A. Persin, R. Ruedy, and D. Zyss, 2019. Improvements in the GISTEMP uncertainty model. Journal of Geophysical Research: Atmospheres, 124(12):6307–6326.

Letterly, A., J. Key and Y. Liu, 2016. The influence of winter cloud on summer sea ice in the Arctic, 1983–2013. Journal of Geophysical Research: Atmospheres, 121(5):2178– 2187.

Lewinschal, A., A.M.L. Ekman, H.-C. Hansson, M. Sand, T.K. Berntsen and J. Langner, 2019. Local and remote temperature response of regional SO_2 emissions. Atmospheric Chemistry and Physics, 19(4): 2385–2403.

Li, S.-M., and L.A. Barrie, 1993. Biogenic sulphur aerosol in the Arctic troposphere: 1. Contributions to total sulfate. Journal of Geophysical Research: Atmospheres, 98(D11):20613–20622.

Li, C., N.C. Hsu, A.M. Sayer, N.A. Krotkov, J.S. Fu, L.N. Lamsal, J.Lee and S.-C. Tsay, 2016a. Satellite observation of pollutant emissions from gas flaring activities near the Arctic. Atmospheric Environment, 133:1–11.

Li, Y., D.K. Henze, D. Jack and P.L. Kinney, 2016b. The influence of air quality model resolution on health impact assessment for fine particulate matter and its components. Air Quality, Atmosphere & Health, 9:51–68.

Li, C., C. McLinden, V. Fioletov, N. Krotkov, S. Carn, J. Joiner, D. Streets, H. He, X. Ren, Z. Li and R.. Dickerson, 2017. India is overtaking China as the world's largest emitter of anthropogenic sulfur dioxide. Scientific Reports, 7:14304.

Liang, T. and J. Aherne, 2019. Critical loads of acidity and exceedances for 1138 lakes and ponds in the Canadian Arctic. Science of the Total Environment, 652:1424–1434.

Libois, Q., G. Picard, J.L. France, L. Arnaud, M. Dumont, C.M. Carmagnola and M.D. King, 2013. Influence of grain shape on light penetration in snow. The Cryosphere, 7(6):1803–1818.

Lidskog, R., J. Johansson and D. Sjödin, 2019. Wildfires, responsibility and trust: public understanding of Sweden's largest wildfire. Scandinavian Journal of Forest Research, 34(4):319–328.

Lihavainen, H., E. Asmi, V. Aaltonen, U. Makkonen and V.-M. Kerminen, 2015. Direct radiative feedback due to biogenic secondary organic aerosol estimated from boreal forest site observations. Environmental Research Letters, 10(10):104005.

Lim, S., X. Faïn, M. Zanatta, J. Cozic, J.-L. Jaffrezo, P. Ginot and P. Laj, 2014. Refractory black carbon mass concentrations in snow and ice: method evaluation and inter-comparison with elemental carbon measurement. Atmospheric Measurement Techniques, 7(10):3307–3324.

Lin, S.-J. and R.B. Rood, 1996: Multidimensional flux-form semi-Lagrangian transport schemes. Monthly Weather Review, 124(9):2046–2070.

Lin, Y., X. Huang, Y. Liang, Y. Qin, S. Xu, W. Huang, F. Xu, L. Liu, Y. Wang, Y. Peng, L. Wang, W. Xue, H. Fu, G.J. Zhang, B. Wang, R. Li, C. Zhang, H. Lu, K. Yang, Yong Luo, Y. Bai, Z. Song, M. Wang, W. Zhao, F. Zhang, J. Xu, X. Zhao, C. Lu, Y. Chen, Yiqi Luo, Y. Hu, Q. Tang, D. Chen, G. Yang and P. Gong, 2020. Community Integrated Earth System Model (CIESM): description and evaluation. Journal of Advances in Modeling Earth Systems, 12(8):e2019MS002036.

Lindberg, H., P. Punttila and I. Vanha-Majamaa, 2020. The challenge of combining variable retention and prescribed burning in Finland. Ecological Processes, 9:4.

Liu, H., D.J. Jacob, I. Bey and R.M. Yantosca, 2001. Constraints from ^{210}Pb and ^{7}Be on wet deposition and transport in a global three-dimensional chemical tracer model driven by assimilated meteorological fields. Journal of Geophysical Research: Atmospheres, 106(D11):12109–12128.

Liu, P.S.K., R. Deng, K.A. Smith, L.R. Williams, J.T. Jayne, M.R. Canagaratana, K. Moore, T.B. Onasche, D.R. Worsnop and T. Deshler, 2007. Transmission efficiency of an aerodynamic focusing lens system: comparison of model calculations and laboratory measurements for the Aerodyne Aerosol Mass Spectrometer. Aerosol Science and Technology, 41(8):721–733.

Liu, J., S. Fan, L.W. Horowitz and H. Levy II, 2011. Evaluation of factors controlling long-range transport of black carbon to the Arctic, Journal of Geophysical Research: Atmospheres, 116(D4).

Liu, Y., J.R. Key, Z. Liu, X. Wang and S.J. Vavrus, 2012a. A cloudier Arctic expected with diminishing sea ice. Geophysical Research Letters, 39(5):L05705.

Liu, X., R.C. Easter, S.J. Ghan, R. Zaveri, P. Rasch, X. Shi, J.-F. Lamarque, A. Gettelman, H. Morrison, F. Vitt, A. Conley, S. Park, R. Neale, C. Hannay, A.M.L. Ekman, P. Hess, N. Mahowald, W. Collins, M. J. Iacono, C.S. Bretherton, M.G. Flanner and D. Mitchell, 2012b. Toward a minimal representation of aerosols in climate models: description and evaluation in the Community Atmosphere Model CAM5. Geoscientific Model Development, 2012, 5(3):709–739.

Liu, D., B. Quennehen, E. Darbyshire, J.D. Allan, P.I. Williams, J.W. Taylor, S.J.-B. Bauguitte, M.J. Flynn, D. Lowe, M.W. Gallagher, K.N. Bower, T.W. Choularton and H. Coe, 2015. The importance of Asia as a source of black carbon to the European Arctic during springtime 2013. Atmospheric Chemistry and Physics, 15(20):11537–11555.

Liu, X., P.-L. Ma, H. Wang, S. Tilmes, B. Singh, R.C. Easter, S.J. Ghan and P.J. Rasch, 2016a. Description and evaluation of a new four-mode version of the Modal Aerosol Module (MAM4) within version 5.3 of the Community Atmosphere Model. Geoscientific Model Development, 9(2):505–522.

Liu, X., H. Sun, T. Feike, X. Zhang, L. Shao and S. Chen, 2016b. Assessing the impact of air pollution on grain yield of winter wheat – a case study in the North China Plain. PLOS ONE, 11(9):e0162655.

Liu, T., L.J. Mickley, M.E. Marlier, R.S. DeFries, M.F. Khan, M.T. Latif and A. Karambelas, 2020. Diagnosing spatial biases and uncertainties in global fire emissions inventories: Indonesia as regional case study. Remote Sensing of Environment, 237:111557.

Loepfe, L., F. Lloret and R.M. Román-Cuesta, 2012. Comparison of burnt area estimates derived from satellite products and national statistics in Europe. International Journal of Remote Sensing, 33(12):3653–3671.

Loewe, K., A.M.L. Ekman, M. Paukert, J. Sedlar, M. Tjernström and C. Hoose, 2017. Modelling micro- and macrophysical contributors to the dissipation of an Arctic mixed-phase cloud during the Arctic Summer Cloud Ocean Study (ASCOS). Atmospheric Chemistry and Physics, 17(11):6693–6704.

Lohmann, U., 2017. Anthropogenic aerosol influences on mixed-phase clouds. Current Climate Change Reports, 3:32–44.

Lohmann, U., J. Feichter, C.C. Chuang and J.E. Penner, 1999. Prediction of the number of cloud droplets in the ECHAM GCM. Journal of Geophysical Research: Atmospheres, 104(D8):9169–9198.

Long, C.M., M.A. Nascarella and P.A. Valberg, 2013. Carbon black vs. black carbon and other airborne materials containing elemental carbon: physical and chemical distinctions. Environmental Pollution, 181:271–286.

Loranty, M.M., W. Lieberman-Cribbin, L.T. Berner, S.M. Natali, S.J. Goetz, H.D. Alexander and A.L. Kholodov, 2016. Spatial variation in vegetation productivity trends, fire disturbance, and soil carbon across Arctic-boreal permafrost ecosystems. Environmental Research Letters, 11(9):095008.

Lorenson, T.D., J. Greinert and R.B. Coffin, 2016. Dissolved methane in the Beaufort Sea and the Arctic Ocean, 1992–2009; sources and atmospheric flux. Limnology and Oceanography, 61(S1): S300–S323.

Lorenzen-Schmidt, H., S. Wessel, W. Unold, S. Solberg, H. Gernandt, F. Stordal and U. Platt, 1998. Ozone measurements in the European Arctic during the ARCTOC 1995 campaign. Tellus B: Chemical and Physical Meteorology, 50(5):416–429.

Loveland, T.R., Z. Zhu, D.O. Ohlen, J.F. Brown, B.C. Reed and L. Yang, 1999. An analysis of IGBP global land-cover characterization process. Photogrammetric Engineering and Remote Sensing, 65(9):1021–1032.

Luben, T.J., J.L. Nichols, S.J. Dutton, E. Kirrane, E.O. Owens, L. Datko-Williams, M. Madden and J.D. Sacks, 2017. A systematic review of cardiovascular emergency department visits, hospital admissions and mortality associated with ambient black carbon. Environment International, 107:154–162.

Lubin, D. and A.M. Vogelmann, 2006. A climatologically significant aerosol longwave indirect effect in the Arctic. Nature, 439:453–456.

Lund, M.T., G. Myhre, A.S. Haslerud, R.B. Skeie, J. Griesfeller, S.M. Platt, R. Kumar, C. Lund Myhre and M. Schulz, 2018. Concentrations and radiative forcing of anthropogenic aerosols from 1750 to 2014 simulated with the Oslo CTM3 and CEDS emission inventory. Geoscientific Model Development, 11:4909–4931.

Lund Myhre, C., B. Ferré, S.M. Platt, A. Silyakova, O. Hermansen, G. Allen, I. Pisso, N. Schmidbauer, A. Stohl, J. Pitt, P. Jansson, J. Greinert, C. Percival, A.M. Fjaeraa, S.J. O'Shea, M. Gallagher, M. Le Breton, K.N. Bower, S.J.B. Bauguitte, S. Dalsøren, S. Vadakkepuliyambatta, R.E. Fisher, E.G. Nisbet, D. Lowry, G. Myhre, J.A. Pyle, M. Cain and J. Mienert, 2016. Extensive release of methane from Arctic seabed west of Svalbard during summer 2014 does not influence the atmosphere. Geophysical Research Letters, 43(9):4624–4631.

Lurmann, F., A.C. Lloyd and R. Atkinson, 1986. A chemical mechanism for use in long-range transport/acid deposition computer modeling. Journal of Geophysical Research: Atmospheres, 91(D10):10905–10936.

Ma, X., K. von Salzen and J. Li, 2008. Modelling sea salt aerosol and its direct and indirect effects on climate. Atmospheric Chemistry and Physics, 8:1311–1327.

Maas, R. and P. Grennfelt (Eds), 2016. Towards Cleaner Air. Scientific Assessment Report 2016. EMEP Steering Body and Working Group on Effects of the Convention on Long-range Transboundary Air Pollution, Oslo. xx + 50pp.

Macdonald, K.M., S. Sharma, D. Toom, A. Chivulescu, S. Hanna, A.K. Bertram, A. Platt, M. Elsasser, L. Huang, D. Tarasick, N. Chellman, J.R. McConnell, H. Bozem, D. Kunkel, Y.D. Lei, G.J. Evans and J.P.D. Abbatt, 2017. Observations of atmospheric chemical deposition to high Arctic snow. Atmospheric Chemistry and Physics, 17(9):5775–5788.

Macdonald, K.M., S. Sharma, D. Toom, A. Chivulescu, A. Platt, M. Elsasser, L. Huang, R. Leaitch, N. Chellman, J.R. McConnell, H. Bozem, D. Kunkel, Y.D. Lei, C.-H. Jeong, J.P.D. Abbatt and G.J. Evans, 2018. Temporally delineated sources of major chemical species in high Arctic snow. Atmospheric Chemistry and Physics, 18(5):3485–3503.

Mackelprang, R., S.R. Saleska, C.S. Jacobsen, J.K. Jansson and N. Taş, 2016. Permafrost meta-omics and climate change. Annual Review of Earth and Planetary Sciences, 44:439–462.

Mackie, A.R., P.I. Palmer, J.M. Barlow, D.P. Finch, P. Novelli and L. Jaeglé, 2016. Reduced Arctic air pollution due to decreasing European and North American emissions. Journal of Geophysical Research: Atmospheres, 121(14):8692–8700.

Madsen, C., P. Rosland, D.A. Hoff, W. Nystad, P. Nafstad and O.E. Næss, 2012. The short-term effect of 24-h average and peak air pollution on mortality in Oslo, Norway. European Journal of Epidemiology, 27:717–727.

Maenhaut, W., G. Ducastel, K. Beyaert, and J.E. Hanssen, 1994. Chemical composition of summer aerosol at Ny-Ålesund, Spitsbergen, and relative contribution of natural and anthropogenic sources to the non-sea-salt sulfate. In: Borrel, P.M., P. Borrel, T. Cvitaš and W. Seiler (Eds). Transport and Transportation of Pollutants in the Atmosphere: Proceedings of EUROTRAC Symposium '94. pp467–471, SPB Academic Publishing, Amsterdam, Netherlands.

Maenhaut, W., K. Beyaert, G. Ducastel, V. Havránek, R. Solomonovic, and J.E. Hanssen, 1997. Long-term measurements of the atmospheric aerosol composition at Ny-Ålesund, Spitsbergen. In: Borrel, P.M., P. Borrel, K. Kelly, T. Cvitaš and W. Seiler (Eds). Proceedings EUROTRAC Symposium '96: Transport and Transformation of Pollutants in the Troposphere Vol. 1. pp183–186, Computational Mechanics Publications, Southampton, UK.

Mahmood R., K. von Salzen, M. Flanner, M. Sand, J. Langner, H. Wang and L. Huang, 2016. Seasonality of global and Arctic black carbon processes in the Arctic Monitoring and Assessment Programme models. Journal of Geophysical Research: Atmospheres, 121(12):7100–7116.

Mahmood, R., K. von Salzen, A.-L. Norman, M. Galí and M. Levasseur, 2019. Sensitivity of Arctic sulfate aerosol and clouds to changes in future surface seawater dimethylsulfide concentrations. Atmospheric Chemistry and Physics, 19, 6419–6435.

Mahowald, N.M., J.-F. Lamarque, X.X. Tie and E. Wolff, 2006a. Sea-salt aerosol response to climate change: last glacial maximum, preindustrial, and doubled carbon dioxide climates. Journal of Geophysical Research: Atmospheres, 111(D5).

Mahowald, N.M., D.R. Muhs, S. Levis, P.J. Rasch, M. Yoshioka, C.S. Zender and C. Luo, 2006b. Change in atmospheric mineral aerosols in response to climate: Last glacial period, preindustrial, modern, and doubled carbon dioxide climates. Journal of Geophysical Research: Atmospheres, 111(D10).

Mahrt, F., J. Wieder, R. Dietlicher, H.R. Smith, C. Stopford and Z.A. Kanji, 2019. A high-speed particle phase discriminator (PPD-HS) for the classification of airborne particles, as tested in a continuous flow diffusion chamber. Atmospheric Measurement Techniques, 12(6):3183–3208.

Makar, P.A., V.S. Bouchet and A. Nenes, 2003. Inorganic chemistry calculations using HETV – a vectorized solver for the SO_4^{2-}–NO_3^-–NH_4^+ system based on the ISORROPIA algorithms. Atmospheric Environment, 37(16):2279–2294.

Makar, P.A., W. Gong, J. Milbrandt, C. Hogrefe, Y. Zhang, G. Curci, R. Žabkar, U. Im, A. Balzarini, R. Baró, R. Bianconi, P. Cheung, R. Forkel, S. Gravel, M. Hirtl, L. Honzak, A. Hou, P. Jiménez-Guerrero, M. Langer, M.D. Moran, B. Pabla, J.L. Pérez, G. Pirovano, R. San José, P. Tuccella, J. Werhahn, J. Zhang and S. Galmarini, 2015a. Feedbacks between air pollution and weather, part 1: effects on weather. Atmospheric Environment, 115:442–469.

Makar, P.A., W. Gong, C. Hogrefe, Y. Zhang, G. Curci, R. Žabkar, J. Milbrandt, U. Im, A. Balzarini, R. Baró, R. Bianconi, P. Cheung, R. Forkel, S. Gravel, M. Hirtl, L. Honzak, A. Hou, P. Jiménez-Guerrero, M. Langer, M.D. Moran, B. Pabla, J.L. Pérez, G. Pirovano, R. San José, P. Tuccella, J. Werhahn, J. Zhang and S. Galmarini, 2015b. Feedbacks between air pollution and weather, part 2: effects on chemistry. Atmospheric Environment, 115:499–526.

Makar, P.A., R.M. Staebler, A. Akingunola, J. Zhang, C. McLinden, S.K. Kharol, B. Pabla, P. Cheung and Q. Zheng, 2017. The effects of forest canopy shading and turbulence on boundary layer ozone. Nature Communications, 8(15243).

Mäkelä, A., S.-E. Enno and J. Haapalainen, 2014. Nordic Lightning Information System: thunderstorm climate of Northern Europe for the period 2002–2011. Atmospheric Research, 139:46–61.

Malm, W.C., J.F. Sisler, D. Huffman, R.A. Eldred and T.A. Cahill, 1994. Spatial and seasonal trends in particle concentration and optical extinction in the United States. Journal of Geophysical Research: Atmospheres, 99(D1):1347–1370.

Malm, W.C., B.A. Schichtel and M.L. Pitchford, 2011. Uncertainties in $PM_{2.5}$ gravimetric and speciation measurements and what we can learn from them. Journal of the Air & Waste Management Association. 61(11):1131–1149.

Malm, W.C., B.A. Schichtel, J.L. Hand and A.J. Prenni, 2020. Implications of organic mass to carbon ratios increasing over time in the rural United States. Journal of Geophysical Research: Atmospheres, 125(5):e2019JD031480.

Malmqvist, E., H.E. Larsson, I. Jönsson, A. Rignell-Hydbom, S.-A. Ivarsson, H. Tinnerberg, E. Stroh, R. Rittner, K. Jakobsson, E. Swietlicki and L. Rylander, 2015. Maternal exposure to air pollution and type 1 diabetes – accounting for genetic factors. Environmental Research, 140:268–274.

Mann, G.W., K.S. Carslaw, D.V. Spracklen, D.A. Ridley, P.T. Manktelow, M.P. Chipperfield, S.J. Pickering and C.E. Johnson, 2010. Description and evaluation of GLOMAP-mode: a modal global aerosol microphysics model for the UKCA composition-climate model. Geoscientific Model Development, 3(2):519–551.

Mann, G.W., K.S. Carslaw, D.A. Ridley, D.V. Spracklen, K.J. Pringle, J. Merikanto, H. Korhonen, J.P. Schwarz, L.A. Lee, P.T. Manktelow, M.T. Woodhouse, A. Schmidt, T.J. Breider, K.M. Emmerson, C.L. Reddington, M.P. Chipperfield and S.J. Pickering, 2012. Intercomparison of modal and sectional aerosol microphysics representations within the same 3-D global chemical transport model. Atmospheric Chemistry and Physics, 12(10):4449–4476.

Manninen, T., K. Anttila, E. Jääskeläinen, A. Riihelä, J. Peltoniemi, P. Räisänen, P. Lahtinen, N. Siljamo, L. Thölix, O. Meinander, A. Kontu, H. Suokanerva, R. Pirazzini, J. Suomalainen, T. Hakala, S. Kaasalainen, H. Kaartinen, A. Kukko, O. Hautecoeur and J.-L. Roujean, 2021. Effect of small-scale snow surface roughness on snow albedo and reflectance. The Cryosphere, 15(2):793–820.

Manousakas, M., O. Popovicheva, N. Evangeliou, E. Diapouli, N. Sitnikov, N. Shonija and K. Eleftheriadis, 2020. Aerosol carbonaceous, elemental and ionic composition variability and origin at the Siberian High Arctic, Cape Baranova. Tellus B: Chemical and Physical Meteorology, 72(1):1–14.

Marais, E.A., D.J. Jacob, J.L. Jimenez, P. Campuzano-Jost, D.A. Day, W. Hu, J. Krechmer, L. Zhu, P.S. Kim, C.C. Miller, J.A. Fisher, K. Travis, K. Yu, T.F. Hanisco, G.M. Wolfe, H.L. Arkinson, H.O.T. Pye, K.D. Froyd, J. Liao and V.F. McNeill, 2016. Aqueous-phase mechanism for secondary organic aerosol formation from isoprene: application to the southeast United States and co-benefit of SO_2 emission controls. Atmospheric Chemistry and Physics, 16(3):1603–1618.

Marelle, L., J.-C. Raut, J.L. Thomas, K.S. Law, B. Quennehen, G. Ancellet, J. Pelon, A. Schwarzenboeck and J.D. Fast, 2015. Transport of anthropogenic and biomass burning aerosols from Europe to the Arctic during spring 2008. Atmospheric Chemistry and Physics, 15(7):3831–3850.

Marelle, L., J.L. Thomas, J.-C. Raut, K.S. Law, J.-P. Jalkanen, L. Johansson, A. Roiger, H. Schlager, J. Kim, A. Reiter and B. Weinzierl, 2016. Air quality and radiative impacts of Arctic shipping emissions in the summertime in northern Norway: from the local to the regional scale. Atmospheric Chemistry and Physics, 16 (4):2359–2379.

Marelle, L., J.-C. Raut, K.S. Law, L.K. Berg, J.D. Fast, R.C. Easter, M. Shrivastava and J.L. Thomas, 2017. Improvements to the WRF-Chem 3.5.1 model for quasi-hemispheric simulations of aerosols and ozone in the Arctic. Geoscientific Model Development, 10(10):3661–3677.

Marelle, L., J.-C. Raut, K.S. Law and O. Duclaux, 2018. Current and future Arctic aerosols and ozone from remote emissions and emerging local sources—modeled source contributions and radiative effects. Journal of Geophysical Research: Atmospheres, 123(22):12942–12963.

Markowicz, K.M., C. Ritter, J. Lisok, P. Makuch, I.S. Stachlewska, D. Cappelletti, M. Mazzola and M.T. Chilinski, 2017. Vertical variability of aerosol single-scattering albedo and equivalent black carbon concentration based on in-situ and remote sensing techniques during the iAREA campaigns in Ny-Ålesund. Atmospheric Environment, 164:431–447.

Markuse, P., 2019. Before/After Comparison of the July/August 2019 Greenland Wildfire: Analysis from Sentinel-2. Available at: https://pierre-markuse.net/2019/08/19/before-after-comparison-of-the-july-august-2019-greenland-wildfire/

Mårtensson, E.M., E.D. Nilsson, G. de Leeuw, L.H. Cohen and H.-C. Hansson, 2003. Laboratory simulations and parameterization of the primary marine aerosol production. Journal of Geophysical Research: Atmospheres, 108(D9).

Marvel, K., B.I. Cook, C.J.W. Bonfils, P.J. Durack, J.E. Smerdon and A. Park Williams, 2019. Twentieth-century hydroclimate changes consistent with human influence. Nature, 569:59–65.

Masrur, A., A.N. Petrov and J. DeGroote, 2018. Circumpolar spatio-temporal patterns and contributing climatic factors of wildfire activity in the Arctic tundra from 2001–2015. Environmental Research Letters, 13(1):014019.

Massling, A., I.E. Nielsen, D. Kristensen, J.H. Christensen, L.L. Sørensen, B. Jensen, Q.T. Nguyen, J.K. Nøjgaard, M. Glasius and H. Skov, 2015. Atmospheric black carbon and sulfate concentrations in Northeast Greenland. Atmospheric Chemistry and Physics, 15(16):9681–9692.

Mastepanov, M., C. Sigsgaard, E.J. Dlugokencky, S. Houweling, L. Ström, M.P. Tamstorf and T.R. Christensen, 2008. Large tundra methane burst during onset of freezing. Nature, 456:628–630.

Mastepanov, M., C. Sigsgaard, T. Tagesson, L. Ström, M.P. Tamstorf, M. Lund and T.R. Christensen, 2013. Revisiting factors controlling methane emissions from high-Arctic tundra. Biogeosciences, 10(7): 5139–5158.

Matsui, H., Y. Kondo, N. Moteki, N. Takegawa, L.K. Sahu, Y. Zhao, H.E. Fuelberg, W.R. Sessions, G. Diskin, D.R. Blake, A. Wisthaler and M. Koike, 2011. Seasonal variation of the transport of black carbon aerosol from the Asian continent to the Arctic during the ARCTAS aircraft campaign. Journal of Geophysical Research: Atmospheres, 116:D05202.

Matsui, H., N.M. Mahowald, N. Moteki, D.S. Hamilton, S. Ohata, A. Yoshida, M. Koike, R.A. Scanza and M.G. Flanner, 2018. Anthropogenic combustion iron as a complex climate forcer. Nature Communications, 9:1593.

Matthew, B.M., A.M. Middlebrook and T.B. Onasch, 2008. Collection efficiencies in an aerodyne aerosol mass spectrometer as a function of particle phase for laboratory generated aerosols. Aerosol Science and Technology, 42(11)884–898.

Matthews, E. and I. Fung, 1987. Methane emission from natural wetlands: global distribution, area, and environmental characteristics of sources. Global Biogeochemical Cycles, 1(1):61–86.

Mauritsen, T., J. Sedlar, M. Tjernström, C. Leck, M. Martin, M. Shupe, S. Sjogren, B. Sierau, P.O.G. Persson, I.M. Brooks and E. Swietlicki, 2011. An Arctic CCN-limited cloud-aerosol regime. Atmospheric Chemistry and Physics, 11(1):165–173.

May, A.A., G.R. McMeeking, T. Lee, J.W. Taylor, J.S Craven, I. Burling, A.P. Sullivan, S. Akagi, J.L. Collett Jr., M. Flynn, H. Coe, S.P. Urbanski, J.H. Seinfeld, R.J. Yokelson and S.M. Kreidenweis, 2014. Aerosol emissions from prescribed fires in the United States: A synthesis of laboratory and aircraft measurements. Journal of Geophysical Research: Atmospheres, 119(20):11826–11849.

McCarty, J.L., E.A. Ellicott, V. Romanenkov, D. Rukhovitch and P. Koroleva, 2012. Multi-year black carbon emissions from cropland burning in the Russian Federation. Atmospheric Environment, 63:223–238.

McCarty, J.L., A. Krylov, A.V. Prishchepov, D.M. Banach, A. Tyukavina, P. Potapov and S. Turubanova, 2017. Agricultural fires in European Russia, Belarus, and Lithuania and their impact on air quality, 2002–2012. In: Gutman G. and V. Radeloff (Eds.). Land-Cover and Land-Use Changes in Eastern Europe after the Collapse of the Soviet Union in 1991, pp. 193–221. Springer.

McConnell, J.R., 2010. New directions: historical black carbon and other ice core aerosol records in the Arctic for GCM evaluation. Atmospheric Environment, 44(21–22):2665–2666.

McConnell, J.R. and R. Edwards, 2008. Coal burning leaves toxic heavy metal legacy in the Arctic. PNAS, 105(34):12140–12144.

McConnell, J.R., G.W. Lamorey, S.W. Lambert and K.C. Taylor, 2002. Continuous Ice-Core analysis using inductively coupled plasma mass spectrometry. Environmental Science & Technology, 36(1):7–11.

McConnell, J.R., R. Edwards, G.L. Kok, M.G. Flanner, C.S. Zender, E.S. Saltzman, J.R. Banta, D.R. Pasteris, M.M. Carter and J.D.W Kahl, 2007. 20th-century industrial black carbon emissions altered Arctic climate forcing. Science, 317(5843):1381–1384.

McConnell, J.R., A. Burke, N.W. Dunbar, P. Köhler, J.L. Thomas, M.M. Arienzo, N.J. Chellman, O.J. Maselli, M. Sigl, J.F. Adkins, D. Baggenstos, J.F. Burkhart, E.J. Brook, C. Buizert, J. Cole-Dai, T.J. Fudge, G. Knorr, H.-F. Graf, M.M. Grieman, N. Iverson, K.C. McGwire, R. Mulvaney, G. Paris, R.H. Rhodes, E.S. Saltzman, J.P. Severinghaus, J.P. Steffensen, K.C. Taylor and G. Winckler, 2017. Synchronous volcanic eruptions and abrupt climate change ~17.7ka plausibly linked by stratospheric ozone depletion. PNAS, 114(38): 10035–10040.

McConnell, J.R., A.I. Wilson, A. Stohl, M.M. Arienzo, N.J. Chellman, S. Eckhardt, E.M. Thompson, A.M. Pollard and J.P. Steffensen, 2018. Lead pollution recorded in Greenland ice indicates European emissions tracked plagues, wars, and imperial expansion during antiquity. PNAS, 115(22)5726–5731.

McConnell, J.R., N.J. Chellman, A.I. Wilson, A. Stohl, M.M. Arienzo, S. Eckhardt, D. Fritzsche, S. Kipfstuhl, T. Opel, P.F. Place and J.P. Steffensen, 2019. Pervasive Arctic lead pollution suggests substantial growth in medieval silver production modulated by plague, climate, and conflict. PNAS, 116(30):14910–14915.

McCoy I.L., D.T. McCoy, R. Wood, L. Regayre, D. Watson-Parris, D.P. Grosvenor, J.P. Mulcahy, Y. Hu, F.A.-M. Bender, P.R. Field, K.S. Carslaw and H. Gordon, 2020. The hemispheric contrast in cloud microphysical properties constrains aerosol forcing. PNAS, 117(32):18998–19006.

McEwen, J.D.N. and M.R. Johnson, 2012. Black carbon particulate matter emission factors for buoyancy-driven associated gas flares. Journal of the Air & Waste Management Association, 62(3):307–321.

McFarquhar, G.M., S. Ghan, J. Verlinde, A. Korolev, J.W. Strapp, B. Schmid, J.M. Tomlinson, M. Wolde, S.D. Brooks, D. Cziczo, M.K. Dubey, J. Fan, C. Flynn, I. Gultepe, J. Hubbe, M.K. Gilles, A. Laskin, P. Lawson, W.R. Leaitch, P. Liu, X. Liu, D. Lubin, C. Mazzoleni, A.-M. Macdonald, R.C. Moffet, H. Morrison, M. Ovchinnikov, M.D. Shupe, D.D. Turner, S. Xie, A. Zelenyuk, K. Bae, M. Freer and A. Glen, 2011. Indirect and semi-direct aerosol campaign. Bulletin of the American Meteorological Society, 92(2):183–201.

McFarquhar, G.M., D. Baumgardner, A. Bansemer, S.J. Abel, J. Crosier, J. French, P. Rosenberg, A. Korolev, A. Schwarzoenboeck, D. Leroy, J. Um, W. Wu, A.J. Heymsfield, C. Twohy, A. Detwiler, P. Field, A. Neumann, R. Cotton, D. Axisa and J. Dong, 2017. Processing of ice cloud in situ data collected by bulk water, scattering, and imaging probes: fundamentals, uncertainties, and efforts toward consistency. Meteorological Monographs, 58(1):11.1–11.33.

McGinnis, D.F., J. Greinert, Y. Artemov, S.E. Beaubien and A. Wüest, 2006. Fate of rising methane bubbles in stratified waters: how much methane reaches the atmosphere? Journal of Geophysical Research: Oceans, 111(C9):C09007.

McGuire, A.D., T.R. Christensen, D. Hayes, A. Heroult, E. Euskirchen, J.S. Kimball, C. Koven, P. Lafleur, P.A. Miller, W. Oechel, P. Peylin, M. Williams and Y. Yi, 2012. An assessment of the carbon balance of Arctic tundra: comparisons among observations, process models, and atmospheric inversions. Biogeosciences, 9(8):3185–3204.

McGwinn, K., 2019. Hikers warned as Greenland wildfire burns out of control. Arctic Today, 16 July 2019. Available at: https://www.arctictoday.com/hikers-warned-as-greenland-wildfire-burns-out-of-control/

McLinden, C.A., S.C. Olsen, B. Hannegan, O. Wild, M.J. Prather and J. Sundet, 2000. Stratospheric ozone in 3-D models: a simple chemistry and the cross-tropopause flux. Journal of Geophysical Research: Atmospheres, 105(D11):14653–14665.

McNamara, S.M., A.R.W. Raso, S. Wang, S. Thanekar, E.J. Boone, K.R. Kolesar, P.K. Peterson, W.R. Simpson, J.D. Fuentes, P.B. Shepson and K.A. Pratt, 2019. Springtime nitrogen oxide-influenced chlorine chemistry in the coastal Arctic. Environmental Science & Technology, 53(14):8057–8067.

McNaughton, C.S., A.D. Clarke, S. Freitag, V.N. Kapustin, Y. Kondo, N. Moteki, L. Sahu, N. Takegawa, J.P. Schwarz, J.R. Spackman, L. Watts, G. Diskin, J. Podolske, J.S. Holloway, A. Wisthaler, T. Mikoviny, J. de Gouw, C. Warneke, J. Jimenez, M. Cubison, S.G. Howell, A. Middlebrook, R. Bahreini, B.E. Anderson, E. Winstead, K.L. Thornhill, D. Lack, J. Cozic and C.A. Brock, 2011. Absorbing aerosol in the troposphere of the Western Arctic during the 2008 ARCTAS/ARCPAC airborne field campaigns. Atmospheric Chemistry and Physics, 11(15):7561–7582.

McWethy, D.B., T. Schoennagel, P.E. Higuera, M. Krawchuk, B.J. Harvey, E.C. Metcalf, C. Schultz, C. Miller, A.L. Metcalf, B. Buma, A. Virapongse, J.C. Kulig, R.C. Stedman, Z. Ratajczak, C.R. Nelson and C. Kolden, 2019. Rethinking resilience to wildfire. Nature Sustainability, 2:797–804.

Medalia, A.I. and F.A. Heckman, 1969. Morphology of aggregates – II. Size and shape factors of carbon black aggregates from electron microscopy. Carbon, 7(5):567–582.

Meinander, O., S. Kazadzis, A. Arola, A. Riihelä, P. Räisänen, R. Kivi, A. Kontu, R. Kouznetsov, M. Sofiev, J. Svensson, H. Suokanerva, V. Aaltonen, T. Manninen, J.-L. Roujean and O. Hautecoeur, 2013. Spectral albedo of seasonal snow during intensive melt period at Sodankylä, beyond the Arctic Circle. Atmospheric Chemistry and Physics, 13(7):3793–3810.

Meinander, O., A. Kontu, A. Virkkula, A. Arola, L. Backman, P. Dagsson-Waldhauserová, O. Järvinen, T. Manninen, J. Svensson, G. de Leeuw and M. Leppäranta, 2014. Brief communication: Light-absorbing impurities can reduce the density of melting snow. The Cryosphere, 8(3):991–995.

Meinander, O., S. Chalov, H. Lappalainen, J. Ekman, K. Eleftheriadis, D. Frolov, A. Hyvärinen, V. Ivanov, N. Karvosenoja, K. Kupiainen, O. Popovicheva, I. Semenkov, L. Sogacheva, and The MSU Workshop Participants, 2019. About black carbon in the Arctic and significance compared to high-latitude dust sources (Finnish-Russian Workshop at the Lomonosov Moscow State University, 17–18 September 2019, in co-operation with MSU, INAR, PEEX, MFA/IBA AND FMI). In: Proceedings of The Center of Excellence in Atmospheric Science (CoE ATM) Annual Seminar 2019. Editors: Laurila, T., A. Lintunen, M. Kulmala (Eds.) pp. 457–465. Finnish Association for Aerosol Research.

Meinander, O., E. Heikkinen, M. Aurela and A. Hyvärinen, 2020a. Sampling, filtering, and analysis protocols to detect black carbon, organic carbon, and total carbon in seasonal surface snow in an urban background and Arctic Finland (>60°N). Atmosphere, 11(9):923.

Meinander, O., A. Kontu, R. Kouznetsov and M. Sofiev, 2020b. Snow samples combined with long-range transport modeling to reveal the origin and temporal variability of black carbon in seasonal snow in Sodankylä (67°N). Frontiers in Earth Science, 8(153).

Meinander, O., P. Dagsson-Waldhauserova, P. Amosov, E. Aseyeva, C. Atkins, A. Baklanov, C. Baldo, S. Barr, B. Barzycka, L. Benning, B. Cvetkovic, P. Enchilik, D. Frolov, S. Gassó, K. Kandler, N. Kasimov, J. Kavan, J. King, T. Koroleva, V. Krupskaya, M. Kusiak, M. Laska, J. Lasne, M. Lewandowski, B. Luks, J. McQuaid, B. Moroni, B. Murray, O. Möhler, A. Nawrot, S. Nickovic, N. O'Neill, G. Pejanovic, O. Popovicheva, K. Ranjbar, M. Romanias, O. Samonova, A. Sanchez-Marroquin, K. Schepanski, I. Semenkov, A. Sharapova, E. Shevnina, Z. Shi, M. Sofiev, F. Thevenet, T. Thorsteinsson, M. Timofeev, N.S. Umo, A. Uppstu, D. Urupina, G. Varga, T. Werner, O. Arnalds and A. Vukovic Vimic, 2021. Newly identified climatically and environmentally significant high latitude dust sources. Atmospheric Chemistry and Physics. Preprint 963.

Meinshausen, M., E. Vogel, A. Nauels, K. Lorbacher, N. Meinshausen, D.M. Etheridge, P.J. Fraser, S.A. Montzka, P.J. Rayner, C.M. Trudinger, P.B. Krummel, U. Beyerle, J.G. Canadell, J.S. Daniel, I.G. Enting, R.M. Law, C.R. Lunder, S. O'Doherty, R.G. Prinn, S. Reimann, M. Rubino, G.J.M. Velders, M.K. Vollmer, R.H.J. Wang and R. Weiss, 2017. Historical greenhouse gas concentrations for climate modelling (CMIP6). Geoscientific Model Development, 10:2057–2116.

Meinshausen, M., Z.R.J. Nicholls, J. Lewis, M.J. Gidden, E. Vogel, M. Freund, U. Beyerle, C. Gessner, A. Nauels, N. Bauer, J.G. Canadell, J.S. Daniel, A. John, P.B. Krummel, G. Luderer, N. Meinshausen, S.A. Montzka, P.J. Rayner, S. Reimann, S.J. Smith, M. van den Berg, G.J.M. Velders, M.K. Vollmer and R.H.J Wang, 2020. The shared socio-economic pathway (SSP) greenhouse gas concentrations and their extensions to 2500. Geoscientific Model Development, 13:3571–3605.

Mekonnen, Z.A., W.J. Riley, J.T. Randerson, R.F. Grant and B.M. Rogers, 2019. Expansion of high-latitude deciduous forests driven by interactions between climate warming and fire. Nature Plants, 5:952–958.

Menon, S. and L. Rotstayn, 2006. The radiative influence of aerosol effects on liquid-phase cumulus and stratiform clouds based on sensitivity studies with two climate models. Climate Dynamics, 27:345–356.

Michaelides, R.J., K. Schaefer, H.A. Zebker, A. Parsekian, L. Liu, J. Chen, S. Natali, S. Ludwig and S.R. Schaefer, 2019. Inference of the impact of wildfire on permafrost and active layer thickness in a discontinuous permafrost region using the remotely sensed active layer thickness (ReSALT) algorithm. Environmental Research Letters, 14(3):035007.

Mijling, B., R.J. van der A and Q. Zhang, 2013. Regional nitrogen oxides emission trends in East Asia observed from space. Atmospheric Chemistry and Physics, 13:12003–12012.

Miller, R.L. and I. Tegen, 1998. Climate response to soil dust aerosols. Journal of Climate, 11(12):3247–3267.

Miller, R.L., R.V. Cakmur, J. Perlwitz, I.V. Geogdzhayev, P. Ginoux, D. Koch, K.E. Kohfield, C. Prigent, R. Ruedy, G.A. Schmidt and I. Tegen, 2006. Mineral dust aerosols in the NASA Goddard Institute for Space Sciences ModelE atmospheric general circulation model. Journal of Geophysical Research: Atmospheres, 111(D6).

Miller, M.E., M. Billmire, L. Bourgeau-Chavez, W.J. Elliot, P.R. Robichaud and L. MacDonald, 2017. Rapid response tools and datasets for post-fire modeling in Boreal and Arctic Environments. AFSC Remote Sensing Workshop: Opportunities to Apply Remote Sensing in Boreal/Arctic Wildfire Management and Science. April 2017, Fairbanks, Alaska, USA. Available at: https://digitalcommons.mtu.edu/mtri_p/290/

Miller, C.E., P.C. Griffith, S.J. Goetz, E.E. Hoy, N. Pinto, I.B. McCubbin, A.K. Thorpe, M. Hofton, D. Hodkinson, C. Hansen, J. Woods, E. Larsen, E.S. Kasischke and H.A. Margolis, 2019. An overview of ABoVE airborne campaign data acquisitions and science opportunities. Environmental Research Letters, 14(8):080201.

Miller, R.L., G.A. Schmidt, L. Nazarenko, S.E. Bauer, M. Kelley, R. Ruedy, G.L. Russell, A.S. Ackerman, I. Aleinov, M. Bauer, R. Bleck, V. Canuto, G. Cesana, Y. Cheng, T.L. Clune, B.I. Cook, C.A. Cruz, A.D. Del Genio, G.S. Elsaesser, G. Faluvegi, N.Y. Kiang, D. Kim, A.A. Lacis, A. Leboissetier, A.N. LeGrande, K.K. Lo, J. Marshall, E.E. Matthews, S. McDermid, K. Mezuman, L.T. Murray, V. Oinas, C. Orbe, C. Pérez García-Pando, J.P. Perlwitz, M.J. Puma, D. Rind, A. Romanou, D.T. Shindell, S. Sun, N. Tausnev, K. Tsigaridis, G. Tselioudis, E. Weng, J. Wu and M.-S. Yao, 2020. CMIP6 historical simulations (1850–2014) with GISS-E2.1. Journal of Advances in Modeling Earth Systems, 13(1):e2019MS002034.

Millet, D.B., M. Baasandorj, D.K. Farmer, J.A. Thornton, K. Baumann, P. Brophy, S. Chaliyakunnel, J.A. de Gouw, M. Graus, L. Hu, A. Koss, B.H. Lee, F.D. Lopez-Hilfiker, J.A. Neuman, F. Paulot, J. Peischl, I.B.

Pollack, T.B. Ryerson, C. Warneke, B.J. Williams and J. Xu, 2015. A large and ubiquitous source of atmospheric formic acid. Atmospheric Chemistry and Physics, 15:6283–6304.

Mills, G., A. Buse, B. Gimeno, V. Bermejo, M. Holland, L. Emberson and H. Pleijel, 2007. A synthesis of AOT40-based response functions and critical levels of ozone for agricultural and horticultural crops. Atmospheric Environment, 41(12):2630–2643.

Mills, G., F. Hayes, D. Simpson, L. Emberson, D. Norris, H. Harmens and P. Büker, 2011. Evidence of widespread effects of ozone on crops and (semi-)natural vegetation in Europe (1990–2006) in relation to AOT40- and flux-based risk maps. Global Change Biology, 17(1):592–613.

Min, C., L. Mu, Q. Yang, R. Ricker, Q. Shi, B. Han, R. Wu and J. Liu, 2019. Sea ice export through the Fram Strait derived from a combined model and satellite data set. The Cryosphere, 13(12):3209–3224.

Mioche, G., O. Jourdan, M. Ceccaldi and J. Delanoe, 2015. Variability of mixed-phase clouds in the Arctic with a focus on the Svalbard region: a study based on spaceborne active remote sensing. Atmospheric Chemistry and Physics, 15(5):2445–2461.

Miyazaki, K., H. Eskes, K. Sudo, K.F. Boersma, K. Bowman and Y. Kanaya, 2017. Decadal changes in global surface NOx emissions from multi-constituent satellite data assimilation. Atmospheric Chemistry and Physics, 17(2):807–837.

Moch, J.M., E. Dovrou, L.J. Mickley, F.N. Keutsch, Y. Cheng, D.J. Jacob, J. Jiang, M. Li, J.W. Munger, X. Qiao and Q. Zhang, 2018. Contribution of hydroxymethane sulfonate to ambient particulate matter: a potential explanation for high particulate sulfur during severe winter haze in Beijing. Geophysical Research Letters, 45(21):11969–11979.

Mölders, N. and G. Kramm, 2018. Climatology of air quality in Arctic cities – inventory and assessment. Open Journal of Air Pollution, 7(1):48–93.

Molinari, C., V. Lehsten, O. Blarquez, C. Carcaillet, B.A.S. Davis, J.O. Kaplan, J. Clear and R.H.W. Bradshaw, 2018. The climate, the fuel and the land use: long-term regional variability of biomass burning in boreal forests. Global Change Biology, 24(10):4929–4945.

Möller, R., M. Möller, P.A. Kukla and C. Schneider, 2016. Impact of supraglacial deposits of tephra from Grímsvötn volcano, Iceland, on glacier ablation. Journal of Glaciology, 62(235):933–943.

Monahan, E.C., D.E. Spiel and K.L. Davidson, 1986. A model of marine aerosol generation via whitecaps and wave disruption. In: Monahan, E.C. and G.M. Niocaill, (Eds.) Oceanic Whitecaps, pp. 167–174. Springer.

Monks, S. A., S.R. Arnold, L.K. Emmons, K.S. Law, S. Turquety, B.N. Duncan, J. Flemming, V. Huijnen, S. Tilmes, J. Langner, J. Mao, Y. Long, J.L. Thomas, S.D., Steenrod, J.C. Raut, C. Wilson, M.P. Chipperfield, G.S. Diskin, A. Weinheimer, H. Schlager and G. Ancellet, 2015. Multi-model study of chemical and physical controls on transport of anthropogenic and biomass burning pollution to the Arctic. Atmospheric Chemistry and Physics, 15(6):3575–3603.

Montzka, S.A., M. Krol, E. Dlugokencky, B. Hall, P. Jöckel and J. Lelieveld, 2011. Small interannual variability of global atmospheric hydroxyl. Science, 331(6013):67–69.

Moore, M.J.K., H. Furutani, G.C. Roberts, R. Moffet, M.K. Gilles, B. Palenik and K. Prather, 2011. Effect of organic compounds on cloud condensation nuclei (CCN) activity of sea spray aerosol produced by bubble bursting. Atmospheric Environment, 45(39):7462–7469.

Morgenstern, O., P. Braesicke, F.M. O'Connor, A.C. Bushell, C.E. Johnson, S.M. Osprey and J.A. Pyle, 2009. Evaluation of the new UKCA climate-composition model – part 1: the stratosphere. Geoscientific Model Development, 2(1):43–57.

Mori, T., N. Moteki, S. Ohata, M. Koike, K. Goto-Azuma, Y. Miyazaki and Y. Kondo, 2016. Improved technique for measuring the size distribution of black carbon particles in liquid water. Aerosol Science and Technology, 50(3):242–254.

Mori, T., K. Goto-Azuma, Y. Kondo, Y. Ogawa-Tsukagawa, K. Miura, M. Hirabayashi, N. Oshima, M. Koike, K. Kupiainen, N. Moteki, S. Ohata, P.R. Sinha, K. Sugiura, T. Aoki, M. Schneebeli, K. Steffen, A. Sato, A. Tsushima, V. Makarov, S. Omiya, A. Sugimoto, S. Takano and N. Nagatsuka, 2019. Black carbon and inorganic aerosols in Arctic snowpack, Journal of Geophysical Research: Atmospheres, 124(23):13325–13356.

Mori, T., Y. Kondo, S. Ohata, Y. Zhao, P.R. Sinha, N. Oshima, H. Matsui, N. Moteki, and M. Koike, 2020. Seasonal variation of wet deposition of black carbon in Arctic Alaska. Journal of Geophysical Research: Atmospheres, 125(16):e2019JD032240.

Moroni, B., D. Cappelletti, L. Ferrero, S. Crocchianti, M. Busetto, M. Mazzola, S. Becagli, R. Traversi and R. Udisti, 2016. Local vs. long-range sources of aerosol particles upon Ny-Ålesund (Svalbard Islands): mineral chemistry and geochemical records. Rendiconti Lincei, 27:115–127.

Moroni B, O. Arnalds, P. Dagsson-Waldhauserová, S. Crocchianti, R. Vivani and D. Cappelletti, 2018. Mineralogical and Chemical Records of Icelandic Dust Sources Upon Ny-Ålesund (Svalbard Islands). Frontiers in Earth Science, 6:187.

Moroni, B., C. Ritter, S. Crocchianti, K. Markowicz, M. Mazzola, S. Becagli, R. Traversi, R. Krejci, P. Tunved and D. Cappelletti, 2020. Individual particle characteristics, optical properties and evolution of an extreme long-range transported biomass burning event in the European Arctic (Ny-Ålesund, Svalbard Islands). Journal of Geophysical Research: Atmospheres, 125(5):e2019JD031535.

Moschos, V., K. Dzepina, D. Bhattu, H. Lamkaddam, R. Casotto, K.R. Daellenbach, F. Canonaco, P. Rai, W. Aas, S. Becagli, G. Calzolai, K. Eleftheriadis, C.E. Moffett, J. Schnelle-Kreis, M. Severi, S. Sharma, H. Skov, M. Vestenius, W. Zhang, H. Hakola, H. Hellén, L. Huang, J.-L. Jaffrezo, A. Massling, J.K. Nøjgaard, T. Petäjä, O. Popovicheva, R.J. Sheesley, R. Traversi, K.E. Yttri, J. Schmale, A.S.H. Prévôt, U. Baltensperger and I. El Haddad, 2022. Equal abundance of summertime natural and wintertime anthropogenic Arctic organic aerosols. Nature Geoscience, 15:196–202.

Moss, R.H., J.A. Edmonds, K.A. Hibbard, M.R. Manning, S.K. Rose, D.P. van Vuuren, T.R. Carter, S. Emori, M. Kainuma, T. Kram, G.A. Meehl, J.F.B. Mitchell, N. Nakicenovic, K. Riahi, S.J. Smith, R.J. Stouffer, A.M. Thomson, J.P. Weyant and T.J. Wilbanks, 2010. The next generation of scenarios for climate change research and assessment. Nature, 463:747–756.

Moteki, N. and Y. Kondo, 2010. Dependence of laser-induced incandescence on physical properties of black carbon aerosols: measurements and theoretical interpretation. Aerosol Science and Technology, 44(8):663–675.

Moteki, N., K. Adachi, S. Ohata, A. Yoshida, T. Harigaya, M. Koike and Y. Kondo, 2017. Anthropogenic iron oxide aerosols enhance atmospheric heating. Nature Communications, 8:15329.

Motos, G., J.C. Corbin, J. Schmale, R.L. Modini, M. Bertò, P. Kupiszewski, U. Baltensperger and M. Gysel-Beer, 2020. Black carbon aerosols in the lower free troposphere are heavily coated in summer but largely uncoated in winter at Jungfraujoch in the Swiss Alps. Geophysical Research Letters, 47(14):e2020GL088011.

Mouteva, G.O., S.M. Fahrni, G.M. Santos, J.T. Randerson, Y.-L. Zhang, S. Szidat and C.I. Czimczik, 2015a. Accuracy and precision of ^{14}C-based source apportionment of organic and elemental carbon in aerosols using the Swiss_4S protocol. Atmospheric Measurement Techniques, 8(9):3729–3743.

Mouteva, G.O., C.I. Czimczik, S.M. Fahrni, E.B. Wiggins, B.M. Rogers, S. Veraverbeke, X. Xu, G.M. Santos, J. Henderson, C.E. Miller and J.T. Randerson, 2015b. Black carbon aerosol dynamics and isotopic composition in Alaska linked with boreal fire emissions and depth of burn in organic soils. Global Biogeochemical Cycles, 29(11):1977–2000.

Mulcahy, J.P., C. Johnson, C.G. Jones, A. Povey, C.E. Scott, A. Sellar, S.T. Turnock, M.T. Woodhouse, N.L. Abraham, M.B. Andrews, N. Bellouin, J. Browse, K.S. Carslaw, M. Dalvi, G.A. Folberth, M. Glover, D.P. Grosvenor, C. Hardacre, R.Hill, B. Johnson, A. Jones, Z. Kipling, G. Mann, J. Mollard, F.M. O'Connor, J. Palmiéri, C. Reddington, S.T. Rumbold, M. Richardson, N.A.J. Schutgens, P. Stier, M. Stringer, Y. Tang, J. Walton, S. Woodward and A. Yool, 2020. Description and evaluation of aerosol in UKESM1 and HadGEM3-GC3.1 CMIP6 historical simulations. Geoscientific Model Development, 13(12):6383–6423.

Mungall, E.L., J.P.D. Abbatt, J.J.B. Wentzell, A.K.Y. Lee, J.L. Thomas, M. Blais, M. Gosselin, L.A. Miller, T. Papakyriakou, M.D. Willis and J. Liggio, 2017. Microlayer source of oxygenated volatile organic compounds in the summertime marine Arctic boundary layer. PNAS, 114(24):6203–6208.

Mungall, E.L., J.P.D. Abbatt, J.J.B. Wentzell, G.R. Wentworth, J.G. Murphy, D. Kunkel, E. Gute, D.W. Tarasick, S. Sharma, C.J. Cox, T. Uttal and J. Liggio, 2018a. High gas-phase mixing ratios of formic and acetic acid in the High Arctic. Atmospheric Chemistry and Physics, 18(14):10237–10254.

Mungall, E.L., J.P.S. Wong and J.P.D. Abbatt, 2018b. Heterogeneous oxidation of particulate methanesulfonic acid by the hydroxyl radical: kinetics and atmospheric implications. ACS Earth and Space Chemistry, 2(1):48–55.

Murray, L.T., D.J. Jacob, J.A. Logan, R.C. Hudman and W.J. Koshak, 2012. Optimized regional and interannual variability of lightning in a global chemical transport model constrained by LIS/OTD satellite data. Journal of Geophysical Research: Atmospheres, 117(D20).

Myhre, G., B.H. Samset, M. Schulz, Y. Balkanski, S. Bauer, T.K. Berntsen, H. Bian, N. Bellouin, M. Chin, T. Diehl, R.C. Easter, J. Feichter, S.J. Ghan, D. Hauglustaine, T. Iversen, S. Kinne, A. Kirkevåg, J.-F. Lamarque, G. Lin, X. Liu, M.T. Lund, G. Luo, X. Ma, T. van Noije, J.E. Penner, P.J. Rasch, A. Ruiz, Ø. Seland, R.B. Skeie, P. Stier, T. Takemura, K. Tsigaridis, P. Wang, Z. Wang, L. Xu, H. Yu, F. Yu, J.-H. Yoon, K. Zhang, H. Zhang, and C. Zhou, 2013. Radiative forcing of the direct aerosol effect from AeroCom Phase II simulations. Atmospheric Chemistry and Physics, 13:1853–1877. https://doi.org/10.5194/acp-13-1853-2013.

Nafstad, P., L.L. Håheim, B. Oftedal, F. Gram, I. Holme, I. Hjermann and P. Leren, 2003. Lung cancer and air pollution: a 27 year follow up of 16,209 Norwegian men. Thorax, 58(12):1071–1076.

Nafstad, P., L.L. Håheim, T. Wisløff, F. Gram, B. Oftedal, I. Holme, I. Hjermann and P. Leren, 2004. Urban air pollution and mortality in a cohort of Norwegian men. Environmental Health Perspectives, 112(5):610–615.

Nagorski, S.A., S.D. Kaspari, E. Hood, J.B. Fellman and S. McKenzie Skiles, 2019. Radiative forcing by dust and black carbon on the Juneau Icefield, Alaska. Journal of Geophysical Research: Atmospheres, 124(7):3943–3959.

Naik, V., A. Voulgarakis, A.M. Fiore, L.W. Horowitz, J.-F. Lamarque, M. Lin, M.J. Prather, P.J. Young, D. Bergmann, P.J. Cameron-Smith, I. Cionni, W.J. Collins, S.B. Dalsøren, R. Doherty, V. Eyring, G. Faluvegi, G.A. Folberth, B. Josse, Y.H. Lee, I.A. MacKenzie, T. Nagashima, T.P.C. van Noije, D.A. Plummer, M. Righi, S.T. Rumbold, R. Skeie, D.T. Shindell, D.S. Stevenson, S. Strode, K. Sudo, S. Szopa and G. Zeng, 2013. Preindustrial to present-day changes in tropospheric hydroxyl radical and methane lifetime from the Atmospheric Chemistry and Climate Model Intercomparison Project (ACCMIP). Atmospheric Chemistry and Physics, 13 (10):5277–5298.

Najafi, M.R., F.W. Zwiers and N.P. Gillett, 2015. Attribution of Arctic temperature change to greenhouse-gas and aerosol influences. Nature Climate Change, 5:246–249.

NASA, 2013. File Specification for GEOS-5 FP (Forward Processing) – GMAO Office Note No. 4 (Version 1.0). Global Modeling and Assimilation Office (GMAO), National Aeronautics and Space Administration (NASA). vi + 63pp.

National Research Council, 2015. Climate Intervention: Reflecting Sunlight to Cool Earth. The National Academies Press. 260pp.

NCAR, 2008. A description of the Advanced Research WRF version 3. National Center for Atmospheric Research (NCAR) of the University Corporation for Atmospheric Research, Boulder, Colorado, USA.

Nemitz E., I. Mammarella, A. Ibrom, M. Aurela, G.G. Burba, S. Dengel, B. Gielen, A. Grelle, B. Heinesch, M. Herbst, L. Hörtnagl, L. Klemedtsson, A. Lindroth, A. Lohila, D.K. McDermitt, P. Meier, L. Merbold, D. Nelson, G. Nicolini, M.B. Nilsson, O. Peltola, J. Rinne and M. Zahniser, 2018. Standardisation of eddy-covariance flux measurements of methane and nitrous oxide. International Agrophysics, 32:517–549.

Nenes, A., S.N. Pandis and C. Pilinis, 1999. Continued development and testing of a new thermodynamic aerosol module for urban and regional air quality models. Atmospheric Environment, 33(10):1553–1560.

Nicely, J.M., D.C. Anderson, T.P. Canty, R.J. Salawitch, G.M. Wolfe, E.C. Apel, S.R. Arnold, E.L. Atlas, N.J. Blake, J.F. Bresch, T.L Campos, R.R. Dickerson, B. Duncan, L.K. Emmons, M.J. Evans, R.P. Fernandez, J. Flemming, S.R. Hall, T.F. Hanisco, S.B. Honomichl, R.S. Hornbrook, V. Huijnen, L. Kaser, D.E. Kinnison, J.-F. Lamarque, J. Mao, S.A. Monks, D.D. Montzka, L.L. Pan, D.D. Riemer, A. Saiz-Lopez, S.D. Steenrod, M.H. Stell, S. Tilmes, S. Turquety, K. Ullmann and A.J. Weinheimer, 2016. An observationally constrained evaluation of the oxidative capacity in the tropical western Pacific troposphere. Journal of Geophysical Research: Atmospheres, 121(12):7461–7488.

Nicely, J.M., R.J. Salawich, T. Canty, D.C. Anderson, S.R. Arnold, M.P. Chipperfield, L.K. Emmons, J. Flemming, V. Huijnen, D.E. Kinnison, J.-F. Lamarque, J. Mao, S.A. Monks, S.D. Steenrod, S. Tilmes and S. Turquety, 2017. Quantifying the causes of differences in tropospheric OH within global models. Journal of Geophysical Research: Atmospheres, 122(3):1983–2007.

Nicely, J.M., T.P. Canty, M. Manyin, L.D. Oman, R.J. Salawitch, S.D. Steenrod, S.E. Strahan and S.A. Strode, 2018. Changes in global tropospheric OH expected as a result of climate change over the last several decades. Journal of Geophysical Research: Atmospheres, 123(18):10774–10795.

Nielsen, I.E., H. Skov, A. Massling, A.C. Eriksson, M. Dall'Osto, H. Junninen, N. Sarnela, R. Lange, S. Collier, Q. Zhang, C.D. Cappa and J.K. Nøjgaard, 2019. Biogenic and anthropogenic sources of aerosols at the High Arctic site Villum Research Station. Atmospheric Chemistry and Physics, 19(15):10239–10256.

Nilsson, J. and P. Grennfelt, 1988. Critical loads for sulphur and nitrogen. Workshop on critical loads for sulphur and nitrogen. 19–24 March 1988, Skokloster, Sweden. 418pp.

NIOSH, 2003. Elemental Carbon (Diesel Particulate). Method 5040 Issue 3. In NIOSH Manual of Analytical Methods, Fourth Edition. National Institute of Occupational Safety and Health (NIOSH), Cincinnati, Ohio, USA.

Nisbet, E.G., 1990. The end of the ice age. Canadian Journal of Earth Sciences, 27(1):148–157.

Nisbet, E.G., M.R. Manning, E.J. Dlugokencky, R.E. Fischer, D. Lowry, S.E. Michel, C. Lund Myhre, S.M. Platt, G. Allen, P. Bousquet, R. Brownlow, M. Cain, J.L. France, O. Hermansen, R. Hossaini, A.E. Jones, I. Levin, A.C. Manning, G. Myhre, J.A. Pyle, B.H. Vaughn, N.J. Warwick and J.W.C. White, 2019. Very strong atmospheric methane growth in the 4 years 2014–2017: implications for the Paris Agreement. Global Biogeochemical Cycles, 33(3):318–342.

Nitzbon, J., S. Westermann, M. Langer, L.C.P. Martin, J. Strauss, S. Laboor and J. Boike, 2020. Fast response of cold ice-rich permafrost in northeast Siberia to a warming climate. Nature Communications, 11:2201.

NOAA GML, 2021. Trends in atmospheric methane. National Oceanic and Atmospheric Administration (NOAA) Global Monitoring Laboratory (GML). Available at: gml.noaa.gov/ccgg/trends_ch4/

Noble, C.A., and K.A. Prather, 2000. Real-time single particle mass spectrometry: a historical review of a quarter century of the chemical analysis of aerosols. Mass Spectrometry Reviews, 19(4):248–274.

Nomokonova, T., K. Ebell, U. Löhnert, M. Maturilli, C. Ritter and E. O'Connor, 2019. Statistics on clouds and their relation to thermodynamic conditions at Ny-Ålesund using ground-based sensor synergy. Atmospheric Chemistry and Physics, 19(6):4105–4126.

Noonan, C.W., T.J. Ward, W. Navidi and L. Sheppard, 2012. A rural community intervention targeting biomass combustion sources: effects on air quality and reporting of children's respiratory outcomes. Occupational & Environmental Medicine, 69(5):354–360.

Norman, A.L., L.A. Barrie, D. Toom-Sauntry, A. Sirois, H.R. Krouse, S.M. Li and S. Sharma, 1999. Sources of aerosol sulphate at Alert: apportionment using stable isotopes. Journal of Geophysical Research: Atmospheres, 104(D9):11619–11631.

North, P.R.J., S.A. Briggs, S.E. Plummer and J.J. Settle, 1999. Retrieval of land surface bidirectional reflectance and aerosol opacity from ATSR-2 multiangle imagery. *IEEE Transactions on Geoscience and Remote Sensing,* 37(1):526–537.

Northington, R.M. and J.E. Saros, 2016. Factors controlling methane in Arctic lakes of southwest Greenland. PLoS ONE, 11(7):e0159642.

Norwegian Polar Institute, 2018. Protocols and recommendations for the measurement of snow physical properties, and sampling of snow for black carbon, water isotopes, major ions and micro-organisms. Kortrapport / Brief Report no. 046. Norwegian Polar Institute, Tromsø, Norway. 27pp.

Nugent, K.A., I.B. Strachan, N.T. Roulet, M. Strack, S. Frolking and M. Helbig, 2019. Prompt active restoration of peatlands substantially reduces climate impact. Environmental Research Letters, 14(12):124030.

O'Connor, F.M., N.L Abraham, M. Dalvi, G. Folberth, P.T. Griffiths, C. Hardacre, B.T. Johnson, R. Kahana, J. Keeble, B. Kim, O. Morgenstern, J.P. Mulcahy, M. Richardson, E. Robertson, J. Seo, S. Shim, J.C. Teixeira, S.T. Turnock, J. Williams, A.J. Wiltshire, S. Woodward and G. Zeng, 2021. Assessment of pre-industrial to present-day anthropogenic climate forcing in UKESM1. Atmospheric Chemistry and Physics, 21(2):1211–1243.

O'Connor, F.M., C.E. Johnson, O. Morgenstern, N.L. Abraham, P. Braesicke, M. Dalvi, G.A. Folberth, M.G. Sanderson, P.J. Telford, A. Voulgarakis, P.J. Young, G. Zeng, W.J. Collins and J.A. Pyle, 2014. Evaluation of the new UKCA climate-composition model – Part 2: The Troposphere, Geoscientific Model Development 7(1):41–91.

O'Neill, B.C., E. Kriegler, K.L. Ebi, E. Kemp-Benedict, K. Riahi, D.S. Rothman, B.J. van Ruijven, D.P. van Vuuren, J. Birkmann, K. Kok, M. Levy and W. Solecki, 2017. The roads ahead: narratives for shared socioeconomic pathways describing world futures in the 21st century. Global Environmental Change, 42:169–180.

O'Neill, H.B., C.R. Burn, M. Allard, L.U. Arenson, M.I. Bunn, R.F. Connon, S.A. Kokelj, S.V. Kokelj, A.-M. LeBlanc, P.D. Morse and S.L. Smith, 2020. Permafrost thaw and northern development. Nature Climate Change, 10:722–723.

Oduber, F., A.I. Calvo, C. Blanco-Alegre, A. Castro, T. Nunes, C. Alves, M. Sorribas, D. Fernández-González, A.M. Vega-Maray, R.M. Valencia-Barrera, F. Lucarelli, S. Nava, G. Calzolai, E. Alonso-Blanco, B. Fraile, P. Fialho, E. Coz, A.S.H. Prevot, V. Pont and R. Fraile, 2019. Unusual winter Saharan dust intrusions at Northwest Spain: air quality, radiative and health impacts. Science of The Total Environment, 669:213–228.

Odum, J.R., T. Hoffmann, F. Bowman, D. Collins, R.C. Flagan and J.H. Seinfeld, 1996. Gas/particle partitioning and secondary organic aerosol yields, Environmental Science & Technology, 30(8):2580–2585.

Oh, Y., B. Stackhouse, M.C.Y. Lau, X. Xu, A.T. Trugman, J. Moch, T.C. Onstott, C.J. Jørgensen, L. D'Imperio, B. Elberling, C.A. Emmerton, V.L. St. Louis and D. Medvigy, 2016. A scalable model for methane consumption in Arctic mineral soils. Geophysical Research Letters, 43(10):5143–5150.

Oh, Y., Q. Zhuang, L. Liu, L.R. Welp, M.C.Y. Lau, T.C. Onstott, D. Medvigy, L. Bruhwiler, E.J. Dlugokencky, G. Hugelius, L. D'Imperio and B. Elberling, 2020. Reduced net methane emissions due to microbial methane oxidation in a warmer Arctic. Nature Climate Change, 10:317–321.

Ohata, S., Y. Kondo, N. Moteki, T. Mori, A. Yoshida, P.R. Sinha and M. Koike, 2019. Accuracy of black carbon measurements by a filter-based absorption photometer with a heated inlet. Aerosol Science and Technology, 53(9):1079–1091.

Ohata, S., T. Mori, Y. Kondo, S. Sharma, A. Hyvärinen, E. Andrews, P. Tunved, E. Asmi, J. Backman, H. Servomaa, D. Veber, K. Eleftheriadis, S. Vratolis, R. Krejci, P. Zieger, M. Koike, Y. Kanaya, A. Yoshida, N. Moteki, Y. Zhao, Y. Tobo, J. Matsushita and N. Oshima, 2021. Estimates of mass absorption cross sections of black carbon for filter-based absorption photometers in the Arctic. Atmospheric Measurement Techniques, 14(10):6723–6748.

Olefeldt, D., M.R. Turetsky, P.M. Crill and A.D. McGuire, 2013. Environmental and physical controls on northern terrestrial methane emissions across permafrost zones. Global Change Biology, 19(2):589–603.

Oliva, P. and W. Schroeder, 2015. Assessment of VIIRS 375 m active fire detection product for direct burned area mapping. Remote Sensing of Environment, 160:144–155.

Olivié, D., L. Höglund Isaksson, Z. Klimont and K. Von Salzen, 2021. Box model for calculation of global atmospheric methane concentration (Version 8.0). Available at: https://zenodo.org/record/5293940#.YYEUAtbP2uN.

Ollison, W.M., W. Crow and C.W. Spicer, 2013. Field testing of new-technology ambient air ozone monitors. Journal of the Air & Waste Management Association, 63(7):855–863.

Olson, D.M., E. Dinerstein, E.D. Wikramanayake, N.D. Burgess, G.V.N. Powell, E.C. Underwood, J.A. D'amico, I. Itoua, H.E. Strand, J.C. Morrison, C.L. Loucks, T.F. Allnutt, T.H. Ricketts, Y. Kura, J.F. Lamoreux, W.W. Wettengel, P. Hedao and K.R. Kassem, 2001. Terrestrial ecoregions of the world: a new map of life on Earth: a new global map of terrestrial ecoregions provides an innovative tool for conserving biodiversity. BioScience, 51(11):933–938.

Olsson, D., C. Johansson and B. Forsberg, 2020. Associations between vehicle exhaust particles and ozone at home address and birth weight. International Journal of Environmental Research and Public Health, 17(11):3836.

Olstrup, H., C. Johansson, B. Forsberg and C. Åström, 2019. Association between mortality and short-term exposure to particles, ozone and nitrogen dioxide in Stockholm, Sweden. International Journal of Environmental Research and Public Health, 16(6):1028.

Omar, A., J. Tackett, M.-H. Kim, M. Vaughan, J. Kar, C. Trepte and D. Winker, 2018. Enhancements to the caliop aerosol subtyping and lidar ratio selection algorithms for level II version 4. EPJ Web of Conferences, 176:02006.

Oshima, N. and M. Koike, 2013. Development of a parameterization of black carbon aging for use in general circulation models. Geoscientific Model Development 6(2):263–282.

Oshima, N., M. Koike, Y. Zhang, Y. Kondo, N. Moteki, N. Takegawa and Y. Miyazaki, 2009a. Aging of black carbon in outflow from anthropogenic sources using a mixing state resolved model: model development and evaluation. Journal of Geophysical Research: Atmospheres, 114(D6).

Oshima, N., M. Koike, Y. Zhang and Y. Kondo, 2009b. Aging of black carbon in outflow from anthropogenic sources using a mixing state resolved model: 2. aerosol optical properties and cloud condensation nuclei activities. Journal of Geophysical Research: Atmospheres, 114(D18).

Oshima, N., Y. Kondo, N. Moteki, N. Takegawa, M. Koike, K. Kita, H. Matsui, M. Kajino, H. Nakamura, J.S. Jung and Y.J. Kim, 2012. Wet removal of black carbon in Asian outflow: Aerosol Radiative Forcing in East Asia (A-FORCE) aircraft campaign. Journal of Geophysical Research: Atmospheres, 117(D3).

Oshima, N., S. Yukimoto, M. Deushi, T. Koshiro, H. Kawai, T.Y. Tanaka and K. Yoshida, 2020. Global and Arctic effective radiative forcing of anthropogenic gases and aerosols in MRI-ESM2.0 Progress in Earth and Planetary Science, 7(38).

Osmont, D., I.A. Wendl, L. Schmidely, M. Sigl, C.P. Vega, E. Isaksson and M. Schwikowski, 2018. An 800-year high-resolution black carbon ice core record from Lomonosovfonna, Svalbard. Atmospheric Chemistry and Physics, 18(17):12777–12795.

Oudin, A., D.O. Åström, P. Asplund, S. Steingrimsson, Z. Szabo and H.K. Carlsen, 2018. The association between daily concentrations of air pollution and visits to a psychiatric emergency unit: a case-crossover study. Environmental Health, 17(4).

Overduin, P.P., S. Liebner, C. Knoblauch, F. Günther, S. Wetterich, L. Schirrmeister, H.-W. Hubberten and M.N. Grigoriev, 2015. Methane oxidation following submarine permafrost degradation: measurements from a central Laptev Sea shelf borehole. Journal of Geophysical Research: Biogeosciences 120(5):965–978.

Pai, S.J., C.L. Heald, J.R. Pierce, S.C. Farina, E.A. Marais, J.L. Jimenez, P. Campuzano-Jost, B.A. Nault, A.M. Middlebrook, H. Coe, J.E. Shilling, R. Bahreini, J.H. Dingle and K. Vu, 2020. An evaluation of global organic aerosol schemes using airborne observations. Atmospheric Chemistry and Physics, 20(5):2637–2665.

Painter, T.H., S. Mackenzie Skiles, J.S. Deems, W.T. Brandt and J. Dozier, 2018. Variation in rising limb of Colorado river snowmelt runoff hydrograph controlled by dust radiative forcing in snow. Geophysical Research Letters, 45(2):797–808.

PAME, 2020. The increase in Arctic shipping 2013–2019: Arctic Shipping Status Report #1. Protection of the Arctic Marine Environment (PAME), Arctic Council, Tromsø, Norway. 25pp.

Pan, X., C. Ichoku, M. Chin, H. Bian, A. Darmenov, P. Colarco, L. Ellison, T. Kucsera, A. da Silva, J. Wang, T. Oda and G. Cui, 2020. Six global biomass burning emission datasets: intercomparison and application in one global aerosol model. Atmospheric Chemistry and Physics, 20(2):969–994.

Pankratova, N., I. Belikov, A. Skorokhod, V. Belousov, A. Artamonov, I. Repina and E. Shishov, 2019. Measurements and data processing of atmospheric CO_2, CH_4, H_2O and $\delta^{13}C_{CH4}$ mixing ratio during the ship campaign in the East Arctic and the Far East seas in autumn 2016. IOP Conference Series: Earth and Environmental Science, 231:012041.

Parfenova, E., N. Tchebakova and A. Soja, 2019. Assessing landscape potential for human sustainability and 'attractiveness' across Asian Russia in a warmer 21st century. Environmental Research Letters, 14(6):065004.

Paris, J.-D., A. Stohl, P. Nédélec, M. Yu. Arshinov, M.V. Panchenko, V.P. Shmargunov, K.S. Law, B.D. Belan and P. Ciais, 2009. Wildfire smoke in the Siberian Arctic in summer: source characterization and plume evolution from airborne measurements. Atmospheric Chemistry and Physics, 9(23):9315–9327.

Parisien, M.-A., C. Miller, S.A. Parks, E.R. DeLancey, F.-N.Robinne and M.D. Flannigan, 2016. The spatially varying influence of humans on fire probability in North America. Environmental Research Letters, 11(7):075005.

Parisien, M.-A., Q.E. Barber, K.G. Hirsch, C.A. Stockdale, S. Erni, X. Wang, D. Arseneault and S.A. Parks, 2020. Fire deficit increases wildfire risk for many communities in the Canadian boreal forest. Nature Communications, 11:2121.

Park, R.J., D.J. Jacob, B.D. Field, R.M. Yantosca and M. Chin, 2004. Natural and transboundary pollution influences on sulfate-nitrate-ammonium aerosols in the United States: implications for policy. Journal of Geophysical Research: Atmospheres, 109(D15).

Park, J., M. Dall'Osto, K. Park, Y. Gim, H.J. Kang, E. Jang, K.-T. Park, M. Park, S.S. Yum, J. Jung, B.Y. Lee and Y.J. Yoon, 2020. Shipborne observations reveal contrasting Arctic marine, Arctic terrestrial and Pacific marine aerosol properties. Atmospheric Chemistry and Physics, 20(9):5573–5590.

Parmentier, F.-J.W., T.R. Christensen, L.L. Sørensen, S. Rysgaard, A.D. McGuire, P.A. Miller and D.A. Walker, 2013. The impact of lower sea-ice extent on Arctic greenhouse-gas exchange. Nature Climate Change, 3:195–202.

Parmentier, F.-J.W., W. Zhang, Y. Mi, X. Zhu, J. van Huissteden, D.J. Hayes, Q. Zhuang, T.R. Christensen and A.D. McGuire, 2015. Rising methane emissions from northern wetlands associated with sea ice decline. Geophysical Research Letters, 42(17):7214–7222.

Parrish, D.D., K.S. Law, J. Staehelin, R. Derwent, O.R. Cooper, H. Tanimoto, A. Volz-Thomas, S. Gilge, H.-E. Scheel, M. Steinbacher and E. Chan, 2013. Lower tropospheric ozone at northern midlatitudes: Changing seasonal cycle. Geophysical Research Letters, 40(8):1631–1636.

Paugam, R., M. Wooster, S. Freitas and M. Val Martin, 2016. A review of approaches to estimate wildfire plume injection height within large-scale atmospheric chemical transport models. Atmospheric Chemistry and Physics, 16(2):907–925.

Pavelka M., M. Acosta, R. Kiese, N. Altimir, C. Brümmer, P. Crill, E. Darenova, R. Fuß, B. Gielen, A. Graf, L. Klemedtsson, A. Lohila, B. Longdoz, A. Lindroth, M. Nilsson, S. Marañon-Jiménez, L. Merbold, L. Montagnani, M. Peichl, M. Pihlatie, J. Pumpanen, P.S. Ortiz, H. Silvennoinen, U. Skiba, P. Vestin, P. Weslien, D. Janouš and W. Kutsch, 2018. Standardisation of chamber technique for CO_2, N_2O and CH_4 fluxes measurements from terrestrial ecosystems. International Agrophysics, 32(4):569–587.

Paytan, A., A.L. Lecher, N. Dimova, K.J. Sparrow, F.G.-T. Kodovska, J. Murray, S. Tulaczyk and J.D. Kessler, 2015. Methane transport from the active layer to lakes in the Arctic using Toolik Lake, Alaska, as a case study. PNAS, 112(12):3636–3640.

Pedersen, C.A., J.-C. Gallet, J. Ström, S. Gerland, S.R. Hudson, S. Forsström, E. Isaksson and T.K. Berntsen, 2015. In situ observations of black carbon in snow and the corresponding spectral surface albedo reduction. Journal of Geophysical Research: Atmospheres, 120(4):1476–1489.

Pedersen, M., T.I. Halldorsson, S.F. Olsen, D. Hjortebjerg, M. Ketzel, C. Grandström, O. Raaschou-Nielsen and M. Sørensen, 2017a. Impact of road traffic pollution on pre-eclampsia and pregnancy-induced hypertensive disorders. Epidemiology, 28(1):99–106.

Pedersen, M., S.F. Olsen, T.I. Halldorsson, C. Zhang, D. Hjortebjerg, M. Ketzel, C. Grandström, M. Sørensen, P. Damm, J. Langhoff-Roos and O. Raaschou-Nielsen, 2017b. Gestational diabetes mellitus and exposure to ambient air pollution and road traffic noise: a cohort study. Environment International, 108:253–260.

Peltola, H., A. Kilpeläinen and S. Kellomäki, 2002. Diameter growth of Scots pine (*Pinus sylvestris*) trees grown at elevated temperature and carbon dioxide concentration under boreal conditions. Tree physiology, 22(14):963–972.

Peltoniemi, J.I., M. Gritsevich, T. Hakala, P. Dagsson-Waldhauserová, Ó Arnalds, K. Anttila, H.-R. Hannula, N. Kivekäs, H. Lihavainen, O. Meinander, J. Svensson, A. Virkkula and G. de Leeuw, 2015. Soot on Snow experiment: bidirectional reflectance factor measurements of contaminated snow. The Cryosphere, 9(6):2323–2337.

Peng, Y., U. Lohmann and R. Leaitch, 2005. Importance of vertical velocity variations in the cloud droplet nucleation process of marine stratus clouds. Journal of Geophysical Research: Atmospheres, 110(D21).

Peng, Y., K. von Salzen and J. Li, 2012. Simulation of mineral dust aerosol with Piecewise Log-normal Approximation (PLA) in CanAM4-PAM. Atmospheric Chemistry and Physics, 12(15): 6891–6914.

Perera, F., A. Ashrafi, P. Kinney and D. Mills, 2019. Towards a fuller assessment of benefits to children's health of reducing air pollution and mitigating climate change due to fossil fuel combustion. Environmental Research, 172:55–72.

Pernov, J.B., R. Bossi, T. Lebourgeois, J.K. Nøjgaard, R. Holzinger, J.L. Hjorth and H. Skov, 2021. Atmospheric VOC measurements at a High Arctic site: characteristics and source apportionment. Atmospheric Chemistry and Physics, 21(4):2895–2916.

Petäjä, T., E.-M. Duplissy, K. Tabakova, J. Schmale, B. Altstädter, G. Ancellet, M. Arshinov, Y. Balin, U. Baltensperger, J. Bange, A. Beamish, B. Belan, A. Berchet, R. Bossi, W.R.L. Cairns, R. Ebinghaus, I. El Haddad, B. Ferreira-Araujo, A. Franck, L. Huang, A. Hyvärinen, A. Humbert, A.-C. Kalogridis, P. Konstantinov, A. Lampert, M. MacLeod, O. Magand, A. Mahura, L. Marelle, V. Masloboev, D. Moisseev, V. Moschos, N. Neckel, T. Onishi, S. Osterwalder, A. Ovaska, P. Paasonen, M. Panchenko, F. Pankratov, J.B. Pernov, A. Platis, O. Popovicheva, J.-C. Raut, A. Riandet, T. Sachs, R. Salvatori, R. Salzano, L. Schröder, M. Schön, V. Shevchenko, H. Skov, J.E. Sonke, A. Spolaor, V.K. Stathopoulos, M. Strahlendorff, J.L. Thomas, V. Vitale, S. Vratolis, C. Barbante, S. Chabrillat, A. Dommergue, K. Eleftheriadis, J. Heilimo, K.S. Law, A. Massling, S.M. Noe, J.-D. Paris, A.S.H. Prévôt, I. Riipinen, B. Wehner, Z. Xie and H.K. Lappalainen, 2020. Overview: Integrative and comprehensive understanding on Polar environments (iCUPE) – concept and initial results. Atmospheric Chemistry and Physics, 20(14):8551–8592.

Peterson, P.K., K.A. Pratt, W.R. Simpson, S.V. Nghiem, L.X. Pérez Pérez, E.J. Boone, D. Pöhler, J. Zielcke, S. General, P.B. Shepson, U. Frieß, U. Platt and B.H. Stirm, 2016. The role of open lead interactions in atmospheric ozone variability between Arctic coastal and inland sites. Elementa: Science of the Anthropocene, 4:000109.

Peterson, P.K., D. Pöhler, J. Zielcke, S. General, U. Frieß, U. Platt, W.R. Simpson, S.V. Nghiem, P.B. Shepson, B.H. Stirm and K.A. Pratt, 2018. Springtime bromine activation over coastal and inland Arctic snowpacks. ACS Earth and Space Chemistry, 2(10):1075–1086.

Petrescu, A.M.R., L.P.H. van Beek, J. van Huissteden, C. Prigent, T. Sachs, C.A.R. Corradi, F.-J.W. Parmentier and A.J. Dolman, 2010. Modeling regional to global CH_4 emissions of boreal and arctic wetlands. Global Biogeochemical Cycles, 24(4):GB4009.

Petzold, A. and M. Schönlinner, 2004. Multi-angle absorption photometry—a new method for the measurement of aerosol light absorption and atmospheric black carbon. Journal of Aerosol Science, 35(4):421–441.

Petzold, A., J.A. Ogren, M. Fiebig, P. Laj, S.-M. Li, U. Baltensperger, T. Holzer-Popp, S. Kinne, G. Pappalardo, N. Sugimoto, C. Wehrli, A. Wiedensohler and X.-Y. Zhang, 2013. Recommendations for reporting "black carbon" measurements. Atmospheric Chemistry and Physics, 13(16):8365–8379.

Péwé, T.L., 1974. Geomorphic processes in polar deserts. In: T.L. Smiley and J.H. Zumberge (Eds). Polar Deserts and Modern Man, pp. 33– 52, The University of Arizona Press.

Pickell, P.D., N.C. Coops, C.J. Ferster, C.W. Bater, K.D. Blouin, M.D. Flannigan and J. Zhang, 2017. An early warning system to forecast the close of the spring burning window from satellite-observed greenness. Scientific Reports, 7:14190.

Pihlatie, M.K., J.R. Christiansen, H. Aaltonen, J.F.J. Korhonen, A. Nordbo, T. Rasilo, G. Benanti, M. Giebels, M. Helmy, J. Sheehy, S. Jones, R. Juszczak, R. Klefoth, R. Lobo-do-Vale, A.P. Rosa, P. Schreiber, D. Serça, S. Vicca, B. Wolf and J. Pumpanen, 2013. Comparison of static chambers to measure CH4 emissions from soils. Agricultural and Forest Meteorology, 171– 172:124–136.

Pincus, R., P.M. Forster and B. Stevens, 2016. The Radiative Forcing Model Intercomparison Project (RFMIP): experimental protocol for CMIP6. Geoscientific Model Development, 9(9):3447–3460.

Pirk, N., T. Santos, C. Gustafson, A.J. Johansson, F. Tufvesson, F.-J.W. Parmentier, M. Mastepanov and T.R. Christensen, 2015. Methane emission bursts from permafrost environments during autumn freeze-in: new insights from ground penetrating radar. Geophysical Research Letters, 42(16):6732–6738.

Pirk, N., M. Mastepanov, F.-J.W. Parmentier, M. Lund, P. Crill and T.R. Christensen, 2016. Calculations of automatic chamber flux measurements of methane and carbon dioxide using short time series of concentrations. Biogeosciences, 13(4):903–912.

Pirk, N., M. Mastepanov, E. López-Blanco, L.H. Christensen, H.H. Christiansen, B.U. Hansen, M. Lund, F.-J.W. Parmentier, K. Skov and T.R. Christensen, 2017. Toward a statistical description of methane emissions from Arctic wetlands. Ambio, 46(1):70–80.

Pisso, I., C. Lund Myhre, S.M. Platt, S. Eckhardt, O. Hermansen, N. Schmidbauer, J. Mienert, S. Vadakkepuliyambatta, S. Bauguitte, J. Pitt, G. Allen, K.N. Bower, S. O'Shea, M.W. Gallagher, C.J. Percival, J. Pyle, M. Cain and A. Stohl, 2016. Constraints on oceanic methane emissions west of Svalbard from atmospheric in situ measurements and Lagrangian transport modeling, Journal of Geophysical Research Atmospheres, 121:14188–14200.

Pisso, I., E. Sollum, H. Grythe, N.I. Kristiansen, M. Cassiani, S. Eckhardt, D. Arnold, D. Morton, R.L. Thompson, C.D. Groot Zwaaftink, N. Evangeliou, H. Sodemann, L. Haimberger, S. Henne, D. Brunner, J.F. Burkhart, A. Fouilloux, J. Brioude, A. Philipp, P. Seibert and A. Stohl, 2019. The Lagrangian particle dispersion model FLEXPART version 10.4. Geoscientific Model Development 12(12):4955–4997.

Pittman, J.V., L.L. Pan, J.C. Wei, F.W. Irion, X. Liu, E.S. Maddy, C.D. Barnet, K. Chance and R.-S. Gao, 2009. Evaluation of AIRS, IASI, and OMI ozone profile retrievals in the extratropical tropopause region using in situ aircraft measurements. Journal of Geophysical Research: Atmospheres, 114:D24109.

Platt, S.M., S. Eckhardt, B. Ferré, R.E. Fisher, O. Hermansen, P. Jansson, D. Lowry, E.G. Nisbet, I. Pisso, N. Schmidbauer, A. Silyakova, A. Stohl, T.M. Svendby, S. Vadakkepuliyambatta, J. Mienert, and C. Lund Myhre, 2018. Methane at Svalbard and over the European Arctic Ocean. Atmospheric Chemistry and Physics, 18(23):17207–17224.

Pohlman, J.W., J. Greinert, C. Ruppel, A. Silyakova, L. Vielstädte, M. Casso, J. Mienert and S. Bünz, 2017. Enhanced CO_2 uptake at a shallow Arctic Ocean seep field overwhelms the positive warming potential of emitted methane. PNAS, 114(21):5355–5360.

Pokhrel, A., K. Kawamura, B. Kunwar, K. Ono, A. Tsushima, O. Seki, S. Matoba and T. Shiraiwa, 2020. Ice core records of levoglucosan and dehydroabietic and vanillic acids from Aurora Peak in Alaska since the 1660s: a proxy signal of biomass-burning activities in the North Pacific Rim. Atmospheric Chemistry and Physics, 20(1):597–612.

Polashenski, C.M., J.E. Dibb, M.G. Flanner, J.Y. Chen, Z.R. Courville, A.M. Lai, J.J. Schauer, M.M. Shafer and M. Bergin, 2015. Neither dust nor black carbon causing apparent albedo decline in Greenland's dry snow zone: implications for MODIS C5 surface reflectance. Geophysical Research Letters, 42(21):9319–9327.

Polishchuk, Y.M., A.N. Bogdanov, I.N. Muratov, V.Y. Polishchuk, A. Lim, R.M. Manasypov, L.S. Shirokova and O.S. Pokrovsky, 2018. Minor contribution of small thaw ponds to the pools of carbon and methane in the inland waters of the permafrost-affected part of the Western Siberian Lowland. Environmental Research Letters, 13(4):045002.

Pommier, M., C. Clerbaux, K.S. Law, G. Ancellet, P. Bernath, P.-F. Coheur, J. Hadji-Lazaro, D. Hurtmans, P. Nédélec, J.-D. Paris, F. Ravetta, T.B. Ryerson, H. Schlager and A.J. Weinheimer, 2012. Analysis of IASI tropospheric O_3 data over the Arctic during POLARCAT campaigns in 2008. Atmospheric Chemistry and Physics, 12(16):7371–7389.

Pope, C.A., III, R.T. Burnett, M.J. Thun, E.E. Calle, D. Krewski, K. Ito and G.D. Thurston, 2002. Lung cancer, cardiopulmonary mortality and long-term exposure to fine particulate air pollution. Journal of American Medical Association, 287(9):1132–1141.

Pope, R.J., N.A.D. Richards, M.P. Chipperfield, D.P. Moore, S.A. Monks, S.R. Arnold, N. Glatthor, M. Kiefer, T.J. Breider, J.J. Harrison, J.J. Remedios, C. Warneke, J.M. Roberts, G.S. Diskin, L.G. Huey, A. Wisthaler, E.C. Apel, P.F. Bernath and W. Feng, 2016. Intercomparison and evaluation of satellite peroxyacetyl nitrate observations in the upper troposphere-lower stratosphere. Atmospheric Chemistry and Physics, 16(21):13541–13559.

Popovicheva, O.B., N. Evangeliou, K. Eleftheriadis, A.C. Kalogridis, N. Sitnikov, S. Echkardt and A. Stohl, 2017. Black carbon sources constrained by observations in the Russian high Arctic. Environmental Science & Technology, 51(7):3871–3879.

Popovicheva, O., E. Diapouli, A. Makshtas, N. Shonija, M. Manousakas, D. Saraga, T. Uttal and K. Eleftheriadis, 2019. East Siberian Arctic background and black carbon polluted aerosols at HMO Tiksi. Science of The Total Environment, 655:924–938.

Porcheron, E., P. Lemaitre, J. Van Beeck, R. Vetrano, M. Brunel, G. Grehan and L. Guiraud, 2015. Development of a spectrometer for airborne measurement of droplet sizes in clouds. Journal of the European Optical Society Rapid Publications, 10:15030.

Portnov, A., S. Vadakkepuliyambatta, J. Mienert and A. Hubbard, 2016. Ice-sheet-driven methane storage and release in the Arctic. Nature Communications, 7:10314.

Posch, M., 2002. Impacts of climate change on critical loads and their exceedances in Europe. Environmental Science & Policy, 5(4):307–317.

Posch, M., W. de Vries and H.U. Sverdrup, 2015. Mass balance models to derive critical loads of nitrogen and acidity for terrestrial and aquatic ecosystems. In: de Vries W., J.P. Hettelingh and M. Posch (Eds). Critical Loads and Dynamic Risk Assessments: Nitrogen, Acidity and Metals in Terrestrial and Aquatic Ecosystems. pp. 171–205. Environmental Pollution, 25. Springer, Dordrecht, Netherlands.

Poulsen, A.H., U.A. Hvidtfeldt, M. Sørensen, R. Puett, M. Ketzel, J. Brandt, J.H. Christensen, C. Geels and O. Raaschou-Nielsen, 2020a. Components of particulate matter air-pollution and brain tumors. Environment International, 144:106046.

Poulsen, A.H., U.A. Hvidtfeldt, M. Sørensen, R. Puett, M. Ketzel, J. Brandt, C. Geels, J.H. Christensen and O. Raaschou-Nielsen, 2020b. Intracranial tumors of the central nervous system and air pollution: a nationwide case-control study from Denmark. Environmental Health, 19(81).

Poulter, B., P. Bousquet, J.G. Canadell, P. Ciais, A. Peregon, M. Saunois, V.K. Arora, D.J. Beerling, V. Brovkin, C.D. Jones, F. Joos, N. Gedney, A. Ito, T. Kleinen, C.D. Koven, K. McDonald, J.R. Melton, C. Peng, S. Peng, C. Prigent, R. Schroeder, W.J. Riley, M. Saito, R. Spahni, H. Tian, L. Taylor, N. Viovy, D. Wilton, A. Wiltshire, X. Xu, B. Zhang, Z. Zhang and Q. Zhu, 2017. Global wetland contribution to 2000–2012 atmospheric methane growth rate dynamics. Environmental Research Letters, 12(9):094013.

Power, M.C., S.D Adar, J.D. Yanosky and J. Weuve, 2016. Exposure to air pollution as a potential contributor to cognitive function, cognitive decline, brain imaging, and dementia: a systematic review of epidemiologic research. NeuroToxicology, 56:235–253.

Prenni, A.J., P.J. Demott, D.C. Rogers, S.M. Kreidenweis, G.M. Mcfarquhar, G. Zhang and M.R. Poellot, 2009. Ice nuclei characteristics from M-PACE and their relation to ice formation in clouds. Tellus B: Chemical and Physical Meteorology, 61(2):436–448.

Prather, M.J., C.D. Holmes and J. Hsu, 2012. Reactive greenhouse gas scenarios: systematic exploration of uncertainties and the role of atmospheric chemistry. Geophysical Research Letters, 39(9):L09803.

Púčik, T., P. Groenemeijer, A.T. Rädler, L. Tijssen, G. Nikulin, A.F. Prein, E. van Meijgaard, R. Fealy, D. Jacob and C. Teichmann, 2017. Future changes in European severe convection environments in a regional climate model ensemble. Journal of Climate, 30(17):6771–6794.

Puett, R.C., A.H. Poulsen, T. Taj, M. Ketzel, C.Geels, J. Brandt, J.H. Christensen, M. Sørensen, N. Roswall, U. Hvidtfeldt and O. Raaschou-Nielsen, 2020. Relationship of leukaemias with long-term ambient air pollution exposures in the adult Danish population. British Journal of Cancer, 123(12):1818–1824.

Punger, E.M. and J.J. West, 2013. The effect of grid resolution on estimates of the burden of ozone and fine particulate matter on premature mortality in the USA. Air Quality, Atmosphere & Health, 6:563–573.

Pureswaran, D.S., A. Roques and A. Battisti, 2018. Forest insects and climate change. Current Forestry Reports, 4:35–50.

Pye, H.O.T., A.W.H. Chan, M.P. Barkley and J.H. Seinfeld, 2010. Global modeling of organic aerosol: the importance of reactive nitrogen (NOx and NO_3). Atmospheric Chemistry and Physics, 10(22):11261–11276.

Qi, L. and S. Wang, 2019. Sources of black carbon in the atmosphere and in snow in the Arctic. Science of The Total Environment, 691:442–454.

Quennehen, B., A. Schwarzenboeck, A. Matsuki, J.F. Burkhart, A. Stohl, G. Ancellet and K.S. Law, 2012. Anthropogenic and forest fire pollution aerosol transported to the Arctic: observations from the POLARCAT-France spring campaign. Atmospheric Chemistry and Physics, 12(14):6437–6454.

Quennehen, B., J.-C. Raut, K. S. Law, N. Daskalakis, G. Ancellet, C. Clerbaux, S.-W. Kim, M. T. Lund, G. Myhre, D. J. L. Olivié, S. Safieddine, R. B. Skeie, J. L. Thomas, S. Tsyro, A. Bazureau, N. Bellouin, M. Hu, M. Kanakidou, Z. Klimont, K. Kupiainen, S. Myriokefalitakis, J. Quaas, S. T. Rumbold, M. Schulz, R. Cherian, A. Shimizu, J. Wang, S.-C. Yoon, and T. Zhu, 2016. Multi-model evaluation of short-lived pollutant distributions over east Asia during summer 2008. Atmospheric Chemistry and Physics, 16(17):10765–10792.

Quinn, P.K., D.J. Coffman, V.N. Kapustin, T.S. Bates and D.S. Covert, 1998. Aerosol optical properties in the marine boundary layer during the First Aerosol Characterization Experiment (ACE 1) and the underlying chemical and physical aerosol properties. Journal of Geophysical Research, 103(D13):16547–16564.

Quinn, P.K., T.L. Miller, T.S. Bates, J.A. Ogren, E. Andrews and G.E. Shaw, 2002. A 3-year record of simultaneously measured aerosol chemical and optical properties at Barrow, Alaska. Journal of Geophysical Research: Atmospheres, 107(D11):AAC 8-1–AAC 8-15.

Raaschou-Nielsen, O., U.A. Hvidtfeldt, N. Roswall, O. Hertel, A.H. Poulsen and M. Sørensen, 2017. Ambient benzene at the residence and risk for subtypes of childhood leukemia, lymphoma and CNS tumor. International Journal of Cancer, 143(6):1367–1373.

Raaschou-Nielsen, O., E. Thorsteinson, S. Antonsen, G.J. Holst, T. Sigsgaard, C. Geels, L.M. Frohn, J.H. Christensen, J. Brandt, C.B. Pedersen and U.A. Hvidtfeldt, 2020. Long-term exposure to air pollution and mortality in the Danish population a nationwide study. EClinicalMedicine, 28:100605.

Rädler, A.T., P.H. Groenemeijer, E. Faust, R. Sausen and T. Púčik, 2019. Frequency of severe thunderstorms across Europe expected to increase in the 21st century due to rising instability. npj Climate and Atmospheric Science, 2:30.

Randles, C.A., A.M. da Silva, V. Buchard, P.R. Colarco, A. Darmenov, R. Govindaraju, A. Smirnov, B. Holben, R. Ferrare, J. Hair, Y. Shinozuka and C. J. Flynn, 2017. The MERRA-2 aerosol reanalysis, 1980 onward. Part I: system description and data assimilation evaluation. Journal of Climate, 30(17):6823–6850.

Rao, S., Z. Klimont, S.J. Smith, R. Van Dingenen, F. Dentener, L. Bouwman, K. Riahi, M. Amann, B.L Bodirsky, D.P. van Vuuren, L. Aleluia Reis, K. Calvin, L. Drouet, O. Fricko, S. Fujimori, D. Gernaat, P. Havlik, M. Harmsen, T. Hasegawa, C. Heyes, J. Hilaire, G. Luderer, T. Masui, E. Stehfest, J. Strefler, S. van der Sluis and M. Tavoni, 2017. Future air pollution in the Shared Socio-economic Pathways. Global Environmental Change 42, 346–358.

Rap, A., N.A.D. Richards, P.M. Forster, S.A. Monks, S.R. Arnold and M.P. Chipperfield, 2015. Satellite constraint on the tropospheric ozone radiative effect. Geophysical Research Letters, 42(12):5074–5081.

Rayner, N.A., D.E. Parker, E.B. Horton, C.K. Folland, L.V. Alexander, D.P. Rowell, E.C. Kent and A. Kaplan, 2003. Global analyses of sea surface temperature, sea ice, and night marine air temperature since the late nineteenth century. Journal of Geophysical Research: Atmospheres, 108(D14).

Raynolds, M.K., D.A. Walker, A. Balser, C. Bay, M. Campbell, M.M. Cherosov, F.J.A. Daniëls, P.B. Eidesen, K.A. Ermokhina, G.V. Frost, B. Jedrzejek, M.T. Jorgenson, B.E. Kennedy, S.S. Kholod, I.A. Lavrinenko, O.V. Lavrinenko, B. Magnússon, N.V. Matveyeva, S. Metúsalemsson, L. Nilsen, I. Olthof, I.N. Pospelov, E.B. Pospelova, D. Pouliot, V. Razzhivin, G. Schaepman-Strub, J. Šibík, M.Y. Telyatnikov and E. Troeva, 2019. A raster version of the Circumpolar Arctic Vegetation Map (CAVM). Remote Sensing of Environment, 232:111297.

Raz-Yaseef, N., M.S. Torn, Y. Wu, D.P. Billesbach, A.K. Liljedahl, T.J. Kneafsey, V.E. Romanovsky, D.R. Cook and S.D. Wullschleger, 2017. Large CO_2 and CH_4 emissions from polygonal tundra during spring thaw in northern Alaska. Geophysical Research Letters, 44(1):504–513.

Reay, D., P. Smith and A. van Amstel, (Eds.), 2010. Methane and climate change. Earthscan Publications Ltd, London, UK. 261pp.

Reeburgh, W.S., 2007. Oceanic Methane Biogeochemistry. Chemical Reviews, 107(2):486–513.

Rehder, G., I. Leifer, P.G. Brewer, G. Friederich and E.T. Peltzer, 2009. Controls on methane bubble dissolution inside and outside the hydrate stability field from open ocean field experiments and numerical modeling. Marine Chemistry, 114(1–2):19–30.

Rein, G., 2016. Smoldering combustion. In: Hurley, M.J., D. Gottuk, J.R. Hall Jr., K. Harada, E. Kuligowski, M. Puchovsky, J. Torero, J.M. Watts Jr. and C. Wieczorek (Eds.). SFPE Handbook of Fire Protection Engineering, pp. 581–603. Springer.

Rein, G., N. Cleaver, C. Ashton, P. Pironi and J.L. Torero, 2008. The severity of smouldering peat fires and damage to the forest soil. Catena, 74(3):304–309.

Reinds, G.J., M. Posch, J. Aherne and M. Forsius, 2015. Assessment of critical loads of sulphur and nitrogen and their exceedances for terrestrial ecosystems in the northern hemisphere. In: de Vries, W., J.P. Hettelingh and M. Posch (Eds). Critical Loads and Dynamic Risk Assessments. pp. 403–417. Environmental Pollution, 25. Springer, Dordrecht.

Reis, S., P. Grennfelt, Z. Klimont, M. Amann, H. ApSimon, J.-P. Hettelingh, M. Holland, A.-C. LeGall, R. Maas, M. Posch, T. Spranger, M.A. Sutton and M. Williams, 2012. From acid rain to climate change. Science, 338(6111):1153–1154.

Reisinger, P., A. Wonaschütz, R. Hitzenberger, A. Petzold, H. Bauer, N. Jankowski, H. Puxbaum, X. Chi and W. Maenhaut, 2008. Intercomparison of measurement techniques for black or elemental carbon under urban background conditions in wintertime: influence of biomass combustion. Environmental Science & Technology, 42(3):884–889.

Remer, L.A., Y.J. Kaufman, D. Tanré, S. Mattoo, D.A. Chu, J.V. Martins, R.-R. Li, C. Ichoku, R.C. Levy, R.G. Kleidman, T.F. Eck, E. Vermote and B.N. Holben, 2005. The MODIS aerosol algorithm, products, and validation. Journal of the Atmospheric Sciences, 62(4):947–973.

Ren, L., Y. Yang, H. Wang, R. Zhang, P. Wang and H. Liao, 2020. Source attribution of Arctic black carbon and sulfate aerosols and associated Arctic surface warming during 1980–2018. Atmospheric Chemistry and Physics, 20(14):9067–9085.

Reyer, C.P.O., S. Bathgate, K. Blennow, J.G. Borges, H. Bugmann, S. Delzon, S.P. Faias, J. Garcia-Gonzalo, B. Gardiner, J.R. Gonzalez-Olabarria, C. Gracia, J. Guerra-Hernández, S. Kellomäki, K. Kramer, M.J. Lexer, M. Lindner, E. van der Maaten, M. Maroschek, B. Muys, B. Nicoll, M. Palahi, J.H. Palma, J.A. Paulo, H. Peltola, T. Pukkala, W. Rammer, D. Ray, S. Sabaté, M.-J. Schelhaas, R. Seidl, C. Temperli, M. Tomé, R. Yousefpour, N.E. Zimmermann and M. Hanewinkel, 2017. Are forest disturbances amplifying or canceling out climate change-induced productivity changes in European forests? Environmental Research Letters, 12(3):034027.

Riahi, K., D.P. van Vuuren, E. Kriegler, J. Edmonds, B.C. O'Neill, S. Fujimori, N. Bauer, K. Calvin, R. Dellink, O. Fricko, W. Lutz, A. Popp, J.C. Cuaresma, S. Kc, M. Leimbach, L. Jiang, T. Kram, S. Rao, J. Emmerling, K. Ebi, T. Hasegawa, P. Havlik, F. Humpenöder, L.A. Da Silva, S. Smith, E. Stehfest, V. Bosetti, J. Eom, D. Gernaat, T. Masui, J. Rogelj, J. Strefler, L. Drouet, V. Krey, G. Luderer, M. Harmsen, K. Takahashi, L. Baumstark, J.C. Doelman, M. Kainuma, Z. Klimont, G. Marangoni, H. Lotze-Campen, M. Obersteiner, A. Tabeau and M. Tavoni, 2017. The Shared Socioeconomic Pathways and their energy, land use, and greenhouse gas emissions implications: an overview. Global Environmental Change, 42:153–168.

Richardson A.D., D.Y. Hollinger, J.K. Shoemaker, H. Hughes, K. Savage and E.A. Davidson, 2019. Six years of ecosystem-atmosphere greenhouse gas fluxes measured in a sub-boreal forest. Scientific data, 6:117.

Riley, K.L., A.P. Williams, S.P. Urbanski, D.E. Calkin, K.C. Short and C.D. O'Connor, 2019. Will landscape fire increase in the future? A systems approach to climate, fire, fuel, and human drivers. Current Pollution Reports, 5(2):9–24.

Rinne J., T. Riutta, M. Pihlatie, M. Aurela, S. Haapanala, J.-P. Tuovinen, E.-S. Tuittila and T. Vesala, 2007. Annual cycle of methane emission from a boreal fen measured by the eddy covariance technique. Tellus B: Chemical and Physical Meteorology, 59(3):449–457.

Robertson, L., J. Langner and M. Engardt, 1999. An Eulerian limited-area atmospheric transport model. Journal of Applied Meteorology and Climatology, 38(2):190–210.

Robinne, F.N., M.-A. Parisien and M. Flannigan, 2016. Anthropogenic influence on wildfire activity in Alberta, Canada. International Journal of Wildland Fire, 25(11):1131–1143.

Rocha, A.V., M.M. Loranty, P.E. Higuera, M.C. Mack, F.S. Hu, B.M. Jones, A.L. Breen, E.B. Rastetter, S.J. Goetz and G.R. Shaver, 2012. The footprint of Alaskan tundra fires during the past half-century: implications for surface properties and radiative forcing. Environmental Research Letters, 7(4):044039.

Rodríguez, B.T., L. Huang, G.M. Santos, W. Zhang, V. Vetro, X. Xu, S. Kim and C.I. Czimczik, 2020. Seasonal cycle of isotope-based source apportionment of elemental carbon in airborne particulate matter and snow at Alert, Canada. Journal of Geophysical Research: Atmospheres, 125(23):e2020JD033125.

Rodriguez-Villamizar, L.A., A. Magico, A. Osornio-Vargas and B.H. Rowe, 2015. The effects of outdoor air pollution on the respiratory health of Canadian children: a systematic review of epidemiological studies. Canadian Respiratory Journal, 22(5):282–292.

Rogers, D.C., P.J. DeMott and S.M. Kreidenweis, 2001. Airborne measurements of tropospheric ice-nucleating aerosol particles in the Arctic spring. Journal of Geophysical Research: Atmospheres, 106(D14):15053–15063.

Rogers, R.R., C.A. Hostetler, J.W. Hair, R.A. Ferrare, Z. Liu, M.D. Obland, D.B. Harper, A.L. Cook, K.A. Powell, M.A. Vaughan and D.A. Winker, 2011. Assessment of the CALIPSO Lidar 532 nm attenuated backscatter calibration using the NASA LaRC airborne High Spectral Resolution Lidar. Atmospheric Chemistry and Physics, 11(3):1295–1311.

Roiger, A., J.-L. Thomas, H. Schlager, K.S. Law, J. Kim, A. Schäfler, B. Weinzierl, F. Dahlkötter, I. Krisch, L. Marelle, A. Minikin, J.-C. Raut, A. Reiter, M. Rose, M. Scheibe, P. Stock, R. Baumann, I. Bouarar, C. Clerbaux, M. George, T. Onishi and J. Flemming, 2015. Quantifying emerging local anthropogenic emissions in the Arctic region: the ACCESS Aircraft Campaign Experiment. Bulletin of the American Meteorological Society, 96(3):441–460.

Romanovskii, N.N., A.V. Gavrilov, V.E. Tumskoy, A.L. Kholodov, C. Siegert, H.-W. Hubberten and A.V. Sher, 2000. Environmental evolution in the Laptev Sea region during Late Pleistocene and Holocene. Polarforschung, 68:237–245.

Romanovskii, N.N., H.-W. Hubberten, A.V. Gavrilov, A.A. Eliseeva and G.S. Tipenko, 2005. Offshore permafrost and gas hydrate stability zone on the shelf of East Siberian Seas. Geo-Marine Letters, 25:167–182.

Ronkainen, T., M. Väliranta and E.-S. Tuittila, 2013. Fire pattern in a drainage-affected boreal bog. Boreal Environment Research, 18(3):309–316.

Rose, N.L. and M. Ruppel, 2015. Environmental archives of contaminant particles. In: Blais, J.M., M.R. Rosen and J.P. Smol (Eds.). Environmental Contaminants – Using natural archives to track sources and long-term trends of pollution. pp 187–221. Springer.

Rubino, M., A. D'Onofrio, O. Seki and J.A. Bendle, 2016. Ice-core records of biomass burning. The Anthropocene Review, 3(2):140–162.

Ruppel, C.D. and J.D. Kessler, 2017. The interaction of climate change and methane hydrates. Reviews of Geophysics, 55(1):126–168.

Ruppel, M.M., E. Isaksson, J. Ström, E. Beaudon, J. Svensson, C.A. Pedersen and A. Korhola, 2014. Increase in elemental carbon values between 1970 and 2004 observed in a 300-year ice core from Holtedahlfonna (Svalbard). Atmospheric Chemistry and Physics, 14(20):11447–11460.

Ruppel, M.M., Ö. Gustafsson, N.L. Rose, A. Pesonen, H. Yang, J. Weckström, V. Palonen, M.J. Oinonen and A. Korhola, 2015. Spatial and temporal patterns in black carbon deposition to dated Fennoscandian Arctic lake sediments from 1830 to 2010. Environmental Science & Technology, 49(24):13954–13963.

Ruppel, M.M., J. Soares, J.-C. Gallet, E. Isaksson, T. Martma, J. Svensson, J. Kohler, C.A. Pedersen, S. Manninen, A. Korhola and J. Ström, 2017. Do contemporary (1980–2015) emissions determine the elemental carbon deposition trend at Holtedahlfonna glacier, Svalbard? Atmospherics Chemistry and Physics, 17(20):12779–12795.

Ruppel, M.M., S. Eckhardt, A. Pesonen, K. Mizohata, M.J. Oinonen, A. Stohl, A. Andersson, V. Jones, S. Manninen and Ö. Gustafsson, 2021. Observed and modeled black carbon deposition and sources in the Western Russian Arctic 1800–2014. Environmental Science & Technology, 55(8):4368-4377.

Sachs, T., M. Giebels, J. Boike and L. Kutzbach, 2010. Environmental controls on CH_4 emission from polygonal tundra on the microsite scale in the Lena river delta, Siberia. Global Change Biology, 16(11):3096–3110.

Salmi, T., A. Määttä, P. Anttila, T. Ruoho-Airola and T. Amnell, 2002. Detecting trends of annual values of atmospheric pollutants by the Mann-Kendall test and Sen's slope estimates - the Excel template application MAKESENS. Publications in Air Quality, No. 31. Finnish Meteorological Institute, 35pp.

Samoli, E., A. Analitis, G. Touloumi, J. Schwartz, H.R. Anderson, J. Sunyer, L. Bisanti, D. Zmirou, J.M. Vonk, J. Pekkanen, P. Goodman, A. Paldy, C. Schindler and K. Kaysouyanni, 2005. Estimating the exposure–response relationships between particulate matter and mortality within the APHEA Multicity Project. Environmental Health Perspectives, 113(1):88–95.

Sampedro, J., S.T. Waldhoff, D.-J. Van de Ven, G. Pardo, R. Van Dingenen, I. Arto, A. del Prado and M.J. Sanz, 2020. Future impacts of ozone driven damages on agricultural systems. Atmospheric Environment, 231:117538.

Samuelsson, P., C.G. Jones, U. Willén, A. Ullerstig, S. Gollvik, U. Hansson, E. Jansson, C. Kjellström, G. Nikulin and K. Wyser, 2011. The Rossby Centre regional climate model RCA3: model description and performance. Tellus A: Dynamic Meteorology and Oceanography, 63(1):4–23.

Sanchez-Marroquin, A., O. Arnalds, K.J. Baustian-Dorsi, J. Browse, P. Dagsson-Waldhauserova, A.D. Harrison, E.C. Maters, K.J. Pringle, J. Vergara-Temprado, I.T. Burke, J.B. McQuaid, K.S. Carslaw and B.J. Murray, 2020. Iceland is an episodic source of atmospheric ice-nucleating particles relevant for mixed-phase clouds. Science Advances, 6(26):eaba8137.

Sand, M., T.K. Berntsen, K. von Salzen, M.G. Flanner, J. Langner and D.G. Victor, 2016. Response of Arctic temperature to changes in emissions of short-lived climate forcers. Nature Climate Change, 6:286–290.

Sand, M., B.H. Samset, Y. Balkanski, S. Bauer, N. Bellouin, T.K. Berntsen, H. Bian, M. Chin, T. Diehl, R. Easter, S.J. Ghan, T. Iversen, A. Kirkevåg, J.-F. Lamarque, G. Lin, X. Liu, G. Luo, G. Myhre, T. van Noije, J.E. Penner, M. Schulz, Ø. Seland, R.B. Skeie, P. Stier, T. Takemura, K. Tsigaridis, F. Yu, K. Zhang and H. Zhang, 2017. Aerosols at the poles: an AeroCom Phase II multi-model evaluation. Atmospheric Chemistry and Physics, 17(19):12197–12218.

Sand, M., T.K. Berntsen, A.M.L. Ekman, H.-C. Hansson and A. Lewinschal, 2020. Surface temperature response to regional black carbon emissions: do location and magnitude matter? Atmospheric Chemistry and Physics, 20(5):3079–3089.

Saunois, M., P. Bousquet, B. Poulter, A. Peregon, P. Ciais, J.G. Canadell, E.J. Dlugokencky, G. Etiope, D. Bastviken, S. Houweling, G. Janssens-Maenhout, F.N. Tubiello, S. Castaldi, R.B. Jackson, M. Alexe, V.K. Arora, D.J. Beerling, P. Bergamaschi, D.R. Blake, G. Brailsford, V. Brovkin, L. Bruhwiler, C. Crevoisier, P. Crill, K. Covey, C. Curry, C. Frankenberg, N. Gedney, L. Höglund-Isaksson, M. Ishizawa, A. Ito, F. Joos, H.-S. Kim, T. Kleinen, P. Krummel, J.-F. Lamarque, R. Langenfelds, R. Locatelli, T. Machida, S. Maksyutov, K.C. McDonald, J. Marshall, J.R. Melton, I. Morino, V. Naik, S. O'Doherty, F.-J.W. Parmentier, P.K. Patra, C. Peng, S. Peng, G.P. Peters, I. Pison, C. Prigent, R. Prinn, M. Ramonet, W.J. Riley, M. Saito, M. Santini, R. Schroeder, I.J. Simpson, R. Spahni, P. Steele, A. Takizawa, B.F. Thornton, H. Tian, Y. Tohjima, N. Viovy, A. Voulgarakis, M. van Weele, G.R. van der Werf, R. Weiss, C. Wiedinmyer, D.J. Wilton, A. Wiltshire, D. Worthy, D. Wunch, X. Xu, Y. Yoshida, B. Zhang, Z. Zhang and Q. Zhu, 2016a. The global methane budget 2000–2012. Earth System Science Data, 8(2):697–751.

Saunois, M., R.B. Jackson, P. Bousquet, B. Poulter and J.G. Canadell, 2016b. The growing role of methane in anthropogenic climate change. Environmental Research Letters, 11:120207.

Saunois, M., A.R. Stavert, B. Poulter, P. Bousquet, J.G. Canadell, R.B Jackson, P.A. Raymond, E.J. Dlugokencky, S. Houweling, P.K. Patra, P. Ciais, V.K. Arora, D. Bastviken, P. Bergamaschi, D.R. Blake, G. Brailsford, L. Bruhwiler, K.M. Carlson, M. Carrol, S. Castaldi, N. Chandra, C. Crevoisier, P. M. Crill, K. Covey, C.L. Curry, G. Etiope, C. Frankenberg, N. Gedney, M.I. Hegglin, L. Höglund-Isaksson, G. Hugelius, M. Ishizawa, A. Ito, G. Janssens-Maenhout, K.M. Jensen, F. Joos, T. Kleinen, P.B. Krummel, R.L. Langenfelds, G.G .Laruelle, L. Liu, T. Machida, S. Maksyutov, K.C. McDonald, J. McNorton, P.A. Miller, J.R. Melton, I. Morino, J. Müller, F. Murguia-Flores, V. Naik, Y. Niwa, S. Noce, S. O'Doherty, R.J. Parker, C. Peng, S. Peng, G.P. Peters, C. Prigent, R. Prinn, M. Ramonet, P. Regnier, W.J. Riley, J.A. Rosentreter, A. Segers, I.J. Simpson, H. Shi, S.J. Smith, L.P. Steele, B.F. Thornton, H. Tian, Y. Tohjima, F.N. Tubiello, A. Tsuruta, N. Viovy, A. Voulgarakis, T.S. Weber, M. van Weele, G.R. van der Werf, R.F. Weiss, D. Worthy, D. Wunch, Y. Yin, Y. Yoshida, W. Zhang, Z. Zhang, Y. Zhao, B. Zheng, Qing Zhu, Qiuan Zhu and Q. Zhuang, 2020. The Global Methane Budget 2000–2017, Earth System Science Data, 12(3):1561–1623.

Sayedi, S.S., B.W. Abbott, B.F. Thornton, J.M. Frederick, J.E. Vonk, P. Overduin, C. Schädel, E.A.G. Schuur, A. Bourbonnais, N. Demidov, A. Gavrilov, S. He, G. Hugelius, M. Jakobsson, M.C. Jones, D. Joung, G. Kraev, R.W. Macdonald, A.D. McGuire, C. Mu, M. O'Regan, K.M. Schreiner, C. Stranne, E. Pizhankova, A. Vasiliev, S. Westermann, J.P. Zarnetske, T. Zhang, M. Ghandehari, S. Baeumler, B.C. Brown and R.J. Frei, 2020. Subsea permafrost carbon stocks and climate change sensitivity estimated by expert assessment. Environmental Research Letters, 15(12):124075.

Sayer, A.M., G.E. Thomas and R.G. Grainger, 2010. A sea surface reflectance model for (A)ATSR, and application to aerosol retrievals. Atmospheric Measurement Techniques, 3(4):813–838.

Sayer, A.M., N.C. Hsu, C. Bettenhausen, Z. Ahmad, B.N. Holben, A. Smirnov, G.E. Thomas and J. Zhang, 2012. SeaWiFS Ocean Aerosol Retrieval (SOAR): Algorithm, validation, and comparison with other data sets. Journal of Geophysical Research: Atmospheres, 117(D3).

Sayer, A.M., L.A. Munchak, N.C. Hsu, R.C. Levy, C. Bettenhausen and M.-J. Jeong, 2014. MODIS Collection 6 aerosol products: comparison between Aqua's e-Deep Blue, Dark Target, and "merged" data sets, and usage recommendations. Journal of Geophysical Research: Atmospheres, 119(24):13965–13989.

Scalabrin, E., R. Zangrando, E. Barbaro, N.M. Kehrwald, J. Gabrieli, C. Barbante and A. Gambaro, 2012. Amino acids in Arctic aerosols. Atmospheric Chemistry and Physics, 12(21):10453–10463.

Schiferl, L. D. and C.L. Heald, 2018. Particulate matter air pollution may offset ozone damage to global crop production. Atmospheric Chemistry and Physics, 18:5953–5966.

Schladitz, A., T. Müller, N. Kaaden, A. Massling, K. Kandler, M. Ebert, S. Weinbruch, C. Deutscher and A. Wiedensohler, 2009. In situ measurements of optical properties at Tinfou (Morocco) during the Saharan Mineral Dust Experiment SAMUM 2006. Tellus B 61(1):64–78.

Schmale, J., J. Schneider, G. Ancellet, B. Quennehen, A. Stohl, H. Sodemann, J.F. Burkhart, T. Hamburger, S.R. Arnold, A. Schwarzenboeck, S. Borrmann and K.S. Law, 2011. Source identification and airborne chemical characterisation of aerosol pollution from long-range transport over Greenland during POLARCAT summer campaign 2008. Atmospheric Chemistry and Physics, 11(19):10097–10123.

Schmale, J., S.R. Arnold, K.S. Law, T. Thorp, S. Anenberg, W.R. Simpson, J. Mao and K.A. Pratt, 2018a. Local Arctic air pollution: a neglected but serious problem. Earth's Future, 6(10):1385–1412.

Schmale, J., S. Henning, S. Decesari, B. Henzing, H. Keskinen, K. Sellegri, J. Ovadnevaite, M.L. Pöhlker, J. Brito, A. Bougiatioti, A. Kristensson, N. Kalivitis, I. Stavroulas, S. Carbone, A. Jefferson, M. Park, P. Schlag, Y. Iwamoto, P. Aalto, M. Äijälä, N. Bukowiecki, M. Ehn, G. Frank, R. Fröhlich, A. Frumau, E. Herrmann, H. Herrmann, R. Holzinger, G. Kos, M. Kulmala, N. Mihalopoulos, A. Nenes, C. O'Dowd, T. Petäjä, D. Picard, C. Pöhlker, U. Pöschl, L. Poulain, A.S.H. Prévôt, E. Swietlicki, M.O. Andreae, P. Artaxo, A. Wiedensohler, J. Ogren, A. Matsuki, S.S. Yum, F. Stratmann, U. Baltensperger and M. Gysel, 2018b. Long-term cloud condensation nuclei number concentration, particle number size distribution and chemical composition measurements at regionally representative observatories. Atmospheric Chemistry and Physics 18(4):2853–2881.

Schmale, J., S. Sharma, S. Decesari, J. Pernov, A. Massling, H.-C. Hansson, K. von Salzen, H. Skov, E. Andrews, P.K. Quinn, L.M. Upchurch, K. Eleftheriadis and R. Traversi, 2022. Pan-Arctic seasonal cycles and long-term trends of aerosol properties from ten observatories, Atmospheric Chemistry and Physics, 22:3067–3096.

Schmeisser, L., J. Backman, J.A. Ogren, E. Andrews, E. Asmi, S. Starkweather, T. Uttal, M. Fiebig, S. Sharma, K. Eleftheriadis, S. Vratolis, M. Bergin, P. Tunved and A. Jefferson, 2018. Seasonality of aerosol optical properties in the Arctic. Atmospheric Chemistry and Physics, 18(16):11599–11622.

Schnaiter, M., E. Järvinen, A. Abdelmonem and T. Leisner, 2018. PHIPS-HALO: the airborne particle habit imaging and polar scattering probe – Part 2: Characterization and first results. Atmospheric Measurement Techniques, 11(1):341–357.

Schulz, H., M. Zanatta, H. Bozem, W.R. Leaitch, A.B. Herber, J. Burkart, M.D. Willis, D. Kunkel, P.M. Hoor, J.P.D. Abbatt and R. Gerdes, 2019. High Arctic aircraft measurements characterising black carbon vertical variability in spring and summer. Atmospheric Chemistry and Physics, 19(4):2361–2384.

Schneider, B., W. Gülzow, B. Sadkowiak and G. Rehder, 2014. Detecting sinks and sources of CO_2 and CH_4 by ferrybox-based measurements in the Baltic Sea: three case studies. Journal of Marine Systems 140 (Part A):13–25.

Scholten, R. and S. Veraverbeke, 2020. Spatiotemporal patterns of overwintering fire in Alaska. Fire Science Highlight (Spring 2020). Alaska Fire Science Consortium. Available at: https://akfireconsortium.files.wordpress.com/2020/03/fsh_2020mar25_holdoverfires-1.pdf

Schöpp, W., Z. Klimont, R. Suutari and J. Cofala, 2005. Uncertainty analysis of emission estimates in the RAINS integrated assessment model. Environmental Science & Policy, 8(6):601–613.

Schuh, A.E., A.R. Jacobson, S. Basu, B. Weir, D. Baker, K. Bowman, F. Chevallier, S. Crowell, K.J. Davis, F. Deng, S. Denning, L. Feng, D. Jones, J. Liu and P.I. Palmer, 2019. Quantifying the impact of atmospheric transport uncertainty on CO_2 surface flux estimates. Global Biogeochemical Cycles, 33(4):484–500.

Schultz, M.G., S. Stadtler, S. Schröder, D. Taraborrelli, B. Franco, J. Krefting, A. Henrot, S. Ferrachat, U. Lohmann, D. Neubauer, C. Siegenthaler-Le Drian, S. Wahl, H. Kokkola, T. Kühn, S. Rast, H. Schmidt, P. Stier, D. Kinnison, G.S. Tyndall, J.J. Orlando and C. Wespes, 2018. The chemistry–climate model ECHAM6.3-HAM2.3-MOZ1.0. Geoscientific Model Development, 11(5):1695–1723.

Schulz, H., M. Zanatta, H. Bozem, W.R. Leaitch, A.B. Herber, J. Burkart, M.D. Willis, D. Kunkel, P.M. Hoor, J.P.D. Abbatt and R. Gerdes, 2019. High Arctic aircraft measurements characterising black carbon vertical variability in spring and summer. Atmospheric Chemistry and Physics, 19(4): 2361–2384.

Schuster, G.L., O. Dubovik and B.N. Holben, 2006. Angstrom exponent and bimodal aerosol size distributions. Journal of Geophysical Research: Atmospheres, 111(D7).

Schutgens, N.A.J., 2020. Site representativity of AERONET and GAW remotely sensed aerosol optical thickness and absorbing aerosol optical thickness observations. Atmospheric Chemistry and Physics, 20(12):7473–7488.

Schutgens, N., A.M. Sayer, A. Heckel, C. Hsu, H. Jethva, G. de Leeuw, P.J.T. Leonard, R.C. Levy, A. Lipponen, A. Lyapustin, P. North, T. Popp, C. Poulson, V. Sawyer, L. Sogacheva, G. Thomas, O. Torres, Y. Wang, S. Kinne, M. Schulz and P. Stier, 2020. An AeroCom/AeroSat study: intercomparison of satellite AOD datasets for aerosol model evaluation. Atmospheric Chemistry and Physics, 20(21):12431–12457.

Schuur, E.A.G., A.D. McGuire, C. Schädel, G. Grosse, J.W. Harden, D.J. Hayes, G. Hugelius, C.D. Koven, P. Kuhry, D.M. Lawrence, S.M. Natali, D. Olefeldt, V.E. Romanovsky, K. Schaefer, M.R. Turetsky, C.C. Treat and J.E. Vonk, 2015. Climate change and the permafrost carbon feedback. Nature, 520:171–179.

Schwaab, J., E.L. Davin, P. Bebi, A. Duguay-Tetzlaff, L.T. Waser, M. Haeni and R. Meier, 2020. Increasing the broad-leaved tree fraction in European forests mitigates hot temperature extremes. Scientific Reports, 10:14153.

Schwander, J., 2007. Ice Core Methods: Chronologies. In: Elias, S.A. (ed.) Encyclopedia of Quaternary Science (pp. 1173-1181). Elsevier, Amsterdam.

Schwartz J., D.W. Dockery and L.M. Neas, 1996. Is daily mortality associated specifically with fine particles? Journal of the Air & Waste Management Association, 46(1):927–39.

Schwarz, J.P., R.S. Gao, D.W. Fahey, D.S. Thomson, L.A. Watts, J.C. Wilson, J.M. Reeves, M. Darbeheshti, D.G. Baumgardner, G.L. Kok, S.H. Chung, M. Schulz, J. Hendricks, A. Lauer, B. Kärcher, J.G. Slowik, K.H. Rosenlof, R.B. Thompson, A.O. Langford, M. Loewenstein and K.C. Aikin, 2006. Single-particle measurements of midlatitude black carbon and light-scattering aerosols from the boundary layer to the lower stratosphere. Journal of Geophysical Research: Atmospheres, 111(D16).

Schwarz, J.P., J.R. Spackman, R.S. Gao, A.E. Perring, E. Cross, T.B. Onasch, A. Ahern, W. Wrobel, P. Davidovits, J. Olfert, M.K. Dubey, C. Mazzoleni and D.W. Fahey, 2010. The detection efficiency of the Single Particle Soot Photometer. Aerosol Science and Technology, 44(8):612–628.

Schwarz, J.P., S.J. Doherty, F. Li, S.T. Ruggiero, C.E. Tanner, A.E. Perring, R.S. Gao and D.W. Fahey, 2012. Assessing single particle soot photometer and integrating sphere/integrating sandwich spectrophotometer measurement techniques for quantifying black carbon concentration in snow. Atmospheric Measurement Techniques, 5(11):2581–2592.

Schwarz, J.P., R.S. Gao, A.E. Perring, J.R. Spackman and D.W. Fahey, 2013. Black carbon aerosol size in snow. Scientific Reports, 3:1356.

Schweiger, A.J., R.W. Lindsay, S. Vavrus and J.A. Francis, 2008. Relationships between Arctic Sea ice and clouds during autumn. Journal of Climate, 21(18):4799–4810.

Scinocca, J.F., N.A. McFarlane, M. Lazare, J. Li and D. Plummer, 2008. Technical Note: The CCCma third generation AGCM and its extension into the middle atmosphere. Atmospheric Chemistry and Physics, 8(23):7055–7074.

Seabrook, J. and J. Whiteway, 2016. Influence of mountains on Arctic tropospheric ozone. Journal of Geophysical Research: Atmospheres, 121(4):1935–1942.

Sebacher, D.I., R.C. Harriss, K.B. Bartlett, S.M. Sebacher and S.S. Grice, 1986. Atmospheric methane sources: Alaskan tundra bogs, an alpine fen, and a subarctic boreal marsh. Tellus B: Chemical and Physical Meteorolgy, 38(1):1–10.

Sedlar, J. and M. Tjernström, 2009. Stratiform cloud-inversion characterization during the Arctic melt season. Boundary-Layer Meteorology, 132:455–474.

Sedlar, J., M.D. Shupe and M. Tjernström, 2012. On the relationship between thermodynamic structure and cloud top, and its climate significance in the Arctic. Journal of Climate, 25(7):2374–2393.

Seidl, R., M.-J. Schelhaas, W. Rammer and P.J. Verkerk, 2014. Increasing forest disturbances in Europe and their impact on carbon storage. Nature Climate Change, 4:806–810.

Seinfeld, J.H. and S.N. Pandis, 2006. Atmospheric Chemistry and Physics: From Air Pollution to Climate Change (2nd Edition). Wiley–Blackwell. 1232pp.

Sellar, A.A., C.G. Jones, J.P. Mulcahy, Y. Tang, A. Yool, A. Wiltshire, F.M. O'Connor, M. Stringer, R. Hill, J. Palmieri, S. Woodward, L. de Mora, T. Kuhlbrodt, S. Rumbold, D.I. Kelley, R. Ellis, C.E. Johnson, J. Walton, N.L. Abraham, M.B. Andrews, T. Andrews, A.T. Archibald, S. Berthou, E. Burke, E. Blockley, K. Carslaw, M. Dalvi, J. Edwards, G.A. Folberth, N. Gedney, P.T. Griffiths, A.B. Harper, M.A. Hendry, A.J. Hewitt, B. Johnson, A. Jones, C.D. Jones, J. Keeble, S. Liddicoat, O. Morgenstern, R.J. Parker, V. Predoi, E. Robertson, A. Siahaan, R.S. Smith, R. Swaminathan, M.T. Woodhouse, G. Zeng and M. Zerroukat, 2019. UKESM1: description and evaluation of the UK Earth System Model. Journal of Advances in Modeling Earth Systems, 11(12):4513–4558.

Serreze, M.C., J.D. Kahl and R.C. Schnell, 1992. Low-level temperature inversions of the Eurasian Arctic and comparisons with Soviet drifting station data. Journal of Climate, 5(6):615–630.

Shaddick, G., M.L. Thomas, H. Amini, D. Broday, A. Cohen, J. Frostad, A. Green, S. Gumy, Y. Liu, R.V. Martin, A. Pruss-Ustun, D. Simpson, A. van Donkelaar and M. Brauer, 2018. Data integration for the assessment of population exposure to ambient air pollution for Global Burden of Disease assessment. Environmental Science & Technology, 52(16):9069–9078.

Shakhova, N., I. Semiletov, A. Salyuk, V. Yusupov, D. Kosmach and Ö. Gustafsson, 2010a. Extensive methane venting to the atmosphere from sediments of the East Siberian Arctic shelf. Science, 327(5970):1246–1250.

Shakhova, N., I. Semiletov, I. Leifer, A. Salyuk, P. Rekant and D. Kosmach, 2010b. Geochemical and geophysical evidence of methane release over the East Siberian Arctic Shelf. Journal of Geophysical Research: Oceans, 115(C8):C08007.

Shakhova, N., I. Semiletov, I. Leifer, V. Sergienko, A. Salyuk, D. Kosmach, D. Chernykh, C. Stubbs, D. Nicolsky, V. Tumskoy and Ö. Gustafsson, 2014. Ebullition and storm-induced methane release from the East Siberian Arctic shelf. Nature Geoscience, 7:64–70.

Shantz, N.C., I. Gultepe, E. Andrews, A. Zelenyuk, M.E. Earle, A.M. Macdonald, P.S.K. Liu and W.R. Leaitch, 2014. Optical, physical, and chemical properties of springtime aerosol over Barrow Alaska in 2008. International Journal of Climatology, 34(10), 3125–3138.

Sharma, S., E. Andrews, L.A. Barrie, J.A. Ogren and D. Lavoué, 2006. Variations and sources of the equivalent black carbon in the high Arctic revealed by long-term observations at Alert and Barrow: 1989–2003. Journal of Geophysical Research: Atmospheres, 111(D14).

Sharma, S., E. Chan, M. Ishizawa, D. Toom-Sauntry, S.L. Gong, S.M. Li, D.W. Tarasick, W.R. Leaitch, A. Norman, P.K. Quinn, T.S. Bates, M. Levasseur, L.A. Barrie and W. Maenhaut, 2012. Influence of transport and ocean ice extent on biogenic aerosol sulfur in the Arctic atmosphere. Journal of Geophysical Research: Atmospheres, 117:D12209.

Sharma, S., M. Ishizawa, D. Chan, D. Lavoué, E. Andrews, K. Eleftheriadis and S. Maksyutov, 2013. 16-year simulation of Arctic black carbon: transport, source contribution, and sensitivity analysis on deposition. Journal of Geophysical Research: Atmospheres, 118(2):943–964.

Sharma, S., W.R. Leaitch, L. Huang, D. Veber, F. Kolonjari, W. Zhang, S.J. Hanna, A.K. Bertram and J.A. Ogren, 2017. An evaluation of three methods for measuring black carbon in Alert, Canada. Atmospheric Chemistry and Physics, 17(24):15225–15243.

Sharma, S., L.A. Barrie, E. Magnusson, G. Brattström, W.R. Leaitch, A. Steffen and S. Landsberger, 2019. A factor and trends analysis of multidecadal lower tropospheric observations of Arctic aerosol composition, black carbon, ozone, and mercury at Alert, Canada. Journal of Geophysical Research: Atmospheres, 124(24):14133–14161.

Sheese, P.E., K.A. Walker, C.D. Boone, P.F. Bernath, L. Froidevaux, B. Funke, P. Raspollini and T. von Clarmann, 2017. ACE-FTS ozone, water vapour, nitrous oxide, nitric acid, and carbon monoxide profile comparisons with MIPAS and MLS. Journal of Quantitative Spectroscopy and Radiative Transfer, 186:63–80.

Sherstyukov, B.G. and A.B. Sherstyukov, 2014. Assessment of increase in forest fire risk in Russia till the late 21st century based on scenario experiments with fifth-generation climate models. Russian Meteorology and Hydrology, 39:292–301.

Sherwen, T., J.A. Schmidt, M.J. Evans, L.J. Carpenter, K. Großmann, S.D. Eastham, D.J. Jacob, B. Dix, T.K. Koenig, R. Sinreich, I. Ortega, R. Volkamer, A. Saiz-Lopez, C. Prados-Roman, A.S. Mahajan and C. Ordóñez, 2016. Global impacts of tropospheric halogens (Cl, Br, I) on oxidants and composition in GEOS-Chem. Atmospheric Chemistry and Physics, 16(18):12239–12271.

Shibata, T., K. Shiraishi, M. Shiobara, S. Iwasaki and T. Takano, 2018. Seasonal variations in High Arctic free tropospheric aerosols over Ny-Ålesund, Svalbard, observed by ground-based lidar. Journal of Geophysical Research: Atmospheres, 123(21):12,353–12,367.

Shindell, D., 2007. Local and remote contributions to Arctic warming. Geophysical Research Letters, 34(14): L14704.

Shindell, D.T., 2016. Crop yield changes induced by emissions of individual climate-altering pollutants. Earth's Future, 4(8):373–380.

Shindell, D. and G. Faluvegi, 2009. Climate response to regional radiative forcing during the twentieth century. Nature Geoscience 2:294–300.

Shindell, D.T., J.L. Grenfell, D. Rind, V. Grewe and C. Price, 2001. Chemistry-climate interactions in the Goddard Institute for Space Studies general circulation model: 1. tropospheric chemistry model description and evaluation. Journal of Geophysical Research: Atmospheres, 106(D8):8047–8075.

Shindell, D.T., G. Faluvegi and N. Bell, 2003. Preindustrial-to-present-day radiative forcing by tropospheric ozone from improved simulations with the GISS chemistry-climate GCM. Atmospheric Chemistry and Physics, 3(5):1675–1702.

Shindell, D.T, G. Faluvegi, N. Unger, E. Aguilar, G. Schmidt, D.M. Koch, S.E. Bauer and R.L. Miller, 2006. Simulations of preindustrial, present-day, and 2100 conditions in the NASA GISS composition and climate model G-PUCCINI. Atmospheric Chemistry and Physics, 6(12):4427–4459.

Shindell D.T., M. Chin, F. Dentener, R.M. Doherty, G. Faluvegi, A.M. Fiore, P. Hess, D.M. Koch, I.A. MacKenzie, M.G. Sanderson, M.G. Schultz, M. Schulz, D.S. Stevenson, H. Teich, C. Textor, O. Wild, D.J. Bergmann, I. Bey, H. Bian, C. Cuvelier, B.N. Duncan, G. Folberth, L.W. Horowitz, J. Jonson, J.W. Kaminski, E. Marmer, R. Park, K.J. Pringle, S. Schroeder, S. Szopa, T. Takemura, G. Zeng, T.J. Keating and A. Zuber, 2008. A multi-model assessment of pollution transport to the Arctic. Atmospheric Chemistry and Physics, 8(17):5353–5372.

Shindell, D., G. Faluvegi, D.M. Koch, G.A. Schmidt, N. Unger and S.E. Bauer, 2009. Improved attribution of climate forcing to emissions. Science, 326(5953):716–718.

Shindell, D.T., O. Pechony, A. Voulgarakis, G. Faluvegi, L. Nazarenko, J.-F. Lamarque, K. Bowman, G. Milly, B. Kovari, R. Ruedy and G.A. Schmidt, 2013. Interactive ozone and methane chemistry in GISS-E2 historical and future climate simulations. Atmospheric Chemistry and Physics, 13(5):2653–2689.

Shiwakoti, S., V.D. Zheljazkov, H.T. Gollany, M. Kleber, B. Xing and T. Astatkie, 2019. Micronutrients in the soil and wheat: impact of 84 years of organic or synthetic fertilization and crop residue management. Agronomy, 9(8):464.

Shupe, M.D. and J.M. Intrieri, 2004. Cloud radiative forcing of the Arctic surface: The influence of cloud properties, surface albedo, and solar zenith angle. Journal of Climate, 17(3):616–628.

Shupe, M.D., 2011. Clouds at Arctic atmospheric observatories. Part II: thermodynamic phase characteristics. Journal of Applied Meteorology and Climatology, 50(3):645–661.

Shupe, M.D., P.O.G. Persson, I.M. Brooks, M. Tjernström, J. Sedlar, T. Mauritsen, S. Sjogren and C. Leck, 2013. Cloud and boundary layer interactions over the Arctic sea ice in late summer. Atmospheric Chemistry and Physics, 13(18):9379–9399.

Shvetsov, E.G., E.A. Kukavskaya, L.V. Buryak and K. Barrett, 2019. Assessment of post-fire vegetation recovery in Southern Siberia using remote sensing observations. Environmental Research Letters, 14(5):055001.

Si, M., E. Evoy, J. Yun, Y. Xi, S.J. Hanna, A. Chivulescu, K. Rawlings, D. Veber, A. Platt, D. Kunkel, P. Hoor, S. Sharma, W.R. Leaitch and A.K. Bertram, 2019. Concentrations, composition, and sources of ice-nucleating particles in the Canadian High Arctic during spring 2016. Atmospheric Chemistry and Physics, 19(5):3007–3024.

Siddika, N., A.K. Rantala, H. Antikainen, H. Balogun, A.K. Amegah, N.R.I. Ryti, J. Kukkonen, M. Sofiev, M.S. Jaakkola and J.J.K. Jaakkola, 2019. Synergistic effects of prenatal exposure to fine particulate matter ($PM_{2.5}$) and ozone (O_3) on the risk of preterm birth: a population-based cohort study. Environmental Research, 176:108549.

Siddika, N., A.K. Rantala, H. Antikainen, H. Balogun, A.K. Amegah, N.R.I. Ryti, J. Kukkonen, M. Sofiev, M.S. Jaakkola and J.J.K. Jaakkola, 2020. Short-term prenatal exposure to ambient air pollution and risk of preterm birth – a population-based cohort study in Finland. Environmental Research, 184:109290.

Sierau, B., R.Y.-W. Chang, C. Leck, J. Paatero and U. Lohmann, 2014. Single-particle characterization of the high-Arctic summertime aerosol. Atmospheric Chemistry and Physics, 14(14):7409–7430.

Siewert, M.B., H. Lantuit, A. Richter and G. Hugelius, 2021. Permafrost causes unique fine-scale spatial variability across tundra soils. Global Biogeochemical Cycles, 35(3):e2020GB006659.

Silva, J.S. and S.P. Harrison, 2010. Humans, climate and land cover as controls on European fire regimes. In: Silva, J.S., F. Rego, P. Fernandes and E. Rigolot (Eds.). Towards Integrated Fire Management–Outcomes of the European Project Fire Paradox, pp. 49–59. European Forest Institute.

Simpson, D., A. Guenther, C.N. Hewitt and R. Steinbrecher, 1995. Biogenic emissions in Europe: 1. estimates and uncertainties. Journal of Geophysical Research: Atmospheres, 100(D11):22875–22890.

Simpson, W.R., D. Carlson, G. Hönninger, T.A. Douglas, M. Sturm, D. Perovich and U. Platt, 2007. First-year sea-ice contact predicts bromine monoxide (BrO) levels at Barrow, Alaska better than potential frost flower contact. Atmospheric Chemistry and Physics, 7:621–627.

Simpson, D., A. Benedictow, H. Berge, R. Bergström, L.D. Emberson, H. Fagerli, C.R. Flechard, G.D. Hayman, M. Gauss, J.E. Jonson, M.E. Jenkin, A. Nyíri, C. Richter, V.S. Semeena, S. Tsyro, J.-P. Tuovinen, Á. Valdebenito and P. Wind, 2012. The EMEP MSC-W chemical transport model – technical description. Atmospheric Chemistry and Physics, 12(16):7825–7865.

Simpson, W.R., U. Frieß, J.L. Thomas, J. Lampel and U. Platt, 2018. Polar nighttime chemistry produces intense reactive bromine events. Geophysical Research Letters, 45:9987–9994.

Simpson, D., R. Bergström, S. Tsyro and P. Wind, 2019a. Updates to the EMEP MSC-W model, 2018-2019. In: Transboundary particulate matter, photo-oxidants, acidifying and eutrophying components. EMEP Status Report 1/2019. pp. 145–152. The Norwegian Meteorological Institute.

Simpson, W., K. Law, J. Schmale, K. Pratt, S. Arnold and J. Mao, 2019b. Alaskan Layered Pollution And Chemical Analysis (ALPACA) White Paper. Air Pollution in the Arctic: Climate, Environment and Societies (PACES). https://alpaca.community.uaf.edu/wp-content/uploads/sites/758/2019/05/ALPACA-whitepaper.pdf

Singh, A., P. Rajput, D. Sharma, M.M. Sarin and D. Singh, 2014. Black carbon and elemental carbon from postharvest agricultural-waste burning emissions in the Indo-Gangetic Plain. Advances in Meteorology, 2014:179301.

Singleton, C.M., C.K. McCalley, B.J. Woodcroft, J.A. Boyd, P.N. Evans, S.B. Hodgkins, J.P. Chanton, S. Frolking, P.M. Crill, S.R. Saleska, V.I. Rich and G.W. Tyson, 2018. Methanotrophy across a natural permafrost thaw environment. The ISME Journal Multidisciplinary Journal of Microbial Ecology, 12:2544–2558.

Sinha, P.R., Y. Kondo, M. Koike, J.A. Ogren, A. Jefferson, T.E. Barrett, R.J. Sheesley, S. Ohata, N. Moteki, H. Coe, D. Liu, M. Irwin, P. Tunved, P.K. Quinn and Y. Zhao, 2017. Evaluation of ground-based black carbon measurements by filter-based photometers at two Arctic sites. Journal of Geophysical Research: Atmospheres, 122(6):3544–3572.

Sinha, P.R., Y. Kondo, K. Goto-Azuma, Y. Tsukagawa, K. Fukuda, M. Koike, S. Ohata, N. Moteki, T. Mori, N. Oshima, E.J. Førland, M. Irwin, J.-C. Gallet and C.A. Pederson, 2018. Seasonal progression of the deposition of black carbon by snowfall at Ny-Ålesund, Spitsbergen. Journal of Geophysical Research: Atmospheres, 123(2):997–1016.

SINTEF, 2013. Particle emission factors for wood stove firing in Norway. SINTEF Energy Research (SINTEF). Trondheim, Norway. 66pp.

Sipilä, M., N. Sarnela, T. Jokinen, H. Henschel, H. Junninen, J. Kontkanen, S. Richters, J. Kangasluoma, A. Franchin, O. Peräkylä, M.P. Rissanen, M. Ehn, H. Vehkamäki, T. Kurten, T. Berndt, T. Petäjä, D. Worsnop, D. Ceburnis, V.-M. Kerminen, M. Kulmala and C. O'Dowd, 2016. Molecular-scale evidence of aerosol particle formation via sequential addition of HIO_3. Nature, 537:532–534.

Sirin, A., A. Maslov, M. Medvedeva, A. Vozbrannaya, N. Valyaeva, O. Tsyganova, T. Glukhova and D. Makarov, 2014. Multispectral remote sensing data as a tool for assessing the need and the effectiveness for peatland restoration. Proceedings of the 9th European Conference on Ecological Restoration. 3–8 August 2014, Oulu, Finland.

Sirin, A., M. Medvedeva, A. Maslov and A. Vozbrannaya, 2018. Assessing the land and vegetation cover of abandoned fire hazardous and rewetted peatlands: comparing different multispectral satellite data. Land, 7(2):71.

Sjostedt, S.J., W.R. Leaitch, M. Levasseur, M. Scarratt, S. Michaud, J. Motard-Côté, J.H. Burkhart and J.P.D. Abbatt, 2012. Evidence for the uptake of atmospheric acetone and methanol by the Arctic Ocean during late summer DMS-Emission plumes. Journal of Geophysical Research: Atmospheres. 117:D12303.

Sjöström, J., F.V. Plathner and A. Granström, 2019. Wildfire ignition from forestry machines in boreal Sweden. International Journal of Wildland Fire, 28(9):666–677.

Skiles, S.M. and T. Painter, 2016. Daily evolution in dust and black carbon content, snow grain size, and snow albedo during snowmelt, Rocky Mountains, Colorado. Journal of Glaciology, 63(237):118–132.

Skjelkvåle, B.L., J. Aherne, T. Bergman, K. Bishop, M. Forsius, L. Forsström, N.A. Gashkina, J.-P. Hettelingh, D. Jeffries, Ø. Kaste, A. Korhola, A. Lappalainen, H. Laudon, J. Mannio, T. Moiseenko, M. Nyman, M. Posch, A.K. Schartau, J. Stoddard, J. Tammi, J. Vuorenmaa, A. Wilander and V. Yakovlev, 2006. Chapter 6: Effects on freshwater ecosystems. In: AMAP Assessment 2006: Acidifying Pollutants, Arctic Haze, and Acidification in the Arctic. Arctic Monitoring and Assessment Programme (AMAP), Oslo, Norway, pp. 64–90.

Skov, H.A.H. Egeløv, K. Granby and T. Nielsen, 1997. Relationships between ozone and other photochemical products at Ll. Valby, Denmark. Atmospheric Environment, 31(5):685–691.

Skov, H., J.H. Christensen, M.E. Goodsite, N.Z. Heidam, B. Jensen, P. Wåhlin and G. Geernaert, 2004. Fate of Elemental Mercury in the Arctic during Atmospheric Mercury Depletion Episodes and the Load of Atmospheric Mercury to the Arctic. Environmental Science and Technology 38(8):2373–2382.

Skov, H., J. Hjorth, C. Nordstrøm, B. Jensen, C. Christoffersen, M.B. Poulsen, J.B. Liisberg, D. Beddows, M. Dall'Osto and J.H. Christensen, 2020. The variability in gaseous elemental mercury at Villum Research Station, Station Nord, in North Greenland from 1999 to 2017. Atmospheric Chemistry and Physics, 20(21):13253–13265.

Smargiassi, A., E.A.L. Sidi, L.-E. Robert, C. Plante, M. Haddad, P. Gamache, R. Burnett, S. Goudreau, L. Liu, M. Fournier, E. Pelletier and I. Yankoty, 2020. Exposure to ambient air pollutants and the onset of dementia in Québec, Canada. Environmental Research, 190:109870.

Smirnov, A., B.N. Holben, I. Slutsker, D.M. Giles, C.R. McClain, T.F. Eck, S.M. Sakerin, A. Macke, P. Croot, G. Zibordi, P.K. Quinn, J. Sciare, S. Kinne, M. Harvey, T.J. Smyth, S. Piketh, T. Zielinski, A. Proshutinsky, J.I. Goes, N.B. Nelson, P. Larouche, V.F. Radionov, P. Goloub, K. Krishna Moorthy, R. Matarrese, E.J. Robertson and F. Jourdin, 2009. Maritime Aerosol Network as a component of Aerosol Robotic Network. Journal of Geophysical Research: Atmospheres, 114(D06204).

Smirnov, N.S., V.N. Korotkov and A.A. Romanovskaya, 2015. Black carbon emissions from wildfires on forest lands of the Russian Federation in 2007–2012. Russian Meteorology and Hydrology, 40:435–442.

Smith, C.J., R.J. Kramer, G. Myhre, K. Alterskjær, W. Collins, A. Sima, O. Boucher, J.-L. Dufresne, P. Nabat, M. Michou, S. Yukimoto, J. Cole, D. Paynter, H. Shiogama, F.M. O'Connor, E. Robertson, A. Wiltshire, T. Andrews, C. Hannay, R. Miller, L. Nazarenko, A. Kirkevåg, D. Olivié, S. Fiedler, A. Lewinschal, C. Mackallah, M. Dix, R. Pincus and P.M. Forster, 2020. Effective radiative forcing and adjustments in CMIP6 models, Atmospheric Chemistry and Physics, 20(16):9591–9618.

Sobhani, N., S. Kulkarni and G.R. Carmichael, 2018. Source sector and region contributions to black carbon and $PM_{2.5}$ in the Arctic. Atmospheric Chemistry and Physics, 18(24):18123–18148.

Sodemann, H., M. Pommier, S.R. Arnold, S.A. Monks, K. Stebel, J.F. Burkhart, J.W. Hair, G.S. Diskin, C. Clerbaux, P.-F. Coheur, D. Hurtmans, H. Schlager, A.-M. Blechschmidt, J.E. Kristjánsson and A. Stohl, 2011. Episodes of cross-polar transport in the Arctic troposphere during July 2008 as seen from models, satellite, and aircraft observations. Atmospheric Chemistry and Physics, 11(8):3631–3651.

Sofronov, M.A., A.V. Volokitina, T. Kajimoto, Y. Matsuura and S. Uemura, 2000. Zonal peculiarities of forest vegetation controlled by fires in northern Siberia. Eurasian Journal of Forest Research, 1:51–57.

Sofronov, M.A. and A.V. Volokitina, 2010. Wildfire ecology in continuous permafrost zone. In: Osawa, A., O.A. Zyryanova, Y. Matsuura, T. Kajimoto and R.W. Wein (Eds.). Permafrost Ecosystems – Siberian Larch Forests. Ecological Studies (Vol. 209). pp. 59–82. Springer.

Sokolik, I.N., A.J. Soja, P.J. DeMott and D. Winker, 2019. Progress and challenges in quantifying wildfire smoke emissions, their properties, transport, and atmospheric impacts. Journal of Geophysical Research: Atmospheres, 124(23):13005–13025.

Solazzo, E., R. Bianconi, R. Vautard, K.W. Appel, M.D. Moran, C. Hogrefe, B. Bessagnet, J. Brandt, J.H. Christensen, C. Chemel, I. Coll, H. Denier van der Gon, J. Ferreira, R. Forkel, X.V. Francis, G. Grell, P. Grossi, A.B. Hansen, A. Jeričević, L. Kraljević, A.I. Miranda, U. Nopmongcol, G. Pirovano, M. Prank, A. Riccio, K.N. Sartelet, M. Schaap, J.D. Silver, R.S. Sokhi, J. Vira, J. Werhahn, R. Wolke, G. Yarwood, J. Zhang, S.T. Rao and S. Galmarini, 2012. Model evaluation and ensemble modelling of surface-level ozone in Europe and North America in the context of AQMEII. Atmospheric Environment, 53:60–74.

Solazzo, E., M. Crippa, D. Guizzardi, M. Muntean, M. Choulga and G. Janssens-Maenhout, 2021. Uncertainties in the Emissions Database for Global Atmospheric Research (EDGAR) emission inventory of greenhouse gases. Atmospheric Chemistry and Physics, 21(7):5655–5683.

Solomon, P.A., D. Crumpler, J.B. Flanagan, R.K.M. Jayanty, E.E. Rickman and C.E. McDade, 2014. U.S. national $PM_{2.5}$ chemical speciation monitoring networks – CSN and IMPROVE: description of networks. Journal of the Air & Waste Management Association, 64(12):1410–1438.

Søreide, J.E., E. Leu, J. Berge, M. Graeve and S. Falk-Petersen, 2010. Timing of blooms, algal food quality and Calanus glacialis reproduction and growth in a changing Arctic. Global Change Biology, 16(11):3154–3163.

SOU, 2019. Betänkande av 2018 års skogsbrandsutredning: Skogsbränderna sommaren 2018. Statens offentliga utredningar (SOU) [In Swedish, translated as: Report of the 2018 forest fire investigation: forest fires in summer 2018. Swedish Government Official Reports (SOU)], Stockholm. 334pp.

Søvde, O.A., M.J. Prather, I.S.A. Isaksen, T.K. Berntsen, F. Stordal, X. Zhu, C.D. Holmes, J. Hsu, 2012. The chemical transport model Oslo CTM3. Geoscientific Model Development, 5(6):1441–1469.

Sparrow K.J. and J.D. Kessler, 2017. Efficient collection and preparation of methane from low concentration waters for natural abundance radiocarbon analysis. Limnology and Oceanography Methods, 15:601–617.

Sparrow, K.J., J.D. Kessler, J.R. Southon, F. Garcia-Tigreros, K.M. Schreiner, C.D. Ruppel, J.B. Miller, S.J. Lehman and X. Xu, 2018. Limited contribution of ancient methane to surface waters of the U.S. Beaufort Sea shelf. Science Advances, 4(1):eaao4842.

Spolaor, A., E. Barbaro, M. Mazzola, A.P. Viola, J. Lisok, F. Obleitner, K.M. Markowicz and D. Cappelletti, 2017. Determination of black carbon and nanoparticles along glaciers in the Spitsbergen (Svalbard) region exploiting a mobile platform. Atmospheric Environment, 170:184–196.

Stamnes, K., S.-C. Tsay, W.J. Wiscombe and I Laszlo, 2000. DISORT, a general-purpose Fortran program for discrete-ordinate-method radiative transfer in scattering and emitting layered media: documentation of methodology. NASA Technical Report, version 1.1.

Stanley, E.H., N.J. Casson, S.T. Christel, J.T. Crawford, L.C. Loken and S.K. Oliver, 2016. The ecology of methane in streams and rivers: patterns, controls, and global significance. Ecological Monographs, 86(2):146–171.

Statistics Norway, 2001. Uncertainties in emissions of long-range air pollutants. Reports 2001/37. Statistics Norway, Olso, Norway. 49pp.

Steinbach, J., H. Holmstrand, K. Shcherbakova, D. Kosmach, V. Brüchert, N. Shakhova, A. Salyuk, C.J. Sapart, D. Chernykh, R. Noormets, I. Semiletov and Ö. Gustafsson, 2021. Source apportionment of methane escaping the subsea permafrost system in the outer Eurasian Arctic Shelf. PNAS, 118(10): e2019672118.

Steinle, L., C.A. Graves, T. Treude, B. Ferré, A. Biastoch, I. Bussmann, C. Berndt, S. Krastel, R.H. James, E. Behrens, C.W. Böning, J. Greinert, C.-J. Sapart, M. Scheinert, S. Sommer, M.F. Lehmann and H. Niemann, 2015. Water column methanotrophy controlled by a rapid oceanographic switch. Nature Geoscience, 8:378–382.

Stengel, M., S. Stapelberg, O. Sus, C. Schlundt, C. Poulsen, G. Thomas, M. Christensen, C. Carbajal Henken, R. Preusker, J. Fischer, A. Devasthale, U. Willén, K.-G. Karlsson, G.R. McGarragh, S. Proud, A.C. Povey, R.G. Grainger, J. Fokke Meirink, A. Feofilov, R. Bennartz, J.S. Bojanowski and R. Hollmann, 2017. Cloud property datasets retrieved from AVHRR, MODIS, AATSR and MERIS in the framework of the Cloud_cci project. Earth System Science Data, 9(2):881–904.

Stephens, M., N. Turner and J. Sandberg, 2003. Particle identification by laser-induced incandescence in a solid-state laser cavity. Applied Optics, 42(19):3726–3736.

Stettler, M.E.J., S. Eastham and S.R.H. Barrett, 2011. Air quality and public health impacts of UK airports. Part I: emissions. Atmospheric Environment, 45(31):5415–5424.

Stevens, B., M. Giorgetta, M. Esch, T. Mauritsen, T. Crueger, S. Rast, M. Salzmann, H. Schmidt, J. Bader, K. Block, R. Brokopf, I. Fast, S. Kinne, L. Kornblueh, U. Lohmann, R. Pincus, T. Reichler and E. Roeckner, 2013. Atmospheric component of the MPI-M earth system model: ECHAM6. Journal of Advances in Modeling Earth Systems, 5(2):146–172.

Stevenson, D.S., P.J. Young, V. Naik, J.-F. Lamarque, D.T. Shindell, A. Voulgarakis, R.B. Skeie, S.B. Dalsoren, G. Myhre, T.K. Berntsen, G.A. Folberth, S.T. Rumbold, W.J. Collins, I.A. MacKenzie, R.M. Doherty, G. Zeng, T.P.C. van Noije, A. Strunk, D. Bergmann, P. Cameron-Smith, D.A. Plummer, S.A. Strode, L. Horowitz, Y.H. Lee, S. Szopa, K. Sudo, T. Nagashima, B. Josse, I. Cionni, M. Righi, V. Eyring, A. Conley, K.W. Bowman, O. Wild and A. Archibald, 2013. Tropospheric ozone changes, radiative forcing and attribution to emissions in the Atmospheric Chemistry and Climate Model Intercomparison Project (ACCMIP). Atmospheric Chemistry and Physics, 13(6):3063–3085.

Stier, P., J. Feichter, S. Kinne, S. Kloster, E. Vignati, J. Wilson, L. Ganzeveld, I. Tegen, M. Werner, Y. Balkanski, M. Schulz, O. Boucher, A. Minikin and A. Petzold, 2005. The aerosol-climate model ECHAM5-HAM. Atmospheric Chemistry and Physics, 5(4):1125–1156.

Stjern, C.W., B.H. Samset, G. Myhre, P.M. Forster, Ø. Hodnebrog, T. Andrews, O. Boucher, G. Faluvegi, T. Iversen, M. Kasoar, V. Kharin, A.Kirkevåg, J.-F. Lamarque, D. Olivié, T. Richardson, D. Shawki, D. Shindell, C.J. Smith, T. Takemura and A. Voulgarakis, 2017. Rapid adjustments cause weak surface temperature response to increased black carbon concentrations. Journal of Geophysical Research: Atmospheres, 122(21):11,462–11,481.

Stjern, C.W., M.T. Lund, B.H. Samset, G. Myhre, P.M. Forster, T. Andrews, O. Boucher, G. Faluvegi, D. Fläschner, T. Iversen, M. Kasoar, V. Kharin, A. Kirkevåg, J.-F. Lamarque, D. Olivié, T. Richardson, M. Sand, D. Shawki, D. Shindell, C.J. Smith, T. Takemura and A. Voulgarakis, 2019. Arctic amplification response to individual climate drivers. Journal of Geophysical Research: Atmospheres, 124(13):6698–6717.

Stohl, A., 2006. Characteristics of atmospheric transport into the Arctic troposphere. Journal of Geophysical Research: Atmospheres, 111(D11).

Stohl, A., C. Forster, A. Frank, P. Seibert and G. Wotawa, 2005. Technical note: The Lagrangian particle dispersion model FLEXPART version 6.2. Atmospheric Chemistry and Physics, 5(9):2461–2474.

Stohl, A., Z. Klimont, S. Eckhardt, K. Kupiainen, V.P. Shevchenko, V.M. Kopeikin and A.N. Novigatsky, 2013. Black carbon in the Arctic: the underestimated role of gas flaring and residential combustion emissions. Atmospheric Chemistry and Physics, 13(17):8833–8855.

Stohl, A., B. Aamaas, M. Amann, L.H. Baker, N. Bellouin, T.K. Berntsen, O. Boucher, R. Cherian, W. Collins, N. Daskalakis, M. Dusinska, S. Eckhardt, J.S. Fuglestvedt, M. Harju, C. Heyes, Ø. Hodnebrog, J. Hao, U. Im, M. Kanakidou, Z. Klimont, K. Kupiainen, K.S. Law, M.T. Lund, R. Maas, C.R. MacIntosh, G. Myhre, S. Myriokefalitakis, D. Olivié, J. Quaas, B. Quennehen, J.-C. Raut, S.T. Rumbold, B.H. Samset, M. Schulz, Ø. Seland, K.P. Shine, R.B. Skeie, S. Wang, K.E. Yttri and T. Zhu, 2015. Evaluating the climate and air quality impacts of short-lived pollutants. Atmospheric Chemistry and Physics, 15(18):10529–10566.

Stone, R.S., S. Sharma, A. Herber, K. Eleftheriadis and D. W. Nelson, 2014. A characterization of Arctic aerosols on the basis of aerosol optical depth and black carbon measurements. Elementa: Science of the Antthropocene, 2(27).

Stralberg, D., X. Wang, M.-A. Parisien, F.-N. Robinne, P. Sólymos, C.L. Mahon, S.E. Nielsen and E.M. Bayne, 2018. Wildfire-mediated vegetation change in boreal forests of Alberta, Canada. Ecosphere, 9(3):e02156.

Stranne, C., M. O'Regan and M. Jakobsson, 2017. Modeling fracture propagation and seafloor gas release during seafloor warming-induced hydrate dissociation. Geophysical Research Letters, 44(16):8510–8519.

Stranne, C., M. O'Regan, M. Jakobsson, V. Brüchert and M. Ketzer, 2019. Can anaerobic oxidation of methane prevent seafloor gas escape in a warming climate? Solid Earth, 10(5):1541–1554.

Ström, L., A. Ekberg, M. Mastepanov and T.R. Christensen, 2003. The effect of vascular plants on carbon turnover and methane emissions from a tundra wetland. Global Change Biology, 9(8):1185–1192.

Stroud, C.A., P.A. Makar, J. Zhang, M.D Moran, A. Akingunola, S.-M. Li, A. Leithead, K. Hayden and M. Siu, 2018. Improving air quality model predictions of organic species using measurement-derived organic gaseous and particle emissions in a petrochemical-dominated region, Atmospheric Chemistry and Physics, 18(18), 13531–13545.

Struthers, H., A.M.L. Ekman, P. Glantz, T. Iversen, A. Kirkevåg, E.M. Mårtensson, Ø. Seland and E.D. Nilsson, 2011. The effect of sea ice loss on sea salt aerosol concentrations and the radiative balance of the Arctic. Atmospheric Chemistry and Physics, 11(7):3459–3477.

Sultan, N., A. Plaza-Faverola, S. Vadakkepuliyambatta, S. Buenz and J. Knies, 2020. Impact of tides and sea-level on deep-sea Arctic methane emissions. Nature Communications, 11:5087.

Super, I., S.N.C. Dellaert, A.J.H. Visschedijk and H.A.C. Denier van der Gon, 2020. Uncertainty analysis of a European high-resolution emission inventory of CO_2 and CO to support inverse modelling and network design. Atmospheric Chemistry and Physics, 20(3):1795–1816.

Svensson, J., J. Ström, M. Hansson, H. Lihavainen and V.-M. Kerminen, 2013. Observed metre scale horizontal variability of elemental carbon in surface snow. Environmental Research Letters, 8(3):034012.

Svensson, J., J. Ström, N. Kivekäs, N.B. Dkhar, S. Tayal, V.P. Sharma, A. Jutila, J. Backman, A. Virkkula, M. Ruppel, A. Hyvärinen, A. Kontu, H.-R. Hannula, M. Leppäranta, R.K. Hooda, A. Korhola, E. Asmi and H. Lihavainen, 2018. Light-absorption of dust and elemental carbon in snow in the Indian Himalayas and the Finnish Arctic. Atmospheric Measurement Techniques, 11(3):1403–1416.

Svensson, J., J. Ström and A. Virkkula, 2019. Multiple-scattering correction factor of quartz filters and the effect of filtering particles mixed in water: implications for analyses of light absorption in snow samples. Atmospheric Measurement Techniques, 12(11):5913–5925.

Szidat, S., T.M. Jenk, H.W. Gäggeler, H.-A. Synal, I. Hajdas, G. Bonani and M. Saurer, 2004. THEODORE, a two-step heating system for the EC/OC determination of radiocarbon (^{14}C) in the environment. Nuclear Instruments and Methods in Physics Research Section B: Beam Interactions with Materials and Atoms, 223–224:829–836.

Szyszkowicz, M., T. Kousha, J. Castner and R. Dales, 2018. Air pollution and emergency department visits for respiratory diseases: a multi-city case crossover study. Environmental Research, 163:263–269.

Szyszkowicz, M., R. Zemek, I. Colman, W. Gardner, T. Kousha and M. Smith-Doiron, 2020. Air pollution and emergency department visits for mental disorders among youth. International Journal of Environmental Research and Public Health, 17(12):4190.

Taj, T., A.H. Poulsen, M. Ketzel, C. Geels, J. Brandt, J.H. Christensen, R. Puett, U.A. Hvidtfeldt, M. Sørensen and O. Raaschou-Nielsen, 2020a. Long-term exposure to $PM_{2.5}$ and its constituents and risk of Non-Hodgkin lymphoma in Denmark: a population-based case-control study. Environmental Research, 188:109762.

Taj, T., A.H. Poulsen, M. Ketzel, C. Geels, J. Brandt, J.H. Christensen, R. Puett, U.A. Hvidtfeldt, M. Sørensen and O. Raaschou-Nielsen, 2020b. Long-term exposure to air pollution and risk of non-Hodgkin lymphoma in Denmark: a population-based case-control study. International Journal of Cancer, 147(7):1874–1880.

Taketani, F., T. Miyakawa, H. Takashima, Y. Komazaki, X. Pan, Y. Kanaya and J. Inoue, 2016. Shipborne observations of atmospheric black carbon aerosol particles over the Arctic Ocean, Bering Sea, and North Pacific Ocean during September 2014. Journal of Geophysical Research: Atmospheres, 121(4):1914–1921.

Tan, Z. and Q. Zhuang, 2015a. Arctic lakes are continuous methane sources to the atmosphere under warming conditions. Environmental Research Letters, 10(5):054016.

Tan, Z. and Q. Zhuang, 2015b. Methane emissions from pan-Arctic lakes during the 21st century: An analysis with process-based models of lake evolution and biogeochemistry. Journal of Geophysical Research: Biogeosciences, 120(12):2641–2653.

Tan, Z., Q. Zhuang and K. Walter Anthony, 2015. Modeling methane emissions from Arctic lakes: model development and site-level study. Journal of Advances in Modeling Earth Systems, 7(2):459–483.

Tan, J., J.S. Fu, F. Dentener, J. Sun, L. Emmons, S. Tilmes, K. Sudo, J. Flemming, J.E. Jonson, S. Gravel, H. Bian, Y. Davila, D.K. Henze,

M.T. Lund, T. Kucsera, T. Takemura and T. Keating, 2018. Multi-model study of HTAP II on sulfur and nitrogen deposition. Atmospheric Chemistry and Physics, 18:6847–6866.

Tarasick, D.W., J. Davies, H.G.J. Smit and S.J. Oltmans, 2016. A re-evaluated Canadian ozonesonde record: measurements of the vertical distribution of ozone over Canada from 1966 to 2013. Atmospheric Measurement Techniques, 9(1):195–214.

Tarasick, D., I.E. Galbally, O.R. Cooper, M.G. Schultz, G. Ancellet, T. Leblanc, T.J. Wallington, J. Ziemke, X. Liu, M. Steinbacher, J. Staehelin, C. Vigouroux, J.W. Hannigan, O. García, G. Foret, P. Zanis, E. Weatherhead, I. Petropavlovskikh, H. Worden, M. Osman, J. Liu, K.-L. Chang, A. Gaudel, M. Lin, M. Granados-Muñoz, A.M. Thompson, S.J. Oltmans, J. Cuesta, G. Dufour, V. Thouret, B. Hassler, T. Trickl and J.L. Neu, 2019. Tropospheric Ozone Assessment Report: Tropospheric ozone from 1877 to 2016, observed levels, trends and uncertainties. Elementa: Science of the Anthropocene, 7:39.

Taylor, K.E., M. Crucifix, P. Braconnot, C.D. Hewitt, C. Doutriaux, A.J. Broccoli, J.F.B. Mitchell and M.J. Webb, 2007. Estimating shortwave radiative forcing and response in climate models. Journal of Climate, 20(11):2530–2543.

Taylor, P.C., S. Kato, K.-M. Xu and M. Cai, 2015. Covariance between Arctic sea ice and clouds within atmospheric state regimes at the satellite footprint level. Journal of Geophysical Research: Atmospheres, 120(24):12656–12678.

Tchebakova, N.M., V.V. Chuprova, E.I. Parfenova, A.J. Soja and G.I. Lysanova, 2016. Evaluating the agroclimatic potential of Central Siberia. In: Mueller, L., A.K. Sheudshen and F. Eulenstein (Eds.). Novel Methods for Monitoring and Managing Land and Water Resources in Siberia. Springer Water. pp. 287–305. Springer.

Tegen, I., D. Neubauer, S. Ferrachat, C. Siegenthaler-Le Drian, I. Bey, N. Schutgens, P. Stier, D. Watson-Parris, T. Stanelle, H. Schmidt, S. Rast, H. Kokkola, M. Schultz, S. Schroeder, N. Daskalakis, S. Barthel, B. Heinold and U. Lohmann, 2019. The global aerosol–climate model ECHAM6.3–HAM2.3 – part 1: aerosol evaluation. Geoscientific Model Development, 12(4):1643–1677.

Terrier, A., M.P. Girardin, C. Périé, P. Legendre and Y. Bergeron, 2013. Potential changes in forest composition could reduce impacts of climate change on boreal wildfires. Ecological Applications, 23(1):21–35.

Tesdal, J.-E., J.R. Christian, A.H. Monahan and K. von Salzen, 2016. Sensitivity of modelled sulfate aerosol and its radiative effect on climate to ocean DMS concentration and air–sea flux, Atmospheric Chemistry and Physics, 16:10847–10864.

Teufel, B. and L. Sushama, 2019. Abrupt changes across the Arctic permafrost region endanger northern development. Nature Climate Change, 9:858–862.

Theesfeld, I. and L. Jelinek, 2017. A misfit in policy to protect Russia's black soil region. An institutional analytical lens applied to the ban on burning of crop residues. Land Use Policy, 67:517–526.

Thomas, G.E., C.A. Poulsen, A.M. Sayer, S.H. Marsh, S.M. Dean, E. Carboni, R. Siddans, R.G. Grainger, B.N. Lawrence, 2009. The GRAPE aerosol retrieval algorithm, Atmospheric Measurement Techniques, 2(2):679–701.

Thomas, J.L., J.-C. Raut, K.S. Law, L. Marelle, G. Ancellet, F. Ravetta, J.D. Fast, G. Pfister, L.K. Emmons, G.S. Diskin, A. Weinheimer, A. Roiger and H. Schlager, 2013. Pollution transport from North America to Greenland during summer 2008. Atmospheric Chemistry and Physics, 13(7):3825–3848.

Thomas, M.A., M. Kahnert, C. Andersson, H. Kokkola, U. Hansson, C. Jones, J. Langner and A. Devasthale, 2015. Integration of prognostic aerosol–cloud interactions in a chemistry transport model coupled offline to a regional climate model. Geoscientific Model Development, 8(6):1885–1898.

Thomas, J.L., C.M. Polashenski, A.J. Soja, L. Marelle, K.A. Casey, H.D. Choi, J.-C. Raut, C. Wiedinmyer, L.K. Emmons, J.D. Fast, J. Pelon, K.S. Law, M.G. Flanner and J.E. Dibb, 2017. Quantifying black carbon deposition over the Greenland ice sheet from forest fires in Canada. Geophysical Research Letters, 44(15):7965–7974.

Thomas, J.L., J. Stutz, M.M. Frey, T. Bartels-Rausch, K. Altieri, F. Baladima, J. Browse, M. Dall'Osto, L. Marelle, J. Mouginot, J.G. Murphy, D. Nomura, K.A. Pratt, M.D. Willis, P. Zieger, J. Abbatt, T.A. Douglas, M.C. Facchini, J. France, A.E. Jones, K. Kim, P.A. Matrai, V.F. McNeill, A. Saiz-Lopez, P. Shepson, N. Steiner, K.S. Law, S.R. Arnold, B. Delille, J. Schmale, J.E. Sonke, A. Dommergue, D. Voisin, M.L. Melamed and J. Gier, 2019a. Fostering multidisciplinary research on interactions between chemistry, biology, and physics within the coupled cryosphere-atmosphere system. Elementa: Science of the Anthropocene, 7:58.

Thomas, M.A., A. Devasthale, M. Tjernström and A.M.L. Ekman, 2019b. The relation between aerosol vertical distribution and temperature inversions in the Arctic in winter and spring. Geophysical Research Letters, 46(5):2836–2845.

Thomason, L.W, 2012. Toward a combined SAGE II-HALOE aerosol climatology: an evaluation of HALOE version 19 stratospheric aerosol extinction coefficient observations. Atmospheric Chemistry and Physics, 12(17):8177–8188.

Thomason, L.W., N. Ernest, L. Millán, L. Rieger, A. Bourassa, J.-P. Vernier, G. Manney, B. Luo, F. Arfeuille and T. Peter, 2018. A global space-based stratospheric aerosol climatology: 1979–2016. Earth System Science Data, 10(1):469–492.

Thompson, D.K. and K. Morrison, 2020. A classification scheme to determine wildfires from the satellite record in the cool grasslands of southern Canada: considerations for fire occurrence modelling and warning criteria. Natural Hazards and Earth System Sciences, 20(12):3439–3454.

Thompson, D.K., B.N. Simpson, E. Whitman, Q.E. Barber and M.-A. Parisien, 2019. Peatland hydrological dynamics as a driver of landscape connectivity and fire activity in the boreal plain of Canada. Forests, 10(7):534.

Thonat, T., M. Saunois, P. Bousquet, I. Pison, Z. Tan, Q. Zhuang, P.M. Crill, B.F. Thornton, D. Bastviken, E.J. Dlugokencky, N. Zimov, T. Laurila, J. Hatakka, O. Hermansen, and D.E.J. Worthy, 2017. Detectability of Arctic methane sources at six sites performing continuous atmospheric measurements. Atmospheric Chemistry and Physics, 17:8371–8394.

Thonat, T., M. Saunois, I. Pison, A. Berchet, T. Hocking, B.F. Thornton, P.M. Crill and P. Bousquet, 2019. Assessment of the theoretical limit in instrumental detectability of northern high-latitude methane sources using $\delta^{13}C_{CH4}$ atmospheric signals. Atmospheric Chemistry and Physics, 19:12141–12161.

Thornhill, G.D., W.J. Collins, R.J. Kramer, D. Olivié, R.B. Skeie, F.M. O'Connor, N.L. Abraham, R. Checa-Garcia, S.E. Bauer, M. Deushi, L.K. Emmons, P.M. Forster, L.W. Horowitz, B. Johnson, J. Keeble, J.-F. Lamarque, M. Michou, M.J. Mills, J.P. Mulcahy, G. Myhre, P. Nabat, V. Naik, N. Oshima, M. Schulz, C.J. Smith, T. Takemura, S. Tilmes, T. Wu, G. Zeng and J. Zhang, 2021. Effective radiative forcing from emissions of reactive gases and aerosols – a multi-model comparison. Atmospheric Chemistry and Physics, 21(2):853–874.

Thornton, B.F., M. Wik and P.M. Crill, 2015. Climate-forced changes in available energy and methane bubbling from subarctic lakes. Geophysical Research Letters, 42(6):1936–1942.

Thornton, B.F., M. Wik and P.M. Crill, 2016a. Double counting challenges the accuracy of high latitude methane inventories. Geophysical Research Letters, 43(24):12,569–12,577.

Thornton, B.F., M.C. Geibel, P.M. Crill, C. Humborg and C.-M. Mörth, 2016b. Methane fluxes from the sea to the atmosphere across the Siberian shelf seas. Geophysical Research Letters, 43(11):5869–5877.

Thornton, B.F., J. Prytherch, K. Andersson, I.M. Brooks, D. Salisbury, M. Tjernström and P.M. Crill, 2020. Shipborne eddy covariance observations of methane fluxes constrain Arctic sea emissions. Science Advances, 6(5):eaay7934.

Thorp, T., S.R. Arnold, R.J. Pope, D.V. Spracklen, L. Conibear, C. Knote, M. Arshinov, B. Belan, E. Asmi, T. Laurila, A.I. Skorokhod, T. Nieminen and T. Petäjä, 2021. Late-spring and summertime tropospheric ozone and NO_2 in western Siberia and the Russian Arctic: regional model evaluation and sensitivities. Atmospheric Chemistry and Physics, 21:4677–4697.

Thygesen, M., G.J. Holst, B. Hansen, C. Geels, A. Kalkbrenner, D. Schendel, J. Brandt, C.B. Pedersen and S. Dalsgaard, 2020. Exposure to air pollution in early childhood and the association with attention-deficit hyperactivity disorder. Environmental Research, 183:108930.

Tilmes, S., A. Hodzic, L.K Emmons, M.J. Mills, A. Gettelman, D.E. Kinnison, M. Park, J.-F. Lamarque, F. Vitt, M. Shrivastava, P. Campuzano-Jost, J.L. Jiminez and X. Liu, 2019. Climate forcing and trends of organic aerosols in the Community Earth System Model (CESM2). Journal of Advances in Modeling Earth Systems, 11(12):4323–4351.

Tobo, Y., K. Adachi, P.J. DeMott, T.C.J. Hill, D.S. Hamilton, N.M. Mahowald, N. Nagatsuka, S. Ohata, J. Uetake, Y. Kondo and M. Koike, 2019. Glacially sourced dust as a potentially significant source of ice nucleating particles. Nature Geoscience, 12:253–258.

Tohjima, Y., J. Zeng, T. Shirai, Y. Niwa, S. Ishidoya, F. Taketani, D. Sasano, N. Kosugi, S. Kameyama, H. Takashima, H. Nara and S. Morimoto, 2021. Estimation of CH_4 emissions from the East Siberian Arctic Shelf based on atmospheric observations aboard the R/V Mirai during fall cruises from 2012 to 2017. Polar Science, 27:100571.

Tomasi C., A. Lupi, M. Mazzola, R.S. Stone, E.G. Dutton, A. Herber V.F. Radionov, B. Holben, M. Sorokin, S.M. Sakerin, S.A. Terpugova, P.S. Sobolewski, C. Lanconelli, B.H. Petkov, M. Busetto and V. Vitale, 2012. An update on polar aerosol optical properties using POLAR-AOD and other measurements performed during in International Polar Year, Atmospheric Environment, 52:29–47.

Tomasi, C., A.A Kokhanovsky, A. Lupi, C. Ritter, A. Smirnov, N.T. O'Neill, R.S. Stone, B.N. Holben, S. Nyeki, C. Wehrli, A. Stohl, M. Mazzola, C. Lanconelli, V. Vitale, K. Stebel, V. Aaltonen, G. de Leeuw, E. Rodriguez, A.B. Herber, V.F. Radionov, T. Zielinski, T. Petelski, S.M. Sakerin, D.M. Kabanov, Y. Xue, L. Mei, L. Istomina, R. Wagener, B. McArthur, P.S. Sobolewski, R. Kivi, Y. Courcoux, P. Larouche, S. Broccardo and S.J. Piketh, 2015. Aerosol remote sensing in polar regions. Earth-Science Reviews, 140:108–157.

Tonneijck, A.E.G., J. Franzaring, G. Brouwer, K. Metselaar and Th.A. Dueck, 2004. Does interspecific competition alter effects of early season ozone exposure on plants from wet grasslands? Results of a three-year experiment in open-top chambers. Environmental Pollution, 131(2):205–213.

Toom-Sauntry, D. and L.A. Barrie, 2002. Chemical composition of snowfall in the high Arctic: 1990–1994. Atmospheric Environment 36(15–16):2683–2693.

Tørseth, K., W. Aas, K. Breivik, A.M. Fjæraa, M. Fiebig, A.G. Hjellbrekke, C. Lund Myhre, S. Solberg and K.E. Yttri, 2012. Introduction to the European Monitoring and Evaluation Programme (EMEP) and observed atmospheric composition change during 1972–2009. Atmospheric Chemistry and Physics, 12(12):5447–5481.

Travis, K.R., D.J. Jacob, J.A. Fisher, P.S. Kim, E.A. Marais, L. Zhu, K. Yu, C.C. Miller, R.M. Yantosca, M.P. Sulprizio, A.M. Thompson, P.O. Wennberg, J.D. Crounse, J.M. St. Clair, R.C. Cohen, J.L. Laughner, J.E. Dibb, S.R. Hall, K. Ullmann, G.M. Wolfe, J.A. Neuman and X. Zhou, 2016. Why do models overestimate surface ozone in the Southeast United States? Atmospheric Chemistry and Physics, 16(21):13561–13577.

Treat, C.C., S.M. Natali, J. Ernakovich, C.M. Iversen, M. Lupascu, A.D. McGuire, R.J. Norby, T. Roy Chowdhury, A. Richter, H. Šantrůčková, C. Schädel, E.A.G. Schuur, V.L. Sloan, M.R. Turetsky and M.P. Waldrop, 2015. A pan-Arctic synthesis of CH_4 and CO_2 production from anoxic soil incubations. Global Change Biology, 21(7):2787–2803.

Treat, C.C., A.A. Bloom and M.E. Marushchak, 2018a. Nongrowing season methane emissions – a significant component of annual emissions across northern ecosystems. Global Change Biology, 24(8):3331–3343.

Treat, C.C., M.E. Marushchak, C. Voigt, Y. Zhang, Z. Tan, Q. Zhuang, T.A. Virtanen, A. Räsänen, C. Biasi, G. Hugelius, D. Kaverin, P.A. Miller, M. Stendel, V. Romanovsky, F. Rivkin, P.J. Martikainen and N.J. Shurpali, 2018b. Tundra landscape heterogeneity, not interannual variability, controls the decadal regional carbon balance in the Western Russian Arctic. Global Change Biology, 24(11):5188–5204.

Trenberth, K.E., 1998. Atmospheric moisture residence times and cycling: implications for rainfall rates and climate change. Climatic Change, 39:667–694.

Tsigaridis, K. and M. Kanakidou, 2007. Secondary organic aerosol importance in the future atmosphere. Atmospheric Environment, 41(22):4682–4692.

Tsigaridis, K., D. Koch and S. Menon, 2013. Uncertainties and importance of sea spray composition on aerosol direct and indirect effects. Journal of Geophysical Research: Atmospheres, 118(1):220–235.

Tuccella, P., J.L. Thomas, K.S. Law, J.-C. Raut, L. Marelle, A. Roiger, B. Weinzierl, H.A.C. Denier van der Gon, H. Schlager and T. Onishi, 2017. Air pollution impacts due to petroleum extraction in the Norwegian Sea during the ACCESS aircraft campaign. Elementa: Science of the Anthropocene, 5:25.

Tunved, P., J. Ström and R. Krejci, 2013. Arctic aerosol life cycle: linking aerosol size distributions observed between 2000 and 2010 with air mass transport and precipitation at Zeppelin station, Ny-Ålesund, Svalbard. Atmospheric Chemistry and Physics, 13(7):3643–3660.

Turetsky, M.R., B. Benscoter, S. Page, G. Rein, G.R. van der Werf and A. Watts, 2015. Global vulnerability of peatlands to fire and carbon loss. Nature Geoscience, 8:11–14.

Turetsky, M.R., B.W. Abbott, M.C. Jones, K. Walter Anthony, D. Olefeldt, E.A.G. Schuur, G. Grosse, P. Kuhry, G. Hugelius, C. Koven, D.M. Lawrence, C. Gibson, A.B.K. Sannel and A.D. McGuire, 2020. Carbon release through abrupt permafrost thaw. Nature Geoscience, 13:138–143.

Turner, D.R., I.-M. Hassellöv, E. Ytreberg and A. Rutgersson, 2017. Shipping and the environment: smokestack emissions, scrubbers and unregulated oceanic consequences. Elementa: Science of the Anthropocene, 5:45.

Turner, A.J., C. Frankenberg and E.A. Kort, 2019. Interpreting contemporary trends in atmospheric methane. PNAS, 116(8):2805–2813.

Turnock, S.T., O. Wild, F.J. Dentener, Y. Davila, L.K. Emmons, J. Flemming, G.A. Folberth, D.K. Henze, J.E. Jonson, T.J. Keating, S. Kengo, M. Lin, M. Lund, S. Tilmes and F.M. O'Connor, 2018. The impact of future emission policies on tropospheric ozone using a parameterised approach. Atmospheric Chemistry and Physics, 18(12):8953–8978.

Turnock, S. T., O. Wild, A. Sellar and F.M. O'Connor, 2019. 300 years of tropospheric ozone changes using CMIP6 scenarios with a parameterised approach. Atmospheric Environment, 213:686–698.

Tuzet, F., M. Dumont, L. Arnaud, D. Voisin, M. Lamare, F. Larue, J. Revuelto and G. Picard, 2019. Influence of light-absorbing particles on snow spectral irradiance profiles. The Cryosphere, 13(8):2169–2187.

Udisti, R., A. Bazzano, S. Becagli, E. Bolzacchini, L. Caiazzo, D. Cappelletti, L. Ferrero, D. Frosini, F. Giardi, Marco Grotti, A. Lupi, M. Malandrino, M. Mazzola, B. Moroni, M. Severi, R. Traversi, A.P. Viola and V. Vitale, 2016. Sulfate source apportionment in the Ny-Ålesund (Svalbard Islands) Arctic aerosol. Rendiconti Lincei: Scienze Fisiche e Naturali, 27(1):85–94.

UN and WHO, 2003. Modelling and assessment of the health impact of particulate matter and ozone: summary report. Joint Task Force on the Health Aspects of Long-range Transboundary Air Pollution (United Nations (UN) Economic Commission for Europe) and World Health Organization (WHO), 2003. 6th meeting of the Task Force on the Health Aspects of Air Pollution. 22–23 May 2003, Bonn, Germany. 15pp.

UNEP, 1997. World Atlas of Desertification. United Nations Environment Programme, 2nd ed., Arnold, London.

Urbanski, S., 2014. Wildland fire emissions, carbon, and climate: emission factors. Forest Ecology and Management, 317:51–60.

US EPA, 2012. Report to Congress on Black Carbon. United States Environmental Protection Agency (US EPA), Washington, DC. xxx + 351pp.

US EPA, 2019. Integrated Science Assessment for Particulate Matter. United States Environmental Protection Agency (US EPA), Washington, DC. lxxxviii + 1668pp.

US EPA, 2020. Integrated Science Assessment for Ozone and Related Photochemical Oxidants. United States Environmental Protection Agency (US EPA), Washington, DC. lxxvi + 1240pp.

USGS, 2009. Snowpack Chemistry Monitoring Protocol for the Rocky Mountain Network; Narrative and Standard Operating Procedures. Administrative Report, 2009. United States Geological Service (USGS), Reston, Virginia, USA. vii + 47pp.

Val Martin, M., R.A. Kahn and M.G. Tosca, 2018. A global analysis of wildfire smoke injection heights derived from space-based multi-angle imaging. Remote Sensing, 10(10):1609.

Valentine, D.L., D.C. Blanton, W.S. Reeburgh and M. Kastner, 2001. Water column methane oxidation adjacent to an area of active hydrate dissociation, Eel river basin. Geochimica et Cosmochimica Acta, 65(16):2633–2640. https://doi.org/10.1016/S0016-7037(01)00625-1

Van Dam, B., D. Helmig, P.V. Doskey and S.J. Oltmans, 2016. Summertime surface O3 behavior and deposition to tundra in the Alaskan Arctic. Journal of Geophysical Research: Atmospheres, 121(13):8055–8066.

van den Berg, L.J.L., C.J.H. Peters, M.R. Ashmore and J.G.M. Roelofs, 2008. Reduced nitrogen has a greater effect than oxidised nitrogen on dry heathland vegetation. Environmental Pollution, 154(3):359–369.

van der Werf, G.R., J.T. Randerson, L. Giglio, T.T. van Leeuwen, Y. Chen, B.M. Rogers, M. Mu, M.J.E. van Marle, D.C. Morton, G.J. Collatz, R.J. Yokelson and P.S. Kasibhatia, 2017. Global fire emissions estimates during 1997–2016. Earth System Science Data, 9(2):697–720.

Van Dingenen, R., F.J. Dentener, F. Raes, M.C. Krol, L. Emberson and J. Cofala, 2009. The global impact of ozone on agricultural crop yields under current and future air quality legislation. Atmospheric Environment, 43(3):604–618.

Van Dingenen, R., F. Dentener, M. Crippa, J. Leitao, E. Marmer, S. Rao, E. Solazzo and L. Valentini, 2018. TM5-FASST: a global atmospheric source-receptor model for rapid impact analysis of emission changes on air quality and short-lived climate pollutants. Atmospheric Chemistry and Physics, 18(21):16173–16211.

van Donkelaar, A., R.V. Martin, M. Brauer and B.L. Boys, 2015a. Use of satellite observations for long-term exposure assessment of global concentrations of fine particulate matter. Environmental Health Perspectives, 123(2):135–143.

van Donkelaar, A., R.V. Martin, R.J.D. Spurr and R.T. Burnett, 2015b. High-resolution satellite-derived $PM_{2.5}$ from optimal estimation and geographically weighted regression over North America. Environmental Science & Technology, 49(17):10482–10491.

van Leeuwen, T.T., G.R. van der Werf, A.A. Hoffmann, R.G. Detmers, G. Rücker, N.H.F. French, S. Archibald, J.A. Carvalho Jr., G.D. Cook, W.J. de Groot, C. Hély, E.S. Kasischke, S. Kloster, J.L. McCarty, M.L. Pettinari, P. Savadogo, E.C. Alvarado, L. Boschetti, S. Manuri, C.P. Meyer, F. Siegert, L.A. Trollope and W.S.W. Trollope, 2014. Biomass burning fuel consumption rates: a field measurement database. Biogeosciences, 11(24):7305–7329.

van Marle, M.J.E., S. Kloster, B.I. Magi, J.R. Marlon, A.-L. Daniau, R.D. Field, A. Arneth, M. Forrest, S. Hantson, N.M. Kehrwald, W. Knorr, G. Lasslop, F. Li, S. Mangeon, C. Yue, J.W. Kaiser and G.R. van der Werf, 2017. Historic global biomass burning emissions for CMIP6 (BB4CMIP) based on merging satellite observations with proxies and fire models (1750–2015). Geoscientific Model Development, 10(9):3329–3357.

Vavrus, S.J., M.M. Holland and D.A. Bailey, 2011. Changes in Arctic clouds during intervals of rapid sea ice loss. Climate Dynamics, 36(7):1475–1489.

Veefkind, J.P. and G. de Leeuw, 1998. A new algorithm to determine the spectral aerosol optical depth from satellite radiometer measurements. Journal of Aerosol Science, 29(10):1237–1248.

Veira, A., G. Lasslop and S. Kloster, 2016. Wildfires in a warmer climate: emission fluxes, emission heights, and black carbon concentrations in 2090–2099. Journal of Geophysical Research: Atmospheres, 121(7):3195–3223.

Venäläinen, A., I. Lehtonen, M. Laapas, K. Ruosteenoja, O.-P. Tikkanen, H. Viiri, V.-P. Ikonen and H. Peltola, 2020. Climate change induces multiple risks to boreal forests and forestry in Finland: A literature review. Global Change Biology, 26(8):4178–4196.

Veraverbeke, S., B.M. Rogers, M.L. Goulden, R.R. Jandt, C.E. Miller, E.B. Wiggins and J.T. Randerson, 2017. Lightning as a major driver of recent large fire years in North American boreal forests. Nature Climate Change, 7:529–534.

Verstraeten, W.W., K.F. Boersma, J. Zörner, M.A.F. Allaart, K.W. Bowman and J.R. Worden, 2013. Validation of six years of TES tropospheric ozone retrievals with ozonesonde measurements: implications for spatial patterns and temporal stability in the bias. Atmospheric Measurement Techniques, 6(5):1413–1423.

Vet, R., R.S. Artz, S. Carou, M. Shaw, C.-U. Ro, W. Aas, A. Baker, V.C. Bowersox, F. Dentener, C. Galy-Lacaux, A. Hou, J.J Pienaar, R. Gillett, M.C. Forti, S. Gromov, H. Hara, T. Khodzher, N.M Mahowald, S. Nickovic, P.S.P. Rao and N.W. Reid, 2014. A global assessment of precipitation chemistry and deposition of sulfur, nitrogen, sea salt, base cations, organic acids, acidity and pH, and phosphorus. Atmospheric Environment, 93:3–100.

Viatte, C., K. Strong, J. Hannigan, E. Nussbaumer, L.K. Emmons, S. Conway, C. Paton-Walsh, J. Hartley, J. Benmergui and J. Lin, 2015. Identifying fire plumes in the Arctic with tropospheric FTIR measurements and transport models. Atmospheric Chemistry and Physics, 15(5):2227–2246.

Virtanen, R., L. Oksanen, T. Oksanen, J. Cohen, B.C. Forbes, B. Johansen, J. Käyhkö, J. Olofsson, J. Pulliainen and H. Tømmervik, 2016. Where do the treeless tundra areas of northern highlands fit in the global biome system: toward an ecologically natural subdivision of the tundra biome. Ecology and Evolution, 6(1):143–158.

Vochezer, P., E. Järvinen, R. Wagner, P. Kupiszewski, T. Leisner and M. Schnaiter, 2016. In situ characterization of mixed phase clouds using the Small Ice Detector and the Particle Phase Discriminator. Atmospheric Measurement Techniques, 9(1):159–177.

Vohra, K., A. Vodonos, J. Schwartz, E.A. Marais, M.P. Sulprizio and L.J. Mickley, 2021. Global mortality from outdoor fine particle pollution generated by fossil fuel combustion: results from GEOS-Chem. Environmental Research, 195: 110754.

Voigt, C., M.E. Marushchak, R.E. Lamprecht, M. Jackowicz-Korczyński, A. Lindgren, M. Mastepanov, L. Granlund, T.R. Christensen, T. Tahvanainen, P.J. Martikainen and C. Biasi, 2017. Increased nitrous oxide emissions from Arctic peatlands after permafrost thaw. PNAS, 114(24):6238–6243.

von Salzen, K., 2006. Piecewise log-normal approximation of size distributions for aerosol modelling. Atmospheric Chemistry and Physics, 6(5):1351–1372.

von Salzen, K., H.G. Leighton, P.A. Ariya, L.A. Barrie, S.L. Gong, J.-P. Blanchet, L. Spacek, U. Lohmann and L.I. Kleinman, 2000. Sensitivity of sulphate aerosol size distributions and CCN concentrations over North America to SOx emissions and H_2O_2 concentrations. Journal of Geophysical Research: Atmospheres, 105(D8):9741–9765.

von Salzen, K., J.F. Scinocca, N.A. McFarlane, J. Li, J.N.S. Cole, D. Plummer, D. Verseghy, M.C. Reader, X. Ma, M. Lazare and L. Solheim, 2013. The Canadian Fourth Generation Atmospheric Global Climate Model (CanAM4). Part 1: Representation of physical processes. Atmosphere-Ocean, 51(1):104–125.

von Schneidemesser, E., J.J. Schauer, G.S.W. Hagler and M.H. Bergin, 2009. Concentrations and sources of carbonaceous aerosol in the atmosphere of Summit, Greenland. Atmospheric Environment, 43(27):4155–4162.

Wåhlström, I. and H.E. Markus Meier, 2014. A model sensitivity study for the sea-air exchange of methane in the Laptev Sea, Arctic Ocean. Tellus B: Chemical and Physical Meteorology, 66(1):24174.

Waigl, C.F., M. Stuefer, A. Prakash and C. Ichoku, 2017. Detecting high and low-intensity fires in Alaska using VIIRS I-band data: an improved operational approach for high latitudes. Remote Sensing of Environment, 199(4):389–400.

Waigl, C.F., A. Prakash, M. Stuefer, D. Verbyla and P. Dennison, 2019. Fire detection and temperature retrieval using EO-1 Hyperion data over selected Alaskan boreal forest fires. International Journal of Applied Earth Observation and Geoinformation, 81:72–84.

Walker, X.J., B.M. Rogers, J.L. Baltzer, S.G. Cumming, N.J. Day, S.J. Goetz, J.F. Johnstone, E.A.G. Schuur, M.R. Turetsky and M.C. Mack, 2018. Cross-scale controls on carbon emissions from boreal forest megafires. Global Change Biology, 24(9):4251–4265.

Walker, X.J., J.L. Baltzer, S.G. Cumming, N.J. Day, C. Ebert, S. Goetz, J.F. Johnstone, S. Potter, B.M. Rogers, E.A.G. Schuur, M.R. Turetsky and M.C. Mack, 2019. Increasing wildfires threaten historic carbon sink of boreal forest soils. Nature, 572:520–523.

Walsh, J.E. and W.L. Chapman, 1998. Arctic cloud-radiation-temperature associations in observational data and atmospheric reanalyses. Journal of Climate, 11(11):3030–3045.

Walter, B.P. and M. Heimann, 2000. A process-based, climate-sensitive model to derive methane emissions from natural wetlands: application to five wetland sites, sensitivity to model parameters, and climate. Global Biogeochemical Cycles, 14(3):745–765.

Walter, K.M., J.P. Chanton, F.S. Chapin III, E.A.G. Schuur and S.A. Zimov, 2008a. Methane production and bubble emissions from Arctic lakes: isotopic implications for source pathways and ages. Journal of Geophysical Research: Biogeosciences, 113(G3):G00A08.

Walter, K.M., M. Engram, C.R. Duguay, M.O. Jeffries and F.S. Chapin III, 2008b. The potential use of synthetic aperture radar for estimating methane ebullition from Arctic lakes. Journal of the American Water Resources Association, 44(2):305–315.

Walter Anthony, K.M. and P. Anthony, 2013. Constraining spatial variability of methane ebullition seeps in thermokarst lakes using point process models. Journal of Geophysical Research: Biogeosciences, 118(3):1015–1034.

Walter Anthony, K.M., D.A. Vas, L. Brosius, F.S. Chapin III, S.A. Zimov and Q. Zhuang, 2010. Estimating methane emissions from northern lakes using ice-bubble surveys. Limnology and Oceanography Methods, 8(11):592–609.

Walter Anthony, K., T. Schneider von Deimling, I. Nitze, S. Frolking, A. Emond, R. Daanen, P. Anthony, P. Lindgren, B. Jones and G. Grosse, 2018. 21st-Century modeled permafrost carbon emissions accelerated by abrupt thaw beneath lakes. Nature Communications, 9 (1):3262.

Wang, X. and D.L. Mauzerall, 2004. Characterizing distributions of surface ozone and its impact on grain production in China, Japan and South Korea: 1990 and 2020. Atmospheric Environment, 38(26):4383–4402.

Wang, X. and J.R. Key, 2005. Arctic surface, cloud, and radiation properties based on the AVHRR Polar Pathfinder dataset. Part I: Spatial and temporal characteristics. Journal of Climate, 18(14):2558–2574.

Wang, Q., D.J. Jacob, J.R. Spackman, A.E. Perring, J.P. Schwarz, N. Moteki, E.A. Marais, C. Ge, J. Wang and S.R.H. Barrett, 2014. Global budget and radiative forcing of black carbon aerosol: constraints from pole-to-pole (HIPPO) observations across the Pacific. Journal of Geophysical Research: Atmospheres, 119(1):195–206.

Wang, X., M.-A. Parisien, S.W. Taylor, J.-N. Candau, D. Stralberg, G.A. Marshall, J.M. Little and M.D. Flannigan, 2017. Projected changes in daily fire spread across Canada over the next century. Environmental Research Letters, 12(2):025005.

Wang, Y., J.H. Jiang, H. Su, Y.-S. Choi, L. Huang, J. Guo and Y.L. Yung, 2018. Elucidating the role of anthropogenic aerosols in Arctic sea ice variations. Journal of Climate, 31(1):99–114.

Wang, S., S.M. McNamara, C.W. Moore, D. Obrist, A. Steffen, P.B. Shepson, R.M. Staebler, A.R.W. Raso and K.A. Pratt, 2019. Direct detection of atmospheric atomic bromine leading to mercury and ozone depletion. PNAS, 116(29):14479-14484.

Wang, J.A., D. Sulla-Menashe, C.E. Woodcock, O. Sonnentag, R.F. Keeling and M.A. Friedl, 2020a. Extensive land cover change across Arctic–boreal northwestern North America from disturbance and climate forcing. Global Change Biology, 26(2):807–822.

Wang, D., J. Guo, A. Chen, L. Bian, M. Ding, L. Liu, Y. Lv, J. Li, X. Guo and Y. Han, 2020b. Temperature inversion and clouds over the Arctic Ocean observed by the 5th Chinese National Arctic Research Expedition. Journal of Geophysical Research: Atmospheres, 125(13):e2019JD032136.

Wang, X., T. Shi, X. Zhang and Y. Chen, 2020c. An overview of snow albedo sensitivity to black carbon contamination and snow grain properties based on experimental datasets across the Northern Hemisphere. Current Pollution Reports, 6:368–379.

Wania, R., I. Ross and I.C. Prentice, 2010. Implementation and evaluation of a new methane model within a dynamic global vegetation model: LPJ-WHyMe v1.3.1. Geoscientific Model Development, 3(2):565–584.

Wania, R., J.R. Melton, E.L. Hodson, B. Poulter, B. Ringeval, R. Spahni, T. Bohn, C.A. Avis, G. Chen, A.V. Eliseev, P.O. Hopcroft, W.J. Riley, Z.M. Subin, H. Tian, P.M. van Bodegom, T. Kleinen, Z.C. Yu, J.S. Singarayer, S. Zürcher, D.P. Lettenmaier, D.J. Beerling, S.N. Denisov, C. Prigent, F. Papa and J.O. Kaplan, 2013. Present state of global wetland extent and wetland methane modelling: methodology of a model inter-comparison project (WETCHIMP). Geoscientific Model Development, 6(3):617–641.

Wanninkhof, R., W.E. Asher, D.T. Ho, C. Sweeney and W.R. McGillis, 2009. Advances in quantifying air-sea gas exchange and environmental forcing. Annual Review of Marine Science, 1:213–244.

Ward, T., B. Trost, J. Conner, J. Flanagan and R. Jayanty, 2012. Source apportionment of $PM_{2.5}$ in a subarctic airshed – Fairbanks, Alaska. Aerosol and Air Quality Research, 12(4):536-543.

Ward, T.J., E.O. Semmens, E. Weiler, S. Harrar and C.W. Noonan, 2017. Efficacy of interventions targeting household air pollution from residential wood stoves. Journal of Exposure Science & Environmental Epidemiology, 27:64–71.

Warwick, N.J., M.L. Cain, R. Fisher, J.L. France, D. Lowry, S.E. Michel, E.G. Nisbet, B.H. Vaughn, J.W.C. White and J.A. Pyle, 2016. Using $\delta^{13}C\text{-}CH_4$ and $\delta D\text{-}CH_4$ to constrain Arctic methane emissions. Atmospheric Chemistry and Physics, 16(23):14891–14908.

Watson, J.G., J. Cao, L.-W.A. Chen, Q. Wang, J. Tian, X. Wang, S. Gronstal, S.S.H Ho, A.C. Watts and J.C. Chow, 2019. Gaseous, $PM_{2.5}$ mass, and speciated emission factors from laboratory chamber peat combustion. Atmospheric Chemistry and Physics, 19(22):14173–14193.

Watson-Parris, D., N. Schutgens, N. Cook, Z. Kipling, P. Kershaw, E. Gryspeerdt, B. Lawrence and P. Stier, 2016. Community Intercomparison Suite (CIS) v1.4.0: a tool for intercomparing models and observations. Geoscientific Model Development, 9(9):3093–3110.

Watts, J.D., J.S. Kimball, A. Bartsch and K.C. McDonald, 2014. Surface water inundation in the boreal-Arctic: potential impacts on regional methane emissions. Environmental Research Letters, 9(7):075001.

WB/GGFR, 2020. Global Gas Flaring Tracker Report. World Bank/Global Gas Flaring Reduction Partnership, Washington DC, USA. 10pp.

Weber, T., N.A. Wiseman and A. Kock, 2019. Global ocean methane emissions dominated by shallow coastal waters. Nature Communications, 10:4584.

Wei, J., Y. Peng, R. Mahmood, L. Sun and J. Guo, 2019. Intercomparison in spatial distributions and temporal trends derived from multi-source satellite aerosol products. Atmospheric Chemistry and Physics, 19(10):7183–7207.

Wendisch, M., A. Macke, A. Ehrlich, C. Lüpkes, M. Mech, D. Chechin, K. Dethloff, C. Barrientos Velasco, H. Bozem, M. Brückner, H.-C. Clemen, S. Crewell, T. Donth, R. Dupuy, K. Ebell, U. Egerer, R. Engelmann, C. Engler, O. Eppers, M. Gehrmann, X. Gong, M. Gottschalk, C. Gourbeyre, H. Griesche, J. Hartmann, M. Hartmann, B. Heinold, A. Herber, H. Herrmann, G. Heygster, P. Hoor, S. Jafariserajehlou, E. Jäkel, E. Järvinen, O. Jourdan, U. Kästner, S. Kecorius, E.M. Knudsen, F. Köllner, J. Kretzschmar, L. Lelli, D. Leroy, M. Maturilli, L. Mei, S. Mertes, G. Mioche, R. Neuber, M. Nicolaus, T. Nomokonova, J. Notholt, M. Palm, M. van Pinxteren, J. Quaas, P. Richter, E. Ruiz-Donoso, M. Schäfer, K. Schmieder, M. Schnaiter, J. Schneider, A. Schwarzenböck, P. Seifert, M.D. Shupe, H. Siebert, G. Spreen, J. Stapf, F. Stratmann, T. Vogl, A. Welti, H. Wex, A. Wiedensohler, M. Zanatta and S. Zeppenfeld, 2019. The Arctic cloud puzzle: using ACLOUD/PASCAL multiplatform observations to unravel the role of clouds and aerosol particles in Arctic amplification. Bulletin of the American Meteorological Society, 100(5):841–871.

Wendl, I.A., J.A. Menking, R. Färber, M. Gysel, S.D. Kaspari, M.J.G. Laborde and M. Schwikowski, 2014. Optimized method for black carbon analysis in ice and snow using the Single Particle Soot Photometer. Atmospheric Measurement Techniques, 7(8):2667–2681.

Wesely, M.L., 1989. Parameterization of surface resistances to gaseous dry deposition in regional-scale numerical models. Atmospheric Environment, 23(6):1293–1304.

Wespes, C., L. Emmons, D.P. Edwards, J. Hannigan, D. Hurtmans, M. Saunois, P.-F. Coheur, C. Clerbaux, M.T. Coffey, R.L. Batchelor, R. Lindenmaier, K. Strong, A.J. Weinheimer, J.B. Nowak, T.B. Ryerson, J.D. Crounse and P.O. Wennberg, 2012. Analysis of ozone and nitric acid in spring and summer Arctic pollution using aircraft, ground-based, satellite observations and MOZART-4 model: source attribution and partitioning. Atmospheric Chemistry and Physics, 12(1):237–259.

Westbrook, G.K., K.E. Thatcher, E.J. Rohling, A.M. Piotrowski, H. Pälike, A.H. Osborne, E.G. Nisbet, T.A. Minshull, M. Lanoisellé, R.H. James, V. Hühnerbach, D. Green, R.E. Fisher, A.J. Crocker, A. Chabert, C. Bolton, A. Beszczynska-Möller, C. Berndt and A. Aquilina, 2009. Escape of methane gas from the seabed along the West Spitsbergen continental margin. Geophysical Research Letters, 36(15):L15608.

Westervelt, D.M., L.W. Horowitz, V. Naik, J.-C. Golaz and D.L. Mauzerall, 2015. Radiative forcing and climate response to projected 21st century aerosol decreases. Atmospheric Chemistry and Physics, 15(22):12681–12703.

Whalen, S.C. and W.S. Reeburgh, 1990. A methane flux transect along the trans-Alaska pipeline haul road. Tellus B: Chemical and Physical Meteorology, 42(3):237–249.

Whalen, S.C. and W.S. Reeburgh, 1992. Interannual variations in tundra methane emission: a 4-year time series at fixed sites. Global Biogeochemical Cycles, 6(2):139–159.

Whaley, C.H., K.S. Law, J.L. Hjorth, H. Skov, S.R. Arnold, J. Langner, J.B. Pernov, et al., 2023. Arctic Tropospheric Ozone: Assessment of Current Knowledge and Model Performance. Atmospheric Chemistry and Physics, 23 (1): 637–61.

Whitman, E., M.-A. Parisien, D.K. Thompson and M.D. Flannigan, 2019. Short-interval wildfire and drought overwhelm boreal forest resilience. Scientific Reports, 9:18796.

WHO, 2008. Health risks of ozone from long-range transboundary air pollution. World Health Organization (WHO) Regional Office for Europe, Copenhagen, Denmark. xiii + 93pp.

WHO, 2012. Health effects of black carbon. World Health Organization (WHO), Regional Office of Europe. viii + 86pp.

WHO Europe, 2013a. Review of evidence on health aspects of air pollution – REVIHAAP project: final technical report. World Health Organization Europe (WHO Europe), Bonn, Germany. vii + 302pp.

WHO Europe, 2013b. Health risks of air pollution in Europe – HRAPIE project: Recommendations for concentration-response functions for cost-benefit analysis of particulate matter, ozone and nitrogen dioxide. World Health Organization (WHO Europe), Copenhagen, Denmark. vi + 54pp.

Wiedinmyer, C., S.K. Akagi, R.J. Yokelson, L.K. Emmons, J.A. Al-Saadi, J.J. Orlando and A.J. Soja, 2011. The Fire INventory from NCAR (FINN): A high resolution global model to estimate the emissions from open burning. Geoscientific Model Development, 4(3):625–641.

Wik, M., P.M. Crill, D. Bastviken, Å. Danielsson and E. Norbäck, 2011. Bubbles trapped in Arctic lake ice: potential implications for methane emissions. Journal of Geophysical Research: Biogeosciences, 116(G3):G03044.

Wik, M., P.M. Crill, R.K. Varner and D. Bastviken, 2013. Multiyear measurements of ebullitive methane flux from three subarctic lakes. Journal of Geophysical Research: Biogeosciences, 118(3):1307–1321.

Wik, M., B.F. Thornton, D. Bastviken, S. MacIntyre, R.K. Varner and P.M. Crill, 2014. Energy input is primary controller of methane bubbling in subarctic lakes. Geophysical Research Letters, 41(2):555–560.

Wik, M., R.K. Varner, K.Walter Anthony, S. MacIntyre and D. Bastviken, 2016a. Climate-sensitive northern lakes and ponds are critical components of methane release. Nature Geoscience, 9:99–105.

Wik, M., B.F. Thornton, D. Bastviken, J. Uhlbäck and P.M. Crill, 2016b. Biased sampling of methane release from northern lakes: a problem for extrapolation. Geophysical Research Letters, 43(3):1256–1262.

Wik, M., J.E. Johnson, P.M. Crill, J.P. DeStasio, L. Erickson, M.J. Halloran, M.F. Fahnestock, M.K. Crawford, S.C. Phillips and R.K. Varner, 2018. Sediment characteristics and methane ebullition in three subarctic lakes. Journal of Geophysical Research: Biogeosciences, 123(8):2399–2411.

Wik, M., B.F. Thornton, R.K. Varner, C. McCalley and P.M. Crill, 2020. Stable methane isotopologues from northern lakes suggest that ebullition is dominated by sub-lake scale processes. Journal of Geophysical Research: Biogeosciences, 125:e2019JG005601.

Wilcox, L.J., E.J. Highwood and N.J. Dunstone, 2013. The influence of anthropogenic aerosol on multi-decadal variations of historical global climate. Environmental Research Letters, 8(2):024033.

Wild, O., A.M. Fiore, D.T. Shindell, R.M. Doherty, W.J. Collins, F. Dentener, M.G. Schultz, S. Gong, I.A. MacKenzie, G. Zeng, P. Hess, B.N. Duncan, D.J. Bergmann, S. Szopa, J.E. Jonson, T.J. Keating and A. Zuber, 2012. Modelling future changes in surface ozone: a parameterized approach. Atmospheric Chemistry and Physics, 12(4):2037–2054.

Wilkinson, S. and W.J. Davies, 2009. Ozone suppresses soil drying- and abscisic acid (ABA)-induced stomatal closure via an ethylene-dependent mechanism. Plant, Cell & Environment, 32(8):949–959.

Wilkinson, S.L., P.A. Moore, D.K. Thompson, B.M. Wotton, S. Hvenegaard, D. Schroeder and J.M. Waddington, 2018. The effects of black spruce fuel management on surface fuel condition and peat burn severity in an experimental fire. Canadian Journal of Forest Research, 48(12):1433–1440.

Wilkinson, S.L., P.A. Moore and J.M. Waddington, 2019. Assessing drivers of cross-scale variability in peat smoldering combustion vulnerability in forested boreal peatlands. Frontiers in Forests and Global Change, 2:84.

Williams, K.D., D. Copsey, E.W. Blockley, A. Bodas-Salcedo, D. Calvert, R. Comer, P. Davis, T. Graham, H.T. Hewitt, R. Hill, P. Hyder, S. Ineson, T.C. Johns, A.B. Keen, R.W. Lee, A. Megann, S.F. Milton, J.G.L. Rae, M.J. Roberts, A.A. Scaife, R. Schiemann, D. Storkey, L. Thorpe, I.G. Watterson, D.N. Walters, A. West, R.A. Wood, T. Woollings and P.K. Xavier, 2018. The Met Office Global Coupled Model 3.0 and 3.1 (GC3.0 and GC3.1) configurations. Journal of Advances in Modeling Earth Systems, 10(2):357–380.

Willis, M.D., W.R. Leaitch and J.P. Abbatt, 2018. Processes controlling the composition and abundance of Arctic aerosol. Reviews of Geophysics, 56(4):621–671.

Willis, M.D., H. Bozem, D. Kunkel, A.K.Y. Lee, H. Schulz, J. Burkart, A.A. Aliabadi, A.B. Herber, W.R. Leaitch and J.P.D. Abbatt, 2019. Aircraft-based measurements of High Arctic springtime aerosol show evidence for vertically varying sources, transport and composition. Atmospheric Chemistry and Physics, 19(1):57–76.

Winiger, P., A. Andersson, S. Eckhardt, A. Stohl and Ö. Gustafsson, 2016. The sources of atmospheric black carbon at a European gateway to the Arctic. Nature Communications, 7:12776.

Winiger, P., A. Andersson, S. Eckhardt, A. Stohl, I.P. Semiletov, O.V. Dudarev, A. Charkin, N. Shakhova, Z. Klimont, C. Heyes and Ö. Gustafsson, 2017. Siberian Arctic black carbon sources constrained by model and observation. PNAS, 114(7):E1054–E1061.

Winiger, P., T.E. Barrett, R.J. Sheesley, L. Huang, S. Sharma, L.A. Barrie, K.E. Yttri, N. Evangeliou, S. Eckhardt, A. Stohl, Z. Klimont, C. Heyes, I.P. Semiletov, O.V. Dudarev, A. Charkin, N. Shakhova, H. Holmstrand, A. Andersson and Ö. Gustafsson, 2019. Source apportionment of circum-Arctic atmospheric black carbon from isotopes and modeling. Science Advances, 5(2):eaau8052.

Winker, D.M., M.A. Vaughan, A. Omar, Y. Hu, K.A. Powell, Z. Liu, W.H. Hunt and S. A. Young, 2009. Overview of the CALIPSO Mission and CALIOP Data Processing Algorithms. *Journal of Atmospheric and Oceanic Technology, 26*(11):2310–2323.

Winker, D.M., J.L. Tackett, B.J. Getzewich, Z. Liu, Z., M.A. Vaughan and R.R. Rogers, 2013. The global 3-D distribution of tropospheric aerosols as characterized by CALIOP. Atmospheric Chemistry and Physics, 13(6):3345–3361.

Winters, N., M.S. Goldberg, P. Hystad, P.J. Villeneuve, K.C. Johnson and the Canadian Cancer Registries Epidemiology Group, 2015. Exposure to ambient air pollution in Canada and the risk of adult leukemia. Science of the Total Environment, 526:153–76.

Winther, M., J.H. Christensen, M.S. Plejdrup, E.S. Ravn, Ó.F. Eriksson and H.O. Kristensen, 2014. Emission inventories for ships in the Arctic based on satellite sampled AIS data. Atmospheric Environment, 91:1–14.

Witek, M.L., M.J. Garay, D.J. Diner, M.A. Bull and F.C. Seidel, 2018. New approach to the retrieval of AOD and its uncertainty from MISR observations over dark water. Atmospheric Measurement Techniques, 11(1):429–439.

Wittmann, M., C.D. Groot Zwaaftink, L. Steffensen Schmidt, S. Guðmundsson, F. Pálsson, O. Arnalds, H. Björnsson, T. Thorsteinsson and A. Stohl, 2017. Impact of dust deposition on the albedo of Vatnajökull ice cap, Iceland. The Cryosphere, 11(2):741–754.

Witze, A., 2021. Is lightning striking the Arctic more than ever before? Nature, 589:11–12.

WMO/GAW, 2016. WMO/GAW Aerosol Measurement Procedures Guidelines and Recommendations 2nd Edition. WMO No. 1177; GAW Report No. 227. World Meteorological Organization (WMO) Global Atmosphere Watch (GAW), Geneva, Switzerland. vi + 93pp.

Wofsy, S.C., S. Afshar, H.M. Allen, E.C. Apel, E.C. Asher, B. Barletta, J. Bent, H. Bian, B.C. Biggs, D.R. Blake, N. Blake, I. Bourgeois, C.A. Brock, W.H. Brune, J.W. Budney, T.P. Bui, A. Butler, P. Campuzano-Jost, C.S. Chang, M. Chin, R. Commane, G. Correa, J.D. Crounse, P. D. Cullis, B.C. Daube, D.A. Day, J.M. Dean-Day, J.E. Dibb, J.P. DiGangi, G.S. Diskin, M. Dollner, J.W. Elkins, F. Erdesz, A.M. Fiore, C.M. Flynn, K.D. Froyd, D.W. Gesler, S.R. Hall, T.F. Hanisco, R.A. Hannun, A.J. Hills, E.J. Hintsa, A. Hoffman, R.S. Hornbrook, L.G. Huey, S. Hughes, J.L. Jimenez, B.J. Johnson, J.M. Katich, R.F. Keeling, M.J. Kim, A. Kupc, L.R. Lait, K. McKain, R.J. Mclaughlin, S. Meinardi, D.O. Miller, S.A. Montzka, F.L. Moore, E.J. Morgan, D.M. Murphy, L.T. Murray, B.A. Nault, J.A. Neuman, P.A. Newman, J.M. Nicely, X. Pan, W. Paplawsky, J. Peischl, M.J. Prather, D.J. Price, E.A. Ray, J.M. Reeves, M. Richardson, A.W. Rollins, K.H. Rosenlof, T.B. Ryerson, E. Scheuer, G.P. Schill, J.C. Schroder, J.P. Schwarz, J.M. St.Clair, S.D. Steenrod, B.B. Stephens, S.A. Strode, C. Sweeney, D. Tanner, A.P. Teng, A.B. Thames, C.R. Thompson, K. Ullmann, P.R. Veres, N.L. Wagner, A. Watt, R. Weber, B.B. Weinzierl, P.O. Wennberg, C.J. Williamson, J.C. Wilson, G.M. Wolfe, C.T. Woods, L.H. Zeng, and N. Vieznor. 2021. ATom: Merged Atmospheric Chemistry, Trace Gases, and Aerosols, Version 2. ORNL DAAC, Oak Ridge, Tennessee, USA. Available at: https://doi.org/10.3334/ORNLDAAC/1925

Woodward, S., 2001. Modeling the atmospheric life cycle and radiative impact of mineral dust in the Hadley Centre climate model. Journal of Geophysical Research: Atmospheres, 106(D16):18155–18166.

World Bank, 2013. On Thin Ice: How Cutting Pollution Can Slow Warming and Save Lives. A Joint Report of the World Bank and the International Cryosphere Climate Initiative. World Bank, Washington D.C. xix + 92pp.

Wotton, B.M., D.L. Martell and K.L. Logan, 2003. Climate change and people-caused forest fire occurrence in Ontario. Climatic Change, 60:275–295.

Wotton, B.M., M.D. Flannigan and G.A. Marshall, 2017. Potential climate change impacts on fire intensity and key wildfire suppression thresholds in Canada. Environmental Research Letters, 12(9):095003.

Wrona, F.J., M. Johansson, J.M. Culp, A. Jenkins, J. Mård, I.H. Myers-Smith, T.D. Prowse, W.F. Vincent and P.A. Wookey, 2016. Transitions in Arctic ecosystems: Ecological implications of a changing hydrological regime. Journal of Geophysical Research: Biogeosciences, 121(3):650–674.

Wu, D.L. and J.N. Lee, 2012. Arctic low cloud changes as observed by MISR and CALIOP: Implication for the enhanced autumnal warming and sea ice loss. Journal of Geophysical Research:Atmospheres, 117:D07107.

Wu, X., L. Deng, X. Song, G. Vettoretti, W.R. Peltier and G.J. Zhang, 2007. Impact of a modified convective scheme on the Madden-Julian Oscillation and El Niño–Southern Oscillation in a coupled climate model. Geophysical Research Letters, 34(16).

Xing Y.F., Y.H. Xu M.H. Shi and Y.X. Lian, 2016. The impact of $PM_{2.5}$ on the human respiratory system. Journal of Thoracic Disease, 8(1):E69–E74.

Xu, X., D.A. Elias, D.E. Graham, T.J. Phelps, S.L. Carroll, S.D. Wullschleger and P.E. Thornton, 2015. A microbial functional group-based module for simulating methane production and consumption: application to an incubated permafrost soil. Journal of Geophysical Research: Biogeosciences, 120(7):1315–1333.

Xu, J.-W., R.V. Martin, A. Morrow, S. Sharma, L. Huang, W.R. Leaitch, J. Burkart, H. Schulz, M. Zanatta, M.D. Willis, D.K. Henze, C.J. Lee, A.B. Herber and J.P.D. Abbatt, 2017. Source attribution of Arctic black carbon constrained by aircraft and surface measurements, Atmospheric Chemistry and Physics, 17(19):11971–11989.

Xu, J., P.J. Morris, J. Liu and J. Holden, 2018. PEATMAP: Refining estimates of global peatland distribution based on a meta-analysis. Catena, 160:134–140.

Xu, W., H.S. He, T.J. Hawbaker, Z. Zhu and P.D. Henne, 2020. Estimating burn severity and carbon emissions from a historic megafire in boreal forests of China. Science of The Total Environment, 716:136534.

Yamagata, S., D. Kobayashi, S. Ohta, N. Murao, M. Shiobara, M. Wada, M. Yabuki, H. Konishi and T. Yamanouchi, 2009. Properties of aerosols and their wet deposition in the arctic spring during ASTAR2004 at Ny-Alesund, Svalbard. Atmospheric Chemistry and Physics, 9(1):261–270.

Yanagiya, K. and M. Furuya, 2020. Post-wildfire surface deformation near Batagay, Eastern Siberia, detected by L-band and C-band InSAR. Journal of Geophysical Research: Earth Surface, 125(7):e2019JF005473.

Yang, Q., C.M. Bitz and S.J. Doherty, 2014. Offsetting effects of aerosols on Arctic and global climate in the late 20th century. Atmospheric Chemistry and Physics, 14(8):3969–3975.

Yang, X., A.-M. Blechschmidt, K. Bognar, A. McClure–Begley, S. Morris, I. Petropavlovskikh, A. Richter, H. Skov, K. Strong, D.W. Tarasick, T. Uttal, M. Vestenius and X. Zhao, 2020. Pan-Arctic surface ozone: modelling vs. measurements. Atmospheric Chemistry and Physics, 20(24):15937–15967.

York, A., U. Bhatt, R. Thoman and R. Ziel, 2017. Wildland Fire in High Latitudes. NOAA Arctic Program – Arctic Report Card: Update for 2017. Available at: https://arctic.noaa.gov/Report-Card/Report-Card-2017/ArtMID/7798/ArticleID/692/Wildland-Fire-in-High-Latitudes

Yoshida, A., N. Moteki, S. Ohata, T. Mori, R. Tada, P. Dagsson-Waldhauserová and Y. Kondo, 2016. Detection of light-absorbing iron oxide particles using a modified single-particle soot photometer. Aerosol Science and Technology, 50(3):1–4.

Yoshida, A., N. Moteki, S. Ohata, T. Mori, M. Koike, Y. Kondo, H. Matsui, N. Oshima, A. Takami and K. Kita, 2020. Abundances and microphysical properties of light-absorbing iron oxide and black carbon aerosols over East Asia and the Arctic. Journal of Geophysical Research: Atmospheres, 125(15):e2019JD032301.

Young, P. J., A.T. Archibald, K.W. Bowman, J.-F. Lamarque, V. Naik, D.S. Stevenson, S. Tilmes, A. Voulgarakis, O. Wild, D. Bergmann, P. Cameron-Smith, I. Cionni, W.J. Collins, S.B. Dalsøren, R.M. Doherty, V. Eyring, G. Faluvegi, L.W. Horowitz, B. Josse, Y.H. Lee, I.A. MacKenzie, T. Nagashima, D.A. Plummer, M. Righi, S.T. Rumbold, R.B. Skeie, D.T. Shindell, S.A. Strode, K. Sudo, S. Szopa and G. Zeng, 2013. Pre-industrial to end 21st century projections of tropospheric ozone from the Atmospheric Chemistry and Climate Model Intercomparison Project (ACCMIP). Atmospheric Chemistry and Physics, 13(4):2063–2090.

Young, A.M., P.E. Higuera, P.A. Duffy and F.S. Hu, 2016. Climatic thresholds shape northern high-latitude fire regimes and imply vulnerability to future climate change. Ecography, 40(5):606–617.

Young, A.H., K.R. Knapp, A. Inamdar, W. Hankins and W.B. Rossow, 2018a. The international satellite cloud climatology project H-series climate data record product. Earth System Science Data, 10(1):583–593.

Young, P.J., V. Naik, A.M. Fiore, A. Gaudel, J. Guo, M.Y. Lin, J.L. Neu, D.D. Parrish, H.E. Rieder, J.L. Schnell, S. Tilmes, O. Wild, L. Zhang, J.R. Ziemke, J. Brandt, A. Delcloo, R.M. Doherty, C. Geels, M.I. Hegglin, L. Hu, U. Im, R. Kumar, A. Luhar, L. Murray, D. Plummer, J. Rodriguez, A. Saiz-Lopez, M.G. Schultz, M.T. Woodhouse and G. Zeng, 2018b. Tropospheric Ozone Assessment Report: Assessment of global-scale model performance for global and regional ozone distributions, variability, and trends. Elementa: Science of the Anthropocene, 6:10.

Yttri, K.E., C. Lund Myhre, S. Eckhardt, M. Fiebig, C. Dye, D. Hirdman, J. Ström, Z. Klimont and A. Stohl, 2014. Quantifying black carbon from biomass burning by means of levoglucosan – a one-year time series at the Arctic observatory Zeppelin. Atmospheric Chemistry and Physics, 14(12):6427–6442.

Yu, Z., J. Loisel, D.P. Brosseau, D.W. Beilman and S.J. Hunt, 2010. Global peatland dynamics since the Last Glacial Maximum. Geophysical Research Letters, 37(13):L13402.

Yu, P., O.B. Toon, C.G. Bardeen, Y. Zhu, K.H. Rosenlof, R.W. Portmann, T.D. Thornberry, R.-S. Gao, S.M. Davis, E.T. Wolf, J. de Gouw, D.A. Peterson, M.D. Fromm and A. Robock, 2019. Black carbon lofts wildfire smoke high into the stratosphere to form a persistent plume. Science, 365(6453):587–590.

Yukimoto, S., H. Kawai, T. Koshiro, N. Oshima, K. Yoshida, S. Urakawa, H. Tsujino, M. Deushi, T. Tanaka, M. Hosaka, S. Yabu, H. Yoshimura, E. Shindo, R. Mizuta, A. Obata, Y. Adachi and M. Ishii, 2019. The Meteorological Research Institute Earth System Model version 2.0, MRI-ESM2.0: description and basic evaluation of the physical component. Meteorological Society of Japan, 97(5):931–965.

Yum, S.S. and J.G. Hudson, 2001. Vertical distributions of cloud condensation nuclei spectra over the springtime Arctic Ocean. Journal of Geophysical Research: Atmospheres, 106(D14):15045–15052.

Zábori, J., R. Krejci, A.M.L. Ekman, E.M. Mårtensson, J. Ström, G. de Leeuw and E.D. Nilsson, 2012. Wintertime Arctic Ocean sea water properties and primary marine aerosol concentrations. Atmospheric Chemistry and Physics, 12(21):10405–10421.

Zamora, L.M., R.A. Kahn, S. Eckhardt, A. McComiskey, P. Sawamura, R. Moore and A. Stohl, 2017. Aerosol indirect effects on the nighttime Arctic Ocean surface from thin, predominantly liquid clouds. Atmospheric Chemistry and Physics, 17(12):7311–7332.

Zanatta, M., M. Gysel, N. Bukowiecki, T. Müller, E. Weingartner, H. Areskoug, M. Fiebig, K.E. Yttri, N. Mihalopoulos, G. Kouvarakis, D. Beddows, R.M. Harrison, F. Cavalli, J.P. Putaud, G. Spindler, A. Wiedensohler, A. Alastuey, M. Pandolfi, K. Sellegri, E. Swietlicki, J.L. Jaffrezo, U. Baltensperger and P. Laj, 2016. A European aerosol phenomenology-5: Climatology of black carbon optical properties at 9 regional background sites across Europe. Atmospheric Environment, 145:346–364.

Zanatta, M., P. Laj, M. Gysel, U. Baltensperger, S. Vratolis, K. Eleftheriadis, Y. Kondo, P. Dubuisson, V. Winiarek, S. Kazadzis, P. Tunved and H.-W. Jacobi, 2018. Effects of mixing state on optical and radiative properties of black carbon in the European Arctic. Atmospheric Chemistry and Physics, 18(19):14037–14057.

Zangrando, R., E. Barbaro, P. Zennaro, S. Rossi, N.M. Kehrwald, J. Gabrieli, C. Barbante and A. Gambaro, 2013. Molecular markers of biomass burning in Arctic aerosols. Environmental Science & Technology, 47(15):8565–8574.

Zdanowicz, C., D. Fisher, J. Bourgeois, M. Demuth, J. Zheng, P. Mayewski, K. Kreutz, E. Osterberg, K. Yalcin, C. Wake, E.J. Steig, D. Froese and K. Goto-Azuma, 2014. Ice cores from the St. Elias Mountains, Yukon, Canada: their significance for climate, atmospheric composition and volcanism in the North Pacific Region. Arctic, 67(5)1:1–107.

Zdanowicz, C.M., B.C. Proemse, R. Edwards, W. Feiteng, C.M. Hogan, C. Kinnard and D. Fisher, 2018. Historical black carbon deposition in the Canadian High Arctic: a 250-year long ice-core record from Devon Island. Atmospheric Chemistry and Physics, 18(16):12345–12361.

Zdanowicz, C., J.-C. Gallet, M.P. Björkman, C. Larose, T. Schuler, B. Luks, K. Koziol, A. Spolaor, E. Barbaro, T. Martma, W. van Pelt, U. Wideqvist and J. Ström, 2021. Elemental and water-insoluble organic carbon in Svalbard snow: a synthesis of observations during 2007–2018. Atmospheric Chemistry and Physics, 21(4):3035–3057.

Zelinka, M.D., T.A. Myers, D.T. McCoy, S. Po-Chedley, P.M. Caldwell, P. Ceppi, S.A. Klein and K.E. Taylor, 2020. Causes of higher climate sensitivity in CMIP6 models. Geophysical Research Letters, 47(1):e2019GL085782.

Zencak, Z., M. Elmquist and Ö. Gustafsson, 2007. Quantification and radiocarbon source apportionment of black carbon in atmospheric aerosols using the CTO-375 method. Atmospheric Environment, 41(36):7895–7906.

Zennaro, P., N. Kehrwald, J.R. McConnell, S. Schüpbach, O.J. Maselli, J. Marlon, P. Vallelonga, D. Leuenberger, R. Zangrando, A. Spolaor, M. Borrotti, E. Barbaro, A. Gambaro and C. Barbante, 2014. Fire in ice: two millennia of boreal forest fire history from the Greenland NEEM ice core. Climate of the Past, 10(5):1905–1924.

Zhang L., S. Gong, J. Padro and L. Barrie, 2001. A size-segregated particle dry deposition scheme for an atmospheric aerosol module. Atmospheric Environment, 35(3):549–560.

Zhang, Q., J.L. Jimenez, M.R. Canagaratna, I.M. Ulbrich, N.L. Ng, D.R. Worsnop and Y. Sun, 2011. Understanding atmospheric organic aerosols via factor analysis of aerosol mass spectrometry: a review. Analytical and Bioanalytical Chemistry, 401:3045–3067.

Zhang, Y.L., N. Perron, V.G. Ciobanu, P. Zotter, M.C. Minguillón, L. Wacker, A.S.H. Prévôt, U. Baltensperger and S. Szidat, 2012. On the isolation of OC and EC and the optimal strategy of radiocarbon-based source apportionment of carbonaceous aerosols. Atmospheric Chemistry and Physics, 12(22):10841–10856.

Zhang L., J.F. Kok, D.K. Henze, Q. Li and C. Zhao, 2013. Improving simulations of fine dust surface concentrations over the western United States by optimizing the particle size distribution. Geophysical Research Letters, 40(12):3270–3275.

Zhang, Z., N.E. Zimmermann, A. Stenke, X. Li, E.L. Hodson, G. Zhu, C. Huang and B. Poulter, 2017. Emerging role of wetland methane emissions in driving 21st century climate change. PNAS, 114(36):9647–9652.

Zhang, R., C. Huang, X. Zhan, H. Jin and X.-P. Song, 2018. Development of S-NPP VIIRS global surface type classification map using support vector machines. International Journal of Digital Earth, 11(2):212–232.

Zhang, X., J. Li., Y. Mo, C. Shen, P. Ding, N. Wang, S. Zhu, Z. Cheng, J. He, Y. Tian, S. Gao, Q. Zhou, C. Tian, Y. Chen and G. Zhang, 2019. Isolation and radiocarbon analysis of elemental carbon in atmospheric aerosols using hydropyrolysis. Atmospheric Environment, 198:381–386.

Zhao, T. X.-P., P.K Chan and A.K. Heidinger, 2013. A global survey of the effect of cloud contamination on the aerosol optical thickness and its long-term trend derived from operational AVHRR satellite observations. Journal of Geophysical Research: Atmospheres, 118(7):2849–2857.

Zhao, X., Y. Lin, Y. Peng, B. Wang, H. Morrison and A. Gettelman, 2017. A single ice approach using varying ice particle properties in global climate model microphysics. Journal of Advances in Modeling Earth Systems, 9(5):2138–2157.

Zhao, A., M.A. Bollasina, M. Crippa and D.S. Stevenson, 2019. Significant climate impacts of aerosol changes driven by growth in energy use and advances in emission control technology. Atmospheric Chemistry and Physics, 19(23):14517–14533.

Zhu, L., E.V. Fischer, V.H. Payne, J.R. Worden and Z. Jiang, 2015. TES observations of the interannual variability of PAN over Northern Eurasia and the relationship to springtime fires. Geophysical Research Letters, 42(17):7230–7237.

Zhu, C., H. Kobayashi, Y. Kanaya and M. Saito, 2017. Size-dependent validation of MODIS MCD64A1 burned area over six vegetation types in boreal Eurasia: large underestimation in croplands. Scientific Reports, 7:4181

Zhu, Y., K.J. Purdy, Ö. Eyice, L. Shen, S.F. Harpenslager, G. Yvon-Durocher, A.J. Dumbrell and M. Trimmer, 2020. Disproportionate increase in freshwater methane emissions induced by experimental warming. Nature Climate Change, 10:685–690.

Zhuang, Q., J.M. Melillo, D.W. Kicklighter, R.G. Prinn, A.D. McGuire, P.A. Steudler, B.S. Felzer and S. Hu, 2004. Methane fluxes between terrestrial ecosystems and the atmosphere at northern high latitudes during the past century: a retrospective analysis with a process-based biogeochemistry model. Global Biogeochemical Cycles, 18(3):GB3010.

Zona, D., B. Gioli, R. Commane, J. Lindaas, S.C. Wofsy, C.E. Miller, S.J. Dinardo, S. Dengel, C. Sweeney, A. Karion, R.Y.-W. Chang, J.M. Henderson, P.C. Murphy, J.P. Goodrich, V. Moreaux, A. Liljedahl, J.D. Watts, J.S. Kimball, D.A. Lipson and W.C. Oechel, 2016. Cold season emissions dominate the Arctic tundra methane budget. PNAS, 113(1):40–45.

Zubko, N., O. Muñoz, E. Zubko, M. Gritsevich, J. Escobar-Cerezo, M.J. Berg and J. Peltoniemi, 2019. Light scattering from volcanic-sand particles in deposited and aerosol form. Atmospheric Environment, 215:116813.

Data References

Chapter 2

Data ref. 2.1. IEA, World Energy Outlook 2018. Available at: https://www.iea.org/reports/world-energy-outlook-2018

Data ref. 2.2. ECLIPSE v6b. Available at: https://iiasa.ac.at/web/home/research/researchPrograms/air/ECLIPSEv6b.html

Data ref. 2.3. ECLIPSE v5a. Available at: https://iiasa.ac.at/web/home/research/researchPrograms/air/ECLIPSEv5a.html

Data ref. 2.4. EDGAR v5.0. Available at: https://edgar.jrc.ec.europa.eu/dataset_ap50

Data ref. 2.5. CLRTAP submission 2017. Available at: https://www.ceip.at/status-of-reporting-and-review-results/2017-submissions

Data ref. 2.6. CLRTAP submission 2020. Available at: https://www.ceip.at/status-of-reporting-and-review-results/2020-submissions

Data ref. 2.7. National reporting to UNFCCC (collected from UNFCCC website on 1.12.2020). Available at: https://unfccc.int/ghg-inventories-annex-i-parties/2020

Chapter 3

Data ref. 3.1. The MEMENTO database, administered by the Kiel Data Management Team at GEOMAR Helmholtz Centre for Ocean Research. Available at: https://memento.geomar.de/

Chapter 4

Data ref. 4.1. Global Fire Emissions Database Version 4s (GFED4s; including small fires). Available at: http://globalfiredata.org/pages/data/#emissions

Data ref. 4.2. Sentinel-2 Global Land Cover (S2GLC) dataset. European Space agency. Available at: https://s2glc.cbk.waw.pl/

Data ref. 4.3. Сведения о лесопожарной обстановке на территории субъектов РФ на 31.12 [Forest fire situation of the constituents of the Russian Federation, 31 December, in Russian]. ФБУ 'АВИАЛЕСООХРАНА', 2019. Available at: https://bit.ly/3c8R6KR

Data ref. 4.4. Total wildland fires and acres (1983–2020). Latest update: 2021. National Interagency Fire Center, Boise, Idaho, USA. Available at: https://www.nifc.gov/fireInfo/fireInfo_stats_totalFires.html

Data ref. 4.5. Emission factors of Global Fire Emissions Database. Available at: https://www.geo.vu.nl/~gwerf/GFED/GFED4/ancill/GFED4_Emission_Factors.txt

Data ref. 4.6. Burned Area Monthly L3 Global 500m (MCD64). Available at: https://lpdaac.usgs.gov/products/mcd64a1v061/

Data ref. 4.7. AMAP SLCF EG Pan-Arctic Fire Emissions Model. Available at: https://doi.org/10.5281/zenodo.4648723

Chapter 5

Data ref. 5.1. Data on atmospheric composition from ground stations. Available at: https://ebas-submit.nilu.no/

Chapter 6

Data ref. 6.1. Samples of atmospheric aerosols from NOAA Regional Aerosol Sampling Stations, National Oceanic and Atmospheric Administration (NOAA). Available at: https://saga.pmel.noaa.gov/data/stations/

Data ref. 6.2. ORNLDAAC, ATom: Merged Atmospheric Chemistry, Trace Gases, and Aerosols. Available at: https://doi.org/10.3334/ORNLDAAC/1581

Data ref. 6.3. Data on atmospheric composition from ground stations. Available at: https://ebas-submit.nilu.no/

Chapter 7

Data ref. 7.1. AMAP SLCF model datasets from ECCC data catalogue entry for model datasets; government of Canada's Open Government Portal (at canada.ca). Available at: https://doi.org/10.18164/e0a0ac5c-d851-45b9-b6d9-4abc29d7d419

Data ref. 7.2 Global Emission Fields (ECLIPSE V6b), 1990–2015 dataset. Latest update: 2019. International Institute for Applied Systems Analysis (IIASA). (https://iiasa.ac.at/web/home/research/researchPrograms/air/ECLIPSEv6b.html)

Data ref. 7.3 NOAA Global Monitoring Surface Ozone Network. Station name, Time start-Time end. 2014. National Oceanic and Atmospheric Administration, Earth Systems Research Laboratory Global Monitoring Division. Boulder, Colorado, USA. (http://dx.doi.org/10.7289/V57P8WBF)

Data ref. 7.4 Villum Station datasets were obtained from: www.villumresearchstation.dk

Data ref. 7.5 Atmospheric Chemistry Experiment – Fourier Transform Spectrometer (ACE-FTS): ACE-FTS v4.1 measurements were obtained from: http://www.ace.uwaterloo.ca. Data quality information is available at https://doi.org/10.5683/SP2/BC4ATC.

Data ref. 7.6 Tropospheric Emission Spectrometer (TES) datasets were obtained from: https://tes.jpl.nasa.gov/tes/data/products/lite

Data ref. 7.7 Measurements Of Pollution In The Troposphere (MOPITT) data were obtained from: https://www2.acom.ucar.edu/mopitt/products.

Data ref. 7.8 Global, non-Arctic satellite-based data were obtained from Dalhousie University. Air Quality: Surface Fine Particulate Matter (PM2.5) Concentrations. Accessed through Resource Watch, www.resourcewatch.org

Data ref. 7.9 NOAA Climate Data Record (CDR) of AVHRR Daily and Monthly Aerosol Optical Thickness (AOT) over Global Oceans (AOT_AVHRR_v03r00_monthly_avg – Version 3.0). National Centers for Environmental Information. Accessed: 30/01/2018–01/02/2020. (https://www.ncei.noaa.gov/access/metadata/landing-page/bin/iso?id=gov.noaa.ncdc:C00977)

Chapter 8

Data ref. 8.1. Ed Dlugokencky, NOAA/GML. Available at: www.esrl.noaa.gov/gmd/ccgg/trends_ch4/

Data ref. 8.2. GISS Surface Temperature Analysis (GISTEMP), Version 4. NASA Goddard Institute for Space Studies, New York city, USA (last accessed 02/14/2020). Available at: https://data.giss.nasa.gov/gistemp/

Chapter 9

Data ref. 9.1.Global Health Estimates: Life Expectancy and Leading Causes of death and disability. Latest update: 2019. World Health Organization (WHO), Geneva, Switzerland. Available at: https://www.who.int/data/gho/data/ themes/mortality-and-global-health-estimates

Data ref. 9.2. Gridded Population of the World, Version 4 (GPWv4). Latest update: 2018. Center for International Earth Science Information Network (CIESEN), Columbia University, United Nations Food and Agriculture Programme (FAO) and International Center for Tropical Agriculture (CIAT). NASA Socioeconomic Data and Applications Center (SEDAC), New York, USA. Available at: http://sedac.ciesin.columbia.edu/ data/collection/gpw-v4/sets/browse

Data ref. 9.3. UN World Population Prospects 2019, Online Edition, Rev. 1, Medium fertility variant, 2020–2100. Latest update: 2019. United Nations (UN) Department of Economic and Social Affairs, Population Division. Available at: https://population.un.org/wpp/Download/ Files/1_Indicators%20(Standard)/EXCEL_FILES/1_Population/ WPP2019_POP_F07_1_POPULATION_BY_AGE_BOTH_SEXES. xlsx

Data ref. 9.4. Global health estimates summary tables: projection of deaths by cause, age and sex, by World Bank Income Group. Latest update: 2018. World Health Organization (WHO), Geneva, Switzerland.

Available at: https://www.who.int/healthinfo/global_burden_disease/GHE_ DthWBInc_Proj_2016-2060.xlsx?ua=1

Data ref. 9.5. Global Agro-ecological Zones (GAEZ V3.0), 2012 datset. Latest update: 2012. International Institute for Applied Systems Analysis (IIASA) and Food and Agriculture Organization (FAO) of the United Nations (last accessed 11/11/2016). Available at: http://www.gaez.iiasa.ac.at/

Data ref. 9.6. Global Agro-ecological Zones (GAEZ V3.0), 2000 dataset. Latest update: 2012. International Institute for Applied Systems Analysis (IIASA) and Food and Agriculture Organization (FAO) of the United Nations. Available at: http://www.gaez.iiasa.ac.at/

Data ref. 9.7. FAOSTAT, Crops (2000 data). Latest update: 2020. Food and Agriculture Organization (FAO) of the United Nations. Available at: http://www. fao.org/faostat/en/#data/QC

Data ref. 9.8. Global Health Data Exchange, GBD 2017 Results Tool. Latest update: 2019. Institute for Health Metrics and Evaluation, University of Washington, Seattle, USA. Available at: https://gbd2017.healthdata.org/gbd- search/

Data ref. 9.9. Global Health Data Exchange, GBD Foresight Visualization Hub. Latest update: 2016. Institute for Health Metrics and Evaluation, University of Washington, Seattle, USA. Available at: https://vizhub.healthdata. org/gbd-foresight/

Data ref. 9.10. United Nations, Department of Economic and Social Affairs, Population Division, 2017. World Population Prospects 2017. United Nations (UN) Department of Economic and Social Affairs, Population Division. DVD Edition.

Data ref. 9.11. United Nations, Department of Economic and Social Affairs, Population Division, 2019. World Population Prospects 2019. United Nations (UN), New York, New York. Available at: https://population.un.org/wpp

Acronyms and Abbreviations

α-pinene	terpene emissions
($O(^1D)$)	excited-state oxygen
μ_{abs}	mean absolute model bias
μ_{rel}	% bias
AAE	average accumulated exceedance
AAOD	absorption aerosol optical depth
AATSR	Advanced Along-Track Scanning Radiometer
AC	Arctic Council Member states
ACCES	De-icing of Arctic Coasts: Critical or new opportunities for marine biodiversity and Ecosystem Services (program)
ACCESS	Arctic Climate Change, Economy and Society (EU Project)
ACE-FTIR	Atmospheric Chemistry Experiment FTIR instrument
ACE-FTS	Atmospheric Chemistry Experiment-Fourier Transform Spectrometer
ACLOUD	Arctic Cloud Observations Using Airborne Measurements during Polar Day (study)
ACSM	Aerodyne Aerosol Chemical Speciation Monitor
ACSM	Aerosol Chemical Speciation Monitor
ACTRIS	Aerosol, Clouds and Trace Gases Research Infrastructure
ADHD	attention deficit hyperactivity disorder
ADOM	Acid Deposition and Oxidant Model
AE	Ångström exponent
AERONET	Aerosol Robotic Network / AErosol RObotic NETwork (NASA)
A-FORCE	the Aerosol Radiative Forcing in East Asia
AIRS	Atmospheric Infrared Sounder
AIS	Automatic Identification Systems
Al/Bc	molar-aluminium-to-base-cation ratio
ALPACA	Alaskan Layered Pollution And Chemical Analysis (study)
AMAP	Arctic Monitoring and Assessment Programme (Arctic Council working group)
AMIP	Atmospheric Model Intercomparison Project
AMS	Aerosol Mass Spectrometer (instrument)
ANN	annual mean AOD
AOD	aerosol optical depth
AOT	aerosol optical thickness
AOT40	accumulated ozone exposure over a threshold of 40 ppb
APG	associated petroleum gas
APM	aerosol particle mass analyzer
APRP	approximate partial radiative perturbation
APS	Aerodynamic Particle Sizer (instrument)
ARCPAC	Aerosol, Radiation and Cloud Processes affecting Arctic Climate (project)
ARCTAS	The Arctic Research of the Composition of the Troposphere from Aircraft and Satellites (mission)

ARM	Atmospheric Radiation Measurement
ASTD	Arctic Ship Traffic Data (database)
ATM	atmospheric transport model
ATom	Atmospheric Tomography mission (NASA)
AVHRR	Advanced Very-High Resolution Radiometer
BC	black carbon
Br	bromine
BVOCs	biogenic volatile organic compounds
$C_{10}H_{16}$	monoterpenes
C^{14}	carbon-14
CABM	Canadian Aerosol Baseline Measurement
CALIOP	Cloud-Aerosol Lidar with Orthogonal Polarization
CALIPSO	Cloud-Aerosol Lidar and Infrared Pathfinder Satellite Observation
CAM	Community Atmosphere Model (version 6)
C-AMS	Aerodyne C-Aerosol Mass Spectrometer (instrument)
CanAM5	Canadian Atmospheric Model version 5
CanAM5-PAM	Version of CanAM5 atmospheric global climate model
CanESM2	Canadian Earth System Model, second generation
CAVM	Circumpolar Arctic Vegetation Map
CB	chronic bronchitis
CCI	Climate Change Initiative (ESA)
CCM	climate chemistry model
CCN	cloud condensation nuclei
CDNC	cloud droplet number concentration(s)
CDR	climate data record
CEDS	Community Emissions Data System (global inventory)
CESM (CESM1, CESM2)	Community Earth System Model (and versions)
CEV	cerebrovascular disease
CFA	continuous flow analysis
CFFEPS	Canadian Forest Fire Emission Prediction System
CFM	climate forcing mitigation
CH_4	methane
CI	confidence interval
CI	chemical ionization
CIAT	International Center for Tropical Agriculture
CIESEN	Center for International Earth Science Information Network
CIESM	Community Integrated Earth System Model
CIS	Community Intercomparison Suite
CIW	cloud ice water
CIWP	cloud ice water path

CL	critical load
CLaci	critical load of acidity
CLAP	continuous light absorption photometer
CLARA-A2	Cloud, Albedo and surface Radiation (AVHRR dataset)
CLE	current legislation (emissions scenario)
CLeutN	critical load of nutrient N
CLIMSLIP	Climate Impacts of Short-lived Pollutants and Methane in the Arctic project
CLM	Community Land Model
CLRTAP	Convention on Long-Range Transboundary Air Pollution
CLW	cloud liquid water
CLWP	cloud liquid water path
Cl	chlorine
CM	crustal material
CM SAF	Climate Monitoring Satellite Application Facility (EUMETSAT)
CMAM	Canadian Middle Atmosphere Model
CMB	chemical mass balance
C_{MBC}	mass concentrations of BC
CMDL	Climate Monitoring and Diagnostics Laboratory
CMIP (CMIP5, CMIP6)	Coupled Model Intercomparison Project (CMIP Phase 5, CMIP Phase 6)
CM-SAF	Climate Monitoring-Satellite Application Facility
CNS	central nervous system
CO	carbon monoxide
CO_2	carbon dioxide
CONUS	contiguous United States
COPD	chronic obstructive pulmonary disease
COSMOS	Continuous Soot Monitoring System
COST	European Cooperation in Science and Technology
COVID-19	Coronavirus disease 2019
CP	crop production
CPC	condensation particle counters
CPL	crop-production losses
CPMA	centrifugal particle mass analyzer
CPS	current policy scenario
CRDS	cavity ring-down spectroscopy
CRE	cloud radiative effect
CSA	Canadian Space Agency
CSN	Chemical Speciation Network
CTM	chemical transport model
CTO-375	chemothermal oxidation method (CTO-375)
CTP	cloud top pressure(s)

CVD	cardiovascular disease
DALYs	disability-adjusted life years
DAO	NASA Data Assimilation Office
DCE	Danish Centre for Environment and Energy
DEHM	Danish Eulerian Hemispheric Model
DIAL	differential absorption lidar
DJF	months December, January, February
DMA	differential mobility analyzer
DMPS	differential mobility particle sizer
DMS	dimethyl sulfide
DOAS	differential optical absorption spectroscopy
DOC	dissolved organic carbon
DRI	Desert Research Institute
DU	mineral dust
EBAS	EBAS database of atmospheric measurements (data repository)
eBC	equivalent black carbon
EC	elemental carbon
ECA	emission control area
ECC	Electrochemical Concentration Cell
ECCC	Environment and Climate Change Canada
ECLIPSE	IIASA GAINS emissions inventories (several versions)
ECT9	EnCan-total-900 (thermal method)
EDGAR	Emissions Database for Global Atmospheric Research
EDS	(SEM-) energy dispersive spectroscopy
EFFIS	European Forest Fire Information System
EG	expert groups
EGBCM	Expert Group on Black Carbon and Methane
EMEP	European Monitoring and Evaluation Programme
EMEP MSC-W	EMEP Meterological Synthesising Centre-West (chemistry transport model)
ENVS	Aarhus University Department of Environmental Science
EPPR	Emergency Prevention, Preparedness and Response
ESA	European Space Agency
ESAS	East Siberian Arctic Shelf
ESI	electrospray ionization
ESM	earth system model
ESRL	Earth System Research Laboratory
ETP	Energy Technology Perspectives (project)
EUCAARI	European Integrated Project on Aerosol Cloud Climate and Air Quality Interactions (campaign)
EUMETSAT	European Organisation for the Exploitation of Meteorological Satellites
EUSAAR-2	standard protocol for measuring atmospheric organic and elemental carbon in European networks

EVA	Economic Valuation of Air Pollution (model system)
FAIR	Findable, Accessible, Interoperable, and Reusable (data principles)
FAO	Food and Agriculture Organization of the UN
FEER	Fire Energetics and Emissions Research (NASA)
FINN	Fire INventory (NCAR)
FireMIP	Fire Model Intercomparison Project
FM14C	Fraction modern, the deviation of a sample's ^{14}C atoms from that of the modern standard
FSU	Former Soviet Union
FTIR	Fourier-transform infrared spectroscopy
GAEZ	Global Agro-Ecological Zones dataset
GAINS	Greenhouse gas–Air-pollution Interactions and Synergies Model
GAW	Global Atmosphere Watch (WMO)
GBD	Global Burden of Disease
GC/MS	gas chromatography / mass spectrometry
GEMM	Global Exposure Mortality Model
GEO	Group on Earth Observations
GEOS	Goddard Earth Observing System
GEOTRACES	international study of the marine biogeochemical cycles of trace elements and their isotopes
GFAS	Global Fire Assimilation System
GFED	Global Fire Emission Database
GGFR	Global Gas Flaring Reduction
GGGRN	Global Greenhouse Gas Reference Network (NOAA)
GISS	NASA Goddard Institute of Space Studies
GISS-E2.1	GISS Earth system model (version 2.1)
GLOMAP	Global Model of Aerosol Processes
GMAO	Global Modeling and Assimilation Office (NASA)
GOES	Geostationary Operational Environmental Satellite (network)
GOME	Global Ozone Monitoring Experiment (ESA)
Gt	gigatonne
GWIS	Global Wildfire Information System
H_2O_2	hydrogen peroxide
H_2S	hydrogen sulfide
H_2SO_4	sulfuric acid gas
HEMCO	Harvard–NASA Harmonised Emission Component
HFCs	hydrofluorocarbons
HFO	heavy fuel oil
HIAPER	High-Performance Instrumented Airborne Platform for Environmental Research
HIPPO	HIAPER Pole-to-Pole Observations (campaign)
HLD	high-latitude dust
HNO_3	nitric acid

HO_2	hydroperoxy radical
$HOONO_2$	aqueous peroxynitric acid
HO_X	hydrogen oxide radicals
HPLC	high performance liquid chromatography
HR	hazard ratio
HRMS	high-resolution mass spectrometry
HTAP	Hemispheric Transport of Air Pollutants (UNECE EMEP)
HTDMA	hygroscopicity tandem differential mobility analyzer
IAM	integrated assessment modelling
IASI	Infrared Atmospheric Sounding Interferometer
IASOA	International Arctic Systems for Observing the Atmosphere
IC	ion chromatography
ICCT	International Council on Clean Transportation
ICOS	Integrated Carbon Observation System
ICP-MS	inductively coupled plasma mass spectrometry
iCUPE	Integrative and Comprehensive Understanding on Polar Environments (program)
IEA	International Energy Agency
IER	Integrated Exposure Response (model)
IFS	Integrated Forecast System
IGBP	International Geosphere-Biosphere Program
IHD	ischemic heart disease
IHME	Institute for Health Metrics and Evaluation
IIASA	International Institute for Applied Systems Analysis
IMO	International Maritime Organization of the UN
IMPROVE	Interagency Monitoring of Protected Visual Environments
INAA	instrumental neutron activation analysis
INP	ice-nucleating particle
INTAROS	Integrated Arctic Observing System (project)
IPCC	Intergovernmental Panel on Climate Change
IPCC AR6	IPCC Sixth Assessment Report
IQR	interquartile range
IR	infrared
IRF	instantaneous radiative forcing
IRR	incidence rate ratio
ISCCP-HGM	International Satellite Cloud Climatology Project (H Gridded Monthly)
ISSW	integrating sphere/integrating sandwich spectrometer
ISTE	Health impacts of air pollution tool (Finnish Institute for Health and Welfare)
JJA	June, July, August (summer)
KARL	Koldewey-Aerosol-Raman-Lidar
KF-CuP	Kain-Fritsch-Cumulus Potential

kt	kilotonne (1000 t)
LAM	limited area model
LDAR	leakage detection and repair
LFO	light fuel oil
LII	laser-induced incandescent
LNG	liquified natural gas
LRI	lower respiratory infection
LRTAP	Convention on Long-range Transboundary Air Pollution (the 'Air Convention')
LSPs	light-scattering particles
LULUCF	land use, land-use change and forest emissions
M12	seasonal mean daytime ozone concentration for a 12-hour daytime period
M7	seasonal mean daytime ozone concentration for a 7-hour daytime period
MAAP	multi-angle absorption photometer
MAC	mass absorption cross-section
MACC	Monitoring Atmospheric Composition and Climate
MADs	median absolute deviations
MAE	mean absolute error
MAM	Modal Aerosol Model
MAM	March, April, May
MAN	Maritime Aerosol Network
MASL	meters above sea level
MATCH	Multiscale Atmospheric Transport and Chemistry (model)
M_{BC}	BC mass concentration
MCL	methyl chloride
MEMENTO	MarinE MethanE and NiTrous Oxide (database)
MERRA	Modern-Era Retrospective analysis for Research and Applications
MFR	maximum technically feasible reduction case
Mg	Megagrams (10^6 kt)
MIPAS	Michelson Interferometer for Passive Atmospheric Sounding
MISR	Multi-angle Imaging Spectroradiometer
MLS	Microwave Limb Sounder
Mm	Megameter
MMM	multi-model mean
MODIS	Moderate Resolution Imaging Spectroradiometer
MOPITT	Measurements Of Pollution In The Troposphere
MOSAiC, MOSAIC	Multidisciplinary drifting Observatory for the Study of Arctic Climate (campaign)
MP	Open-Multi-Processing
MPLNET	Micro-Pulse Lidar Network (NOAA)
MRAD	minor restricted activity days
M_{rBC}	total mass concentration of refractory BC

MRI	Meteorological Research Institute
MRI-ESM2	Earth system model (from the MRI of the Japanese Meterological Agency)
MRR	mortality rate ratio
MS	mass spectrometry
MSA	methanesulfonic acid
Mt	Megatonne
N	nitrogen
N	number of data points compared
N_2O	nitrous oxide
N_2O_5	dinitrogen pentoxide
NAPS	National Air Pollution Data Surveillance Program
NAtChem	Canadian National Atmospheric Chemistry (data repository)
NCAR	National Centre for Atmospheric Research
NCD	non-communicable disease
NCEP	National Center for Environmental Prediction
NDACC	Network for the Detection of Atmospheric Composition Change
NDCs	nationally determined contributions of the Paris Climate Agreement
N_{dep}	N depositions
NESAL	northeast Siberian Arctic lowlands
NETCARE	NETwork on Climate and Aerosols: addressing key uncertainties in Remote Canadian Environments
NFC	no further control case
NH_3	ammonia
NH_4	ammonium ions
NHL	non-Hodgkins lymphoma
NH_X	reduced nitrogen
NIOSH-5040	thermo-optical (T-O) technique used to determimine carbon mass on filters (protocol)
nm	nanometers
NMHCs	non-methane hydrocarbons
NMVOCs	non-methane volatile organic compounds
NO_2	nitrogen dioxide
NO_3	nitrate ions
NOAA	United States National Oceanic and Atmospheric Administration
NorESM	Norwegian Earth System Model (global climate model)
NO_X	nitrogen oxides
NO_y	nitrogen oxides, excluding N_2O
NPF	new particle formation
NPP	net primary production
NPS	new policy scenario
NS	not significant
NSAT	near-surface air temperature

O_3	ozone
OA	organic aerosol
OC	organic carbon
ODE	ozone-depletion event
OH	hydroxyl radical
OMA	one-moment aerosol
OMI	Ozone Monitoring Instrument
OPC	optical particle counter
OR	odds ratio
ORCHIDEE	Organizing Carbon and Hydrology in Dynamic EcosystEm (model)
O_X	odd-oxygen (= $O+O_3$)
PAHs	polycyclic aromatic hydrocarbons
PAM	Piecewise lognormal approximation Aerosol Model
PAMARCMiP	Polar Airborne Measurements and Arctic Regional Climate Model Simulation Project
PAME	Protection of the Arctic Marine Environment (Arctic Council working group)
PAN	peroxyacyl nitrates
PATMOS-x	Pathfinder Atmosphere Extended Program (NOAA)
Pb	lead
PFCs	perfluorocarbons
PIXE	particle-induced x-ray emission
PM_1	ultra fine particulate matter
PM_{10}	coarse particulate matter
$PM_{2.5}$	fine particulate matter
PMF	positive matrix factorization
POLARCAT	Polar Study using Aircraft, Remote Sensing, Surface Measurements and Models, of Climate, Chemistry, Aerosols, and Transport (study)
POM	primary organic matter
POPs	persistent organic pollutants
ppb	parts per billion
ppbv	parts per billion by volume
PRR	prevalence rate ratio
PRSQs	Policy Relevant Science Questions
PSAP	particle soot absorption photometer
PSCFs	probability source contribution functions
PTR-MS	Proton Transfer Reaction ToF Mass Spectrometer
QFED	Quick Fire Emissions Dataset
R	correlation coefficient
RAD	restricted activity days
RAL	Rutherford-Appleton Laboratory (Oxford)
rBC	refractory BC
RCP	Representative Concentration Pathway

RH	relative humidity
RHA	respiratory hospital admissions
RMSD	root mean standard error
RNO_3	Alkali nitrates
RR	relative risk
RTP	regional temperature potential
RWC	residential wood combustion
RYL	relative yield losses
S	sulfur
SALSA	Sectional Aerosol module for Large Scale Applications (model)
SCAC	Swedish Climate and Clean Air Research (program)
SDA	spectral de-convolution algorithm
S_{dep}	S depositions
SDGs	Sustainable Development Goals of the UN
SDS	Sustainable Development Scenario
SeaWiFS	Sea-viewing Wide-field-of-view Sensor
SEDAC	NASA Socioeconomic Data and Applications Center
SEM	scanning electron microscopy
SF_6	sulfur hexafluoride
SIA	secondary inorganic aerosols
SIC	sea-ice concentrations
SLCF	short-lived climate forcer
SLCP	short-lived climate pollutant
SMB	simple mass balance model
SMPS	scanning mobility particle sizer
SO_2	sulfur dioxide
SO_4	sulphate
SOA	secondary organic aerosol
SOA	secondary organic aerosols
SOMO35	sum of ozone means over 35 ppb
SON	months September, October, November
SP2	single particle soot photometer
SS	sea salt
SSA	single scattering albedo
SSPs	Shared Socioeconomic Pathways
SST	sea surface temperature
StD	standard deviation
STEAM3	Ship Traffic Emission Assessment Model
SWAMPS-GLWD	Sustainable Wetlands Adaptation and Mitigation Program – Global Lakes and Wetlands
TCCON	Total Carbon Column Observing Network

TEM	transmission electron microscopy
TES	Tropospheric Emission Spectrometer
Tg	Teragrams (1000 kt)
THL	Finnish Institute for Health and Welfare
TM5-FASST	TM5-Fast Scenario Screening Tool (source-receptor model)
TOA	top of the atmosphere
TOAR	Tropospheric Ozone Assessment Report (database)
TOT	thermal-optical transmittance (EC-OC technique)
TROPOMI	TROPOspheric Monitoring Instrument
TSP	total suspended particles
UKCA	United Kingdom Chemistry and Aerosol scheme
UKESM1	UK Earth System Modelling project (earth system model)
UN	United Nations
UNECE	United Nations Economic Commission for Europe
UNFCCC	United Nations Framework Convention on Climate Change
US EPA	United States Environmental Protection Agency
UT	upper troposphere
UV	ultraviolet
VBS	volatility basis set
VIIRS	Visible Infrared Imaging Radiometer Suite
VMR	volume mixing ratio
VOCs	volatile organic compounds
VPDB	Vienna Peedee belemnite
WAD2M	Wetland Area Dynamics for Methane Modeling (dataset)
WB	World Bank
WDCA	World Data Center for Aerosols (WMO)
WDCGG	World Data Centre for Greenhouse Gases (WMO)
WHO	World Health Organization
WLD	work loss days
WMO	World Meteorological Organization
WRF-Chem	Weather Research and Forecasting model with online coupled chemistry
XRD	x-ray diffraction

Arctic Monitoring and Assessment Programme

The Arctic Monitoring and Assessment Programme (AMAP) was established in June 1991 by the eight Arctic countries (Canada, Denmark, Finland, Iceland, Norway, Russia, Sweden and the United States) to implement parts of the Arctic Environmental Protection Strategy (AEPS). AMAP is now one of six working groups of the Arctic Council, members of which include the eight Arctic countries, the six Arctic Council Permanent Participants (Indigenous Peoples' organizations), together with observing countries and organizations.

AMAP's objective is to provide 'reliable and sufficient information on the status of, and threats to, the Arctic environment, and to provide scientific advice on actions to be taken in order to support Arctic governments in their efforts to take remedial and preventive actions to reduce adverse effects of contaminants and climate change'.

AMAP produces, at regular intervals, assessment reports that address a range of Arctic pollution and climate change issues, including effects on health of Arctic human populations. These are presented to Arctic Council Ministers in 'State of the Arctic Environment' reports that form a basis for necessary steps to be taken to protect the Arctic and its inhabitants.

This report has been subject to a formal and comprehensive peer review process. The results and any views expressed in this series are the responsibility of those scientists and experts engaged in the preparation of the reports.

The AMAP Secretariat is located in Tromsø, Norway. For further information regarding AMAP or ordering of reports, please contact the AMAP Secretariat (The Fram Centre, P.O. Box 6606 Stakkevollan, N-9296 Tromsø, Norway) or visit the AMAP website at www.amap.no.

AMAP Secretariat

The Fram Centre,
P.O. Box 6606 Stakkevollan,
N-9296 Tromsø, Norway

T +47 21 08 04 80
F +47 21 08 04 85

www.amap.no

ISBN – 978-82-7971-202-2

ARCTIC COUNCIL

AMAP
Arctic Monitoring and Assessment Programme